NIST SPECIAL PUBLICATION 756

U.S. DEPARTMENT OF COMMERCE/National Institute of Standards and Technology

Laser Induced Damage in Optical Materials: 1987

ASTM

STP 1038

The National Institute of Standards and Technology[1] was established by an act of Congress on March 3, 1901. The Institute's overall goal is to strengthen and advance the Nation's science and technology and facilitate their effective application for public benefit. To this end, the Institute conducts research to assure international competitiveness and leadership of U.S. industry, science and technology. NIST work involves development and transfer of measurements, standards and related science and technology, in support of continually improving U.S. productivity, product quality and reliability, innovation and underlying science and engineering. The Institute's technical work is performed by the National Measurement Laboratory, the National Engineering Laboratory, the National Computer Systems Laboratory, and the Institute for Materials Science and Engineering.

The National Measurement Laboratory

Provides the national system of physical and chemical measurement; coordinates the system with measurement systems of other nations and furnishes essential services leading to accurate and uniform physical and chemical measurement throughout the Nation's scientific community, industry, and commerce; provides advisory and research services to other Government agencies; conducts physical and chemical research; develops, produces, and distributes Standard Reference Materials; provides calibration services; and manages the National Standard Reference Data System. The Laboratory consists of the following centers:

- Basic Standards[2]
- Radiation Research
- Chemical Physics
- Analytical Chemistry

The National Engineering Laboratory

Provides technology and technical services to the public and private sectors to address national needs and to solve national problems; conducts research in engineering and applied science in support of these efforts; builds and maintains competence in the necessary disciplines required to carry out this research and technical service; develops engineering data and measurement capabilities; provides engineering measurement traceability services; develops test methods and proposes engineering standards and code changes; develops and proposes new engineering practices; and develops and improves mechanisms to transfer results of its research to the ultimate user. The Laboratory consists of the following centers:

- Computing and Applied Mathematics
- Electronics and Electrical Engineering[2]
- Manufacturing Engineering
- Building Technology
- Fire Research
- Chemical Engineering[3]

The National Computer Systems Laboratory

Conducts research and provides scientific and technical services to aid Federal agencies in the selection, acquisition, application, and use of computer technology to improve effectiveness and economy in Government operations in accordance with Public Law 89-306 (40 U.S.C. 759), relevant Executive Orders, and other directives; carries out this mission by managing the Federal Information Processing Standards Program, developing Federal ADP standards guidelines, and managing Federal participation in ADP voluntary standardization activities; provides scientific and technological advisory services and assistance to Federal agencies; and provides the technical foundation for computer-related policies of the Federal Government. The Laboratory consists of the following divisions:

- Information Systems Engineering
- Systems and Software Technology
- Computer Security
- Systems and Network Architecture
- Advanced Systems

The Institute for Materials Science and Engineering

Conducts research and provides measurements, data, standards, reference materials, quantitative understanding and other technical information fundamental to the processing, structure, properties and performance of materials; addresses the scientific basis for new advanced materials technologies; plans research around cross-cutting scientific themes such as nondestructive evaluation and phase diagram development; oversees Institute-wide technical programs in nuclear reactor radiation research and nondestructive evaluation; and broadly disseminates generic technical information resulting from its programs. The Institute consists of the following divisions:

- Ceramics
- Fracture and Deformation[3]
- Polymers
- Metallurgy
- Reactor Radiation

[1]Headquarters and Laboratories at Gaithersburg, MD, unless otherwise noted; mailing address Gaithersburg, MD 20899.
[2]Some divisions within the center are located at Boulder, CO 80303.
[3] Located at Boulder, CO, with some elements at Gaithersburg, MD.

Laser Induced Damage in Optical Materials: 1987

Proceedings of a Symposium sponsored by:

National Institute of Standards and Technology
(formerly National Bureau of Standards)
American Society for Testing and Materials
Office of Naval Research
Department of Energy
Defense Advanced Research Project Agency
Air Force Office of Scientific Research

October 26-28, 1987

NIST (formerly NBS), Boulder, Colorado 80303

Edited by:

Harold E. Bennett
Naval Weapons Center
China Lake, California 93555

Arthur H. Guenther
Air Force Weapons Laboratory
Kirtland Air Force Base, New Mexico 87117

David Milam
Lawrence Livermore National Laboratory
Livermore, California 94550

Brian E. Newnam
Los Alamos National Laboratory
Los Alamos, New Mexico 87545

M.J. Soileau
University of Central Florida
Orlando, Florida 32816

NOTE: As of 23 August 1988, the National Bureau of Standards (NBS) became the National Institute of Standards and Technology (NIST) when President Reagan signed into law the Omnibus Trade and Competitiveness Act.

BOULDER DAMAGE SYMPOSIUM

U.S. DEPARTMENT OF COMMERCE, C. William Verity, Secretary

NATIONAL INSTITUTE OF STANDARDS AND TECHNOLOGY, Ernest Ambler, Director
(formerly National Bureau of Standards)

Issued October 1988

Library of Congress Catalog Card Number: 88-600576

National Institute of Standards and Technology
Special Publication 756, 650 pages (Oct. 1988)
CODEN: XNBSAV

U.S. GOVERNMENT PRINTING OFFICE
WASHINGTON: 1988

For sale by the Superintendent of Documents, U.S. Government Printing Office, Washington, DC 20402-9325

Foreword

The Proceedings contain the papers presented at the Nineteenth Symposium on Optical Materials for High-Power Lasers held at the National Institute of Standards and Technology in Boulder, Colorado, on October 26-28, 1987. The Symposium was jointly sponsored by the National Institute of Standards and Technology, the American Society for Testing and Materials, the Office of Naval Research, the Defense Advanced Research Projects Agency, the Department of Energy, and the Air Force Office of Scientific Research. The Symposium was attended by over 190 scientists from the United States, Canada, the United Kingdom, India, Japan, France, Taiwan, and the Federal Republic of Germany. It was divided into sessions devoted to the following topics: Materials and Measurements, Mirrors and Surfaces, Thin Films, and, finally, Fundamental Mechanisms. The Symposium Co-Chairmen were Dr. Harold E. Bennett of the Naval Weapons Center, Dr. Arthur H. Guenther of the Air Force Weapons Laboratory, Dr. David Milam of the Lawrence Livermore National Laboratory, Dr. Brian E. Newnam of the Los Alamos National Laboratory, and Dr. M. J. Soileau of the University of Central Florida. They also served as editors of this report.

The editors assume full responsibility for the summary, conclusions, and recommendations contained in the report, and for the summaries of discussion found at the end of each paper. The manuscripts of the papers presented at the Symposium have been prepared by the designated authors, and questions pertaining to their content should be addressed to those authors. The interested reader is referred to the bibliography at the end of the summary article for general references to the literature of laser damage studies. The Twentieth Annual Symposium on this topic will be held in Boulder, Colorado, October 26-28, 1988. A concerted effort will be made to ensure closer liaison between the practitioners of high peak power and the high average power community.

The principal topics to be considered as contributed papers in 1988 do not differ drastically from those enumerated above. We expect to hear more about improved scaling relations as a function of pulse duration, area, and wavelength, and to see a continuing transfer of information from research activities to industrial practice. New sources at shorter wavelengths continue to be developed, and a corresponding shift in emphasis to short wavelength and repetitively pulsed damage problems is anticipated. Fabrication and test procedures will continue to be developed, particularly in the diamond turned optics and thin film areas. It is our intention to pause and reflect on progress over the past twenty years of the Symposium on Optical Materials for High Power Lasers. It will be our pleasure to present a comprehensive array of tutorial lectures by distinguished workers in the field of laser induced damage in optical materials.

The purpose of these symposia is to exchange information about optical materials for high-power lasers. The editors will welcome comment and criticism from all interested readers relevant to this purpose, and particularly relative to our plans for our Gala Twentieth Annual Symposium.

H.E. Bennett, A.H. Guenther
D. Milam, B.E. Newnam, and M.J. Soileau
Co-Chairmen

Disclaimer

Certain papers contributed to this publication have been prepared by non-NIST authors. These papers have not been reviewed or edited by NIST; therefore, the National Institute of Standards and Technology accepts no responsibility for their accuracy, nor for their comments or recommendations.

Certain commercial equipment, instruments, and materials are identified in this publication in order to explain the experimental procedure adequately. Such identification in no way implies approval, recommendation, or endorsement by the National Institute of Standards and Technology, nor does it imply that the equipment, instruments, or materials identified are necessarily the best available for the purpose.

CONTENTS

Surfaces and Mirrors

Thin Films

Fundamental Mechanisms

OPENING COMMENTS - 19TH ANNUAL DAMAGE SYMPOSIUM

D. Milam
Lawrence Livermore National Laboratory
University of California
P.O. Box 5508, L-490
Livermore, California 94550

The chairmen of the 1987 Boulder Damage Conference wish first to acknowledge continued support by the National Institute of Standards and Technology. Access to NIST facilities and contributions by individuals in that organization have provided a stable and comfortable environment during this series of 19 conferences. For the 1987 meeting, we had the assistance of Bob Kamper, Director, NIST Boulder, of Aaron Sanders, Leader of the Optical Electronic Metrology Group, and of an administrative staff: Susie Rivera, Edit Haakinson, and Ann Mannos. Major contributions to the organization and operation of the conference were again made by Pat Whited of the Air Force Weapons Laboratory.

This year we will have 73 papers presented by authors from 15 countries. As in previous years, the majority of the authors are affiliated with either a university or a commercial organization, while the remainder are affiliated with a national laboratory.

As has become typical, the topic most often discussed will be damage in thin films. This effort has consumed 30 to 55 percent of our effort in each year since 1977. Including the papers at this conference, we have heard 265 reports of studies related to some aspect of the production of damage resistant films. Sixteen different processes for making films have been investigated. Conservatively estimated, execution of this work required at least 100 man years. Since many participated without sharing authorship, the total effort expended was probably much greater than the conservative estimate.

Progress is apparent. Films made by several processes are better than they were 20 years ago, and our industrial facilities can now coat substrate with diameter exceeding 1 m. Films with higher density, lower stress, and lower scatter have been produced by several ion-assisted technologies. Solution-deposited silica antireflection coatings have excellent damage resistance. We have learned much about making coatings for both ultraviolet and infrared applications. Other examples of progress could be cited.

However, with few exceptions, progress has been incremental and many questions remain unanswered. The fundamental mechanism for damage in films is still a subject of debate. Large coaters do not produce films with quality equal to those that have been made in smaller research machines. And, after having studied 15 competing processes, we still rely heavily on a technique that was available 20 years ago, electron-beam evaporation.

Considering the magnitude of our past effort and the number of unresolved issues, it is possible without being overly cynical to question whether these issues can be resolved by a larger but similar effort. Note that I do not question whether progress is possible; past effort did produce a few exceptional optical coatings with thresholds 2-5 times larger than thresholds of commercially available films. We have not reached a fundamental limit.

It is more difficult to suggest what else should be done than it is to cite unresolved issues. Without pretending to know the specific steps that should be taken, I would comment on two general topics. The first is my growing concern that we have not established an adequate flow of real information from research into production. The hypothesis underlying much of our research is that information obtained through the relatively inexpensive study of small samples made in small research machines can be transferred to improve large coatings made in production machines. However, large coatings do not have thresholds as large as those frequently reported in studies of small samples. When sliced into the black and white version, this implies either that research concepts have been evaluated by production groups and found to be ineffective, or that research concepts have not been evaluated. If the former is true, is it because the research data are wrong, or do fundamental differences in large and small coaters prevent transfer of information? If the results are not being evaluated, is this caused simply by the press of production schedules and the large cost of doing research in large machines? Some rather blunt comment by our production community, which could be made without divulging the detailed proprietary aspects of coating production, would be of great value.

The second general concern is the now elderly problem of identifying the defects responsible for coating damage. Work done between 1972 and 1974 indicated that damage to coatings is initiated in very small volumes. The few exceptions are instances where spatially averaged absorption is important -- in coatings used in the far UV or far IR or those used in lasers operating at high average power. Much effort has been spent in the study of these defects, but their basic nature remains a mystery. My belief is that nonstoichiometric subvolumes are the defects which most often determine the damage resistance. However, I reach this conclusion through a rather circuitous argument and cannot prove that it is correct. Other candidates are impurities from the substrate itself, from compounds used in polishing or cleaning of the substrate, or from the coating chamber, or film imperfections such as pinholes, grain boundaries, or local areas of poor adhesion. Lacking identification of the limiting defect, we are left with the two general routes we have so far followed -- the somewhat random search for a coating process that makes perfect films, or the somewhat random tuning of existing coating processes. Since our search pattern would be narrowed by that ability to remove even some of the contenders from the list, identification of limiting defects is the most important issue before us.

Laser Induced Damage in Optical Materials

Nineteenth ASTM Symposium
October 26-28, 1987

The Nineteenth Annual Symposium on Optical Materials for High-Power Lasers (Boulder Damage Symposium) was held at the National Institute of Standards and Technology in Boulder, Colorado, October 26-28, 1987. The Symposium was held under the auspices of ASTM Committee F-1, Subcommittee on Laser Standards, with the joint sponsorship of NIST, the Defense Advances Research Project Agency, the Department of Energy, the Office of Naval Research, and the Air Force Office of Scientific Research. Over 190 scientists attended the Symposium, including representatives of the United Kingdom, France, Japan, India, Canada, and the Federal Republic of Germany. The Symposium was divided into sessions concerning Materials and Measurements, Mirrors and Surfaces, Thin Films, and, finally, Fundamental Mechanisms. As in previous years, the emphasis of the papers presented at the Symposium was directed toward new frontiers and new developments. Particular emphasis was given to materials for high power apparatus. The wavelength range of the prime interest was from 10.6 μm to the uv region. Highlights included surface characterization, thin film substrate boundaries, and advances in fundamental laser-matter threshold interactions and mechanisms. The scaling of damage thresholds with pulse duration, focal area, and wavelength was discussed in detail. Harold E. Bennett of the Naval Weapons Center, Arthur H. Guenther of the Air Force Weapons Laboratory, David Milam of the Lawrence Livermore National Laboratory, Brian E. Newnam of the Los Alamos National Laboratory, and M.J. Soileau of the University of Central Florida were co-chairmen of the Symposium. The Twentieth Annual Symposium is scheduled for October 26-28, 1988, at the National Institute of Standards and Technology, Boulder, Colorado.

Key words: laser damage; laser interaction; optical components; optical fabrication; optical materials and properties; thin film coatings.

1. Introduction

The Nineteenth Annual Symposium on Optical Materials for High-Power Lasers (Boulder Damage Symposium) was held, as in previous years, at the National Institute of Standards and Technology in Boulder, Colorado, October 26-28, 1987. The Symposium was held under the auspices of the ASTM Committee F-1, Subcommittee on Laser Standards, with the joint sponsorship of NIST, the Defense Advanced Research Projects Agency, the Department of Energy, the Office of Naval Research, and the Air Force Office of Scientific Research. Approximately 190 scientists attended the Symposium, including representatives of the United Kingdom, France, Japan, India, Canada, and the Federal Republic of Germany. The Symposium was divided into sessions concerning Materials and Measurements, Mirrors and Surfaces, Thin Films, and, finally, Fundamental Mechanisms. In all, approximately 80 technical presentations were made. Harold E. Bennett of the Naval Weapons Center, Arthur H. Guenther of the Air Force Weapons Laboratory, David Milam of the Lawrence Livermore National Laboratory, Brian E. Newnam of the Los Alamos National Laboratory, and M. J. Soileau of the University of Central Florida were co-chairmen of the Symposium. Alexander J. Glass of Hillcrest Associates is Conference Treasurer and Aaron A. Sanders of the National Institute of Standards and Technology acts as Conference Coordinator.

The purpose of these symposia is to exchange information about optical materials for high power lasers. The authors welcome comments and criticism from all interested readers relevant to this purpose and particularly relative to our plans for the Twentieth Annual Symposium, scheduled for October 26-28, 1988, at the National Institute of Standards and Technology, Boulder, Colorado.

2. Overview

Our objective in this section is to give the reader a sense of the emphasis and general concerns of this year's symposium. Although we do not review all of the excellent work presented, some of the highlights are touched upon briefly.

Measurements and Materials

Several of the 21 papers in this session described new or improved testing facilities. In terms of shear volume, the most notable success was the testing, in a production environment, of large (30 kg) samples of Nd-doped phosphate glass. Microscopic platinum inclusions produced visibly detectable damage when the sample was raster scanned across a beam emitted by a standard 10 ns, 20 Hz Nd:YAG laser. A second new apparatus allowed testing with 16 ns, 1064 nm pulses at pulse repetition rates not previously available, 60-120Hz.

An elaborate scheme for detecting damage permitted observation, with 75 ps resolution, of the evolution of bulk damage. A picosecond pulse, with variable time delay, was used to probe and photograph damage induced by a second pulse. Automated detection of damage through recording of laser-induced plasma or detection of light forward scattered from the damaging pulse was also discussed.

The passive identification of defects that would cause damage was the subject of two experimental papers. Both found that damage-prone defects strongly scattered light at the test wavelength. A postmortem diagnostic x-ray topography was successful in locating damage more subtle than that detectable by optical microscopy.

Among studies of damage in laser materials, the most controversial was a discussion of bulk damage tests with 100 ps, 532 nm pulses in KBr. Analysis of recombination radiation indicated damage was caused by four-photon absorption, not avalanche breakdown. Another paper reported that damage thresholds in plastics scaled inversely with spot size.

Several improvements in optical materials were also reported. Phosphate laser glass free of platinum inclusions has been produced by two corporations. This progress was attributed to the high solubility of platinum in molten phosphate glass. Crystals of KDP with increased damage resistance were produced by eliminating microbes from

growth solutions by ultraviolet irradiation. Two papers indicated that both transient and residual coloring of silica under ionizing radiation could be minimized through use of highly purified silica.

Two relatively new materials were introduced, KCl doped with ReO_4^- as a potential modulator material for the 10.6 μm wavelength and carbon composites as substrates for large lightweight mirrors.

Laser-induced damage in silicon avalanche photodiodes and a characterization of a CCD array camera were also presented.

Surfaces and Mirrors

The principal topics treated in the 16 papers in this session were devoted to fabrication and characterization of surfaces, studies of the physical mechanisms of damage, and optical components for RF-linac free electron lasers.

A major accomplishment in surface preparation i.e. the ion milling of silica surfaces to depths of 10 μm without causing serious degradation in surface finish or damage resistance, may allow surface figuring through this process. A second group described the fabrication, through polishing of a SiC layer deposited on graphite, of mirrors for the ArF excimer laser. It was also reported that subsurface damage on polished substrates of molybdenum or tungsten could be largely eliminated by float polishing these substrates with SiO_2 abrasives.

The possibility of automated surface characterization was addressed in a paper which described the incorporation of dark-field microscopy with a raster scanned, automated device. Presently the pixel size is 50 μm. A comparison of three other surface diagnostics, surface second harmonic generation, LEED and AES, was made by employing them to monitor initial cluster formation during deposition of Ag films on Cu substrates. The diagnostics produced similar results.

Four papers described experimental studies of matter ejected from surfaces under laser irradiation. Although this work has so far produced few firm conclusions regarding the physics of damage, it was apparent from the range of topics addressed that desorption may become a primary tool for surface studies.

Several authors reported damage thresholds for optical components subjected to irradiation by the 1-100 μsec trains of short-duration pulses emitted by a RF-linac free electron laser. Coatings of $ZnSe/ThF_4$ on ZnS substrates failed at time-averaged intensities of 500-700 kW/cm^2 in an FEL operated at a wavelength of 8-12 μm. Gold surfaces in an FEL operating at 3.2 μm survived at 1 MW/cm^2, but failed when the operating wavelength was changed to 2.7 μm. A damage test facility with a source that mimics the FEL pulse format has been constructed. Initial results indicate that some dielectric coatings survive at up to 500 MW/cm^2 averaged over the total pulse train.

Other papers discussing more conventional damage tests contained some rather significant results. Thresholds measured with 16 ns, 1064 nm pulses incident at rates of 6-120 Hz were independent of pulse repetition rates. Dielectric surfaces withstood irradiation at 5-10 times the fluence required to damage metal surfaces. Both observations indicate that single-pulse fluence is the limiting parameter under these conditions. In a study relevant to laser-pumped dye lasers, it was found that silica surfaces covered by cyclohexane failed at $0.8 J/cm^2$ under irradiation by 10 ns, 308 nm pulses, whereas surfaces covered by dioxane survived at 2-4 J/cm^2, the level at which damage occurred for silica substrates in air.

Thin Films

As in previous years, the session on thin films attracted the largest participation, indicating the continuing interest in development of improved coatings. While progress was apparent, no major advances were reported. An illustration of the incremental progress evident was from an experiment which demonstrated that the use of 248 nm UV light to clean substrate surfaces led to a 50% improvement in damage thresholds of 355 nm AR coatings deposited on substrates, so cleaned.

The search for a deposition technique that produces films with fewer defects continues unabated. The possibility of depositing films from ionized clusters of atoms was treated in two papers, one that discussed techniques for producing clusters through condensation and one reporting that ionized cluster deposition of BaF_2, produced films with good resistance to damage at both 1.06 and 10.6 μm. Oxide films made by metal-organic chemical vapor deposition had large refractive indices, but only moderate damage thresholds. Diamond films can now be produced, but they consist of isolated small crystals and are presently not sufficiently smooth to serve as optical films.

Use of ions during deposition, either as an assist or directly through ion plating was the subject of several papers. In general, films made through these processes have increased refractive index, reduced absorption and, in some instances, improved thresholds. A primary claim was that ion assist allowed deposition of improved films of substrates held at temperatures below 150°C.

Rugate films were treated in a tutorial paper, and fabrication through laser-flash deposition of a 15-cycle SiO_2 - Si_3N_4 rugate filter described. Controlling film thickness with 3 Å resolution and index to within 1%, produced a film with nearly theoretical reflectance at the rejection band and only a 10-nm error in band position.

There were two reports of deposition of HR coatings from colloidal suspensions. In both instances, this technique produced single-layer oxide films with excellent damage resistance, but HR coatings of Al_2O_3 had lower thresholds comparable to those of the high quality e-beam deposited films.

The companion to deposition is proper characterization of films. The conference heard several papers on ellipsometry, measurement of absorption and thermal diffusivity. Two were particularly novel. Absorption in the dielectric spacing layer of an intracavity etalon was measured by recording the temperature-induced shift of the passband frequency. Both visible and XUV 58(nm) ellipsometry were successfully used to measure formation of monolayers of oxide on metal films.

Several papers addressed the physics of thin film damage. Three of these were studies of matter ejected from coatings during laser irradiation. The result most firmly established was emission of Fe from Si_2O_3/SiO_2 coatings during the initial irradiations of a test site. In other experiments aimed at ranking metallic coatings in small-spot 10.6 μm tests, ranking was independent of three criteria, surface distortion, physical damage to coatings, and substrate damage. The Ramans spectra of films under static loading, a model which calculated net scattering due to contributions from film interfaces, and the effects produced by CO_2 laser annealing of films were also discussed.

Several sets of damage thresholds measured with recently constructed facilities were reported. The IR materials ZnSe, Ge, CdTe and CdS were tested with 10-100 μsec, 10.6 μm pulses; some samples survived thousands of tests at fluences above 10 J/cm^2 at the other end of the spectrum a visible wavelength source of 50 ns pulses at repetition rates to 30 kHz was used to test optical coatings. The principal result was that large visible defects caused initiation of damage which quickly spread over the irradiated area. In initial tests using 36,000 irradiations by 1064 nm, 16 ns pulses at rates from 6-120 Hz, median coating thresholds ranged from 8-18 J/cm^2 and highest measured thresholds were in excess of 30 J/cm^2. In contrast, metals damaged at 1-4 J/cm^2. Thresholds were the same for either 6 or 120 Hz. Thresholds of components for use at 248 nm were tested at that wavelength with both 11 ns and 36 ns pulses. The mean power law scaling exponent was 0.3. A final paper indicated that desorption of water might be responsible for the increase in threshold sometimes observed in multiple shot testing.

Fundamental Mechanisms

A total of eight papers were submitted in the Fundamental Mechanisms session. Topics covered included the role of thermal shock in continuous wave laser damage, thermal modeling of pulsed laser damage, the role of multiple photon absorption in short wavelength pulsed laser damage, laser-induced particle emission and fundamental mechanism of laser damage to polymers. The thermal model presented for CW laser damage incorporated the elastic properties of materials with their thermal response to predict laser damage (such as slip) prior to melting.

The particle emission study was done in a clean ultra-high vacuum system using pulsed and cw 1.06 micron lasers. The authors found that desorbed water and carbon

could be detected for both cw pulsed irradiations prior to damage, consistent with laser conditioning observed by others. The authors concluded that a reasonable explanation for the observed desorption is vibrational excitation of the molecule-surface atom oscillator system.

The ever controversial subject of intrinsic damage reclaimed renewed attention in three papers dealing with bulk damage in wide-gap materials. One paper interpreted the lack of a strong temperature dependence in 532 nm, picosecond pulsed damage in NaCl and KBr to be evidence for intrinsic 4-photon induced damage. A second paper dealt exclusively with reports measured of intrinsic damage in KBr at 532 nm. The author claimed that damage is due to 4-photon absorption without avalanche formation. They infer a temperature rise of the sample up to melting by monitoring σ-luminescence from self-trapped excitons. The paper was lively debated at its conclusion. Among the questions raised was the calibration of the σ-luminescence yield with temperature (done for T=50 to 75°K) and the extrapolation of this calibration to the melting point of the samples (1007° K). A third paper focused upon the evolution of the present understanding of the complex nonlinear phenomenon associated with bulk damage as well as questions regarding the "intrinsic vs. extrinsic" nature of damage. These primary conclusions were a) that earlier claims of intrinsic damage due to avalanche breakdown are incorrect b) that for $M \leq 4$ damage is dominated by multiphoton absorption whereas for $M \geq 5$ avalanche breakdown dominates and c) that intrinsic multiphoton dominated damage has been observed in NaCl and KBr at 532 nm. The lively debate that followed these papers can be taken as evidence that the subject of intrinsic damage remains controversial.

The paper on damage to optical polymers established that factors of 10 to 100 improvements in multi-shot damage thresholds were possible by adding selective additioners to the polymers. The observed increases were attributed to vibrational energy transfer from polymer macromolecules to additive molecules which suppress the laser created radicals. The authors proposed methods of creating new polymers with damage thresholds comparable to silicate glasses and crystals, as previously reported by Soviet workers.

3. Acknowledgments

The editors would like to acknowledge the invaluable assistance of Mr. Aaron A. Sanders and the other involved staff members of the National Institute of Standards and Technology in Boulder, Colorado, for their interest, support, and untiring efforts in the professional operation of the symposium. Particular thanks to Ms. Susie Rivera for her lead in the preparation and publication of the proceedings as well as Ms. Edit Haakinson, and to Ms. Pat Whited of the Air Force Weapons Laboratory and Ms. Ann Mannos for conference coordination.

4. References

[1] Glass, A.J.; Guenther, A.H., eds. Damage in Laser Glass, ASTM Spec. Tech. Pub;. 469, ASTM, Philadelphia. PA; 1969.

[2] Glass, A.J.; Guenther, A.H., eds. Damage in Laser Materials, Nat. Bur. Stand. (U.S.) Spec. Publ. 341; 1970.

[3] Bloembergen, N. Fundamentals of Damage in Laser Glass, National Materials Advisory Board Publ. NMAB-271, National Academy of Sciences; 1970.

[4] Glass, A.J.; Guenther, A.H., eds. Damage in Laser Materials: 1971, Nat. Bur. Stand. (U.S.) Spec. Publ. 356; 1971.

[5] Bloembergen, N. High Power Infrared Laser Windows. National Materials Advisory Board Publ. NMAB-356; 1971.

[6] Glass, A.J.; Guenther, A.H., eds. Laser Induced Damage in Optical Materials: 1972, Nat. Bur. Stand. (U.S.) Spec. Publ. 372; 1972.

[7] Glass, A.J.; Guenther, A.H., eds. Laser Induced Damage in Optical Materials: 1973, Nat. Bur. Stand. (U.S.) Spec. Publ. 387; 1973.

[8] Glass, A.J.; Guenther, A. H. Laser Induced Damage in Optical Materials: A Conference Report. Appl. Opt. 13 (1): 74-88; 1974.

[9] Glass, A.J.; Guenther, A.H., eds. Laser Induced Damage in Optical Materials: 1974, Nat. Bur. Stand. (U.S.) Spec. Publ. 414; 1974.

[10] Glass, A.J.; Guenther, A.H. Laser Induced Damage in Optical Materials: 6th ASTM Symposium. Appl. Opt. 14 (3): 698-715; 1975.

[11] Glass, A.J.; Guenther, A.H., eds. Laser Induced Damage in Optical Materials: 1975, Nat. Bur. Stand. (U.S.) Spec. PUbl. 435; 1975.

[12] Glass, A.J.; Guenther, A.H. Laser Induced Damage in Optical Materials: 7th ASTM Symposium. Appl. Opt. 15 (6): 1510-1529; 1976.

[13] Glass, A.J.; Guenther, A.H., eds. Laser Induced Damage in Optical Materials: 1976. Nat. Bur. Stand. (U.S.) Spec. Publ. 462; 1976.

[14] Glass, A.J.; Guenther, A.H. Laser Induced Damage in Optical Materials: 8th ASTM Symposium, Appl. Opt. 16 (5): 1214-1231; 1977.

[15] Glass, A.J.; Guenther, A.H., eds. Laser Induced Damage in Optical materials: 1977, Nat. Bur. Stand. (U.S.) Spec. Publ. 509; 1977.

[16] Glass. A.J.; Guenther, A.H. Laser Induced Damage in Optical Materials: 9th ASTM Symposium, Appl. Opt. 17 (15): 2386-2411; 1978.

[17] Glass, A.J.; Guenther, A.H. Laser Induced Damage in Optical Materials: 1978, Nat. Bur. Stand. (U.S.) Spec. Publ. 541; 1978.

[18] Glass, A.J.; Guenther, A.H., eds. Laser Induced Damage in Optical Materials: 10th ASTM Symposium, Appl. Opt. 18 (13): 2212-2229; 1979.

[19] Bennett, H.E.; Glass, A.J.; Guenther, A.H.; Newnam, B.E. Laser Induced Damage in Optical Materials: 1979, Nat. Bur. Stand. (U.S.) Spec. Publ. 568; 1979.

[20] Bennett, H.E.; Glass, A.J.; Guenther, A.H.; Newnam, B.E. Laser Induced Damage in Optical Materials: 11th ASTM Symposium, Appl. Opt. 19 (14): 23375-2397; 1980.

[21] Bennett, H. E.; Glass. A.J.; Guenther, A. H.; Newnam, B.E. Laser Induced Damage in Optical Materials: 1980, Nat. Bur. Stand. (U.S.) Spec. Publ. 620; 1981.

[22] Bennett, H.E.; Glass, A.J.; Guenther, A.H.; Newnam, B.E. Laser Induced Damage in Optical Materials: 12th ASTM Symposium, Appl. Opt. 20 (17): 3003-3019; 1981.

[23] Bennett, H.E.; Guenther, A.H.; Milam, D.; Newnam, B.E. Laser Induced Damage in Optical Materials: 1981, Nat. Bur. Stand. (U.S.) Spec. Publ. 638; 1983.

[24] Bennett, H.E.; Guenther, A.H.; Milam, D.; Newnam, B.E. Laser Induced Damage in Optical Materials: 13th ASTM Symposium, Appl. Opt. 22 (20): 3276-3296; 1983.

[25] Bennett, H.E.; Guenther, A.H.; Milam, D.; Newnam, B.E. Laser Induced Damage in Optical Materials: 1982, Nat. Bur. Stand. (U.S.) Spec. Publ. 669; 1984.

[26] Bennett, H.E.; Guenther, A.H.; Milam, D.; Newnam, B.E. Laser Induced Damage in Optical Materials: 14th ASTM Symposium, Appl. Opt. 23 (21): 3782-3795; 1984.

[27] Bennett, H.E.; Guenther, A.H.; Milam, D.; Newnam, B.E. Laser Induced Damage in Optical Materials: 1983, Nat. Bur. Stand. (U.S.) Spec. Publ. 688; 1985.

[28] Bennett, H.E.; Guenther, A.H.; Milam, D.; Newnam, B.E. Laser Induced Damage in Optical Materials: 15th ASTM Symposium, Appl. Opt. 25 (2): 258-275; 1986.

[29] Bennett, H.E.; Guenther, A.H.; Milam, D.; Newnam, B.E. Laser Induced Damage in Optical Materials: 1984, Nat. Bur. Stand. (U.S.) Spec. Publ. 272; 1986.

[30] Bennett, H.E.; Guenther, A.H.; Milam, D.; Newnam, B.E. Laser Induced Damage in Optical Materials: 16th ASTM Symposium, Appl. Opt. 26 (5): 813-827; 1987.

[31] Bennett, H.E.; Guenther, A.H.; Milam, D.; Newnam, B.E. Laser Induced Damage in Optical Materials: 1985, Nat. Bur. Stand. (U.S.) Spec. Publ. 746; 1987.

[32] Bennett, H.E.; Guenther, A.H.; Milam, D.; Newnam, B.E. Laser Induced Damage in Optical Materials: 1986, NIST (U.S.) Spec. Publ. 752; 1988.

Manuscript Received
8-15-88

Influence of Optical Components for Laser Processing

A. Giesen, S. Borik, U. Schreiner

Institut für Strahlwerkzeuge IFSW, Universität Stuttgart
Pfaffenwaldring 43, D 7000 Stuttgart 80, West Germany

In order to make full use of the potential of today's high-power lasers it is desirable for numerous applications in material processing to achieve a diffraction limited intensity distribution in the focal plane. Therefore, in addition to the mode of the laser beam the properties of the optical components used for beam guiding and beam shaping are essential. Due to partial absorption of the high-power laser's radiation these components have transient optical properties. In order to investigate this behavior different experiments to evaluate the surface quality, the absorption and the optical deformation under irradiation have been performed.

Key words: optical deformation; focussing systems; surface quality; absorption.

1. Introduction

Material processing by high-power lasers requires specific power-densities ranging from 10^3 to 10^7 W/cm^2, which are obtained by appropriate focussing the radiation of the laser onto the workpiece. In most cases the process-efficiency can be increased by optimizing the beam quality at the workpiece, especially for cutting and welding.

Progress in laser applications stimulates the development of the laser-source itself. Due to this feedback, CO_2-lasers are now available which operate at beam-power levels up to 5 kW in low-order mode.

Regarding the focussability of laser-radiation, it is known that the phase distribution is more essential than the intensity distribution. Best focus parameters (small focus diameter and large Rayleigh-length) and therefore highest intensities are obtained with plane or spherical phase-fronts (for homogeneous intensity profiles).

In order to transmit the good beam-quality of the laser-source to the processing-area it is necessary to have a beam-guiding system which does not cause phase-front aberrations exceeding $\lambda/10$ to $\lambda/4$. Otherwise a measurable degradation of the focus properties will occur. This limit is given for the complete system, since all the optical components of the system work together. Thus the optical quality of every single component has to be better than $\lambda/10$.

Regarding beam-guiding systems for high-power lasers the behavior of the optical components under irradiation has to be taken into account because it is a dominant factor for the stability of the beam parameters during processing. A certain percentage of the irradiated power is absorbed by each of the individual components. Caused by this absorption and the subsequent heating a time-dependent deformation is observed which gives rise to a deformation of the phase-front. Also for these deformations of the components the limit given above must not be exceeded.

This contribution deals with measurements concerning the deformation of optical components. In particular, the time-dependent behavior of deformations due to laser-irradiation is discussed. Furthermore, the properties of focussing mirror systems are investigated.

2. Optical Deformation under Irradiation

Measurements of the deformation of optical components have been carried out by interferometry. The object to be tested was placed in an interferometer and was irradiated simultaneously by a high-power laser (Fig. 1). By taking photographs of the interferogram at different time steps after starting the irradiation the time-dependence of the deformation is obtained.

Fig. 2 shows measured values of the deformation for OFHC Cu mirrors with different water-cooling systems (commercial and own development) and for ZnSe windows (one uncoated and one at both sides with an AR-coating) as a function of irradiation time. From these data the following results can be derived:

- The deformation of water-cooled Cu mirrors is rather small (less than 1 μm after 1 min of irradiation time at laser-power of 2.5 kW). In accordance with the acceptable limit for the deformation given above no serious consequences for the focussability should be expected. This has been confirmed by additional measurements of the focus-parameters which will be discussed in detail in the next chapter.

- The deformation of uncoated ZnSe is more than three times larger (3 μm after 20 sec at 2.5 kW). This deformation will have consequences in cases of critical processes.

- ZnSe with an AR-coating on each side shows an extremly strong deformation. Already 10 sec after starting the irradiation a deformation of 5 μm is observed, reaching the maximum density of fringes of the interferogram that could be photographed. Note that these measurements were performed at a power level reduced to 50% compared to the other curves.

From these facts it can be concluded that the observed deformation of AR-coated ZnSe is primarily due to the absorption of the AR-coatings. Hence, all transmitting optical components provided with AR-coatings will experience changes of their optical properties. As an example, Fig. 3 shows the time-dependence of the focal length of a ZnSe lens used for cutting (f = 127 mm). Note that the transient behavior occurs within time intervals comparable to those being typical for some applications.

As such a severe deformation is caused by a relative low absorption of only 0.3%, it is important to use only optical elements of highest quality. Hence, a strict quality control appears advisable.

Furthermore it is important to mention that all these measurements were done using new components without damage or contamination. Components used in industrial environment will become contaminated by evaporation and dust. This causes an enhanced absorption and hence increased deformation leading to larger phase-front aberrations and worse focus-parameters. The measurements referred above implicate that this effect will be much more serious for transmitting optics than for reflecting ones.

3. Focussing Systems

Focussing of laser beams for material-processing can be done by lenses or focussing mirror systems. For applications with high-power lasers mirrors have some significant advantages compared to lenses:

- Metal mirrors can be provided with highly efficient water-cooling systems, whereas lenses can be cooled only at their circumferential areas. Combined with the good thermal conductivity the optical deformation of mirrors is much smaller in spite of their higher absorption.

- The damage threshold of metal optics is much higher than that of transmitting optics.

- Off-axis-parabolic mirrors are free from spherical aberration. This effect is limiting the aperture ratio of lenses to values of D:f < 1:4.

- The absence of chromatical aberration allows adjustment of the focus on the workpiece by a simple visible laser.

For cutting applications (where highest power-density is requiered) only with lenses the necessary optical quality could be achieved in the past. The use of focussing mirror systems was restricted to welding and surface-treatment. Today, however, improved diamond-turning processing of metal surfaces allows the production of all geometrical forms needed (parabolic etc.). At present metal mirrors can achieve an optical quality comparable or even better (no spherical aberration) to the quality of lenses.

Fig. 4 shows the interferogram of a focussing mirror system consisting of a plano and an off-axis-parabolic mirror (angle of deflection 45°, effective focal length 153 mm, aperture 40 mm). Fringes represent lines of constant deviation from the ideal shape. The maximum deviation turns out to be 0.3 μm or $\lambda/30$ at λ = 10.6 μm meaning that the focus of this optical system is limited only by diffraction. Furthermore, the roughness can be determined to be less than 0.05 μm (peak-to-valley) so that scattering of light is much less than 1% [1].

A disadvantage of focussing mirror systems is their larger sensitivity to misalignment compared to that of lenses. Fig. 5 shows the astigmatism Δf (distance between sagittal and meridional focal lengths f_s and f_m) which is significant of this effect. The full line represents the theoretical result [2]:

$$\Delta f = f_m - f_s = -2 \cdot S \cdot \tan \alpha \cdot \Delta\varphi$$

(S: effective focal length, α: angle of deflection, $\Delta\varphi$: angle of misalignment).
When the focus parameters should not be significantly changed by this astigmatism Δf, the astigmatic distance should not exceed half the Rayleigh-length. For the focussing system referred above in combination with the laser used in this experiments the Rayleigh-length was measured to be 1.2 mm (see Fig. 7). Therefore, the tolerable angle of misalignment is limited to 5 mrad.

Compared to this 45°-system the sensitivity to misalignment of a 90°-off-axis system is 2.4 times larger as shown in Fig. 5 (dotted line). On the other hand, for a lens of a focal length of f = 127 mm the corresponding angle would be 90 mrad neglecting other optical distortions as shown in Fig. 6.

With an instrument as described in [3] measurements of the laser focus were carried out. Fig. 7 shows the focussing properties of the 45°-off-axis mirror system at different time steps. The full circles represent the laser beam radius immediatly after switching on the laser, the open circles show the beam radius after one minute of irradiation time. The laser power was 1.3 kW. The picture demonstrates the good stability of the optical properties of the focussing system. No change in focus position and focus spot size can be observed.

For cutting applications one has to assist the process by applying a gas jet. Usually this gas jet is collinear to the laser beam. Therefore the focussing system has to be sealed by a ZnSe window. This additional AR-coated window which is mounted at the entrance of the focussing mirror system causes changes of the optical properties with time as is shown in Fig. 8. After one minute of irradiation time the focal length has been shortened by 0.5 mm and the radius of the focal spot has enlarged by about 10% (open circles). Thus the AR-coated window acts as a lens with a time and laser power dependent focal length with an additional distortion of the beam giving rise to an enlargement of the focus spot size. The results for the focussing mirror system with a window are similar to those of an AR-coated ZnSe lens, see Fig. 3.

4. Static Deformation of Optical Components

In addition to the dynamic deformation due to thermal effects attention must be paid to static deformations caused by attaching the components to their mounts. While substrates like ZnSe or Si show little deformation, OFHC Cu mirrors are easily deformed by inadequate mountings and mounting procedures. Further efforts are needed in this field.

5. Conclusions

Changes of the optical properties of various optical components have been observed during laser irradiation at power levels well below the damage threshold. Transmitting components, in particular those with coatings (antireflecting), show a very large deformation due to absorption causing a significant degradation of the laser beam quality. In contrast to this, with reflecting metal optics the beam quality will not be significantly degraded since their deformation is lower more than an order of magnitude.

6. References

[1] K. Du, P. Loosen, G. Herziger, Proceedings of "Laser 87, Optoelectronic in Engineering", Munich 1987, pp. 478-482

[2] P. Henneberg, c/o Carl Zeiss, Oberkochen, private communication

[3] G. Herziger, E. Beyer, R. Kramer, P. Loosen, F. Rühl, Proceedings of "Laser Advanced Materials Processing", Osaka 1987, 37 (1987)

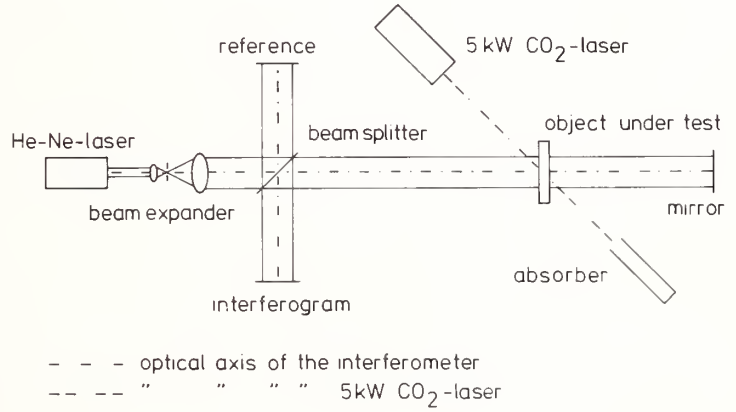

Figure 1.
Interferometer for measurements of the optical deformation.

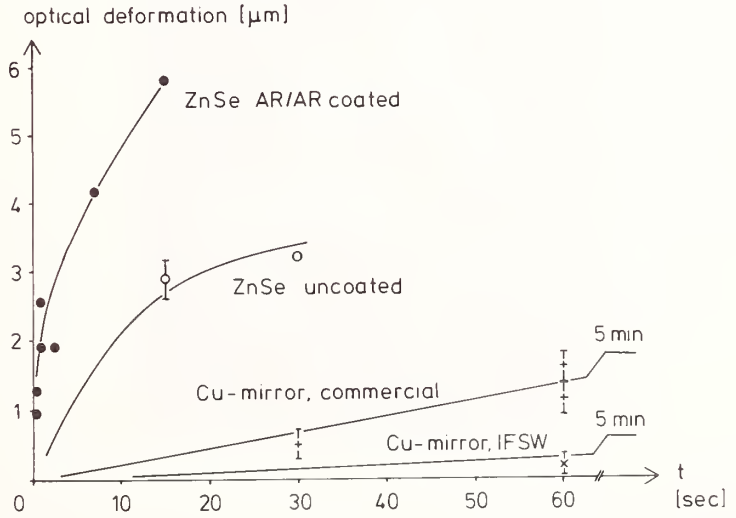

Figure 2.
Time-dependence of the optical deformation of several components.
Laser-power: 2.5 kW for Cu mirrors and ZnSe uncoated,
1.25 kW for ZnSe AR-coated.

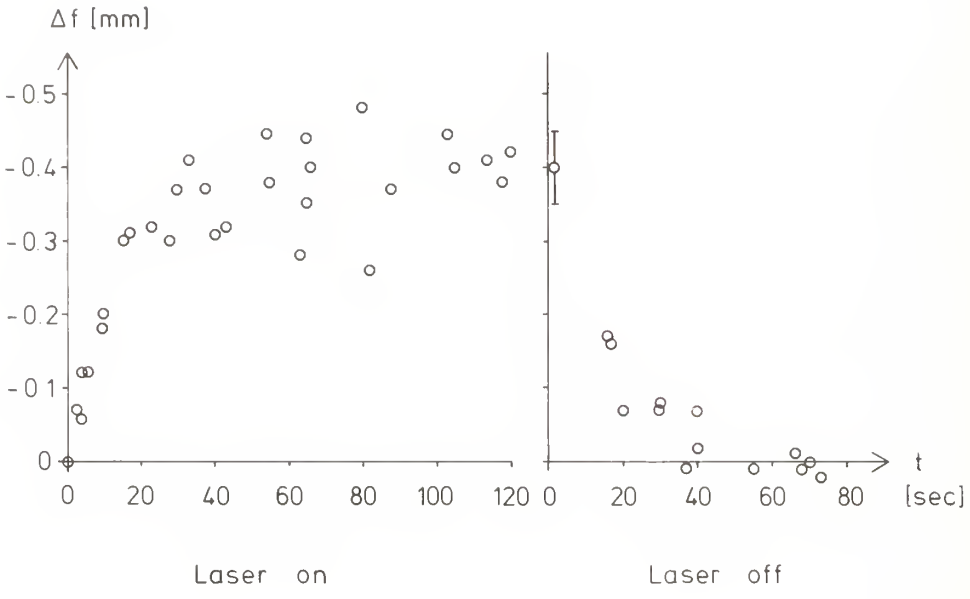

Figure 3.
Time-dependence of the focal length of a ZnSe lens, f = 127 mm, laser-power 1.3 kW.

Figure 4.
Interferogram (λ = 633 nm) of the focussing mirror system as described in the text.

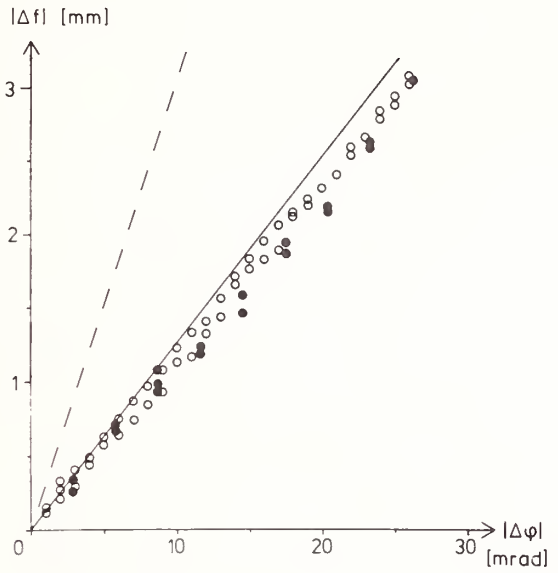

Figure 5.
Astigmatism Δf as function of the angle Δφ of misalignment for the mirror system, the interferogram of which is shown in Fig. 4.
Full and open circles: measured misalignment in two axes,
full line: theoretical curve [2], dotted line: theoretical curve for a mirror system with a deflection of 90°.

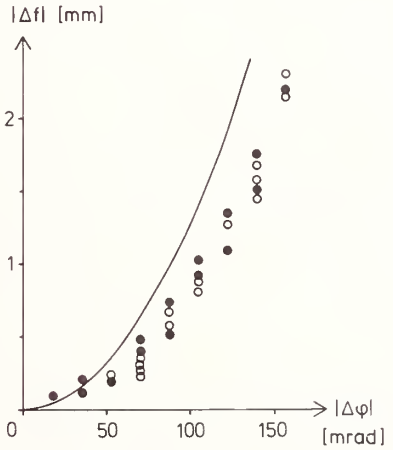

Figure 6.
Astigmatism Δf as function of the angle Δφ of misalignment for a lens, f = 127 mm. Full curve: theoretical values for a thin lens.

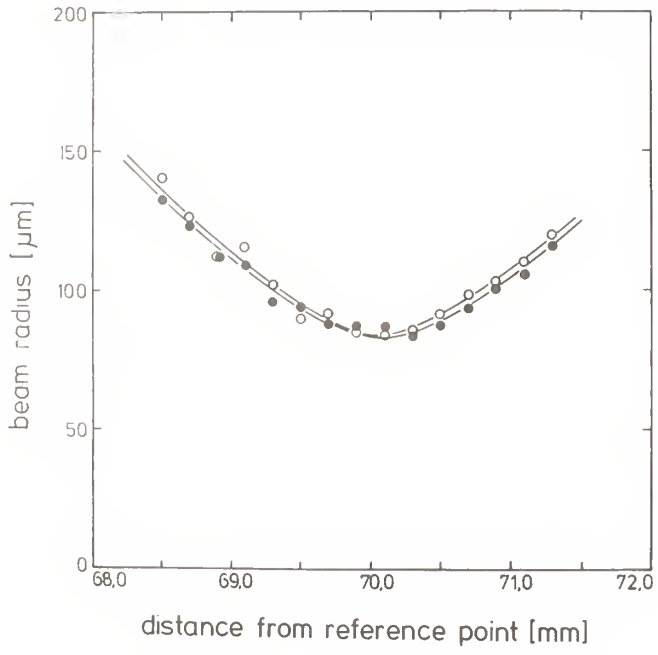

Figure 7.
Beam radius in the focal region of the focussing mirror system, laser power: 1.3 kW, laser mode: TEM_{01}*.
Full circles: beam radius after switching on the laser,
open circles: beam radius after 1 min of irradiation time.

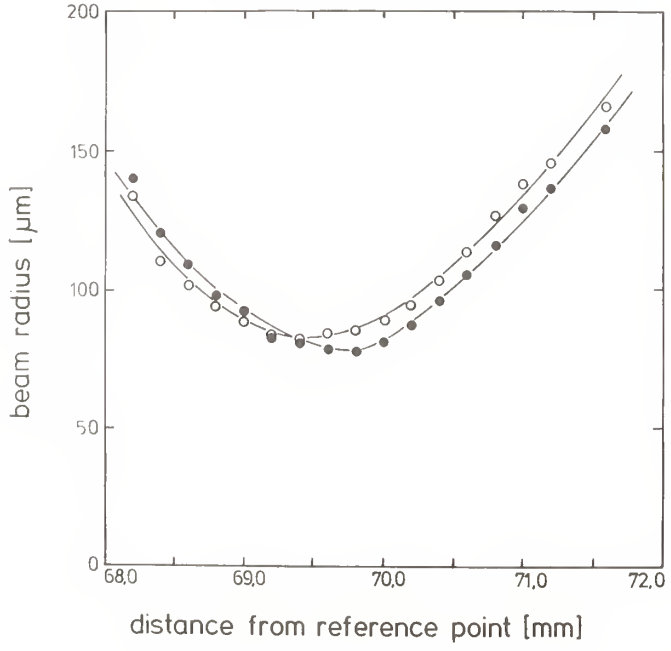

Figure 8.
Beam radius in the focal region of the focussing mirror system with an additional AR-coated ZnSe window (see text). Symbols and parameters see Fig. 7.

Manuscript Received
8-10-88

MATERIALS FOR AEROSPACE/LARGE OPTICS

W. W. Ernst
SPACE-FORSCHUNGSGRUPPE (SFBF)
Schloßhofstr. 9, 7801 Buchenbach, FRG

Abstract

For use in large mirrors in outer space, where low mass is a critical need, 3 D-CFK developments are under our investigation since 8 years. Precision replication future technologys taken from a negative form are our candidates for the ESO, VLT monolithic primarys. In our option we use a Nasmyth Focus, because of mirror stability.

Introduction

The fact that it takes from ten to fiftheen years to complet a large astronomical telescope, wheter in space or on the ground is a to long time range. Furthermore, astronomical techniques are changing rapidly, and there is a need to have in every place of the instrument a future technology located. Several mirror designes have been investigated 1. Cost will then become a major concern, when big apertures are to heavy (20 tons) an the spheres will change figure under his own weight.

Telescope designoptions

Reflecting telescopes have traditionally built around simple monolithic primary mirrors. Larger than 5 to 6 meters in diameter monolithic mirrors become increasingly heavy and difficult to cast, handle and support. Recently, the need for very large aperture telescopes (VLT) on the ground has promoted three new approaches:

1. the telescope array, or $(MMT)^2$, composed of a number of parallel pointing telescopes with their beams combined to a common focus.
2. the segmented primary mirror $(SMT)^3$, where the primary mirror is a mosaic of common-focus mirrors supported by actuators which maintain optical alignment.
3. the thin adaptive primary mirror[4], also supported on actuators.

The segmented primarys

Unfortunately, the greatest problem of segmented primary arrays may be the recombination of all individual beams in phase. Adjusting optical paths with an accuracy on the order of the wavelength is a major challenge. Telescop arrays are very attractive from an optical point of view because resolution increases linearly with the overall aperture size, while the collecting power varies as its square. The thin adaptive primary is very similar to the segmented mirror scheme, but without the advantage of modularity. Active control of large optical surfaces has been proposed[5,6], but requires a large number of actuatores with inherently low overall reliability.

Conclusion

Among these approches, the segmented primary scheme appears the most attractive, but is still not fully satisfactory compared to traditional telescopes with passive primaries. Not only might such support systems have low reliability, but when the weigth of these actuatores and of necessary supporting structures are taken into account, the mass-saving over a light-weight passive large mirror may not be significant. A very-high-precision 3 D-CFK 8 meter primary taken from the shape of the master negative form can be released and multiple times used. A preliminary look at a possible design of such a 8 meter primary is presented in Fig. 1.

Proposed concept

However, in certain specific application areas, replication is the fabrication method of choice. Technologys for space should also be used for the VLT of ESO to be affordable to the astronomical community, it will be essential to reduce costs drastically. The proposed primarys are 3 D-Carbon composite honeycombed monoliths, supported by three pads. The primarys are fabricated to diffraction-limited quality. The deformable secondary mirrors are used to correct the residual primary mirror defects.

Small-scale research of 1,5 meter Carbon composite mirrors and long term tests[7] in 3 D-Structures was of great value in the generation of new scientific ideas in subject of large optics. Development in carbon-composite materials and the creation of new future technologys, with scientests working in small groups (SFBF) brings success. Furthermore, such small projects offer the flexibility for rapid

changes in research directions, so that innovation is encouraged.

The fact that 3 D-CFK structures have a near 0 thermal expansion rate and gives a drastical mass reduction was one of among aspects to use these materials for large optics.

Another ascpects was the possibility to build large replication negative forms, Figure 2, with a high quality surface.

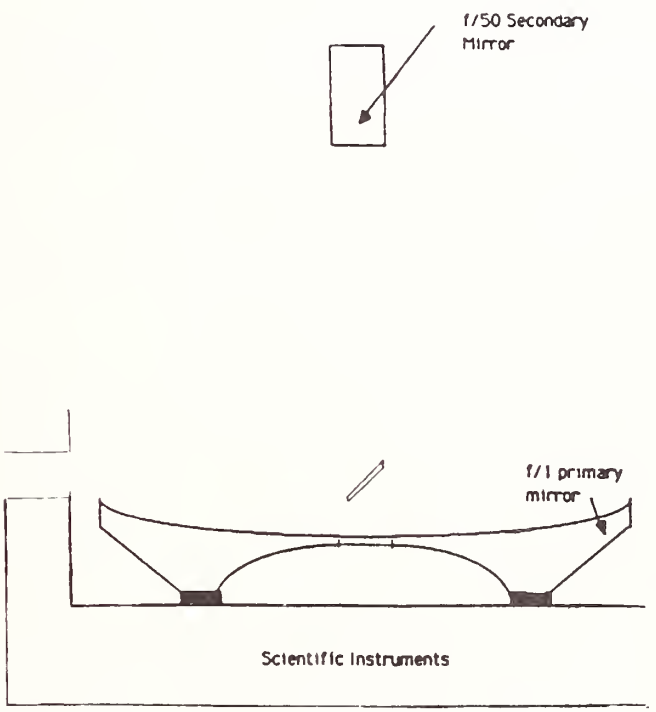

Fig. 1: Schematic section of the proposed 3 D-CFK very fast aspheric 8 m very-high-precision replicated primary mirror for the VLT.

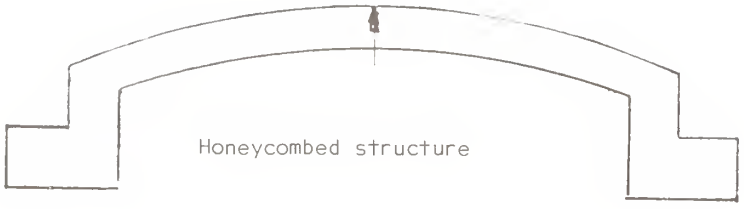

Fig. 2: Schematic section of a negativ form
to be used for replication.

The large physical size of a 8-meter monolithic mirror, of course brings problems in subject above. A laser-interferometric correction with testglas of such a large negative surface will hard to do, but we think with already existing technologys its possible.

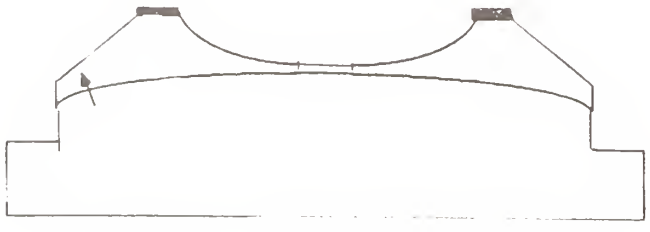

Fig. 3: Very-high-precision negative form
with a proposed mirror.

The replication process involves the transfer of a film or a stack of films from a master surface to a machined base of substrate. New matrix materials for a 3 D-CFK layer and rapid changes in using this, (Diamond) promis to be successful. Next step in this way is a 2,4-meter f/1.6, mass ca. 200 kg 3 D-CFK honeycombed monolith (BMFT-Project).

Conclusions

There is no doubt that many long-term deformation is to verify and need to be studied thoroughly before any serious proposal for a super 8-meter 3 D-CFK monolith can be formulated.

We think our carbon fiber mirror developments are the technology of the future. The Arizonas Dr. Roger Angel, who will build 8-meter mirrors made of glass, is the most innovative in this way. Ironically, Angel takes much of his inspiration from the past.

The proposed approach may offer the best chance to put a future technology into the ESO VLT-Project, because our master negative can be used multiple times which is very economically.

Acknowledgement

I wish to thank P. Y. Bely, Space Telescope Science Institute, Baltimore, and Dr. Raymond N. Wilson, ESO, Garching for inspiring this proposal.

References

1. Bunner, A. N. Optical arrays for future astronomical telescopes in space, SPIE Proc. 546, 1985.
2. Beckers, J. M. Ulrich, B. L., and Williams, J. T., Performance of the Multiple Mirror Telescope (MMT)I, Advanced Techn. Telescopes II SPIE Proc. 332, p. 9, 1983
3. Nelson, J. et al., The segmented-mirror..., Advanced Technology Telescopes II, SPIE Proc. 444, 1983, p. 274.
4. Wilson, R. N. Very Large Telescopes, ESO Prox., p. 173, 1983.
5. Wilson, R. N. Very Large Telescopes, ESO Prox., p. 173, 1983.
6. Hansen, J. G. R., Richard, R. M., Swanson, R. H., Deformable primary mirror for a space telescope, Appl. Opt., Vol. 21 no. 14, 1982.
7. Ernst, W. W., Sterne und Weltraum, 11, 1985, Low mass mirrors in large optics, SPIE Proc. 655, p. 405, 1986.

Production and Properties of Perrhenate-doped Alkali Halide Crystals

O. H. Nestor

Harshaw/Filtrol Partnership
Cleveland, Ohio 44139

and

J. F. Figueira

Los Alamos National Laboratory
Los Alamos, New Mexico 87545

Manuscript Received 2-12-88

The growth and selected properties of single crystals of KCl doped with ReO_4^- is described. The crystals have been used as saturable absorbers to modulate and control CO_2 laser radiation. ReO_4^- ion concentrations in excess of 10^{17} cm^{-3} were achieved in KCl with good optical quality. The room temperature absorption of the ReO_4^- ion in KCl was centered at 936.8 cm^{-1} with 1.5 cm^{-1} linewidth and with absorption cross-section determined to be $(0.46 + 0.02) \times 10^{-16}$ cm^2. The addition of Li^+ as a second dopant resulted in a splitting of the ReO_4^- resonance into two components at 957.5 cm^{-1} and 900.7 cm^{-1}.

The characteristically sharp resonance of ReO_4^- was not detected in NaCl grown with $NaReO_4$ additions to the melt. Only with addition of Ca^{++} as a co-dopant was the ReO_4^- resonance observed. The absorption, detected as a very weak resonance through a 92 mm path length, was centered at 946.0 cm^{-1} with linewidth of 6 cm^{-1}, overlapping the P(20) transition in the 10 micron CO_2 band.

Key words: alkali halides; Bridgman-Stockbarger; CO_2 laser radiation; crystal growth; dopant distribution; double-doped crystals; non-linear material; perrhenate ion absorption; potassium chloride; saturable absorber; sodium chloride.

1. Introduction

In a collaborative program between Los Alamos National Laboratory and Cornell University, investigators identified a new class of nonlinear materials that have a variety of potential applications to CO_2 lasers [1]. These materials are based on the selective introduction of impurity ions into normally transparent alkali halides. The ions are optically active in the infrared, producing absorptions in the 10 micron wavelength region. The first successful demonstration of this concept was made using a KCl crystal host doped with the perrhenate ion ReO_4^-. This material has been successfully used as a room-temperature passive pulse compressor for P(28)-transition CO_2 laser pulses [2] and as a short pulse generator for P(26) radiation at 105°K using optical free-induction decay [3].

In parallel to the LANL/Cornell program, a collaborative effort between LANL and Harshaw/Filtrol was undertaken to identify potential problems in producing large crystals of perrhenate doped alkali halides. The program was designed to produce large crystals of KCl:ReO_4^- with the eventual extension to NaCl single crystal and hot forged hosts. Of particular interest were the dopant concentrations achievable and the associated optical quality, particularly since residual strains in the Czochralski(Cz)-grown Cornell crystals completely destroyed their infrared optical quality. The approach at Harshaw was based on another melt-growth process, the Bridgman-Stockbarger (B-S) technique, successfully applied in the production of large NaCl windows for the Antares project at Los Alamos.

An additional point of interest in the present work was the possibility that the perrhenate absorption in NaCl would be shifted to the region of the P(20) CO_2 transition at 944.2 cm^{-1} and hence that saturable absorption might be realized for this dominant CO_2 laser line. This possibility was projected by the LANL/Cornell team upon considering the size of the perrhenate ion relative to the lattice parameters of KCl (3.2A) and NaCl (2.8A).

The perrhenate ion is estimated to measure approximately 3.1 A in radius, based on similarities between the perrhenates and periodates of potassium as well as of sodium [4], and the

published I-O bond distance in the periodate $(IO_4)^-$ ion[5]. The perrhenate ion is then tightly constrained by the crystal field of either host lattice, KCl or NaCl, but more so in NaCl wherein the restoring force for the vibrational mode is effectively greater and the resonance frequency is accordingly higher.

Because of the dopant-lattice size relationship, it can be expected that the segregation coefficient, ratio of dopant level in the solid phase to that in the melt, would be <<1 for both the B-S and Cz melt processes and that there would be a large variation in dopant concentration along the length of the crystal.

2. Crystal Production and Evaluation

The crystals produced in this investigation were grown by the Bridgman-Stockbarger process. Growth materials were melted and crystallized in platinum crucibles in selected gases at one atmosphere pressure. A series of KCl crystals was grown in helium and several crystals were grown in argon. NaCl crystals were grown in N_2, air or O_2, options spanning a range of possible effects on the oxidation state of the dopant.

Starting materials for growth of doped KCl crystals were once-grown crystals produced from Harshaw-purified KCl powder plus $KReO_4$ powder (4N purity from Cerac, Inc.) covering decade steps in the range 0.001-10. weight percent (0.00026 - 2.5 mol percent). Starting materials for doped NaCl crystals were Harshaw-purified NaCl powder plus $NaReO_4$ powder (4N purity from Apache Chemicals, Inc.) added at levels of 0.005, 0.10, 1.0 and 10.0 weight percent (0.0011-2.1 mol percent) in a series of runs. Anticipating a segregation coefficient <<1 and rather limited melt stirring during growth, the dopant was concentrated in the lower (first-to-be-solidified) end of the crucible with the intent of reducing the variation in ReO_4^- content along the length of the crystal.

Double-doped crystals of KCl and NaCl were grown with the second dopant selected to adjust the crystal lattice for a desired effect on the ReO_4^- absorption peak. The second dopant for KCl was lithium, added as LiCl, and for NaCl it was calcium, added as $CaCl_2$.

Crystals were grown at rates of 1.25-1.60 mm/hr to sizes ranging from 36 mm diameter x 82 mm length to 64 mm diameter x 195 mm length. Samples were taken for transmission spectroscopy, dopant analysis and optical evaluation. The primary spectroscopic evaluations were done with a Nicole Fast Fourier Transform Spectrometer. Perrhenate concentrations were established by neutron activation analysis and by a standard colorimetric technique, assuming all rhenium present as ReO_4^-. Samples were examined for Tyndall scattering and, under polarized white light, for strain.

3. Results

3.1 KCl

3.1.1 Crystal Quality

Figure 1 shows a 64 mm diameter x 190 mm long crystal grown from a charge containing 0.26 mol percent (1.0 weight percent) $KReO_4$ at loading and sections of the KCl crystal double-doped with ReO_4^- and Li^+. The KCl:ReO_4 crystals grown in this work were generally of good internal quality except at high dopant levels. Strain as viewed between cross polarizers was at a very low level, an improvement sought relative to the original Czochralski-grown crystals (Figure 2). Typical bulk defects encountered with dopant additions at or below 0.26 mol percent $KReO_4$ were low-to-moderate haze and small discrete scattering centers, such as gas bubbles or voids or perhaps particulate inclusions.

Surface defects were encountered in some of the more highly doped crystals. These occurred in the form of pits or channels, such as that evident in the lower crystal in Figure 1, a crystal grown from a melt doped to the 0.26 mol percent level. It is surmised that there occurs a nucleation process for such defects that depends on the local melt composition and the proximity of a surface, such as the crucible wall. This is suggested further by inclusions at the crystal wall (Figure 3) found in one of the crystals doped with 0.26 mol percent $KReO_4$. A possible extension of such process was found in the interior of a crystal grown from a melt of 2.5 mol percent $KReO_4$; therein a 39 mm long channel was nucleated in the surrounds of optically clear crystal and grew to a diameter in excess of 1 mm. A scanning electron micrograph of this defect is shown in Figure 4. It was shown to contain Re, K and Cl, the latter in non-stoichiometric

ratio. This crystal gave indication of an upper limit on the $KReO_4$ concentration in the form of high density of inclusions and boundaries between 5°-10° misoriented grains, both evident in the latter-grown part of the crystal (Figure 5).

3.1.2 ReO_4^- Distribution

The dopant distributions measured in this work require that the surface and bulk concentrations be distinguished. This was suggested by the findings discussed above and further by analytical results shown in Figure 6 applying to a slab taken from the cone section of the crystal of Figure 3. The data of Figure 6 represent colorimetric determinations accurate and precise to within 2 percent down to the ppm range. It is seen that an order-of-magnitude difference in the surface to bulk concentrations was measured in this example.

With the segregation coefficient <<1 and perfect mixing, a significant increase in dopant content can be expected along the length of the crystal. In order to smooth out the expected variation, the dopant load was concentrated in the cone end of the crucible. Figure 7 shows the variation measured colorimetrically along the surface of two crystals, one grown with a starting concentration of 0.26 mol percent (1.0 wt percent) $KReO_4$ in the melt and the other with 0.026 mol percent. The upper curve data point at 1 cm from the start of growth represents the average of the determinations detailed in Figure 6. Order-of-magnitude variation in dopant concentration is seen in the results of Figure 7, even as moderated by the non-uniform initial doping of the charge. The effect of the initial concentration of the dopant is evident. The ensuing decline in dopant concentration is understood to follow from the mixing that occurred (over 40 hours) in the melt. The increase that then follows is that representative of a segregation coefficient <1.

The general level of the dopant surface contents of the two crystals surveyed in Figure 7 are not in the same ratio as that of the respective starting compositions: the surface concentrations in general are disproportionately high for the 1.0 wt percent $KReO_4$ doping relative to the 0.1 wt percent doping. Again, it is presumed this signals that the wall effect becomes more significant with increasing doping.

Bulk concentration data are shown in Figure 8 as a function of starting compositions. These results are based on neutron activation methodology and apply to slabs normal to the growth direction, taken from 195 mm long crystals at fixed locations corresponding to 90 percent of the crystal grown, a standardizing procedure adopted in light of the longitudinal variation in the ReO_4^- concentration. This result indicates that a controllable dopant concentration can be achieved in the bulk material in KCl, with ReO_4^- concentrations approaching 10^{17} cm^{-3} in highly doped samples.

3.1.3 $KCl(ReO_4)$ Spectroscopy

Figure 9 shows a typical room temperature absorption spectrum of $KCl:ReO_4^-$ in the 10 micron region. Coupling this with neutron activation-determined dopant concentrations yields a value of $(0.46 \pm 0.02) \times 10^{-16}$ cm^2 for the absorption cross section at 936.8 cm^{-1}. Thus, absorption coefficients in excess of 4 cm^{-1} can be obtained in highly doped single crystal samples.

The KCl crystal double-doped with Li^+ and ReO_4^- was of good quality, having only low haze in the first half of a 63 mm diameter x 115 mm long crystal and moderate haze with decorated mosaic boundaries in the second half. The 10 micron absorption for this crystal is characterized by two resonances at 957.5 cm^{-1} and 900.7 cm^{-1}, instead of the single line at 936.8^{-1} seen in $KCl:ReO_4^-$. This change is attributed to the removal of degeneracy in the fundamental vibrational mode of the ReO_4^- ion.

3.2 NaCl

Crystals grown from melts charged with 0.022 mol percent (0.1 wt percent) $NaReO_4$ surpassed their KCl counterparts in quality. That from a 2.1 mol percent $NaReO_4$ melt was comparable to its high-doped KCl counterpart, exhibiting reasonable quality over the first-grown half, but hardly translucent over the last-grown half.

NaCl crystals singly-doped with ReO_4^- did not exhibit the sharp resonance characteristic of the ReO_4^- ion. They exhibited only broad absorption in the 10 micron wavelength region. Such absorption was attributed to a collective lattice mode of vibration that by experimentation was shown to be extremely difficult to saturate.

Only when Ca^{++} was added as a co-dopant was the sharp ReO_4^- absorption detected. Growth of NaCl doped with ReO_4^- and Ca^{++} was predicated on utilizing Ca to expand the NaCl lattice such that the ReO_4^- ion could be accommodated [6]. A double-doped crystal, grown in nitrogen from a melt charged with 0.21 mol percent $NaReO_4$ plus 0.0062 mol percent $CaCl_2$, exhibited the ReO_4^- absorption resonance, though very weakly even through a 92 mm path. The resonance at room temperature is shown in Figure 10. It is centered at 946.0 cm^{-1} with bandwidth of 6 cm^{-1}, overlapping the desired 944.2 cm^{-1} P(20) transition in the 10 micron CO_2 band. The ReO_4^- ion concentration was below the detection threshold of the neutron activation technique (2 x $10^{14}/cm^3$). Based on assuming equal transition probabilities in KCl and NaCl, the estimated average ReO_4^- concentration in the spectroscopically probed path was 1.6 x 10^{14} cm^{-3}.

Other double-doped crystals were grown with ReO_4^-/Ca^{++} ratios in the 1-10 range and with Ca^{++} up to 0.5 mol percent. These had an absorption peak at 946 cm^{-1} with absorption coefficient in the 0.3-0.9 percent/cm range. This is probably too low to be of practical interest for CO_2 lasers.

4. Summary

This research has shown that ReO_4^- ion concentrations in the range 10^{17} cm^{-3} and higher can be achieved in large KCl crystals of good optical quality grown by the Bridgman-Stockbarger process. KCl:ReO_4^- crystals exhibiting room-temperature absorption at 936.8 cm^{-1} suitable for pulse compression and short pulse generation in the 10 micron CO_2 band can be produced.

The use of Li^+ as a second dopant with ReO_4^- in KCl yielded resonances at 957.5 cm^{-1} and 900.7 cm^{-1}, apparently removing degeneracy in the fundamental vibrational mode of the ReO_4^- ion.

The characteristically sharp resonance of ReO_4^- was not detected in NaCl grown with $NaReO_4$ additions to the melt. Only with the addition of Ca^{++} as a co-dopant was the ReO_4^- resonance detected. The room-temperature absorption was shifted relative to that in KCl and was observed at 946.0 cm^{-1} with a 6 cm^{-1} bandwidth, hence overlapping the 944.2 cm^{-1} P(20) transition. However, this was a very weak absorption, presumed to be so because of low ReO_4^- ion concentration even in the Ca^{++} expanded lattice.

5. Acknowledgement

The authors are grateful to the following contributors to this investigation: Joseph J. Ursic and David A. Hammond, Harshaw/Filtrol, for the growth of crystals; Arthur F. Greene, Harshaw/Filtrol, for colorimetric determinations of the perrhenate ion distributions; Berle Bunker, LANL, for neutron activation analyses for Re-concentrations; and Albert J. Sievers, Cornell University, for advice concerning double dopant combinations.

6. References

[1] R. K. Ahrenkiel, J. F. Figueira, C. R. Phipps, Jr., D. J. Dunlavy, S. J. Thomas and A. J. Sievers, "A New Saturable Absorber for the CO_2 Laser Using Doped KCl," Appl. Phys. Letter. 33, 705 (1978).

[2] J. F. Figueira, R. K. Ahrenkiel and D. Dunlavy, "Nonlinear Optical Properties of the Perrhenate Ion in KCl," SPIE Vol. 190, LASL Conference on Optics '79, p. 293 (1979).

[3] R. K. Ahrenkiel, J. F. Figueira and D. Dunlavy, "Generation of Ultrashort CO_2 Pulses by Free-Induction Decay in KCl:ReO_4," SPIE Vol. 190, LASL Conference on Optics '79, p. 332 (1979).

[4] R. W. G. Wyckoff, "Crystal Structures" (Interscience Publ. Inc., New York), Table VIIIA. 5.

[5] A. F. Wells, "Structural Inorganic Chemistry" (Clarendon Press, 1975, 4th Ed.), p. 344.

[6] The authors gratefully acknowledge this suggestion by Professor A. Sievers, Cornell University.

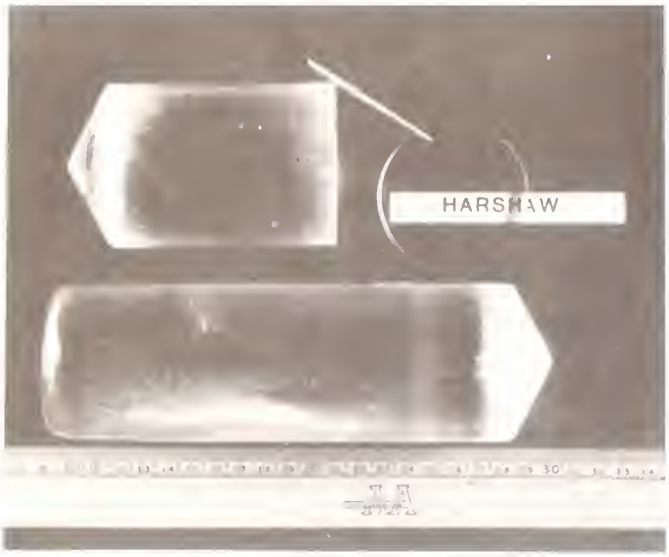

Figure 1. Crystals produced in this program. Lower: $KCl(ReO_4)$ of typical size, 63 mm diameter x 195 mm long. Upper: $KCl(ReO_4,Ca)$.

Figure 2. Strain comparison of $KCl(ReO_4)$ crystals. Upper: Czochralski-grown in the LANL/Cornell program. Lower: Bridgman-Stockbarger grown in the present program.

Figure 3. Inclusions near periphery of $KCl(ReO_4)$ crystal.

Figure 4. Scanning electron micrograph of defect in a $KCl(ReO_4)$ crystal grown from melt with 2.5 mol % $KReO_4$.

Figure 5. High inclusion density zones and grain boundaries in heavily doped KCl(ReO_4) crystal.

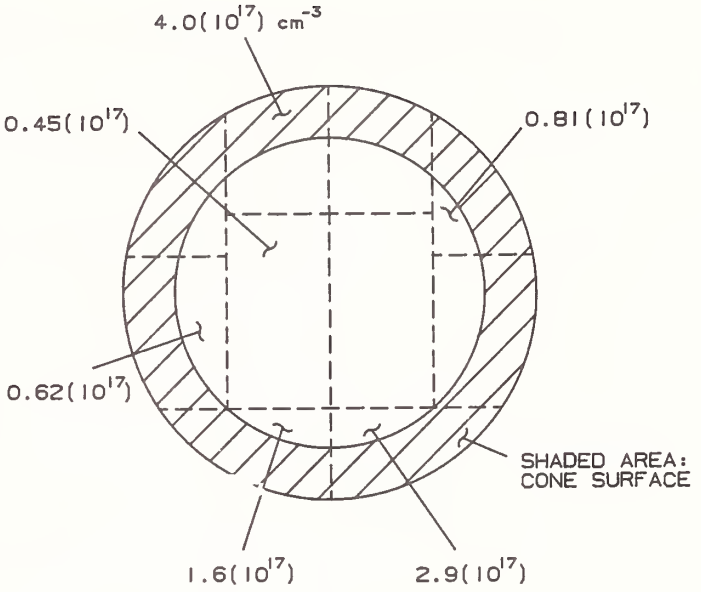

Figure 6. Colorimetrically determined ReO_4^- concentration distribution across section of KCl(ReO_4) crystal.

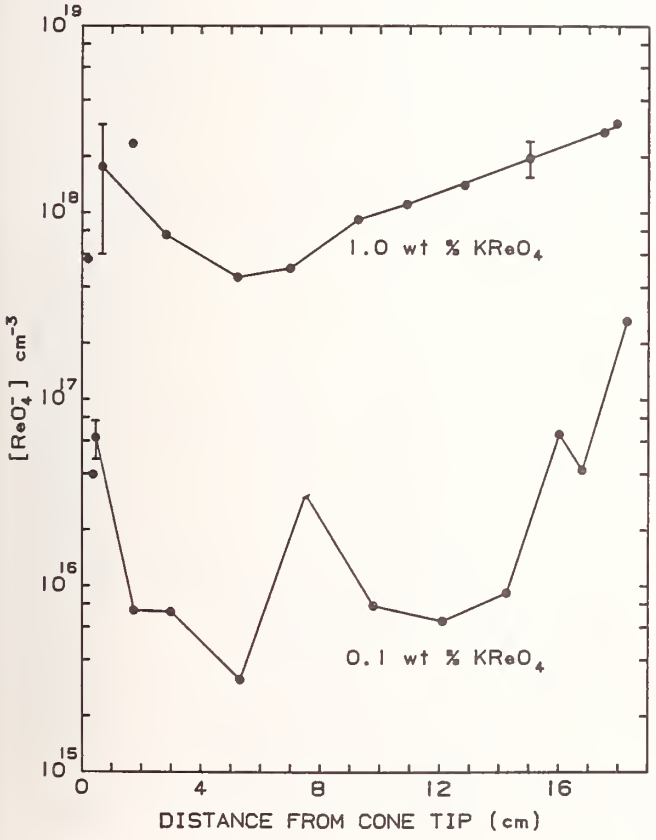

Figure 7. Colorimetrically determined ReO_4^- concentration distribution along surface of KCl(ReO_4) crystal.

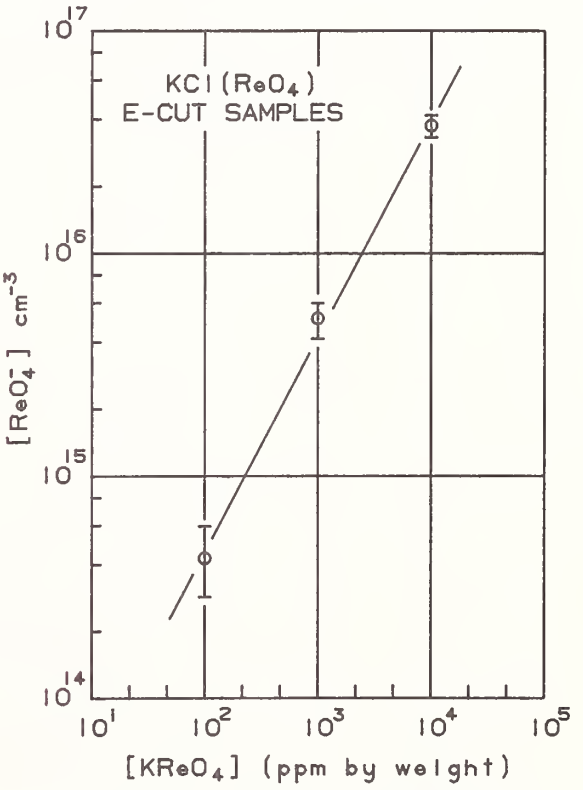

Figure 8. Dopant concentration (determined by neutron activation analysis) within KCl(ReO_4) crystals as a function of the initial dopant loading in the melt.

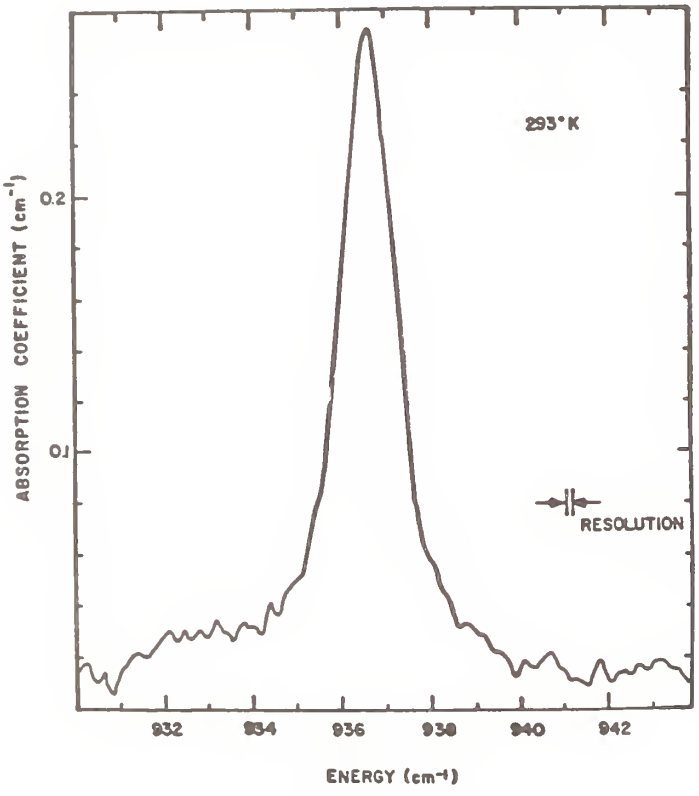

Figure 9. Room temperature absorption spectrum of $KCl(ReO_4)$ in the 10 micron region.

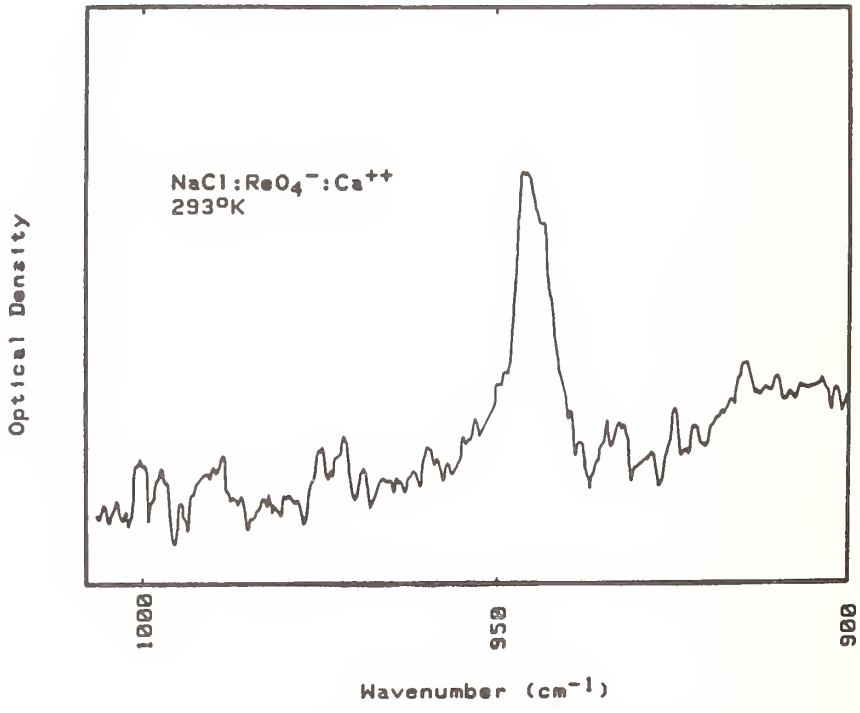

Figure 10. Room temperature absorption spectrum of $NaCl(ReO_4,Ca)$ in the 10 micron region.

Manuscript Received
10-16-87

Solubility of Pt in Nd Phosphate Laser Glass

T. Izumitani, M. Matsukawa and H. Miyade

Research & Development Center, HOYA CORPORATION
Tokyo, JAPAN

Abstract

Solubility of Pt was measured in order to make Pt inclusion free laser glass. Pt solubility increased with decreasing temperature. The solubilities were measured in the atmosphere of O_2, air and N_2 and decreased in the order of O_2 > air > N_2. The Pt solubility of phosphate glass was higher than that of silicate glass and decreased in the order of LHG-5 > LHG-8 > HAP-3 > LHG-10 > LSG-91H. Pt deposition mechanism is considered that Pt dissolve into the melt in ionic state but some of them are easily reduced to atomic state and deposited as metallic inclusions due to supersaturation.

Key words: Solubility, platinum, atmosphere, temperature, glass composition, laser damage, Pt deposition mechanism, reactive atmosphere processing.

1. Introduction

In March 1985, a laser damage was observed on the laser glass disc in the high power laser equipment, NOVA, at UCLL. The cause of the damage was fine Pt inclusions present in the laser glass, due to an increase in the influence of NOVA'S laser beam from a value of 3.5 J/cm^2 to 8 ~ 10 J/cm^2. A disc contains 35 ~ 1,000 Pt inclusions with 8 ~ 75μm size, and cracks grew from 80 to 1,000μm by radiation of laser beam.

For this reason, a study has started to manufacture Pt inclusion free laser glass. In the summer 1986 a technology for manufacturing Pt inclusion free phosphate laser glass has been achieved, resulting in a reduction of Pt inclusion number from 1000/l to 0.1/l (with smaller size than 5μm).

The process consists of ionization of dissolved Pt particle in glass because no damage occurs if Pt is ionized. It was necessary to know Pt solubility in the glass for obtaining fundamental data on Pt inclusion. If Pt dissolution could be suppressed below the solubility, the deposition of Pt inclusion can not occur. But almost no data on Pt solubility in the glass is known, therefore, Pt solubility variation with temperature, atmosphere and composition was measured. Further, efforts were made to ionize Pt by RAP treatment using $POCl_3$. Our success in making Pt inclusion free laser

glass was based on these efforts. The following are descriptions of studies on Pt solubility.

2. Experimental

To measure Pt solubility, a given quantity of Pt was added to a glass batch, and after melting, stirring in a quartz crucible and keeping at a given temperature, the glass was bubbled with a given gas, then it was cast. Figure 1 shows an example of melting schedule. The existence of Pt crystal was examined by using microscope (magnification: 80 ~ 40). The solubility at a given temperature was determined according to a limit value for Pt existence.

Quantitative determination of Pt in the glass was carried out as follows: A glass sample was decomposed by using acid, Pt was then coprecipitated by means of Te-Sn(II) process and separated from glass constituent. The precipitate was dissolved in the aqua-regia to convert Pt into a chloride. Pt was then determined from the solution by using P-nitrosodimethylaniline colorimetry.[1)]

Table 1 shows Pt amount added vs. found. As shown in the Figure, Pt content corresponds very well to the amount added.

3. Results

3.1 Pt solubility vs. temperature

Figure 2 shows the solubility of LHG-8 in function with the temperature. Reducing of the solubility was clearly observed as the temperature decreases. Such tendency is similar to that of Ar and N_2 solubility in the glass, suggesting that the dissolution be of no chemical character but a physical one. Namely, the solubility is defined by Pt present in form of atom or metal in the glass.

3.2 Pt solubility vs. atmosphere

Pt solubility depends also on the atmosphere. As shown in Figure 3, the solubility is the highest in O_2 atmosphere, lowest in N_2 and middle in Ar showing a close value to N_2. The fact can be easily understood, provided the solubility is defined by metallic or colloidal Pt dissolved amount. Because Pt ions were reduced to atomic state under N_2 atmosphere resulting in a increase of metallic Pt deposit which grew to colloids, a low solubility was observed.

3.3 Pt solubility vs. chemical composition

As shown in Figure 4, Pt solubility decreases according to the order: LHG-5 > LHG-8 > HAP3 > LHG-10 > LSG-91H. The order corresponds to phosphate, silico-phosphate, phospho-fluoride and silicate. Pt solubility is high in phosphate glass and it decreases when SiO added as glass component. By 1979 fluoro-phosphate glasses were found to be laser damaged easily. The reason for it is attributed to a low Pt

solubility in the fluoro-phosphate glass.

For the mechanism of Pt deposition it can be considered that Pt dissolves in form of ion into the melt from the Pt crucible wall, these Pt ion is then reduced into an atomic Pt due to oxygen partial pressure condition, and Pt colloids are formed from the supersaturated atomic Pt resulting finally in a deposition of Pt metal. As is shown by its relationship with the temperature and the atmosphere, Pt solubility is considered to be, therefore, determined by the atomic Pt.

LIII X-ray absorption threshold resonance[2] may be effective to make a distinction between ionic and metallic Pt.

3.4 Effect of RAP treatment on Pt dissolution

Being made clear that Pt deposit occurs due to the presence of atomic Pt, a trial was made to ionize Pt by using RAP treatment. $POCl_3$ gas was used as treatment gas[3].

250ppm Pt has dissolved by bubbling with $POCl_3+O_2$; this Pt was insoluble under O_2 atmosphere at 1,250℃.

(1) Pt ionization by $POCl_3+O_2$ treatment

Figure 5 shows results of UV absorption when dissolved under $POCl_3+O_2$ atmosphere. Absorption can be clearly observed at 255nm, caused by Pt oxychloro-complex by treated with $POCl_3$ resulting in a ionization.

(2) Pt evaporation by $POCl_3+O_2$ treatment

Figure 6 shows variation of Pt amount, Cl_2 and the optical density at 255nm resulted from twice repeated processes for Pt added phosphate glass, LHG-8, consisting of bubbling with $POCl_3+O_2$ followed by keeping in O_2 atmosphere. As shown in the Figure, bubbling with $POCl_3+O_2$ caused a 40% reduction of Pt. Increase of Cl_2 content and coloration is also shown. By returning to O_2 atmosphere, no change of Pt content was observed with decrease in Cl_2 content and coloration.

As mentioned above, it is clear that bubbling with $POCl_3+O_2$ evaporate Pt in form of $PtCl_4$ and reduce Pt dissolved in the glass.

In brief, bubbling with $POCl_3+O_2$ appears to dissolve Pt colloid by a) reducing Pt dissolved through evaporation of Pt and b) ionizing Pt.

4. Conclusions

1) Pt solubility in glasses was measured and determined relationships between this solubility and the temperature, the atmosphere and the chemical composition.

2) The solubility appears to be defined by forming of metallic Pt.

3) Pt inclusion free phosphate laser glasses have been produced successfully by bubbling with $POCl_3+O_2$.

REFERENCES

1) C.W. Fuller, G. Himworth and J. Whitehead, Analyst 96 (1971) 177
2) F.W. Lytle, P.S.P. Wei and G.B. Greegor, J. Chem. Phys. 76 (1979) 4849
3) M. Matsukawa, K. Takeuchi, T. Izumitani, U.S. Pat. Appl. 894,058 (1986)

Table 1 Determination of platinum in phosphate glass.

Pt (ppm)	
Added	Found
50	50
100	100
125	125
150	143
200	188

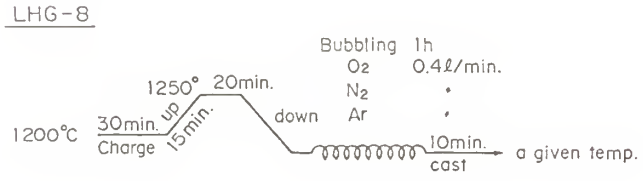

Fig. 1 An example of melting schedule of Pt containing laser glass at a given temp. and a given atmosphere.

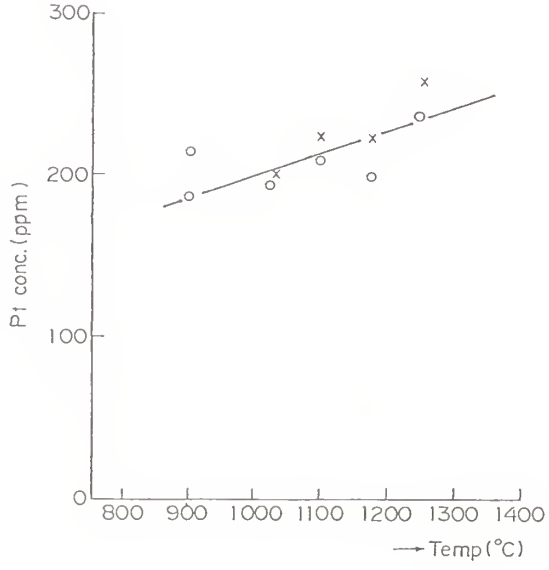

Fig. 2 Relationship between Pt solubility and temperature.

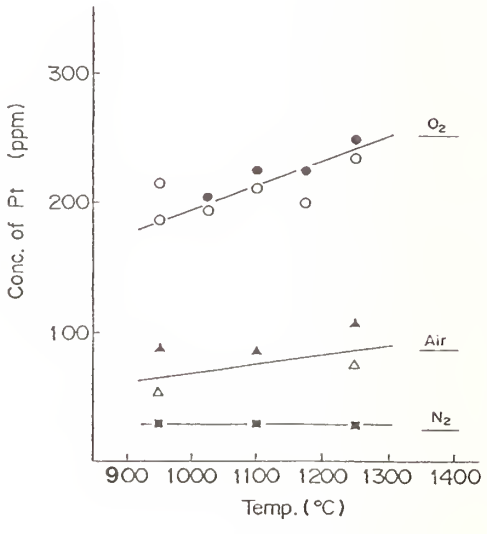

Fig. 3 Effect of atmosphere on Pt solubility

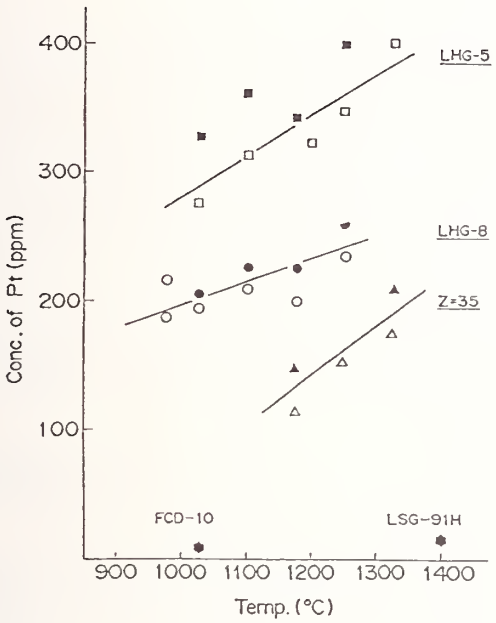

Fig. 4 Relationship between Pt solubility and glass composition

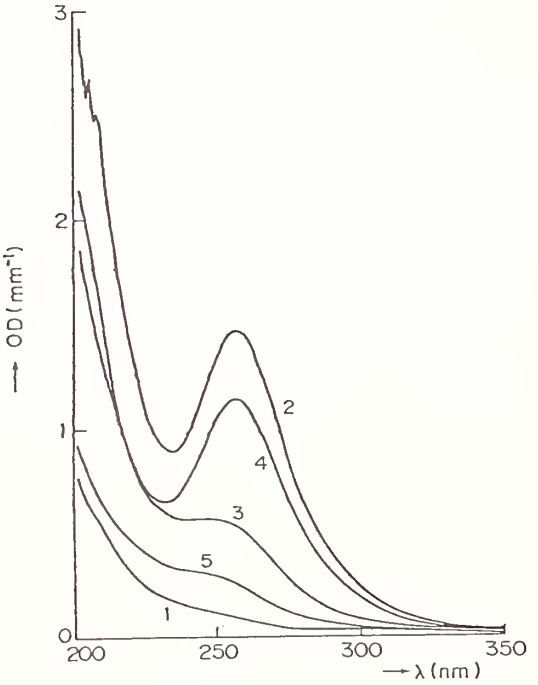

Fig. 5 UV absorption spectrum of the Pt containing glass melted in the $POCl_3 + O_2$ atmosphere.

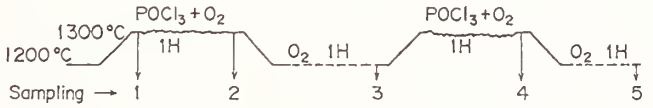

Sample	1	2	3	4	5
Pt (ppm)	180	111	110	60	60
Cl (ppm)	86	511	154	415	86
OD at 255nm	0.14	1.48	0.57	1.15	0.29

Fig. 6 Effect of $POCl_3 + O_2$ bubbling on the Platinum content

A questioner pointed out that there are three parameters which the platinum content depends on (1) temperature, (2) glass composition, and (3) atmosphere. Two of the variables should be specified as constant when the third one is varied. The author replied that the phosphate glass was measured in an oxygen atmosphere, 1250 C or 1300 C or 1000 C depending on the glass. The author did not understand why the phosphate glass had such a high solubility for platinum and the silicate glass did not.

Manuscript Received
2-22-88

Effect of Residual Organic Carbon in Mother Solution of Potassium Dihydrogen Phosphate on Damage Threshold of the Crystals for High Power Lasers

A.Yokotani, T.Sasaki, K.Yoshida, T.Yamanaka S.Nakai and C.Yamanaka

Institute of Laser Engineering, Osaka University
2-6 Yamada-Oka Suita, Osaka 565 JAPAN

We obtained the damage-resistant crystals of potassium dihydrogen phosphate (KDP) by reducing organic impurities in the growth solution. To prevent organic impurity exuded from the wall of growth vessel, Pyrex glass was used. The residual organic impurities which mainly derived from KDP raw powder were reduced by photo-chemical dissociation using the combination of ultraviolet light and an oxidant (hydrogen peroxide). The resultant total organic carbon (TOC) of the solution was less than 0.1ppm. The damage threshold of the crystals grown from this solution were always high (20-22 J/cm^2), which is about three times higher than that of crystals grown by conventional methods.

Key wards : potassium dihydrogen phosphate; crystal; harmonic generation; high power laser; laser fusion; damage threshold; microbes; residual organic carbon; photo-chemical dissociation

1. INTRODUCTION

Potassium dihydrogen phosphate (KDP) crystals are used widely in laser engineering as frequency multipliers to obtain short wavelength lasers. Especially in laser fusion, very large (clear aperture of 20-40cm) KDP crystals are necessary. Fig.1 shows a large KDP crystals which we developed for fusion lasers and the maximum size is $38x42cm^2$ in cross section, 50cm in height. The crystals which was used in laser fusion must have high damage thresholds whereas typical as-grown crystals have bulk laser damage threshold of $6-9J/cm^2$.[1,2]

KDP crystals are usually grown from aqueous solutions in the temperature range between 60-20•C. Microbes are sometimes observed in the KDP solution during the long growth term despite stirring of the solution. If these microbes or their carcasses which are made of organic materials are incorporated into the growing crystals, the damage threshold will show values lower than the intrinsic value because the damage threshold of the organic material is much lower than that of the inorganic materials.[3]

In our previous papers, we detected an organic impurity derived from microbes incorporated in the crystal[4] and we tried to grow KDP crystals in sterilized solution to prevent the growth of microbes in the solution[5]. In the ref.5, we obtained the results that the bulk laser damage threshold of the crystals grown in the sterilized solution was considerably increased as shown in fig. 2. However, the damage threshold was not always high, therefore, we considered that the low damage threshold even when the solution was sterilized might be caused by organic material, a contamination from the wall of growth vessels or organic impurities in the KDP raw powder and deionized water for the solution. Thus in this paper, we tried to reduce the residual organic impurities in the solution to as low as possible during the growth in order to obtain damage resistant crystals.

2. ORGANIC IMPURITY FROM THE WALL OF THE VESSELS

We examined whether the organic impurities exuded from the wall of the growth vessel. The total organic carbon (TOC) in the solution was measured by total organic carbon analyzer DC-80 (Dohman Co.). The sensitivity was 0.05ppm. The measured values were independent of KDP concentration in the solution.

We measured the TOC in the solution during the crystal growth for two types of growth vessels

which made of polyester and pyrex glass. We used the deionized water supplied by an ultra pure water system (NANO pure ; Barnstead Co.) and commercially supplied KDP raw material (guaranteed reagent). The results are shown in fig.3. In the case of polyester vessel TOC in the solution at the growth starting point was about 1ppm and increased about 10 ppm after 40 days of growth period. In the case of Pyrex glass vessel, TOC in the solution did not change at all during 40 days (about 1ppm). Therefore we adopted the Pyrex glass vessel for the following experiments.

Even if the Pyrex glass vessel was used, the prepared solution contained TOC about 1ppm. The deionized water from NANO pure system contained TOC about 0.05ppm. Accordingly we concluded that the KDP raw material contained considerable amount of organic impurities.

3. PHOTO-CHEMICAL DISSOCIATION OF ORGANIC IMPURITIES IN KDP RAW MATERIAL

We tried to remove the residual organic impurities mainly due to KDP raw material by photo-chemical reaction. Preliminary experiments were performed using KDP solution 500ml. The experimental setup was shown in fig.4. KDP solution which contained TOC of approximately 1ppm was introduced into a Pyrex glass tube of 50mm in diameter, 300mm in length. A low pressure mercury lamp with a Suprasil quartz tube and an input power 20W was inserted into the tube. We used two types of oxidant, oxygen (O_2) and hydrogen peroxide (H_2O_2), both of which did not affect on crystal growth. Oxygen gas was supplied into the tube through a gas dispersion. The flow rate was 50 and 100ml/min. The alternative oxidant, H_2O_2, was doped into the solution. The doped quantity were 10ppm, 100ppm, and 1000ppm.

The results are shown in fig.5. In the case of only UV lamp, the effect of photo-dissociation was very small. By adding the oxidant, TOC in the solution was reduced more quickly. Compared to O_2, H_2O_2 was more effective. Hydrogen peroxide of 100 ppm was adequate to oxidize the organic carbon in the solution, and higher H_2O_2 concentration were not more effective (The most adequate concentration of oxidant may depend on the power of mercury lamp). Using H_2O_2, we could reduce TOC in the KDP solution to as little as 0.05ppm which was the limit of the sensitivity of the carbon analyzer.

4. IMPROVEMENT OF THE BULK LASER DAMAGE THRESHOLD BY REDUCING RESIDUAL ORGANIC MATERIALS IN THE SOLUTION

4.1. CRYSTAL GROWTH

We grew KDP crystals from the organic reduced solution by the technique mentioned above. All components of the growth unit contacting to the solution consisted of glass and stainless steel. These components were baked at 400•C for 4 hours to barn out the surface contamination of organic materials before the growth. The KDP solution of 9 liters was introduced into the growth vessel by using an ultra filter with a cut-off molecular weight of 6000, then H_2O_2 of 100ppm was doped. After UV irradiation of 24 hours by Suprasil mercury lamp (20W), we confirmed the residual organic carbon was less than 0.1ppm, after which the growth was started. The crystal was grown by the temperature dropping method (approximately from 55•C to 45•C). The UV lamp did not irradiate the solution during growth, but no microbe existed in the solution. The KDP crystal of which size was about 5x5cm^2 in cross section and about 7cm in height, was grown in about 40 days. An increase in TOC in the solution was not found after growth.

4.2. MEASUREMENT OF THE DAMAGE THRESHOLD

We measured the bulk laser damage threshold of the crystals grown in this method. Measurement of the bulk laser damage threshold was performed using a Nd^{3+}:$LiYF_4$ (YLF) laser (wavelength 1.053μm) in a transverse and longitudinal single mode with a 1-ns pulse. The pulse was focused into Z-cut KDP samples by a lens with focal length 3.5cm.

The surface of KDP crystal were finished by a combination of a diamond turning and wet polishing with 0.05μm aluminum oxide powder. The damage was observed by eye. A He-Ne was also used to identify small damage spots by utilizing the scattering from the damage spots. The focal point was moved shot by shot.(1-on-1 damage)

4.3. RESULTS OF THE DAMAGE THRESHOLD MEASUREMENT

The results of the damage threshold measurement are shown in fig.6. We investigated 5 crystals which were grown from the organic-reduced solution and denoted A,B,C,D, and E for each crystals. The crystals A,B, and C were grown in the solution which contained TOC of 0.6-0.9ppm using only ultra filtration. They have high damage thresholds (14-18J/cm^2). The crystals D and E were grown in the solution of TOC below 0.1ppm, which was prepared using ultra filtration and UV irradiation with H_2O_2. The high damage thresholds (20-22J/cm^2) of the crystals are about three times higher than those in crystals grown by conventional methods (6-9J/cm^2).

The relation between organic impurity concentration in the solution and the damage threshold of grown crystals is shown in fig.7. There is a strong correlation between these two values. The damage threshold tends to saturate with reducing TOC. We think that the threshold of about 20J/cm^2 may be the intrinsic damage threshold of KDP crystal.

5. DISCUSSION AND CONCLUSION

Damage resistant KDP crystals (20-22J/cm^2) could be stably grown by reducing the residual organic impurities in the solution using photo-chemical dissociation. V.V.Azarov *et al.*[6] reported that the damage threshold as influenced by the dislocation in the KDP crystal and the crystalwith many dislocations presented low damage threshold. On the other hand, H.Newkirk *et al.*[2] showed no direct relation between the dislocation in KDP crystals and the damage threshold. We used KDP samples with few dislocations, in which the organic impurities seemed to play a main role in causing bulk laser damage. Therefore, we conclude that the main reason for the low damage threshold of KDP crystals grown by conventional methods is evidently due to organic impurities incorporated in the crystals. This technique can be applied to growth of other crystals from water solution for use in high power lasers.

6. References

[1] Swain, J.E.; Stokowski,S.E.; Milam,D.; Rainer,F.; Improving the bulk laser damage resistance of potassium dihydrogen phosphate crystals by pulsed laser irradiation. Appl. Phys. Lett. 40; 1982 February. 350 p.

[2] Newkirk,H; Swain,J.E; Stokowski,S.E.; Milam,D. X-ray topography of laser-induced damage in potassium dihydrogen phosphate crystals. J. Cryst. Growth 65; 1983. 651p.

[3] Laser Program Annual Repts.; Lawrence Livermore National Lab. UCRL-50021-82. 1982. 7-29.

[4] Yokotani,A.; Nishida,Y.; Fujioka,K.; Sasaki,T.; Yamanaka,T.; Yamanaka,C. A chromogenic limulus test for detection of micobes that decreases the laser damage threshold of potassium dihydrogen phosphate crystals. J. of Appl. Phys. 61(9); 1987 May. 4696p.

[5] Yokotani,A.; Sasaki,T.; Yashida,K.; Yamanaka,T.; Yamanaka,C. Improvement of the bulk laser damage threshold of potassium dihydrogen phosphate crystals by ultraviolet irradiation. Appl. Phys. Lett. 48; 1986 April. 1030p.

[6] Azarov,V.V.; Atroshchenko,L.V.; Danileiko,Yu.K.; Kolybaeva,M.I.; Minaev,Yu.P.; Nikolaev,V.N.; Sidrin,A.V.; Zakharkin,B.I. Influence of structure defects on the internal optical strength of KDP single crystals. Sov. J. Quantum. Electron. 15; 1985 January. 89 p.

Fig.1. Large KDP crystals developed for laser fusion at ILE. (38cm x 42cm in cross section, 50cm in height)

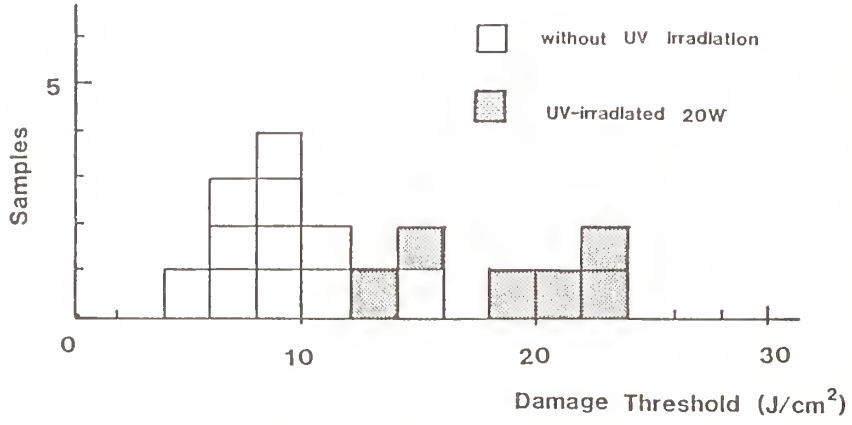

Fig.2. Damage threshold of KDP crystals which grown in the sterilized and the unsterilized solutions.

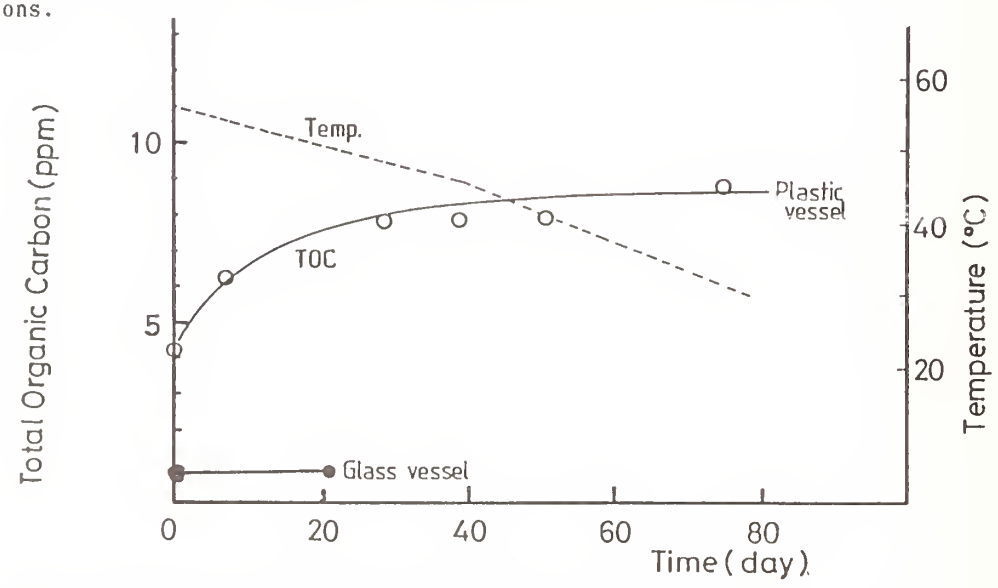

Fig.3. Change in TOC in the KDP solution during the growth.

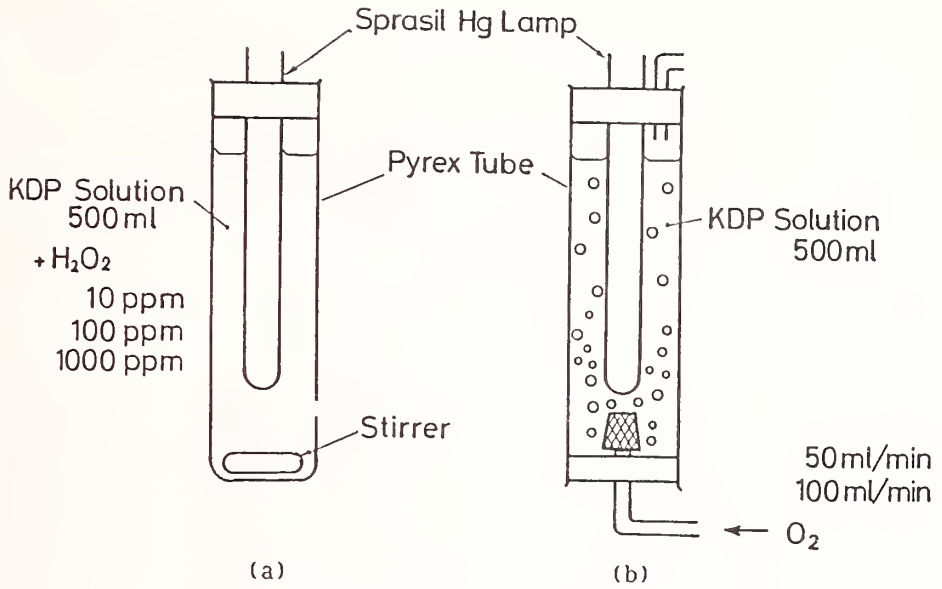

Fig.4. Experimental setup of the preliminary experiments for reducing the organic impurities using UV light.
(a) Photo dissociation by using oxidant H_2O_2 and(b)O_2.

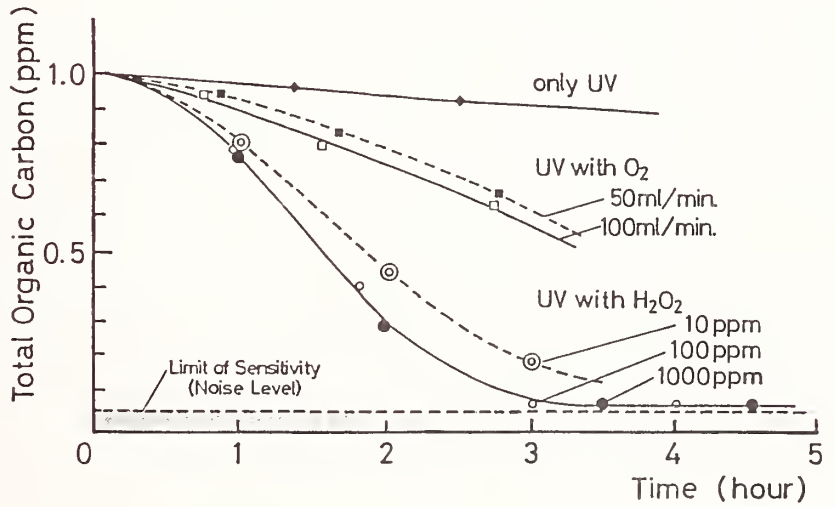

Fig.5. Results of the preliminary experiments.

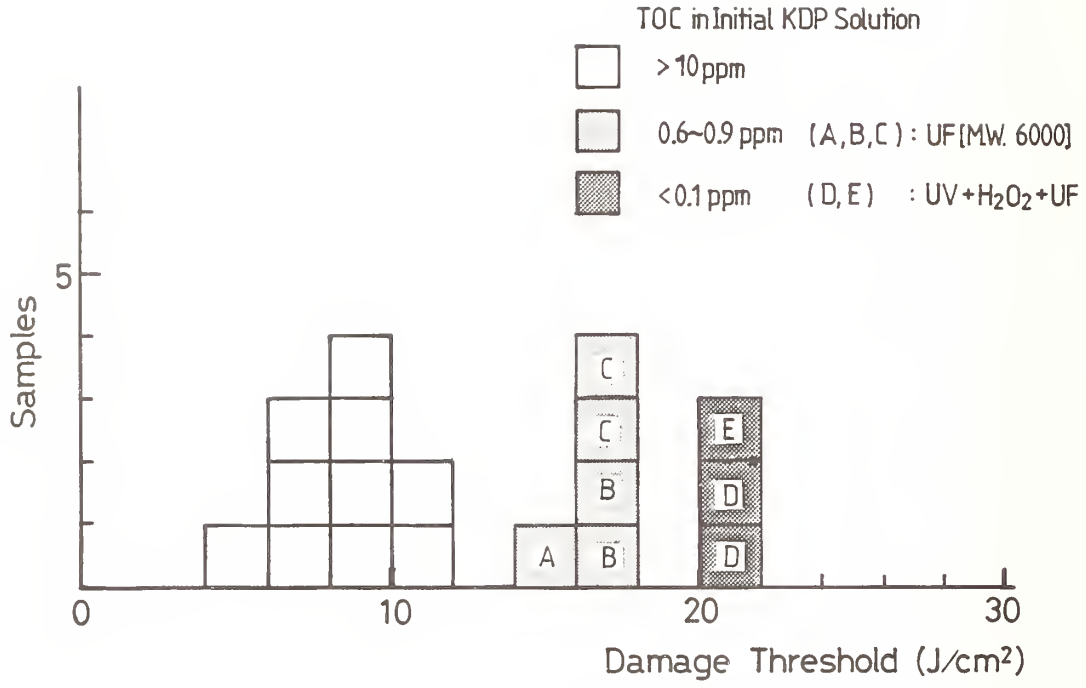

Fig.6. Histogram of the bulk laser damege threshold measured for KDP crystals grown in the organic-reduced solution.

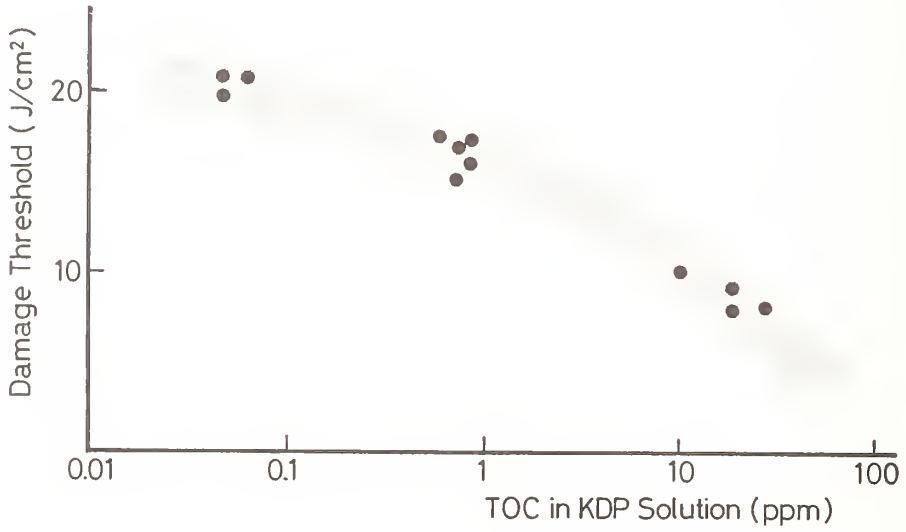

Fig.7. Relation between the damage threshold of KDP crystals and TOC concentration in the solution.

Manuscript Received
2-8-88

Laser Damage on Zinc Selenide and Cadmium Telluride using the Stanford Mark III Infrared Free Electron Laser

Stephen V. Benson, Eric B. Szarmes, Brett A. Hooper[1], Edwin L. Dottery[2], John M. J. Madey

Stanford Photon Research Laboratory,
Stanford University, Stanford, CA 94305

We have encountered intracavity optical damage, and have estimated fluence damage thresholds, in samples of CVD zinc selenide which have been used as intracavity Brewster plate output couplers for the Stanford Mark III infrared free electron laser. For spot radii of approximately 1.4 mm and wavelengths in the range of 3 μm to 4 μm, we have determined damage thresholds ranging from 8.2 J/cm^2 to 11.3 J/cm^2 for optical macropulses of 2 μs duration and 15 Hz repetition rate, with corresponding circulating micropulse intensities on the order of 5 GW/cm^2; in most cases catastrophic damage seemed to occur due to the coalescence of tiny pits in the surface. We also report on damage threshold measurements for uncoated cadmium telluride at 3.2 μm, and observe a fluence dependent damage threshold of approximately 6.3 J/cm^2 for macropulses scaled (via $\tau^{1/2}$) to a 1 μs duration. Finally, we observe a lowering of the damage threshold of uncoated CdTe in the presence of the laser harmonics, presumably due to free carrier absorption of the fundamental.

Key Words: Brewster plate; catastrophic damage; CdTe; chemical vapor deposition (CVD); free electron laser; macropulse; micropulse; ZnSe

1. Introduction

Intracavity optical elements for free electron laser oscillators are necessarily restricted to materials which possess high vacuum stability, mechanical and optical stability under extreme levels of gamma and neutron radiation, and appropriate optical qualities over a generally wide wavelength range. Ultimately, they must withstand very intense circulating optical radiation, and it is this quality which in principle limits the power available from the devices.

The Stanford Mark III free electron laser uses a nearly confocal, 1.8 meter broadband optical cavity with silver coated, diamond turned copper mirrors and Brewster plate output coupling using a suitable uncoated dielectric. In the past, the choice for this Brewster plate has been CVD zinc selenide, which initially was found to be suitable in all respects. The configuration of the vacuum chamber allows for the insertion of other intracavity elements, and a cadmium telluride electro-optic loss modulator is being considered for future cavity dumping experiments. The laser is driven by a 45 MeV RF linear accelerator which typically yields macropulses of a few microseconds duration at a repetition rate of 15 Hz, each macropulse consisting of a train of roughly picosecond duration micropulses repeated at the RF frequency of 2.857 GHz. The design range for the cavity is 1 μm to 8 μm, and the device has been operated in wavelengths ranging from 1.5 μm to 5.5 μm with typical spectral widths under 1%. A complete description of the Mark III free electron laser can be found in the literature [1,2].

As indicated, the choice of CVD zinc selenide as an output coupler was motivated by several factors. It is stable under high vacuum and is sufficiently lossless and dispersionless over the entire wavelength range of the laser. Our samples have shown no evidence of physical or optical degradation due to bremsstrahlung and neutrons on the order of several hundred rad/hour, and have survived circulating optical macropulse fluences up to 15 J/cm^2 (micropulse intensities on the order of 5 GW/cm^2). However, in August of 1987 the electron gun of the Mark III accelerator was modified to produce a more intense beam, and the damage threshold of zinc selenide was quickly surpassed. [We are presently operating with calcium fluoride Brewster plates which have survived circulating macropulse fluences of

---

[1]Laser Institute, Veterans Administration and University of Utah Medical Centers, Salt Lake City, Utah.

[2]Department of Physics, United States Military Academy, West Point, NY 10996

58 J/cm^2 and have not appeared to have appreciably radiation-darkened after several hundreds of hours of operation.] Up until the present date, the laser has not been operated with an intracavity cadmium telluride element.

The purpose of this paper is to describe the optical damage which was observed in several of our zinc selenide Brewster plate output couplers; we first explain the output coupling scheme and then present estimates for the corresponding fluence damage thresholds. We also describe an experiment we have developed to assess the damage threshold of cadmium telluride, and we present preliminary damage threshold measurements on uncoated cadmium telluride samples. Finally, we report observations of the lowering of the CdTe damage threshold in the presence of the laser harmonics, which bears directly upon experiments using CdTe as an intracavity element for free electron lasers.

2. Output Coupling Method

The output coupling method of the Mark III is unique to all currently operating free electron lasers. A schematic view of the system is shown in figure 1. The optical mode is horizontally polarized and broadband output coupling is achieved by inserting an uncoated transparent plate near Brewster's angle. The angle of this plate can then be varied by $\pm 1°$ to provide a small range of output couplings. The mechanical configuration allows for one of several Brewster plates to be inserted so that different materials or angles can be chosen, and the entire assembly is housed in a vacuum chamber that maintains a vacuum of 5 microTorr. In order to provide the experimenter with all of the outcoupled power, one of the Brewster plates is provided with an external second-reflection cavity mirror which serves to reflect the leftward travelling macropulses back through the Brewster plate. The longitudinal position of this mirror is chosen so that micropulses from the outcoupled macropulses are interleaved, thereby doubling the average power during the macropulse.

The Brewster plates are manufactured with surfaces parallel to an accuracy of 5 arc seconds and are polished to a scratch-dig of 20-10 and a flatness of $\lambda/100$ at 10.6μm. However, due to the finite thickness of the plates (typically 1 - 2 mm), the front and back surface reflections on a single pass are displaced transversely on the order of a millimeter and temporally by several tens of picoseconds; it is sufficient to consider only those two reflections. As a result, the outcoupled macropulse is slightly broadened in the horizontal direction. Furthermore, the curvature of the second-reflection mirror leads to a skewed reflection of one of the beams relative to the other (greatly exaggerated in figure 1), which complicates the use of this mirror. These points will be discussed more fully in section 4.

3. Zinc Selenide Damage

3.1. General Description

Intracavity optical damage was encountered on a total of eight zinc selenide Brewster plates inserted at angles between 59.6° and 61.6° and operated at wavelengths in the range of 3 μm to 4 μm. Seven of these exhibited manifest catastrophic damage in which laser output decreased by as much as 80% and cavity losses increased by as much as a factor of two, usually in under one second. Catastrophic in this sense is taken to mean self-quenching. In the one exception, the damage was less severe, with output power dropping only slightly and cavity losses increasing by less than 40%.

We found that the thresholds for catastrophic damage are primarily fluence dependent. In particular, we operated the laser in one instance for several hours at saturation with macropulse widths under 1 μs, observing no evidence of damage. However, almost immediately after increasing the pulsewidth to 2 μs the power dropped and catastrophic damage was induced in the Brewster plate. Increasing the fluence in this manner does not alter the modal spot size, the peak intensity of the micropulses, the repetition rate of the micropulses, or the average intensity of the macropulses. Accordingly, no dependence on these quantities could be established, and so the damage thresholds reported in paragraph 3.3 are presented in units of fluence.

3.2. Morphology

All instances of optical damage to the Brewster plates appeared to be thermally induced, beginning at absorbing defects near the surfaces and leading in cases of catastrophic damage to the coalescence of molten pits or thermal fracturing. Vacuum preparation of the Brewster plates involved only gentle blowing of dust off of the surfaces or, in a few cases, careful drag wiping with methanol. In six cases out of eight, the damage started on the surface farther from the cavity mirror; in the other two cases the damage started on the nearer surface. The prevalence of surface damage

indicates a surface absorption mechanism not present in the interior of the plates. Such absorption could occur as the consequence of grinding and polishing, for example, by the inclusion of microscopic particles of polishing compound. It is also possible that surface contaminants could play a role. As an example, Lewis and Arthur [3] have performed investigations on the effects of extrinsic surface absorption processes on the infrared properties of CVD zinc selenide. In particular, they measured the infrared spectral transmittance of a sample exposed to laboratory air for a few days and found a dominant absorption around 2900 cm^{-1} (3.4 μm) due to $-CH_n$ vibrational modes. It is possible that hydrocarbons were absorbed in our samples, either from the methanol or directly from the air, which acted as nuclei for subsequent thermal damage; this hypothesis is consistent with the observation of surface defects in our samples and the fact that the samples were operated in the vicinity of 3.4 mm when catastrophic damage was induced.

The photomicrograph in figure 2a shows how optical damage is induced at a large number of random absorbing sites on the surface of a zinc selenide plate. These damage sites appear as small molten pits (fig. 2b) with evidence of thermal deformation occurring in the material between them. The growth of these damage sites can lead to catastrophic damage in the form of a coalesced molten crater (fig. 3), or in the form of bulk fracture due to thermal stress (fig. 4a,b). However, it is not clear that the fracture originates between two pits; in particular, figure 5b shows a single molten pit with evidence of fracture lines at the bottom, although catastrophic damage in this case was clearly due to the coalescence of pits (fig. 5a).

There are notable differences in the two forms of catastrophic damage. In particular, the density of surface pits is much smaller in the fractured case, and the ring of discoloration (actually a surface film) which appears around the damage crater in figure 3 is absent in figure 4a. Furthermore, the damage crater in figure 4b consists of a very clean fracture which contrasts with the 'dirty' crater appearing in figure 3. Finally, of the seven cases of catastrophic damage observed in our zinc selenide Brewster plates, thermal fracturing occurred in only two cases. This leads us to conclude that a coalesced molten crater is the primary form of catastrophic damage, unless fracturing quenches the laser before further pitting and melting can occur. All of these types of damage are consistent with a fluence dependent damage threshold.

3.3. Damage Thresholds

Fluence damage thresholds for the various types of damage were derived from five out of eight ZnSe Brewster plates for macropulses of 2 μs duration. The relevant data are summarized in table 1. The damage thresholds were obtained by measuring the outcoupled energy with a pyrometer and dividing by the round trip output coupling calculated for the given angle of incidence. Corrections were included for the losses on all of the transport mirrors. The second-reflection mirror was employed in all cases, and the angles were accurately inferred using an alignment helium-neon laser outcoupled through the side Brewster window. The $1/e^2$ beam radii ω were calculated from the structure of the mode, and the circulating beam area was taken as $\pi\omega^2/2$. Finally, the damage thresholds were adjusted for *normal incidence* by rescaling the area by the obliquity factor, $\cos(\theta_{incidence})$.

Table 1. CVD Zinc Selenide Damage Thresholds
(Adjusted for Normal Incidence)

Sample	Wavelength (μm)	Beam Radius (mm)	Angle of Incidence	Damage Threshold 2 μs; (J/cm^2)	Run Time Before Onset of Damage	Type of Damage
1	3.0 - 4.0	1.4	61.6°	**11.3±1.6**	< 10 min	(b)
2	3.0-4.0	1.4	61.6°	**11.3±1.6**	<1 1/2 hr	(c)
3	3.6	1.39	60.4°	**10.8±0.9**	< 20 min	(a)
4	3.2	0.31	59.6°	**8.7±0.6**	< 2 hr	(a)
5	3.33	1.34	61.6°	**8.2±0.6**	< 6 hr	(b)

(a), catastrophic coalescence of pits; (b), catastrophic fracture; (c), non-catastrophic pitting

The errors in the damage thresholds for samples 1 and 2 account mainly for the imprecise knowledge of the wavelengths, and hence the beam areas, in those cases. The errors in the remaining thresholds are due to a partial vignetting of the outcoupled beam in the transport system for which we were able to derive a correction factor. All of the thresholds are scaled by this factor, but it was only determined to within eight percent.

The dominant variable in the thresholds for catastrophic damage appears to be in the run time before onset of damage. There is no apparent dependence of threshold on the type of damage. Since pitting leads to both types of catastrophic damage and this damage is only observed after running for some time, the lowest reported threshold - 8.2 J/cm^2 - may be closer to the actual value for the formation of pits alone. Finally, we note that the actual micropulse fluences corresponding to the macropulse damage threshold of 8.2 J/cm^2 were approximately 1.4 mJ/cm^2. Autocorrelation measurements of the micropulse durations have yielded minimum pulsewidths of 500 fs, so that scaling the macropulse damage threshold down to the micropulse duration using the $\tau^{1/2}$ scaling law[§] would yield a micropulse threshold of 4.1 mJ/cm^2. Since this threshold is larger than the actual micropulse fluence, we conclude that the $\tau^{1/2}$ scaling law is at least consistent with our observation that damage was not due to micropulse effects.

4. Cadmium Telluride Damage

The circulating intensities which are currently achievable in the Mark III free electron laser using calcium fluoride Brewster plates are potentially great enough to damage other intracavity optical elements. Since we are considering the use of a cadmium telluride electro-optic cell for future cavity dumping experiments, we have undertaken a project to characterize the damage threshold of cadmium telluride and have performed preliminary damage studies on uncoated cadmium telluride samples in air at 3.2 μm, which we report on here. The experimental configuration is conventional, but the Mark III pulse structure provides several independently adjustable quantities which can be varied to determine the damage thresholds under different experimental controls. These variable quantities are summarized in figure 6.

4.1. Experimental Procedure

The experimental beamline is shown in figure 7. The horizontally polarized beam enters the apparatus with a spot radius of 8.4 mm and is collimated to a radius of 1.58 mm in a compromise between vignetting and damage on the downstream optical components. A germanium Brewster plate filters the coherent laser harmonics and a zinc selenide pickoff plate samples the incident beam for the energy measurement using a Ge:Au detector; this detector is calibrated to the full pulsewidth at the start of each damage test using a pyrometer placed at the sample position.The cadmium telluride sample is located on a micrometer stage behind the final focusing lens, and sample transmission is monitored with a second Ge:Au detector. Neutral density filters ensure that these detectors remain below saturation.

Preliminary damage threshold measurements were concerned with isolating fluence effects from peak intensity effects. Accordingly, the procedure involved placing the sample at a fixed position beyond the focus of the lens (ensuring front surface damage), and then slowly increasing the macropulse width from its minimum value until damage occurred. The procedure was then repeated at virgin sites on the sample for various spot sizes, with sample preparation involving only the gentle blowing of dust off of the surface. In all cases, damage was indicated by a drop in the transmission Ge:Au detector signal followed almost immediately by arcing and pitting; this occurred *only after* increasing the macropulse width beyond a certain value, with peak and average intensities varying usually by no more than 15 %. The corresponding macropulse energies were obtained by integrating the oscilloscope traces for the calibrated Ge:Au sampling detector.

4.2. Damage Thresholds

The 3.2 μm diffraction limited beam used for these damage tests was outcoupled from the laser using a 66°, 1mm thick calcium fluoride Brewster plate yielding up to 30 mJ/macropulse. The second-reflection mirror was not employed. The macropulse energies were determined in the manner outlined above and the beam areas $\pi\omega^2/2$ were calculated from Gaussian propagation formulae based on measurements of waist radius and distances to the sample. Tables

---

[§]This scaling law should apply if the damage is due either to surface melting or thermal stress induced fracture, in which the onset of damage is determined either by the temperature rise or temperature gradient at the surface.

2a,b summarize the results of the damage tests. The three passes in table 2a were performed with the coherent harmonics filtered out of the beam, while the three passes in table 2b included those harmonics.

The finite thickness of the output coupler was neglected in the calculations of beam area. The peak micropulse intensities were calculated from peak average powers measured from the oscilloscope traces for the sampling detector and assume a 1 ps micropulse duration. The errors in the fluence values are derived from a 12 % random error observed in previous damage tests on cadmium telluride, and the final column in each of tables 2a,b gives the fluence damage thresholds scaled from the actual pulsewidths to a 1 μs pulsewidth assuming the $\tau^{1/2}$ scaling law. This law should yield fairly accurate scalings since the pulsewidths are already on the order of 1 μs.

Table 2a. Damage Thresholds for Uncoated Cadmium Telluride; **no harmonics**

Pass #	Spot Size (μm)	Peak Micropulse Intensity (GW/cm^2)	Damage Fluence (J/cm^2)	Macropulse Width (μs)	Damage Fluence 1 μs; (J/cm^2)
1	270	1.9	5.0 ± 0.6	0.45	7.6 ± 0.9
2	370	1.3	5.2 ± 0.6	0.70	6.2 ± 0.7
3	420	0.9	8.5 ± 1.0	1.8	6.3 ± 0.8

Table 2b. Damage Thresholds for Uncoated Cadmium Telluride; **harmonics included**

Pass #	Spot Size (μm)	Peak Micropulse Intensity (GW/cm^2)	Damage Fluence (J/cm^2)	Macropulse Width (μs)	Damage Fluence 1 μs; (J/cm^2)
1	160	2.3	5.6 ± 0.7	0.39	9.0 ± 1.1
2	300	0.7	4.5 ± 0.5	1.1	4.3 ± 0.5
3	500	0.3	2.9 ± 0.3	1.8	2.2 ± 0.3

We see that the 1 μs fluence thresholds from table 2a are quite independent of peak intensity and show only a slight decrease for increasing spot size; this is consistent with the observation that damage was primarily due to the macropulse fluence. [We also find that the damage fluences scaled from 1 μs to 1 ps via $\tau^{1/2}$ are larger than the actual micropulse fluences encountered, so that the $\tau^{1/2}$ scaling law is not inconsistent with our observations.] In comparison, table 2b shows a marked decrease of damage threshold with spot size, and the thresholds are significantly lower than those for comparable spot sizes in the case where harmonics were filtered. This leads us to speculate that free carriers produced by the coherent laser harmonics reduce the damage threshold by causing increased absorption of the fundamental. The most important contribution to free carrier generation is expected to be from the third harmonic which contains 0.03% of the power at the fundamental. The effects are difficult to quantify, however, because the propagating mode structure of the harmonics is unknown, and different wavelengths will focus to different incident intensities as the sample position is varied.

4.3. Future Experiments

Considerations for future characterization of the damage threshold include holding the macropulse width constant and varying the incident intensity by means of crossed polarizers placed in front of the ZnSe pickoff plate. This will allow the ratio of sampling and transmission detector signals to remain constant so that the latter can be used to accurately monitor the onset of damage as the incident intensity is varied. We will continue to concentrate on multishot, single-site damage studies since this is the realistic mode of operation in a free electron laser. We also intend to investigate average power effects independently of peak intensity by employing the second-reflection mirror to outcouple the entire macropulse. In this case, the skewed reflection from this mirror can be appropriately eliminated by means of an aperture so that the incident mode size can be accurately assessed.

As a final note, we record here that the silver coated, diamond turned copper cavity mirrors used in our laser have exhibited *no evidence* of any damage under incident fluences up to 58 J/cm^2, which fluence was achieved using a 62° calcium fluoride Brewster plate. We hope to increase this fluence to 100 J/cm^2 in the near future in order to demonstrate an even higher damage resistance for these mirrors under the unique pulse structure and wavelength regime of our laser.

5. Summary and Conclusions

In this paper we have described observations of intracavity damage on samples of CVD zinc selenide used as output couplers in the Stanford Mark III free electron laser, and we have derived fluence damage thresholds ranging from 8.2 J/cm^2 to 11.3 J/cm^2 for macropulses of 2 μs duration and wavelengths in the range of 3 μm to 4 μm. Spot sizes were approximately 1.4 mm and peak micropulse intensities were on the order of 5 GW/cm^2. The optical damage seemed to occur at defects near the surfaces in the form of pitting and melting and led in cases of catastrophic (self-quenching) damage to a coalesced molten crater or bulk fracture due to thermal stress. The initiation of surface pitting may be correlated with hydrocarbon absorption in the surfaces [3], since the vibrational modes of -CH_n are consistent with the wavelengths at which damage was observed. However, this hypothesis cannot be confirmed with the present data because no correlations were obtained among the wavelength, damage threshold, or run time before onset of damage.

We have also presented preliminary results in an experiment to characterize the damage threshold of cadmium telluride. Damage thresholds for uncoated samples in air at 3.2 μm were approximately 6.3 J/cm^2 for macropulses scaled to a 1μs duration using the $\tau^{1/2}$ law, and these thresholds were generally independent of spot size and peak intensity for cases in which the laser harmonics were filtered from the beam. However, tests including the laser harmonics yielded significantly lower damage thresholds, leading us to speculate that free carriers produced by the coherent laser harmonics reduced the damage threshold by causing increased absorption of the fundamental. Finally, we described future experiments in which other parameters such as peak intensity and average macropulse power will be varied in order to map the damage threshold dependence on these parameters.

We wish to gratefully acknowledge II - VI Incorporated, Saxonburg, PA for donating the cadmium telluride samples used in these damage studies. We would also like to thank Brian Newnam and Dave Deacon for helpful discussions, and James Haydon for operating the Mark III accelerator during the cadmium telluride tests. This work was supported by Army contract DAAL03-86K-0122 and Los Alamos National Laboratory contract 9XFH1725G1.

7. References

[1] Benson, Stephen. V.; Schultz, John; Hooper, Brett A.; Crane, Richard; Madey, John M. J.; Status Report on the Stanford Mark III Infrared Free Electron Laser; presented at the ninth international FEL conference, Sept. 1987, Williamsburg, VA.

[2] S. V. Benson, J. M. J. Madey, J. Schultz, M. Marc, W. Wadensweiler, G. A. Westenskow; Nucl. Inst. and Meth. A250 (1986) 39.

[3] K. L. Lewis and G. S. Arthur; Surface and Free Carrier Absorption Processes in CVD Zinc Selenide; Nat. Bur. Stand. (U.S.) Spec. Publ. 669, 1982.

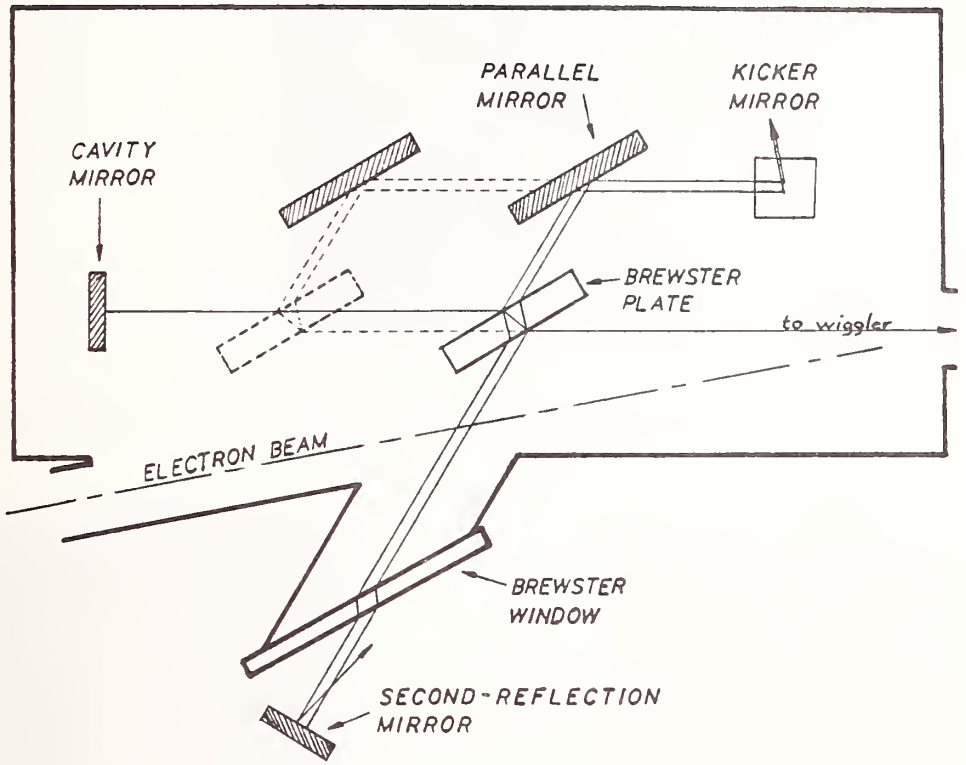

Figure 1. Output coupling system for the Mark III free electron laser.

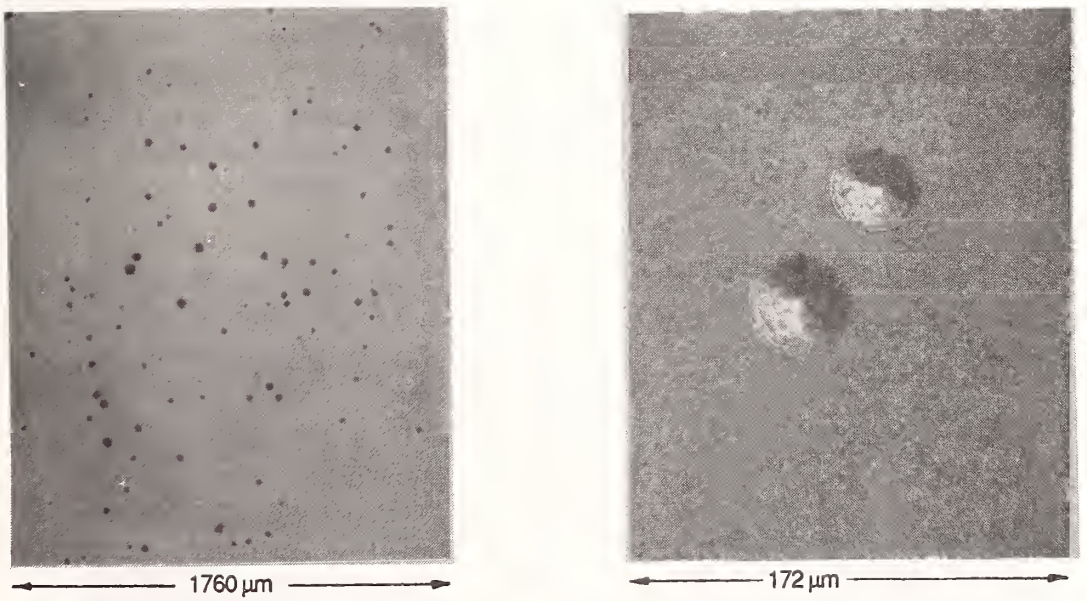

(a) (b)

Figure 2. Non-catastrophic surface pitting in a sample of CVD ZnSe; (a), photomicrograph showing random pitting; (b), photomicrograph showing structure of individual pits. Note the distortion between the pits and the occurrence of smaller damage damage sites.

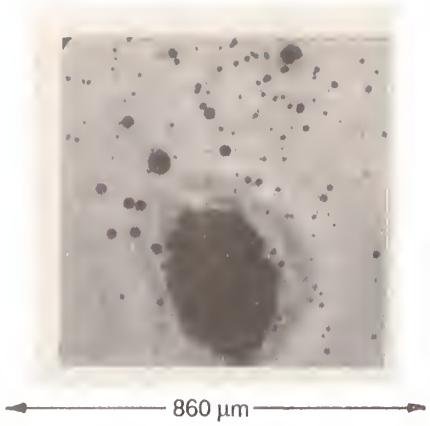

Figure 3. Photomicrograph of catastrophic damage in a sample of CVD ZnSe due to coalescence of molten pits

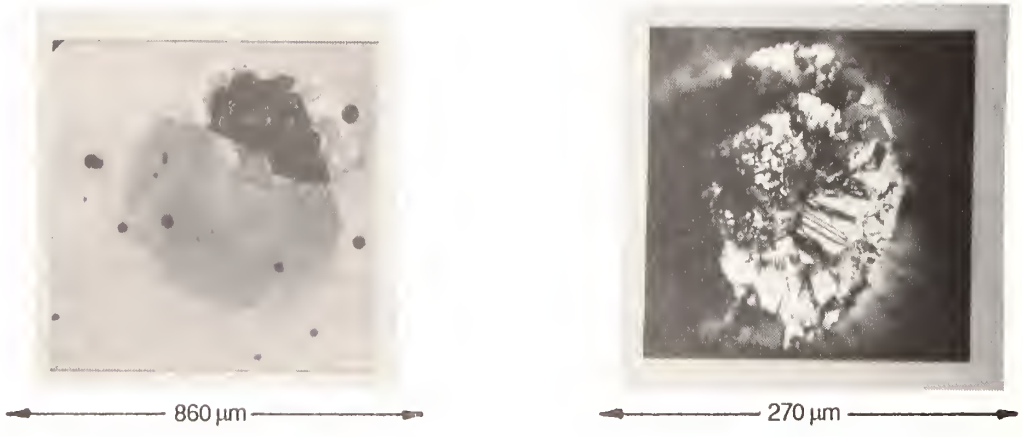

Figure 4. Catastrophic damage in a sample of CVD ZnSe showing thermal fracture; (a), photomicrograph showing large scale structure of damage site; (b), image in polarized light showing clean, fractured pit.

Figure 5. Electron micrographs of catastrophic damage in ZnSe; (a), crater showing coalescence of pits around the edges; (b), single pit showing fracture lines at the bottom.

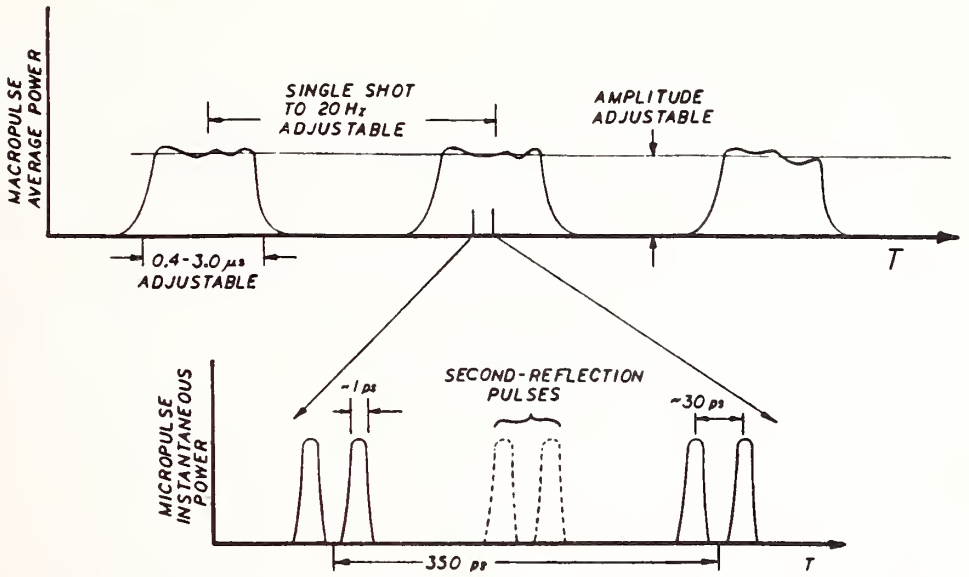

Figure 6. Optical output pulse structure of the Mark III free electron laser

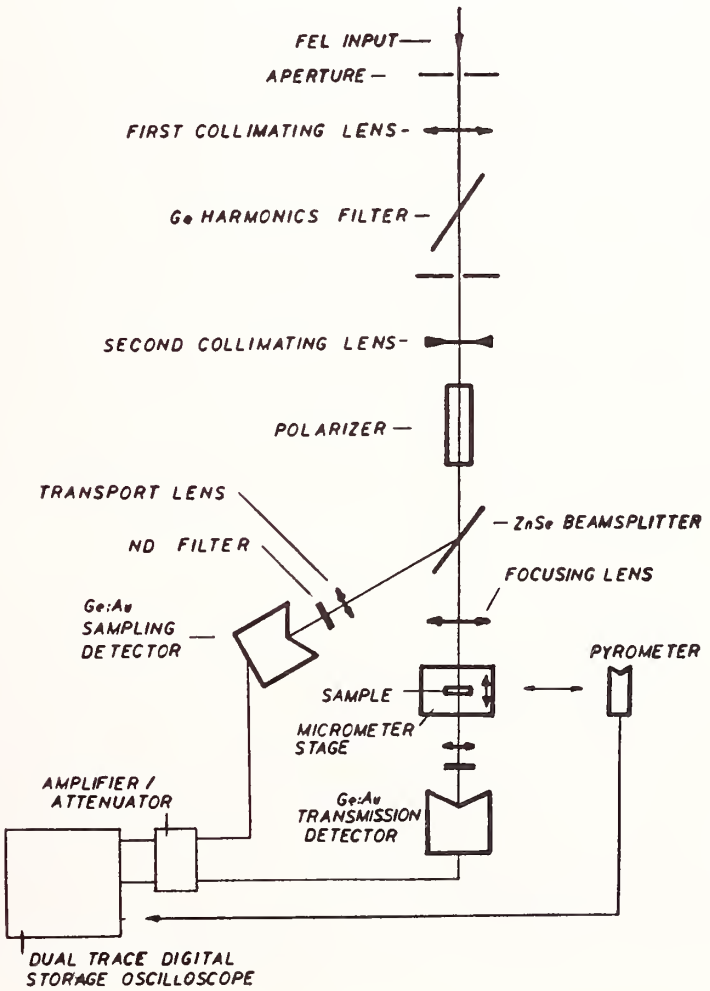

Figure 7. Optical beamline for damage studies on cadmium telluride

Manuscript Received
1-20-88

Laser Damage in Silicon Avalanche Photodiode

M.A. Acharekar

Litton Systems, Inc.
Laser Systems Division
Orlando, FL 32854-7300

Silicon Avalanche photodiodes (APDs) are widely used for detection of visible and near infrared laser radiation. The laser damage of the APD investigated using a Q-switched Nd:YAG laser pulse of 15 ns duration is reported in this paper. Two types of laser damage threshold measurements were performed on the APDs. The minimum flux level of 1064 nm laser radiation resulting in degraded signal-to-noise ration (SNR) is considered the primary type of detector damage. This type of detector damage can be defined in terms of a rearrangement of electrical charge in the semiconductor resulting in increased noise current and therefore poor SNR. The second type of laser damage threshold measurements were performed where the laser power on the detector was increased to the level producing not only a decrease in SNR, but also resulting in visible deformation on the surface of the detector. This type of detector damage can be defined in terms of a rearrangement of some of the atoms of the crystal due to the thermal effects of the laser pulses.

Key Words: APD; Avalanche Photodetector; detectors for Nd:YAG laser; Laser damage threshold of APD; Silicon Detector.

1. Introduction

Silicon avalanche photodiodes (APDs) are widely used for detection of visible and near infrared laser radiation. The laser damage has been studied for the detector materials (see ref. 1-5). However, the laser damage threshold measurement data for the APD have not been sufficiently studied. Kruer et.al., (ref. 6) at the Naval Research Laboratory, Washington, D.C., investigated silicon P-N photodiodes and reported a damage threshold of 3.8 giga watts per sq. cm for 17 nsec pulses of 1.06 micron. The damage threshold data for the APD was collected at Litton Laser Systems, Orlando, FL.

A brief description of the detector configuration and the theory of operation is provided in this section.

A silicon photodiode, a solid-state device that converts incident light into an electric current, consists of a shallow diffused P-N junction, normally a P on N configuration (ref. 7). Diffused silicon sensors can be divided into four different types depending upon their processing method as shown in figure 1.

1) Planar Diffusion Type: In this configuration, the junction surface of the silicon chip is passivated by a thermally grown oxide layer (SiO_2) yielding photodiodes with a low level dark current.

2) Low-Capacitance Planar Diffusion Type: This is a high speed version of the planar diffusion type photodiode. This type makes use of highly pure, high resistance N-type material to enlarge the depletion layer and thereby decrease the junction capacitance, lowering the response time.

3) PIN Type: This improved version of the low capacitance planar diffusion device makes use of an extra high resistance I layer between the P and N layers to improve the response time.

4) Avalanche Type: If a reverse bias is applied to a P-N junction and a high field formed within the depletion layer, photon carriers will be accelerated by this field. They will collide with atoms in the field and produce secondary carriers. These secondary carriers will also collide and produce more carriers. The process occurs repeatedly and is known as the avalanche effect. Since it results in the signal being amplified, this type of device is ideal for detecting extremely low levels of light.

A brief theory of operation of the silicon photodiode (ref. 8, 9) is also provided in this section. Figure 2(a) shows a cross-section of a photodiode. The P-layer material at the light sensitive surface and the N material at the substrate form a P-N junction which operates as a photoelectric converter. The usual P-layer for a silicon photodiode is formed by selective diffusion of boron to a thickness of approximately 1 micron, and the neutral region at the junction between P and N layers is known as the depletion layer. By varying and controlling the thickness of the outer P-layer, bottom N-layer and substrate N-layer, as well as the doping concentration, the spectral and frequency responses can be controlled.

PHOTODIODE TYPES

TYPE	CONSTRUCTION	FEATURES
PLANAR DIFFUSION TYPE	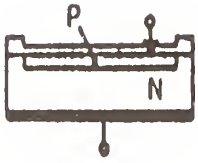	SMALL DARK CURRENT
LOW CAPACITANCE PLANAR DIFFUSION TYPE	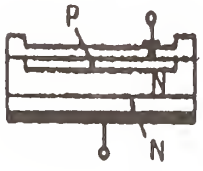	SMALL DARK CURRENT FAST RESPONSE
PIN TYPE	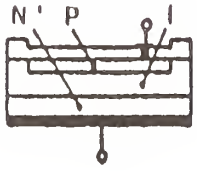	ULTRA-FAST RESPONSE
AVALANCHE TYPE	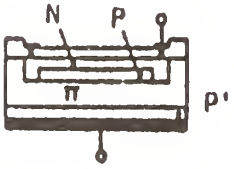	HIGH GAIN ULTRA-FAST RESPONSE

FIGURE 1.0

(a) PHOTODIODE CROSS-SECTION

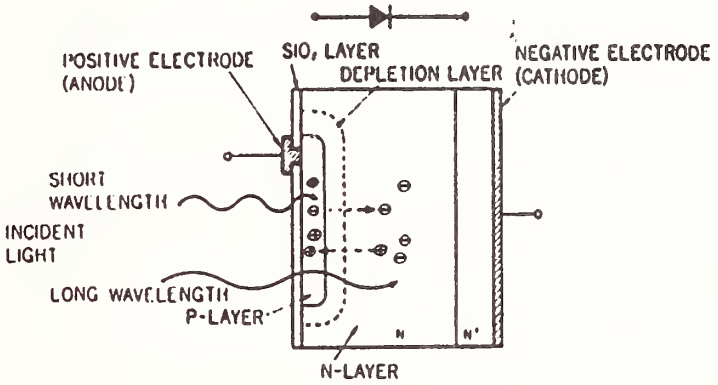

(b) PHOTODIODE P-N JUNCTION STATES

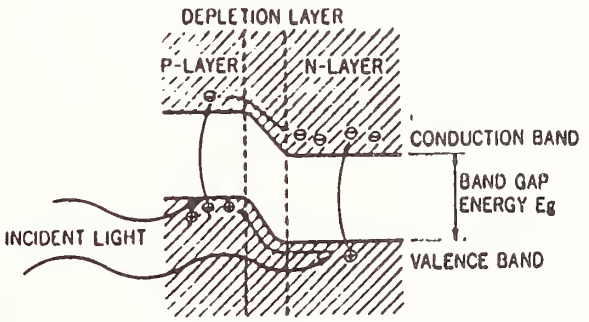

FIGURE 2.0

When light is allowed to strike a photodiode, the electrons within the crystal structure become stimulated. If the light energy is greater than the bandgap energy Eg, the electrons are pulled up into the conduction band, leaving holes in their places in the valence band (see figure 2(b)). These electron-hole pairs occur throughout the P-layer, depletion layer and N-layer materials. In the depletion layer the electric field accelerates the electrons toward the N-layer and holes toward the P-layer. Of the electron-hole pairs that are generated in the N-layer, the electrons, along with the electrons that have arrived from the P-layer, are left in the N-layer conduction band, while the holes diffuse through the N-layer up to the P-N junction while being accelerated, and collected in the P-layer valence band. In this manner, electron-hole pairs which are generated in proportion to the amount of incident light are collected in the N-layer and P-layer. This results in a positive charge in the P-layer and negative charge in the N-layer. If an external circuit is connected between the P and N-layers, electrons will flow away from the N-layer and holes from the P-layer toward the opposite electrode.

Laser damage produced in these semiconductor devices can be categorized into two different types. The minimum flux level of the laser radiation resulting in a permanent degradation of signal-to-noise ratio (SNR) is considered the primary type of detector damage. This type of detector damage can be defined in terms of a rearrangement of electrical charge in the semiconductor. The second type of detector damage not only increases SNR, but also results in visible deformation on the detector surface. This type of detector damage can be defined in terms of a physical rearrangement of some of the atoms of the crystal due to the thermal effects of the laser pulses. In order to understand the silicon detector damage, a brief review of noise in photodiodes is provided in section 2. of this paper.

2. Pulse Detection in Noise

The detection of a laser pulse of duration τ immersed in white noise is analyzed in the RCA Electro-Optics handbook and briefly reviewed in this section. In figure 3, a mathematical description of the threshold detection process is shown. For clarity, the figure shows separately the effect of the match filter on the rectangular signal pulse and the white noise. At the filter output, the signal current is denoted by i_s, a triangular pulse of peak amplitude I_s (the same amplitude as the rectangular input pulse). The filter output noise current i_n is Guassian with root mean square (RMS) value I_n given by:

MATHEMATICAL DESCRIPTION OF THRESHOLD DETECTION PROCESS

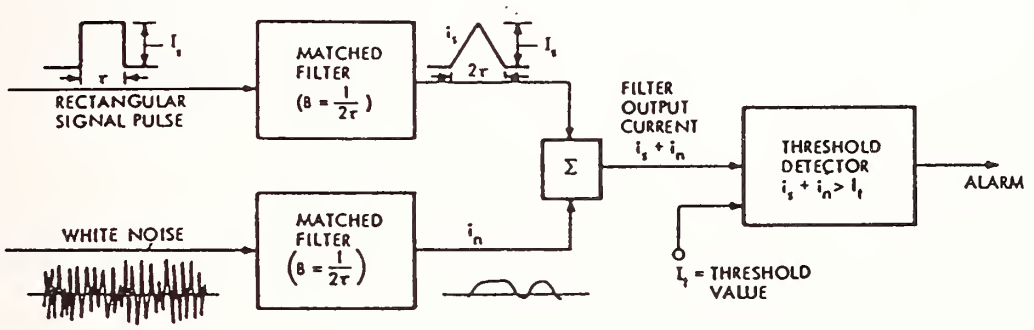

FIGURE 3.0

$$I_n = \sqrt{i_n^2} = \sqrt{W/2\tau} \qquad (1)$$

where W = Single sided power spectral density of input white noise,
τ = Input pulse duration.

The average false alarm rate $\overline{FAR}$ is the average number of times per second the output noise current i_n exceeds the threshold value I_t of the detector. This rate is given by Rice (ref. 10):

$$\overline{FAR} = \frac{1}{2\sqrt{3}\tau} e^{-I_t^2/2I_n^2} \qquad (2)$$

As seen in the equation, $\overline{FAR}$ decreases rapidly with the increase in the detector threshold value. When the signal is present, the probability that it will be detected P_d is very nearly the probability that the signal plus noise exceeds the threshold I_t at the instant of signal peak (ref. 11):

$$\begin{aligned} P_d &= P(i_s + i_n > I_t) \cong P\,(i_n > I_t - I_s) \\ &\cong \tfrac{1}{2}\,(1 + \operatorname{erf}\,(I_s - I_t/\sqrt{2}\,I_n)) \end{aligned} \qquad (3)$$

Thus, if the threshold I_t has been set according to equation (2) to achieve a given false alarm rate, then the peak signal to RMS noise current ratio I_s/I_n required to obtain a specified probability of detection P_d can be obtained using equation (3).

The total mean square shot noise for a photodiode can be given by:

$$\overline{i_n^2} = 2q\,(I_{bd} + I_R + I_{sd} + I_{bg} + I_s)B, \qquad (4)$$

where q = the charge on an electron,
B = the bandwidth,
I_{bd} = the bulk dark current,
I_R = the current due to detector damage,
I_{sd} = the surface dark current,
I_{bg} = the current due to background, and
I_s = the optical signal current.

And for 100 percent modulation for RMS signal current is $i_s = I_s/\sqrt{2}$. Then the available signal power is (ref. 12):

$$P_{av} = \frac{i_s^2}{4\, R_s\, \omega_o^2\, c^2} \quad , \tag{5}$$

where R_s = the series resistance and
C = the parallel combination of the diode and parasitic capacitance, and
ω_o = the resonant frequency.

The signal-to-noise ratio becomes

$$SNR = \frac{I_s^2}{2\,(i_n^2 + 4\, kTB/R_s\, \omega_o^2\, c^2)} \, . \tag{6}$$

The last term in the denominator represents the Johnson noise, and

k = Boltzmann's current
T = absolute temperature.

In a practical photodiode the optical signal current I_s is negligible in comparison to the other current terms in equation (4). Then, by solving equation (6), for I_s we will get:

$$I_s = \frac{\eta q\, P_s}{h\nu} \, , \tag{7}$$

where P_s = the signal power,
η = the quantum efficiency,
h = Planck's constant, and
ν = the frequency of light.

Thus, we obtain the well known expression (ref. 13) for P the signal power,

$$P = \frac{h\nu}{\eta q} \left(\frac{2\, SNR\, i_n^2}{G^2} \right)^{\frac{1}{2}} \, . \tag{8}$$

This is the generalized equation for the silicon detector, where G is the current gain = 1 for a PIN or P-N photodiode, and by inserting gain, the equation can be used for avalanche photodiode. For SNR = 1, P is the noise equivalent power (NEP).

3. Theoretical Background

The two types of laser damage thresholds are observed for the APDs. The first type of laser detector damage is defined in terms of a rearrangement of electrical charge (REC) in the semiconductor and will generate an additional shot noise term. The second type is defined in terms of a rearrangement of the atoms (REA) of the crystal and results in a localized leakage path, causing the detector to short circuit. It may be noted that the REC type of detector damage should be considered the laser damage threshold since it is a catastrophic, permanent failure of the detector, rather than a gradual degradation as occurs with gamma and neutron radiation. The REC and REA types of detector damage will require two different models. It is clear that the model for the REC detector damage will be similar to the models for gamma and neutron radiation degradation. The important difference between the REC type detector damage and the damage in the detector due to gamma and neutron radiation is that the REC damage is generally localized, while the nuclear damage of the detector is over the entire detector area.

The second term in equation (4) for shot current is the noise current due to the laser damage of the detector, and its RMS value can be given by the relation:

$$\overline{i^2_{REC}} = \sqrt{2}\, qB \left(\frac{A_r}{A}\right) G^2 \quad , \tag{9}$$

where A_r = the area of the detector damaged by a laser,
A = the total detector area, and
G = the detector current gain.

It may be noted that for PIN and P-N silicon photodiodes with gains equal to one, this noise current will not significantly affect the false alarm rate. however, the following numerical example will show that in the APD the REC type of damage plays an important role.

For $G = 100$,
$B = 50$ MHz,
$A_r/A = 0.000001$,

The RMS value of noise current I_{REC} will be 400 nA for the APD with this very small A_r/A ratio, which will result in an acceptable false alarm rate.

Most of the published data of the silicon detector can be classified as the REA type of laser damage. The laser damage threshold is characterized by a temperature rise at the irradiated surface. A brief review of the thermal model developed (ref. 14) is summarized here. The model treats a semi-infinite solid irradiated by a Gaussian beam. The energy density required to damage the sample can be given by:

$$E_o = E\Delta T \left[1 + \frac{\delta\tau\alpha\pi^{\frac{1}{2}}}{a \tan^{-1} (4\delta\tau/a^2)^{\frac{1}{2}}} \right] , \qquad (10)$$

where $$E_{\Delta T} = \frac{\Delta T \rho s}{(1 - R) \alpha} \qquad (11)$$

and Δ_t = the increase in surface temperature required for damage (melting in this case),

α = the absorption coefficient,

R = the reflectivity,

s = the specific heat,

ρ = the density,

δ = the laser pulse width, and

a = the beam radius.

The first term in equation (10) is dominant at short times, where thermal conduction is not important and the temperature change is determined by the depth (α^{-1}) over which the energy is absorbed. The second term is dominant at long times where the heat diffusion distance, $\sqrt{(\delta\tau)}$, is much greater than the absorption depth (α^{-1}). In the limit of $4\delta\tau << a^2$ then $\tan^{-1}(4\delta\tau/a^2)^{\frac{1}{2}}$ becomes $(4\delta\tau << a^2)^{\frac{1}{2}}$ and equation (11) will be:

$$E_o \cong E_{\Delta T} \left[1 + \sqrt{\left(\frac{\delta\pi\alpha^2\tau}{4} \right)} \right] . \qquad (12)$$

In the limit of $4\delta\tau << a^2$ then $\tan^{-1}(4\delta\tau/a^2)^{\frac{1}{2}}$ becomes $\pi/2$ and equation (11) will be:

$$E_o \cong E_{\Delta T} \, 2\delta\tau\alpha/a\sqrt{\pi} \quad . \qquad (13)$$

Thus the irradiation time dependance of the damage thresholds exhibits three distinct regions of behavior. For short times where heat diffuses a distance that is small compared to the absorption depth (α^{-1}) and the beam radius (a), no appreciable energy leaves the absorption region. In this short

time limit, E_0 is approximately constant and power density P_0 varies inversely as τ. For intermediate times, E_0 is proportional and P_0 is inversely proportional to the square root of the irradiation time. In the long time limit, a steady state thermal distribution exists and the detector surface reaches a terminal temperature for a given power density. In this time region, P_0 approaches a constant asymptote and E_0 approaches an asymptote which increases linearly with irradiation time.

4. Experimental

APDs were exposed to pulses of 1.064 micron radiation, using Litton Laser Systems model P-3 laser. Model P-3 uses a 5 mm diameter by 50 mm long Nd:YAG laser rod and provides output energy of 53.2 mJ per pulse for repetition rates up to 20 Hz. The laser uses a Pockels cell Q-switch to produce pulse widths of 15 ns. The experimental set-up used is shown in figure 4. As seen in the figure, although the detector active area is significantly smaller than the laser beam diameter, for the purpose of alignment, an LLS model PL-100 laser was used. Model PL-100 uses a GaAs laser diode with collimating optics.

The power density was varied by using glass filters. The beam profile of the model P-3 laser is approximately Gaussian and, by using 0.5 mm diameter aperture, only the center portion of 5 mm diameter beam was used. The energy density of this pulse laser was measured by a EG&G model 580 radiometer using a 90-10 beam splitter. The beam splitter provided 10 percent of the beam for continuous measurement. The power was varied by using a combination of glass filters in front of the laser, rather than reducing input power to the laser flashlamp in order to keep the beam quality (profile) the same at different laser output power levels.

The silicon detectors selected for the laser damage threshold measurements were RCA models C30954E and C30904-54E APDs. The difference between models C30954E and C30904-54E is the mechanical package. Model C30904-54E uses fiber optics of a core diameter 0.5 mm and numerical aperture 0.6 in front of the detector chip as an integral part. The characteristics of the detectors are shown in Table I. It may be noted that each detector was found to provide high responsivity of 0.36 A/W at 1064 nm wavelength.

The APD under test was first characterized for its critical parameters, namely, the dark current and responsivity. Then the detector was placed with its pre- and post-amplifier on the laser damage threshold measuring test fixture. The detector and the aperture were aligned on the fixture using the GaAs diode laser which was aligned with the Nd:YAG laser. The laser damage

EXPERIMENTAL SET-UP

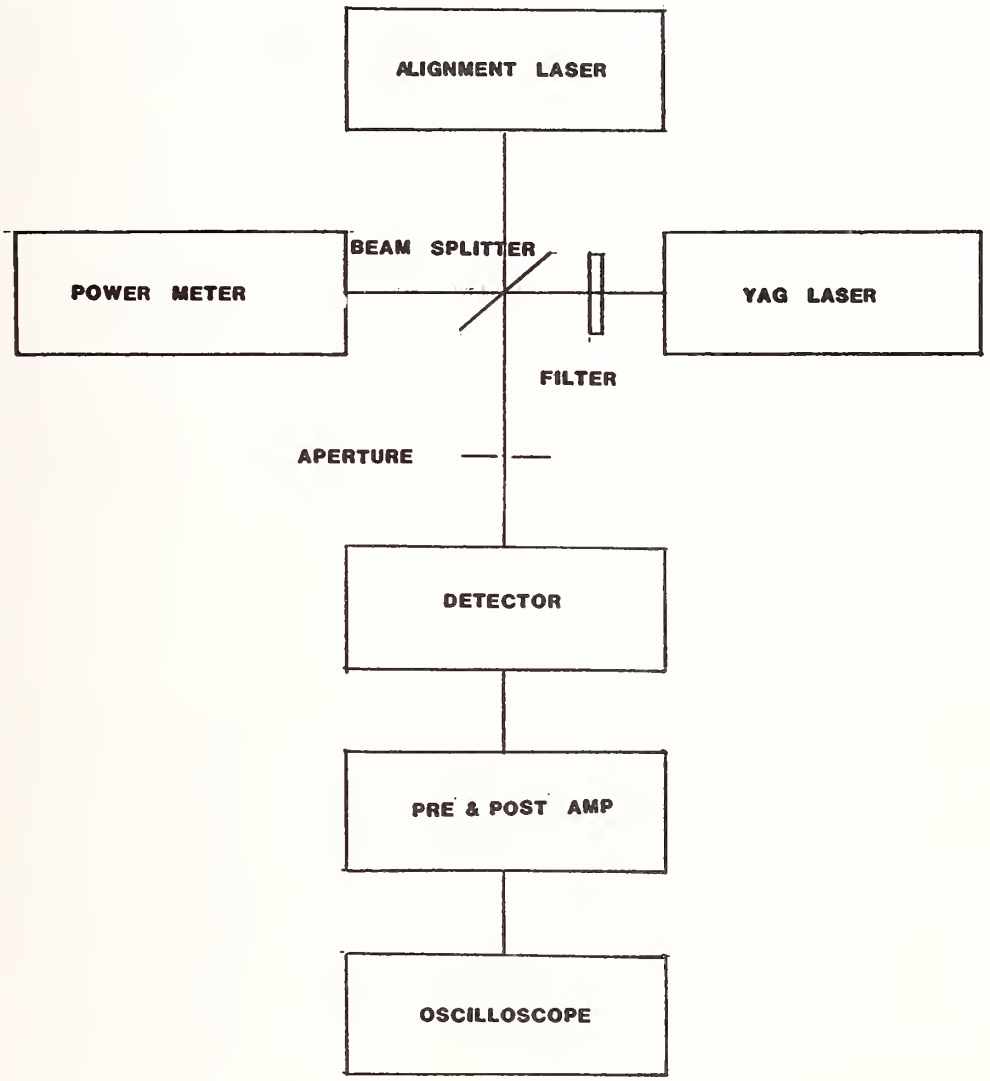

FIGURE 4.0

Table I. AVALANCHE PHOTODIODE CHARACTERISTICS

	RCA C30954E			RCA C30904-54E		
Diameter (mm)	0.8			0.8		
Area (sq.mm)	0.5			0.5		
Light Pipe Core (mm)	-			0.5		
Package	L-569			L-1048		
APD Serial No.	8616	7520	7519	0601	0597	0566
Operating Voltage (V)	418	364	420	365	364	386
Breakdown Voltage (V)	462	418	470	408	412	426
Dark Current (nA)	45	39	34	30	30	38
Responsivity (A/w)	0.36	0.36	0.36	0.36	0.36	0.36
Laser Damage Threshold	-	0.302	>0.302	-	0.099	2.183

measurements were performed at 19.9 Hz repetition rate and 15 ns pulse width pulses of the Nd:YAG laser. The power density on the detector was increased in steps.

5. Results and Conclusions

The data collected for the laser damage threshold are also summarized in Table I. Although the number of parts damaged during the tests were small, it may be noted that the APDs' damage threshold was measured to be significantly smaller than 3.8 giga watts per sq. cm previously reported for the silicon PIN photodetector (ref. 1). The APDs damaged during these measurements were evaluated for the dark current and the responsivity. The data collected show that the responsivity of the detector was not significantly changed, while the dark current was increased by several orders of magnitude. Furthermore, the dark current magnitude was proportional to the ratio A_r/A for the detector. In equation (9) the relationship between

the dark current and ratio A_r/A is shown. A photograph of this damage is shown in figure 5(b). This damage sight is not visible to the naked eye [see figure 5(a) microscope magnification 15x]. In this REC type of detector damage it may be noted that the damage sight is not circular.

In figure 6, the REA type of detector damage is shown. In this type of laser damage, threshold is characterized by the temperature rise at the irradiated surface. The molten material can be seen in figure 6(b), at 250x magnification. This type of damage not only increases the dark current but also decreases the responsivity of the detector. The REA type of damage threshold can be obtained using equation (10) which is plotted in figure 7. The figure also shows the REC type of laser damage threshold data obtained.

6. Acknowledgements

This work was performed at and supported by Litton Systems, Inc., Laser Systems division, Orlando, FL. The author wishes to acknowledge the work of Mr. Roger Zenrick in the detector damage threshold measurements and Ms. Gretchen Cleary for collecting photographs of the damaged detectors. The author also wishes to thank Lauryn Erndl, Jackie Gibson, and Phyllis Heatley for assistance in preparing this manuscript.

PHOTOMICROGRAPH FOR AVALANCHE PHOTODETECTOR
(MAG. 15X)

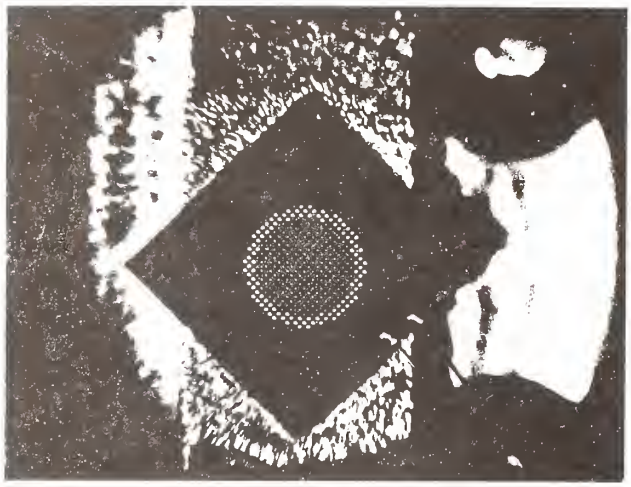

PHOTOMICROGRAPH OF REC TYPE DETECTOR DAMAGE
(MAG. 90X)

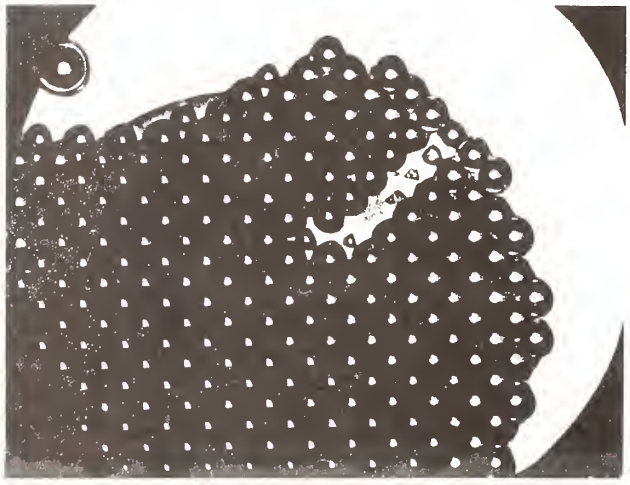

101387-11

FIGURE 5.0

PHOTOMICROGRAPH OF REA TYPE DETECTOR DAMAGE
(MAG. 180X)

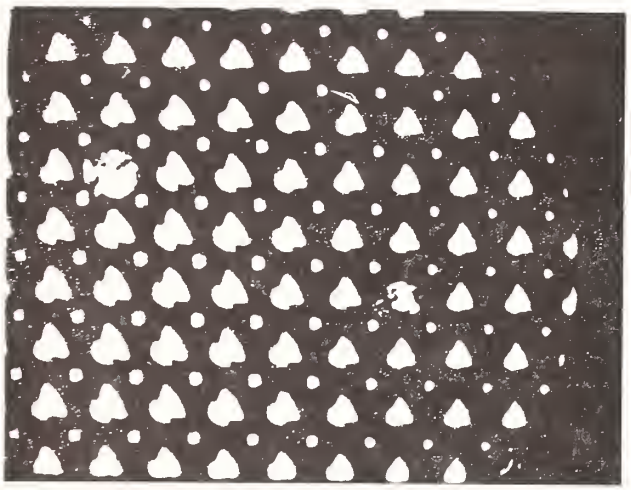

PHOTOMICROGRAPH OF REA TYPE DETECTOR DAMAGE
(MAG. 360X)

101387-12

FIGURE 6.0

LASER DAMAGE THRESHOLD OF SILICON DETECTOR

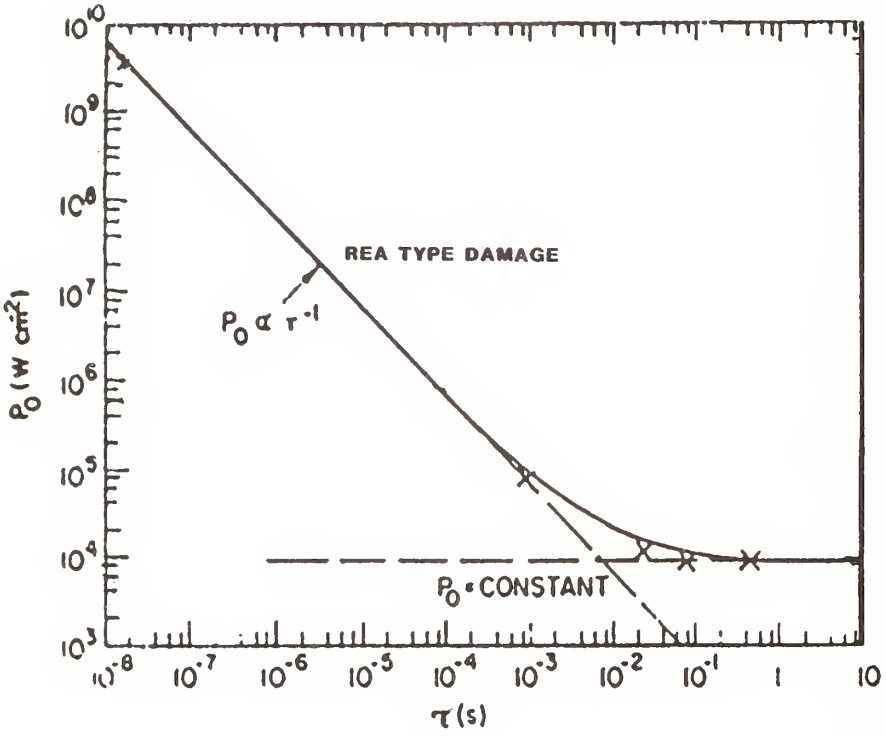

FIGURE 7.0

7. References

1. F. Bartoli, L. Esterowitz, R. Allen, and M. Kruer, J. Appl. Phys. 47, 2875 (1976).

2. J. Davit, NBS Spec. Publ. 387 (1973).

3. V.I. Kovalev, V.V. Morozov, and P.S. Faizullov, Sov. J. Quantum Electron. 4, 1208 (1975).

4. Y. Matsuoka, and A. Usami, J. Phys. D. 7, 1259 (1974).

5. A. Grindberg, R. Mekhtieo, S. Ryokin, V. Salamanov, and I. Yaroshetski, Sov. Phys. Solid State 9, 1085 (1967).

6. M. Kruer, R. Allen, L. Estereowitz, and F. Bartoli, Opt. and Quantum Electron. 8, 453 (1976).

7. D.H. Seib, and L.W. Aukerman, "Advances in Electronics and Electron Physics," Vol. 34, p. 169, Academic Press, New York (1973).

8. K.D. Stock, Appl. Opt. 25, 832 (1986).

9. P.P. Webb, R.J. McIntyre, and J. Conradi, RCA Rev. 35, 234 (1974).

10. S.O. Rice, Bell Syst. Tech. J. 24, 46 (1945).

11. F.J. Gardiner, "RCA Electro-Optics Handbook," p. 110, 2nd edition, RCA, Lancaster, PA (1978).

12. L.W. Aukerman, F.L. Vernon, and Y Song, Opt. Eng. 23, 678 (1984).

13. K.W. Mitchell, IEEE Tran. Nucl. Sc. NS-25, 1545 (1978).

14. F. Bartoli, L. Esterowitz, M. Kruer, and R. Allen, Appl. Opt. 16, 2934 (1977).

Multiphoton Photoconductivity and Laser Induced Damage in Alkali-Halide Crystals under Picosecond Pulses from YAG:Nd Laser and its Harmonics

S.V. Garnov, A.S. Epifanov, S.M. Klimentov,
A.A. Manenkov, and A.M. Prokhorov

General Physics Institute of the Academy of Sciences
Moscow, USSR

The results are presented of studying photoconductivity induced by picosecond pulses of the second, third, and fourth harmonics of YAG:Nd-laser in KCl, NaCl, KBr, KI crystals. The processes of multiphoton photoexcitation of nonequilibrium carriers are revealed up to the 4-th order and the corresponding multiphoton absorption coefficients are measured. Drift mobility of thermalized nonequilibrium electrons is measured. The role of multiphoton absorption in laser-induced damage in crystals is discussed. With a view to elucidating the role of impurities (inclusions) in the laser induced damage in alkali-halide crystals in the picosecond region, impurity photoconductivity is studies depending on thermal treatment of crystals.

Key Words: alkali-halide crystals; drift mobility; multiphoton absorption; photoconductivity; picosecond laser pulse damage.

1. Introduction

The role of multiphoton absorption in laser induced damage to transparent solids has been discussed in a series of works (see reviews [1,2] and references therein). It has been theoretically proved that multiphoton absorption may serve as source of seed electrons for their successive multiplication in the impact ionization process, or may directly lead to the material damage due to generation a large number of nonequilibrium carriers in the conduction band, enough for strong heating of the lattice. An essential role of multiphoton processes in laser induced damage in semiconductors and dielectrics has been pointed out in some works (see, for instance, [3,4]), but so far there is no reliable evidence of a decisive role of these processes in laser induced damage. More over, only some works [5,9] (see also references in [10]) and [11-13] which appeared later, are devoted to experimental research of multiphoton processes in wide-gap dielectrics. It is likely that sufficiently reliable results have been obtained in only a few studies of multiphoton processes [8-9, 11-13].

The present paper reports a detailed study of the use of picosecond pulses of the second, third and fourth harmonics of the Nd:YAG laser in multiphoton excitation of free carriers (electrons) in chemically pure (without injected impurities) KCl, NaCl, KBr, and KI crystals. As an investigative technique we selected picosecond laser photoconductivity ([9,13]. It is the most efficient and straightforward way to record carriers, and features both high sensitivity and temporal resolution, making it advantageous over the photoacoustic and luminescence techniques used in [11] and [12]. Because the threshold intensity for laser damage by picosecond pulses is large, we were able to study excitation for multiphoton processes over a wide range of intensities under conditions not influenced by breakdown phenomena. This allows us to measure the dependence of the photoconductivity signal on laser intensity, and to unambiguously identify the intrinsic absorption.

Besides intrinsic photoconductivity caused by multiphoton interband transitions in the alkali-halides matrix, we have also studies extrinsic photoconductivity associated with photoionization of uncontrollable (parasitic) impurity present in some samples. An interest to this investigation is associated, in particular, with elucidating how these impurities affect the laser induced damage process. In case of damage by nanosecond laser pulses, a decisive

role of inclusions is well established [1,2], whereas for damage by shorter pulses the influence of impurities has not so far been studied enough to make definite conclusions. In section 6 of this paper we present the results of studying the influence of the thermal treatment of crystals on both the extrinsic photoconductivity and the thresholds of picosecond laser damage.

2. Experimental

We used pulses of the fourth, third and second harmonics of a picosecond YAG:Nd laser that was developed especially for this work. The laser exhibited enhanced stability of spatial, temporal and energy parameters of high-power pulses produced at high conversion efficiency (tens of percent) from the fundamental, $\lambda = 1.064$ μm. In this case, the beam retained its Gaussian beam distribution. The pulse duration at the fundamental frequency was 55-60 ps; harmonic pulses were shorter by $\sqrt{n}$ where n is the harmonic number.

The experimental arrangement for recording the photoconductivity signal is shown in Fig. 1. Cleaved, 3x15x15 mm^3 alkalihalide samples were placed between electrodes. A bell-shaped electric pulse with duration of 100 μs and magnitude, U_0, up to 4 KV was applied to the electrode in synchronism with the laser irradiation. The photocurrent signal was directly taken by a cable with a wave resistance R=50 Ohm. The signal was recorded with a wide-band oscilloscope. The recording circuit was carefully screened, so that the noise level did not exceed 1 mV in the 0-500 MHz band. Temporal resolution was limited by the oscilloscope band width to be 1 ns. (Special investigation has shown the intrinsic temporal resolution to be not worse than 100 ps.

To exclude surface photoconductivity, the electrodes were made slightly smaller than the crystal dimensions, and the crystals were constantly heated, by a halogen lamp or by warm air, to a temperature of 50-60°C. The influence of the electrodes was also excluded, since neither direct nor scattered radiation got on them. Note that the "parasitic" signal from surfaces of crystals and electrodes had a characteristic irregular shape and life time of 5-10 times that of the legitimate signal. Sites in the crystal were irradiated only once to prevent accumulation effects, particularly of laser-induced radiation defects. To increase radiation intensity, the input beam was slightly focussed by a lens of long focal length to diameter of 0.3-1.0 mm at the entrance surface of the crystal.

3. Absorption Coefficient Measurement Procedure

The measurements of the multiphoton absorption coefficients presented are based on comparison of the corresponding photoconductivity signals with that at two-photon excitation of free carriers with the known two-photon absorption coefficients [8]. This approach improves the measurement accuracy by eliminating, for instance, some uncertainty in the geometry of the interaction volume and in the characteristics of the recording circuit.

According to the definition of the K-photon absorption coefficients, β_k:

$$\frac{\lambda}{I}\frac{dI}{dZ} = -\sum_{k=1} \beta_k I^{k-1} \qquad (1)$$

where I=I (r,z,t) is the intensity of a beam propagating through a sample with a length l, r, and Z are transverse and longitudinal coordinates, respectively, and t is time.

In case of weak absorption, when

$$\beta_k \cdot I^{k-1}(r,o,t) \cdot l \ll 1$$

the number of the electrons N_k, appeared in the conduction band may be written as:

$$N_k = n_k \cdot V_k \qquad (2)$$

where n_k is effective electron concentration, V_k is an effective interaction volume.

For a Gaussian pulse with the intensity distribution:

$$I(r,o,t) = I_0 \cdot \exp(-\frac{r^2}{r_0^2}) \cdot \exp(-\frac{t^2}{\tau^2})$$

the introduced parameters appeared to be equal:

$$n_k = \beta_k \cdot \frac{I_0^k}{k \cdot \hbar\omega} \cdot t_k \quad , \quad V_k = \frac{\pi r_0^2 \, l}{k} \qquad (3)$$

where ω is the exciting light frequency, $t_k = (\frac{\pi}{k})^{\frac{1}{2}} \tau$ is the effective pulse width.

One can show that the amplitude U_{pc} of the photoconductivity voltage, recorded by oscilloscope, has the form:

$$U_{pc} = \alpha N_k \frac{e \mu U_0}{L^2} R \psi (\frac{\tau_r}{\tau_t}) \qquad (4)$$

Here e and μ are the charge and drift mobility of the electrons, L is the distance between the electrodes, α is a geometric factor describing deviation from the plane capacitor approximation (α = I), ψ is the signal transfer function, τ_r is the electron recombination time, τ_t is the transient characteristic time of the recording apparatus.

Formula (4) has been obtained assuming that the external field screening by free carriers is absent (this was certainly fulfilled in the experiment at relatively low concentrations of free carriers) and that the electron recombination is linear:

$$n_k = n_k(0) \exp(-t/\tau_r) \qquad (5)$$

The latter condition was probably also realized in the experiment, since the values n_k did not exceed 10^{-14} cm^{-3}, at which quadratic recombination made no contribution, and the recorded photoconductivity signal had an exponential shape. Note that expression (4) was carefully experimentally controlled. Checked were the signal linearity to the applied voltage U_0, proportionality of U_{pc} to $1/L^2$ and 1, dependence of U_{pc} upon r_0 and τ_t.

From (2) and (3,4) one can readily obtain expressions for the ratios of the multiphoton absorption coefficients. At a given value of U_{pc} and equal spot sizes of the exciting radiation beams, they have the form:

$$\frac{\beta_2}{\beta_3} = \frac{4\sqrt{2}}{9\sqrt{3}} \cdot \frac{\omega_2}{\omega_3} \cdot \frac{\tau_3}{\tau_2} \cdot \frac{I_0^{3},_3}{I_0^{2},_2} \qquad (6)$$

$$\frac{\beta_2}{\beta_4} = \frac{\sqrt{2}}{8} \cdot \frac{\omega_2}{\omega_4} \cdot \frac{\tau_4}{\tau_2} \cdot \frac{I_0^{4},_4}{I_0^{2},_2} \qquad (7)$$

Indices 2, 3, 4 at ω, τ, and I_0 denote the frequency, pulse width, and intensity of the laser radiation leading to the two-, three-, and four-photon excitation of the free carriers.

Relationships (6) and (7) show that the accuracy of determining the ratios of the multiphoton absorption coefficients depends only on the accuracy of determining laser pulse parameters. This requires a rigorous laser stability and beam quality which are satisfied in our laser system.

4. Experimental Results

For the crystals examined, the dependence of photoconductivity voltage on laser intensity are presented in figures 2 and 3. All the measurements were made under identical conditions, i.e. at equal geometric sizes of the samples (L=3 mm, l=10 mm), equal laser beam cross-section ($\pi r_0^2 = 4.10^{-3}$ cm^2), at the same applied voltage U_0 = 3.6 KV and the same recording circuit (τ_t = ' ns). The obtained results are seen to be well described by power functions (dotted lines) with the powers k=2, 3, and 4, corresponding to two-, three-, and four-photon excitation of free carriers. The multiphoton absorption coefficients obtained from these experimental results are listed in the table. To determine them we have used the two-photon absorption coefficients directly measured by N. Bloembergen at at. [8] for a great number of wide-gap crystals at λ = 0.266 μm and λ = 0.355 μm (fourth and third harmonics of a picosecond YAG:Nd laser). Analysis of the errors associated with the accuracy of the energy, pulse width, and beam radius measurements (10, 20, and 15 percent, respectively) has shown that with due regard to the spread of the experimental data and accuracy of β_2, the value of the multiphoton absorption coefficients cannot differ from the presented ones more than by a factor of 2.2 for 225_2, and by a factor of 2.8 for β_4.

Our results can be compared with the previously published results which are, in our opinion, most reliable [11, 12]. For KI at λ = 0.532 μm, the three-photon absorption cross section is $\delta_3 = 6 \times 10^{-81}$ cm^6 sec^2 [11], which corresponds to a calculated absorption of 4.9×10^{-22} cm^3 W^{-2}. The four-photon absorption cross section for NaCl at λ = 0.532 μm, $S_4 = 1.5 \times 10^{-14}$ cm^8 s^3 [12], corresponds to an absorption coefficient of 0.65×10^{-36} cm^5 W^{-3}. The published result for KI agrees with our data; for NaCl there is a discrepancy. Note, however, that the accuracy of our results are determined by the accuracy of measurements of β_2 and of laser parameters. When photoacoustic or luminescence measurements are used, the accuracy is influenced by an adopted model of the transfer of electron energy to the lattice, and the error can be as large as an order of magnitude [12].

Our approach to measuring multiphoton absorption coefficients may be used for determining their spectral dependencies. As an example we present the value of the two-photon absorption coefficient at $\lambda = 0.355$ μm we have measured: β_2 3.6×10^{-11} cm W^{-1}. A considerable decreasing of the absorption coefficient at this wavelength compared to its value at $\lambda = 0.266$ μm (obtained in [8]) is due to the fact that transitions of the carriers into the conduction band proceed in this case from the edge of the valence band (the energy gap for KBr is 7.3 eV, the YAG:Nd laser third harmonics energy is 3.51 eV). Note also that the signal is quadratically dependent on intensity (see Fig. 3). This indicates that the two-photon excitation process prevails over the three-photon process in the given intensity range.

5. Electron Drift Mobility Measurement

Calibration of the photoconductivity signal by the known two-photon absorption allows use of formula (4) for determining drift mobility of the thermalized nonequilibrium electrons. An error in determining μ is mainly due to a geometrical factor α and signal transfer function ψ. Analysis shows, however, that the uncertainty in the value of μ does not exceed 50-70%. The μ values measured by this procedure are listed in the table.

It is worth noticing that for KCl, NaCl, and KI crystals the obtained values of drift mobility are by an order of magnitude less than those of Hall's mobility [15], whereas fir KBr their values actually coincide.

6. Impurity Photoconductivity

Excitation of free carriers due to impurity photoionization has been studied on KCl crystals which contained OH^- and other impurities. The 0.355 μm radiation in these samples was revealed to give rise, along with intrinsic electron excitation, to extrinsic excitation into the conduction band, which is indicated by the intensity dependence of photoconductivity shown in figure 4. It has two characteristic parts: linear at low intensities (extrinsic excitation), and superlinear at high intensities. This can be easily understood if one takes into account in expression (4) contributions of the three-photon (intrinsic) and single-photon (extrinsic) absorption. Indeed, in the case:

$$U_{pc} \sim \pi r_0^2 \left(\beta_1 \cdot I_0 + \frac{1}{9\sqrt{3}} \beta_3 \cdot I_0^3\right) \qquad (8)$$

where β_1 is the linear absorption coefficient, whose value is equal to 7.10^{-5} cm^{-1}. At an intensity $I'_0 = 1.5 \times 10^{10}$ W cm^{-2} both terms in (7) become equal. At intensities higher I_0 three-photon absorption starts to play a decisive role.

When investigating temperature dependencies of the photoconductivity signal it was revealed that the KCl samples, whose photoconductivity at $\lambda = 0.355$ μm was evidently extrinsic, sharply changed their properties after thermal treatment in the following way: heating up to the temperature close to the melting point ($T=T_m-(5\ 10)°C$), holding at this temperature for about 30 min, and then fast cooling. After this treatment the intensity dependence of the photoconductivity voltage became close to cubic and actually coincided with that obtained in the originally pure samples, thus indicating an intrinsic three-photon excitation of the carriers.

A similar thermal treatment has been used in the study of laser-induced damage in these crystals [16]. Heat treatment increased the threshold for crystals that initially had low threshold, but did not alter high-threshold crystals. For instance, for KCl at $\lambda = 1.064$ μm, heat treatment produced a five fold increase in threshold to a value approaching that of the best crystals. Since the same pattern was observed in our study of photoconductivity, we assume there is a correlation between temperature-induced reduction of extrinsic picosecond laser photoconductivity temperature-induced increase of damage

resistance in the nanosecond range. One may also assume a similar correlation exists for damage thresholds of picosecond laser breakdown. To test this, we made comparative measurements at both $\lambda = 1.064$ μm and $\lambda = 0.355$ μm, of the bulk damage threshold of initially pure and doped KCl crystals. The laser radiation was focused into the samples by a lens with focal length of 45 mm. Samples were tested before and after thermal treatment, but the treatment did not effect thresholds measured at either wavelength.

7. Discussion

Our investigations showed that photoexcitation of free carriers in wide-band dielectrics can be efficiently studied by measurement of picosecond laser photoconductivity. It enables reliable recording of multiphoton processes and accurate measurements of relevant absorption coefficients. The high sensitivity allows detection of low-concentration impurities in crystals and measurement of their ionization cross sections.

At intensities near the breakdown threshold (I 10^{12} W cm^{-2}) multiphoton absorption may provide an essential heating of the crystal and cause damage. Indeed, at an intensity of $I_0 = 5 \times 10^{12}$ W cm^{-2} in NaCl and KCl, effective absorption coefficients for 2-, 3-, and 4-photon excitation of carriers are 104 cm^{-1} ($\lambda = 0.266$ μm), 10^2 cm^{-1} ($\lambda = 0.355$ μm) and 5×10^2 cm^{-1} ($\lambda = 0.532$ μm), respectively.

From our study of picosecond extrinsic photoconductivity and thermal treatment, we conclude that impurities and inclusions have less impact on picosecond laser damage than in damage induced by longer (nanosecond) pulses.

However, a special study is certainly required to make a definite statement about the role of inclusions and impurities on ultrashort-pulse damage.

8. Figure Captions

Figure 1. Experimental arrangement used for recording photoconductivity.
Figure 2. Intensity dependence of photoconductivity voltage in KCl and NaCl.
Figure 3. Intensity dependence of photoconductivity voltage in KBr and KI.
Figure 4. Intensity dependence of impurity photoconductivity in KCl at $\lambda = 0.355$ μm before and after thermal treatment.

8. References

[1] Walker, T.W.; Guenther, A.H.; Nielsen, P.E. IEEE J. Quantum Electr., QE-17, 1981, 2053.

[2] Manenkov, A.A.; Prokhorov, A.M. Uspelchi Physicheskikh Nauk, 1986, 148, 180.

[3] Danileiko, Yu.K.; Lebedeva, T.P.; Manenkov, A.A.; Sidorin, S.V. Soviet JETP, 74, 765 (1978).

[4] Merkle, L.; Bass, M.; Swimm, R.T. Opt. Engin. 1983, 22, 405.

[5] Dneprovsky, V.S.; Klyshko, D.N.; Penin, A.N. Soviet JETP. Pis'ma v Redaktsiyu, 1966, 3, p. 385.

[6] Aseev, G.I.; Kats, M.L.; Nikol'sky, V.K. Soviet JETP. Pis'ma v Redaktsiyu, 1968, 8, 174.

[7] Catalano, I.M.; Cingolomi, A.; Minafra, A. Phys. Rev., 1972, B5, 1629.

[8] Liu, P.; Yen, R.; Smith, W.L.; Lotem, H.; Bachtel, J.H.; Bloembergen, N.; Adhow, R.S. Phys. Rev. 1978, B17, 4620.

[9] Williams, R.T.; Klein, P.H.; Marquardt, C.L. Laser induced damage in optical materials. NBS spec. publ. 509, p. 481. US Govern. Print. Office, Washington, 1978.

[10] Nathom, V.; Guenther, A.H.; Mitra, S.S. JOSA 1985, B2, 294.

[11] Brost, G.; Braunlich, P.; Kelly, P. Phys. Rev., 1984, B30, 4675.

[12] Jones, S.C.; Shen, X.A.; Braunlich, P.F.; Kelly, P.; Epifanov, A.S. Phys. Rev., 1987, B35, 894.

[13] Garnov, S.V.; Epifanov, A.S.; Klimentov, S.M.; Manenkov, A.A.; Prokhornov, A.M. Soviet JETP Letters, 1987, 45, 399.

[14] Garnov, S.V.; Epifanov, A.S.; Klimentov, S.M.; Manenkov, A.A.; Izvestiya, A.N. SSSR, ser. physicheskaya, 1987, 51, 1447.

[15] Seager, C.H.; Envin, D. Phys. Rev., 1970, B2, 3421.

[16] Gorshkov, B.G.; Danileiko, Yu.K.; Epifanov, A.S.; Lobachev, V.A.; Manenkov, A.A.; Sidorin, A.V. Soviet JETP, 1977, 72, 1171.

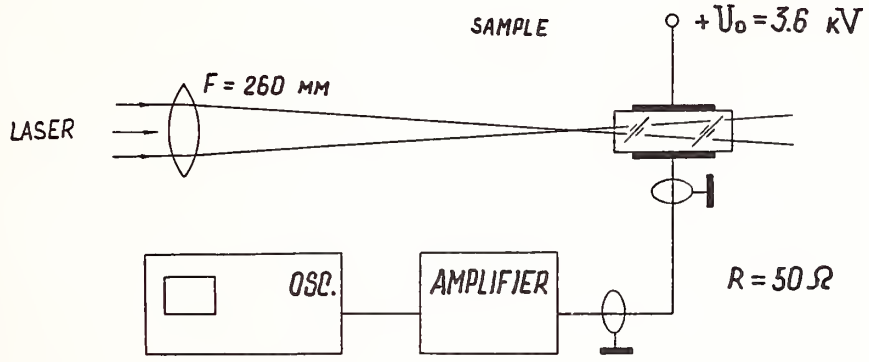

EXPERIMENTAL ARRANGEMENT USED FOR PHOTOCONDUCTIVITY DETECTION

Figure 1

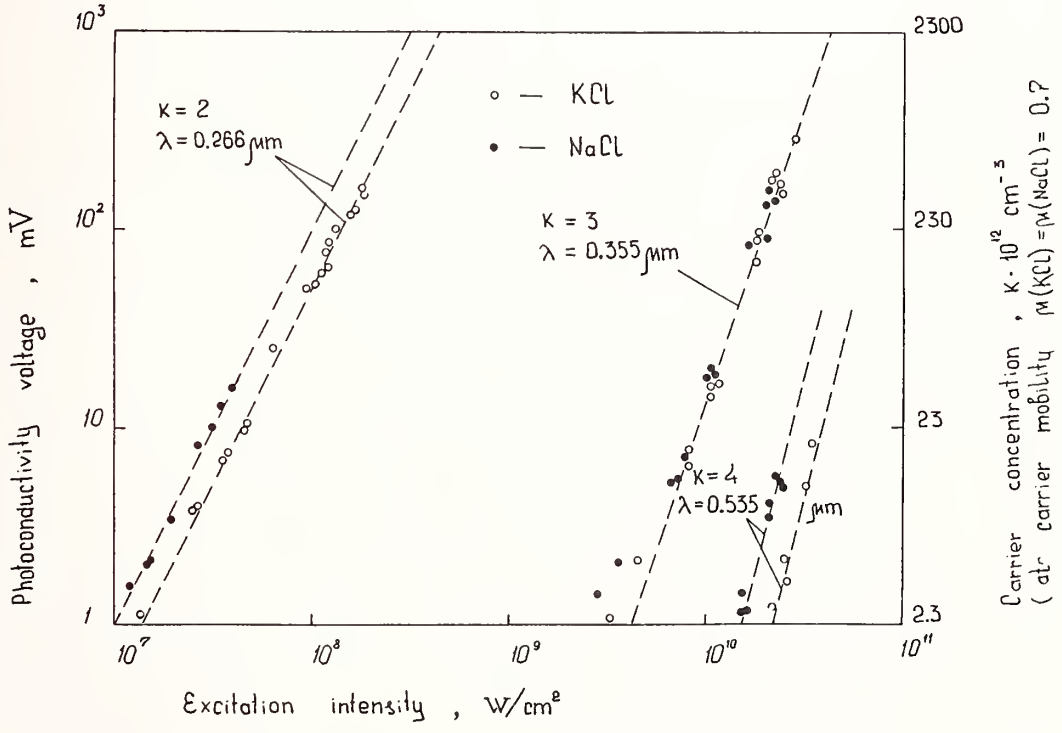

Figure 2

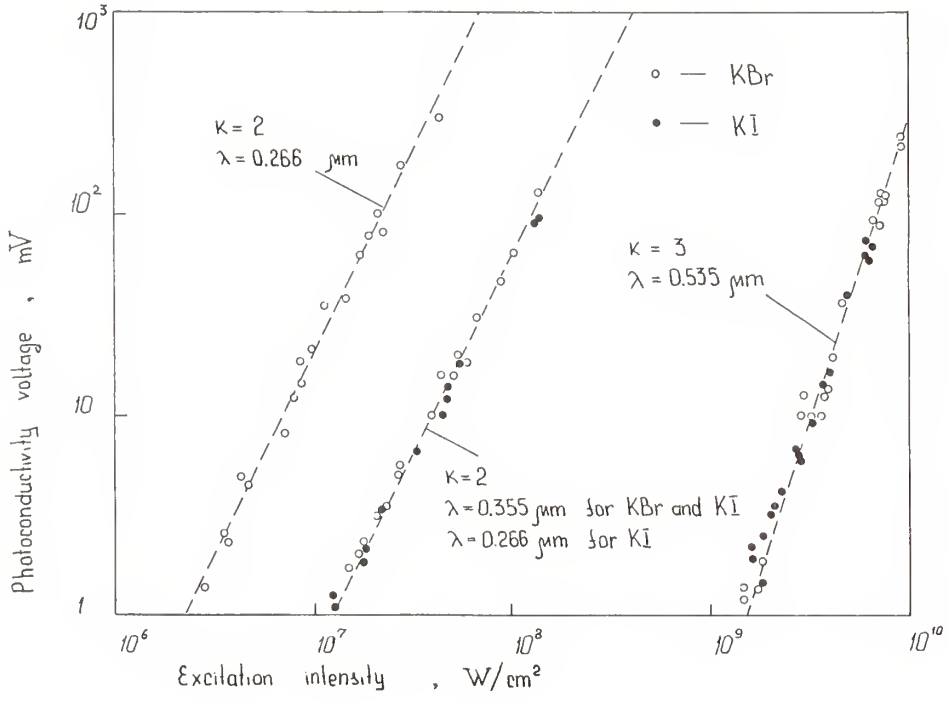

Intensity dependences of photoconductivity in KBr and KI

Figure 3

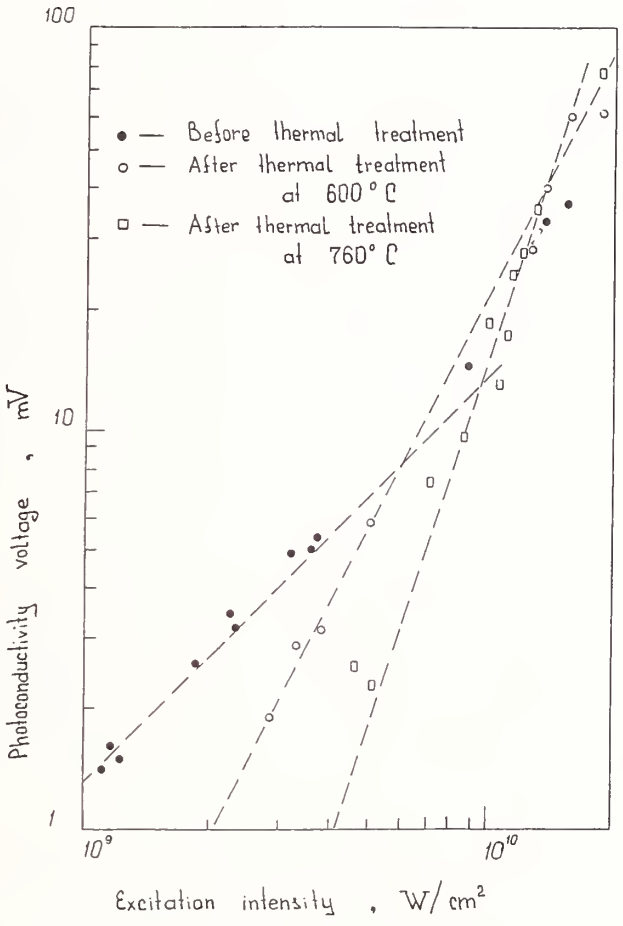

Impurity photoconductivity in KCl

Figure 4

Table

Multiphoton Absorption Coefficients and Drift Mobilities

	$\beta_2^*, 10^{-9}$ cm·W^{-1} (λ, μm)	$\beta_3, 10^{-24}$ cm^3·W^{-2} (λ, μm)	$\beta_4, 10^{-36}$ cm^5·W^{-3} (λ, μm)	μ, cm^2·V^{-1}·S^{-1}
KCl	I.7 (0.266)	4.7 (0.355)	I.8 (0.532)	0.69
NaCl	3.5 (0.266)	6.6 (0.355)	8.3 (0.532)	0.67
KBr	2.0 (0.266)	2.6 (0.532)	-	23
KI	3.3 (0.266)	200 (0.532)	-	0.54
	7.3 (0.355)	430 (0.532)		

* - after Bloembergen et al. Phys. Rev. 1978, B17, 4620

Table 1

Manuscript Received
2-23-88

Radiation-Induced Absorption In Fused Silica

G. H. Miley, R. Chapman, J. Nadler, and W. Williams

University of Illinois, Nuclear Engineering Department
103 S. Goodwin Ave., Urbana, IL 61801

The transient radiation-induced absorption in fused silica due to neutron and γ-ray irradiation has been investigated. Transient absorption coefficients at 325 nm have been measured during and after pulsed reactor (TRIGA) irradiation. Radiation-induced absorption results from the generation of color centers.

Most of the previous efforts have been concerned with the permanent effects due to low dose rate steady-state irradiations. This study focuses on the transient effects due to pulsed irradiations and their dependence on dose rate and total dose. The transient absorption coefficient increases very rapidly to a maximum value during the pulse, then decreases over a time period >1000 seconds to a permanent value after the pulse. In general, the absorption coefficient is found to increase with increasing dose rate and total dose.

Key words: color center; Corning 7940; fused silica; radiation-induced optical absorption; reactor irradiation; transient absorption; nuclear pumped laser; free electron pumped laser.

1. Introduction

Optical components of Nuclear-Pumped Laser (NPL) and Free Electron Laser (FEL) systems may be exposed to intense environments. The radiation-induced optical absorption (α) in the window and substrate materials resulting from pulsed irradiation can have a great impact on the optical performance of those materials. Typically, α reaches a maximum value (α_{max}) during pulsed irradiation and then decreases to an asymptotic permanent value afterwards. This phenomena can lead to incorrect gain measurements in the development of laser systems. Measurements of gain in such systems must take into account the transient radiation-induced absorption in the system optics. In addition, laser operation itself can be severely effected.

A schematic of the radiation-induced absorption mechanisms is given in figure 1. Excellent review papers [1,2] on radiation-induced absorption have been published and therefore only a brief description of the processes involved will be discussed here. Radiation-induced absorption is due to the formation of color centers. γ-rays interact with the material to produce Compton electrons and the neutrons interact to produce secondary electrons. At the same time, the neutrons and Compton electrons cause atom displacements to create defects in the material through momentum transfer. The Compton and secondary electrons then interact with the material to generate electron-hole pairs. Also, the electron-hole pairs recombine non-radiatively to create defects. The electrons or holes then become trapped at the radiation-created defects or inherent defects to form color centers.

Most of the previous efforts have concentrated on the permanent absorption [1,2,3] resulting from low dose rate steady-state irradiations. Prior studies of the transient radiation-induced absorption resulting from pulsed irradiation have been made at 215 nm [4] and at 257 nm [5]. The present study focuses on the transient radiation-induced absorption at 325 nm in type-III (≈1200 ppm OH) fused silica (Corning 7940) as a result of pulsed reactor (TRIGA) irradiation. The radiation characteristics of the TRIGA reactor pulses are given in table 1. Presented in the table are the neutron and γ fluxes and fluences for three typical different size single pulses. The size of the pulses are characterized in terms of excess reactivity ($). All of the irradiations and absorption measurements presented in this paper were done at room temperature, although during the radiation pulse the temperature of the sample was raised ≈8 °C.

2. Experimental

A schematic of the experimental set-up is given in figure 2. A sample of the optical material to be studied was placed in a multi-pass optical cavity which was then positioned adjacent to the reactor core in the through-port of the TRIGA reactor. The multi-pass cavity utilizes a Lissajou-type resonator which increases the sensitivity of the absorption

Table 1. TRIGA Reactor Pulse Characteristics

Reactivity ($)	3.00	2.50	1.75
Peak			
γ Dose Rate (MRad/s)	35	21	7.4
Thermal Neutron Flux (n/cm²s)	4.3×10^{15}	2.6×10^{15}	8.9×10^{14}
Fast Neutron Flux (n/cm²s)	4.0×10^{15}	2.4×10^{15}	8.3×10^{14}
Total			
γ Dose (MRad)	0.50	0.39	0.21
Thermal Neutron Fluence (n/cm²)	6.2×10^{13}	4.8×10^{13}	2.9×10^{13}
Fast Neutron Fluence (n/cm²)	5.7×10^{13}	4.5×10^{13}	2.7×10^{13}
Pulse Width FWHM (ms)	13	17	29

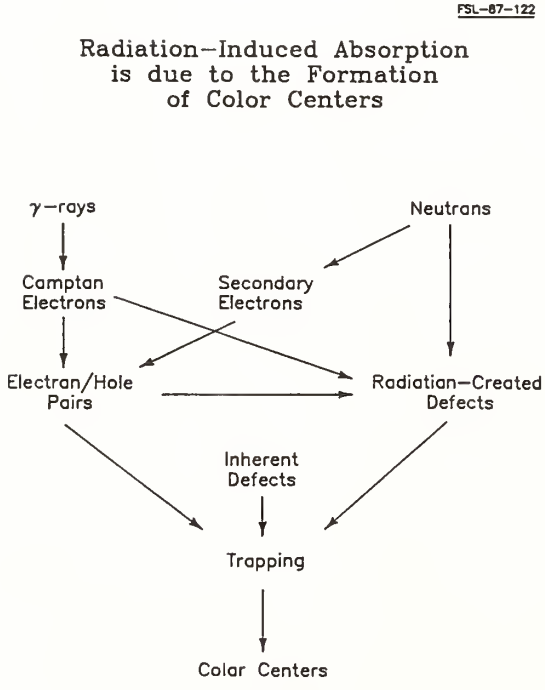

Figure 1. Schematic of radiation-induced absorption mechanisms.

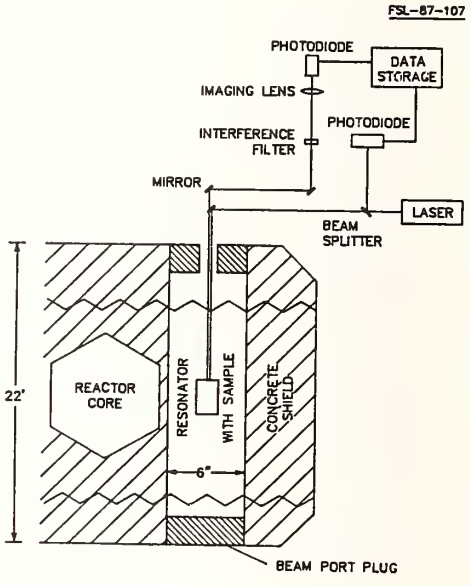

Figure 2. Schematic of experimental set-up.

measurements ≈40 times due to an increase in path length through the sample. A diagram of the multi-pass cavity is given in figure 3. The mirrors are UV-enhanced aluminum and the lens is fused silica. These materials were chosen to minimize the effects of irradiation on the performance of the cavity.

Laser light from a He-Cd laser with a wavelength of 325 nm was directed through the sample and multi-pass cavity. The output of the multi-pass cavity was then measured by photodiode detectors and stored on a digital oscilloscope. A narrow band-pass filter ($\Delta\lambda$ = 2.5 nm) was used to reduce the background signal due to the fluorescence of the sample. A laser reference signal was obtained by splitting the laser beam before it entered the multi-pass cavity to allow accurate measurements of the absorption on long time scales after the irradiation pulse.

The effects of the pulsed irradiation on the multi-pass cavity optics have been determined and were found to account for 3% of the total maximum absorption measured during the reactor

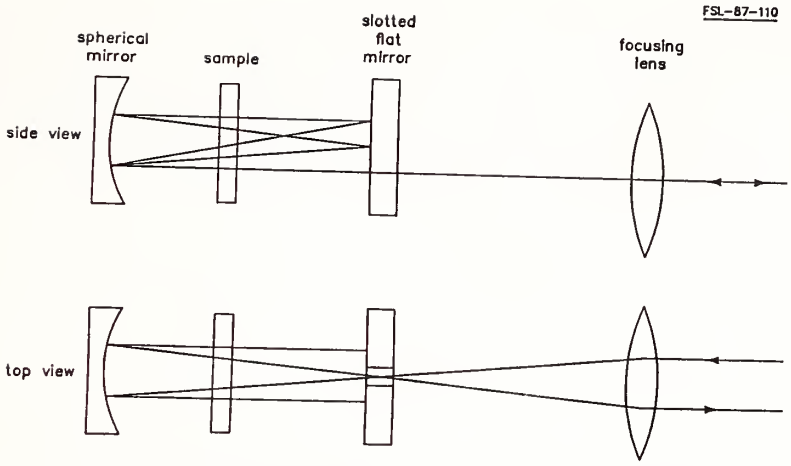

Figure 3. Diagram of multi-pass (Lissajou-type) resonator.

pulse and for 75% of the total absorption measured at a time of 1000 s after the reactor pulse. The absorption attributed to the cavity optics were subtracted from the total measured absorption to yield the absorption coefficients for the fused silica.

3. Results

The radiation-induced absorption (α) as a function of time for a \$3.00 pulse at room temperature is given in figure 4. α reaches a maximum value (α_{max}) of 0.0070 cm^{-1} during the pulse then asymptotically approaches a permanent value afterwards. α_{40} and α_{1000} are the absorption coefficients at 40 and 1000 s after the pulse respectively, and are labeled on the curve in figure 4. α for the fused silica decreases to 0.0001 cm^{-1} at a time of 1000 s after the pulse. This corresponds to a recovery of 99%.

The transient radiation-induced absorption in fused silica at 325 nm is compared to previous work [4] at 215 nm in figure 5. The previous work was done on the same material (Corning 7940) and at the same reactor (University of Illinois' TRIGA). At 215 nm, α is found to reach a maximum of 0.077 cm^{-1} with a recovery of 53% to 0.036 cm^{-1}. Since these experiments were done at different times with different apparatus, and different quality Corning 7940 samples, etc., there remains some uncertainty about the validity of a direct comparison. Still the large difference in α illustrates a strong wavelength dependence as α_{max} is an order of magnitude greater at 215 nm than at 325 nm. In addition, the recovery of α proceeds slower and to a lesser extent at 215 nm than at 325 nm. These results suggest that different color centers are responsible for absorption at 325 nm vs. 215 nm.

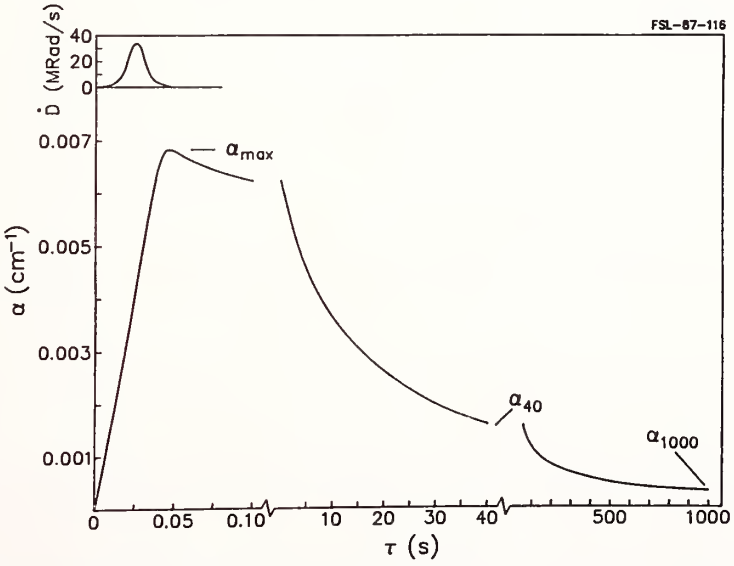

Figure 4. Radiation-induced absorption as a function of time.

The radiation-induced absorption as a function of time for a series of $3.00 reactor pulses is given in figure 6. The pulses are 17 minutes apart with a dose of 0.5 MRad each. α_{max}, α_{40}, and α_{1000} for each pulse in the series of pulses shown in figure 6 are given in figure 7 as functions of dose. In general, α increases with increasing accumulated dose. If the color centers are formed at the inherent defects, α would become saturated with increasing dose. And if the color centers are formed at the radiation-created defects, α would be approximately linear with increasing dose. The experimental data shows a combination of both of these trends.

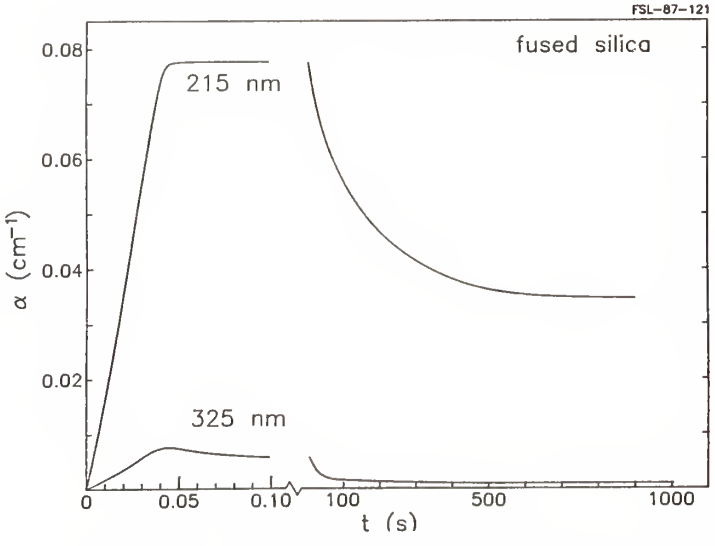

Figure 5. Comparison of radiation-induced absorption at 215 nm vs. 325 nm.

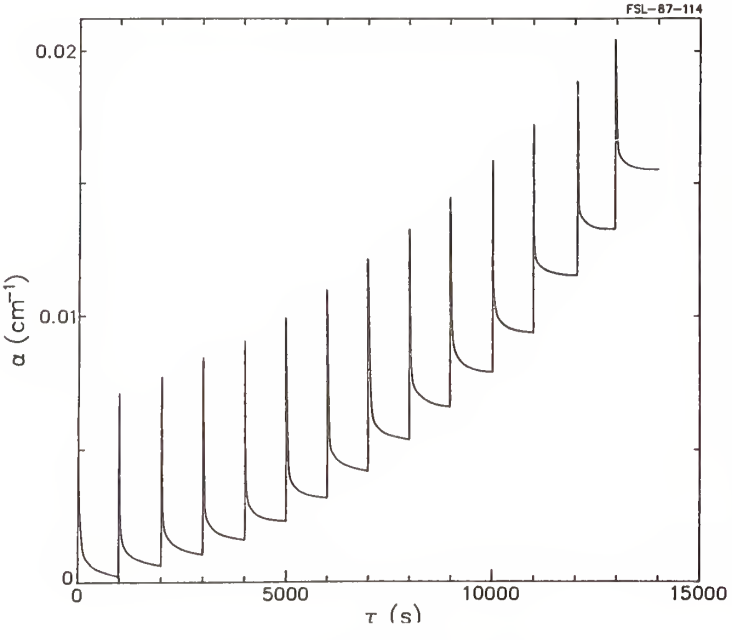

Figure 6. Radiation-induced absorption as a funtion of time for a series of pulses.

At low accumulated doses the color centers responsible for α_{max} (the short-term color centers) are formed at both the inherent and radiation-created defects. At high accumulated doses, the short-term color centers are mainly formed at the radiation-created defects. These results are presented in terms of α_{max}/D, α_{40}/D, and α_{1000}/D in figure 8. α_{40}/D and α_{1000}/D increase with increasing dose indicating that the material recovers to a lesser extent as the accumulated dose increases. This suggests that the fused silica network bonds, broken to create the defects,

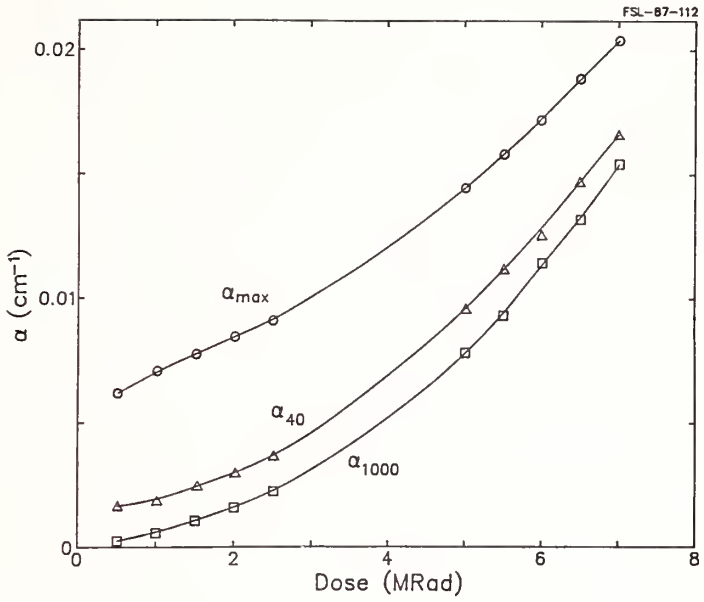

Figure 7. α_{max}, α_{40}, and α_{1000} for each pulse in a series of pulses.

reform to a lesser extent as the accumulated dose increases (i.e., the annealing of the long-term color centers decreases as the accumulated dose increases).

Some points about this data can be clarified by considering relative changes in α for each pulse. α' is defined as the relative absorption coefficient. It measures the absorption as a result of one pulse in a series of pulses and is normalised with the transmission through the sample just prior to the particular pulse of interest. The difference between α and α' is illustrated in figure 9. α'_{max}, α'_{40}, and α'_{1000} are given in figure 10 as functions of accumulated dose for a series of pulses. α'_{max} is found to exhibit a maximum with increasing dose indicating that the maximum relative absorption coefficient is not constant for a series of pulses. α'_{40} and α'_{1000} increase with increasing dose suggesting that the long-term color centers anneal to a lesser extent as the accumulated dose increases. α' as a function of time is given in figure 11 for a sample that had previously received 1.0 MRad and 6.5 MRad. At the lower accumulated dose, α' recovers to a greater degree (99%) than at the higher accumulated dose (73%). This again indicates that the long-term color centers anneal to a lesser extent as the accumulated dose increases.

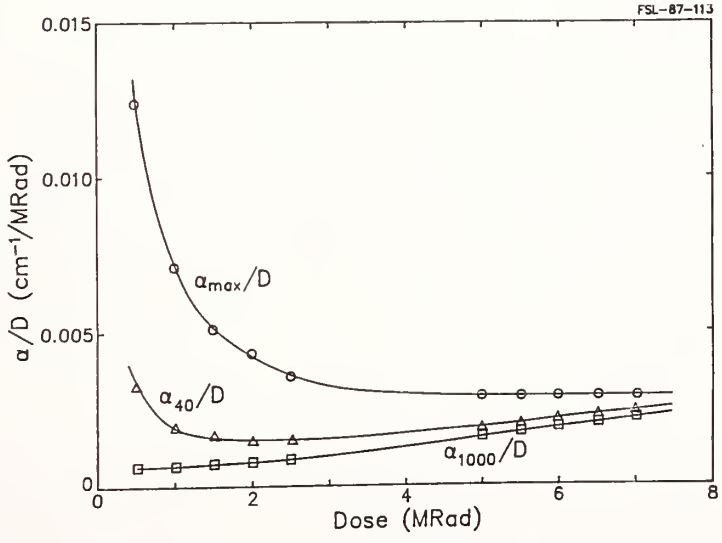

Figure 8. α'_{max}, α'_{40}, and α'_{1000} for each pulse in a series of pulses.

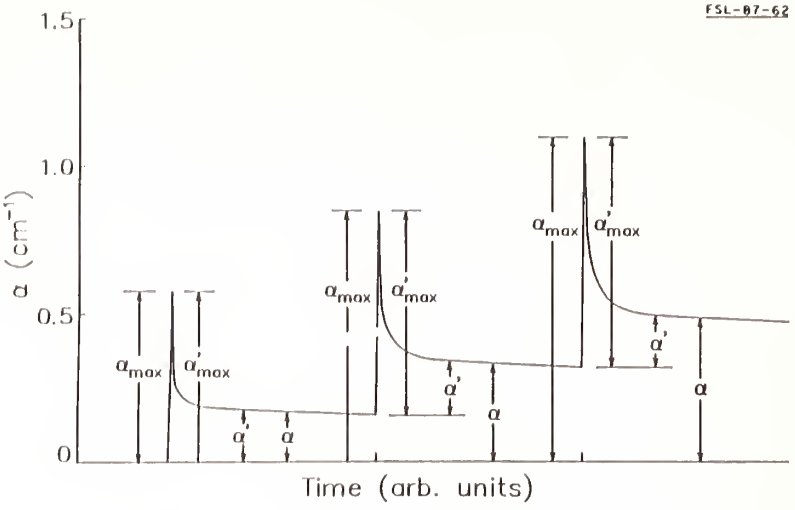

Figure 9. Definition of α and α'.

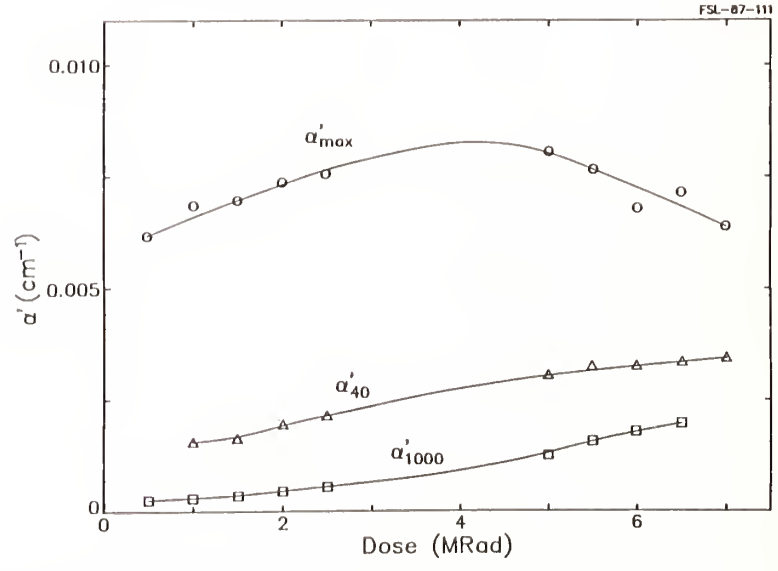

Figure 10. α'_{max}, α'_{40}, and α'_{1000} as functions of accumulated dose.

α'_{max} and α'_{max}/D as functions of three different size single pulses are given in figures 12 and 13, respectively. The different size reactor pulses are characterized in terms of the maximum dose rate during the pulse; the total dose is also shown. α'_{max} increases and α'_{max}/D decreases with increasing maximum dose rate. However, since the integrated dose of a pulse also increases with increasing pulse size (i.e., the maximum dose rate and integrated dose of a reactor pulse are coupled), figures 12 and 13 could also be presented in terms of the dose of the different size reactor pulses and would exhibit the same trends. Indeed, the trends observed in the figures are similar to those that would be expected for α as a function of dose (i.e., the 0 - 0.5 Mrad range of figures 7 and 8). This negative curvature in figure 12 is termed a dose effect because it shows a similar behavior as that seen in figure 7. If the curvature in figure 12 were positive, going contrary to what would be expected by the increasing dose alone, it would be termed a dose rate effect since it would only be attributable to the increasing dose rate. Therefore, over the range of maximum dose rates shown in figures 12 and 13, α'_{max} and α'_{max}/D do not appear to exhibit any dose rate effects. Earlier work [6] on Pyrex at 632.8 nm is compared to the current work on fused silica at 325 nm in figures 14 and 15. The percent change in α'_{max}/D as a function of three different size single pulses for Pyrex and fused silica is given in figure 14. α'_{max}/D increases with increasing maximum dose rate for Pyrex and decreases with increasing maximum dose rate for fused silica. Thus, Pyrex exhibits an interesting dose rate effect whereas fused silica appears to exhibit only a dose effect. The normalized absorption coefficient as a function of time for Pyrex and fused silica is given in figure 15. Fused silica recovers slower but to a greater extent than Pyrex.

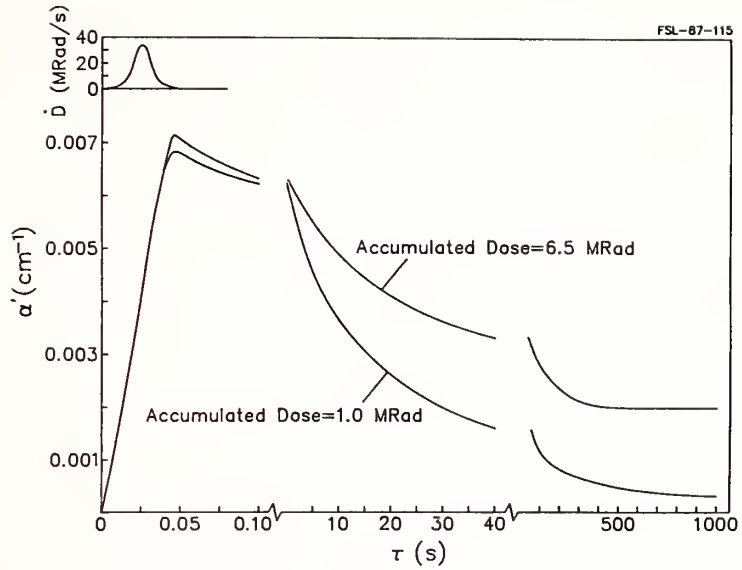

Figure 11. α' for a sample at accumulated doses of 1.0 and 6.5 MRad.

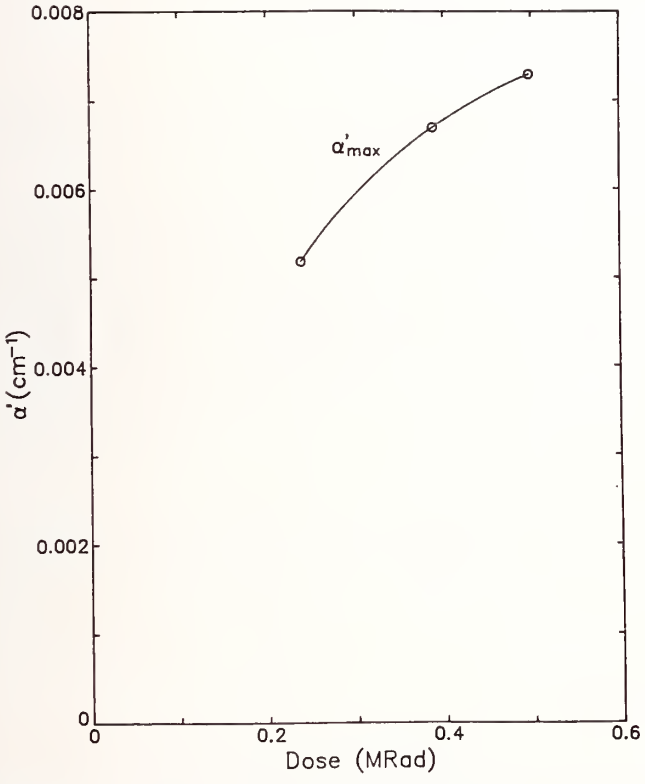

Figure 12. α'_{max} vs. dose for 3 different single pulse sizes.

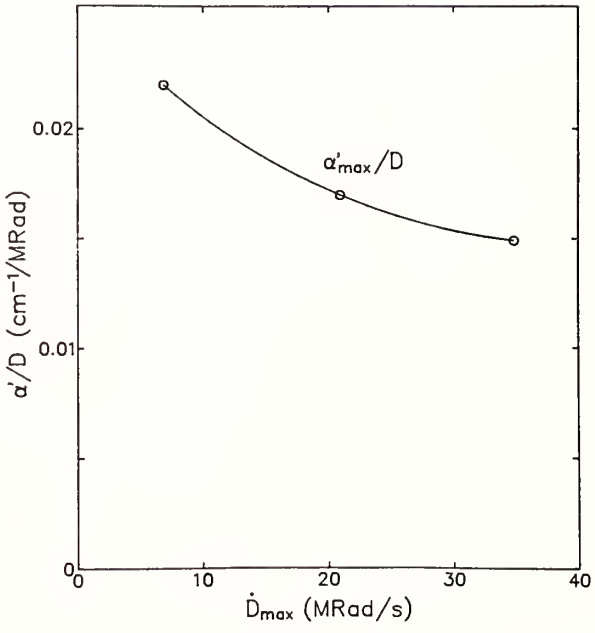

Figure 13. α'_{max}/D vs. maximum dose rate.

4. Conclusions

A multi-pass technique has been developed to enable high-sensitivity measurements of very small transient radiation-induced absorption coefficients. Utilizing this technique, the transient radiation-induced absorption in fused silica (type-III) at 325 nm has been investigated. For a fresh sample, α is found to reach a maximum value of 0.0070 cm^{-1} during a 0.5 MRad reactor pulse and then decreases to 0.0001 cm^{-1} at a time of 1000 s after the pulse. Therefore, α recovers to 99% of its initial value. However, as the accumulated dose on the

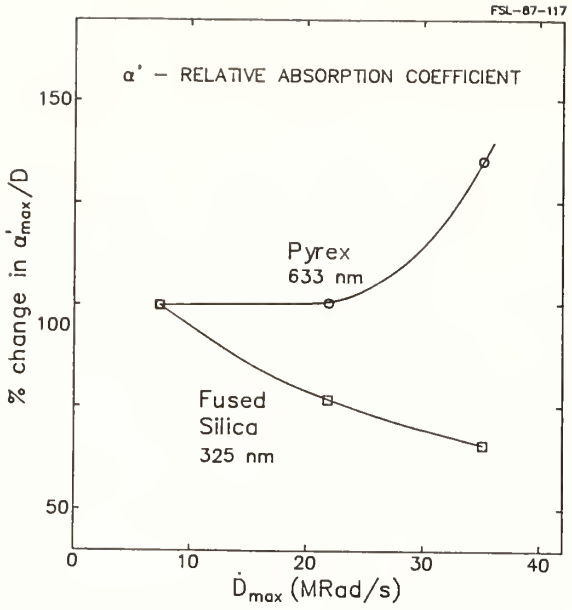

Figure 14. Comparison of fused silica at 325 nm to Pyrex at 633 nm. Note that the data is normalized to one pulse size.

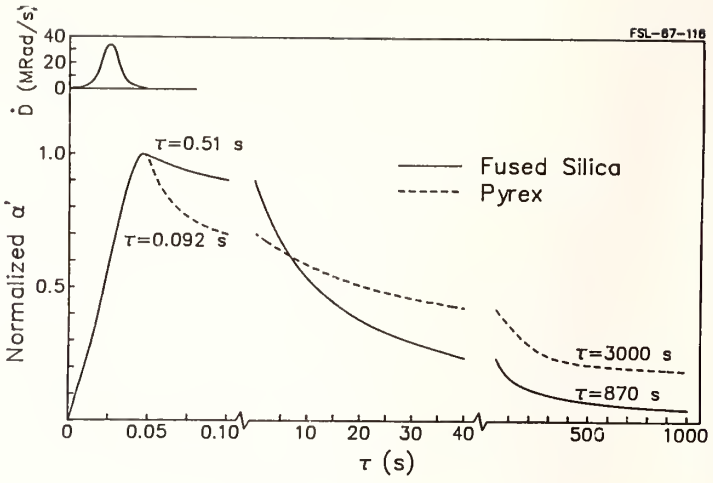

Figure 15. Comparison of α' vs. time for fused silica at 325 nm and Pyrex at 633 nm.

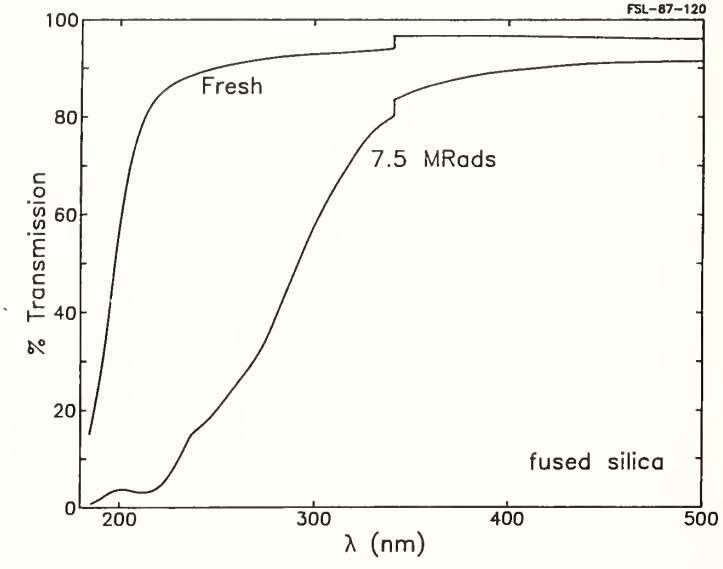

Figure 16. Transmission spectra of fresh and irradiated fused silica.

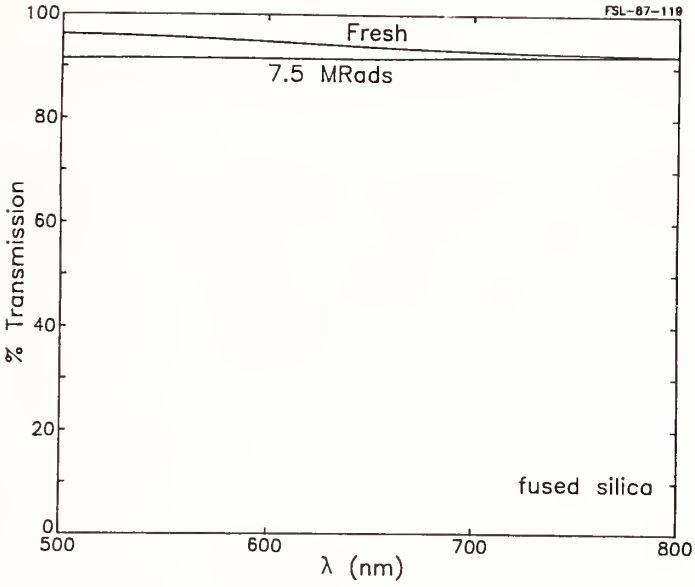

Figure 17. Continuation of figure 16.

sample is increased, the recovery is reduced. For example, after the dose is about 6.5 MRad, a 73% recovery is observed.

A previous study of radiation-induced absorption in fused silica at 215 nm found that α reached a maximum value of 0.077 cm^{-1} during a 0.5 MRad reactor pulse with a subsequent recovery of 53% to 0.036 cm^{-1}. The fact that α exhibits such different behavior at the two wavelengths is characteristic of absorption by color centers. Earlier work done on Pyrex (Corning 7740) at 632.8 nm showed an interesting dose rate effect. The maximum α reached during a single reactor pulse normalized with the total integrated dose of that pulse (α'_{max}/D) was found to increase with increasing pulse size (D_{max}, the maximum dose rate of the reactor pulse). This dose rate effect was not observed in fused silica (Corning 7940).

This work was supported by Sandia National Laboratory under contract number 01-0371, and by EG&G Idaho, Inc. under contract number C87-101376-2. The authors would like to thank Corning Glass Works for providing the samples used in this study.

5. References

[1] Griscom, D. L. "Nature of Defects and Defect Generation in Optical Glasses," SPIE Radiation Effects in Optical Materials 541; 38; 1985.

[2] Levy, P. "Overview of Nuclear Radiation Damage Processes: Phenomenological Features of Radiation Damage in Crystals and Glasses," SPIE Radiation Effects in Optical Materials 541; 2; 1985.

[3] Friebele, E. J.; Higby, P. L. "Radiation Effects in Amorphous SiO_2 for Window and Mirror Substrates," 19th Annual Symposium on Optical Materials for High Power Lasers, 1987.

[4] Palma, G. E.; Gagosz, R. M. "Optical Absorption in Fused Silica During Irradiation Annealing of the C-Band," J. Phys. Chem. Solids 33; 177; 1972.

[5] Brannon, P. J.; Morris, R. W.; Gerrardo, J. B. "Nuclear Radiation Induced Absorption in Optical Materials," SPIE Southwest Conference on Optics 540; 451; 1985.

[6] Miley, G. H., Chapman, R., Kislev, H., Nadler, J., and Williams, W., "Radiation-Induced Absorption in Pyrex," Southwest Optics '87 Conference; 1987 February 11-13; Albuquerque, NM.

How did the author distinguish losses in the resonator from losses in the sample? The author replied he ran the resonator without the sample and calibrated the experiment in this way.

Another questioner wondered if the dose rate effects reported could be explained by the different compaction properties of pyrex as compared to fused silica? In zircon, which is a zirconium silicate crystalline material, the material swells. Is there a correlation? The author replied that pyrex swells also but he had not looked at pyrex in that detail. Pyrex is only 81% silicon dioxide and also contains boron, which would interact with the neutrons in the reactor more strongly per dose than SiO_2. The fused silica was type 3, 1200 ppm OH, Corning 7940.

Manuscript Received

2-5-88/sar

Radiation Effects in Amorphous SiO_2 for Windows and Mirror Substrates

E.J. Friebele and P.L. Higby*

Naval Research Laboratory
Washington, DC 20375

Amorphous SiO_2 is material with unique physical properties, including excellent optical transmission in the uv spectral range and a low coefficient of thermal expansion at cryogenic temperature. These properties make it an attractive candidate for excimer laser windows and as a surveillance mirror substrate. However, in both of these applications the silica may be exposed to substantial doses of ionizing radiation, either from the scattered electrons and x-rays from the laser pump or from the natural and/or enhanced on-orbit space radiation environment. This paper reports the effects of ionizing radiation on the uv transmission and density of SiO_2. Current mirror substrates are fabricated from fused natural quartz. However, the greater purity of *synthetic* silica leads to increased uv transmission and greater radiation resistance. Therefore, measurements have been made on a large suite of silica samples, including fused quartz, synthetic silica fabricated by flame hydrolysis, plasma fusion, or new techniques. In some cases the observed radiation sensitivity has been related to fabrication technique and impurity contents.

Key Words: density, ionizing radiation effects, laser windows, mirror substrates, silica, surface deformation, uv transmittance

1. Introduction

Amorphous silica is an important material for many technological applications because of its broad transmission window, which extends from < 0.20 to > 2.5 μm. In addition, silica is a strong, stable, low density material with a coefficient of thermal expansion near zero at cryogenic temperatures. These properties make silica attractive for both excimer laser windows and surveillance mirror substrates.

The properties of silica, and in particular their response to ionizing radiation, are determined to a large extent by the type and concentration of impurities such as alkali, aluminum, chlorine, and hydroxyl; in turn these are influenced by the mode of glass formation. Bruckner [1] classified silica into 4 types according to fabrication process: **Type I** is fused from natural quartz in an electric arc and contains [OH] < 5 ppm, [Al] = 30-100 ppm, and [Na] = 1-4 ppm as the most significant impurities. **Type II** is fused from natural quartz in a flame and contains [OH] = 150-400 ppm, the other impurities being similar. **Types III and IV** are synthetic and are prepared, respectively, by hydrolysis of $SiCl_4$ in a hydrogen-oxygen (or hydrocarbon-oxygen) flame, or reaction of $SiCl_4$ with O_2 and fusion in a plasma. The most significant difference between Types III and IV silica is the OH content, which is 1200 ppm in the former and < 3 ppm in the latter.

Since Bruckner's work in 1970, new ways of making silica have emerged. In particular, the modified chemical vapor deposition process [2] is extensively used to deposit very high purity low-OH silica for optical fiber waveguide applications. Various techniques for drying silica made by flame hydrolysis have been developed, and sol-gel fabrication [3] can be used to make both thin film and bulk forms. Although there have been extensive studies of the effects of radiation on the optical transmission [4] and physical properties [5,6] of Types I-IV silica, there have been few investigations of the more recently-developed forms. This paper reports a comparative study of the radiation-induced optical absorption in a suite of amorphous silica samples fabricated by different techniques. The radiation-induced compaction and the resultant deformation of polished surfaces are also presented. Correlations between optical absorption and fabrication techniques have been attempted, and the defect center responsible for the observed radiation damage has been identified by correlating the density and deformation results with spectral measurements by optical and electron spin resonance (ESR) spectroscopies.

*Sachs Freeman Assoc., Inc., Landover, MD 20785

2. Experimental

2.1 Samples Studied

Table 1 contains a list of the silica samples studied. Because of the higher metallic impurity content (and hence greater radiation-induced optical absorption) of Types I and II silica, the emphasis of the optical studies was on the synthetic materials, while Type II fused silica was used for the density and deformation measurements since it is currently a candidate for mirror substrates.

Table 1. Samples Used in the Present Study

Silica		OH Content (ppm)
Type II:	Heraeus Optosil	30-50
	Heraeus Ultrasil	30-50
Type III:	Heraeus Suprasil 2	1200
	Heraeus Fluosil SS1.2	1200
Type IV:	Heraeus Suprasil W2 (O_2 Plasma)	< 3
	Mitsubishi (Ar Plasma)	< 3
Other:	Heraeus Suprasil 200	200
	Heraeus Suprasil 300	<< 1
	Heraeus Suprasil 310	260
	NRL MCVD	< 1

2.2 Optical Absorption

The optical measurements were performed on samples 3-5 mm thick, which were polished and measured before and after irradiation. All optical, density and deformation samples in this study were electron-irradiated at 23 C to various doses with a 2 MeV Van de Graaff accelerator. Following exposure to the highest dose, the samples were subjected to 10 min isochronal anneals with temperature increments of 50 C. Optical absorption measurements were made between 0.185-0.800 μm on a Cary 17D spectrophotometer interfaced to an IBM PC computer. Gaussian resolutions were performed on all spectra following conversion of the abscissa from wavelength to energy.

Because of the problem of uniqueness of resolving spectra into Gaussian bands, the following methodology was adopted: First, the spectrum obtained after a sample was exposed to the highest dose was resolved into the minimum number of component bands. Then, the spectra after each anneal were likewise resolved, varying only the height of the component bands while keeping the same central energy and width. This procedure constrains the effect of annealing to changing the *concentration* of defect centers, whereas allowing the peak energy and width of the bands to vary with annealing could be interpreted as allowing the *physical nature* of the color centers to change.

However, it became evident that this procedure of minimum number of bands might not have physical meaning. For example, an excellent fit to the experimental spectrum of irradiated Suprasil W2 shown as the heavy line in figure 1 could be obtained with 3 bands, and excellent resolutions of all the spectra recorded after anneals from 23 to 750 C could likewise be obtained by varying only the heights of these bands.[7] In this case the large peak near 0.22 μm shown in figure 1 was fit with a band centered at 5.71 eV. However, it is well known from the early work of Weeks and Sonder [8] that the E_1' center absorption is at 5.85 eV, while that of the E_2' center is at 5.5 eV (see table 2 for a description of these centers).[9] Since the ESR spectra of the E' centers were easily detected in all irradiated silicas, the correct resolution of the 0.22 μm band is into two components at 5.5 and 5.85 eV, resulting in the 4 band fit for the radiation-induced absorption shown in figure 1.

Figure 1 illustrates the point that it is insufficient to resolve optical spectra into a minimum number of Gaussian components; rather, one must be constrained by the results of other spectroscopies and prior studies on more "well-behaved" samples such as the Type III Corning 7940 used by Weeks and Sonder[8] where the E_1' center band at 5.85 eV is clearly resolved since there is apparently an absence of the E_2' center band at 5.5 eV.

2.3 Density

The densities of Optosil and low CTE Zerodur and Astro Sitall glass-ceramic materials were measured in a density gradient column.[10] Solutions of bromoform and carbon tetrachloride were

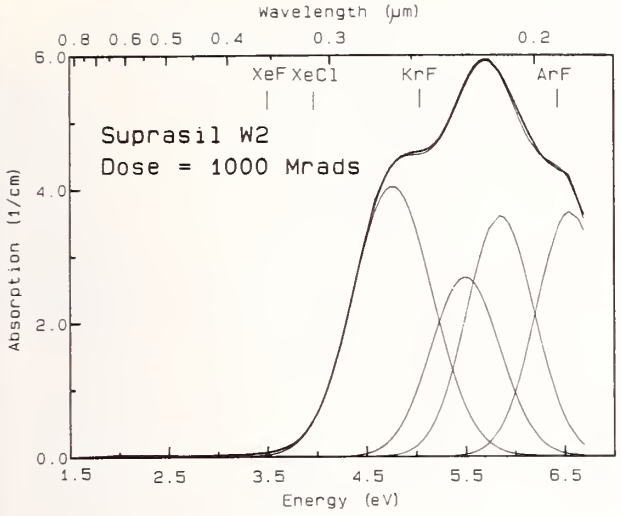

Figure 1. Optical absorption spectrum of irradiated Type IV Suprasil W2 (heavy line) showing Gaussian resolution and component bands (light lines). Primary excimer laser wavelengths are shown at the top of the figure.

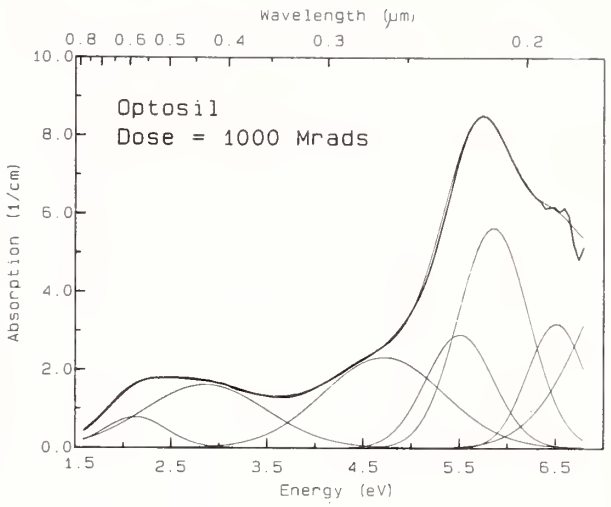

Figure 2. Optical absorption spectrum of irradiated Type II Optosil fused silica (heavy line), Gaussian resolution, and component bands (light lines). The two bands absorbing in the visible (<3.5 eV) are associated with alkali and aluminum impurities.

mixed in the proportions necessary to acquire a gradient spanning the desired density range. Irradiated and unirradiated samples of each material were simultaneously placed in the column in order to accurately measure the change in density due to irradiation. Standards with a precision of 0.0005 g/cc were used for calibration. The sensitivity of the column to density changes was approximately 0.00008 g/cc for silica, and approximately 0.0006 g/cc for the glass ceramics, the difference between the two being due to the larger gradient required in the latter case.

2.4 Surface Deformation

Samples of Optosil and Ultrasil 5-10 mm thick were polished to $\lambda/20$ and irradiated with a collimated beam (masked with a 2 cm thick aluminum block containing a 5 mm diameter hole) to doses of 1×10^9 rads. For comparison, similar samples of two types of Zerodur and a sample of Astro Sitall were also measured. The plates examined qualitatively with a Bausch and Lomb 4.5" Para-Plane Gauge and measured quantitatively with a DekTak profilometer with a resolution of 100 Å. The deformation was measured as a function of dose and annealing temperature.

3. Results and Discussion

3.1 Optical Absorption

The radiation-induced optical spectra of the different synthetic silica samples of this study could all be resolved into the same 4 component bands near 4.7, 5.5, 5.85, and 6.5 eV; a typical resolution of Suprasil W2 (figure 1) shows these bands and slight evidence of the band at 2.0 eV. As shown in Table 2, correlations have been previously established between several of the radiation-induced optical bands in silica and specific defect centers. These include bands at 2.0,[11] 5.5,[9] 5.85,[8] and 7.6 eV,[12] which have been attributed, respectively, to the nonbridging oxygen hole center ≡Si-O· and an electron trap, the E_2' center, the E_1' center, and the peroxy radical ≡Si-O-O·.

The growths of the intensities of these 4 bands have been measured as a function of dose: an example for Suprasil 2 is shown in figure 3. In general, for doses $\leq 2 \times 10^8$ rads the radiation-induced band intensities $\Delta\alpha$ have been found to follow a power law

$$\Delta\alpha = AD^B \qquad (1)$$

where D is the dose and A and B are constants. At doses $>2 \times 10^8$ rads significant saturation is observed. The values of 0.62-0.75 measured for the exponent for the bands in Suprasil 2 for doses $\leq 2 \times 10^8$ rads compare favorably with the exponent of 0.64 in the power law dependence of the radiation-induced compaction (Section 3.2). Interestingly, we have found much lower values of B in the 0.17-0.27 range for the growth of the optical bands in Optosil, in analogy with the lower power

Table 2. Summary of Radiation-Induced Optical Bands in SiO_2.
Peak Energy (E_o) and Width (W) at Half-Maximum Given in eV, f is the Oscillator Strength

Label	E_o	W	f	Occurrence	Defect
	8.2			γ-Irradiation	
	8.0			γ-Irradiation	
E	7.6	0.5	0.65	Pure SiO_2	Peroxy Radical
D	7.15	0.8		Heavy ion irrad.	
C	6.05			Impure SiO_2	
E_1'	5.85	0.6	0.14	Pure/lightly doped	Hole trapped in neutral O vacancy
E_2'	5.5	0.4	0.28	Pure SiO_2	E_1' + proton
	5.3	0.4		Alk-Doped SiO_2	E_1' + alkali
B_2	5.1	0.4		Heavy ion irrad.	Neutral O vacancy
D_o	4.7			Pure SiO_2	
B	3.95	1.2		Impure SiO_2	
A_3	2.90	1.5		Impure SiO_2	"Bare" Al center
A_2	2.55	0.8		Impure SiO_2	Al Center variant
	2.0	0.26		Pure SiO_2	Nonparamagnetic e^- trap
	2.0	0.33		Pure SiO_2	NBOHC
A_1	1.85	0.7		Impure SiO_2	Al center variant

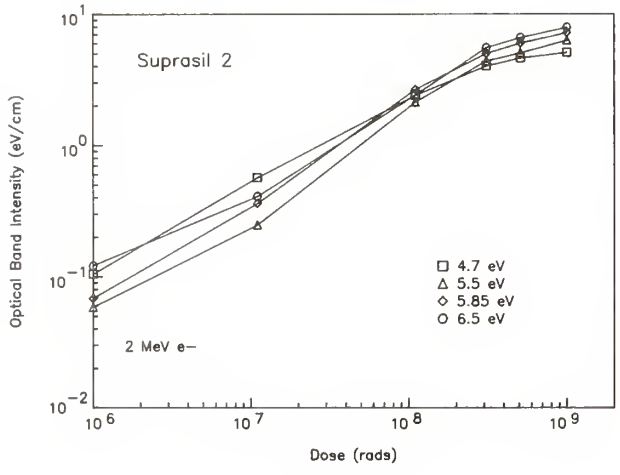

Figure 3. Intensities (product of height and width at half maximum) of component Gaussian bands in irradiated Type III Suprasil 2 vs. dose. Growths approximate a power law for doses < 2 x 10^8 rads with exponents of 0.62-0.75.

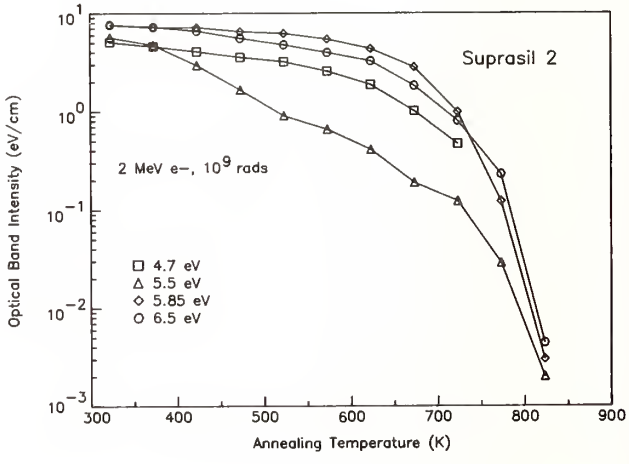

Figure 4. Thermal annealing of the intensities of the component Gaussian optical bands in irradiated Suprasil 2.

law dependence of compaction of this material, as described below.[6] These results, although not in complete agreement in the case of Optosil, suggest an interrelationship between the color centers giving rise to the optical absorption and the structural changes causing densification.

Following irradiation to 10^9 rads, annealing experiments were carried out to investigate the thermal stability and annealing temperature of the various optical bands. Results for Suprasil 2 are shown in figure 4. These studies have also shown that the stability of the uv induced absorption varies significantly among the different silica samples.[7] The E_1' center anneals near 550 K in Suprasil W2, near 825 K in Suprasil 2 (figure 4) and at temperatures >900 K in the other silicas shown in Table 1. This sample-to-sample variation in defect center stability cannot be attributed solely to OH content. For example, Suprasil W2 and Suprasil 300 both have low OH contents, but the annealing temperatures of their E_1' centers are quite different, at 550 and 1050 K, respectively.[7]

Although Types I and II fused silica are not candidates for window applications, it is instructive to compare the radiation-induced absorption spectrum of a synthetic silica such as Suprasil W2 with that of a Type II silica such as Optosil (figures 1 and 2). Note that the same 4 bands at 4.7, 5.5, 5.85 and 6.5 eV are evident in the uv spectral region in both samples. However,

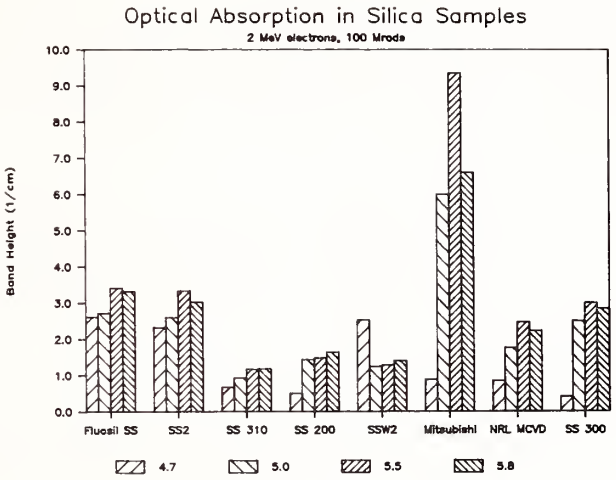

Figure 5. Comparison of Gaussian band heights of various synthetic silicas exposed to 10^8 rads. Samples are plotted from left to right in order of decreasing OH content.

there are additional bands in the visible region in irradiated Optosil which are associated primarily with the alkali and aluminum impurities present in fused natural quartz. The band near 2.2 eV is analogous to the A_1 band in irradiated crystalline quartz, and the band near 3.0 eV is the A_3 band.[13] At lower doses a band near 3.9 eV is evident, which is likely the B band.[13] It is these impurity-related bands which give irradiated quartz its grey-brown, "smoky" color and make it useless for window applications in radiation environments. In contrast, there are no strong induced absorptions in the visible spectral region in irradiated synthetic silica, and the material remains water white after exposure to doses as high as 10^9 rads.

The relative intensities of the 4 bands at 4.7, 5.5, 5.85 and 6.5 eV in all irradiated silicas vary considerably among the different samples. A bar chart comparing the band heights is shown in figure 5. Although it has been traditionally thought that low OH content silica is more radiation-sensitive than high OH, the results in figure 5 show that the noticeable differences between the silicas cannot be attributed simply to OH content. Note that the Fluosil SS and Suprasil 2 samples have 1200 ppm OH, while lower induced loss is measured in Suprasil 200 and 310 with approximately 200 ppm OH. Although more damage is evident in the 5.5, 5.8 and 6.5 eV bands in Suprasil 300 with $<<1$ ppm OH, the intensity of the 4.7 eV band is actually the least in any of the samples measured. Likewise, there is wide variation in the radiation sensitivity of the Suprasil W2, Mitsubishi, and NRL MCVD silicas in spite of the fact that all have approximately the same OH content. These results indicate that the details of the fabrication process, such as the type of plasma used to deposit Type IV silica (or perhaps the level of Cl_2 which is incorporated during deposition and drying [14]), have a strong influence on its radiation damage.

Of particular concern for excimer laser window application are the induced bands absorbing at emission wavelengths; the primary laser lines are shown in figure 1. The XeF and XeCl lines are on the tail of the 4.7 eV band with the former at sufficiently long wavelength that linear absorption should not be a problem. On the other hand, the KrF and ArF lines are located in regions of significant absorption from the 4.7 and 5.5 eV, or 5.85 and 6.5 eV bands, respectively. The relatively intense net optical absorptions at these laser wavelengths suggests that the windows may have difficulty surviving high laser powers in the presence of high radiation fields.

Thus, the 4.7 eV radiation-induced band is likely a major contributor to excimer laser window failure in radiation environments. Figure 5 shows that the greatest heights are measured in the high-OH Fluosil and Suprasil 2 samples and in low-OH Suprasil W2. In contrast, the 4.7 eV band height is much less in the low-OH Mitsubishi and MCVD silicas and least in the new Suprasil 200 and Suprasil 300 samples. These results are further evidence that the fabrication process by which silica is made has a significant influence on its subsequent radiation sensitivity.

Although linear absorption by the radiation-induced optical bands will degrade the window performance, multiphoton absorption processes may play an important role as well. Soileau et al.[15] measured virtually no difference between the 1.06 μm laser damage thresholds of Type III Spectrosil A and B and Type IV Spectrosil WF silicas before and after irradiation. However, when the same measurement was made at 0.53 μm, as much as a 30% decrease in damage threshold occurred in the irradiated samples in spite of the fact that there are no induced absorption bands at this

wavelength. The culprit here was two photon absorption by the 4.7 eV (0.264 μm) band, and indeed Soileau et al. found good agreement between his data and a model which assumed that free carriers were initially generated by two-photon absorption at 0.266 μm and then multiplied by the avalanche process.[15] Thus, in considering the survivability of high power laser windows in radiation environments, it is imperative to consider not only those radiation-induced bands absorbing at the laser wavelength, but also bands at shorter wavelengths which may absorb by multiphoton processes.

3.2 Density

The increases in density of Type II Optosil silica and the Zerodur and Astro Sitall glass-ceramic materials induced by 2 MeV electron irradiation are shown in figure 6. There appears to be a monotonic increase in compaction ($\Delta\rho/\rho$, where ρ is the density of the unirradiated material) with dose in the glass-ceramic materials and Optosil. The lines in figure 6 are linear regression analyses of the compaction data to a power law:

$$(\Delta\rho/\rho)_C = C(D)^B \qquad (2)$$

where $(\Delta\rho/\rho)_C$ is the calculated compaction, D is the dose, and C and B are the intercept and slope. The B value of 0.3 measured here for Optosil irradiated $\leq 10^9$ rads [6] should be contrasted to the linear growth (B = 1) reported by Norris and EerNisse [16] for electron-irradiated Type I Infrasil and Type III Corning 7940 fused silicas for doses < 10^{10} rads. (Norris and EerNisse report saturation of the radiation-induced compaction at doses >10^{10} rads with B = 0.45 at these high doses.) Primak and Kampwirth report a value of B=0.66 [17] for gamma-irradiated Suprasil, and we have measured exponent values of 0.64 and 0.67 for electron-irradiated Suprasil 2 and Suprasil W2 (unpublished work).

The origin of these discrepancies is not known, but it seems likely that both the impurity and OH content and the fabrication process have a strong influence. Although the impurity levels of Infrasil and Optosil should be similar, the OH content of Type I Infrasil is < 8 ppm while that of Optosil is 30-50 ppm. It is also possible that the sample used in the earlier study might have had a higher or different impurity content. In contrast, similar values of B are found for the Type III and Type IV synthetic silicas.

Annealing experiments have been carried out on Optosil. The compaction remains stable for annealing temperatures <450 K and then releases slowly up to about 700 K. In this range approximately 60% of the compaction is released. At higher temperatures, the compaction releases rapidly, and the density approaches its pre-irradiation value after an anneal near 750-800 K. We have attempted to correlate the annealing behavior of the compaction with that of the various paramagnetic defect centers in irradiated Optosil. The best agreement has been found with the OHC, although there is considerable scatter in the density data due to the large gradient used in the column for this measurement. These experiments are being repeated and will be reported at a later time.

3.3 Surface Deformation

A particularly deleterious manifestation of radiation-induced compaction can occur in the form of surface deformation of large mirror substrates. If the substrate is uniformly exposed to radiation of sufficient energy to fully penetrate the faceplate and supporting structure, the compaction will change the radius of curvature as the whole structure shrinks. However, in space where the proton and electron energy spectra are highly peaked at low energy, the irradiation will not fully penetrate the faceplate and support. More severe deformation of the surface will occur in this case.

As shown in figure 7, the radiation-induced surface deformation of the samples studied was found to be most severe in the Zerodur and Astro Sitall glass ceramics and less in Type II Optosil silica,[18] in analogy with the radiation-induced compaction of these materials shown in figure 6. We observed that the maximum depth of the deformation decreased with increasing sample thickness due to the counteracting effects of the limited penetration depth of the electron beam and the restoring force exerted by the undamaged part of the substrate below the damaged area. The deformation depth increased with dose with a power law dependence similar to the growths of the optical absorption and compaction. However, the exponents for growth of the deformation were considerably less that those of the density, varying from 0.1 for Optosil to 0.37 for the glass ceramics. It seems reasonable to attribute these lower values to the effects of the undamaged substrate.

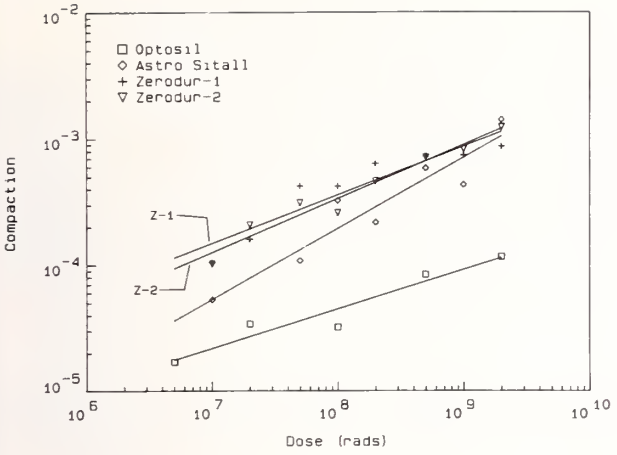

Figure 6. Compaction of Type II Optosil fused silica and low expansion coefficient Zerodur and Astro Sitall glass ceramics vs. electron dose. Lines are regression fits to a power law (see text).

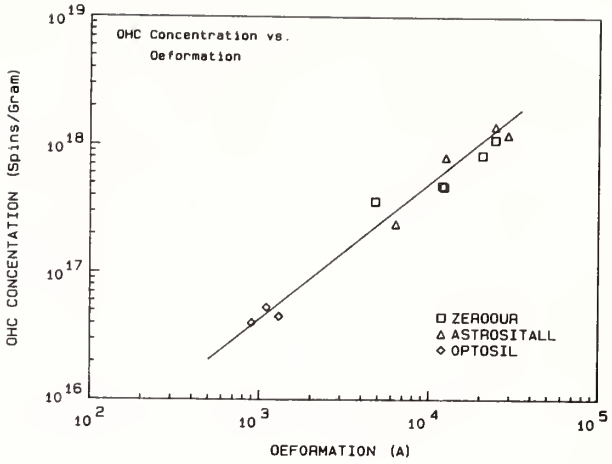

Figure 7. Correlation of peak radiation-induced surface deformation in fused silica and two glass ceramics with the concentration of paramagnetic oxygen hole centers determined by ESR. The line represents a slope of one.

ESR spectra were measured for Optosil and the two glass ceramics following each irradiation, and a number of paramagnetic defect centers were observed, including the E' center, the NBOHC, and the peroxy radical in Optosil, and OHC's, (Ti^{3+}+Zr^{3+}) centers, Fe^{3+}, and two As-related centers in the glass ceramics.[19] Of all these centers, the OHC has been found to correlate most closely with compaction.[19] As shown in figure 7, good agreement was also found between the surface deformation depth and the concentration of OHC's in these materials.[18] The points fall on a line having a slope of one, suggesting that the OHC is the major paramagnetic defect center associated with compaction and surface deformation in the dose region studied here.

4 Model for Radiation Damage in Silica

The traditional, one dimensional model of OHC formation during irradiation consists of radiolytic hole trapping by a non-bridging oxygen compensated by a proton or alkali:

$$\equiv Si - O^{-M^+} + h^+ \text{ ----> } \equiv Si - O\cdot + M^+ \qquad (3)$$

where M^+ represents the proton or alkali ion and ≡Si - O· is the paramagnetic OHC. Following hole trapping, the alkali diffuses away from the OHC site and trapped alternately with electrons on an alkali cluster.[20] The radiolytic protons bond together to form hydrogen molecules.

It is difficult to envision how the OHC formation described in equation 3 could result in compaction at high doses. Rather, it seems plausible that bond breaking might result in a net *expansion* of the silica glass matrix, and in any event, the formation mechanism requires impurities, which are present in only limited quantities in synthetic silica. Rather, we propose the model for radiation damage shown in figure 8.

It is well known that the intermediate range structure of silica consists of rings of SiO_4 tetrahedra.[21] When exposed to radiation, a Si atom at the site of a strained bond in a large membered ring traps an electron and relaxes into a planar configuration. The previously-bonded oxygen would then be left with one electron in a non-bonding orbital--hence, it would be a paramagnetic OHC. Subsequent rebonding of the large-membered rings results in the formation of smaller-membered rings. Evidence that smaller rings do indeed form has been presented by Bates, et al. using Raman spectroscopy;[22] neutron irradiation of amorphous SiO_2 caused the 606 cm^{-1} band to increase significantly in intensity relative to the band at 440 cm^{-1}. The 606 cm^{-1} "defect" band has been assigned to three-membered rings in the silica structure while the 440 cm^{-1} band is generally associated with six-membered tetrahedral rings.[21] The shift in ring statistics to smaller average ring size would explain the observed density increase after irradiation [22].

The model proposed in figure 8 does not fully explain the correlation between density or deformation and OHC concentration since the formation of two closed, 3-membered rings from a 6-membered ring would annihilate an OHC involved in the intra-ring bonding. However, in order for the rings to form, substantial rearrangement of the surrounding glass matrix may be required, and

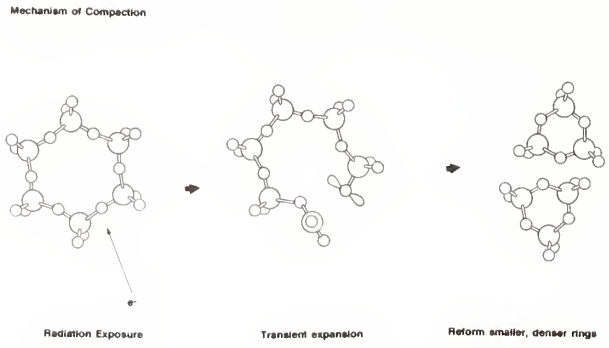

Figure 8. Model for radiation-induced compaction in fused silica due to the breaking of Si-O bonds in 6-membered rings and subsequent rebonding to form 3-membered rings.

the OHC may transfer to an oxygen involved in inter-ring bonding. In any event, the correlations established here between the concentration of OHC's, the density and the surface deformation, together with the similar growth behaviors of the density, deformation and optical band intensity are strong evidence of the important role of electronic defect centers in the radiation damage of amorphous silica.

5 Conclusions

The results of the present study have shown that ionizing radiation has a significant effect on the optical and physical properties of amorphous SiO_2. The radiation-induced degradation in uv transmission, the compaction and its resultant effect on mirror surface quality must all be taken into account in considering silica for excimer laser window or surveillance mirror substrate applications. However, considerable variations in radiation sensitivity with fabrication or processing techniques have been demonstrated in this study. Thus, judicious choice of materials may provide sufficient radiation hardness for most applications, and it seems likely additional advances in hardening will be forthcoming as new fabrication processes are developed and refined.

The authors would like to thank D.L. Griscom for helpful discussions and suggestions and A. Kreutzer, Amersil, Inc., and A. Sakar, Lightwave Technologies, Inc., for providing samples.

6. References

[1] R. Bruckner, J. Non-Cryst. Solids 5: 123-175; 1970.
[2] W.G. French, R.E. Jaeger, J.B. MacChesney, S.R. Nagel, K. Nassau and A.D. Pearson, Optical Fiber Telecommunications, S.E. Miller and A.G. Chynoweth, Ed. (Academic Press, New York, 1979), pp. 233-262.
[3] S.P. Mukherjee, J. Non-Cryst. Solids 42: 477-488; 1980.
[4] For extensive reviews, see: E.J. Friebele and D.L. Griscom, Treatise on Materials Science and Technology Vol. 17: Glass II, M. Tomozowa and R.H. Doremus, Ed. (Academic Press, New York, 1979), pp. 257-351; R.T. Williams and E.J. Friebele, CRC Handbook of Laser Sci. and Tech., III: Optical Materials, M.J. Weber, Ed. (CRC Press, Inc., Boca Raton, FL, 1986), pp. 297-449.
[5] For a recent review, see: M. Rajaram and E.J. Friebele, "The effects of nuclear radiation on the physical properties of low expansion coefficient materials," J. Non-Cryst. Solids (in press).
[6] P.L. Higby, E.J. Friebele, C.M. Shaw, M. Rajaram, E.K. Graham, D.L. Kinser and E.G. Wolff, "A survey of radiation effects on the physical properties of low expansion coefficient glasses and ceramics," J. Am. Ceram. Soc. (in press).
[7] E.J. Friebele, P.L. Higby and T.E. Tsai, "Radiation-induced optical absorption in amorphous silicas prepared by different techniques," J. Non-Cryst. Solids (in press).
[8] R.A. Weeks and E. Sonder, Paramagnetic Resonance 2: 869; 1963.
[9] C.M. Nelson and R.A. Weeks, J. Am. Ceram. Soc. 43: 396-399; 1960.
[10] ASTM D1505-68 "Standard Method of Test for Density of Plastics by the Density-Gradient Technique".
[11] E.J. Friebele, D.L. Griscom and M.J. Marrone, J. Non-Cryst. Solids 71: 133-144; 1985.
[12] M. Stapelbroek, D.L. Griscom, E.J. Friebele, and G.H. Sigel, Jr., J. Non-Cryst. Solids 32: 313-326; 1979.
[13] K. Nassau and B.E. Prescott, Phys. Stat. Sol. A 29: 659-663; 1975.
[14] D.L. Griscom and E.J. Friebele, Phys. Rev. B 34: 7524-7533; 1986.

[15] M.J. Soileau, N. Mansour, E. Canto and D.L. Griscom, Defects in Glasses, MRS Proceedings Volume 61, F.L. Galeener, D.L. Griscom and M.J. Weber, Ed. (Materials Research Society, Pittsburgh, 1986), pp. 205-211.
[16] C. B. Norris and E. P. EerNisse, J. Appl. Physics 45: 3876-3882; 1974.
[17] W. Primak and R. Kampwirth, J. Appl. Phys. 39: 5651-5658; 1968.
[18] M. Rajaram, T.-E. Tsai, and E.J. Friebele, "Radiation-induced surface deformation in low thermal expansion glasses and glass-ceramics," J. Am. Ceram. Soc. (in press).
[19] T.-E. Tsai, P.L. Higby, E.J. Friebele, and D.L. Griscom, J. Appl. Phys. 62: 3488-3490; 1987.
[20] D.L. Griscom, J. Non-Cryst. Solids 6: 275-282; 1971.
[21] F. Galleener, Sol. State Comm. 44: 1037-1040; 1982.
[22] J. B. Bates, R. W. Hendricks and L. B. Shaffer, J. Chem. Phys. 61: 4163-4176; 1974.

A question was raised as to whether by annealing the original vibration spectra could be reobtained. The speaker replied that some of the color centers could be annealed out, although the annealing temperature for some of them is really quite high, around 900 K to 1000 K. Some of the compaction can also be annealed out. However, the rebonding and reconfiguration of the three-membered rings does not get annealed out and one must remelt the glass.

Another question was what type of ionizing radiation and hence what penetration depth was required for compaction. The author replied that one could see compaction with any type of radiation; penetrating or not. However, to get a good view of the deformation it is nice to have a sample that is thicker than the damage so that everything is deposited in a layer within the sample. They see compaction as low as 8 x 10+6 Rads. The surface deformation at that level is largely unmeasurable in silica. The deformation curves shown were at 10+9 Rads.

In response to a question about the difference between electron, x-ray and gamma ray environments, the speaker noted that a Rad is a Rad, energy deposited in a material. The difference is in the depth of penetration. The gamma rays are fully penetrating, whereas the electrons are not fully penetrating. The depth of 2 Mev electrons is approximately 2 mm. The damage, however, is roughly equivalent. Low energy electrons, which are deposited mainly on the surface, can induce greater compaction because of the surface strain which is already there.

A questioner suggested that the density of color centers had to be at least enough to ionize in a single photon or low order multiphoton step in order for them to change the damage threshold. Their density therefore had to be at least 10+17 or 10+18/cc. The reason is that at damage there are probably about 10+18 free carriers and the defects must contribute a sizeable fraction of that before they will influence the damage threshold. The speaker replied that in the samples tested the defect concentrations were probably in this order.

Another listener commented that one had to be careful in dismissing smaller concentrations of defects because although their absorption might be small, they might have a profound effect on the initiation of exponential processes such as dielectric breakdown.

Manuscript Received
3-17-88

Ultrafast Imaging of Optical Damage in PMMA.

Taehyoung Zyung, Hackjin Kim, Jay C. Postlewaite and
Dana D. Dlott*

School of Chemical Sciences
University of Illinois at Urbana Champaign
505 S. Mathews Ave.
Urbana, IL. 61801

A new imaging system with ultrafast (75 ps) time resolution, the "picosecond microscope" is used to study the damage dynamics of PMMA irradiated at 532 nm. A small diameter (50 μm), intense laser pulse is used to damage the PMMA, and a larger diameter, delayed probe pulse is imaged onto a video camera detector. The resultant time-dependent images are a "motion picture" of the damage process.

Key words: optical damage, PMMA = polymethyl methacrylate, ultrafast spectroscopy, ablation, shock waves, microscopy

1. Introduction

Optical damage is an example of a *spatially inhomogeneous* solid state chemical reaction. In order to develop a thorough understanding of the mechanism(s) of optical damage, it is necessary to perform experiments which measure the formation of damaged areas with both *temporal* and *spatial* resolution. In other words the ideal technique is ultrafast microscopy.

In this work, we describe an apparatus for ultrafast microscopy, and apply the technique to the problem of optical damage in a transparent polymer. A preliminary report of this work has appeared in Chemical Physics Letters [1].

The first usage of ultrafast imaging, by Fork, Downer and Shank [2], was a study of the melting of a silicon surface irradiated by intense subpicosecond pulses. In that work the recording medium was motion picture film, and the spatial resolution was about 5 μm. In our experiments we use diffraction limited optics, providing a spatial resolution of better than 1 μm, and the recording medium is a video camera and computer. The advantage of digital image acquisition, compared to film, is the ease of signal averaging and the ability to use standard techniques of digital image analysis.

There has been recent interest in the use of polymers for optical materials [3], and in the laser machining of polymers via ablative photodecomposition [4]. The best characterized optical polymer [5], PMMA (polymethyl methacrylate), is chosen for our optical damage studies, which used single shot damage with 75 ps, 532 nm laser pulses. In this case material damage occurs mainly via photothermal effects [4].

The deposition of a considerable fraction of the incident laser pulses via nonlinear absorption processes results in violent damage. Using our ultrafast imaging system, we have observed the growth of a dark, absorbing volume in the PMMA which we term the damage "core". When the sample is damaged in air, some of the polymer is ablated, generating a hypersonic shock wave in the air, which propagates outward from the core. When the sample is damaged in vacuum, we observe the generation of a large amplitude acoustic wave which propagates through the PMMA at the velocity of sound.

---

* Author to whom correspondence should be addressed.

2. Experimental

These experiments were performed with a home-built laser system which has been previously described [6]. The laser pulses are extremely well characterized, possessing a clean gaussian spatial profile, a gaussian temporal profile, and a gaussian spectrum. They are transform limited. This system produces 532 nm pulses of energies up to E = 650 μJ whose duration, measured by background free autocorrelation, is t_p = 77 ± 2 ps, where t_p is the full width at half maximum. The irradiating power of the damage pulses is calculated using the formula

$$P = E/[t_p \pi(\omega_0)^2] , \quad (1)$$

where ω_0 is the gaussian beam radius. The peak power at the center of the pulse is roughly 20% greater than P.

The experimental setup for ultrafast imaging is diagrammed in figure 1. The laser pulse is split into a damage and a probe pulse, whose intensity is about one-sixth of the damage pulse. The p-polarized damage pulse passes through a thin-film polarizer (CVI Corp.), and is focused onto the sample in a low vacuum chamber (≈ 10^{-2} torr) to a spot size (gaussian beam radius) of ω_o = 50 μm. The probe pulse is up-collimated and a half-wave plate is used to make the pulse s-polarized. This probe pulse is sent along a variable delay. It is then imaged onto the sample in a counterpropagating geometry. The spot size of the probe, ω_o = 250 μm, is much larger than the excitation so that the probe flux is less than one percent of the damage flux, and the probe alone does not produce damage. After passing through the sample, the probe pulse is reflected from the thin-film polarizer and is imaged onto the camera with a computer-optimized achromatic lens (Melles Griot, Inc.).

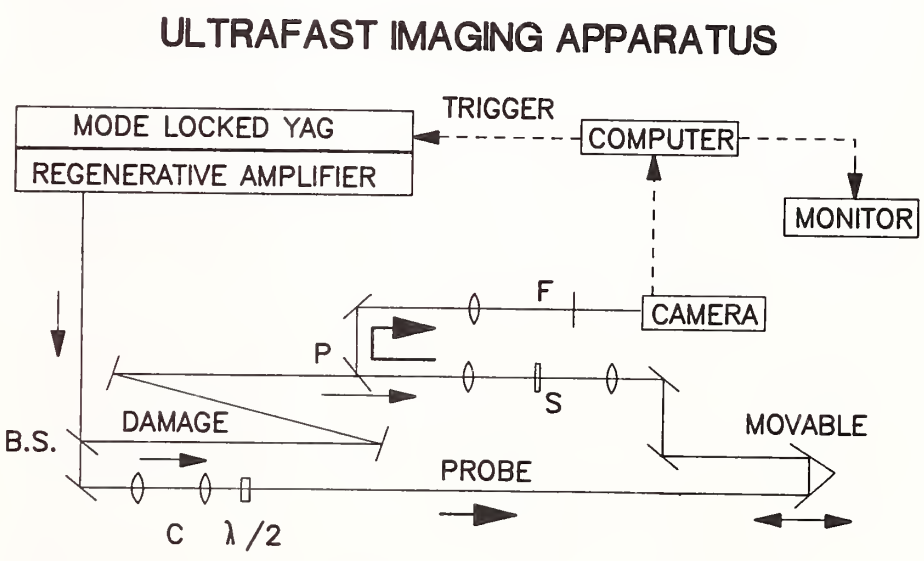

Figure 1. The damage pulses and probe pulses are counterpropagating and orthogonally polarized. The laser is described in [6]. Key: BS = beam splitter, P = polarizing beam splitter, C = beam collimator, F = calibrated neutral density filters, S = PMMA sample, λ/2 = half wave plate.

The probe pulse spatial profile is detected with a video camera (Panasonic). The video output of this camera is acquired with a computer (IBM PC AT) and video frame grabber (DT2803, Data Translation, Inc.), which resolves each image into 256 x 256 pixels with eight bit intensity resolution. In our experiments, each pixel corresponds to a region roughly 1 μm^2. The PMMA samples were 1/32 inch thick, much less than the confocal parameter of the laser pulses to insure uniform irradiation. The images were obtained at various delay times -200 ps $\leq t_d \leq$ 17 ns, where negative delay denotes that probe *precedes* damage.

3. Results and Discussion

Plots of dynamic images taken at different delay times and the permanent damage are shown in figure 2. The plots are of the "wire grid" type, where the height above the plane of the image represents *decreased* transmittance of the probe laser pulse. The images are obtained by subtracting the probe pulse profile from the dynamic image. A background correction is also performed to remove noise at the level of the lowest digitized bits. The images are representative individual damage events. Images in the left column are acquired with a laser power P = 54 GW/cm^2 with the sample in the ambient atmosphere, and images in the right column are obtained with P = 42 GW/cm^2 under vacuum. Note the different magnification in each column.

In air and vacuum, the damage volume (bottom of each column) is cylindrical, with a diameter about 40% as large as the laser beam diameter. This indicates that damage, which is induced via nonlinear absorption, occurs pre-

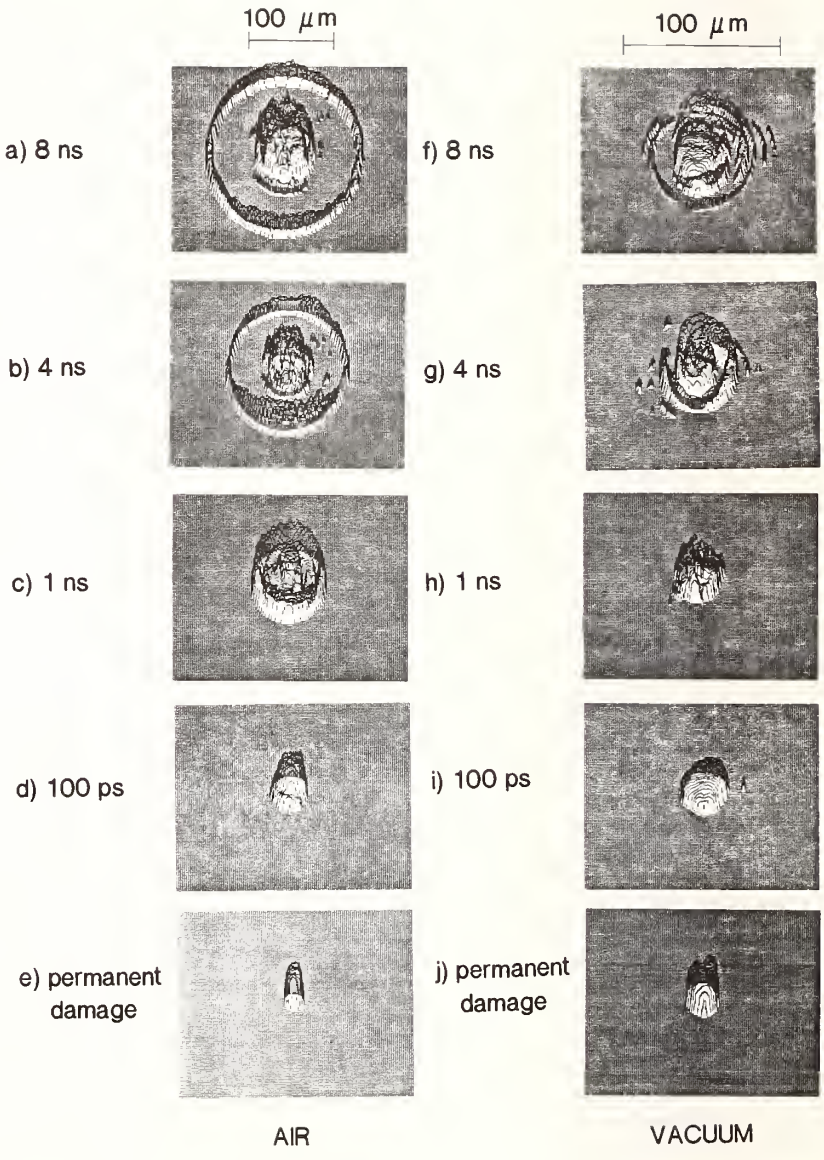

Figure 2. Dynamic damage images obtained from optical damage of PMMA in air (left column) and in vacuum (right column). Note the change in magnification in each column. At bottom is the image of permanent damage. The delay times are indicated next to each image.

ferentially at the hot center of the laser pulse. In air, an expanding ring, which is clearly visible in figure 2 a-c propagates outward from the damage core at high velocity, which in its initial stages is as much as twenty times the velocity of sound in air. This ring, not observed in vacuum, is caused by a shock wave in the air above the damage region. We also observe another ring which propagates away from the core, but at a much slower velocity (e.g. fig. 2, top). The time dependent radii of the ring patterns are plotted in figures 3a and 3b.

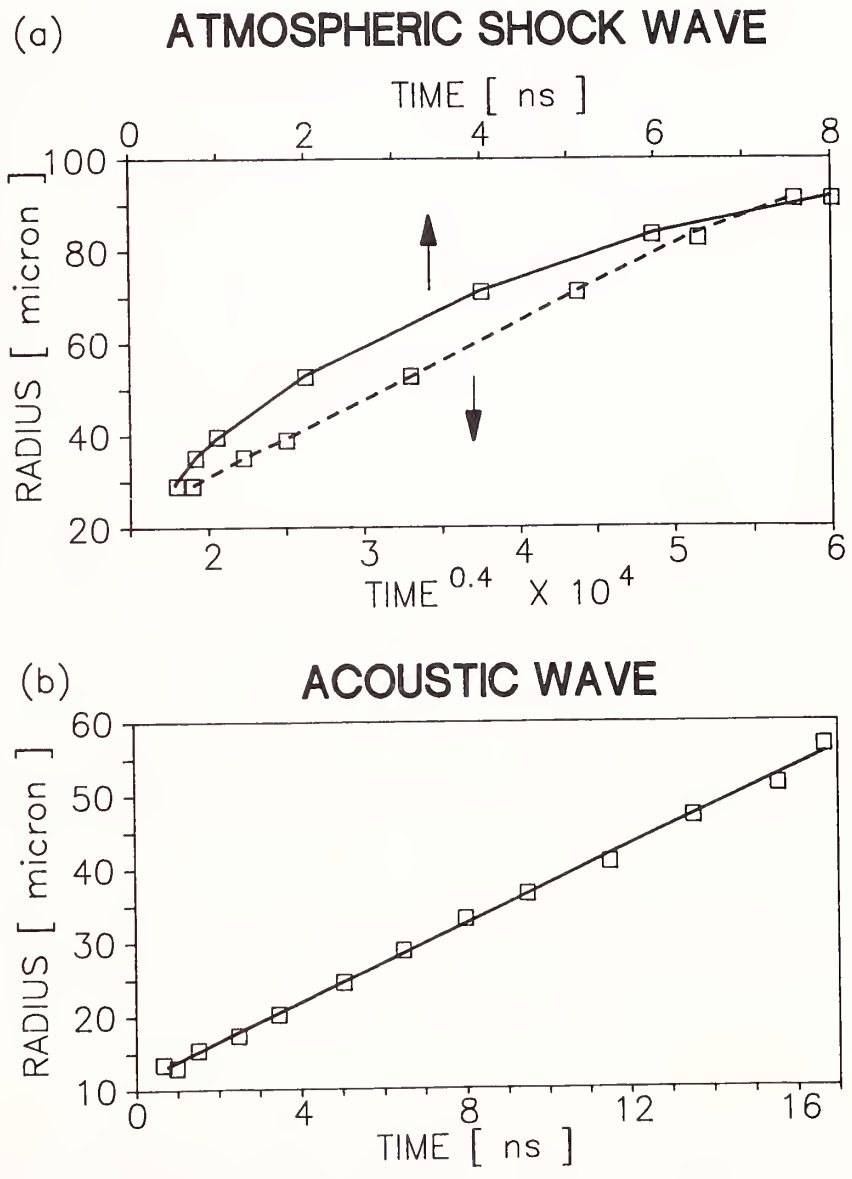

Figure 3. (a) Time-dependent radius of laser produced atmospheric shock wave (*open squares*). The initial velocity is roughly twenty times the velocity of sound. The radius $R \propto (\text{time})^{0.4}$ as predicted by eq. 2. (b) Time-dependent radius of laser produced stress wave in PMMA (*open squares*) is a linear function of time.

The hydrodynamic theory of shock waves [7] gives the relationship between the radius of the shock wave and the energy deposited by the damage process,

$$R = \xi_0 \left(\frac{E}{\rho} \right)^{0.2} t^{0.4} , \qquad (2)$$

where R is the radius of the shock wave, t is the time, E is the energy deposited into the air, ρ is the density of air, and ξ_0 is a known constant related to the heat capacity of air, with a value near unity. The time dependent radius of the shock wave in figure 3a (*open rectangles*) is a nonlinear function of time (*solid curve*, upper axis), but when plotted versus $t^{0.4}$, a linear relation is obtained (*broken line*, lower axis) whose slope gives a direct measurement of the deposited energy, E. In one experiment, we used an incident pulse energy of 370 μJ, yielding an incident power of 27 GW/cm^2. Under these conditions, the energy of the atmospheric shock wave was 130 $\pm$ 20 μJ, representing a 35% conversion efficiency of laser pulse into shock wave. This conversion efficiency is not highly dependent upon the incident intensity; when the laser power is lowered by one-half, the conversion efficiency was hardly changed, i.e. the energy in the shock ring was almost one-half.

Figure 3b shows the time dependent radius of the ring pattern in vacuum [*open rectangles*]. The radius is now a linear function of time, with the slope yielding the velocity V = 2.67 $\pm$ 0.04 km/s, within experimental error the velocity of sound in PMMA, V = 2.70 km/s. Unlike the atmospheric shock wave, its propagation is nearly independent of the damage laser intensity.

Observation of the growth of the damage core region was investigated using a new ultrafast technique involving image processing. It is clear from figure 2 that at early values of t_d the shock and acoustic waves overlap spatially with the core to some extent, e.g. figures 2d, 2i, 2h, making it difficult to observe core growth independently. Unlike UV laser ablation [4], the optical damage process using 532 nm light does not result in a reproducible damage core, but rather the spatial extent and shape of the core varies somewhat in each damage event. This variation is caused by large scale heating effects which are unimportant in UV damage processes [4]. In order to overcome these difficulties, we found a method to process the dynamic probe pulse image to determine the time dependent transmission through the damaging sample *by projecting from each image an area of the exact size and shape of the permanent damage created on that laser pulse* [1]. Using this method of image processing, we can determine a normalized, spatially projected absorbance, $A(t_d)$ which has the property that $A(t_d = -\infty) = 0$ and $A(t_d = \infty) = 1$. The spatially projected absorbance is defined as

$$A(t_d) = \frac{\iint dx\, dy \left\{ \left[I_0(x,y) - I(x,y,t_d) \right] \theta \left[I_0(x,y) - I_p(x,y) \right] \right\}}{\iint dx\, dy \left[I_0(x,y) - I_p(x,y) \right]} , \qquad (3)$$

where $\theta(z)$ is the step function which is 1 for $z > 0$ and 0 for $z \leq 0$. The physical interpretation of $A(t_d)$ is as follows. First the probe pulse gaussian background, $I_p(x,y)$ is subtracted from the permanent damage, $I_0(x,y)$ and the dynamic damage image, $I_p(x,y,t_d)$. Then the region of the dynamic image which overlaps the permanent damage is projected out of the image,

and the resultant is integrated over all space. Finally the integral is normalized so that $A(t_d = -\infty) = 0$ and $A(t_d = +\infty) = 1$.

Figure 4 shows the normalized absorption ratio of the core region of a sample in vacuum as a function of delay time, t_d, at three laser powers. Each data point is the average of 10-20 damage events, and the error bars ($\pm\sigma$) are about 5%. If optical damage were imagined to be a linear, well-behaved process, the time dependence of damage build-up would be the sigmoidal curve obtained by integrating the gaussian laser pulse autocorrelation function (*solid curve*). However it is observed that increasing the laser damage pulse power will shift the damage build up to earlier values of the delay time, indicating that optical damage core formation is initiated at the leading edge of high power pulses and towards the trailing edge of lower power pulses. At ca. 100 ps, each build up curve overshoots unity, but at long delay, the curves return to unity. The overshoot indicates that at small delay times, $t_d \leq 1$ ns, the core attenuates the probe pulse *more* than the permanent damage image. This additional attenuation is due to the early influence of the acoustic and shock waves.

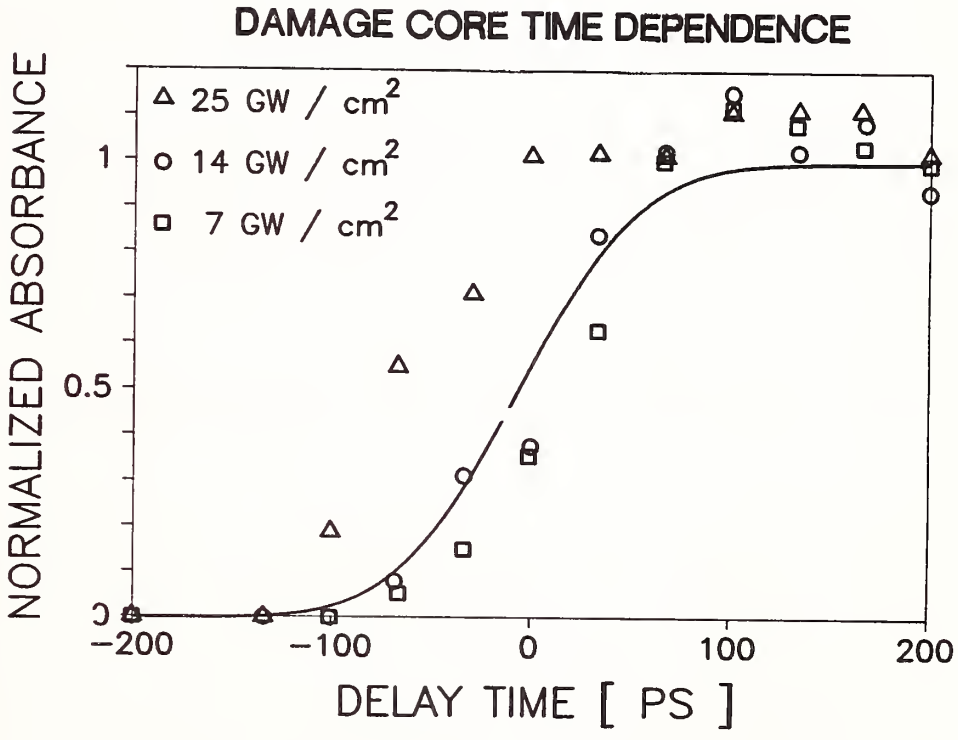

Figure 4. Time dependent growth of spatially projected, normalized absorption ratio of the dark damage core at three laser powers. The *solid curve* is the apparatus function which would describe the build-up of a linear, well-behaved process.

4. Conclusion

The qualitative picture of the damage process which emerges as a result of these experiments is that severe damage is produced in the leading edge of a powerful laser pulse, but near the trailing edge with a less powerful pulse. This implies the existence of a threshold value of the flux (J/cm^2), which may depend upon the pulse duration [4]. Upon reaching this threshold flux value, fragments of polymer are ablated into the space above the sample,

probably via local heating, where they temporarily screen the surface from the damaging pulse. The recoil of this ablation launches the acoustic wave in the solid. In air, the ablated fragments continue to absorb the laser light and transfer their energy to the air, which becomes superheated, and moves outward at velocities as great as twenty times the velocity of sound. In vacuum, where no shock wave is observed, the ablated fragments move away from the blast core more rapidly because they are not slowed by air resistance. In air, roughly 50% of the laser pulse energy can be converted into atmospheric shock wave, while in vacuum a larger fraction of the laser pulse is converted into material damage.

These results suggest that it might be possible to selectively enhance or impede optical damage processes by using properly shaped laser pulses [8] which interact more or less with the cloud of ablated material. The rate of dissipation of this cloud may be responsible, in part, for the dependence of damage thresholds on pulse duration at constant fluence. Workers attempting to use optical damage to write on plastic with high spatial resolution should consider the possibility of nonlocalized material damage due to shock and acoustic wave formation.

This research is supported by the US Army Research Organization through grant DAALO-86-K-0135, and by the National Science Foundation, Division of Materials Research, by grant NSF DMR 84-15070.

5. References

[1] Kim, H.; Postlewaite, J. C.; Zyung, T; Dlott, D. D. Ultrafast imaging of optical damage dynamics and laser-produced wave propagation in PMMA. Chem. Phys. Lett. (in press).

[2] Downer, M. C.; Fork, R. L.; Shank, C. V. Femtosecond imaging of melting and evaporation at a photoexcited silicon surface. J. Opt. Soc. Am. B. 2(4): 595-598 (1985).

[3] O'Connell, R. M; Saito, T. T. Plastics for high-power laser application: a review. Opt. Eng. 22(4): 393-399 (1983).

[4] Srinivasan, R. Ablation of Polymers and Biological Tissue by Ultraviolet Lasers. Science 234: 559-565 (1986).

[5] O'Connell, R. M.; Deaton, T. F.; Saito, T. T. Single- and multiple-shot laser damage properties of commercial grade PMMA. Opt. Eng. 23(5): 682-688 (1984).

[6] Postlewaite, J. C.; Miers, J. B.; Reiner, C. C.; Dlott, D. D. Picosecond Nd:YAG regenerative amplifier with electrooptic VFET pulse switchout. IEEE J. Quant. Electron (in press).

[7] Zel'dovich, Y. B.; Raizer, Y. P.: Physics of Shock Waves and High-Temperature Hydrodynamic Phenomena. New York; Academic Press, 1967.

[8] Warren, W. S.; Silver, M. S.: The art of pulse crafting: applications to magnetic resonance and laser spectroscopy. Adv. Mag. Res. 12: 247-383 (1988).

Recent Progress in Understanding Fundamental Mechanisms of Laser Induced Damage in Optical Polymers

K.M. Dyumaev, A.A. Manenkov, A.P. Maslyukov,
G.A. Matyushin, V.S. Nechitailo, and A.M. Prokhorov

General Physics Institute of the Academy of Sciences
Moscow, USSR

Damage studies in polymers of acrylic and methacrylic type with low-molecular additives like water, alcohols, and similar compounds are presented. It was established that some additives significantly (by a factor of 10 to 100) increases multi-shot laser damage resistance of polymers. Vibration energy transfer (vibrational cross-relaxation) from polymer macromolecule to additive molecules which suppress the laser created absorbing radicals was shown to be attributed to such damage resistance increase. A mechano-chemical mechanism of laser damage in polymers is proposed which includes laser excitation of vibration states and creation of absorbing "hot radicals". Basing on this mechanism we proposed methods of physical modification of polymers with high laser damage resistance comparable with that of silicate glasses and crystals.

Key Words: laser induced damage; low-molecular additives in polymers; mechano-chemical laser damage mechanism; optical polymers; physical modification of polymers; vibrational cross-relaxation.

1. Introduction

Large efforts have recently been made to get an insight into the mechanisms of laser induced damage in polymers as a class of optical materials. Since optical polymers have physical and chemical properties essentially different from those of other optical materials (inorganic glasses and crystals), one may naturally expect that the mechanisms of laser induced damage in transparent polymers will also considerably differ from the damage mechanisms in crystals and glasses.

Rather a large number of works have been devoted to elucidation of the laser induced damage mechanisms in polymers [1-7]. Various mechanisms have been suggested, such as multi quantum photodestruction of macromolecules [3], thermochemical reaction of carbon-black formation in the matrix surrounding inclusions 4-6 and others [1,2,7]. However, a detailed analysis of the available experimental data based on these mechanisms has shown that these mechanisms fail to account for all the series of results obtained. In particular, these mechanisms do not account for inherently optical damage resistance in ordinary (nonmodified) polymers and considerable (up to two orders of magnitude) difference in the thresholds of single-pulse and multipulse damage in polymers [8].

In this connection we have carried out extensive, systematic investigations of the major regularities of laser induced damage in optical polymers [8,9] enabling us to offer an adequate mechanism of optical breakdown in polymers, based on an account of mechano-chemical processes in the matrix surrounding the absorbing defect [10]. In the present work we point out the major peculiarities of laser induced damage to polymers, present new experimental data on laser induced damage in acryl-series polymers with various low-molecular additives, discuss the proposed mechano-chemical mechanism of laser induced damage which explains all the major regularities of optical breakdown in polymers. Based upon this mechanism, we present an efficient technique of physical modification of polymers that leads to new modified polymers with damage resistance comparable to that of the most damage-resistant inorganic glasses and crystals.

2. Major Peculiarities of Laser Induced Damage in Polymers and New Experimental Results

Many experiments, including investigation of the influence of monomer purification, spot-size dependence and, spatial fluctuations of the damage thresholds have indicated that absorbing defects play an essential role in the processes of laser induced damage in polymers as well as in optical materials of other classes of materials (inorganic glasses and crystals) [11]. Optical breakdown in polymers has, however, some peculiarities, compared to the other materials. These peculiarities, having been so far established, are as follows: relatively low damage resistance (10-100 times lower) of usual (nonmodified) polymers, compared to high resistance of crystals and glasses [9]; great (up to two orders of magnitude) difference in the thresholds of single-pulse and multipulse damage in polymers [8]; sharp decreasing (more than 10 times) of the single-pulse damage threshold in polymers, compared to initial monomers [9]; strong temperature dependence of the multipulse damage threshold near the glass transition temperature [9]; remarkable increase of the damage resistance of polymers on introducing plasticizers [9]; absence of laser radiation self-focusing in polymers even at intensities essentially exceeding the damage threshold [9]; noticeable higher surface damage threshold compared to the bulk [9] (other optical materials usually feature a reverse relationship of the surface and bulk damage thresholds).

In our recent research we have established that the low-molecular additives introduced into a polymer have a markedly selective influence on its optical strength, thus enhancing its laser damage resistance [10]. This very important result is shown in figure 1 presenting the multipulse damage threshold of polymethylmethacrylate (PMMA) versus concentration of a series of additives: propanol, butanol, hexanol, butyronitrile, and cyclohexanol. Mixing of butanol and hexanol into PMMA is seen to increase its laser damage resistance most strongly, whereas butyronitrile and cyclohexanol in the same concentrations only slightly increase the damage resistance.

Further investigations have shown that mixing of water, whose molecules form hydrogen bonds with the molecules of the other additives (alcohol type), has a stronger effect on the polymer optical damage resistance. Figure 2 illustrates this result presenting multipulse damage threshold versus water concentration for PMMA containing propanol and dibutyl phthalate. Injection of water (even in small concentrations (1%)) into mixture with propanol is seen to result in an essential (more than 10 times) increasing of the damage threshold, whereas in mixture with dibutyl phthalate water addition does not influence the damage threshold.

Note that the results presented on essential influence of low-molecular additives upon the laser damage resistance of polymers cannot be accounted for by any chemical transformations in the matrix, since the injected additives are chemically inert compounds. We assume the effect to be associated with the physical interaction of the additive molecules with the polymer macromolecules preventing the chemical processes of radical formation in the matrix under laser irradiation. Proceeding from this concept we have offered the following model of laser induce damage in polymers [10].

3. Theoretical Model

According to our model, damage is initiated by the absorbing inclusions and defects. Due to laser heating, impulse thermoelastic stresses arise in the polymer matrix around the inclusions and defects, which lead, by means of mechano-chemical reactions, to the appearance of vibrationally excited (hot) radicals absorbing laser radiation, thus, enhancing absorption in the matrix surrounding the defects. In other words, an absorption wave propagates in the polymer around an inclusion which finally leads to macrodamage. In the framework of this model, the influence of low-molecular additives on the polymer laser damage resistance is associated with the radical formation suppression due to energy transfer from a macromolecule to additive molecules. Since radicals appear in polymers from the excited vibrational states of macromolecules, the influence of low-molecular additives is evidently associated with

the energy transfer between the excited vibrational states of macromolecule and higher vibrational states of the additive molecules. This energy transfer reduces lifetimes of the macromolecules excited states and, as a result, decreases the efficiency of the radical generation.

Mathematical analysis of the polymer damage mechanism offered has been made solving the heat transfer equation with a nonlinear thermal source

$$Q = (\chi_d + \chi_r)\cdot I \qquad (1)$$

where χ_d is the light absorption coefficient of defect, and

$$\chi_r = \sigma_r C_a \tau_r K_{mch} \qquad (2)$$

is the absorption coefficient of hot radicals (σ_r and τ_r are absorption cross-section and lifetime of hot radicals, respectively, K_{mch} is the rate constant of mechanochemical reaction of their formation, C_a is the concentration of the chemical bonds from which the radicals are formed). Solution of this equation has shown that laser heating of the defect and surrounding matrix has an essentially nonlinear temporal character. Solutions show an asymptotically fast temperature increase and allows one to determine the threshold intensity of a N pulse damage event [10]:

$$I_N = \frac{D\ E_a}{\tau_a(\sigma_s)} \qquad (3)$$

where D is the thermoelastic parameter, E_a is the activation energy of hot radicals formation, τ_a is the vibrational relaxation time of the chemical bonds from which hot radicals are formed, σ_s is the residual stress parameter.

When mixing low-molecular additives into a polymer, the vibrational relaxation time is reduced as follows

$$\tau_a' = \frac{\tau_a}{1 + W_{cr}\cdot\tau_a} \qquad (4)$$

where W_{cr} is the vibrational cross-relaxation rate, and for the N-pulse damage threshold we have

$$I_N = DE_a \frac{1 + W_{cr}\ \tau_a(\sigma_s)}{\tau_a(\sigma_s)} \qquad (5)$$

where

$$\tau_a(\sigma_s) = \tau_0(1 + \delta\sigma_s) \qquad (6)$$

τ_0 and δ are parameters.

It is seen that in case of strong vibrational cross-relaxation ($W_{cr}\tau_a >>1$), which occurs at an efficient interaction of the additive molecules with macromolecules (in particular, in case where vibrational states of macromolecules and additive molecules are overlapped to give rise to resonance energy exchange), the multipulse damage threshold essentially depends on the type of low-molecular additive characterized by the W_{cr} value. In case of weak vibrational cross-relaxation ($W_{cr}\tau_a<<1$) the multipulse damage threshold is determined by visco-elastic properties of the matrix characterized by a breaking strength of the polymer, σ_b to which residual stresses tend at multiple laser irradiation.

In the framework of the considered model, the accumulation effect observed at multiple laser irradiation of a polymer is associated with accumulation of residual thermoelastic stresses around the absorbing defects at their laser heating from pulse to pulse. These stresses increase the lifetime of the excited vibrational states of the macromolecules from which the absorbing hot radicals are formed (see (6)), as well as the rate of mechanochemical reaction of radicals formation.
The theoretical model developed qualitatively explains all the observed features of laser induced damage in polymers. In particular, the influence of the matrix viscoelastic properties depending on both the temperature (most strongly near the glass transition temperature), and the injection of plasticizers [9], is associated with the lifetime change of the excited vibrational states of the macromolecules giving birth to the absorbing radicals due to variation of internal stresses in these molecules. Therefore, the polymer temperature rise and mixing of plasticizers into it lead to a remarkable increase of its laser damage resistance.
Selective influence of low-molecular additives upon optical damage resistance of the polymer is associated, as seen from formulae (4) and (5), with the efficiency of vibrational cross-relaxation between the additive molecules and macromolecules. Indeed, OH-groups of hydrogen-bound water molecules have the vibration frequency multiple to that of the carbonyl group ($\rightleftharpoons$C=O) in the PMMA macromolecule responsible for the formation of acyl radicals (-C=O), whereas free OH-groups have the vibration frequency is essentially different from that of carbonyl group [12]. Therefore, for interaction of bound OH-groups with PMMA macromolecules, strong vibrational cross-relaxation should be observed and, hence, laser damage resistance of the polymer with this additive should considerably increase; and for free OH-groups - weak vibrational cross-relaxation which does not practically affect the damage resistance. This expectation is experimentally confirmed.

4. Conclusion

The investigations carried out on laser induced damage in polymers and the developed theoretical model have shown that optical breakdown of polymers is associated with the absorbing defects initiating, due to laser heating, mechanochemical reactions of absorbing radicals formation. The analysis of the suggested damage mechanism offers ways for physical modification of polymers in order to increase their optical damage resistance: 1) plasticization lowering the induced elasticity limit; 2) mixing low-molecular additives efficiently preventing the formation of the absorbing radicals due to vibrational cross-relaxation. The experiments have supported this concept and allowed us to produce modified acryl-series polymers with laser damage resistance comparable with that of the most damage-resistant crystals and glasses. For instance, modified PMMA has the damage threshold at the 1.06 μm wavelength and 10 ns laser pulse duration equal to $I_1 = 5.10^{11} W/CM^2$, silicate glass K8 and fused quartz - $I_1 = 7.10^{11} W/cm^2$. These results illustrate attractive opportunities of wide application of modified polymers in laser optics.

6. References

[1] Ashkinadze, B.M.; Vladimirov, V.I.; Likhachev, V.A.; Ryvkin, S.M.; Salamanov, V.M.; Yaroshetsky, I.D. Soviet JETP, 1966, v.50, p. 1187.

[2] Barenblatt, G.I.; Vsevolodov, N.N.; Mirkin, L.I.; Pilipetsky, N.F.; Raizer, Yu.P. Soviet JETP Letters, 1967, v.5, p.87.

[3] Agranat, M.B.; Krasyuk, I.K.; Novikov, N.P.; Perminov, V.P.; Yudin, Yu.I.; Yampol'sky, P.A. Soviet JETP, 1971, v.60, p.1748.

[4] Orlov, A.A.; Ulyakov, P.I. Soviet JAMTP, 1976, No1, p.127.

[5] Butenin, A.V.; Kogan, B.Ya. Kvantovaya Elektronika 1976, v.3, p.1136.

[6] Liberman, M.A.; Tribel'sky, M.I. Soviet JETP, 1978, v.74, p.194.

[7] Kovalev, A.A.; Makshantsev, B.I.; Pilipetsky, N.F.; Sidorin, Yu.V.; Stonik, O.G. Kvantovaya Elektronika, 1980, v.7, p.1287.

[8] Manenkov, A.A.; Matyushin, G.A.; Nechitailo, V.S.; Prokhorov, A.M.; Tsaprilov, A.S. Laser Induced Damage in Optical Materials: 1982, NBS Spec. Publ. 669, p.436.

[9] Dyumaev, K.M.; Manenkov, A.A.; Maslyukov, A.P.; Matyushin, G.A.; Nechitailo, V.S.; Prokhorov, A.M. Laser Induced Damage in Optical Materials: 1981, NBS Spec. Publ. 638, p.31.

[10] Dyumaev, K.M.; Manenkov, A.A.; Maslyukov, A.P.; Matyushin, G.A.; Nechitailo, V.S.; Prokhorov, A.M. Izvestiya AN SSSR, Ser. Phys., 1985, v.49, p.1084.

[11] Manenkov, A.A.; Nechitailo, V.S. Kvantovaya Elektronika, 1980, v.7, p.616.

[12] Smith, A. Applied IR spectroscopy. Moscow, "Mir", 1982, 328 p.

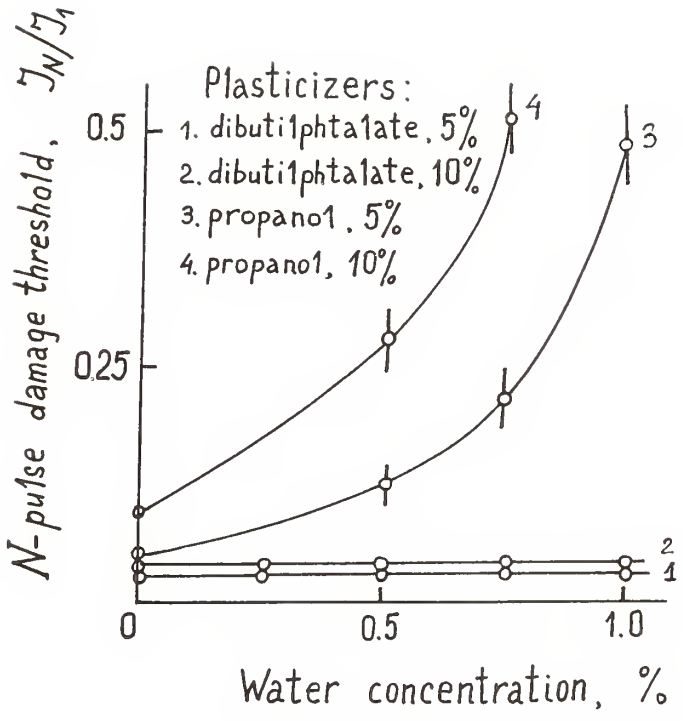

Fig. 2. Dependence of N-pulsed damage threshold, I_N, (N=200) upon water additive concentration in plasticized PMMA. I_1 is the single-pulse damage threshold in non-modified PMMA.

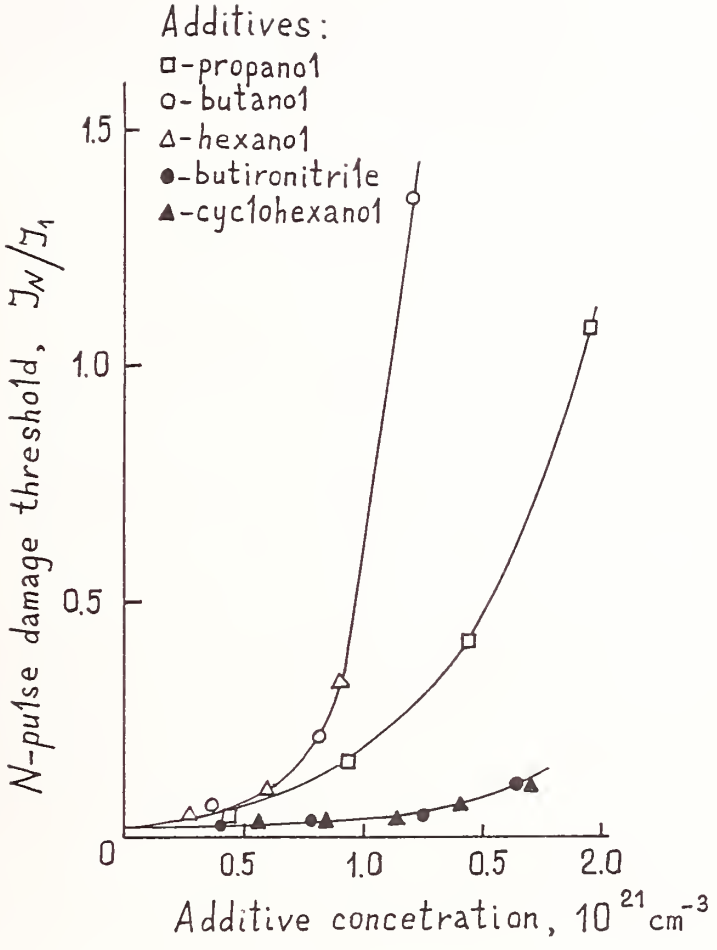

Fig. 1. Dependence of N-pulse damage threshold, I_N, (N=200) upon the additives concentration in Pmma. I_1 is the single-pulse damage threshold in non-modified PMMA.

Manuscript Received
3-17-88

Large Scale Damage Testing in a Production Environment*

C. L. Weinzapfel, G. J. Greiner, C. D. Walmer,
J. F. Kimmons, E. P. Wallerstein,
F. T. Marchi and J. H. Campbell

Lawrence Livermore National Laboratory
University of California
P.O. Box 5508, L-491
Livermore, California 94550

J. S. Hayden
Schott Glass Technologies, Inc.
400 York Avenue
Duryea, PA 18642

K. Komiya and T. Kitayama
Hoya Corporation
572 Miyazawa-cho, Akishima-shi
Tokyo, 196, Japan

We are using laser damage test systems on a production scale to scan large castings of laser glass for the presence of damage-causing platinum inclusions. These systems support glass melting production lines at two plants; one is in the U.S. (Schott Glass Technologies, Inc.) and the other is in Japan (Hoya Corporation).

The damage test systems are designed to scan an entire glass casting using the pulsed output from a commercial Nd:YAG laser. The system is fully automated and operates unattended. Following testing, the glass casting is removed from the system and visually inspected for the presence of Pt-damage sites. We routinely test polygonally-shaped castings that are about 0.5 meter in size, weigh approximately 30 kg and contain about 7 liters of glass. It takes roughly 6 to 8 hours to test a piece of this size. To date the systems have been in use about 12 hours-per-day, up to 5 days-a-week for a period of about 15 months. Of the approximately 300 disks that have passed the damage test so far, sixty-two percent of the disks have no platinum inclusions at all and ninety-two percent have an inclusion density of less than 0.2 per liter.

Key Words: damage test system, Pt-inclusions, large scale damage testing, laser disks.

1. Introduction

Prior to 1987 laser glass sold for use in high power lasers was limited in performance and durability due to the presence of damage- causing defects.[1,2] The Pt-inclusions originate from the platinum crucibles that are used in melting the glass.[3-5] We discovered Pt-inclusion damage to be a serious problem at the LLNL 100-kJ Nova laser system during start-up in early 1985. The large aperture Nd:doped phosphate amplifier disks experienced isolated bulk damage.[6,7] The platinum particles vaporize when subjected to Nova's high pulse-power levels causing fractures within the glass around the metallic inclusions (fig. 1).[6,10] These fractures interfere with the laser beam propagation.[11]

Often, the size of the inclusion that can lead to damage is less than 5-20 μm in diameter. These are too small to be seen visually and many of the optics are too large for inspection by conventional microscopy. Damage is then only found after purchase, installation, and actual use of these optics. At this point, replacement of the damaged optics is usually a costly as well as a time consuming operation.

---

*Work performed under the auspices of the U.S. Department of Energy by the Lawrence Livermore National Laboratory under contract number W-7405-ENG-48.

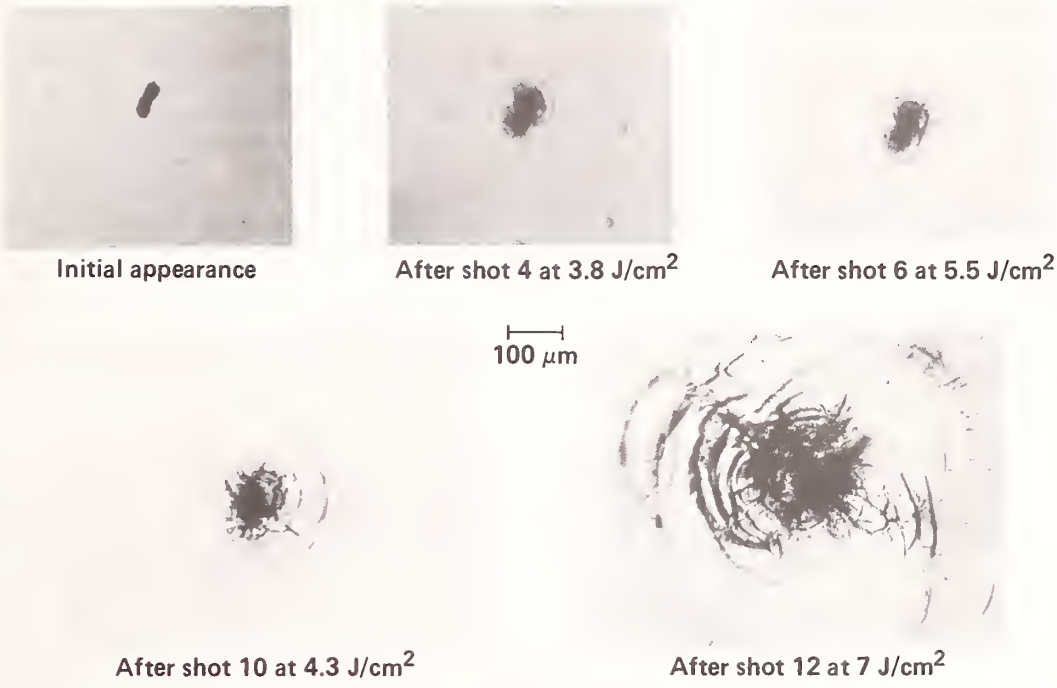

Figure 1. Growth of damage around a platinum inclusion when exposed to multiple irradiation of 1.06 μm laser light at 1 ns. Data are from Gonzales and Milam.[6]

Recently two optical glass companies (Hoya Corp., Tokyo, Japan and Schott Glass Technologies Inc., Duryea, PA) working with LLNL, have successfully completed research to eliminate the platinum inclusions during the melting process. Also, during this time we developed a large-area damage test system to test for the presence of platinum in all new glass being produced. One of these damage systems has been installed at each of the glass companies and is integrated into the production process.

In the past, QA damage tests have been confined to small optical samples such as witness samples or to lot testing. Also much of the damage testing has been done in a research environment. When there is an extremely low density of inclusions it is impossible for small area damage testing to be effective. Consequently, large optics that contain very few damaging defects are certified as inclusion-free based on damage tests performed on a few small samples.

We have developed a damage system designed to test an entire large laser optic under the fluence conditions it would see in application. Our damage test system not only provides 100% QA testing for these large optics but it is also fully automated and is being successfully used in a production plant environment. This has established a trend at our Laboratory that will be required for all future optical components used in high peak power lasers.

2. Description of the Glass Damage Test System

The damage test system uses a commercial Q-switched YAG laser (Lumonics, Inc. Model 750) and movable x-y stage to automatically scan the entire volume of glass for the presence of damage producing defects (fig. 2). The maximum output is 780 mJ at an 8 ns pulse width and approximately a 20 HZ repetition rate. The laser produces a slightly diverging, 8 mm diameter beam that is collimated by a 5 m focal length positive lens (fig. 3). The beam is directed towards the sample by high energy dielectric-coated mirrors. A 2 m focal length positive lens is used to reduce the beam to a 2 mm spot on the test sample. The spot size and therefore the laser fluence can be changed by varying the position of the 2 m lens. This allows the operating conditions of the laser to remain the same. A beamsplitter, located between the 2 m lens and the test sample, sends a portion of the beam to a vidicon camera and a calorimeter. Both the vidicon camera and calorimeter are the same distance from the beam splitter as the sample. The vidicon camera is part of our beam profile system that is described in further detail below. A helium-neon laser is co-aligned with the YAG laser to assist in beam path alignment and sample positioning.

Figure 2. Photograph showing the physical layout of the LLNL damage test system.

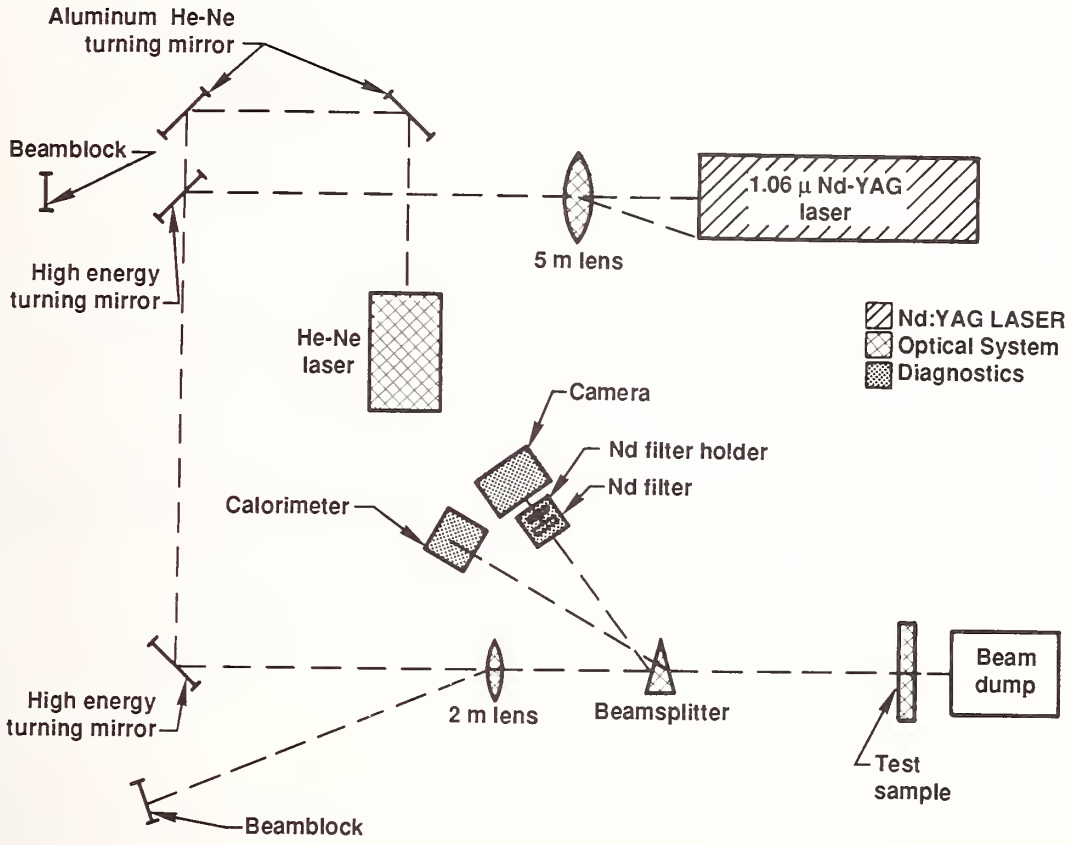

Figure 3. Schematic drawing of the optical layout of the damage test system.

The test sample is mounted on a commercial stage drive (Daedal, Inc. Model 00X-0140) capable of movement along the x and y axes. The stage can carry a piece of glass over one meter in diameter and weighing as much as 100 kg. However the maximum scan area is 60 x 60 cm. The stage moves the sample continuously in front of the laser beam. The scan speed can be varied in order to produce single or multiple shots through the entire test sample. Typically, we use scan rates that give between 10 to 100 shots through the entire volume.

The laser beam diagnostics and stage movements are all controlled by a Hewlett-Packard model HP-310 computer. The computer is connected to the system using standard HPIB and GP10 interfaces and a model 3421 Data Acquisition System for system control (fig. 4).

The laser power output is continuously monitored by a calorimeter whose output is read by the system controller. The spatial profile of the beam is monitored by a commercially available beam profile system (Big Sky Software Corp., Bozeman, Montana). This beam profiler consists of a General Electric CID TN 2509 camera, a Poynting PRoducts frame grabber, and a monitor. A typical profile of the laser beam is a contour plot and an x-y cross section of the beam showing beam diameter, and minimum and maximum fluences required for testing (fig. 5). A 3-dimensional plot of the beam can also be shown if desired.

Because of the short pulse width of the laser trigger, we designed and built an interface that allows us to synchronize the laser with the frame grabber at 17.8 Hz. This interface also provides signal isolation between the laser and the frame grabber. Both the hardware and software packages of the profiler have been integrated into the laser, stage, and diagnostic control system. The system carries out a beam profile measurement automatically at a frequency established by the operator.

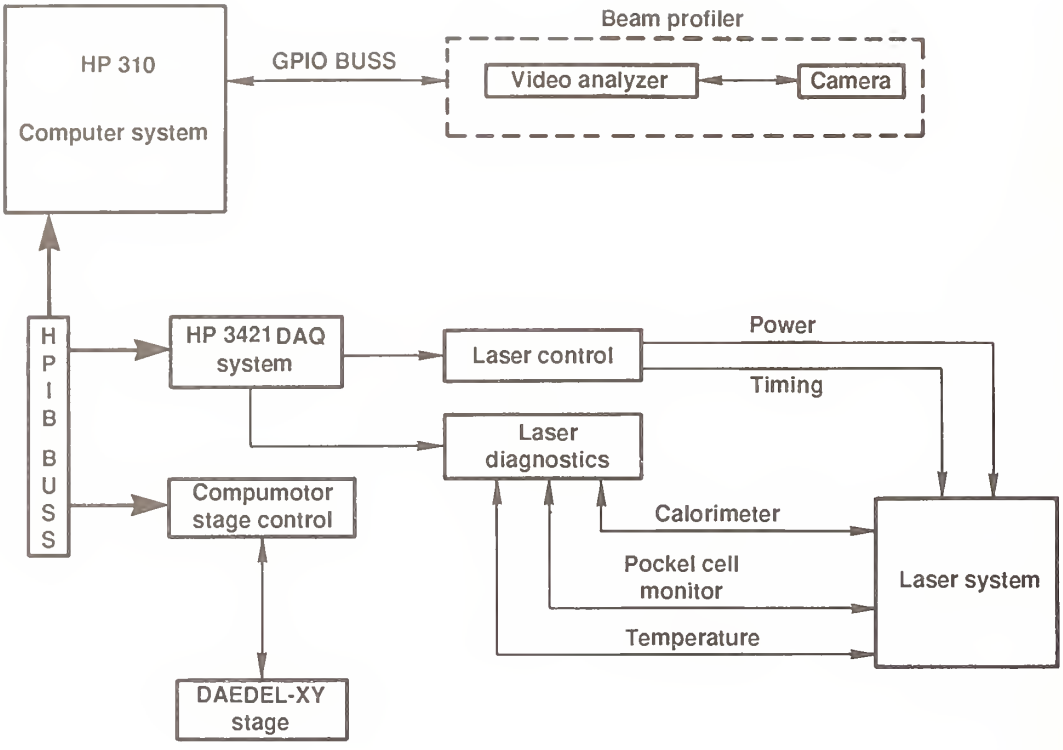

Figure 4 Block diagram of the monitoring and control system of the damage test apparatus.

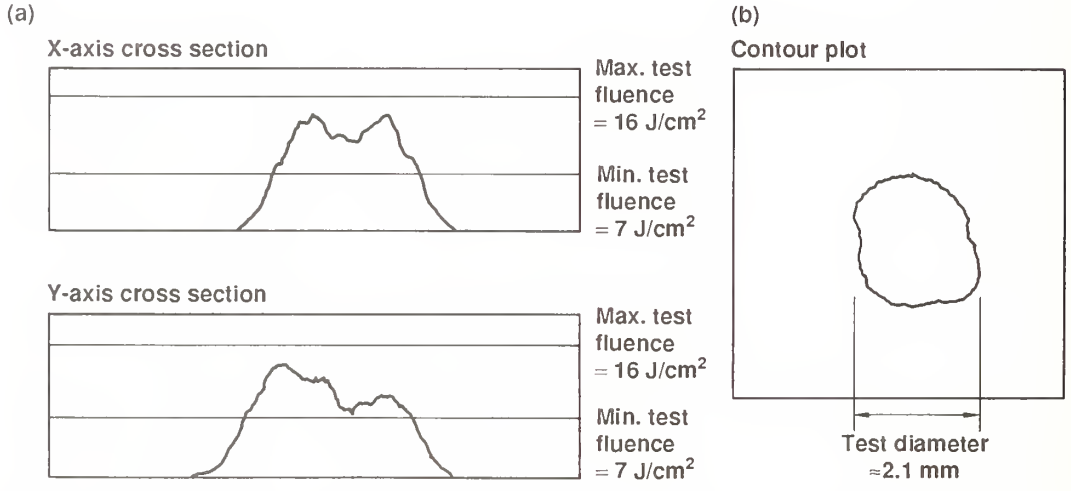

Figure 5 (a) An x and y cross-sectional plot of the laser beam. The maximum test fluence is 16 J/cm^2 and the minimum test fluence is 7 J/cm^2.
(b) Plot of a single contour shows the effective test diameter of the beam at 7 J/cm^2.

The laser beam characteristics are passed automatically from the beam profiler software to the main control software. There the data is compared with the required operating specifications. If a problem develops within the system it performs a controlled system shutdown while preserving all data taken to that point. This feature allows us to safely and reliably use the system unattended for periods up to 16 hours or more.

The laser, the optical train and the sample are contained in a class 10000 clean room or enclosure to minimize damage to the test sample from dust contamination.

3. Test Specifications

Table 1 summarizes several of the disk material properties as well as the Pt damage test specifications. Our manufacturing goal was to have no more than an average of 2 inclusions per disk; each disk contains about 7 liters of glass. This is about a 1000-fold improvement over the original Nova disks (the Pt inclusion density in the original Nova disks ranged from about 100 to 10,000 per disk) (fig. 6).

A few small damage inclusions do not necessarily render the optic unusable. But even particles less than 10 microns may grow to several hundred or even thousands of microns over a period of 100 shots (e.g. see fig. 1). We have found that most damage sites will attain their maximum size after approximately 50 to 60 shots. We can accept a certain number of damaging inclusions in each piece of glass as long as the damage size remains below the limits given in Table 1.

Table 1. Summary of material properties, Pt-inclusion damage test specifications for the Nova 46- and 31.5-cm glass laser disks.

Material Properties	
Glass-Type:	phosphate glass (Hoya LHG-8, Schott LG-750)
Stimulated emission cross-section:	$\sim 4 \times 10^{-20}$ cm^2
Fluorescence lifetime:	$\geq$ 350 µs
Nd^{+3} doping level:	2 ($\pm$0.1) x 10^{20} Nd ion/cm^3
Absorption at 400 nm:	$\leq$ 0.25/cm
Absorption at 1.05 µm:	$<$ 0.0015/cm
Pt Inclusion Damage Specifications	
Number of Inclusions:	No more than 10 metallic particles or other types of inclusions within the clear aperture volume (volume ~ 7 L).
Minimum distance between inclusions:	25 mm
Average number of inclusions: (manufacturing goal)	No more than 2 per disk (i.e. $<$ 0.3 inclusion/liter)
Inclusions after damage testing:	1 damage spot $\leq$ 0.5 mm (largest dimension) and remainder $\leq$ 0.25 mm (largest dimension)
Damage test conditions:	Wavelength: 1053 to 1064 nm fluence: $\geq$ 7 $\pm$ 1 J/cm^2 in the glass pulse width: 8 ns No. of shots: 100

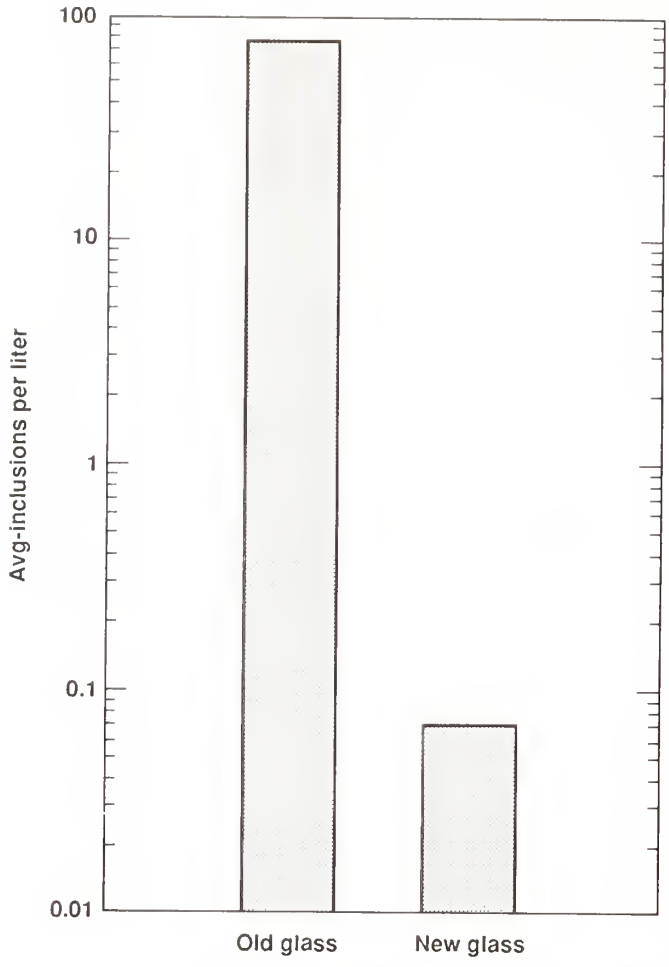

Figure 6 The average number of inclusions per liter of new Nova glass compared to the old Nova glass. This new glass shows a 1000-fold improvement over the old glass.

4. Test Procedure

Schematic diagrams of the glass production process and QA Pt-damage testing are shown in figure 7a and b. All of the Nova laser glass is damage tested after it has been coarse annealed and inspection polished.

During an actual test the glass is manually loaded onto the stage and locked into place. The desired test program is entered into the computer which then starts the laser. An initial beam profile is run to verify proper fluence and beam shape. The sample is then irradiated at normal incidence with 10 shots per site at a fluence level of 7 to 14 J/cm^2 (fig. 8). At this fluence, any platinum inclusions in the glass will produce optically visible damage sites. This fluence corresponds to about twice the damage threshold for platinum inclusions in glass for an 8 ns pulse width.[6,10]

A typical scan takes approximately 6 to 8 hours to complete for a large Nova disk. At the end of a scan the computer automatically shuts down all system operations.

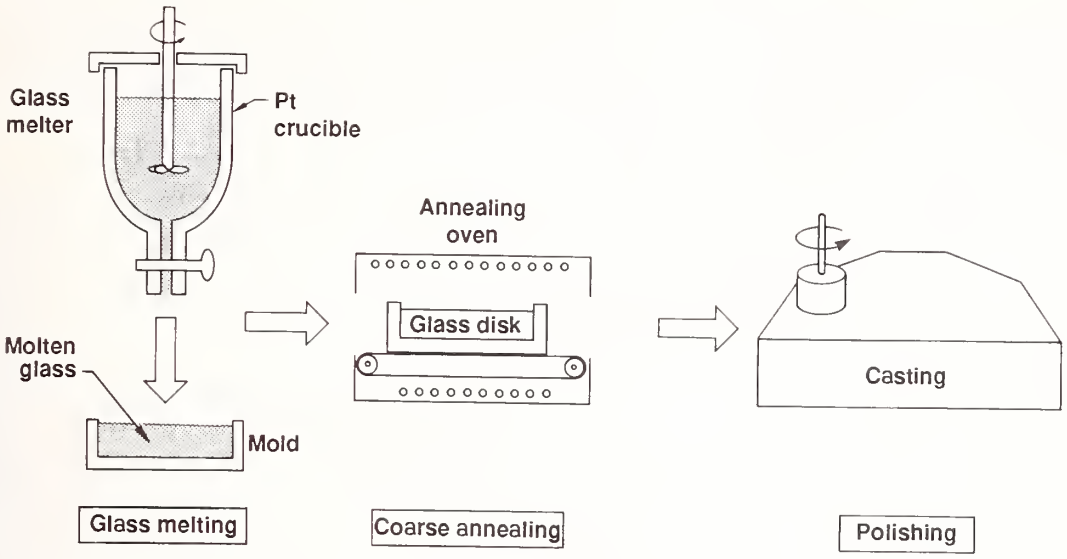

Figure 7 (a) Schematic diagram of the laser glass production process.

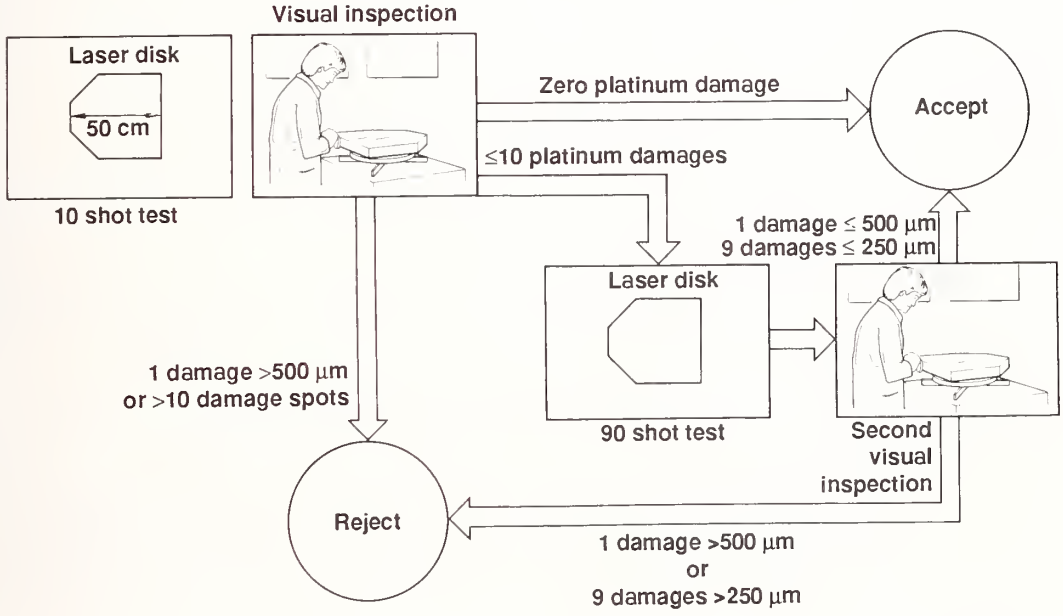

Figure 7 (b) The laser glass is damage tested and visually inspected after it has been coarse annealed and inspection polished. If any damage sites are found the individual sites are retested with 90 shots each and inspected a second time for maximum damage growth.

The test sample is then removed and taken to a separate inspection area (fig. 7b). The sample is mounted on a stationary or rotating stage with a black base. The room is darkened and a visual inspection is performed by illuminating the sample from the side with an intense white-light source. Visual inspection after this type of testing has proven to be very efficient and generally takes no more than about one hour to inspect a 60 x 40 x 5.4 cm disk.

When damage sites are found they are identified, marked and sized using optical microscopy (40X). Then an additional 90 shot test is performed on each damage site. The purpose of the 90-shot test is to grow the damage to it's maximum dimension. The 90-shot test usually takes 5 to 10 minutes to set up and then only a few minutes for each damage site. After the 90 shot test the damage sites are remeasured for growth. If the damage site is still within specifications (Table 1) the glass is accepted.

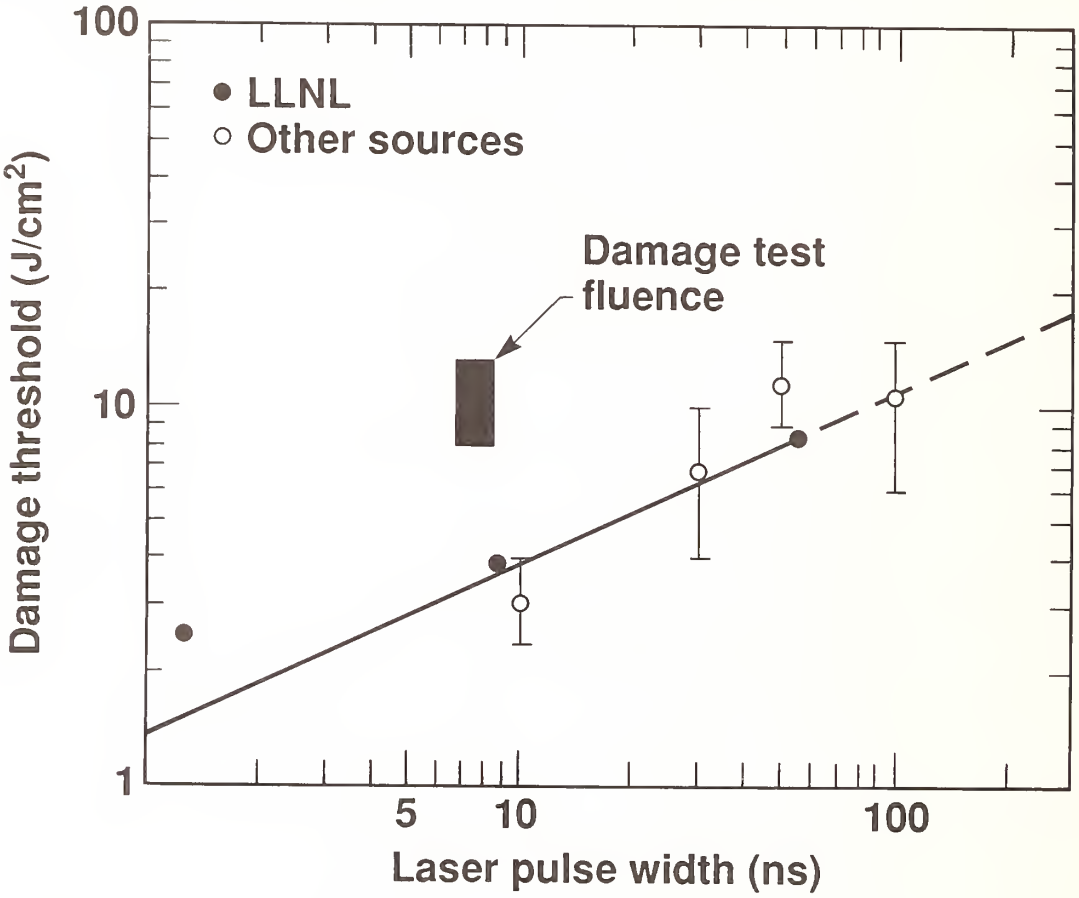

Figure 8 Pt damage threshold vs. pulse width for 1.06 μm laser light. The points are experimental data and the solid line is a model calculation by Pitts et al.[10] The shaded area is the operating fluence we use in the damage tests. Note that it is approximately twice the Pt-damage threshold yet is below the threshold for damage of an inspection polished surface.

5. Current Status

Test facilities have been established at each of the laser glass production plants and at LLNL. Production melting of the new Nova glass began in December 1986. The glass production order is for about 350 disks. Each glass casting is being damage tested using these new systems.

At this writing the systems have been in use for about 15 months. They operate 6 to 12 hours a day, 5 to 6 days a week. Approximately $2.5\text{-}3.0 \times 10^5$ shots are put on each piece of glass. Production is 90% complete with 62% of the acceptable disks having zero platinum inclusions and 92% having two platinum inclusions or less (fig. 9).

We have found the laser damage test systems have performed admirably in this production environment. We have experienced less than 5% down-time during production. The lasers themselves are very sturdy; although designed for research applications we have turned them into production lasers with only a few modifications. Specifically, we have upgraded the water chillers, redesigned the heat exchanger, and installed new flashlamp leads, a pockels cell monitor, and a beam profiler to continuously monitor the shape and energy of the beam. During the production operation we established a thorough maintenance schedule for the lasers. Some months as many as 10 million shots were fired requiring that the flashlamps be changed every 2 to 4 weeks.

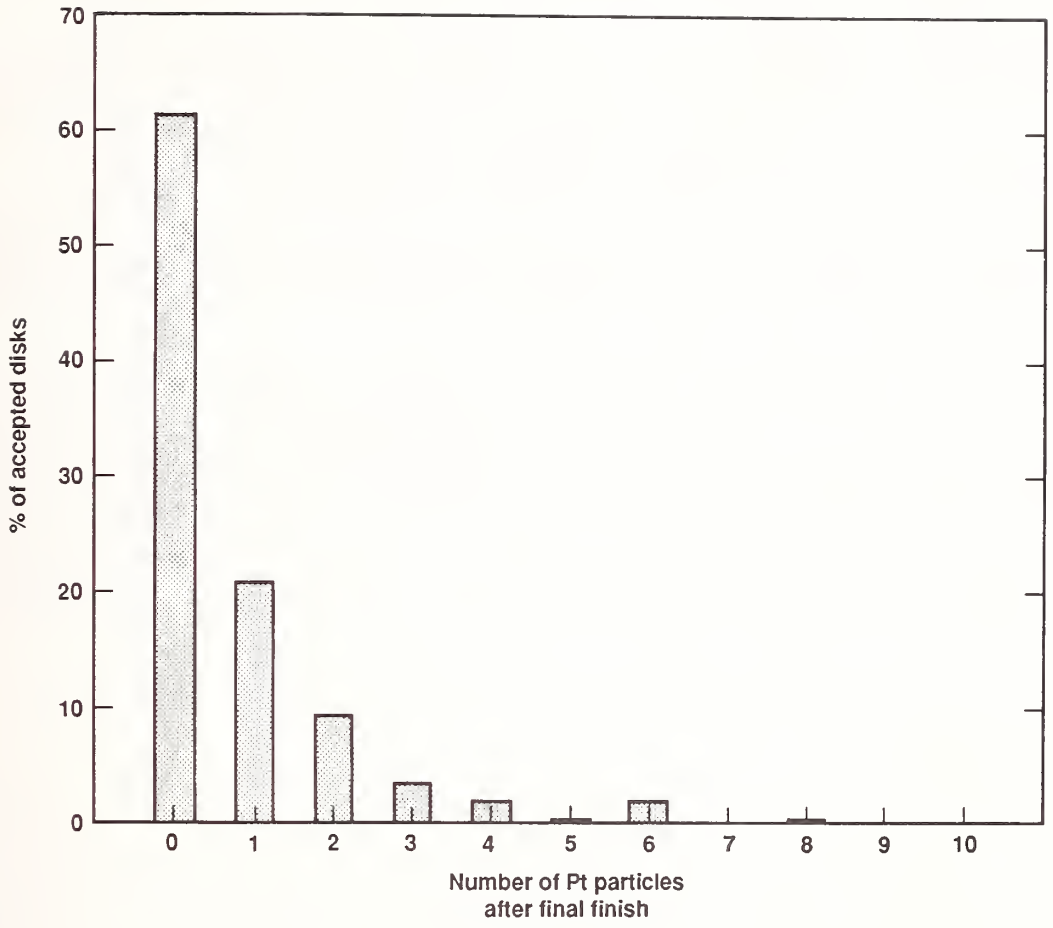

Figure 9 Percentage of laser disks having between zero and 10 Pt-inclusions per disk. The Nova specification allows up to 9 damage spots less than 250 μm and 1 less than 500 μm. Note that 62% of all disks have zero Pt-inclusions.

The authors gratefully acknowledge the technical contributions of Dr. D. Milam in certain phases of this work. The efforts of Mr. K. Kita and Mr. H. Kowa of Hoya Corporation, and Mr. F. Carrotto of Schott Glass Technologies, Inc. We also wish to thank Mr. John Grens for his work on the inclusion detector system and the scan control software.

6. References

1. National Academy of Science, National Academy of Engineering, Fundamentals of Damage in Laser Glass, Publ. NMAB-271, Washington, D.C. (1970).

2. R. W. Hopper and D. R. Uhimann, "Mechanism of Inclusion Damage in Laser Glass", J. Appl. Phys. 41, 4023-4037 (1970).

3. P. V. Avizonis and T. Farrington, "Internal Self-Damage of Ruby and Nd-Glass Lasers", Appl. Phys. Lett. 7 (1965).

4. R. J. Ginther, "The contamination of glass by Platinum", J. Non-crystalline Solids 6, 294 (1971).

5. J. Campbell, "Eliminating Platinum Inclusions in Laser Glass", Energy and Technology Review, Lawrence Livermore National Laboratory Report, March-April 1986, p. 12-23.

6. C. W. Hatcher, "Assessment of Laser Glass Damage on the Nova System", 1985 Laser Program Annual Report, Lawrence Livermore National Laboratory UCRL-50021-85, p. 6-4 to 6-6.

7. D. Milam, C. W. Hatcher and J. H. Campbell, "Platinum Particles in the Nd:doped Disks of Phosphate Glass in the Nova Laser", in Laser Induced Damage in Optical Materials: 1985; Proceedings of the Boulder Damage Symposium, Oct. 1985, Boulder, Colorado.

8. R. P. Gonzales and D. Milam, "Evolution During Multiple-Shot Irradiation of Damage Surrounding Isolated Platinum Inclusions in Phosphate Laser Glasses", in Laser Induced Damage in Optical Materials: 1985; Proceedings of the Boulder Damage Symposium, Oct. 1985, Boulder, Colorado.

9. J. Campbell, "Replacement of Nova Laser Glass", 1986 Laser Program Annual Report, Lawrence Livermore National Laboratory UCRL-50021-86, Section 4, in press.

10. J. H. Pitts, "Modeling Laser Damage Caused by Platinum Inclusions in Laser Glass", in Laser Induced Damage in Optical Materials: 1985; Proceedings of the Boulder Damage Symposium, Oct. 1985, Boulder, Colorado.

11. J. A. Fleck, Jr., J. R. Morris, and E. S. Bliss, "Small-Scale Self-Focusing Effects in a High Power Glass Laser Amplifier", IEEE J. Quantum Electronics, Vol. QE-14, No. 5, May 1978.

Manuscript Received 12/16/87/sar

A New Average-Power Damage Test Facility at LLNL*

E. A. Hildum, F. Rainer, and D. Milam

Lawrence Livermore National Laboratory
University of California
P.O. Box 5508, L-490
Livermore, California 94550

We describe a new facility for studying damage induced by 1064-nm, 16-ns, 0.6-J laser pulses at repetition rates up to 120 Hz. This facility is built around four commercial 30-Hz Nd:YAG lasers fired under computer control. The beams from the four lasers are combined using thin-film polarizers and rotating half-wave plates to obtain a single irradiated spot on a test target. We also describe computer controlled beam diagnostics based on a commercial video frame-grabber.

This facility has been used to compile a database of damage thresholds for a variety of materials under average power conditions. Details of this database are presented in a companion paper.

Key Words: average power; beam combining; beam profiling; damage testing; laser fluence measurements; laser induced damage; thermal accumulation.

1. Introduction

Various laser systems under development at LLNL require optical components which can survive high fluences of 1064-nm radiation at pulse repetition frequencies (PRF's) ranging from hundreds to thousands of Hz. Under these conditions, slowly accumulating damage can cause catastrophic component failure at fluences well below the single-shot damage threshold. Heat accumulation may also adversely affect component damage thresholds at higher PRF's. Optical elements in some proposed systems may be required to survive as many as 10^9 shots. We have conducted a damage test facility which addresses these issues using commercially available lasers.

With the moderately high PRF (up to 120 Hz) available in this facility, it is practical to put several million shots on a single site to evaluate component lifetimes. Though this is a small number in comparison to 10^9, it should be sufficient to estimate the Weibull distribution[1,2] for particular components and coatings. 10^6 shots is comparable to, or in excess of the design lifetime of several interesting systems. Surface defect densities can be probed by scanning an area of the sample.

If optical components suffer detectable heat accumulation under irradiation at 120 Hz, they are likely to be unsuitable for use in laser systems operating at PRF's above several kilohertz. We can detect small local temperature excursions in an irradiated sample area with an infrared imaging system.

2. Laser light source

The 1064-nm light source is a composite of four commercial Nd:YAG lasers (Quantel). Each laser can deliver 0.8-J, 16-ns pulses at repetition rates up to 30 Hz. The four lasers are fired in succession under computer control to produce a series of equally spaced pulses at 120 Hz. Thermal considerations require the flashlamps to be fired at 30 Hz to maintain oscillator cavity alignment. Lower PRF's are obtained by Q-switching only selected pulses.

---

*Work performed under the auspices of the U. S. Department of Energy by Lawrence Livermore National Laboratory under Contract No. W-7405-ENG-48.

The outputs of the four lasers are combined pairwise into a single beam with thin film polarizers and rotating half-wave plates (fig. 1). The combiners each accept two orthogonally polarized input beams with 30-Hz PRF's and produce a single linearly polarized beam with 60 Hz PRF (fig. 2). The input beams are superposed on a thin film polarizer to produce a single beam whose polarization flips 90 degrees on alternate pulses. To obtain linear polarization, we rotate every other pulse 90 degrees with a stepping-motor driven half-wave retardation plate. The two 60-Hz beams are similarly merged with a third combiner with a faster rotator. Since the wave plate must rotate 45 degrees between successive pulses, the rotation rates are 450 RPM for both 30-Hz combiners and 900 RPM for the 60-Hz combiner. By varying the orientation of a final half-wave plate, the output polarization can be set to any desired angle. Stacked rubber isolation pads attenuate the vibration caused by the stepping motors to easily tolerable levels.

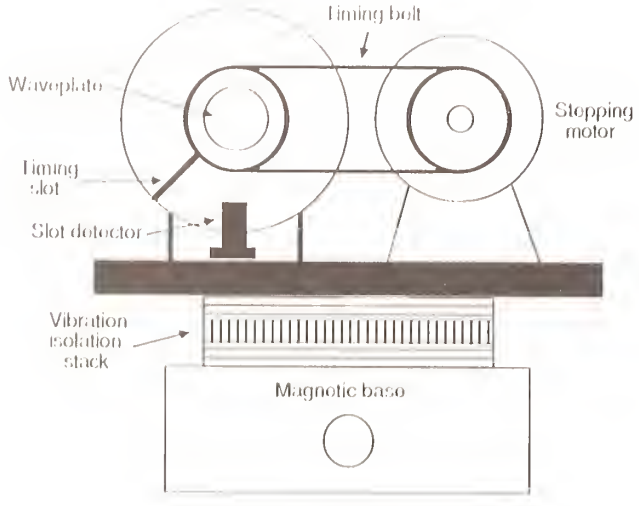

Figure 1. Beam Combiner

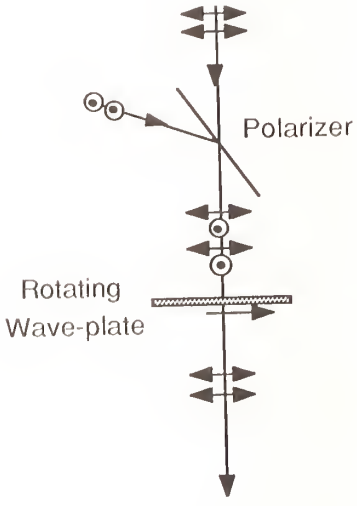

2. Beam Combiner Schematic

Similar function can be obtained by replacing the motorized wave plates with Pockels' cells which are fired for alternate pulses. Early efforts to use a system based on KD*P (92% deuterated) Pockels' cells had to be abandoned because of thermal stress-induced birefringence. If the deuteration level of the KD*P had been higher (lowering absorption at 1064 nm) this method would probably have succeeded. Pockel's cell combiners are more elegant and flexible, and do not vibrate the optical table. An AR coated 2.5-m focal length lens focuses the composite beam onto a roughly 0.6-mm spot on a test sample.

3. Beam Diagnostics

In practice, it is difficult to adjust four separate lasers to produce identical output beams. To adequately characterize the laser light source, it is necessary to measure the energy and fluence in the sample plane during damage testing. We use three separate diagnostics (shown schematically in fig. 3) to determine beam parameters. A charge-injection-device (CID) solid state video camera (General Electric TN2505-A4) monitors the spatial energy distribution in the sample plane. Individual pulse energies are obtained from a large area silicon photodiode (PIN8/LC). Average power is determined with a surface absorbing calorimeter (Scientech 36-0001). The CID camera and photodiode are calibrated with respect to the calorimeter.

We extract diagnostic light from the main beam with an uncoated fused silica wedge placed after the final focusing lens. Additional wedges direct portions of this light into the three photodetectors. Neutral density filters in the camera and photodiode beams select the operating fluence range.

The photosensitive array of the CID camera coincides optically with the test sample image plane. The imager consists of 377 horizontal by 242 vertical elements with horizontal spacing 23.3 microns and vertical spacing 27.2 microns, corresponding to an image about 26 pixels wide and 22 pixels high for a 0.6-mm sample spot. The camera can grab single laser shots with the help of an electro-mechanical shutter (Vincent Associates 225L).

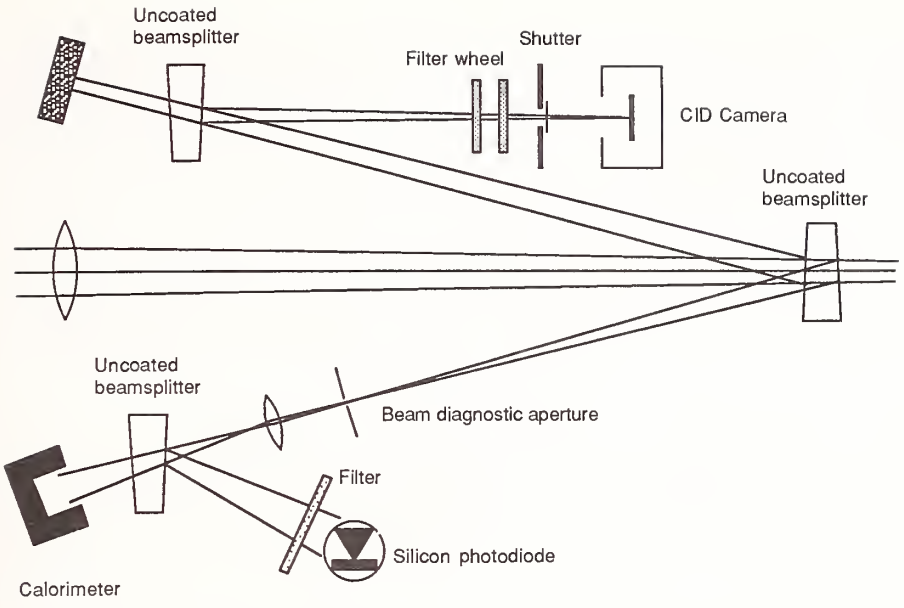

Figure 3. Beam Diagnostic Configuration

A pre-amplifier and gated integrator (Evans Assoc. 4130) condition output from the silicon photodiode. The integrated photocurrent signal is finally digitized and logged by the lab computer.

4. Sample Diagnostics

Optical microscopy is our main damage diagnostic. We use Nomarski (interference phase contrast) microscopy to examine and photograph samples before and after test irradiation. Under some circumstances, light- or dark-field microscopy may also be used. These techniques highlight phase artifacts in the transparent materials used for most coatings and substrates. A rotatable mounting positions samples repeatably in the laser beam or under the microscope. We do not observe the sample with the microscope during irradiation.

An infrared imaging camera (Inframetrics Model 600) can be used to observe samples during irradiation. This camera is sensitive to IR radiation in the 8 to 12 micron range, which covers the room temperature black-body peak. Sample temperature can be displayed on a video monitor in false color and recorded on a video tape recorder for future review. The IR imager can resolve temperature differences of 0.1/C.

5. Computer Control System

A single commercial microcomputer (Compaq Deskpro 286) controls the operation of our damage test facility. Add-in boards in the computer provide other specialized functions needed for laboratory control and monitoring.

An eight (differential) channel, 12-bit analog to digital converter board (Data Translation DT2821) in the computer monitors analog signals from the beam diagnostics. One A to D channel is presently used for digitizing pulse energy information from the photodiode energy monitor.

A commercial video frame-grabber (Data Translation DT2851) digitizes video output from the CID camera and displays the acquired images in false color on a video monitor. Single frames can optionally be stored for subsequent analysis. A crystal-controlled clock on the frame grabber board generates the video horizontal and vertical drive signals for the CID camera, and provides the master clock for the entire lab system. A video frame processor (Data Translation DT2858) handles all computationally intensive operations on video data (e.g. frame averaging and histogramming), freeing the main processor for real-time control tasks.

A custom laser timing and trigger board (LTTB) generates timing signals for the four lasers, the beam combiner stepping motors, the gated integrator, and the camera shutter. The board can monitor the beam combiner position sensors. An interrupt controller on the LTTB expands the interrupt capabilities of the computer to accomodate the additional demands for main processor attention.

The computer system is shown schematically in figure 4.

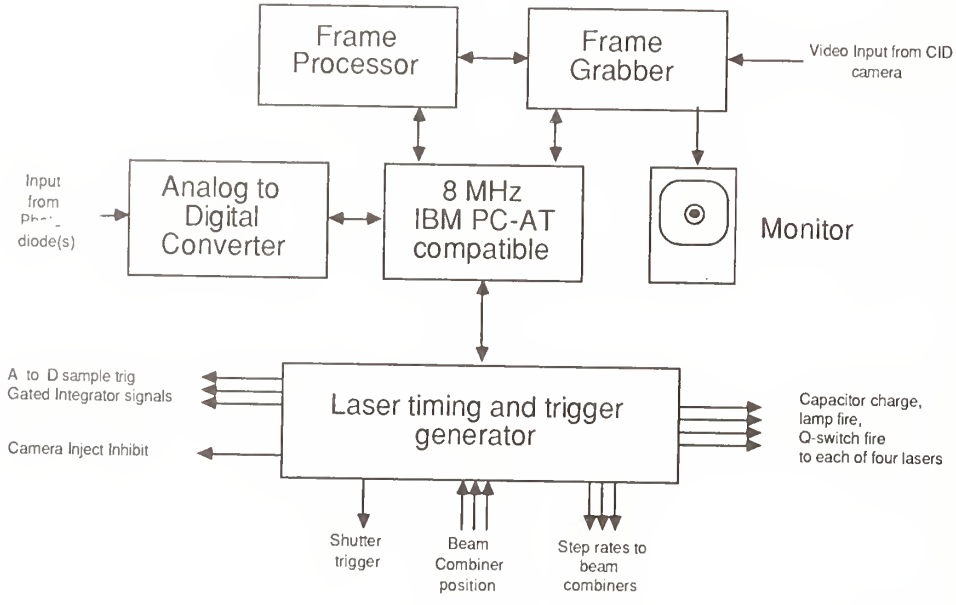

Figure 4. Computer System

6. Lab Control Software

Menu-driven software allows a single operator to control the damage test facility from the computer console. A wide range of critical parameters can be set and optimized during operation, and data from the various diagnostic instruments can be displayed in graphical form in real time. Most of the code is written in C (Mark Williams Co.), though interrupt handlers and several low level routines are implemented in assembly language. The central kernel of the program contains a menu interpreter, display controller, and command dispatcher. A variety of program modules support other command- and device-specific functions.

All operating parameters of the four lasers may be set through various commands. The PRF may be varied, though in practice the lasers are only aligned for a particular flashlamp firing rate. Slower rates may be achieved by firing the Q-switches at multiples of the pulse repetition period. In addition, delays between flashlamp and Q-switch firing can be optimized individually for each laser while the system is
running.

While the lasers are firing, their pulse energies are continuously monitored and histogrammed. The pulse energy histogram can be displayed in real time, and dumped to a graphics printer at the conclusion of a test. The computer calibrates the photodiode energy detector during every damage test by comparing the average single pulse energy with the average power measured by the calorimeter. Tests do not begin until the lasers have come to thermal equilibrium. Under these circumstances, typical pulse to pulse energy variations are in the 5 to 10 percent range, so it is not necessary to take the calorimeter time constant into consideration.

We extract fluence at the sample surface from digitized CID camera data. Capture and analysis of single video frames requires about 0.5 s, giving a maximum sampling rate of 2 Hz, or approximately every 60th pulse. The computer analyzes the video frame by calculating a histogram of pixel values in a circular region corresponding in size to the beam diagnostic aperture (see fig. 3). We take the maximum pixel value with ten or more pixels in this region to represent the maximum fluence in the sample plane. The numerical value of the maximum fluence is derived from the camera calibration, which is determined by comparing the video pixel histogram with the average power measured by the calorimeter. The video histogram and a record of maximum single-pulse fluences accumulate for the duration of a test. In a 5-minute test run, the camera records 600 video frames, producing 1) a histogram of 600 maximum single-pulse fluence values, and 2) a video histogram containing all pixel values from 600 video frames. The maximum fluence histogram can be displayed graphically and dumped to a graphics printer. Typical fluctuations in maximum single-pulse fluence are in the 15 to 20% range.

7. Test Procedure

In a typical test run, a sample is first examined and photographed using Nomarski microscopy. The sample is then rotated into the beam path and irradiated for up to 5 minutes at a particular fluence. If light emission or visible evidence of damage appears during the test, the beam is blocked and the test ends. Damage is, as usual, defined as any observable modification of the surface. At the conclusion of a test, the computer plots the pulse energy and maximum single-pulse fluence histograms for each laser. Average fluence (averaged over the diagnostic beam aperture) and the mean of the maximum single-pulse fluence histogram are also displayed. Approximately 10 tests at different sites determine the damage threshold of the sample. The damage threshold is taken to be the average of the maximum non-damaging fluence and the minimum damaging fluence.

8. Results

Data obtained during development of this facility is summarized in a companion paper entitled "Database of Average-Power Damage Thresholds at 1064 nm".

9. Summary

We have constructed a facility for testing critical optical components under average-power conditions at 1064 nm. This facility is well suited for investigating shot-number effects and component lifetimes. To a lesser extent, heat accumulation can be studied; components which suffer detectable thermal build-up under our test conditions are likely to cause problems at higher repetition rates and fluences. We have automated the laser operation and beam diagnostics sufficiently that one person can perform damage tests.

10. Disclaimer

Equipment makes and model numbers are included for reference purposes only and do not constitute an endorsement of the respective manufacturers by LLNL.

11. References

1. J. H. K. Kao, Technometrics 1, 389 (1959).

2. P. H. H. Fischer and K. W. Nissen, IEEE Trans. Elect. Insul. EI-11, 37 (1976).

Manuscript Received
5-31-88

Developments in Beam Profiling with a CCD Area Array Detector

Robert M. O'Connell and Rui J. Ferreira
Department of Electrical and Computer Engineering
University of Missouri, Columbia
Columbia, Missouri 65211

Alan F. Stewart
AFWL/ARBD
Kirtland AFB, NM 87117

Measurements and calculations of the performance of a frame-transfer CCD area array sensor in a beam profiling system are presented. The measured dark current and photosensitivity pattern noise of the sensor are shown to be better than those of previously studied self-scanned imaging devices. Calculated modulation transfer functions agree with previous measurements, verifying that the CCD sensor should be able to adequately resolve spatial frequencies up to 50 mm^{-1}. A logarithmic video amplifier was successfully interfaced with the CCD camera and an 8-bit image processor for the acquisition of laser beam images with improved contrast.

Key Words: area array sensor; beam profiling; charge-coupled device; dark current; logarithmic video amplifier; modulation transfer function; photosensitivity pattern noise.

1. Introduction

In a recent report, we compared a frame transfer CCD camera with a CID camera for use with an 8-bit image processor in the beam profiling system of a laser damage testing facility. The CCD camera (VSP Labs Model SC 505) was found to be more compatible with the image processor and to have the important performance advantages of a lower dark current pattern noise and a wider spatial frequency bandwidth. The dynamic ranges of both devices were similar, but modest.

Because of the apparent superiority of the CCD camera in the beam profiling system, we have restricted recent studies to that particular device. In this report, we present the results of the following investigations on the CCD camera:

1) Measurements of the photosensitivity pattern noise of the camera sensor with no protective faceplate, which was unavoidably present in our previous measurements and caused interference fringes [1];

2) Calculations of the modulation transfer function of the camera sensor for comparison with previous measurements [1];

3) The use of a logarithmic video amplifier to improve the contrast of relatively low intensity components in the acquired laser beam image.

2. Photosensitivity Pattern Noise

Photosensitivity pattern noise, which is a measure of the spatial uniformity of sensor responsivity to uniform illumination, can be expressed as the ratio of the sensor pixel signal standard deviation to the mean pixel signal [2]. To uniformly illuminate the CCD sensor, the optical arrangement illustrated in figure 1 was used to produce an Airy diffraction pattern, whose main lobe was 8 cm wide at the 6.0 mm x 4.5 mm sensor. By monitoring the camera video output with an oscilloscope, it was possible to optimize the relative positions of the Airy disc and the camera sensor as well as to ascertain that the sensor illumination was uniform. The neutral density filters shown in figure 1 were used to adjust the intensity of the illumination.

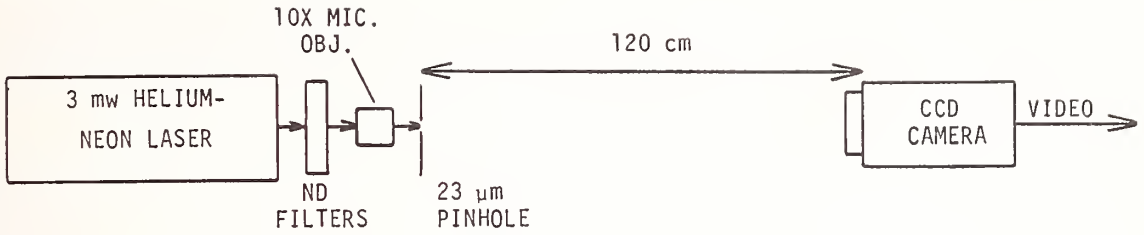

Figure 1. Optical arrangement used to produce uniform illumination of the CCD sensor.

To obtain pattern noise data, the camera video output, which is in standard RS 170/NTSC format, was input directly to the 8-bit image processor (RCI trapix 5500). Using system software, the gain and offset of the image processor were automatically adjusted to suppress background noise and optimize use of the 256 grey level range of the image processor. Data frames corresponding to dark current (no illumination) and two illumination intensities were then acquired and stored for subsequent analysis.

The stored pattern noise data frames were analyzed using system software to calculate the mean grey level $\bar{g}$ and the grey level standard deviation σ of the following: all 512 x 482 pixels in each frame, the central 256 x 256 pixels in each frame, and the central 128 x 128 pixels in each frame. The results, along with the corresponding $\sigma/\bar{g}$ ratio (the percent pattern noise) for each case are given in table 1. Thus, for example, the dark current and photosensitivity pattern noises of the central 256 x 256 pixel region (2.5 x 2.4 mm) of the sensor, which is large enough for many laser damage test beams, are 6.5% and less than 1%, respectively.

Table 1. Grey level mean $\bar{g}$, standard deviation σ, and percent pattern noise $\sigma/\bar{g}$ of the CCD camera under conditions of no illumination (dark current) and two levels of uniform illumination. A, B, and C refer, respectively, to the entire 512 x 482 pixel sensor, the central 256 x 256 pixel region, and the central 128 x 128 pixel region.

	Dark Current			Medium Illumination			Higher Illumination		
	A	B	C	A	B	C	A	B	C
$\bar{g}$	9.1	9.1	9.1	134.5	135.0	135.4	215.2	216.8	217.0
σ	0.61	0.59	0.60	1.65	1.36	1.31	2.01	1.51	1.44
$\sigma/\bar{g}$ (%)	6.8	6.5	6.5	1.2	1.0	0.97	0.93	0.70	0.66

3. Modulation Transfer Function (MTF)

The MTF or spatial frequency response of the camera sensor characterizes its ability to resolve fine details, e.g., hot spots, in the beam profile. In our previous study, we measured the MTF of the CCD camera by recording images of a USAF resolution test target and using system software to determine grey levels in appropriate portions of the images.

For purposes of comparison with the measured results, in the present study we have calculated the MTF of the CCD sensor. Because they are architecturally and operationally different in the horizontal and vertical directions, CCD area array sensors have distinct horizontal and vertical MTF's [3]. The net MTF in either direction is the product of component MTF's that account for pixel geometry, diffusion of signal charge, and, in the vertical direction only for frame transfer CCD sensors, signal charge transfer inefficiency.

The geometry component of MTF is found by Fourier transforming (in spatial frequency space) the light-sensitive portion of a sensor pixel [3]. Convenient expressions of the horizontal and vertical results are, respectively,

$$MTF_{gh} = \text{sinc}\ [(\pi f/2f_n)\ (\Delta x/p)] \qquad (1)$$

and

$$MTF_{gv} = \text{sinc}\ [(\pi f/f_n)\ (\Delta x/p)] \qquad (2)$$

where

f = spatial frequency in mm^{-1},

f_n = Nyquist limited spatial frequency,

Δx = signal sensitive extent of the pixel in the respective direction,

and p = pixel center-to-center spacing.

The factor of 2 difference in the arguments of eq (1) and eq (2) is due to the fact that our CCD camera operates in a 2:1 interlaced format (standard video). Thus, the Nyquist limits are equal to 1/2p and 1/p in the horizontal and vertical directions, respectively [4].

Although the arguments of eq (1) and eq (2) could both be simplified to ($\pi f \Delta x$), the forms given allow MTF calculations in terms of the light-sensitive fraction of the pixel ($\Delta x/p$) and the Nyquist frequency. Using manufacturer's data for our CCD camera sensor, we determined that $\Delta x/p \simeq 1$ and $p = 10\ \mu m$ and $15.6\ \mu m$ in the horizontal and vertical directions, respectively, corresponding to Nyquist frequencies of 50 mm^{-1} and 64.1 $mm.^{-1}$ Figure 2 shows computer-generated plots of eq (1) and (2) based on these values.

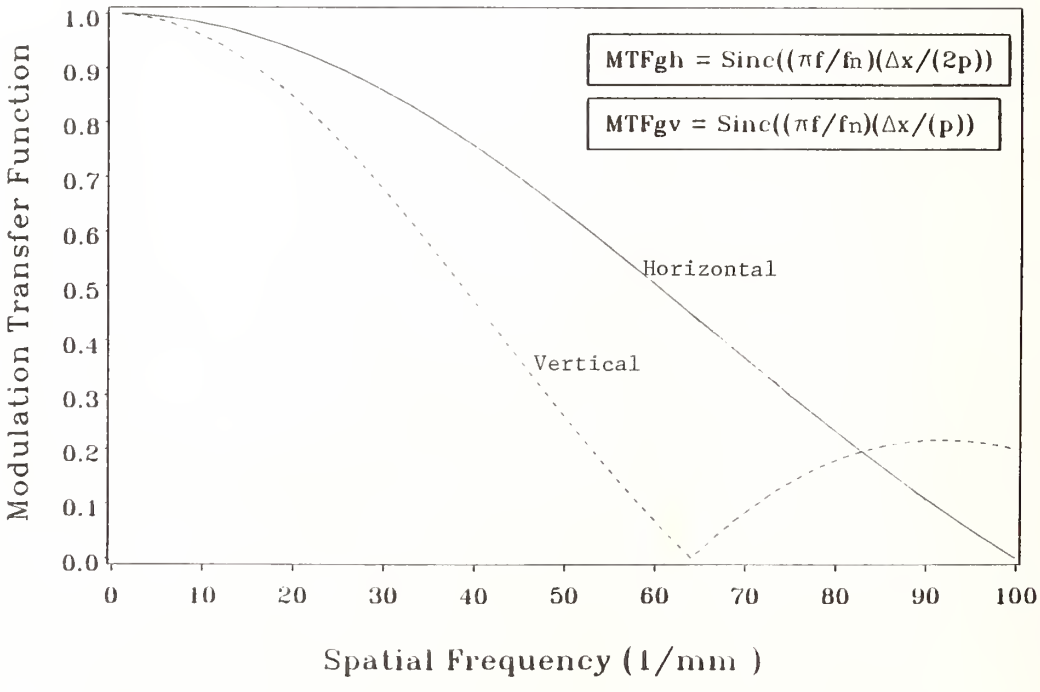

Figure 2. Calculated pixel geometry components of the CCD sensor MTF in the horizontal and vertical directions.

The diffusion component of MTF accounts for the loss of signal due to photons that are absorbed outside the sensor CCD depletion regions [5]. The effect is approximately the same in both the horizontal and vertical directions, and can be expressed as

$$MTF_d = \frac{1 - [\exp(-\alpha L_d)/(1 + \alpha L)]}{1 - [\exp(-\alpha L_d)/(1 + \alpha L_o)]} , \qquad (3)$$

where the quantity L is obtained from the relation

$$\frac{1}{L^2} = \frac{1}{L_o^2} + (2\pi f)^2 , \qquad (4)$$

L_o = diffusion length of signal change,

L_d = width of the CCD depletion layer,

and α = material optical absorption coefficient.

Figure 3 shows the results of plotting eq (3) with $\alpha = 1000\ cm^{-1}$, $L_d = 4\ \mu m$, and $L_o = 7\ \mu m$ and $10\ \mu m$. We subsequently determined that $\alpha = 4000\ cm^{-1}$ and $L_o = 30\ \mu m$ are probably better values for those parameters [5,6]; however an examination of eq (3) reveals that whereas increasing L_o tends to lower the MTF curve (see figure 3), increasing α tends to raise it. Thus the result shown in figure 3 for $L_o = 10\ \mu m$ is reasonable.

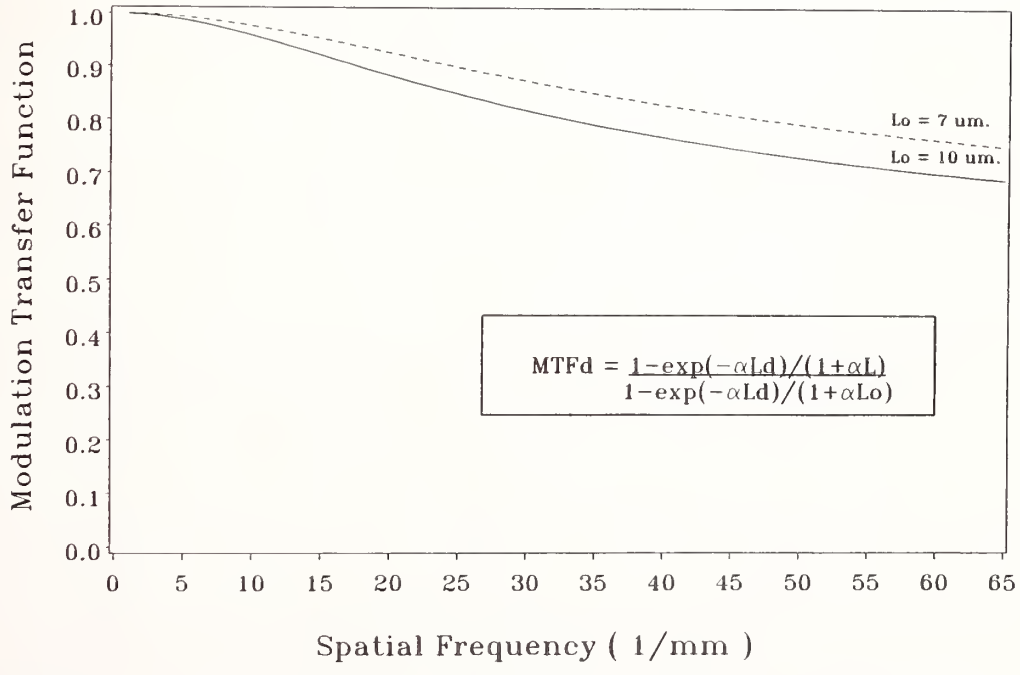

Figure 3. Calculated diffusion component of the CCD sensor MTF for $L_d = 4\mu m$ and $\alpha = 1000\ cm^{-1}$. Results are valid in both the horizontal and vertical directions.

In frame transfer CCD sensors, images are continually transferred vertically from the imaging portion of the sensor to the storage portion [4]. During this transfer, some of the charge stored in each pixel is left behind and added to the charge in trailing pixel signals. This effect results in a so-called transfer inefficiency component of MTF in the vertical direction, which is given [3] by the expression

$$MTF_t = \exp[-\eta\epsilon(1 - \cos(\pi f/f_n))], \quad (5)$$

where ϵ = the fraction of charge left behind in each transfer

and η = total number of transfers.

Equation 5 is plotted in figure 4 for an inefficiency product $\eta\epsilon = 0.3$, which was found to be the case in previous measurements on a frame transfer CCD sensor [7].

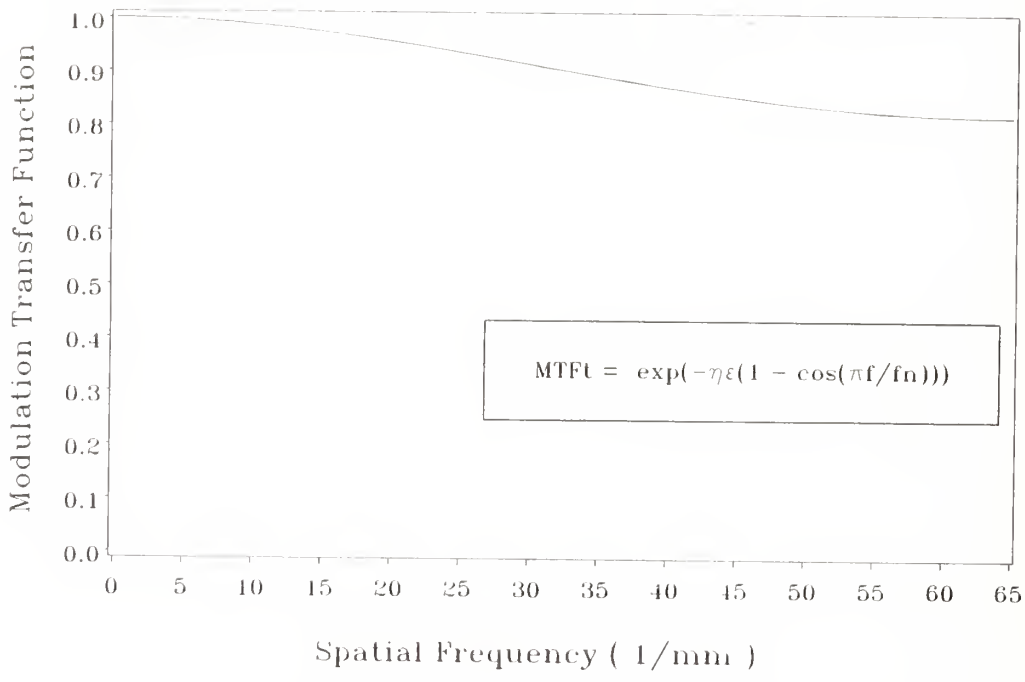

Figure 4. Calculated transfer inefficiency component of the CCD sensor MTF in the vertical direction for $\eta\epsilon = 0.3$. There is no transfer inefficiency in the horizontal direction.

Total MTF's consist of the products of geometric, diffusion, and transfer inefficiency components in the vertical direction and geometric and diffusion components in the horizontal direction. The appropriate curves from figures 2, 3 (L_o = 10 μm), and 4 along with their products are shown in figures 5 and 6, respectively, for the vertical and horizontal directions.

The net vertical and horizontal MTF's from figures 5 and 6 are compared to our previously measured results [1] in figures 7 and 8, respectively. The dashed curves through the data points in figures 7 and 8 were obtained with a spline-based curve fitting routine [8]. These calculated and measured results are in reasonably good agreement, which suggests that image grey levels can be used to provide a fairly reliable indication of sensor spatial frequency bandwidth. However, the scatter in the measured data also suggests that other MTF measurement methods, e.g., those based on the camera output video signal [9], are more accurate. The general agreement between the calculated and measured results also supports the earlier conclusion [1] that the CCD area array sensor should be able to resolve structural details in laser beam profiles with spatial frequencies up to 50 mm^{-1}

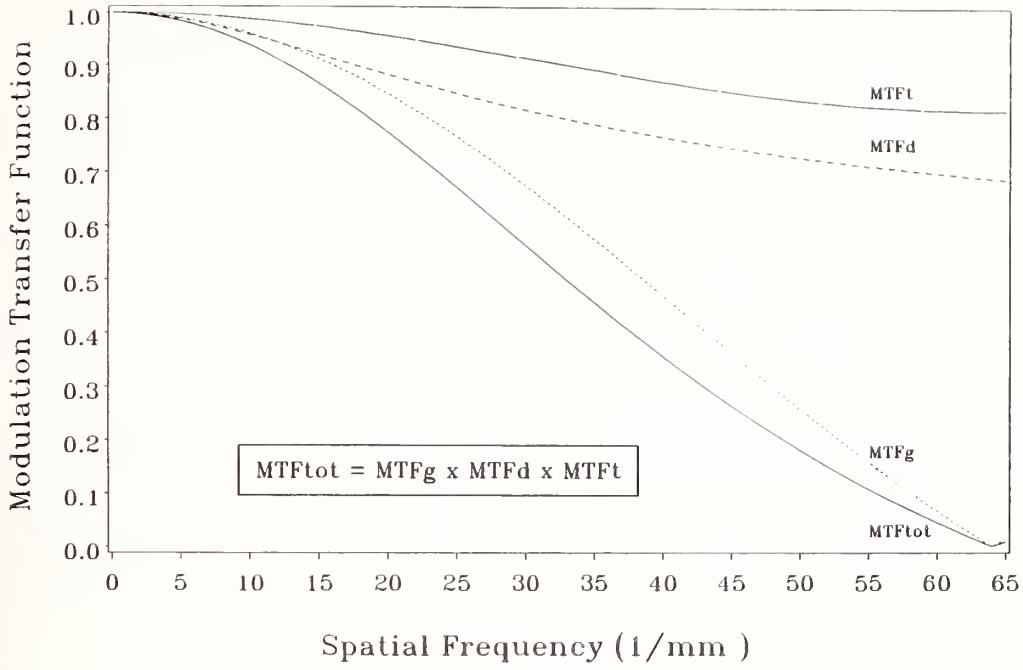

Figure 5. Calculated total MTF of the CCD sensor in the vertical direction. Component curves are from figures 2, 3 (L_o = 10 μm), and 4.

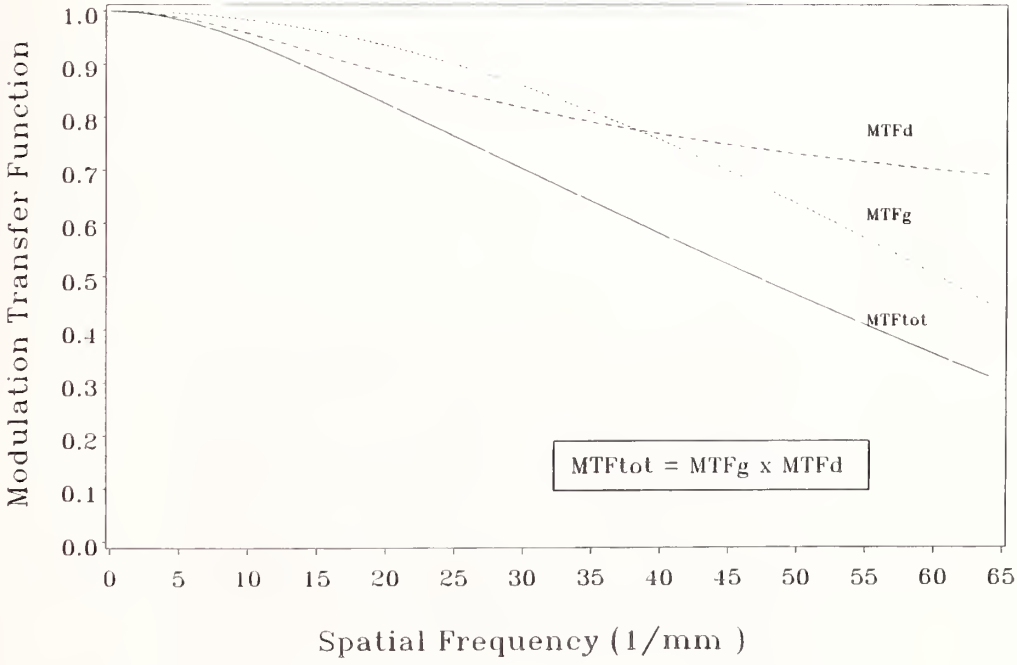

Figure 6. Calculated total MTF of the CCD sensor in the horizontal direction. Component curves are from figures 2 and 3 (L_o = 10 μm).

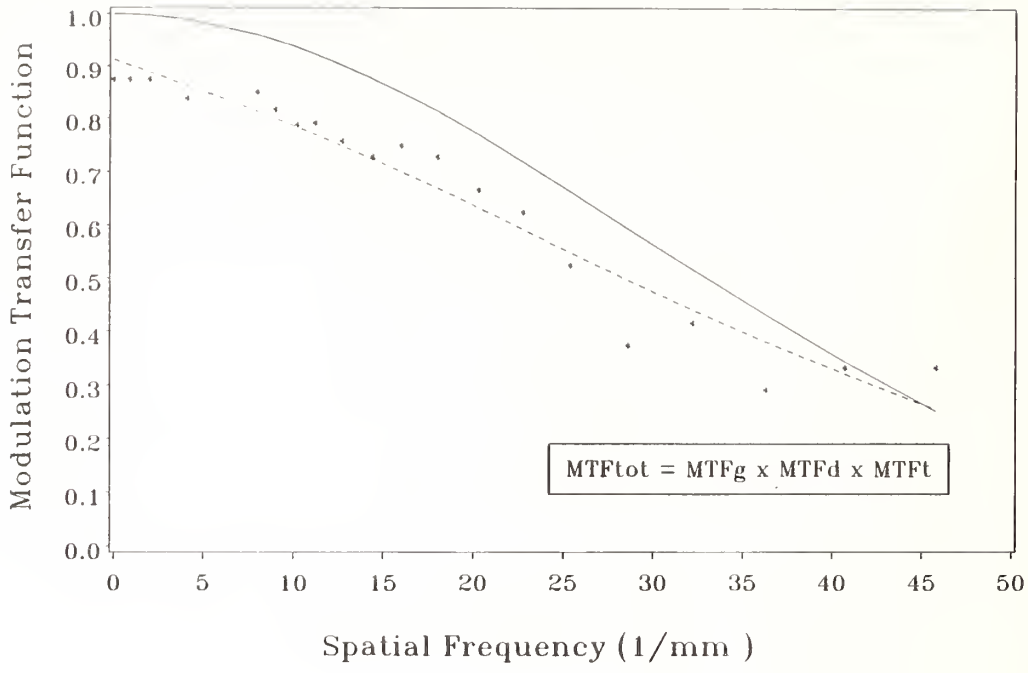

Figure 7. Comparison of the calculated total MTF of the CCD sensor in the vertical direction (solid curve) with the previously measured result [1].

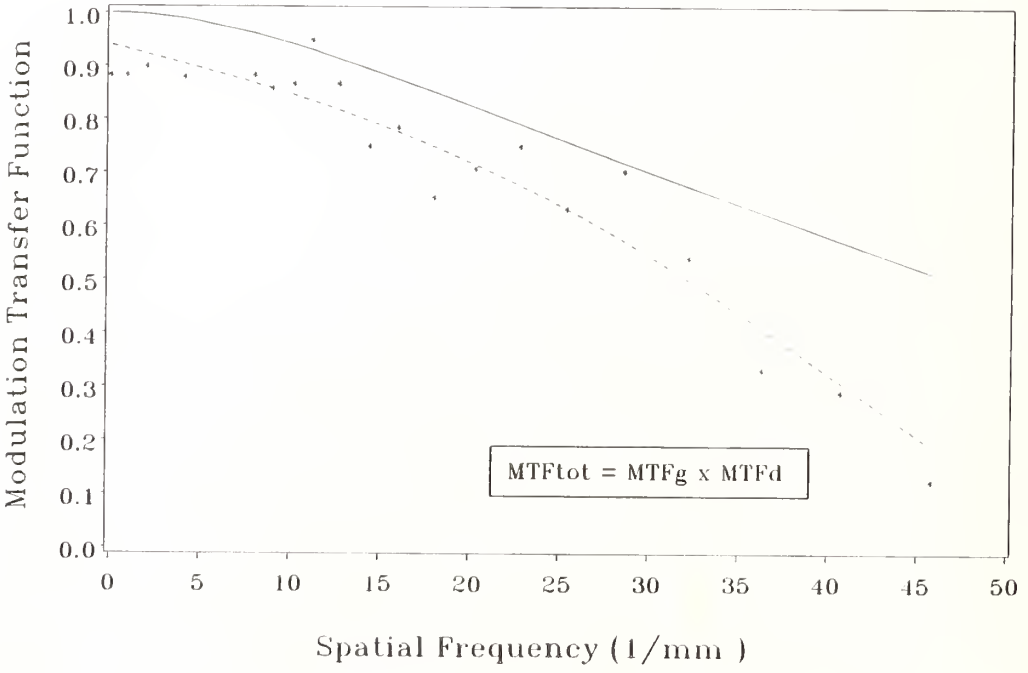

Figure 8. Comparison of the calculated total MTF of the CCD sensor in the horizontal direction (solid curve) with the previously measured result [1].

4. Logarithmic Video Amplifier for Contrast Enhancement

To improve the contrast of low intensity components in the imaged laser beam, we studied the effects of using a logarithmic video amplifier (MVP Electronics DCL-80-20) to modify the output of the CCD camera before it enters the 8-bit image processor. In principle, the logarithmic amplifier should magnify the smallest intensity components the most and the largest intensity components the least, thereby improving the contrast of the smaller components.

Feeding the composite camera output, which includes both video information and blanking signals, into the amplifier proved unacceptable because the amplified blanking signals were too large for the image processor. It was thus necessary to amplify only the video component of the camera output. To do this, we modified the camera output circuitry so that the video information and blanking signals could be joined externally, after either sending the video information through the logarithmic amplifier or bypassing it. The modification is illustrated in figure 9.

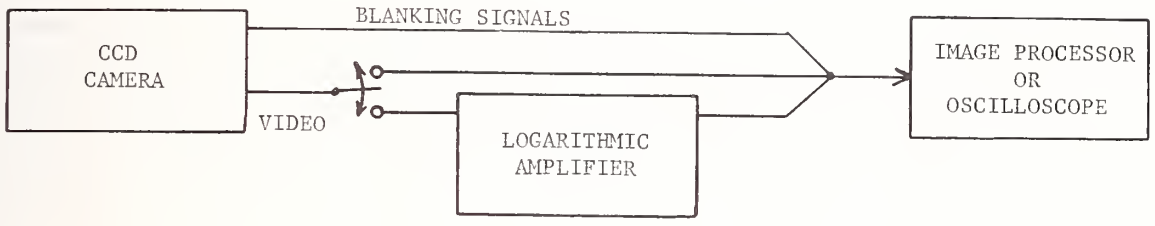

Figure 9. Arrangement used to study the effects of a logarithmic amplifier on the CCD camera output signal. With the camera modification, blanking and video signals are superimposed after the video signal is optionally amplified.

To evaluate the effect of the logarithmic amplifier on an optical signal, we used an oscilloscope to observe the video signal associated with the image of a gaussian helium-neon laser beam. To avoid saturation of the CCD camera sensor, neutral density filters were used to attenuate the beam such that approximately only one-half of the 2.65 volt video voltage window of the camera was used. In figure 10, oscilloscope traces (storage mode) of both the unamplified and amplified video signals are superimposed. The inner and outer envelopes represent, respectively, the gaussian beam profile and its logarithmically amplified counterpart. It can be seen in the figure that the logarithmic amplifier operated on the weaker signals more than on the stronger ones, as expected. For example, whereas the peak of

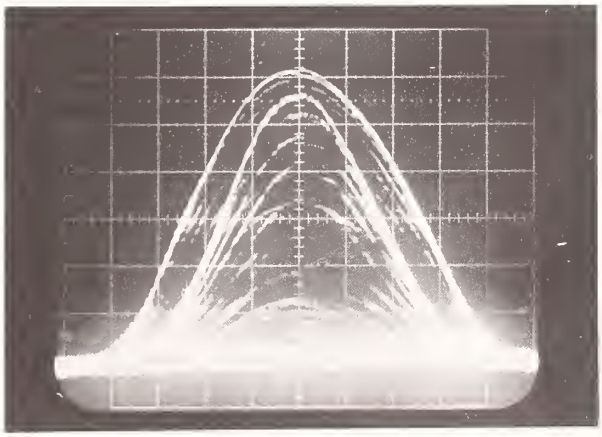

Figure 10. Superimposed storage oscilloscope traces of the camera video signal associated with a gaussian laser beam. Inner envelope: unamplified gaussian signal. Outer envelope: logarithmically amplified signal. Horizontal: 2 μsec/div. Vertical: 0.2 volts/div.

the gaussian signal was amplified by a factor of only 1.09 (or 9%), the $1/e^2$ point of the gaussian signal was amplified by a factor of 2.64 (or 164%). When either signal (amplified or unamplified) was input to the 8-bit image processor, the corresponding beam image was displayed as expected, i.e., without saturating the voltage window of the image processor. It is thus clear that logarithmic amplification can be used to improve the contrast of low intensity components in beam profiles without saturating the voltage window of the image processor.

5. Summary and Conclusions

The dark current and photosensitivity pattern noises of the CCD area array sensor are less than 7% and 1%, respectively, over the entire sensor area. Thus the device is virtually free of geometric distortion and superior in this regard to the CID camera studied earlier [1].

The calculated MTF's agree reasonably well with the previously measured results [1]. Thus, the CCD camera should provide adequate resolution of beam profile structure with spatial frequencies up to 50 mm^{-1}.

With a slight modification to the CCD camera output circuitry, the logarithmic video amplifier can be used with the 8-bit image processor to improve the contrast of low intensity components in measured laser beam images. An important next step in this work will be to calibrate the amplifier so that image-inversion software can be written, which will allow the automatic display of laser beam images that have been logarithmically amplified for contrast improvement and converted back to a linear format for observation and analysis.

---

*Research sponsored by the Air Force Office of Scientific Research/AFSC, United States Air Force, under Contract F49620-85-0013. The United States Government is authorized to reproduce and distribute reprints for governmental purpose notwithstanding any copyright notation hereon.

6. References

[1] O'Connell, R.M., and Stewart, A.F. Performance characteristics of a beam profiling system consisting of various solid state imaging devices and an 8-bit image processor. Proceedings of the 18th Annual Symposium on Optical Materials for High Power Lasers, Boulder, CO., 1986.

[2] McColgin, W.C. and Stancampiano, C.V. Analysis and measurement of pattern noise in color-filter arrays for image sensors. IEEE Trans. Electron Devices ED-32(8): 1411; 1985.

[3] Barbe, D.F. Imaging devices using the charge-coupled concept. Proc. IEEE 63(1): 38; 1975.

[4] Sèquin, C.H. Interlacing in charge-coupled imaging devices. IEEE Trans. Electron Devices ED-20(6): 535; 1973.

[5] Seib, D.H. Carrier diffusion degradation of modulation transfer function in charge coupled imagers. IEEE Trans. Electron Devices. ED-21(3): 210; 1974.

[6] Dash, W.C. and Newman, R. Intrinsic optical absorption in single-crystal germanium and silicon at 77°K and 300°K. Phys. Rev. 99: 1151; 1955.

[7] Joyce, W.B. and Bertram, W.J. Linearized dispersion relation and Green's function for discrete-charge-transfer devices with incomplete transfer. Bell Syst. Tech. J. 50: 1741; 1971.

[8] Ferreira, R.J. Modulation transfer function of self-scanned imaging devices. M.S. Thesis. University of Missouri-Columbia. 1987.

[9] Sèquin, C.H.; Morris, F.J.; Shankoff, T.A.; Tompsett, M.F. and Zimany, E.J., Jr. Charge-coupled area image sensor using three levels of polysilicon. IEEE Trans. Electron Devices ED-21(11): 712; 1974.

Manuscript Received
9-29-88

A Sensor for Production Oriented Damage Testing at 1.06μm

J. W. Arenberg, C. L. Schoen*, and D. W. Mordaunt

Hughes Aircraft Company
Electro-Optical and Data Systems Group
El Segundo, California 90245

Detection for production laser damage testing at 1.06μm may be accomplished by a single scheme of flash detection. This scheme uses the test wavelength, 1.06μm, to detect catastrophic damage events and is sufficient to detect the plasma associated with catastrophic damage, the failure morphology typical of production damage testing.

The detection scheme consists of a fiber optic bundle used as a light pipe and a photomultiplier tube as a detector. When introduced into the target area, the collection end of the light pipe is the only element of the detector that need be in proximity to the target area. Since the light pipe has a wide acceptance angle, precise location and orientation of the light pipe end is not required. Therefore, the detector may be moved in and out easily without compromising detector performance. The detector is used in conjunction with electronics that allow the user to define a non-damage level of scatter. When damage occurs and the characteristic plasma plume is formed, a comparator detects the signal exceeding the set threshold and registers a damage event.

The simplicity and low cost aspects of the detection scheme make it a good candidate for all production damage testers at 1.06μm. Furthermore, the detection apparatus may be linked electronically to the test laser to shut off the test source upon detection of damage to prevent gratuitous damage to the sample under test. The incorporation of such a binary damage detector is suitable for use in an automated and, therefore, enclosed (Class I) damage tester for use on factory floors.

Key words: damage detection; laser damage; production testing.

1. Introduction and Background

This paper describes the development of a sensor for production oriented laser damage testing. Following this introduction, a resume of the desired attributes of a sensor for production oriented damage testing is presented. Then the particular implementation will be introduced and discussed.

It is worth noting that the sensor described herein was initially intended to be a scatter probe similar to one previously described [1]. The difference between the scatter probe described by Seitel and Babb and the intended operation of the present sensor was the wavelength of operation. Seitel's and Babb's sensor requires an additional He-Ne laser and measures the change in scatter of the 0.6328μm radiation. The intended sensor was designed to detect change in the 1.06μm test laser itself with no additional beams required.

2. Attributes of a Sensor for Production Oriented Testing

The two main differences between sensors used in research oriented damage testing and production oriented damage testing are the subtlety of the degradation and the quantification of degradation. The researcher is interested in the evolution of the damage morphology as a function of irradiation and frequently defines damage as the first observable permanent change in the optic under test. The laser manufacturer is interested in damage that will impact laser operation and frequently defines damage to be catastrophic [2,3], since the more subtle pitting of optics does not usually affect the performance or typical laser systems now in production.

*Current address is: LLNL/TRW, P. O. Box 5513, Livermore, California

Thus, the attributes of a damage sensor for production differ from the requirements of a sensor for research oriented damage testing in the requirements of quantification. The research oriented sensor must be capable of detecting small changes in the surface of the optic, while the production oriented sensor should only detect catastrophic events. Here the difference becomes clear. The research oriented sensor returns an analog result related in some way to surface change while the production sensor returns a binary signal indicating damage or no damage.

3. Concept, Implementation and Operation

The basic attribute of the sensor is the ability to detect and report catastrophic damage to the optic under test. There is a plasma spark associated with catastrophic failure of an optic and it is this plasma spark that is detected.

To implement this concept of plasma spark detection, a light pipe consisting of a fiber optic bundle is used to collect and guide the radiated light to a detector. This dectector puts out a signal proportional to the energy that is collected by the light pipe. This signal is compared to a threshold level. If the signal exceeds the threshold level, the discriminator generates a logic pulse which then shuts off the laser and allows for inspection of the surface.

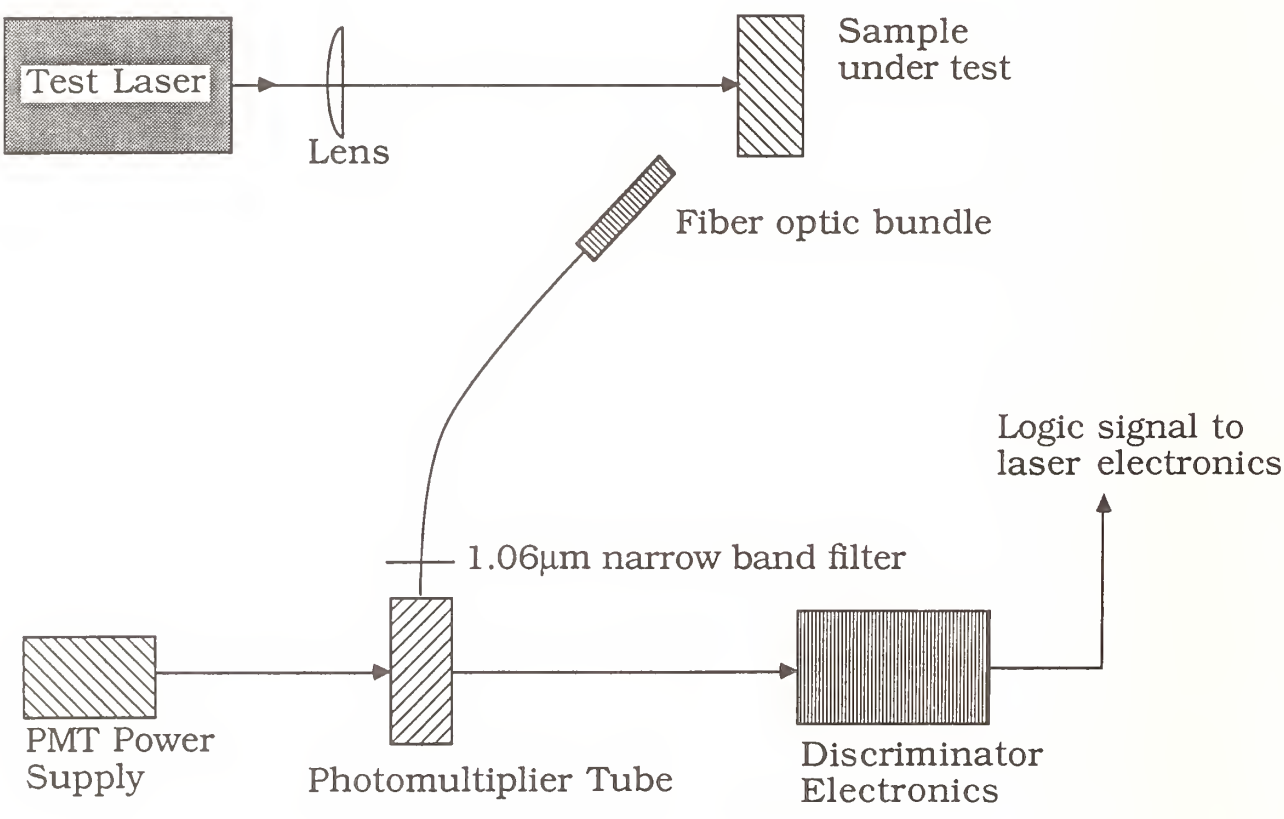

Figure 1. Schematic of Flash detector

A layout of the sensor is shown in figure 1. The 1.06μm interference filter is an artifact from the attempt to design a scatter probe. Its presence does not hinder the performance of the sensor and provides a needed filter against background illumination.

The precise specification of equipment should not be necessary to construct an operational sensor. The discriminator, for example, can be an off-the-shelf device, such as are common in many NIM crates, or can be built for the explicit purpose as in the present case. The ability to set a threshold level enables the user to "calibrate" the sensor for the size of the plasma spark typical of the damage test station.

In the particular sensor assembled at Hughes, it was found that the ability of the sensor to detect damage was relatively insensitive to angular orientation of the fiber optic bundle. Also, the sensor was found to operate with as much as 14dB of attenuation between the spark and the collecting end of the fiber.

4. Discussion

There are several advantages to the sensor described above that make it an attractive option for damage detection in a production oriented environment.

The first is alignment insensitivity, the ability of the sensor to tolerate minor angular misalignments, which allows for the rapid removal and replacement of the fiber optic bundle. Thus, minimal time and operator training are necessary to successfully remove and replace the fiber bundle. The small size of the fiber bundle allows for placement in the crowded area near the target plane. This is further reinforced by the fact that other sources and collection optics are not needed.

The binary nature of the discriminator output and the ability to adjust the level to detect the plasma spark associated with catastrophic failure makes this sensor an attractive option for damage detection in a fully enclosed damage test station. This allows construction and operation of a fully enclosed, Class I laser damage test station in a normal production environment. The amount of operator training and skill needed to recognize a plasma spark and adjust the discriminator level accordingly is minimal. This minimal training requirement is in contrast to the rather difficult job of observing and calibrating subtle changes in the optic under test.

In conclusion, it is the authors' contention that the device described above is a useful damage detection sensor for production oriented applications and can be assembled from common laboratory equipment. Although the sensor described in this paper is intended to operate with a 1.06μm damage tester, it is really the plasma spark that is detected, and the device should operate well at any laser wavelength where a plasma spark accompanies catastrophe failure of the optic under test.

5. References

[1] Seitel, S. C.; Babb, M. T. Laser induced damage detection and assessment by enhanced surface scattering. 18th symposium on optical materials for high power lasers; 1986 October; Boulder, CO. Proceedings to be published.

[2] Arenberg, J. W.; Frink, M. E.; Mordaunt, D. W.; Lee, G.; Seitel, S. C.; Teppo, E. A. Correlation of laser damage tests at 1.06μm varying modal content and irradiance history. 18th symposium on optical materials for high power lasers; 1986 October; Boulder, CO. Proceedings to be published.

[3] Mordaunt, D. W.; Arenberg, J. W.; Frink, M. E. Production oriented laser damage testing at Hughes Aircraft Company. 18th symposium on optical materials for high power lasers; 1986 October; Boulder, CO. Proceedings to be published.

The composition and design of the coatings tested was requested. The speaker replied that he did not know the answer since these were vendor samples. However, it was worth noting that of the 12 designs analysed the one which conditioned the most and the one which conditioned the least were from the same coating coated at the same time by the same vendor. The porosity of the films has not been checked. A weight loss technique was suggested. The author believes that water plays a large role in coating anomalies. The possibility of getting contaminants from the chamber wall onto the optic was discussed.

Another participant pointed out that in his experience water would reenter porous films within minutes or faster after it was removed from the vacuum chamber. The speaker replied that he had reported work last year suggesting that on samples he had studied the time constant was on the order of days.

- MANUSCRIPT NOT RECEIVED -

MAPPING OF SURFACE DEFECTS OF OPTICAL COMPONENTS BY A HIGH SPEED SURFACE ANALYSIS SYSTEM

Ramin Lalezari and Robert Knollenberg
PMS-ELECTRO OPTICS
1855 South 57th Court
Boulder, Colorado 80301

ABSTRACT

A scanning darkfield laser scatterometer is used to produce maps of surface defects on optical component surfaces. This instrument was originally developed for the examination of silicon wafers. The short depth of filed, high resolution darkfield imaging design of the scattering measurement head, enables the instrument to examine the cleanliness and surface condition of transparent as well as opaque optical surfaces, including coated surfaces.

The measurement system consists of a laser illuminated darkfield optical head mounted on a linear translation stage, a spinning chuck, and a data acquisition and display system. The instrument is capable of resolving the ac scattered light component to two parts in 10^9 for scattering sites smaller than the pixel size (50 microns). The dc sensitivity of the instrument is roughly one part in 10^6 (1 ppm).

The instrument has been successfully used in inspecting mirror substrates before and after coating and in developing cleaning techniques. Operation of the system and some data will be presented.

Manuscript Received
3-4-88

Scattered Light as a Laser Damage Diagnostic

Alan F. Stewart and Arthur H. Guenther
Air Force Weapons Laboratory
Kirtland AFB, New Mexico 87117-6008

ABSTRACT

Laser light scattering from thin film coatings was evaluated as a diagnostic indicator for an automated 1-on-1 laser damage test facility. While variations in scattered light has been effectively used in bulk damage testing for many years, a dependable diagnostic of similar ilk for threshold phenomena of surfaces and thin film coatings has not been universally accepted. The data collected in this study indicates that measurement of scattered light is effective when surface damage morphologies mimic the larger scale phenomena observed in bulk damage. When individual micron diameter pits form on the surface, as can frequently be the case, this diagnostic is less reliable. In addition, when the overall scatter level from the surface is high, as in poor quality optics, the change in scattered light becomes undetectable with the onset of damage.

Key words: laser induced surface/thin film damage, scattering, damage indicator.

I. Introduction

Laser induced damage in 1-on-1 testing of surfaces and thin film coatings has been an area of intensive study for many years. [1-7] The determination of a true threshold value has been the subject of much debate because of the statistical nature of testing procedures and how the onset of damage was defined. In an ideal experiment for the determination of an absolute damage threshold, a purely statistical test could be employed with a large sample set using a fail-safe determination of the onset of damage. A considerable amount of surface area must be tested at each fluence level and a large number of identical samples must be tested to obtain the required statistics to accurately define a threshold for a specific set of samples.[5] The amount of testing required is impractical because of many reasons, e.g., human fatigue, experimental errors as well as cost. As a result, most studies published to date present enough data to indicate trends and bracket with some level of confidence the expected performance levels for a given coating or surface. Of course what is generally wanted is an indicator of performance for full size optical components.

A number of techniques have been described the literature which make use of scattered light, either at the fundamental or at another wavelength in an attempt to determine the onset of laser damage or to study the mechanisms of laser damage. [3,8-11] In this study, we examined the use of both off axis and near angle (to the specular reflected beam) scattered laser light as automated diagnostic indicators for threshold determinations in 1-on-1 laser damage testing of thin film coatings. Scattered light has been used effectively for many years in bulk damage testing where the onset of damage is marked by a large fracture zone in the material. The data collected in this study involving some 5000 individual sites indicates that scattered light variations works well when surface damage morphologies mimic the larger scale phenomena observed in bulk damage. When micron diameter pits form on the surface, this diagnostic is less reliable. And when the overall initial scatter level from the surface is high, the change in scattered light becomes undetectable and thus, uncorrelated with the onset of damage.

II. Experiment

An extensive series of laser damage tests were conducted in support of an experiment to be described elsewhere in these proceedings. [12] 1-on-1 laser damage tests were conducted using a single mode Nd:YAG laser system. The laser damage testing protocol employed and the system specifications have been reported in the literature over the past several years. [6,7] Two different experimental configurations were assembled to determine the viability of scattered light as a laser damage indicator. Off axis scattered light as depicted in figure 1 was the initial thrust of this investigation. This technique was of particular interest due to the known sensitivity of variable angle scatterometer measurements to small scale surface imperfections. [13,14] A chopped helium neon laser probe beam illuminated the area of the

surface under test. The probe beam was incident on the sample surface at an angle of 30 degrees from normal and was focused to match the diameter of the 1.064 micron damage test beam. The Gaussian profile of the probe beam was thus elongated in the plane of incidence. The damage test beam was incident on the sample surface at 4 degrees from normal and also exhibited a Gaussian profile. The specularly reflected beam was blocked. In all other respects, damage testing was conducted following standard procedures. [6,7] The implementation of a scattered light diagnostic probe is very dependent on the footprint of the intensity profile and the overlap between the two beams at the sample surface. It should be noted that both probe and damage test beams exhibited some pointing jitter. A larger margin for error due to beam jitter would have resulted from utilization of a larger probe beam diameter but with correspondingly lower intensities on the sample surface and reduced sensivity. Scattered light from the sample surface was collected using a Questar QM-1 long working distance microscope positioned 110cm from the sample. The microscope viewed the sample surface at 10 degrees off normal and 10 degrees from the specular beam in the plane of incidence. The 8.8cm microscope aperture collected light from a solid angle of 0.006 steradians. The image from the microscope passed through a paritally reflecting beamsplitter to a video camera for observation of the sample surface. The beamsplitter was coated as an 80% reflector at 633nm. The reflected red light was incident on a laser line interference filter followed by a photomultiplier tube.

The photomultiplier signal was processed by an amplifier with a bandpass filter on the input synchronous to the chopping frequency of the probe laser. Amplifier gain settings varied between 20 and 5000 to obtain an output signal of 1 volt for the different samples tested. The chopped signal was then processed by a transient digitizer which averaged 60 waveforms. The averaged waveform was then analyzed to obtain a root mean square amplitude. Scatter levels were measured in this fashion before and after each shot. Both the absolute scatter level and the fractional change in this level were recorded. Scattering from bare low scatter surfaces (<400 PPB/Str) were easily measurable using this system. Data obtained on coated surfaces during this study indicated a noise level of about 1% for typical meaurements. The principal source of the recorded noise level was triggering instability and resolution in the transient digitizer.

Near angle scattered light measurement, as depicted in figure 2, was later investigated as an alternative technique. Again, a chopped helium neon laser probe beam was used to illuminate the area of the sample surface under test. The probe beam in these tests was focussed to twice the diameter of the 1.064 micron damage beam. The angle ofincidence of the probe beam was 30 degrees from normal to the sample surface. The specularly reflected beam was blocked by a "negative pinhole". [9-11] Scattered light was collected by a lens which imaged the test surface onto the enrance aperture of the photomultiplier tube. The photomultiplier output signal was processed in the same manner as described above. In all other respects, damage testing was conducted following standard procedures. After the conclusion of testing, each irradiation site was carefully examined under a Nomarski microscope at magnifications up to 400X. Any noticeable change of the sample surface was identified as damage. This was the only criteria used for the determination of damage in this study.

The samples tested in this study provided a broad variation in properties and damage thresholds. Single layer coatings of Al_2O_3 and Ta_2O_5 were prepared using electron beam and reactive sputtering. Hafnium oxide coatings were prepared using ion assisted electron beam deposition. These coatings were deposited in a half wave thickness at 1.06 microns. The substrates were superpolished fused silica with extremely low scatter surfaces (<400 PPB/str). Before damage testing, the coated substrates were subjected to a laser annealing treatment at various power levels. For each set of samples, it was observed that average scattering levels increased dramatically above an annealing level of 50 W/cm2. As reported elsewhere in these proceedings [12], the properties of these coatings in terms of damage thresholds and scattering levels varied considerably with microstructures that ranged from polycrystalline to amorphous. Thus, the light scatter diagnostic was evaluated with samples exhibiting a very extensive range of properties.

III. Data

The scattered light variation data collected for this study has been plotted in figures 3- 6 for four sets of samples tested. For purposes of defining a performance level, a 20% change in scattering was selected as the cutoff point--significantly above the noise level of the measurement data, but otherwise an arbitrary choice. In figures 3-6, two groups of data are plotted. First, the percentage number of damaged sites (determined from microscopy data) which exhibited a change in scatter level of 20% or more are plotted. A perfect damage diagnostic

would provide 100% correlation between the occurrence of damage (microscopy) and a measurable change in signal. The second data set plotted is the percentage of undamaged sites which exhibited a change in scatter level of 20% or more. For a perfect damage diagnostic, this error rate would be 0%. The off axis scatter data plotted in figure 3 for Al_2O_3 coatings deposited using reactive sputtering appears to be the most understandable. As the annealing power level (and thus the average scattering level) is increased from 0 to 100 Watts per square centimeter, the number of damage sites registering a change in scatter above 20% declines steadily from 94% on down to 5%. Thus, the majority of the damaged sites escape detection at the higher annealing power levels. The fraction of undamaged sites which had significantly altered scatter levels is consistently below 4% for this whole series of samples. Off axis scatter data obtained on Ta_2O_5 coatings fabricated using reactive sputtering and electron beam deposition was less encouraging. The data plotted in figures 4 and 5 shows that the scatter diagnostic was much less efficient as a damage indicator for these films in general. In figure 4, data obtained on sputtered Ta_2O_5 films actually shows a crossover for one sample where a measured change in the scattering level correlated to undamaged sites more often than to those which had damaged. The efficiency of the off axis scatter diagnostic falls to below 50% for highly scattering samples annealed at higher power levels. The signal-to-noise of scattered light as a diagnostic indicator is inadequate for the detection of small scale damage features on annealed electron beam and sputtered Ta_2O_3 films.

Near angle scattering was used as a diagnostic indicator for the data obtained on ion assisted hafnium oxide films plotted in figure 6. As in figure 3 for Al_2O_3films, the data shows a steadily decreasing efficiency of the diagnostic with increasing anneal power. At an anneal power of 125 W/cm2, near angle scattered light permitted the detection of only 5% of the sites damaged by the incident 1.064 micron beam. While the near angle scatter diagnostic fell from 76% for unannealed films to 5% efficiency for films annealed at 125 W/cm2, the background scattering level of these coatings rose by a factor of 156 as determined from measurements on a variable angle scatterometer. [14] The error rate for near angle scattered light detection is zero for all practical purposes and is lower than that observed in off axis scattered light data.

IV. Analysis

Several factors controlled the performance of the light scatter damage diagnostics as described above. Damage morphology played a significant role in determining the applicability of these diagnostics for thin film studies. The morphology observed on the Al_2O_3 sputtered films was unique in that every site involved the complete ablation or uniform modification of the film under the beam footprint. This morphology was very definitive and unusual for coating damage at 1.064 microns. [3] Damage morphologies observed on the Ta_2O_5 and HfO_2 films tested were much more typical of thin film damage with small pitting occuring near threshold. Not surprisingly, the efficiency of detection of damage in these films fell to 75-80%.

Another important factor was the overall background scattering level of the film under test. Typical scattering levels measured on single layer films on superpolished fused silica have averaged 1-5 PPM/str over the past few years. [14] The coatings annealed at power levels above 50W/cm2 and tested as part of this study exhibited scattering levels 50 - 700 times higher. These levels are considerably higher than for typical films and serve only to bracket the performance of these diagnostics.

The detection of the pitting damage morphology may serve as a reasonable ranking parameter for a damage indicator. The total area of a film modified by the damaging beam might be only 2-4 square microns within a total beam footprint of 10,000 square microns. As our standard technique, microscopy requires that the operator must exercise some judgement in identifying the very small features associated with the onset of laser damage. The question facing him is whether a suspicious 1 micron diameter spot is a native coating defect or a laser damage feature.* Without a perfect deterministic method to compare with, the microscope remains as our standard.

* This nearly becomes a philosophical discussion since if N-on-1 testing were being performed, that site might grow to macroscopic dimensions on the next shot. From this perspective, N-on-1 testing is much more deterministic than 1-on-1 testing. From a practical standpoint, some laser systems do not lend themselves to N-on-1 testing because of shot to shot reproducibility in energy, pointing or beam profile.

The measurement of off axis or near angle scattered light does not seem to be able to provide the resolution, compared to microscopy, for the identification of small scale damage features.

For control samples, which had not been annealed, the average was only 70% detection of damage sites. This phenomena can be correlated with the damage morphology observed in all coatings other than the data in figure 3. For the majority, but not all, of the coatings tested in this and other studies of thin film damage, the initiation of damage occurs with the formation of micron diameter pits. The integrated effect of a few isolated pits within the much larger area of the probe and damage beams does not seem to significantly alter the scatter levels measured by these techniques.

The error rate, as defined by the number of undamaged sites registering large changes in scattering is relatively high for the off axis data plotted in figures 3-5 with values ranging from 4-30%. The performance of the near angle scatter diagnostic as plotted in figure 6 is acceptably low with a near zero error rate. A test facility could rely on the near angle scattered light as providing a number equal to or higher to the actual damage threshold.

However, 57% of the samples tested in the off axis diagnostic mode had sites with measurable changes in the scattering level below the actual damage threshold. Every damage investigator has obediently watched as weakly bonded particulates on the surface get blown off by the laser leaving a pristine surface behind (and as we would define it - an undamaged surface but perhaps in an excited electronic or chemical state). Even with careful cleaning, these sites can not be eliminated as these particulates could have settled out of the air or have been ejected from a neighboring site. There is also the possibility of a high power damage beam annealing the coated surface resulting in reduced scatter levels. A site which is annealed by the high power beam will have different properties easily observable under the microscope and thus will not escape detection. A light scatter damage indicator would also presumably detect this type of phenomena.

It is important to note that the collection optics sufficiently discriminated against scatter from back surface damage to remove this a possible complication. In fact, the majority of the sites tested in the Al_2O_3 data set of figure 3 experienced back surface damage.

IV. Comparison to Other Techniques

Several other techniques have been used in an attempt to resolve the question of the onset of damage on coatings and surfaces. Most methods have demonstrated limited applicability and limited success. We attempted to replicate the high levels of success reported by Franck, et al, [9,10], who developed the near angle scatter diagnostic technique.

A comparison of the test data shows that considerably reduced performance results from our implementation of either the near angle scatter or off axis scatter diagnostics. One possible discrepancy might be the acceptance angle for scatter collection. We have not optimised the size of the negative pinhole used. Clearly, with optimization, the NWC technique samples near angle scatter at much smaller angles closer to the specular direction. This may permit the detection of scatter level changes on the order of 1 part in 10,000 corresponding to the formation of a single pit.

Another apparent difference in the data, is that this laboratory has tested primarily single layer coatings on transparent substrates and bare surfaces whereas the NWC group has been more involved in testing single or multilayer coatings on metal substrates. The relationship between the probe beam and fundamental wavelengths with the coating structure cannot be ignored for the implementation of a diagnostic indicator. Clearly, the removal of a small area of a film with an optical thickness of 1/2 or 1 wave may not result in large changes in the reflectance or scattering of a surface at specific wavelengths. Much larger changes in scatter have been measured in this laboratory with the onset of even small damage features in testing of multilayer high reflectance films.

A third complication in comparison of this technique with others is how the microscopist sets the criteria for the occurrence of damage. We examine each site at magnifications up to 400x using a Nomarski microscope and even then it is sometimes difficult to discriminate between native coating defects and laser damage induced features near threshold. The type of microscope employed can change the criteria selected as the microscopist sets his own discrimination levels.

A third alternative to the test procedures described here, and which has seen limited use, would be a pixel by pixel comparison of television picture frames of the sample surface taken before and after each exposure event. [15] This technique suffers somewhat from the 8 bit resolution of the television system. The effective resolution of the scatter collection system used in this study after initialization for a given sample was 10 bits but without the spatially resolved information a television picture contains.

V. Conclusions

With optimization to permit detection at the 10-100 PPM level, the near angle scatter probe developed at NWC may be able to provide the performance levels required for use in an automated laser damage test facility. Off axis scattered light as a diagnostic indicator provides low performance levels as measured on a wide variety of samples. It is unlikely that the off axis light scattering technique described here can be relied upon sufficiently to allow complete automation of a test facility.

A damage test usually involves observation of the sample under test followed by post mortem microscopy. This allows the investigator to study the area under test with high resolution, looking for changes over an area equal to a Polaroid picture or a quadrant of a television screen. The development of a similar high resolution technique for the damage diagnostic will be required for automation in testing.

List of References

1. J. H. Parks and D. A. Rockwell, "Surface Studies With Acoustic Probe Techniques", Nat. Bur. Stand. (U.S.) Spec. Publ. #435, 1975, pp 157-163.

2. J. R. Bettis, R. A. House, A. H. Guenther and R. Austin, "The Importance of Refractive Index, Number Density, and Surface Roughness in the Laser Induced Damage of Thin Films and Bare Surfaces", Nat. Bur. Stand. (U.S.) Spec. Publ. #435, 1975, pp 289-295.

3. T. W. Walker, A. H. Guenther, and P. E. Neilsen, "Optical Techniques for the Determination of Pulsed Laser Damage in Thin Films", Nat. Bur. Stand. (U.S.) Spec. Publ. #541, 1978, pp 226-234.

4. D. Milam, opening remarks at Laser Induced Damage in Optical Materials: 1987.

5. F. Rainer, D. Milam, and W. H. Lowdermilk, "Laser Damage Thresholds of Thin Film Optical Coatings at 248nm", Nat. Bur. Stand. (U.S.) Spec. Publ. #638, 1981, pp 339-343.

6. Alan F. Stewart and Arthur H. Guenther, "Laser Damage Test Results on Balzers Round Robin Thin Film Samples", Appl. Opt. 23, 3774 (1984).

7. John A. Kardach, Alan F. Stewart, Arthur H. Guenther and John K. McIver, "Photon Induced Desorption and Emission From Thin Film Dielectric Surfaces", Nat. Bur. Stand. (U.S.) Spec. Publ. # tbd; 1986, pp tbd.

8. M. B. Moran, R. H. Kuo, and C. D. Marrs, "Scatter Mapping of Laser Illuminated Coating Defects", Nat. Bur. Stand. (U.S.) Spec. Publ. #tbd; 1986, pp tbd.

9. J. B. Franck, S. C. Seitel, V. A. Hodgkin, W. N. Faith and J. O. Porteus, "Automated Pulsed Testing Using a Scatter-Probe Damage Monitor", Nat. Bur. Stand. (U.S.) Spec. Publ. 727; 1984, pp 71-76.

10. J. O. Porteus, C. J. Spiker and J. B. Franck, "Correlation Between Local HeNe Scatter and Defect Initiated Laser Damage at 2.7 microns", Nat. Bur. Stand. (U.S.) Spec. Publ. #tbd; 1985, pp tbd.

11. S. C. Seitel and Mark T. Babb, "Laser-Induced Damage Detection and Assesment by Enhanced Surface Scattering", Nat. Bur. Stand. (U.S.) Spec. Publ. # tbd; 1986, pp tbd.

12. Alan F. Stewart, Arthur H. Guenther, and Fred E. Domann, "The Properties of Laser Annealed Dielectric Films", Nat. Bur. Stand. (U.S.) Spec. Publ. #tbd; 1987, pp tbd.

13. J. M. Bennett and W. K. Stowell, "Round-Robin Testing of Low Scatter Optics", Nat. Bur. Stand. (U.S.) Spec. Publ. 688, 1983, pp 183-190.

14. W. K. Stowell and Lt. Jeff Brown, AFWAL/AADO-2, Wright-Patterson AFB, OH 45433.

15. John Jolin, Los Alamos National Laboratory, Private Communication

He Ne LIGHT SCATTERING PROBE AND COLLECTION OPTICS INCORPORATED INTO THE 1064 nm LASER DAMGE TEST FACILITY

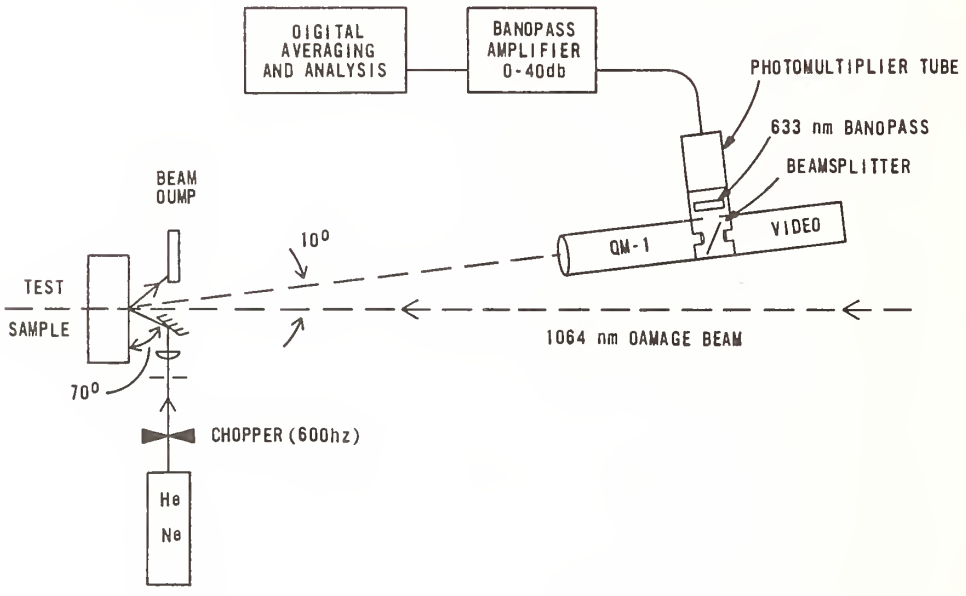

Fig. 1 Off axis light scatter detection system installed in the Nd:YAG laser damage test facility

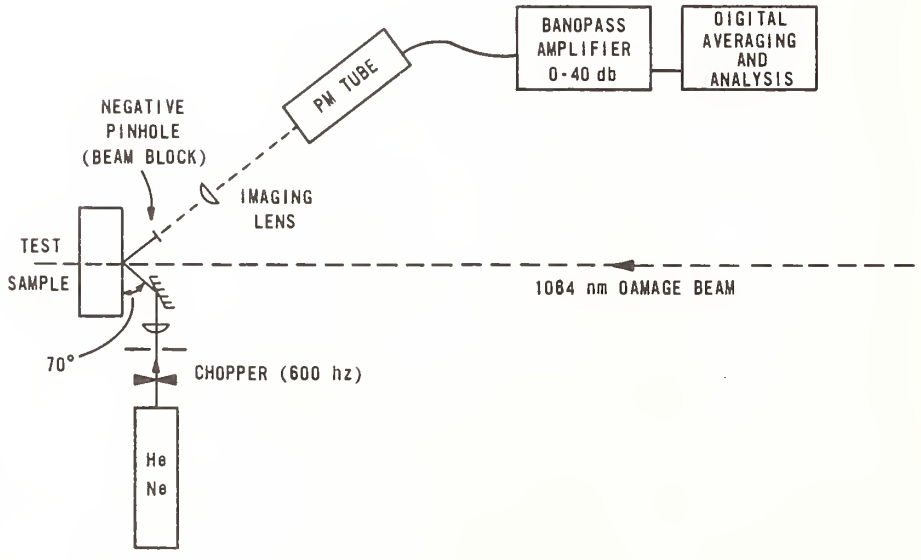

Fig. 2 Near angle scatter detection system installed in the Nd:YAG laser damage facility

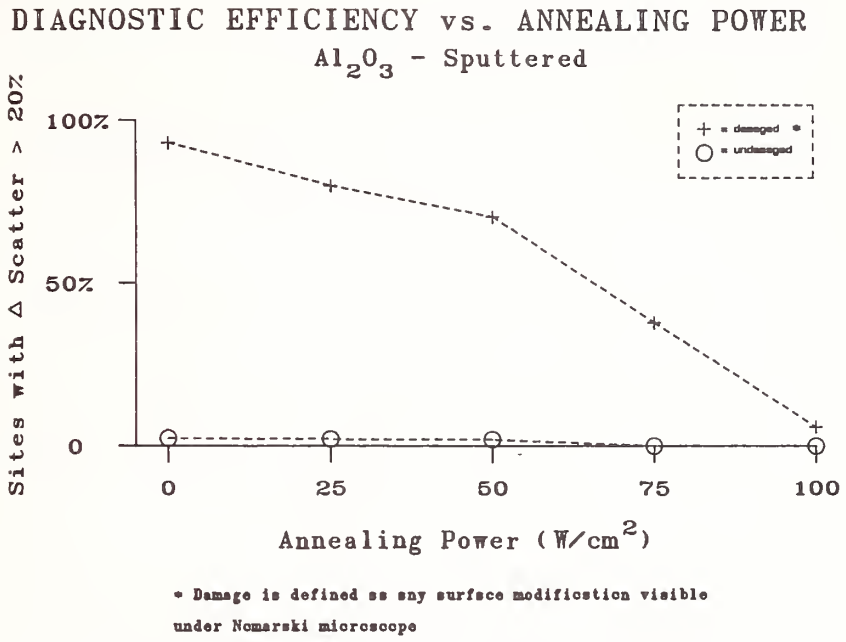

Fig. 3 Off axis scatter data: diagnostic efficiency measured on thin film coatings of Al_2O_3 deposited using reactive sputtering

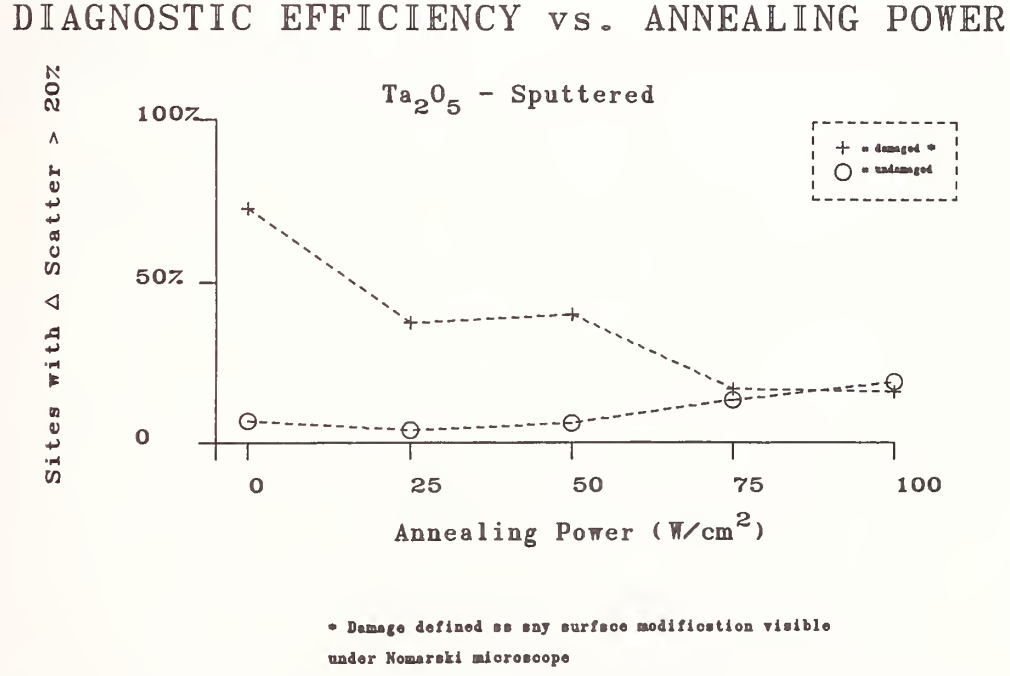

Fig. 4 Off axis scatter data: diagnostic efficiency measured on Ta_2O_5 thin film coatings deposited using reactive sputtering

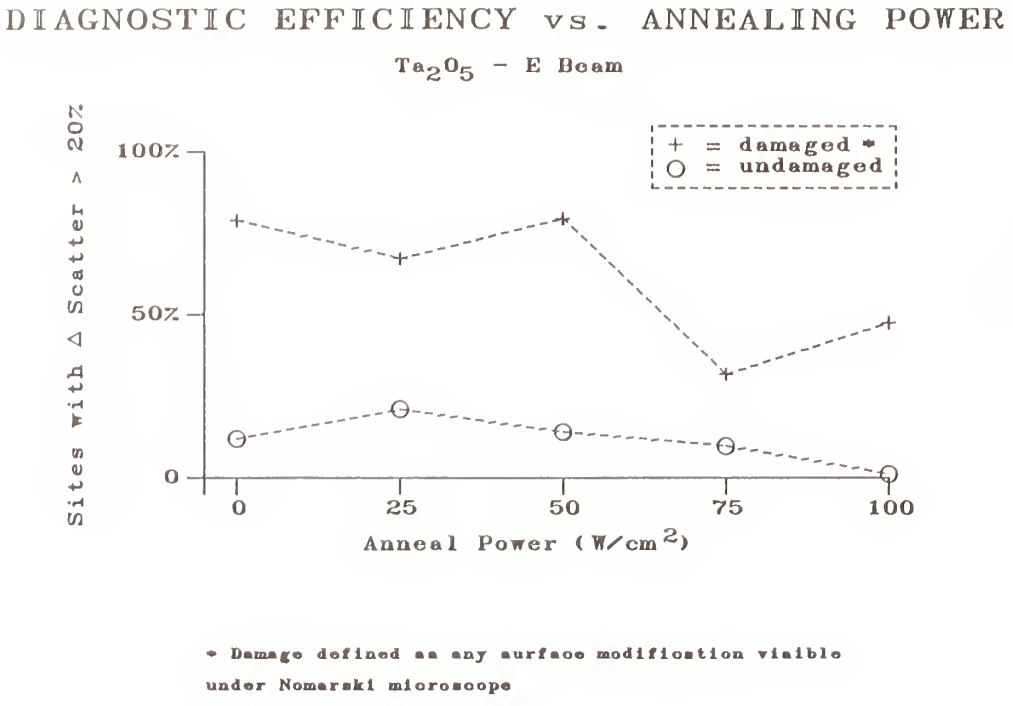

Fig. 5 Off axis scatter data: diagnostic efficiency measured on Ta_2O_5 thin film coatings deposited using electron beam evaporation

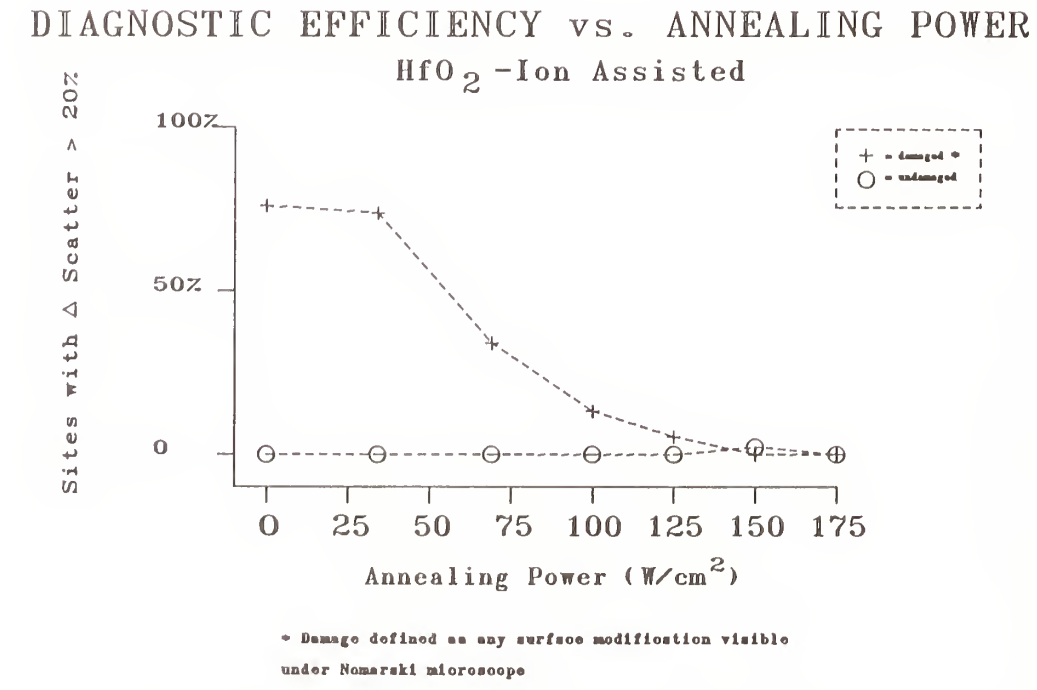

Fig. 6 Near angle scatter data: diagnostic efficiency measured on HfO_2 thin film coatings using on assisted electron beam process

- MANUSCRIPT NOT RECEIVED -

THE GROWTH AND STABILITY OF Ag LAYERS ON Cu(110) MONITORED BY SECOND-HARMONIC GENERATION

R. E. Muenchausen, M. A. Hoffbauer and T. N. Taylor
Los Alamos National Laboratory
Los Alamos, NM 87545

ABSTRACT

Understanding the fundamental limits for laser/optical mirror fabrication is directly relevant to the development of mirrors with improved durability and damage thresholds. Ag layers deposited in ultra-high vacuum on a well characterized, single-crystal Cu(110) substrate as a function of substrate temperature have been analyzed using Auger electron spectroscopy (AES) and low-energy electron diffraction (LEED) in order to answer questions concerning substrate overlayer formation and film degradation at the early stages of growth (~ 10 monolayers).[1]

Another aspect of this work has centered on developing diagnostics transferable from UHV to "real-world" environments. Optical second-harmonic generation (SHG) was chosen due to its surface specificity and experimental simplicity. The observed SH intensity as a function of Ag deposition even at submonolayer coverages. A comparison between the observed SH intensity and polarization dependence with the AES and LEED analysis indicates that optics SHG provides a fingerprint of the nucleation of Ag clusters.

[1] Taylor, T.N.; Hoffbauer, M.A.; Maggiore, C.J.; Beery, J.G. The growth and stability of Ag layers on Cu(110). J. Vac. Sci. Technol. A 5(4): 1625-1629; 1987 July/August.

- MANUSCRIPT NOT RECEIVED -

SUPER-POLISHED SILICON CARBIDE MIRROR FOR XUV RADIATION

K. Yoshida, Y. Kato and S. Nakai
Institute of Laser Engineering, Osaka University
Suita, Isaka 565, Japan

K. Kurosawa and W. Sasaki
College of Engineering, University of Osaka Prefecture
Sakai, Osaka 591, Japan

ABSTRACT

We have coated a large silicon carbide (SiC) thin film on the graphite substrate by thermal CVD method. The surface of the SiC is first lapped and then polished with a precision ring-polisher. The roughness of super-polished SiC surface was about 5 Arms. This super-polished SiC surface is expected to be useful as a grazing incidence mirror for XUV radiation.

We have applied this SiC as a high reflectance mirror for the argon excimer laser (λ=126 nm), and obtained peak output power of more than 14 MW (MgF_2 output mirror and 3 mm in beam diameter) without any damage on the SiC mirror surface. The output power and power density on the cavity mirror are the highest in comparison to the previous results obtained with other mirrors.

Manuscript Received
1-6-88

Ultrafine polishing of tungsten and molybdenum mirrors for CO_2 laser

M. Yamashita, S. Hara and H. Matsunaga

Manufacturing Development Laboratory, Mitsubishi Electric Corp.
Amagasaki, Hyogo 661, Japan

A study has been performed experimentally to determine the polishing methods for high-power laser mirrors. This paper presents ultrafine polishing of tungsten (W) and molybdenum (Mo) which cannot be turned by a diamond tool.

Samples were prepared by five methods: lapping with SiC abrasives of 4000-grit size; lapping with 3 μm diamond powder; float polishing with SiO_2 powder; Ar ion beam etching; and electrolytic polishing. The finished surfaces are characterized using several techniques, including profilometry, electron probe microanalysis, X-ray diffraction, calorimetric technique with cw CO_2 laser and so on.

The surfaces lapped with 3 μm diamond powder have damaged layers of about 2 μm deep in the case of W and about 3 μm deep in the case of Mo. In either case, however, if about 1 μm thickness of the damaged layer is removed by float polishing from the lapped surface, the layer which increases absorptance at 10.6 μm wavelength will be almost removed.

Key words: Tungsten; molybdenum; laser mirror; CO_2 laser; polishing; reflectance; absorptance; damaged layer; surface roughness; surface analysis; chemical composition.

1. Introduction

Tungsten (W) and molybdenum (Mo) are materials of interest for high-power laser mirrors because they have high melting points, sufficient stiffness, excellent thermal diffusivity, and low thermal expansion. However,it is not possible at present to diamond turn W and Mo. The most widely used method for obtaining optical surfaces on W and Mo is by mechanically polishing the bulk materials.

The purpose of this paper is to explain the development of high-power laser mirrors that have high geometrical accuracies and high reflectances at 10.6 μm wavelength.

In this paper, effects of the damaged layer (or plastically deformed layer), chemical composition and surface roughness on the specular reflectance of W and Mo are described from the machining point of view. However, as it is difficult to measure the specular reflectance with high accuracy, the absorptance is measured using calorimetric technique that has high precision of measurement of the order of 10^{-4}.

2. Experimental procedure

Samples of 18 x 18 x 2 mm and 75 mm in diameter x 10 mm thick in dimensions were used in this experiment; the former was used to investigate effects on the specular reflectance at 10.6 μm wavelength and the latter could be used as a mirror for CO_2 laser. A polishing machine of 12 inch in diameter was used in this experiment.

Samples were prepared by five methods (shown in tables 1 and 2): (1) lapping with SiC abrasives of 4000-grit size; (2) lapping with 3 μm diamond powder; (3) float polishing with SiO_2 powder; (4) Ar ion beam etching; and (5) electrolytic polishing. The method of number 2 was preceded by number 1. The methods of number 3 to 5 were preceded by number 2 and were carried out, varying the amount of stock removal from the lapped surface with the method of number 2.

The absorptance was determined by calorimetry using a 20 W cw CO_2 laser. Its precision was within ±0.03%. In order to analyze the geometrical properties of finished surfaces, Nomarski interference microscope of Union Optical Co., Talystep of Rank Taylor Hobson, TOPO 2D of WYKO Co. and Zygo Mark III of Zygo Co. were used after rinsing the samples in water. X-ray diffractometer (XD) of Rigaku Electric Co. was used to analyze the damaged layer. And then, Auger electron spectrometer (AES) of JEOL and Electron probe microanalyzer (EPMA) of JEOL were used to analyze the chemical composition of the finished surface.

3. Experimental results and discussion

3.1 Absorptance

Tables 1 and 2 show surface roughness, absorptance, and total integrated scattering (TIS) calculated with rms roughness. At first, surface roughness of both W and Mo decreases with increase of the amount of stock removal by float polishing. However, excessive polishing causes an irregular surface due to crysrallographic anisotropy, especially in the case of Mo. Consequently, surface roughness gradually increases.

Table 1. Surface roughness, absorptance, and total integrated scattering on tungsten.

	Amount of stock removal from the surface lapped with 3μm diamond (μm)	Surface roughness (Å rms)	Absorptance (%)	Total integrated scattering [TIS]
Lapping with SiC abrasives of 4000-grit size	——	420	11.30	2.5×10^{-3}
Lapping with 3μm diamond	0	66	3.30	6.1×10^{-5}
Float polishing with SiO_2 powder	0.4	64	1.59	5.8×10^{-5}
	0.9	28	1.45	1.1×10^{-5}
	2.1	36	1.43	1.8×10^{-5}
Ar ion beam etching	2.2	1960	1.88	5.3×10^{-2}
Electrolytic polishing	4.5	585	1.45	4.8×10^{-3}
	7.0	645	1.50	5.8×10^{-3}

$TIS = 1 - \exp[-(4\pi\delta/\lambda)^2]$; δ: rms roughness, λ: wavelength

Table 2. Surface roughness, absorptance, and total integrated scattering on molybdenum.

	Amount of stock removal from the surface lapped with 3μm diamond (μm)	Surface roughness (Å rms)	Absorptance (%)	Total integrated scattering [TIS]
Lapping with SiC abrasives of 4000-grit size	——	430	11.46	2.6×10^{-3}
Lapping with 3μm diamond	0	55	3.61	4.3×10^{-5}
Float polishing with SiO_2 powder	0.1	43	1.87	2.6×10^{-5}
	0.7	280	1.69	1.1×10^{-3}
	1.9	446	1.66	2.8×10^{-3}
Ar ion beam etching	2.8	2110	1.70	6.1×10^{-2}
Electrolytic polishing	5.0	454	1.67	2.9×10^{-3}

$TIS = 1 - \exp[-(4\pi\delta/\lambda)^2]$; δ: rms roughness, λ: wavelength

Figure 1 shows the relationship between the absorptance and the methods of surface finishing. The surfaces of W and Mo obtained by float polishing have the lowest absorptances, 1.43% for W and 1.66% for Mo. Both lapped surfaces with SiC abrasives of 4000-grit size and lapped surfaces with 3 μm diamond powder have higher absorptances than finished surfaces by Ar ion beam etching in spite of smoother surfaces. This is because each surface has its own damaged layer and chemical composition. W has lower absorptance than Mo except for the surfaces finished by Ar ion beam etching.

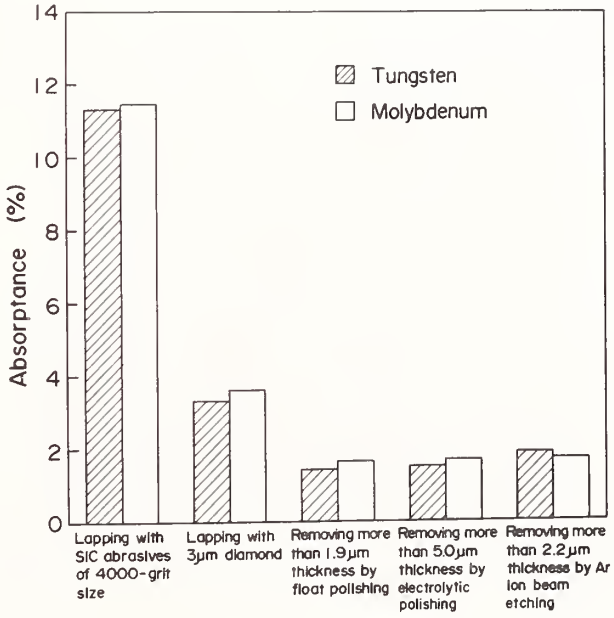

Figure 1. Relationship between the absorptance and the methods of surface finishing.

Figures 2 and 3 show the relationship between the absorptance and the amount of stock removal from the surface lapped with 3 μm diamond. In both cases of W and Mo, the absorptances decrease with increase of thicknesses removed by float polishing, and converge to the constant values, 1.43% for W and 1.66% for Mo. These constant values are identical with the absorptances of the surfaces finished enough by electrolytic polishing. On the contrary, the absorptance of the surface finished by Ar ion beam etching is about 0.4% higher than that constant value, especially in the case of W.

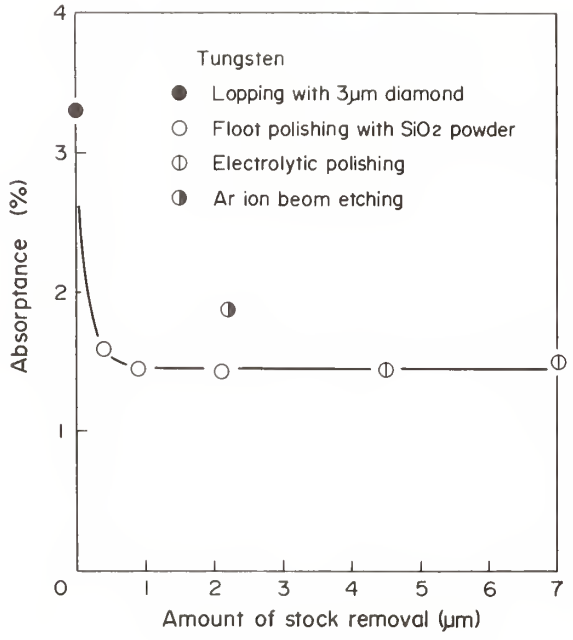

Figure 2. Relationship between the absorptance and the amount of stock removal from the surface lapped with 3 μm diamond on tungsten.

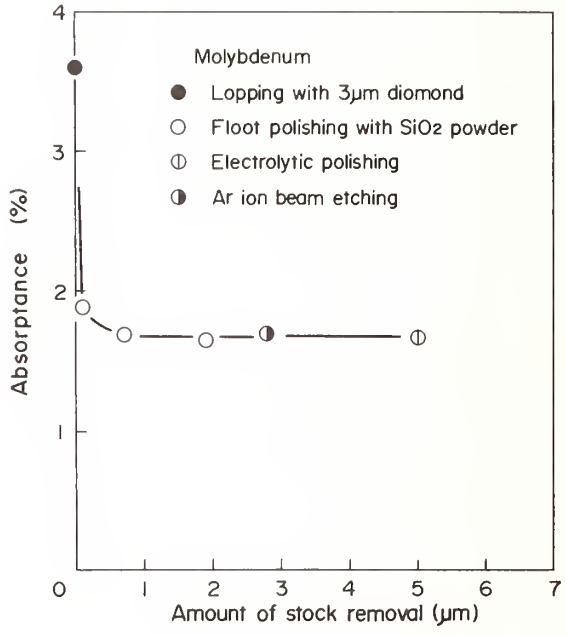

Figure 3. Relationship between the absorptance and the amount of stock removal from the surface lapped with 3 μm diamond on molybdenum.

3.2 Damaged layer

Figures 4 and 5 show the relationship between the half value width of diffraction line from (310) surface and the amount of stock removal from the surface lapped with 3 μm diamond. The half value widths decrease with the increase of the amounts of stock removal from the surfaces lapped with 3 μm diamond in both cases of W and Mo. These half value widths converge to the constant values of about 2 μm in the case of W and about 3 μm in the case of Mo. From these figures, it can be estimated that the damaged layers generated by lapping with 3 μm diamond are about 2 μm in the case of W and about 3 μm in the case of Mo, and none of the polishing methods shown in figures 4 and 5 generate damaged layers that can be evaluated by this analysis.

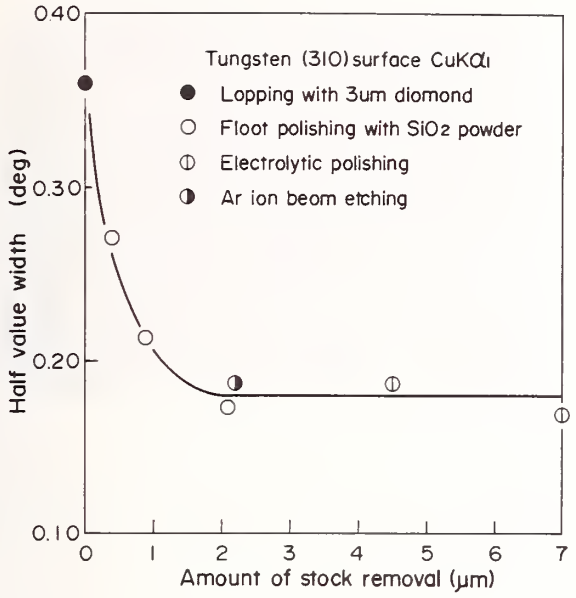

Figure 4. Relationship between the half value width of diffraction line from (310) surface and the amount of stock removal from the surface lapped with 3 μm diamond on tungsten.

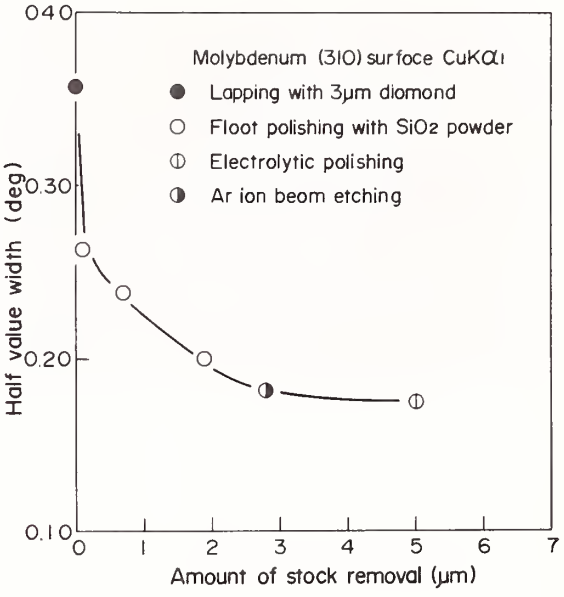

Figure 5. Relationship between the half value width of diffraction line from (310) surface and the amount of stock removal from the surface lapped with 3 μm diamond on molybdenum.

3.3 Chemical composition

Several samples shown in tables 1 and 2 were analyzed with EPMA and AES. The results are shown in table 3. From this table and reference figures listed in it, the following typical facts are clear.

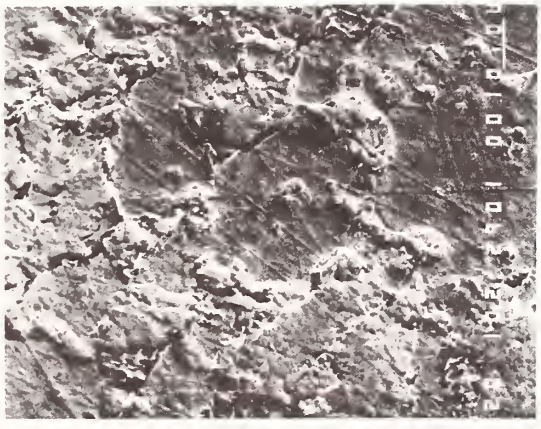

Figure 6. Scanning electron micrograph of the tungsten surface after removing 2.2 μm thickness from the lapped surface by Ar ion beam etching.

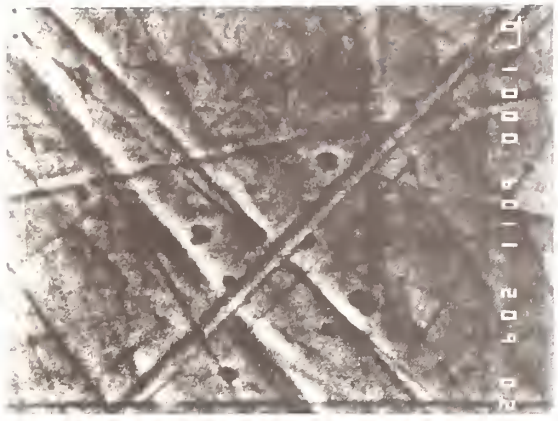

Figure 7. Scanning electron micrograph of the molybdenum surface lapped with 3 μm diamond.

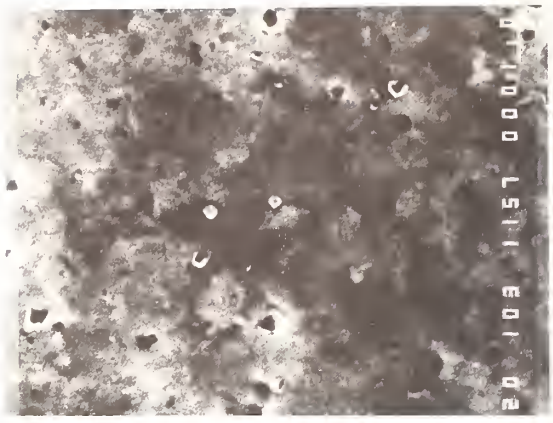

Figure 8. Scanning electron micrograph of the molybdenum surface after removing 0.1 μm thickness from the lapped surface by float polishing.

Table 3. Chemical composition analyzed with EPMA and AES.

		Electron probe microanalysis (EPMA)		Auger electron spectroscopy (AES)
		Result	Reference	Result
Tungsten (W)	Lapped surface with 3μm diamond	The amount of carbon detected at holes was two times larger than the bulk	——	————
	Surface after removing 0.4μm thickness by float polishing	Many holes of about 1μm in diam. were observed, but contaminations were not detected at the places	——	Contaminations were not detected
	Surface after removing 2.2μm thickness by Ar ion beam etching	Infinitesimal argon was detected.	Fig.6	————
Molybdenum (Mo)	Lapped surface with 3μm diamond	The amount of carbon detected at holes was ten times larger than the bulk.	Fig.7	————
	Surface after removing 0.1μm thickness by float polishing	Many holes smaller than 1μm in diam. were observed, and infinitesimal silicon was detected at the places.	Fig.8	Contaminations were not detected, but something was likely to exist.
	Surface after removing 0.7μm thickness by float polishing	Contaminations were not detected.	——	————
	Surface after removing 2.8μm thickness by Ar ion beam etching	Argon and carbon were detected.	——	————

1) In both cases of W and Mo, many holes of about 1 μm in diam. were observed on the surface lapped with 3 μm diamond and not a little carbon was detected at the places.
2) In the case of Mo, many holes smaller than 1 μm in diam. were observed on the surface after removing 0.1 μm thickness from the lapped surface by float polishing, and traces of silicon were detected at the places.
3) In both cases of W and Mo, traces of argon were detected at grain boundaries on the surface finished by Ar ion beam etching.

3.4 Reflectance

TIS shown in tables 1 and 2 is given by

$$TIS = 1-\exp[-(4\pi\delta/\lambda)^2]$$

where δ is the rms roughness and λ is the wavelength. In this experiment, the wavelength λ is 10.6 μm and δ is the experimental value. Specular reflectance should be regarded as an important factor for laser mirrors and corresponds to the value which is given by subtracting absorptance and TIS from one. Therefore, in order to raise the specular reflectance, it would be necessary to reduce not only the absorptance but also TIS.

Figures 9 and 10 show TIS and specular reflectances calculated in this way. From these figures and TIS shown in tables 1 and 2, in the case of W, it is found that TIS of the lapped surface with 3 μm diamond and that of the finished surfaces by float polishing are of the order of 10^{-5}, which accounts for only 0.001-0.006% of reflectance, while TIS of the finished surfaces by electrolytic polishing is of the order of 10^{-3}, which accounts for as much as 0.5-0.6% of reflectance and so cannot be ignored.

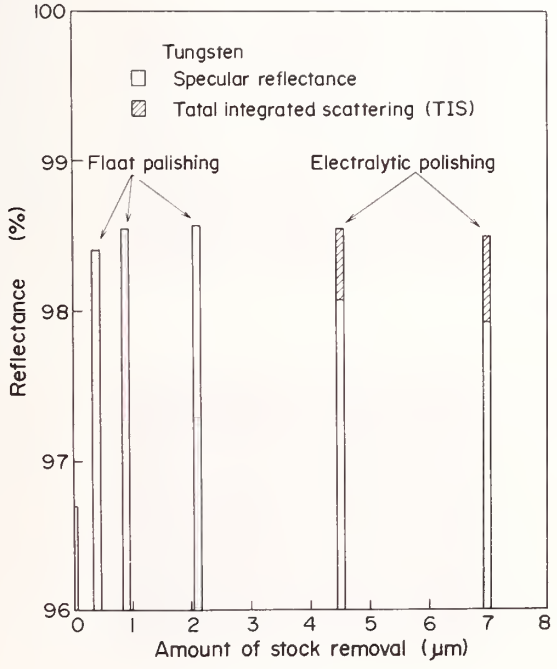

Figure 9. Relationship between the reflectance and the amount of stock removal from the surface lapped with 3 μm diamond on tungsten.

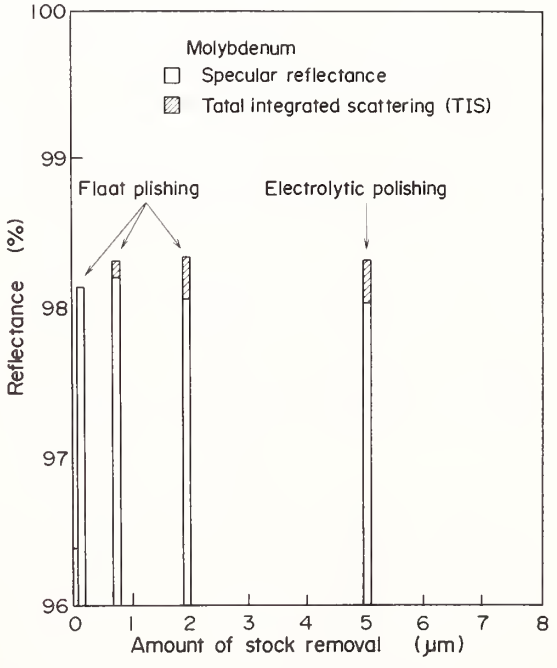

Figure 10. Relationship between the reflectance and the amount of stock removal from the surface lapped with 3 μm diamond on molybdenum.

Therefore, the finished surface by electrolytic polishing has large amounts of scattering because of its large surface roughness, so that it is not suitable for the laser mirrors. By contrast, the surface finished by float polishing has the best quality because of its small amounts of scattering and high specular reflectance. On the other hand, in the case of Mo, it is found that TIS of the lapped surface with 3 μm diamond and that of the surface after removing 0.1 μm thickness by float polishing are of the order of 10^{-5}, while TIS of the others is of the order of 10^{-3}. This is because steps at grain boundaries which appear on the polished surface due to anisotropy of stock removal rate based on crystallographic orientation are greater in the case of Mo than in the case of W. Therefore, it is an important key to determine the amount of stock removal, considering damaged layer, chemical composition and surface roughness (i.e. absorptance and TIS), especially in the case of Mo.

4. Mirrors made on an experimental basis

Mirrors of 75 mm in diam. x 10 mm thick were finished by float polishing considering experimental results mentioned above.

Figure 11 shows the polishing process of W and Mo. Figure 12 shows the appearance and the flatness of W and Mo mirrors finished by float polishing. The result shows that the peak-to-valley flatness is less than $\lambda/60$. Where λ is the wavelength of 10.6 μm. Figures 13 and 14 show Nomarski micrographs and surface profiles of W and Mo mirrors finished by float polishing. From these figures, the polished surface of the W mirror has very small surface roughness of 9.7 Å rms. On the other hand, the surface roughness of the Mo mirror is 29 Å rms larger than that of the W mirror, but is small enough for the mirrors used in the wavelength of 10.6 μm. The absorptances were measured with 500 W cw CO_2 laser and found to be at most 1.38% for W and 1.59% for Mo.

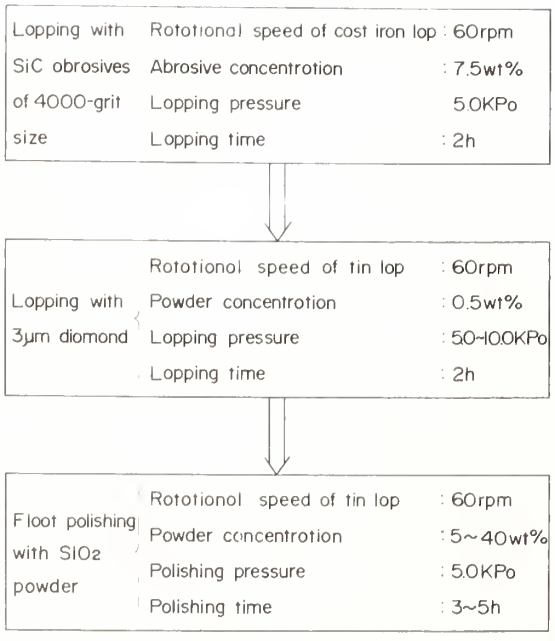

Figure 11. Polishing process of tungsten and molybdenum.

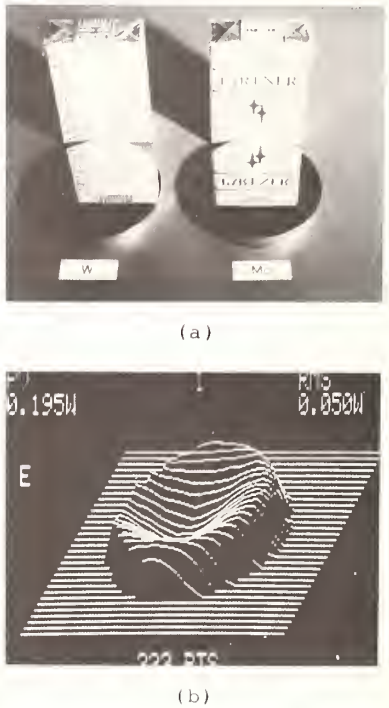

(a)

(b)

Figure 12. Appearance (a) and flatness (b) of tungsten and molybdenum mirrors finished by float polishing.

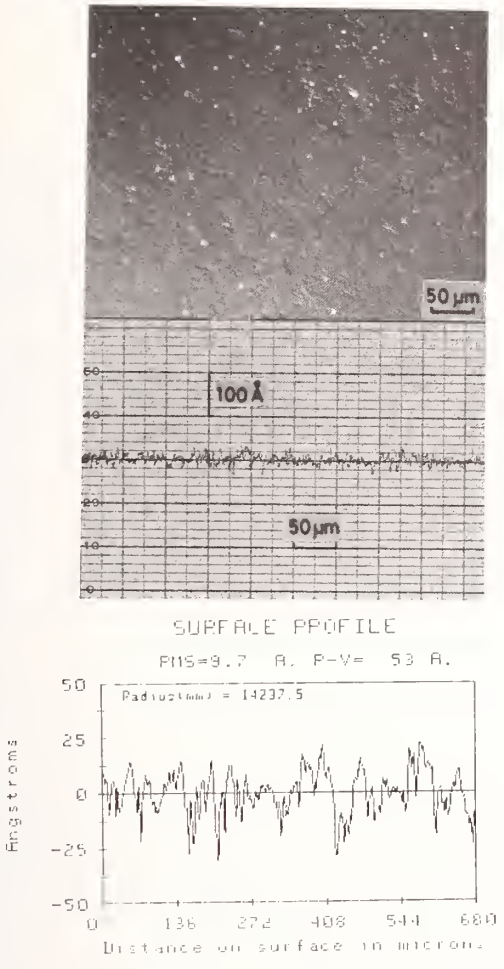

Figure 13. Nomarski micrograph and surface profiles of tungsten mirror finished by float polishing.

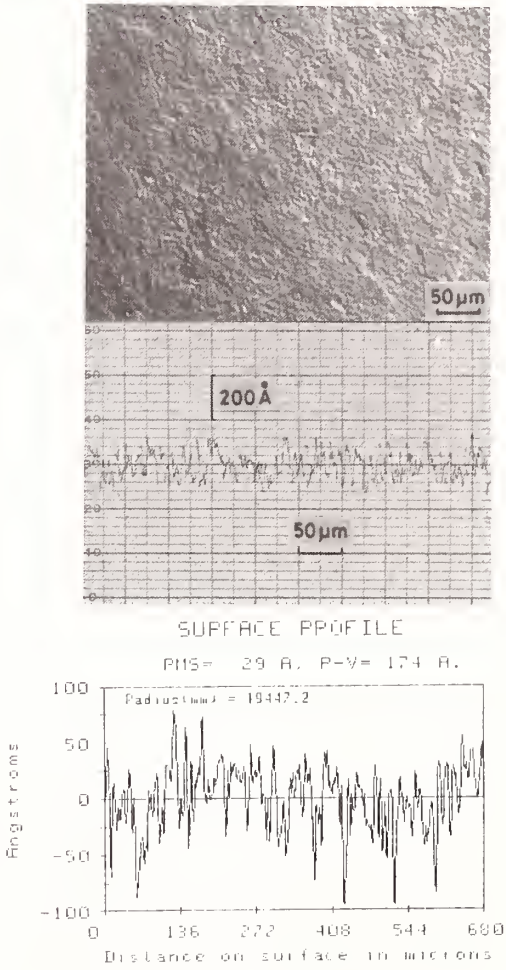

Figure 14. Nomarski micrograph and surface profiles of molybdenum mirror finished by float polishing.

5. Conclusions

W and Mo mirrors for CO_2 laser were polished by various methods, and were examined by profilometry, interferometry, calorimetric technique, EPMA, AES, and XD. The results obtained can be summarized as follows:

1) The surfaces lapped with 3 µm diamond powder have damaged layers of about 2 µm deep in the case of W and about 3 µm deep in the case of Mo. In either case, however, if about 1 µm thickness of the damaged layer is removed by float polishing from the lapped surface, the layer which increases absorptance at 10.6 µm wavelength will be almost removed.

2) In the case of W, it is found that the absorptance of the surface after removing 0.4 µm thickness from the lapped surface by float polishing is about 0.18% higher than the absorptance of the surface after removing more than 0.9 µm thickness, and this difference seems to be caused mainly by the damaged layer.

3) In the case of Mo, it is found that the absorptance of the surface after removing 0.1 μm thickness from the lapped surface by float polishing is about 0.18% higher than the absorptance of the surface after removing more than 0.7 μm thickness, and this difference seems to be caused not only by the damaged layer but also by contamination on the surface by SiO_2 powder.

4) Contamination by carbon was detected on the surface lapped with 3 μm diamond powder, and this may cause increase of the absorptance in company with the damaged layer.

5) The surface finished by Ar ion beam etching has scarcely any damaged layer, but Ar detected on the surface may cause increase of the absorptance, especially in the case of W, because the amount of Ar is greater than that on the Mo surface.

6) W and Mo of 75 mm in diam. can be finished by float polishing to the surface roughness of 9.7 Å rms and 29 Å rms and to the absorptances of 1.38% and 1.59%, respectively.

The authors would like to thank Prof. Y. Namba of Chubu University for encouraging this work and helpful advice.

6. References

[1] Y. Namba, Specular spectral reflectance of AISI 304 stainless steel at near-normal incidence, SPIE, 362, 93-103 (1983).
[2] Jean M. Bennett, Philip C. Archibald, John P. Rahn, and A. Klugman, Low-sctter molybdenum surfaces, Appl. Opt., 22, 24, 15 Dec. (1983).
[3] Jean M. Bennett, Joseph J. Saffer, Y. Shibano, and Y. Namba, Float polishing of optical materials, Appl. Opt., 26, 4, 15 Feb. (1987).
[4] A. Mitsuishi, Optical Absorption of High Power Infrared Laser Materials, The Review of Laser Engineering, 6, 1, 3-15 (1978).
[5] T. Miyata, T. Ono and T. Iwabuchi, Development of Optics for High-Power cw CO_2 Lasers, The Review of Laser Engineering, 13, 2, 129-147 (1985).

In response to a question of how the thickness removed was measured, the speaker replied that a mark was made on the surface. The ratio of length to depth was 30.5 to one, so that a depth of 0.1 μm could be measured.

- MANUSCRIPT NOT RECEIVED -

A NEW FORMING TECHNOLOGY USING LASER DAMAGE

Yoshiharu Namba
Chubu University
Kasugai, Aichi 487, Japan

- MANUSCRIPT NOT RECEIVED -

UV LIGHT CLEANING OF SILICA SURFACES FOR IMPROVED LASER DAMAGE OF AR COATINGS

K. Yoshida, H. Yoshida, Y. Kato and S. Nakai
Institute of Laser Engineering, Osaka University
Suita, Osaka 565, Japan

M. Ohtani
Physical & Chemical Technology Dept. 1
Canon Inc.
Ohta-ku, Tokyo 146, Japan

ABSTRACT

The glass substrates for the optical coatings have many contaminations on the surface which can not be removed by standard optical cleaning techniques. Especially, it is very difficult to remove the polishing compound which is buried into the silica substrates.

In this report, the improvement of laser damage threshold due to UV light cleaning is presented. The excimer laser, Xe flashlamps, and Xe arc-lamp have been used as UV light sources. The damage threshold of the AR coating on the silica surface which was cleaned with KrF laser light has increased by 50% at 355 nm.

Laser induced surface emission of neutral species and its relationship to optical surface damage processes*

Manuscript Received 3-17-88

L. L. Chase and L. K. Smith
Lawrence Livermore National Laboratory
P.O. Box 5508, L-490, Livermore, California 94550

Abstract

The laser-induced emission of neutral constituents and impurities from surfaces of several optical materials is shown to be correlated with optical surface damage thresholds. The characteristics of the emission can be utilized to investigate physical processes involved in the absorption of laser energy at the surface. Examples are given of neutral emission correlated with catastrophic surface heating, changes in surface stoichiometry, and thermally-induced cracking.

Key words: damage; mass spectroscopy; sodium fluoride, surface damage; surfaces; zinc sulfite

Introduction

Two fundamental problems involved in understanding and controlling optical surface damage involve identifying the initial mechanism for deposition of laser energy at the surface and the resulting physical processes that precipitate catastrophic failure. There are several possible interaction mechanisms that could account for the absorption of laser energy at the surface of a nominally transparent optical material. These are illustrated in Fig. 1, which shows the valence and conduction bands of a typical optical material. We shall be concerned here with optical damage to such a material caused by irradiation with laser light having a photon energy much less than the optical bandgap energy. Direct absorption of light by the intrinsic material can result only from multiphoton excitation across the bandgap or by multiphonon absorption. In the first case, electrons and holes are generated, and in the second case, heating of the material results directly from the excitation. Both of these direct excitation processes are very weak, and the energy density deposited in the near-surface region is certainly too low to cause direct thermal failure of the material. It is possible, however, that free carriers produced by the multiphoton process could nucleate an avalanche process. There are also extrinsic absorption processes that produce free carriers or direct heating near the surface of a "real" optical material. These are illustrated in Fig. 1 by the presence of surface states or defects that can supply "cheap" electrons or holes by direct absorption of the laser light, or by highly absorbing particles embedded in the surface region.

The problem of detecting these surface absorption processes is formidable because they may be very localized and cause unobservably small changes in the transmitted or reflected laser intensities and average surface temperatures. In the present work, we have investigated the possibility of observing the interaction of the laser with the surface by detecting neutral atoms or molecules emitted as a result of the laser excitation. It is also possible, and much easier, to detect ions and electrons. In general, however, it is found that, at least for ion beam or electron beam excitation of surfaces, the primary emitted species are neutrals.[1] In previous work on ZnS, we also found this to be the case for laser excitation at 1.06 μm.[2]

There are several characteristics of the emitted neutrals that could, in principle, provide evidence regarding the nature of the interaction of the laser beam with the surface:

(1) Emission yields as a function of laser fluence, photon energy and surface preparation can help to identify the type of optical absorption process.
(2) The identity and relative abundance of the emitted species can be used to infer the physical process causing surface ablation, and to search for changes in surface composition caused by the laser excitation.
(3) The time dependence of the neutral emission following initiation or termination of laser excitation can be significant for a variety of reasons. Temperatures of the emitted particles can be obtained from time-of-flight data, if there is not too large a time delay between laser excitation and emission. On the other hand, a measurable time delay may help to identify the ablation process.
(4) The spatial dependence of the emission can be used to locate regions susceptible to ablation and optical damage.

*Work performed under the auspices of the Division of Materials Sciences of the Office of Basic Energy Sciences, U.S. Department of Energy by Lawrence Livermore National Laboratory under Contract No. W-7405-ENG-48.

If neutral emission is to be a very useful method for surface damage research, it must be established that it is caused by the same interaction of the laser with the surface that precipitates the observable damage event. In addition the emission must be detectable at fluence levels considerably below the threshold for significant optical damage so that it probes the initial interaction of the laser beam with the surface, rather than a catastrophic breakdown of the surface, which will always result in copious neutral, ion and electron emission. To the best of our knowledge, only one previous investigation of neutral or ion emission was successful in establishing these properties. This is the work of Schmid, et.al., who observed multiphoton-induced emission of halogen atoms from alkali-halides using ruby laser excitation.[3] It is the aim of the present work to explore the possibility of utilizing neutral emission as a probe of optical surface damage processes in various types of optical materials. We have therefore selected for study a set of representative types of optical materials. These include fused silica, and single crystals of ZnS, NaF, Al_2O_3, and BaF_2.

Experimental procedure

The experiments are carried out in two UHV systems with base pressures of 5×10^{-10} and 2×10^{-9} torr, respectively. At these pressures, the adsorbed impurities accumulate at a rate very much less than a monolayer between laser shots. The samples were optically polished, cleaned with ethanol, and blown free from dust and other particles just before insertion in the vacuum system. Prior to laser excitation, a heater on the sample holder was used to desorb contaminants from the surfaces at temperatures up to 500C in UHV. The experiments on fused silica were done in the vacuum system with lower ambient pressure using a variable-pulsewidth (1 - 10 ns) Nd:glass laser at a wavelength of 1.05 μm and a beam diameter of 1 mm. A vidicon and calorimeter system provided accurate fluence measurements. For the other materials, the smaller vacuum system with higher base pressure was used, and a Q-switched YAG:Nd laser, providing pulses of 5-8 ns duration at the fundamental and first three harmonics (1.06 μm, 0.532 μm, 0.355 μm, and 0.266 μm), was used for excitation with beam diameters of about 500 μm. Fluence estimates with this second laser system were made by measuring the beam diameter with a travelling knife-edge, and a calorimeter measured the total pulse energy. Optical damage was identified visually by increased scattering of a probe laser beam. The optical damage thresholds quoted in this work are therefore to be regarded as estimates of relative thresholds for the various samples and laser wavelengths.

A quadrupole mass spectrometer (QMS) was mounted in the line-of-sight to the sample at a distance of 11.3 cm to detect the emitted neutrals. The response time of the detection system was limited to about 10 μs because of the transit-time dispersion in the quadrupole system. Pulse counting and digital storage were used to record the signals from the microchannel plate detector. Data were obtained with increasing fluence on each new spot on the sample, starting from about an order of magnitude below the observed damage threshold. At most, about ten to twenty shots were taken at each spot on the surface before damage occurred or the spot was abandoned.

The time-of-flight from the sample to the ionizer on the QMS is inversely proportional to the particle velocity. For a Maxwellian distribution of particle velocities characterized by a temperature T, the detected signal will have the time-dependence

$$S = K\, t^{-4} \exp[-(t_0/t)^2] \qquad (1)$$

where $t_0 = (M/2kT)^{1/2}d$, M is the particle mass, d is the sample-detector distance, and K is a normalizing constant. This distribution has a maximum at a time delay $t_p = t_0/\sqrt{2} = d(M/4kT)^{1/2}$ This relationship is plotted in Fig. 2 for various masses of interest for the samples studied in this work. We see that for temperatures up to a few thousand K, the time delay provides a sensitive measure of the effective temperature of the particles, particularly for those of large mass. Of course, Eq. 1 is valid only if the emission occurs within a time interval smaller than t_p after the laser pulse.

Experimental Results

Synopsis

A summary of the samples studied, laser wavelengths, and general characteristics of the observed emission is given in Table 1. Al_2O_3 is the only material for which unambiguous evidence of emission of surface constituents below the optical damage threshold could not be obtained. In all cases, of course, desorption of surface contaminants was found, usually at a very low level, after thermal cleaning of the surface. For fused silica, ZnS and NaF, one or more Maxwellian-shaped components were dominant at low fluences. At higher fluences, we also

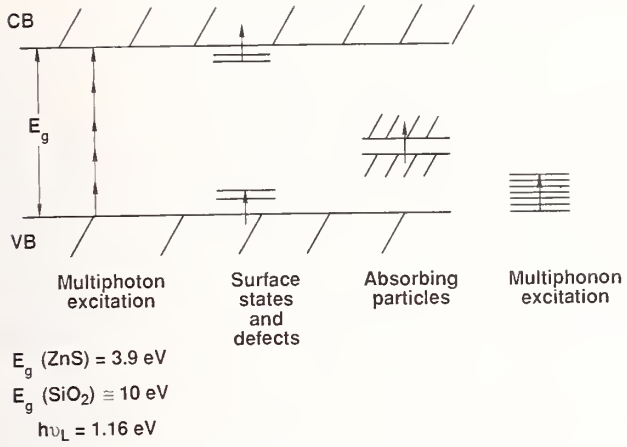

Fig. 1. Possible mechanisms for absorption of light on the surface of a nominally transparent medium.

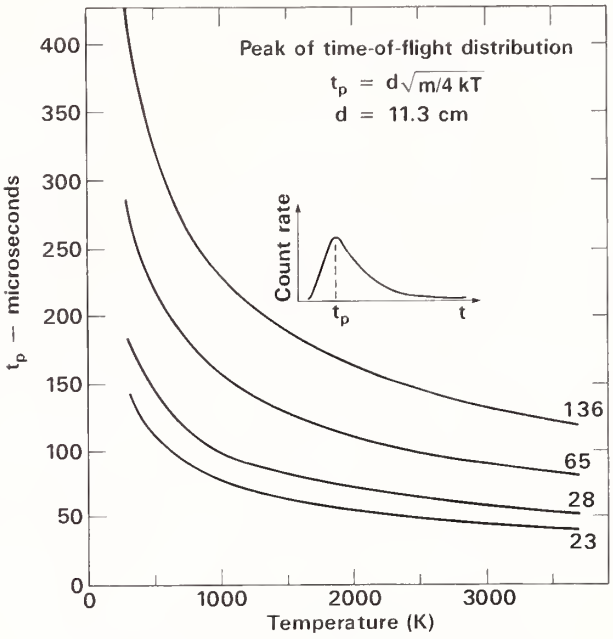

Fig. 2. Relationship between the time delay of the peak of the time-of-flight distribution and the particle temperature. A Maxwellian distribution of particle velocities is assumed. Numbers at the right of each curve are masses, in atomic units.

Table 1. Summary of optical materials and neutral emission characteristics

Sample	Wavelengths	Emitted Species	Characteristics
Fused silica	1064 nm	Si, SiO, O, O_2, OH	Maxwellian, HE neutrals
ZnS crystal	1064, 532 355, 266	Zn, S, S_2	Complex HE neutrals
NaF crystal	1064, 532 355, 266	Na, F	Maxwellian, cleaving, cracking, HE neutrals
Al_2O_3 crystal	1064, 532 355, 266	No predamage emission observed	
BaF_2 crystal	1064, 532 355, 266	Ba, F	HE neutrals only

observed emission of high-energy (HE) neutrals from these materials, as well as BaF_2. The results obtained for BaF_2 are interesting, because of the contrast with the work of Matthias, et. al., who observed copious emission of fluorine neutrals and Ba^+ ions from vacuum-cleaved surfaces of BaF_2 excited by a dye laser.[4,5,6] By contrast, we have investigated emission from polished and air-cleaved surfaces, from which these laser-induced emission components are completely absent, despite the fact that one of our wavelengths, 0.532 μm, is close to one of the resonant peaks for the desorption identified by Matthias, et. al.[5] Presumably, the

surface states that are active on the vacuum-cleaved surface are neutralized by exposure to air and polishing procedures. This demonstrates the sensitivity of the laser-induced emission to surface conditions. The remainder of this discussion will be focused on fused silica, ZnS and NaF, since the most significant results have been obtained for those materials.

Fused silica

Figure 3 shows a set of oscilloscope photographs giving the time-of-flight (TOF) characteristics of the emission of Si and SiO from four different spots on fused silica following 1 ns laser pulses at 1.05 μm. (It is worth mentioning that common surface contaminants, CO, N_2, and CO_2 have the same masses as Si and SiO. By introducing these gases into the chamber, we were able to do control experiments which verified that they were not responsible for the observed emission.) Occasionally, two distinct Maxwellian components were found in a single shot for fused silica; these presumably result from emission from different regions in the laser spot. At fluences near the damage threshold the number of high energy particles (i.e., at small time delays) increases, and a "spike" develops near zero time delay. By comparing data taken with the QMS ionizer on and off, we found that this spike consisted mostly of neutrals, although a fraction are ions. These high energy (HE) neutrals are a common feature of several of the materials studied at fluences close to the threshold for observable damage. In the trace on the lower right of Fig. 3 the damage threshold has been exceeded, and copious emission of energetic ions and neutrals is observed. The damage morphology produced in such events consists of a number of small craters, typical of nanosecond-pulse damage on fused silica.

Two examples of fits to time-of-flight profiles of SiO with assumed Maxwellian velocity distributions are shown in Fig. 4 for different fluences and sample temperatures. There is no reason why a single effective particle temperature should characterize emission from a $1mm^2$ region. Nevertheless, the fits to a single Maxwellian are quite reasonable. The most interesting aspect of these results is the low effective temperatures, in some cases well below the temperature at which the surfaces were cleaned prior to laser excitation. This shows that the emission process does not result primarily from heating of the surface by the laser beam. This common feature of the emission from several of the materials will be discussed later.

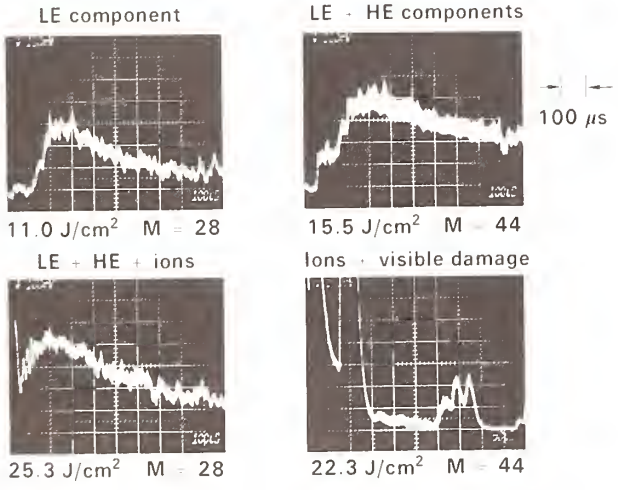

Fig. 3. Some typical TOF distributions for Si and SiO emitted from a fused silica surface following excitation with a 1.05 μm, 1 ns laser pulse. LE and HE refer to the Maxwellian ("low energy") and "high energy" components, respectively.

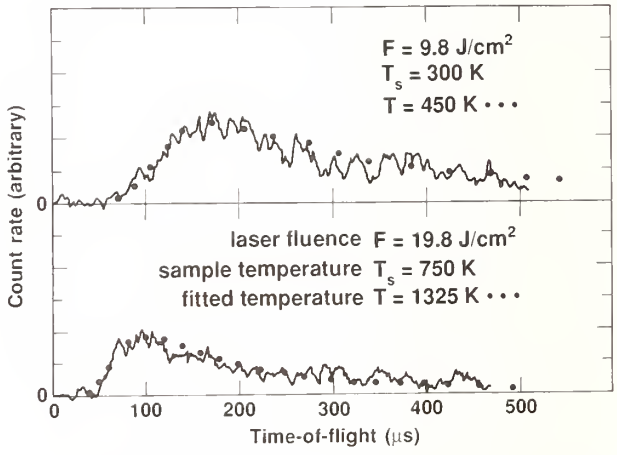

Fig. 4. TOF distributions for SiO emitted from fused silica following a one ns laser pulse at 1.05 μm. The dotted curves are fits to Eq. 1.

Zinc sulphide

ZnS was selected for these studies because it is an example of a wide-bandgap semiconductor, which is used as a material for optical coating, but also because it has a small enough optical bandgap, E_g = 3.9 eV, that measurements can be made with photon energies both above and below E_g using Nd:YAG laser wavelengths up to the fourth harmonic. In addition, we previously investigated ion and electron emission from ZnS and conjectured that the primary emission

component must be neutrals;[2] the present work confirms that hypothesis. TOF data for the emission of Zn from a ZnS single crystal is shown in Fig. 5 for excitation with an 8 ns pulse at 1.064 μm. Near the threshold for observation of neutral Zn emission, about 4 J/cm^2, a gradual onset of the signal suggests that the emission occurs for a time interval of several hundred microseconds, and then the signal decreases due to pumping and adsorption on the chamber walls. At fluences above about 8 J/cm^2, however, a peak develops at a time delay of about 250 μs, which we attribute to promptly emitted Zn particles with a kinetic temperature < 1000K. This behavior is also observed for the emission of S and S_2 and shows that very little surface heating is required in order for the emission to occur. As the damage threshold is approached, however, this peak shifts very rapidly to shorter time delays, indicating characteristic temperatures of several thousand Kelvin. Simultaneously, a spike, due to HE neutrals, appears. Even after the laser shots in the two upper traces in Fig. 5, no visible evidence of optical damage could be detected, although the apparent particle temperature of ~ 10^4K suggests that either the sample surface or the emitted gas of Zn atoms is hot enough to cause local surface modification. This spot on the sample did, in fact, damage catastrophically on the next shot at 11 J/cm^2.

Similar data has been obtained at 532 nm, 355 nm, and 266 nm. As the wavelength decreases, the general characteristics of the TOF distributions are unchanged, which suggests that the same processes are involved in the emission at all four laser wavelengths. On the other hand, the threshold fluences at which emission is observed, and at which optical damage occurs, gradually decrease. We have compared the thresholds for observable neutral Zn emission with the observed optical damage thresholds obtained by taking shots at successively higher fluences on a single site until optical damage occurred. This comparison is shown in Fig. 6, in which the two thresholds for each wavelength are plotted on separate axes. This figure shows that there is a rough correlation between these two thresholds for wavelengths that span the region of optical transparency of ZnS. At 266 nm, however, the emission threshold is very low, below 10 mJ/cm^2, while there is still a measurable optical damage threshold of about 0.5 J/cm^2.

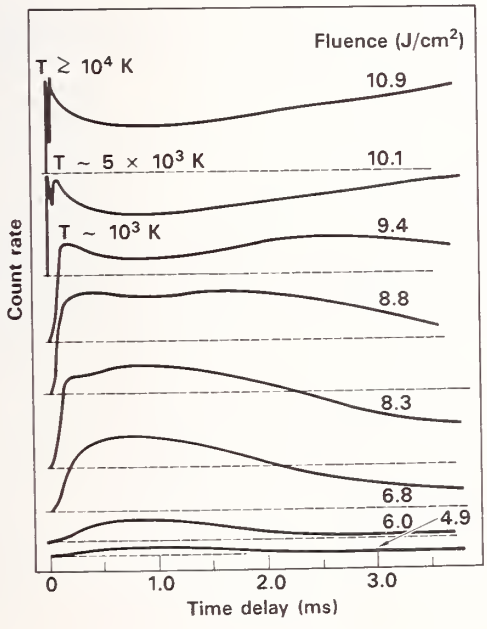

Fig. 5 TOF data for Zn emission from ZnS following a series of 1.06 μm, 8 ns long laser pulses with the indicated fluences. Labelled temperatures are estimates based on the time delay t_d of the peak of the "Maxwellian" emission component. The sharp spike near zero time delay in the two upper curves is the HE neutral emission.

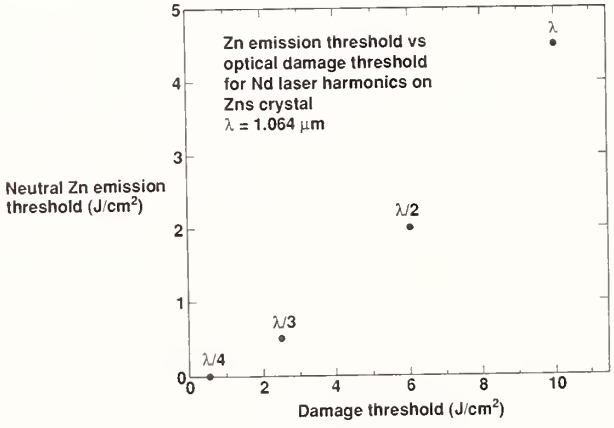

Fig. 6 The threshold for observable neutral Zn emission from ZnS plotted against the optical damage threshold for the four Nd:YAG laser wavelengths.

A potentially important characteristic of the neutral emission is its effects on the surface composition. In Fig. 7a, the signals recorded on successive shots at 266nm with the mass spectrometer set to masses of 68 (Zn), 64 (Zn + S_2), and 32 (S) are compared. The presence of a prompt TOF peak in the mass 64 and 32 data, and the absence of such a feature in the m = 68 trace, suggest that the Zn emission is time-delayed after the laser pulse, but the sulfur emission is not. At fluences close to the damage threshold a prompt TOF peak appears even on the Zn emission signal, as shown in Fig. 7b, although the apparent temperature indicated by the time delay of this peak is lower than the temperature obtained from the corresponding peaks in the S or S_2 data. This suggests that during, and possibly after, a laser pulse the surface composition can be altered by the laser ablation. A possibly related effect is shown in Fig. 8, which shows that the emission observed on consecutive shots on the same site decreases ("bleaches") by an amount that varies with the fluence. As the fluence approaches the damage threshold the bleaching is greatly reduced, if not eliminated. We also observed this bleaching behavior for fused silica and, to a lesser extent, for NaF.

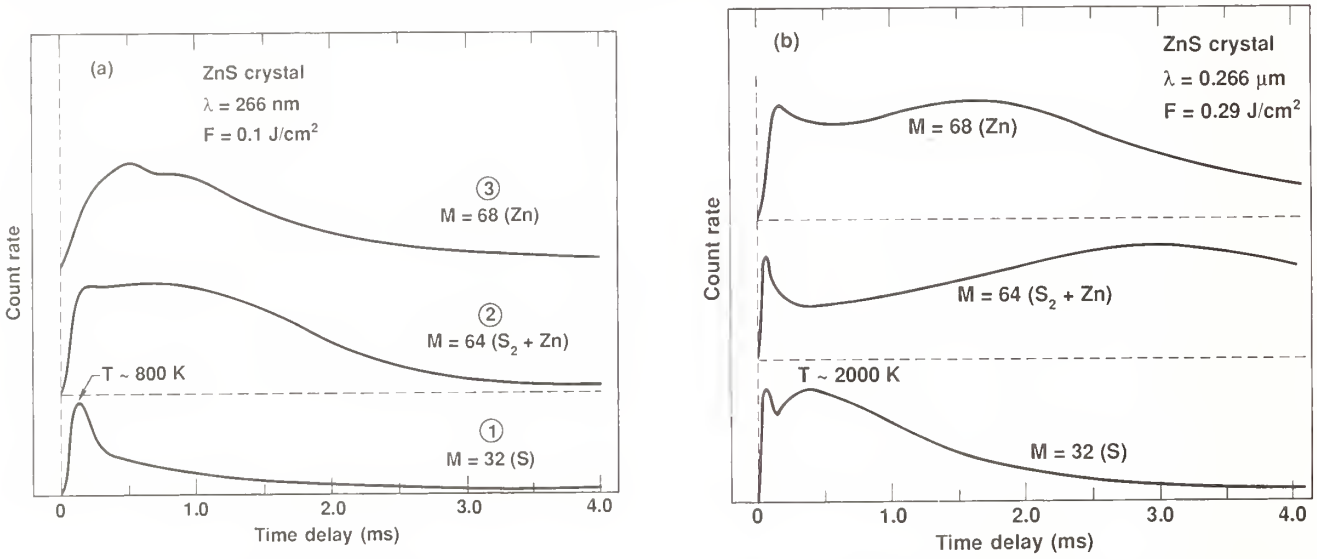

Fig. 7 TOF data for emission of Zn, S, and S_2 from ZnS following laser excitation at 266 nm. Fluences are (a) 0.1 J/cm^2 and (b) 0.29 J/cm^2.

Arlinghaus, et. al.,[7] have investigated the laser-induced emission of Zn from ZnS using laser fluorescence detection. In that experiment, which is performed with a repetitively-pulsed excimer laser at a wavelength of 308 nm, the apparent surface temperatures at the lowest fluences are over 2000K, much higher than those observed near threshold in the present work, and there is no evidence of delayed Zn emission. At this time it is not clear why the laser fluorescence and mass spectrometer measurements differ in those two respects. The major difference between the two measurements is the total number of laser pulses involved in making the measurements. It is likely, however, that, if the ablation causes a change in surface composition, this process reaches a steady state in the repetitively-pulsed experiment, whereas it may not in the measurements with the mass spectrometric detection, where not more than ten to fifteen pulses are used on a single spot. This difference can be resolved with the mass spectrometer experiments by studying a surface area that has undergone many shots.

Sodium fluoride

The experiments were done on single crystals of NaF that were cleaved and subsequently polished. The neutral emission characteristics were similar at all four Nd laser wavelengths, except for a gradual decrease in the threshold fluence with decreasing wavelength, which was similar to the behavior observed for ZnS. The same two characteristic features found for fused silica and ZnS were also present in NaF. Figure 9 shows a TOF distribution of the neutral Na emission following a 266 nm pulse at a fluence of 3.8 J/cm^2, about one-half the observed optical damage threshold. An approximately Maxwellian distribution with a maximum at t_p = 200 μs is indicative of a particle temperature of about 300K, very close to the sample temperature. This cold emission is accompanied by a feature at a very short time delay, which was recorded on the same shot by a second transient recorder with a time resolution of 10 μs. This peak is shown in the inset of Fig. 9, from which the transit time (9.6 μs) in the mass spectometer has been subtracted. This feature was not present when the mass spectrometer was set to transmit other masses, and it was absent or greatly reduced when the ionizer filament was turned off, so

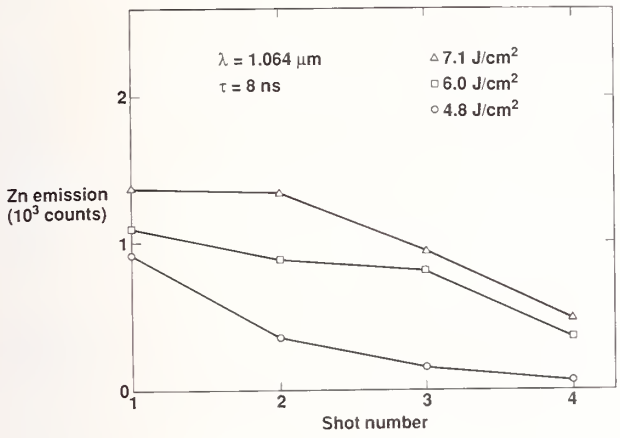

Fig. 8 Total yield of Zn emission for successive laser excitation pulses at 1.064 μm and at three laser fluences.

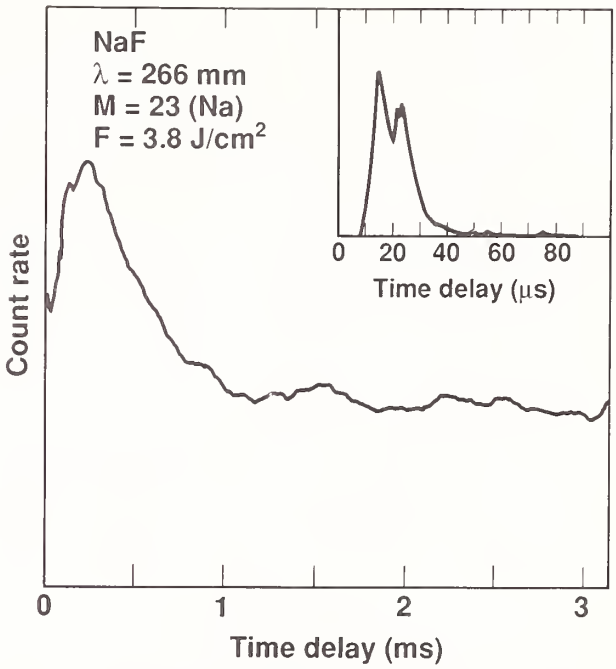

Fig. 9 Time dependence of Na emission from NaF following excitation at 266 nm at a fluence of 3.8 J/cm^2. Inset is the initial 100 μs portion of the data.

it is not caused by scattered or emitted light, and there are very few emitted ions. The very short time delay of this pulse is indicative of very high energies, on the order of 10 - 100 eV. The TOF data shown in Fig. 10 suggests a likely explanation for the emission of the HE neutrals. The lower trace was taken at a laser fluence just below the optical damage threshold at the wavelength of 266 nm. The Maxwellian emission and the HE emission at small time delays were both observed on this shot. The upper trace was the next shot, at a slightly higher fluence, on the same spot. The surface was optically damaged, and a large emission of Na was observed at small time delays. In addition, there is a series of aperiodic spikes that persist for at least tens of milliseconds after the laser pulse. These spikes are often followed by Maxwellian-like tails. In the damaged region, many large and small cleavage cracks were observed after this shot. The similarity of these sharp spikes to the HE neutral components observed immediately after the laser pulse at lower fluences shows that microscopic cleaving of the surface is a very likely origin for the HE neutrals.

Since the neutral emission from NaF had only a slight tendency to bleach on consecutive shots, it is meaningful to examine the dependence of the emission yield on the laser fluence for consecutive shots on the same spot. (Ideally, it would be preferable to move to a different spot for each shot, but the total useable surface area of the samples was not adequate for this.) The yield of Na as a function of fluence for excitation at 266 nm is shown in Fig. 11. Emission starts fairly abruptly at a threshold of 1.5 - 2.0 J/cm^2 and rises nearly linearly up to the damage threshold at 7.5 J/cm^2. This behavior is qualitatively similar to that observed for fused silica and ZnS, although the bleaching effect was too pronounced for those materials to give a meaningful plot of yield versus fluence.

Discussion

A central question regarding the observed neutral emission is that of its relationship to optical damage mechanisms. Strictly speaking, any emission of surface constituents is optical damage. If, however, the emission involves desorption of atoms more or less uniformly distributed over the surface, it is not necessarily related to the type of damage that impairs the optical quality of the surface. The ubiquitous correlation observed between the threshold for observable neutral emission and the threshold for observable optical damage is the strongest evidence that these two phenomena are related. For all of the materials studied, with the exception of Al_2O_3, the emission threshold fluence is about 10 - 40 percent of the optical damage threshold for all laser wavelengths at which the materials are transparent and for the two pulse widths (1 ns and 10 ns) used with fused silica. In fused silica and ZnS the rapid

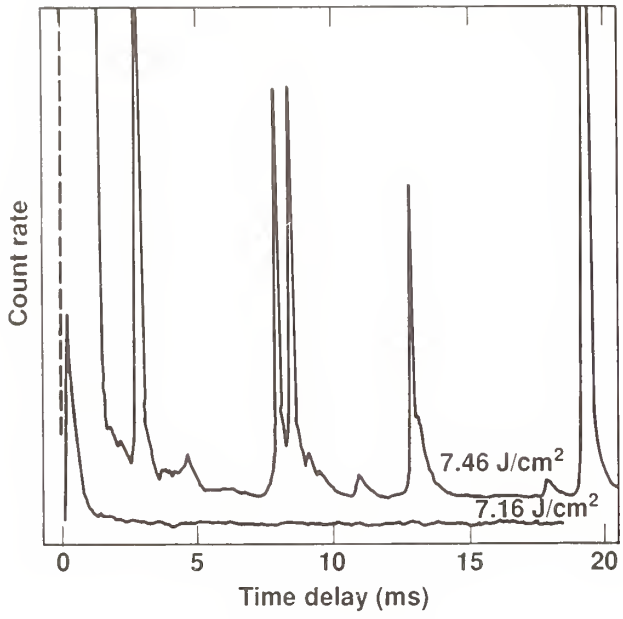

Fig. 10 Time dependence of the emission of Na from NaF after two laser shots. On the second of the two shots, at 7.46 J/cm^2, the sample damaged catastrophically.

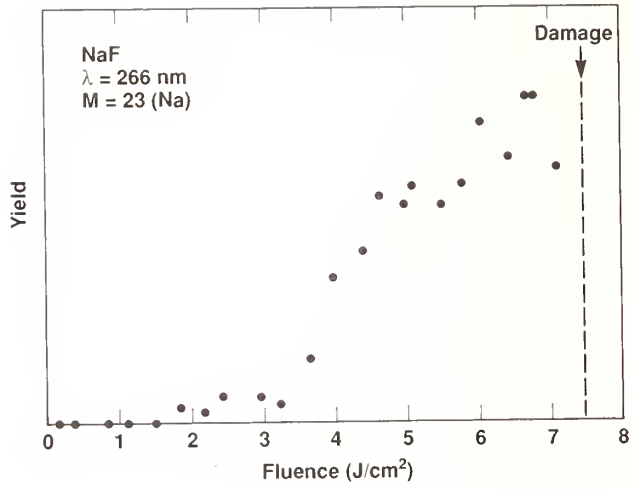

Fig. 11 Yield of laser-induced emission of Na from NaF as a function of fluence with excitation at 266 nm for successive shots of increasing fluence on a single spot.

increase in the effective particle temperature, to values typical of an optical breakdown plasma just below the optical damage threshold, also suggests a connection with damage events. In NaF and BaF_2 neutral emission has always been observed to include the HE neutrals that are most likely the result of cracking or cleaving, which means that some degree of damage occurs on each laser shot. We conclude from these observations that the neutral emission results from the same interaction of the laser with the surface that precipitates optical damage.

Although these investigations are still far from complete because of the small number of materials studied and the lack of information concerning the effects of surface treatment and other variables, it is possible to draw some conclusions regarding the cause of the emission. Consider first the multiphoton interband excitation mechanism in Fig. 1. The dependence of the Zn emission threshold on laser wavelength in Fig. 6 is far too slow to be consistent with multiphoton absorption, since the absorption at 1.06 μm would correspond to a five-photon process, and at 0.355 μm to a two-photon process. At the peak intensities (~ 10^8 W/cm^2) involved in these experiments, these multiphoton transition rates would differ by many orders of magnitude.[8] Data similar to that in Fig. 6 is obtained for NaF, BaF_2, and fused silica.

Desorption caused by thermal excitation (evaporation or sublimation) is also an unlikely cause of the neutral emission. The most straightforward argument in support of this conclusion is that the characteristic temperatures of the Maxwellian emission components of fused silica, ZnS, and NaF are in the range 300K to 800K at the lowest fluences for which they are detectable. Not only are these temperatures far below the melting (or sublimation, for ZnS) temperatures, but they are comparable with the temperatures at which the surfaces are cleaned, and no emission is observed during the cleaning. It is conceivable, however, that the time-of-flight distributions are not an accurate measure of surface temperature. The experiments on ZnS at the fourth harmonic provide some additional evidence that the surface temperature rise is very small. The absorption coefficient of ZnS at 266 nm is known, as are its relevant thermal properties. We have modelled the temperature rise of ZnS due to illumination at 266nm by using the solutions of the thermal diffusion equations including the presence of bulk heating by the laser.[9] We conclude that, at the threshold fluence (10 mJ/cm^2) for observation of Zn neutrals, the temperature rise at the surface is at most 50K, assuming that all of the energy absorbed from the laser is converted immediately into heat. Since the carrier lifetime in ZnS is on the order of a millisecond, it is possible that only the photon energy in excess of the bandgap energy is effective in heating the surface during the duration of the laser pulse, so the temperature rise may be as small as 20K.

It has been suggested that microscopic cleaving or cracking can result from rather small increases in surface temperature because of the large surface stresses accompanying differential thermal expansion.[10] This is a likely cause of the high energy neutrals observed just below the damage threshold in most of the materials that we studied. Indeed, copious charged and neutral emission ("fractoemission"), as well as visible discharge, has been observed to accompany the fracture of numerous materials.[11] Although no measurements of their energy distributions have been reported, the very rapid spikes in Fig. 9, which undoubtedly result from cleavage of the NaF sample, are evidence of very high velocities, since most of the neutrals reach the detector in a time interval much shorter than the width of the Maxwellian component in the lower trace. Presumably, this emission can also result from the growth of existing cracks near the surface. In addition to the direct damage caused by the crack initiation and propagation, the high gas densities and ionization levels produced by this localized phenomenon can also precipitate local optical breakdown, which could grow catastrophically due to surface bombardment.

The Maxwellian-like emission from fused silica and ZnS is clearly observed even without the HE neutrals at low fluences, so it cannot be attributed to any mechanism of thermal origin, including cracking. It is most likely that this emission results from electronic excitation of defects or surface states. The carriers released by this process can cause bond breaking, followed by desorption of atoms. There is a large body of literature documenting this type of desorption, from semiconductors and insulators, resulting from ion and electron bombardment, and from excitation by photons at frequencies above the optical bandgap.[12] It is not unreasonable to presume that if there is a distribution of defect levels within the bandgap of materials like fused silica, ZnS and NaF, the carriers released from these defects by excitation at photon energies below the bandgap will also cause desorption, although the yield will be much lower. The wavelength dependence of the threshold fluence for observable emission, exemplified by the ZnS data in Fig. 6, is consistent with this assumption. The F-center, which is a singly-charged sulfur vacancy, is an example of a defect in ZnS that absorbs throughout the visible, and photoconductivity measurements show that free carriers are produced by this absorption.[13] Recent measurements of laser-induced Ba ion emission from vacuum-cleaved BaF_2 show sharp resonances arising from surface states,[4,5,6] so such levels deep in the bandgap exist for ionic materials as well.

Despite its rather innocuous appearance, the electronic desorption discussed in the preceding paragraph may play a central role in optical damage. For example, the energy transferred to the surface, either by the primary excitation process or by subsequent excitation of the free carriers released by the absorption, is a possible source of the heating that can cause cracking or cleaving, thus releasing many HE neutrals and ions. The carriers might also precipitate avalanche ionization. These consequences will be most likely if the absorbing defects are clustered in small regions, perhaps in the vicinity of cracks, grain boundaries, dislocations or foreign particles. If the emission alters the composition of the surface, a catastrophic, positive feedback into the density of absorbing defects could result. For this reason the possibility of delayed or unequal emission of Zn or S from ZnS is very significant. This could produce S vacancies, and possibly F-centers, at the surface. Obviously, this surface ablation could also reduce the damage threshold for multiple-pulse excitation. Laser annealing studies on GaAs show that the emission yield of As becomes larger than that of Ga as the surface temperature increases,[14] so surface composition changes due to laser ablation may be a common phenomenon.

Conclusions

Laser-induced neutral emission appears to be a common precursor to observable optical surface damage. Not only is it a signature of the interaction of the light with the surface, but it may be a cause of optical damage. In order to further evaluate its significance, it is important to investigate the spatial dependence of the emission and obtain quantitative information on the relative yields of various surface constituents. The wavelength dependence of the emission yield is also an important piece of evidence to use in identifying the absorbing centers.

References

1. D. Menzel, "Electronically Stimulated Desorption", Appl. Phys. A38, 191 (1985); also see references therein.

2. W. J. Siekhaus, L. L. Chase and D. Milam, "Temporal Distribution of Electron and Ion Emission Caused by Laser Excitation of Optical Surfaces in Ultra-high Vacuum", Proceedings of the 1985 Symposium on Materials for High-power Lasers, to be published as a National Bureau of Standards Special Publication.

3. Ansgar Schmid, Peter Braunlich and Pieter Rol, "Multiphoton-induced Directional Emission of Halogen Atoms from Alkali Halides", Phys. Rev. Lett. 35, 1382 (1975).
4. J. Reif, H. Fallgren, W. E. Cooke, and E. Matthias, "Wavelength Dependence of Laser-Induced Sputtering from the (111) Surface of BaF_2", Appl. Phys. Lett. 49, 770 (1986).
5. J. Reif, H. B. Nielsen, O. Semmler, and E. Matthias, "Multiphoton Processes at the (111) Surface of BaF_2 Crystals", Physica Scripta 35, 532 (1987).
6. E. Matthias, J. Reif, H. B. Nielsen, E. Westin and A. Rosen, "Multiphoton-induced Desorption From BaF_2", these conference proceedings.
7. A. Arlinghaus, W. F. Calaway, C. E. Young, M. J. Pellin, D. M. Gruen and L. L. Chase, "Laser Fluorescence Spectroscopy of Zinc Neutrals Originating from Laser Irradiated and Ion-Bombarded Zinc Sulfide and Zinc Surfaces", in these proceedings.
8. Vaidya Nathan, A. H. Guenther and S. S. Mitra, "Review of Multiphoton Absorption In Crystalline Solids", J. Opt. Soc. Am. B2, 294 (1985).
9. J. H. Bechtel, "Heating of Solid Targets With Laser Pulses", J. Appl. Phys. 46, 1585 (1975).
10. V. P. Krutyakova and V. N. Smirnov, "Electron Emission from Alkali Halide Crystals Irradiated by a Pulsed CO_2 Laser", Sov. Phys. Tech. Phys. 24, 1085 (1979).
11. See, for example, J. T. Dickinson, L. C. Jensen and M. R. McKay, "Neutral Molecule Emission from Fracture of Crystalline MgO", J. Vac. Sci. Technol. A5, 1162 (1987), and references cited therein.
12. For a recent review, see Noriaki Itoh, "Laser Sputtering in the Electronic Excitation Regime: Comparison With Electron and Ion Sputtering", Nuc. Inst. Methods B27, 155 (1987).
13. K. Leutwein, A. Raufer, and J. Schneider, "Optical and Photoelectric Properties of the F-center in ZnS", Sol. St. Commun. 5, 783 (1967).
14. A. Pospieszczyk, M. Abdel Harith, and B. Stritzker, "Pulsed Laser Annealing of GaAs and Si: Combined Reflectivity and Time-of Flight Measurements", J. Appl. Phys. 54, 3176 (1983).

In fitting the temperature to the emission how can you be sure, particularly in cases where there is a very high temperature, that you are not observing a laser plasma electron ion neutral coupling so the temperature observed is not at all indicative of the surface temperature? The speaker replied that the suggestion is probably correct for ZnS when you don't get temperatures of 10,000 K without plasma. On the other hand, when measuring neutral emission characterized by temperatures of 300 K to 1000 K it is definitely not true since you cannot have a hot plasma at 1000 K.

Laser Induced Particle Emission as a Precursor to Laser Damage*

Manuscript Received
2-16-88

Fred E. Domann** and Alan F. Stewart

Air Force Weapons Laboratory

Kirtland Air Force Base, NM 87117-6008

and

Arthur H. Guenther

Air Force Weapons Laboratory

Kirtland Air Force Base, NM 87117-6008

Mass spectrometry was used to investigate particle emission, specifically contaminant species, as a possible precursor to laser damage. Experiments were carried out in a clean ultra-high vacuum chamber with a background pressure of 4×10^{-8} Pa. Both pulsed (8 ns) and CW Nd:YAG lasers operating at 1.06 microns were used to irradiate a variety of samples which included uncoated Si, fused silica coated with films of Al_2O_3, MgF_2, or ZrO_2, and Si coated with a SiO_2/ZrO_2 stack. In the pulsed laser experiments, both 1-on-1 and N-on-1 irradiations were investigated. Emitted particles were mass analyzed with a quadruple mass spectrometer which recorded the partial pressure of a given species as a function of time.

Single pulse damage thresholds found in this study were consistent with those reported in the literature. Important differences are exhibited in pulse radiation data depending upon whether the laser fluence is above or below the damage threshold as well as upon the type of sample irradiated. In CW laser experiments, fluence was sufficient to cause damage only in the SiO_2/ZrO_2 multilayered coating due to absorption by the Si substrate. CW irradiation also resulted in desorption signals at lower fluences than was possible with pulsed radiation.

KEY WORDS: laser damage; mass spectroscopy; fluence; damage threshold.

1.0 Introduction

It has been shown that optical dielectric breakdown as a result of laser radiation is frequently preceded by changes in electrical properties or emission of charged and neutral particles. Yasojima, et al., have shown that dielectric breakdown in alkali-halide crystals was preceded by a dramatic increase in electrical conductivity. [1] Sharma, et al., have reported that increasing photoconductivity in silicate glasses by multiphoton electron-hole production was a precursor to dielectric breakdown and mechanical damage. [2] Numerous other investigators have reported observations of laser induced charged and neutral particle emission from semiconductors such as CdS and Si. [3,4,5] The authors of this work have previously studied the charge emission and surface conductivity of ThF_4, Al_2O_3 and Ta_2O_5 coatings on fused silica, irradiated with 1.06 μm pulses.[6] The results of that study showed that while charge emission for the oxide coatings occurred at roughly 10% of the damage threshold fluence, the data indicated no clear systematic dependence of charge emission on laser fluence. Thorium fluoride exhibited no charge emission below the single pulse damage threshold. In addition, the emission of neutral particles from dielectric coatings was studied and it was found that at or above the threshold fluence for neutral particle emission the single saturated the detection electronics. [7]

The objective of this work was to monitor the emission of neutral particles, primarily carbon and water, as precursors to laser damage under pulsed and CW Laser radiation at 1.06 μm, to identify the emitted species with mass analysis, and to determine the respective threshold laser fluences for their emission.

2.0 Experimental

* Work supported by AFOSR

**UURP Fellow. University of Wisconsin-Platteville, Platteville, Wisconsin 53818-3099.

2.1 Laser Systems

The pulsed laser used in these experiments was a passively Q-switched Quantel Nd:YAG laser with one amplifier module. The 1.06 μm pulses were of 8.0 ± 1 ns duration, and a single axial and longitudinal mode. The amplified beam passed through a rotating half-wave plate and fixed reflection mode polarizer attenuator. A 2.0 m focal length lens was used to bring the beam to a focus at the sample surface. The $1/e^2$ radius of the beam at the target was 356 μm, measured with a linear diode array, and was Gaussian. The pulse energy was measured using a pyroelectric energy meter which sampled a split-off portion (5.43%) of the beam. With these data, the laser fluence (energy/area) was defined for each shot.

The CW Laser was a Lasermetrics Nd:YAG laser with two in-line pumped cavities separated by a shutter. The beam power was controlled by adjusting the power delivered to arclamps and was measured using a thermopile detector which sampled a 1.9% split-off portion of the beam. A 20 cm focal length lens was used to focus the beam to a $1/e^2$ radius of 1.6 mm at the target surface.

2.2 Samples

The target samples used in these experiments included: a) single crystal <1,1,1> silicon disks 1.5" in diameter and 3/8" thick, super polished on both sides; b) Al_2O_3 coating on fused silica, $3\lambda/4$ at 1064nm optical thickness; c) ZrO_2 coating on fused silica, $\lambda/2$ at 1064nm optical thickness; d) an SiO_2/ZrO_2 high reflectance stack designed for 514 nm (used in CW experiments only). All coatings tested were electron beam deposited by Optical Coating Laboratory, Inc. (OCLI). In each case, samples were prepared by cleaning on a spin cleaner with a methanol rinse, N_2 blow-off, collodion application and removal (on coating side only), followed by an N_2 blow-off.

2.3 Vacuum Chamber

The experimental chamber was a stainless steel cylindrical chamber with an xyz plus rotational motion manipulator which supported the samples. The system was pumped with a 60 l/s ion pump, and the system pressure was monitored with a nude ion gauge. Typically, the system pressure was reduced from atmosphere to about 4×10^{-8} Pa after a 48-hour bake at 200°C. The laser input and output ports were type #705G glass and transmitted about 86% at 1.06 μm.

2.4 Mass Spectrometer

The mass spectrometer was a Quadrex Residual Gas Analyzer (RGA) Model 100 with a mass range of 1-100 amu. The minimum detectable partial pressure of this instrument is 6.5×10^{-8} Pa and $M/\Delta M \geq 2M$. Several video output modes are possible including a 20 amu scan and a single peak monitor. Because the RGA utilized a Be-Cu electron multiplier which must be isolated from the atmosphere, a straight through valve was placed between the vacuum chamber and the RGA sensors. Thus the sensor was 30 cm from the sample surface and was aimed normally to it. The sensitivity of the RGA was such, however, that the 30 cm separation did not seem to cause inadequate sensitivity for the peaks studied.

A block diagram of the experimental apparatus is shown in Figure 1.

2.5 Procedure

Pulsed laser and CW laser desorption experiments were performed in this study with slightly different procedures for each set of experiments. Irradiation of surfaces using the pulsed laser was conducted in both the 1-on-1 and N-on-1 modes. In all CW experiments, a new site was selected for each measurement as no signal was observed for multiple irradiations of a given site on the samples tested.

In the pulsed laser experiments, the RGA was tuned to the desired mass in the single peak monitor mode, with the video cursor making a complete sweep across the screen in 25.7s. The laser was fired just after the cursor began a new sweep across the screen, resulting in a video display of the partial pressure of the selected species as a function of time.

In CW Laser experiments, a sheet of graphite was used as a manual shutter because we found that opening the laser's shutter resulted in a significant energy pulse with a duration on the order of one second before the output settled down to the selected steady state value. After the arclamp current was adjusted to a level which resulted in the desired beam power and the RGA cursor had started a new trace, the graphite block was removed from the beam path until the RGA

cursor reached the end of its trace. As in the pulsed laser experiments, the RGA cursor sweep time was set at 25.7s.

3.0 Results

3.1 1-on-1 Experiments

Figure 2 shows a typical RGA response to a single laser pulse on Al_2O_3 for a fluence of 16 J/cm^2. The leading edge of the response is limited by the response time of the detection electronics, and the decay of the response appears to be exponential. The quantity of removed species, in the case of H_2O, is taken to be proportional to the height of the RGA response. Figure 3 is a plot of typical RGA responses for masses 12, 18, and 27 for increasing fluence. As is typical with measurements of this sort, there were significant fluctuations in yield for nearly equal laser fluences. These fluctuations are believed to be due to variations in water concentration from site to site. Our single pulse damage threshold (SPDT) is defined simply as the lowest fluence that resulted in visible damage under a microscope at 100x. The SPDT for Al_2O_3 was found to be 11 J/cm^2. Figure 3 shows that the threshold fluence for the removal of water was essentially coincidental with damage. Figure 3 also shows that aluminum (mass 27) is removed with a threshold fluence of about 12 J/cm^2, or about 110% of the SPDT. The removal of aluminum is an obvious indicator of damage to the coating and provides a good check on the SPDT. From these data, one must conclude that water desorption is not a precursor to damage for 8 ns laser pulses. On the other hand, carbon (mass 12) is desorbed with a threshold of about 9 J/cm^2, or about 80% of the SPDT.

Figure 4 shows that the observed threshold fluence for H_2O removal from ZrO_2 is approximately 8 J/cm^2, or about 3.5 times the SPDT of 2.3 J/cm^2. No carbon peak was observed below the SPDT. This is not surprising since the threshold fluence for carbon desorption from Al_2O_3 of 8 J/cm^2 is well above the SPDT for ZrO_2. It is important to note that the mechanism or bonding which allows the incorporation of carbon within these films may vary considerably with the chemical nature of the film as well as the deposition process used in fabrication.

Figure 5 is a plot of RGA carbon and water peaks versus laser fluences incident on a bare silicon substrate. Because the RGA signal was extremely sensitive to laser fluence and varied over three decades, the data are plotted on a semi-logarithmic scale. The 1.5 J/cm^2 SPDT found in this experiment is in good agreement with that found in the literature. [8] Interestingly, the threshold fluence for carbon removal from Si of less than 0.2 J/cm^2 is well below that of the oxides studied, and well below the SPDT for Si. Evidently, very loosely bound carbon was present on the silicon surface.

3.2 N-on-1 Experiments

The RGA signals resulting from N-on-1 pulses on the oxide coatings depended upon whether the laser fluence was above or below the damage threshold for the coating being irradiated. The fluence level for the data shown in Figure 6 was slightly below the SPDT at 9.6 ± 0.5 J/cm^2 (recall that the SPDT for Al_2O_3 was 11 J/cm^2).

Since the quantity of removed species increases with laser fluence as shown in earlier figures, the number of pulses required to remove all of an absorbed impurity varied with the fluence. With laser fluences slightly below the damage threshold, Figure 6 shows that about eight pulses are required for complete carbon desorption from Al_2O_3. We note here that the apparent exponential decrease in the RGA signal, as well as the number of pulses required for complete carbon removal are very similar to those reported by Gibson and Wilson for H_2O removal from ZnS under CO_2 laser pulses of 100 ns. [9]

Due to its low damage threshold, no N-on-1 data below the damage threshold were obtained for ZrO_2.

For silicon, N-on-1 experiments below the damage threshold, indicated that all carbon was removed after one or two shots, and no water peak was observed.

In N-on-1 experiments with fluences above the SPDT, the oxide coated samples exhibited similar yield versus pulse profiles, but differed in the number of pulses required for the RGA signals to return to background as shown in Figure 7-9. Figures 7 and 8 show the water and carbon signal profiles respectively for 30-on-1 laser pulses. Note that the fluence level used for water removal was greater than that used for carbon removal. Figure 9 shows the carbon peaks for successive pulses on ZrO_2 at an average fluence of 3.84 J/cm^2. The fluctuations in RGA signal are due in part to fluctuations in fluence for successive shots. Comparing the RGA carbon

signal profiles for fluences below and above the damage threshold (Figures 6 and 8) for Al_2O_3 reveals an important difference which was typical of all such comparisons. Below the damage threshold the desorption signal resulting from the first pulse is greater than that from subsequent pulses. Above the damage threshold, the RGA signal is found to build to some maximum value before decreasing to the background level. This seems to be strong evidence that post-damage fluences remove impurity species from within the bulk of the coating as it is removed by successive shots, or possibly from between the coating and substrate. Finally, the RGA profile of carbon from ZrO_2 (Figure 9) exhibits a rapid decrease in signal for pulses 7-11 and a shoulder for pulses between 12 and 19. A reasonable interpretation of these data may be that large carbon signals during the first part of the pulsing sequence are due mainly to carbon within the ZrO_2 film, while after about ten pulses, after the coating has been largely removed, the signal is primarily due to carbon at the coating substrate interface.

Figure 10 shows the RGA response for N-on-1 pulses on silicon, with a laser fluence of approximately 6.6 J/cm^2. The response profile is essentially featureless, and is simply a measure of carbon as an impurity in the silicon bulk.

3.3 CW Laser Experiments

Samples studied under CW 1.06 μm radiation included Al_2O_3, ZrO_2, and a multilayer coating stack of SiO_2/ZrO_2. The beam diameter was 3.21 mm and the total beam power ranged up to 300 Watts. Thus, the maximum intensity available at the sample surface was 3.5 kW/cm^2. Figure 11 shows a typical RGA response for the desorption of C from ZrO_2. Figures 12 and 13 show desorption signals from Al_2O_3 and ZrO_2 respectively. Each data point represents the peak in the RGA signal obtained while the shutter was open. Although the desorption signals varied greatly for a given radiation intensity, several important features are evident in these data. First, since none of these samples were damaged by the radiation, it is indeed possible to clean a coated surface with intensities well below the damage threshold. It is important to note, however, that a larger surface area was irradiated with the CW Laser than with the pulsed laser, so direct comparison between signal strengths cannot be made. In addition, contaminants which are tightly bound to the surface might be removed only by the higher intensities used in pulsed radiation. Secondly, water is a more tenacious contaminant than carbon, i.e., has a greater desorption energy. Last, the magnitude of the desorption signal from Al_2O_3 was significantly smaller than that from ZrO_2, although the significance of this fact is unclear. It may have been due simply to a greater level of contaminant coverage.

Finally, the coating stack of SiO_2/ZrO_2 was found to damage, i.e., crystalize as a result of the first exposure to an intensity of 1170 W/cm^2. This was caused by intense absorption and heating in the silicon substrate beneath the coating.

4.0 Discussion and Conclusion

In the preceding paragraphs, a given contaminant was said to be "removed" rather than desorbed when an RGA signal was accompanied by laser damage. For laser fluences and intensities below the damage threshold, there were no clear indications of sample heating, suggesting that the signal was due strictly to surface contaminants, and thus were referred to as "desorption." Under pulsed radiation, it is possible to desorb carbon from Al_2O_3 and Si at fluences below the damage threshold, while water is not found to desorb under pulsed radiation for any of the samples tested. Thus, carbon appears to be a reliable precursor to laser damage for Al_2O_3 and Si, but not for ZrO_2.

Pulsed N-on-1 studies below the damage threshold yielded desorption responses in agreement with findings by other investigators, as is the number of pulses (15) required to clean a particular site.[9]

CW irradiation yielded RGA signals that varied from site-to-site, but did demonstrate that both water and carbon could be removed with 1.06 μm radiation without damaging the surface for Al_2O_3 and ZrO_2, and that on the average carbon was more easily removed than water.

The results of this study suggest that in vacua, photon desorption may provide a viable means to clean a substrate prior to coating. However, the coupling mechanism between the incident photons and the adsorbed contaminants is not well understood. The 1.064 micron radiaiton used in this study is not known to be strongly absorbed by water or most hydrocarbons. Free carbon would strongly absorb this wavelength.

One mechanism frequently considered to cause desorption from a surface is the excitation of molecular vibration levels. The photon energy of the Nd:YAG lasers used in this experiment is given by

$$E_{\nu} = 12400\text{eV} - \mathring{A}/\lambda = 1.17\text{eV}.$$

Typical values of molecular vibration levels are represented by the three fundamental vibrational transitions in free H_2O molecules. These are 0.198, 0.466, and 0.661 eV transitions.[10] Infrared active transitions in CO_2 are similar in energy. Quite clearly, the photon energy does not match the vibrational transitions in free water. However, in a recent paper by N. Russo, et al., the authors report binding energies of H_2O on Si(100) ranging from 0.09 to 1.19 eV depending upon the geometric nature of the bond.[11] Thus it is tempting to consider the incident photons as causing vibrational excitations in the water molecule-surface atom oscillator system. In this system, the theoretical binding energy of 1.19 eV is an acceptable match with our photon energy of 1.17 eV. The data also showed that carbon signals well above background levels resulted from both pulsed and CW irradiation. However, significant CO and CO_2 peak were not observed, even though CO_2 should be a common contaminant resulting from exposure to the atmosphere. This finding is entirely consistent with chemisorption and desorption studies of other systems. Russo and coworkers report that the dissociative desorption of H_2O from Si requires about half (2.5eV) the energy compared to that required for molecular (5eV) H_2O desorption. That is, the Si(100) actually catalyzes the water dissociation.[11] A similar effect has been reported for N_2 dissociation on Fe crystals.[12] Thus it is reasonable to assume that adsorbed hydrocarbons were dissociated leading to the signals detected.

5.0 References

[1] Yasojima, Yoshiyuki; Ohmori, Yutaka; Okumura, Norio; Inuishi, Yoskio. "Optical dielectric breakdown of alkali-halide crystals by Q-switched lasers," Jap. J. Appl. Phys. 14(6): 815-823; June 1975.

[2] Sharma, Bhim S.; Rieckhoff, Kaus E. "Laser-induced photoconductivity in silicate glasses by multiphoton excitation, a precursor of dielectric breakdown and mechanical damage. Can. J. Of Phys. 45: 3781-3791; 1967.

[3] Namiki, A.; Watabe, K.; Fukano, H.; Nishiguki, S.; Noda, T. "Behavior of positive ions ejected from laser irradiated CdS," J. Appl. Phys. 54(6): 3443-3447; June 1982.

[4] Namiki, A.; Watabe, K.; Fukamo, H.; Nishigaki, S.; Noda, T. "Ejection of atoms and molecules from highly excited CdS," Sur. Sci. 128: L242-L248; 1983.

[5] Lui, J.M.; Yen, R.; Kurz, H.; Bloembergen, N. "Phase transformation on a charged particle emission from a Si crystal surface induced by ps laser pulses," Appl. Phys. Lett. 39(9): 755-757; 1981 Nov 1.

[6] Becker, M.F.; Domann, F.E.; Stewart, A.F. and Guenther, A.H. "Charge emission and related precursor events associated with laser damage," Fifteenth Annual Symposium: Optical Materials for High Power Lasers, Nat. Bur. Stand. Special Publ.; 1983.

[7] Becker, M.F.; Domann, F.E.; Stewart, A.F. and Guenther, A.H. Unpublished.

[8] Domann, F.; Becker, M.; Guenther, A. and Stewart, A. "Charged particle emission related to laser damage," Appl. Optics 25(9): 1371-1373; 1986.

[9] Gibson, D. and Wilson, A. CO_2 laser induced damage in a model thin film system: ZnS on Ge. "Laser Induced Damage in Optical Materials," Nat. Bur. Stand. Special Publ.; 1985.

[10] Levine, I.N. Molecular spectroscopy, John Wiley and Sons, 1975 (263-264).

[11] Russo, N.; Toscano, M.; Barone, V. and Lelj, F. "On the chemisorption of water on the (100) surface of silicon," Sur. Sci. 180(1987) 599-604.

[12] Hayward, D.O. and Trapnell, B.M. Chemisorption. Butterworth, London, 1964.

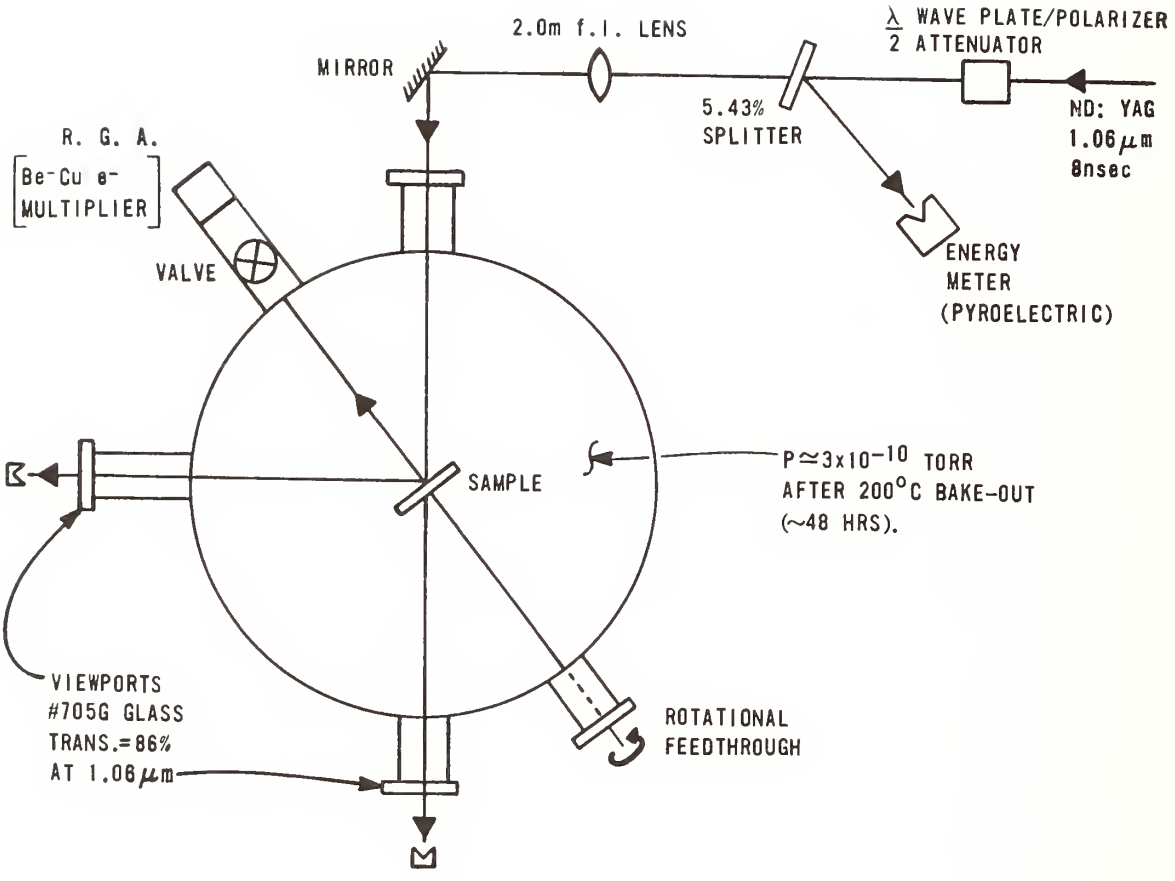

Figure 1. Schematic diagram of experimental apparatus.

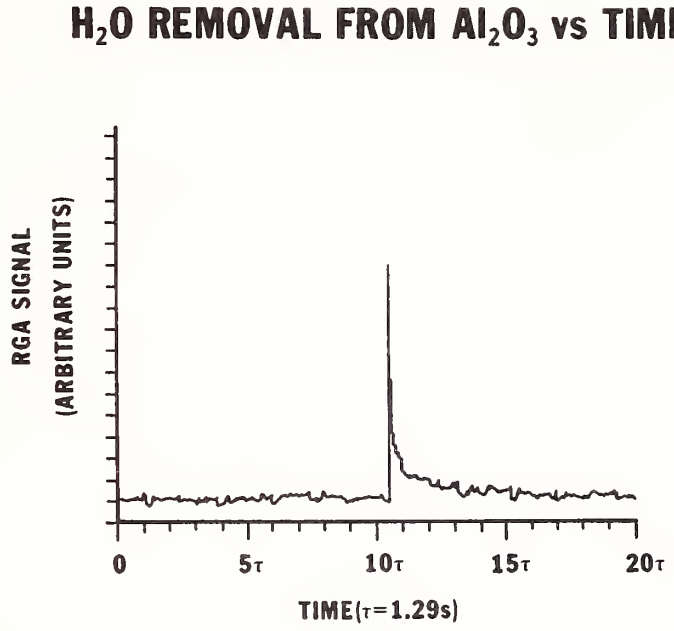

Figure 2. A typical RGA output showing the H_2O peak resulting from a 1-on-1 shot on Al_2O_3.

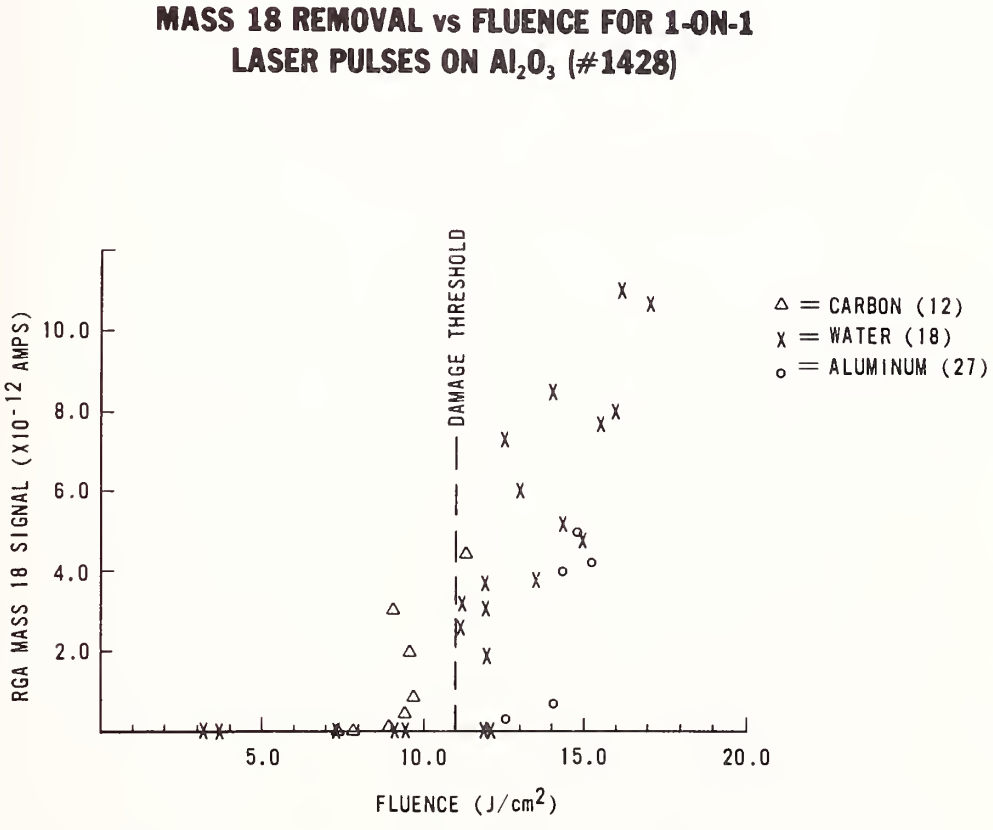

Figure 3. RGA peak heights versus laser fluence for masses 12, 18, and 27 from Al_2O_3.

MASS 18 REMOVAL vs FLUENCE FOR 1-ON-1 LASER PULSES ON ZrO_2

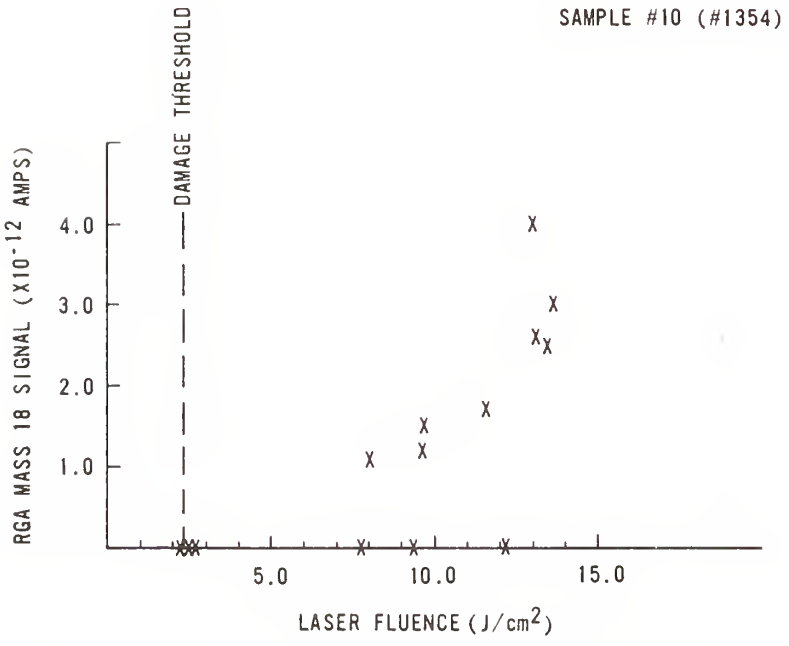

Figure 4. RGA peak height versus laser fluence for mass 18 from ZrO_2.

LOG_{10} (MASS 12/18 SIGNAL) vs LASER FLUENCE FOR 1-ON-1 LASER PULSES ON Si

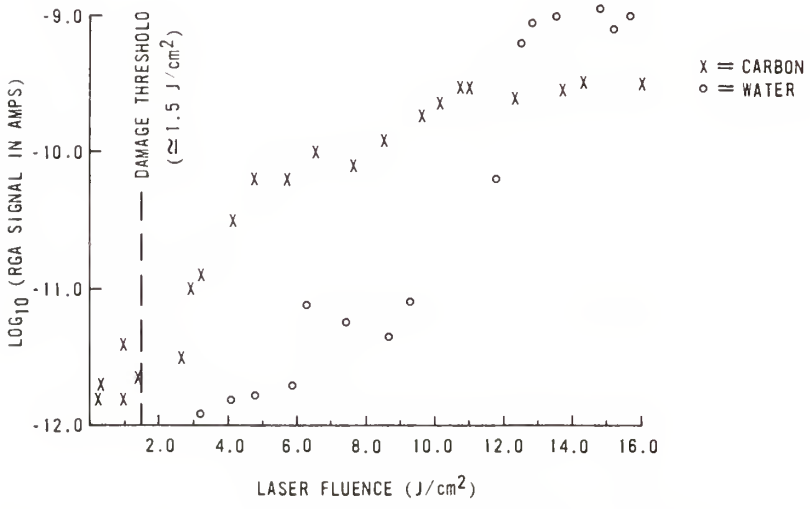

Figure 5. RGA peak height versus laser fluence for mass 18 from bare Si.

C DESORPTION FROM Al_2O_3 FOR SUCCESSIVE LASER PULSES

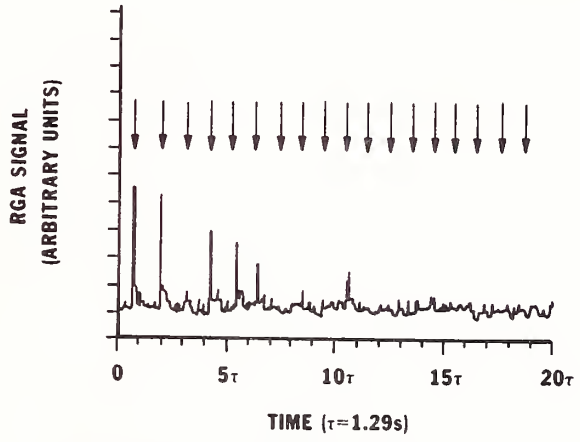

Figure 6. RGA peak heights for successive laser pulses for mass 12 from Al_2O_3.

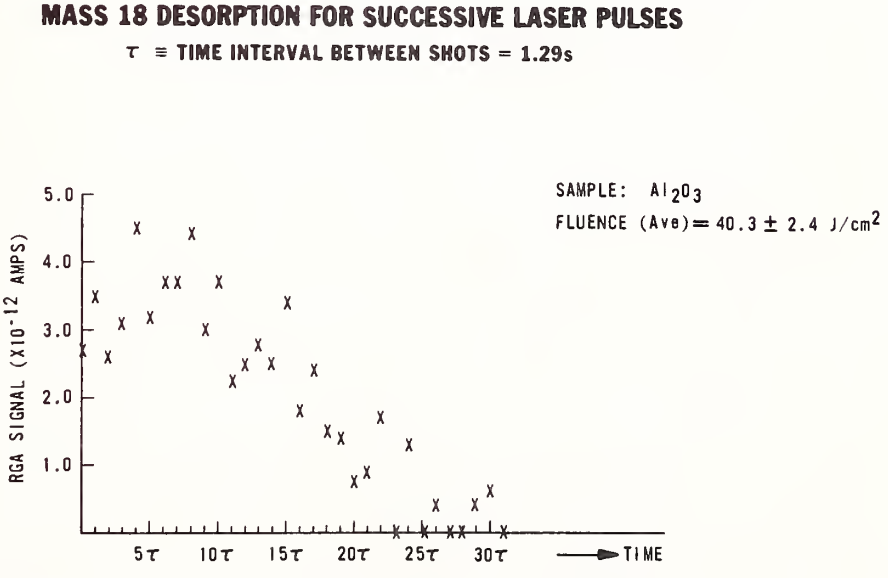

Figure 7. Water signal from Al_2O_3 for 30-on-1 laser pulses.

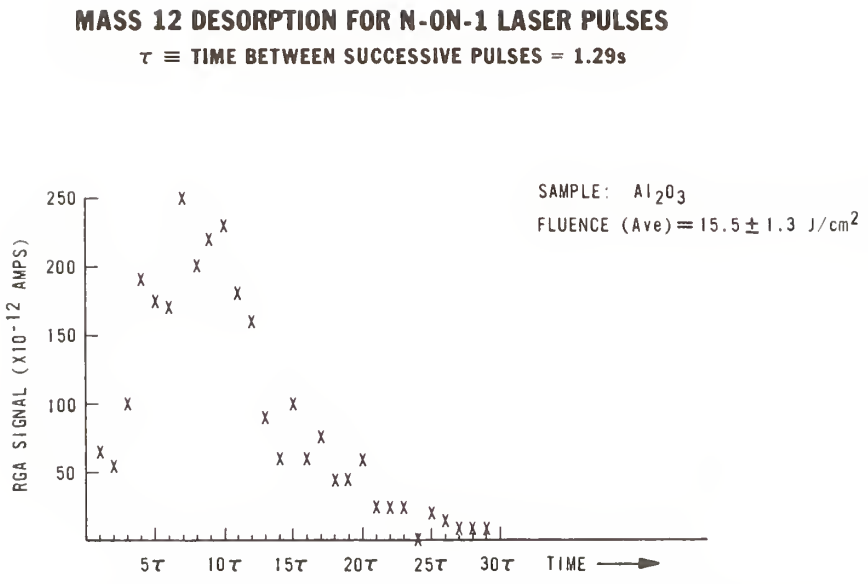

Figure 8. Carbon signal from Al_2O_3 for 30-on-1 laser pulses.

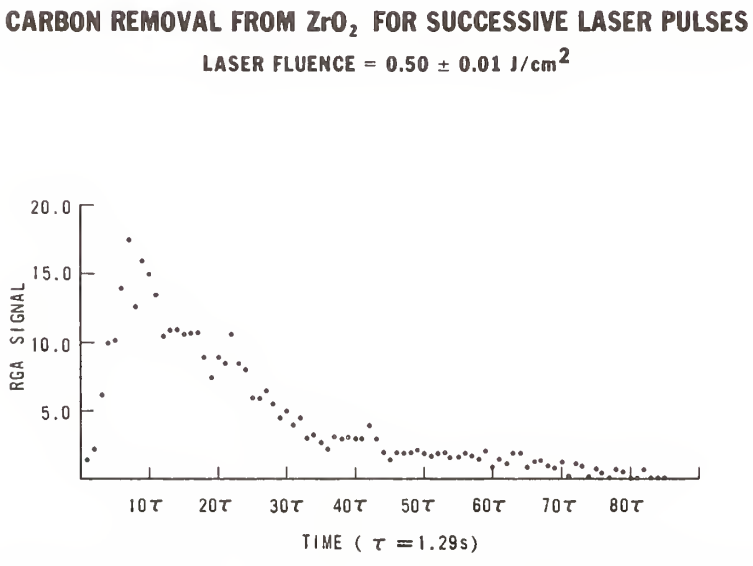

Figure 9. Carbon signal from ZrO_2 for 30-on-1- laser pulses.

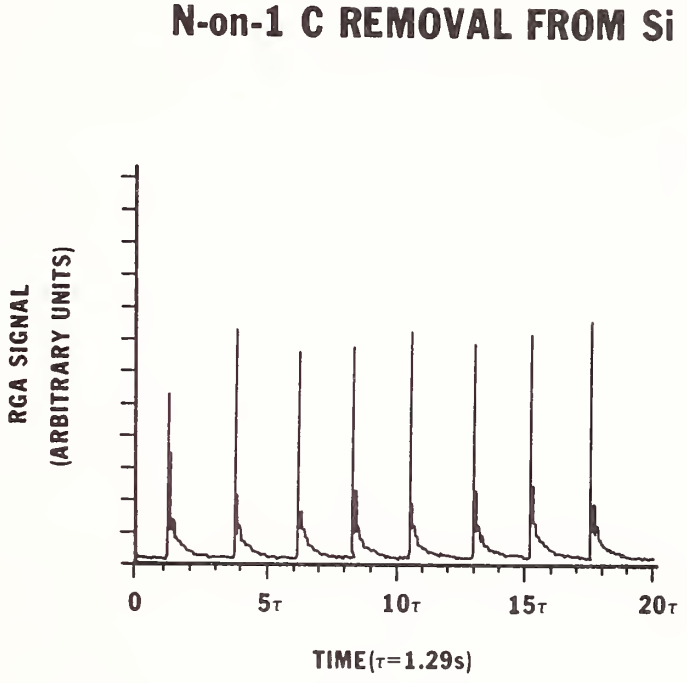

Figure 10. Carbon removal from Si for 8-on-1 laser pulses. Fluence = 6.6 J/cm^2

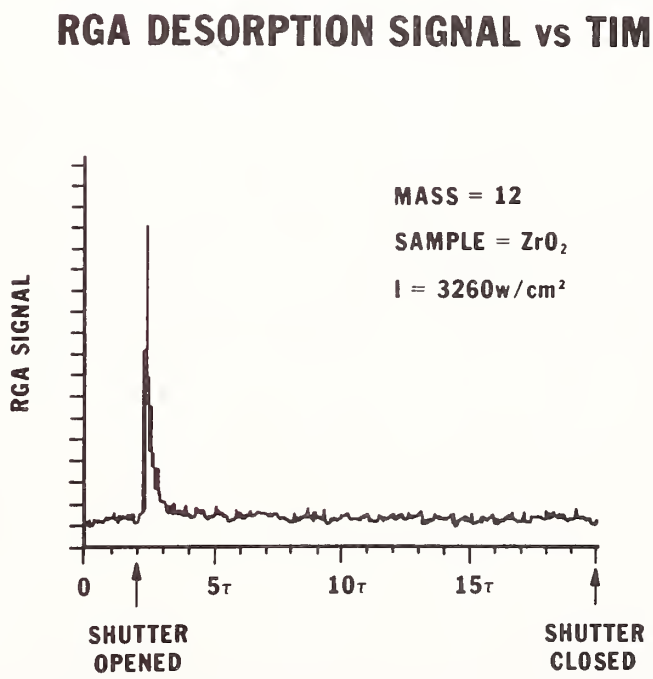

Figure 11. Typical RGA response for carbon desorption from ZrO_2 under CW radiation.

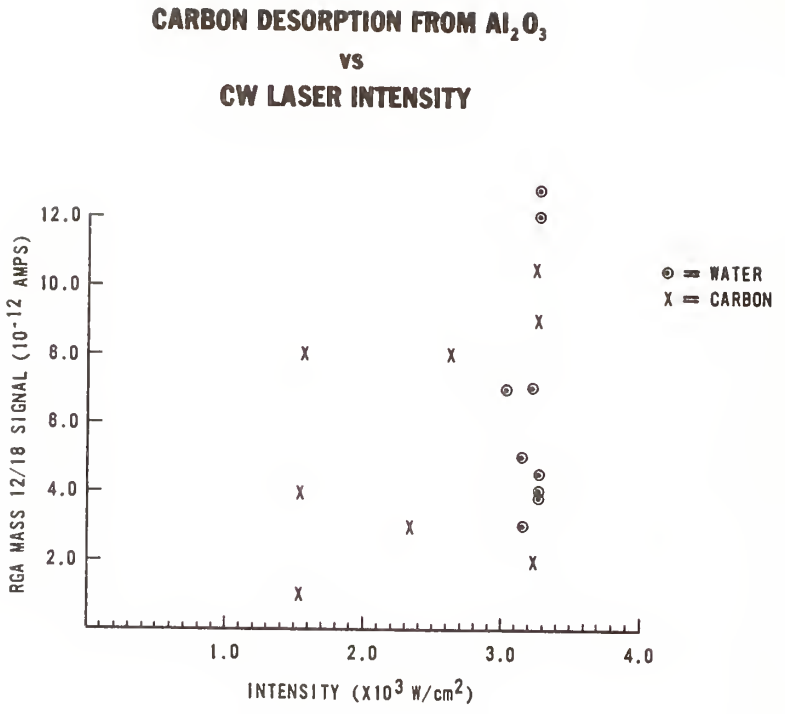

Figure 12. Carbon and water desorption signals from Al_2O_3 under CW radiation. Each data point represents desorption from a virgin site.

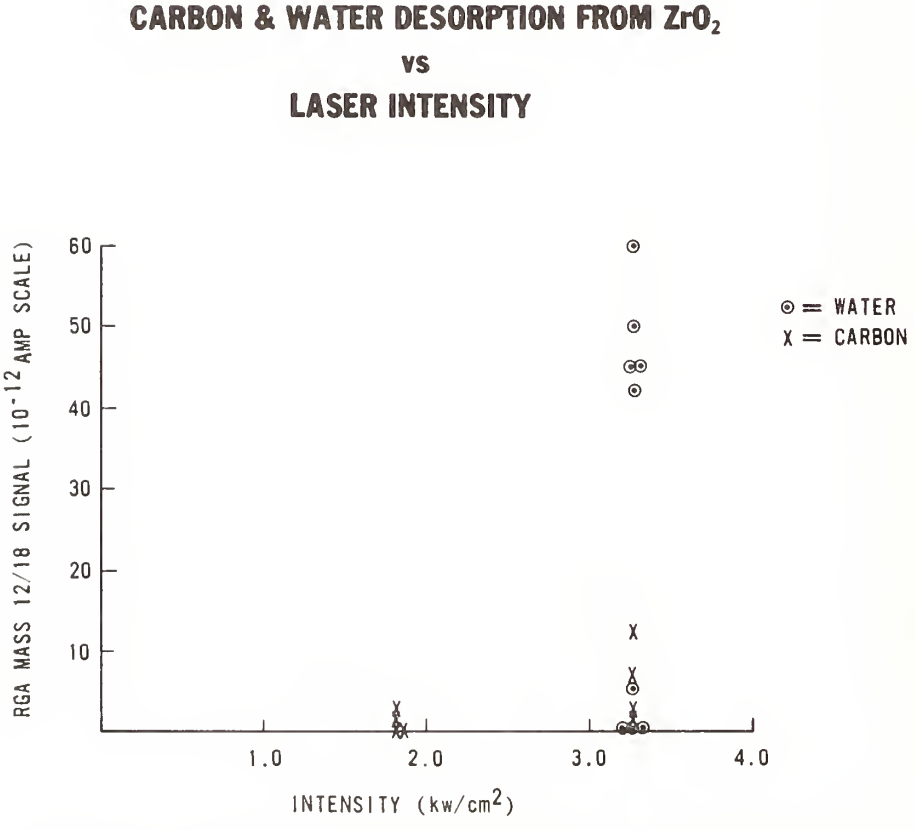

Figure 13. Carbon and water desorption signals from ZrO_2 under CW radiation. Each data point represents desorption from a virgin site.

Manuscript Received 12/16/87/sar

A Chemical Precursor to Optical Damage? Studies by Laser Ionization Mass Spectrometry

N. S. Nogar and R. C. Estler*

Chemical and Laser Sciences Division
Los Alamos National Laboratory
Los Alamos, New Mexico 87545

*Permanent Address: Department of Chemistry
Fort Lewis College
Durango, Colorado 81301

Mass spectrometry has been used in conjunction with Nomarski microscopy to characterize the initiation of optical damage in selected commercial optics. For a sample with a Al_2O_3/SiO_2 multilayer coating (351 nm) on a Si substrate, our results suggest layer by layer removal of the coating material with low-fluence irradiation at 1.06 μ. In addition, carbon impurities were observed in the low-damage threshold sample. For the Sc_2O_3/SiO_2 multilayer coated (351 nm) 7940 substrates, transient iron signals were observed at each increasing fluence level, with concomitant appearance of small circular (10 μ) pits in the surface. These pits were also associated with macroscopic damage features due to threshold testing.

Key words: optics, lasers, mass spectrometry

1. Introduction

Optical damage is often assumed to initiate by a localized absorption at chemical or physical defect sites in otherwise damage-resistant optical coatings and substrates.[1-3] Propagation of damage through either thermal runaway or avalanche-breakdown mechanism can be modeled once an initial source of electrons, localized high field, or thermal evaporation is identified.[4-6] Small levels of chemical impurities including residual polishing compound and absorbing inclusions, or physical imperfections, such as grain boundaries or misoriented microcrystals, are among the candidates for initiation sites.[7] While the participation of these source defects has long been assumed, there has been surprisingly little direct evidence to support their existence. In most previous studies, the identity and concentration of these defects was unknown, and in those cases where chemical impurities were observed, there was usually little evidence of a one-to-one correspondence between the defects and the onset of optical damage.

We report here a mass spectral study of damage in two sets of commercial optics. Mass spectroscopy has been used previously to examine the adsorption of surface contaminants on optical materials,[8] and to characterize the dynamics of macroscopic damage events.[9,10] In the present work, we have identified, in at least one case, a chemical contaminant associated with initiation of the damage event.

2. Experimental

In all experiments, the photodesorption/photoablation products were monitored by mass spectrometry, using one of two mass spectrometer systems. A quadrapole (QMS) apparatus was equipped with electron impact ionization, while the time-of-flight (TOF) apparatus utilized multiphoton photoionization for the production of ions. Samples examined in these experiments were commercial reflective optics of two types: Al_2O_3 /SiO_2 multilayer coating (351 nm) on a Si substrate, and Sc_2O_3/SiO_2 multilayer coating (also 351 nm) on a 7940 substrate. Each sample was

secured in a holder attached to a 15-cm stainless steel rod for mounting within the mass spectrometer vacuum can. The substrates were placed near (1.5-3 cm) the source regions in both mass spectrometer systems, and were manipulated by mounting the rods on a rotation-push/pull feedthrough (Varian Model 1371). The samples could thereby be rotated so as to provide a fresh surface for exposure to the laser beam.

Nomarski micrographs were taken of the samples both before and after exposure, using a commercial microscope (Nikon). Images were recorded on Polaroid Type 53 film. A series of alignment marks on the samples were used to locate the photographed sites.

The source region of the QMS (Extrel, C-50) was equipped with an axial ionizer modified to allow a variety of laser/substrate interactions. In one configuration, the high intensity laser beam passed through the ionizer, radiating the substrate at normal incidence.[11] The spalled material was ejected perpendicular to the quadrapole axis. In a second geometry, the substrate was mounted on the axis of the quadrapole. The desorption laser hit the surface at a 45-degree incidence angle, ejecting the spalled material directly along the QMS trajectory axis (Fig 1). Qualitatively, both arrangements produced the same results, however, the axial configuration was several orders of magnitude more sensitive in detecting desorbed species. Primary ions produced by the damaging laser were detected by turning off the electron impact ionizer, while survey electron impact mass spectra were typically acquired at an energy of 70 eV. Ions were detected by a channel-electron multiplier, and the signal amplified and detected by a boxcar integrator (PARC 162/164) synchronized to the output of the desorption/ablation laser. Unit mass resolution is possible with this apparatus throughout the range of interest, 4-200 au. A base pressure of $\leq 1 \times 10^{-8}$ Torr was maintained in this vacuum chamber by an ion pump and/or turbomolecular pump.

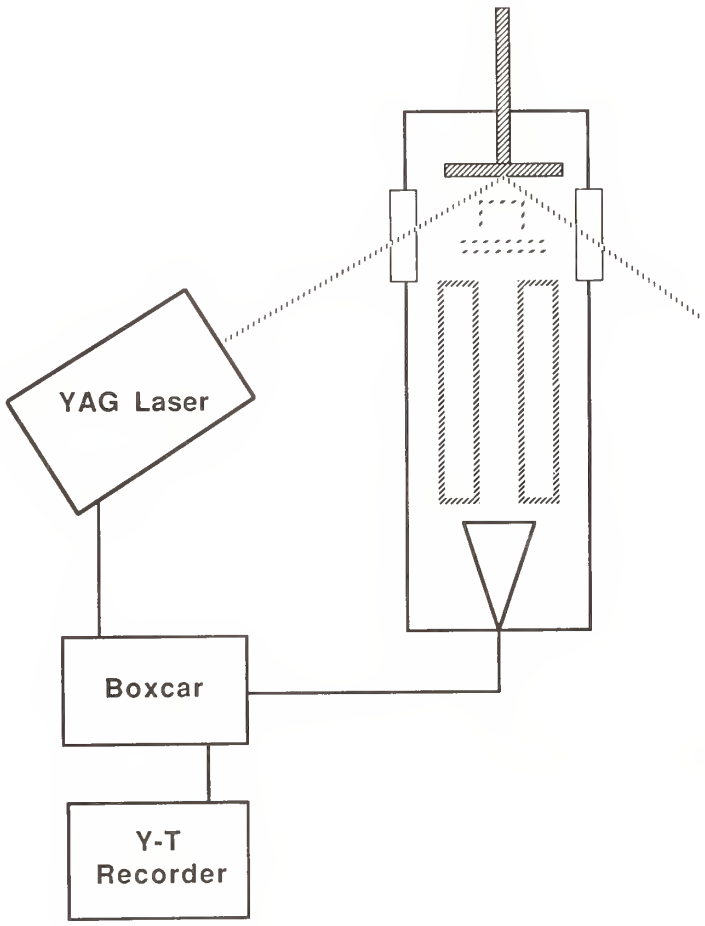

Figure 1. Experimental schematic for the "on-axis" quadrapole mass spectrometer configuration.

The source region of the TOF allowed optical access by both the desorption and interrogation laser beams.[12] Ions were again detected by a channel-electron multiplier, and the signal processed with either the boxcar integrator or transient recorder (Tektronix 2430). The latter was very important since the multiplex detection allowed acquisition of a full mass spectrum for each laser shot, and facilitated the observation of transient signals. The mass resolution of this instrument was ≈2 au in the range 2-200 au. A base pressure of ≤1 x 10^{-7} Torr was maintained by a L-N_2 trapped oil diffusion pump.

Desorption/damage was initiated by the fundamental (1.06 μ) output of a Nd^{+3}:YAG laser (Quanta Ray/Spectra Physics Model DCR 1A). The laser was equipped with filled-beam optics, and produced a beam whose spatial profile was somewhat more sharply peaked than for a gaussian beam. The Q-switched output was 10 ns FWHM in duration, and smooth within the resolution of our electronics (≈2 ns). The output of this laser was focused to a diameter of 500 μ at the front surface of the sample of interest. Beam diameters were determined by burn patterns on photographic film[13].

The timing sequence was initiated by the Q-switch synch-out from the YAG laser. When using the quadrapole mass spectrometer, this signal triggered directly the boxcar averager gated to accept signal from laser-generated species. In experiments using the time-of-flight mass spectrometer, the YAG laser synch-out was passed through a variable delay (Tektronix 7904/7B85), a pulse generator (BNC 8010) and then to the trigger of a XeCl excimer laser (Lambda Physics EMG 101). The UV output from this laser was used to pump a tunable dye laser (Lambda Physics FL 2002) which could then probe, via multiphoton ionization, the material spalled by the laser damage event. Typical pulse energies were 1-5 mJ (12 ns FWHM) at 394 nm using the laser dye QUI (Lambda Physics). The identity of the spalled material could be determined by ion flight times and by varying the ionization wavelength, while velocity distributions could be measured by changing the delay between the damage and interrogation lasers.

3. Results and Discussion

Since the type of information obtained for the two sets of samples was qualitatively different, they shall be discussed separately.

3.1. Al_2O_3 / SiO_2 multilayer-coated Si substrate.

Two samples were examined, one having a relatively high macroscopic damage threshold (10 J/cm² @ 351 nm), while the other exhibited a low threshold (5 J/cm² @ 351 nm). Figure 2 shows typical low sensitivity mass spectra for either sample obtained with the quadrapole mass spectrometer system, and 70 eV electrons. The bottom trace is due to background gases (no sample irradiation), and exhibits small peaks corresponding to water, nitrogen, residual hydrocarbons, argon and carbon dioxide. At low fluences (1-3 J/cm² @ 1.06 μ), as damage was just beginning, results were typified by trace b, which exhibits an increase in the water-related signal (mass 16-18), and the appearance of aluminum (mass 27) and silicon (mass 28). At higher fluences (7-10 J/cm² @ 1.06 μ), or longer radiation times, the dielectric coating was removed, and a signal due primarily to bulk silicon was observed, Fig. 2. When a higher sensitivity was used, it was possible to detect a number of other species, both ionic and neutral, in the laser generated plume (see Table I). In most experiments, the signal due to neutral species was ≥100 times the signal due to primary ions[14] (those generated directly by 1.06 μ pulses). It is interesting to note that the carbon ions and neutrals were observed only for the low damage threshold sample, suggesting a correlation with the presence of this impurity.

Our experiments showed a factor of 10 decrease in signal for Si_2^+ relative to Si^+, and another order of magnitude decrease for Si_3^+ relative to Si_2^+. Although the large silicon clusters reported in some previous laser vaporization studies[15] were not seen in this work, this is not surprising since the vaporization and expansion conditions were dramatically different. In the previous studies, the irradiation intensities were considerably higher, which should lead to a higher local density of gas phase silicon atoms, and the spalled material was expanded through a supersonic jet, which should lead to an increase in cluster formation. Both of these effects tend to skew the previously observed distributions toward higher cluster sizes.

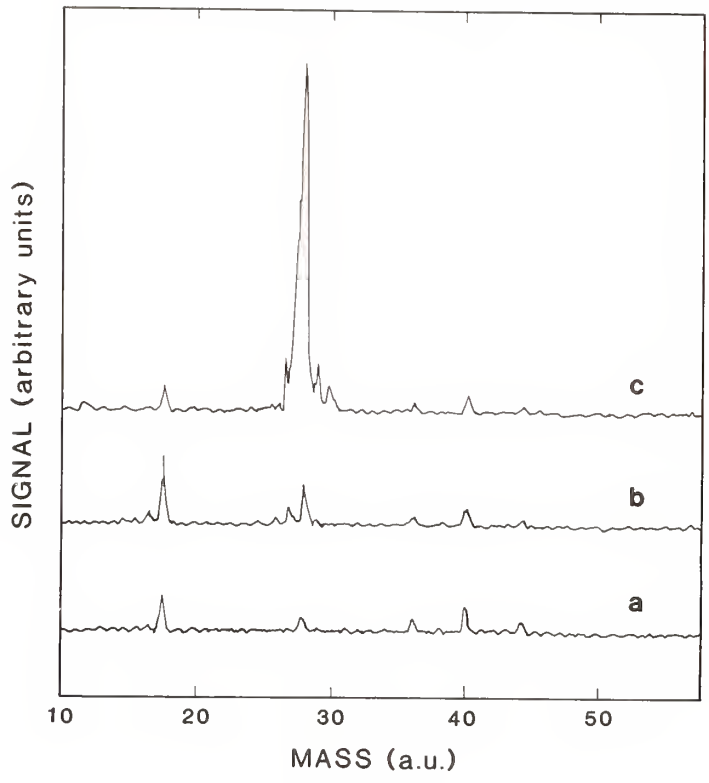

Figure 2. Low sensitivity mass spectra of laser-generated plume from Al_2O_3/SiO_2 multilayer coated Si substrate, obtained with 70 eV electron impact ionization. Lower trace (a) shows background gases. Trace (b) shows a characteristic spectrum for low laser fluence, while trace (c) is a typical trace for high fluence irradiation.

Table I. Ionic and neutral species observed by mass spectrometry in the laser desorption/laser ablation of coated optical samples.

Sample	Neutral Species[a]	Ionic Species[b]
Al_2O_3 / SiO_2 on Si	C*, Al, Si, SiO, Al_2O	C^+,Si^+, Si_2^+, Si_3^+, SiO_2^+ Al^+, AlO^+, AlO_2^+, O_2^+, H_3O^+
Sc_2O_3 /SiO_2 on 7940	Si, Sc, ScO, O_2, Sc_2O#	Si^+, Sc^+, Sc_2^+ Fe#

[a]Required post-desorption ionization (laser or electron-impact) to observe by mass spectrometry
[b]Ions produced directly in the desorption process
*Indicates only observable in low-damage threshold sample
#Indicates transient signal (see text for details)

Figure 3 displays the time-dependent Al^+ signal due to 70 eV electron impact ionization of neutrals removed from the surface by laser desorption. This data was acquired at low fluence (1.5 J/cm^2 @ 1.06 μ), corresponding the onset of damage at this site. After the initial few hundred laser shots, it appears that there is some periodicity (see tick marks on the upper horizontal axis), corresponding to a period of ≈1200 laser shots, superimposed on a roughly exponential decay in this signal. This suggests that we may be observing layer by layer removal of the multilayer dielectric coating, although the radial growth of the damage spot may certainly be occurring concurrently. Roughly complimentary behavior was observed for the Si^+ signal (periodicity, with a phase shift relative to the aluminum signal), although for silicon, the interpretation is complicated by the 28 au background due to molecular nitrogen. In spite of this interference it was very clear from a spectacular rise in the silicon signal, with a concomitant drop in the aluminum signal, when the coatings were removed completely and the substrate material irradiated directly.

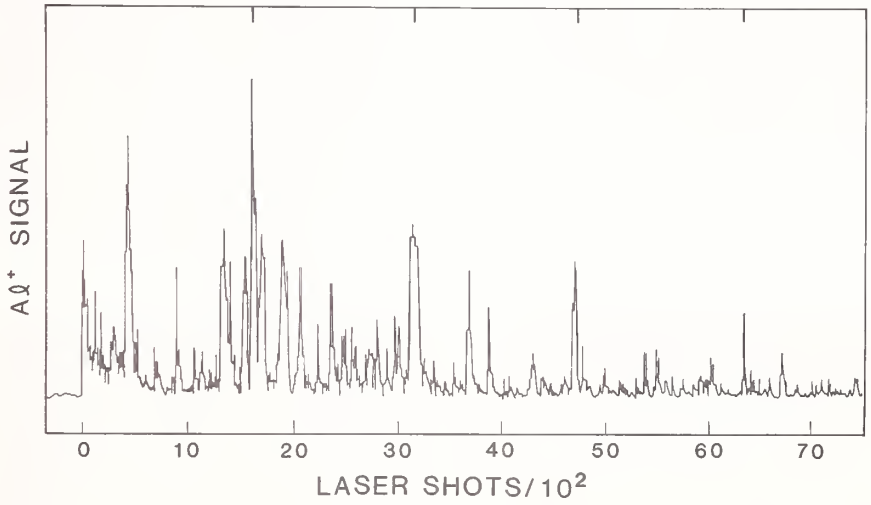

Figure 3. Time-dependent Al^+ signal generated from electron-impact ionization of plume desorbed at low fluence from the Al_2O_3/SiO_2 multilayer coated Si substrate. Tick marks on the upper vertical axis are coincident with periodic maxima in the signal.

3.2. Sc_2O_3 /SiO_2 multilayer coated 7940 substrate

Table I. shows the species typically observed in the plume of material spalled from two samples (high damage threshold, 10.3 J/cm^2 @ 351 nm, and low damage threshold, 3.8 J/cm @ 351 nm) of the Sc_2O_3/SiO_2 multilayer coated 7940. Those species not designated as transient were detected via 70 eV electron impact in the quadrapole mass spectrometer, and could be observed for extended periods (≥10^3 laser shots) at low fluence (1-3 J/cm^2 @ 1.06 μ) irradiation of a single site.

The "transient" species were observed only by TOF mass spectrometry, in combination with laser ionization. Figure 4 shows typical TOF mass spectra, with the lower vertical axis indicating flight time, and the upper corresponding to mass. The lower trace (a) is the (null) mass spectrum observed when the YAG laser fires, but no photons impinge on the sample. This display is the result of a four-shot average, and displays the mass range from ≈4 to 250 au. The deflection immediately following t=0 is the result of r.f.i. due to firing the ionization (excimer-pumped dye) laser. The time between firing the desorption- and excimer lasers (≈14 μs) was adjusted to address particles having a velocity normal to the surface of ≈7x10^4 cm/s. This time delay was found empirically to maximize the observed signal.

The middle trace (b) of Fig. 4 is typical of the mass spectra observed when the desorption laser fluence is just sufficient (100 mJ/cm^2) to produce any detectable signal. In this case, the only observable signal (equivalent to 1-2 ions detected per laser shot) occurs at mass 56. Since

the ionization laser is tuned to the $^5G_5$ (50703.9 cm^{-1}) $\leftarrow$ $^5G_4$ (0.000 cm^{-1}) two-photon transition in iron (394.4 nm), and since the observed signal is sharply peaked at this wavelength, both the mass and optical spectral signatures suggest that were are observing iron desorbed from the sample.[16] It is important to note that for a particular location on the sample, this signal could only be observed for 2-6 shots at a given fluence of the desorption laser. In order to observe subsequent signal, either the location of irradiation had to be changed or the fluence raised. The uppermost trace (c) of Fig. 4 shows a signal generated at significantly higher fluence (6.4 J/cm^2). In addition to the iron signal observed in trace (b), signal is now also present at 28 au, corresponding to silicon, and at ≈106 au, corresponding to Sc_2O. Note that although the 28 au and 106 au signals are smaller than that observed for 56 au, this does not necessarily indicate that more iron is being removed from the surface than silicon or scandium. Since ionization is affected by a multiphoton photoionization process in which the ionization wavelength is tuned to resonance with an iron transition, the ionization efficiency is expected to be much greater (by perhaps 10^2 to 10^3) than for the non-resonant ionization of silicon- or scandium-containing fragments. Based on previous results with this apparatus,[12,17] and the magnitude of the observed iron signal, the number of *ground state iron atoms* removed from the surface lies in the range 10^4-10^5 assuming the distribution is spatially isotropic and kinetically thermal. It should be noted that this does not place an upper limit on the *total* amount of material removed from these pits. Iron clusters, coating material and other impurities may be desorbed and detected with much lower efficiency than for ground state iron atoms.

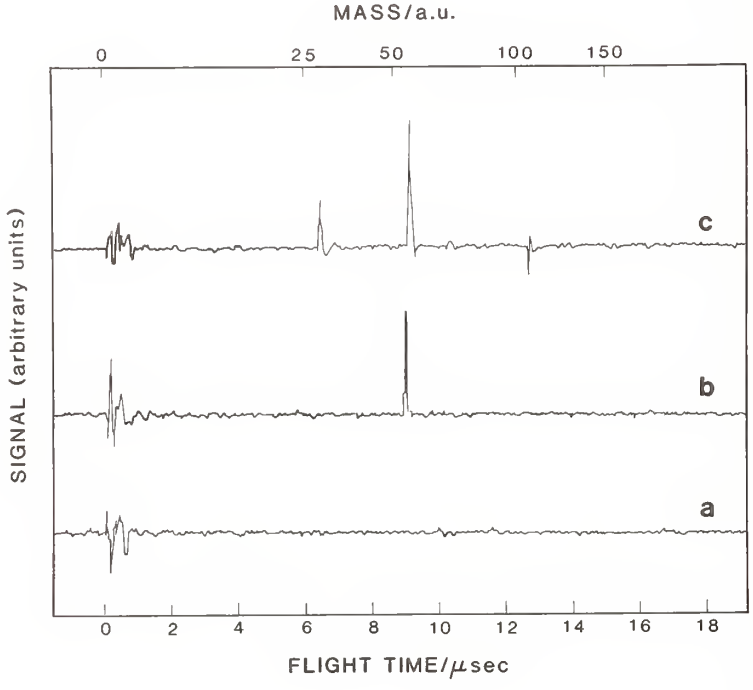

Figure 4. Time-of-flight mass spectra of laser-generated plume from Sc_2O_3/SiO_2 multilayer coated 7940 substrate, obtained with laser multiphoton photoionization at 394 nm. Trace (a) was generated with no plume present, and shows only r.f.i. pickup at t=0, when the ionization laser fires. Trace (b) displays a signal at mass 56 (Fe) due to low-fluence irradiation of the sample, while trace (c) shows additional signals at mass 28 (Si) and mass 106 (Sc_2O).

These results can be profitably compared with evidence provided by Nomarski photographs of the samples. Figure 5 displays, at 420x magnification, a section of the sample prior to laser irradiation (upper level), while the central feature shows the results of irradiation below the fluence necessary to initiate macroscopic damage. Irradiation conditions were similar to those used to obtain the mass spectrum in Fig 4b. A number round pits, approximately 10 μ in diameter, can be observed within the field of view. A slight shading in the background surrounding these pits can also be observed in some instances, suggesting that some thermal deformation

occurred. Several of these circular blemishes were typically observed within the (YAG) laser footprint following experiments in which a transient iron signal was observed. In addition, the density of these pits increases with the maximum fluence to which the sample was exposed for the mass spectrometric diagnostics. Figure 5 (lower right) shows, for comparison, a macroscopic damage feature produced by an excimer laser in threshold damage testing. Several features should be noted. First, the damage test figure appears to be both larger and deeper than the circular features of 4b. And secondly, a circular feature, similar to those in 5b, can be seen to the left of center in the damage pit. In fact, for all cases in which a macroscopic damage feature was photographed, one or more of these circular features was observed within the damage footprint. In addition, each of these circular features appear to have grown from its center as marked by a deeper central damage site.

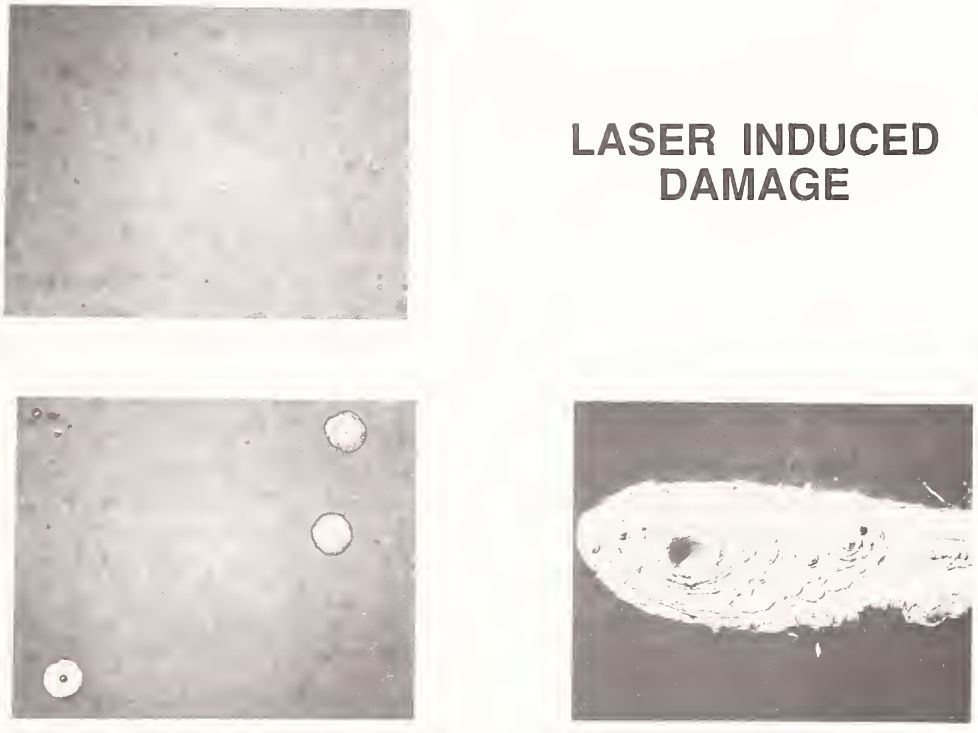

Figure 5. Nomarski micrographs (420X) of Sc_2O_3/SiO_2 multilayer coated 7940 substrate. Upper left shows an unirradiated surface. Lower left displays a surface subjected to low-fluence irradiation, while lower right shows a surface subjected to high-fluence irradiation, resulting in macroscopic damage.

The appearance of small pits within the irradiated area, and the concomitant detection of iron emission from the surface, strongly suggests a correlation. We believe that the observed signals are due the presence of small, iron-containing micro-inclusions in the optical coatings. Low fluence irradiation removes near-surface contaminants with minimal damage, while higher-fluence irradiation may remove more deeply imbedded, or lower susceptibility, contaminants, with concomitant removal of surrounding coating material.

This interpretation is consistent with a number of observations. In particular, previous reports[18,19] have cited a laser-annealing effect. That is, a gradual increase in the fluence with which a sample is irradiated results in a higher measured damage threshold than for immediate irradiation at high fluences. This can be rationalized by low fluence removal of included impurities below the threshold for macroscopic damage. In addition, the association, in our experiments, of the circular pits with the macroscopic damage sites suggests that at high fluences, absorption by impurity inclusions can result in a high local temperature or field to cause macroscopic damage.

In conclusion, the combination of a method (RIMS) having high sensitivity, and good spatial and temporal resolution, with an imaging capability, such as micrography, provides a powerful tool for the study of optical damage processes. Imaging capabilities are vital, in general, for the detection of inhomogenously distributed impurities. Work is under way to introduce imaging capabilities directly into RIMS analysis.

5. References

[1] Wood, R. M. Laser Damage in Optical Materials, Boston, Adam Hilger,1986.

[2] Smith, W. L. Laser-Induced Breakdown in Optical Materials. Opt. Engin. 17; 489-503; 1978.

[3] Ready, J. F. Effects of High-Power Laser Radiation, New York, Academic, 1971.

[4] Hurt, H. H.; The Effect of Defects on the Laser Damage Performance of Metal Mirror Surfaces, Proc. 16th Ann. Symp. on Laser Induced Damage in Opt. Mat., 1984; NBS Special Publication 727; Oct. 1986, Pp. 66-70.

[5] Siekhaus, W. J.; Kinney, J. H.; Milam, D.; Chase, L. L. Electron Emission from Insulator and Semiconductor Surfaces Below the Optical Damage Threshold, Appl. Phys. A39, 163-166; 1986.

[6] Lange, M. R., McIver, J. K., and Guenther, A. H., Laser Induced Damage of a Thin Film with an Absorbing Inclusion: Thermal Considerations of Substrates and Absorption Profiles, Proc. 15th Ann. Symp. on Laser Induced Damage in Opt. Mat., 1983; NBS Special Publication 688; Nov. 1985, Pp. 448-453.

[7] Johnson, L. F., Ashley, E. J., Donovan, T. M., Franck, J. B., Woolever, R. W., and Dalbey, R. Z., Scanning Electron Microscopy Studies of Laser Damage Initiating Defects in ZnSe/ThF_4 and SiH/SiO_2 Multilayer Coatings, Proc. 15th Ann. Symp. on Laser Induced Damage in Opt. Mat., 1983; NBS Special Publication 688; Nov. 1985, Pp. 356-370.

[8] Allen, S. D.; Porteus, J. O.; Faith, W. N. ; Franck, J. B. Contaminant and Defect Analysis of Optical Surfaces by Infrared Laser Induced Desorption. Appl. Phys. Lett. 45; 997-999; 1984.

[9] Estler, R. C.; Apel, E. C.; Nogar, N. S. Laser Mass Spectrometric Studies of Optical Damage in CaF_2. J. Opt. Soc. Am. B., 4, 281-286; 1987.

[10] Levine, L. P.; Ready, J. F.; Bernal, E. G. Production of High-Energy Neutral Molecules in the Laser-Surface Interaction. IEEE J. Quant. Elec. QE-4; 18-23; 1968.

[11] Estler, R. C.; and Nogar, N. S. Mass Spectrometric Identification of Wavelength Dependent UV-Laser Photoablation Fragments from Polymethylmethacrylate. Appl. Phys. Lett., 49, 1175-1177; 1986.

[12] Nogar, N. S.; Estler, R. C.; and Miller, C. M. Pulsed Laser Desorption for Resonance Ionization Mass Spectrometry. Anal. Chem. 57; 2441-2444 ; 1985.

[13] Avizonis, P. V.; Doss, T T.; Heinlich, R. Measurements of Beam Divergence of Q-Switched Ruby Laser Rods. Rev. Sci. Inst. 38; 331; 1967.

[14] The authors would like to thank D. A. Dahl and J. E. Delmore, EG&G Idaho, for an IBM-compatible copy of SIMION, an ion optics program which we used to estimate the relative transmission efficiencies of neutral and ionic species in our apparatus.

[15] Heath, J. R.; Liu, Y.; O'Brien, S. C.; Zhang, Q-L; Curl, F.K.; Tittel, F. K.; Smalley, R.E. Semiconductor Cluster Beams: One and Two Color Ionization Studies of Si_x and Ge_x. J. Chem. Phys. 83; 5520-5526; 1985.

[16] Standard tests, including duplicate experiments with alternate samples and with no sample, were performed in order to insure that the iron signal originated with the sample and not from other parts of the apparatus.

[17] Apel, E. C.; Anderson, J. E.; Estler, R. C.; Nogar, N. S.; Miller, C. M. Use of Two Photon Excitation in Resonance Ionization Mass Spectrometry. Appl. Opt. 26; 1045-1050; 1987.

[18] Frink, M. E.; Arenberg, J. W.; Mordaunt, D. W.; Seitel, S. C.; Babb, M. T.;, Teppo, E. A. Temporary Laser Damage Threshold Enhancement by Laser Conditioning of Antireflection-coated glass, Appl. Phys. Lett. 51; 415-417; 1987.

[19] Franck, J. B.; Soileau, M. J. A Technique for Increasing the Optical Strength of Single-Crystal Sodium Chloride and Potassium Chloride Through Temperature Cycling, Proc. 15th Ann. Symp. on Laser Induced Damage in Opt. Mat., 1981; NBS Special Publication 638; p. 114.

Manuscript Received
2-1-88

Ion Emission Kinetics of Laser Damage to Semiconductor and Dielectric Thin Film Surfaces

Jahja I. Trisnadi[1], Yong Jee[2], Rodger M. Walser, and Michael F. Becker
The University of Texas at Austin
Center for Materials Science and Engineering and
Department of Electrical and Computer Engineering
Austin, TX 78712-1084

In these experiments we used time-of-flight energy analysis to determine the kinetic processes occurring at laser damage on surfaces. A triaxial charge collector of relatively large area was designed for use in the target vacuum chamber. It could be biased in several ways to detect either positive or negative charge, and it could resolve charged particle time-of-flight over a field free region of about 6 cm. The laser system was a Q-switched Nd:YAG laser with 10 ns pulses at 1064 nm. Measurements were made on single crystal germanium wafers and on half-wave delectric thin film samples of ThF_2 and MgF_2 on fused silica.

On germanium, ion emission was only detected when the surface morphology indicated boiling. This occurred at about 1 J/cm^2 or a little over twice the melt or damage onset fluence. For thin film samples, ion emission correlated with surface damage. For all samples, ion velocity distributions and the observed correlation between kinetic energy and ion flux were characteristic of laser heated plasma processes following charge emission.

Key words: laser damage; ion emission; charge emission; germanium; thorium fluoride; magnesium fluoride.

1. Introduction

In these experiments, our objective was to study the kinetics of charge emission in conjunction with laser induced surface damage. If sufficient sensitivity could be obtained, pre-damage emission could also be studied. Ion velocity data obtained from time-of-flight measurements should give information about the kinetics of the laser-surface-plasma interaction near the damage threshold. Our experiments in this direction were directly motivated by the observation of pre-damage charge emission from dielectric films and metal surfaces [1,2] and from the observation of surface charging on dielectric thin films after laser damage [3].

In general, there is a long history to the study of laser induced emission of ions from both insulating and semiconduction materials. Probably the most quantitatively studied examples are single crystal alkali halides [4-6]. And, emission from semiconductors has been examined for silicon [7,8], gallium arsenide [9], cadmium selenide [10], cadmium sulfide [11], cadmium telluride and zinc sulfide [12,13].

2. Experimental Apparatus and Samples

The laser used in these experiments was a Q-switched Quantel Nd:YAG laser operated at the fundamental wavelength of 1064 nm at a repitition rate of 10 Hz and with a 10 ns pulselength (FWHM). The optical layout is shown in figure 1. The beam was attenuated with a fixed dielectric reflector and a variable attenuator consisting of a rotating half-wave plate and a fixed thin film polarizer. Irradiations were controlled by a computer driven shutter, and the computer also collected data from a reference energy meter on every pulse in order to compile irradiation statistics. The reference energy meter was calibrated at the start and end of each data taking session against another energy meter near the sample location. Each calibration also consisted of measuring the beam spot size at an equivalent focal plane using the scanning knife edge method. Depending on the sample type, either a 45 cm or a 100 cm focusing lens was used. Spot sizes were typically 135 μm and 350 μm (1/e^2 radius) respectively.

The charge collector was designed to allow field free drift from the sample to the collector and with a second biasable grid to exclude particles of the opposite polarity. The collection area was made as large as possible to improve sensitivity while still maintaining a 50 Ω transmission line structure. The central charge collection electrode was 1.5 cm in diameter. The triaxial collector and its associated circuitry is diagrammed in

[1]Department of Physics
[2]Microelectronics and Computer Technology Corp. (MCC), Austin, TX

figure 2. Provision has been made to bias the collection electrode and capacitatively couple the transient signal. In practice it was found that the second grid electrode was not used and connected to ground potential (bias #1 = 0 V). A bias of ±30 V was applied to the collection electrode (bias #2) and it was used to reject the undesired polarity of charge. The collector was placed about 6 cm from the target sample at 30° to the sample normal and laser beam axis. These in turn were enclosed in a vacuum chamber dry pumped by an adsorption pump and an ion pump. Typical operating vacuum was $<10^{-6}$ torr ($<1.3 \times 10^{-4}$ Pa). Care was taken to place the ion pump sufficiently far from the sample location so that stray magnetic fields or ions did not affect the experiments.

The samples used in the experiments included germanium wafers and thorium fluoride and magnesium fluoride coatings on fused silica substrates. The germanium wafers were single crystal, polished on one side, flat wafers for semiconductor device processing. The dielectric thin film samples were both a half-wave thick at 1064 nm and obtained from the Air Force Weapons Laboratory. The MgF_2 films were coated onto ultra-polished substrates and were measured by TIS to have a 20 Å RMS surface roughness after coating.

3. Data

Data was collected by irradiating the sample with single pulses both above and below the damage threshold fluence. Waveforms from the triaxial charge collector were recorded on a fast oscilloscope with separate tests being conducted to record positive and negative charge. A new sample site was selected for each test. Representative ion flux versus time and ion flux versus velocity distributions for germanium are shown in figure 3. Although the waveforms are generally peaked in the center, they do not resemble those for a thermal equilibrium distribution in many specific ways. This aspect will be discussed later. Not shown on the figure are the electrons which arrive in about 10-20 ns and are seen when the bias is +30 V for observing negative charge. Detailed data were not collected for the electrons because the pulse was not fully resolved in time. When all the charge was added together, the expanding plasma was found to be approximately neutral. Since the data were noisy, and positive and negative charge were not collected simultaneously for a single shot, this conclusion can only be approximate.

The waveforms were characterized by determining the arrival time of the fastest ions, the arrival time of the peak of the ion flux waveform, which gives data for the most probable ion velocity, and the pulse height, which is proportional to the ion flux at the most probable velocity. Since the laser energy of each shot was recorded, these three ion parameters could be correlated with laser fluence and with the occurrence of damage. Damage for these experiments was determined by subsequent Nomarski micrography after the sample was removed from the vacuum chamber. Any visible change in the sample at up to 200x magnification was considered to be damage. However, since the number of sites was limited, only approximate damage onset fluences were measured, and detailed damage probability versus fluence curves were not generated.

Kinetic energy data for the germanium samples is shown in figure 4 for positive and negative ions. In computing the kinetic energy, the mass of a single germanium atom was used. Only the most probable kinetic energy is shown in the figure since the data for the peak kinetic energy are similar and are just shifted slightly higher in energy. This was true for all the samples in this study. The ion energy was observed to increase monotonically with fluence as expected, and there was considerable site-to-site fluctuation in the data as had been observed in other charge emission experiments [1-3]. Although the data was noisy, the most probable ion kinetic energy was quite highly correlated with the peak ion flux, as shown for positive germanium ions in figure 5. This is suggestive of plasma density dependent heating and will be discussed later.

Detectable charge emission appeared to have a distinct onset fluence which was around 1 J/cm^2 for germanium. Subsequent microscopic examination led us to conclude that whereas germanium had a melting threshold fluence of about 0.5 J/cm^2, charge emission was not detected until the boiling threshold was reached. An example of the surface morphology above the boiling onset is shown in the center region of figure 6. When boiling did not occur, no charge was detected; and a melt boundary ring was observed surrounding a relatively flat or slightly rippled region. A melt ring can also be seen in figure 6 surrounding the boiled area.

The thin film samples showed qualitatively similar charge emission behavior to that of germanium. Only the damage threshold fluences were higher, and there was no melting-boiling distinction to be made. The most probable ion velocity squared (proportional to most probable kinetic energy) versus fluence is plotted in figure 7 for thorium fluoride thin films. Since we were unable to uniquely assign a mass to the ejected ions, the velocity data has not been converted to kinetic energy for the two types of thin film sample. Again, similar behavior for positive and negative ions was observed, and there was a noticeable onset fluence for charge emission. This emission onset was later correlated with the onset of microscopically visible damage to the thin films. In figure 8, most probable velocity squared is plotted versus ion flux. Much of the site-to-site fluctuation in kinetic energy was removed when the data was correlated in this way.

The behavior of magnesium fluoride thin films was very similar to that of thorium fluoride films. The damage and ion emission onset was higher, about 50 J/cm^2; and a smaller range of fluences was explored due to equipment limitations. It should be pointed out that this damage onset was not unreasonabley high considering the limited data set from which it was derived and the fact that the test was conducted with a relatively

small spot size at 1064 nm. A larger spot size or more data points would reveal the effect of sparsely distributed defects and lower the observed damage threshold. The onset of charge emission was again consistently correlated with microscopically visible damage. Most probable kinetic energy and peak ion flux for MgF_2 were also closely correlated, and the data are shown in figure 9. No deviation from the behavior of the other samples was observed.

4. Discussion

In these experiments on charge emission kinetics, we found that the triaxial charge collector was only able to detect charge emission when either damage occurred to a thin film or boiling occurred on germanium. These events were always accompanied by a visible flash which was never observed in the absence of a charge emission signal. We do know from previous experiments, however, that thin film samples emit positive and negative ions prior to damage at fluences down to 1/20 of the damage threshold [1,2]. The quantity of charge emitted below damage threshold was several orders of magnitude smaller than that emitted at damage. Hence, an apparent threshold behavior is not unexpected when lower sensitivity observations are made. The sensitivity of the triaxial collector seems to be limited by three factors: 1) limited solid angle of acceptance at the end of a field free drift region; 2) placement away from the sample surface normal; and 3) lack of gain or charge multiplication in the detection process. The removal of one or more of these limitations should allow the detection of pre-damage ion emission and the analysis of their energies.

In all cases, once charge emission was detected, the plasma was found to be approximately neutral and contain both positive and negative ions as well as electrons. Charge emission was always observed coincidently with either boiling for germanium or with surface damage on the thin films. This is entirely consistent with a laser melting model for the damage of semiconductors with nanosecond pulses where the photon energy is above the material's bandgap. In this model, pulses near threshold melt the surface and occasionally leave ripples. Higher fluence pulses are able to initiate boiling at the center of the melt region.

It was informative to observe the consistent correlation between most probable ion kinetic energy and the peak ion emission flux for all the samples. This suggests a plasma heating process which is strongly dependent on charge density. Fluctuations in the quantity of material ejected from the surface can cause correlated fluctuations in the ion kinetic energy even in the presence of a relatively constant laser fluence. This is further substantiated by the summary data in table 1 which shows data from all the samples near the charge emission onset. Using the most probable velocity in table 1 as a starting point, the most probable kinetic energy at emission onset is calculated assuming that the mass of the ion is that of the lightest constituent atom. Although the kinetic energy distributions are not particularly thermal in shape, the most probable kinetic energy can be fit to a Maxwell-Boltzmann distribution at a characteristic temperature. The temperaures obtained in this manner are shown in table 1 and are unrealistically high for surface temperatures. They are not, however, inconsistent with a laser heated plasma in which the ions and electrons are easily heated by the laser beam to nonequilibrium states. We conclude that the time-of-flight measurements in these experiments served to characterize the laser heated plasma above the sample surface which is observed as the damage flash. More detection sensitivity would be required to observe pre-damage emission and to characterize its kinetics.

This research was supported by the Texas Advanced Technology Research Program. Yong Jee acknowledges the support of a Department of Electrical and Computer Engineering Post Doctoral Fellowship.

5. References

[1] M.F. Becker, F.E. Domann, A.F. Stewart, and A.H. Guenther, "Charge emission and related precursor events associated with laser damage," Laser Induced Damage in Optical Materials: 1983, Natl. Bur. Stand. U.S. Spec. Publ. 688 (1983).

[2] F.E. Domann, M.F. Becker, A.H. Guenther, and A. F. Stewart, "Charged particle emission related to laser damage," Appl. Opt. 26, 1371 (1986).

[3] M.F. Becker, A.F. Stewart, J.A. Kardach, and A.H. Guenther, "Surface charging in laser damage to dielectric surfaces," Appl. Opt. 26, 805 (1987).

[4] A. Schmid, P. Braunlich, and P. Rol, "Multiphoton-induced directional emission of halogen atoms from alkali halides," Phys. Rev. Lett. 35, 1382 (1975).

[5] J. Reif, H. Fallgren, W.E. Cooke, and E. Matthias, "Wavelength dependence of laser-induced sputtering from the (111) surface of BaF_2," Appl. Phys. Lett. 49, 770 (1986).

[6] J. Reif, H. Fallgren, H.B. Nielsen, and E. Matthias, "Layer-dependent laser sputtering of BaF_2 (111)," Appl. Phys. Lett. 49, 930 (1986).

[7] J.M. Liu, R. Yen, H. Kurz, and N. Bloembergen, "Phase transformation on and charged particle emission from a silicon crystal surface, induced by picosecond laser pulses," Appl. Phys. Lett. 39, 755 (1981).

[8] Y.K. Jhee, M.F. Becker, and R.M. Walser, "Charge emission and precursor accumulation in the multiple-pulse damage regime of silicon," J. Opt. Soc. Am. B 2, 1626 (1985).

[9] A.L. Huang, M.F. Becker, and R.M. Walser, "Laser-induced damage and ion emission of GaAs at 1.06 microns," Appl. Opt. 25, 3864 (1986).
[10] I.N. Aleksandrov and T.T. Bykova, "Laser-induced ion emission from cadmium selenide," Sov. Phys. Tech. Phys. 25, 727 (1980).
[11] A. Namiki, K. Watabe, H. Fukano, S. Nishigaki, and T. Noda, "Behavior of positive ions ejected from laser-irradiated CdS," J. Appl. Phys. 54, 3443 (1983).
[12] W.J. Siekhaus, J.H. Kinney, and D. Milam, "Predamage threshold electron emission from insulator and semiconductor surfaces," Laser Induced Damage in Optical Materials: 1983, Natl. Bur. Stand. U.S. Spec. Publ. 688 (1983).
[13] W.J. Siekhaus, L.L. Chase, and D. Milam, "Temporal distribution of electron and ion emission caused by laser excitation of optical surfaces in ultra-high vacuum," Laser Induced Damage in Optical Materials: 1985, Natl. Bur. Stand. U.S. Spec. Publ. (1985).

Table 1. Emission kinetics at onset of charge emission

Sample and Specie	Emission Onset Fluence J/cm^2	Most Probable Velocity km/s	Most Probable Kinetic Energy[1] eV	Temperature[2] K x10^3
Ge +ions	1.1	4.3	7	81
-ions	1.0	4.0	6	70
ThF_4 +ions	22	16.0	25	290
-ions	20	13.4 (0.8)[3]	18 (6)[3]	210 (69)[3]
MgF_2 +ions	50	24	79	910

1 Assumes mass of ion is that of the lightest ion.
2 Assumes the most probable velocity is fit to a Maxwell-Boltzmann distribution.
3 Values for an anomalous event.

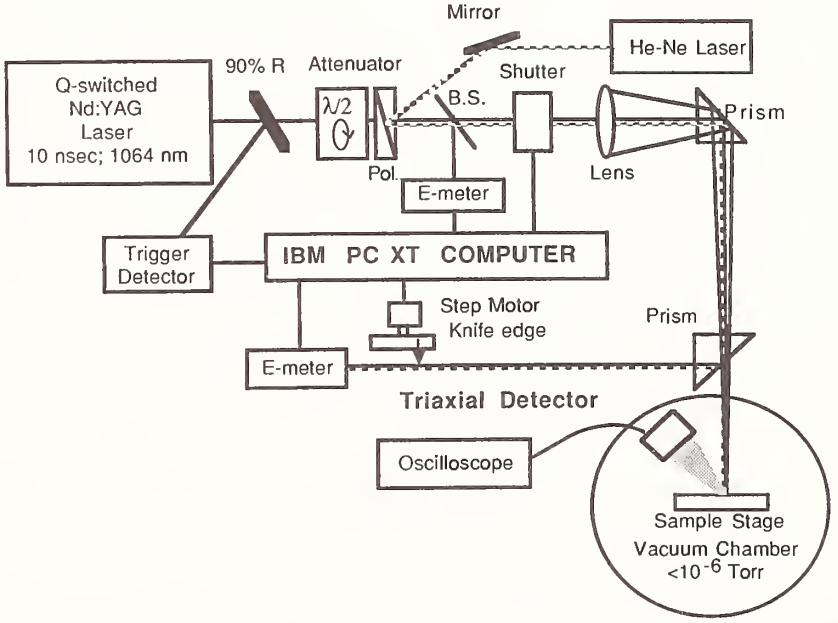

1. Optical experimental layout.

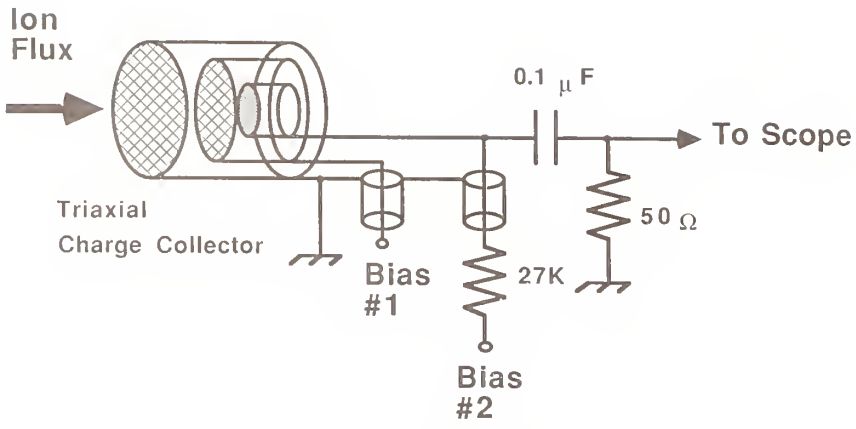

2. Diagram and electrical connection of the triaxial charge collector.

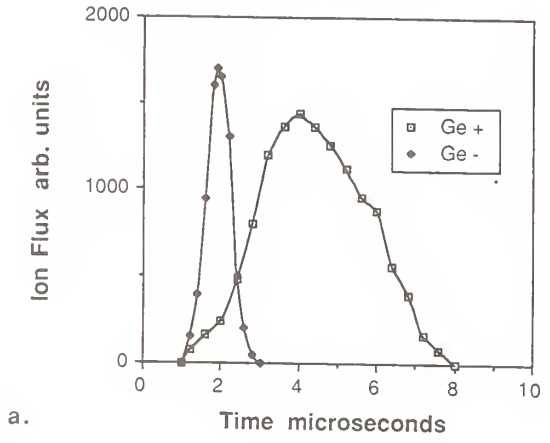

a.

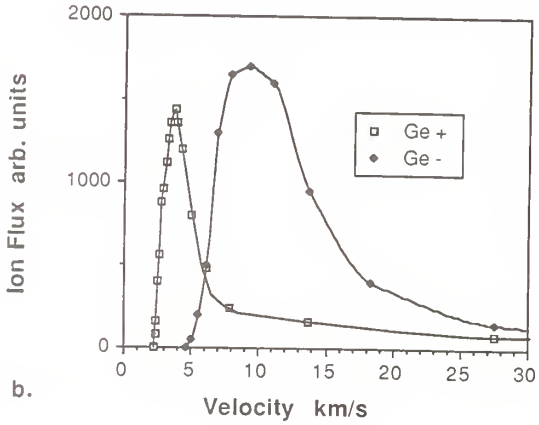

b.

3. Representative data for: a. ion flux versus time waveforms, and b. ion flux versus velocity, for positive and negative germanium ions.

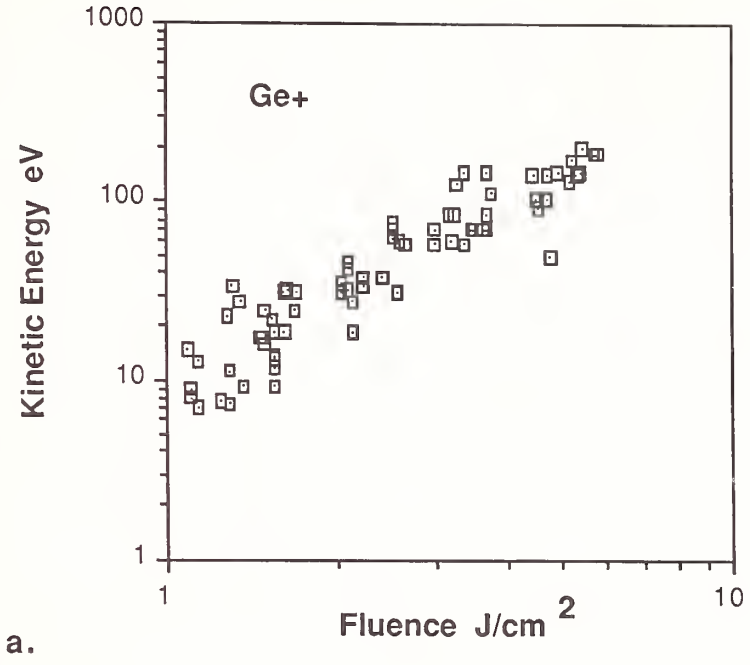

a.

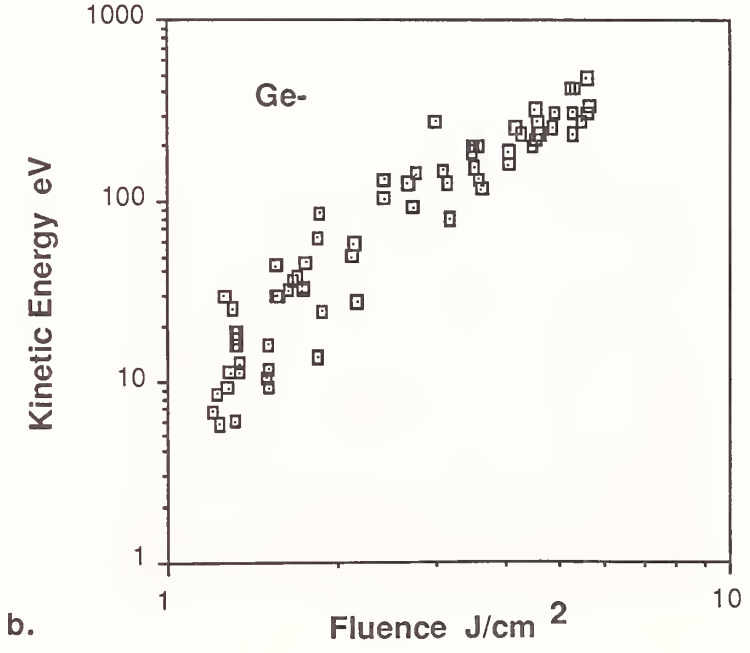

b.

4. Most probable ion kinetic energy versus laser fluence for germanium irradiated above the boiling threshold: a. positive ions; b. negative ions.

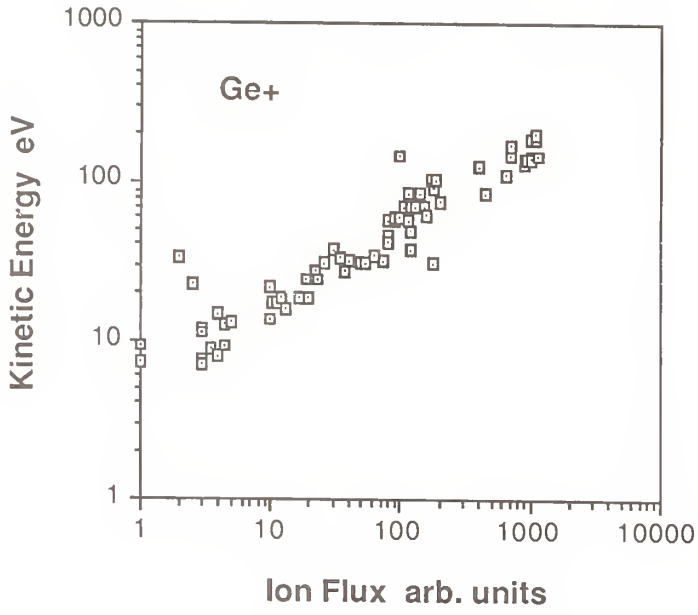

5. Correlation plot of most probable ion kinetic energy versus ion flux at the most probable energy for positive germanium ions.

6. Optical Nomarski micrograph at 200x of a germanium damage site showing a melt ring surrounding a boiled region at the beam center.

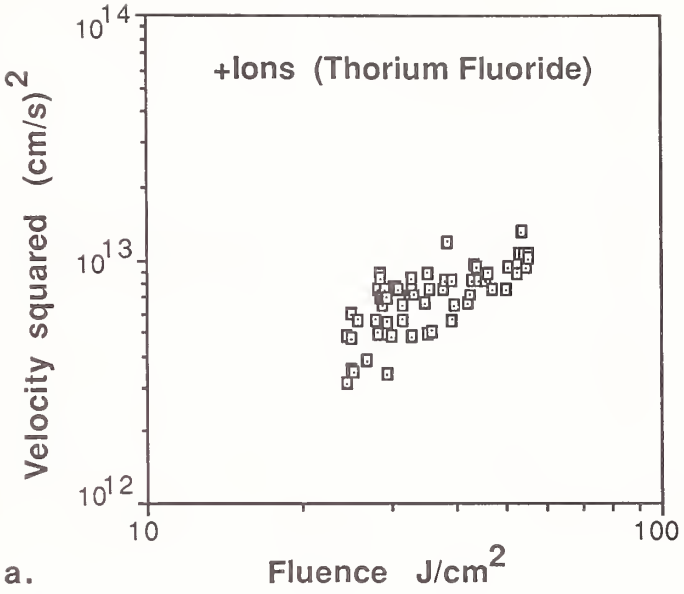

a.

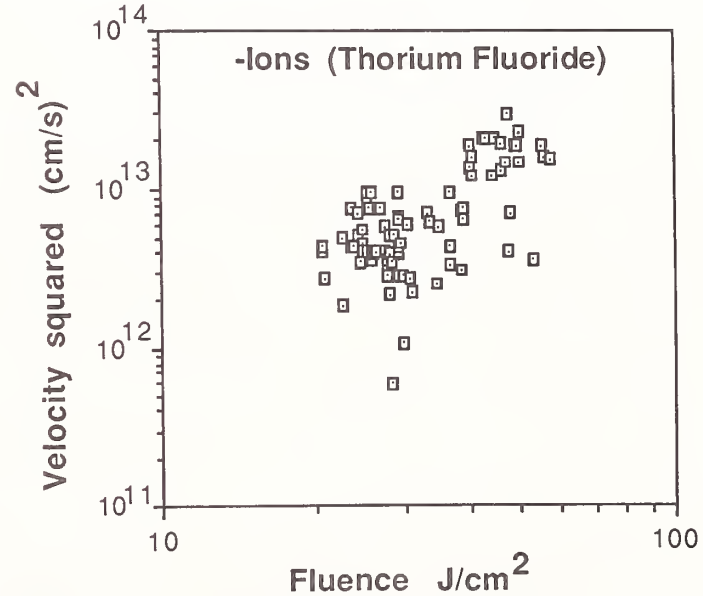

b.

7. Most probable ion velocity squared versus laser fluence for thorium fluoride thin films: a. positive ions; b. negative ions.

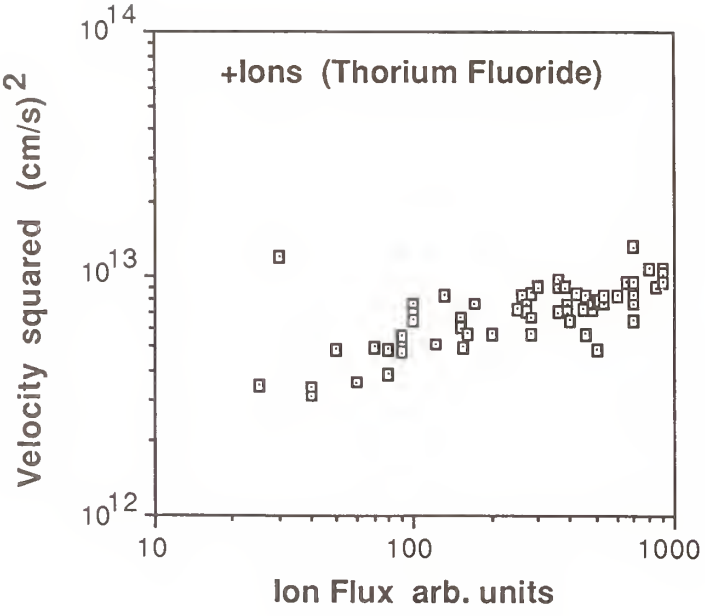

8. Correlation plot of most probable ion velocity squared versus ion flux at the most probable energy for positive ions emitted for thorium fluoride thin films.

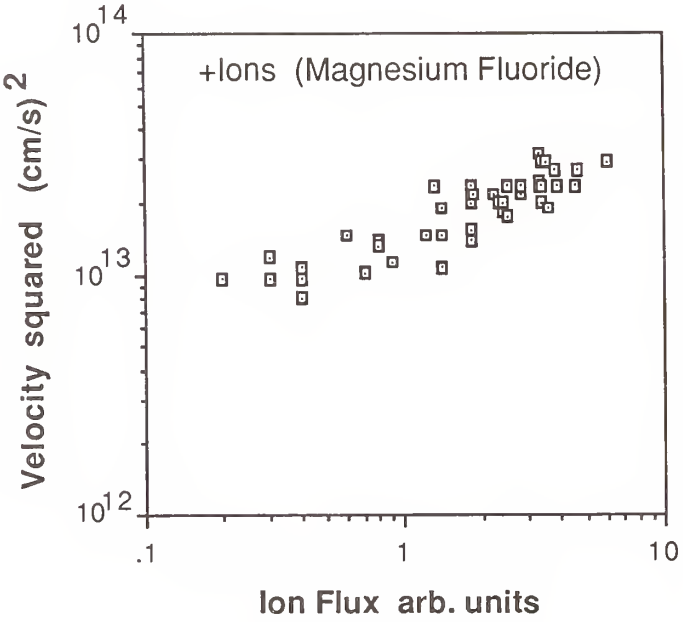

9. Correlation plot of most probable ion velocity squared versus ion flux at the most probable energy for positive ions emitted for magnesium fluoride thin films.

Manuscript Received
10-26-87

Laser Induced Desorption and Second Harmonic Generation from the (111) Surface of Barium Fluoride

J. Reif, H.B. Nielsen, O. Semmler, P. Tepper, and E. Matthias

Freie Universität Berlin, West Germany

and

E. Fridell, E. Westin, and A. Rosén

Chalmers University, Göteborg, Sweden

The desorption of positive ions from the (111) surface of BaF_2 induced by visible laser light with photon energies far below the bandgap (in the green (500-560 nm) and blue (410-440 nm) spectral regions) shows sharp resonances (~ 0.01 eV). Cluster calculations indicate that there exist occupied and excitonic surface states which facilitate resonant multiphoton photoemission from the surface. This, in turn, leads to a localized positive charge-up which results in the emission of positive ions. The influence of surface states seems to be present also in air judging from experiments on surface second harmonic generation which exhibit both a pronounced surface anisotropy and a wavelength dependent second harmonic yield.

Key words: BaF_2; surface ionization; ion emission; surface states; multiphoton processes

1. Introduction

Numerous studies in the past years [1] have evidenced that surface decomposition plays an important role in optical damage to laser components. However, the microscopic processes involved in surface breakdown are not yet well understood. One attempt to avoid damage is to optimize the polishing and cleaning of optical surfaces [1], assuming that granularity or dirt particles may under irradiation of sufficiently high laser intensities lead to extremely high local electrical fields and hence serve as seeds for the ignition of a plasma discharge which, in turn, leads to the destruction of the surface.

On the other hand, it has been shown that intense laser radiation can induce defects in the bulk of transparent media, such as color centers. These may then migrate to the surface and subsequently lead to decomposition [2,3].

In this contribution we present evidence that resonantly enhanced multiphoton absorption at the surface of divalent ionic crystals can lead to desorption of positive ions already at laser intensities far below the commonly quoted breakdown threshold [3,4,17] for these optical materials. This effect may be considered as a precursor step for surface damage. We show that the process strongly depends on the existence of occupied and excited states in the bandgap of a non-stoichiometric surface.

For our investigations [5], we have hitherto chosen the (111) surface of bariumfluoride as a prototype material, which can be used for optical components in the VUV and IR. In the following, we first describe the result of cluster calculations, which predict the existence of surface states. Then we demonstrate experimental proof of this prediction by resonant multiphoton ionization and subsequent emission of positive ions from the surface. Finally we report on first results from experiments on surface second harmonic generation which yield information about the electronic surface structure in an ambient gas atmosphere.

2. Cluster Calculations

Modelling a crystal surface by a planar cluster in an embedding potential is one way to calculate surface properties starting from microscopic molecular principles [6]. In our case of BaF_2 (111) we use a 10-atom planar cluster in C_{3v} geometry (see Fig. 1) to present the non-stoichiometric barium rich surface. We do so, since we assume an appreciable number of loosely bound upper layer fluorine atoms to be lost during the surface preparation, i.e. by cleaving the crystal.

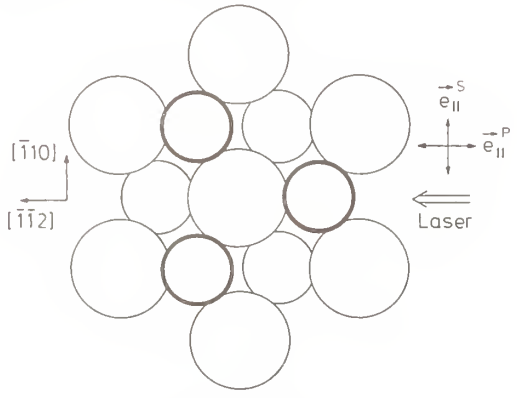

Figure 1.
Schematic representation of the BaF_2(111) surface (large circles: barium; small circles: fluorine). In the non-stoichiometric 10-atom cluster, used in the calculations, the three fluorines (bold circles) above the barium plane are missing.

For the calculations we used the discrete variational embedded cluster method with the potentials determined by the local density approximation. A detailed description of the technique can be found in the literature [7]. In short, the molecular wavefunctions were expanded as linear combinations of atomic orbitals (LCAO-method) for the constituent ions in the cluster, with the addition of some virtual orbitals, i.e. $Ba^{++}(Xe6s^0 6p^0 5d^0)$ and $F^-(1s^2 2s^2 2p^6 3s^0)$. The effect of the surrounding crystal lattice is taken into account by the potential of a half-sphere consisting of 21 Ba^{++} and 41 F^- ions. The molecular potential as well as this embedding potential were constructed using an expression for the exchange and correlation energy which is derived from a homogeneous electron gas [8].

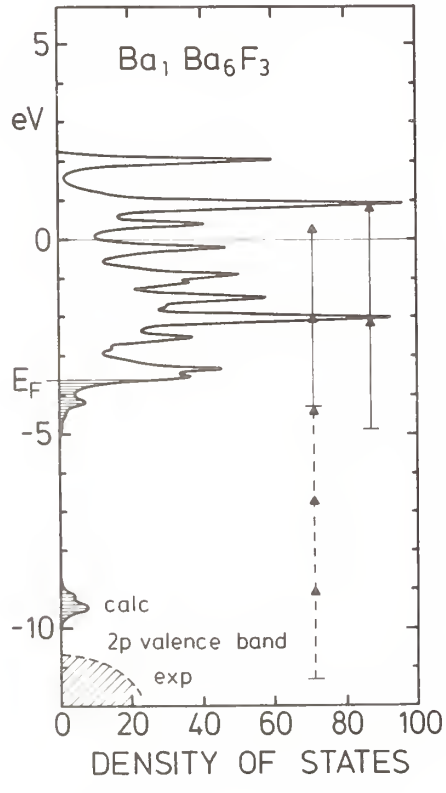

Figure 2.
Density of states obtained from the calculations for a non-stoichiometric 10-atom cluster representing BaF_2 (111). The arrows indicate possible multiphoton interactions for green (left) and blue (right) light. Also indicated is the experimentally found position of the 2p valence band [9] (shaded: occupied levels).

The results of the calculations are illustrated by a density of states plot (DOS) in figure 2. This curve is obtained when each molecular energy level is arbitrarily broadened with a Lorentzian lineshape of 0.1 eV width. Relaxation is taken into account for an ionizing excitation from the level corresponding to the F(2p) band. The most important result of these calculations is the prediction of occupied surface states and a rich structure of unoccupied states in the middle and in the upper half of the bandgap, respectively. As a check, calculations for a cluster representing the crystalline bulk revealed no occupied states in the middle of the bandgap. It must be stated here, however, that these results are up to date only qualitative in nature.

In order to probe the existence of such a predicted electronic structure and to reveal its relation to laser-induced damage processes in transparent materials, two principally different approaches were followed experimentally.

1) In ultra-high vacuum, laser-induced emission of electrons and ions from in situ cleaved, clean BaF_2 (111) surfaces was investigated.

2) In air, we measured the second harmonic of the incident laser frequeny, generated in reflection at a polished BaF_2 (111) surface [10,11].

3. Experiments on Ionization and Desorption

A comparatively simple set-up was used in all experiments. The light from a pulsed tunable dye laser pumped by the third harmonic of a Nd:YAG laser, or the second harmonic of the Nd:YAG laser itself was weakly focused onto the sample to give a pulse intensity of less than 50 MW/cm² at a pulse duration of about 8 ns and a repetition rate of 10 Hz. The actual intensity of the linearly polarized laser could be varied by rotating a half-wave retarding Fresnel-rhomb in front of a Glan linear polarizer, thus conserving a well defined linear polarization and spatial distribution of the laser beam. For the experiments on electron and ion emission, high purity single crystals of BaF_2 (manufacturer: Karl Korth, Kiel) were kept in ultra-high vacuum (about $5x10^{-10}$ hPa) and *in situ* cleaved for each set of experiments. This procedure was hoped to prepare a reproducible and clean surface. The angle of incidence was about 70°, and care was taken that no transmitted or reflected high intensity light hit the metal parts of the vacuum chamber. Electrons and ions emitted from the surface could be analyzed by a quadrupole mass spectrometer or a biased grid system and were detected by an electron multiplier. By use of an additional ionizing current the mass spectrometer was also sensitive to the emission of neutrals.

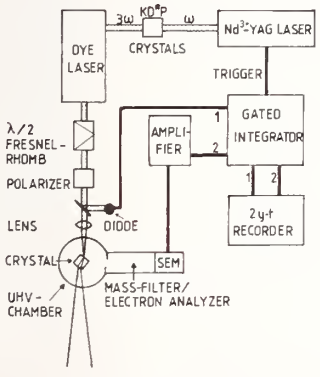

Figure 3.
Set-up for the experiments in ultra-high vacuum.

In all experiments, the signals from the detectors as well as from beam monitoring photodiodes were processed by gated integrators and then recorded.

When shining the unfocused light of the frequency doubled Nd:YAG laser at 532 nm onto the sample, already for an average intensity of 6 MW/cm² the desorption of neutral fluorine (F^0) could be observed. However, it ceased within about 20 s under constant irradiation. When the intensity was slightly increased, the signal reappeared and died out again with the same time constant. This could be repeated for increasing intensities up to a point where visible damage occured and $F^{(0)}$ came off the surface for longer periods (cf. Fig. 4). No time correlation between individual laser pulses and the fluorine emission could be established by means of gated signal processing. Until present, we do not know whether this is a sign for thermal desorption or whether it is due to apparative effects, such as insufficient pump speed for fluorine.

However, this experiment provides a first indication, that our assumption of a non-stoichiometric surface is reasonable since the upper fluorine layer is easily desorbed from the

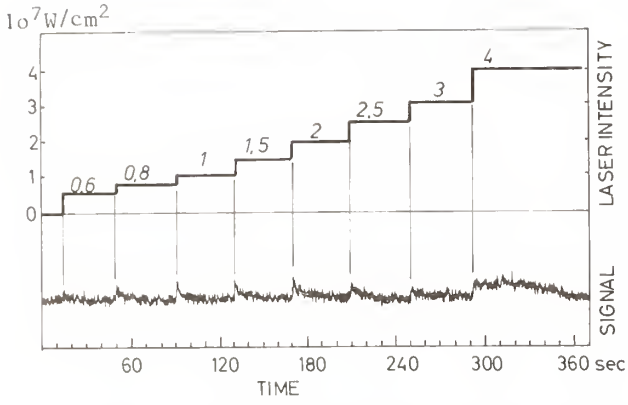

Figure 4.
Emission of neutral fluorine from BaF_2 (111) under constant irradiation with 532 nm light at a pulse rate of 10 Hz and increasing average intensity. For the relatively low apparent damage threshold it should be noted, that the Nd:YAG laser beam in this experiment contained hot spots with an intensity at least 10 times higher than the average, and damage only occurred at these spots.

surface. In order to substantiate the findings of the cluster calculations, we then performed experiments with a tunable dye laser in the blue (stilbene 410...450 nm) and green (coumarine 152; 500...560 nm) spectral ranges.

3.1 Ion emission under blue dye laser irradiation

When focusing the blue dye laser onto the sample to give an intensity of about 50 MW/cm², we observed the emission of the positive ions Ba^+, F^+, $(BaF)^+$, and Ba^{++}, time-correlated to the individual laser pulses. When the laser was continuously pulsing at a fixed wavelength, we again observed a rapid decrease of the ion signal, as is shown in Fig. 5.

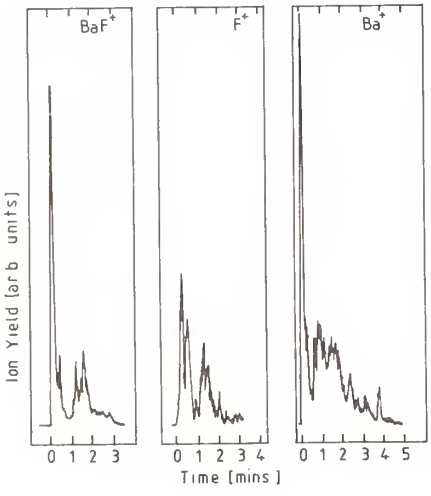

Figure 5.
Emission of positve ions from BaF_2 (111) under continuously pulsing laser irradiation at 429 nm (=2.9 eV) (pulse energy 50 MW/cm², repetition rate 10 Hz).

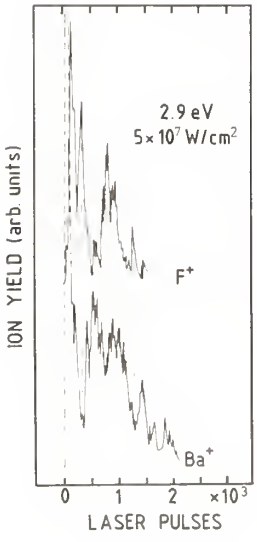

Figure 6.
Comparison of the decrease of the Ba^+ and F^+ signals with irradiation time. The dashed-dotted lines are drawn to emphasize the anticorrelation of Ba^+ and F^+ emission.

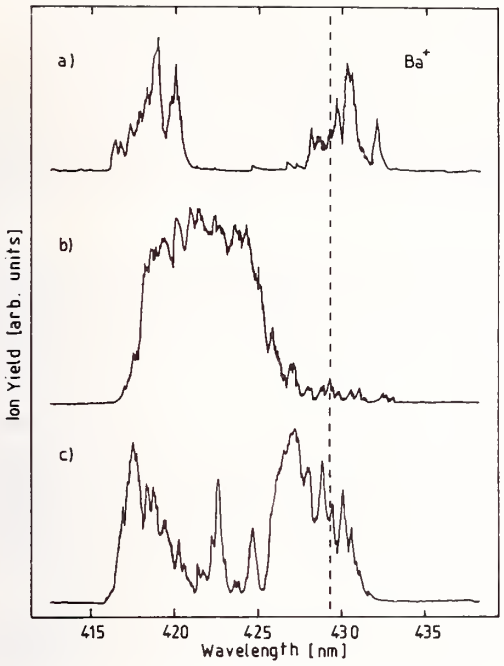

Figure 7.
Emission of Ba^+ as a function of incident laser wavelength at constant laser intensity over the entire scan (50 MW/cm²). a), b), and c) represent three consecutive scans at the same interaction spot under identical conditions. The dashed line represents the laser wavelength used for the results of Figs. 5 and 6

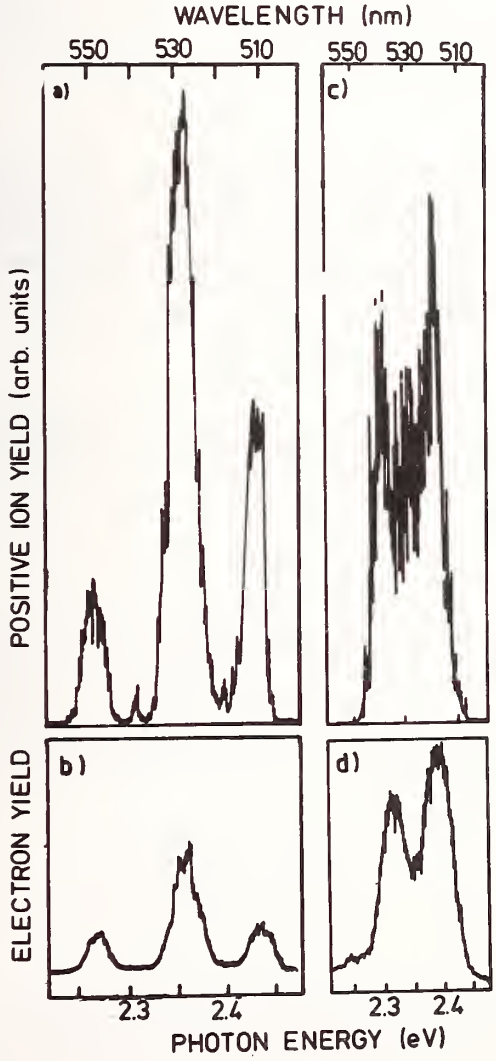

Figure 8.
Positive ion (a,c) and electron (b,d) yields from BaF_2 (111) as a function of green laser wavelength (laser intensity about 5 MW/cm²). In (a,b), the projection of the laser polarization onto the surface is parallel to the $[\bar{1}\bar{1}2]$ direction, in (c,d) it is parallel to $[\bar{1}10]$ (cf. figure 1).

By comparing the results for F^+ and Ba^+ (cf. figure 6), one observes a strong anticorrelation, giving rise to the assumption of layer-by-layer ablation [12]. This is further supported by the result shown in Fig. 7. The dependence of the ionization signal on the laser wavelength changes from scan a) to b) and about recovers in scan c). There are two important points about this result: Firstly, the pronounced resonance structure is in good qualitative agreement with the predictions of our theoretical model [13]. Secondly, the change in chemical environment by taking away one layer of F^+ resp. Ba^+ changes the fine structure of the spectrum, i.e. the energy of the surface states involved.

It should be noted here, that we also searched for the emission of neutral barium. However, the results with the additional ionization current on and off did not differ significantly, which means that either the desorption of Ba^0 is rather weak or the atoms immediately condense at cooler nearby surfaces.

3.2 Ion and electron emission under green dye laser radiation

With the green dye laser, we again obtained a pronounced wavelength dependence of the ion signal (cf. figure 8). By a more sensitive detection scheme, using biased grids instead of the mass filter, we were able to measure the ion signal at substantially lower laser intensities, i.e. in Fig.8 at 5 MW/cm^2. Thus, we avoided the rapid bleeding out of the signal (cf. figures 5,6) and obtained reproducible results from a single interaction spot over long periods of time. Also, by changing the bias polarity, we were able to measure electrons instead of ions. There were no negative ions emitted from the surface. They could easily have been distinguished from electrons by their substantially longer flight time to the detector. The electron yield also shows a pronounced dependence on laser wavelength which is practically identical to that for positive ions, as can be seen from figure 8.

Apparently, the spectral fine structure depends strongly on the azimuthal direction of the laser polarization. This probably reflects the symmetry of the excited electronic states in their surrounding crystal field.

4. Discussion of Results

The photon energies in the blue and green spectral regions are not sufficient to overcome the bandgap of about 10 eV of the optically transparent material. Even if one takes into account the theoretically predicted occupied surface states in the middle of the bandgap (figure 2), the energy of one photon does not suffice to ionize electrons from the surface. However, the combined energy of several photons does. If we measure the intensity dependence of the ionization signals at a fixed wavelength, we find that ionization and desorption are indeed multiphoton processes (fig. 9).

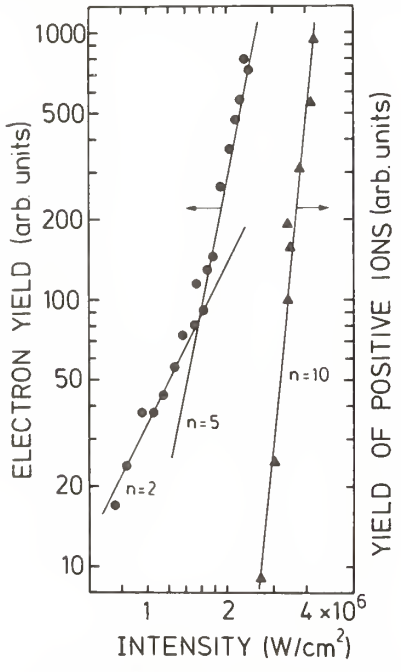

Figure 9.
Intensity of electron (dots) and ion (triangles) yields at a laser wavelength of 518 nm. The solid lines indicate the number of photons involved.

From lowest order perturbation theory, which certainly holds in our case since the resonances are extremely broad compared to atomic physics, the yield in an n-photon process is generally found to be proportional to the n-th power of the input intensity. Thus, for electrons we find that

2 photons are required at lower intensities, while for higher intensities the ionization is a five-photon process (dynamic resonances should play no role in this intensity range). The low intensity result confirms the theoretical prediction of occupied surface states in the middle of the bandgap. The five-photon absorption most probably originates from the valence band (cf. the arrows in figure 2). The conspicuous resonance structures must then be due to enhancement by the empty surface states. We found in our experiments, that the electron yield spectra do not change in shape when going from a two- to a five-photon process. Hence, the resonant steps must be identical in both cases.

For the ion emission, we find that 10 photons are necessary to create one ion. On the other hand, from the evident similarity of the yield spectra, we find that intrinsically the same absorption process should lead to both electron and ion emission. Our conclusion from this is, that two electrons must be emitted to set free one ion. This idea is supported by the fact, that a pure 10-photon-process should originate far below the Ba (5p) band, which is located at a binding energy corresponding to 8 photons [9]. Following a recent theory of Itoh and Nakayama [15], two adjacent holes, generated by ionization of two electrons, may concentrate on a fluorine ion. Their combined energy should be about twice the bandgap, i.e. 21.4 eV [9]. This would be sufficient to reverse the charge of the free negative fluorine ion, which requires about 20.8 eV and certainly can be taken as an upper limit for the bound ion. Consequently, the combination of two holes would make the surface electrostatically instable and would result in Coulombic expulsion of positive ions from the surface. Since we observe only positive ions, this hypothesis appears rather plausible.

In order to confirm this model, we present a rough estimation of the probability for finding two holes created simultaneously at adjacent positions. The estimate is based on lowest order perturbation theory.

The number N_k of electrons emitted per laser pulse by a k-photon absorption is given by [16]

$$N_k = \frac{N_o}{k-1}\,\sigma_k\,\frac{n^k}{\tau^{k-1}} \qquad (1)$$

where N_o denotes the number of absorbers, $\sigma_k[cm^{2k}\ s^{k-1}]$ is the k-photon cross section, $n\ [cm^{-2}]$ is the photon flux per laser pulse and $\tau[s]$ accounts for the pulse duration.

For non-resonant processes we take from the literature

$$\sigma_2 \simeq 10^{-50}\ cm^4\ s \qquad [16,17]$$

and $$\sigma_5 \simeq 10^{-140}\ cm^{10}\ s^4 \qquad [3,17] \qquad (2a)$$

Experimentally, we find that $N_2 = N_5$ at an intensity of 1.6×10^6 W/cm², corresponding to $n \simeq 2.7 \times 10^{16}\ cm^{-2}$. Applying Eq.(1) and assuming Bepp's two-photon cross section $\sigma_2 \simeq 10^{-50}\ cm^4 s$ [16], we obtain

$$\sigma_5 \simeq 10^{-123}\ cm^{10} s^4 \qquad (2b)$$

which is in strong disagreement with earlier observations [3,17]. We must, however, take into account that we observe strong resonances. If we assume, like indicated in figure 2, that in the two-photon process both photons and in the five-photon process the last two-photons are each resonant, we have to modify the cross sections. Because of the relatively large width of the resonances, lowest order perturbation theory may still be applied. Then, the k-photon cross section is given by the square of the k-photon transition matrix element between ground state $|g\rangle$ and final state $|f\rangle$

$$\sigma_k \propto \left|\langle f|U^{(k)}|g\rangle\right|^2 \qquad (3)$$

which can be rewritten in the form [18]

$$\sigma_k \propto \left|\frac{d^k}{\prod_{\nu=1}^{k}\left[(\Omega_\nu - \nu\omega + \frac{i\Gamma_\nu}{2})\right]}\right|^2 \qquad (4)$$

Here d is a generalized transition dipole moment, Γ the width and $\hbar\Omega$ the energy of the ν-th real intermediate state, and $\hbar\omega$ the photon energy. For the resonant processes we obtain from this

$$\sigma_2^{res} \propto \frac{4d^4}{(\hbar\Gamma)^2} \tag{4a}$$

and $$\sigma_5^{res} \propto \frac{16d^{10}}{(\hbar\Gamma)^4(\hbar\omega)^2(2\hbar\omega)^2} = \frac{4d^{10}}{(\hbar\Gamma)^4(\hbar\omega)^4}$$

where the width Γ of all intermediate states is assumed to be equal (see also fig. 8). This has to be compared to the nonresonant case (with $\hbar\Omega \simeq k(\hbar\omega)$)

$$\sigma_2^{non} \propto \frac{d^4}{(\hbar\omega)^2} \tag{4b}$$

and $$\sigma_5^{non} \propto \frac{d^{10}}{(\hbar\omega)^2(2\hbar\omega)^2(3\hbar\omega)^2(4\hbar\omega)^2} = \frac{d^{10}}{576(\hbar\omega)^8}$$

From the experiment, we find the ratio $\omega/\Gamma \simeq 100$ (cf. figure 8). Hence we obtain the ratios

$$\frac{\sigma_2^{res}}{\sigma_2^{non}} = 4\left(\frac{\omega}{\Gamma}\right)^2 = 4 \times 10^4 \tag{5}$$

and $$\frac{\sigma_5^{res}}{\sigma_5^{non}} = 2304\left(\frac{\omega}{\Gamma}\right)^4 \simeq 2.3 \times 10^{11}$$

By combination with Eq.(2a) this yields

$$\sigma_2^{res} \simeq 4 \times 10^{-46}\ cm^4\ s \tag{6a}$$

and $$\sigma_5^{res} \simeq 2.3 \times 10^{-129}\ cm^{10}\ s^4$$

whereas the procedure of Eq.(2b) with σ_2^{res} gives

$$\sigma_5^{res} \simeq 4 \times 10^{-119}\ cm^{10}\ s^4 \tag{6b}$$

The two cross sections still differ by ten orders of magnitude. If we consider, however, that a surface is a highly complex system, we inevitably have to take collective effects on all electrons into account [19], which become more effective the more photons are involved and therefore will further increase σ_5^{res}. We also expect that the density of states in the F(2p) band is considerably higher than that of the surface states, thus affecting N_0 in Eq.(1). If we incorporate that into the cross section instead, we estimate (6b) should be a reasonable approximation for the ionization cross section at higher intensities . With this cross section and Eq.(1), the number of electrons emitted from the interaction spot per pulse at the threshold intensity for ion detection (2.8×10^6 W/cm^2 corresponding to 4.7×10^{16} photons/cm^2) is given by:

$$N = 5.5\ N_0 \times 10^{-4} \tag{7}$$

Likewise, the probability of emitting two electrons from close to each other may be approximated by the square of the one electron probability, i.e.

$$P(2e^-) \simeq \left(\frac{N}{N_0}\right)^2 \simeq 3 \times 10^{-7} \tag{7a}$$

In order to evaluate the number of irradiated atoms susceptible to resonant multiphoton ionization, we assume that the abundancy of non-stoichiometric surface spots is of the order of 10^{-6}. Then, for a laser spot of 1 mm^2 and a geometrical cross section of about 5×10^{-14} mm^2, we

obtain $N_0 \simeq 2 \times 10^7$ and

$$N(2e^-) \simeq 6 \qquad (7b)$$

as the number of paired holes per laser pulse. When the electrons are emitted simultaneously, shielding effects disturbing the spectral structure of the surface states only play a minor role. For a sequential emission of two electrons only the first one must show a pronounced spectral dependence for the resultant ion emission to obey the same wavelength correlation. Furthermore, diffusion of holes can only increase the occurence of paired holes. From all this, the proposed mechanism of positive ion emission appears plausible.

5. Surface second harmonic generation

The experiments described so far had to be performed in ultra-high vacuum to guarantee clean surfaces and to assure easy detection of ions and electrons. Naturally, it is of interest to test whether the observed influence of surface states also persists in gaseous environment, where the surface is likely to be covered by a gas layer. In order to obtain this spectroscopic information, we use in our laboratory the generation of reflected surface second harmonic generation.

5.1 Second harmonic generation at the surface of a cubic medium

The interaction of light with matter is characterized by a resulting polarization **P** which is connected to the electric light field **E** by the susceptibility χ

$$\mathbf{P}(t) = \chi\, \mathbf{E}(t) \qquad (8)$$

If the intensity of the driving field becomes stronger, the response of the matter is no longer linear, and the polarization may be expanded in a power series of the electric field

$$\mathbf{P}(t) = \chi\, \mathbf{E}(t) + \chi^{(2)}:\mathbf{E}(t)\mathbf{E}(t) + \chi^{(3)}:\mathbf{E}(t)\mathbf{E}(t)\mathbf{E}(t)+\ldots \qquad (9)$$

where the expansion coefficients $\chi^{(k)}$ are tensors of rank (k+1) since **E** and **P** are vectors. In the electric dipole approximation, even terms vanish in a medium with inversion symmetry for parity reasons. Hence, for a cubic crystal like barium fluoride there should be no second order polarization which is the origin for second harmonic generation. However, Bloembergen et al. [20] demonstrated that nonetheless second harmonic generation occurs as well at the surface due to the electric field discontinuity as in the bulk due to the electric quadrupole and magnetic dipole interactions. In a more complete derivation, Shen and collaborators [21] have shown recently, that there occur also surface contributions in dipole approximation because of the broken symmetry at the surface. Obviously, the dipole contribution is most interesting for spectroscopic investigations because it images local electronic wavefunctions at the surface [22]. By applying Bloembergen's formalism [20], one can show that the bulk contributions as well as the effect due to the field discontinuity normal to the surface vanish for the electrical vectors of both fundamental and second harmonic being perpendicular to the plane of incidence (s-polarization), i.e. being parallel to the surface [23]. Experiments under this condition are, however, subject to a forthcoming publication [24]. Here, we restrict ourselves to experiments with projected polarization components normal to the surface (e.g. 45° polarization or p-polarization), for which the signal is at least one order of magnitude stronger than for s-polarization (about 10^{-13} times the fundamental).

5.2 Experiments on barium fluoride

For the experiments on second harmonic generation, the sample was a polished slice of the crystal described above, mounted in air in order to maintain easier manipulation. The generated second harmonic light was separated from the fundamental by means of optical filters and a dispersive prism and could be analyzed by a linear polarizer and a monochromator. It was detected by a solar blind photomultiplier with Cs-Te cathode.

As early as 1968, Wang and Duminsky [25] observed second harmonic generation of ruby laser light at the surface of BaF_2. Since then, the substance has not attracted much attention. In our experiments, starting with the second harmonic of the Nd:YAG laser at 532 nm as a fundamental, we obtained a conversion efficiency which was about three orders of magnitude higher than at 694 nm, indicating a resonance enhancement like the one observed for the emission of electrons and ions.

In the experiments great care has to be taken to make sure that one really observes the second harmonic generation and not generates a plasma at the surface which may also emit radiation in the wavelength range of the second harmonic. This is demonstrated in Fig. 10.

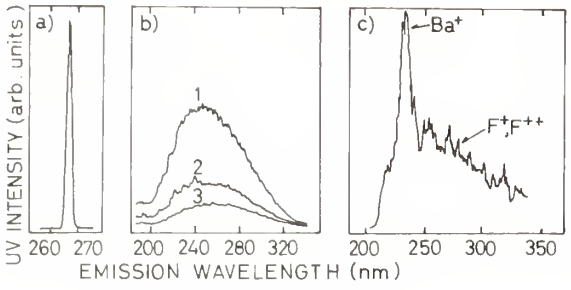

Figure 10.
Spectra for UV emission from the surface of BaF_2 in air irradiated by 532 nm laser light.
a) Second harmonic generation at a cleaved (111) surface (laser intensity ~40 MW/cm²). The observed linewidth is given by the resolution of the monochromator, the line itself is as narrow as the laser bandwidth.
b) Radiation from a plasma generated at a cleaved (111) surface (laser intensity ~40 MW/cm²). The signal is about 10 times stronger compared to (a).Traces (1), (2), and (3) denote successive scans after 0, 12, and 18 min of continued irradiation at 10 Hz.
c) UV emission generated by irradiating BaF_2 powder at an intensity of about 100 MW/cm².

Second harmonic generation only depends on the induced nonlinear polarization. The emitted wavelength must be exactly half that of the fundamental, and the bandwidth is determined by that of the fundamental. Plasma generation, on the other hand, results in the presence of a larger number of excited ions. These may release their energy by radiating at many different eigenfrequencies, giving rise to a broadband emission as in figure 10b). An experiment on bariumfluoride powder, where the laser radiation burned a hole into the sample, reveals the origin for the broadband radiation by showing pronounced emission lines of the excited ions involved (Fig. 10c). For the fundamental intensity the transition range between second harmonic generation and plasma ignition is narrow. It depends on individual spot characteristics which are not known in detail and must be subject of further investigations. The intensity dependence of both processes confirms the two-photon process for second harmonic generation whereas the plasma generation varies with the fifth power of the laser intensity, similar to the electron emission observed in ultra-high vacuum (cf. section 3.2). Similar to the experiments with the blue dye laser (cf. section 3.1) at about the same intensity, the plasma signal dies out with ongoing irradiation, indicating a change in the surface properties, whereas the second harmonic signal remains constant with time. In summary, we found that the laser intensity should be less than 20 MW/cm² to make sure no plasma radiation is observed. The only way to increase the second harmonic intensity is then to increase the size of the interaction spot.

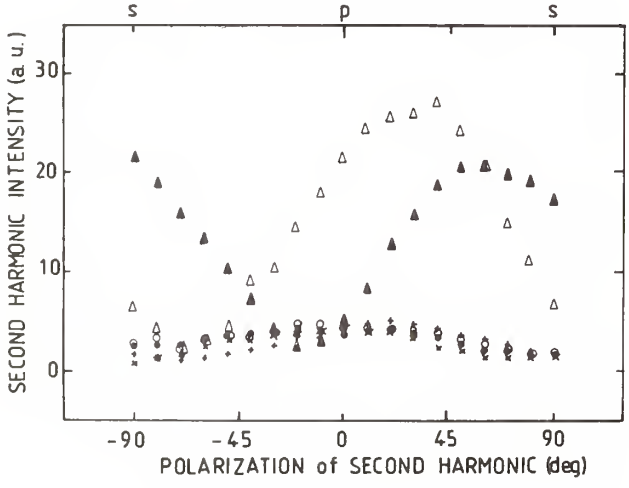

Figure 11.
Polarization of second harmonic for different fundamental polarizations; crosses: s-polarized, circles: p-polarized, triangles: 45° polarized. The azimuthal orientation for full symbols differs by 90° from that for open symbols.

When we analyzed the degree of polarization of the second harmonic light for three different polarizations of the fundamental (s,p, and 45°), we found a different behavior for two azimuthal orientations differing by 90° (open and full symbols in figure 11). This is a result of the rotational anisotropy (cf. figure 1) of the surface and transforms into the result of figure 12, when both polarizations are kept fixed and the crystal is rotated about its normal.

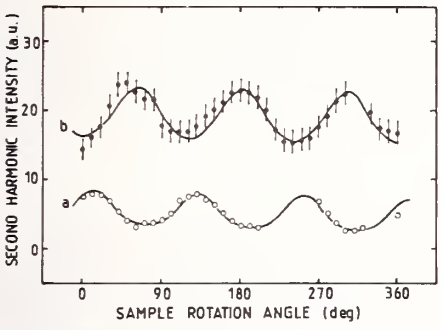

Figure 12.
Second harmonic intensity as a function of the rotation angle when the sample is rotated about its normal.
a) s-polarized fundamental, p-polarized second harmonic
b) 45°-polarized fundamental, 30°-polarized second harmonic to give maximum signal.

Only the dipole contribution may be anisotropic, whereas the normal-to-surface field gradient contribution should be isotropic because there should be no effect on the gradient within the dimension of one wavelength. When the non-linear polarisation contains both contributions, as is the case in fig. 12a) and b), the angular dependence of the second harmonic field amplitude is given by [26].

$$E_{SH} \propto A + B \cos 3\varphi \qquad (10a)$$

and the intensity by

$$I_{SH} \propto |A+B \cos 3\varphi|^2 \qquad (10b)$$

with A being the isotropic contribution, B the anisotropic part and φ the angle of crystal rotation. The solid lines in figure 12, obtained by this formula, fit the experimental data well. The fit parameters A and B confirm the above assumption that only the dipole part of the signal is sensitive to the anisotropy. In both fits, B is about equal, whereas the isotopic part for curve b) is twice that for curve a), corresponding to the increased role of the normal-to-surface component. This shows also that the increase in total signal for the b)-situation does not originate from the pure surface dipole contribution.

When we used the green dye laser to measure the dependence of the second harmonic generation on the fundamental wavelength, we found several very narrow resonances on a broad background spectrum (figure 13). From fluorescence spectra these spikes were identified as flare-ups of plasma emission. They were very reproducible for one specific sample but did not appear with others. A tentative interpretation is that on this specific sample there exists an adsorbate layer which facilitates absorption of the fundamental or second harmonic at certain wavelengths and thus triggers the ignition of a plasma.

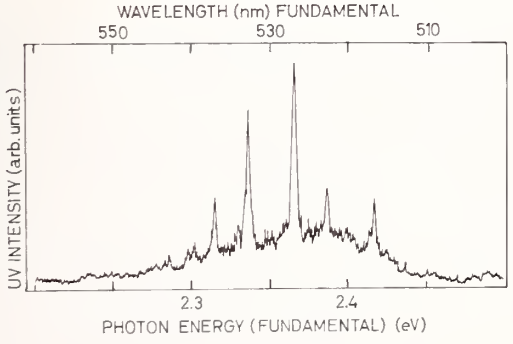

Figure 13.
Excitation spectrum for second harmonic generation. The resonances reflect the onset of plasma radiation. They are very reproducible in wavelength, but only appear on one specific sample.

6. Conclusion

In this paper we demonstrate the importance of intrinsic surface states at non-stoichiometric surfaces of optical materials. They strongly enhance the probability of multiphoton processes. These lead for visible light at intensities far below the damage threshold to ionization and ion desorption. The latter is a precursor of surface decomposition eventually terminating in the generation of a plasma and optical damage. By using second harmonic generation, we have found an indication that these surface states are not only present on clean freshly cleaved surfaces, but also in air on polished surfaces. This leads to the conclusion that, in order to increase the damage threshold for optical components, it is necessary (1) to avoid certain wavelengths which would be multiphoton resonant and (2) to prepare stoichiometric surfaces with as little impurity contaminations as possible.

5. Acknowledgements

This work was supported by the Deutsche Forschungsgemeinschaft, Sfb 6 and Sfb 161 (expired), the Swedish Natural Science Research Council, and the Swedish Board for Technical Development. One of us (J.R.) wants to thank Prof. N.H. Tolk at the Vanderbilt University, Nashville, TN, for his hospitality during the preparation of this resumé. We gratefully acknowledge the technical assistance of E. Arndt, and many fruitful discussions with Dr. P. West. We also want to express our thanks to S. Lemma and Mrs. D. Mallwitz for the final realization of this manuscript.

References

[1] see the proceedings of the previous Boulder conferences on **Laser Induced Damage in Optical Materials**, quoted in the introductory article to this volume by H.E. Bennett, A.H. Guenther, D. Milam, and B.E. Newnam
[2] A. Schmid, P. Bräunlich, and P.K. Rol; Phys.Rev.Lett. 35, 1382 (1975);
R. Smoluchowski; Phys.Rev.Lett. 35, 1385 (1975)
[3] P. Bräunlich, A. Schmid, and P. Kelly; Appl. Phys. Lett. 26, 150 (1975)
[4] F. Rainer, W.H. Lowdermilk, and D. Milam; NBS Special Publication 669, 157 (1984)
[5] J. Reif, H.B. Nielsen, O. Semmler, E. Matthias, E. Westin, and A. Rosén; Physica Scripta 35, 532 (1987)
[6] N.C. Amaral, B. Maffeo, and D. Guenzburger; Phys. Stat. Sol.(b) 117, 141 (1983)
[7] A. Rosén, E. Westin, E. Matthias, H.B. Nielsen, and J. Reif; to be published in Physica Scripta
[8] U. von Barth and L. Hedin; J. Phys. C5, 1629 (1972)
[9] W. Pong, C.S. Inouye, and S.K. Okada; Phys.Rev.B18, 4422 (1978)
[10] N. Bloembergen, R.K. Chang, and C.H. Lee; Phys.Rev.lett. 16, 986 (1966)
[11] Y.R. Shen; Ann.Rev.Mater.Sci. 16, 69 (1986)
[12] J. Reif, H. Fallgren, H.B. Nielsen, and E. Matthias; Appl.Phys.Lett. 49, 930 (1986)
[13] J. Reif, H. Fallgren, W.E. Cooke, and E. Matthias; Appl.Phys.Lett. 49, 770 (1986)
[14] E. Matthias, H.B. Nielsen, J. Reif, A. Rosén, and E. Westin; J.Vac.Sci. & Technol., in print (Sept./Oct. 1987)
[15] N. Itoh and T. Nakayama; Phys. Lett. 92A, 471 (1982)
N. Itoh, T. Nakayama, and T.A. Tombrello; Phys.Lett. 108A, 480 (1985)
[16] H.B. Bepp; Phys. Rev. 149, 25 (1966)
[17] J.M Catalano, A. Cingolani, and A.N. Minafra; Phys. Rev. B5, 1629 (1972)
[18] H.B. Bepp and A. Gold; Phys. Rev. 143, 1 (1966)
[19] G. Wendin, L. Jönsson,and A. L'Huillier; Phys. Rev. Lett. 56, 1241 (1986)
A. L'Huillier, L. Jönsson, and G. Wendin; Phys. Rev. A33, 3938 (1986)
A. L'Huillier and G. Wendin; J. Phys. B20, L37 (1987)
[20] N. Bloembergen, R.K. Chang, S.S. Jha, and C.H. Lee; Phys. Rev. 174, 813 (1968)
[21] P. Guyot-Sionnest, W. Chen, and W.R. Shen; Phys.Rev. B33, 8254 (1986)
[22] P. Guyot-Sionnest and Y.R. Shen; Phys. Rev. B35, 4420 (1987)
[23] O. Semmler; Diplomarbeit, Freie Universität Berlin (1986), unpublished
[24] J. Reif, P. Tepper, E. Matthias, E. Westin, and A. Rosén; to be published in Appl. Phys. B.
[25] C.C. Wang and A.N. Duminski; Phys. Rev. Lett. 20, 668 (1968)
[26] H.W.K. Tom and G.D. Aumiller; Phys. Rev. B33, 8818 (1986)

Manuscript Received
10-26-88

Multiphoton Absorption Near Surface Damage Thresholds of Ionic Crystals and Metals

E. Matthias, S. Petzoldt, A.P. Elg, P.J. West, and J. Reif

Fachbereich Physik, Freie Universität Berlin,
D-1000 Berlin 33, FRG

By means of acoustic probe beam deflection we have measured the energy of acoustic pulses released during the interaction of intense laser pulses with solid surfaces. This technique is well suited to determine surface damage thresholds. We find that for a sufficiently high defect density at the surface the primary energy absorption is by multiphoton ionization, even within a certain energy interval **above** the damage threshold. The order of the multiphoton process corresponds to the bulk band gap of ionic materials or, for metals, to the work function. "Inert" surfaces with a low density of surface defects, like MgF_2 and CaF_2, on the other hand, show evidence for dielectric breakdown.

Key words: Ablation; Acoustic probe beam deflection; Damage threshold; Multiphoton absorption; Surface defect states.

1. INTRODUCTION

The field of irreversible laserlight interactions with surfaces can be subdivided into two areas: (1) One in which the laser intensity is low, and only individual atoms, molecules, or ions are desorbed, leaving behind a **local** microscopic defect center. The rate of desorption per laser pulse and surface area is small in this case, i.e., no macroscopic damage occurs and the optical properties of the surface remain unaltered. The nature of desorption can either be thermal, due to laser heating, or bond breaking by electronic transitions driven by the laser light [1]. (2) The other area is the one where at sufficiently high laser intensities a large amount of material is ablated and where the optical properties of the surface are deteriorated to a point usually described as macroscopic surface damage [2-4]. At these laser intensities it is commonly assumed that the high electric field causes an avalanche breakdown [5] and ignites a plasma which, in turn, strongly interacts with the surface, thereby causing further removal of material [6]. Although some models exist for bulk breakdown [7-9], it is not entirely clear to what extent these can be applied to explain surface damage mechanisms. Therefore, in order to develop a more detailed microscopic picture of the ablation process, it is still necessary to acquire more specific data about its various stages, preferentially by different experimental techniques.

Over the years considerable efforts have been spent in the investigation of both intensity ranges. In general, however, the approaches were rather different. Ablation has been of interest for laser damage and surface modifications and was consequently approached very application oriented [6]. Laser-induced desorption (mostly thermal), on the other hand, has been a valuable tool of surface physics, of particular interest for studying adsorbate bonding [1,10,11]. It seems that in most cases the two fields have been treated as separated areas of research, and only occasionally was their connection emphasized [12-16]. In this contribution we address the question whether or not laser-stimulated desorption of individual particles and the large scale removal of material are merely quantitatively different sequels of the same basic energy intake mechanism. For some transparent materials we present experimental evidence that indeed the primary energy absorption mechanism near and even above the damage threshold is multiphoton ionization, provided there exists a sufficiently large density of defect states to enhance the multiphoton absorption cross section. In contrast, for small defect densities dielectric breakdown is identified, presumably in the air directly in front of the surface, and consequently plasma-surface interaction is expected to be the damage producing mechanism.

In this paper we report on measurements of the energy of the acoustic pulse emitted from surfaces in air during laser irradiation. The results provide evidence for multiphoton absorption in the upper surface layers, in line with earlier conclusions about laser-induced non-thermal desorption from cleaved BaF_2 surfaces in UHV [17,18]. The connection between results obtained in ambient air and under UHV conditions is, however, by no means obvious. Nevertheless, the fact that we observe in both cases the same order of multiphoton process, with the number of photons matching the band gap energy, indicates that any effect of adsorbates in air cannot exceed the energy of one photon, which is the uncertainty when determining the order of the multiphoton absorption. It is even conceivable that adsorbate-induced defect states within the band gap promote multiphoton transitions. Also for strongly absorbing materials like metals we find evidence for multiphoton absorption corresponding to the work function of the material. The very fact that band properties of such different materials as metals and insulators can be recognized by the order of the multiphoton absorption above the damage threshold, implies that the threshold itself is determined by the bandstructure.

2. EXPERIMENTAL DETAILS

The well-known mirage effect [19,20], i.e., probe beam deflection due to a transient change of the refractive index, can be employed to measure the intensity of the shock waves generated at surfaces by high-power laser pulses [21,22]. Since shock waves signal the removal of material or the existence of a plasma in front of the surface, it was expected that by monitoring the acoustic pulses, the damage threshold could be determined. For that purpose we have set up an experiment [23], the principle of which is sketched in figure 1.

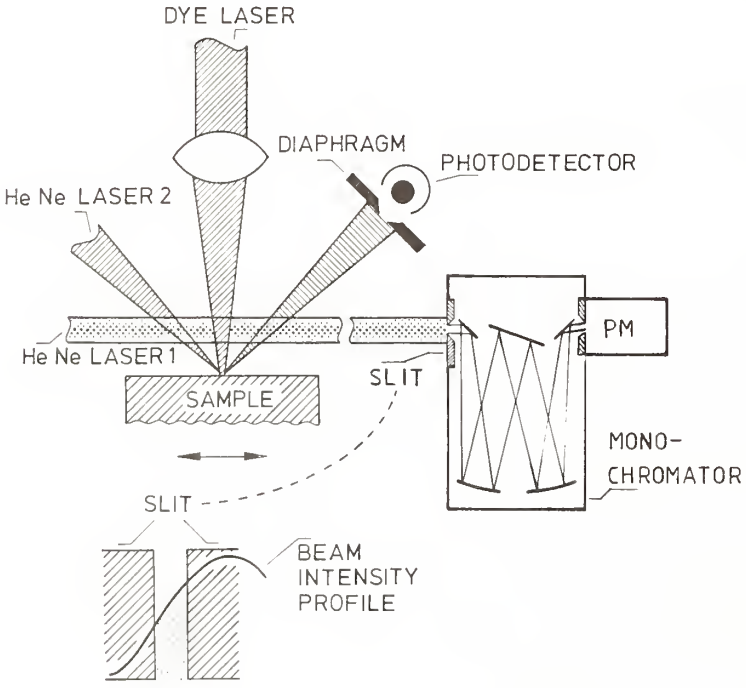

Figure 1. Principle scheme of the experimental set up. The HeNe laser #1 experiences the deflection due to acoustic pulses. The reflected intensity of HeNe laser #2 monitors surface damage.

A Nd:YAG pumped dye laser was focused onto the sample surface to produce the required power density. The laser intensity was varied by polarization optics (Fresnel rhomb and Glan prism) without changing the beam properties. The acoustic pulse emitted from the irradiated surface spot was detected by the deflection of the HeNe probe laser beam due to the associated transient gradient of the refractive index [19]. The HeNe beam had a waist of typically 120 μm and was running parallel to the surface at a few mm distance. As indicated in figure. 1, the deflection moved the intensity profile across a 40 μm slit, resulting in an intensity change at the photomultiplier. The slit was part of a monochromator in order to discriminate against the background light from the illuminated surface spot. A detailed analysis [24] shows that the deflection angle β is given by

$$\tan\beta = \frac{l_o}{2\varepsilon_o n_o} \frac{c_v}{c_p} \frac{\alpha}{kT} \frac{\partial p}{\partial z}\Bigg|_{z=z_o} \qquad (1)$$

where n_o is the refractive index of the ambient gas, l_o is the extension of the pressure pulse along the probe beam, T the temperature, $p = p_o + \Delta p(t)$ the pressure, and α the molecular polarizability of the ambient gas. The sensitivity of the experiment was such that a deflection angle of 4×10^{-7} rad corresponding to a pressure gradient of 5×10^{-6} bar/mm could be detected.

The second HeNe-laser beam shown in figure 1 was used to monitor the optical quality of the surface. Any decrease in reflected intensity indicates scattering losses caused by surface deterioration. This established technique [25] for measuring damage thresholds was intended to control the reliability of the acoustic beam deflection method. It turned out that both techniques yield identical results and are well comparable as far as their analytical potential is concerned (c.f. fig.5 below).

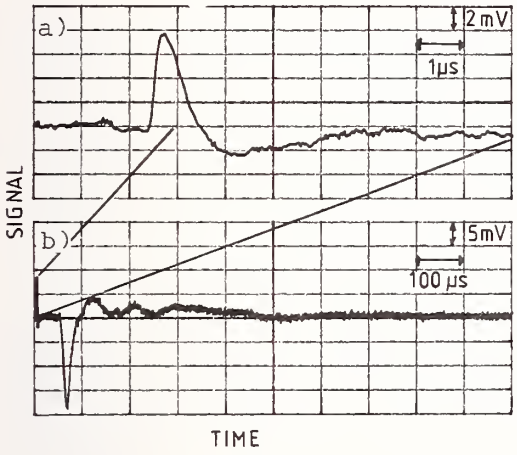

Figure 2. Typical deflection signals obtained from a predamaged surface of BaF_2 with HeNe probe laser beam #1 at a distance of 2 mm from the surface (cf. fig.1). The lower part (b) of the figure shows the total signal during 1 ms. The first spike corresponds to the acoustic deflection signal which is displayed on an expanded scale (x100) in part (a).

A typical single shot single trace obtained by the acoustic beam deflection technique is displayed in figure 2. The lower part (b) of this figure represents the total deflection signal. One can clearly distinguish two types of signals with opposite polarity. The first one appears after a few μs and originates from the acoustic wave. It is shown in figure 2(a) on a time scale expanded by a factor of 100. The second signal in figure 2(b) starting at about 50μs is presently not completely understood and will not be discussed here any further.

The shape of the deflection signal in figure 2(a) is nearly identical for all materials that we investigated. The time integral of it is proportional to the amplitude Δp of the acoustic pulse. Its total energy E in turn is proportional to $\int(\Delta p)^2 dt$ and can therefore be evaluated from the original signal S in figure 2(a) by the relation [24]:

$$E \propto [(c_p/c_v) \cdot p_o \rho]^{-1/2} \int dt \left[\int_o^t S \, dt' \right]^2 \qquad (2)$$

The inner integration extends to about 10 μs, as displayed in figure 2(a). It has been shown elsewhere that the photoacoustic energy is to a good approximation proportional to the volume of material removed by the laser shot [23].

That we are indeed observing an acoustic pulse is demonstrated in figure 3. Here the time delay of the signal with respect to the laser pulse was measured as a function of distance between surface and probe beam for two different excitation intensities. In order to obtain a high spatial resolution the probe beam was narrowed to a waist of about 10 μm. The right part of figure 3 (c and d) shows the corresponding velocities as a function of distance. The shockwave nature is obvious. For 0.2 GW/cm^2 the pulse speed thermalizes in less than 1 mm, while for 0.8 GW/cm^2 more than 2 mm are needed. In all further experiments care was taken to ensure that the probe beam was at distances where the acoustic pulse was slowed down to the normal speed of sound.

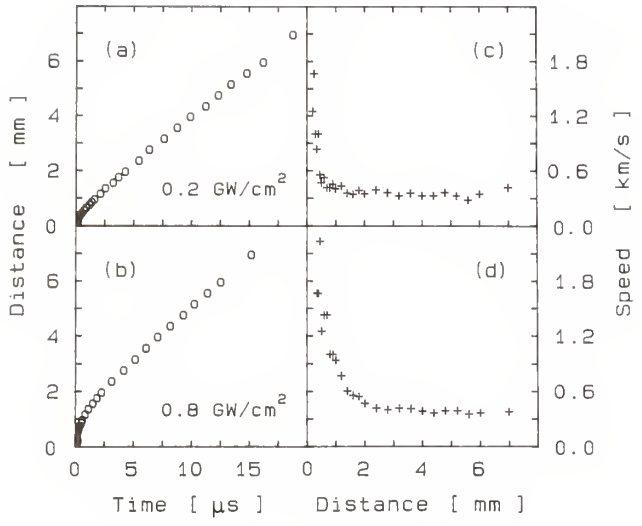

Figure 3. Parts (a) and (b) show for two different intensities the time delay of the deflection signals with respect to the damaging laser pulse as a function of distance between the HeNe probe beam and the surface. In (c) and (d) the corresponding speed of the acoustic pulse is plotted.

The fully computer-controlled experimental procedure was to choose the intensity at random by turning the Fresnel rhomb with a step motor and have a second motor advance the sample in well-defined steps between two successive laser pulses. After evaluating the acoustic energy according to eq. (2), a typical set of data for 300 laser shots shows an intensity dependence as illustrated in figure 4. The intensity scale of the excitation laser was arrived at by carefully measuring the spatial beam profile with both the burn pattern and the knife edge technique, and by monitoring the pulse energy for each shot and converting it with the average pulse length. The data in figure 4 are representative for a situation where the sample advance between successive shots is about 1/100 of the spot diameter, which in this case was 280 μm. Above 0.3 GW/cm² the acoustic energy rises steeply. Below this threshold there are no signals of the type shown in figure 2(a) present and the data define the noise level. An actual measurement consists of typically 500-1000 laser shots, but instead of plotting the individual values for each shot the signals are usually averaged over a certain intensity interval.

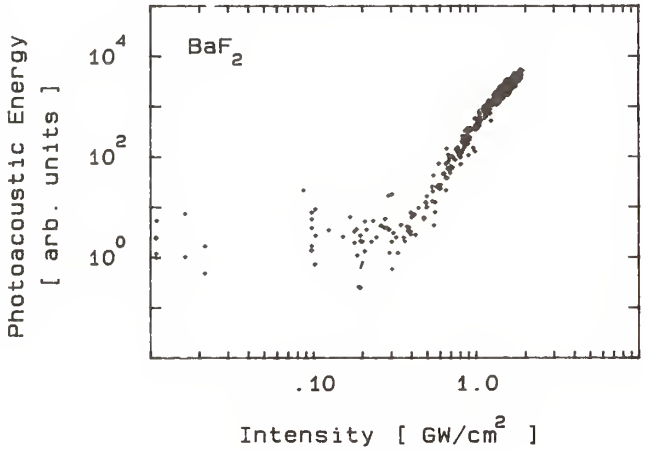

Figure 4. A typical set of 300 non-averaged data points evaluated from the acoustic signals by eq.(2). In this case the spot advance between the individual shots was small compared to the spot diameter (predamage).

3. RESULTS FOR FLUORIDE CRYSTALS

In order to determine single shot damage thresholds the sample must be advanced by a distance large compared to the spot diameter to make sure that the interaction takes places each time at a virgin spot (1-on-1). This type of measurements, using highly polished samples of CaF_2, MgF_2, and quartz (for comparison) and laser light of 530 nm, leads to the results displayed in figure 5. Each data point for the acoustic energy (asterisk) represents an average of about 10 individual signals, as described above. Circles indicate the reflected intensity of the second HeNe-laser (cf. fig.1).

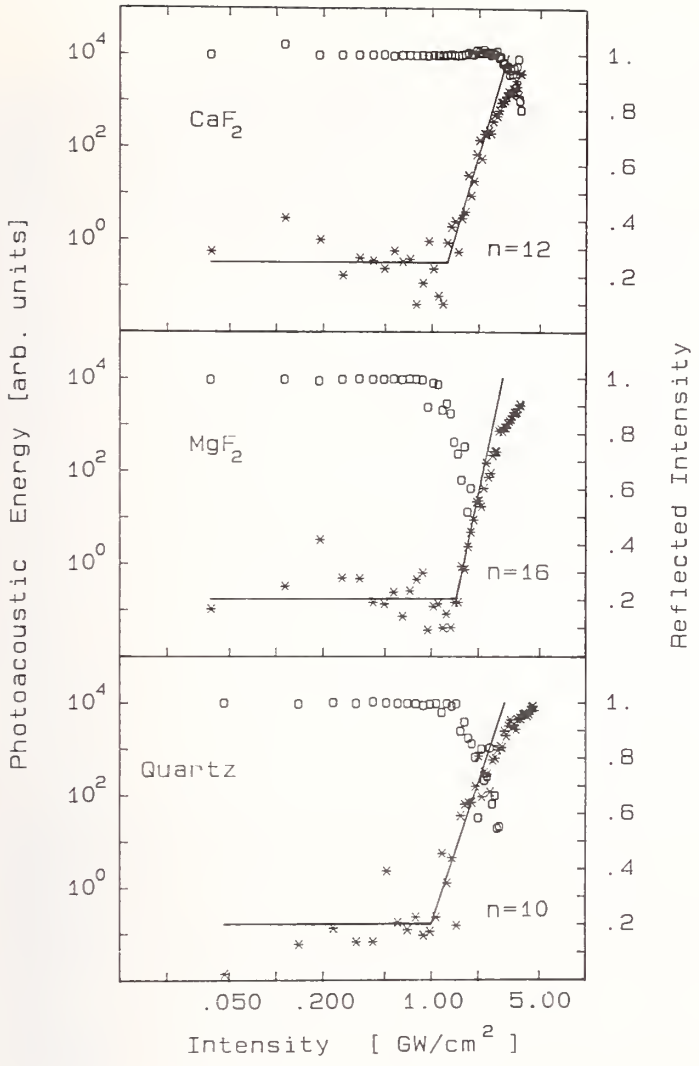

Figure 5. Single shot (1-on-1) acoustic pulse energy (asterisks) and reflectance (circles) data for optical grade CaF_2, MgF_2, and quartz as a function of laser intensity. The solid lines indicate the slope n closely above the damage threshold and, below threshold, the average background (no acoustic signal).

The agreement between the onsets of increase of acoustic energy and decrease of reflected intensity is striking, demonstrating the sensitivity of the acoustic deflection technique. For all three surfaces this threshold is comparable and about 1 GW/cm². Another feature of the data in figure 5 is for all three materials the steep increase of the acoustic energy above the threshold, with slopes of 10 and higher. We interpret this as evidence for avalanche breakdown [5]. The fact that the threshold is almost independent of the material itself for these very clean and inert surfaces supports this view. Surface damage is then produced by plasma-surface interaction [6]. At intensities larger than 2 GW/cm² the slopes become considerably smaller in all three cases. This signals the formation of a dense plasma which absorbs a significant fraction of the incoming photon flux. Above this point heating of the plasma and its feedback onto the surface govern the ablation rate.

The data in figure 6 are recorded in exactly the same manner as the ones in figure 5, and again the surfaces of both BaF_2 and LiF were highly polished and of optical quality. Yet the intensity dependence of the acoustic energies is remarkably different from that seen in figure 5. Not only are the surface damage thresholds significantly lower for these two materials but also the slopes of the acoustic energy increase are notably smaller. In fact the slopes agree surprisingly well with the number of photons required to bridge the band gap. Hence we conclude that damage on surfaces of BaF_2 and LiF is initiated by multiphoton absorption, the order of which is given by the slope.

The question arises why for some materials a 5-photon transition, which normally has an extremely small cross section, can take place with measurable intensity, whereas it is not observed for others. In accordance with earlier results on multiphoton-induced desorption [17,18], we postulate that a sufficiently large density of defect states in the band gap is needed to resonantly

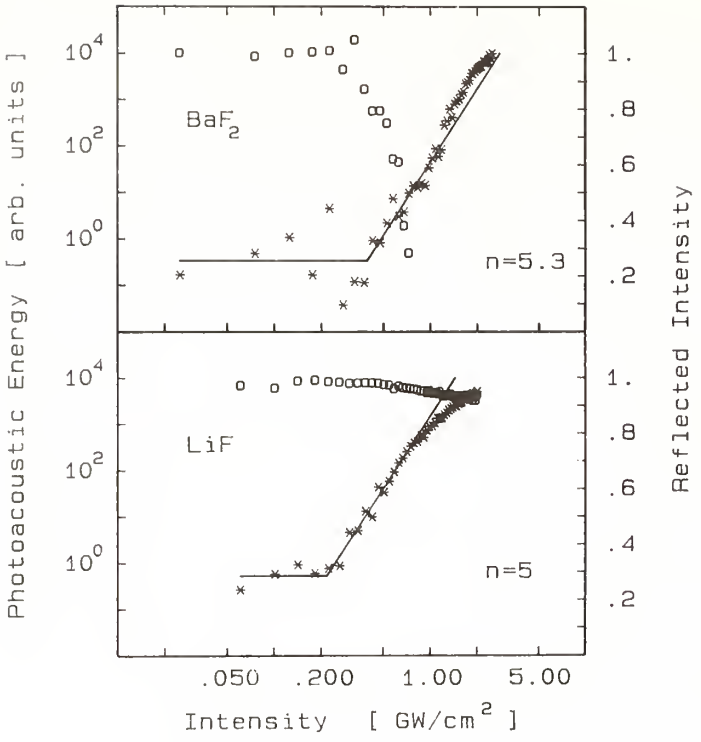

Figure 6. Single shot (1-on-1) acoustic pulse energy (asterisks) and reflectance (circles) data for optical grade BaF_2 and LiF as a function of laser intensity. The solid line indicates background and slope n closely above the damage threshold.

enhance the multiphoton transition probability. For fluoride crystals, these defect states can be due to either gross structural defects, a non-stoichiometric surface like for example missing fluorine atoms, adsorbates, or intrinsic impurities [26]. The latter seems unlikely in these cases, since we do not expect impurities in large enough concentrations at the surface of optical quality material. Missing fluorine, equivalent to surface F centers, leads to occupied and unoccupied states in the band gap [27]. Therefore, the data in figures 5 and 6 could imply that there is a larger deficiency of fluorine atoms at the surfaces of BaF_2 and LiF compared to MgF_2 and CaF_2. Whether that would be an equilibrium situation at room temperature or whether the onset of the laser pulse would generate F centers, must be left unanswered at this time. Concerning adsorbate-induced defect states it should be remembered that BaF_2 and LiF are about two orders of magnitude better soluable in water than MgF_2 and CaF_2, indicating stronger dipole forces at the surface of LiF and BaF_2, which in turn may be linked to a greater non-stoichiometry of the surface.

Structural defects can be mimicked much easier, at least in a qualitative manner, by using rough surfaces or predamaging the spot by preceding laser shots. In fact, the data points in figure 4 were taken with sample advance steps small compared to the spot diameter, which means that the excitation laser always hit a heavily damaged surface. The threshold observed under these conditions was 0.3 GW/cm², in good agreement with the result presented for BaF_2 in figure 6. Also the slopes (n=5) in both figures are mutually consistent and compare well with the ratio between the 11.0 eV band gap of BaF_2 and the photon energy of 2.34 eV (cf. table 1). This essentially proves that for both a polished and a predamaged surface of BaF_2 there exists a sufficiently high density of defect states in the band gap that a multiphoton absorption of the order of five can take place. The exact nature of these states is not yet understood. A similar conclusion must be drawn for LiF.

To further check the conjecture of multiphoton absorption in case of surfaces with a high structural defect density, we have also measured predamaged surfaces of MgF_2, CaF_2, and LiF, all of optical grade, by advancing the focal spot for each consecutive laser shot by only 1/40 of the spot diameter. In addition we studied a cleaved BaF_2 surface, using the same procedure. (A cleaved surface could have areas of both low and high defect density which, however, is irrelevant as long as the advancing step size is small.) The results are shown in figure 7. The difference between these data and the ones in figures 5 and 6 is evident. In all cases we find a damage threshold of approximately 0.1 GW/cm². As summarized in table 1, the slopes agree well with the band gap of the material in case of MgF_2 and BaF_2 but differ by about one photon energy in case of LiF and CaF_2. This difference may indicate the general uncertainty of the slopes, but it may also have specific physical reasons.

Table 1. Comparison of band gap energies for the investigated fluoride crystals with the observed order of multiphoton absorption at 530 nm.

Sample	band gap (eV)	observed slope n	n•hν (eV)
LiF	13.5[a]	4 ± 1	9.36 ± 2.34
CaF_2	12.1[b]	4 ± 1	9.36 ± 2.34
MgF_2	≈ 11[c]	5 ± 1	11.70 ± 2.34
BaF_2	11.0[b]	.5 ± 1	11.70 ± 2.34

[a]Ref.[28], [b]Ref.[29], [c]Ref.[30]

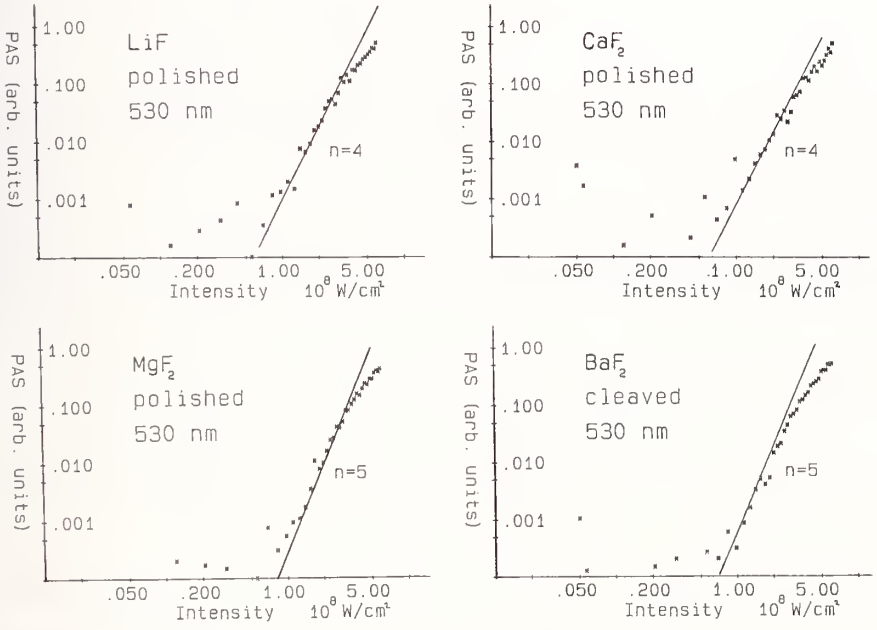

Figure 7. Acoustic pulse energy data from predamaged (step advance small compared to spot diameter) surfaces of LiF, CaF_2, MgF_2 and BaF_2. The solid lines indicate the slope n in a selected intensity range above the damage threshold.

4. RESULTS FOR METALS

In view of earlier reports on multiphoton ionization from metals [31] it was compelling to investigate the intensity dependence of the acoustic pulse energy for metal surfaces. If the assumption is correct that surface ionization plays an essential role in initiating damage, we expect for metals to see slopes related to the work function, strictly speaking for the molten metal as long as we use nanosecond pulse lengths [32]. The results for polished and cleaned silver, copper, and aluminum samples are shown in figure 8. The measurements for Cu and Al were done with a spot advance much smaller and the one for Ag with a spot advance much larger than the spot diameter. The data verify the low thresholds of metals for vaporizing surface material, due to their strong optical absorption. The observed slopes are indicated in figure 8 and listed in table 2.

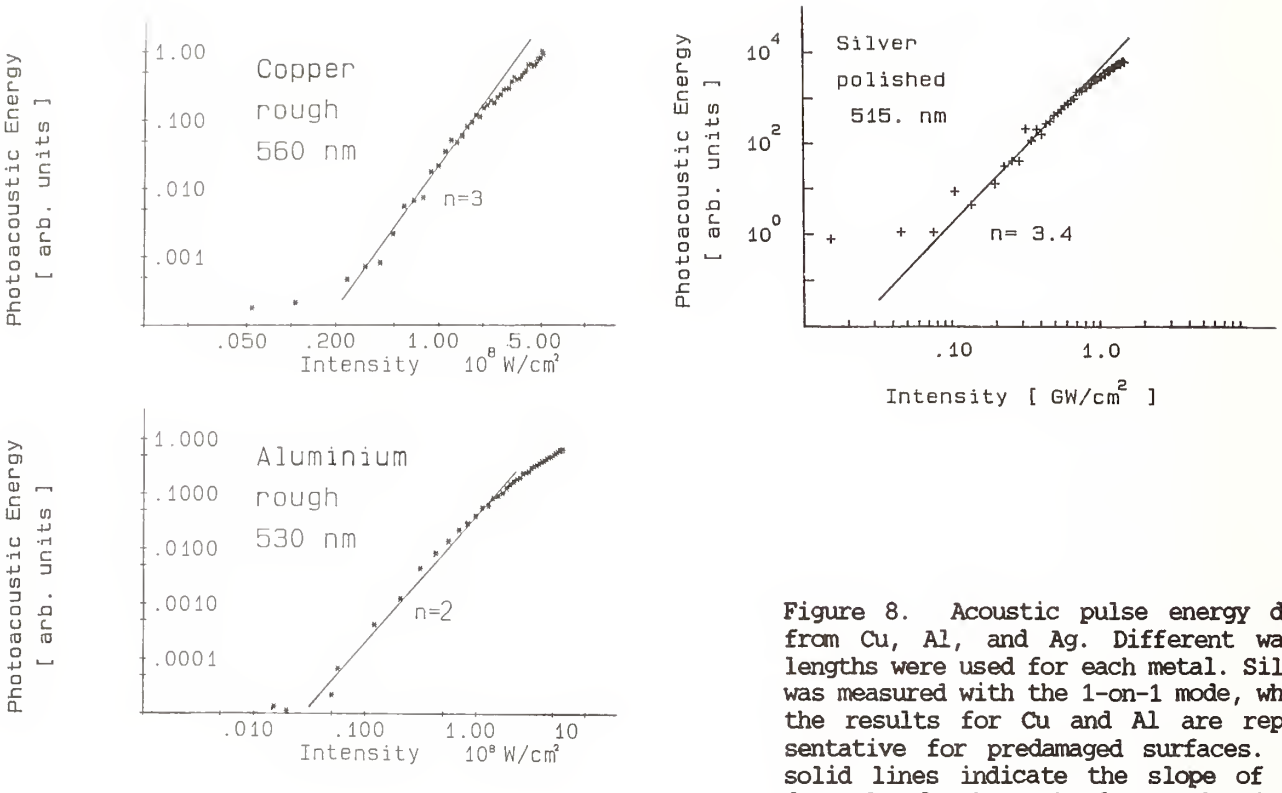

Figure 8. Acoustic pulse energy data from Cu, Al, and Ag. Different wavelengths were used for each metal. Silver was measured with the 1-on-1 mode, while the results for Cu and Al are representative for predamaged surfaces. The solid lines indicate the slope of the data closely above the damage threshold.

Table 2. Comparison of work functions for Al, Cu, and Ag with the observed order of multiphoton absorption.

metal	work function (eV)[a]	observed slope n	λ(nm)	n•hν (eV)
Al	4.28	2 ± 1	530	4.68 ± 2.34
Cu	4.65	3 ± 1	560	6.64 ± 2.21
Ag(100)	4.64	3 ± 1	515	7.22 ± 2.41

[a]Ref.[23]

Note that different wavelengths were used for the three materials. For copper with a work function of 4.65 eV three photons of 560 nm are required to emit an electron. Aluminum has a lower work function of only 4.28 eV and hence two photons of 530 nm are adequate for photoemission. In silver two photons of 515 nm should have been sufficient to eject an electron, but here we observe a slope of 3. Whether or not the multiphoton ionization in silver is influenced by the strong 4d band remains to be seen. In any case there can be no doubt that the removal of material from the surface of metals is, in the range of 10^7 W/cm², initiated by multiphoton ionization. Like for the wide band gap materials we see in figure 8 at higher intensities a clear deviation from the straight line, which again indicates the onset of a different physical process, namely the heating of a dense vapor plasma [6].

5. CONCLUSIONS

The acoustic beam deflection method was found to be a reliable technique for measuring optical damage thresholds. The origin of the shockwave is at the moment not understood in every detail, but we follow the general opinion that it arises from a plasma formed outside the surface [6,21]. This technique is independent of surface quality and capable of distinguishing between multiphoton

absorption and avalanche breakdown in laser-surface interactions. The results indicate that avalanche breakdown takes place at very inert surfaces with a low defect density. Materials that qualify in this category are CaF_2, MgF_2, and fused quartz, all polished to optical quality. In contrast, we find that other materials like optical grade LiF and BaF_2 apparently have a sufficiently high density of surface defect states such that multiphoton processes bridging the band gap can occur. The exact nature of the defect states on surfaces of LiF and BaF_2 is not known, it could be non-stoichiometry, structural or adsorbate induced defects. As to the latter, one might speculate that in ambient air water molecules adsorbed at the surface contribute.

The influence of structural defects was qualitatively shown by predamaging the surface with preceeding laser shots. In that case no avalanche effects were observed and the data show three clearly distinct domains: (1) One below the threshold where the intensity is too low to generate an acoustic signal. (2) An intermediate intensity range where the photoacoustic energy increases with the n'th power of the laser intensity, and $n \cdot h\nu$ exceeds the band gap of the crystal or the work function of the metal. (3) High intensities where the dependence of the acoustic energy on the laser intensity becomes weaker and indicates the formation of a dense plasma which is heated by absorbing most of the incoming laser light.

For us the most interesting domain is the intermediate one in which the acoustic energy discloses multiphoton absorption. The correlation of the order of the multiphoton process with band gap or work function proves that the primary process is multiphoton ionization. The amount of material removed must then be proportional to the energy deposited by this initial excitation, and sufficient in quantity to feed a plasma, which in turn generates the shockwave. In this intensity domain, however, the plasma must still be transparent for the incoming laser light, such that the energy is absorbed in the surface layers of the material. The observation of material properties like band gap and work function above the damage threshold proves that the threshold intensity crucially depends on surface quality as well as on band structure.

If we briefly recall the results on laser-induced non-thermal desorption of positive ions from cleaved surfaces of BaF_2 [17, 18], presented at last years symposium, it becomes evident that a 5-photon ionization occurs both for desorption at intensities in the MW/cm^2 range and for damage at two orders of magnitude higher intensities. The transition from desorption, creating only local microscopic defects to damage with macroscopic surface modification, therefore seems to be merely a quantitative change of the rate of material removal from a given surface area, with the basic physical processes remaining the same. Of course the rate increase with intensity has, for ns pulse widths, cumulative character since each local defect generated by desorption will further amplify the multiphoton absorption rate.

This work was supported by the Deutsche Forschungsgemeinschaft, Sfb 337.

6. REFERENCES

[1] Chuang, T.J., J. Vac. Sci. Technol. B3: 1408-1420; 1985.

[2] Lowdermilk, W.H., and Milam, D., IEEE J.Quant. Electr. QE-17: 1888-1903; 1981.

[3] Wood, Roger M. Laser damage in optical materials. Bristol; Adam Hilger IOP Publishing Ltd., 1986.

[4] Rothenberg, J.E., and Kelly, R., Nucl. Instr. Meth. B1: 291-300; 1984.

[5] Epifanov, A.S., IEEE J. Quant. Electr. QE-17: 2018-2022; 1981.

[6] von Allmen, M. Laser-Beam Interactions with Materials. Heidelberg; Springer Verlag; 1987.

[7] Walker, T.W., Guenther, A.H., and Nielsen, P., IEEE J. Quant. Electr. QE-17: 2053-2065; 1981.

[8] Jones, S.C., Shen, X.A., Braunlich, P.F., Kelly, P., and Epifanov, A.S., Phys. Rev. B35: 894-897M 1987.

[9] Braunlich, P., Jones, S.C., Shen, X.A., Casper, R.T., and Kelly, P., Proc. 1987 Boulder Damage Symposium.

[10] Hall, R.B., J. Phys. Chem. 91: 1007-1015; 1987.

[11] Zhu, X.D., Shen, Y.R., and Carr, R., Surface Sci. 163: 114-120; 1985.

[12] Rousseau, D.L., Leroi, G.E., and Falconer, W.E., J. Appl. Phys. 39: 3328-3332; 1968.

[13] Nakayama, T., Okigawa, M., and Itoh, N., Nucl. Instr. Meth. B1: 301-306; 1984.

[14] Siekhaus, W.J., Kinney, J.H., Milam, D., and Chase, L.L., Appl. Phys. A39: 163-166; 1986.

[15] Chase, L.L, and Smith, L.K., Proc. 1987 Boulder Damage Symposium.

[16] Bräunlich, P.F., Brost, G., Schmid, A., and Kelly, P., IEEE J. Quant. Electr. QE-17: 2034-2041; 1981.

[17] Reif, J., Nielsen, H.B., Semmler, O., Tepper, P., Matthias E., Fridell, E., Westin, E., and Rosén, A., Proc. 1986 Boulder Damage Symposium.

[18] Matthias, E., Nielsen, H.B., Reif, J. Rosén, A., and Westin, E., J.Vac. Sci. Technol. B5: 1415-1422; 1987.

[19] Boccara, A.C., Fournier, D., Jackson, W., and Amer, N.M., Optics Lett. 5: 377-379; 1980.

[20] Koren, G., Appl. Phys. Lett. 51: 569-571; 1987.

[21] Bobin, J.L., Durand, Y.A. Langer, Ph.P., and Tonon, G., J. Appl. Phys. 39: 4184-4189; 1968.

[22] Belikova, T.P., Savchenko, A.N., and Sviridenkov, E.A., Soviet Phys. JETP 27: 19-23; 1968.

[23] Petzoldt, S., Elg, A.P., Reichling, M., Reif, J., and Matthias, E., Appl. Phys. Lett. 53: in print; 1988.

[24] Petzoldt, S., Diplomarbeit, FU Berlin; 1988.

[25] Franck, J.B., Seitel, S.C., Hodgkin, V.A., Faith, W.N., and Porteus, J.O., NBS Special Publication 727: 71-76; 1986.

[26] Allen, S.D., Porteus, J.O., Faith, W.N., and Franck, J.B., Appl. Phys. Lett. 997-999; 1984.

[27] Rosén, A., Westin, E., Matthias, E., Nielsen, H.B., and Reif, J., Physica Scripta T23: 184-190; 1988.

[28] Gout, C., and Pradal, F., J. Phys. Chem. Solids 29: 581-592; 1968.

[29] Rubloff, G.W., Phys. Rev. B5: 662-684, 1972.

[30] American Institute of Physics Handbook, 3rd edition: pp. 9-18; 1972.

[31] Lompre, L.A., Thebault, J., and Farkas, G., Appl. Phys. Lett. 27: 110-112; 1975.

[32] Kelly, R., and Rothenberg, J.E., Nucl. Instr. Meth. B7/8: 755-763; 1985.

[33] CRC Handbook of Chemistry and Physics, 66th edition: E-86; 1985-1986.

In response to a question of whether the measurements were made in air and a plasma spot was seen, the author replied yes but the plasma was too weak to affect the beam incident on the surface. The questioner disagreed, pointing out that sometimes the plasma was so intense that it completely reflected the beam. The speaker replied that they had done the same measurements through the crystal and had identified the same type of heat signal. Up to the point where the experimental points deviate from the theoretical slope he felt that he was clearly looking at a surface multiphoton absorption and therefore cold.

Manuscript Received
2-22-88

Laser Fluorescence Spectroscopy of Zinc Neutrals Originating from Laser-Irradiated and Ion-Bombarded Zinc Sulfide and Zinc Surfaces

H.F. Arlinghaus, W.F. Calaway, C.E. Young, M.J. Pellin, D.M.Gruen

Materials Science, Chemistry, and
Chemical Technology Divisions
Argonne National Laboratory
Argonne, IL 60439 USA

L.L. Chase

Lawrence Livermore National Laboratory
University of California
P.O. Box 5508
Livermore, CA 94550 USA

Time-of-flight (TOF) measurements, employing high-resolution laser-induced fluorescence spectroscopy (LFS) as a probe, have been used to measure the yield and velocity distribution of Zn atoms ejected from a ZnS single crystal under irradiation by 308 nm photons. By comparison with the known ion sputtering yield for pure zinc, the absolute yield was determined to be 10^9 atoms/pulse at a laser fluence of 30 mJ/cm^2. The velocity distribution of the Zn atoms could be fitted by a Maxwell-Boltzmann distribution, having a characteristic temperature of 2360 K. In addition, Doppler-shift techniques have been combined with TOF measurements in order to separate prompt from delayed emission of ablated atoms, as well as to probe possible molecular or cluster fragmentation. The results obtained suggest the possibility of molecular or cluster emission from ZnS.

Key words: delayed emission; laser damage; laser fluorescence spectroscopy; Maxwell-Boltzmann distribution; molecular or cluster fragmentation; time of flight; zinc sulfide.

1. Introduction

The application of high-power lasers to a variety of technologies is frequently limited by the ability to produce optical components capable of transmitting intense laser beams without incurring damage. As has been previously observed and well documented at this conference, laser-induced damage to the surface of an optical component often initiates failure of that component. From this observation, it is apparent that understanding optical surface damage is of crucial importance in the development of optical components that can withstand high-power laser irradiation. Nevertheless, the nature of this damage is still not well understood. In an attempt to better understand the damage process, experiments have been initiated that employ various spectroscopic and surface analysis techniques in a study aimed at elucidating fundamental damage mechanisms in optical materials.

Several researchers have observed the emission of ions and neutrals from optical material surfaces illuminated by laser radiation at power densities below the damage threshold of the material [1-4]. Determining the yield and the kinetic energy distribution of particles produced during laser radiation is key information needed to determine the mechanism responsible for the ejection of particles from a surface. Knowledge of this mechanism will allow a better understanding of the ener-

gy transfer mechanism between an optical field and the near-surface region of a solid material. Presently, there are only a few velocity measurements of particles ejected from laser-ablating materials [5].

Laser-induced fluorescence spectroscopy (LFS) provides a powerful tool to measure both atomic densities and velocity distributions of ejected particles and has been widely used for some time to study sputtering due to ion bombardment. It appears that LFS techniques are just as well suited for obtaining information relevant to the optical damage process, yet very few experiments of this type have been reported [6,7]. Further, LFS is a very sensitive technique when compared to mass spectrometry (MS) of electron-ionized neutrals.

In the work reported here, LFS has been used to measure the yield and the velocity distribution of Zn atoms ejected from ZnS. This wide band-gap semiconductor has some practical application as an optical coating material, and it serves nicely as a prototype for this class of materials, which are of considerable practical significance. In addition, emission of neutral atoms and charged particles from ZnS during laser irradiation has been observed previously by MS techniques and some estimates of particle velocities have been made [1,8].

Due to the relatively short interaction time between a pulsed laser and optical material, the most convenient method for determining particle velocities is by time of flight (TOF). This is accomplished by detecting ejected particles a known distance from a target at some time after the ablating laser strikes the target. The capabilities of this type of experiment have been expanded as described in this paper by incorporating a high-resolution tunable laser into the LFS system in order to obtain Doppler-shifted velocity profiles of ablated atoms as a function of TOF. As described in this paper, it is possible from such data to separate prompt from delayed emission of ablated atoms as well as to probe possible molecular or cluster fragmentation. It is believed that this is the first time that such LFS experiments have been performed and that this new technique will become a useful tool in solving a variety of problems.

2. Experimental

The experimental arrangement consists of an ablating laser, a LFS detection system, an ultra high vacuum (UHV) system, and computer-controlled electronics. The experimental arrangement is depicted in figure 1. The ablating laser is

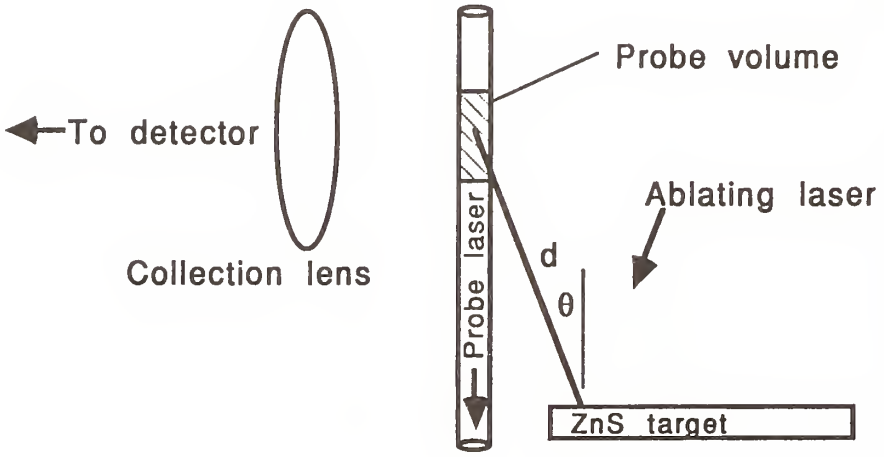

Figure 1. Experimental arrangement. In the present configuration the probe laser is propagating perpendicular to the ZnS target.

directed onto a sample target suspended in the UHV chamber. The interaction of this laser with the sample causes atoms to be ejected from the surface. At some later time, a second (probe) laser is triggered which is tuned to a resonant transition of the atom or molecule of interest. The beam from the probe laser passes near the target exciting the ejected atoms or molecules causing them to fluoresce. Light collection optics are used to image fluorescence from a volume element at a known distance from the sample onto a photomultiplier. The timing between the two lasers and the frequency of the probe laser are varied so that the Doppler-shifted frequency spectrum for the particle of interest can be recorded as a function of TOF.

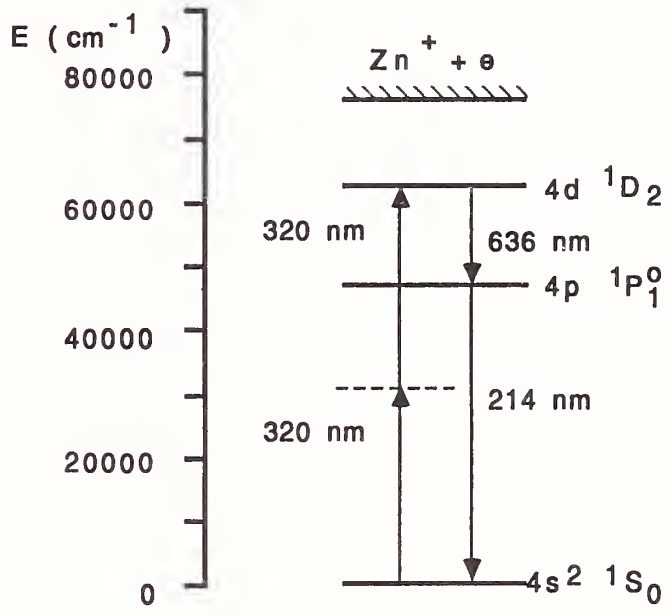

Figure 2. Partial energy level diagram of zinc.

All experiments were conducted on hexagonal melt grown ZnS crystals from Eagle Picher, which were wafers approximately 1 mm thick and polished to an optical quality surface on both sides. The samples were rinsed using methanol, placed in the UHV chamber, and evacuated to a base pressure of 3×10^{-10} mbar. For these initial experiments, Zn atoms were chosen for interrogation. Figure 2 shows a partial energy level diagram for Zn. As shown in figure 2, a two-photon resonance excitation using 320 nm light was used to produce fluorescence at 636 nm. Although it was not possible to saturate the transition, this detection scheme worked well and resulted in acceptable signal levels.

The probe laser (LFS) system is shown schematically in Figure 3. It consists of a narrow-band cw oscillator followed by a three-stage high-power, pulsed amplifier chain. The system was used previously for measuring velocity and electronic state distributions of several species of sputtered atoms [9,10]. For the present experiments, the system was optimized to have sufficient power in the tunable UV probe beam for multiphoton resonant excitation. The cw ring dye laser (Spectra Physics 380A) was pumped by an argon ion laser (Coherent CR-12) and was operated as a single-mode device with ~20 MHz linewidth and a maximum scan length of 35 GHz. The tunable cw beam was continuously monitored by two etalons that provide calibration of the frequency scale and allow monitoring of the mode quality. An iodine fluorescence detector was used to identify the exact wavelength of the ring laser. The three flowing dye cells were transversely pumped by the output of an excimer

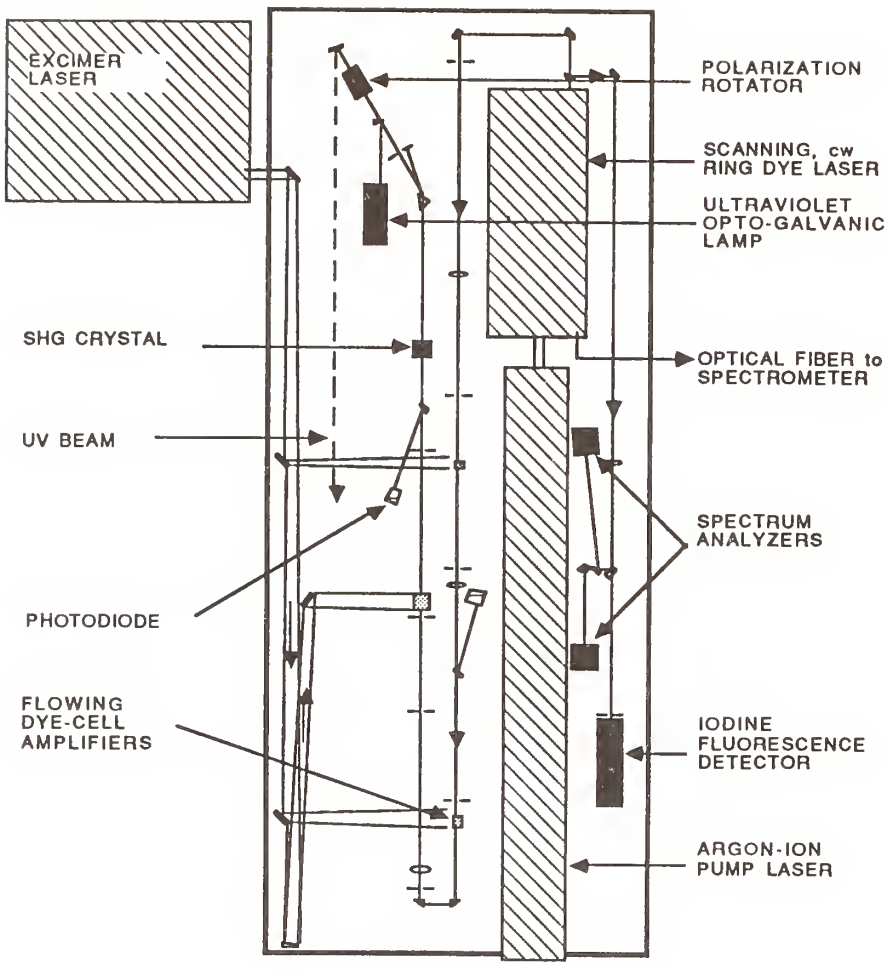

Figure 3. High-resolution tunable UV laser system.

laser (Lumonics, 861-T) operating with XeCl at 308 nm. For the experiments with Zn, DCM was used for the ring dye and for the dye in the amplifier cells. Frequency doubling the amplified visible output of the ring laser produced up to 1.3 mJ/pulse of narrow-band UV light. The UV linewidth was estimated to be in the range of 350 MHz.

For all of the experiments reported here, a Lambda Physik (model EMG 201 MSC) excimer laser was used as the ablating laser. This laser was operated with XeCl to produce an output wavelength of 308 nm which is well into the ZnS interband absorption edge at ~325 nm [11]. With unstable resonator optics, the output from this laser is 350 mJ with a pulse width of 30 ns. For these experiments, the output of the ablating laser is attenuated by a series of quartz plates and then focused to a spot size of 1.2 x 2.4 mm in order to produce fluences in the range 10 to 100 mJ/cm^2, which is well below the single-pulse damage threshold of ZnS [1,12].

A high-efficiency light-collection system consisting of a combination of two lenses and a concave mirror was used to focus the emitted photons onto the photomultiplier. The alignment of the lenses and mirror is such that only photons emanating from a sharply defined probe volume can reach the photomultiplier. A narrow bandpass interference filter with transmission at 636 nm was used to assure that only fluorescence from the excited Zn atoms was detected by the cooled photomultiplier (EMI model 9659 QB). The signal from the photomultiplier was digitized within 100 ns gates coincident with the probe laser pulse. Quartz plates were used to pick off a fraction of the probe UV signal as well as the ablation UV signal. These integrated UV signals were detected by fast photodiode circuits and recorded

along with the Zn fluorescence signal, iodine fluorescence signal, and 3-GHz etalon output by a Digital Equipment Corporation 11/23 microcomputer through a CAMAC interface.

3. Results and Discussion

Typical Doppler-shifted spectra for Zn atoms ablated from a ZnS surface at various delay times are shown in figure 4. With shorter delay times (TOF), the observed fluorescence signal shifts to lower probe laser frequency, and the width increases. This is consistent with what would be expected for a Doppler-shifted TOF experiment. Using TOF, the velocity, v, can be calculated as the distance, d, an atom travels divided by the TOF, t. The Doppler-shift is then given by:

$$\nu = \nu_o \left(1 - \frac{d \cos\theta}{c\, t} \right) \tag{1}$$

where, ν is the measured frequency,

ν_o is the frequency of transition at zero velocity,

θ is the angle between the direction of the light propagation vector and the velocity vector of the atom,

and c is the velocity of light.

Two factors contribute to the width of the Doppler profile, the velocity spread due to the size of the probe volume, and the frequency spread due to the bandwidth of the probe laser. If d_{min} and d_{max} are the minimum and maximum distance a particle can travel and still remain in the probe volume, then the width of the Doppler profile is given by:

$$\Delta\nu = \nu_o \frac{\Delta d}{c\, t} \tag{2}$$

where $\Delta d = d_{max} - d_{min}$. For comparison with laboratory data, the above effect must be convolved with the laser bandwidth.

As shown in eqs 1 and 2, both frequency shift and spectral width of the fluorescence signal are inversely proportional to the delay time (TOF). This results in the broadening of the fluorescence signal for shorter delay times which is observed in figure 4. Since the Doppler profile shifts as it broadens, the fluorescence signal should broaden for shorter delay times only in the direction of lower frequencies, i.e., lower wave numbers. However, as is depicted in figure 5, the experimental results for a delay time of 2.5 μs show broadening toward both lower and higher wave numbers when compared to the 4-μs results. To better see this effect, the minimum and maximum frequencies of the Doppler profile, defined as 25% of the maximum signal, have been plotted versus 1/t in figure 6. As derived from eq 1, the resulting curves are expected to be straight lines.

The data in figure 6 show that at short delay times the high-frequency data deviate substantially from a straight line towards higher frequencies. This indicates that there are particles in the probe volume with velocities too slow to have travelled from the sample to the volume at constant velocity in time, t. One possible explanation for this result is that ZnS molecules or clusters are fragmenting, producing Zn atoms that have a velocity distribution containing a slow velocity component. Fragmenting molecules or clusters may produce a wide variety of velocity components in all directions. This may explain why for long-delay times, as depicted in figure 6, a broadening is observed in both frequency directions. It is also interesting to note that at a given t, the low wave number edge shows no deviation from linearity. This result suggests that we are not detecting any delayed emission of Zn atoms, which is contrary to measurements determined by mass

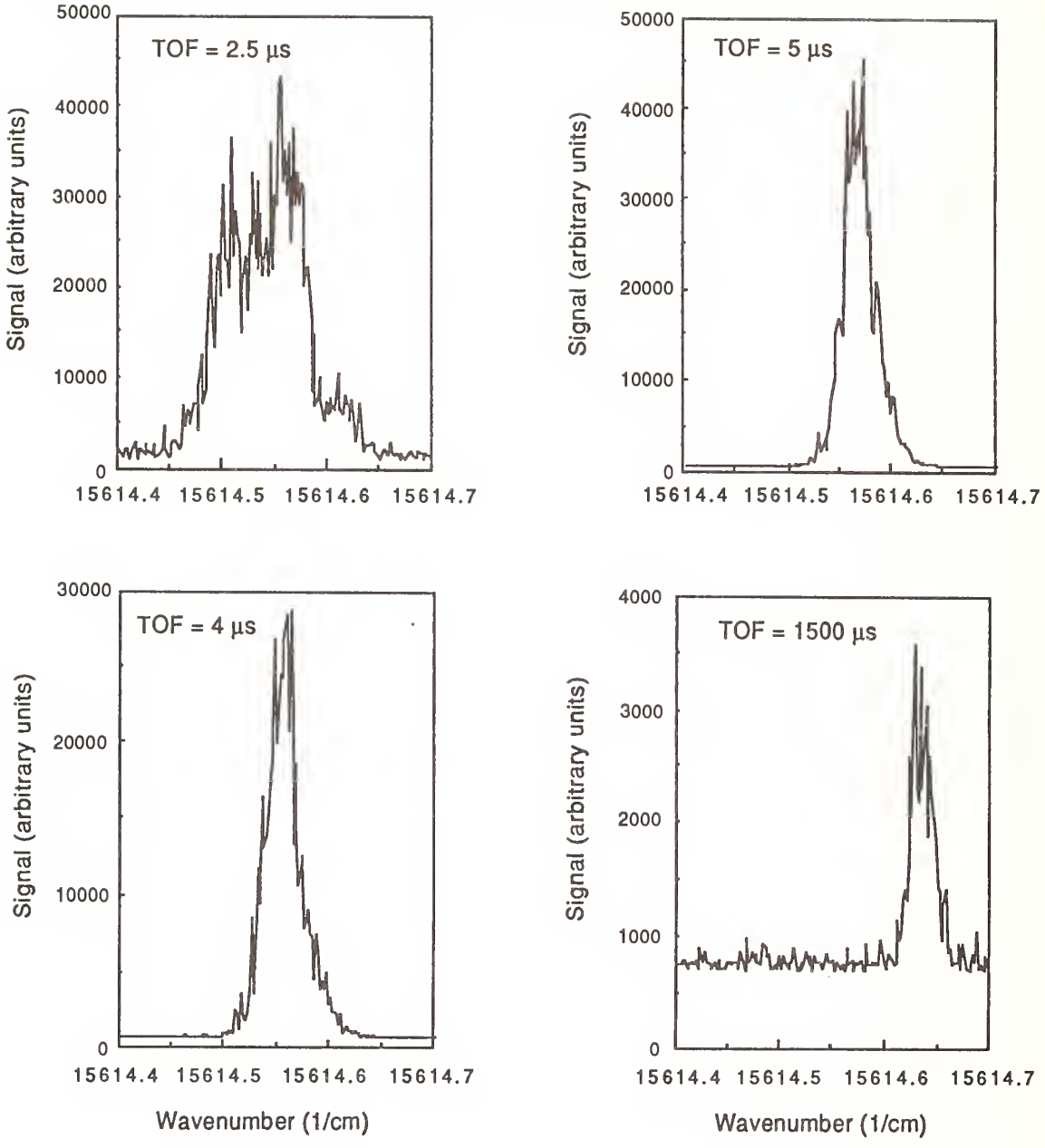

Figure 4. Doppler-shifted laser-induced fluorescence spectra of Zn atoms at various delay times after ablation from a ZnS surface. For these experiments the center of the probe volume was 9 mm from the target at an angle of 23°.

spectroscopic technique [1].

Spontaneous fragmentation of ionic clusters, displaying fragmentation patterns from which neutral atom formation may be inferred, has been observed by other authors [13-15]. It is surprising that ablation from a solid surface occurs at such low laser fluences, let alone cluster emission. In our studies to date, we have not examined the stability of the clusters or the details of spontaneous fragmentation. It is quite possible that the probe laser may cause the decomposition of ZnS molecules or clusters arriving in the probe volume. This possibility will be examined in future experiments where the occurrence of cluster emission with damage is to be studied in more detail.

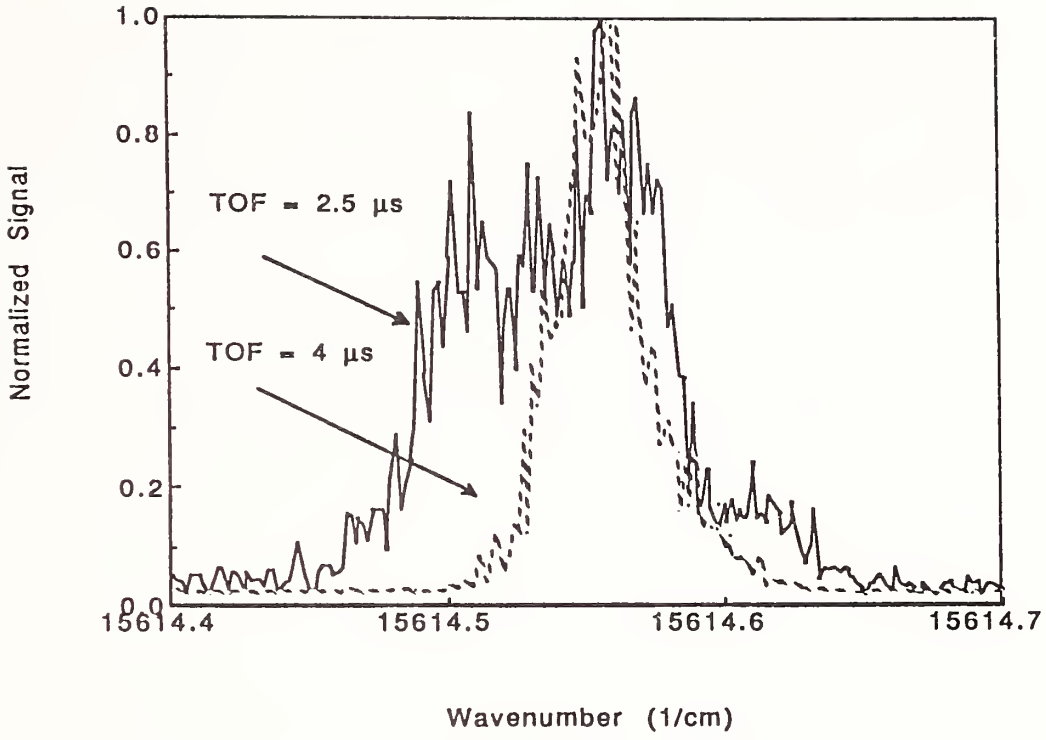

Figure 5. Doppler-shifted laser-induced fluorescence spectra of Zn atoms for delay times of 2.5 μs and 4 μs.

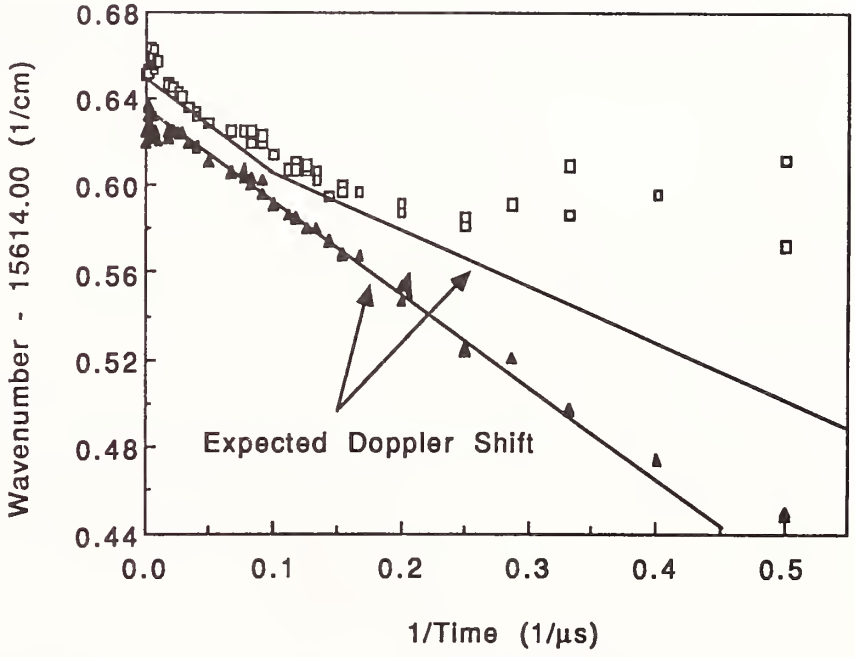

Figure 6. Doppler shift of Zn atoms in the probe volume as a function of time of flight. Triangle: low-frequency edge; square: high-frequency edge. The triangles and squares represent data obtained from the low and high frequency edge of the Doppler profile respectively. The solid lines were calculated from eq 1 taking in account the probe UV laser bandwidth.

Measuring the fluorescence signal at the appropriate frequency for each corresponding delay time, (i.e., a single velocity component out of the velocity integral) and plotting those numbers against the velocity, as determined from the delay time, results in the velocity distribution as given in figure 7. If the experimental velocity distribution has its origin in a thermal process, then the data should follow a Maxwell-Boltzmann distribution. For such processes, the number density of atoms, N, (ejected during a short pulse) which reside in a volume located at a distance, d, from a point on the surface and at an angle, q, from that point can be expressed as a function of the reduced velocity, u, as follows:

$$N(u) = \frac{Q}{d^3} \frac{2\cos\theta}{\pi} u^4 \exp\left(-u^2\right) \tag{3}$$

where, Q = total number of atoms ejected per pulse,
and θ = angle between ejection velocity vector and surface normal.

The reduced velocity, u, is related to the velocity by u = v/v* with

$$v^* = \sqrt{\frac{2kT}{M}} \tag{4}$$

where, k = Boltzmann constant,
T = temperature,
and M = atomic mass.

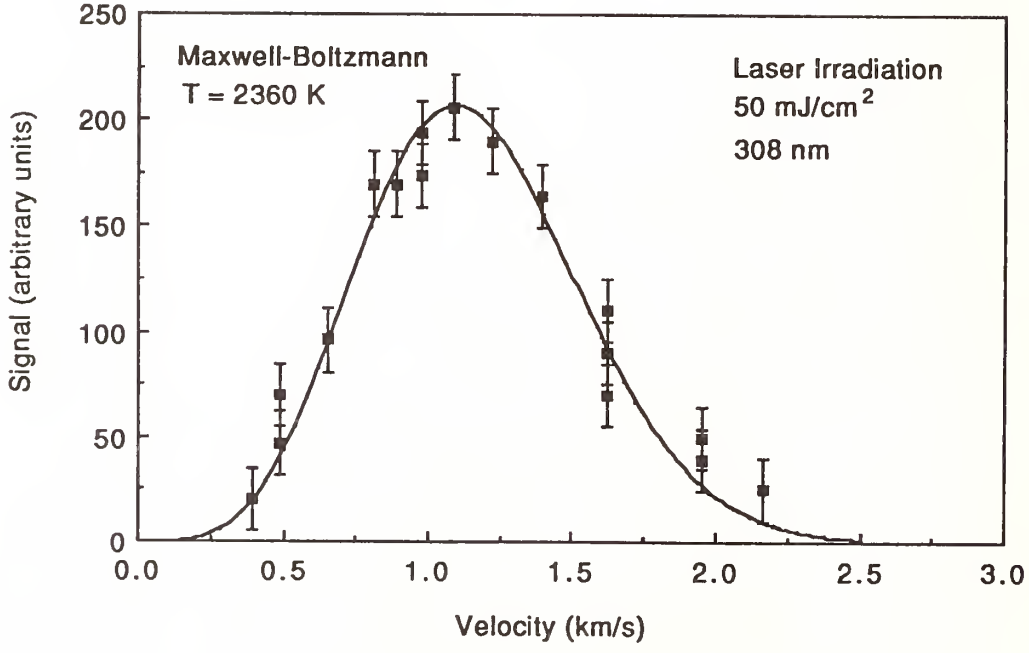

Figure 7. Velocity distribution of Zn atoms ablated from a ZnS surface. The data are represented by the squares while the solid line is a Maxwell-Boltzmann fit to that data.

Equation 3 was fit by applying the Levenberg-Marquaedt nonlinear least-squares method [16] to the data and the calculated distribution is plotted in figure 7 as a

solid line. As can be seen from figure 7, the velocity distribution appears to be thermal in nature. The calculated Maxwell-Boltzmann velocity distribution fits the data well at a kinetic temperature of 2360 K with an associated uncertainty of 100 K. As can also be seen from figure 7, the error associated with the data is substantial. The conclusion we draw from these experiments is that there are inherently large variations in the number of ejected particles during the ablation process. This fact, coupled with the shot-to-shot fluctuations in laser intensities, substrate morphology, and contributions due to fragmenting clusters, leads to the somewhat larger than desired error limits for each data point.

The absolute yield of Zn atoms produced by the laser irradiation was ascertained by comparison with sputtering experiments in which the velocity distributions of Zn atoms ejected by ion bombardment of single crystal ZnS, and metallic Zn targets were measured using the same apparatus. The yield of laser-induced emission was then obtained from the known ion sputtering yield for Zn [17]. In this manner the magnitude of the absolute Zn yield from ZnS, due to 0.9 mJ irradiation at 308 nm on a 3 mm^2 area, was determined to be 10^9 atoms/pulse. This corresponds to $2x10^{-8}$ atoms/photon.

The mechanism responsible for the ejection of the neutral Zn particles is not well characterized. The kinetic temperature of 2360 K as determined from the velocity distribution is in fact higher than the sublimation temperature of ZnS (1450 K). However, calculations, which model the laser irradiation as a bulk heating process, suggest that the temperature of the ZnS surface is lower than 1000 K. Recently, it has been shown that certain electronic-sputtering mechanisms do lead to thermal velocity distribution of laser desorbed neutrals [7]. Therefore, the creation of "color centers" or other related electronic defects due to the incident photons may cause the formation of neutrals on the surface as well as the ejection of such neutrals. Other schemes which postulate small isolated surface regions of microscopic dimension that become superheated are also a possible mechanism. Clearly, additional measurements are necessary in order to gain more detailed information on the mechanism for atomic and cluster emission during laser irradiation in order to link this phenomenon to optical damage processes. In future experiments, the dependence of the Zn velocity distribution on the ablating laser fluence will be investigated in more detail. In addition, experiments will be conducted to examine the wavelength dependence of the damage process through the visible and infrared regions.

4. Conclusions

The Doppler-shifted LFS TOF technique has been shown to be a very sensitive and effective method for obtaining information on particle emission from laser-irradiated surfaces. Neutral Zn atom ejection from ZnS is observed at very low laser fluences (<50 mJ/cm^2) when samples are illuminated at wavelengths above the band gap of ZnS. The velocity distribution of the Zn atoms is thermal with a characteristic temperature around 2360 K and an absolute yield of 10^9 atoms/pulse. The width of the Doppler-profile spectra at short delay times lends indirect evidence to the possibility of molecular or cluster emission from ZnS. For 308 nm radiation and at fluences below 100 mJ/cm^2, no evidence of delayed emission of Zn atoms has been observed. Further studies are needed in order to determine which mechanism is responsible for optical damage in ZnS.

Work performed under the auspices of the U.S. Department of Energy, BES-Materials Sciences, under Contract W-31-109-ENG-38 (ANL) and Contract W-7405-ENG-48 (LLNL).

5. References

[1] Chase, L. L.; Smith, L. K. Laser-induced surface emission of neutral atomic and molecular constituents of optical materials. This conference.

[2] Matthias, E.; Reif, J.; Nielsen, H. B. Multiphoton-induced desorption from $BaF_2(111)$. This conference.

[3] Matthias, E.; Nielsen, H. B.; Reif, J. Multiphoton-induced desorption of positive ions from barium fluoride. J. Vac. Sci. Technol. B5(5): 1415-1422; 1987.

[4] Schmid, A.; Bränlich, P. Multiphoton-induced directional emission of halogen atoms from alkali halides. Phys. Rev. Lett. 35(20): 1382-1385; 1975.

[5] see,.for example: Itoh, N. Laser sputtering in the electronic excitation regime: comparison with electronic and ion sputtering. Nucl. Instr. and Meth. B27: 155-166; 1987.

[6] Dreyfus, R. W.; Kelly, R.; Walkup, R. E. Laser-induced Fluorescence study of laser sputtering of graphite. Nucl. Inst. and Meth. B23: 557-561; 1987.

[7] Stoffel, N. G.; Riedel, R.; Colavita, E.; Margaritondo, G.; Haglund, Jr., R. F.; Taglauer, E.; Tolk, N. H. Photon-stimulated desorption of neutral sodium from alkali halides observed by laser-induced fluorescence. Phys. Rev. B32(10): 6805-6808; 1985.

[8] Siekhaus, W. J.; Kinney, J. H.; Milam, D.; Chase, L. L. Electron emission from insulator and semiconductor surfaces by multiphoton excitation below the optical damage threshold. Appl. Phys. A39: 163-166; 1986.

[9] Young, C. E.; Gruen, D. M.; Pellin, M. J.; Calaway, W. F. Narrow Band, near UV, high repetition rate laser induced fluorescence system for use as an edge diagnostic in fusion machines. Fusion Techn. 6: 434-446; 1984.

[10] Young, C. E.; Calaway, W. F.; Pellin, M. J.; Gruen, D. M. Velocity and electronic state distribution of sputtered Fe atoms by laser-induced fluorescence spectroscopy. J. Vac. Sci. Technol. A2(2): 693-697; 1984.

[11] Landolt Börnstein, N.S., Vol. 17b, 1982, 63 p.

[12] Wood, Roger M. Laser damage in optical materials. Bristol: Adam Hilger; 1986.

[13] Kasuya, A.; Nishina, Y. Dynamical characteristics of laser vaporization process in group IV elements. Nishina, Y.; Ohnushi, S.; Sugana, S., ed. Proceedings of the 1st NEC Symposium, Berlin; New York, Springer Verlag; 1987.

[14] Cole, S. K.; Liu, K. Metastable decay of photoionized niobium clusters I. A new experimental method. Submitted to J. Chem. Phys.

[15] Begemann, W.; Meiwes-Broer, K. H.; Lutz, H. O. Unimolecular decomposition of sputtered Al_n^+, Cu_n^+, and Si_n^+ clusters. Phys. Rev. Let. 56(21): 2248-2251; 1986.

[16] Press, William H.; Flannery, Brian P.; Teukolsky, Saul A.; Vetterling, William T. Numerical recipes : the art of scientific computing. Cambridge: Cambridge universdity press; 1986.

[17] Benninghoven, A. A mass spectrometrical method for measuring sputtering rate and secondary ion emission coefficients of solids by thin layers. Z. angew. Phys. 27(1): 51-55; 1969.

Manuscript Received
2-22-88

Damage to Fused Silica Windows while Under Simultaneous Exposure to Flowing Solvents and Laser Radiation at 308 nm

Billie R. Mauro, Stephen R. Foltyn and Virgil Sanders

Los Alamos National Laboratory
Los Alamos, NM 87545

This paper reports the results of a study to determine the degrading effects of flowing dye solvents on the laser damage threshold of fused-silica windows at 308 nm. Thresholds were measured at the SiO_2/solvent interface in a test cell. Bare SiO_2 tested in air at 308 nm (20 ns) typically exhibits a threshold ranging from 4 to 10 J/cm^2; with the solvent cyclohexane in contact, a threshold as low as 0.3 J/cm^2 was measured. The damage data indicate that window lifetime (number of shots) is independent of fluence at higher levels, and asymptotically approaches infinity at levels near threshold. Dielectric coatings were tested as possible damage-resistant barriers between the solvent and SiO_2; the results show some improvement in damage threshold. When cyclohexane is replaced with the solvent dioxane, thresholds measured for SiO_2 windows are within the range cited above for thresholds measured in air.

Key words: cyclohexane; dioxane; dye solvents; fused silica; optical damage; simultaneous exposure; window lifetime

1. Introduction

This study was undertaken in order to investigate the cause of damage to fused-silica windows on preamplifier and oscillator cells in a large XeCl-pumped-dye-laser system that contained the dye solvent cyclohexane. It was observed that damage in the system always first appeared as the deposition of carbon or carbon compounds on the inner faces of both the pump and output windows of the cells. These deposits of carbon strongly absorb laser light and lead to catastrophic failure of the window surfaces at fluence levels far lower than the damage threshold for the same window material tested in air.

2. Test Conditions

The laser used in this study is a Lambda Physik excimer laser, model EMG203, operating at 308 nm with a pulse duration of 20 ns. Figure 1 demonstrates the experimental layout of the laser-damage test facility. The experimental set-up incorporates a flow simulator with replaceable test windows (shown in fig. 2). Normal test conditions include a solvent flow rate of four gallons per minute, a clearing ratio of two, a laser spot size of 1 mm x 12 mm, and a pulse-repetition rate of 200 Hz. The test plane is located at the SiO_2/solvent interface of the test cell. While the cell window is simultaneously exposed to flowing solvent and laser radiation, damage is observed visually with a 60x telescope and video camera. The damage threshold is determined to be the highest test-plane fluence at which no damage occurs in 10^6 shots. Cyclohexane and dioxane are the only laser-dye solvents studied in this series of tests; Corning 7940 is the window material.

3. Test Results

3.1. Cyclohexane Data

Experimental results for near-uv dye lasers pumped with pulses from a XeCl laser have shown that the solvent will effect the operation of a dye laser -- particularly its photochemical stability [1]. Therefore, initial tests for this experiment utilized the solvent cyclohexane alone; no laser dye was added to the solvent. Damage, appearing as the deposition of carbon or carbon compounds, was produced at fluence levels as low as 0.4 J/cm^2; yet thresholds for bare SiO_2 tested in air at this facility range from 4 to 10 J/cm^2 and carbon deposits are not a part of the damage morphology. The fused-silica damage data for cyclohexane (fig. 3) indicate asymptotic behavior at threshold and, at fluences above threshold, all damage is delayed and occurs at approximately 10^5 shots. Tests at varied pulse-repetition rates (100 to 200 Hz), solvent-flow rates (2 to 4 gpm), and clearing ratios (1 to 3) reveal no significant dependence of damage on any of these parameters.

In an attempt to improve on the window damage threshold when in contact with cyclohexane, two other window materials were tested. Sapphire windows exhibit threshold behavior at 1.3 J/cm^2 and the damage also appears as carbon deposits. Sapphire windows tested in air at this facility produced a damage threshold of 2 J/cm^2. A MgF_2 window could not be damaged in 10^6 shots at up to 3.3 J/cm^2, which was the maximum test-plane fluence attainable with the 1 x 12 mm beam. However, previous tests of MgF_2 in air at 248 nm and 351nm have produced thresholds of 19 and 20 J/cm^2 respectively [2]. Dielectric coatings were tested as possible damage-resistant barriers between the solvent and SiO_2. As seen in the following table, thicker coatings (10,000 Å) can improve damage threshold nearly 1.5 times while thinner coatings provide little or no improvement. These combined results imply that the window is not simply a passive surface that collects the products of photo-dissociation, but is an active participant in the reactions.

Table 1. Coatings as Barriers between SiO_2 and Cyclohexane

Materials Tested	Damage Threshold (J/cm^2)
Al_2O_3 single layer (10,000 Å) on SiO_2	1.9
Al_2O_3 antireflector (~1,000 Å) on SiO_2	1.1
Al_2O_3 single layer (100 Å) on SiO_2	0.8
uncoated SiO_2 companion sample	0.8

3.2. Dioxane Data

A major improvement in damage threshold occurs when the solvent dioxane is used. As seen in figure 4, the thresholds exceed those measured in cyclohexane by an order of magnitude. (It was necessary to reduce the spot size to .5 mm x 2 mm in order to attain greater test-plane fluences. Appropriate cross checks were made to ensure that the higher damage threshold could not be attributed to a decreased spot size.) Further, no carbon deposits were observed on the cell windows -- damage appears to be a surface-roughening process similar to that seen on samples tested in air. Although companion samples tested in air and in dioxane produce nearly the same damage thresholds (8 to 10 J/cm^2), those tested in dioxane appear to produce delayed damage. (This might be attributed to a partial index match between the dioxane and SiO_2 which could make damage more difficult to see.)

4. Conclusions

The data for SiO_2 windows tested in cyclohexane suggest that damage is independent of repetition rate or flow conditions. Further, damage near threshold occurs after an accumulation of shots depending on fluence, while at values above threshold, damage occurs after a fixed number of shots regardless of test-plane fluence. A thick dielectric coating is able to protect the SiO_2 surface at test-plane fluences up to nearly 1.5 times the damage threshold for uncoated SiO_2, while thinner coatings show little or no improvement. Finally, the data suggest that cyclohexane damage is a photochemical process rather than a photodeposition process, and the photochemical process is more pronounced for SiO_2 windows than for Al_2O_3 or MgF_2 windows.

For tests in the solvent dioxane, no photochemical deposition is observed in the damage mechanism. Fused-silica damage thresholds depend upon test-plane fluence, and, while damage appears to be delayed, thresholds are comparable to those measured for SiO_2 windows tested in air.

7. References

[1] P. Cassard, P. B. Corkum, A. J. Alcock. Characteristics of XeCl pumped uv dye lasers. Appl. Phys. 25, 17-22 (1981).

[2] L. J. Jolin, Los Alamos National Laboratory (unpublished test results).

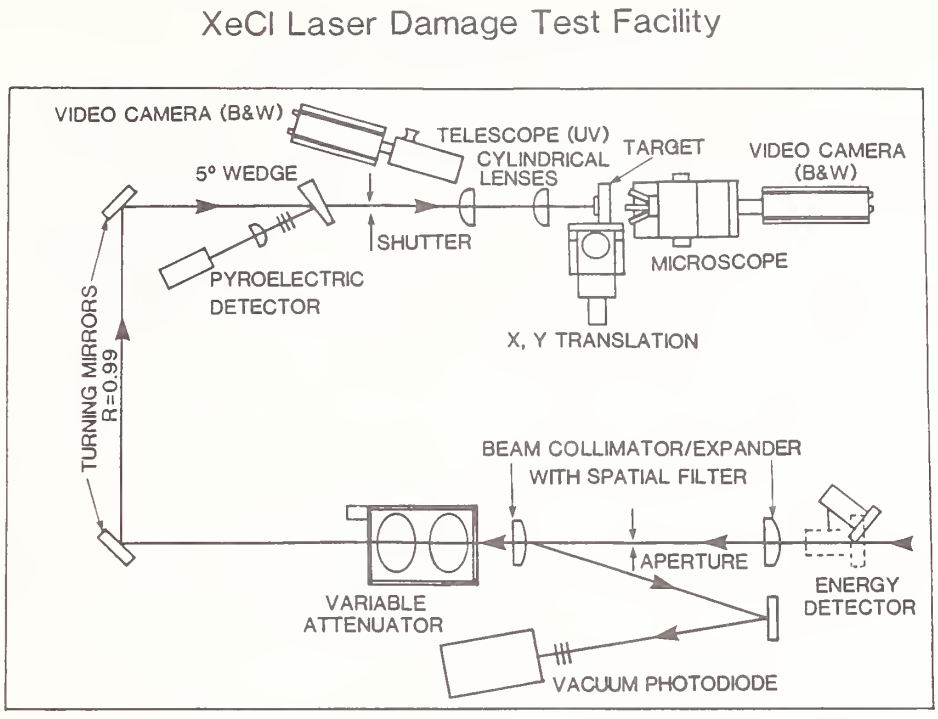

Figure 1. Line drawing of the laser damage test facility.

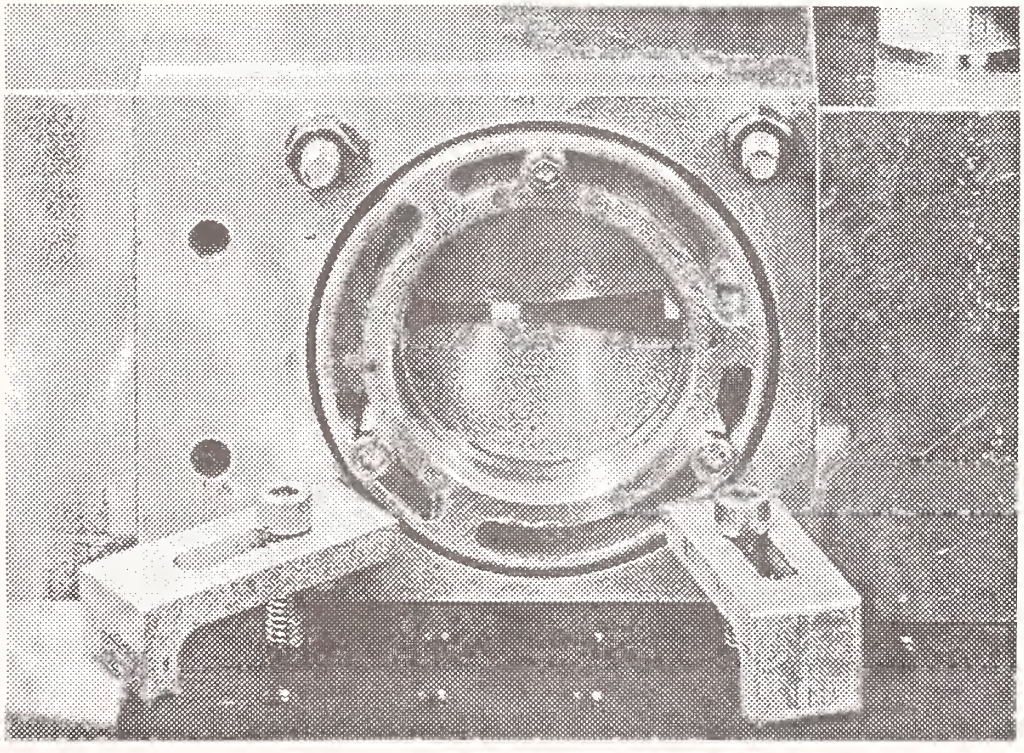

Figure 2. Test cell that incorporates flowing dye solvents and replaceable test windows.

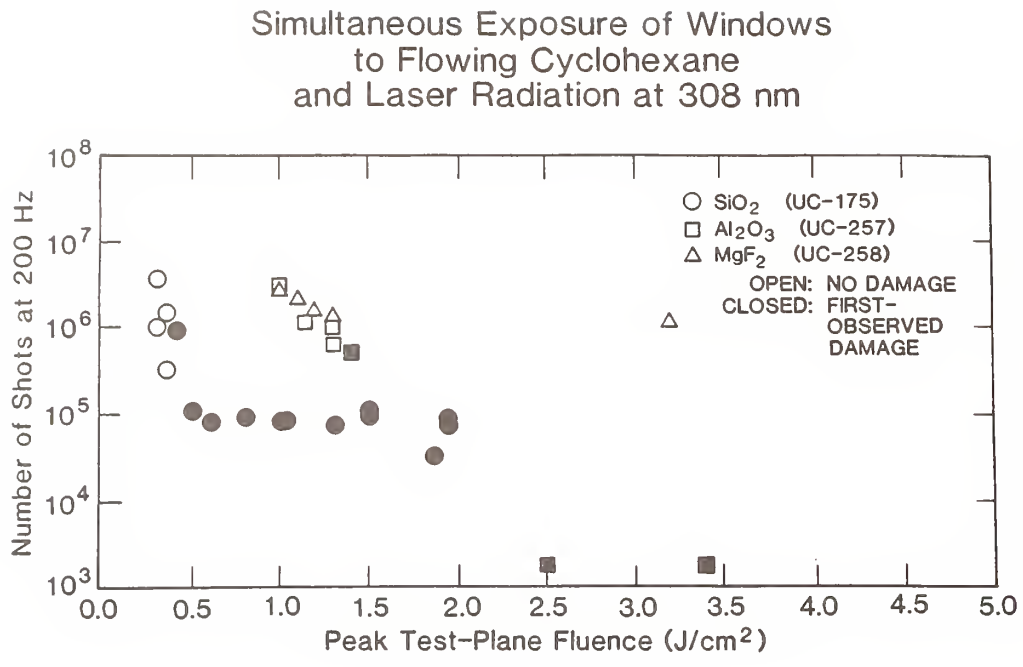

Figure 3. Cyclohexane test data for SiO_2, Al_2O_3, and MgF_2 windows.

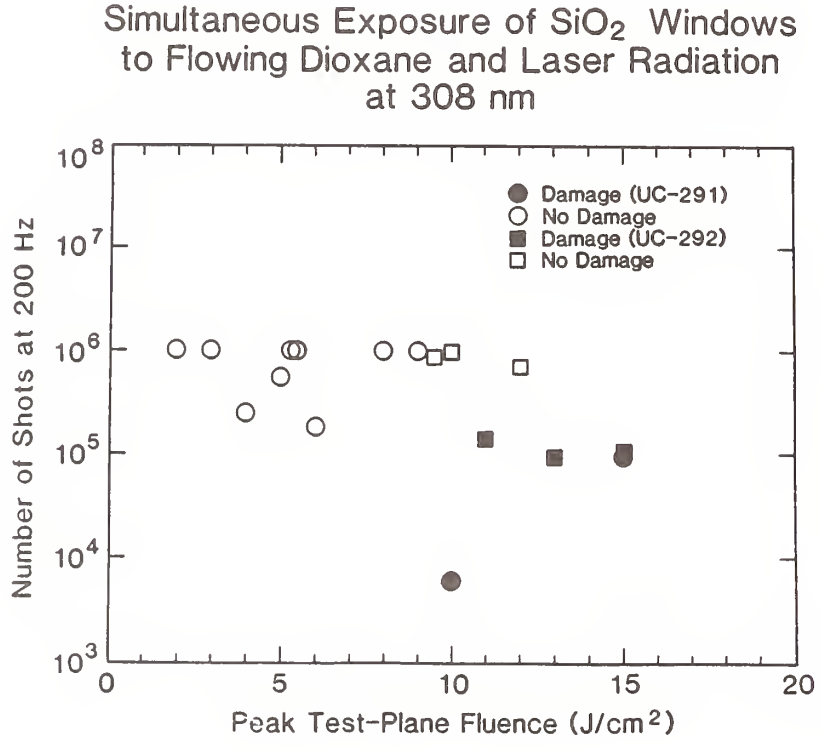

Figure 4. Dioxane test data for SiO_2 windows.

Manuscript Received
1-12-88

LASER DAMAGE STUDIES of ION BEAM MILLED FUSED SILICA

S. R. Wilson, D. W. Reicher, J. R. McNeil

University of New Mexico
Department of Electrical and Computer Engineering
Center for High Technology Materials
Albuquerque, NM 87131

J. J. McNally

Department of Physics
USAFA/DFP
United States Air Force Academy, CO 80840

Kent Stowell

AFWL/ARBD
Kirtland AFB
Albuquerque, NM 87117

D. Milam, R. Gonzales, and F. Rainer

Lawrence Livermore National Laboratory
University of California
P. O. Box 5508, L-490
Livermore, CA 94550

Ion beam figuring is a promising optical fabrication technique in which substrate material is removed from an optical component by selectively ion beam milling the surface. The effects of ion beam milling on the properties of the optical surface are not completely understood. One area of investigation is the influence of ion beam milling on the laser damage threshold of the substrate. The ion milling process removes part of the damage layer at the surface of the optic formed during fabrication, and this might result in modification of laser damage behavior.

As part of an investigation of the ion beam figuring process, a study was undertaken to determine the effect of ion milling on the laser damage threshold of fused silica. Fused silica substrates were ion milled to depths up to ten microns using a 1500 eV, 40mA Argon ion beam from a Kaufman ion source. The milled substrates were then subjected to laser damage testing using a 1064 nanometer wavelength laser. The tests were performed using one nanosecond pulse width single shot pulses and sixteen nanosecond pulse width thirty Hz pulses. The results indicate that ion beam milling has no significant influence on the damage threshold.

Key words: ion beam, laser damage, fused silica, ion milling.

1. Introduction

The fabrication of optical surfaces by sputtering is a process which has been of interest to many researchers since it was first attempted two decades ago. Recent technical developments in ion sources and phase measurement interferometers have pushed this technology to a practical level, where the sputtering is accomplished by ion beam milling. Figure 1 illustrates the experimental arrangement. This has been discussed in References 1 and 2. The effects of sputtering on the properties of optical materials are numerous. These include changes in surface roughness, stoichiometry, crystal structure, and optical constants. The effect of ion beam milling on the laser damage threshold is presently unknown, but a modification of the damage threshold would not be unexpected.

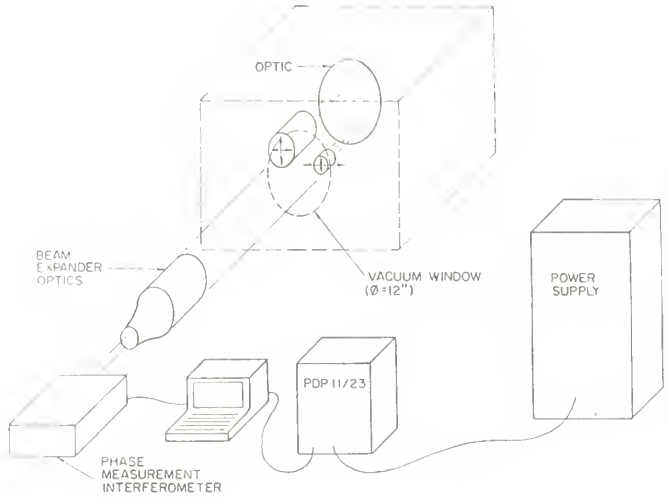

Figure 1.

A major advantage of ion beam milling is that no foreign materials are in contact with the optical surface. This produces a surface which should differ substantially from one produced by conventional processes. In order to investigate the influence of the differences in process on laser damage threshold several fused silica samples were subjected to ion beam milling and then laser damage tested.[1]

2. The Damage Layer

The damage layer of a polished surface, sometimes referred to as the Beilby layer, consists of several distinct regions. A diagram of these regions is shown in Figure 2. At the top is the redeposition region which consists of silicon dioxide formed by the indicated reaction. Below this is a region of hydrolyzed silicon, and then an area where hydrogen ions have replaced ions extracted from the glass. In addition to the chemical alteration of the glass, the water diffusion region also contains fine fractures of the glass and the ion exchange region contains course fractures of the glass. These fractures may be the result of the grinding process and promote the penetration of the water and ions into the glass. The thickness of each region in the damage layer is of the order of tens of microns. Finally the chemically unaltered glass is found.

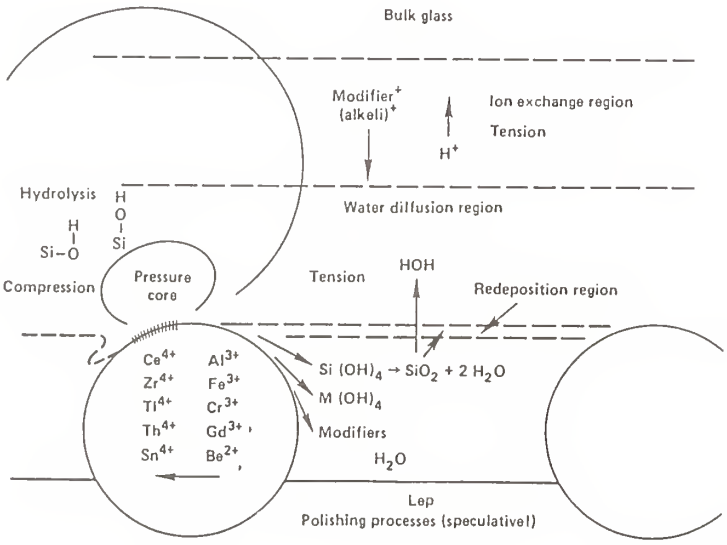

Figure 2.

3. Sample Preparation

Fused silica samples were obtained from Lawrence Livermore National Laboratory. The samples were cleaned using soap and water, followed by drag wipe cleaning with optical grade ethanol. The samples were placed in aluminum holders covered, and loaded in a vacuum chamber. The samples were then milled between 3 and 10 microns using a 1500 eV, 30mA neutralized argon ion beam produced by a Kaufman ion source. These mill depths were chosen because they are typical of what occurs in the ion beam figuring process. The distance from the sample to the ion source was approximately eight inches. A shield was placed over half of the sample. Due to the shielding, each sample had a milled and unmilled area. The experimental arrangement is shown in Figure 3.

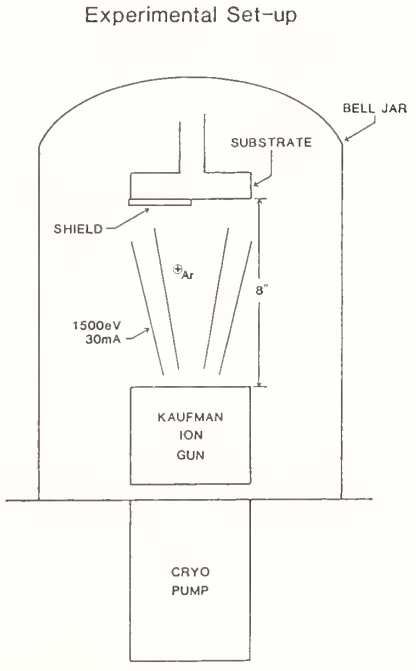

Figure 3.

The samples were then packaged in protective holders, sealed, and sent to LLNL for laser damage testing. The testing was performed using the VPL damage facility with one nanosecond 1064 nanometer pulses at ten degrees incidence. Some additional testing was done using the REPTILE facility with sixteen nanosecond 1064 nanometer pulses at a pulse repetition frequency of thirty Hz. This facility is illustrated in Figure 4. Both the incident (front) and exit (rear) surfaces were examined after testing. Front surface damage is more difficult to detect near threshold. Rear surface damage is easier to detect and is often observed at lower thresholds than the front surface damage.

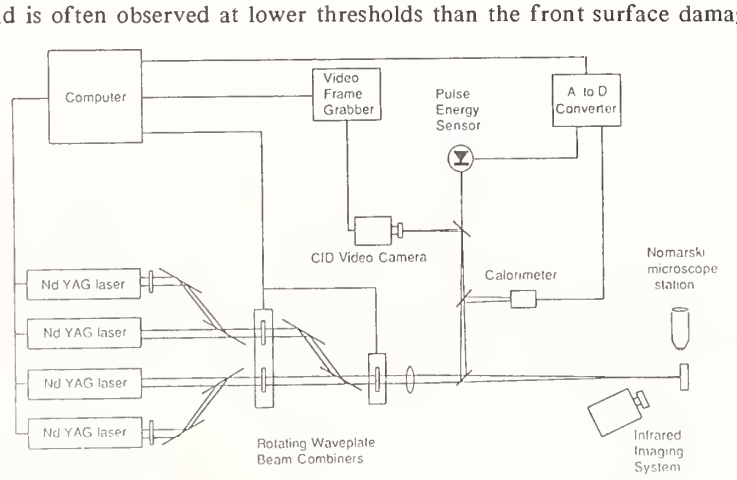

Figure 4.

4. Laser Damage Results

The results from the laser damage tests are shown in Figure 5. The results are categorized by the surface treatment (polished or milled), and which surface was observed for damage (front or rear).

Laser Damage Results from Ion Beam Milled Fused Silica

Test #	Sample #	PRF (Hz)	PW (ns)	Scan	Milled Front Surface (J/cm^2)	Polished Front Surface (J/cm^2)	Milled Rear Surface (J/cm^2)	Polished Rear Surface (J/cm^2)
V2765	3519	SS	1	None	16.5±2.5			16.5±2.5
V2767	3519	SS	1	None		17.0±2.5	17.0±2.5	
R130	3519	30	16	Scan	〉45.5		〉 46.2	
V2766	3551	SS	1	None	〈 19.7	18.8±2.8	17.6±2.6	〈 19.7
R128	3551	30	16	Single		46.5±7.0	38.8±5.8	
V2771	3892	SS	1	None		20.7±3.1		

Figure 5. PRF = Pulse Repetition Frequency PW = Pulse Width

Scan = Beam Scanned Across Sample

From the data it can be seen that within the limits of experimental error no difference in laser damage threshold was observed. The damage thresholds for all of the single-shot tests rank among the higher ones measured for bare polished fused silica. A large data base of results for bare fused silica using 30 Hz PRF was not available, but the results obtained for these samples are consistent with preliminary data taken by the REPTILE facility.

5. Discussion

Based on these damage results, there appears to be no difference in the laser damage threshold between the milled and unmilled surfaces. This is the trend for both the single-shot and 30 Hz PRF data.

The lack of a modified laser damage behavior for the milled surfaces indicates that ion beam milling does not produce any further surface damage. Since the redeposition region was probably removed, it seems this portion of the damage layer is not significantly involved in laser damage. It can therefore be hypothesized that the laser damage is induced in the lower lying portions of the damage layer. If this is true, then improved grinding and polishing techniques should result in improved laser damage thresholds.

6. Summary

The laser damage threshold data obtained in this investigation indicates that ion beam milling can safely be used to figure fused silica substrates for use in high power applications. If the grinding and polishing steps prior to figuring can be improved, it may be possible to increase the damage threshold. Additional areas of investigation include the investigation of deeply milled (50 microns or more) surfaces such that the chemically unaltered layer is exposed, and the influence of ion beam milling on the laser damage threshold coated optics. In the latter, the coating can be applied to the surface which has been milled without breaking vacuum, thus providing a very clean substrate coating interface. Even if it is necessary to figure the optic and remove it from vacuum, improved damage threshold may result from the removal of surface contaminates.

References

1. S.R. Wilson and J.R. McNeil, "Neutral Ion Beam Figuring of Large Optical Surfaces", Workshop on Optical Fabrication and Testing Technical Digest 1987, Vol. 19, (Optical Society of America, Washington, DC 1987) pp. 109-114.

2. S.R. Wilson and J.R. McNeil, "Neutral Ion Beam Figuring of Large Optical Surfaces", SPIE Proceeding, 1987.

Manuscript Received
4-22-88

DIAMOND, A POTENTIALLY NEW OPTICAL COATING MATERIAL*

Albert Feldman, Edward N. Farabaugh, and Y. N. Sun**
Ceramics Division
Institute for Materials Science and Engineering
and
Edgar S. Etz
Center for Analytical Chemistry

National Bureau of Standards
Gaithersburg MD 20899

The ability to synthesize diamond films at low pressures offers the possibility of superior optical coatings for severe environments. This is because of diamond's great hardness, high thermal conductivity, and chemical inertness. However, several problems must be overcome before practical diamond optical coatings can be made. They include difficulties in film nucleation, high substrate temperatures, and large film surface roughness leading to high optical scatter.

Key words: Auger spectroscopy, carbon, chemical vapor deposition, CVD, diamond films, electron energy loss spectroscopy, infrared spectroscopy, Raman spectroscopy, surface roughness, thin films, x-ray diffraction.

1. Introduction

At present, many optical materials are subject to degradation due to several factors, including chemical attack from corrosive environments such as in excimer lasers, physical abrasion, or erosion damage from atmospheric conditions such as wind, rain, and dust impact. Because of the hardness of diamond, its high thermal conductivity, and its chemical inertness, diamond films offer the possibility of a superior protective optical coating material that is transparent over an extensive range of the spectrum. Diamond is both the hardest material known and the material with the highest thermal conductivity.[1] In addition, it is stable to reasonably high temperatures (900K in the presence of oxygen, 1800K in the absence of oxygen).

Until recently, there has been interest in the U.S. on 'diamond-like' films,[2,3] hard carbon films usually containing a substantial molar fraction of hydrogen. These films go under the name of diamond-like carbon (DLC), amorphous hydrogenated carbon, and i-carbon. However, because of significant advances made in the Soviet Union[4,5] and Japan,[6] in depositing 'true' diamond films, interest in the U.S. has shifted to the area of diamond films as well.[7] Several methods are used to produce diamond films, all based on chemical vapor deposition (CVD) of diamond from an atmosphere of several percent methane and the remainder hydrogen. These include hot filament CVD,[6] electron-assisted CVD,[8,9] microwave plasma-assisted CVD,[10] RF discharge CVD,[11] DC discharge CVD,[12] laser-assisted deposition,[13] and remote plasma CVD.[14] In addition, other organic compounds can be used to produce diamond.[15] While many approaches have been used to produce diamond films, it is not yet clear which method is superior. The availability of commercial apparatus for diamond film deposition by the microwave plasma method suggests that is the most favorable. A microwave discharge deposits a greater amount of energy into the plasma compared to an RF discharge [16] and, thus, would appear to be more efficient. However, other methods cannot be ruled out, particularly in the absence of detailed mechanistic information regarding the deposition process.

* Work supported in part by U. S. Army ARDEC Integrated Optical Logic Program directed by G. Vezzoli.
** Guest scientist from Lanzhou Institute of Physics, Lanzhou, People's Republic of China

In this paper, we discuss the work being done at NBS on diamond film deposition. We have been depositing diamond films by the hot filament CVD method; the films have been verified to be diamond by x-ray diffraction, Raman spectroscopy, Auger electron spectroscopy, and electron energy loss spectroscopy. Scanning electron microscopy has been used to examine the morphology of the films.

2. Diamond Film Research at NBS

We have been depositing diamond films using the hot filament chemical vapor deposition method.[5] The method was chosen for its simplicity and for scale-up possibilities. The deposition chamber, shown in figure 1 consists of a fused silica envelope bolted to a brass flange. The flange contains a gas inlet for the reactive gases, a gas outlet to a mechanical pump, and electrical feedthroughs for filament power, biasing voltages and a thermocouple temperature sensor. In the chamber, the reactive gases flow through a narrow fused silica tube onto a heated tungsten filament which is suspended above the substrate holder. The reactive gas is a mixture of 0.47% methane and the remainder hydrogen. The thermocouple was embedded in the substrate holder in order to monitor the substrate temperature. Specimen substrates are typically 1 cm^2. Substrate materials were Si single crystal wafers, silica, and sapphire.

The gas flow rate was externally controlled by a needle valve and monitored by a flow meter. Prior to installation in the deposition apparatus, the flow meter had been calibrated by measuring the speed of hydrogen filled soap bubbles propagating through a specially constructed graduated pipette connected in series with the flow meter. The gas pressure was controlled by means of a needle valve connected between the deposition chamber and the mechanical vacuum pump; the pressure is read by means of both a thermocouple vacuum gauge and a diaphragm gauge.

The filament, which is made from tungsten wire 0.005" in diameter and 1.5" long, is wound around a mandrel to form a five turn coil with a coil diameter of 0.045"; if the turns are not present, the filament breaks during heating. The filament power is controlled by means of a power supply capable of operating in a constant voltage mode or a constant current mode. It was found that for the first several hours of gas flow, the resistance of the filament changed by a least a factor of two. T. Moustakas, reporting at the recent Second Annual Diamond Initiative Seminar in Durham, N. C. has found the same effect which he has shown to be due to conversion of W to W_2C. In order to stabilize the filament characteristics, the filament is run for several hours in the reactive gas environment prior to the start of the deposition.

During some our earlier depositions, a voltage was maintained between the filament and the substrate holder, typically 100V biased positive with respect to the filament. This resulted in an emission current from the filament of about 10mA. The method, which is called electron assisted CVD (or EACVD), was reported to yield denser diamond films than the simple hot filament method. [8] However, because we have been unable to discern any difference between films made with the field applied and films made without the field applied, we have ceased applying bias voltages during our depositions.

The deposition is carried out as follows: the apparatus is inserted into a gold furnace and the temperature is raised to the desired nominal substrate temperature, 700 or 800 deg C; the temperature is considered nominal because the specimen surface can be significantly higher than the substrate holder due to radiative heating from the filament. The gas flow is then started, a typical flow rate being 50 ccm. Next, the filament power is turned on; the input power is about 60W and the filament temperature is about 1800 deg C as measured by an optical pyrometer. This begins the deposition. The deposition is stopped by evacuating the deposition chamber and shutting off the power, first to the filament and then to the furnace. Deposition are usually done overnight, typically for 17 hrs. Table 1 summarizes a typical set of deposition conditions.

Our first successful depositions were made on silicon wafer substrates. The deposited material consisted of crystalline particles having polyhedral shapes typical of the diamond particles described in the literature. Examples of the particles we have obtained are shown in figure 2. Subsequently, we were able to deposit these particles on sapphire and silica substrates as well. The sizes of the particles, as measured by SEM, were in the range 3-10μm. Micro-Raman spectra were obtained from individual particles; a typical spectrum is shown in figure 3. The spectrum consists of a sharp Raman line with very little background centered at 1322 cm^{-1}, which is 10cm^{-1} below the Raman line of natural diamond. The origin

of this shift is not known; if the shift were due to stress effects, the magnitude of the stresses, calculated on the basis of the measured stress dependence of Raman shifts in natural diamond,[17] would have to be about $3x10^9$pa isostatic tensile stress. Also shown in the figure is the Raman spectrum of a gem quality diamond, lines from a mercury spectral lamp used for calibration, and a line due to the Si substrate material.

Because of the sparseness and small size of our diamond particles, we were unable to use x-ray diffraction to verify the presence of the diamond structure. We were able to deposit continuous diamond films by rubbing the surfaces of our substrates with diamond paste.[18] The specimen was then thoroughly washed to remove the paste. Figure 4 shows scanning electron micrographs of one such film under different powers of magnification. Observe that the films are extremely rough, consisting of merged crystallites showing triangular faces corresponding to the [111] crystallographic faces.

Table 1. Typical Parameters Used to Deposit Diamond Films by the Hot Filament CVD Method

gas mixture: 0.47% methane, remainder hydrogen
flow rate: 50 ccm
base pressure: 0.1 torr
deposition pressure: 40 torr
filament: W wire
power to filament: 60W
filament temperature: 1800 °C (approx)
substrate temperature range: 700-800 °C
substrates: silicon predominantly, also silica, sapphire
substrate dimensions, typical: 1 cm^2.

X-ray diffraction measurements were made on the deposited films both with a Read thin-film diffraction camera and with a powder diffractometer. The Read camera photographs shown in figure 5 show a one-to-one correspondence of the diffraction lines in natural diamond abrasive powder with the diffraction lines in the film. The diffractometer allowed us to obtain accurate lattice constants. Table 2 compares the lattice spacings of a diamond film we have made with the lattices spacings of natural diamond.

Table 2. DIAMOND LATTICE SPACINGS (Angstroms)

hkl	natural diamond	NBS diamond film
111	2.060	2.0606
220	1.261	1.2620
311	1.0754	1.0760
400	0.8916	0.8921
331	0.8182	0.8184

A Raman spectrum from one of our films is shown in figure 6. This spectrum differs significantly from the spectrum of the diamond particle. A sharp peak is observed at $1334cm^{-1}$ which is near the position of the Raman peak of natural diamond at $1332cm^{-1}$. However, the peak in the film spectrum is considerably broader. Near $1510cm^{-1}$, another Raman peak attributable to another allotropic phase of carbon, perhaps diamond-like carbon (DLC) can be observed. Thus, this film appears to be a mixture of tetrahedral diamond and DLC. Also observed in the diamond film spectrum is a significant background signal extending over a large wavelength range which is attributed to specimen luminescence. The luminescence signal peaks at a wavelength in the vicinity of 738nm (1.68ev). A similar band in irradiated natural diamond has been attributed to isolated lattice vacancies.[19]

Two other techniques have been used to verify the presence of diamond in our films, Auger electron spectroscopy [20,21] and electron-energy loss spectroscopy.[20] Figure 7 shows the spectra we have obtained from our diamond films and from graphite placed in our surface analysis facility. The differences we observe in the spectra of our diamond films and in the spectra of graphite are consistent with the data reported in the literature.

X-ray diffraction, SEM, and Raman spectroscopy used together, appear to be the best techniques for evaluating the quality of diamond films. X-ray diffraction confirms the crystal structure; however, it is not sensitive to other forms of carbon that may be present in the films such as DLC. Raman spectroscopy appears to be the most sensitive technique for observing other forms of carbon in the films. An important goal would be to be able to use Raman spectroscopy to determine the ratio of diamond and DLC material in a film. SEM is important for examining the morphology of the films. The other techniques, Auger spectroscopy and electron energy loss spectroscopy are surface techniques, and, hence, would be sensitive to surface contamination. It would appear that these techniques would not be sensitive enough to quantitatively obtain ratios of diamond and DLC in films.

The use of currently available diamond films as optical coatings is not presently feasible due to the large optical scatter these films exhibit. However, such films might be usable as infrared coatings at wavelengths longer than 10μm. Figure 8 shows a single pass transmission spectrum of a diamond film on a silicon substrate taken in a Fourier transform infrared spectrometer. The general features of the spectrum are an increasing optical density as the frequency increases, the appearance of interference fringes at the lower frequencies, and high optical transmissivity at frequencies less than 1000 cm^{-1}. We believe that the large optical attenuation at the higher frequencies is due mainly to optical scatter and not to absorption.

3. Technical Challenges to the Use of Diamond Optical Films

Before diamond films can be used as optical coatings, several problems must be overcome.

The mechanism for the diamond forming process is not understood. In the various plasma assisted deposition methods, there is little detailed atomic and molecular level knowledge of the actual species present in the CVD gas nor of their interactions with the substrate or the film. Crucial to the quantitative understanding of the CVD formation of diamond is a detailed knowledge of the identity, reaction rates, spatial distribution, and thermochemistry of the atomic, molecular, and ionic species present in the reactive gas flow as a function of processing conditions, and how their interactions affect the deposition process.

In the case of the filament method, it is unknown what processes are occurring. It will be necessary to clarify the importance of the filament temperature, the filament electron emission, the filament composition (W, WC, other metals), and the filament shape. Sagging of the filament is a major problem with the filament method because after several depositions, the filament, which is located above the specimen, comes into contact with the specimen. If this method is to have practical applications, means must be found either to prevent sagging or to cause sagging to be of no consequence.

The substrate temperature is a critical factor in the deposition of diamond. These temperatures are high, typically in the range 600-1050 °C. Unless the deposition temperature can be lowered significantly, the application of diamond film technology will be restricted to substrate materials that can withstand these high temperatures. Some optical applications will be difficult to implement at current temperatures because many of the commonly used optical materials such as plastics would melt, and the optical figure frequently required in precision optics would be destroyed.

Currently, the diamond films that are deposited have significant surface roughness (about 2μm peak to valley. 0.4μm average roughness). These roughness values would prevent the use of diamond as an optical coating in the near infrared, visible and near ultraviolet because of the large optical scatter that would occur.

The purity of the diamond films would be critical in optical applications. Small amounts of graphitic carbon in the films would adversely affect the transmissivity of the films. Methodologies must be developed for quantifying carbon in these films in forms other than diamond.

Finally, there are problems of nucleation of diamond on various substrate materials. As discussed above, special surface preparation was required before a continuous diamond film could be formed on the silicon substrates. We suspect that although the specimens had been cleaned after rubbing with diamond paste, residual diamond remains embedded in the surface acting as nucleation sites for the diamond deposition. However, the question of the need to provide nucleation sites by seeding has not been answered definitively. In order to obtain smoother films, higher nucleation densities must be obtained. An alternative means for obtaining smooth diamond films would be epitaxial growth of single crystal diamond films. Although diamond films can be grown epitaxially on diamond substrates, it is not clear that diamond could be grown epitaxially on other substrates. In this regard, lattice matching diamond to other crystalline materials would be difficult because diamond has an extremely small lattice constant.

4. Summary

The ability to synthesize diamond films at low pressures offers the possibility of superior optical coatings for severe environments. This is because of diamond's great hardness, high thermal conductivity, and chemical inertness. However, several problems must be overcome before practical diamond optical coatings can be made. They include difficulties in film nucleation, high substrate temperatures, and large film surface roughness leading to high optical scatter.

We would like to thank the following individuals for their assistance: from NBS, D. Minor for SEM work, R. Faltynek for FTIR spectroscopy, S. Jahanmir for surface roughness measurements and Peter Schenck for useful discussions regarding the chemistry of diamond film formation; from North Carolina State University, R. Nemanich and R. Shroder for examining one of our films on their Raman spectrometer; from Penn State University, A. Badzian for useful discussions, especially with regard surface preparation.

5. References

[1] J. E. Field, editor, The Properties of Diamond (Academic Press, London, 1979).

[2] S. Aisenberg and R. Chabot, "Ion-Beam Deposition of Thin Films of Diamond-like Carbon," J. Appl. Phys. 42, 2953 (1971).

[3] B. V. Derjaguin and D. B. Fedoseev, "The Sythesis of Diamond at Low Pressure," Sci. Amer. 233, 102-9 (1975).

[4] B. V. Spitsyn, L. L. Bouilov, and B. V. Derjaguin, "Vapor Growth of Diamond on Diamond and Other Surfaces," J. Cryst. Growth 52, 219 (1981).

[5] S. Matsumoto, Y. Sato, M. Tsutsumi, and N. Setaka, "Growth of Diamond Particles from Methane-Hydrogen Gas," J. Mater. Sci. 17, 3106 (1982).

[6] A. Badzian, B. Simonton, T. Badzian, R. Messier, K. E. Spear, and R. Roy, in: "Infrared and Optical Transmitting Materials," R. W. Schwartz, ed. (SPIE, Bellingham, WA, 1986), SPIE Conf. Vol. 683, p. 127.

[7] R. Roy, "Diamonds at low pressure," Nature 325, 17-8 (1987).

[8] A. Sawabe and T. Inuzuka, "Growth of Diamond Films by Electron-Assisted Chemical Vapor Deposition," Appl. Phys. Lett. 46, 146 (1985).

[9] A. Sawabe and T. Inuzuka, "Growth of Diamond Thin Films by Electron-Assisted Chemical Vapor Deposition and Their Characterization," Thin Solid Films, 137, 89 (1986).

[10] Y. Saito, S. Matsuda, and S. Nigita, "Synthesis of Diamond by Decomposition of Methane in Microwave Plasma," J. Mater. Sci. Lett. 5, 565 (1986).

[11] Z. Has and S. Mitura, "Nucleation of Allotropic Carbon in an External Electric Field," Thin Solid Films 128, 353-60 (1985).

[12] K. Suzuki, A. Sawabe, H. Yasuda, and T. Innzuka, "Growth of Diamond Thin Films by DC Plasma Chemical Vapor Deposition," Appl. Phys. Lett. 50, 728 (1987).

[13] K. Kitahama, K. Hirata, H. Nakamatsu, S. Kawai, N. Fujimori, T. Imai, H. Yoshimo, and A. Doi, "Synthesis of Diamond by Laser-Induced Chemical Vapor Deposition," Appl. Phys. Lett. 49, 634 (1986).

[14] Second Annual Diamond Technology Initiative Seminar, Durham NC, 7-8 July, 1987.

[15] Y. Hirose, and Y. Terasawa, "Synthesis of Diamond Thin Films by Thermal CVD Using Organic Compounds," Jpn. J. Appl. Phys. Part 2 25, L519 (1986).

[16] M. R. Wertheimer and M. Moisan, "Comparison of microwave and lower frequency plasmas for thin film deposition and etching," J. Vac. Sci. Technol. A 3, 2643-9 (1985).

[17] B. J. Parsons, Proc. R. Soc. Lond. A252, 397-417 (1977).

[18] A. Badzian, private communication.

[19] Reference [1] above, p.44.

[20] P. G. Lurie and J. M. Wilson, "The Diamond Surface I. The structure of the clean surface and the interaction with gases and metals," Surface Science 65, 453-75 (1977).

[21] T. J. Moravec and T. W. Orent, "Electron spectroscopy of ion beam and hydrocarbon plasma generated diamond-like carbon films," J. Vac. Sci. Technol. 18, 226-8 (1981).

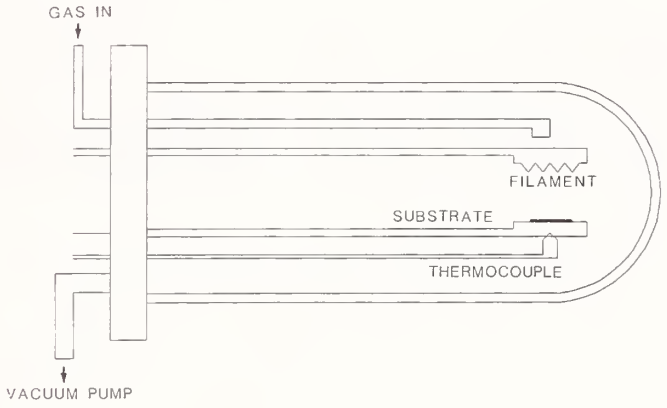

Figure 1. Schematic diagram of the hot filament CVD apparatus for depositing diamond films.

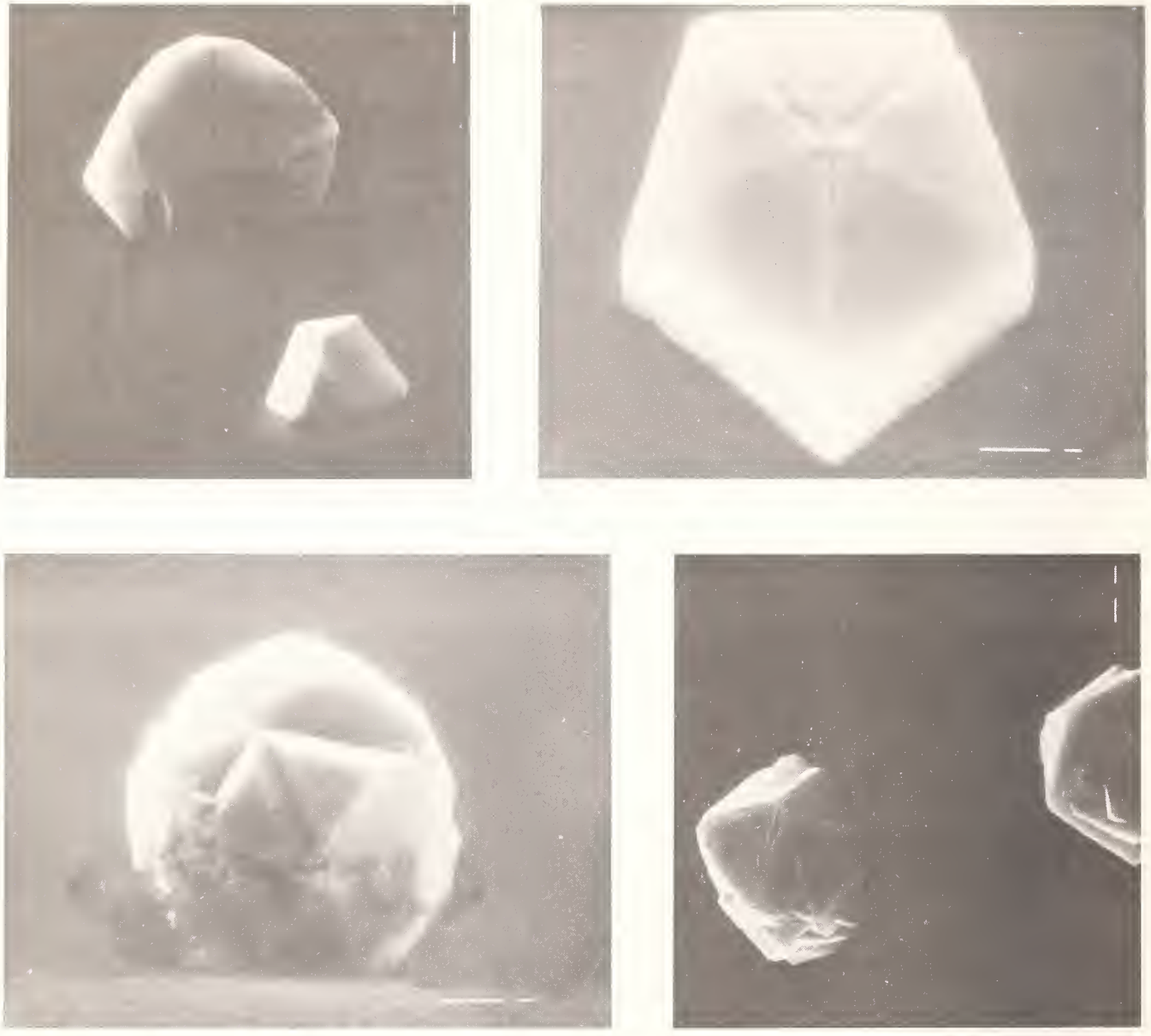

Figure 2. Scanning electron micrographs of diamond particles deposited by the hot filament CVD process on a Si substrate. A 1μ scale is given by the lower white line in the upper left and lower right micrographs and by the left white line in the upper right and lower left micrographs.

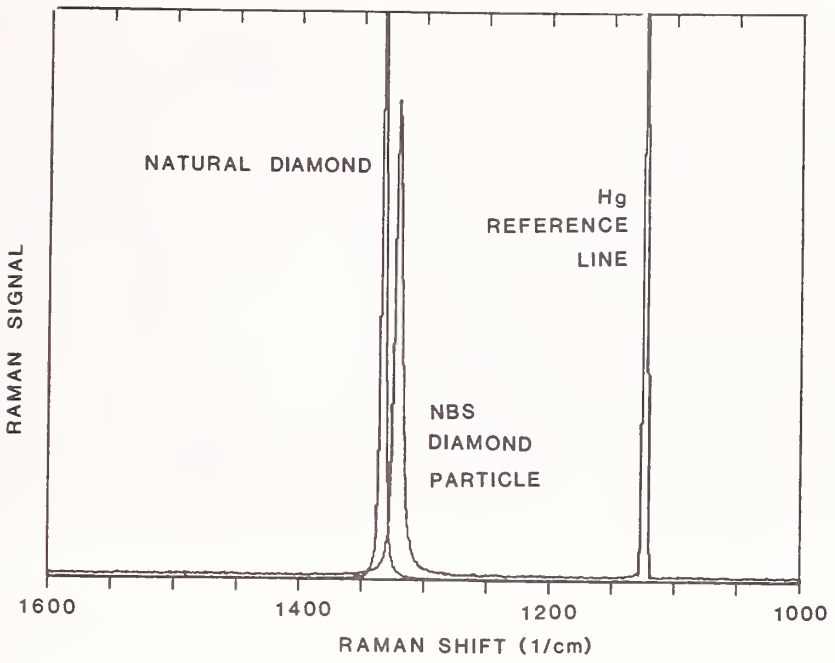

Figure 3. Micro-Raman spectrum of a diamond particle.

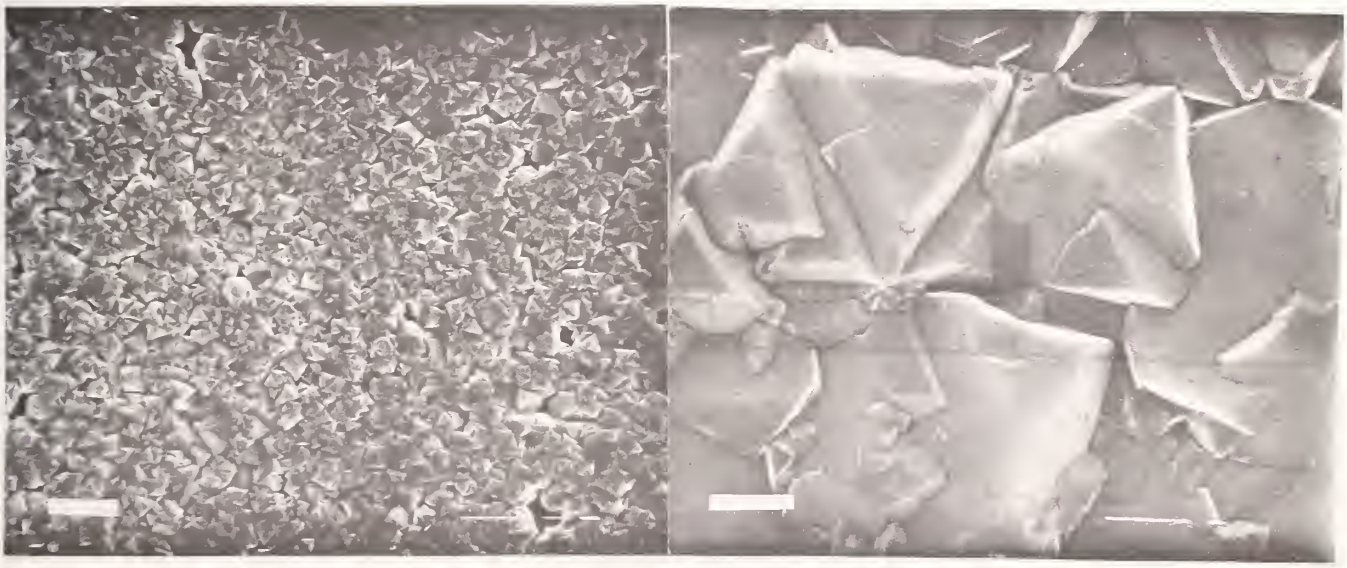

Figure 4. Scanning electron micrographs of NBS diamond film deposited by the hot filament CVD process on a Si substrate. The scale for each micrograph is given by the white bar in the lower left hand corner. In the left micrograph the bar represents 10μm; in the right micrograph the bar represents 1μm.

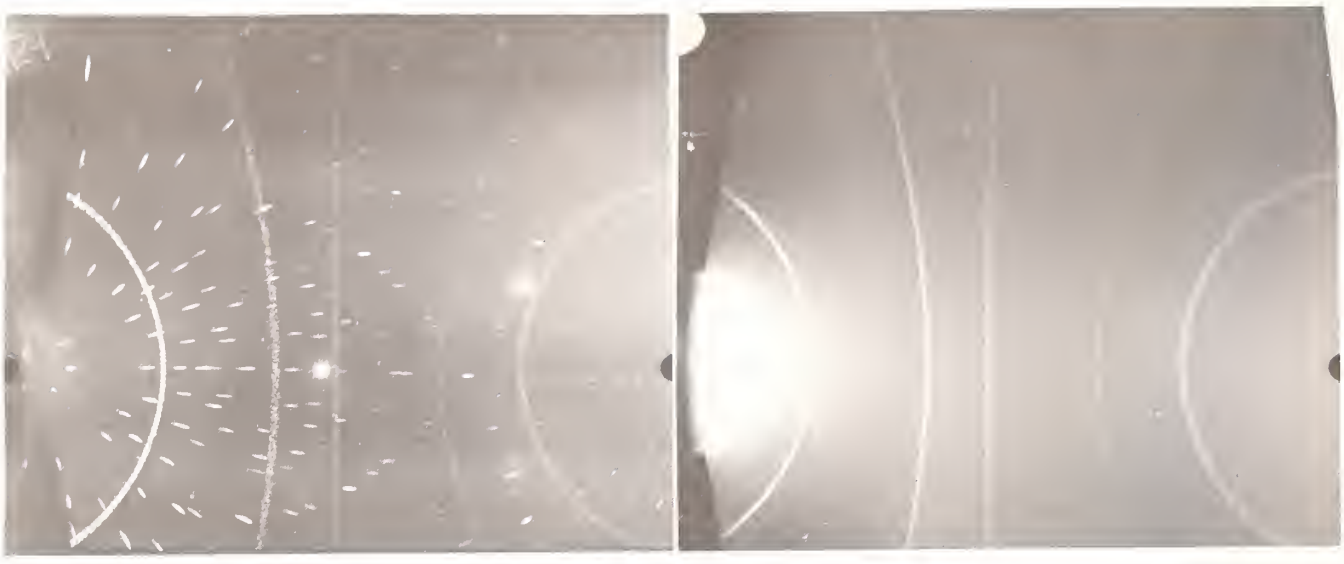

Figure 5. Diffraction patterns from a diamond film (left pattern) and from natural diamond powder (right pattern) obtained with a Read camera. The spots on the pattern from the diamond film are due to diffraction from the silicon substrate.

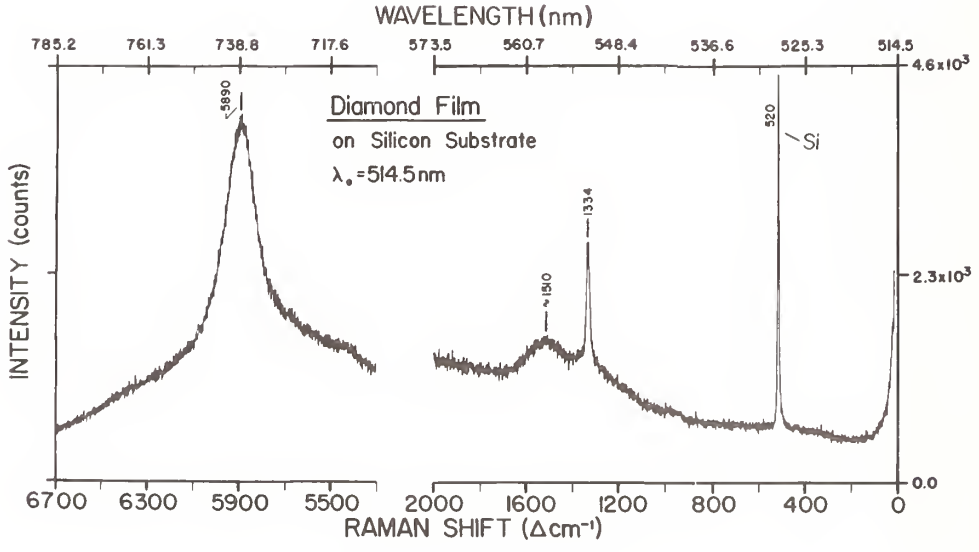

Figure 6. Raman spectrum of NBS diamond film.

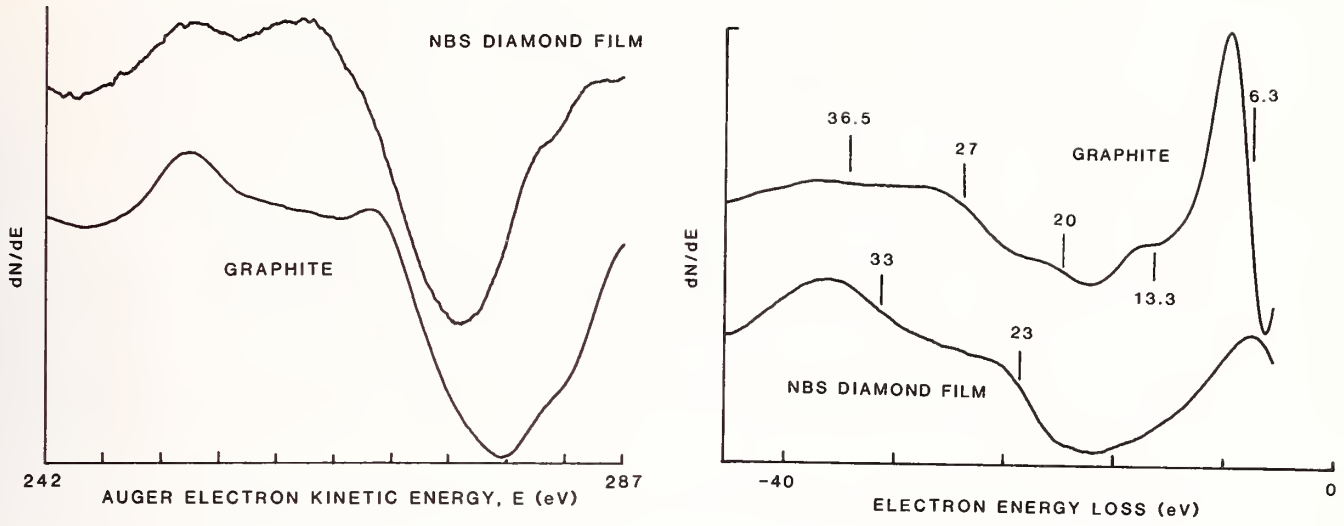

Figure 7. Auger and electron energy loss spectra of NBS diamond film and of graphite.

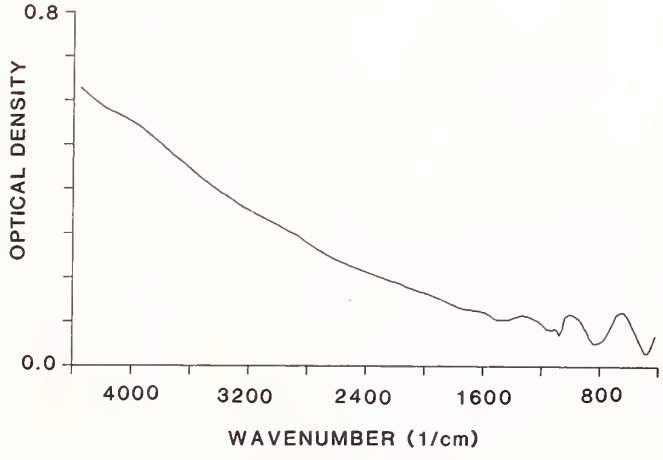

Figure 8. Fourier transform infrared transmission spectrum of NBS diamond film.

A questioner wondered if scratching the surface was required so that the diamond flux could nucleate on the diamond particles in the paste used for scratching. The author replied that they did clean the surfaces off after scratching them so they didn't believe that embedded diamond particles were required. However, they could not be certain yet. Some diamond particle nucleation does occur even if one does not scratch the surface. They scratch the surface by taking some commercial diamond paste and make perhaps ten swipes on the surface with a CueTipand then clean it off. They have tried <100> and <111> orientations of the silicon substrate and found no difference in the resultant films. They deposit at a rate of about 0.1 m/hr. Some depositions have lasted 60 hours. In the literature rates of 60 m/hr or higher have been reported. There is graphite present, although it is not clear where on a microscopic scale. There is probably a silicon carbide layer between the diamond and the silicon substrate. The higher the hydrogen content the less graphite, the less hydrogen in the film and the better the quality of the diamond. Also the lower the deposition rate.

In regard to film hardness the author has sent some films to the Tribology group at the Bureau of Standards for a wear analysis. He believes the crystallites have true diamond properties.

The thermal conductivity has been measured on a series of films as a function of gas composition. At the lowest methane concentrations, which are the highest hydrogen concentrations, the thermal conductivity is best and is at least as good as natural diamond.

Manuscript Received 12/21/87/sar

WAVELENGTH DEPENDENCE OF EDGE FILTER ABSORPTION

L. J. Basegio and M. K. von Gunten
Spectra-Physics, Inc.
Mountain View, California

ABSTRACT

Laser isotope separation and free electron laser programs have driven the need for optical coatings which function in environments of high average power density. Low absorption is the key requirement for these coatings to prevent catastrophic laser damage and to minimize wavefront deformation caused by localized heating of the coating and substrate. Dichroic edge filters have been utilized in wavelength separation applications; however, the intrinsic absorption of these designs at the edge limits their power handling capability for closely spaced wavelengths. In order to fully understand the absorption behavior and to optimize the performance of these designs, measurement of absorption as a function of wavelength has been undertaken, with particular emphasis on the transition region.

The absorption measurements have been performed with a calorimeter which utilizes a matched thermistor bridge and an ultra-precision instrumentation amplifier in conjunction with both discrete and tunable laser sources. Several types of edge filter coatings have been measured. These measurements have been performed over the wavelength region from the stopband through the edge region into the passband. This empirical data is compared to theoretical predictions.

Key words: absorption; coatings; filters; free electron laser; isotope separation; thin films

INTRODUCTION

Thin film theory predicts that a multilayer optical coating will exhibit absorption that can vary dramatically with the wavelength of the incident light. Over broad wavelength ranges, dispersion in the complex refractive index can produce significant differences in absorption. Over narrower wavelength ranges, where dispersion may not be significant, changes in the standing wave electric fields within the coating can also produce dramatic differences in absorption. In the case of an edge filter, in the narrow transition region from high reflectance to high transmittance, changes in the standing wave electric fields can be the dominant mechanism for changes in absorption.

When developing thin film edge filters with minimal absorption as the critical design parameter it has become necessary to characterize the absorption of the stack for a range of wavelengths that include the transition region. In the following treatment we discuss the theoretical calculation of absorption for two long-wave-pass edge filters and compare the predicted values to the measured values obtained from coated samples of the two designs.

The comparison consists of the following:

1. Several samples are measured for absorption from each of two coating runs. The samples are measured through a wavelength range that includes points in the stopband, in the edge region, and in the pass band. The wavelength increment used is 5nm.

2. The extinction coefficient is adjusted for one or both coating materials to allow the theoretical prediction at the wavelength of interest to be in close agreement with that obtained by measurement.

3. The resultant curves are plotted and compared.

THEORETICAL MODEL FOR ABSORPTION

The model used for the absorption calculation is the matrix formulation of thin film theory. (1) Here it is assumed that R+T+A=1. Losses due to scatter are ignored in this approach.

For normal incidence:

$$R = [(n(0)B-C)/(n(0)B+C)]\ \mathrm{CONJ}[(n(0)B-C)/(n(0)B+C)]$$

$$T = 4n(0)\mathrm{Re}(N(m))/[(n(0)B+C)\ \mathrm{CONJ}(n(0)B+C)]$$

$$A = 1-R-T = 4n(0)\mathrm{Re}[B\ \mathrm{CONJ}(C)-N(m)]/[(n(0)B+C)\ \mathrm{CONJ}(n(0)B+C)]$$

$$\begin{bmatrix} B \\ C \end{bmatrix} = \left(\prod_{r=1}^{q} \begin{bmatrix} \cos(d(r)) & (i\sin(d(r))/N(r) \\ iN(r)\sin(d(r)) & \cos(d(r)) \end{bmatrix} \right) \cdot \begin{bmatrix} 1 \\ N(m) \end{bmatrix}$$

where,

d(r) = phase thickness of rth layer = 2 pi N(r)t(r)cosQ(r)/lambda
n(0) = index of incident medium (assumed real)
N(m) = exit medium complex refractive index; N(m)=n(m)-ik(m)
N(r) = complex refractive index of the rth layer; N(r)=n(r)-ik(r)
t(r) = physical thickness of the rth layer
Q(r) = angle of incidence in the rth layer
pi = 3.14159...
lambda = wavelength.

A computer program performs calculations based on this model and plots the results. The assumed value for the HfO2 extinction coefficient is 5.0EE-7 with a real index of 2.016. The index used for SiO2 is 1.444 with no extinction coefficient. It is assumed that the absorption in the SiO2 layers is negligible in comparison to the absorption in the HfO2 layers. The theoretical absorption plots in this paper do not include the substrate absorption.

COATING ABSORPTION MEASUREMENT - INSTRUMENT AND PROCEDURE

The device used to measure absorption was constructed at Spectra-Physics. It is essentially a laser calorimeter. The device could also be considered a modified bolometer. The analysis used is a lumped analysis whereby the slopes of the heating and cooling curves are measured and absorption of the optic (substrate and thin film assembly) is computed using this data and the thermal mass of the substrate. (2)

$$P(a)=mC([dT/dt](up) - [dT/dt](down))$$

P(a)=power absorbed by coated substrate
mC=thermal mass of substrate
[dT/dt](up)=rate of temperature rise on heating
[dT/dt](down)=rate of temperature decrease on cooling

The central assumption in the lumped analysis is that at any instant in time, the sample is at thermal equilibrium. The method, in principle, allows one to ignore heat dissipation mechanisms by assuming that at a given temperature the heat losses are identical for both the heating and cooling portions of the curve.

Errors associated with this approach have been previously discussed by Bernal. (3) The primary errors are due to temperature gradients within the sample from non-uniform heating. The degree of error is dependent on factors such as the thermal conductivity and aspect ratio of the substrate. The substrates used in this work were selected on the basis of low absorption, favorable aspect ratio, and small thermal mass - essential for measurement of low levels of absorption with low incident power.

A block diagram of the apparatus is given in Figure 1. A Spectra-Physics 2020 Argon laser is used to pump a Spectra-Physics model 375 dye laser. The dye laser is set up for R6G dye and is continuously tunable from 570-630 nm. Output power levels range from 200mW to 900mW depending on the wavelength. The beam is directed through a weak positive lens (E) that focuses the beam to a diameter more suitable for a small substrate. The incident power is measured prior to the measurement at location (P).

The focused beam passes through an aperture (F) and then into the entrance window (C) of the calorimeter. The entrance window has a broad-band anti-reflection coating on both surfaces that reduces the reflectance in the dye band to less than 0.1% per surface. Inside the calorimeter there are several adjustable iris apertures (G) used for control and adjustment of scattered light, and two optical mount/sensor assemblies (A&B). One of the assemblies (A) holds the optic under test, the other assembly (B) holds a "reference" optic of identical thermal mass. The samples are 7.75mm diameter, 4mm thickness, flat, fused silica substrates polished to 10-5 surface quality. The differential signal obtained from the two sensor assemblies is amplified and displayed on an HP model 7044A X-Y recorder.

The reflected beam is brought out through the entrance window at a slight angle and is blocked by the aperture. The transmitted beam leaves the system through the exit window (D) and is terminated in beam block (H). The exit window is also coated with an anti-reflection coating.

The differential sensor configuration is designed to minimize the influence of ambient temperature fluctuations.(4) Sensors and electronic components were selected and assembled with significant attention to temperature coefficients, thermal EMFs, and low noise circuitry. The sensitivity of the system is 40 millivolts per millidegree C. Noise reduction is obtained by the standard techniques of EMI shielding, single point grounding, and by use of sample and hold techniques prior to and as a part of amplification.

Absolute accuracy of the system appears to be within a factor of two when compared to results obtained by LLNL (5). Lack of available data in the visible wavelength range makes absolute accuracy statements very difficult. Measurement of uncoated test samples identical to the test substrates of this paper yields values between 2ppM and 5ppM for fused silica. Repeatability of a given measurement is generally within 10% to 25%. The statements just made do not apply to coatings that scatter excessively; measurements made on such optics have questionable value and indicate higher than the actual absorption loss.

The procedure for measuring absorption is as follows: The part is inspected for surface contamination and cleaned. Test and reference optics are mounted in their respective mounts, the calorimeter is closed and the system allowed to come to thermal equilibrium. Once equilibrium has been established, as indicated by a stable signal traced by the XY recorder, the wavelength is selected and verified using a spectrometer. The incident power is measured and the sweep on the XY recorder is started. At some predetermined point the beam block is removed. The start of the temperature rise is examined for the presence of excessive scatter, indicated by an instant jump of the pen. The system is realigned if necessary. The temperature is allowed to increase to a level that allows good resolution of both time and voltage. XY recorder sensitivities are adjusted accordingly. At some predetermined level the beam is blocked and the cooling cycle begins - this

point will also be examined for rapid changes. In general, there should be several seconds before the temperature begins to fall. The optic is allowed to cool to a level determined by calculation requirements. A typical calorimeter trace is shown in Figure 2.

COATING DESIGN AND PERFORMANCE

The coatings were produced in a 28 inch Balzers 710 stainless steel bell jar with a CTI 10 inch cryogenic high vacuum pump and a water cooled baffle. This system is capable of achieving a base pressure of 2.0EE-7 Torr vacuum with a pumping speed of 3000 lps (air). The chamber is equipped with electron beam evaporation sources, an optical monitoring system, radiant quartz heaters with automatic control, automatic gas bleed, a residual gas analyzer, and a planetary rotation system. The coatings are analyzed for spectral performance on a Beckman ACTA MVII double beam ratio recording spectrophotometer. The spectral trace was performed in transmission on the same sample as the calorimeter trace.

Two long wave pass designs were coated on fused silica substrates. One design was a 33 layer Hafnium Oxide and Silicon Dioxide optimized long wave pass coating and the other a 41 layer coating. Process parameters such as deposition rate, backfill pressure, and substrate temperature were optimized to produce low absorption coatings. The same coating processes were utilized on the 33 layer and 41 layer coatings. Figure 3 represents the theoretical transmittance and absorptance values of the 33 layer coating based on the previously described refractive index and extinction coefficient values. Figure 4 presents the same information except for the 41 layer coating. Figures 5 and 6 represent the actual measured results of transmission and absorption of the 33 layer and 41 layer coating, respectively. Transmission traces have not been adjusted for the Fresnel reflectance of the uncoated side of the sample. Actual data points have been plotted for absorption with an interpolated curve.

Several interesting features should be considered in comparison of the theoretical plots of the 33 layer and 41 layer long wave pass designs. The transmission cuton is more rapid in the case of the 41 layer design. However, absorption of this design is higher by 50% over the 33 layer design. Note also the transmission and absorption curves of the 41 layer design have more structure than the 33 layer version. Considering the measured result plots, both coatings are red shifted by approximately 1%. Structure in the sidebands of the transmission curves is similar to theoretical predictions. The absorption curves also are similar to theoretical predictions in the fact that both rise and fall in value around the stopband edge. Good agreement with theory is obtained in the absorption value in the stopband and at the peak of the curve. Departure from theory is evident in the location of the absorption peak, however, a more detailed analysis of absorption at this peak is appropriate and may provide better correlation with theoretical predictions.

CONCLUSIONS

Basic electromagnetic theory predicts a certain wavelength dependence of absorption when one or both coating materials have a finite extinction coefficient. This behavior is verified with careful measurements. The absolute magnitude of the absorption may differ due to many factors which include; non-ideal coating materials, interface contributions, substrate contributions, and lack of absolute precision in the layer thicknesses and the measurement analysis. While quantitative agreement cannot be established because of the adjustments made to the coating material constants, qualitative agreement with the basic theory has been demonstrated. The very low measured values are also significant in that they represent the state of the art for electron beam deposited metal oxide coatings. The results of these measurements are in close agreement with measurements perfor-

med by LLNL using a completely different technique. (5)

REFERENCES

1. Macleod, H.A., Thin Film Optical Filters, 2nd edition, Macmillan Publishing Co., N.Y., 1986, pp. 32-40.

2. Holman, J.P., Heat Transfer, 3rd edition, McGraw-Hill, 1972, pp. 86-88.

3. Bernal, E.G., Appl. Opt. 14, No. 2, 1975, pp. 314-321.

4. DeBell, G.W., The Design and Measurement of Low Absorptance Optical Interference Coatings, Doctoral Thesis, Univ. Rochester, 1972.

5. Draggoo, V.G., Morton, R.G., Sawicki, R.H., Bissinger, H.D., "Optical Coating Absorption Measurement for High Power Laser Systems", SPIE Vol. 622, High Power and Solid State Lasers, 1986, pp. 186-190.

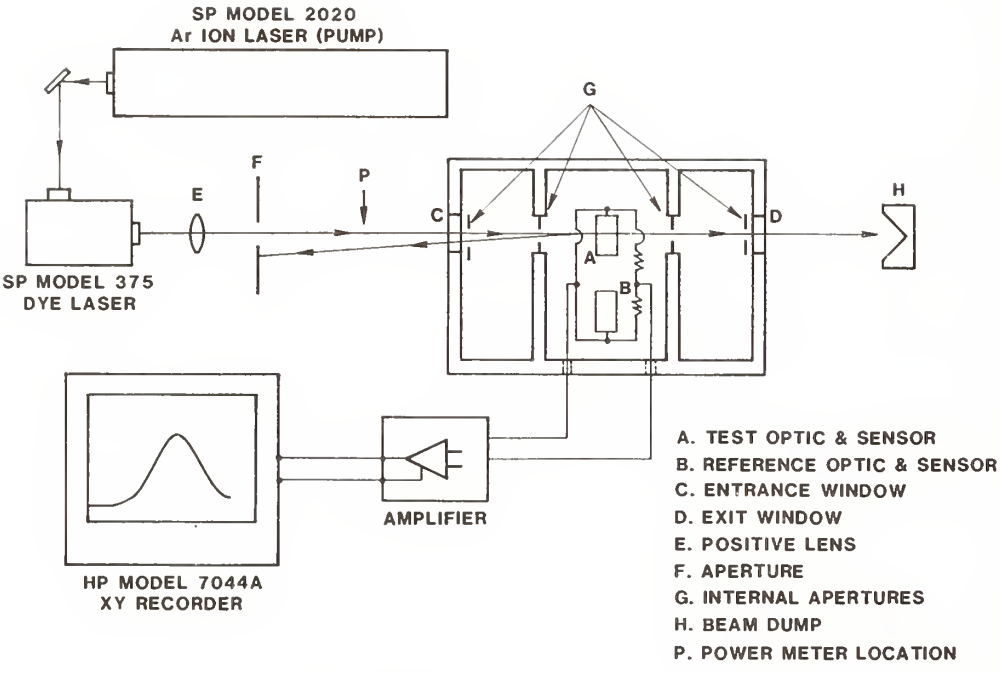

FIGURE 1. CALORIMETER BLOCK DIAGRAM

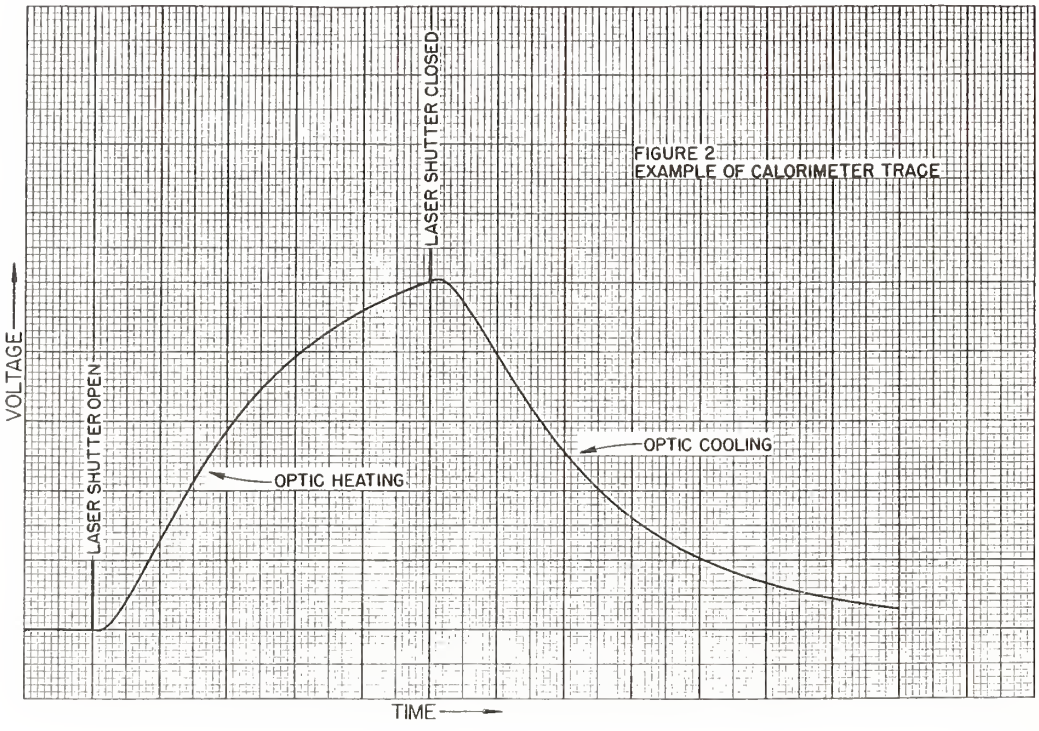

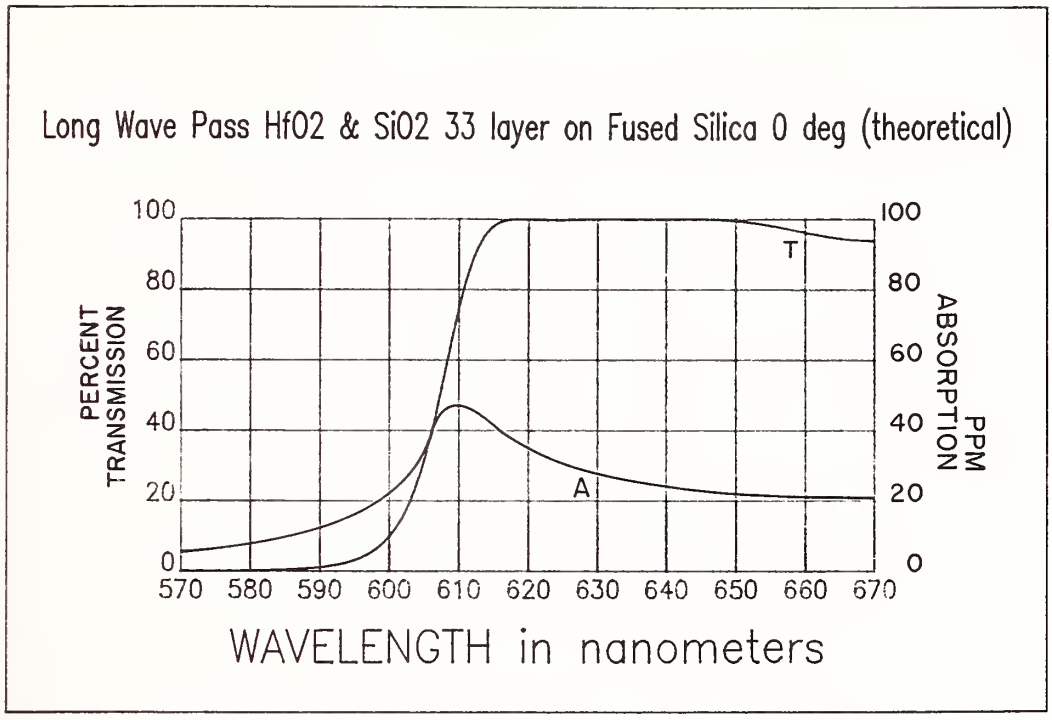

FIGURE 3

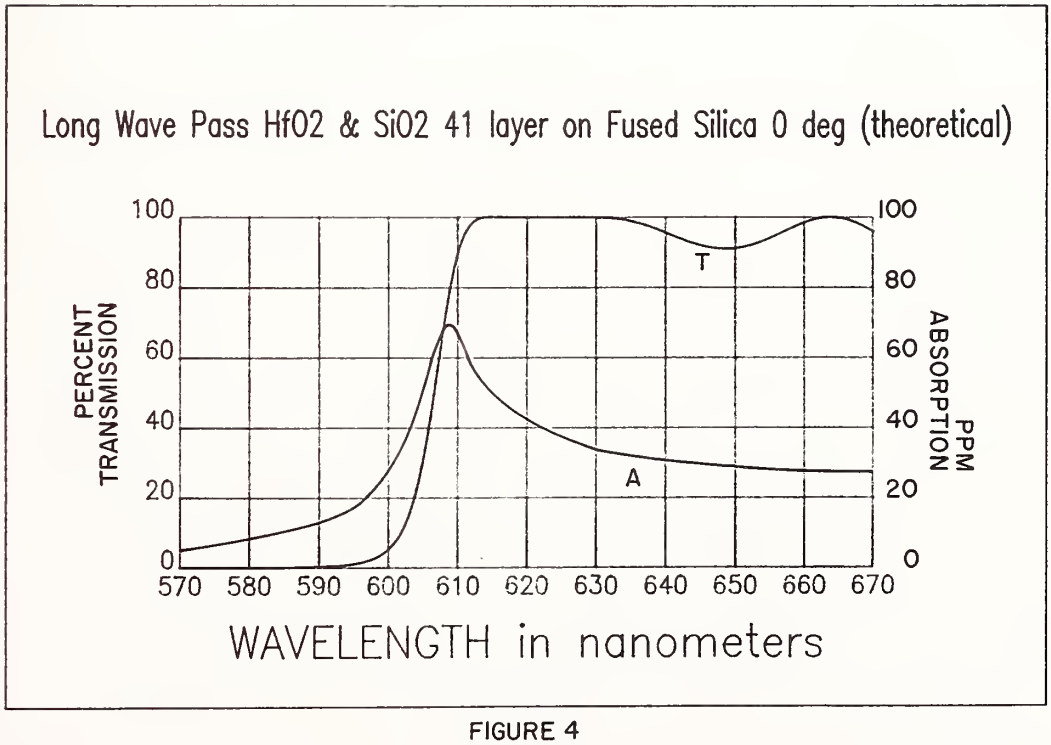

FIGURE 4

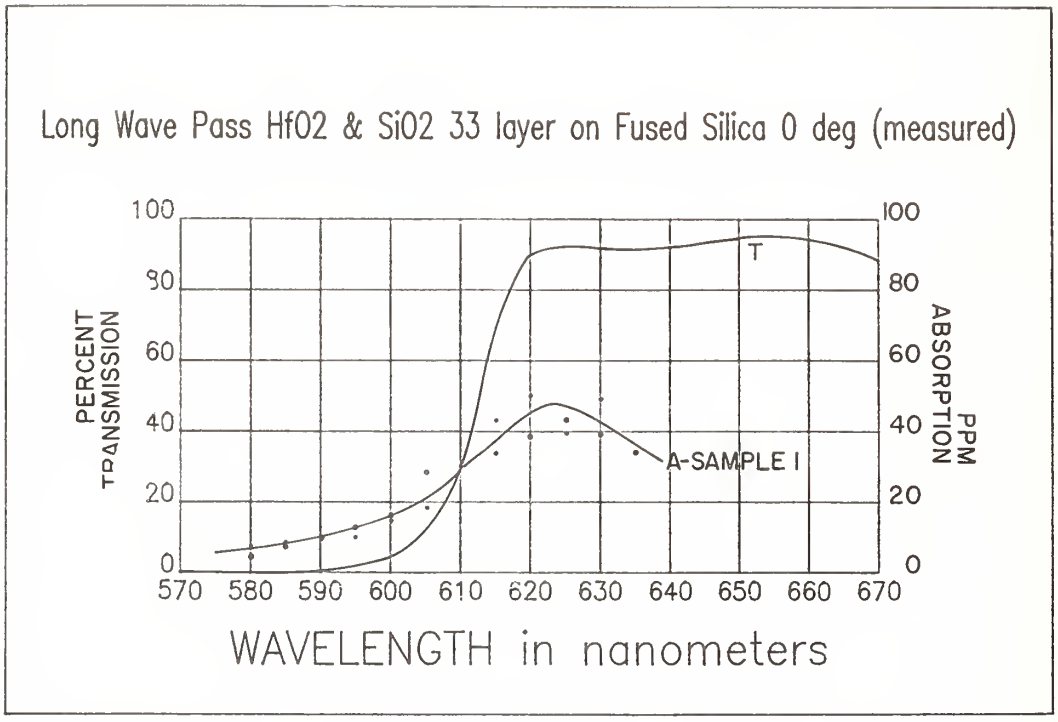

FIGURE 5

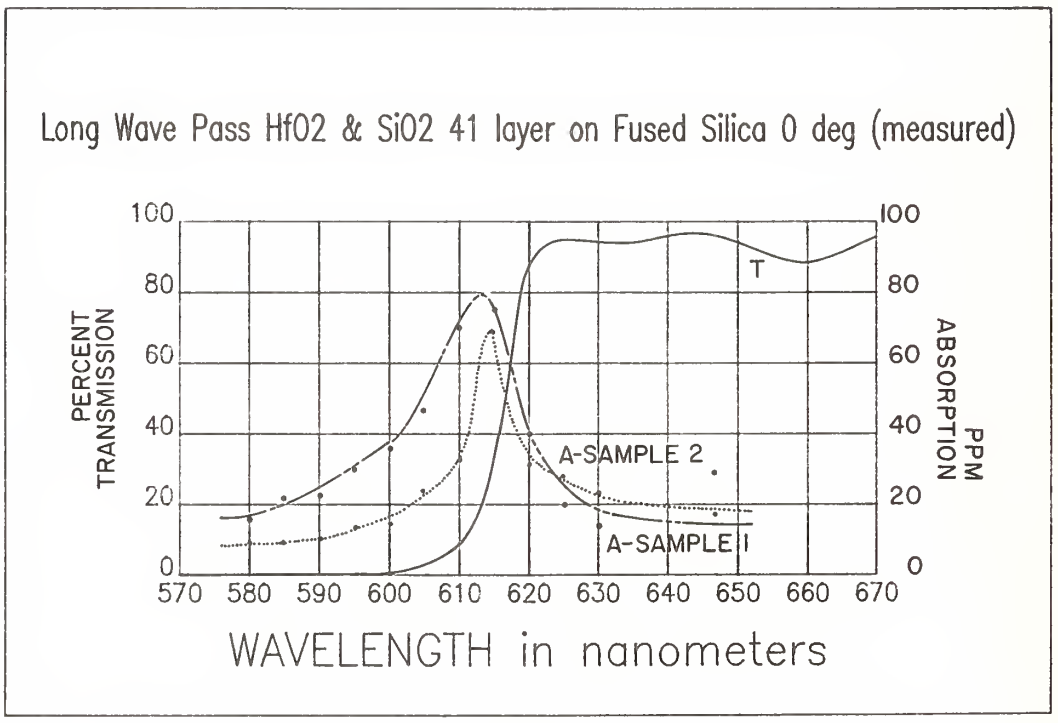

FIGURE 6

Manuscript Received
1-4-88

Minimizing scattering in multilayers: Technique for searching optimal realization conditions

C. Amra

Laboratoire d'Optique des Surfaces et des Couches Minces - Unité Associée au CNRS (U.A. 1120) - Ecole Nationale Supérieure de Physique de Marseille
Domaine Universitaire de St Jérôme - 13397 Marseille Cedex 13 - France

Reducing losses in optical coatings implies a search for optimal realization conditions of multidielectric coatings to obtain minimal absorption and scattering. Numerous works have been devoted to the absorption problem. Here we deal with scattering minimization. Scattering from a coated substrate is a function of numerous factors that can be successively measured: substrate roughness, interfaces roughness, cross-correlation state between interfaces. First, the substrate roughness is determined by scattering measurement before coating. Then, the interfaces roughness depends on the grain size of the material in thin film form. For a given material, we find that the grain is, in a large extent, function of the preparation conditions of the layer. And mainly, when a whole layer stack is concerned, the spatial distribution of the scattered light depends on the cross-correlation state between successive interfaces. With a scattering vector theory and an apparatus for measuring scattering curves at our disposal, we can show how it is possible to determine the interface roughness and the cross-correlation state, by a systematic comparison between theory and experiment. In order to eliminate any ambiguity in interpreting the experimental results, we must work with multilayer stacks the design of which is chosen so that the scattering curves have an aspect very different according to the cross-correlation state.

Key words: interface correlation; multilayers; optical filters; roughness; scattering.

1. Introduction

Though many works /1,2/ have been devoted to the study of absorption in optical multilayers, there are many applications (mirrors for lasers and gyrolasers, Fabry-Perot filters for optical multi-demultiplexing, ...) where scattering losses are mainly responsible for the limitation of filter performances. So we are dealing here with light scattering from surfaces and interfaces of optical multilayers.

We have already described the experimental /3/ and theoretical /4/ tools we developed in Marseilles for this study; let us recall that the scattering distribution can be measured in the whole space (25 000 data points), and then interpreted by matching the parameters involved in the theoretical model. Owing to these two tools that are theory and experiment, our investigations in scattering phenomenon have well gone forward:

- In a first stage, measurements of scattering from only one surface enabled us to show /3/ that the roughness spectrum, which characterizes the surface defects/5/ is independent of the illumination and observation conditions; such results are in good agreement with theory.
- Then we were interested in the study of scattering from one single layer /6, 7/, and we demonstrated that a deposited layer could exactly reproduce the substrate defects, provided that the deposition conditions have been well adapted. In such a case, the two interfaces (air/layer) and (layer/substrate) are quasi proportional and their cross-correlation coefficient is close to unity: the scattered waves from one and other interface are in phase cancellation, which leads to reduction of total integrated scattering ("antiscattering effect"). Then, by studying the ratio of the top interface (air/layer) roughness to the substrate roughness, we obtain precious information concerning the microstructure of the material in thin film form, and especially on the grain size which characterizes this microstructure.
- In the case of a multilayer mirror, the Aluminum technique /8/ pointed out the fact that roughness has its origins in two different phenomena: it can be due

to reproduction of substrate defects (case of perfectly correlated surfaces) or to the material microstructure (case of uncorrelated surfaces).

Now that such information is at our disposal, the question is to know whether it is possible to generalize "antiscattering effect" to multilayer systems, owing to destructive interferences between scattered waves. It is obvious that the first problem lies in the choice of the multilayer design; but as far as we know that scattering will only be reduced with perfectly correlated surfaces, we have first to make sure that we control the different parameters involved in scattering phenomenon. In spite of numerous results /9/ we obtained concerning the cross-correlation coefficient between interfaces, the determination of these parameters and of the associated roughnesses remains a difficult problem /10/, especially if the number of layers is high.

We show here how we can solve this problem, by using specific multilayer designs deduced from theory. The scattering of these stacks is so sensitive to the scattering parameters that we can determine them without any ambiguity. Such multilayers are then produced, using Ion Assisted Deposition, and both cross-correlation laws and roughnesses are deduced from scattering measurements. It then appears that we can characterize our deposition conditions with accuracy, from a point of view of scattering.

2. Search of specific multilayer design

In this section, we only present theoretical results, for a sample illuminated in natural light at normal incidence. The wavelength under study is $\lambda_0 = 630$ nm. The study is limited to scattering in the half space containing the specular reflection direction. We do not describe the analytical calculation that enabled us to choose the multilayer designs; we only verify by numerical computation that such designs are well adapted to our study.

The idea lies in the fact that (as an analogy with antiscattering effect),when a half-wave ($\lambda_0/2$) high-index layer is deposited on a substrate, the scattered waves from the new interface (air/layer) are in phase cancellation with those of the (layer/substrate) interface, which minimizes scattering losses. So we can expect that the same effect will occur if we deposit an odd number of successive alternated high- and low-index half-wave layers on a substrate: as the modulus of the electric field is the same at interfaces (Fig. 1), the corresponding scattering sources /11/ have magnitudes that are nearly the same; therefore scattering will be reduced, provided that these sources are in phase cancellation two by two. Obviously such phenomena only occur in the case where the interfaces are perfectly correlated; in such a case, we demonstrate (using analytical calculation) that scattering in the specular reflection direction do not depend on the number of layers. From a point of view of total integrated scattering, such results remain identical, as it is shown in table I:

For perfectly correlated surfaces and identical roughnesses at each interface, scattering losses do not change before and after coating, whatever the number of layers of the stack. On the other hand, we find in the case of uncorrelated surfaces that scattering losses are very sensitive to the number of layers: with 11 layers for instance, such losses are 138 times higher than that of the substrate before coating. It then appears that specific half-wave multilayer designs will give us access, using a careful comparison between theory and experiment, to the key parameters of scattering.

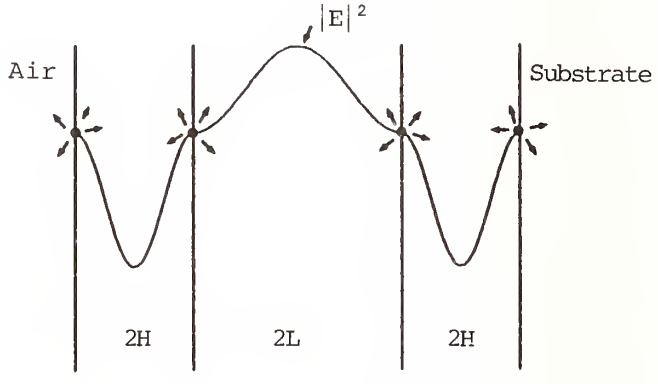

Figure 1:
Scattering phenomenon in a multilayer stack made of an odd number of alternated half-wave ($\lambda_0/2$) high index (2H) and low-index (2L) layers. We have plotted the square of the modulus of the electric field inside the stack. The sample is illuminated at $\lambda_0 = 630$ nm. The value of this field at interfaces is strongly related to the magnitude of the corresponding scattering source.

N	Coating	$D_0\ 10^6$	η_0	$D_1\ 10^6$	η_1
0	Bare substrate	23		23	
1	2H	649	28.2	23	1
3	2H 2L 2H	1153	50	24	1.1
5	2H 2L 2H 2L 2H	1660	72.2	26	1.2
11	2H 2L 2H ...	3175	138	28	1.2

Table I:
Scattering losses D integrated in the half-space containing the specular reflection direction, calculated before and after deposition of an odd number of alternated half-wave high-index (2H) and low-index (2L) layers. The substrate is a usual glass with refractive index $n_s = 1.52$. The materials are TiO_2 and SiO_2. N is the number of layers of the stack. Scattering is calculated at the wavelength $\lambda_0 = 630$ nm in the case of identical roughnesses at each interface, for two extreme values ($\alpha = 0$ and $\alpha = 1$) of the cross-correlation coefficient between interfaces. D_0 and D_1 are scattering losses that correspond to $\alpha = 0$ and $\alpha = 1$ respectively.
In the same way, η_0 and η_1 are the ratio of scattering after coating to scattering before coating, respectively for $\alpha = 0$ and $\alpha = 1$. For these theoretical results, we assume that the roughness spectra at each interface can be approximated with the Fourier Transform of the sum of an exponential and a gaussian function /3, 8/, with respective parameters: $(\delta_{exp}, L_{exp}) = (1.5\ nm, 2000\ nm)$ and $(\delta_g, L_g) = (1\ nm, 200\ nm)$.

3. Experimental results

We produced the preceding specific multilayers using Ion Assisted Deposition /12, 13/. The materials are TiO_2 and SiO_2. In order to point out the possible influence of the substrate quality, each multilayer was simultaneously produced on three black glasses with very different micropolishes. Scattering of every sample was measured before and after coating, at the wavelength $\lambda_0 = 630$ nm. The experimental results are presented in Table II, and they are concerning stacks that have one, three and five alternated half-wave ($\lambda_0/2$) high-index and low-index layers:

Sample	$D_N\ 10^6$	Coating	$D_T\ 10^6$	η
A27	8.9	2H	13.6	1.53
A29	41.6	2H	9.5	0.23
A23	82.6	2H	18.9	0.23
A31	9.7	2H 2L 2H	17.9	1.85
A22	40.1	2H 2L 2H	9.9	0.25
A32	80.6	2H 2L 2H	16.6	0.21
A36	25.2	2H 2L 2H 2L 2H	39.7	1.58
A21	42.0	2H 2L 2H 2L 2H	13.5	0.32
A33	110.5	2H 2L 2H 2L 2H	15.9	0.14

Table II:
Measured scattering losses from rough samples before (D_N) and after (D_T) deposition of an odd number of alternated half-wave high-index (2H) and low index (2L) layers. The materials are TiO_2 and SiO_2. All substrates were usual opaque glasses. Scattering is measured at the wavelength $\lambda_0 = 630$ nm. η is the ratio of scattering after and before coating: $\eta = D_T/D_N$.

First we notice that a unity value of η(predicted by theory in the case of identical roughnesses and perfectly correlated surfaces - see Table I) is not obtained. However, the curves of figure 2 and 3 will give us a complete understanding of these results.

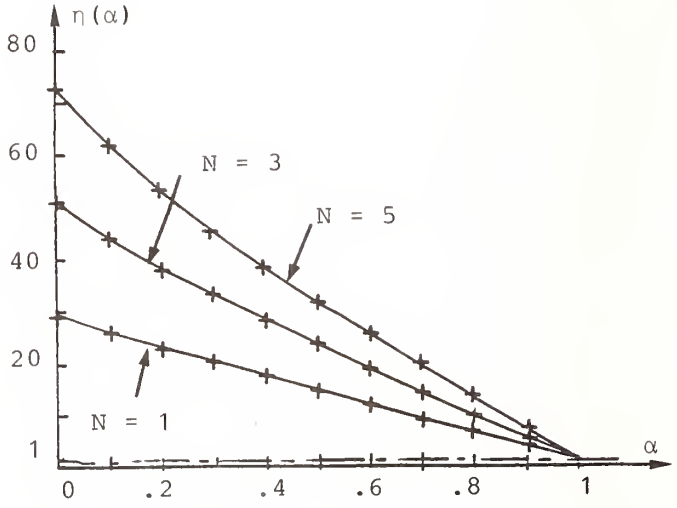

Figure 2:
Calculated variations of the ratio $\eta = D_T/D_N$ (scattering after coating/scattering before coating) as a function of the cross-correlation coefficient α between interfaces, in the case of identical roughnesses at each interface. These results concern multilayer stacks made of an odd number of alternated half-wave ($\lambda_0/2$) high index (TiO_2) and low index (SiO_2) layers. Scattering is calculated at the wavelength λ_0 = 630 nm. N is the number of layers of the stack.

In figure 2 we plotted the calculated variations of the ratio η (scattering after coating/scattering before coating) as a function of the cross-correlation coefficient α /9/ between interfaces, in the case of identical roughnesses. Let us remark that, whatever the number of layers, only the value $\alpha = 1$ (correlated surfaces) leads to a unity value for η: it is not possible to reduce scattering without modifying the interface roughnesses.

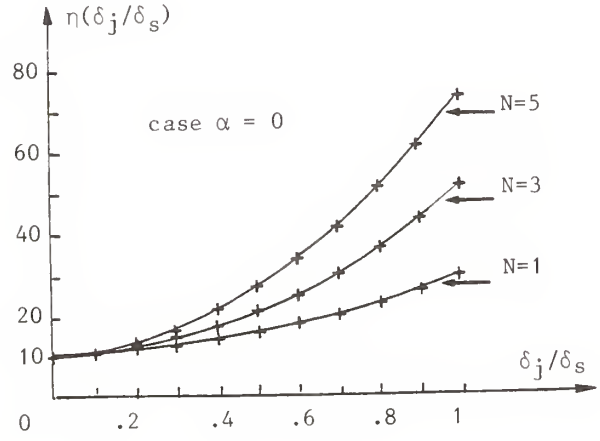

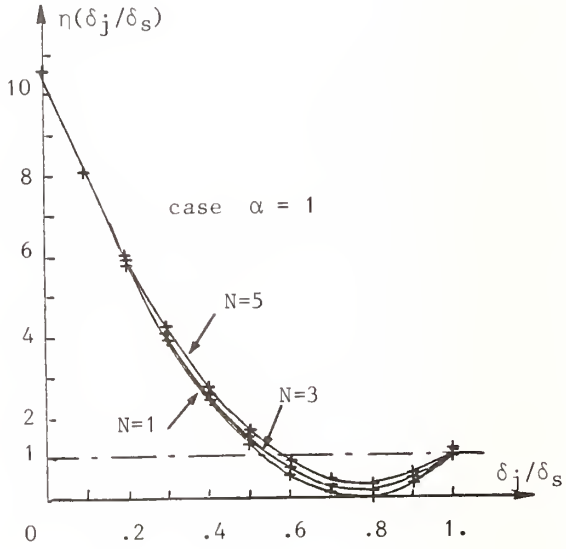

Figure 3:
Calculated variations of the ratio $\eta = D_T/D_N$ as a function of the ratio (δ_j/δ_s) of the roughness at interfaces, for two extreme values of the cross-correlation coefficient between interfaces. Figure 3a corresponds to $\alpha = 0$, while figure 3b corresponds to $\alpha = 1$. The stacks are made of an odd number of alternated half-wave ($\lambda_0/2$) high index (TiO_2) and low index SiO_2 layers. Scattering is calculated at the wavelength λ_0 = 630 nm. We assumed that all roughnesses δ_j at interfaces (except that of the substrate) were identical, but smaller than the roughness substrate; then the ratio (δ_j/δ_s) is in the range [0; 1].

Figure 3 gives us the calculated variations of η as a function of the ratio δ_j/δ_s (interface roughness δ_j / substrate roughness δ_s), for two extreme values ($\alpha = 0$ and $\alpha = 1$) of the cross-correlation coefficient. Whatever the number of layers, the case of uncorrelated surfaces ($\alpha = 0$) never leads to reduction of scattering: the smallest value for η is greater than 10 in the case $\alpha = 0$. Such results obviously show the interest of the preceding half-wave multilayers for the study of the scattering parameters: the curves $\alpha = 0$ and $\alpha = 1$ get more different as the number of layers increases.

Let us now interpret the experimental results of Table II by comparing them with the calculated values of figures 2 and 3.

(2H) designs

The conclusions are presented in Table III. The case of uncorrelated surfaces is never possible, whatever the roughness at interfaces. For A23 and A29 samples, the only interpretation is:

$$\alpha \cong 1 \text{ and } \delta_j/\delta_s \text{ close to } 0.7 \text{ ou } 0.8$$

As for the best micropolish (A27), correlation must be perfect ($\alpha = 1$) but the roughness is close to 0.5 or 1.

Sample	A27 ($9\ 10^{-6}$)	A29 ($42\ 10^{-6}$)	A23 ($83\ 10^{-6}$)
η	1.53	0.23	0.23
α ($\delta_j = \delta_s$)	≈1.0	No solution	No solution
δ_j / δ_s ($\alpha = 0$)	No solution	No solution	No solution
δ_j / δ_s ($\alpha = 1$)	≈ .5 or ≈ 1.0	≈ .7 or ≈ .8	≈ .7 or ≈ .8

Table III:

Interpretation of the experimental results of Table II for a (2H) stack with the help of figure 2 and figure 3. We give below each sample the scattering before coating (A27 has scattering losses equal to $9\ 10^{-6}$ for instance). η is the ratio of scattering after and before coating: $\eta = D_T/D_N$. The value of $\alpha(\delta_j=\delta_s)$ is deduced from figure 2, while the ratio $\delta_j/\delta_s(\alpha=0 \text{ or } \alpha=1)$ is deduced from figure 3.

(2H 2L 2H) and (2H 2L 2H 2L 2H) designs

The conclusions (Tables IV and V) are exactly the same as the preceding of Table III. Experiment can never be interpreted with uncorrelated surfaces. For the samples (A22, A32, A21, A33), we find that $\alpha \cong 1$ and $\delta j/\delta_s$ close to 0.7 or 0.8. As for the best micropolishes (A31 and A36) α is close to unity but $\delta j/\delta_s$ can be 0.5 or 1.

So we conclude for these multilayers that interfaces are practically homothetic: our deposition conditions lead to a cross-correlation coefficient near unity. As for the roughness, we find a slight diminution with respect to the substrate roughness; it would be interesting to control such reduction by adapting the ion beam power during the assisted deposition.

Sample	A31 ($10\ 10^{-6}$)	A22 ($40\ 10^{-6}$)	A32 ($81\ 10^{-6}$)
η	1.85	0.25	0.21
α ($\delta_j = \delta_s$)	≈1.0	No solution	No solution
δ_j / δ_s ($\alpha = 0$)	No solution	No solution	No solution
δ_j / δ_s ($\alpha = 1$)	≈ .5 or ≈ 1.0	≈ .7 or ≈ .8	≈ .7 or ≈ .8

Table IV:
Interpretation of experimental results of Table II for a (2H 2L 2H) stack, with the help of figures 2 and 3. We give below each sample the scattering before coating. η is the ratio of scattering after and before coating: $\eta = D_T/D_N$. The value of $\alpha(\delta_j=\delta_s)$ is deduced from figure 2, while the ratio $\delta_j/\delta_s(\alpha=0$ or $\alpha=1)$ is deduced from figure 3.

Sample	A36 ($25\ 10^{-6}$)	A21 ($42\ 10^{-6}$)	A33 ($111\ 10^{-6}$)
η	1.58	0.32	0.14
α ($\delta_j = \delta_s$)	≈1.0	No solution	No solution
δ_j / δ_s ($\alpha = 0$)	No solution	No solution	No solution
δ_j / δ_s ($\alpha = 1$)	≈ .5 or ≈ 1.0	≈ .7 or ≈ .8	≈ .7 or ≈ .8

Table V:
Interpretation of the experimental results of Table II for a (2H 2L 2H 2L 2H) stack, with the help of figures 2 and 3. We give below each sample the scattering before coating. η is the ratio of scattering after and before coating: $\eta = D_T/D_N$. The value of $\alpha(\delta_j=\delta_s)$ is deduced from figure 2, while the ratio $\delta_j/\delta_s(\alpha=0$ or $\alpha=1)$ is deduced from figure 3.

4. Conclusion

We were interested in an attempt to generalize antiscattering effect to multilayer systems. As far as such effect only occurs in the case of perfectly correlated surfaces, the first difficulty was to determine the key parameters of scattering, in order to possibly control them in a second stage. We demonstrated how the use of specific half-wave multilayers enabled us to determine both cross-correlation coefficients and roughness at interfaces: for the coatings produced by ion assisted deposition in our laboratory, we find a perfect correlation between interfaces and a slight reduction of interface roughness with respect to the substrate roughness.

Now that we have such information at our disposal, we must introduce scattering parameters in the filter design conception to obtain simultaneously well defined spectral properties (a high reflection coefficient for instance) and minimal scattering losses; we have the theoretical tools for this type of study.

From a point of view of experiment, we must not forget that it is *a priori* possible to modify the preparation conditions of the layers obtained by ion assisted deposition. To which extent is it possible to control the roughness at each interface? The ideal would be to produce multilayers with roughnesses that exactly correspond to a criterion of minimal scattering losses. Then, in spite of the unavoidable substrate defects and the grain size of the materials in thin film form, we could appreciably reduce scattering in optical multilayers.

References

1 J.H. Apfel, Optical coating design with reduced electric field intensity, Appl. Opt., 16, 1880-1885, (1977)

2 C.K. Carniglia and J.H. Apfel, Maximum reflectance of multilayer dielectric mirrors in the presence of slight absorption, J.Opt.Soc.Am., 70, 523-534,(1980)

3 P. Roche and E. Pelletier, Characterizations of optical surfaces by measurement of scattering distribution, Appl. Opt., 23, 3561-3566, (1984)

4 P. Bousquet, F. Flory and P. Roche, Scattering from multilayer thin films: theory and experiment, J. Opt.Soc.Am., 71, 1115-1123, (1981)

5 J.M. Elson and J.M. Bennett, Relation between the angular dependence of scattering and the statistical properties of optical surfaces, J.Opt.Soc.Am., 69, 31-47, (1979)

6 C. Amra, G. Albrand and P. Roche, Theory and application of antiscattering single layers: antiscattering antireflection coatings, Appl.Opt., 25, 2695-2702 (1986)

7 P. Roche, E. Pelletier and G. Albrand, Antiscattering transparent monolayers: theory and experiment, J.Opt.Soc.Am., 1, 1032-1033, (1984)

8 P. Roche, C. Amra, E. Pelletier, Measurement of scattering distribution for characterization of the roughness of coated or uncoated substrtes, SPIE Proceedings, Thin Film Technologies II, 652, 256-263, (1986)

9 C. Amra, P. Roche, E. Pelletier, Interface roughness cross-correlation laws deduced from scattering diagram measurements on optical multilayers: effect of the material grain size, J.Opt. Soc.Am. B, 4, 1087-1093, (1987)

10 J.M. Elson, J.P. Rahn and J.M. Bennett, Light scattering from multilayer optics: comparison of theory and experiment, Appl. Opt., 19, 669-679, (1980)

11 C. Amra, Scattering distribution from multilayer mirrors - Theoretical research of a design for minimum losses. To be published in "Laser damage in optical materials", (1986)

12 P.J. Martin, H.A. Macleod, R.P. Netterfield, G.C. Pacey, W.G. Sainty, Ion Beam Assisted Deposition of optical films, Appl. Opt., 22, 178, (1983)

13 F. Flory, G. Albrand, C. Montelymard, E. Pelletier, Optical study of the growth of Ta_2O_5 and SiO_2 layers by Ion Assisted Deposition, SPIE Proceedings, Thin Film Technologies II, 652, 248-253, (1986)

In response to a question on whether in order to minimize scatter one would have to give up something in reflectance or transmittance the author replied that in principle nothing is given up. To minimize scattering for a specific design depends entirely on which design is considered. For instance, if we wish to minimize scattering in a mirror, we must have anticorrelated surfaces and we can shift the electric field within the stack. To minimize scattering in a Fabry-Perot filter we must have perfectly correlated surfaces because scattering is very low if we have correlated surfaces. For each application we must control the scattering parameters to choose the best design.

Manuscript Received
10-27-87

A Comparison of Various Rugate Filter Designs

C. K. Carniglia

Martin Marietta Astronautics Group, Laser Systems Technology
P.O. Box 9316, International Airport
Albuquerque, NM 87119

A rugate filter is a multilayer reflector with a continuously varying refractive index profile. The performance desired from such a filter is the reflection of light at a single band centered at some wavelength λ_0 without the associated reflectance bands at the harmonics $\lambda_0/3$, $\lambda_0/5$,. . . . Three index profiles are compared: sinusoidal variation of refractive index, sinusoidal variation of dielectric constant and sinusoidal variation of the natural log of the refractive index. The latter profile gives complete suppression of the reflectance bands at the harmonics.

Key Words: gradient index; interference filter; reflector; rugate filter

A rugate filter is commonly described as an interference filter in which the variation in refractive index with depth is sinusoidal. The desired property of such a filter is that it reflect light at a given band centered at a wavelength λ_0 and have minimal reflectance at all other wavelengths. At the 1986 Boulder Damage Symposium, an exact solution was presented by Becker [1] for the case in which the dielectric constant of the coating varied sinusoidally. The purpose of this paper is to compare three rugate index profiles and to show that the optimum profile is one in which the logarithm of the refractive index varies sinusoidally with optical thickness [2].

Consider three different sinusoidal profiles for the refractive index n(x) of a thin film coating:

$$n(x) = a_1 \cos(2k_0 x) + b_1, \tag{1}$$

$$\varepsilon(x) = n^2(x) = a_2 \cos(2k_0 x) + b_2, \tag{2}$$

and

$$\ln[n(x)] = a_3 \cos(2k_0 x) + b_3. \tag{3}$$

Here x is the optical thickness of the coating, given by

$$x(t) = \int_0^t n(t')\, dt', \tag{4}$$

where t is the physical distance measured from the substrate. In eqs (1) - (3), k_o is given by

$$k_o = 2\pi/\lambda_o, \tag{5}$$

which ensures that the filters have their rejection bands at λ_o.

The profile given by eq (1) corresponds to the common definition of a rugate filter; namely, the refractive index varies sinusoidally. Equation (2) corresponds to a sinusoidal variation of the dielectric constant ϵ. This profile results when two materials are combined in such a way that their mixing fraction varies sinusoidally if the refractive index of the composite mixture followes a Drude mixing model [3]. This profile is also amenable to an analytical solution in terms of Mathieu functions [1].

The third profile is suggested by a common line of reasoning which leads to the concept of a sinusoidal profile. Loosely speaking, the variation in reflectance with wavelength is related to the Fourier transform of the refractive index profile. For example, a standard multilayer quarter-wave stack reflector has an index profile which is a "square wave". The Fourier transform of a square wave has resonances at the odd harmonics. These correspond to the reflection bands actually observed for a quarter-wave stack reflector at $\lambda_o/3$, $\lambda_o/5$, $\lambda_o/7$, etc. The Fourier transform of a sinusoidal profile has no harmonics. Rather, it has only a contribution at the fundamental frequency or wavelength. Thus, a sinusoidal index profile should eliminate the higher order reflection bands.

The actual relationship between the index variation and the spectral performance of the filter can be expressed in many ways. However, all of these involve the log of the refractive index. For example, one relationship between n(x) and the transmittance T(λ) for a filter is [4]

$$\ln[n(x)] = (2/\pi) \int_0^\infty [Q(k)/k] \sin[\phi(k) - kx]\, dk, \tag{6}$$

where

$$Q^2(k) = \frac{1}{2} \left[\frac{1}{T(k)} - T(k) \right] \tag{7}$$

is a function of transmittance expressed in terms of $k = 2\pi/\lambda$. The phase factor $\phi(k)$ must be an odd function to ensure that n(x) is real. Note that it is ln[n(x)] which is the Fourier transform of the performance and which should therefore vary sinusoidally to eliminate the higher order rejection bands. Such an index profile is given by eq (3).

In eqs (1) - (3), the coefficients a_i and b_i are chosen using two constraints. First, the refractive index is allowed to vary between a minimum value of n_L and a maximum value of n_H. Second, the profile is assumed to start and end with the minimum index n_L. This choice was made arbitrarily for the purposes of this discussion, and the actual terminations of the multilayer are determined by the exact requirements of the filter. The values of a_i and b_i determined by these constraints are given in table 1. A single period of each profile is shown in figure 1.

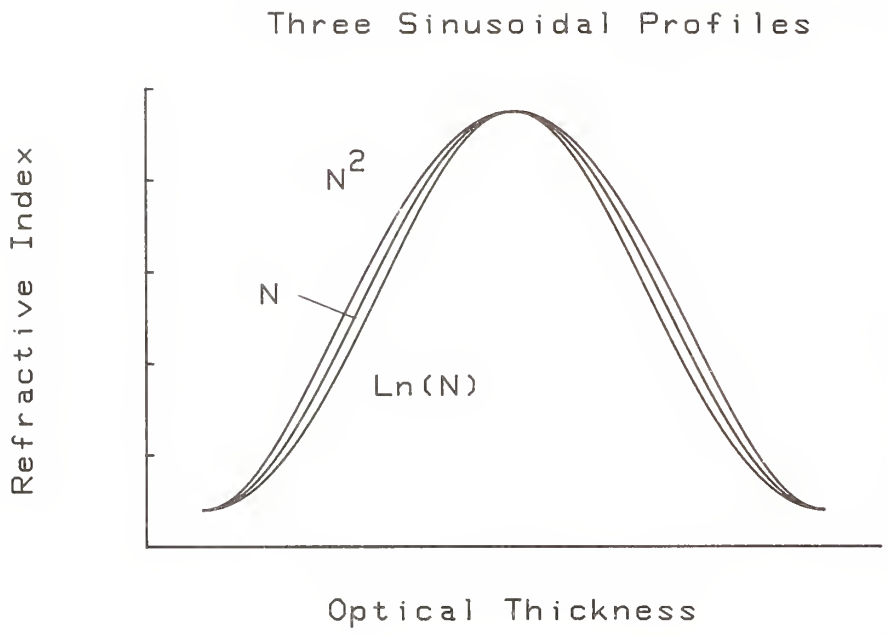

Figure 1. Refractive index profiles versus optical thickness as given by eq (1) - (3) and table 1.

Table 1. Coefficients for Rugate Index Profiles

i	1	2	3
a_i	$(n_L - n_H)/2$	$(n^2_L - n_H{}^2)/2$	$[\ln(n_L/n_H)]/2$
b_i	$(n_L + n_H)/2$	$(n^2_L + n_H{}^2)/2$	$[\ln(n_L n_H)]/2$

To calculate the spectral performance of filters with these three profiles, it is convenient to approximate the continuous profile by a number of discrete index steps of equal optical thickness. The approximation of the logarithmic profile by six discrete index levels is illustrated in figure 2. Expressions for the determination of the index levels are given elsewhere [2,5]. When approximating a continuous profile by discrete steps, one must recognize that higher order resonances will occur. In the case of a profile with m index levels as shown in figure 2, the first non-zero order occurs at $\lambda_0/(2m - 3)$. One must also be sure to use enough steps to provide a satisfactory approximation to the performance of the rugate filter over the wavelength range near the primary reflectance band at λ_0. Experimentation with various numbers of layers shows that m = 6 is sufficient.

Figure 3 illustrates the spectral reflectance curves for multilayers having stepped-index profiles approximating eqs (1) - (3). For this figure, values of $n_L = 1.38$ and $n_H = 2.25$ were chosen [5], with a substrate index of 1.52. Six index levels were used to approximate the profiles and six repetitions of the basic period were used in each case. The wavelength has been expressed relative to a value of $\lambda = 1$. It can be seen that the sinusoidal n^2 profile (broken curve) has a significant reflectance at a relative wavelength of 0.5, corresponding to the second order or $\lambda_0/2$. The sinusoidal index profile (dashed curve) has a smaller peak, while the sinusoidal ln(n) profile (solid curve) has no peak at all at $\lambda_0/2$. At shorter wavelengths, the differences between the curves become negligible; a slight deviation being observed for the n^2 profile at $\lambda_0/3$.

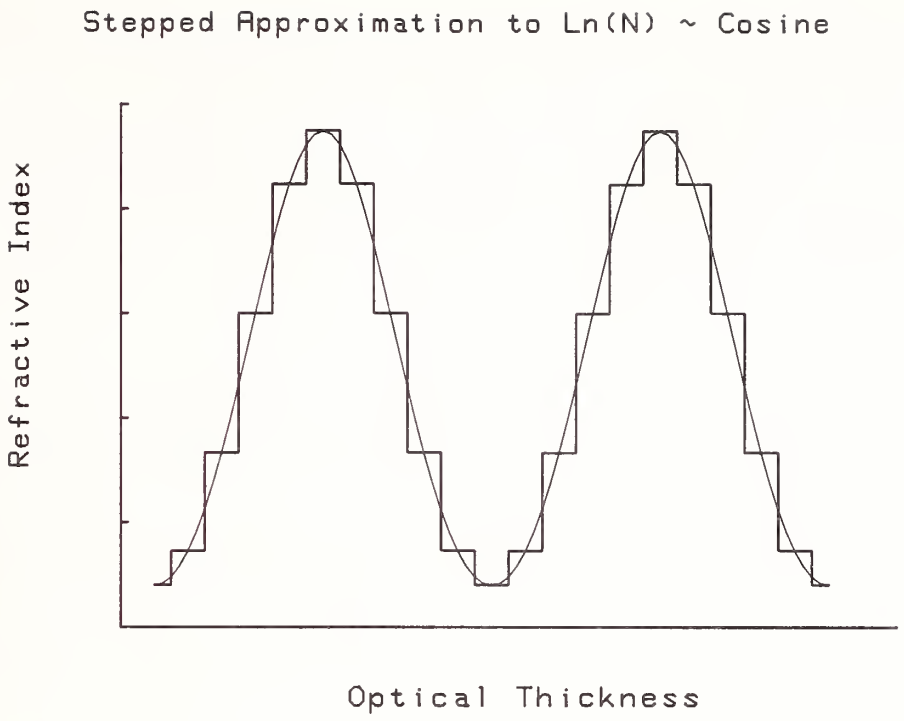

Figure 2. Approximation of a continuous index profile by a series of discrete steps of equal optical thickness.

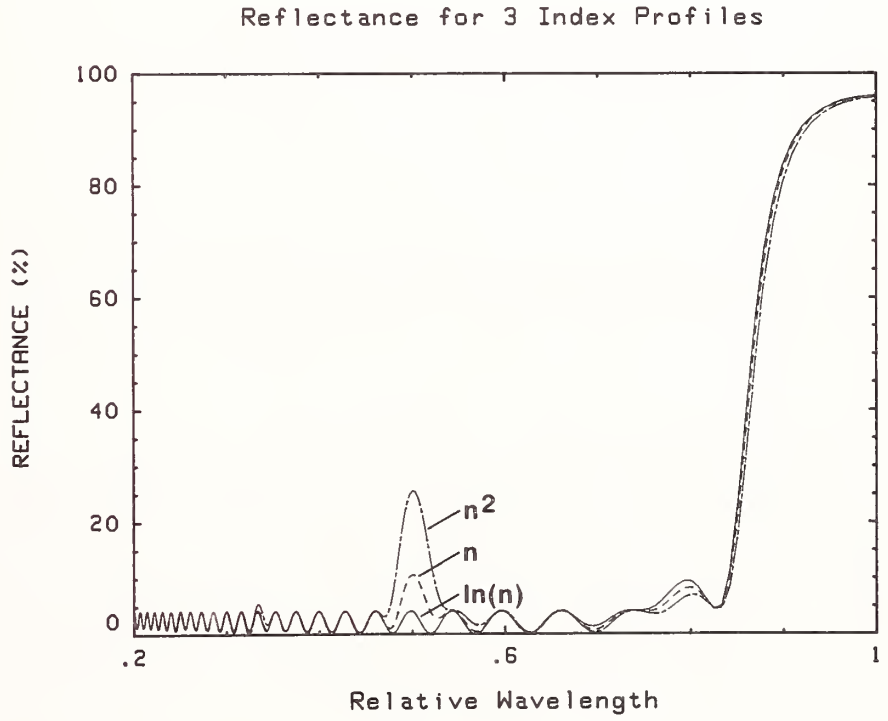

Figure 3. Reflectance versus wavelength for the three rugate filter designs, illustrating the behavior at wavelengths of 1/2 and 1/3 relative to $\lambda_0 = 1$. The designs consist of six repetitions of the periods given by eqs (1) - (3), and values of $n_H = 2.25$ and $n_L = 1.38$ have been assumed. A substrate index of 1.52 was also used.

The actual height of the reflective peak at $\lambda_o/2$ depends on two factors: the number of repetitions of the basic period and the index ratio n_H/n_L. The number of repetitions of the basic period is determined by the desired reflectance at λ_o, while the index ratio may be determined by the desired spectral width of the reflectance band at λ_o. As an example, for 10 repetitions of the basic period, the values of the peak reflectance at $\lambda_o/2$ for the three profiles are plotted against index ratio in figure 4. (Note: The actual wavelength of the peak is about 0.496 λ_o.) For high index ratios, the second order reflectance peak becomes significant, especially for the profile with a sinusoidally varying dielectric constant. On the other hand, for the logarithmic profile, there is no peak at $\lambda_o/2$, as indicated by the nearly constant value of reflectance versus index ratio.

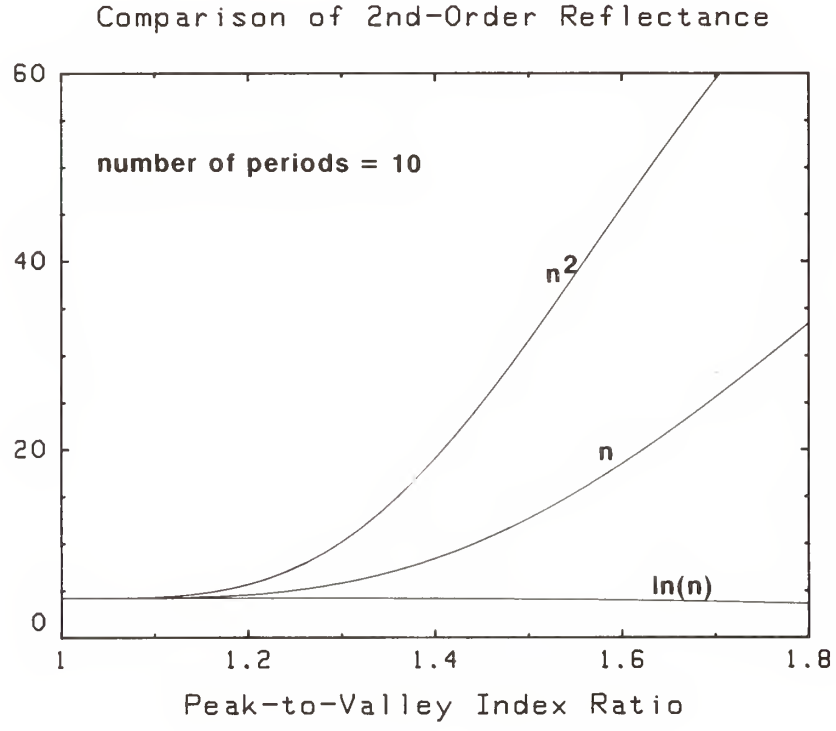

Figure 4. The height of the reflectance peak at $\lambda_o/2$ for three filter designs. The designs consist of ten repetitions of the periods given by eqs (1) - (3). The peak-to-valley ratio is n_H/n_L, and a value of $n_L = 1.38$ was assumed. A substrate index of 1.52 was used.

For low index ratios, the differences between the three profiles are smaller, becoming essentially negligible below $n_H/n_L = 1.1$. This was the range of interest of the work reported by Becker [1]. For these low index ratios, a larger number of repetitions of the basic period would be required to achieve a high reflectance at λ_o.

In summary, three slightly different index profiles for rugate filters have been compared. The major difference in the performance of the three designs occurs at $\lambda_o/2$. The design in which the log of the refractive index varies sinusoidally is found to have no unwanted reflectance bands.

References

[1] Becker, Roger J. Analysis of rugate filter behavior. To be published in the Proceedings of the Eighteenth Annual Symposium on Optical Materials for High Power Lasers (1986).

[2] Carniglia, C.K. A comparison of several short-wave-pass filter designs. Appl. Opt. (submitted for publication).

[3] Jacobsson, R. Inhomogeneous and coevaporated homogeneous films for optical applications, chapter 8 in Phys. of Thin Films. George Haas, ed. New York: Academic Press; 1975. 51-98.

[4] Dobrowolski, J.A.; Lowe, P. Optical thin film synthesis program based on the use of Fourier transforms. Appl. Opt. 17 (19): 3039; 1978, Oct 1.

[5] Baumeister, Philip. Simulation of a rugate filter via a stepped-index dielectric multilayer. Appl. Opt. 25 (16): 2644-2645; 1986 August 15.

Which relation is in best agreement with experiment? The author replied that people usually are trying to make very narrow Rugate filters, so they have down in the region where the various curves nearly coincide. A more important practical problem is that the dispersion of the coating materials means that if one is correct at the fundamental one may still be off in sideband regions.

The damage threshold of these Rugate coatings is not well known. Back in 1975 and 1976, the Air Force and DARPA were trying to smear out interfaces to improve the damage threshold by eliminating the field discontinuity at the interface. Results were mixed. In some cases the damage threshold improved, in others no effect was seen. In theory Rugate filters should be very damage resistant if interfaces are bad, since there are no sharp interfaces. Also, the deposition is a continuous process so that no contaminant layer can form in between depositions. However, one of the practical problems is that in mixing materials one may change their absorption drastically. They have discovered this for mixtures of zirconia and yttria.

How narrow a bandwidth can one get for a Rugate filter? The author replied that the bandwidth is made narrower by making the two indices very close together. In Arizona he believes they have succeeded in depositing Rugate coatings with indices of 1.45 and 1.46.

It was suggested that if the indices were very close together, the filter might be rather sensitive to radiation. The speaker pointed out that if the indices were both shifted together by the same amount by radiation it might be OK. If they were shifted differently, the filter wouldn't work.

- MANUSCRIPT NOT RECEIVED -

COMPARATIVE STUDY OF REACTIVELY EVAPORATED VS. ION-PLATED TiO_2 THIN FILMS

Karl H. Guenther
Center for Applied Optics
University of Alabama in Huntsville

Boon Loo
Chemistry Department
University of Alabama in Huntsville

Hans K. Pulker
Basic Research Laboratory
BALZERS AG, Liechtenstein

Andreas Saxer
c/o ENEA - Casaccia
Via Anguillarese
Rome 00060, Italy

Steven C. Seitel
Montana Laser Optics, Inc.
Bozeman, Montana

ABSTRACT

Single-layer thin films of TiO_2 deposited on glass substrates by means of standard reactive evaporation (from a boat) and by means of the novel deposition technique of ion-plating were characterized with a transmission electron microscope, a Raman microprobe, a thermal deflection spectrometer, and a Talystep stylus-type surface profiling instrument. With each deposition technique, single-layer coatings of different thicknesses were produced, from one QWOT up to 12 QWOT (@ 633 nm). The thickness dependence of microstructure, surface roughness, and absorption for the two groups of coatings will be presented, together with laser damage threshold measurements at 532 nm.

- MANUSCRIPT NOT RECEIVED -

ION ASSISTED DEPOSITION OF OPTICAL THIN FILMS AT REDUCED SUBSTRATE TEMPERATURE

Forrest L. Williams and J. R. McNeil
University of New Mexico
Center for High Technology Materials
Albuquerque, NM 87131

J. J. McNally
Dept. of Physics
USAFA/DFP
U.S. Air Force Academy, CO 80840

G. J. Exarhos
Battelle Northwest Laboratory
PSL-1108
Battelle Boulevard
Richland, WA 99352

ABSTRACT

Ion assisted deposition (IAD) involves bombarding a thin film with low energy ions (E_i <1 keV) while it is being deposited. We have investigated the application of this technique to deposit optical thin films onto substrates at low temperature (T < 150°C). Since conventional deposition methods require heating the substrate to temperatures of -300°C, IAD is important for coating substrate materials that cannot be subjected to elevated temperature.

In this study, we have observed that optical coatings of Al_2O_3, Ta_2O_5 and TiO_2 deposited at low temperature using IAD have higher values of refractive index compared to similar films produced without IAD. In addition, the optical absorption of Al_2O_3 and Ta_2O_5 thin films can be decreased by applying IAD to deposit these materials. We were unable to detect visible absorption of TiO_2 thin films produced in this study. We also present results correlating Raman spectra and optical scatter of these films to IAD conditions. Which suggests that IAD TiO_2 at low temperature can promote anatase crystallites in the film, with a corresponding increase in optical scatter.

*Work supported in part by Air Force Weapons Laboratory Contract F29601-86-K-0207

Manuscript Received
8-29-88

OPTICAL PROPERTIES OF LOW ENERGY ION ASSISTED DEPOSITED TiO_2 FILMS

M.Ghansyam Krishna, K. Narasimha Rao,
M.Adinarayana Murthy and S.Mohan

Instrumentation and Services Unit,
Indian Institute of Science,
Bangalore-560 012, India.

Absorption in TiO_2 films limits their efficiency and stability against high power laser radiation. The optical absorption in single layer TiO_2 films is greatly influenced by deposition parameters such as the rate of deposition, oxygen partial pressure, substrate temperature and the starting material. It is also observed that low energy ion assisted deposition enhances the reactivity and results in reduction of absorption.

In this investigation, single layers of TiO_2 films have been prepared using ionized oxygen (produced using a Heitmann source) and TiO as the starting material. The optical properties (refractive index n, and extinction coefficient k) and the laser induced damage threshold as a function of deposition parameters has been studied. The discharge currents were varied between 0 and 400 mA with the rate of deposition being 9 and 18 nm/min. The oxygen pressure was maintained at 2×10^{-4} torr. At low deposition rates, in situ optical monitoring of transmission has shown absorption free single layers for moderately low discharge currents (200 mA) whereas at higher deposition rates absorption free films were obtained at higher currents. The damage threshold of these films was found to be directly dependent on the absorption.

Variation in damage threshold values is explained on the basis of film composition, structure and optical properties.

Keywords: absorption coefficient;discharge current;laser induced damage threshold;low energy ions;refractive index;TiO_2 films.

1. Introduction

It is a well documented fact that optical coatings are the "weak links" in any high energy laser system. The laser induced damage threshold (LIDT) of these coatings apart from being influenced by laser parameters such as spot diameter, pulse, width and mode of operation also depends on the coating technique and deposition parameters.

Some of the more important properties of optical films which are studied in relation to damage resistance are absorption

coefficient,refractive index, stress, thermal conductivity etc. Various deposition techniques have been extensively used with a view to increase the damage thresholds of optical coatings used in laser systems.

This paper reports preliminary results on optical properties of single layer TiO_2 films deposited using a low energy ion assisted deposition process. The low energy ions of oxygen are produced using a Heitmann type discharge source [1] and the starting material (TiO) is evaporated from an electron beam gun. The effect of discharge currents and rate of deposition on the optical properties viz. refractive index, absorption coefficient and LIDT of single layer TiO_2 films is investigated.

2. Experimental Techniques

Single layer TiO_2 films were deposited in a standard high vacuum system used as the experimental chamber. It was pumped using an oil diffusion-rotary pump combination and ultimate vacuum of the order 10^{-6} torr could be routinely obtained. A quartz crystal monitor (FTM3 of M/s Edwards) and an optical monitor (OMS 2000 of M/s Leybold Heraeus) were used to monitor the film thickness during deposition. The substrates were well polished (25mm dia) fused quartz plates. They were first, cleaned with detergent and running tap water. They were then vapour degreased in an iso-propyl alcohol bath.

The substrates were rotated during deposition to obtain uniform thickness. The starting material TiO was evaporated from a 6kW electron beam source (M/s Leybold Heraeus model ESV6). Films were deposited at ambient temperature and an oxygen partial pressure of 2×10^{-4} torr. The rate of deposition was kept at 9nm/min and 18nm/min. The discharge current was varied between 0 to 400 mA. The films were monitored at 1060 nm and coated to a thickness of 280 nm geometrical thickness.

The transmittance and reflectance of the films were recorded using a dual beam spectrophotometer (Hitachi Model 330 UV-Vis and IR) with an accuracy of $\pm 0.2\%$. The refractive index and absorption coefficient were calculated using the envelope technique[2]. The LIDT was measured using the set up described earlier [3].

3. Results and Discussion

The insitu transmission curves for a film of thickness 280 nm prepared in neutral oxygen and ionized oxygen (ion current=200mA) are shown in (fig.1). There is a marked change in the transmission maximum on increasing the discharge current. Films deposited without discharge show lower transmission indicating a reduced oxygen content in these films. However, the introduction of ionized oxygen enhances reactivity and hence there is an increase in transmission.

The variation of n and k with discharge current for two deposition rates 9nm/min and 18nm/min is shown in (fig.2). The index of refraction changes insignificantly with an increase in discharge current for both rates of deposition. The decrease in absorption with an increase in discharge current is, however, significant. This can be attributed to an increase of oxygen content in the film due to increased reactivity in the

presence of oxygen ions. Similar observations have been made by Allen [4]and Kuster et al [5]. The absorption in films deposited at the higher deposition rate is only marginally higher indicating that the oxygen content has changed only nominally.

The dispersion curves for n and k are shown in (fig.3). For both the deposition rates i.e., 9nm/min and 18nm/min the refractive index as well as absorption coefficient show a decrease with increasing wavelength. The increase in refractive index with rate of deposition could be due to increased packing density. It appears that the variation in discharge current does not have much influence on the refractive index and its variation with wavelength.

The increase in k values at shorter wavelengths is due to the intrinsic absorption edge (at 380 nm) of this material. In the films deposited in neutral oxygen the observed increase in k at longer wavelengths has also been reported by Allen [4]. who attributes this to oxygen deficiency. The absorption in films deposited at the higher rate of deposition is marginally higher.

Laser damage measurements made on the films are shown in table 1. With an increase in discharge current there is an increase in LIDT values. The highest damage threshold was obtained for the film deposited at a discharge current of 200mA and the deposition rate of 9nm/min. This can be directly correlated with the absorption coefficient of this film. The spot diameters used were .35mm and 1.05mm. The change in spot diameter did not influence the laser damage threshold values because it was well above the minimum required for any such effect to be observed.

4. Conclusions

Single layer films of TiO_2 have been deposited using a low energy ion assisted process. The absorption coefficient of these films has been optimized as a function of discharge current. The films deposited at 200mA were found to have the lowest absorption coefficient and highest laser damage threshold. The change in rate of deposition from 9nm/min to 18nm/min has not affected the optical properties significantly.

The authors would like to thank Prof.E.S.Rajagopal,Chairman,ISU for his encouragement and keen interest in this study.

5. References

[1] Heitmann,W.;Appl.Opt.,Vol.10;2414-8;1971.

[2] Swanpoel,R.;J.Phys.E: Sci. Instrum.,Vol.16;1214-22;1983.

[3] Narasimha Rao,K.,Adinarayana Murthy,M.,Mohan,S.,and Ramakrishna Rao,M.;

Proceedings of XIV ASTM Annual Symposium on Laser Induced Damage in

Optical Materials,1985 October,Boulder,USA.

[4] Allen,T.H.,Proceedings of SPIE;Vol.325;93-99;1982.

[5] Kuster,H.,and Ebert,J.;Thin Solid Films;Vol.70;43-47;1983.

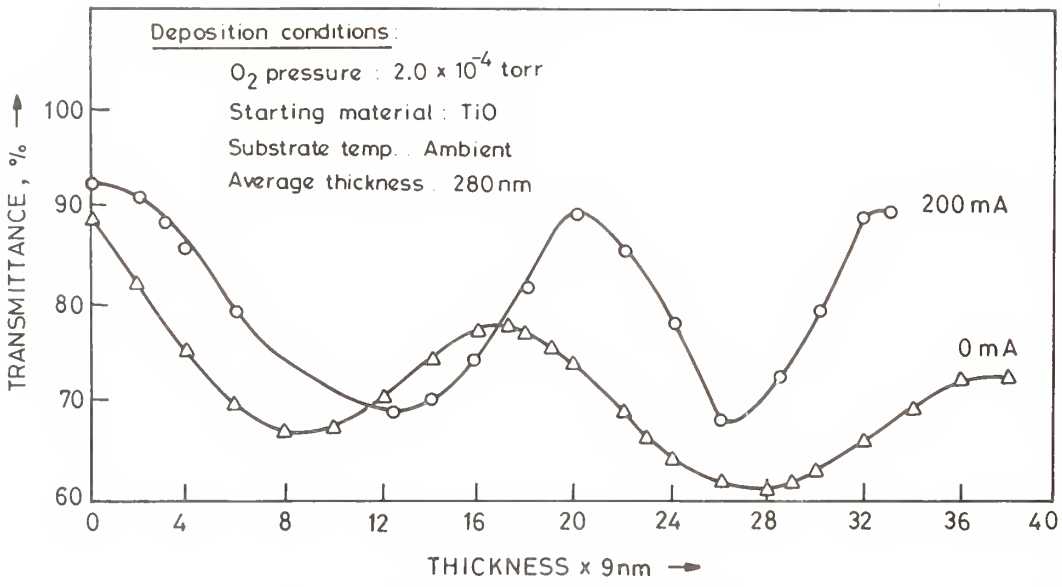

Figure 1. Insitu transmittance with thickness.

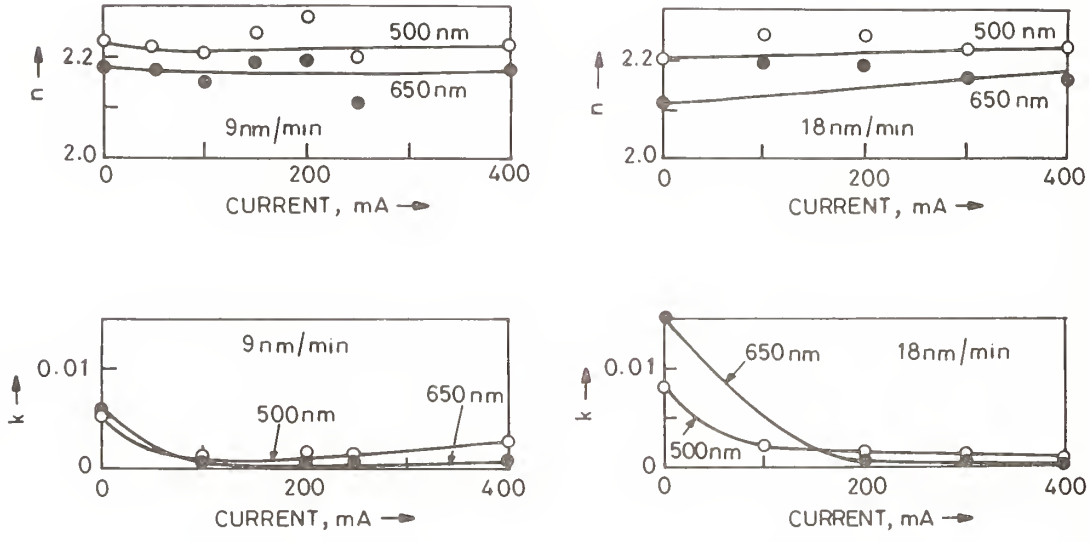

Figure 2. Variation of refractive index (n) and extinction coefficient (k) with discharge current.

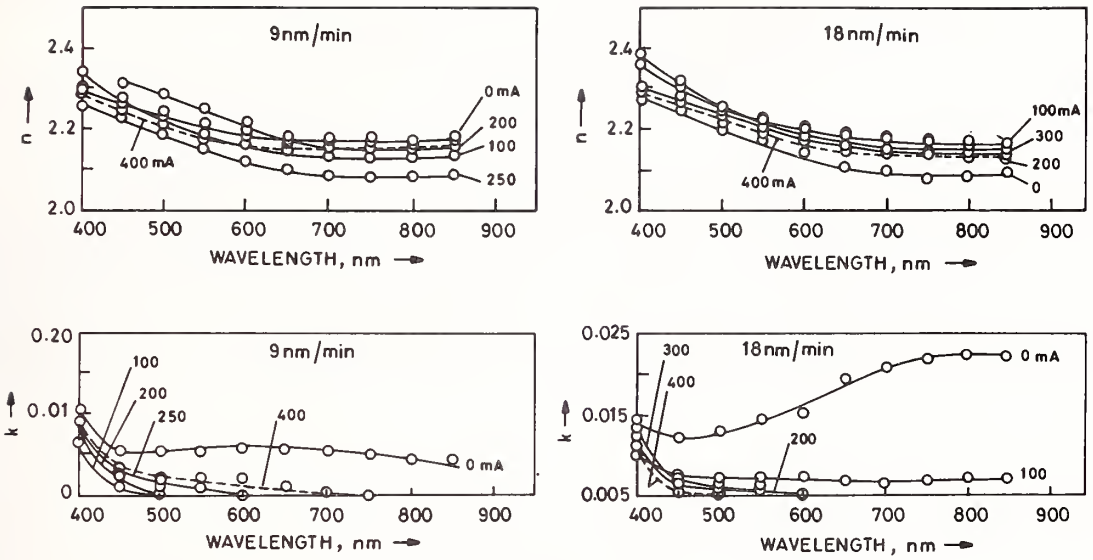

Figure 3. Variation of refractive index (n) and extinction coefficient (k) with wavelength.

Table: 1 Measured laser damage thresholdsstudies

Rate of deposition :	9 nm/min
Working pressure :	2×10^{-4} torr
Laser used :	Nd : YAG

Discharge current (mA)	k (650 nm)	power density J/cm^2
0	0.007	3.6
50		3.6
100	0	3.7
150		3.6
200	0	4.6
250	0	3.9
400	0.001	3.7

Manuscript Received
3-17-88

HR Coatings Prepared from Colloidal Suspensions*

Ian M. Thomas, John G. Wilder and
Raymond P. Gonzales

Lawrence Livermore National Laboratory
University of California, P.O. Box 5508, L-483
Livermore, CA 94550

ABSTRACT

We have now established that sol-gel HR coatings prepared from colloidal oxide suspensions are superior to those prepared from solutions of precursor materials. Our investigation of single coatings of ZrO_2, HfO_2 and $Al_2O_3 \cdot H_2O$ prepared from suspensions has indicated that those from $Al_2O_3 \cdot H_2O$ have the highest laser damage threshold at 1064 nm. We have prepared HR coatings by stacking $Al_2O_3 \cdot H_2O$ and SiO_2, also prepared from suspension, in the conventional manner achieving reflectivity of 99% with 35 layers. The damage threshold of these materials has however only been about half that of single coats of the component oxides.

Key words: alumina-silica, HR coatings, laser damage, Sol-gel coatings.

1. Introduction

There are two methods used for the preparation of coatings by the sol-gel method.

(a) Application of a precursor solution to a substrate with subsequent conversion of the precursor to an oxide on the substrate surface. This normally requires water and heat.

(b) Application of a colloidal suspension of an oxide to a substrate with subsequent evaporation of the suspending medium. This can usually be accomplished at room temperature.

In our previous investigations[1] we have utilized both methods for the preparation of HR multilayer stacks. Method (a) is the easiest because of the ready availability of a number of suitable precursor materials in contrast to the difficulty in preparing suitable colloidal suspensions required in method (b). However we have now found that method (a) becomes unsatisfactory once the number of layers exceeds about 10 for reasons that are illustrated in Fig. 1. The conversion of the precursor material to oxide involves shrinkage, due to the necessary removal of the residual reactive groups, and this always gives rise to crazing and peeling because of the resultant stress. No amount of curing of the lower layers prior to the application of the upper layers eliminated the problem. We have therefore abandoned this method entirely in favor of coatings prepared from colloidal suspensions. This method is more difficult to carry out because of the necessity for preparing suitable suspensions but gives rise to completely stress-free films which can readily be stacked (illustrated in Fig. 2).

2. Preparation of Suspensions

A considerable amount of effort was directed towards the preparation of suitable colloidal suspensions, these being ones in which the particles were monodispersed, all about the same size and in the size range of 100-300 Å. We had previously been able to prepare suitable suspensions of SiO_2 and TiO_2 [2] and further effort now allowed us to prepare suspensions of $Al_2O_3 \cdot H_2O$, HfO_2 and ZrO_2. These were all prepared by the hydrolysis of suitable precursors in large quantities of water followed by a reflux period which allowed the precipitated oxides to crystallize. These were adoptions of the method of Yoldas for alumina[3] and Clearfield for zirconia[4]:

$$2\ Al(OR)_3 + 4\ H_2O \rightarrow Al_2O_3 \cdot H_2O + 6\ ROH$$
$$ZrOCl_2 + H_2O \rightarrow ZrO_2 + 2\ HCl$$
$$HfOCl_2 + H_2O \rightarrow HfO_2 + 2\ HCl$$

---

*Work performed under the auspices of the U.S. Department of Energy by Lawrence Livermore National Laboratory under Contract No. W-7405-ENG-48.

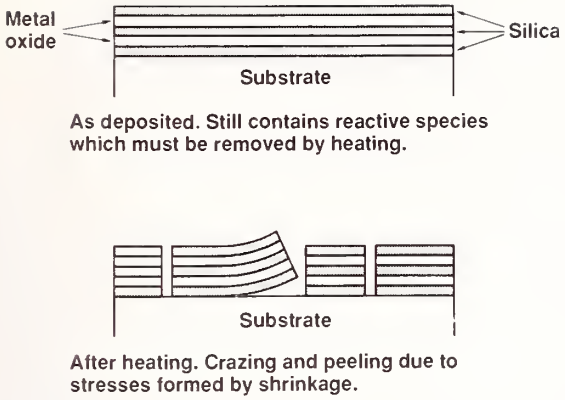

Figure 1.

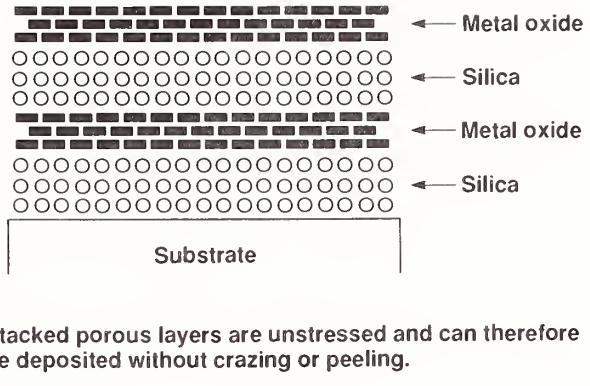

Figure 2.

The alumina was obtained as boehmite in the form of thin plates approximately 300 x 300 x 50 Å and the HfO_2 and ZrO_2 as approximately spherical agglomerates 300-500 Å in diameter containing monoclinic microcrystals.

3. Preparation of Coatings

Single coatings of all of these oxides were prepared by spinning onto fused silica substrates followed by an air dry. All coatings were porous and consequently of low refractive index. The indices and laser damage thresholds of single coats under two different conditions are shown in Table 1.

		Damage at 1064 nm · J/cm ^{2}	
Oxide	Index	10 ns, single shot	16 ns, 120 Hz
SiO_2	1.20	30-40	30-40
$Al_2O_3 \cdot H_2O$	1.43	20-30	30
ZrO_2	1.55	10-20	10-15
HfO_2	1.52	15-20	15-20
TiO_2	1.75	15-20	2-5

Table 1. Laser damage thresholds and refractive indices of single oxide coatings.

It is immediately apparent that the $Al_2O_3 \cdot H_2O$ coatings compare very favorably with our silica coatings in laser damage and that TiO_2 coatings fail dramatically when subjected to a high repetition rate. We therefore decided to concentrate efforts on the preparation of multilayer coatings using our two best materials, SiO_2 and $Al_2O_3 \cdot H_2O$, as the low and high index components.

By spinning on alternating coats of silica and alumina suspensions onto a fused silica substrate with several minutes air dry in between coats, HR dielectric mirror samples were readily obtained. These were arranged such that they had maximum reflection at 1064 nm and all samples reported contained ten pairs or more resulting in reflections of greater than 85%. It was found that 35 layers were required to give reflection of 99%.

4. Laser Damage Thresholds

Laser damage threshold measurements were carried out at 1064 nm with single shot pulses of 10 ns duration. The results are shown in Fig. 3. These show quite a wide spread and average about 12 J/cm^2, a disappointingly low figure in view of the high thresholds of the individual oxide components. We have so far no explanation for these low figures. One observation of possible significance is that the damage threshold decreases and the number of damage sites increases as the number of layers in a coating increases. This suggests that absorptive sites

are being introduced with each successive coating layer and that, even though the density of sites is not increasing, the laser damage threshold of these sites is decreasing. The threshold level of each absorptive site is therefore not constant but depends on the coating thickness. A possible explanation of this is that a large quantity of gas is liberated when a site damages (perhaps CO_2 and H_2O from the decomposition of organic entities) and this can escape without damaging the coating when it is thin but not when it is thick. The inherent weakness of the particle-particle bonding in these coatings would allow easy separation by expanding gas. We intend to investigate this further.

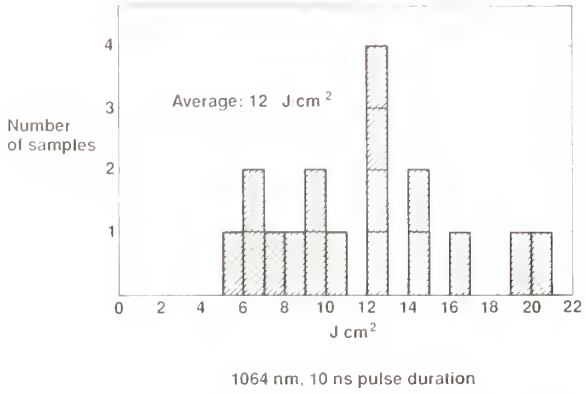

Figure 3. Laser damage thresholds of $Al_2O_3 \cdot H_2O$-SiO_2 multilayer coatings.

5. Summary

We have prepared coatings of ZrO_2, HfO_2 and $Al_2O_3 \cdot H_2O$ from colloidal suspensions of the relevant oxides. All are porous and consequently of low refractive index. $Al_2O_3 \cdot H_2O$ coatings had the highest laser damage threshold at 1064 nm and this oxide was used in combination with SiO_2 to prepare HR coatings. About 35 layers were required to attain 99% reflectivity. The laser damage threshold was however about half that of single coats of the component oxides.

6. References

[1] Thomas, I.; Wilder, J.; Gonzales, R.; George, D. "1064 nm and 350 nm Laser Damage Thresholds of High Index Films Deposited from Organic Solutions and Sols", Boulder Damage Symposium, Boulder, Colorado, November 1986.

[2] Thomas, I. "Single Layer TiO_2 and Multilayer TiO_2-SiO_2 Optical Coatings Prepared from Colloidal Suspensions", Applied Optics, 26, 4688 (1987).

[3] Yoldas, B. E. "Alumina Sol Preparation from Alkoxides", Amer. Ceram. Soc. Bull. 54, 289 (1975).

[4] Clearfield, A. "Crystalline Hydrous Zirconia", Inorg. Chem. 3, 146 (1964).

Is it difficult with two materials of so nearly the same index of refraction to get the proper center wavelength? The speaker replied that it was but they had succeeded in getting some good coatings.

The effect of bacteria should also be considered. The speaker replied that they were now working on this problem seriously. They have put hydrogen peroxide into the salt solutions prior to coating and irradiated with uv light for several hours. Organic residues adsorbed onto the coating after deposition must also be considered, since the coating has a large surface area and behaves somewhat like activated charcoal.. The coatings may have to be used in vacuum. Thick coatings are affected, thin coatings are not. They do not have any direct evidence for organic effects in the films except that when uv-ozone, which will oxidize carbon, is used on thick silica coatings the damage threshold was improved. The same technique did not work for alumina.

It was pointed out that Sandy Asher used polymer spheres which he deposited to make Bragg reflection devices. This technology may be important here.

Manuscript Received
12-20-87

1064 nm and 350nm Radiation Stability of Low Density ThO_2-SiO_2 High-Reflective Coatings Deposited from Sols

H. Floch , J.J. Priotton
and
J.F. Mengue , C. Cordillot

Commissariat à l'Energie Atomique, Centre d'Etudes de Limeil-Valenton
B.P. n° 27, 94190 VILLENEUVE-SAINT-GEORGES, FRANCE

We maintain our effort together with the Lawrence Livermore National Laboratory in the research for high damage threshold optical coatings prepared from colloidal oxide suspensions, we have recently observed that single layers of ThO_2 exhibits up to 12-13 J/cm^2 under single pulse laser irradiation at 1064nm wavelength and 1ns pulse duration. Associating this thoria with the silica reported earlier/1,2/, multilayer HR-coatings have been also elaborated by laying down quaterwave thick alternating coats, at room temperature. In this manner, we have achieved reflectivity adjacent to 97-98% with 21 layers. The laser-induced breakdown of these mirrors has unfortunately only been about 8-9 J/cm^2, lower than the one of the high index thoria component.

Key words : Laser damage, ThO_2, thoria-silica coatings, sol, HR-coatings, sol-gel coatings.

I - Introduction

It is important to differentiate the sol-gel coating method using colloidal suspensions (sols) with another variation which is far more common /3/. This variation involves the application of a metal organic monomer or polymer precursor solution to a substrate followed by conversion to the inorganic oxide by a combination of water and heat. Making use of solutions (gels) it is possible to obtain hard, abrasion-resistance coatings of near-theoretical density if final processing temperatures of 400-500°C are used. However, these coatings begin to crack and peel after about nine layers are applied because of the stress built up and this has been reported to reduce laser damage resistance and the ability to form multilayer systems /4/.

After notable effort and investigations directed by I.M.Thomas */5-7/ at Lawrence Livermore National Laboratory (LLNL) for the preparation of HR multilayer dielectric stacks, they finally have demonstrated that the employment of colloidal oxide systems are superior to those prepared from solutions of precursor materials /8/. Unluckily, it has not always been possible to prepare suitable oxide suspensions with some oxides. Recent developments at LLNL and in our lab tend however to change this situation.

This specific paper describes the preparation and properties of single-layer thoria coatings prepared from a colloidal ThO_2 suspension. The use of these coatings associated with coatings from colloidal silica to built multilayer HR-coatings and the caracteristics of these films is also treated. All coatings were tailored for 1053nm wavelength or its harmonics ; this being the wavelengths of interest in our 20KJ neodynium-doped glass Phebus laser facility operating at Limeil-Valenton C.E.A laboratory.

2 - Colloidal thoria suspensions

The colloidal oxide route has been used much less frequently and has only been reported in optical application for antireflective SiO_2 /1-2/ and Al_2O_3 /9/ coatings and very recently for reflective coatings /6-8/. The use of inorganic colloids also has its advantages and disavantages. In colloidal suspensions the suitable precursor is already chemically converted to oxide prior to application to a substrate and only the removal of the suspending medium is required. This leaves a substantially strain-free oxide coating which normally requires little or no heat subsequent treatment. Nevertheless the coatings are porous and of comparatively low refraction index. They are also mechanically brittle because only the point contact energy between particles keeps the coating intact. The idea to utilize thoria as a high index candidate for laser damage resistant HR-coatings is the result of fact

that thorium dioxide has a high melting point temperature (~ 3050°C) and therefore is stoutly refractory. After a sustained work, we have found that a colloidal suspension of ThO_2 can be obtained by the hydrolysis of the thorium nitrate tetrahydrate salt in large excess of water followed by a liquid-liquid extraction of the solubilizing anion species using a water-insoluble base as depicted by O'Connor/10/.

The overall reaction can be represented by the following equation :

$$Th(NO_3)_4 + 2H_2O \xrightarrow[60°C]{\text{organic base}} ThO_2 + 4\ HNO_3$$

and the chemical procedure is described in figure 1. After solvent exchange, this suspension can be used to prepare porous ThO_2 coatings with an index of about 1.5-1.6 by application to suitable substrates at room temperature. The thoria was synthesized in the amorphous form and transmission electron microscopy (TEM) indicated that the thoria particles were roughly spherical 300-400 Å in diameter and substantially monodispersed. See figure 2.

3 - Coating procedure

All coating suspensions were filtered through a 0.2 micron teflon membrane filter and then applied by spinning on 5cm diameter and 5mm thick fused silica substrates. All coatings, which consist of layers of discreet ThO_2 particles, are therefore porous (~ 50-55%). It is similar to the porous silica AR coating prepared from colloidal silica developed by Thomas /1/. See figure 3.

Coatings of thoria are strain-free and remain as such, and optically unchanged, even when heated to high temperatures below the sintering temperature of the oxide particles. This property is in contrast with the stressed coatings prepared from a thorium metal organic precursor in solution (gel) in which heat is required after deposition for complete conversion to dense oxide /11/.

A number of HR-coatings have been prepared by spinning on quaterwave thick alternating coats of colloidal thoria and colloidal silica from suspensions. Up to twenty successive layers have been spun-coated at room temperature with about 20 minutes drying time between coats. Eventually, this coating process could have been shortened by using mild heat from an infrared lamp, or by exposing the coated samples under microwave radiance. These samples have remained intact with no shrinkage or peeling. Figure 4 shows the

* I.M.THOMAS is a doctor in chemistry working on the optical coatings by the sol-gel process at Lawrence Livermore National Laboratory (California)

transmission spectrum of a 21-layer coating whose reflectance is ~ 98% at 1.064µm. By changing the thickness of the individual oxide layers, unstressed HR-coatings with reflection maxima at wavelengths from 0.3µm to several microns could be elaborated.

4 - Laser damage thresholds caracteristics

Laser-induced damage threshold tests were carried out at 1064nm and 350nm with single shot pulses respectively of 1ns ans 3ns irradiation duration. The damage thresholds of single thoria coatings at 1064nm are shown in Fig.5. ThO_2 ranges from 10-15 J/cm^2 with an average of 12,3 J/cm^2. These are low packing density coatings of comparatively low index, about 1.55. It is obvious that thoria coatings are more damage-resistant compared to titania porous sol-gel coatings /7,14/ that tend to fail with massive damage in the thoria laser-energy breakdown range. Damage thresholds at 1064nm of multilayered coatings of this thoria with colloidal silica as the low-index component (n ~ 1,22) are presented in Fig.6. It is immediately apparent that thick multilayer stacks containing nine to fifteen layers have a low figure, averaging 8,7 J/cm^2, comparatively to the high thresholds of the respective oxide materials. Although a long sol dialysis restores slightly the threshold values, we remain convinced that others absorptive sources exist in the oxide coatings.

Single layers and multicoated systems operating at 350nm have also been damage-measured at this wavelength. See figures 7 and 8. There was quite a wide variation in the damage thresholds of the coatings at 350nm, in view of the previous values obtained at 1064nm. Respectively thoria monocoats and thoria-silica multicoats averaged around 3.6 J/cm^2 and 2.6 J/cm^2. There is a definite evidence that these low figures are not related to the nominal thoria UV cut-off wavelength (~250nm) but probably to the presence of residual nitrate entities. Effectively, as is well known, the NO_3^- anion has for solutions and crystalline nitrates /12/ absorption bands in the wavelength region of 302nm. Depending on the concentration and on the nature of the cation and the solvent, this band can shift somewhat. As a matter of fact, we observed (see histograms in figures 7 and 8) that the dialysis of the initial sol improved appreciably the damage threshold values. In order to change the anion stabilizer in the suitable suspensions, we intend to substitute the nitrate by the chloride metallic precursor, In this case, there is no major absorption risk because the maximum of absorption band of the chloride anion is at 181nm, as reported by Terenin /12/.

In spite of careful dialysis or resin ion-exchange, it remains unfortunatly difficult for HR-coatings to restore completly the laser-resistance figure like the high thresholds of the individual oxide components. We have so far no accurate explanation for this phenomenon, but one significant interpretation could be stated through recent investigations reported by

Thomas /13/. Thus, by depositing thick porous silica from suspension in alcohol /1,2/, they observed a drastic reduction in laser damage threshold at 350nm. One possible explanation for this result was that absorptive species were being trapped in the lower layers. Based on this premise, after coating they undertook to use ozone treatment at low temperature to remove the carbonaceous impurities. Immediatly, this was found to correct damage thresholds to the levels measured in single layers. In multilayered HR-coatings, we probably are faced to the same disturbing phenomenon because of the large number of layers, so we plan to investigate the oxidization of all the eventual parasitic organic species.

5 - Conclusion

At Limeil-laboratory and LLNL high laser damage threshold coatings are of particular interest and this has prompted investigation of sol-gel systems. So, we are enquiring into the possibility to prepare highly reflective optical coatings for laser glass that will survive, with minimal damage, relatively high energy laser shots. In continuation of this common effort, we have prepared coatings of ThO_2 from colloidal suspensions. All coatings are porous with low refraction index compared to dense thoria. This relevant oxide could be an acceptable high-index candidate for HR-systems with regard to the most promising Al_2O_3, H_2O component investigated by Thomas at LLNL. Disappointingly the laser-resistance of all sol-gel multilayer structures was much lower than the one of single coatings of the constituent oxides.

Aknowledgements

The authors are indebted to I.M.THOMAS for contribution and very helpful discussions in chemistry and to M.NOVARO and A.ROUSSEL for advices in optical coatings designs.

Could one make broadband coatings using the technique described? The author replied no, not yet. The thickness of the coating can be adjusted by varying the speed of rotation and observing spectrophotometrically.

References

1 I.M.Thomas, "High laser damage threshold porous silica antireflective coatings", Appl. Opt., 25, 1481 (1986).

2 H.Floch, J.J.Priotton and I.M.Thomas, "Porous silica sol-gel coatings for Nd : glass high-power pulsed laser uses" plenum publishing corp. in the press.

3 H.Schroeder, "Properties and applications of oxides layers deposited on glass from organic solutions", Opt. Acta. 9, 249 (1962).

4 R.S.Sokolova, "Internal stresses in thin oxide films deposited from hydrolyzable solutions", Sov. J. Opt. Technol, 41, 15 (1974).

5 I.M.Thomas, "Optical coatings by the sol-gel process", Optics News, 12, 18 (1986).

6 I.M.Thomas, J.Wilder, R.Gonzales and D.George, "1064nm and 350nm laser damage thresholds of high index films deposited from organic solutions and sols" ; 18th Boulder Damage symposium, Colorado, November 1986.

7 I.M.Thomas, "Single layer TiO_2 and multilayer TiO_2- SiO_2 optical coatings prepared from colloidal suspensions", Applied Optics, in the press.

8 I.M.Thomas, J.Wilder and R.Gonzales, "HR coatings prepared from colloidal suspensions" ; 19th Boulder Damage Symposium, Colorado, October 1987.

9 B.Yoldas, "Investigations of porous oxides as an antireflective coating for glass surfaces", Appl. Optics, 19, 1425 (1980)

10 T.L.O'Connor, Dedham and Mass, "Metal oxide aquasols and their preparation by liquid-liquid ion exchange", US.patent 3, 256, 204 (1966)

11 T.N.Krylova, R.S.Sokolova et al, "Radiation stability of oxide coatings obtained from solutions", Sov. J. Opt. Technol., 41,12 (1974)

12 A.N.Terenin, Usp. Fiz. Nauk 18, 1 (1937)

13 I.M.Thomas, J.Wilder and A.Lee, D.George, "Influence of post-deposition treatment by UV light and oxygen (ozone) on 350nm damage thresholds of SiO_2 films deposited from sols" ; 18th Boulder Damage symposium, Colorado, November 1986.

14 H.Floch, J.J.Priotton, "TiO_2 colloidal comme matériau haut-indice dans les lasers de puissance" Rapport C.E.A, in the press.

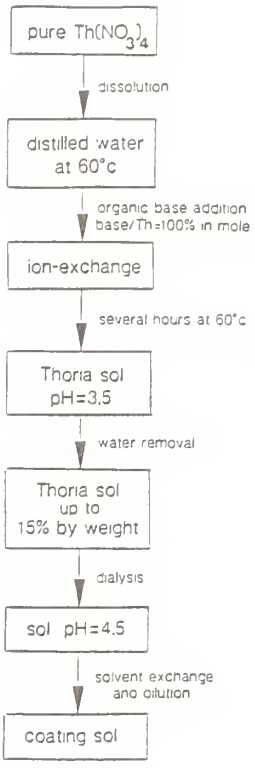

Figure 1. Thoria sol preparation.

Figure 2.

Colloidal thoria particles are roughly spherical (Ø~40nm) and monodispersed.

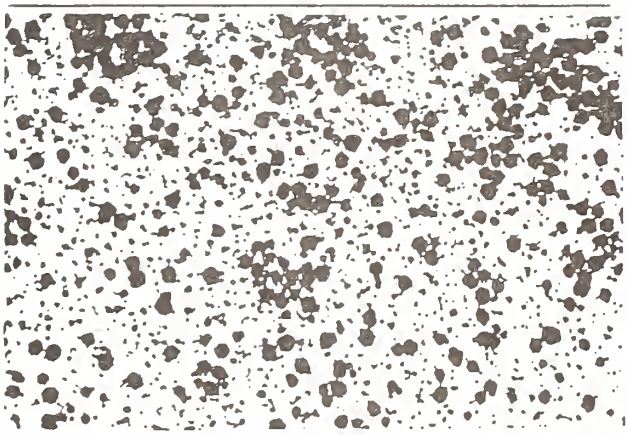

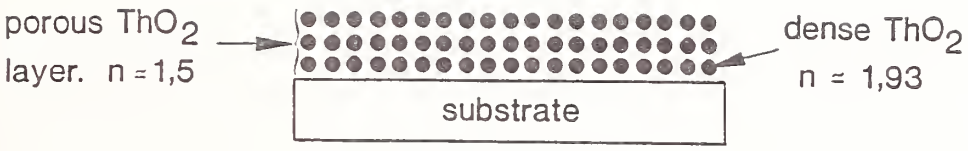

Figure.3

ThO_2 colloids give porous coatings.

Figure 4.

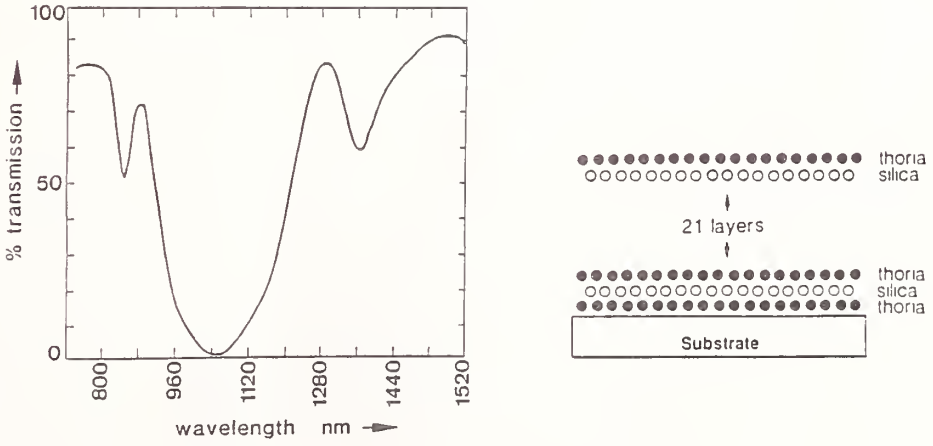

A 21-layers ThO_2-SiO_2 HR-film gives about 98% reflection on fused silica substrate.

Figures 5 & 6 show respectively the radiation stability of ThO_2 and ThO_2–SiO_2 coatings at 1064nm – 1ns.

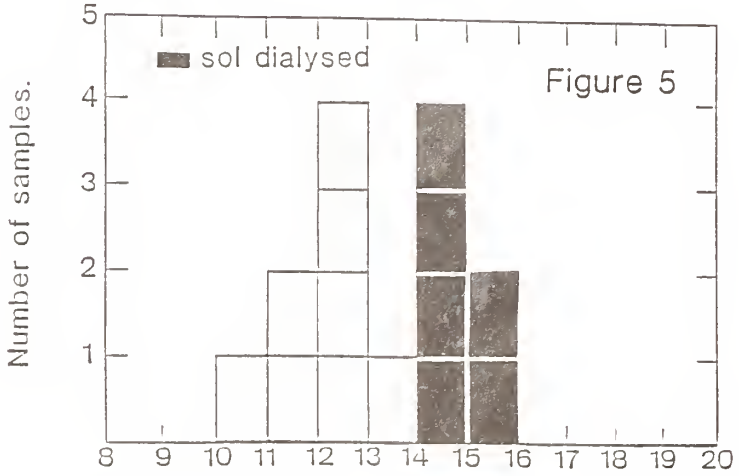

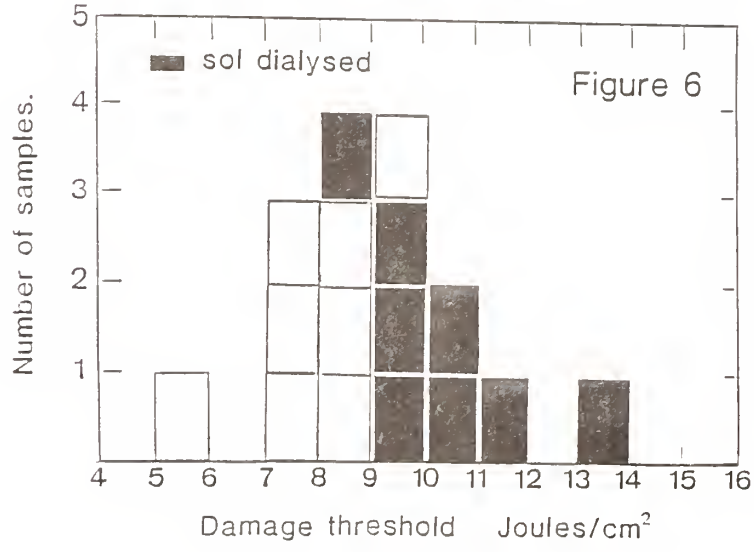

Figures 7 & 8 show respectively the radiation stability of ThO_2 and ThO_2-SiO_2 coatings at 350nm – 3ns.

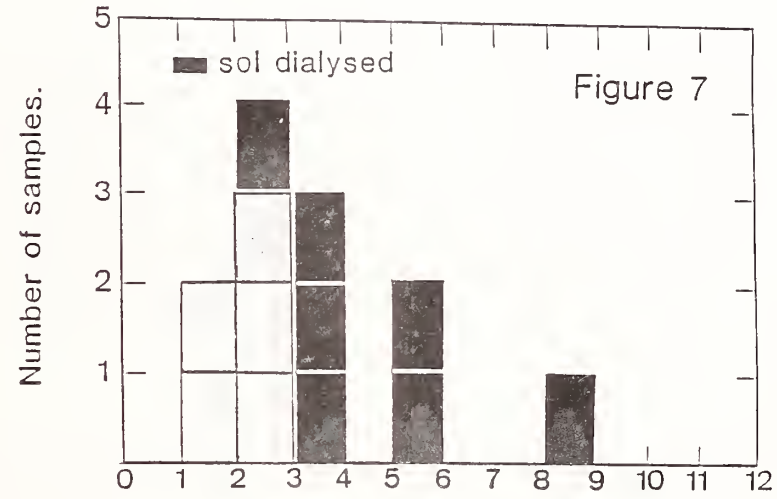

Figure 7

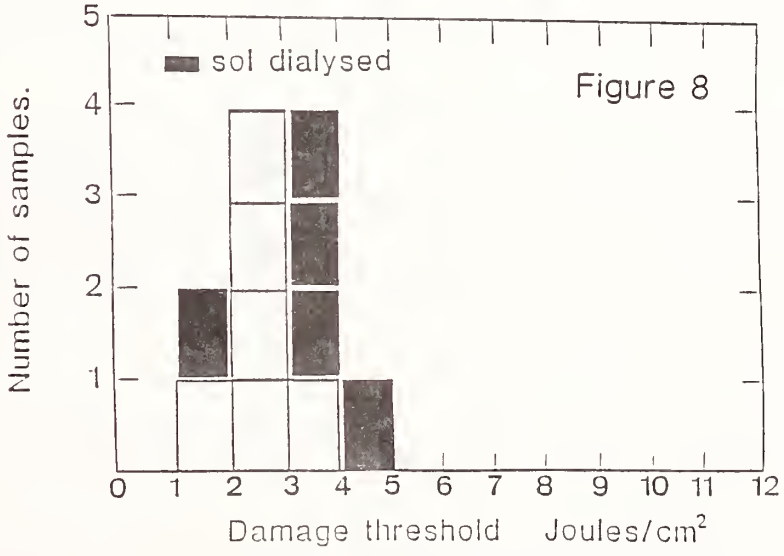

Figure 8

Manuscript Received
3-17-88

Oxide Optical Coatings Prepared by Metal-Organic Vapor Deposition*

Raymond Brusasco

Lawrence Livermore National Laboratory
University of California, P.O. Box 5508, L-483
Livermore, California 94550

ABSTRACT

We prepared films of alumina, zirconia and hafnia by Chemical Vapor Deposition (CVD) for evaluation as high refractive index optical components for high power laser applications. Films with high index of refraction (1.89-1.63) but with rather low single shot laser damage thresholds (4-10 J/cm^{-2}) were prepared by high temperature (400°C) thermal decomposition. Lower temperature deposition with chemical assist improves some optical properties and laser damage thresholds at the expense of a lower index of refraction.

Key Words: chemical vapor deposition, alumina, hafnia, zirconia, laser damage.

1. Introduction

Chemical Vapor Deposition (CVD) has been used extensively in the microelectronics industry to prepare thin films of oxides and other materials.[1] However, the application of CVD to the preparation of optical films has not been studied to any detail. The reviews by Gribov et. al.,[1] and by Jacobson[2] discuss optical coating by CVD but their discussion is limited in scope and does not discuss the problems in preparing films suitable for high power laser operation. The relatively high index of refraction for alumina reported by Aboaf[3] (1.59-1.61) and for zirconia (1.94) and hafnia (2.02) as reported by Balog et al.[4] is attractive for preparing highly reflective coatings in a minimum number of deposition steps. The object of this study is to survey the use of CVD to prepare high index thin films and examine the preparative details with regard to optical performance and laser damage thresholds and morphology. For initial studies, only single layers prepared by thermal and chemical decomposition methods are examined.

2. Experimental

CVD reactions were done in a horizontal silica reactor with a diameter of 140 mm at the substrate. The reactor is shown schematically in Fig. 1. Argon was used as the carrier gas. The substrates were held in a solid gold retainer fitting into an internally heated, gold plated, copper substrate holder in a cold wall deposition arrangement. Actual surface temperatures were calibrated under operating conditions by a thermocouple. Liquid reagents were admitted via bubblers held at 28°C. The reactor outlet and assembly area was contained in an Integrated Air Systems clean bench.

Aluminum tert-butoxide (ATB) was prepared by an exchange reaction between aluminum isopropoxide and tert-butanol in benzene. The aluminum isopropoxide was prepared by reacting aluminum metal wire with isopropanol using a small amount of iodine as a catalyst. Zirconium tert-butoxide (ZTB) was prepared by synthesizing zirconium diethylamide and reacting with tert-butanol. Hafnium tert-butoxide was prepared in an analogous manner. The substrates used for this study were optically polished, fused silica. They were cleaned in hot sulfuric acid with ammonium persulfate for 15 minutes, then rinsed in distilled water and ethanol and finally drag wiped with an ethanol soaked lens tissue.

---

*Work performed under the auspices of the U.S. Department of Energy by the Lawrence Livermore National Laboratory under contract number W-7405-ENG-48.

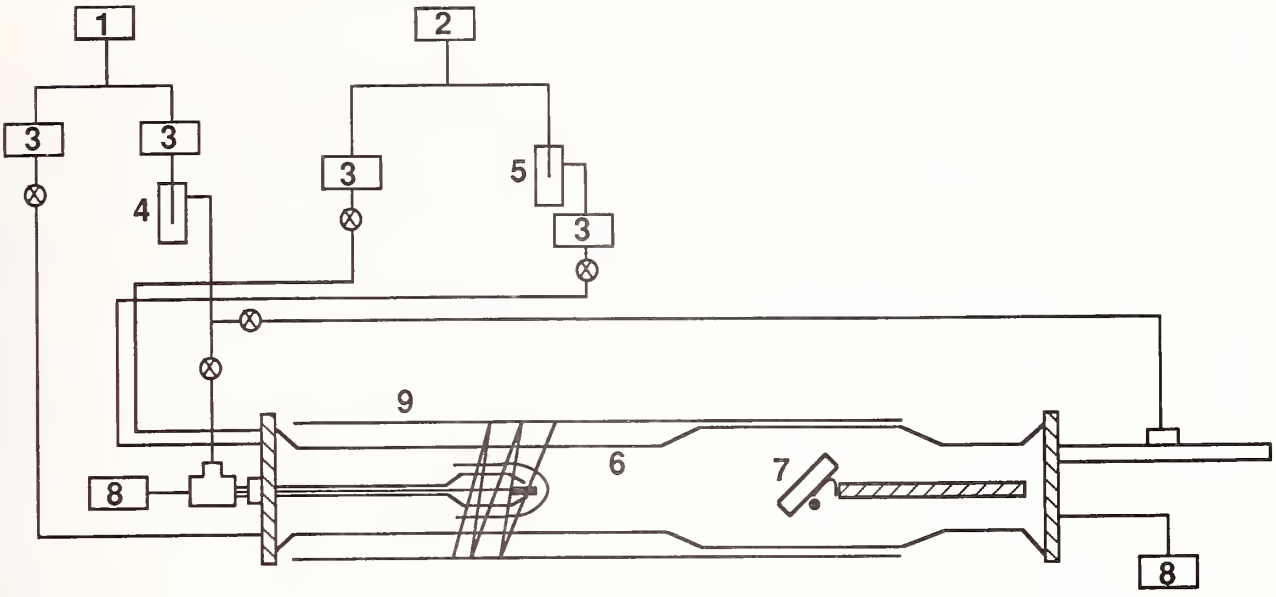

1) Argon
2) Oxygen
3) Brooks mass flow controllers
4) Liquid alkoxide bubbler
5) Tert-butanol bubbler
6) Silica reactor tube
7) Internally heated gold retainer
8) Pressure and temperature controls
9) External heater

Figure 1. Schematic diagram of MOCVD reactor.

The reaction conditions used for all film depositions are listed in Table 1. The reactions fell into three basic types: simple thermal decomposition at high temperature (400°C), simple thermal decomposition at low temperature (250°C) and chemically assisted deposition (CAD) at low temperature (250°C with tert-butanol added to the reaction gas).

Table 1.

Carrier gas flow	100 sccm
Source gas flow	100 sccm
Reactor pressure	500 mTorr
Deposition angle	45°
Substrate surface temperature	400°C (High temp.)
	250°C (Low temp.)

The indices of refraction were calculated from optical spectra using transmission minima at or near 400 nm using equation 1. The transmission was corrected for reflectance of the substrate rear surface.

$$n = n_s \left(\frac{1 + (T)^{1/2}}{1 - (T)^{1/2}} \right)^{1/2} \qquad (1)$$

3. Results and Discussion

Table 2 compares the indices of refraction determined in this study with index values reported in the literature for other CVD films. It can be seen that our values at 400°C are similar to those of other workers with the differences attributable to differences in starting materials, methods and temperatures. Scanning Electron Microscope examinations of the high temperature films reveal a smooth, low contrast film surface without pits or cracks to 0.2 micron resolution, indicating a nonporous coating which is consistent with the index of refraction data. The X-ray diffraction data shows the alumina films to be amorphous while the zirconia and hafnia display a crystalline phase. The X-ray diffraction data are given in Table 3 along with a comparison of values in the JCPDS[6] file. The observable zirconia phase is cubic while the hafnia pattern consists of a weakly crystalline monoclinic phase.

Table 2.

Material	n	Reference
Al_2O_3	1.60	3
	1.63	this work (400°C)
	1.50	this work (250°C)
ZrO_2	1.94	4
	2.05	5
	1.89	this work (400°C)
	1.72	this work (250°C)
HfO_2	2.02	4
	1.87	this work (400°C)
	1.64	this work (250°C)

Table 3.

d_{obs}	d_{JCPDS}	Index	Notes
2.930	2.93	111	Zirconia film prepared at
2.545	2.55	200	400°C - JCPDS data taken
1.797	1.801	220	card no. 27-997
1.535	1.534	311	
3.18	3.15	11I	Hafnia film prepared at 400°C
2.84	2.82	111	JCPDS data taken from card
2.58	2.59	002,020	6-0318
1.80	1.807	220	

Figure 2 shows a typical UV-VIS transmission spectrum for an alumina film prepared at 400°C. The film curve exhibits the familiar interference pattern associated with a film whose index is greater than that of the substrate. The curve maxima do not coincide with the blank substrate curve with the transmission loss becoming more pronounced at shorter wavelength. This result indicates that there is some loss of transmission which could be due to absorbing centers or a graded index in the film. It is not possible to determine the cause of the displacement simply from the optical transmission spectrum. This curve is representative in its general features of all materials in this study.

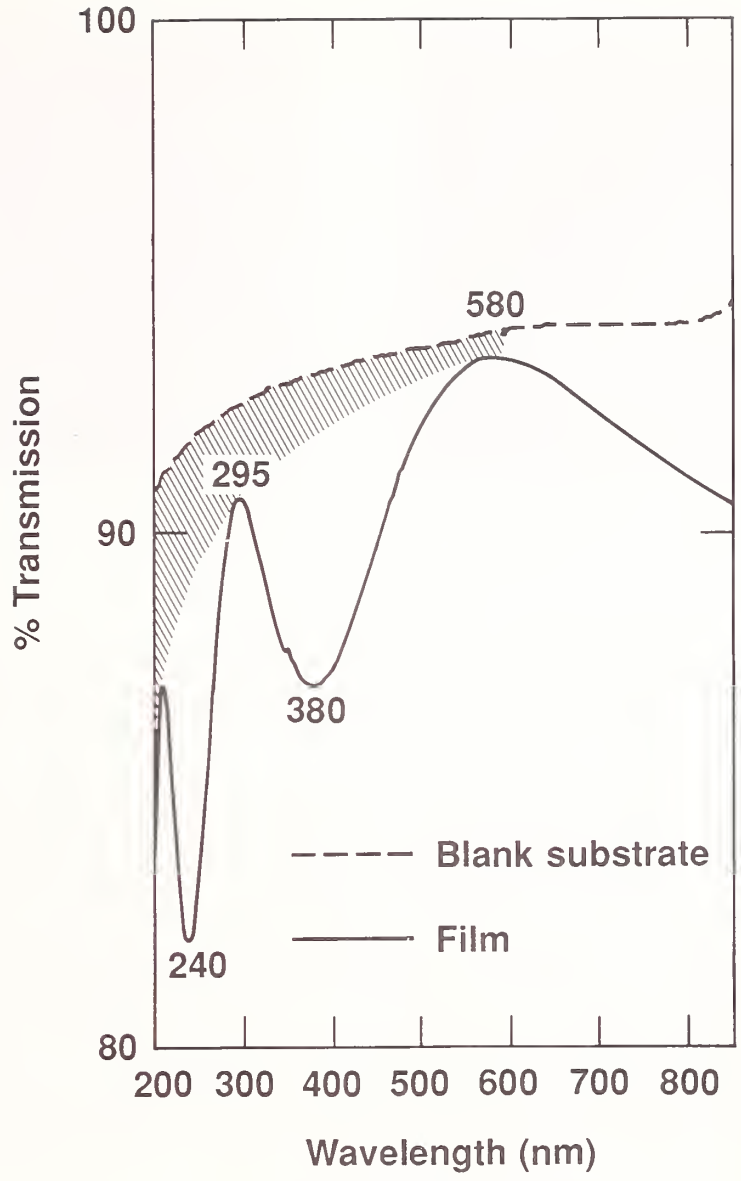

Figure 2. UV-VIS transmission spectrum of alumina film prepared at 400°C.

The laser damage data is shown in Table 4. The damage thresholds tend to be much lower than that for materials prepared by, for example, sol-gel method. The damage figures are insensitive to the thickness of the film and such deposition conditions as flow rate, presence or absence of additional oxygen during deposition, deposition rate, or post-deposition treatments consisting of air annealing in a furnace and treatments with (H_2O_2 or O_3) and UV light. These facts demonstrate the chemical inertness of the damage nucleation site. Figure 3 shows that damage begins at a multitude of sites which rapidly increase in size as the fluence increases. The transmission loss in the UV-VIS spectrum is considered to be a major contributor to the low damage thresholds.

Table 4.
Single Shot Laser Damage Threshold (400°C Deposition)

Material	Threshold (J/cm^{-2}) ± 10%
Alumina	4.0
Zirconia	7.0
Hafnia	10.0

Single Shot Test, 1-on-1, 1060 nm, 10 ns duration

(a) (b)

Figure 3. Appearance of laser damage under 100X optical microscopy. Single shot, 1.06 micron, 10 ns pulse duration, 1-on-1 measurement. (a) Before irradiation; (b) After irradiation.

Figure 4 shows an alumina film prepared at 250°C using the Chemical Assisted Deposition method. The displacement of the transmission maxima from the bare substrate curve is considerably reduced. This is a general result for all films prepared at lower temperatures. The X-ray diffraction data show all films to be amorphous. The damage thresholds are given in Fig. 5. It is seen that, for each material, the threshold obtained by the CAD method is improved over those films deposited at higher temperature. The effect of simply lowering the deposition temperature without adding t-butanol gave damage results intermediate between high temperature and CAD films. There is a dependence of the damage threshold on the thickness of the films which was not seen at higher deposition temperatures. Alumina and hafnia damage levels decrease with increasing thickness while the zirconia shows a slight tendency to increase with increasing thickness. Figure 6 shows the damage morphology of these films has changed to a few small damage sites which do not grow to a significant degree well above the threshold fluence. The index of refraction of films prepared at low temperature is always reduced. It is not clear whether this lowered index in the zirconia and hafnia films is due to amorphization or increased porosity.

While deposition at 250°C generally improved the optical spectra and the damage threshold, greatest improvement was seen when additional tert-butanol was admitted to the reaction zone (CAD method). The tert-butanol dehydrates into water and isobutylene upon encountering the hot substrate surface according to Reaction 2.

$$H_3C - \underset{\displaystyle CH_3}{\overset{\displaystyle CH_3}{\overset{|}{\underset{|}{C}}}} - OH \xrightarrow{\Delta} H_2O + H_3C-\overset{\displaystyle CH_2}{\overset{||}{C}}-CH_3 \qquad (2)$$

The water formed at the substrate surface assists in the decomposition of the source material. The consistently higher performance of the films prepared by CAD methods implies that the deposition chemistry plays an important role in improving optical and damage performance. Additional research is needed to determine what physical and compositional changes in the film were made with the CAD method so that further improvements can be made.

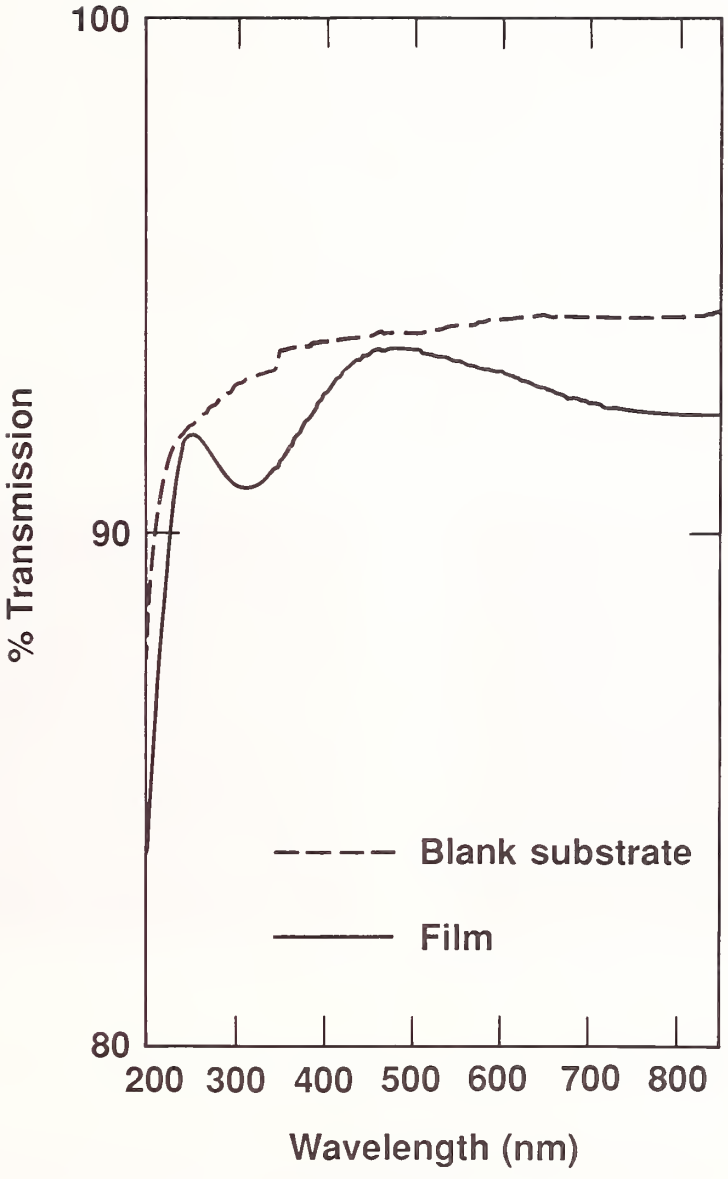

Figure 4. UV-VIS transmission spectrum of alumina film prepared at 250°C using Chemical Assisted Deposition method.

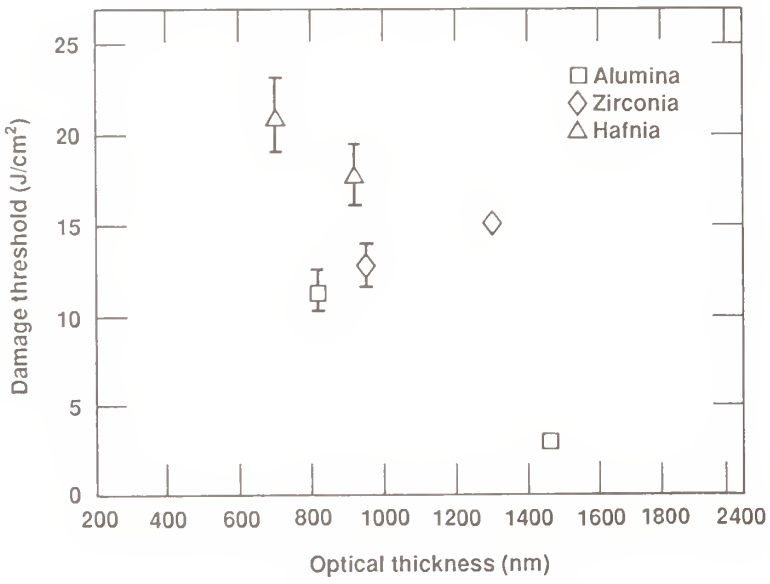

Figure 5. Laser damage threshold as a function of film thickness. Films prepared using Chemical Assisted Deposition method.

(a) (b)

Figure 6. Appearance of laser damage under 100X optical microscopy. Single shot, 1.06 micron, 10 ns pulse duration, 1-on-1 measurement. (a) Before irradiation; (b) After irradiation.

4. References

[1] Gribov, B. G.; Baranenkov, I. V.; Petrov, V. N.; Koshchienko, A. K.; Kozyrkin, B. I., Sov. J. Opt. Technol, 53(5), 296, 1986.

[2] Jacobson, M. R., SPIE Opt. Thin Films, 325, 123, 1982.

[3] Aboaf, J. A., J. Electrochem. Soc., 114(9), 945, 1967.

[4] Balog, M.; Schieber, M.; Patai, S.; Michman, M., J. Cryst. Growth, 17, 298, 1972.

[5] Balog, M.; Schieber, M.; Michman, M.; Patai, S., Thin Solid Films, 47, 109, 1977.

- MANUSCRIPT NOT RECEIVED -

DEPOSITION WITH ULTRA-FINE PARTICLES

Arthur C. Day
Photon Sciences, Inc.
Bothell, WA 98011

ABSTRACT

A study has been initiated into the possible uses of deposition with ultra-fine particles and/or clusters. The starting point was the Ionized Cluster Beam technique reported by Takagi et. al. Experimental studies in this laboratory strongly suggest that clusters cannot, in general, be formed in an adiabatic expansion of a pure metal vapor as had been claimed, although other mechanisms cannot be ruled out. Numerical simulations have also been carried out which support our conclusion.

However, it is well known that small particles or clusters can be condensed in a low pressure quenching gas. Work is now being directed toward exploiting these particles to produce materials composed of nanometer-sized "splats" somewhat analogous to those in plasma spray coatings. It is hoped this radical departure from the usual columnar structures of deposited materials can lead to improved damage thresholds in many types of optical coatings. The feasibility of this new approach will be discussed along with its potential merits.

Manuscript Received
3-23-88

CLUSTER BEAM DEPOSITION FOR OPTICAL THIN FILMS

E.M. Waddell and B.C. Monachan
Pilkington Defence Systems
Barr & Stroud
Caxton Street, Anniesland
Glasgow, G13 1HZ, Scotland

and

K.L. Lewis, T. Wyatt-Davies and A.M. Pitt
Royal Signals and Radar Establishment
St. Andrews Road, Malvern
Worcs. WR14 3PS England.

ABSTRACT

A study has been carried out of the deposition of films of barium fluoride using cluster beam techniques. The effect of different aspects of the deposition process has been assessed including deposition temperature, cluster source geometry and acceleration voltage. X-ray measurements suggest that a transition temperature exists between 200 and 300°C above which dense oriented films of excellent crystallinity are produced. At lower temperatures the films are of a different orientation, are less than theoretical density and are optically inhomogeneous. However an enhancement of laser damage threshold at 1.06μm has been observed for films produced at 200°C. The transition temperature itself can be influenced by cluster source geometry and acceleration voltage used during deposition. The films have been used for anti-reflection of ZnSe substrates and, under optimum conditions, have laser damage thresholds at 10.6μm significantly in excess of the uncoated substrate material.

INTRODUCTION

The technique of ionised cluster beam deposition (ICB) has been suggested as having some potential for improving the microstructure of thin films. Publications by Takagi et. al., (1) indicate that significant effects can be produced on adatom migration, nucleation density, sticking coefficient and enhancement of chemical reactivity. These are the fundamental factors likely to influence the optical and physical properties of the growing film and the ICB technique therefore has some potential for improvement over conventional deposition techniques. A good example for comparison of different deposition techniques is afforded by the case of the growth of TiO_2. For example, in a study of TiO_2 deposition from a reactive ionised cluster beam, Fukushima et al., (2) were able to prepare stoichiometric films at 350°C at oxygen partial pressures of $1\text{-}2\times10^{-4}$ mbar and, by increasing ionisation current from 0 to 400mA, could increase refractive indices at 0.6μm from, 2.0 to 2.6. The position of the fundamental absorption edge was also affected by varying the cluster accelerating voltage with resulting energy gaps in excess of 3.55eV. In comparison, amorphous sputtered films would give values in the range 3.2 to 3.5eV. Changes in the ionisation current and acceleration voltage also influence the relative concentrations of anatase and rutile phases in the film. In general, increase in ionisation current favoured the formation of rutile phase deposits whilst use of high acceleration voltages (>5kV) favoured the anatase phase. In comparison, when TiO_2 films are produced by ion-assisted deposition (IAD), refractive indices are lower, typically 2.45 at 0.6μm (3). Furthermore, significant levels of optical absorption due to the presence of oxygen vacancies are introduced by argon ion bombardment although these can be reduced considerably by using oxygen ion bombardment at energies of the order of 300eV. For IAD, both ion energy and flux are important factors in determining film properties (4).

It is thus appropriate to explore the application of ICB deposition for optical thin films with particular reference to coatings for high energy lasers. This paper will be concerned with an assessment of film growth using cluster beam sources with particular reference to barium fluoride. This is a material of considerable interest for application over a wide range of wavelengths, but by conventional techniques, requires high deposition temperatures to ensure stable dense films. A comparison is made with films deposited under conventional conditions.

EXPERIMENTAL

The essential requisites for ICB deposition are a cluster source, an electron source capable of ionising the cluster beam by impact ionisation and a means of applying a potential to accelerate the resulting ionised clusters towards the substrate. The cluster source used in this work consists of a carbon crucible with an orifice through which the evaporating material streams. Unlike a Knudsen cell, the cluster source operates in a regime where significant adiabatic cooling

of the vapour stream occurs, sufficient to form atomic or molecular aggregates. Takagi (5) have shown, using time of flight techniques, that in the case of tellurium, cluster sizes range from 500 to 1500 atoms with the distribution of high mass clusters dependent on source temperature.

In this work, the technique has been realised in a Balzers box coater by using a resistively heated cluster source and effecting ionisation of the ensuing cluster beam by impact ionisation from an incident electron beam. Acceleration voltages were applied using a metallic grid structure. The films were deposited under conditions of conventional high vacuum at pressures of typically 1×10^{-6}mbar. Conventional films were deposited in the same equipment by replacing the source with a conventional boat.

The microstructure of the films was assessed by X-ray diffraction using Cu Kα radiation (λ = 1.542Å). However, since the penetration depth of such X-rays in barium fluoride is small, the assessment only gives an indication of the structure near the surface of the film. By using Mo Kα radiation (λ = 0.711Å) it was possible to explore the distribution of diffraction lines throughout the whole thickness of the film.

The degree of surface roughness was measured using a modified Aphastep profilometer (Tencor Instruments) and correlated with integrated optical scatter values determined by a spectroscopic technique using an integrating sphere attachment to a Perkin-Elmer Lamda 9 spectrophotometer. Laser induced damage thresholds were determined at 10.6µm using a previously described facility (6) based on a TEA laser and at 1.064µm using a facility which produces a well characterised pulse from a Quantel YG481A Nd:YAG laser.

ORIENTATION OF BARIUM FLUORIDE FILMS

Significant differences were found in the microstructures of the ICB films at different growth temperatures. At room temperature (using Cu Kα radiation), the films produced by conventional evaporation showed a distribution of diffracted intensities characteristic of randomly oriented polycrystalline deposits, as shown by the intensity values in Table 1. Replacement of the conventional source with the cluster source produced a change in film orientation with an enhancement of the (220) reflection. This enhancement was more apparent at higher acceleration voltages.

In films produced at 200°C, the diffracted intensities of the conventionally deposited films were very weak, suggesting a more amorphous structure. The change to a cluster source produced an immediate increase in (422) orientation of the film. This characteristic was more pronounced at higher acceleration voltages. In films grown at an acceleration voltage of -2kV, the (111) reflection was almost absent when the film was examined using Cu Kα X-rays (λ = 1.542Å). However when examined using Mo Kα radiation (Table 2) it was found that the (111) diffraction line was now present indicating the initial growth of the film occurred at (111) orientation, changing to (422) at an intermediate position within the film. Such transient phenomena have also been found in barium fluoride films deposited by molecular beam techniques, although in this case, initial growth was of a more amorphous character (7).

A 300°C, the crystallinity of the ICB films is greatly increased as shown by the higher intensity of the diffraction lines (Table 1). The film grown from a conventional source shows (111) preferred orientation, but this changes to (200) when the ionised cluster source is used.

TABLE 1 X-RAY DIFFRACTION RELATIVE INTENSITIES PRODUCED BY BARIUM FLUORIDE FILMS UNDER DIFFERENT GROWTH CONDITIONS.

			REFLECTIONS								
Sample	temp	-kv	111	200	220	311	222	400	331	420	422
591	60	C	184	155	73	56	0	27	5	2	9
576	60	0	28	61	182	68	0	12	6	6	6
577	60	1	46	10	448	68	0	0	10	11	8
578	60	2	12	13	420	67	0	0	8	15	4
579	60	3	99	32	239	107	0	5	9	15	4
581	60	5	19	132	532	100	0	24	12	8	8
592	200	C	13	0	18	29	0	12	6	13	11
584	200	0	34	0	3	53	0	0	0	9	70
585	200	1	33	0	0	41	0	0	0	0	81
586	200	2	8	0	0	34	0	0	0	0	101
589	200	5	29	0	3	43	0	0	0	0	74
618	300	C	300	129	58	65	12	24	10	6	18
614	300	2	300	1300	30	30	10	220	-	-	-

C denotes conventional deposition

TABLES 2 X-RAY DIFFRACTION INTENSITIES FOR Mo RADIATION REFLECTIONS

Sample	temp	-kV	111	200	220	311	222	400	422
591	60	C	52	54	27	24	0	15	0
577	60	1	12	6	138	27	0	0	0
585	200	1	43	0	0	26	0	0	41
586	200	2	48	0	0	20	0	0	35
614	300	2	29	168	6	7	0	48	0

The largest change in film orientation was usually produced when the conventional source was replaced by the cluster source. The effect of acceleration voltage was merely to accentuate the tendency for any particular orientation already produced by the cluster beam.

OPTICAL SCATTER MEASUREMENTS

The degree of back-scatter produced by the films was measured using the integrating sphere technique as a function of wavelength between 300 and 700nm. A preliminary study of the glass substrates used for these experiments showed that the background scatter levels are low (0.8%) at wavelengths of 300nm or greater, but that the magnitude of the scatter increased considerably below 300nm, reaching values of about 13% at 200nm. Since this was a substrate related effect, it was decided to carry out scatter measurements on the deposited barium fluoride films at 312.5nm (32000cm^{-1}). Values for λ /4 (λ=10.6μm) thicknesses are listed in Table 3. This wavelength was selected since it was well away from the absorption edge of the different substrates used.

TABLE 3 BACK SCATTER VALUES FOR BARIUM FLUORIDE FILMS DEPOSITED BY CONVENTIONAL AND IONISED CLUSTER BEAM DEPOSITION, = 312.5nm

Sample	temp	kV	% Scatter at 312.5nm
591	60	C	3.5
576	60	0	1.4
577	60	1	3.0
578	60	2	3.6
579	60	3	3.8
580	60	4	4.1
581	60	5	3.9
592	200	C	6.4
584	200	0	3.4
585	200	1	3.3
586	200	2	2.6
587	200	3	4.1
588	200	4	3.9
589	200	5	4.5
642	250	C	3.7
637	250	0	2.0
638	250	1	0.8
639	250	2	0.7
618	300	C	1.1
613	300	0	0.5
615	300	1	0.4
614	300	2	0.6

For conventionally deposited films, scatter values are dependent on the deposition temperatures, with films deposited at 300°C being indistinguishable from uncoated substrates. However, it can also be seen from the table that the most significant change in the optical scatter value at each growth temperature is brought about by the use of the cluster source. The acceleration voltage has some effect, but is negligible in comparision except at 250°C. The correlation between scatter and surface roughness was explored using the set of λ/4 (λ = 10.6μm) BaF_2 films produced at 200°C. The results are shown in figure 1 and highlight the variation in crystallite size at the different deposition conditions.

OPTICAL PROPERTIES OF ICB BARIUM FLUORIDE FILMS

Measurements of optical transmission and reflection of the films on various substrates were carried out using integrating sphere techniques and so include contributions from scattered light. The reflectivity spectra of all λ /4 (λ = 10.6μm) films produced at 300°C suggest that

they are dense and relatively well behaved, with maxima of 8.1% and minima of 6.8% as shown in figure 2. However, films produced at lower temperatures have generally lower reflectivities, with minima in the case of 200°C films of about 6% and maxima of 7%. A small amount of absorption is present in these films, sufficient to give a 1% to 3% drop in transmission, but this is insufficient to produce any change in reflectivity. It is suggested that non uniformity in film density throughout the thickness of these films is giving rise to a grading of refractive index. This would explain the low reflectivity and the low peak to peak modulation in reflectivity, and would be in accordance with the X-ray diffraction results. By assuming that the graded index structure can be approximated by a series of individual discrete layers, each 1/16th of the thickness of the whole film, it has been possible to assign values to the refractive indices of each of these 16 sublayers on the basis of an iterative computer algorithm to produce the best fit of the measured reflectivity data. Dispersion of refractive index was assumed in the form.

$$n_\lambda = n + 3.835\times10^8/\lambda^4 \quad (\lambda \text{ in nm}).$$

The estimated index profile for such a film is shown in figure 3. In order to check the accuracy of this estimate, separate films were deposited with thicknesses of $\lambda/40$, $2.2\,\lambda/40$ and $3.3\,\lambda/40$ at λ 10.6μm. The calculated index profiles for each of these films is plotted in figure 4 and compared with the initial part of the data for the $\lambda/4$ case. Agreement is good, suggesting that our technique for extracting the refractive index profile is valid. It is notable that the results for all four films suggest that the films are uniformly dense for $\lambda/40$ at 10.6μm or $\lambda/4$ at 1.06μm.

Clearly, on the basis of the reflectivity measurements, a transition temperature occurs between deposition temperatures of 200°C and 300°C. At temperatures above a critical value, the film grows with (100) orientation and is dense, whilst at lower temperatures the films are primarily of (422) orientation and are graded with the majority of the film being of less than theoretical density. This may be a consequence of a dendritic microstructure of the type previously found for low temperature polycrystalline films produced by MBE (7). We have determined that the transition temperature can be influenced by varying the diameter of the orifice of the cluster source. For conventional sources, the critical temperature is between 260 and 270°C. This can be reduced to 240°C by using a 1mm orifice, and to 220°C with a 0.5mm diameter orifice.

LASER DAMAGE EXPERIMENTS AT 1.06μm

The laser induced damage thresholds (LIDT) of a series of optically thick BaF_2 ($10\,\lambda/4$) films on BK7 glass were determined at 1.06μm using a 15ns FWHM pulse width laser. The results are summarised in figure 5 and show a surprising dependence on the ICB growth conditions. At all temperatures, the LIDT values of conventionally deposited films were low, with films produced at 300°C being marginally better than those produced at room temperature. However, when a cluster source is used, significant differences are found for the different deposition temperatures, with an enhancement of LIDT by a factor of up to 3 for films deposited at 200°C. Variation of acceleration voltage also has an effect at this temperature, largely however to reduce the LIDT at high acceleration voltage.

The LIDT values of thin ($\lambda/4$) films of BaF_2 on glass are considerably higher, and for 200°C films, approach the LIDT of the uncoated substrate (55-65J/cm²). The variation with film thickness is shown for the selected cases of 200°C, and 300°C with zero acceleration voltage, in Table 4.

TABLE 4 VARIATION OF 1.06μm LIDT WITH FILM THICKNESS FOR ICB BaF_2 FILM

Optical thickness in units of $\lambda/4$	LIDT (J/cm²)	
1	39.3	18.4
2.4	24.1	-
3.6	18.4	-
10	13.8	9.3
Deposition temperature	200°C	300°C

Although the thick films ($10\,\lambda/4$ @ 1.06μm) deposited at 200°C are not dense throughout their thickness, they do appear to have a dense layer next to the substrate as do the thinner films deposited at this temperature. The LIDT measurements therefore suggest that a dense layer next to the substrate is functional in producing high laser induced damage thresholds.

LASER DAMAGE EXPERIMENTS AT 10.6μm

For LIDT experiments at 10.6μm, BaF_2 films were deposited on ZnSe substrates. LIDT values are given in Table 5 and clearly show the advantages afforded when compared with conventional films.

TABLE 5 LASER DAMAGE THRESHOLDS AT 10.6μm

Film/Substrate	Deposition Temperature deg C°	Acceleration Voltage kV	LIDT/Jcm^{-2}
U/C ZnSe	-	-	63.9 - 78.8
BaF_2/ZnSe	250	conventional	60.5 - 61.6
	300	conventional	68.2 - 74.8
BaF_2/ZnSe	250	0	85.8 - 86.9
	300	0	107 - 113

Barium fluoride is a good refractive index match for ZnSe and can be considered as a good practical example of a single layer anti-reflection coating. Conventionally deposited films have a lower damage threshold than the substrate, even when deposited at 300°C. In comparison, films deposited from a cluster source, even with zero acceleration voltage, show significant improvement with values at 300°C very similar to values for polycrystalline MBE deposited films previously found by Lewis et.al.,(7). Some of the enhancement is achieved as a result of the production of theoretically dense films, which do not absorb atmospheric moisture as shown in figure 6. These films also show strong X-ray diffraction lines, indicative of a high degree of crystalline order, and would be expected to have thermophysical properties more like those of bulk material.

ACKNOWLEDGEMENTS

The authors would like to express their appreciation of the assistance given by many of their colleagues and of the Management of Barr & Stroud for permission to publish this paper.

REFERENCES

1. T. Takagi: J. Vac. Sci. Technol., A2 (2), 382 (1984).
2. K. Fukushima, I. Yamada and T. Takagi: J. Appl. Phys. 58 (11) 4146 (1985).
3. T.H. Allen: Proc. Int. Ion Eng. Congress - ISIAT 83 and IPAT 83 1305 (1983).
4. J.R. McNeil, G.A. Al-Jumaily, K.C. Jungling and A.C. Barron: Applied Optics 24 486 (1985).
5. T. Takagi, Proc. 5th Int. Conference Ion and Plasma Assisted Techniques IPAT 85 52 (1985).
6. D.R. Gibson and A.D. Wilson: Proc. 1984 Boulder Damage Symposium, NBS Spec. Publication 727 100 (1986)
7. K.L. Lewis, A.M. Pitt, N.G. Chew, A.G. Cullis, T.J. Wyatt-Davies, L. Charlwood, O.D. Dosser and I.T. Muirhead: Proc., 1986 Boulder Damage Symposium (to be published).

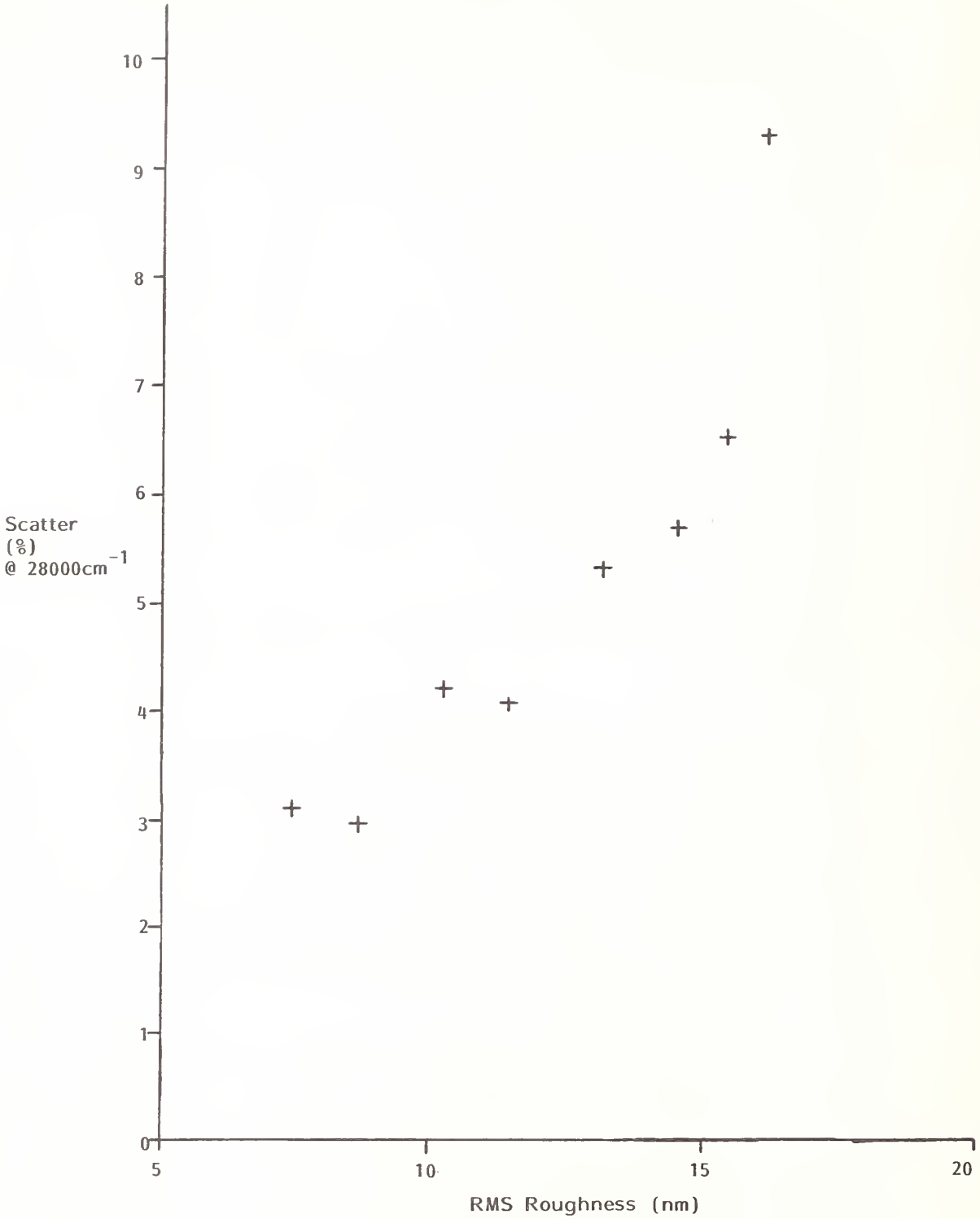

The measured total back scatter at 28000cm^{-1} vs RMS roughness of optically thick BaF_2 films on glass.

Film thickness 10 $\lambda/4$, λ= 1.06μm

Deposition by conventional and ICB techniques.

FIGURE 1

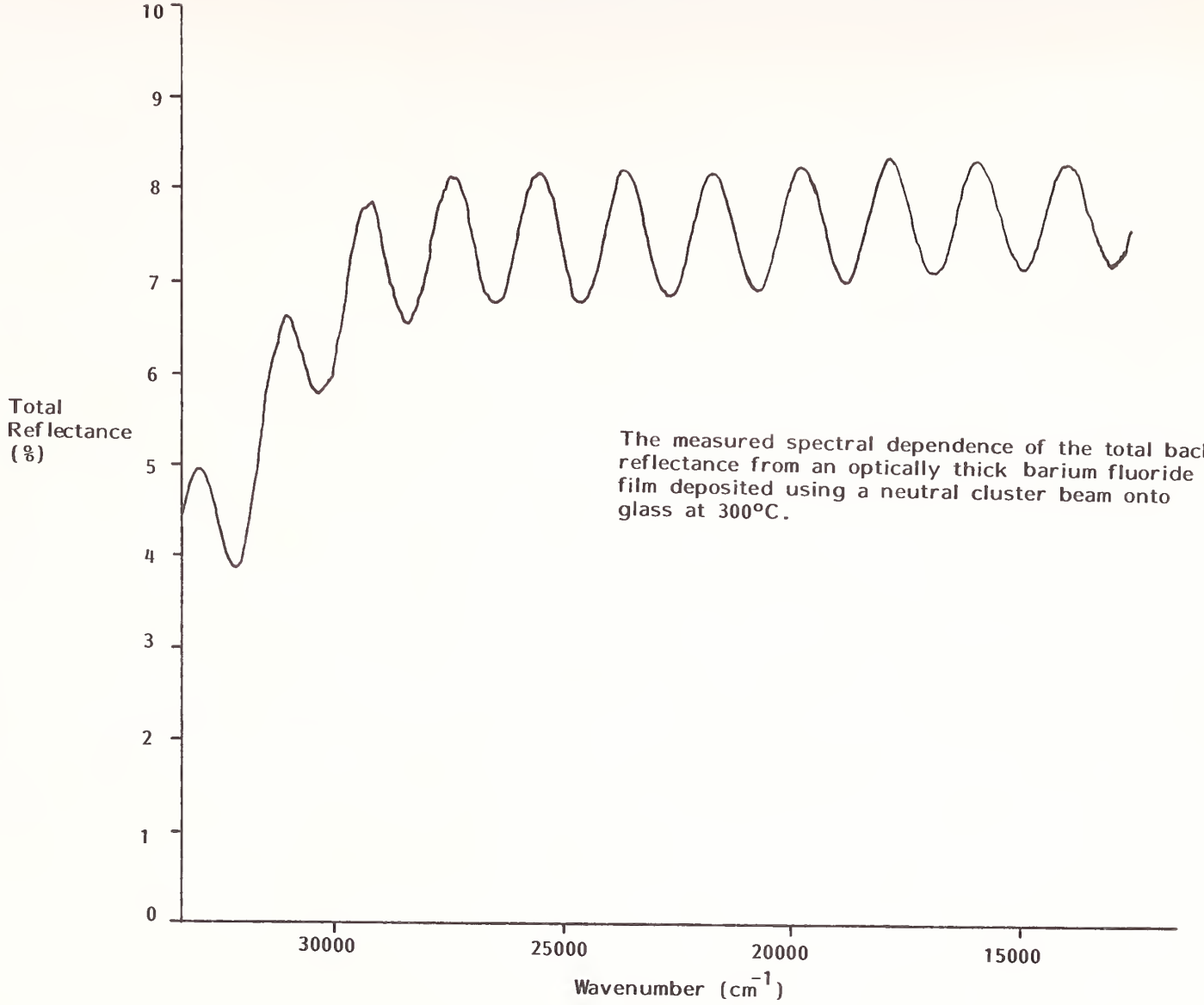

FIGURE 2

The measured spectral dependence of the total back reflectance from an optically thick barium fluoride film deposited using a neutral cluster beam onto glass at 300°C.

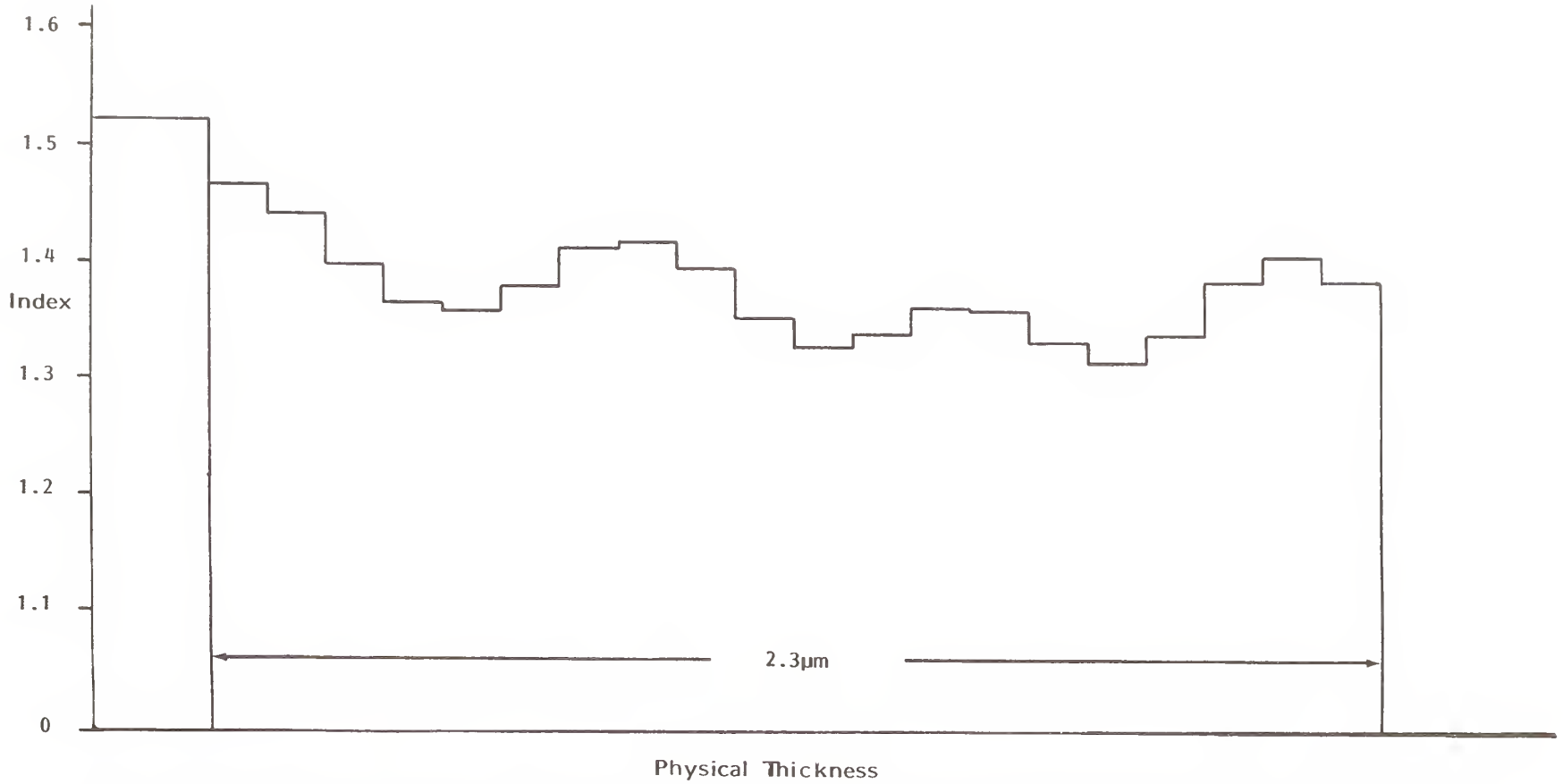

The calculated refractive index profile computed to match th measured total back reflectance from an optically thick barium fluoride film deposited on glass at 200°C by a neutral cluster beam.
Dispersion is assumed to be of the form $n_\lambda = n + 3.835 \times 10^8/\lambda^4$ (λ in nm)

FIGURE 3

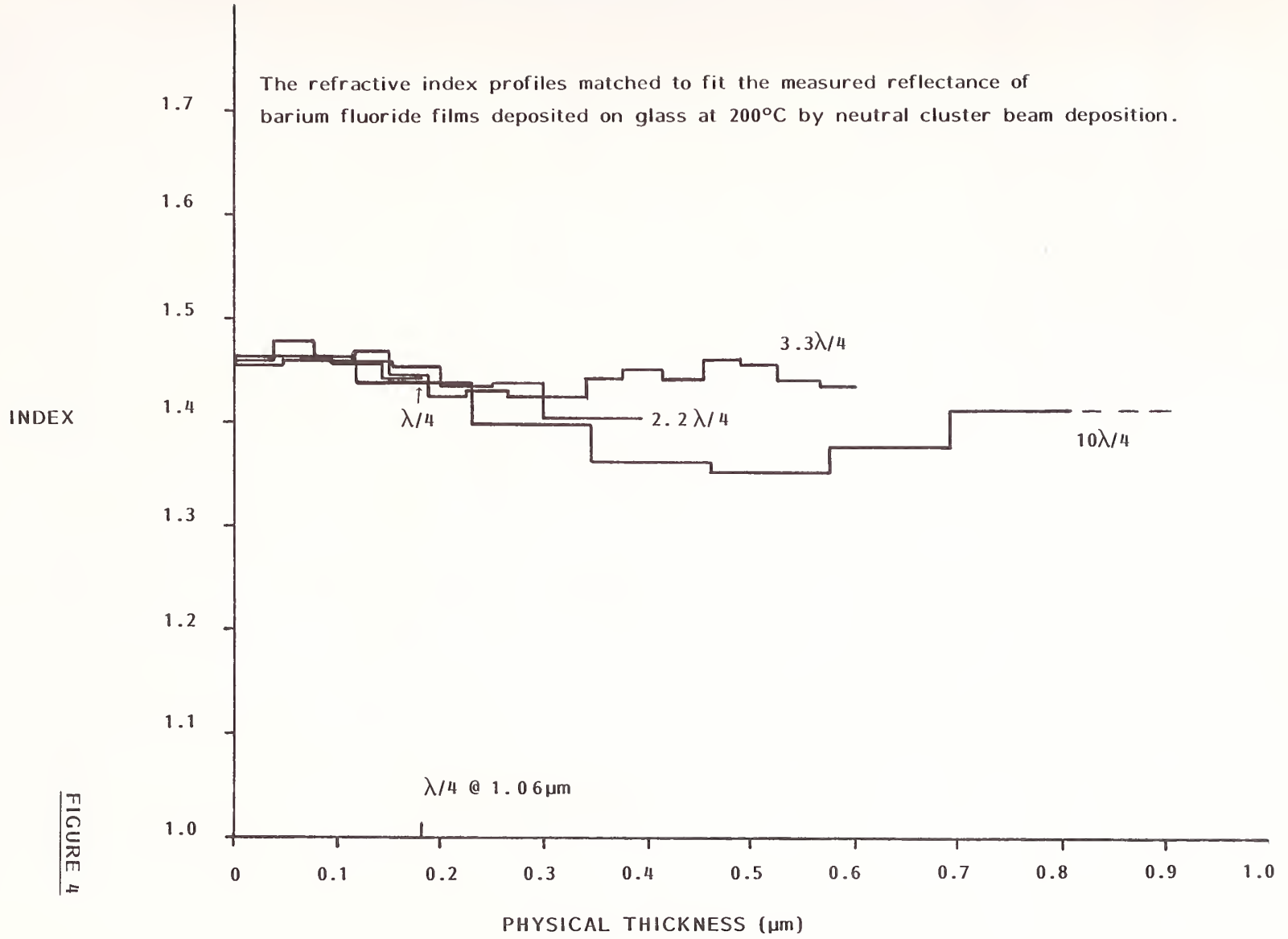
The refractive index profiles matched to fit the measured reflectance of
barium fluoride films deposited on glass at 200°C by neutral cluster beam deposition.
INDEX
1.7
1.6
1.5
1.4
1.3
1.2
1.1
1.0
3.3λ/4
λ/4
2.2λ/4
10λ/4
λ/4 @ 1.06μm
0
0.1
0.2
0.3
0.4
0.5
0.6
0.7
0.8
0.9
1.0
PHYSICAL THICKNESS (μm)

FIGURE 4

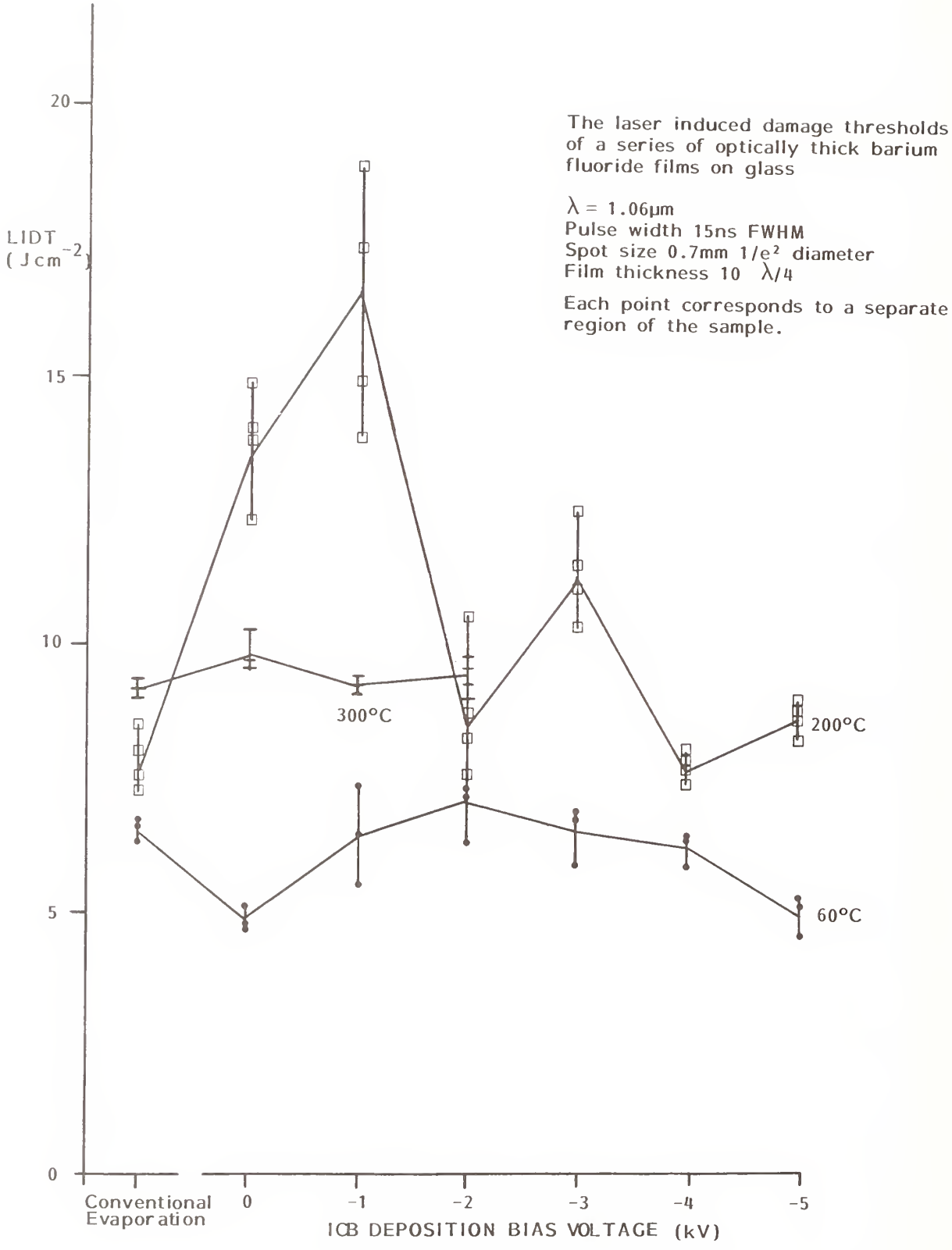
The laser induced damage thresholds of a series of optically thick barium fluoride films on glass
λ = 1.06μm
Pulse width 15ns FWHM
Spot size 0.7mm 1/e² diameter
Film thickness 10 λ/4
Each point corresponds to a separate region of the sample.
LIDT (Jcm⁻²)
20
15
10
5
0
300°C
200°C
60°C
Conventional Evaporation
0
-1
-2
-3
-4
-5
ICB DEPOSITION BIAS VOLTAGE (kV)

FIGURE 5

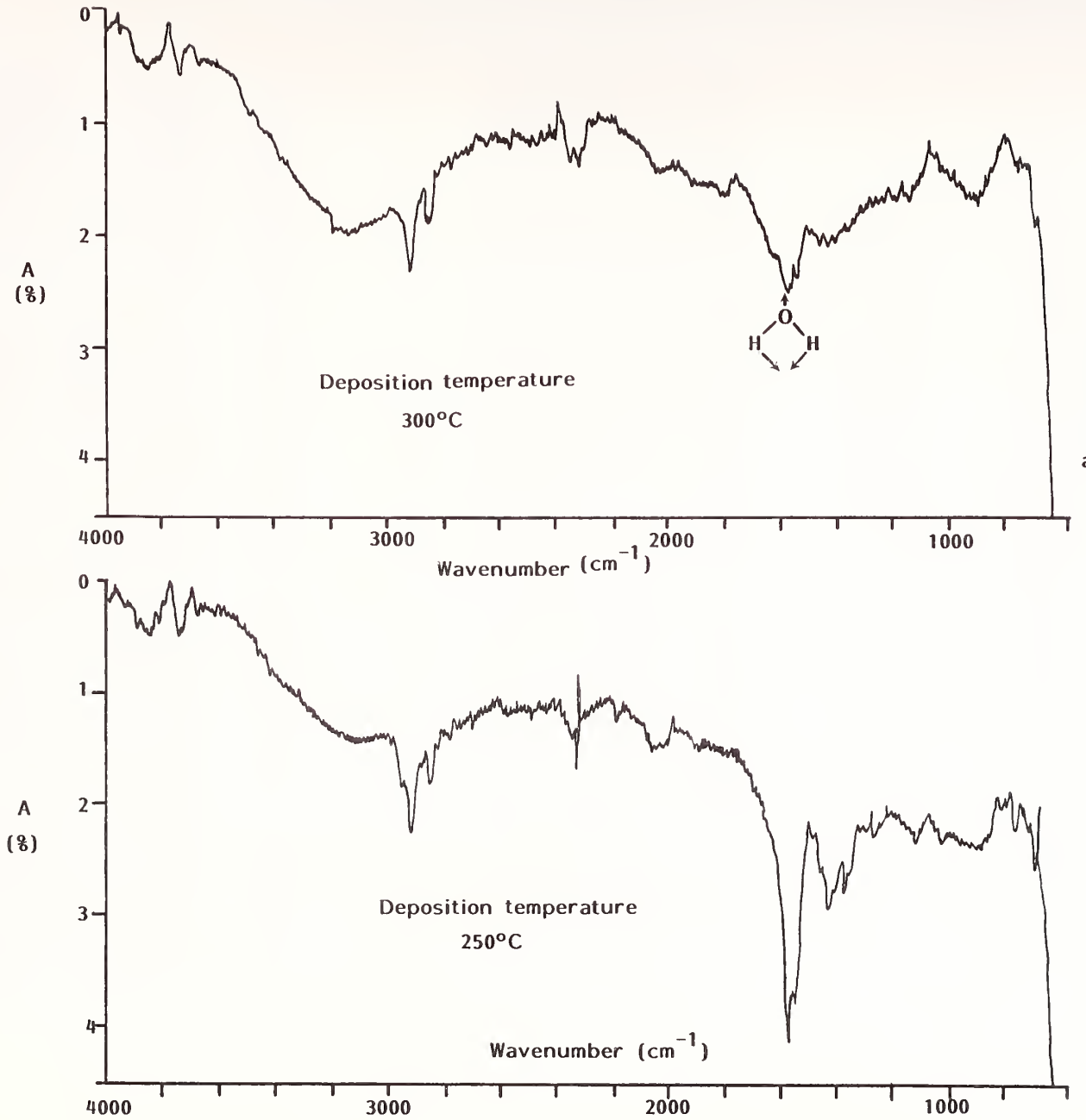

The measured absorption (A = I-T-R) for two films deposited by neutral cluster beam deposition from a 0.5mm diameter orifice. The one deposited at 300°C shows lower absorption due to water.

FIGURE 6

Manuscript Received
3-2-88

Measurement of HR coatings absorptance at 10.6 microns by Mirage Effect

P.J. BARON
Laboratoires de Marcoussis
91460- Marcoussis-France

A. CULOMA
Etablissement Technique Central de l'Armement
94114 Arcueil- cedex -France

A.C. BOCCARA and D. FOURNIER
Ecole Supérieure de Physique et de Chimie Industrielles
75231 Paris -cedex 05 - France

To get a high optical quality beam from a High Power Laser (HPL), optical distorsions must be minimized. For a CW CO_2 HPL, the key parameter is absorptance. Generally, High Reflective (HR) coated mirrors exhibit absorptance less than one percent. A photothermal measurement method of absorptance (Mirage Effect) seems to be adequate to reach the required resolution. In this paper we present a method of absolute measurement of HR coatings absorptance at 10.6 microns. The measurement key point is calibration. The linearity of the deflection angle versus absorptance predicted by the theory led us to calibrate our experimental set up with a strongly absorbing sample which could be measured by reflection. (scattering neglected). The first step is to verify the signal linearity versus absorbed power and its evolution as a function of chopping frequency in order to neglect convective transfers. Measurements performed on different HR coated mirrors are presented.

Key words: CO_2 lasers; mirage effect; photothermal deflection; reflectors

1. Introduction

The quest for ever better beam quality and the drive to ever higher power levels require high grade coated mirrors. For CW CO_2 High Power Laser, the key parameter is optical absorptance.

Photothermal Deflection Method (Mirage Effect) emerges as an adequate technique for investigating optical coatings absorptance (1). In this paper, we present a technique dedicated to measure the absolute optical absorptance of High Reflective (H.R) coated mirrors used at 10.6 microns. Due to the numerous parameters (geometrical, thermal, optical,...) involved in this method, we have chosen to calibrate our experiment with High Absorbing (H.A) samples.

Measuring the reflection and the deflection signals on the H.R and H.A samples, we can deduce the absolute optical absorptance of the H.R one.In section 2, we present the simplified measurement principle.In section 3, we deal with experimental considerations in order to validate the assumptions made in Sec.2. Some results performed on different H.R coated mirrors are presented.

2. Simplified Principle of the measurement

2.1. 1-D- simplified theory (Fig.1)

When a sample is irradiated with a modulated laser beam (frequency f), its surface will exhibit periodic temperature fluctuations which will in turn induce a modulated reflective index gradient in a layer of gas adjacent to the sample surface. According to Ref 2, neglecting convective transfer, the gas temperature at steady state follows the equation :

$$T(x)= T_{dc}(x)+\Delta T_m \exp\left(-\frac{x}{\mu_g}\right)\exp j\left(\omega t - \frac{x}{\mu_g}\right)$$

with x = distance above the sample surface (m)

$T_{d.c}$ (x) = d.c temperature

w = $2\pi f$

$\mu_i = \frac{2k_i}{\rho_i C_i w}$ = thermal diffusion length of material i at frequency f (m)

ΔT_m = a.c amplitude of the sample surface temperature

k_i = thermal conductivity of material i (w/m.k)

ρ_i = density of material i (kg/m^3)

C_i = Specific heat of material i (J/ kg. K)

In the case of surface absorptance for an optically opaque solid,

one obtain

$$\Delta T_m \cong \frac{a\Phi_0}{2f}\frac{1}{\rho_s C_s \mu_s} = \frac{a\Phi_0}{2\sqrt{f}}\frac{\Pi}{k_s\rho_s C_s}$$

with a = optical absorptance

Φ_o = incident intensity (w/m^2)

The a.c deflection signal can be written

$$\psi_{ac} \cong \frac{\pi}{2}\frac{1}{n}\frac{dn}{dt}\frac{\rho_g C_g}{k_g}\frac{1}{k_s\rho_s C_s} a\phi_0 \exp(-A\sqrt{f}\,x)\cos\left(\omega t - \frac{x}{\mu_g} + \frac{\pi}{4}\right)$$

with l = width of interaction

n = gas refractive index

$$A = \frac{\Pi \rho_g C_g}{k_g}$$

x = distance between the probe beam and the sample surface.

This last equation shows that a.c deflection signal amplitude is proportional to the incident intensity ($\Phi_\circ$), the optical absorptance (a) and depends exponentially on the distance x and the square root of the chopping frequency (f)

2.2. Calibration

This technique consists in doing simultaneous reflection (R) and deflection (S) measurements on a H.R sample. In a second step, we measure the reflection ($R_\circ$) and deflection ($S_\circ$) on a H.A sample positioned in the same experimental configuration.

With the assumption made in Sec.2.1 i.e deflection signal proportional to the absorbed power, these 4 experimental data lead to :

$$a = \frac{(1-\delta)\left(1-\frac{R}{R_0}\right)}{1-\frac{RS_0}{R_0 S}} \cong \frac{1-\frac{R}{R_0}}{1-\frac{RS_0}{R_0 S}}$$

with δ = optical diffusion factor

The validity of this calibration method requires :

- a constant incident power
- a constant chopping frequency
- a accurate repositioning of H.A sample in order to maintain the probe beam and surface sample distance
- identical substrates

The H.A samples are two layers of SiO_2 and Al_2O_3 deposited on the same H.R sample substrate

3. Experimental considerations

3.1. Experimental configuration

Experiments were performed to validate the assumption made in Sec.2.1. The experimental configuration is represented in Fig2 . A CO_2 laser, intensity stabilized by optogalvanic method (S.A.T), provides the pump beam. The typical beam power is 7 Watt, with 3.1 mrad half divergence. A mechanical chopper is used to modulate the beam which is focused with a 6 inches focal length lens . A O.5 mW He-Ne laser is used as the probe beam. The periodic deflection of the He-Ne beam is monitored by a position sensor (UDT spot 9 D) - The S/N ratio of the signal is improved by a lock in Amplifier (EGG). A pyroelectric detector monitores the power of the reflected beam.

3.2. Signal dependance on chopping frequency (Ref 3)

Fig 3 and 4 show the dependance of the Logarithm of the signal versus the square-root of the chopping frequency for different HR and HA samples. We have verified the linearity of these two quantities (correlation factor > 98 %). According to Ref 3, we see a slight bending at low frequencies (< 20 Hz). In our experiment (chopping frequency f = 70 Hz) convective heat transfer can be neglected.

3.3. Signal dependance on incident power

Fig 5 shows the signal dependance on incident power. These measurements have been performed on HA samples. Incident power has been decreased from 1.6 W to 0.1 W. The lower power level corresponds to a H.A sample signal equal to the one obtained on a H.R sample at the higher power level . We have verified the linearity (correlation factor > 99.9 %)

3.4. Signal dependance on optical absorptance

Fig 6 and 7 show the signal dependance on optical absorptance. We have verified the linearity of the deflection signal upon the optical absorptance in the range of 4 ‰ to 90 % (correlation factor > 99.9 %). Optical absorptance of different H.R samples (Table 1) calibrated with different H.A samples are listed in Table 2.

4. Conclusion

The simplified 1-D model used in this preliminary experiment needs further improvements to take into account the thicknesses and thermal properties of the multilayers coatings. A more sophisticated model could bring more informations about the deflection phase signal wich has not been considered in this paper.

This study has been supported by D.R.E.T. .We thank Mr MOUCHART for supplying us the H.A. samples.

References

1. A.C. BOCCARA , D. FOURNIER , W. JACKSON , N.M. AMER ,Optics Letters 5 No9 ,377 (1980)

2. J. BADOZ , D. FOURNIER , A.C. BOCCARA ,J. Optics (Paris),11 No6 ,399 (1980)

3. G. ROUSSET , F. CHARBONNIER , F. LEPOUTRE , J.Appl.Phys. 56 (7), 2093 (1984)

GEOMETRY OF THE 1-D MODEL

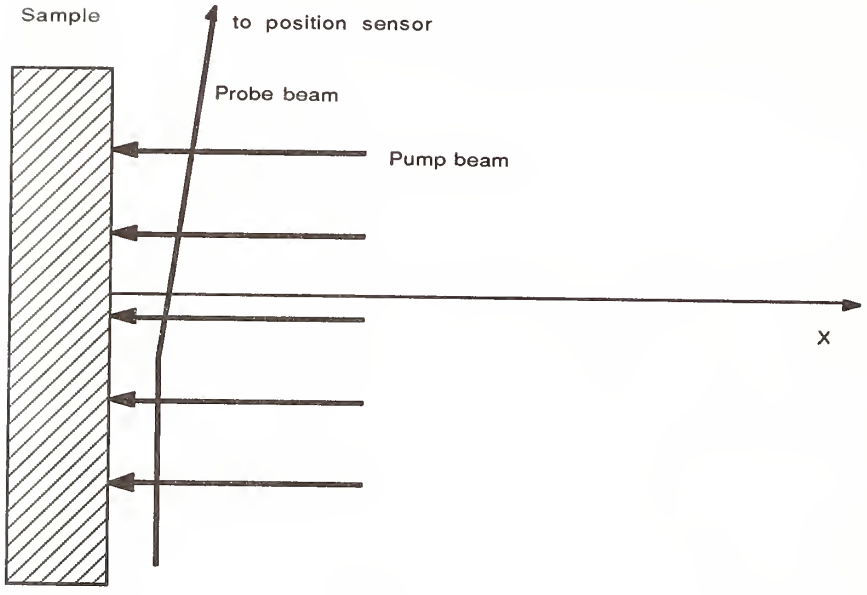

FIG 1

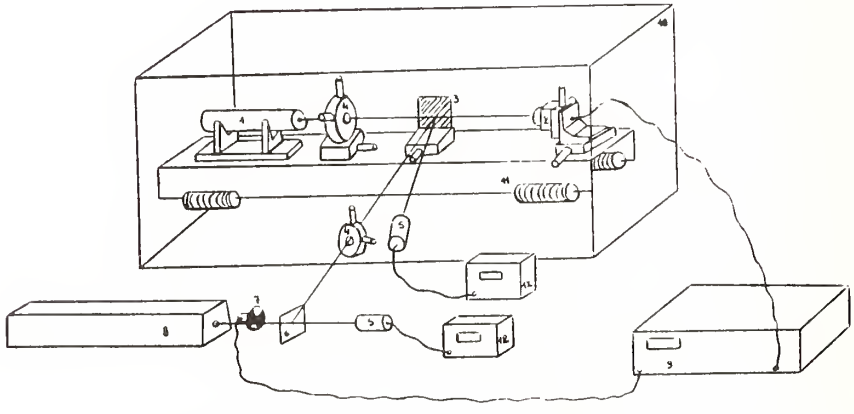

1- Probe laser 2- Position sensor 3- Sample holder 4- Focusing lens 5- Optical detector

6- Beam splitter 7- Chopper 8- Pump laser 9-Lock-in Amplifier 10-Plexiglas box

11- Optical bench with rubber cushions 12- Digital voltmeter

FIG 2

DEFLECTION SIGNAL VERSUS FREQUENCY (silicon substrate ; x=constant)

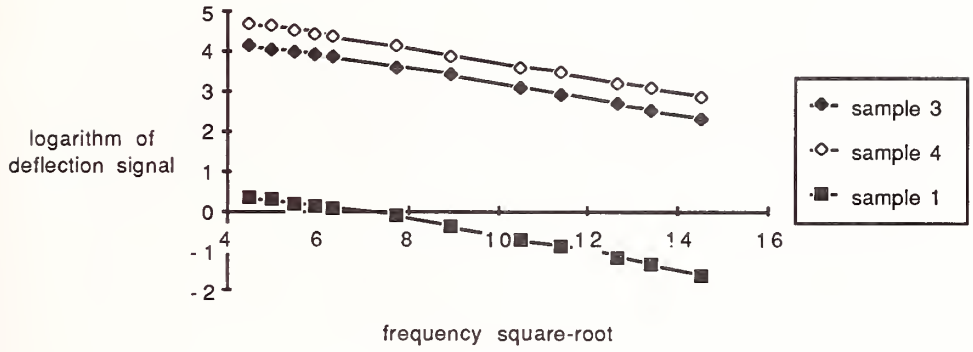

Fig 3

DEFLECTION SIGNAL VERSUS FREQUENCY (molybdenum substrate ; x=constant)

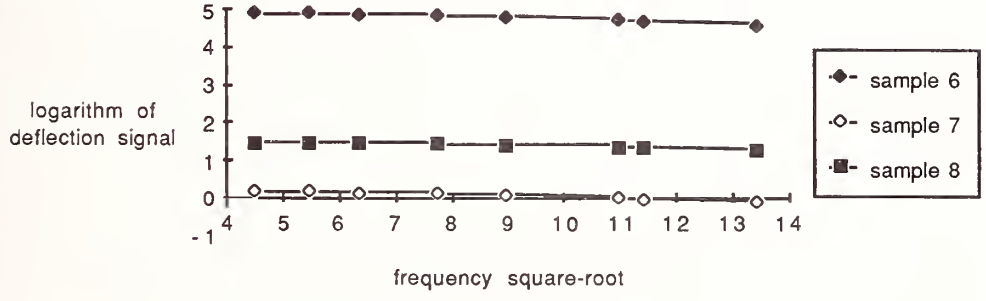

Fig 4

DEFLECTION SIGNAL VERSUS INCIDENT POWER (f=70 Hz ; x=constant)

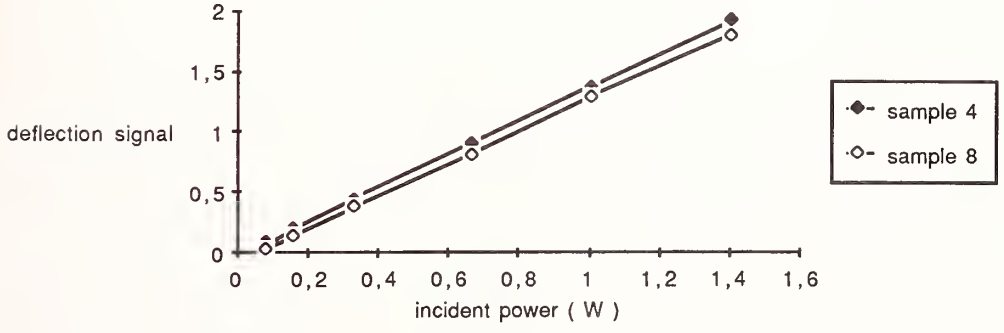

fig 5

DEFLECTION SIGNAL VERSUS OPTICAL ABSORPTION
(molybdenum;f=70Hz;x=constant)

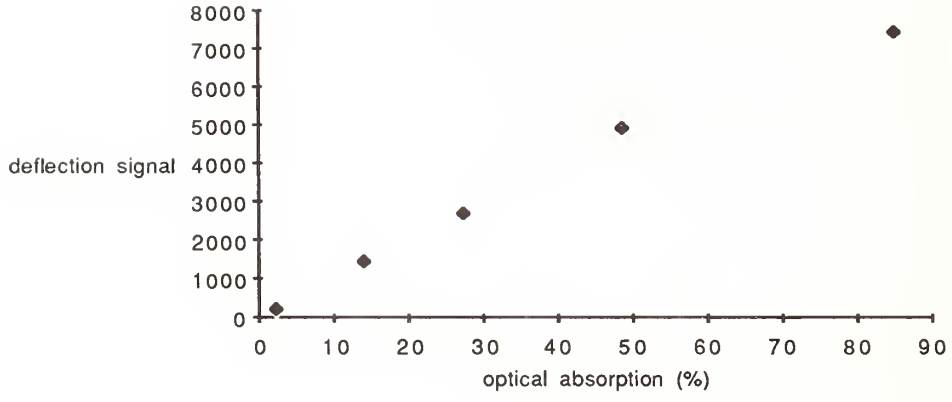

Fig 6

DEFLECTION SIGNAL VERSUS OPTICAL ABSORPTION
(silicon ; f=70 Hz ; x=constant; w=weight in the linear regression)

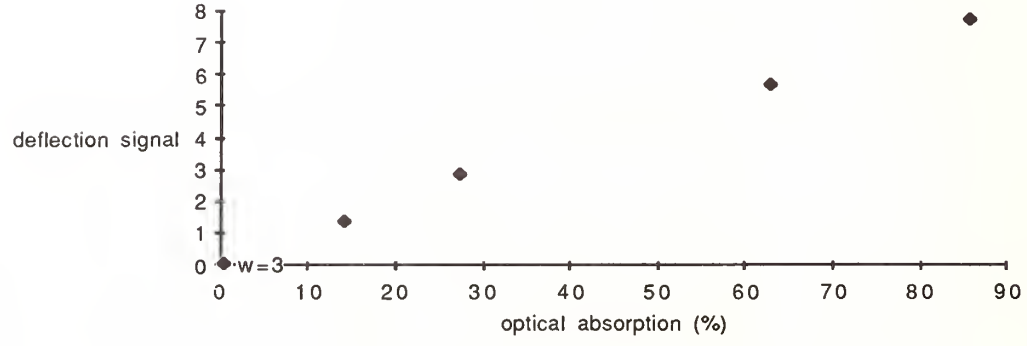

Fig 7

SAMPLES TABLE (TABLE 1)

Sample number	Substrate	Coating
1	silicon	Ag + dielectric protective coatings
2	silicon	Au + dielectric protective coatings
3	silicon	absorbing coatings ;thickness e1; a=14,5%
4	silicon	absorbing coatings ;thickness e2; a=27,6%
5	silicon	absorbing coatings ;thickness e3; a=60,4%
6	molybdenum	without coating
7	molybdenum	absorbing coatings ;thickness e4; a=14%
8	molybdenum	absorbing coatings ;thickness e5; a=27,3%
9	molybdenum	absorbing coatings ;thickness e6; a=48,7%

RESULTS (TABLE 2)

HR/HA	3	4	5	7	8	9	AVERAGE	Σ
1	0,41%	0,39%	0,44%	-	-	-	0,42%	0,06
2	0,53%	0,51%	0,57%	-	-	-	0,55%	0,06
6	-	-	-	2,08%	2,25%	2,17%	2,17%	0,07

Manuscript Received 5-24-88
sar

BASIC STUDIES OF OPTICAL COATING THERMAL PROPERTIES

Randall T. Swimm

Center for Laser Studies
University of Southern California
Los Angeles, CA 90089-1112

Characteristics of a technique to measure the thermal transport properties of coatings are discussed. The measurement technique is based on interferometry using thermal diffusion waves. Initial measurements of thermal transport in single-layer metal coatings are described.

Key words: bonding, coatings, delamination, diffusion wave interfermetry, diffusion waves, laser induced damage, metal coatings, nickel coatings, optical coatings, thermal contact resistance, thermal diffusion waves, thermal transport, thermal waves, thin films.

1. Introduction

The goal of the present research is to characterize the thermal transport properties of thin-film dielectric coatings. The motivation is that for the case of laser-induced coating damage dominated by absorbing inclusions in a thermally-dissipative host coating, the thermal transport properties of the coating are critical. Initial work (references summarized in [1]) has indicated that thermal transport in optical dielectric coatings is substantially impaired relative to corresponding bulk transport values.

2. Background

2.1. Sample Choice Justification

The first step in this research was to develop a probe technique based on diffusion-wave interferometry (Ref. 1). The next step has been to study a simple model system consisting of a thin-metal coating deposited on a substrate, in an effort to test and refine the measurement system. The simplified metal coating sample is of interest for two reasons. First, it is a requirement (Ref. 1) of the measurement technique that a thin metal

overlayer be deposited on the dielectric coatings under study. Thus, it is advantageous to examine the properties of metal coatings separately. Second, the simplest possible sample design is preferred during system development in order that the system behavior may be reliably understood. The research effort to date has been confined to system development, using single-layer metal coating samples.

2.2. Measurement System Physics

The measurement method ad the associated theoretical analysis have been described previously (Ref. 1). Briefly, the measurement involves generating a critically-damped thermal diffusion wave at the outer surface of the metal coating by periodic (sinusoidal) laser heating, and allowing the diffusion wave to probe the coating structure. Specifically, the diffusion wave is partially reflected at discontinuities of the sample thermal properties. The partially-reflected diffusion waves return to the sample surface where they interfere with the instantaneous heating generated by the pump laser beam. The phase shift between the periodic heating and the resultant steady-state periodic temperature response at the sample surface constitutes the desired data. The surface temperature modulation is monitored by a HeNe probe laser beam reflected off the coating. The intensity of the probe laser beam is modulated by the temperature modulation of the reflectance of the metal coating. In the interest of simplicity and tractability, operation is sought in a regime in which radial heat flow may be neglected, thereby allowing a one-dimensional theoretical model to be employed.

2.3. Theoretical Analysis

The thermal boundary value problem is solved (Ref. 1) assuming a piecewise constant approximation, and including a nonzero thermal contact resistance between the metal coating and the substrate. The single-layer coating model contains four adjustable parameters: the coating thermal conductivity, the coating thermal diffusivity, the thermal contact resistance, and the coating thickness. By adjusting the parameters of the model, the measured data are to be fit, and the thermal transport

properties of the coating are to be determined, within the piecewise constant approximation. Corrections for the nonzero optical depth of the pump laser beam have not been included yet.

3.0. Results

3.1. Measurement Conditions

The sample studied was a 1000 A-thick nickel coating deposited on a fused silica substrate using electron-beam deposition. The modulation frequency of the pump laser beam was varied from 100 Hz to 100 kHz. The measurement system has been modified relative to that described in Ref. 1 by the addition of a preamplifier and a tunable narrow-band filter between the signal detector and the lock-in analyzer.

3.2. General Observations on Data

The measured data and two model calculations are shown in Fig. 1. The phase shift between pump and probe ($+ 45^{o}$) is plotted versus the square root of the modulation frequency. The phase oscillation is the result of diffusion wave interference. The two limiting theoretical curves were generated using the formulation described in Ref. 1. Before proceeding further with a description of the analysis, one must note that the experimental data cover an insufficient dynamic range to allow four adjustable parameters to be fitted. The only solution to this problem will be to extend the dynamic range of the measurement system and measure more data, not merely to force an analysis onto the existing data. With that caveat, consider the following observations.

3.3. Plausible Limiting Assumptions

The experimental data are sufficient to provide two conditions on the four parameters. In order to gain insight into the range of possible solutions, two additional constraints must be arbitrarily specified. The upper theoretical curve in Fig. 1 was generated by assuming 1) that the thermal contact resistance between the coating and the substrate is zero, and 2) that the thickness of the coating is 1000 A as measured during deposition. The lower theoretical curve was generated by assuming 1) that the coating displayed bulk-like thermal transport properties, and

identically 2) that the thermal conductivity and the thermal diffusivity are related to the corresponding bulk values by the same factor (here, identically 1). (This would appear to be a reasonable approximation since the coating density is expected to be within 20% of the bulk value, and since Decker (Ref. 2) has shown that coating speific heat is approximately equal to the bulk value.) It must be emphasized that the sensitivity of the model to these arbitrary assumptions may be excessive, and that these assumptions could even result in order of magnitude errors in the other parameters. More experience with the behavior of the model is needed.

3.4. Implications Regarding Measurement System

Let us consider first what the comparison of data and theory implies about the measurement system. Two problems are evident. At the high frequencies, the data do not extend into the range necessary to discriminate between the two model calculations. At the low frequencies, the two model calculations are nearly identical, but the models fail to agree wtih the data. For these reasons, the measurement system, as it presently exists, clearly does not possess sufficient dynamic range to allow a single-layer coating to be characterized.

3.4.1. Response to High-Frequency Nonuniqueness

The problem at high frequencies may be attacked in one of two ways. Either the modulation frequency limit of the measurement system must be increased, preferably by at least one order of magnitude, or thicker coatings must be studied. The characteristic frequencies of the interference oscillations are proportional to the reciprocal of the square of the coating thickness (Ref. 1). Therefore, a coating three times as thick would exhibit interference structure shifted about one decade lower in modulation frequency (assuming identical thermal diffusivity).

3.4.2. Response to Low-Frequency Departure

The departure of the one-dimensional model from the data at low frequencies is expected. A requirement of the one-dimensional model is that radial heat flow be insignificant. This condition will be satisfied provided that the pump beam spot diameter is large compared to the thermal

diffusion length in every layer. The thermal diffusion length varies as the square root of the modulation period. Therefore, below a certain frequency the one-dimensional model fails. The departure of the data from the one-dimensional model at low frequencies in Fig. 1 is presumed to be caused by three-dimensional heat flow effects. The frequency of onset of three-dimensional heat flow may be reduced by employing a larger pump beam spot size, subject to signal-to-noise ratio considerations. The 100 mW argon ion laser that serves as the pump laser in the present system will soon be replaced by a 6W argon ion laser under AFOSR funding (Ref. 3). If the pump beam spot is enlarged to produce the same spot intensity as is presently used, then the frequency for onset of three-dimensional heat flow should be reduced by a factor of approximately sixty.

3.5. Implications Regarding The Sample

As for what a comparison of the theory and data implies about the sample, the results bracket a very broad range. The upper theoretical curve in Fig. 1, in which it is arbitrarily assumed that the thermal contact resistance is zero and the coating thickness is 1000 Å, corresponds to a value for the thermal diffusivity 4 x 10^3 times lower than bulk values (let this ratio be called b) and a value for the thermal conductivity 5 x 10^3 times lower than bulk values. However, the lower theoretical curve, in which it is arbitrarily assumed that the thermal transport parameters are bulk-like, and identically that the thermal conductivity and thermal diffusivity are related to their corresponding bulk values by the same factor, corresponds to a coating thickness of 1.7 x 10^3 Å, and a thermal contact resistance parameter h equal to 400. Finally, it is observed that for the range of solutions for which h >> 1, the relation h b remains nearly constant, where b is the assumed common factor by which the coating thermal diffusivity and thermal conductivity are reduced relative to corresponding bulk values. Following Ref. 1, the parameter h = 400 corresponds in this sample to a thermal contact resistance R equal to approximately 0.05 cm^2K/W. This about one order of magnitude smaller than the equivalent values of thermal contact resistant reported by Jacobs (Ref.

4), and similarly for the values of thermal contact resistance reported by Gitzhofer (Ref. 5) on ZrO_2: Y_2O_3 coatings deposited on nickel substrates by plasma deposition.

As stated above, the dynamic range of the data is insufficient to allow a unique determination of the model parameters to be obtained, as so the specific sample properties discussed above are merely limiting possibilities.

4.0. Discussion

4.1. Common Factor oF Alternative Techniques

It is now possible to place the present method in context with alternative approaches to thermal properties measurement. Two common techniques involve either measuring a temperature drop between two points in a sample, or measuring the transit time for a thermal disturbance to diffuse from one point in a sample to another. In most cases, measurements performed on a single sample yield effective thermal transport parameters representing a spatial average over inhomogeneities. The determination of contributions due to contact resistance or other inhomogeneities may require the measurement of a set of samples of nominally identical thermal transport properties, but of graduated thicknesses. The important point is that a single sample generally yields only a single set of effective thermal transport parameters using these methods.

4.2. Unique Characteristic of Present Technique

In the present approach, no corresponding set of effective transport parameters is obtained from the data. Instead, the data contains a depth-resolved record of the thermal transport, encoded in the form of interference oscillations. Consequently, a great deal of information may potentially be obtained from a single sample (e.g. diffusivity, conductivity, contact resistance and layer thickness of each stratified layer), but equally great demands are placed on the data and analysis. The intrinsic nature of the present approach is therefore quite different from that of the methods described above. The former are poorly suited to yield detailed data on inhomogeneities. The present is poorly suited to ignore

that detail.

4.3. Future Direction

The present research will continue under AFOSR funding (Ref. 3). Efforts will center on adequately representing sample inhomogeneity in order to account for the data, and on pgrading the measurement system dynamic range to the extent required by sample inhomogeneity. Single-layer metal coatings on dielectric substrates will continue to play a prominant role in these studies. Research will continue toward the goal of characterizing two-layer samples containing a dielectric layer. The direction of the research will be defined by the strengths of the measurement technique.

5.0. Summary

The goal of this project is to experimentally characterize the thermal transport properties of dielectric optical coatings. Efforts to date have been primarily devoted to refining the measurement system to the point where meaningful results can be obtained. Characterization has been confined to single-layer metal coatings initially, for reasons of simplicity of data analysis. Measurements indicate that in its present configuration, the measurement system is incapable of characterizing single layer metal coatings, but the improvements necessary to allow such coatings to be characterized are apparent. The upgrade of the system necessary to permit characterization of single layer metal coatings is in progress. The suitability of the upgraded system to the study of two-layer sample coatings consisting of a dielectric layer overcoated with a thin metal overlayer remains to be demonstrated. The complementary nature of the present approach to alternative approaches is discussed.

6.0 Acknowledgement

This research was supported by a contract from the Air Force Weapons Laboratory.

7.0 References

[1] Swimm, Randall T., and Hou, Lisa, "Basic Studies of Optical Coating Thermal Properties", Proceedings of 1986 Boulder Damage Symposium, to be published in a Special NBS Publication.

[2] Decker, D.L., Koshigoe, L.G., and Alshley, E.J., Nat. Bur. Stand. (U.S.), Spec. Publ. 727, 291 (1986).

[3] Swimm, Randall T., "Thermal Transport Studies of Optical Coatings, Interfaces, and Surfaces by Thermal Diffusion Wave Interferometry", contract number AFOSR-88-0038.

[4] Jacobs, Stephen D., LLE Review Quarterly Report 29, 30 (1986).

[5] Gitlzhofer, Francois; Pawlowski, Lech; Lombard, Didier; Martin, Christian, and Kaczmavek, Ryszard; and Maher Boulos, High Temperatures-High Pressures 17, 563 (1985).

Figure 1. Phase vs. square root of modulation frequency for a 1000 A Ni coating deposited by electron beam evaporation onto a fused silica substrate. Curve a) is for h = 0 (zero thermal contact resistance). Curve b) is for b = 1 (bulk-like coating thermal diffusivity). High-frequency limit of measurement system is insufficient to distinguish between theoretical models a) or b) for a nickel coating of 1000 A thickness. Departure of theoretical models from data as frequency is diminished indicates failure of one-dimensional approximation as thermal diffusion length in nickel coating approaches value of pump spot radius. Error bars indicate one standard deviation. Phase is corrected for sign of temperature coefficient of reflection of Ni coating.

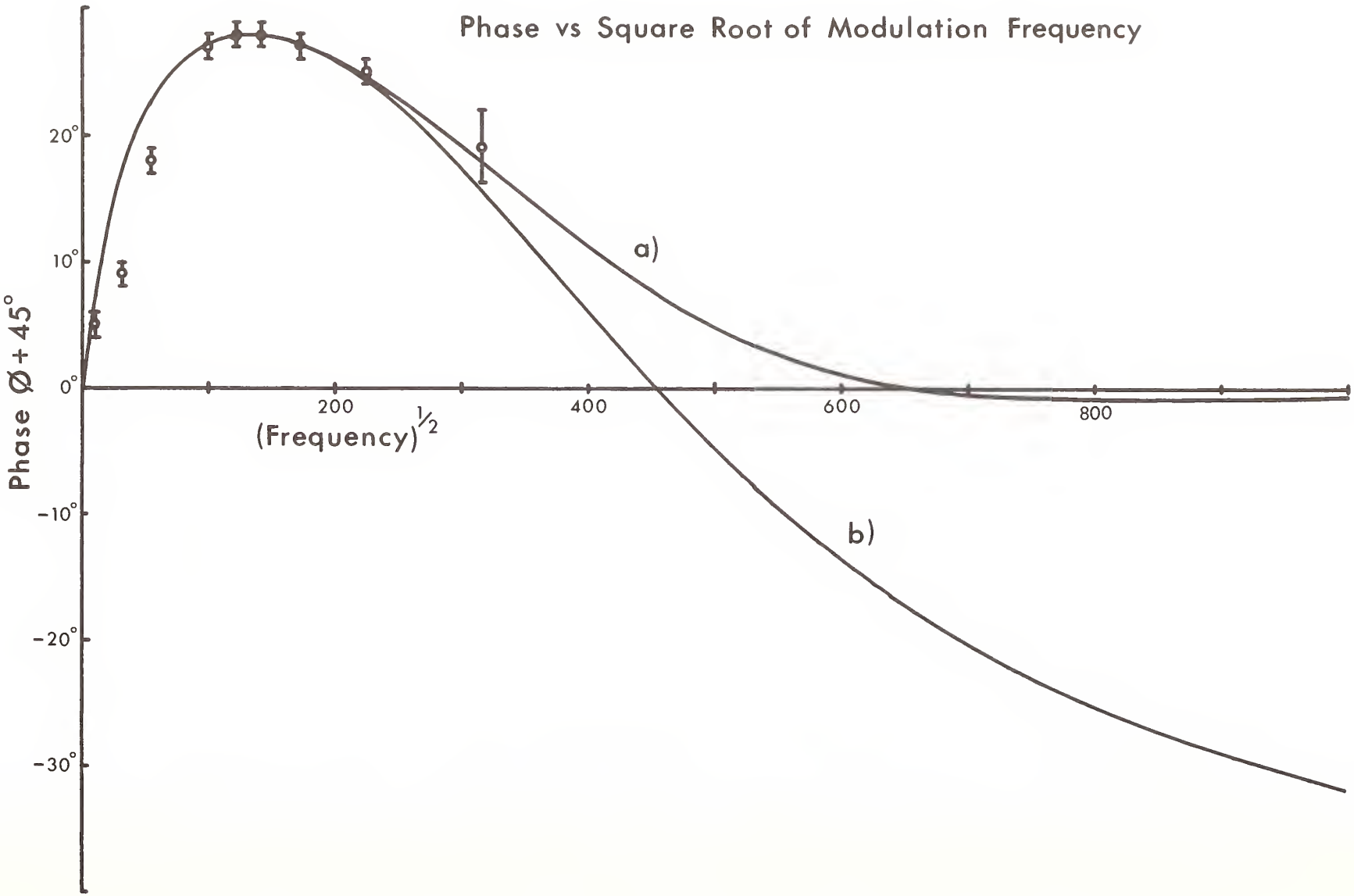
Phase vs Square Root of Modulation Frequency
Phase Ø + 45°
20°
10°
0°
-10°
-20°
-30°
200
400
600
800
(Frequency)^1/2
a)
b)

How were the other values of contact resistance obtained which the author compared his result to. The author replied that Steve Jacobs published the thermal conductivity of an interface assuming a specified thickness. Going backward and taking the thickness he gave and divide by the conductivity he quoted one obtains values within an order of magnitude of the values reported in this paper.

It was also suggested that thermal contact resistance might be related to adhesion strength. The author agreed that that was an interesting possibility and it would be useful to try to correlate contact resistances with adhesion. It may provide a non-destructive method for testing adhesion.

The author suggested a possible engineering application if adhesion and contact resistance are related. It may be possible to get a signature of a coating. If one were to deposit a small metal dot off to the side of the stack, it may be possible to monitor adhesion over a period of time, perhaps years, by measuring the phase signature and find out whether the coating, perhaps on a large window or mirror, is debonding. A pulloff technique would ruin the window, but using a technique such as that described here with a small portable instrument one could check on the status of the coating non-destructively.

In addition to the thermal reflectance measured there is also an effect that Amer has used called the bump effect. You get a distortion of the surface presumably due to thermal effects throughout the material. Will that affect the results reported in this paper? The speaker replied that of all the beautiful systematic errors he has encountered in this investigation that has been one of the most persistent. The system is now immune to that effect. One just located the pump spot exactly centered within the probe spot. One is then not on a gradient and there is therefore no lateral deflection.

Manuscript Received
10-23-87

Studies of the Thermal Stability of Thin Film Structures

K L Lewis, A Miller, I T Muirhead* and J Staromlynska

Royal Signals and Radar Establishment
Malvern, Worcs WR14 3PS, UK

Key words: bistability; damage; dielectric coatings; multilayer mirrors; zinc selenite

1. Introduction

Interest is currently being shown in the role of thermal transport in determining the laser damage threshold of thin film structures. Experimental evidence [1] suggests that the thermal conductivity of materials in thin film form may be significantly different to that in bulk, and that this is probably related to the microstructure of the film. A recent paper by Abraham and Ogilvy [2] presents a linear theory of heat conduction in an etalon filter structure with a weakly absorbing spacer layer. This allows the calculation of temperature distribution at the centre of the spacer for given values of film thermal conductivity. For spacer layers with significant temperature dependences of the refractive index (eg ZnSe near its fundamental absorption edge), the temperature rise induced by laser heating can be followed in principle as the change in transmission produced as the etalon sweeps along the edge of one of its characteristic fringes. When the appropriate cavity conditions are met, optical bistability can occur with incident powers typically in the milliwatt regime with focussed laser beams. This power depends on such parameters as the effective optical nonlinearity of the material, the design of the etalon and wavelength. The heatsinking of the device, normally on a glass substrate, will affect both the switching power and the switching speed. Although the absorption coefficient of the spacer, α, varies rapidly with wavelength near the band gap, the temperature dependence of the refractive index as measured [3] is much less sensitive to wavelength. It may also be noted that thick polycrystalline samples have shown dispersive optical bistability at 476nm, whereby a polished etalon of ZnSe provides feedback [4,5]; bistability due to increasing absorption in which the feedback is inherent in the thermally induced absorption edge shift was also achieved in this type of sample [5].

The first report of passive optical bistability in a semiconductor in 1978 employed ZnS as a spacer layer between dielectric multilayer reflectors. Although originally discussed by Karpushko and Sinitsyn [6] in terms of an electronic nonlinearity, it has since been well characterised as a thermally induced dispersive mechanism [7–9]. Interest in optical bistability employing interference filters based on visible band gap II–VI semiconductors has increased in the last few years because of the potential of these structures as test-beds for early all-optical computing systems. Although electronic nonlinearities would be preferred in terms of speed and operational stability, thermo-optic interference filters are attractive because they can be uniformly fabricated in large areas and therefore offer a very high degree of parallel processing capability with room temperature, visible light operational convenience. Most effort has involved ZnSe since it is an established thin film coating material and provides a band gap energy which is resonant with the dominant 514nm green output of the argon laser.

Potential areas of application of bistable filters impose stringent requirements on the individual devices in terms of uniformity, stability, switching power, switching speed, signal gain etc. To this end, bistable device research has already addressed these parameters in some detail. For instance, Wherrett et al [10] have theoretically analysed filter designs for minimum switching power in terms of mirror reflectivities and spacer layer absorption and thickness, making comparison with experimental results on different filters. Optimisation of the filter design in terms of heat sinking and element isolation has also been discussed from an analysis of heat flow under conditions of bistability [2,3,10]. Switching times have been measured and analysed as a function of laser spot size by Mathew et al [11]. Recently, high power pulses have been used to switch ZnSe bistable etalons through fast electronic nonlinearities [12].

ZnSe filters have now been operated over a wide range of wavelengths. The absorption edge of ZnSe films is generally less abrupt than bulk material, such that significant absorption is apparent well below the band gap energy. By optimising mirror reflectivities for different wavelengths and introducing absorbing layers external to the etalon [13], bistable operation may be extended into the infrared. External absorbing layers have led

*OCLI Optical Coatings, Dunfermline, Fife KY11 5JE, Scotland

to further original device concepts such as those employing more than one thermally coupled cavity in order to enhance signal gain [14]. The results presented in this paper are appropriate to the case with absorption occuring only within the etalon.

Although bistability effects can be produced at incident powers of 10–20mW, this translates into power densities of about 10kW/cm^2 for the typical spot widths used for etalon assessment. Since the repeated production of a bistable loop depends on a controlled excursion of refractive index over a small range, it is essential that the etalon structure is stable and free from effects that produce drift, eg desorption of water from pores or varying levels of stress. Earlier work on UHV film fabrication addressed the feasibility of producing films with high resistance to damage induced by pulsed laser irradiation. In the case of ZnSe,, the film laser damage threshold to CO_2 laser pulses at 10.6μm was greater than that of an uncoated ZnSe substrate, whilst the refractive index was identical [15]. More recent work on fluoride deposition [16] has highlighted the potential of barium and lead fluoride as low index materials for use over a wide range of wavelengths. Techniques have been developed for the control of the microstructure of the films offering the potential of novel structures including graded index designs.

Optical bistability has already been reported for ZnSe filters fabricated with molecular beam (MB) deposited spacer layers of different thicknesses (using the same UHV machine) but employing conventional, thermally evaporated dielectric mirror stacks [3]. These UHV deposited, thick spacers were found to give much improved long term stability. In addition, the dependence of critical power level on thickness was found to be consistent with theory [10]. One of these filters is used for comparison in the present studies. The second filter discussed in this work was fabricated entirely in UHV.

Initial work has addressed the transient processes leading to a change in filter transmission when subjected to incident laser irradiation. These are fundamental in determining the amount of energy coupled into the thin film structure and allow conclusions to be drawn on the viability of the technique for the assessment of the thermal properties of thin film structures. Such factors also have important implications for the performance of filters in optical bistability experiments.

2. Experimental Details of Etalon Fabrication and Assessment

Two etalon structures are compared here. Both were fabricated with relatively thick MB deposited ZnSe as the spacer layer. The difference between the samples lies in the method of producing the partially reflecting mirrors. One has conventional, thermally evaporated multilayer dielectric coatings as mirrors, OC3102, while the other sample, AP245, was constructed entirely by MB techniques. Both filters were deposited on glass substrates with small built-in wedges allowing ease of control of initial etalon detuning.

The thermally evaporated mirrors consisted of two-period high/low index coatings comprising $\lambda/4$ thick ZnSe and ThF_4 layers with peak reflectivities centred at 514nm on either side of a 4.3μm MB deposited spacer. Optical bistability at 514nm (argon), 633nm (He-Ne) and 647nm (krypton) has already been described for this filter in a previous publication [3]. The completely MB grown filter was built up by first depositing a two-period stack comprising $\lambda/4$ thick layers of ZnSe and BaF_2 (n=1.45) centred at 633nm, followed by a 6.7μm thick ZnSe spacer and finally a matching two period mirror to complete the etalon.

The MB layers were deposited in a Vacuum Generators load-locked UHV system fitted with 3 Knudsen sources and *in situ* surface diagnostics (Auger and x-ray photoelectron spectroscopy). The source materials were contained wihin high purity graphite crucibles which were carefully outgassed following baking of the entire deposition chamber at 180°. The ZnSe source was ultra-high purity polycrystalline ZnSe which had previously been prepared by chemical vapour deposition from a mixture of zinc vapour and hydrogen selenide. The barium fluoride source was high purity crystalline optical grade material. Source temperatures were adjusted to give deposition rates of 0.9μm/h for ZnSe (896°C) and 0.7μm/h for BaF_2 (1185°C) at pressures of 10^{-8}mbar. The substrate (glass) temperature during growth for the entire MB deposited layer was 300°C. The multilayers were exceptionally smooth with no evidence of surface texture visible by Normarski interference microscopy.

The microstructure of the films was assessed by scanning electron microscopy (SEM) of cleaved cross-sections. This is reasonably effective in revealing the nature of the film morphology, although as a technique is not able to resolve fine detail as in transmission electron micrography (TEM). Earlier TEM work had revealed [15] that ZnSe films produced by the MB technique were polycrystalline and exhibited a columnar morphology. This is clearly shown in the SEM cross-section in Fig. 1a for filter AP245. At higher magnification (Fig. 1b), the films appear to be uniformly dense, although the SEM is unable to distinguish individual crystallites. X-ray diffraction studies show that the 300°C films have a high degree of preferred orientation with (111) ZnSe lattice planes parallel to the substrate. The (111) diffraction line is narrow, with half-width similar to that of bulk chemically vapour-deposited ZnSe, indicative of good crystallinity. This evidence implies that the

MB ZnSe films should have thermophysical properties approaching that of bulk material.

A c.w. krypton laser provided output at several wavelengths between 476 and 676nm. The laser output was focussed to a spot size of ω_o = 12μm ($1/e^2$ intensity radius) on the sample after passing through an acousto-optic modulator to provide control of the incident power. The samples were held normal to the beam with adjustment of initial detuning of the etalon accomplished by moving the slightly wedged samples transversely across the beam. A schematic diagram of the experimental layout is given in Fig. 2.

Fig. 3 gives the transmission spectrum of the entirely MB deposited filter, AP245, measured using a spectrometer with a small light spot on the sample in order to minimise spatial variations in this slightly wedged etalon. Transmission measurements were also carried out using low power, focussed krypton laser radiation in order to determine precise maximum and minimum values by fully resolving the fringes. From these results, given in Table 1, peak mirror reflectivities of about 70% were deduced aassuming equal values of reflectivity for front (R_F) and back (R_B) mirrors and values of αD were estimated at five wavelengths where α is the absorption coefficient and D is the etalon spacer layer thickness.

Table 1: Sample AP245

λ	Tmax%	Tmin(%)	αD	R(%)
521	23	8	0.63	52
531	28	7	0.47	57
568	38	3.5	0.24	69
647	62	3	0.09	70
676	73	4	0.07	67

The reflectivities may be compared with the theoretically predicted values of R_F = 81% and R_B = 74% assuming no absorption in the stack. The ZnSe absorption coefficient varies from approximately 100 to 1000cm^{-1} going from 676 to 521nm. The absorption edge in this sample is less abrupt than for bulk polycrystalline ZnSe, as found for conventional, thermally evaporated thin films [7].

3. Non-linear Absorption Effects Under CW and Time Resolved Conditions

The simplest way to study such an etalon structure would be to carry out measurements at wavelengths out of resonance and assess the changes in absorption induced by heating. For a semiconductor, changes in absorption would be induced by shift of the fundamental absorption edge to longer wavelengths as a result of lattice heating. For sample AP245 at 476nm, etalon fringes are not apparent because of the high absorption coefficient close to the band gap energy, Fig. 3, and because the mirror configuration was optimised for 632nm operation. Nonlinear absorption and any permanent absorption changes can thus be distinguished from refractive index changes which otherwise dominate etalon performance. Fig. 4a shows the nonlinear input-output characteristic obtained at 476nm when the incident power density was ramped up to 18KW/cm^2 and down again in 10 seconds (spot size same as for bistability conditions). Laser induced heating causes the increased absorption at high power due to the shift of the absorption edge to longer wavelengths. Permanent changes in transmission were monitored under conditions of repetitive cycling of the input power. Very little change was observed for the first 5 minutes. However, during the next few minutes the characteristic altered substantially through that shown in Fig. 4b to Fig. 4c. Here the low level transmission of the sample has not changed substantially but the input-output characteristic is much closer to linear. This is evidence, not so much of a bleaching effect but of a reduction in non-linear absorption coefficient.

These processes were explored in further detail in time resolved studies at 476nm, using fresh regions of the filter. The temporal response of the transmitted light was detected when square pulses of 10ms duration were incident on the filter. Fig. 5a shows the transmission response to an input power density of 18KW/cm^2. A spike occurs as the incident irradiance is suddenly increased, followed by a fall in transmitted light as the filter heats and shifts its band gap energy to longer wavelengths. The time constant for the filter to reach equilibrium at a transmission of about 0.5% is of the order of 10μs under these conditions. A temperature rise ΔT of about 150°C is estimated from:

$$\Delta T = \frac{P \alpha \tau}{V_P \rho A D}$$

where $P\alpha$ is the absorbed power, C_P and ρ are the specific heat and density of ZnSe respectively, A is the

heated area and D the film thickness. The 10μsec time constant at first sight may be thought to be associated with thermal diffusivity effects in the filter. However, other factors were shown to be having some effect as a result of analysis of transient response following repetitive pulses. Bursts of 6 pulses, each 18KW/cm^2 and 10ms in duration with equal off periods were shone ontol the sample. Fig. 5b shows how the transmission changed after a number of these bursts,, each burst separated by at least one second. Note that the peak transmission of the spike decreased and the associated time to reach an equilibrium increased slightly. A more extreme excitation condition was then employed in this example whereby the 10msec square pulses excited the sample continuously for some time. The effect was to cause a net increase in the high power transmission, together with a much longer time constant, eventually reaching several hundred microseconds (Fig. 5c). This form of transmission characteristic stabilised after 5 minutes but, again, the low power transmission of the sample was not substantially altered. The behaviour is thus similar to that found under CW irradiation, with the same reduction in non-linear absorption coefficient.

If the time constant associated with non-linear absorption was due to a thermal diffusivity process, it would imply that the filter site irradiated has been converted after 5 minutes exposure into a region of lower thermal conductivity. This is not reasonable from a physico-chemical point of view since annealing would be expected to give rise to a less amorpohous structure, with larger crystalline content and hence higher thermal conductivity. Furthermore, the true thermal constant of the system should manifest itself during the leading edge of the irradiation step function. At present this cannot be explored because of an inability to increase the response bandwidth of the modulator and detector system available. However, it is clearly evident that the experimental behaviour is complex and may imply participation from transitions between relatively long lived energy states within the band gap.

Non-linear Refraction and Optical Bistability

Optical bistability was observed in both samples at the five krypton laser wavelengths listed in Table 1. Input-output characteristics measured at 531nm are shown for the MB sample AP245 in Fig. 6. Results for different initial detunings of the etalon are illustrated, each obtained by choosing different locations on the filter. Fig. 6b represents the critical condition for bistability, ie a non-hysteretic characteristic with vertical slope. Slightly increasing the detuning from this condition produces bistability at higher incident power. For the laser spot size used with this filter, the critical power level for bistability at 531nm is thus approximately 11mW.

Critical powers, measured at the available output wavelengths of the krypton laser between 521nm (green) and 676nm (red) are plotted as a function of wavelength in Fig. 7. A minimum critical power of 9.5mW is obtained at 568nm (yellow). This optimum is a trade-off between the larger nonlinearity at shorter wavelengths due to higher absorption plus slightly larger optothermal coefficient (dn/dT), against the higher absorption causing a reduction in the finesse of the etalon. Also plotted are the corresponding results for the filter, OC3102, with thermally evaporated mirrors. In this case, the minimum switching power was found to be 5mW at 531nm.

An expression giving the wavelength dependence of the critical switching irradiance I_c for optothermal devices has been derived by Wherrett et al [10]. The critical switching power P_c can be derived from this as

$$P_c = \frac{\lambda f}{\delta n/\delta T}$$

where f is a function of etalon reflectivity and spacer absorption. This function is plotted for the two samples in figures 7(a) and (b) given the etalon parameters extracted from transmission measurements and employing the same vertical scaling for both cases. If zero dispersion in $\delta n/\delta T$ is assumed, the predicted wavelength dependences show the correct general shapes but predict lower critical values in the red than measured. This may be due to the usual experimental difficulty encountered in reliably extracting low absorption coefficients from thin structures. However, some dispersion in $\delta n/\delta T$ does exist close to the band gap energy and this would also increase the switching power at long wavelengths relative to those nearer the band edge. This is illustrated in Fig. 7 by simply assuming a linear wavelength dependence for $\delta n/\delta T$ such that its value is a factor of 3 greater at 521nm compared to 676nm.

Although some residual drift of the bistable loops was still apparent in these initial MB structures, essentially stable conditions could be maintained under continuous operation for periods of several hours under certain conditions. Fig. 8 shows an example of bistable operation maintained over long tiemescales at a wavelength of 568nm (yellow) in sample AP245; the input power was continuously ramped up and down at 0.5Hz with the maximum incident power density on each cycle reaching 35KW/cm^2,. Single cycle, input-output characteristics are shown at fixed times. Only small changes in the bistable loop are observed during the first three hours and only after seven hours has the loop begun to deteriorate significantly. At other wavelengths, faster

deteriorations of the bistable loop were recorded. For instance, experiments conducted at 647nm under similar conditions to that described above for 568nm resulted in the bistable loop permanently moving to lower power and reducing in size, consistent with a gradual decrease in refractive index reducing the etalon detuning. The bistable loop disappeared in about one hour, showing a critical switching power of 20mW, close to that measured on a fresh region of sample (see Fig. 7). Since the films were fabricated with a slight wedge, different wavelengths necessitate using different parts of the filter in order to achieve the appropriate initial detuning for bistability. Thus, the long term stability differences noted here may depend at least partly on material factors which vary across the sample.

4. Conclusions

Assessment of thermally induced absorption processes in multilayer filter structures based on etalons has shown that under both CW and transient conditions the behaviour of the filters is complex and cannot be explained on a simple linear basis. It is necessary to introduce additional phenomena to explain some of the effects observed – these may be associated with transitions between long-lived energy states within the energy gap of the material.

The work has demonstrated that thick ZnSe etalons can be fabricated entirely by ultra-high vacuum, molecular beam techniques. These initial filters are mechanically stable and exhibit optical bistability. The wavelength dependence of the critical switching power is found to follow the general theoretical predictions of Wherrett et al [10] as the absorption close to the band gap energy increases with photon energy. Further improvements in mirror reflectivities and optimisation of the design should allow low power optical bistability with high through output at the longer wavelengths.

Although some drift of the bistable loop was still apparent at high incident power levels in these structures, stable conditions could be maintained under continuous operation for periods of many hours at 568nm in these initial studies. Further progress in this new materials technology is likely to lead to further improvements in the performance of opto-thermal devices and allow novel structures to be fabricated because of the high degree of control available with MB techniques.

Acknowledgments

We have benefitted from many stimulating discussions on optical bistability in opto-thermal devices with members of the opto-electronics group at Heriot-Watt University and in particular we acknowledge the help of B S Sherrett and D Hutchings. Thanks are also due to O D Dosser of RSRE for her skills in the SEM studies.

5. References

[1] D L Decker, L G Koshigoe and E J Ashley, Proc. 1984 Boulder Damage Symposium, NBS SP 727 291 (1986)

[2] E Abraham, I J M Ogilvy, Appl. Phys. B 42 31 (1987)

[3] Y T Chow, B S Wherrett, E Van Stryland, B T McGuckin, D Hutchings, J G H Mathew, A Miller, K L Lewis, J.Opt.Soc.Am. B 3 1535 (1986)

[4] M R Taghizadeh, I Janossy, S D Smith, Appl.Phys.Lett. 46 331 (1985)

[5] A K Kar, B S Wherrett, J.Opt.Soc.Am. B 3 345 (1986)

[6] F V Karpushko, G V Sinitsyn, J.Appl.Spectrosc. 29 1323 (1978)

[7] S D Smith, J G H Mathew, M R Tagjozadeh, A C Walker, B S Wherrett, A Hendry, Opt. Commun. 51 357 (1984)

[8] G R Olbright, N Peyghambarian, H M Gibbs, H A Macleod, F Van Milligan, Appl.Phys.Lett. 45 1031 (1984)

[9] I Janossy, M R Taghizadeh, J G H Mathew, S D Smith, IEEE J.Quant. Electron. QE-21 1447 (1985)

[10] B S Wherrett, D Hutchings, D Russell, J.Opt.Soc.Am. B 3 351 (1986)

[11] J G H Mathew, M R Taghizadeh, E Abraham, I Janossy, S D Smith in "Optical Bistability III" ed. H M Gibbs, P Mandel, N Peyghambarian, S D Smith (Springer-Verlag, Berlin, 1986) pp57-60

[12] J Y Bigot, A Daunois, R Leonelli, M Sence, J G H Mathew, A C Walker, S D Smith, Appl.Phys.Lett. 49 844 (1986)

[13] A C Walker, Optics Commun. 59 145 (1986)

[14] N C Craft, S D Smith, Technical Digest of topical meeting on Photonic Switching, Lake Tahoe (Optical Society of America, 1987), paper TuC3-1

[15] K L Lewis, J A Savage, A G Cullis, N G Chew, L Charlwood, D W Craig in Proc. 1984, Boulder Laser Damage Symposium, NBS Spec. Publication 727 162 (1986)

[16] K L Lewis, A M Pitt, N G Chew, A G Cullis, T J Wyatt-Davis, L Charlwood, O D Dosser, I T Muirhead in Proc. 1986 Boulder Laser Damage Symposium

6. Figures

Fig. 1: Scanning electron micrographs of cleaved cross-sections of MB filter structure. The outer reflector layers are barely discernable in (a)

Fig. 2: Schematic diagram of experimental layout used for filter assessment

Fig. 3: Transmission of complete molecular beam deposited ZnSe etalon, sample AP245, with mirror reflectivities peaked at 640nm. Note that the fringes are not fully spatially resolved by the spectrometer. See Table 1 for small spot size transmission results using the krypton laser

Fig. 4: Nonlinear absorption at 476nm, (a) initial conditions; (b) after 5 minutes of continuous cycling and (c) after 10 minutes

Fig. 5: Temporal dependence of the transmission of 40mW, 10ms duration pulses, (a) initial conditions, (b) after a total of 800 pulses and (c) after 5 minutes of continuous repetitive illumination (2.5×10^5 pulses)

Fig. 6: Input-output transmission characteristics for a ZnSe etalon fabricated by molecular beam deposition and measured at 531nm for three different initial cavity detunings obtained by making use of a slight wedge built into the structure

Fig. 7: Measured critical switching powers as a function of laser wavelength. The diamonds are the results for the entirely molecular beam deposited sample, AP245; the squares are results obtained for a similar filter with mirrors fabricated by conventional thermal evaporation, OC 3102. The lines are the predicted wavelength dependences using the theory of Wherrett et al [3] for these etalon structures

Fig. 8: Long-term drift assessment of bistable loop at λ = 568nm. Time, a) 0, b) 1, c) 2, d) 3,, e) 7 hours

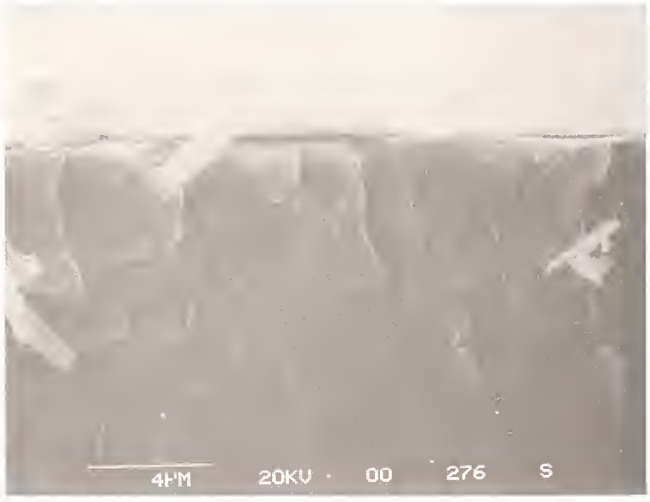

Fig. 1: Scanning electron micrographs of cleaved cross-sections of MB filter structure. The outer reflector layers are barely discernable in (a)

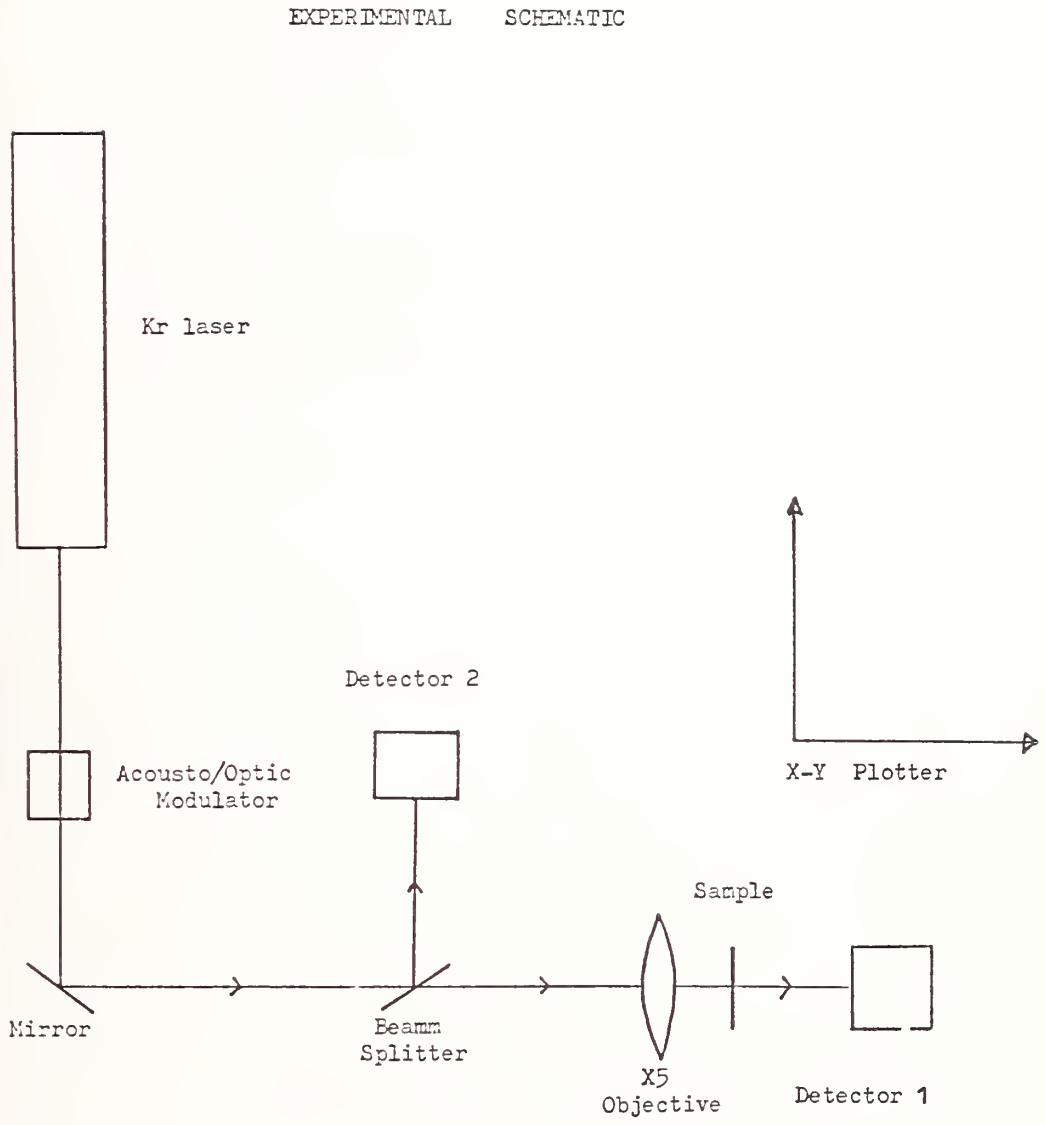

Fig. 2: Schematic diagram of experimental layout used for filter assessment

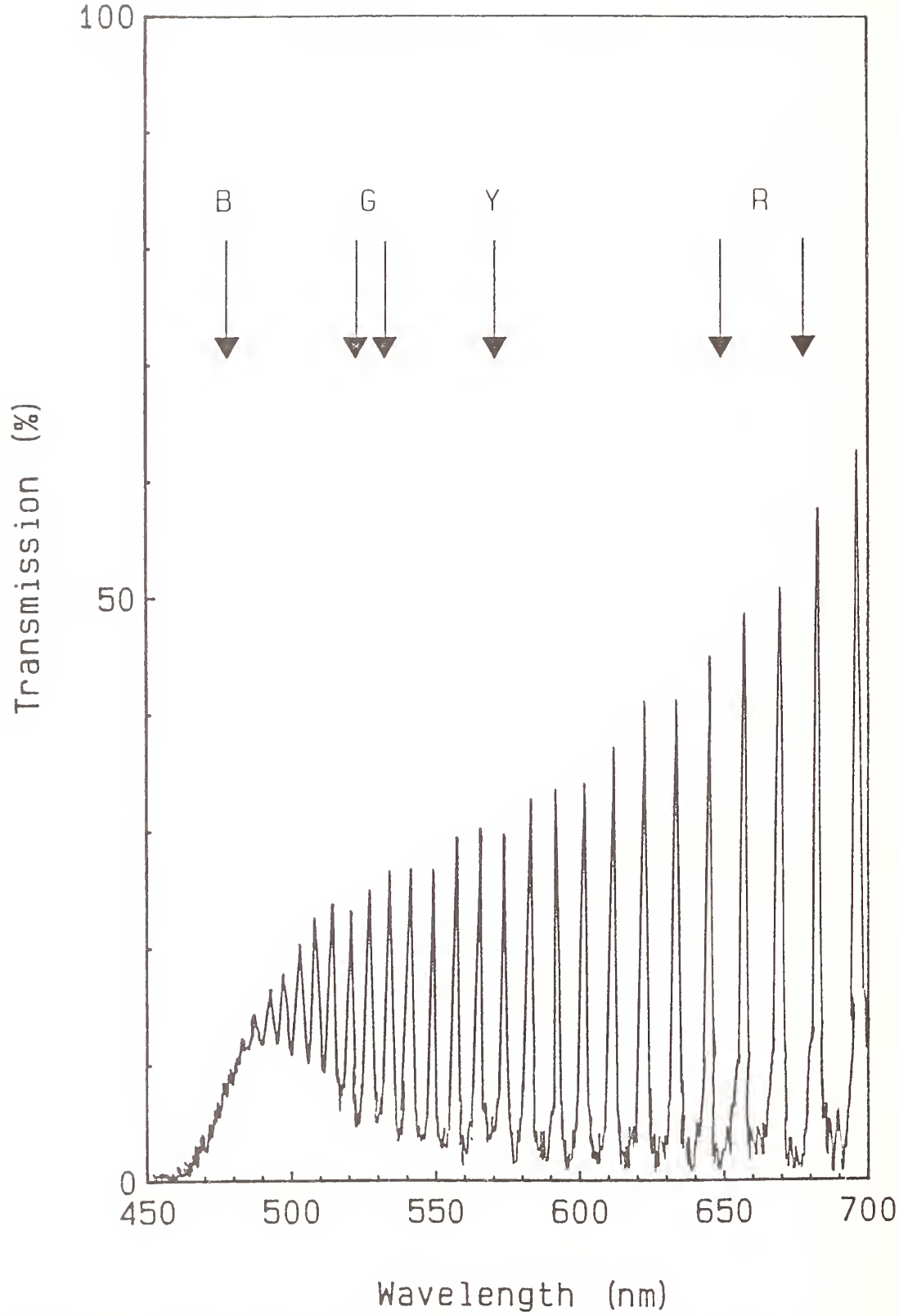

Fig. 3: Transmission of complete molecular beam deposited ZnSe etalon, sample AP245, with mirror reflectivities peaked at 640nm. Note that the fringes are not fully spatially resolved by the spectrometer. See Table 1 for small spot size transmission results using the krypton laser

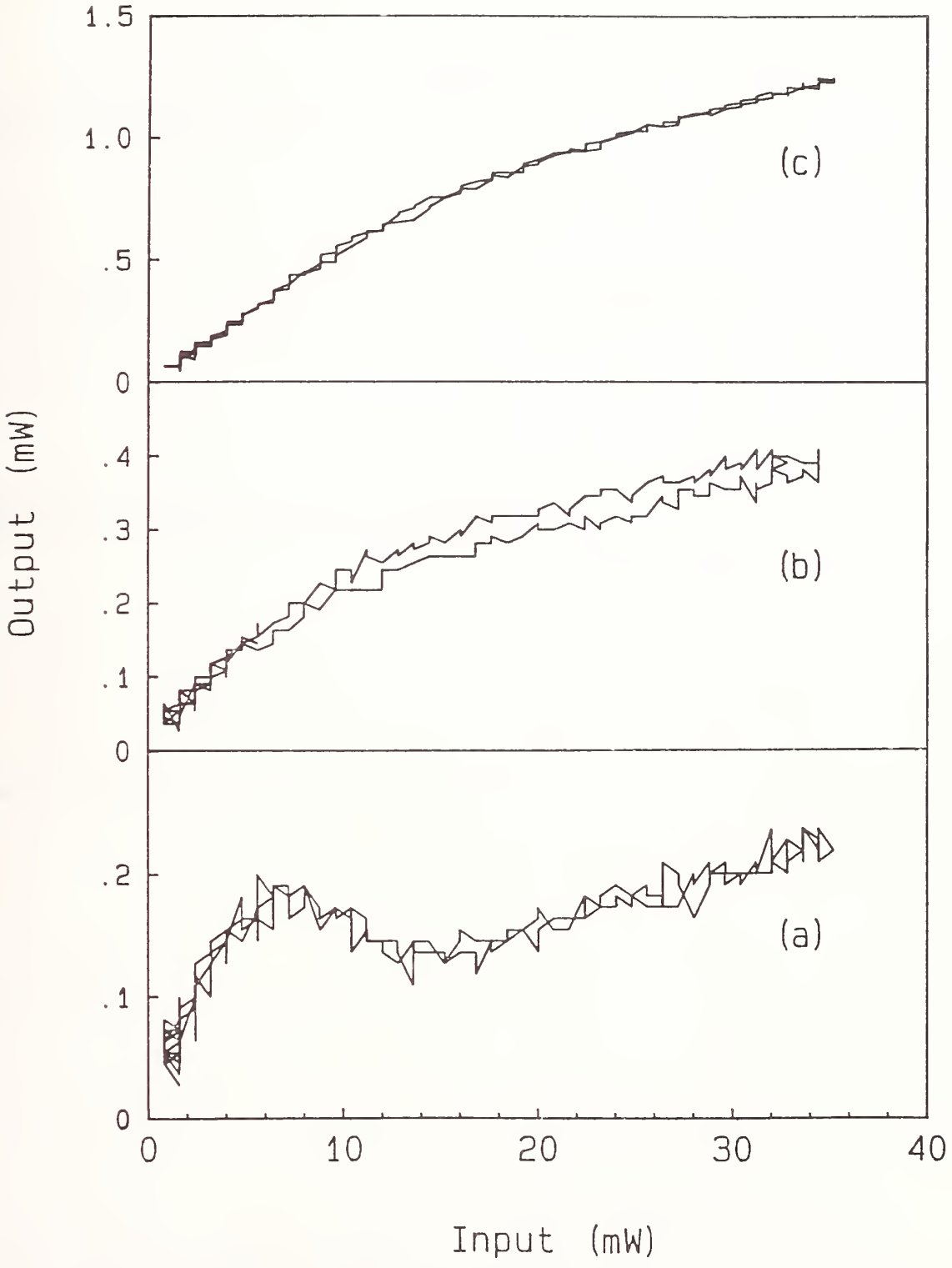

Fig. 4: Nonlinear absorption at 476nm, (a) initial conditions; (b) after 5 minutes of continuous cycling and (c) after 10 minutes

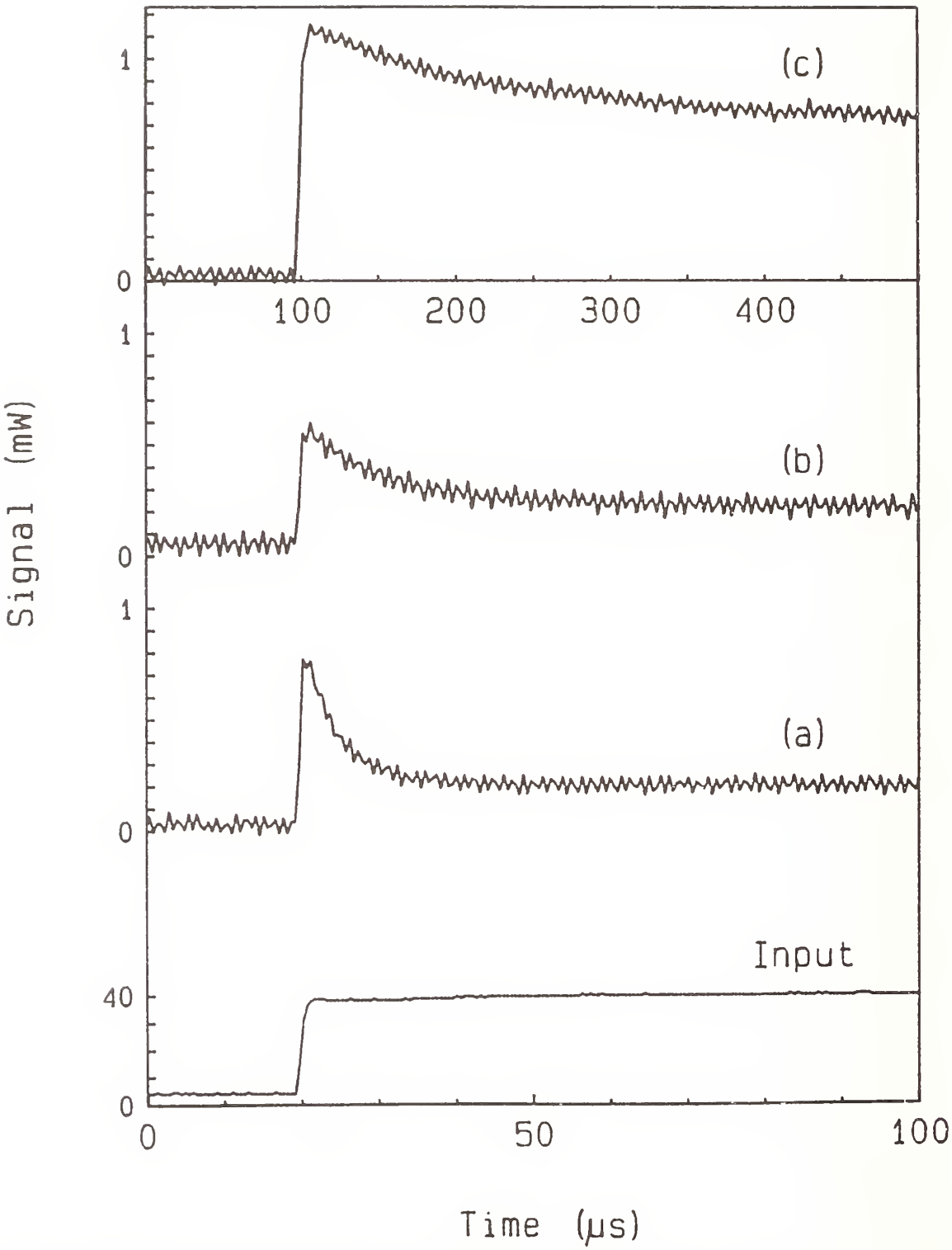

Fig. 5: Temporal dependence of the transmission of 40mW, 10ms duration pulses, (a) initial conditions, (b) after a total of 800 pulses and (c) after 5 minutes of continuous repetitive illumination (2.5×10^5 pulses)

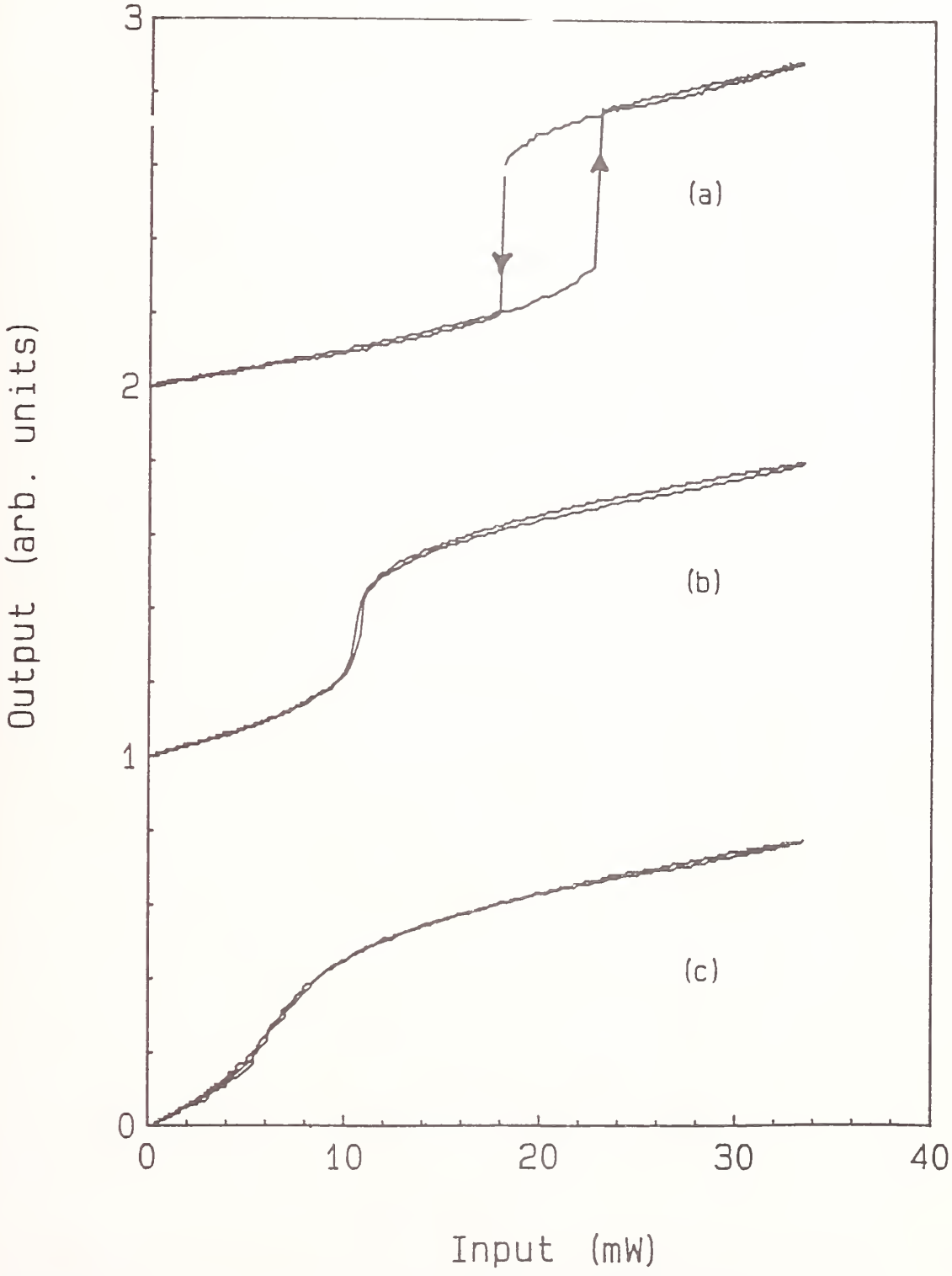

Fig. 6: Input–output transmission characteristics for a ZnSe etalon fabricated by molecular beam deposition and measured at 531nm for three different initial cavity detunings obtained by making use of a slight wedge built into the structure

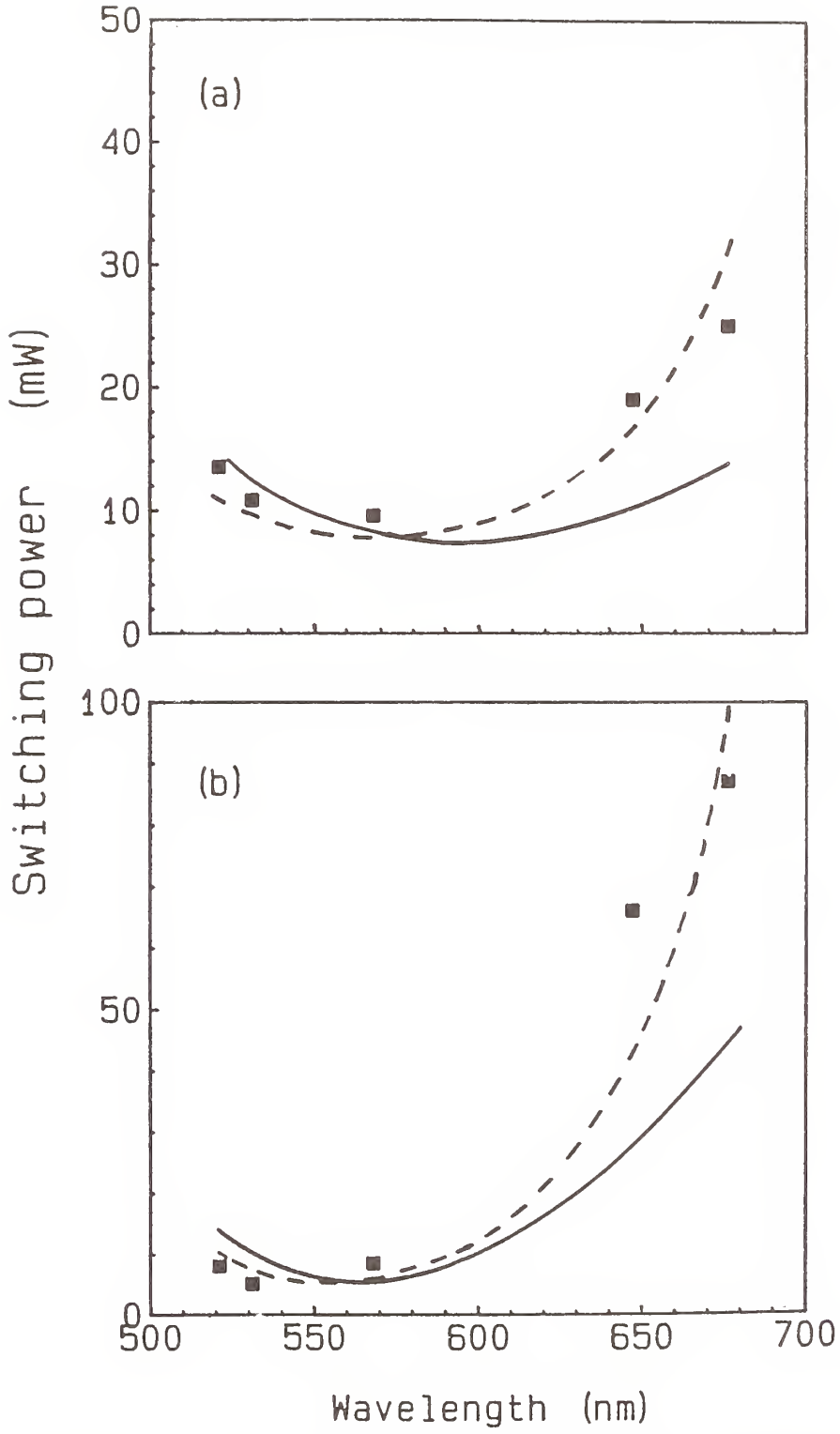

Fig. 7: Measured critical switching powers as a function of laser wavelength. The diamonds are the results for the entirely molecular beam deposited sample, AP245; the squares are results obtained for a similar filter with mirrors fabricated by conventional thermal evaporation, OC 3102. The lines are the predicted wavelength dependences using the theory of Wherrett et al [3] for these etalon structures

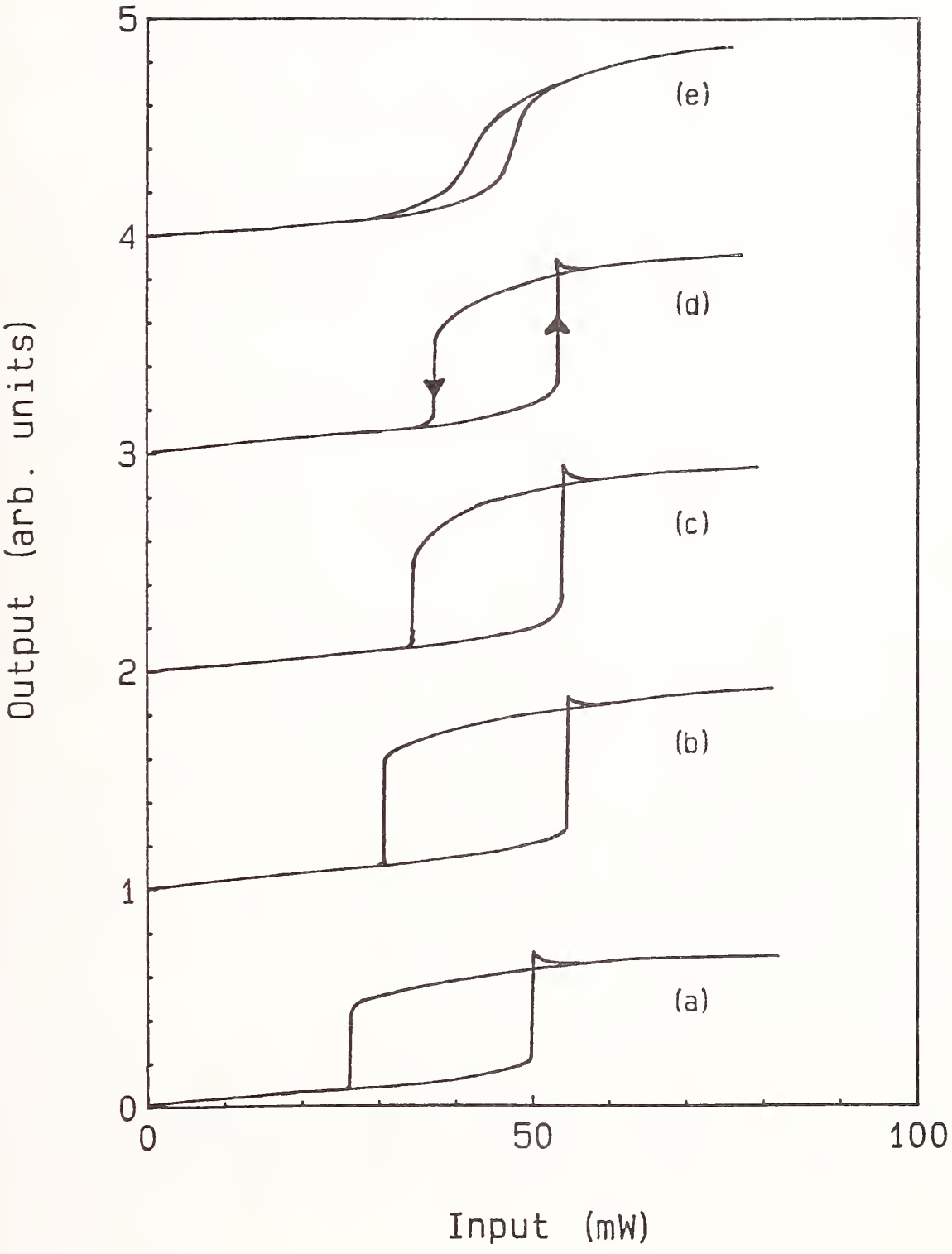

Fig. 8: Long-term drift assessment of bistable loop at λ = 568nm. Time, a) 0, b) 1, c) 2, d) 3,, e) 7 hours

Manuscript Received 12/16/87/sar

Raman Studies of Inherent and Applied Stress in Thin Optical Films

G. J. Exarhos, W. S. Frydrych, K. F. Ferris, and N. J. Hess*

Pacific Northwest Laboratory**
Richland, Washington 99352

Vibrational mode frequency shifts have been shown to correlate with strain in optical coatings the extent of which is dependent upon film deposition conditions. The presence of strain and strain inhomogeneity in thin films as well as crystallite phase and phase homogeneity affects the optical properties, environmental durability, and laser damage resistance. The influence of these variables on the response and stability of optical thin films can be effectively probed using Raman spectroscopy. Molecular vibrational spectra for several sol-gel and sputter-deposited TiO_2 films have been recorded at variable pressures approaching 100 kbar using a diamond anvil cell. Results demonstrate the presence of reversible pressure-induced phase transformations and suggest that introduction of voids in the film microstructure can influence the pressure at which such transformations are observed.

Key words: strain; phase transformations; Raman spectroscopy; sol-gel films; sputter-deposited films; hydrostatic pressure; microstructure.

1. Introduction

Previous work in this laboratory has demonstrated that laser Raman spectroscopy is a sensitive probe of crystalline phase and phase homogeneity in dielectric films.[1,2] In addition, spatially resolved measurements have been used to profile strain and strain heterogeneity in pristine and laser-damaged optical films through frequency shifts of the allowed lattice phonon lines.[3,4] Such measurements are performed using a laser microprobe, which is basically an optical microscope (with a spatial resolution on the order of several micrometers) that is interfaced to the spectrometer. Raman measurements of catastrophic damage regions to an anatase/silica multilayer coating have revealed the existence of the higher density rutile phase and extensive development of inhomogeneous strain fields into the undamaged region of the coating.[4] Damage-induced strain is quantified from measurement of the strong 143 cm^{-1} E_g mode which exhibits a pressure-dependent shift of 0.3 cm^{-1}/kbar in anatase.[5] These results indicate that both crystalline phase and strain are important parameters which control the optical properties of thin films as well as their environmental stability; the pressure-dependent optical measurements reported in this article are mandated by these results.

Interfacial strain in thin films can result from inherent materials properties, variation of deposition parameters, and thermal processing of the deposited film. For plasma vapor-deposited films, in which substrate heating is appreciable during deposition, the mismatch in thermal properties between substrate and film materials may be sufficient to generate significant interfacial strain upon cooling. In some cases, laser annealing of the coated substrate can modify interfacial strain. However, in amorphous films, such thermal treatments can also induce a crystalline phase transformation that can significantly alter the optical properties.

*Department of Geology, University of Washington, Seattle, WA 98195.
**Pacific Northwest Laboratory is operated by Battelle Memorial Institute for the U. S. Department of Energy under Contract DE-AC06-76RLO 1830.

The magnitude of interfacial strain in sol-gel deposited films can be controlled through alteration of solution chemical equilibria and condensation kinetics. Three consecutive chemical equilibria appear to be important in developing an extended molecular network in solution [6,7]: metal ion complexation, hydrolysis, and condensation to a polymeric oxide precursor. Chemical control of the complexation reaction will fix the metal cation in localized geometries, which eventually lead to development of a specific crystalline phase of the oxide film being deposited. Thermal treatment leads to loss of the organic material. Solution chemistry, therefore, controls the oxide phase and phase homogeneity that results in the processed film. Strain can also be introduced in sol-gel films by the same mechanisms.

In this work, Raman spectroscopy has been used to determine interfacial strain and phase homogeneity in sol-gel and sputter-deposited films. The vibrational mode frequencies for a number of TiO_2 films and bulk materials have been evaluated for their pressure dependence from ambient pressures to 100 kbar using a diamond anvil cell. Reversible pressure-induced phase transformations have been identified for both anatase and rutile phases of TiO_2. The presence of voids in the sol-gel deposited films is shown to influence the onset of the pressure-induced phase transformations. Vibrational data also indicate an increase in compressibility for sol-gel films over the bulk material.

2. Experimental

Dielectric films were deposited on silica substrates using both reactive sputter deposition and sol-gel techniques. Titanium dioxide was sputtered in an argon/oxygen atmosphere using a radio frequency discharge. Substrate temperature, gas composition, discharge power, and distance between substrate and the titanium target were varied to control the crystalline phase of the deposited material. Sol-gel films were deposited on silica substrates using spin-coating techniques. Ethanolic solutions of titanium ethoxide or titanium tetrachloride were used as starting solutions. Addition of HCl or other volatile chloride-containing specie such as a quaternary alkyl-ammonium chloride was used to force preferential growth of the rutile phase over the anatase phase, which resulted when no additional chloride ion was present.[4] Heat treatment at moderate temperatures induced removal of the volatile organic species and formation of a uniform film. Film thicknesses ranged from 200 to 1000 nm. Dielectric films were mechanically removed from the substrate for insertion into a diamond anvil cell for pressure studies.

The Raman scattering measurement is similar to that reported in the literature.[8] The pressure cell consisted of two Class II low fluorescence diamonds, each mounted in a hardened stainless steel holder of a Merrill-Bassett design.[9] A hole, 200 micrometers in diameter, was drilled into an inconel gasket (.5 mm thick) located between the flat diamond faces. Film samples were placed in the cavity along with a small crystallite of ruby, which served as the pressure sensor through known pressure-dependent frequency shifts of the 14,404 cm^{-1} R_1 laser-excited fluorescence lines. A 4:1 methanol/ethanol solution admitted to the cavity was used as the pressure medium. In order to verify hydrostatic conditions in the cell, the fluorescence bandwidth, doublet splitting, and intensity of the R_1 features were monitored. Raman spectra of samples mounted in the pressure cell were excited at normal incidence in a backscattering geometry using the Raman microprobe (Spex Model 1482). A long focal length, all-reflecting objective (Ealing, 36 power, 0.5 numerical aperture) allowed viewing inside the cell and imaging of the probe excitation (514.5 nm, 300 milliwatts) onto the sample. Scattered light was directed to a 0.85 meter Spex Model 1403 double spectrometer and analyzed in a photon-counting mode. A white light source on the far side of the diamond anvil cell allowed transmission spectra to be recorded as a function of applied pressure using the Raman spectrometer. Film integrity at high pressures was verified through the appearance of interference fringes in the transmission spectrum. Spectra were recorded at applied pressures from 1 bar to 100 kbar at 298°K.

3. Results and Discussion

Raman spectra of anatase (bulk powder) and a sol-gel processed TiO_2 film (0.2 micrometers thick) at an applied pressure of 70 kbar are shown in Figure 1

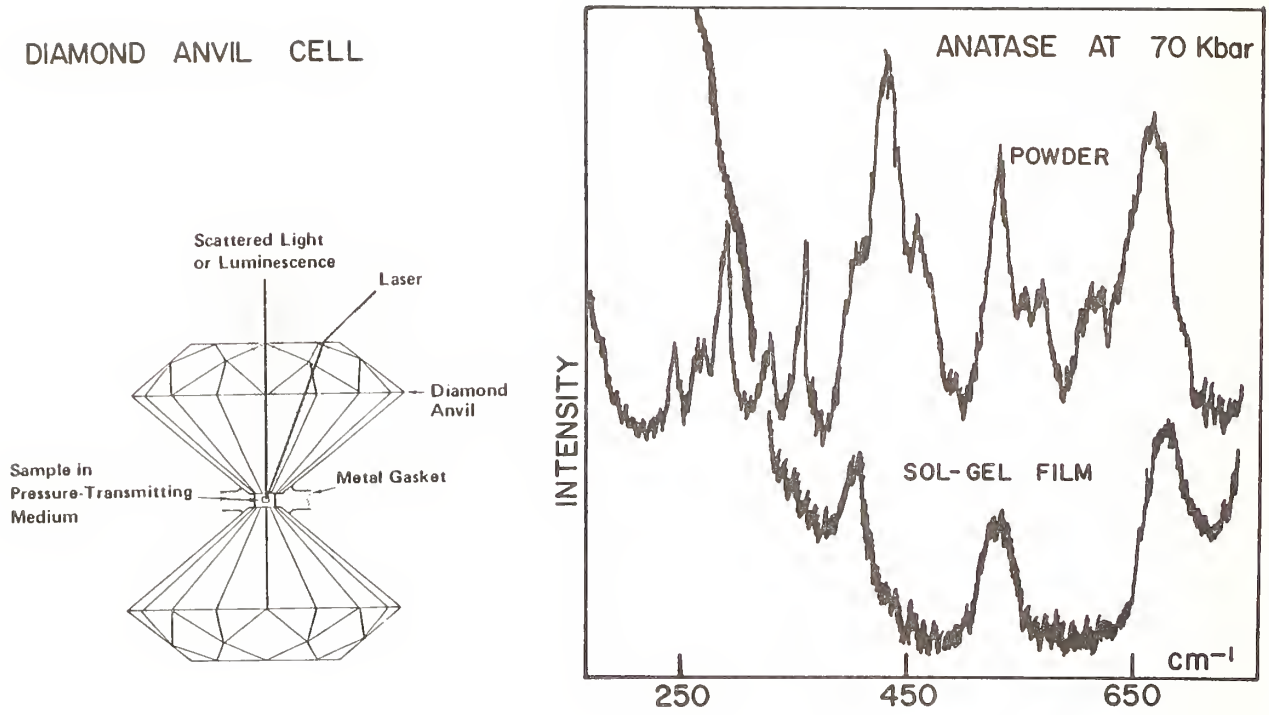

Figure 1. Raman spectra of bulk anatase and a sol-gel film at an applied pressure of 70 kbar in the diamond anvil cell show contrasting behavior.

along with a schematic diagram of the diamond anvil cell. The sol-gel film exhibits the same number of vibrational modes at a pressure of 70 kbar that is seen at 1 bar (ambient); however, the modes observed at high applied pressure are shifted to considerably higher frequencies. A different situation exists for the bulk material where band splitting and appearance of new vibrational modes, observed at elevated pressures, are indicative of a pressure-induced phase transformation. 5,10 Upon gradual release of pressure, the simple anatase spectrum is recovered and the film maintains its integrity, demonstrating the reversibility of the transition. Rapid release of pressure leads to disintegration of the film.

A sol-gel prepared rutile film also exhibits pressure-induced vibrational shifts to higher frequencies. In this case, vibrational bandwidths narrow as a function of applied pressure. The observed splitting of the 235 cm^{-1} mode into weak features at 254 cm^{-1} and 322 cm^{-1}, as seen in Figure 2, is indicative of a pressure-induced phase transformation. An applied pressure of ca. 64 kbar was necessary to induce the observed transformation. The reversibility of this transformation has also been observed. However, similar measurements performed on sputter-deposited rutile films at applied pressures up to 60 kbar show no evidence for this phase transformation; only pressure-induced frequency shifts of the Raman-allowed modes and line narrowing are seen. Single-crystal rutile material shows no evidence for a pressure-induced phase transition up to ca. 60 kbar. Previous work on rutile single crystals to much higher pressures indicates onset of a pressure-induced phase transformation at about 70 kbar. However, the observed transformation is very sluggish and irreversible, which may indicate second-order behavior on the basis of the time-dependence of the phenomenon. Sputter-deposited films are expected to undergo an analogous, albeit reversible, phase transformation.

Preliminary measurements seem to indicate that sputter-deposited titania films exhibit behavior that is similar to the bulk material in regard to presure-dependent phase transformation phenomena. The transformation behavior in sol-gel films is different from that seen in the bulk or single-crystal material, and the observed reversibility may be characteristic of the two-dimensional nature

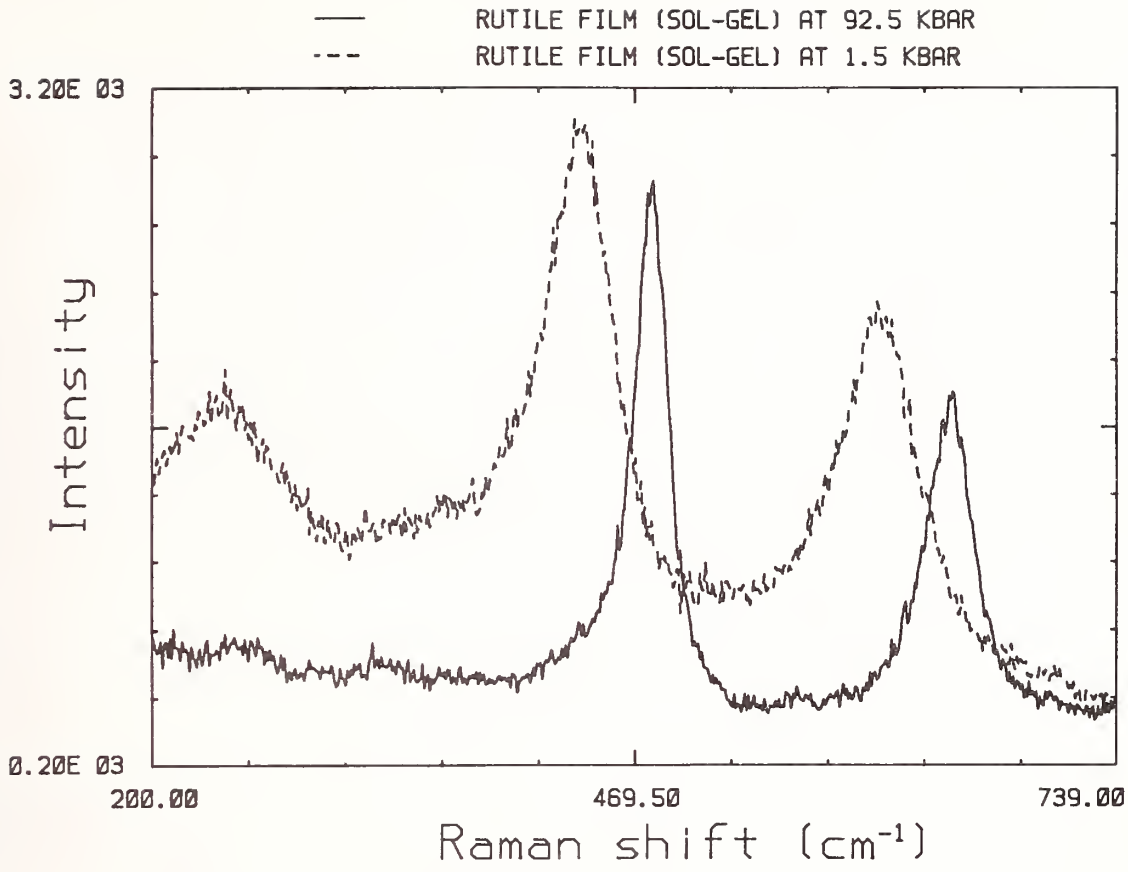

Figure 2. Raman spectra of a sol-gel prepared rutile film (1.0 micrometer thick) as a function of applied pressure.

of the films. This contrasting behavior warrants further consideration and is the subject of continuing work.

Relationships between the microscopic vibrational properties and macroscopic physical properties of condensed phase materials can be derived from lattice dynamics considerations.[11] The frequency variation (ω_i) of each allowed vibrational mode with applied pressure at constant temperature is proportional to the isothermal compressibility of the material (κ) according to equations (1) and (2).[11] The proportionality constant in these equations is the mode Grüneisen

$$(\delta w_i/\delta P)_T = \kappa\gamma_i\omega_i \quad (1)$$

$$(\delta \ln\omega_i/\delta P)_T = \kappa\gamma_i \quad (2)$$

parameter (γ_i), which varies for each vibrational mode. Therefore, the bulk compressibility can be determined from pressure-dependent measurements of molecular vibrational frequencies. Figure 3 illustrates this pressure variation for the two phases of titanium dioxide studied. Results are displayed for the 440 cm^{-1} E_g and 608 cm^{-1} A_{1g} modes of rutile, and the 143 cm^{-1} and 638 cm^{-1} E_g modes of anatase. The slope variations are attributed to differing values of the Grüneisen parameters, which are related to the anharmonicity of each mode.

All rutile phase materials investigated, including both sol-gel and plasma-vapor deposited films, exhibit the same dependence of mode vibrational frequency on applied pressure. This result implies that the bulk compressibilities for rutile films and single crystal are equivalent. A different result is seen for anatase phase materials. A larger frequency variation for the Raman-active modes with increasing pressure is observed for the sol-gel deposited

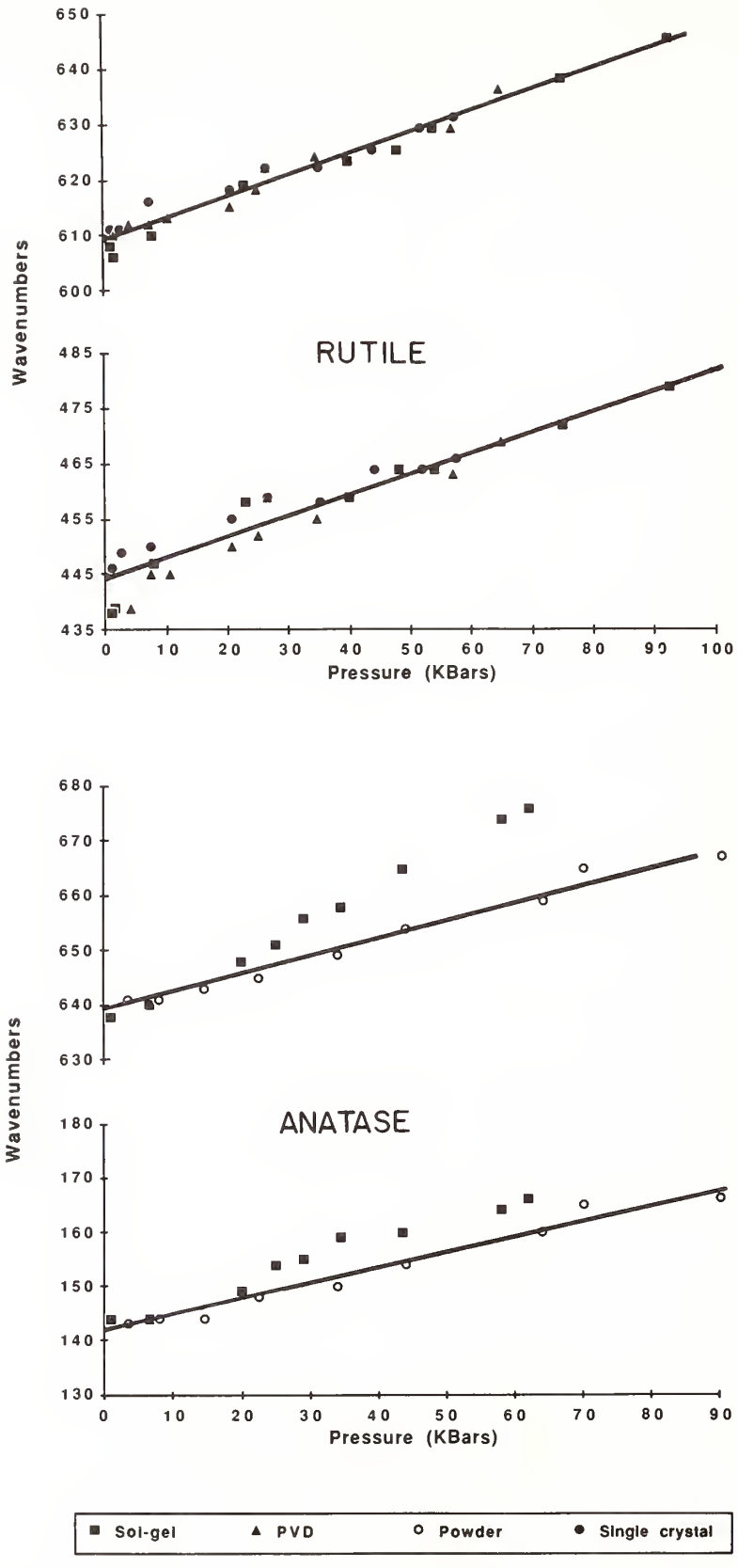

Figure 3. The pressure dependence of the two strongest vibrational mode frequencies for both anatase and rutile phases of thin film and bulk TiO_2.

film when compared with that exhibited by the bulk material. Results suggest that anatase sol-gel films are characterized by a higher compressibility than the bulk material.

This conclusion requires that thin film and bulk TiO_2 materials exhibit identical Grüneisen parameters for each particular allowed vibrational mode. Since this factor arises from anharmonicity in the vibrational potential energy well, invariance is expected, especially when considering highly localized vibrational modes. A qualitative indication of mode anharmonicity can be inferred from studies of vibrational linewidths as a function of applied pressure. The pressure dependence of the bandwidth at half-maximum for the A_{1g} rutile mode at 608 cm^{-1} and the E_g anatase mode at 638 cm^{-1} was determined for bulk crystals, plasma vapor-deposited films, and sol-gel deposited films. Figure 4 summarizes these results and indicates a similar pressure dependence of the linewidths for a specific vibrational mode. It is also noteworthy that the A_{1g} rutile mode narrows with increasing pressure, while the E_g anatase mode broadens over the same pressure range. This trend suggests that the anatase mode becomes more anharmonic at higher pressures while the rutile mode becomes more harmonic, which may explain the greater tendency of anatase to undergo pressure-induced phase transformations. The linewidth measurements support the contention that the Grüneisen parameter is invariant for a particular vibrational mode in a fixed crystalline phase. Thus, we have attributed the anomalous behavior of the

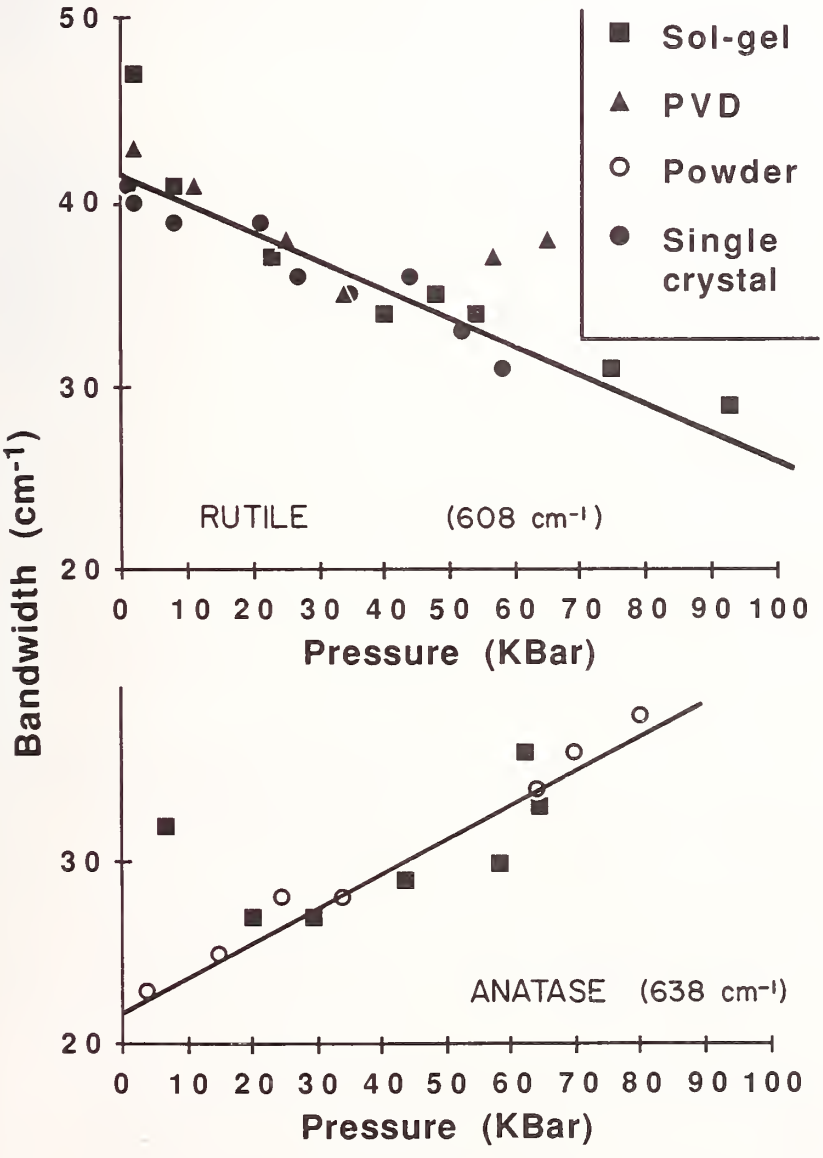

Figure 4. Linewidth variation as a function of applied pressure for anatase and rutile phases of TiO_2.

vibrational frequency variation with applied pressure in sol-gel anatase films to a greater compressibility of the material.

The higher compressibility of sol-gel deposited anatase films can be attributed to the presence of voids randomly distributed in the thin film. This lower density phase appears to be more susceptible to void formation during annealing. Indirect evidence of voids in such films is provided by pressure-dependent transmission measurements. In general, the fringe spacing allows film thickness (l) to be determined from the wavelengths corresponding to adjacent peak maxima or minima (λ_i) and the refractive index (n) of the film according to equation (3).

$$2\,nl = (\lambda_1 \cdot \lambda_2)/(\lambda_1 - \lambda_2) \qquad (3)$$

The variation in fringe spacing for plasma vapor-deposited rutile and sol-gel deposited anatase thin films is shown in Figure 5. A slight monotonic decrease in film thickness as a function of increasing hydrostatic pressure is observed for the high-density rutile phase film. The sol-gel anatase film again exhibits anomalous behavior and appears to increase in thickness to a pressure of about 35 kbar, and then decrease in thickness. This behavior can be explained in terms of displacement of air in the voids by the higher index pressure medium (alcohol), leading to an effective increase in film thickness due to the higher composite index. A critical pressure is reached when all air has been expelled from the voids and the film begins to compress. This model requires the presence of very small voids on the order of 10 angstroms or less. Microstructural studies are currently in progress to verify the presence of the proposed void structure and quantify average void size.

4. Conclusion

Raman spectroscopy has been used to probe perturbation of molecular structure in dielectric films resulting from inherent and applied stress. Frequency shifts in the allowed lattice phonon lines correlate with applied pressure and can be used to profile strain heterogeneity in thin films. By means of a diamond anvil cell, Raman microprobe measurements are reported that follow changes in the vibrational spectrum of titania films at pressures up to 100 kbar. Using the same arrangement, transmission spectra of the films can be obtained over the same pressure range.

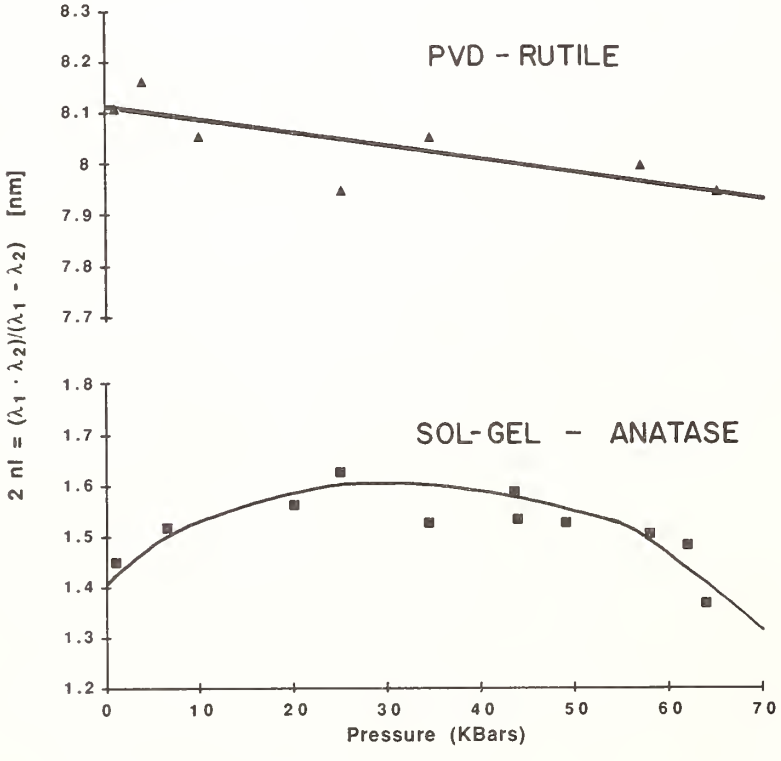

Figure 5. Relative change in film thickness with applied pressure.

Pressure-dependent vibrational spectra of plasma vapor-deposited rutile films exhibit vibrational frequency shifts and linewidth variations consistent with single-crystal behavior. Sol-gel deposited rutile films transform reversibly into a TiO_2-II structure at pressures above 70 kbar. A similar transformation is observed in bulk materials, but the relatively long time periods required for complete transformation to a phase isostructural with α-PbO_2 and the irreversibility of the transformation suggest a second-order phenomenon. An analogous phase transformation also has been observed in rutile crystals under nonhydrostatic conditions.[10,12] The microstructure associated with the sputter-deposition process may induce these films to behave in a nonhydrostatic manner. The two-dimensional nature of the thin film may offer lower impedance to propagation of the transformation throughout the film. Sol-gel deposited anatase films exhibit an anomalous pressure-dependent frequency response when compared with that of the bulk powder. These results suggest that the film is more compressible, resulting from an abundance of microscopic voids formed during processing. The presence of these voids is apparently responsible for suppressing the reversible pressure-induced phase transformation observed in the bulk material.

This work has been supported by the Materials Sciences Division of the Office of Basic Energy Sciences, U. S. Department of Energy. One of the authors (NJH) gratefully acknowledges support through a NORCUS (Northwest College and University Association for Science) fellowship.

5. References

[1] Exarhos, Gregory J. High-temperature Raman studies of phase transitions in thin film dielectrics. Mater. Res. Soc. Symp. Proc. 48:461-469; 1985.

[2] Exarhos, G. J. Raman determination of molecular structure and physical properties of dielectric coatings. J. Vac. Sci. Technol. A 4(6):2962-2968; 1986.

[3] Exarhos, G. J.; Friedrich, D. M. Raman microprobe characterization of dielectric films following high-energy pulsed laser irradiation. Microbeam Analysis--1987; San Francisco, CA: San Francisco Press, Inc.; 147-149; 1987.

[4] Exarhos, Gregory J. Raman characterization of molecular bonding and phase homogeneity in thin optical films. SPIE Vol. 678 Optical Thin Films II: New Developments; 51-58; 1986.

[5] Ohsaka, T.; Yamaoka, S.; Shimomura, O. Effect of hydrostatic pressure on the Raman spectrum of anatase (TiO_2); Solid State Commun. 30:345-347; 1979.

[6] Mukherjee, S. P. Sol-gel processes in glass science and technology; J. Non-Cryst. Solids 42(1-3); 477-488; 1980.

[7] Sakka, S. Sol-gel synthesis of glasses: present and future. Am. Ceram Soc. Bull. 674(11); 1463-1466; 1985.

[8] Hemley, R. J.; Bell, P. M.; and Mao, H. K. Laser techniques in high-pressure geophysics. Science 237(4815): 605-612; 1988.

[9] Merrill, L.; Bassett, W. Miniature diamond anvil pressure cell for single-crystal x-ray diffraction studies. Rev. Sci. Instrumen. 45: 290-294; 1974.

[10] Hara, Y.; Nicol, M. Raman spectra and the structure of rutile at high pressures. Phys. Stat. Sol. (b) 94: 317-322; 1979.

[11] Samara, G. A.; Peercy, P. S. Pressure and temperature dependence of the static dielectric constants and Raman spectra of TiO_2 (rutile). Phys. Rev. B. 7(3) 1131-1148; 1973.

[12] Mammone, J. F.; Sharma, S. K.; Nicol, M. Raman study of rutile (TiO_2) at high pressures. Solid State Commun. 34: 799-802; 1980.

A questioner asked if in the hydrostatic pressure measurements account was taken of the change in refractive index of the sample with pressure as well as dimensional changes. The presenter replied yes.

To the question of "what does it all mean" the author replied that among other things the presence of voids in the films seems to prevent a phase transformation. One of the cause they suspect for radiation damage to the coatings seems related to a phase transformation. If one can design a film with voids in it one may be able to suppress this radiation damage mechanism. Perhaps this result explains why some of the sol gel films appear to give higher damage thresholds than other types of film structures. Why the voids repress the phase transformations is not clear yet.

It was suggested that perhaps the grain size also affected phase transformations and might explain sol gel film behavior.

Optical Measurements of Surface Oxide Layer Formation on Metal Films

Marion L. Scott

Materials Science and Technology Division
Los Alamos National Laboratory
Los Alamos, NM 87545

Manuscript Received
12-1-87/sar

We have employed two optical techniques which give complementary indications of the formation of monolayers of oxide on freshly evaporated aluminum and silicon thin films. Visible ellipsometry is utilized to observe the growth of the initial monolayer of oxide on these films. From these data, we deduce the pressure and coverage dependence as well as the growth rate for the initial monolayer arising from these surface reactions. In addition, extreme ultraviolet (XUV) reflectance vs angle of incidence measurements at 58.4 nm wavelength clearly indicate the growth of oxide on the surface of our freshly deposited aluminum and silicon films as well. We have utilized this reflectance data to deduce the optical constants of aluminum and silicon at 58.4 nm. We find that previous XUV measurements of these optical constants were hampered by the presence of oxides. We also determined that the XUV reflectivity performance of aluminum films freshly deposited in our UHV system does not degrade appreciably when stored for four weeks in a helium atmosphere of 2×10^{-9} Torr.

Key words: aluminum; ellipsometry; oxidation; reflectance; silicon; UHV films; XUV.

1. Introduction

Applications for XUV grazing incidence reflectors range from resonator mirrors for an XUV free-electron laser to imaging optics for XUV photolithography and synchrotron optics [1,2]. These applications can take advantage of the total-external-reflectance (TER) which occurs for aluminum and silicon in the extreme ultraviolet (XUV). The performance of these grazing incidence reflectors can be significantly degraded by the presence of oxide surface layers that form on the thin film reflectors when they are exposed to the atmosphere [3-8]. We have undertaken a study of the formation of surface oxide layers that form on aluminum and silicon thin films deposited in our ultra-high vacuum (UHV) deposition system [9]. We utilize in situ visible ellipsometry to observe the time evolution of the surface oxidation and in situ XUV reflectometry to determine material optical constants and the loss of XUV reflectance from the oxidized surface.

2. UHV Deposition and Analysis Chamber

Our UHV chamber is capable of a base pressure of 2×10^{-10} Torr when it is fully baked at 200°C for 24-48 hours. The pumps on the system are oil-free (sorption/ion/cryo pumps) to avoid any problems with carbon contamination. Heating of our chamber is accomplished with a combination of quartz lamps inside the chamber and external heating tapes. The electron beam source and quartz crystal thin film thickness monitor are water cooled. The pump down sequence for this chamber, which includes a bakeout, requires one and a half to two days. The chamber is illustrated schematically in figure 1.

A 7.5 cm diameter silicon substrate is attached to an adjustable sample holder which can be translated in three orthogonal directions and rotated about the plane of incidence for ellipsometry and reflectance measurements. The material in the shuttered e-beam source is evaporated onto the substrate with the film thickness controlled by a quartz crystal monitor.

3. Visible Ellipsometer

The in situ visible ellipsometer employed on our UHV chamber is a Gaertner model L104ALC, rotating analyzer, automated ellipsometer with a helium-neon laser light source. The source and detector modules of the ellipsometer are located outside the UHV chamber and view the sample through fused silica windows. In order to avoid problems with stress and temperature induced birefringence in the fused silica windows, we utilized a differential measurement of the ellipsometric parameter delta. Thus, only changes in delta were used to calculate the change in surface oxide layer thickness.

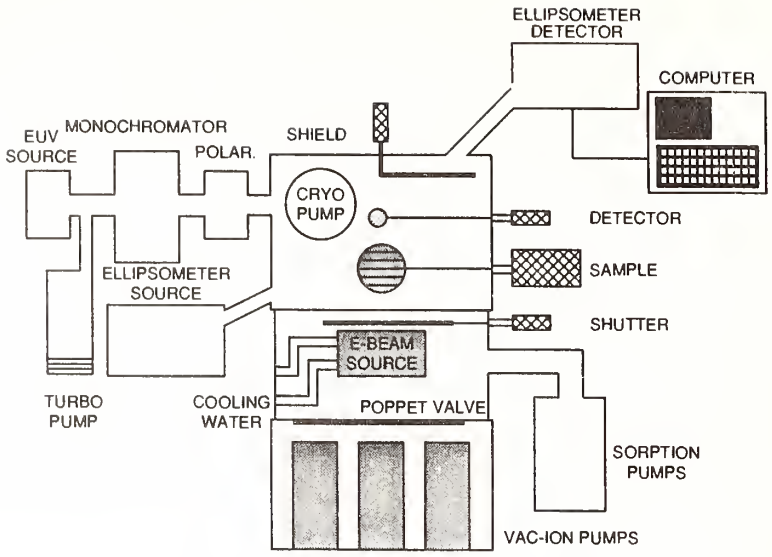

Figure 1. Schematic drawing of our UHV deposition and analysis system. All vacuum pumps are oil-free. The in situ visible ellipsometer and XUV reflectometer are used to measure the oxidation of freshly evaporated films.

3.1 Aluminum Film Oxide Layer

The growth of a monolayer of oxide on the surface of a thin film is adequately modeled by the time evolution of the fractional coverage parameter Θ, given by

$$\frac{d\Theta}{dt} = R*P*(1-\Theta)^n \qquad (1)$$

where R is the rate constant, P is the pressure, n is the order parameter, and t is the time. The ellipsometer data for aluminum exposed to 2×10^{-8} Torr of oxygen is given in figure 2a and the solid curve is a fit of eq. (1) to this data. The value for R found from this fit is 2.89×10^{6} [monolayers/Torr*min]. In addition, we find that the order parameter n = 1, which implies that this is a first order reaction. Another set of data which was taken on aluminum exposed to 1×10^{-8} Torr of oxygen is given in figure 2b and the solid curve is calculated from eq. (1) with the rate constant and order parameter deduced from the previous experiment. The fit to the data in figure 2b is good, which indicates that the linear pressure dependence in eq. (1) is correct for this reaction. The measured rate constant for aluminum indicates a sticking coefficient of .05, which means that only 5 out of 100 oxygen molecules that strike the fresh aluminum surface "stick" to the surface.

A second set of ellipsometric experiments was performed on fresh aluminum exposed to water vapor instead of oxygen. The results of these experiments are indicated in figures 3a and 3b for water vapor pressures of 2×10^{-8} Torr and 1×10^{-8} Torr, respectively. These data also fit equation (1) using the same rate constant and order parameter that were obtained for the oxygen data. However, there is a time delay at the start of the reaction for water vapor. The time delay scales linearly with the pressure as can be seen from these two figures. This time delay may be caused by the formation of initial nucleation sites before the aluminum surface reaction can proceed.

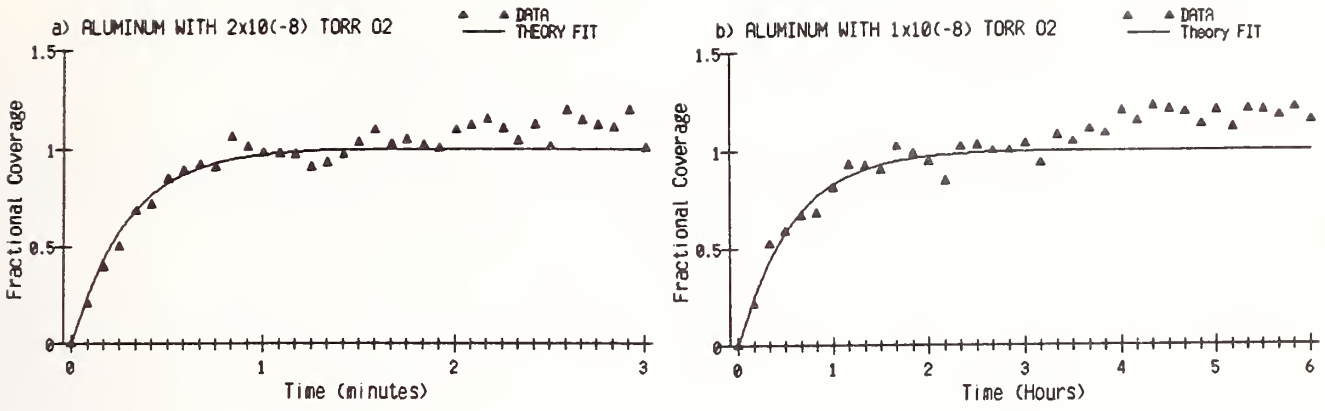

Figure 2. The growth of a monolayer of oxide on a freshly deposited aluminum film exposed to a) 2 x 10^{-8} Torr and b) 10^{-8} Torr of oxygen is shown in this ellipsometer data. The solid curves are calculated from a fit of eq. (1) to the data in a) and this fit yields the parameters given in the text.

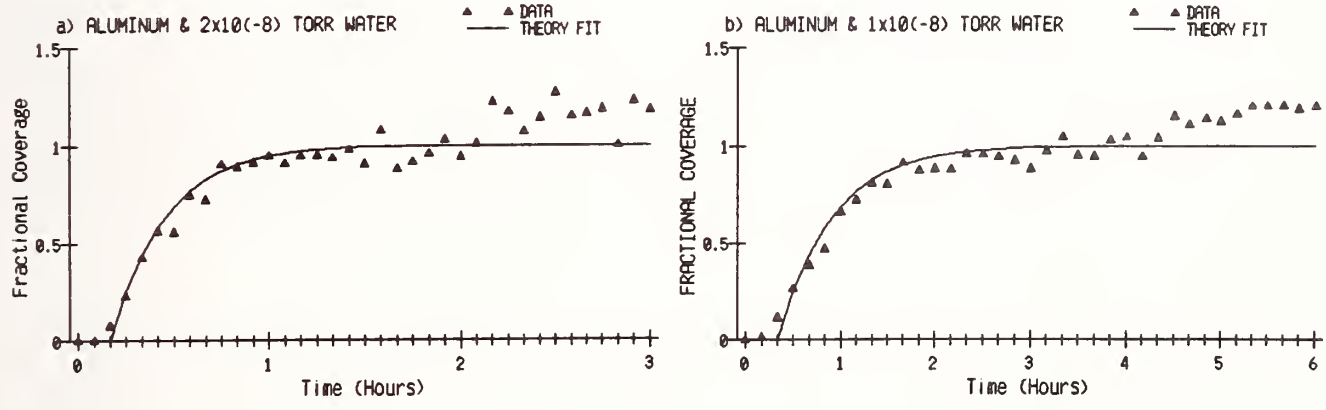

Figure 3. The growth of a monolayer of oxide on a freshly deposited aluminum film exposed to a) 2 x 10^{-8} Torr and b) 10^{-8} Torr of water vapor is shown in this ellipsometer data. The solid curves are calculated with eq. (1) using parameters fit to the data in figure 2a with the addition of a time delay at the beginning of the run.

3.2 Silicon Film Oxide Layer

We have evaporated silicon films onto specially prepared silicon substrates in a manner analagous to the experiments performed with aluminum. The special preparation of the substrates involved evaporating aluminum films, which were subsequently oxidized, onto the silicon substrates. Unlike aluminum, silicon is relatively transparent to the 632.8 nm HeNe ellipsometer source and this preparation was required to enhance the sensitivity of the ellipsometer to the formation of silicon oxide on the surface of freshly deposited silicon.

The results of our ellipsometer measurements of oxide growth on silicon are indicated in figures 4a and 4b for oxygen pressures of 1 x 10^{-7} Torr and 5 x 10^{-8} Torr, respectively. The indicated fit of eq. (1) to these data yields a rate constant R = 6.3 x 10^{5} [monolayers/Torr*min] and linear pressure dependence. The order parameter for the silicon/oxygen reaction is found to be 2, which indicates that this is a second order reaction.

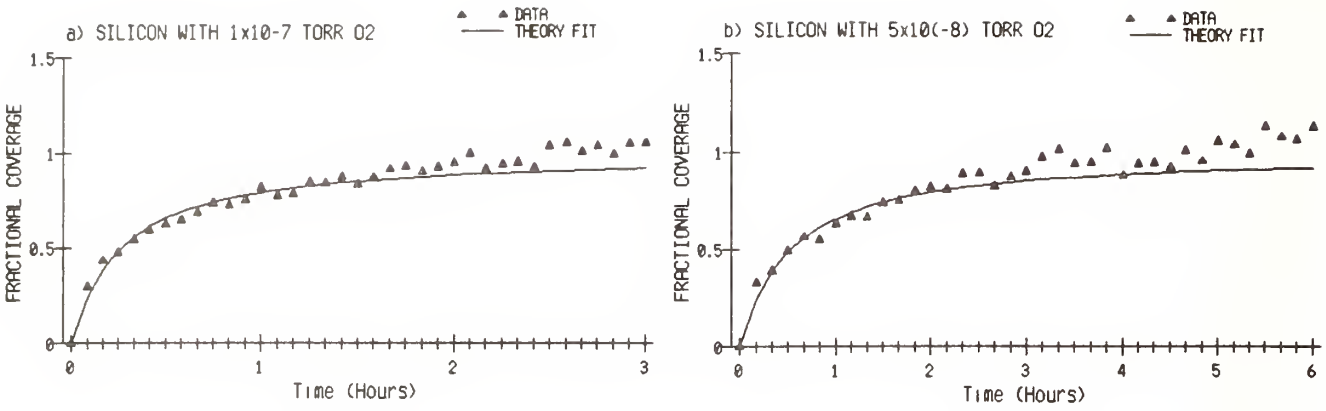

Figure 4. The growth of a monolayer of oxide on a freshly deposited silicon film exposed to a) 10^{-7} Torr and b)5 x 10^{-8} Torr of oxygen is shown in this ellipsometer data. The solid curves are calculated from a fit of eq. (1) to the data in a) and this fit yields the parameters given in the text.

4. XUV Reflectometer

The in situ XUV reflectometer, which is an integral part of our UHV vacuum chamber, consists of a capillary discharge source, a simple grating monochrometer, an imaging microchannel plate detector, and a sample holder with several degrees of freedom (our XUV polarizer was not used in these measurements). The detector and sample can be rotated about the plane of incidence in order to measure reflectance vs angle of incidence. The sample can also be positioned in x,y,z translations for proper alignment. There is no window between the gas discharge source and the UHV chamber due to the excessive absorption of XUV photons that would be caused by such a window. The error in our XUV reflectance measurements is estimated to be ±2% of the measured value.

4.1 Aluminum Film Reflectance

Reflectance vs angle of incidence measurements were performed on a freshly evaporated aluminum film at 58.4 nm in our UHV system. In addition, we exposed the sample to sufficient oxygen in our chamber to form a monolayer of surface oxide and we then remeasured the reflectance. Finally, we vented the chamber to air for about 35 minutes before pumping the chamber down again and remeasuring the reflectance. The results of these measurements are given in figure 5. The calculated curves in figure 5 utilized previously published optical constants for the oxides of silicon and aluminum [10,11]. The optical constants for the aluminum were fit to the reflectance data for the fresh aluminum film and then used in all three calculated curves. The optical constants derived from this analysis are given in table 1. The constants given in the column labeled "old" are from reference 10.

The reflectance data in figure 5 indicate that there is a strong total-external-reflectance (TER) effect in aluminum at 58.4 nm wavelength. In addition, this data indicates that a surface oxide layer has a very serious degrading effect on the XUV reflectance of aluminum films.

4.2 Silicon Film Reflectance

We measured the reflectance vs angle of incidence at 58.4 nm for a freshly deposited silicon film as shown in figure 6. We then performed surface oxidation and reflectance measurements on this silicon sample similar to those already described for aluminum. The optical constants of the oxide layers were obtained from published values as in the aluminum case [10,11]. The optical constants for silicon were obtained from a fit to the reflectance data from the freshly deposited film and these constants were used in the three calculated curves in figure 6. The optical constants obtained from this work are compared to previously published values in table 1.

The XUV reflectance of silicon shows a pronounced TER effect that is not quite as dramatic as that of aluminum due to the higher absorption of silicon (see k values in table 1). It is

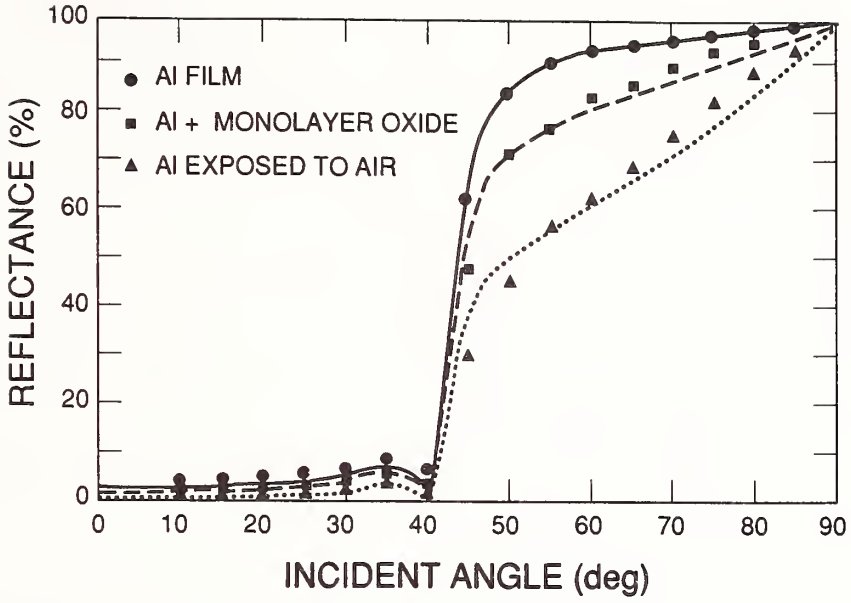

Figure 5. Reflectance vs angle of incidence for an aluminum film at 58.4 nm wavelength. The solid line is calculated for aluminum that is oxide-free (corresponding to the ● data). The dashed line is calculated for aluminum with one surface monolayer of oxide (corresponding to the ■ data). The dotted line is calculated for aluminum with three surface monolayers of oxide (corresponding to the ▲ data).

Table 1. Optical constants at 58.4 nm

Material		Old	This Work
Aluminum	n	0.715	0.700±0.005
	k	0.024	0.010±0.002
Silicon	n	0.637	0.637±0.005
	k	0.054	0.042±0.003

also evident from these reflectance measurements that the presence of surface oxide on silicon degrades the XUV reflectance but not as dramatically as the aluminum case.

5. Reflector Lifetime

The lifetime of a UHV aluminum reflector can also be evaluated with the XUV reflectance measurement outlined in this paper. In order to accomplish this measurement, we overcoated the oxidized aluminum sample with a fresh layer of aluminum in the UHV system. We measured the reflectance vs angle of incidence for this fresh film (indicated in figure 7) and then allowed the film to sit in the UHV chamber for 4 weeks. The pressure in the UHV chamber during this life test was greater than 2×10^{-9} Torr (mostly helium from our XUV source). After the four weeks of elapsed time, the reflectance was remeasured and this result is given in figure 7. We were very pleased to observe that the reflectance degradation during this life test was minimal.

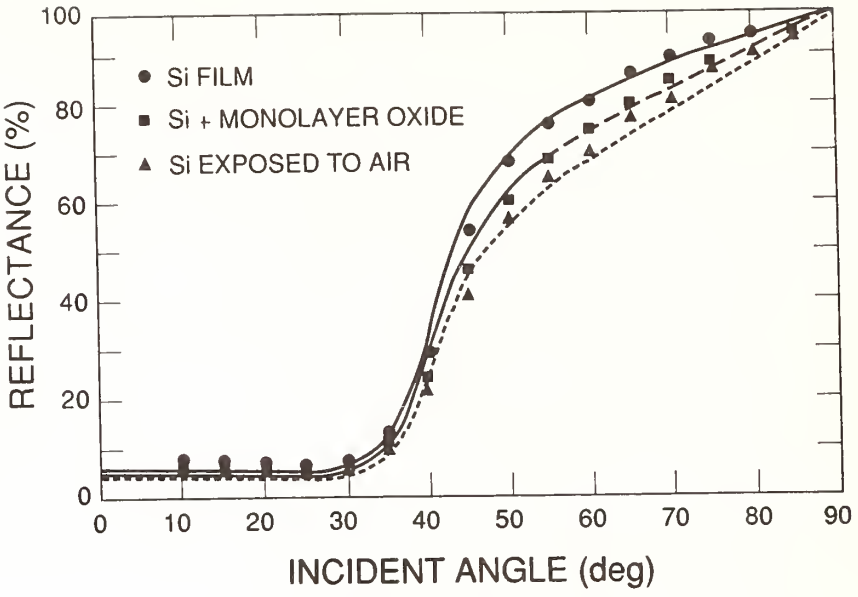

Figure 6. Reflectance vs angle of incidence data for a silicon film at 58.4 nm wavelength. The solid line is calculated for silicon that is oxide-free (corresponding to the ● data). The dashed line is calculated for silicon with one surface monolayer of oxide (corresponding to the ■ data). The dotted line is calculated for silicon with two surface monolayers of oxide (corresponding to the ▲ data).

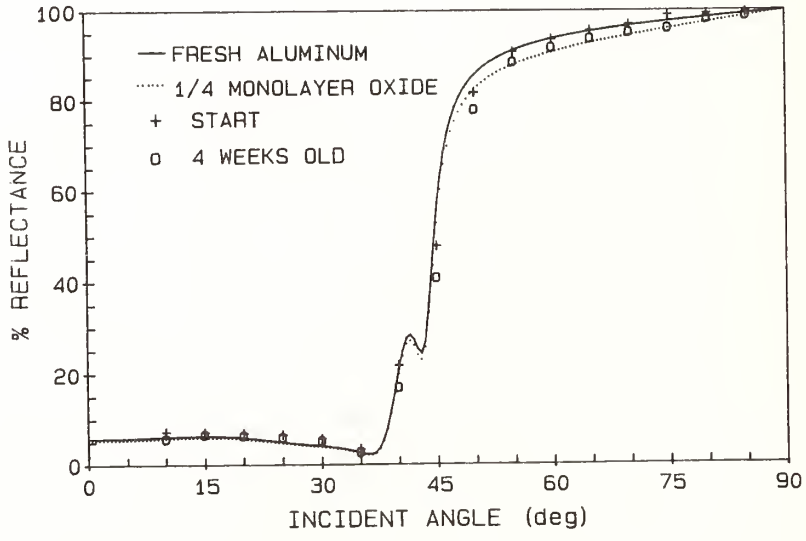

Figure 7. Reflectance vs angle of incidence for a fresh aluminum film overcoating a previously deposited and oxidized aluminum film (solid line and + data). This same film is measured again after four weeks in our UHV system at a helium pressure of 2×10^{-9} Torr or greater (dotted line and o data). The interference effect seen between 35° and 45° is due to subsurface reflections from the substrate and overcoated aluminum plus oxide layers.

6. Conclusions

The formation of surface oxides on aluminum and silicon films freshly deposited in an UHV system have been observed with visible ellipsometry. A monolayer of surface oxide forms on the aluminum when exposed to sufficient oxygen or water vapor with a sticking coefficient of .05 in each case. There is a significant time delay before the start of the formation of the oxide monolayer for water vapor, whereas there is no delay in the case of oxygen exposure. Similarly, a monolayer of surface oxide forms on fresh silicon, when exposed to a sufficient quantity of oxygen, with a .01 sticking coefficient. Silicon does not form an oxide in our UHV chamber when exposed to water vapor pressures as high as 10^{-4} Torr.

XUV reflectance vs angle of incidence measurements on aluminum and silicon films freshly evaporated in our UHV chamber and subsequently exposed to oxygen indicate substantial reductions in reflectance caused by the oxide. Optical constants determined by our measurements indicate lower absorption values for both aluminum and silicon than previously published values. The lower values of the absorption index k obtained in this study are probably due to the high purity of the starting material and the lack of any oxidation during the deposition in our UHV chamber.

A four week life test for an aluminum reflector indicated that minimal degradation of the reflectance occurs when the mirror is kept in an UHV system with minimal oxygen and water vapor partial pressures.

The authors would like to acknowledge the financial support provided to this project by the Institutional Research and Development funds of the Los Alamos National Laboratory.

7. References

[1] Atwood, D. T., ed., Short wavelength optics for future free-electron lasers, AIP Conf. Proc. Proc. 118, 294 (1984).

[2] Newnam, B. E., Multifaceted metal mirror designs for soft x-ray and EUV free-electron laser resonators, in Laser induced damaged in optical materials: 1985, eds. H. E. Bennett, A. H. Guenther, D. Milam, and B. E. Newnam NBS Spec. Pub. to be published (1987).

[3] Scott, M. L., P. N. Arendt, B. J. Cameron, B. E. Newnam, D. Windt, and W. Cash, Extreme ultraviolet multilayer reflectors, in Short wavelength coherent radiation: Generation and applications, AIP Conf. Proc. 147, 260 (1986).

[4] Johnson, E. D., S. L. Hulbert, R. F. Garrett, G. P. Williams, and M. L. Knotek, In situ reactive glow discharge cleaning of optical surfaces, Rev. Sci. Instrum. 58(6), 1042 (1987).

[5] Scott,, M. L., P. N. Arendt, B. J. Cameron, R. Cordi, B. E. Newnam, D. Windt, and W. Cash, Metal reflectors in the EUV, SPIE 691, 20 (1986).

[6] Hartmann, H., R. Nord, H. Schwille, and E. Bachor, ROSAT experience on x-ray optics contamination, SPIE 733, 210 (1987).

[7] Burkett, W., B. Aschenbach, and H. Brauninger, Effects of mirror contamination observed in the ROSAT programme, SPIE 733, 217 (1987).

[8] J. P. Chauvineau, J. Corno, D. Decanini, L. Nevot, and B. Pardo, Characteristics of multilayered structures for soft x-ray mirrors, SPIE 563, 248 (1985).

[9] Scott, M. L., P. N. Arendt, B. J. Cameron, and B. E. Newnam, Contamination layers on EUV reflectors, SPIE 733, 156 (1987).

[10] Palik, E. D., ed., Handbook of optical constants of solids. Orlando: Academic Press; 1985. 804 p.

[11] H. J. Hageman, W. Gudat, and C. Kunz, Optical constants from the far infrared to the x-ray region: Mg, Al, Cu, Ag, Au, Bi, C, and Al_2O_3, DESY SR Report #74/7 (1974).

In response to a question the speaker commented that the partial pressures of oxygen and water vapor in his system are very low, in that 10-11 Torr range.

A second question was how to put a monolayer of oxygen on the metal studies? The speaker replied that they simply expose it to oxygen and monitor the oxide thickness using the ellipsometer.

A third question concerned the purity of the aluminum used in the deposition. The speaker replied that the aluminum was 99.999% pure, which may account for the low k value found. Another contributing factor may be that the evaporation was carried out in ultra high vacuum. With a conventional vacuum system it is almost impossible to avoid incorporating some oxide in the film.

Manuscript Received
3-4-88

The Properties of Laser Annealed Dielectric Films

Alan F. Stewart and Arthur H. Guenther
Air Force Weapons Laboratory
Kirtland AFB, NM 87117

Fred E. Domann
University of Wisconsin, Platteville
Platteville, Wisconsin 53818

ABSTRACT

The annealing of dielectric thin film coatings has been explored in an attempt to identify the potential benefits of this method of post deposition treatment. Single layer coatings fabricated using several different deposition techniques were annealed and subsequently characterized. All properties so determined evidenced substantial changes as a result of the annealing process. Film microstructure, optical absorption levels, and laser damage thresholds varied considerably with annealing power levels. Although oven annealing is known to improve the performance of certain types of multilayer films, significant improvements were seen only in certain films over a limited range of annealing conditions. As a consequence of this, there were changes in other important optical properties, which will be discussed as well.

Key words: laser annealing, thin films, optical properties, laser damage

I. Introduction

The process of annealing to affect improved material properties has a long established history. Steel and glass are annealed to improve their mechanical properties making them less brittle and more ductile. This is accomplished by careful control of the resultant microstructure, usually through thermal cycling which promotes uniform grain growth within the material [1]. The final properties of the material are quite sensitive to the specifics of the annealing cycle. A rapid quenching of heated steel results in a hard but durable material suitable for a fine edged sword. Longer cooling cycles result in steels with other characteristics and uses.

Semiconducting materials such as silicon have been annealed using lasers as well as by flashlamps. Typically, annealing of silicon results in epitaxial regrowth of the material allowing the use of additional treatment such as ion implantation which can leave residual damage in surface layers [2]. Usually, the annealing process has been found to remove crystalline defects which strongly affect the electrical properties of the material. Depending on the details of the process employed, impurities in the semiconductor can be forced to remain where they are, or can be caused to diffuse into the surrounding material in a controlled fashion.

Most all of the processes used to produce semiconductor and dielectric thin film coatings create films with extensive numbers of defects and measurable levels of impurities. In both optical and electronic applications, these defects and impurities define the yield or the ultimate utility. For semiconductor materials, more diagnostic techniques have been perfected and hence a greater number of defect types have been identified and studied. The low laser damage thresholds observed in optical thin film coatings have frequently been attributed to the presence of film defects, impurities, inclusions, or other inhomogeneities [3]. For dielectric films deposited under otherwise ideal conditions for a given process, these defects, inclusions, and impurities remain largely unidentified.

In addition to controlling or eliminating defects and impurities, laser processing of materials has permitted the controlled alteration of microstructure in several materials including fused silica, silicon, and metallic glasses [4-7]. Laser annealing or polishing of fused silica surfaces has resulted in high laser damage

thresholds through the removal of contaminants, the fusing of microcracks and/or the formation of unusual chemical bonding [4,5]. Picosecond pulses have been used to anneal silicon or metallic glasses resulting in direct phase transitions from crystalline to amorphous [6,7]. The potential for control of microstructure, in the bulk as well as at or near the surface of bulk materials, is obvious.

The intent of this study was to determine if beneficial changes could be induced in dielectric thin film coatings through a laser annealing process. The regrowth of a dielectric thin film coating into a more "defect free" structure was a potential objective of this study although we have no direct way of determining that the film was "defect free". Thus, for laser processed optical coatings, the transmission, reflection, scattering, damage threshold and absorption were measured. The observed changes provided us with only indirect information on the resultant microstructure, band structure and alteration or removal of defects.

The utility of annealing of dielectric films should not be based solely on the results of this work. A set of experimental conditions were selected based on the results of an earlier preliminary experiment and also on the convenience of the particular approach taken [8]. These conditions were held invariant throughout the experiment. However, it is clear that specific processing conditions would need to be developed for each material studied and each deposition process employed in the initial film fabrication. Additional work required to fully explore the utility of laser annealing might include annealing in different ambient atmospheres, annealing with various duty cycles, a direct comparison with oven annealing and an evaluation of the effects of the time factor in the heating and cooling cycles on resultant film properties including a complete thermal heat-flow analysis.

II. Experiment

To determine if laser processing could induce beneficial changes in dielectric films, a large number of samples were prepared, processed, and tested. The samples were selected to be representative of oxide dielectric films in common use. Where possible, films of a given material were prepared using more than one deposition process. These films were irradiated under controlled conditions and then extensively characterized.

Experimental conditions for the annealing process were selected to replicate the earlier work whenever possible [8]. As before, a large 15 kilowatt carbon dioxide laser was used at reduced power levels for this study. The 10.6 micron beam had a nearly uniform intensity profile and a diameter of 8.9 cm at the sample plane. Samples were scanned across the beam at 1.5 cm/sec resulting in a dwell time of 5.9 sec.

Two significant improvements over the earlier work were implemented in this study. Samples were held by a vacuum chuck assembly during translation across the beam. This assembly, detailed in Figure 1, allowed for precise alignment of the sample surface during irradiation. Another advantage was that the sample holder provided a uniformly cool heat sink at the back surface of the sample. This feature was found to be especially important in the irradiation of the fused silica calorimetry/stress wafers which were only 0.25 mm thick. The original sample holder design for this size substrate had channels cut into its surface as shown in Figure 1. Upon irradiation, these channels left permanent signatures in the optical thickness of the dielectric film on the wafer. The redesigned holder, shown in Figure 1, provides suction only on the outside rim with a recessed interior resulting in uniformly annealed films over the central area.

The second improvement was real-time monitoring of sample surface temperatures during the experiment using an infrared camera system [9]. A complete thermal history of each sample was recorded on video tape. With this data, we attempted to replicate surface temperatures on calorimetry wafers that had been observed on full size samples. Typical power loadings used in the annealing process and the resultant surface temperatures are listed in Table 1.

Table 1. Power Loadings and Temperatures Recorded

1.5 and 2" SiO_2 substrates		1.0 " SiO_2 wafers	
25 W/cm2	380°C	10.5 W/cm2	370°C
50	660	13.3	600
75	900		
100	1250		

The annealing process, as described here, is a surface treatment, although both the coating and the substrate are affected. The temperature dependence of the penetration depth of 10.6 micron light in fused silica has been measured [10]. At room temperature, the penetration depth is 34 microns and decreases to 4 microns at 1800°C. Given the high absorption of fused silica, and the 200-400 nm thickness of the coating, the infrared camera system measured temperatures representative of the ambient coating temperature.

III. Samples

Single layer dielectric coatings were deposited on fused silica substrates with a 1/2 wave optical thickness at 1064nm. The 1.5" and 2" diameter substrates were superpolished by a commercial firm for ultralow scatter/roughness surfaces. Stress wafers were included in the sample set for calorimetry and film stress measurements. Scattering levels were measured on a selected group of the larger substrates and then all were coated.

Three deposition processes were selected for study - electron beam, reactive sputtering, and sol gel. The sample set and representative film properties are described in Table 2. Electron beam coatings of Al_2O_3 and Ta_2O_5 were prepared by the Developmental Optics Facility [11]. A second set of Al_2O_3 and Ta_2O_5 films were prepared using reactive sputtering at Battelle, Pacific Northwest Laboratories [12]. TiO_2 sol gel coatings were prepared at Lawrence Livermore National Laboratory [13]. Except for the sol gel coatings, which were prepared individually, all films of the same type were deposited at the same time during the same coating run. All films received were of excellent quality with few blemishes noted upon visual inspection.

Table 2. Thin Film Coating Samples[1]

Deposition Process	Film Material	Refractive Index[2]
Electron Beam	Al_2O_3	1.63
	Ta_2O_5	2.01
Reactive Sputtering	Al_2O_3	1.64
	Ta_2O_5	2.13
Sol Gel	TiO_2	1.8

1) Nominally $\lambda/2$ at 1064 nm.
2) At 633nm, from spectrophotometric data.
3) Film thickness selected for T max at 500nm.

Prior to irradiation, all films were measured in a spectrophotometer for transmission over the range of 190 to 800 nm[14]. The coating uniformity measured was almost as good as the measurement uncertainty of 0.5%. In addition, the scattering levels of selected films were measured for comparison with the uncoated substrates.

Each sample was clensed prior to irradiation using a spin cleaning system which dispensed spectroscopic grade methanol followed by a nitrogen blow off. Collodion was then applied to the coated surface and stripped off with tape. Finally, samples were stored in sealed containers before mounting on the vacuum chuck assembly for processing.

Power levels used for sample irradiation were selected after analysis of data obtained on an initial series of samples which were irradiated at 25, 50, 75 and 100 W/cm2. Spectrophotometer transmission curves were compared with pre-test data. It

was observed, as in the preliminary work, that the optical transmission of annealed coatings steadily diminished for samples irradiated at power levels above 50 W/cm2. At 25 and 50 W/cm2, changes in the optical transmission were small, but measurable, and appeared to be potentially beneficial. Therefore, the remaining samples were irradiated at 25 and 50 W/cm2.

IV. Post-Irradiation Characterization

After annealing, the treated films were analyzed using a number of techniques. Characterizations performed included optical transmission, ellipsometry, x-ray diffraction, stress, optical absorption at 351nm, laser damage testing at 1064nm, and surface scattering at 633nm. All measurements except surface scattering were performed at the Air Force Weapons Laboratory.

Spectrophotometric Data

Optical transmission was measured on annealed films and then compared with data from the virgin samples. As in the earlier study, changes were observed in the transmission curves which indicated a modification of the films optical thickness. Data recorded from samples irradiated at 50 W/cm2 is summarized in Table 3. In contrast to the earlier work, transmission maxima at the halfwave points were observed to shift to shorter as well as longer wavelengths. Shifts of a few nm were observed to occur in both directions even within a given sample set. For some samples, an increased modulation depth was observed in the transmission scans indicating a larger refractive index. In most scans, the overall transmission of the samples was lower after irradiation. For power levels of 75 and 100 W/cm2 it was observed consistently that film transmission levels were greatly reduced at shorter wavelengths. Further analysis of these scans as per reference 15 provided refractive index data for the annealed films which was compared with ellipsometric data.

Table 3. Summary of Spectrophotometric Data from Samples Annealed at 50 W/cm2.

Sample	λ_{hw} Shift UV	IR	Modulation Depth	Transmission at UV edge (% Change)
Al_2O_3, e.b.	20 ← - 40 nm		(λ)[3]	-2 - -6%
Ta_2O_5, e.b.	6 ← - → 10 nm		(λ), ↑	-2 - -4%
Al_2O_3, r.s.	2 - → 10 nm		(λ), ↑	+0.5 - 1%
Ta_2O_5, r.s.	2 - → 10 nm		↓	NC
TiO_2, sol	NA		NA	-4%

1) Transmission maxima or half wave points.
2) Modulation depth is related to refractive index.
3) Varies with wavelength.

Transmission data recorded on reactive sputtered Ta_2O_5 films annealed at each power level appears in Figure 2. Shifts of the transmission maxima towards longer wavelengths are clearly in evidence for each annealed film. At the higher power levels, this shift is nearly 40nm. The transmission for films annealed at the higher power levels is reduced by up to 15% at the shorter wavelengths. Because of this sharp reduction in film transmittance, it is difficult to be certain from Figure 2 that the modulation depth, and hence the refractive index, is altered in the transmission scans of the annealed films. Film refractive indices obtained from these curves are plotted in Figure 3 and a small decrease in index with increasing anneal power level is apparent.

Data obtained on reactive sputtered films of Al_2O_3 differed in some respects. As in the Ta_2O_5 data, shifts were observed in transmission maxima towards longer wavelengths by 2-10nm. In the other distinguishing features of these scans, these two film materials behaved quite differently. The transmission scans for the Al_2O_3 films showed a slightly increased modulation depths consistent with an increased refractive index. However, the modulation depth and the spacing of the transmission maxima changed with wavelength after annealing. As plotted in Figure 4, refractive indices dropped slightly before increasing for the film irradiated at 100 W/cm2. In

Al_2O_3 films, the UV cutoff shifted towards shorter wavelengths with higher transmissions overall in this region.

The data obtained on electron beam deposited coatings of Ta_2O_5 and Al_2O_3 indicated that these films were susceptible to significant thickness changes due to the annealing process. Ta_2O_5 films processed at 50 W/cm2 or higher experienced shifts of transmission maxima towards the UV by 6-10nm. Unirradiated control samples were observed to shift in the opposite direction, i.e., towards the IR by 2-4nm in comparing pre and post annealing transmission scans. The modulation depth in these transmission scans increased although the overall transmission was reduced by 6-20% at the shorter wavelengths. In addition, the modulation depth was seen to change with wavelength in the data for these coatings - a disturbing feature for a single layer film discussed in Appendix A. Refractive index data taken from these scans is plotted in Figure 5.

Annealing of the Al_2O_3 films fabricated by electron beam deposition resulted in crazing of the films annealed at 50 W/cm2 or higher. Films annealed at 25 W/cm2 survived and had 6% higher transmission at 220nm. However, these films also exhibited a modulation depth which varied with wavelength. As the majority of these films did not survive the annealing process, only the absorption could be measured on wafer samples.

Analysis of the TiO_2 sol gel films from spectrophotometric data is somewhat different, since the usual thin film interference modulation pattern does not appear. The transmission scans recorded show only a peak in the transmission near 500nm with a cut-off at 320nm. After annealing, the TiO_2 sol gel films had lower peak transmittances by 4% or more for films irradiated at 50 W/cm2 or higher. A small shift towards the UV was also observed in the transmission maxima at the higher power levels.

Ellipsometry Data

Films annealed at all power levels were analyzed using ellipsometry. A standard commercial ellipsometer operating at 633nm was used for testing the complete set of annealed films [16]. Unfortunately, data obtained on the TiO_2 sol gel films could not be analyzed with our current modelling capabilities. The remaining films were measured, and the data is plotted along with the spectrophotometric data in Figures 3-5. A consistent increase in the refractive index of the electron beam deposited Ta_2O_5 was measured along with a slightly increasing film thickness. The opposite trend was measured in Ta_2O_5 deposited using reactive sputtering. Reactive sputtered Al_2O_3 films did not change significantly in either refractive index or thickness according to the ellipsometry data.

The apparent inconsistency between refractive indices, obtained from ellipsometric and spectrophotmetric data in Figures 3-5, is due to the difficulty of modelling inhomogeneous films. Significant progress has been made recently in analysis of spectrophotometric and ellipsometric data incorporating a model of an inhomogeneous film structure [Appendix A]. While either data set may be off in absolute magnitude, the trends in the derived refractive indices are replicated for the most part.

Film Scattering Measurements

A selection of films irradiated at 25 and 50 W/cm2 and appropriate controls were evaluated using a variable angle scatterometer at the Air Force Avionics Laboratory [17]. Samples were evaluated three times - as bare surfaces, coated surfaces and after annealing. The scattering levels obtained on the uncoated substrates provided an average value of 40 PPB/steradian - a very smooth surface in comparison to conventionally polished optics which normally exhibit scattering at the 1 PPM/steradian level[17]. After coating deposition, average levels increased by a factor of 100. After annealing, the average scattering levels recorded on films annealed at 25 and 50 W/cm2 did not change significantly. This data verified total integrated scatter data recorded in the preliminary study[8]. Films annealed at higher power levels were crystallized and scattering levels for these films were two to four orders of magnitude higher.

X-Ray Diffraction Data

An x-ray diffractometer was used to determine the crystalline structure of the films used in this study. Control samples and films irradiated at power levels up to 50 W/cm2 appeared to be completely amorphous with no visible structure. With one exception, coatings showed some evidence of crystallization after annealing at power levels of 75 and 100 W/cm2.

Sputtered and electron beam deposited Ta_2O_5 coatings crystallized into the orthorhombic structure. Data taken on films irradiated at 100, 75, 50 W/cm2 and a control is plotted in Figure 6. Diffracted intensities did not change significantly between samples irradiated at 75 and those irradiated at 100 W/cm2.

The structural modification of Al_2O_3 coatings could not be detected by x ray diffraction even on samples irradiated at the highest annealing power levels. Films fabricated by reactive sputtering survived the highest annealing powers and scattered light intensely. However, no definitive peaks appeared in the x-ray data.

The TiO_2 sol gel films, which were initially amorphous, became polycrystalline at high annealing powers. Raman spectroscopic analyses provided by Dr Greg Exarhos of Battelle verified the formation of anatase and rutile bonding in these films. X-ray diffraction data proved to be unreliable and may indicate that the technique is sensitive to the unusual microstructure of sol gel films.

Film Stress

Residual stress in coatings deposited on fused silica stress wafers was inferred from an interferometric technique which determined the flexure of each substrate wafer [18]. An increase in compressive stress with film annealing was observed only in Ta_2O_5 films. Data recorded on several wafers annealed at each power density has been averaged and is plotted in Figure 7 for electron beam and reactive sputtered Ta_2O_5 films. Even though substantial differences exist in the properties and microstructure of these two types of films, the slopes determined in the rate of increase in film stress are the similar.

Optical Absorption Data

Coatings deposited on fused silica wafers and annealed at two power levels were measured for optical absorption at 351nm using a laser calorimeter system. The calorimeter, which has been described elsewhere, is capable of determining absorptions as low as 20 PPM [19]. Absorption levels measured on these samples were large and the data is plotted in figures 8-10. From the peak temperatures recorded on wafers and larger size samples in Table 1, it is clear that the highest temperatures recorded on the wafers (600 degrees°C) corresponded to larger samples annealed at 50 W/cm2. Calorimetry data taken on these wafers shows that for most of the samples tested, the absorption drops by 5 to 90% as the annealing power increases. The one exception is the Ta_2O_5 films deposited using the e beam process. Annealing these films increased the absorption levels by a factor of 3.

Laser Damage Data

Testing was performed at 1064nm using a ND:YAG laser system and test procedures which have been described previously [20]. The test parameters were as follows:

pulse duration	-	7 nsec (FWHM) single mode
spot size	-	710 microns 1/e2 diameter
sites tested	-	144
type of test	-	1-on-1
damage determination	-	Nomarski microscopy, 200X, any observable change.

Two samples annealed at 25 and 50 W/cm2 of each type were tested. An unannealed sample and one sample each annealed at 75 and 100 W/cm2 were also tested.

Laser damage test data is plotted in Figures 11-13. In every type of film studied, the damage morphologies observed remained consistent up to the 50 W/cm2 level and then changed dramatically for samples annealed at 75 and 100 W/cm2. It was somewhat unusual that for the Ta_2O_5 samples prepared using electron beam deposition, the observed damage site morphology seemed to be independent of the incident fluence level after annealing at the higher power levels. This observatin may demonstrate the sensitivity of thin film damage thresholds to substrate contamination.

The laser damage thresholds plotted in figure 11 of Al_2O_3 films deposited by reactive sputtering remained unchanged after annealing, even though the film crystalline structure, surface appearance, scattering levels, transmissivity, and the morphology of the damage sites changed considerably over the different annealing levels. These were unusual samples in that no pitting was observed in the damage morphology. The characteristic morphology consisted of a uniformly round area of complete film ablation or alteration. Damage in these films was thus absorption dominated. [21]

Table 4. Summary of Annealed Film Characterization Data

Anneal Power W/cm2	0	25	50	75	100	
Refractive	1.64	1.64	1.57	1.59	1.78	Al_2O_3, rs
Index	2.12	2.13	2.11	2.08	2.06	Ta_2O_5, rs
at 500nm	2.01	2.04	2.03	2.02	2.06	Ta_2O_5, eb
	1.8	-	-	-	-	TiO_2, sol
Absorption	0.192	-	0.115	-	-	Al_2O_3, rs
at 351nm	0.265	0.323	0.208	-	-	Ta_2O_5, rs
(%)	0.698	1.920	-	-	-	Ta_2O_5, eb
	8.650	8.230	8.210	-	-	TiO_2, sol
Crystal	Amorphous	A	A	A	A	Al_2O_3, rs
Structure	A	A	A	orthorhombic		Ta_2O_5, rs
	A	A	A	"	"	Ta_2O_5, eb
	A	A	A	Rutile/anatase		TiO_2, sol
Stress	352	-	354	-	-	Al_2O_3, rs
(MPa)	181	318	432	-	-	Ta_2O_5, rs
	128	261	-	-	-	Ta_2O_5, eb
	0	0	0	-	-	TiO_2, sol
Laser Damage	12.2	10.8	11.1	11.7	11.3	Al_2O_3, rs
Threshold	5.4	2.6	3.5	2.1	0.9	Ta_2O_5, rs
at 1064nm	2.7	2.3	1.8	3.3	4.8	Ta_2O_5, eb
(J/cm2)	4.8	4.4	2.6	6.0	7.9	TiO_2, sol
Scattering	-26%	-26%	277%	1000%+	1000%+	Al_2O_3, rs
at 633nm	-54%	39%	-31%	"	"	Ta_2O_5, rs
(PPM/Str)	-18%	37%	22%	"	"	Ta_2O_5, eb
	6%	-1%	-11%	"	"	TiO_2, sol
Peak Temp	20°C	380°C	660°C	900°C	1250°C	

Data obtained on Ta_2O_5 deposited by reactive sputtering is plotted in Figure 12. A clearly defined trend towards reduced damage thresholds with increased annealing power is shown. Further examination of the damage data from the perspective of determining the probability for damage at a given fluence led to a second trend - the slope of a probability curve or the spread in fluences resulting in either damaging or nondamaging events increases with annealing power. Damage morphologies consisted of pitting at low damaging fluences and larger features at higher fluences. The change in slope with annealing power was evident in the damage morphologies as well since small sites which were identical in appearance were observed at high damaging fluences and at threshold on samples annealed at 75 and 100 W/cm2. While very small

sites are commonly observed in coating damage studies well above the threshold, the number of such occurrences changed considerably after annealing.

In Figure 13, laser damage threshold data obtained on Ta_2O_5 films fabricated using electron beam deposition and the TiO_2 sol gel coatings are plotted. In both plots the damage threshold appears to decrease to a low level at 50 W/cm2 and then increase again at the higher power levels.

V. Analysis Summary

The data taken using each of the various characterization techniques has been collected into Table 4. It is clear that the largest changes occurred in the annealed coatings in all categories at power levels of 75 W/cm2 or higher. Between 50 and 75 W/cm2, refractive index, absorption, laser damage threshold and scattering data continued or reversed trends seen at lower power levels. The optical properties seem to correlate well with changes in film structure seen in the x-ray diffraction data. The majority of the films which were amorphous, became polycrystalline after annealing at power levels of 75 and 100 W/cm2. The onset of crystallization led to either improvements in laser damage threshold and slight increases in refractive index or a reduced damage threshold and refractive index.

In a more qualitative sense, the data collected in this study encompasses several areas of topical interest concerning thin film structure and the role of contaminants such as water and hydrocarbons. For instance, the changes observed in transmission scans of annealed films are clearly due to several phenomena. The sol gel and electron beam deposited films all showed shifts towards the UV of transmission maxima indicating a reduced optical thickness. This is probably due to the known porosity and water content of these types of films. [22,23] The reactive sputtered films, which are known to be dense and non-porous, invariably shifted towards longer wavelengths. [24] Severely reduced film transmission at shorter wavelengths are a direct result of very large increases in scattering which could not be accounted for in the absorption data but does correlate well with the x-ray diffraction data. Competing processes of water removal and densification or crystallization led to the majority of the observed phenomena.

VI. Interpretation

The data presented is consistent with a model of film microstructure and bonding which changes when thermal energy from the annealing process is added to the system. The additional energy promotes the growth of crystallites within the film which alter the optical properties, such as increased scattering. Depending on the initial state of the film, these changes may be beneficial or deleterious.

In electron beam deposited films, the original microstructure is known to be small scale polycrystalline or amorphous [22]. These films have less than the bulk packing density resulting in a film which is porous and has variable properties depending on the ambient humidity - as observed in the shifting transmission data recorded on unannealed films. In the films tested in this survey, the spectrophotometric and ellipsometric data indicated the annealed films density with higher refractive indices and become optically thinner. The laser damage threshold increases with the onset of crystallization along with light scattering and the film's mechanical stress. These phenomena are consistent with the growth of crystallites within the film. Only the optical absorption data seems unusual since absorption in the UV increases in Ta_2O_5 and decreases in Al_2O_3 films with annealing. The growth of crystallites within the Ta_2O_5 films does apparently result in the rupturing of preexisting bonding and a concommitant increase in the optical absorption. The Al_2O_3 films tested were probably not stoichiometric and thus became fully oxidized with the anneal process resulting in lower absorption.

In most respects, the sol gel films tested in this study behaved in a similar fashion to the electron beam deposited films. These films have a microstructure which is very porous and resembles many layers of packed spherical particles [23]. Like the electron beam deposited coatings, annealing at high power levels resulted in higher damage thresholds and increased light scattering. Optical absorption measurements in the UV near the band edge for TiO_2 showed only a very slight decrease in absorption.

In the sputtered films, the microstructure is known to be amorphous and dense providing nearly bulk properties [24]. The spectrophotometric and ellipsometric data indicates that the refractive index decreases for these films with an increase in film optical thickness. The laser damage threshold decreases or remains unchanged along with increases in light scattering and the mechanical stress. As before, these phenomena are consistent with the growth of crystallites within the film - with a film that is initially dense and the growth of crystallites disrupts existing bonding patterns. The small decreases measured in optical absorption in annealed sputtered films may indicate some small deviation from completely stoichiometric oxides.

VII. Conclusions

The objective of this study was to examine the effect of a laser annealing process on the properties of several types of dielectric films. The samples tested were selected to be representative of the parameter space of film characteristics from the most popular deposition techniques available. Data collected as part of this study shows significant differences in the properties of the films and the strong influence of the initial film microstructure on the properties of the annealed film.

The process of annealing modifies the film characteristics by affecting the film microstructure as a result of the formation of crystallites. The initial film microstructure is significantly altered by the growth of crystallites which evolve within the existing matrix. In a film with a densely packed microstructure, these crystallites may rupture bonds and for all practical purposes destroy the integrity of the film. In less dense films, the nucleation of crystallites may actually increase the packing density resulting in a film with generally improved optical and mechanical properties.

The ability to control film microstructure through a post deposition process has been demonstrated in this study. The annealing process used in this study promotes crystaline growth within the film microstructure. The analogy of annealing and hardening of metals ends here since there is no available means to "cold work" the thin film coating and create a fine grained film once it has been annealed. From the data presented, the annealing process can result in improved properties in some performance criteria. However, the process is relatively uncontrolled and trade-offs are involved in performance.

The results of this paper are complementary to the observation that a post deposition baking at comparable temperatures can notably improve the performance of sputtered films [25]. A model which may account for this phenomenon begins with the assumption that the lowest energy state for a coating material such as Ta_2O_5 <u>in thin film form</u> may be the glassy amorphous phase so often found as opposed to the crystalline state of the bulk material. The free energy of the large surface area of the film in comparison to the free energy of the bulk of the film may dictate the glassy amorphous phase. Sputtered films are known to have nearly bulk packing densities and contain very small scale nucleated crystallites of a particular crystalline phase when deposited [26]. As depicted in Figure 14, the free energy of crystallites within the film is such that they may be above or below the critical size for growth. When heated in an oven, crystallites smaller than the critical radius break up and go back into the solution or liquid phase of the surrounding glassy film. Crystallites larger than the critical radius continue to grow. The important difference between this type of baking procedure and the laser annealing performed in this study is the time factor involved. An overnight bake allows a gradual redistribution of free energy in the film system as bonding patterns shift slowly into the lowest energy condition of a uniform glassy film.

The authors wish to thank the following individuals for their outstanding contributions to this study: Willie Kunzler, Dan Oshea, and C. Miglionico of AFWL/SU, David Gallant of Rockwell Power Systems and W. Kent Stowell of AFWL/ARBD for measurements performed; Ian Thomas of Lawrence Livermore National Laboratory, Walter T. Pawlewicz of Pacific Northwest Laboratory and Steve Tuenge of Martin Marietta Aerospace for coating fabrication; Adam Rusek of AFWL/ARBD for microscopy and sample holder design.

List of References:

1. Richard A. Flinn and Paul K. Trojan, "Engineering Materials and Their Applications", second edition, Houghton Mifflin Co, Boston, 1981, pp 90-96.

2. D.S. Gnanamuthu, "Laser Surface Treatment," Opt. Engr. Vol 19, 783(1980).

3. M.R. Lange, J.K.McIver and A.H. Guenther, "An Initial Study of: The Inclusion Model for Repetitively Pulsed Laser Damage," Nat. Bur. Stand. (U.S.) Spec. Publ. 727, 1984, pp 382-393.

4. P.A. Temple, D. Milam, and W.H. Lowdermilk, "CO2 Laser Polishing of Fused Silica Surfaces for Increased Laser Damage Resistance at 1.06 microns," Nat. Bur. Stand. (U.S.) Spec. Publ. 568, 1979, pp 229-236.

5. Annetta J. Weber, Alan F. Stewart, Gregory Exarhos, and W. Kent Stowell, "An Investigation of Laser Polishing of Fused Silica Surfaces," Nat. Bur. Stand. (U.S.) Spec. Publ. 1986: to be published.

6. P.L. Liu, R. Yen, N. Bloembergen, and R.T. Hodgson, " ", Appl. Phys. Lett. 34, 864, 1979.

7. A.P. Radinski and A. Calka, "Modification of Pd-Si Metallic Glasses by Picosecond Laser Annealing," Phys. Rev. Lett. 57(24), 3081, 1986.

8. Anetta J. Weber, Alan F. Stewart and Gregory J. Exarhos, "An Investigation of Laser Processing of Thin Film Coatings," Nat. Bur. Stand. (U.S.) Spec. Publ. 1986: to be published.

9. Model 600 camera system from Inframetrics Inc., 12 Oak Park Dr., Bedford, MA 01730.

10. Anthony D. McLachlan and Fred P. Meyer, "Temperature Dependence of the Extinction Coefficient of Fused Silica for CO2 Laser Wavelengths," Appl. Opt. 26, 1728(1987).

11. Mr. Steve Tuenge, Martin Marietta Aerospace, Albuquerque, New Mexico.

12. Dr. Walter T. Pawlewicz, Battelle Pacific Northwest Laboratories, P.O. Box 999, Richland, WA 99352.

13. Dr. Ian Thomas, Lawrence Livermore Laboratory, P.O.Box 5508, Livermore, CA 94550.

14. Model 2320, Varian Associates Inc., Instrument Group, 220 Humboldt Ct., Sunnyvale, CA 94089.

15. D.P. Arndt, et al, "Multiple Determination of the Optical Constants of Thin Film Coating Materials," Appl. Opt. 23(20), 3571,1984.

16. Gaertner Scientific Corp., 1201 Wrightwood Ave. Chicago, IL 60614.

17. Robert M. Silva, Fred D. Orazio Jr., and W. Kent Stowell, "Scatter Evaluation of Supersmooth Surfaces," Musikant, Solomon, ed. Proceedings of SPIE Vol 362: Scattering in Optical Materials; 1982 Aug 25-27; San Diego, CA pp 71-76.

18. "Handbook of Thin Film Technology", Maissel and Glang, editors, McGraw-Hill Inc., New York, 1970, pp 12.22-12.32.

19. A.F. Stewart and G.J. Gallant, "Ultraviolet Thin Film Coating Characterization," Nat. Bur. Stand. (U.S.) Spec. Publ. 727, 1984, pp. 272-284.

20. Alan F. Stewart and Arthur H. Guenther, "Laser Damage Test Results on Balzers Round Robin Thin Film Samples," Appl. Opt. 23, 3774 (1984).

21. S.M.J. Akhtar, D. Ristau, and J. Ebert, "Thermal Conductivity of Dielectric Films and Correlation to Damage Threshold at 1064nm", Nt. Bur. Stand. (U.S.) Spec. Publ, 1985.

22. H.A. Macleod and D. Richmond, "Moisture Penetration Patterns in Thin Films", Thin Solid Films, 37 (1976) 163-169.

23. I.M. Thomas, J.G. Wilder and W.H. Lowdermilk, "High Damage Threshold Porous Silica Antireflective Coating", Nt. Bur. Stand. (U.S.) Spec Publ. 727, 1984, pp 205-210.

24. W.T. Pawlewicz, G.J. Exarhos and W.E. Conaway, "Structural Characterization of TiO_2 Optical Coatings by Raman Spectroscopy," Appl. Opt. 22, 1837 (1983).

25. Private communication with Sam Holmes of Northrup Research and Technology Center, One Research Park, Palos Verdes Penninsula, CA 90274 and with Tony Lauderback of Ojai Research Corp., Ojai, CA.

26. R. Rujkorakarn, L.S. Hsu, and C.Y. She, "Crystallization of Titania Films by Thermal Annealing," Nat. Bur. Stand. (U.S.) Spec. Publ. 727, 1984, pp. 253-261.

27. S. Mallavarpu is a US Air Force National Research Council Resident Research Associate at the Air Force Weapons Laboratory. Modelling developed by Dr. Charles Carniglia, Thin Film Designer Software Inc., Albuquerque, New Mexico.

28. K. Vedam, L. D'Aries and Arthur H. Guenther, "Nondestructive Depth Profiling of Transparent Thin Films by Spectroscopic Ellipsometry," Nat. Bur. Stand. (U.S.) Spec. Publ. 1986: to be published.

A questioner was puzzled why the density increased but the index decreased. The author replied that he felt that the physical structure of the porous films was collapsing and when crystallites grow within the sputtered films that grow within the existing matrix without rupturing the overall structure of the film. In the tantalum pentoxide films a roughening of the surface but no apparent cracks. In the aluminum oxide sputtered films cracks are seen opening up in the surface relieving stress. That also occurs in electron beam deposited films as part of the damage morphology. There are physical changes going on in the films but why the density increases but the index decreases is a puzzle.

Another questioner pointed out that a phenomenon in bulk ceramics is known as transformation toughening. For example, in ZrO_2 people dope it to stabilize a particular phase. When these samples crack, there is a great amount of stress present near the crack tip which causes a transformation to a different phase which prevents the crack from going farther. Can there be an analogy in thin films so that increased stress improves the damage threshold? The author replied that he knew of no evidence to support such an interpretation. The electron beam deposited films are initially porous and the growth of new crystal grains within the film appear to fill up existing pores within the material and not causing a large increase in residual stress. He does not have stress data taken on films annealed above 50 W/cm^2, however, so that the above conclusion is not certain.

The samples were irradiated in air and held in a vacuum chuck assembly. One questioner suggested that there might be implications for manufacturers who are baking their samples after their coatings. The author agreed, saying that one of the motivations for the study was the industrial practice of baking ion-beam deposited films to improve their damage threshold. Films in an amorphous phase are not in equilibrium, the equilibrium condition is a crystalline phase. Perhaps a slow oven bake promotes nuclei which return to the glassy matrix. However, in this experiment the heating takes 6 seconds so that the activation energy for crystal growth, which is of the order of 0.1 eV, is not allowed enough time to be effective.

The questioner also reminded the audience that the Russians reported about 4 years ago that if they baked their samples in an oven of hydrogen or oxygen free of water that the damage resistance went up. Was the water content controlled in these experiments? The speaker replied that although the water was not controlled, the properties of the films after baking were stable for several months. Water, however, would not necessarily diffuse in or out.

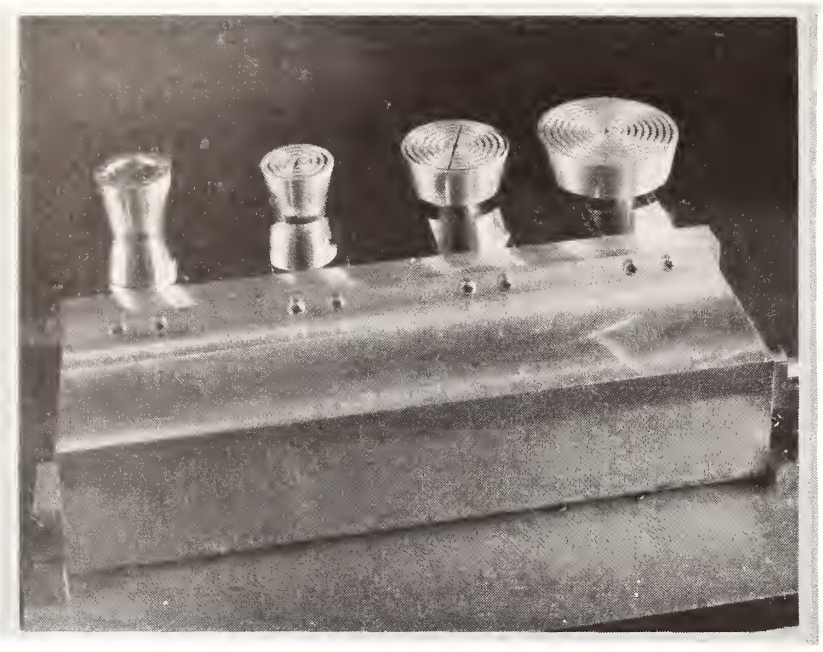

Fig. 1 Detail of sample holder, vacuum chuck assembly for laser annealing experiments

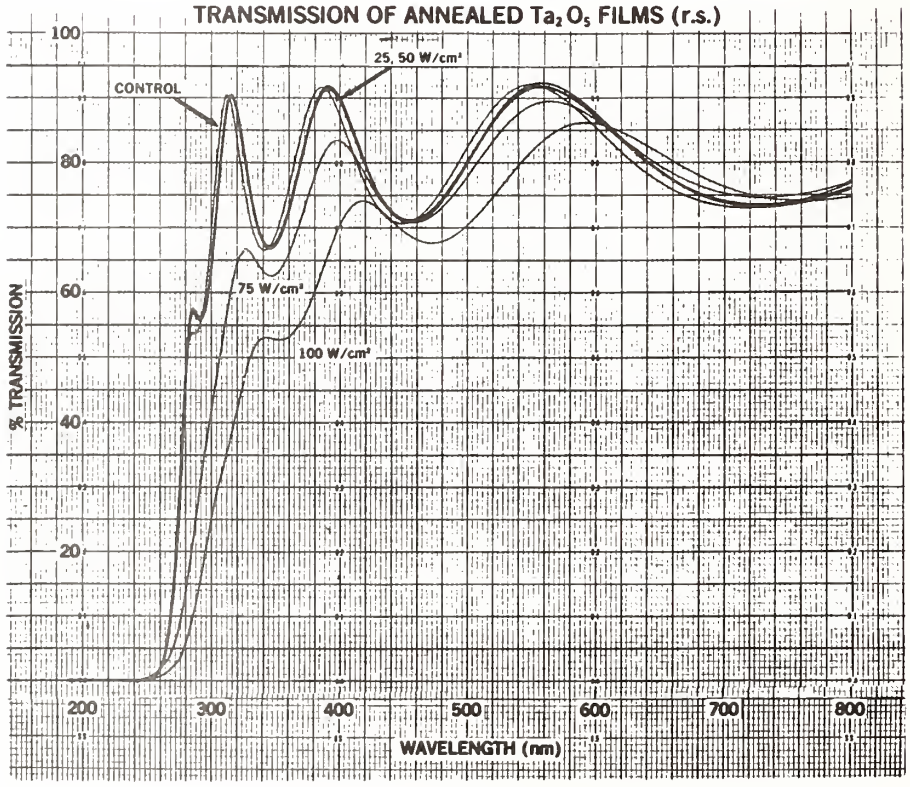

Fig. 2 Spectrophotometer transmission data on set of annealed reactive sputtered Ta_2O_5 films

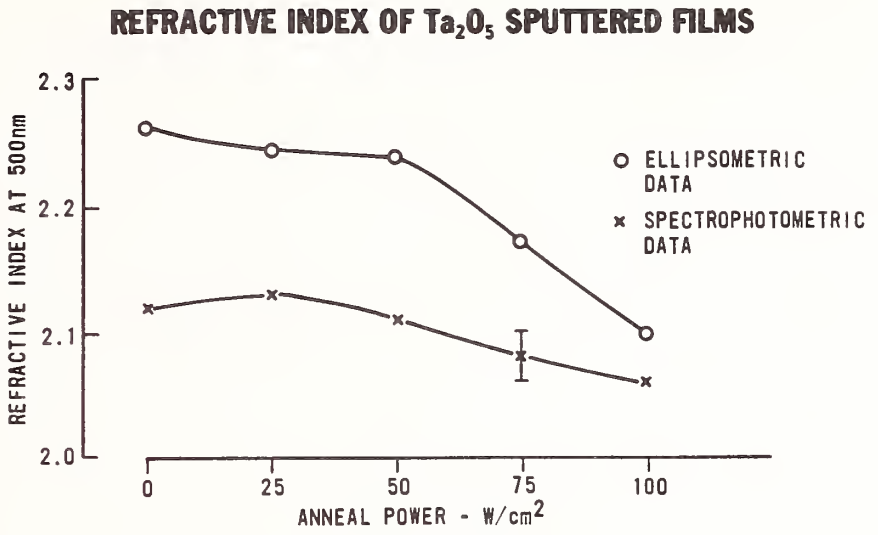

Fig. 3 Refractive indices determined from spectrophotometric and ellipsometric analysis of sputtered Ta_2O_5 films annealed at various power levels

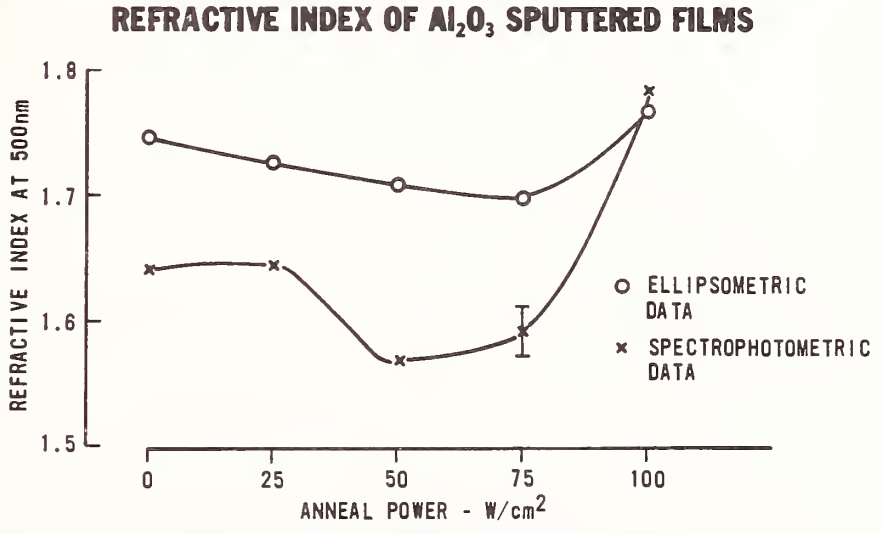

Fig. 4 Refractive indices determined from spectrophotometric and ellipsometric analysis of sputtered Al_2O_3 films annealed at various power levels

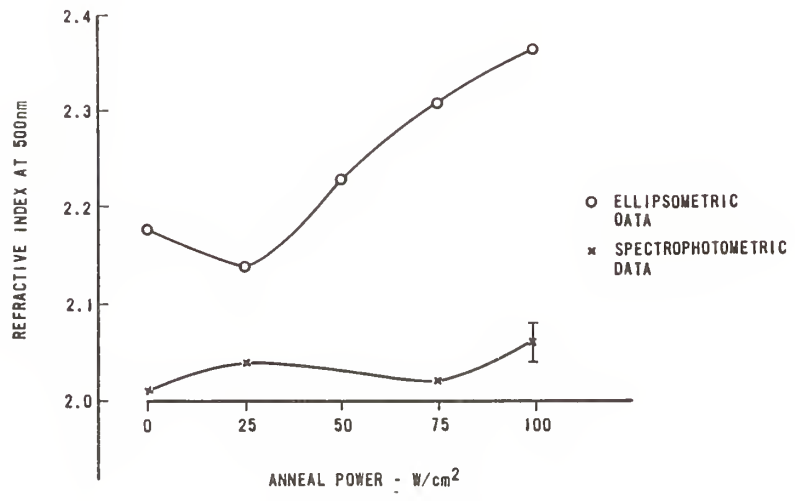

Fig. 5 Refractive indices determined from spectrophotometric and ellipsometric analysis of Ta_2O_5 films fabricated using electron beam deposition and annealed at various power levels

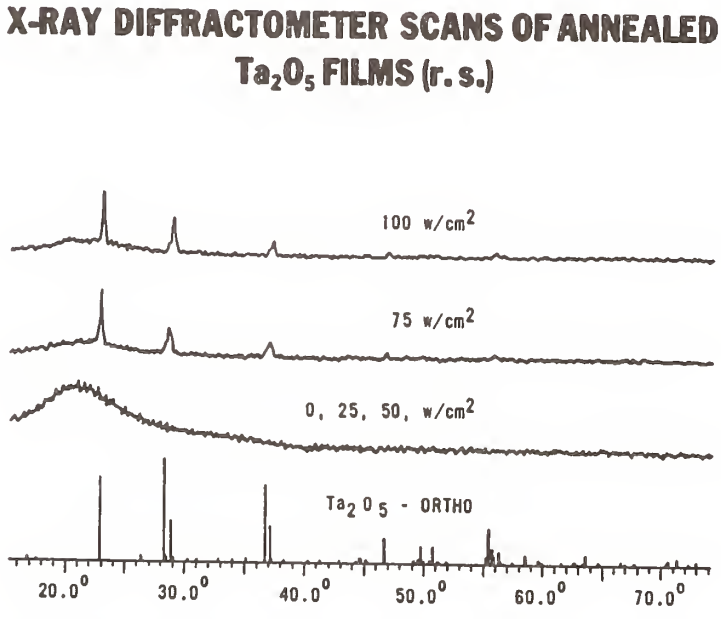

Fig. 6 X-ray diffractometer data taken on set of annealed reactive sputtered Ta_2O_5 films

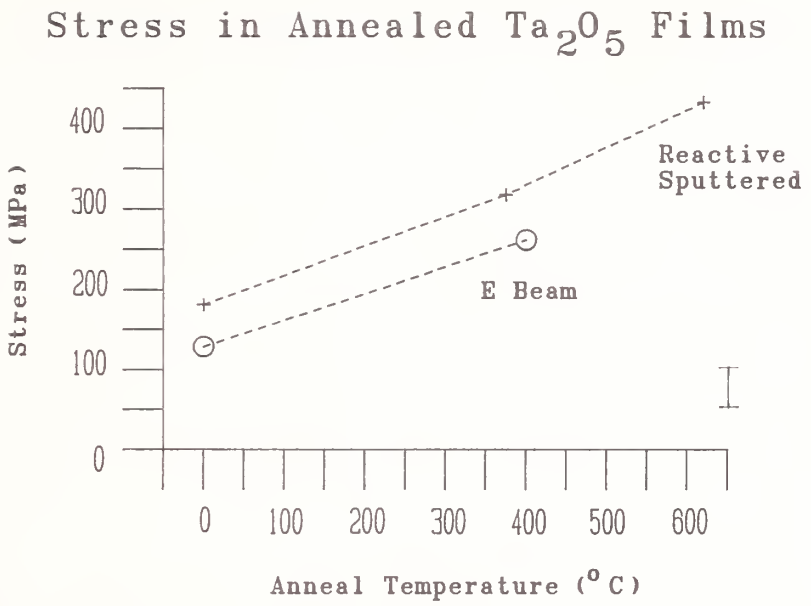

Fig. 7 Residual compressive stress measured in annealed Ta_2O_5 films fabricated by electron beam and reactive sputtering

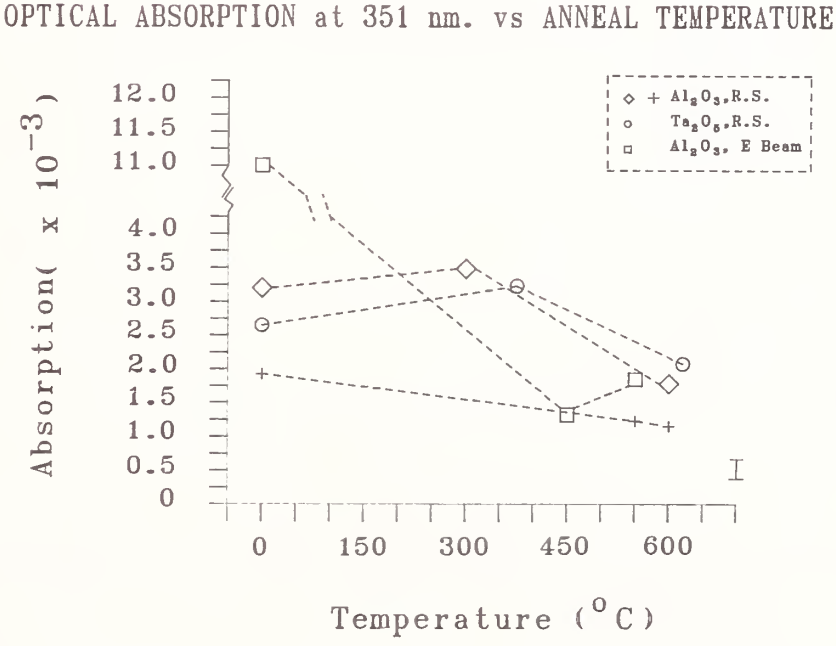

Fig. 8 Optical absorption at 351 nm measured on Al_2O_3 films fabricated by electron beam and reactive sputtering and data obtained on Ta_2O_5 films fabricated by sputtering

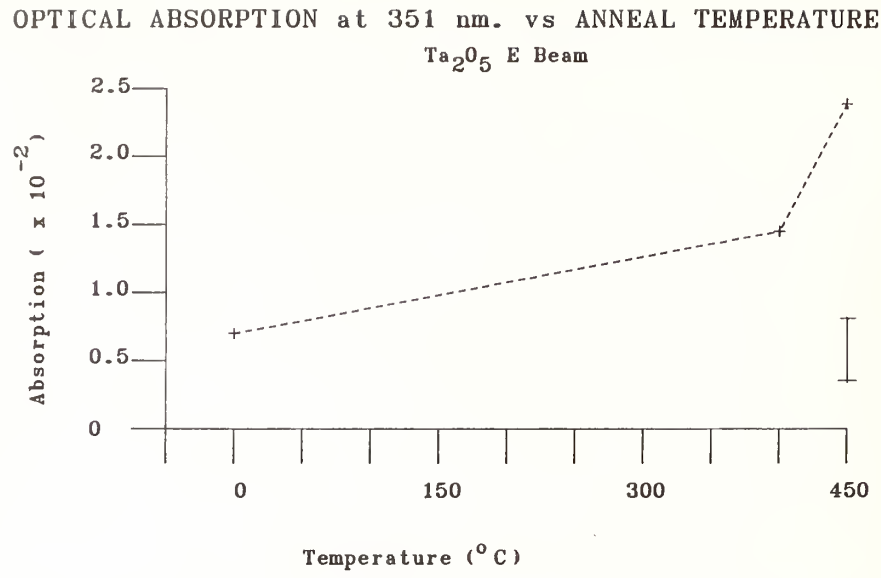

Fig. 9 Optical absoprtion at 351 nm measured on Ta_2O_3 films fabricated by electron beam deposition

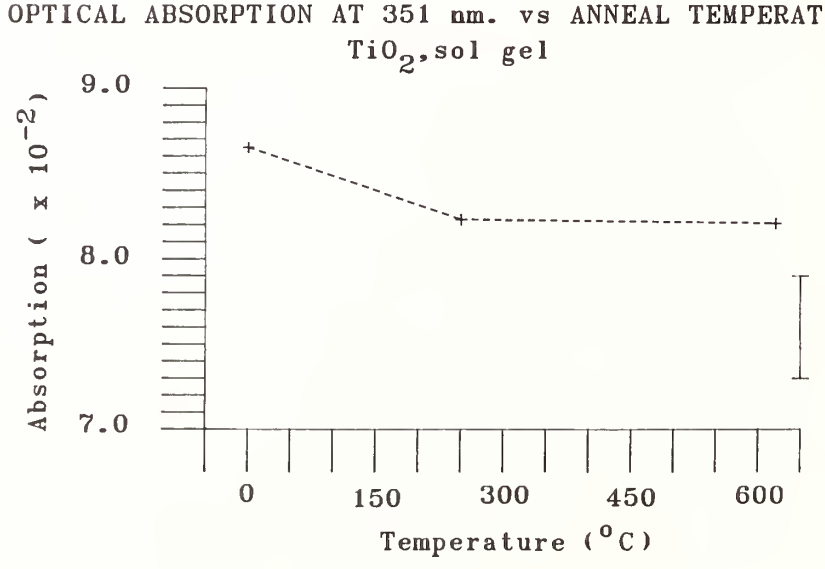

Fig. 10 Optical absorption in TiO_2 films deposition by the sol gel technique

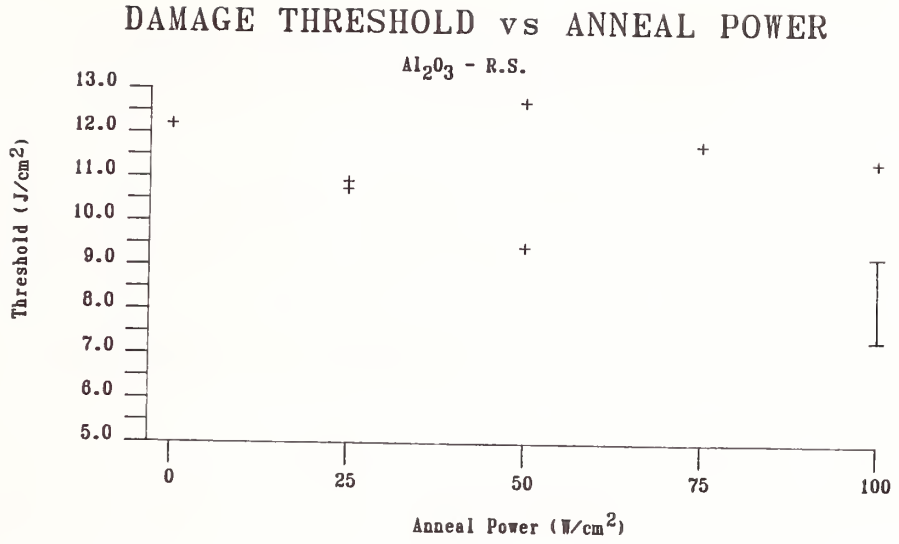

Fig. 11 Laser damage thresholds measured at 1064 nm on annealed Al_2O_3 films fabricated by reactive sputtering

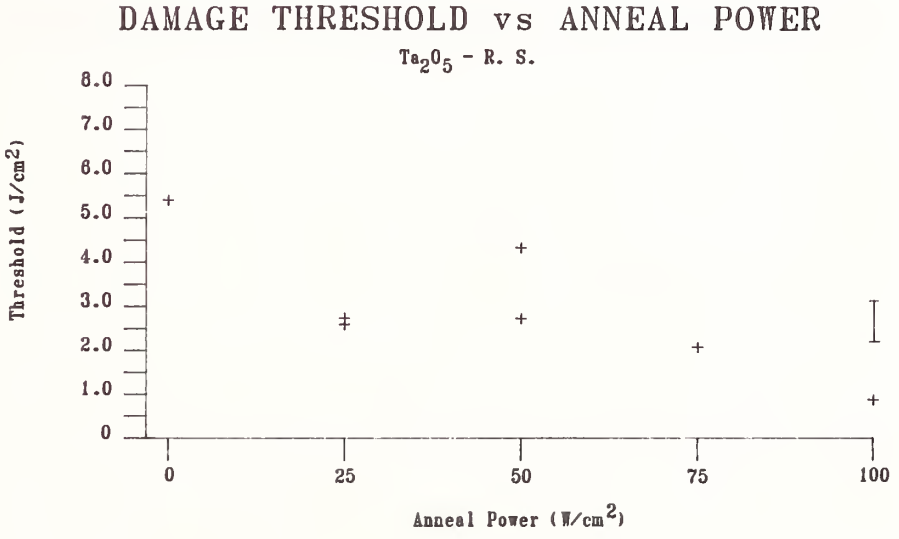

Fig. 12 Laser damage thresholds measured at 1064 nm on annealed Ta_2O_5 films fabricated by reactive sputtering

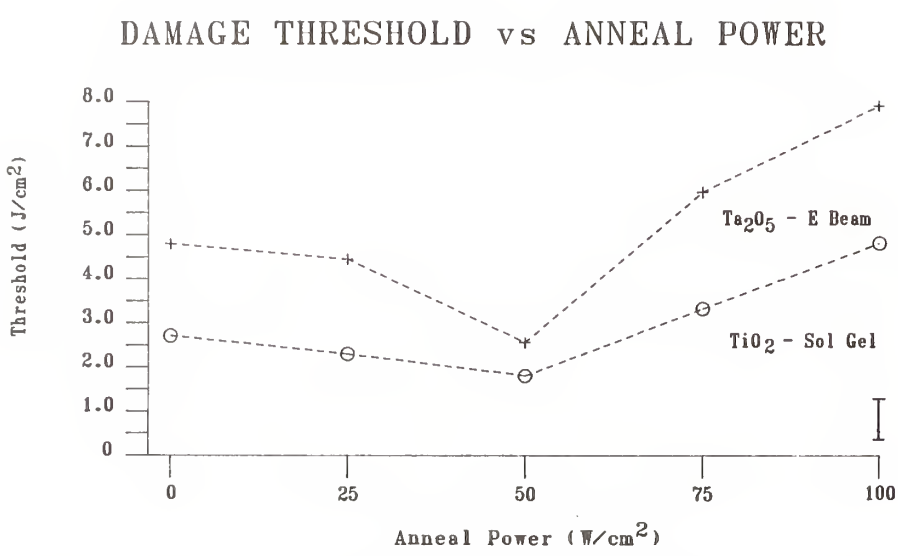

Fig. 13 Laser damage thresholds measured at 1064 nm on annealed films of electron beam Ta_2O_5 and sol gel TiO_2

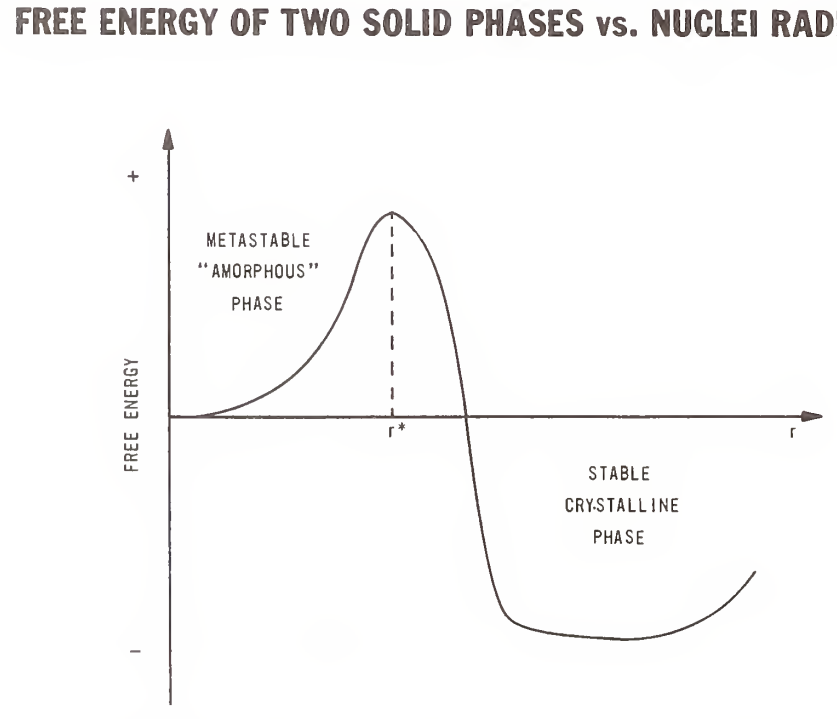

Fig. 14 Free energy of two solid phases vs. nuclei radius

List of Figures:

Manuscript Received
2-22-88

Video Image Processing of Laser-Illuminated Coating Defects*

J. E. Auborn and M. B. Moran

Physics Division, Research Department
Naval Weapons Center, China Lake, California 93555-6001

A video microscopy system has demonstrated the ability to detect and locate defects nondestructively in multilayer optical coatings. The system uses laser-excited scattering to illuminate defects responsible for laser-induced damage in multilayer dielectric mirrors. Scatter intensity maps and contours can be generated by digitizing the video image of scattering from individual defects. These can reveal characteristic defect scatter features that can be related to a damage probability. Due to the relatively low resolution of the stored video image, the scattering from a defect may be contained in only a few pixels. Using digital-enhancement techniques such as cross correlation, noise filtering, and Laplacian edge enhancement combined with fast-Fourier transforms, it is possible to increase the resolution of the characteristic features of a scattering defect for a more detailed analysis. Examples of these techniques for a dielectric mirror will be presented and discussed.

Key words: coating defects; defect scattering; laser damage; thin films; video-enhancement techniques; video image processing.

1. Introduction

Video microscopy using laser illumination can be used as a tool to examine optical coating defects responsible for laser-induced damage [1].[1] Due to the relatively low resolution inherent in the video process, the ability to identify the defects that act as damage initiators can be limited severely. The present study seeks to identify and provide information on defect characteristics by the use of video-enhancement techniques. This nondestructive technique could provide a more efficient and economical means of quality assessment than laser damage testing. The work reported here was designed to develop further the method of defect indentification and characterization in order to address this need [2]. Examples of the application of these video techniques will be presented.

2. Experimental

The laser-illumination studies were performed previously in the Naval Weapons Center's visible wavelength damage facility. This facility has been described in detail in the literature [3]. A tunable dye-laser source provides plane-polarized 0.4-J, 0.5-μs pulses in a reproducible smooth spatial profile in the 460- to 530-nm wavelength range. The attenuated laser beam is focused on the sample surface at near-normal incidence using a 280-mm focal length lens. The spatial profile of the focused beam is a flat-topped Gaussian (420 μm in diameter at the $1/e^2$ intensity) with a 240-μm-diameter area of constant (to ±5%) intensity. An area approximately 1×0.8 mm^2 is viewed by the video-imaging microscopy system (VIMS) at an angle of 15° from the laser beam in the plane of the laser polarization. This sample was also irradiated with a chopped 25-W tungsten-halide lamp to see if the coating defects were visible with a broadband light source. The coating defects could not be seen by this method [4]. The VIMS consists of a close-focusing Questar Model QM-1 telescope, a color video camera, and broadcast-quality recording system. A three-tube Saticon camera was used to observe defect illumination and damage. The video-image-processing system (VIPS) is a recent addition to the overall laser damage facility. The VIPS consists of an Eigen F-100 digital image processor and a Hewlett-Packard Model 216 computer controller.

---

*Work supported by Navy Independent Research funds.
[1]Numbers in brackets indicate the literature references at the end of the paper.

The Eigen F-100 is designed to grab a single video field (256 × 512 pixels) or frame (512 × 512 pixels) and detail the image in its solid state memory. The video input can be any national television standard code source (video camera or videotape). The digitized video data can be stored in the F-100's integral 20-Mbyte Winchester disk or transferred to the computer for analysis or storage on floppy disks. The Winchester disk allows 100 video fields (50 frames) to be stored. Other important features include (1) dynamic resolution of 256 gray levels, (2) five levels of noise reduction, (3) simultaneous display of two fields, (4) contrast and level controls, and (5) burst mode (stores two frames per second to the Winchester disk). All functions are computer controlled by means of an IEEE 488 interface.

The Hewlett-Packard Model 216 computer was specially outfitted to handle the large matrices of digital video data. Internal RAM memory had to be 3.5 Mbytes or larger. This requirement is dictated by the number of pixels being analyzed. Other features include (1) floating point math coprocessor, (2) 1-Mbyte disk storage, and (3) Hewlett-Packard extended BASIC 3.0. A BASIC complier will soon be implemented to increase the computational speed.

3. Software

Special video image-analysis software (VIAS) was written to accomplish three tasks: (1) provide control of the Eigen FL-100 and to access its digitized video data, (2) provide a means to plot the digitized video in useful formats, and (3) perform image-analysis techniques to enhance the image quality.

The Eigen control portions of the VIAS invoke commands from the F-100 and facilitate data transfer between the F-100 and the computer. Commands for the F-100 include access to the internal hard disk, control of various display modes, status of the F-100, and selection of specific groups of pixels or entire fields to send to or receive from the computer.

The digital video images can be displayed before and after image processing in several ways. The video pixel information can be output through the F-100 to any standard video monitor, video recorder, or plotted on the computer in either contour, surface, or gray map plots. Contour and surface plots treat the image as a pseudo three-dimensional surface where X and Y remain the same, but the gray level intensity is treated as a height or third dimension. Contour plots like topographical maps draw lines along areas of equal height to produce a plot looking "down" at the image. Surface plots look at the "surface" of the image from the side and partially above or below the edge. Features behind other features can be hidden or, if one chooses, drawn with the obscured lines shown. A density of dots proportional to the gray level of that pixel is provided by gray map plots; the video output of the F-100 provides a much better means, however, as it uses real gray levels.

4. Image-Enhancement Techniques

The original images from the video tape can be noisy and limited in resolution. To enhance what can be seen, several image-processing techniques have been implemented in VIAS.

4.1. Averaging and Filtering

4.1.1. Local Averaging

To eliminate image noise, many different filtering schemes can be used. One of the simplest schemes is local averaging, which substitutes the average value of a 3 × 3 block around a pixel for that pixel. This method will eliminate pixels that differ greatly from their neighbors. The effect is to blur the image slightly; this must be considered a trade-off with the advantage of eliminating noise. Many variations exist using different size and shape blocks around each pixel.

4.1.2. Median Filtering

A method of filtering that will not blur the image is median filtering. As in local averaging, the 3 × 3 block of pixels surrounding each pixel is used; in median filtering, the pixel value closest to the average is used. This will preserve edges, but still eliminate single spots of noise. Again, many variations of median filtering can be used employing different blocks of pixels. A side effect of median filtering is that thin lines or small spots will be made thinner, but they will not blur as in local averaging.

4.1.3. Min/Max Filtering

Another type of filtering used in VIAS is min/max filtering, where the local minimum or maximum of a block of pixels is used to replace the central pixel. This is similar to using thresholds to segment portions of the image from the background.

4.1.4. Thresholding

Thresholding can be used to eliminate unwanted portions of the image. For example, a noisy low-level background can be eliminated if the portions of the image of interest are of a higher gray level; with subsequent scaling, the image can be substantially improved. An extreme of thresholding is to quantize the image into two gray levels: those above a given threshold and those below. This technique is called quantization.

4.2. Scaling

4.2.1. Gray Scale Adjustment

Since most images will be made under conditions where the full range of gray levels is not used, a scaling option can be implemented to spread the image over the complete 256 gray levels available. This scaling operation tends to increase the contrast of the image. Also, it can be performed in nonuniform ways: Portions of the gray scale (i.e., the top 1/4) are stretched to cover a wider range (usually the top 156 gray levels), while the rest of the gray scale is compressed into what remains. This technique can be used to enhance greatly certain features of the image over the background.

4.2.2. Histograms and Co-occurrence Matrices

Histograms of the number of pixels in each gray level can be generated to show where to perform thresholding and scaling operations. More information about the image can be found through co-occurrence matrices. The co-occurrence matrix is a measure of how often each gray level occurs adjacent to every other gray level. In pictures with little change in gray levels, most of the co-occurrence matrix will be near the diagonal, as most pixels will have gray levels that are the same as those of its neighbors. Various parameters such as the texture of an image can be learned from the co-occurrence matrix.

4.3. Edge Enhancement

Edges are important features in most images, so a Laplacian function can be optioned in VIAS to enhance these image edges. Either the Laplacian itself that contains only the edge information can be displayed or, to enhance edges, the Laplacian can be subtracted from the original image.

4.4. Interpolation

Due to the small size of the defects (5-25 μm) examined with VIAS, it is desirable to expand areas of the image that are of interest. A subroutine of VIAS will expand each pixel into four pixels (this number can be changed). This is a zero-order interpolation, because the values of the pixels have not been changed. The resultant image appears blocky; however, subsequent use of averaging or filtering provides a image close to the original.

4.5. Fast-Fourier Transform

Discrete Fourier transforms may be performed using a fast-Fourier transform (FFT) algorithm [5]. The greatest use of FFTs is in analysis, but another use in image analysis is spatial filtering. For example, to filter out high frequencies, one needs only to eliminate the portions of a FFT near the edges, keep those near the center, and then reverse the transform. The result will be the image with the higher frequencies filtered out. Similarly, masking out the center of the FFT will filter out low frequencies. Convolution and correlation are functions that are made much easier to calculate when using Fourier transforms. These functions are also implemented in VIAS.

5. Discussion

The laser illuminator defects were observed in an antireflection multilayer dielectric coating designed for 500 nm, which was developed for protective use on laser windows. This coating consisted of alternating layers of aluminum nitride and aluminum oxide on a fused-quartz substrate [6,7]. The coating was measured to be approximately 90% transmissive at the laser illumination wavelength of 515 nm. The laser-illuminated area was approximately 1 × 0.8 mm.

The progression from defect illumination to laser-induced damage as the laser intensity increases is shown in figure 1. These video fields were recorded immediately following a nondamaging [fig. 1(a)] and subsequent damaging [fig. 1(b)] pulse of higher intensity. Damage was initiated at defects A and C. Defect B did not damage at the higher intensity laser pulse. The areas digitized for analysis are enclosed by the solid white rectangles. The rectangles enclose approximately 50 × 50 pixels. Smaller subset arrays were analyzed from these large arrays to highlight details.

Various views of a 60 × 277 array of pixels encompassing points A, B, and C are presented in figures 2 and 3. The scatter intensity map [fig. 2(a)], contour map [fig. 2(b)], and a histogram of the number of pixels having a certain gray level [fig. 2(c)] are representations of the video data without applying any image-processing techniques. Very little detail can be observed, and most of the features are obscured by the background noise. Figure 3 shows the same views of this area with image-analysis techniques applied. The techniques used included thresholding, 3 × 3 pixel averaging, scaling, linear interpolation, and 1% Laplacian edge enhancement. The scatter map [fig. 3(a)] and contour map [fig. 3(b)] show the enhanced detail that clearly highlights points A, B, and C and their surrounding topographies. The histogram [fig. 3(c)] represents (1) a narrowing of gray scale levels by the averaging and thresholding techniques and (2) an increase in the number of pixels caused by the interpolation and scaling operations.

Scatter intensity maps and contour maps of point A with and without image processing are presented in figures 4 and 5, respectively. The image-processing techniques employed were quadratic interpolation, thresholding, 3 × 3 pixel median smoothing, zoom enlargement, and gray level scaling. Clearly, the scatter maps presented in figures 4(a) and 5(a) are very different. In figure 4(a), the background intensity nearly hides the two peaks of this defect. Figure 5(a) shows how this information can be amplified to better discern any features the defect might have. The loss of resolution after amplification is due to the median smoothing. This type of smoothing can be adjusted to retain subtle features.

The difference in the contour maps [figs. 4(b) and 5(b)] is readily evident. The squarish features in figure 5(b) are due to the zoom enlargement technique, where each pixel in figure 4(b) is made into four pixels. The two areas of high intensity are clearly depicted in figure 5(b). These techniques provide a means to discriminate subtle features that are close to the background in intensity.

Figures 6 and 7 are representations of a B-type defect [8] that did exhibit laser-induced damage.Illuminated defects with characteristics of a B-type defect (i.e., a singular defect aggregate with no distinct contour features) produced laser-induced damage only 50% of the time. Using the same techniques as figure 4, no features were evident in the comparison of the unprocessed scatter map [fig. 6(a)] and the processed scatter map [fig. 7(a)]. However, a comparison of the unprocessed contour map [fig. 6(b)] and the processed contour map [fig. 7(b)] highlights two distinct areas of high intensity in the image-processed contour map. This contour map [fig. 7(b)] now has the same features of laser-illuminated defects A and C, which produced laser-induced damage 100% of the time. Analysis of the other B-type defects that did damage with these techniques produced similar results about 35% of the time. The remaining defects of this type had too low a resolution to resolve any features.

A comparison of histograms in figures 6(c) and 7(c) shows the broadening of the number of gray scale levels used after image processing. The number of pixels that had a certain gray level was reduced, but the overall spread of gray levels increased. This technique allows information to be extracted from any background noise.

The FFT of the video data on defect C after laser-induced damage occurred is presented in figure 8(a). The areas digitized for analysis are enclosed by the solid white rectangles. Approximately 32 × 32 pixels are enclosed by the rectangles. The upper rectangle encircles the original damage area. The bottom rectangle is the video reconstruction of the FFT. A scatter map [fig. 8(b)] and a contour map [fig. 8(c)] are provided for comparison. The FFT is particularly useful for spatial filtering: Either the high or low frequencies can be deleted and the transform may be reversed to depict the video image with these frequencies removed. This method is useful to remove constant instrument noise. Another use of the transform is the compression of the digitized video data for storage or transmission. It is possible that a transform, either optical or computational, could be used to identify damaging defects. Further work in this area is continuing.

6. Summary

By using video-analysis techniques, we have shown that even low-resolution video data can be used to discriminate between nondamaging and damage-initiating, laser-illuminated coating defects. These techniques increase the discrimination and correlation of the laser-illuminated-defect features to a probability of laser-induced damage.

Future plans involving the video-analysis techniques will emphasize the fast-Fourier transform code and methods to increase computational speed. Correlation of sample response will continue to include (1) polarization effects, (2) wavelength and pulse-width effects, and (3) spatial intensity profile distribution and surface scatter. Analysis of this type of information will continue to aid in the understanding of laser-induced damage to optical materials.

7. References

[1] Marrs, C. D.; Porteus, J. O.; Palmer, J. R. "Nondestructive defect detection in laser optical coatings," J. Appl. Phys. 57; 1719; 1985.

[2] Moran, M. B.; Kuo, R. H.; Marrs, C. D. "Scatter intensity mapping of laser-illuminated coating defects," 18th annual symposium on optical materials for high power lasers; Boulder, CO; Nat. Bur. Stand.; 1986 November 3-5. (Proceedings in process.)

[3] Marrs, C. D.; Faith, W. N.; Dancy, J. H.; Porteus, J. O. "Pulsed laser-induced damage of metals at 492 nm," Appl. Opt. 21; 4063; 1982.

[4] Marrs, C. D. Unpublished results.

[5] Ramirez, R. W. The FFT, fundamentals and concepts. New York; Prentice-Hall, Inc.; 1985.

[6] Koshigoe, L. G.; Johnson, L. F.; Donovan, T. M.; Marrs, C. D. Characterization of aluminum nitride/aluminum oxide reactively sputtered antireflection coatings. China Lake, CA; Naval Weapons Center; Technical Publication 6651; 1985.

[7] Johnson, L. F.; Ashley, E. J.; Donovan, T. M.; Franck, J. B.; Woolever, J. B.; Dalbey, R. Z. "Scanning electron microscopy studies of laser damage initiating defects in zinc selenide/thorium fluoride and silicon hydride/silicon oxide multilayer coatings," in Proceedings of the 16th annual symposium on optical materials for high power lasers, Bennett, H. E.; Guenther, A. H.; Milam, D.; Newnam, B.E., ed. 1984 October 15-17; Boulder, CO; Nat. Bur. Stand. (U.S.) Spec. Publ. 727; 1986 October. Pp. 356-370.

[8] Moran, M. B.; Kuo, R. H.; Marrs, C. D. "Scatter intensity mapping of laser-illuminated coating defects," 18th annual symposium on optical materials for high power lasers; Boulder, CO; Nat. Bur. Stand.; 1986 November 3-5. (Proceedings in process.)

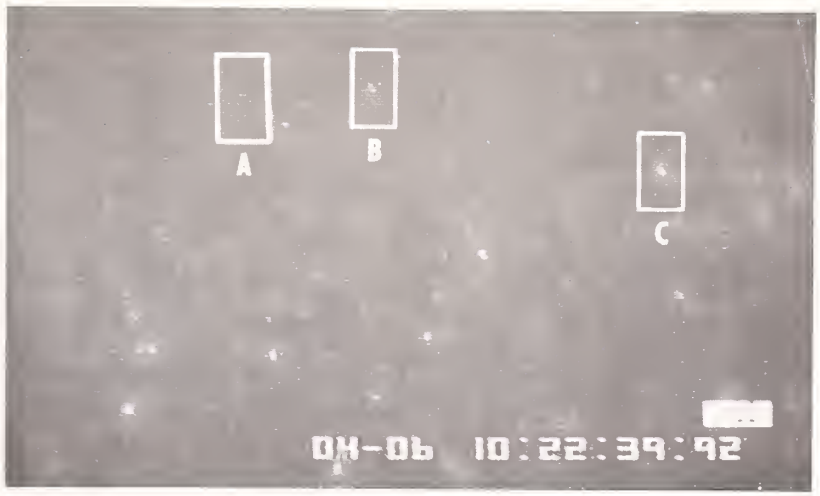

(a)

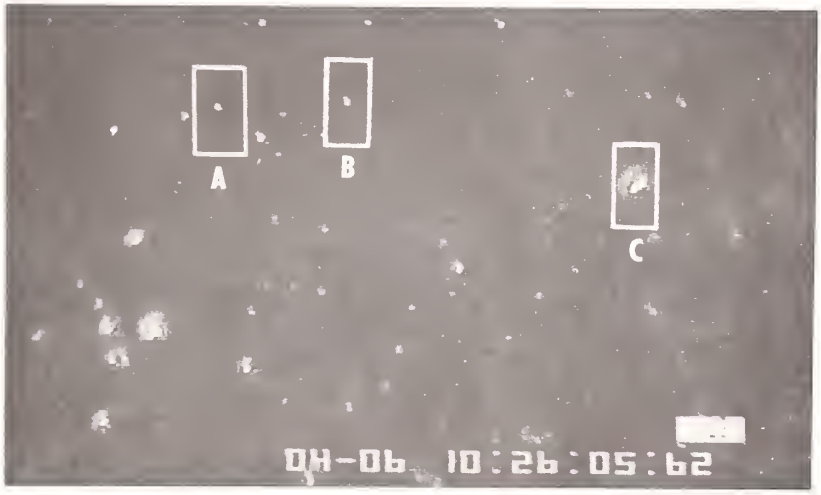

(b)

Figure 1. Illuminated defects of aluminum nitride/aluminum oxide/aluminum nitride multilayer antireflection coating for 500 nm during (a) predamage laser pulse and (b) damaging laser pulse; 1-mm FOV. Note illuminated defects A, B, and C.

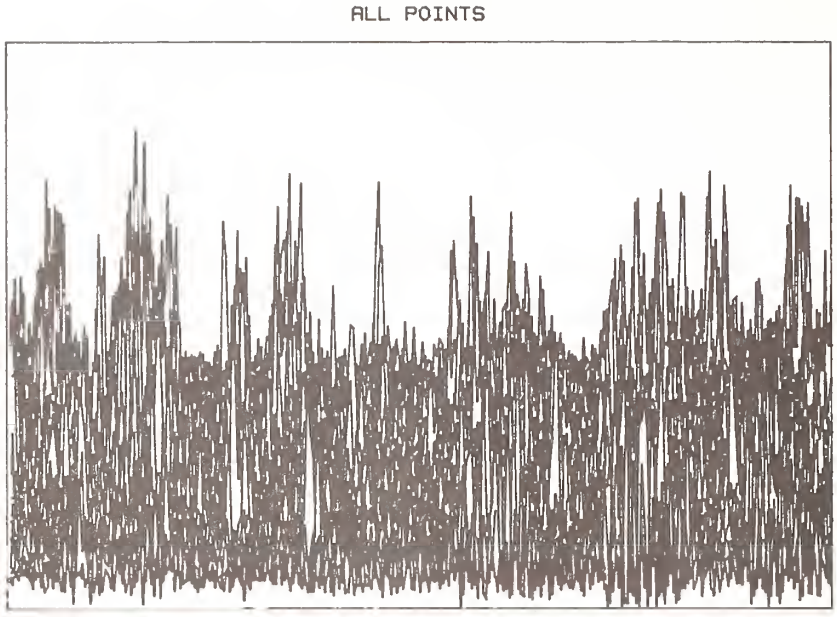

(a)

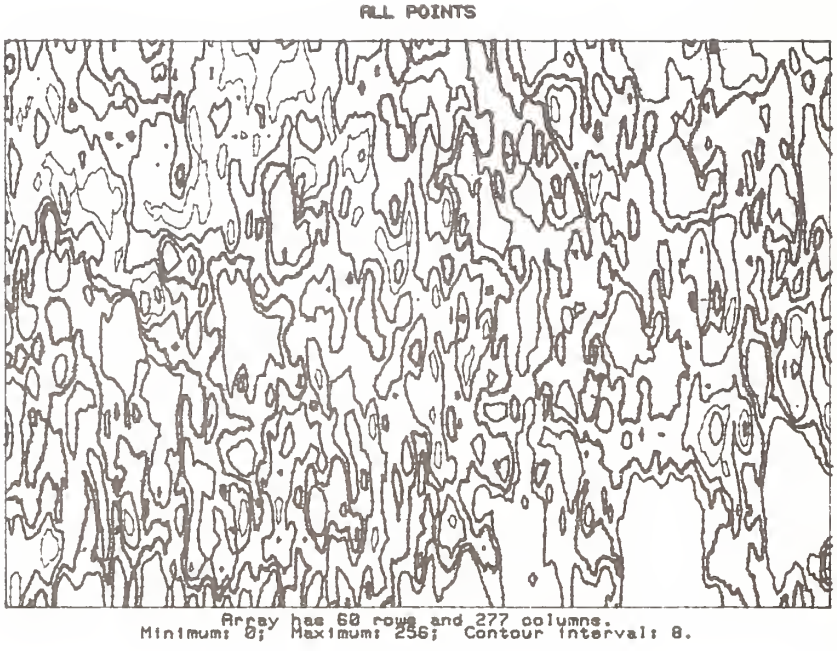

(b)

Figure 2. Various views of a 60 × 277 array of pixels encompassing points A, B, and C. The views are presented without any image-processing techniques applied. The views are (a) scatter intensity map, (b) contour map of scatter intensity, and (c) histogram of the number of pixels with a certain gray level.

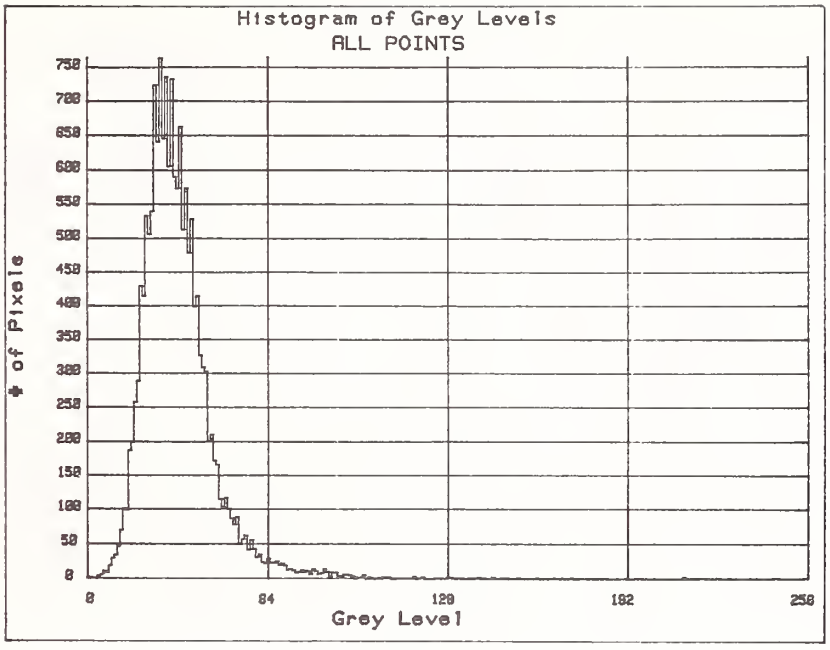

(c)

Figure 2. (Contd.)

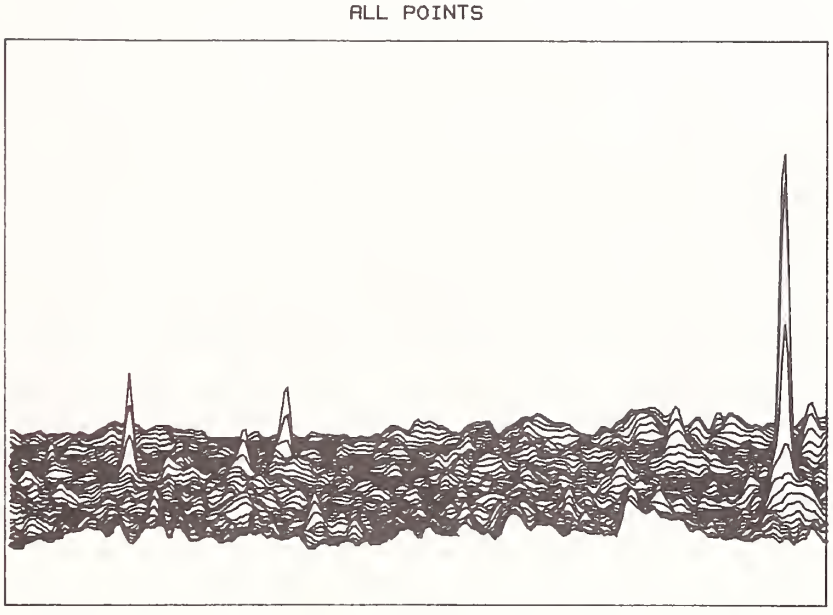

(a)

Figure 3. Views of the array of pixels encompassing points A, B, and C with image-processing techniques applied. The techniques used were thresholding, 3 × 3 average smoothing, scaling, linear interpolation and a 1% Laplacian edge enhancement. The views are (a) scatter intensity map (here the points are very clearly defined), (b) contour map (again the points and topographies are very much sharper), and (c) histogram of gray levels (notice the narrowing of gray scale levels, but the increase in the number of pixels).

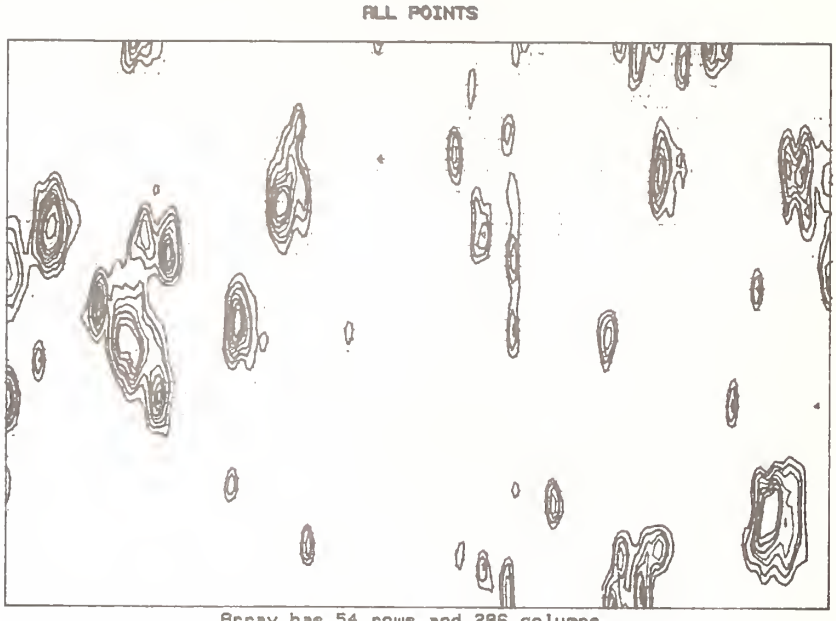

(b)

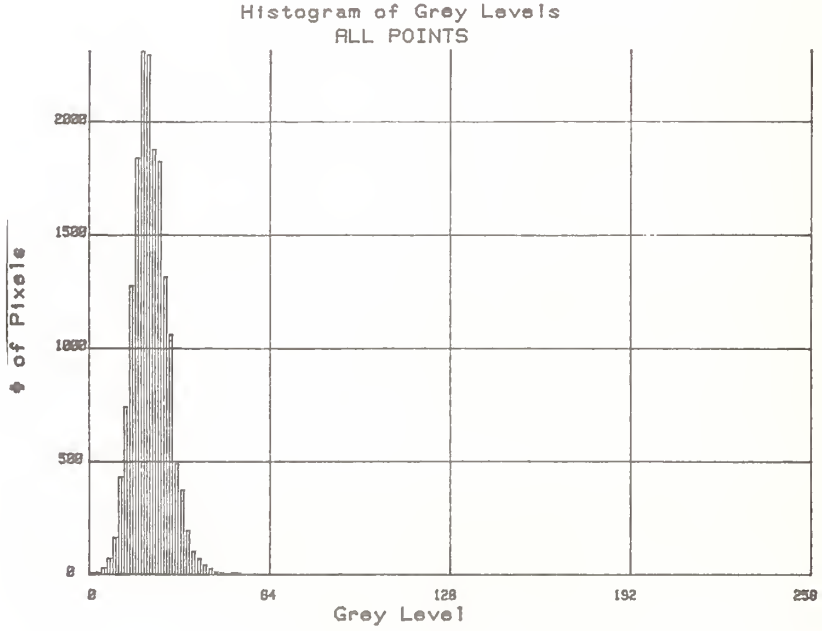

(c)

Figure 3. (Contd.)

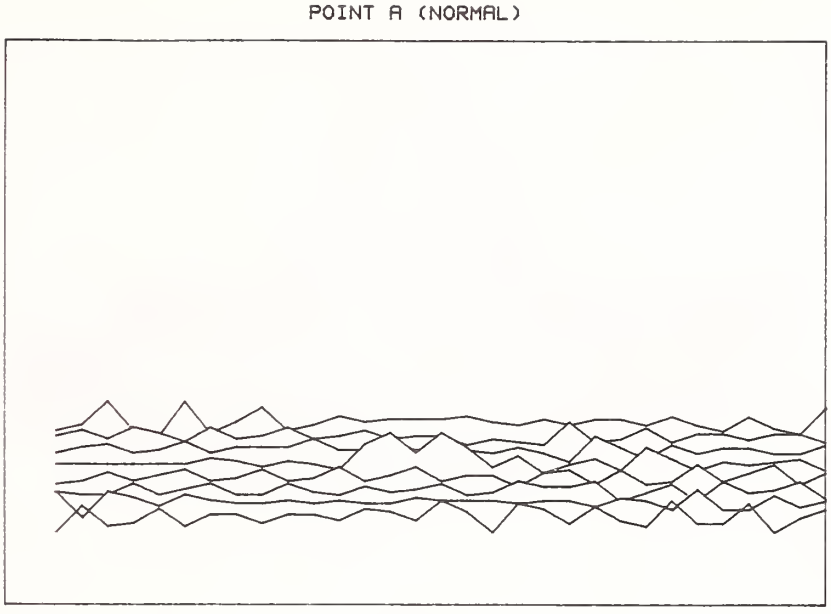

(a)

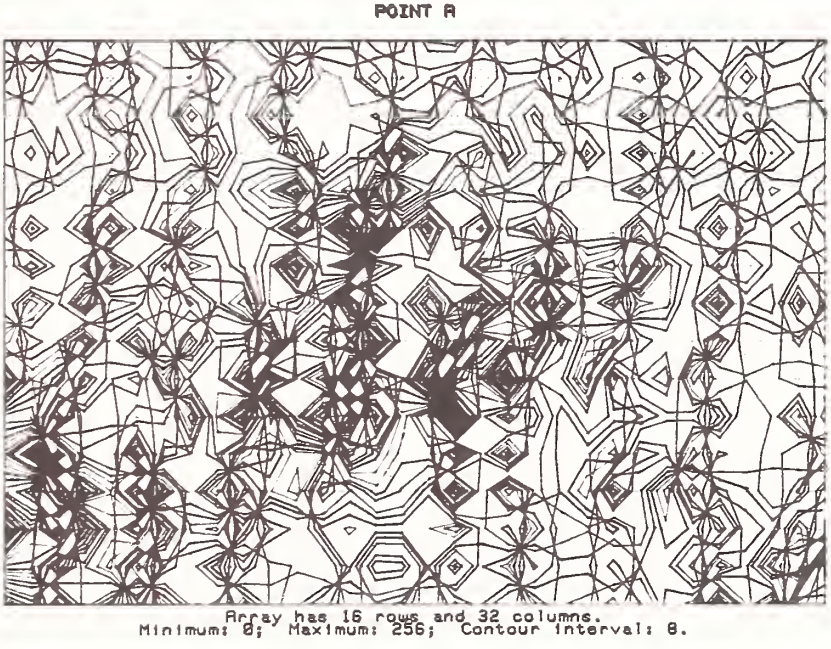

(b)

Figure 4. (a) Scatter intensity map and (b) contour of point A without image processing applied.

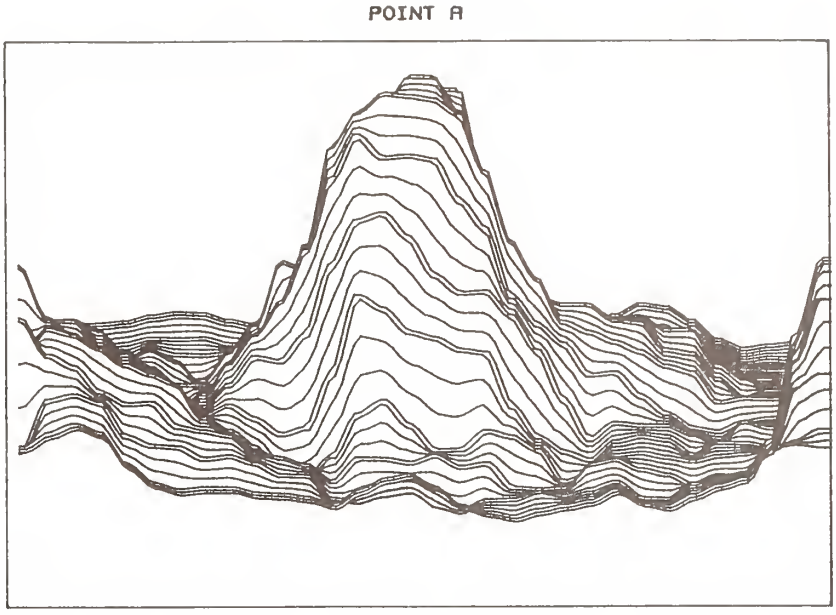

(a)

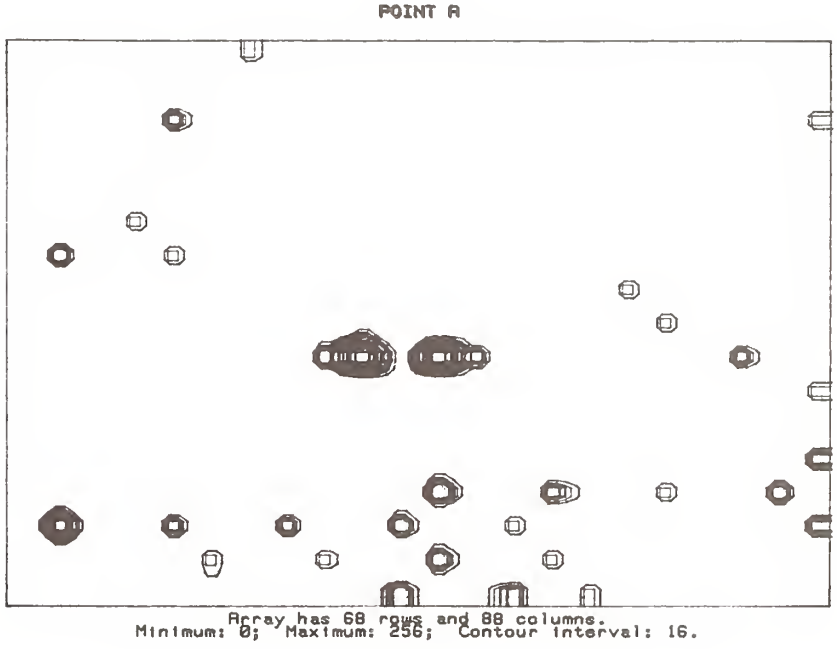

(b)

Figure 5. (a) Scatter intensity map and (b) contour of point A with image processing applied. The image-processing techniques used were quadratic interpolation, thresholding, 3 × 3 median averaging, and scaling.

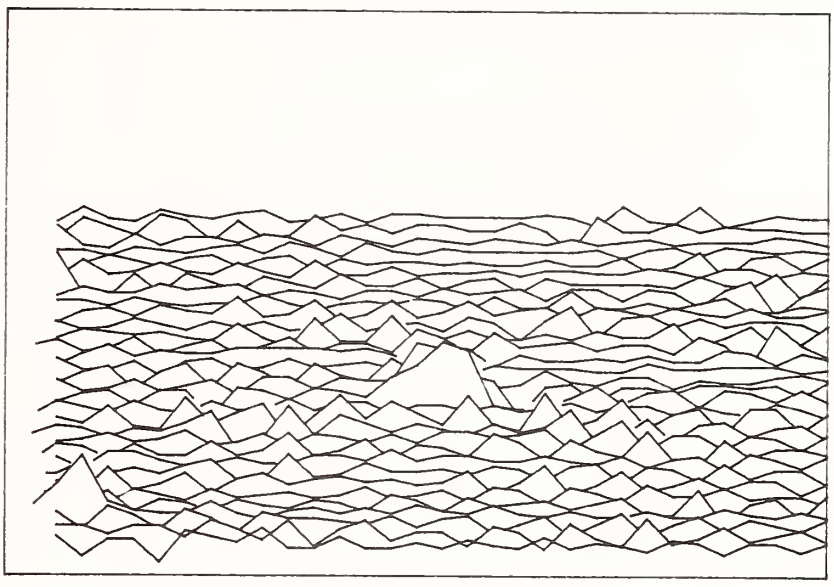

(a)

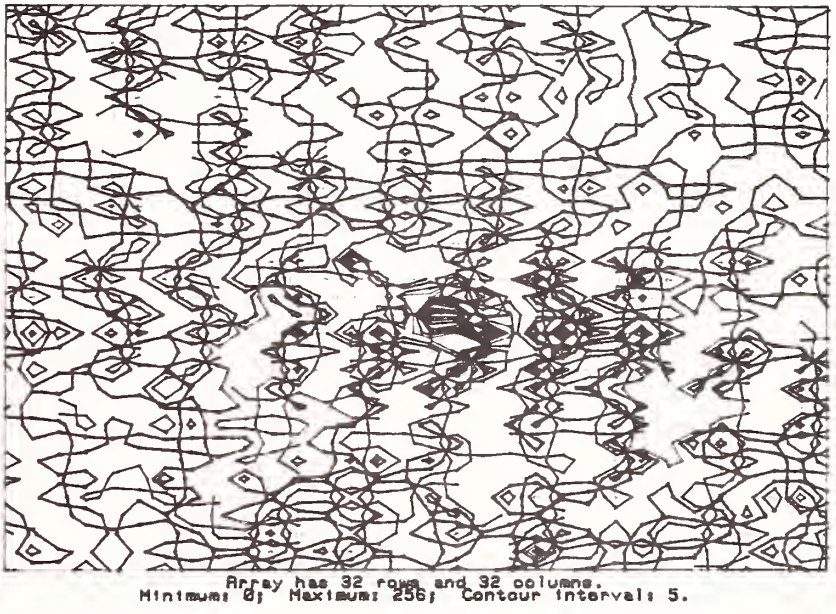

(b)

Figure 6. Views of a point-B-type laser-illuminated defect that did exhibit laser damage. They are presented without image-processing techniques applied. The views are (a) scatter intensity map (notice very little difference from background), (b) contour map (poor resolution of defect contours), and (c) a histogram of gray levels for this defect.

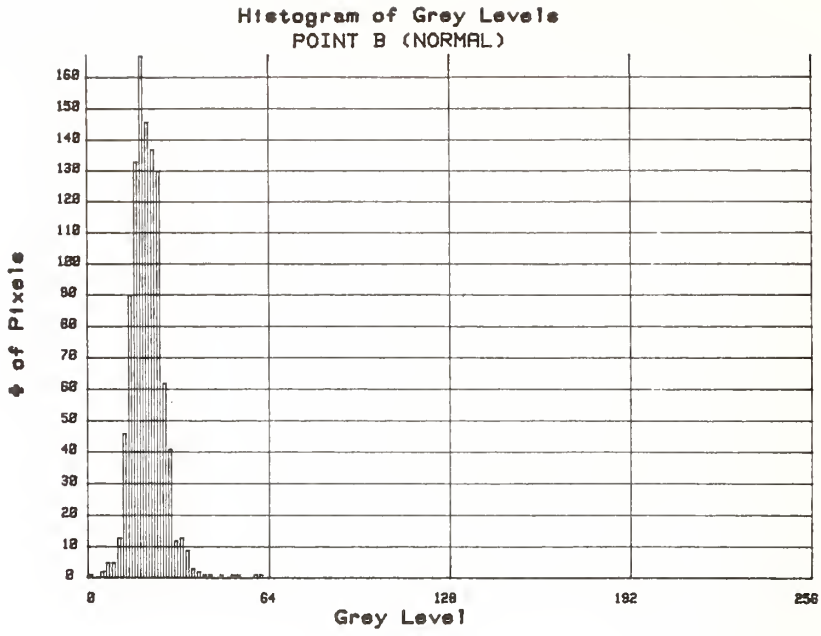

(c)

Figure 6. (Contd.)

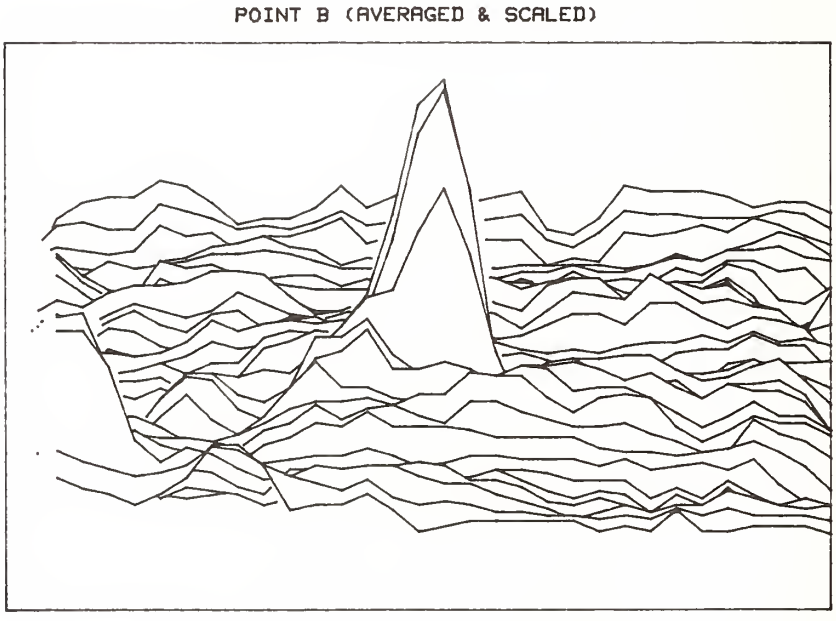

(a)

Figure 7. Same views of the point-B-type defect with image-processing techniques of local maximum smoothing and scaling applied. The views show (a) scatter intensity map (notice the clear distinction of point over background), (b) contour map (now shows two distinct regions of high intensity scatter -- more easily seen in color). This correlates with the contours seen for points A and C that damaged 100% of the time. Figure 7(c) shows a histogram of gray levels (notice the more even spread of pixels and the increase in span of gray levels).

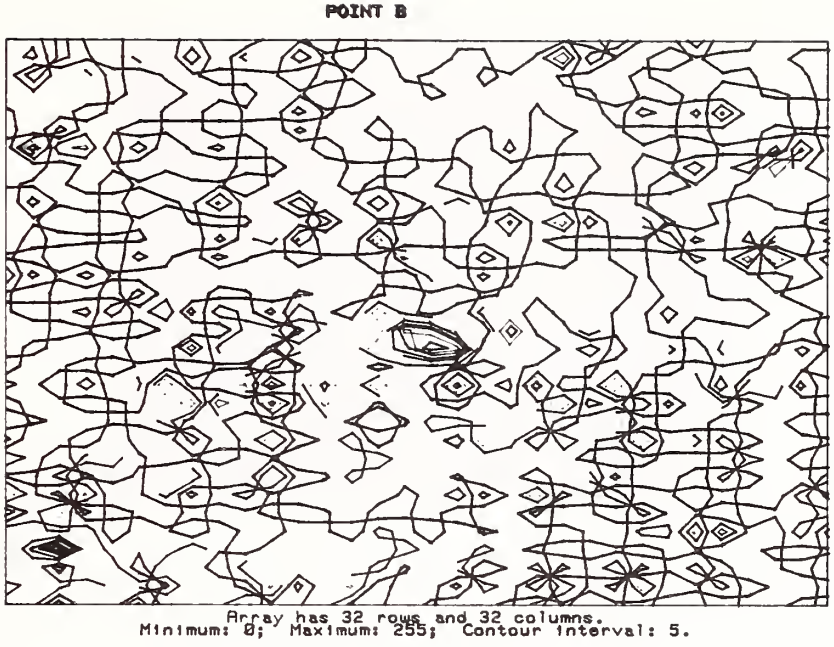

(b)

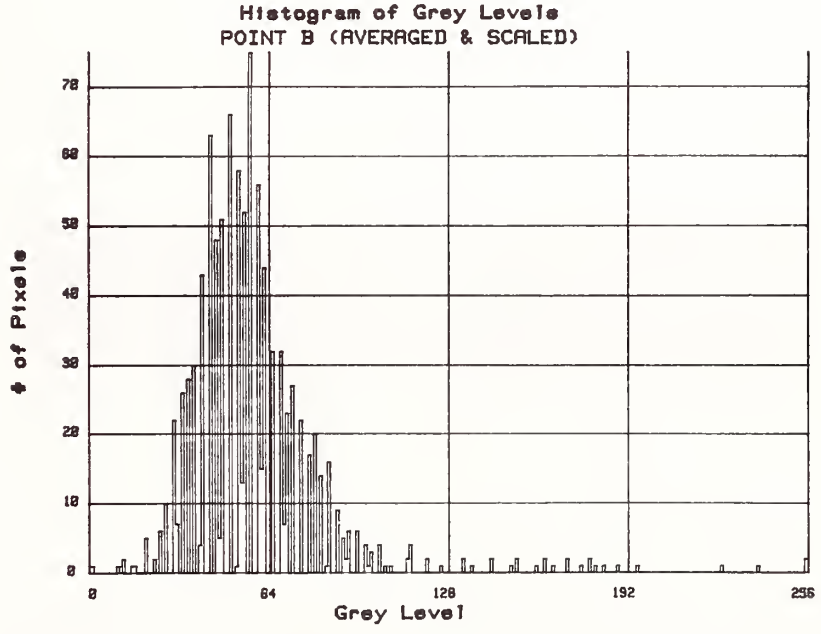

(c)

Figure 7. (Contd.)

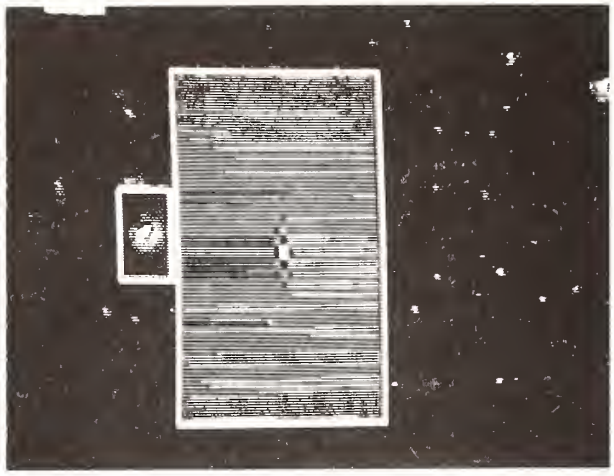

(a)

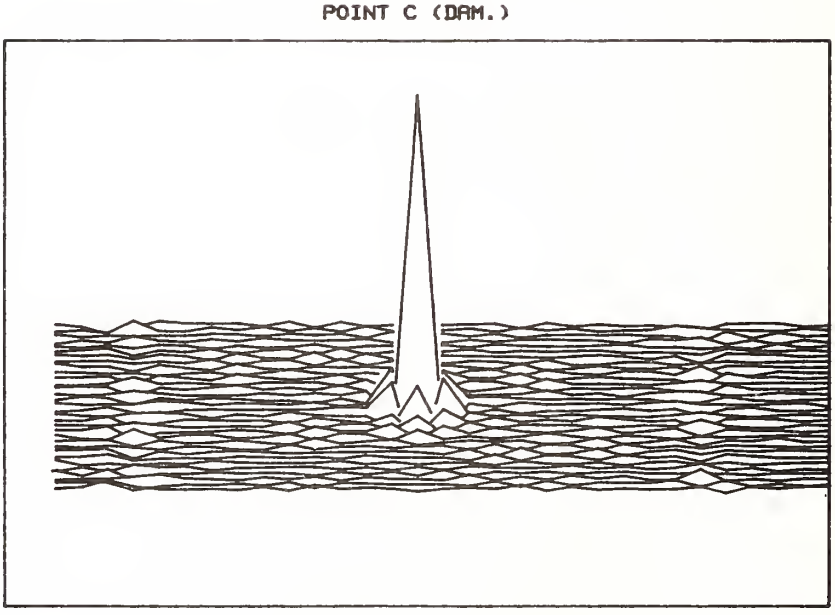

(b)

Figure 8. Figure 8(a) is a photograph of the damaged point-C scatter (left boxed area). The right larger boxed area is an enlarged video image of its fast-Fourier transform. Figures 8(b) and (c) show the scatter surface map and the contours of the transform of point C, respectively.

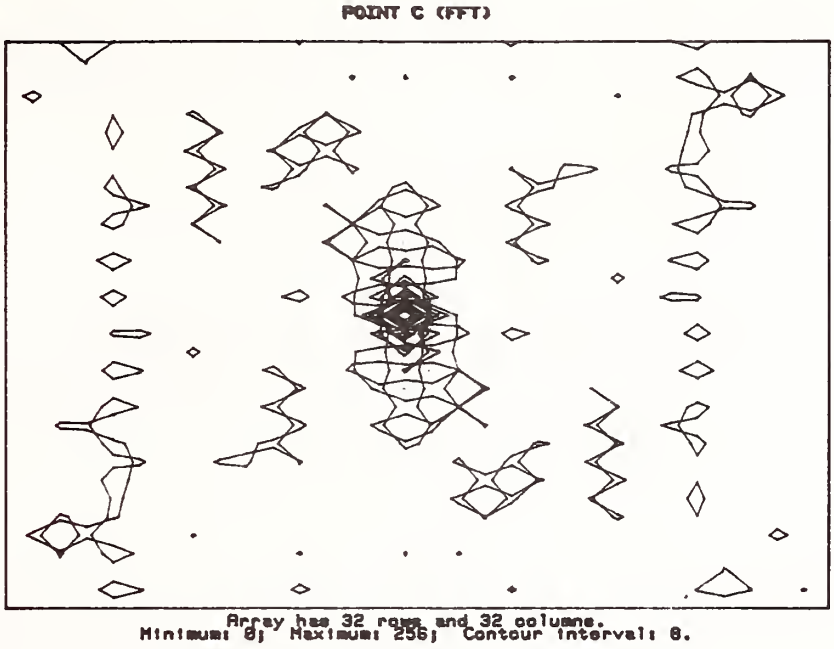

(c)

Figure 8. (Contd.)

- MANUSCRIPT NOT RECEIVED -

OPERATIONAL LIMITS FOR $ZnSe/ThF_4$ MULTILAYER MIRRORS IN THE LOS ALAMOS FREE-ELECTRON LASER OSCILLATOR*

Brian E. Newnam and Steven C. Bender
Los Alamos National Laboratory
Los Alamos, New Mexico 87545

ABSTRACT

The Los Alamos free-electron oscillator is driven by an rf linear accelerator at an energy of ~20 MeV. This L-band linac delivers electrons in a 100-μs-long train of micropulses (~10-ps width) each separated by 46 ns. A semi-confocal resonator ($g_1 g_2$ = 0.87 to 0.95) is used to maximize the optical intensity within the magnetic undulator by which extraction of energy from the electrons and optical gain are maximized.

For operation in the spectral range of 8 to 12 μm. multilayer dielectric reflectors of $ZnSe/ThF_4$ on ZnSe substrates have been used for the end mirrors. At moderate laser power, these reflectors have performed without evidence of deterioration in the multiple environment of laser photons, gamma rays and neutrons [1]. However, when the time-average optical intensity on the mirrors exceeded the range of 500 to 700 kW/cm^2, the resonator losses increased and the output power dropped [2]. Post inspection revealed coating damage in the form of a collection of many elongated pits plus one or two larger (1 x 1 mm^2) pits penetrating to the ZnSe substrate. The damage mechanism most consistent with the observed morphology is heating of microscopic absorbing defects leading to film rupture by excessive stress.

[1] "Optical performance of the Los Alamos free-electron laser," B. E. Newnam, et al., IEEE J. Quantum Electron. QE-21, 867 (1985).

[2] "Recent results from the Los Alamos free-electron laser," D. W. Feldman, et al., IEEE J. Quantum Electron. QE-23, 1476 (1987).

* Work performed under the auspices of the U.S. Department of Energy and supported by the U.S. Army Strategic Defense Command.

Manuscript Received
5-23-88

Damage Threshold of Oscillator Mirrors in Mark III FEL

David A. G. Deacon

Deacon Research
900 Welch Road, Suite 203, Palo Alto CA 94304

Stephen V. Benson, John M. J. Madey, John Schultz

Stanford Photon Research Laboratory
Stanford CA 94305

We have observed damage of gold resonator mirrors in the Mark III FEL with 1.2 microsecond macropulses at a fluence threshold of 21 J/cm^2. This number agrees with YAG laser damage measurements scaled by the square root of the ratio of the pulse lengths. Silver coated mirrors have not shown damage up to an equivalent threshold of 40 J/cm^2. Work aimed at increasing the pulse energy on the silver mirrors is continuing; we expect to extend these measurements in the near future.

key words: FEL; gold; mirror damage; scaling; silver

The Mark III FEL has been designed with metal mirrors and coatings so that the tuning capability inherent in the free electron laser may be exploited [1]. Output coupling is performed with an intracavity Brewster plate whose angle can be adjusted away from the Brewster angle to vary the output coupling. Thermal laser damage has been observed both in the Brewster plates and in the resonator mirrors. Another paper in this conference [2] discusses the measurements which have been made on candidate intracavity materials. In this paper, we discuss the damage thresholds we have inferred from the resonator mirror data, and review the implications.

The damage problem is aggravated in the Mark III by the fact that the length of the optical resonator has been made short to optimize the laser power in the short electron beam macropulse, so the intensity at the mirrors is high. In our initial work with this

To be published: Proc. Boulder Damage Symp., Laser Induced Damage in Optical Materials: 1987, NBS Pub., US Govt. Printing Ofc., Washington DC 20402.

machine, we used resonator mirrors fabricated from molybdenum substrates with an e-beam evaporated gold coating and titanium binder layer [3]. These mirrors were damaged during operation. The replacement mirrors, fabricated from copper substrates, with a silver coating and chromium binder layer [4], have performed without damage at somewhat higher fluence levels.

A knowledge of the time structure of the Mark III FEL is important in interpreting the damage results we have measured. As in all RF linac FELs, the laser produces a series of picosecond scale micropulses during the few microsecond (adjustable) macropulse. Typical values for the Mark III are 1 ps and 2 microseconds.

For the conditions under which damage occurred, the mirrors are exposed [5] to a fluence for each of the 3500 micropulses of 6 mJ/cm^2, or an average fluence during the macropulse of about 21 J/cm^2. The laser wavelength was 2.7 microns and the macropulse length 1.2 microseconds. Under the same conditions but at the slightly longer wavelength of 3.1 microns, no damage was obtained during three weeks of operations. The major uncertainty in the calculation of the damage threshold from our data is the laser spot size on the mirrors. The theoretical beam waist at the mirrors, 1.39 mm, is easily obtained from the Gaussian beam formulas. However, due to the optical guiding present in the FEL [6], the Strehl ratio is not unity. In view of our measurements of the Strehl ratio, we estimate the effective mode size to be 17% larger than the TEM_{oo} mode size at the mirrors [7].

The damage threshold of these mirrors at 1.06 microns was measured for us at Livermore [8] on the REPTILE testing facility, with 16 ns YAG laser pulses. The threshold for severe surface pitting was observed at 1.4 J/cm^2. Scaling the single pulse threshold using the well known relation that the thermal damage threshold scales as the square root of the pulse length, we derive an expected threshold for the micropulse and the macropulse of 11 mJ/cm^2 and 12 J/cm^2 respectively. The absorption coefficient of Au is lower at 3 microns by a factor of 1.8 [9], yielding an expected damage thresholds at 3 microns of 20 mJ/cm^2 and 22 J/cm^2, respectively. Although the observed micropulse fluence remains a factor of three below the expected threshold, the macropulse fluence equals the expected threshold for damage. We conclude that the damage probably is initiated by thermal slip in the gold, and that it is the accumulation of absorbed energy during the macropulse which eventually heats the coating above the slip temperature.

As indicated above, there is not enough energy in the micropulses to drive the coating temperature above the scaled threshold for plastic deformation. As a result, we have not been able to verify the scaling of the mechanism to the 1 ps regime. Some variation in the thermal properties of the gold might be expected to appear at very short time scales, although such changes will affect the thermal threshold only as the square root of their values. In the absence of such effects, the root(tau) scaling relation should continue to hold for bulk gold down to pulse durations of 0.1 ps

where the thermal diffusion depth becomes equal to the skin depth.

The dependence of the observed damage on the laser wavelength leads to the question of whether water adsorbed on the mirrors might play a role in the damage, since the absorption coefficient of water vapor changes by more than four orders of magnitude between 3.2 and 2.7 microns. Two factors argue against this speculation. First, the absorption of liquid water changes by less than a factor of ten over this range since its spectrum [10] is much broadened and smoothed. The spectrum of adsorbed water will be intermediate between those of the liquid and the gas because of the electronic interaction with the surface. Second, at 10^{-6} Torr, only a monolayer exists on the mirror surfaces unless trapped by structural irregularities in the evaporated gold films.

The most likely possibility is that the laser operated close to the threshold at 3.1 microns, and above threshold at 2.7 microns. The output power was initially 50% higher during the operation at 2.7 (for a few seconds before the mirrors damaged). Although the absorption coefficient of bulk gold is essentially the same at the two wavelengths [9], the change in the peak power may have been enough to drive the mirrors beyond the threshold.

As mentioned above, the silver coated copper mirrors [4] we have used since the observation of gold mirror damage have not yet shown signs of damage at higher fluence levels than could be sustained by the gold mirrors. The highest fluence levels these mirrors have yet experienced [11] are about 60 J/cm^2 in the 2.5 microsecond macropulse.

This work was supported by the Office of Naval Research, Contract No. N0014-85K-0535, and the US Army Research Office, Contract No. DAAL03-86K-0122.

References

[1] S.V. Benson, J.M.J. Madey, J. Schultz, M. Marc, W. Wadensweiler, G.A. Westenskow, "The Stanford Mark III infrared FEL", Nucl. Instr. & Meth. A250 39 (1986).

[2] S.V. Benson, E.B. Szarmes, B.A. Hooper, E.L. Dottery, "Laser damage on ZnSe and CdTe using the Stanford Mark III infrared FEL", this conference proceedings.

[3] Spawr substrates, evaporated coatings applied at Stanford University.

[4] These mirrors were fabricated by Perkin Elmer (1986), M. McGuirk, 761 Main Ave., Norwalk CT 06856.

[5] Extracted energy 0.14 mJ, outcoupling 0.04%, 60% transport efficiency.

[6] J.E. LaSala, D.A.G.Deacon, J.M.J.Madey, "Optical Guiding in a Free Electron Laser Oscillator", Phys. Rev. Lett. 59 2047-2050 (1987).

[7] Using the Strehl ratio of 0.7 and the assumed beam envelope formulas in B.E. Newnam, R.W. Warren, R.L. Sheffield, J.C. Goldstein, C.A. Brau, "The Los Alamos FEL oscillator: optical performance", Nucl. Instr. & Meth. A237 187-198 (1985).

[8] F. Rainer, D. Milam, Lawrence Livermore National Laboratory.

[9] AIP Handbook, Third Edition, McGraw-Hill, New York (1982) 6-138.

[10] W.G. Driscoll, W. Vaughan (eds.) Handbook of Optics, p. 15-28, McGraw-Hill, New York, (1978).

[11] Extracted energy 30 mJ, outcoupling 2.5%, 60% transport efficiency.

- MANUSCRIPT NOT RECEIVED -

LASER INDUCED DAMAGE MEASUREMENTS OF FREE ELECTRON LASER OPTICAL COMPONENTS

L. John Jolin, Virgil E. Sanders, Steven J. Salazar, CLS-6
Chemical and Laser Sciences Division
Los Alamos National Laboratory
Los Alamos, NM 87545

ABSTRACT

A study of free electron laser (FEL) related optical damage is currently under way at Los Alamos National Laboratory. A single burst of the FEL has been simulated using a Nd:YAG laser system operating at 1064 nm. The laser is a modelocked, 100 microsecond, pulse selected system operating at 10 pulses per second.

Damage thresholds for conventionally deposited dielectric high reflectors as well as bare metals have been studied and the results are reported. Some high reflectors have demonstrated laser induced damage thresholds of greater than 5 megawatts/cm^2 average pulse power.

Also, reported are damage data for a non-modelocked laser configuration.

Manuscript Received 12/16/87/sar

Database of Average-Power Damage Thresholds at 1064 nm*

F. Rainer, E. A. Hildum, and D. Milam

Lawrence Livermore National Laboratory
Livermore, CA 94550

We have completed a database of average-power, laser-induced, damage thresholds at 1064 nm on a variety of materials. Measurements were made with a newly constructed laser at the Lawrence Livermore National Laboratory (LLNL) to provide design input for moderate and high average-power laser projects. The measurements were conducted with 16-ns pulses at pulse-repetition frequencies ranging from 6 to 120 Hz. Samples were typically irradiated for times ranging from a fraction of a second up to 5 minutes (36,000 shots). We tested seven categories of samples which included antireflective coatings, high reflectors, polarizers, single and multiple layers of the same material, bare and overcoated metal surfaces, bare polished surfaces, and bulk materials. The measured damage thresholds ranged from < 1 J/cm^2 for some metals to > 46 J/cm^2 for a bare polished glass substrate.

Key words: antireflective coatings; bare substrates; bulk damage; damage; e-beam coatings; laser-induced damage; metallic coatings; polarizers; reflectors; sol-gel coatings; thin films.

1. Introduction

We have constructed the REPTILE (Repetition Laser Experiment) Facility to conduct laser-induced damage studies on a variety of material types at moderate pulse-repetition frequencies (PRF) ranging up to 120 Hz at 1064 nm. The facility supports the development of damage resistant materials needed for several laser projects at the Lawrence Livermore National Laboratory. It supplements our data gathering capabilities at low PRF from our single-shot damage-test facilities, and provides an efficient means to conduct the following types of tests: PRF dependent studies, thermal accumulation effects, N-on-1 irradiations, lifetime tests, and large area scans. Details of the facility design and computer control system are presented in a companion paper at these proceedings. [1]

2. Laser parameters at the sample plane

The pulses from four commercial YAG lasers, each operating at 30 Hz, are interleaved to yield PRF's up to 120 Hz. At the sample plane we obtain pulse energies up to 0.6 J with peak fluences > 40 J/cm^2. The spatial profile is nominally Gaussian with spot sizes adjusted to be typically 0.5 to 1.0 mm diameter FWHM. Peak fluence can be controlled by varying the spot size and/or by ejecting a fraction of the beam energy with a polarizer-waveplate pair. The output polarization can be set to alternate between S and P from pulse to pulse, or remain fixed at any orientation of linear polarization. The average energy of the four lasers is monitored by a calorimeter. Individual laser pulse energies are measured with a PIN diode which is calibrated with the calorimeter. We use a computer to generate a histogram of pulse energy distributions for each laser and calculate peak fluences either by means of apertured calorimetry or by integrating the spatial profile obtained from a CID video camera at the sample plane. The profile is displayed in a false color format on a TV monitor. We take the average of all peak fluence calculations for all four lasers to yield a peak fluence value for a particular irradiation interval. A second PIN diode measures the temporal profile.

3. Sample diagnostics and irradiation conditions

We examine the test samples for damage by comparing pre- and post-irradiation photographs generated by Nomarski, bright field or dark field microscopy at typical magnifications of 100.

*Work performed under the auspices of the U. S. Department of Energy by Lawrence Livermore National Laboratory under Contract No. W-7405-ENG-48.

These techniques have been described extensively at previous Boulder Damage Symposia and elsewhere. [2] We also monitor the accumulation of heat on the sample surface by means of an infrared imaging camera which can resolve temperature rises of 0.1° C in spatial elements nominally 0.2 mm square.

Most tests were conducted at a PRF of 120 Hz. However, until we implemented a technique for combining the total energy of each of the four lasers into one collinear beam, irradiations at relatively high fluence or with single linear polarization were limited to a maximum PRF of 60 Hz. For instance, all polarizers and high-threshold bare substrates were irradiated at 60 Hz. For isolated instances, we also conducted tests at PRF's ranging from 6 to 30 Hz to compare PRF effects. Our standard procedure was to irradiate a fixed site on the sample for up to five minutes (36,000 shots) before examining it again for damage. We interrupted the irradiation if obvious damage was observed, typically manifested by a plasma, by the emission of coating debris (often accompanied by considerable noise), or by increased scatter of light from a collinear He-Ne laser beam. About 10 sites were irradiated at different fluences to establish a damage threshold fluence, defined to be the mean between the highest non-damaging fluence and the lowest damaging fluence. In some circumstances we scanned the sample continuously through the irradiating beam, usually at about 0.1 mm/min, and then conducted scanned microscopy after the irradiation scan was completed. Our samples were usually mounted at 10° incidence to the input beam to avoid interference effects from rear surface reflections. Polarizers and some special reflectors were tested at their design angles which ranged up to 66°.

4. Databases of laser damage thresholds

4.1 General observations

We conducted over 200 damage tests on samples in seven different categories. These were supplied to us by more than 20 sources both from within LLNL and from commercial vendors. Our databases contained results from a broad spectrum of samples representing state of the art technology, current optics in use on one of the laboratory's laser systems, and both current and old developmental research samples. None of the results of the individual categories of databases is necessarily representative of the highest, lowest or average damage thresholds attainable within that category. Moreover, in some cases they represent evolutionary development of improved thresholds or parameter studies, which may encompass a large spread in thresholds.

Half way through our test program we installed an infrared imaging camera to observe the accumulation of heat on the irradiated sample under PRF conditions. To first order, we found no discernible difference in sample thresholds between those measured at 120 Hz and lower PRF's. In general we found that there was very little macroscopically observable sample heating. Temperature changes were usually on the order of a few tenths of a degree Celsius. As expected, partially absorbing bulk materials yielded the highest surface temperature rises, usually no more than 4° C. Since the smallest resolving element of the camera was about 0.2 mm square, probable heating of micron-sized defects from which damage often originated was not resolvable. Typically, damage occurred within the first fraction of a second of irradiation, although observable damage was sometimes delayed by as long as 235 seconds after the start of irradiation. Catastrophic failure, either delayed or early, usually produced a plasma with temperature of hundreds of degrees. The camera, however, reads a time-averaged temperature which vastly underestimates the short-lived maximum temperature in the plasma.

4.2 Antireflective (AR) coatings

A typical database comparing e-beam-deposited and sol-gel-fabricated coatings is shown in Fig. 1. The histograms display the number of samples that were tested whose damage thresholds fell within a given window 2-J/cm^2 wide. The e-beam coatings were a variety of multi-layer coating designs deposited on either fused silica or BK-7. We further categorize the samples by material used for the high index-of-refraction layers. The low-index materials were either silica or magnesium fluoride. The best AR was a tantala/silica stack, but then, so was the worst. The large spread in thresholds is attributable to variations in coating design and deposition parameters. This threshold distribution, as well as those that follow can obviously be skewed at will by further tests of particular designs. Therefore, tests of more samples of the optimum design for each material combination would yield tighter distribution groupings for tantala, zirconia and titania based AR's.

The sol-gel AR's are single- and multiple-layer porous coatings of the one material noted, primarily silica. These were deposited at LLNL by a variety of processing techniques to establish the optimum parameters for producing high damage threshold AR's. The spread in silica thresholds

represents improvements in the deposition process rather than intrinsic variability in the sol-gel process. In addition, these coatings were deposited on either fused silica, calcium fluoride or KDP crystals. The lowest silica thresholds were those on KDP which did not have particularly clean or well polished surfaces. In general we found that the optimally deposited sol-gel AR's had thresholds comparable to the best e-beam deposited coatings.

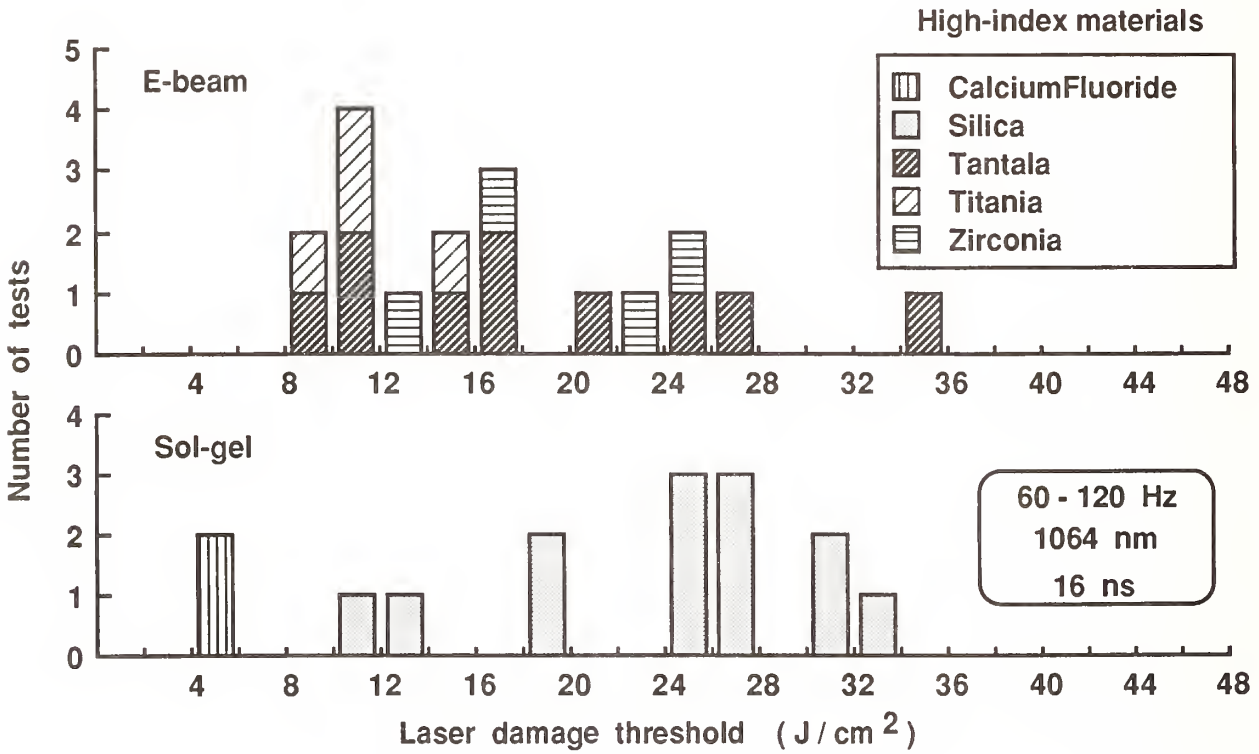

Figure 1. Distribution of laser damage thresholds of 33 e-beam- and sol-gel-deposited anti-reflective coatings. Spreads in the threshold for a particular material combination are attributable to different coating designs or deposition parameters.

4.3 Highly reflective (HR) coatings

We tested 32 HR coatings of greatly varied coating designs. These are shown in Fig. 2. Four different vendors supplied e-beam-deposited HR's on fused silica, BK-7, SiC, or Cu substrates. The low-index material for each sample was silica, although for four samples the vendors did not disclose the constituent materials. Because the number of samples for each material combination is relatively low, and parameter and vendor variations are large, it would be imprudent to discount any material combination based on these tests. The highest threshold sample was a titania/silica stack developed as a research coating several years ago. Most of the other titania/silica coatings were variations of the optimum design so that gaps in the distribution could readily be filled by selecting different HR designs. Samples which had high damage thresholds when measured with single, 1-ns pulses several years ago still had correspondingly high thresholds under our current PRF conditions.

All of the sol-gel HR coatings were fabricated at LLNL and consisted of multiple-layer stacks of the materials listed alternating with sol-gel-deposited silica layers. All were deposited on fused silica substrates. As will be shown later, all of these coatings had thresholds notably lower than those of single or multiple layers of the individual constituent materials. Contrasted with AR designs tested, the sol-gel HR's failed to yield thresholds comparable to the best e-beam HR's. In particular, it can be noted that some of the best e-beam HR coatings were titania/silica combinations, whereas these combinations with sol-gel processing had some of the lowest thresholds.

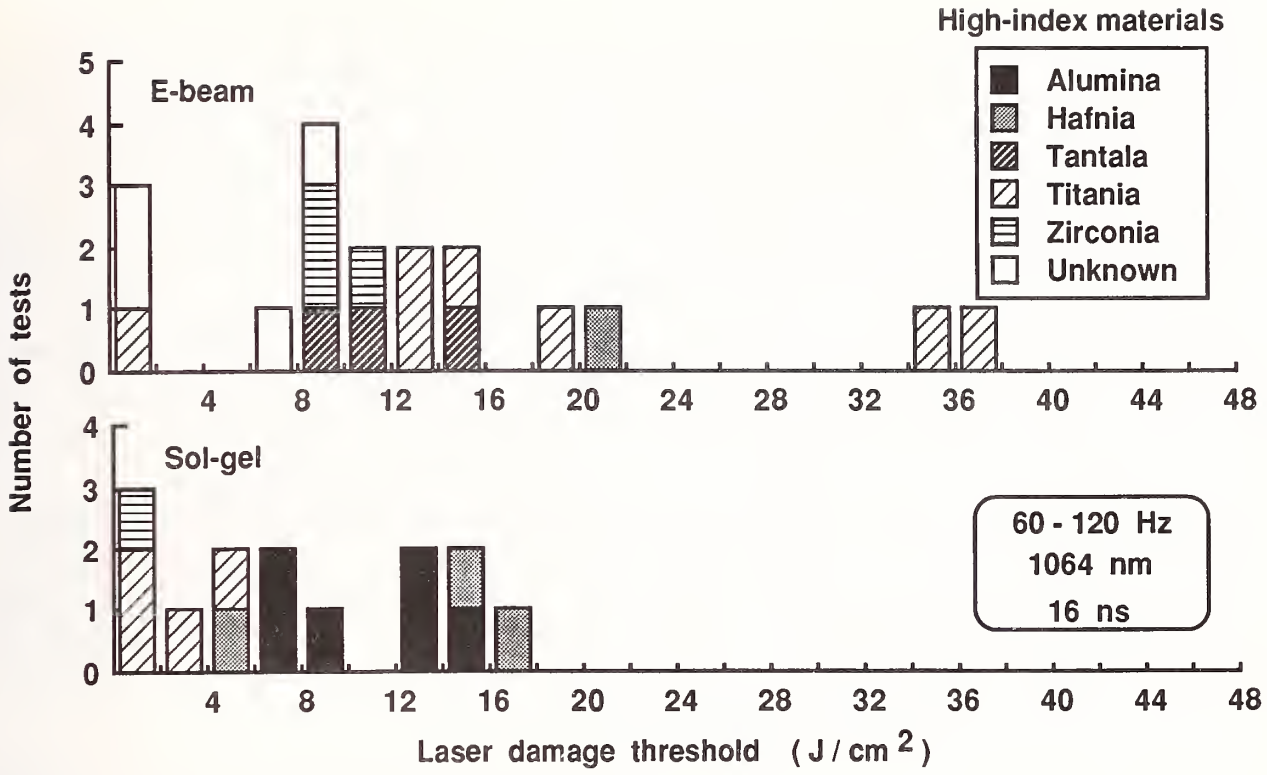

Figure 2. Laser damage thresholds of 32 e-beam- and sol-gel-deposited highly reflective coatings. All samples are comprised of multi-layer stacks of the designated high-index material and silica. Materials of some e-beam coatings were not specified by the vendors.

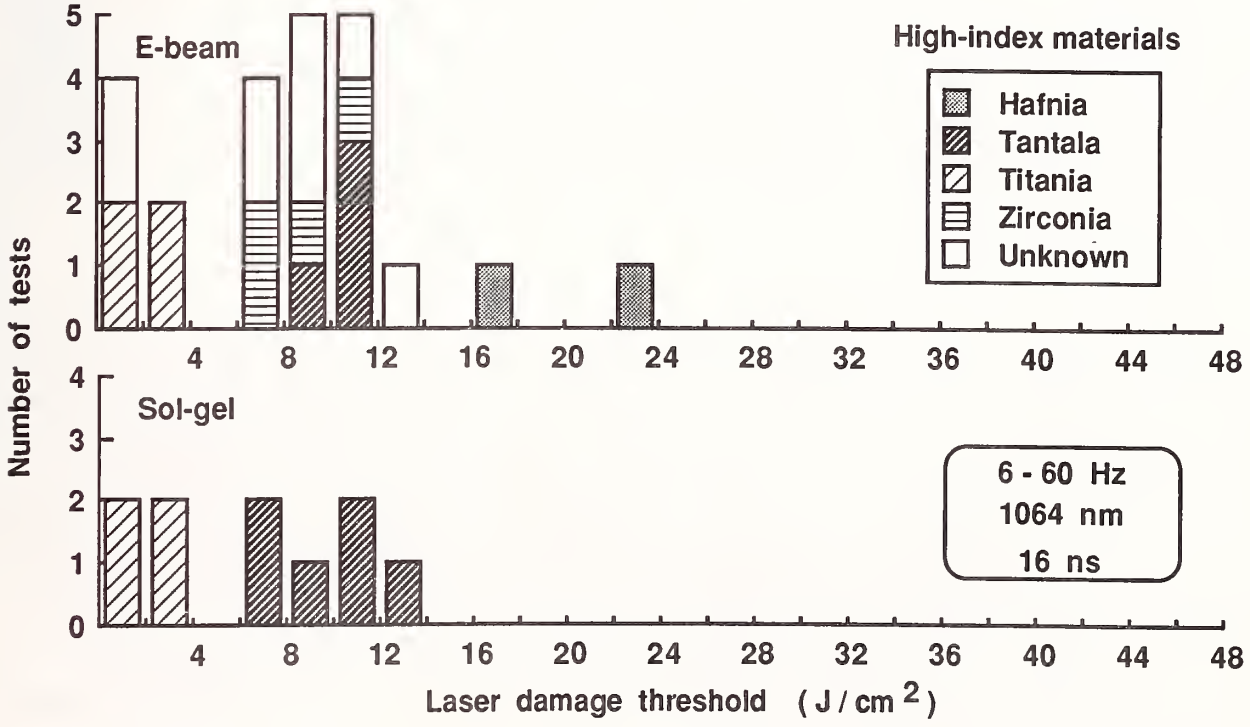

Figure 3. Laser damage thresholds of 33 e-beam and sol-gel deposited polarizers. Except for those listed as unknown, all e-beam deposited polarizers consisted of multi-layer stacks of the materials listed plus silica. The sol-gel polarizers were all single layer coatings.

4.4 Polarizers

Our tests include 33 damage threshold measurements of e-beam and sol-gel deposited polarizers shown in Fig. 3. All but two tests were conducted at 60 Hz. Each sample was irradiated at its optimum design angle of incidence which ranged from 55° to 66°. Seven different vendors supplied e-beam deposited polarizers, although not all provided information on the coating design or the constituent materials. All of the designs provided were multi-layer stacks of silica and the high-index materials identified in the figure. The identified substrates were either fused silica or BK-7. Most of the tests were conducted with P-polarized pulses. However, six samples were also tested at the same angle of incidence with S-polarization irradiation. Of these we noted that the S-polarization threshold was 20% lower for two samples, identical for another two, and indeterminate for the remaining two. As with our HR tests, we must emphasize that the database is too small to exclude any material combination from high threshold polarizer designs. Typically we found polarizers to have a higher density of coating defects than HR's but only a small fraction of the defects actually proved to be the source of damage. Once damage was initiated we found a greater tendency for both the magnitude and number of damage points to grow. The highest thresholds were obtained from research grade hafnia/silica combinations.

All of the sol-gel polarizers were single-layer coatings fabricated on fused silica substrates for process development at LLNL. Although sol-gel coatings were exceptionally clean in comparison with the e-beam-coated polarizers, damage accumulated similarly with successive irradiations. Damage to the titania samples grew particularly rapidly with successive shots compared to the tantala samples. For the limited number of tantala and titania polarizers tested we found thresholds to be comparable to their e-beam material counterparts. However, the degree of polarization in the sol-gel samples is not optimum and is obtained only at high angles of incidence, up to 66°. Only one sample was tested at both P- and S-polarization with a 16% drop in threshold for the latter.

4.5 Single and multiple layers of a single material

All single material tests were conducted with LLNL-fabricated sol-gel coatings on fused silica substrates. We tested 51 samples which are detailed in Fig. 4. The highest thresholds were obtained from alumina coatings although zirconia, hafnia, and tantala coatings also yielded promising thresholds. The two silica coatings were special designs to produce a frosted surface effect. Otherwise, silica coatings, previously listed as AR's, had thresholds comparable to those of aluminas. Possibly because of the extra handling involved, multi-layer coatings made by alternating different materials had lower thresholds than those of the individual constituent materials. We conducted no specific tests to see if the same effect applied to multiple layers of the same material. With these, as with other sol-gel coatings, we often observed a faint emission of white light from the surface for the first fraction of a second of irradiation. We conclude that this is produced by the combustion of residual solvent trapped in the outer portion of these porous coatings. Post-irradiation microscopy showed no evidence of damage in these situations. This shows that light emission from an irradiated sample is not a conclusive indicator of coating damage.

4.6 Bare and overcoated metals

We have examined a limited number of different metallic surfaces which were either plated on substrates or were formed by polishing or diamond-turning bare metal substrates. In addition, most of the samples also had e-beam deposited dielectric coatings to form either a protective layer or a dielectric HR. The results of 17 damage tests on samples supplied by eight different vendors are summarized in Fig. 5. The variety in metals, surface preparation, coatings, vendors, and handling history makes it difficult to note more than a few superficial observations. The highest threshold was 4.3 J/cm^2 for a diamond-turned copper substrate with a dielectric HR stack, yet a comparable sample had a notably lower threshold. All other metals had thresholds of 2 J/cm^2 or less. Molybdenum and copper mirrors which had no dielectric overcoats or HR's fared worse than their counterparts with dielectric coatings. We found in all cases that damage was highly dependent on existing observable artifacts. Under threshold level irradiation damage nucleated at these artifacts but did not grow with repeated irradiation. However, a slight increase in fluence typically caused massive damage. Slow heat accumulation, on the order of 2-3° C over a span of a few minutes, was observed with the infrared camera. However, the temperature of micron-sized artifacts was not resolvable. Basically, all of the metallic samples had among the lowest thresholds of the various categories tested.

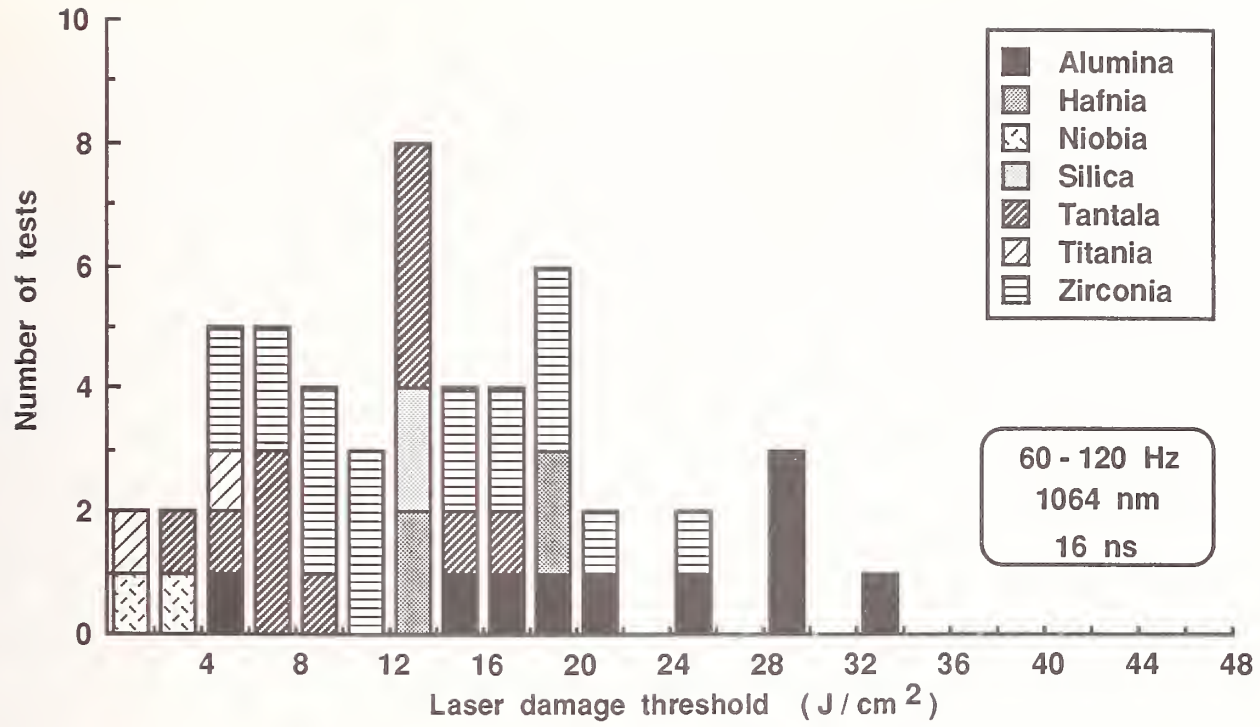

Figure 4. Laser damage thresholds of 51 single and multiple-layer sol-gel samples of a single material. All were fabricated at LLNL on fused silica substrates. The two silica tests were for frosted type coatings. All other silica tests are listed under the AR database.

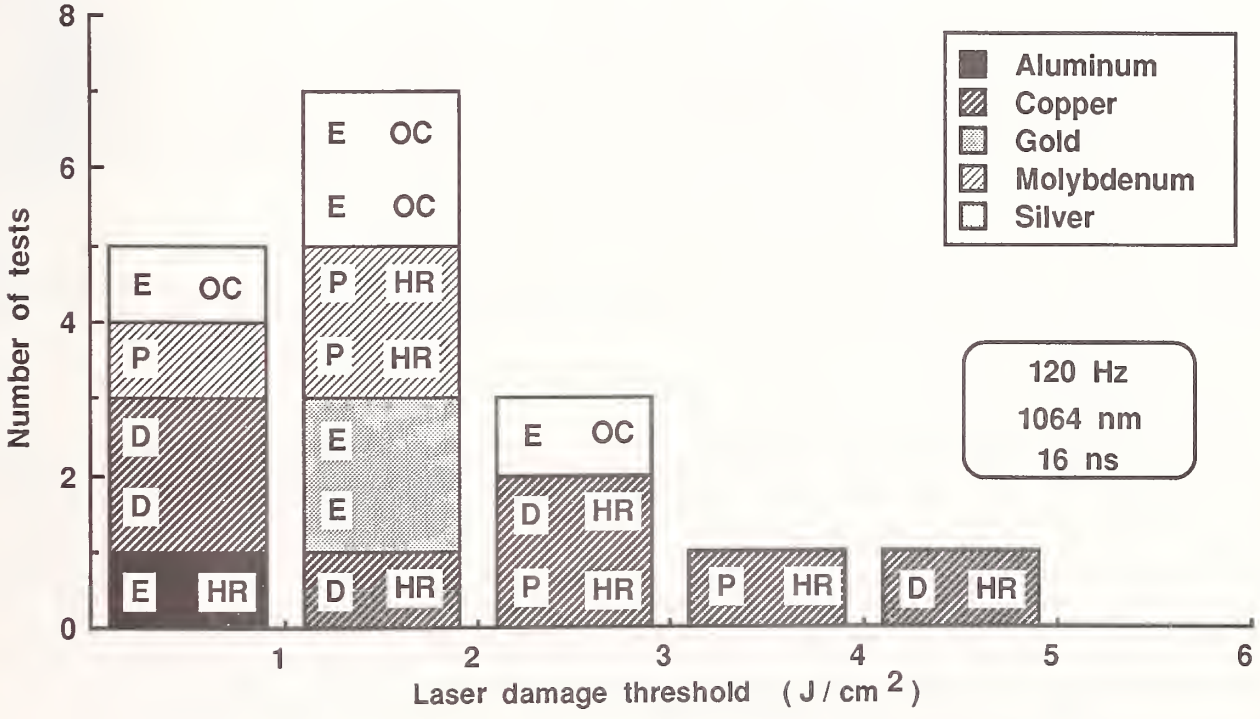

Figure 5. Laser damage thresholds of 17 metallic reflectors from 8 vendors. The metal surface preparation was by diamond turning (D), electroplating (E), or polishing (P). Some samples had dielectric overcoats of a few layers (OC) or a full high reflector stack (HR).

4.7 Bare polished surfaces

We conducted damage tests on four categories of non-metallic bare polished substrates: fused silica, calcium fluoride, non-linear crystals and silicon carbide (Fig. 6). Besides actual differences in materials, other factors influencing the level and spread in damage thresholds of these materials are the quality of polishing or surface preparation and the degree of handling prior to testing. Two thirds of the threshold measurements are for exit-surface irradiation. Rear-surface damage is both easily detected and the more likely failure mode for a bare, highly transparent substrate irradiated at near normal incidence. [3] Unsurprisingly, the highest thresholds were obtained for fused silica, ranging from 25.3 to > 46 J/cm^2. In several cases, limitations on available fluence prevented us from inducing any damage at all. We found no degradation to damage thresholds when the fused silica was subjected to final figuring by ion milling. [4] Among the non-linear crystals tested were KDP, KD*P and LAP (l-arginine phosphate). All exhibited large-area temperature rises of 3-5° C with damage occurring 3-235 seconds after the start of irradiation. Polishing differences, rather than material type, appeared to be the dominant factor in damage level.

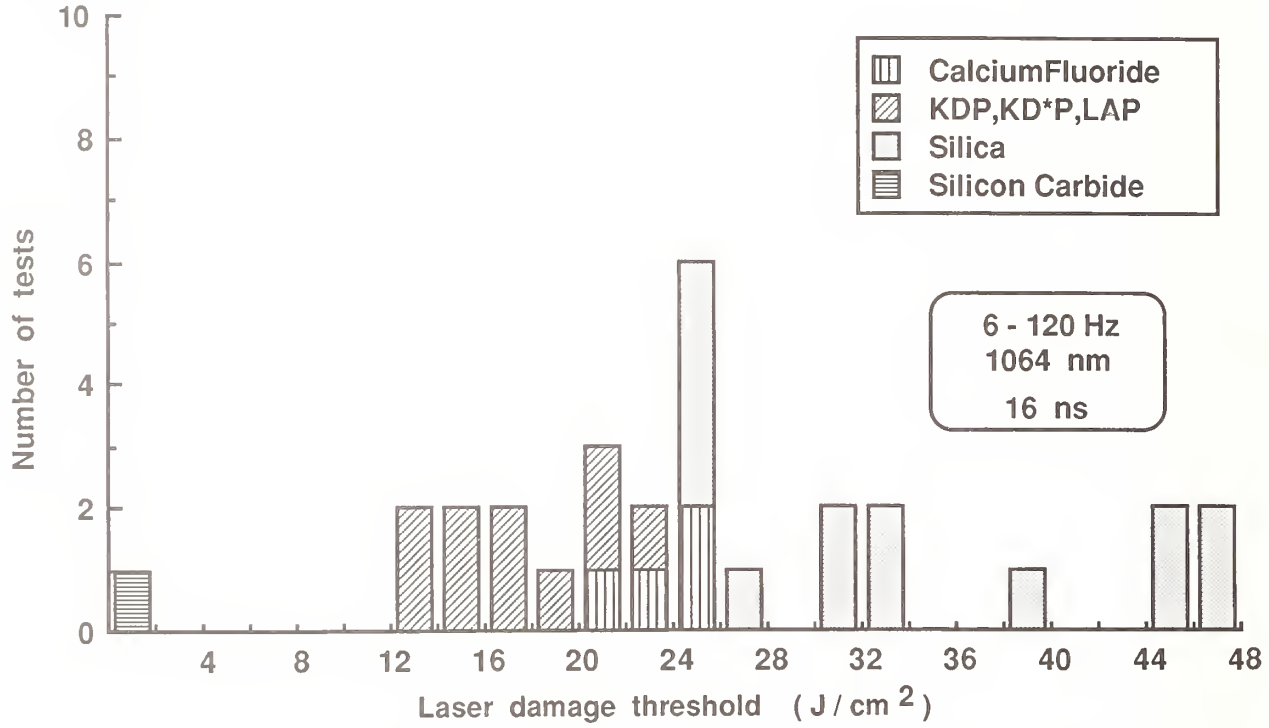

Figure 6. Laser induced damage thresholds of 29 bare polished, ion-milled, or etched surfaces of dielectric substrates. Measurements were made both on the entrance and exit surfaces.

4.8 Bulk materials

Many of the materials used in the bare surface tests were also examined for damage within the bulk material itself (Fig. 7). Bulk damage was usually first detected by increased scattering of light from a collinear He-Ne laser beam. This was followed by more detailed microscopy through the bulk of the substrate. It was occasionally difficult to differentiate between rear surface and bulk damage when massive damage propagated quickly from near the rear surface into the bulk with repeated irradiation. For the non-linear materials, the threshold for isolated bulk damage was typically 30% lower than the threshold for surface damage. In the calcium fluoride crystals, the threshold for surface pitting was less than that for bulk damage which was not observed except in instances where surface pitting grew under repeated irradiation and propagated into the bulk. We list both an indeterminate threshold and number of tests for fused silica. We conducted many tests of bare and AR coated samples for which we were never able to induce bulk damage at fluences exceeding 36 J/cm^2.

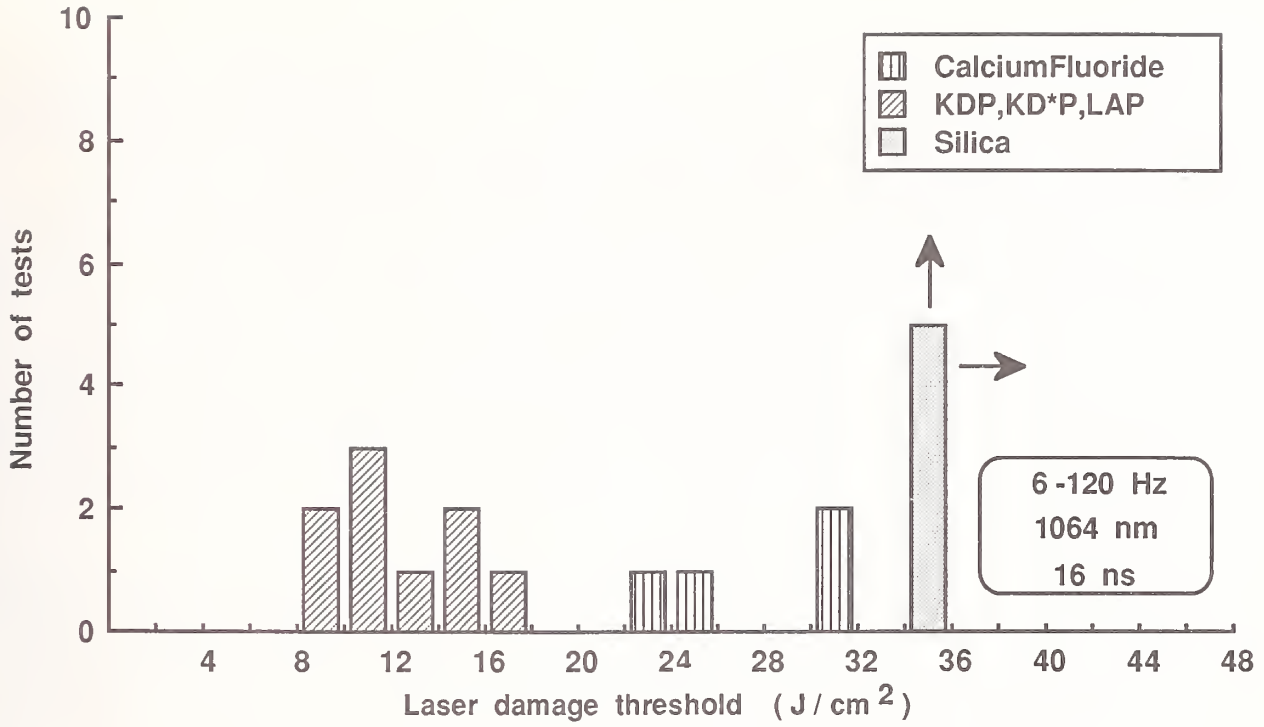

Figure 7. Laser induced damage thresholds of bulk materials. Damage was readily observed in non-linear crystals at fluences averaging 30% less than surface thresholds. No damage was observed in calcium fluoride before massive damage from the rear surface propagated into the bulk material. No bulk damage was observed in any fused silica sample at fluences exceeding 36 J/cm^2.

4.9 Summary

In table 1, we summarize the results of all damage tests conducted with the REPTILE facility to date. We list the maximum, median and minimum thresholds obtained within each sample category, but stress that the threshold distribution can be skewed readily by the choice of samples selected for testing. The reported tests were neither exhaustive nor systematic and are not necessarily indicative of the potentials for materials or designs.

Table 1. Summary of Laser Damage Thresholds
1064-nm, 16-ns Pulses at 6-120 Hz

Category	Type	# of Tests	Threshold (J/cm^2) Max.	Median	Min.
AR	E-beam, sol-gel	33	35	18	5
HR	E-beam, sol-gel	32	>36	9	1
Polarizer	E-beam, sol-gel	33	>23	8	1
Single layer	Sol-gel	51	32	13	1
Metal	Polished, turned, plated, coated	17	4	1	<1
Bare surface	Polished, milled, etched	29	>46	25	2
Bulk material	Silicas, fluorides, crystals	>13	>36	>14	9

5. Conclusions

A database of laser-induced damage thresholds of seven categories of samples, comprising more than 200 tests, was compiled on the REPTILE Damage Test Facility. The tests were conducted with 16-ns, 1064-nm pulses at PRF's ranging from 6 to 120 Hz. Although often including only a minimal number of samples, the individual databases provide rudimentary guidelines on the status of thresholds of currently available optics. Highest thresholds were obtained for clean well-polished fused silicas whose thresholds for both bulk and surface damage readily exceeded 36 J/cm^2. Non-linear crystals that we tested were limited by their bulk damage thresholds although they had relatively poorly polished surfaces. Optimized deposition for both e-beam and sol-gel AR coatings yielded thresholds of 30 to 35 J/cm^2. The best research-grade, e-beam-deposited, HR coatings also achieved high thresholds up to 36 J/cm^2. However, most e-beam HR's and all sol-gel HR's achieved, at best, only half that level. Probably because polarizers are usually more complex coatings requiring more handling, they had somewhat lower thresholds than comparable HR coatings. During the development of many of the above sol-gel coatings we tested many single- or multiple-layer sol-gel films of only one material. In general we found that their individual high thresholds were not attained when combined with other materials to produce coating stacks. Lowest in threshold of all the categories tested were metallic coatings. Even with otherwise good quality e-beam deposited HR stacks deposited over them, metallic coatings failed to yield thresholds higher than 4.3 J/cm^2.

One of our principal goals with REPTILE was to determine if PRF effects would come into play at or below 120 Hz. Although we did encounter samples which took up to several minutes to fail catastrophically, microscopic damage was usually already evident from the first fraction of a second of irradiation. Moreover, we found no significant difference in thresholds between PRF data measured on REPTILE versus single-shot thresholds at the same pulse duration from other damage facilities. We detected negligible heat accumulation in our samples over the course of five minutes of irradiation. However, we cannot rule out possible thermal effects due to unresolvable micron-sized defects.

In general we found REPTILE to provide a very flexible means of producing definitive thresholds with a rapid turnaround. In particular, it has proved to be especially effective for both lifetime and large area damage test irradiations.

6. References

[1] Hildum, E. A.; Rainer, F; Milam, D. A new average-power damage test facility at LLNL. Boulder Damage Symposium. 1987, October 26-28.

[2] Rainer, F.; Deaton, T. F. Laser damage at short wavelengths. Appl. Opt. 21(10); 1722-1724; 1982 May 15.

[3] Crisp, M. D.; Boling, N. L.; Dube, G. Importance of Fresnel reflections in laser surface damage of transparent dielectrics. Appl. Phys. Lett. 21; 364-366; 1980.

[4] Wilson, S. R.; Reicher, D. W.; McNeil, J. R.; McNally, J. J.; Milam, D.; Gonzales, R.; Rainer, F. Laser damage studies of ion milled fused silica. Boulder Damage Symposium. 1987, October 26-28.

Manuscript Received 12/21/87/sar

Causes of Damage in Multilayer Dielectric Coatings Exposed to High Average Power Visible Laser Radiation

David M. Aikens and John R. Taylor

Lawrence Livermore National Laboratory
PO Box 5508, Livermore, CA. 94550

Causes of damage in multilayer dielectric coatings exposed to high average power visible lasers have been examined. Damage has been seen to be related to coating defects, surface contamination, and coating absorption. Defects and contamination, particularly those larger than 4um, have been observed to significantly lower the damage threshold for high reflective coatings. Attempts have been made to visually evaluate defects and surface contamination prior to damage in order to find correlation with the damage threshold. The methods used to evaluate coating defects and conduct high average power damage testing as well as test results are presented. This work demonstrates the value of controlling sources of defects in manufacture and contamination for use in high average power visible laser systems.

1. Introduction

This work was conducted over a six month period to study the factors leading to the damage of dielectric optic coatings when used in high average power laser systems. The objective has been to better understand the mechanisms involved, predict an operational damage threshold under a set of operating conditions, and to identify corrective measures which will lead to a reduction in damage during operation. Damage tests were performed using the Laser Isotope Separation Laser Demonstration Facility at Lawrence Livermore National Laboratory. Preliminary results indicate a dependence on coating absorption and defects as well as surface contaminants. When these limiting conditions are minimized, there are indications that the potential coating design damage threshold is dramatically higher than the coating damage threshold generally observed.

1.1. Definitions

The following terms are defined for use in this discussion:

Potential Damage Threshold - The minimum power density required for catastrophic damage of a given coating design, assuming no surface defects or contaminants greater than 4 um.

Local Damage Threshold - The minimum power density required to initiate catastrophic damage of a small area of coating within an area measuring typically less than 1 mm^2 assuming a given set of conditions and a uniform illumination over the area of interest.

Operational Damage Threshold - The minimum power density required to cause catastrophic damage to a coating when a significant area is illuminated under normal operating conditions. The area sampled must have a significant probability of including typical defects and contaminants. The operational damage threshold represents the practical limit to using the coating in a high average power laser system and is probably the closest to the threshold identified with single pulse or low repetition rate testing.

2. Test Methodology

Testing was performed using three methods. The first method was to locate, under very low power, a small area of a coating with no visible defects or contaminants, and then irradiate that area with progressively higher powers. This test was used to measure the potential damage threshold of coatings. This type of test was run 23 times on 8 different coatings for a particular laser application. The results are listed in table I. The potential damage threshold was lower for high absorption (>100 ppm) coatings, and could not be measured for the very low absorption coatings tested.

Table I

Potential damage threshold for high reflection coating

Coating	No. of Tests	Coating Absorption	Observed Damage	Estimated Potential Damage Threshold
CØ – 1	2	Low	None	High
CØ – 2	9	Low	None	High
CØ – 3	1	Low	None	High
CØ – 4	3	Low	None	High
CØ – 5	2	High	2	5 – 20 kW/cm^2
CØ – 6	3	High	3	5 – 20 kW/cm^2
C45 – 1	1	Low	None	High
C45 – 2	2	High	1	5 – 20 kW/cm^2

The second test method involved choosing an area of coating which is of interest, typically due to visible defects or contaminants, and then irradiating that area with increasingly larger power densities in order to ascertain the local damage threshold. Contaminants were sometimes intentionally added to the coating for this purpose. The results are shown in table II.

Table II

Local damage threshold for high reflection coatings

Coating	No. of Tests	Estimated Potential Damage Threshold	Local Absorption	Observed Damage	Estimated Local Damage Thresholds for Defects/Contaminants
CØ – 1	2	High	Low	1	Fairly high for small defects
CØ – 2	25	High	Low – High	22 out of 25	3 – 20 kW/cm^2
CØ – 3	1	High	High	0	High for small defects
CØ – 6	3	5 – 20 kW/cm^2	High – very high	3	6 – 20 kW/cm^2

The third test method involved scanning the laser over a fairly large section of coating at successively higher powers until catastrophic damage occurred in order to directly estimate the coating operational damage threshold. The results from this test are listed in table III.

Table III

Operational damage threshold for high reflection coatings

Coating	No. of Tests	Coating Absorption	Estimated Potential Damage Threshold	Estimated Local Damage Threshold	Damage Observed During Scanning	Estimated Operational Damage Threshold
CØ – 2	6	Low	high	3 – 20 kW/cm^2	5 out of 6	4 – 17 kW/cm^2
CØ – 7	1	Low			1	14 kW/cm^2
C45 – 3	1	Low			0	High
C45 – 4	1	Low			1	4 kW/cm^2

2.1. Absorption and the Damage Threshold

The potential damage threshold is higher for coatings with low absorption as can be seen in table I. This same relationship can be seen in figure 1 for the operational damage threshold of another type of high reflector coating. The method for absorption measurement is that described by V. Draggoo et al. [1]

2.2. Defects and the Damage Threshold

All observed damage was defect or contaminant related. For high reflection, low absorption coatings, this statement has been confirmed at various power levels and with various coatings. For these coatings, it was seen that no damage occurred unless a defect could be seen as a source of bright scattered under low power magnification. In the cases where a defect was present, the catastrophic damage originated from the defect site, and spread to fill the entire laser illuminated area.

The rate at which damage spread increased as the power density was increased. An example of a damage sequence from a defect and the resultant damage site is shown in figure 2. For high reflection, high absorption (>100 ppm) coatings the size of the defect which results in damage may be smaller than observed for low absorption coatings. Since low absorption coatings were the primary interest, this was not studied.

For the purpose of this work, no differentiation is made between contaminants and defects. Further work is planned to identify defect and contaminant types and materials. Numerous papers [2-5] discuss the make up of defects and contaminants and their relation to laser damage in optical thin film coatings.

The presence of a defect or contaminant generally resulted in a drop in the local damage threshold as can be seen in table II. When sufficient measurements of local damage thresholds are made, the lower levels shown in table II are seen to agree fairly well with the operational damage thresholds listed in table III.

3. Experimental Details

3.1. Coatings Under Test

The coatings tested were developed for use with high repetition rate or CW visible laser systems. Tests were primarily conducted on high reflector coatings but antireflection, beamsplitter, and dichroic coatings were also tested. A variety of coating vendors supplied coatings for test with absorption as high as 10,000 ppm. The low absorption coatings (<100 ppm) were developed under previous contracts.

The coatings are produced on standardized 76.2 mm diameter, 19 mm thick fused silica substrates. All substrates are polished using a process to remove subsurface damage and to produce <5 A RMS surface roughness. High reflection coatings are designed for specific angles of incidence, usually either 0-10° or 45°. Samples were cleaned prior to test using a standard drag wipe technique. The coatings tested were designed for high reflection over specific wavelength applications, and only common dielectric materials were used.

3.2. Test Facility

Tests were performed in the Laser Isotope Separation Laser Demonstration Facility by diverting the beam to be used for test into the optical test area where the beam was reimaged and reduced in size on the test optic. Care has been taken in this setup to ensure that the test sample is located at the exit pupil of the relay optics, which in turn is an image of the laser amplifier cavity. This is done so that the beam is far from image space which ensures the removal of any Fresnel structure from the beam profile. This is shown schematically in figure 3. A picture of the test area is included as figure 4. Both a thermal imaging camera that measures the temperature rise of the irradiated part and a CCD camera with a lens providing 20X magnification so that the coating surface can be viewed as it is irradiated and translated under the beam. Defects and contaminants greater than 4 um can be seen from the scattered light.[6] Details of the surface condition and the damage event are recorded on video

tape for later slow motion viewing. The video image is processed so that relative variations in brightness can be measured. Defects as seen in the video system and in microscopic size characterization are shown in figures 5 and 6.

This facility provides power continuously at visible wavelengths and at a specific polarization. Test conditions are given in table IV. Incremental increases in laser power is produced by adjusting operating efficiency, adding pump power, or adding amplifiers in the laser chain. Additional control of power density is provided by changing beam size. This facility is unique in its high average power and flexibility. It is also a large facility which presents scheduling problems and requires a number of technicians to operate.

Table IV

Test conditions

Wavelength range:	**500–650 nm**
Power:	**100–350 Watts**
Repetition rate:	**4.3 kHz**
Pulse width:	**80 ns**
Beam size:	**0.5–8 mm diameter**
Test duration:	**10–100 seconds/test area**

3.3. Beam Characteristics

The beam size is measured directly in the video camera by comparison to a graduated scale and can be adjusted by positioning the beam formatting optics.. Beam power is monitored at power meters which are part of the laser system and is periodically checked at the test site. Because of the size and large number of optical components, the most time consuming part of using this facility for testing is the time required to characterize the spatial beam profile. The beam profile is examined using an in house image analysis program and a false color presentation. Optical alignment is then made to optimize uniformity. A typical beam profile is shown in figure 7.

3.4. Characterization of Damage and Damage Threshold

From test results it can be seen that the probability of damage is variable even within a single part. Statistical differences exist at different points in the coating which cause the local damage threshold to vary from spot-to-spot. Defects in the coatings which can be seen by scattered light and surface contaminants have been the origin of virtually all damage that we have observed for the high reflector coatings. Not all defects or contaminants cause damage at low levels. In addition, there may be other variables that contribute to the statistically varied nature of the damage but no damage occurred under test conditions that did not originate from a known defect or contaminant. Examples of other variables could be defects that were not visible by reflected light or defects that were too small to be seen by the video detection method that was used. These conditions are currently thought to be insignificant since unaccounted damage was not observed.

The first onset of damage as the threshold is approached usually requires seconds or minutes of exposure representing thousands of pulses before damage starts. Most damage progresses rapidly after it is first observed, often taking less than 100 msec to progress from ignition to catastrophic optic damage. It is clear in almost all cases that the damage originates at a defect or contaminant site and then grows until the coating in the full beam area has been blown away. The damage site generally reproduces the details of the beam shape very closely as seen in figure 2. Significant stress fracture in the surrounding coating material indicates the effects of high levels of local heating. In rare cases involving low damage thresholds in the presence of contaminants, the time it takes from onset to full beam damage has been seconds or minutes. This may be associated with how well the contaminant conducts heat to the coating, as alluded to by Bennett. [7]

In order to best characterize the operational damage threshold for a given coating, the beam must be moved over sufficient area to give a high probability that typical defects and other possible variables were encountered. Since typical coating defect densities we have seen range from approximately 0.1 - 10 / mm^2, a path of 40 mm is scanned on the part covering approximately 40 mm^2 or about 1% of the total clear aperture. Between 4 and 400 defects should be irradiated by this procedure.

4. Conclusions

In our test of multilayer dielectric high reflection coatings exposed to high average power lasers, we have observed low damage thresholds of <5000 watts/cm^2 when absorption was very high (10^{-3}). For coatings optimized for low coating absorption, coating defects were observed to limit the damage threshold to 5000-20,000 watts/cm^2 and surface contamination was associate with damage levels below 1000 watts/cm^2 in some cases. In areas of low absorption coatings where these limiting defects and surface contamination were not present, coating damage was not observed indicating the potential that exists if cleanliness and production processes can be controlled during the coating process and in laser system operation.

This work was performed under the auspices of the U. S. Department of Energy by Lawrence Livermore National Laboratory under contract No. W-7405-Eng-48. Many people contributed to this test program but a special effort was made by W. K. Eickelberg, R. M. Hamilton and D. L. Saunders from LLNL and J. D. Prosise from Martin Marrietta, Oak Ridge.

5. References

[1] Draggoo, V. G., Morton, R. G., Sawicki, R. H., and Bissenger, H. D. Optical Coating Absorption Measurement for High Power Laser Systems, Proceedings of the Socie Photo-Optical Instrumentation Engineers Conference 622,186 (1986).

[2] Guenther, K. H. Modular defects in dielectric multilayers and thick single layers. Opt. 20 1034 (1981).

[3] Bloembergen, N. Role of cracks, pores, and absorbing inclusions on laser induced damage threshold at surfaces of transparent dielectrics. Appl. Opt. 12, 661 (197

[4] Rosasco, G. J. and Bennett, H. S. Internal field resonance structure: Implications optical absorbtion and scattering by microscopic particles. JOSA 68, 1242 (1978

[5] Guenther, K. H. Microstructure of vapor-deposited optical coatings. Appl. Opt. 23, 3806 (1984).

[6] Bennett, J. M., Burge, D. K., Rahn, J. P, and Bennett, H. E. Standards for Optical Surf Quality Using Total Integrated Scattering, Proceedings of the Society of Photo-Optical Instrumentation Engineers Conference Vol. 181: 124-132 (1979).

[7] Bennett, H. E., Glass, A. J., Guenther, A. H., Newman, B. E. Laser induced damage in optical materials. NBS U.S. Spec. Publ. (1981)

A question was raised of whether average power was the appropriate quantity to use for ranking the materials reported since 80 nsec pulses were used with a high repetition rate. Alternately one could use Joules/cm^2. The author replied that although everyone else is talking in J/cm^2, they believe that average power may be the appropriate parameter. They have begun to look at the relation between high and low rep rate but at the moment average power is what the use. The question is a valid one. It is not clear to them that the damage threshold would stay the same is the J/cm^2 per pulse remained the same and the rep rate was decreased. Some samples did not damage. What levels were they tested at? The speaker replied that most damage thresholds were in the 5 to 20 Kw/cm^2 and they could go at least 5 to 10 times higher than that. The limit was not the same for every test that was run.

In response to another question, the speaker defined high absorption as 10^{-4} or 100 ppm and low absorption was 10 ppm. In the chart only high and slow absorption samples were tested. In the curve, which was for a different set of reflectors for different applications, the absorption was mainly intermediate between high and low absorption. The absorption was measured by using a thermal camera to measure the temperature rise and then using a computer code called TSO developed at Livermore to determine absorption.

They have only verified the absorption values indirectly by looking at wavefront distortion and believe that the absorption values are perhaps good to 30%. At least it is repeatable to that value.

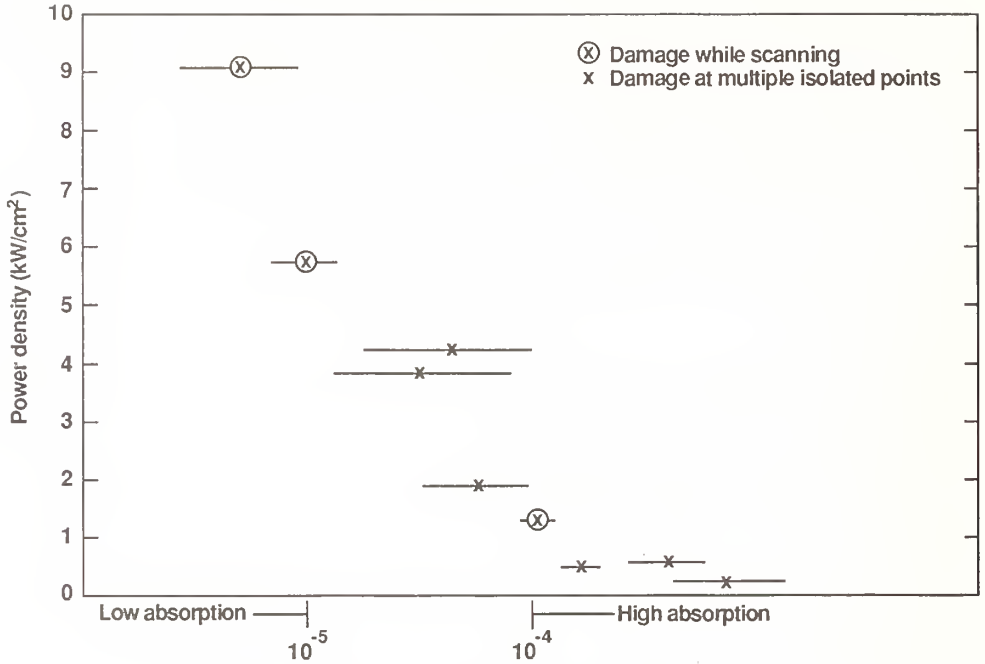

Figure 1 High reflector for visible laser

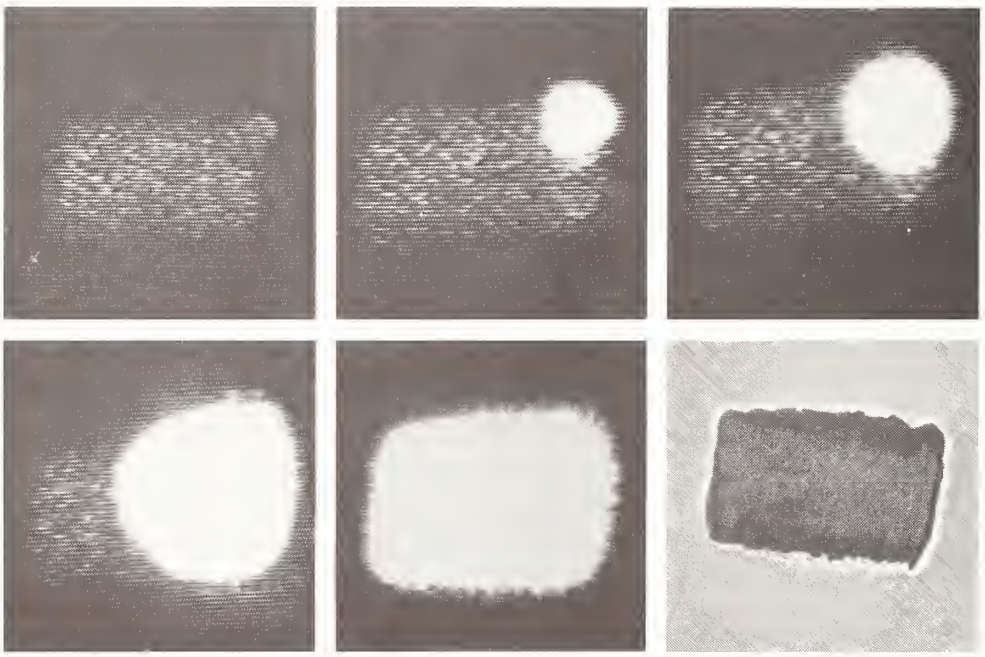

Figure 2 Defect related damage

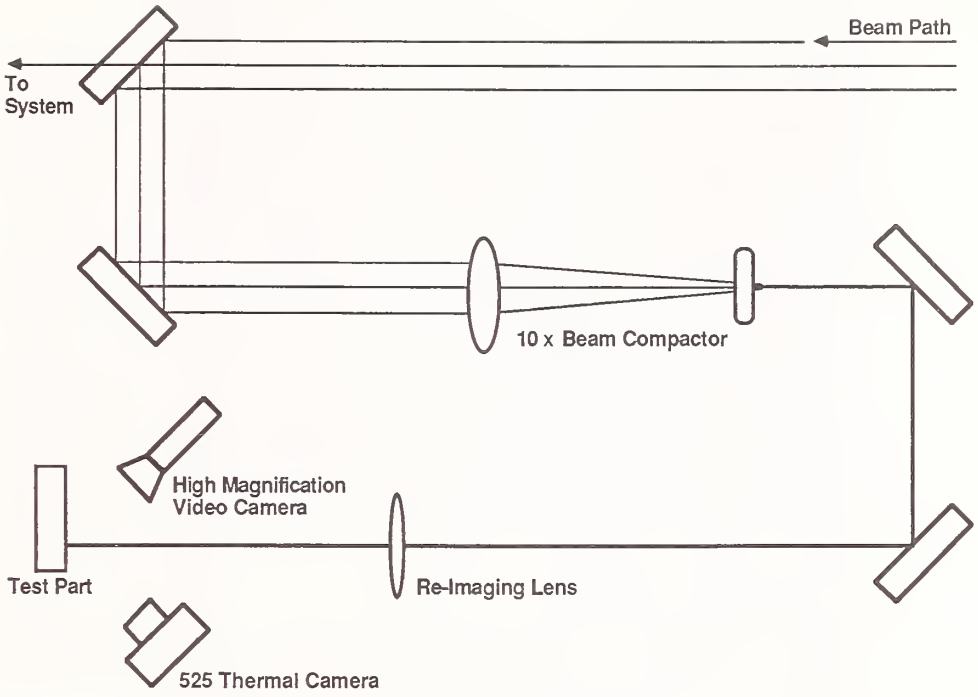

Figure 3 Test schematic

Figure 4 Test area

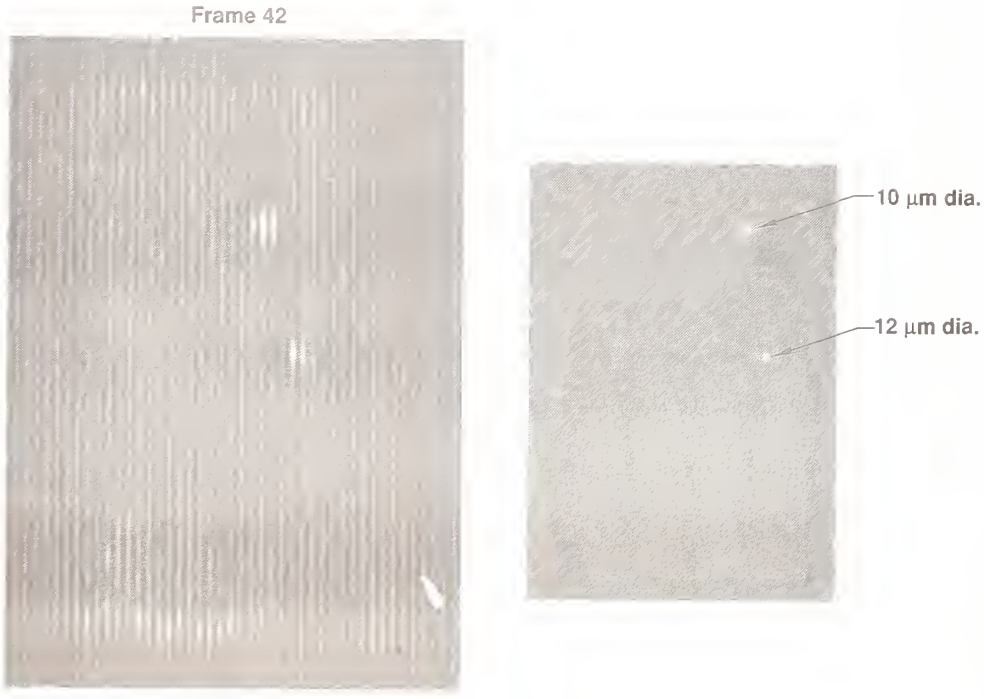

Figure 5 Visual coating defects

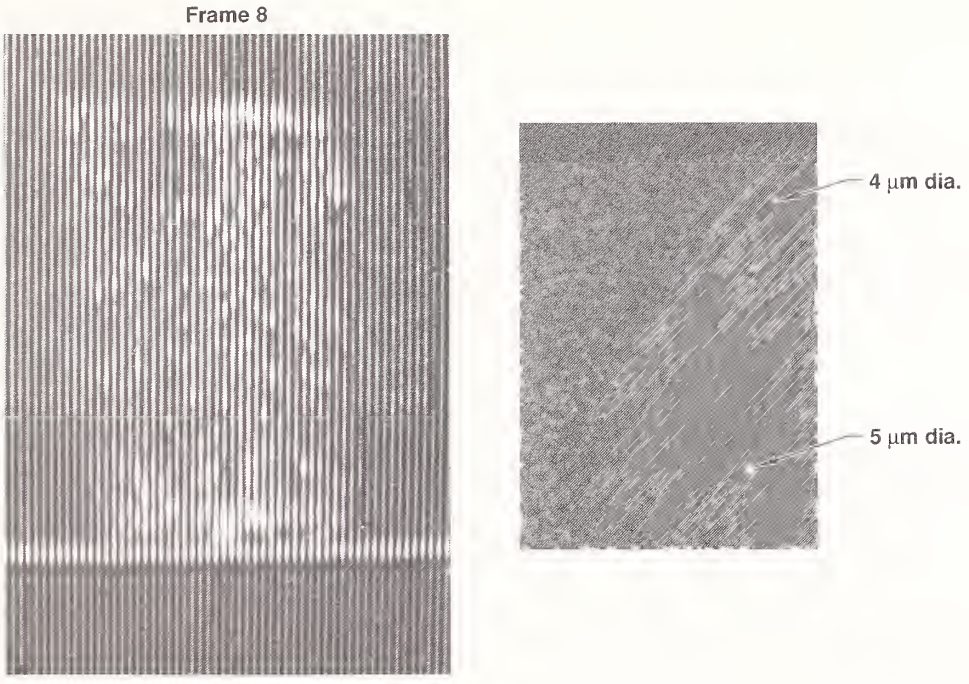

Figure 6 Visual coating defects

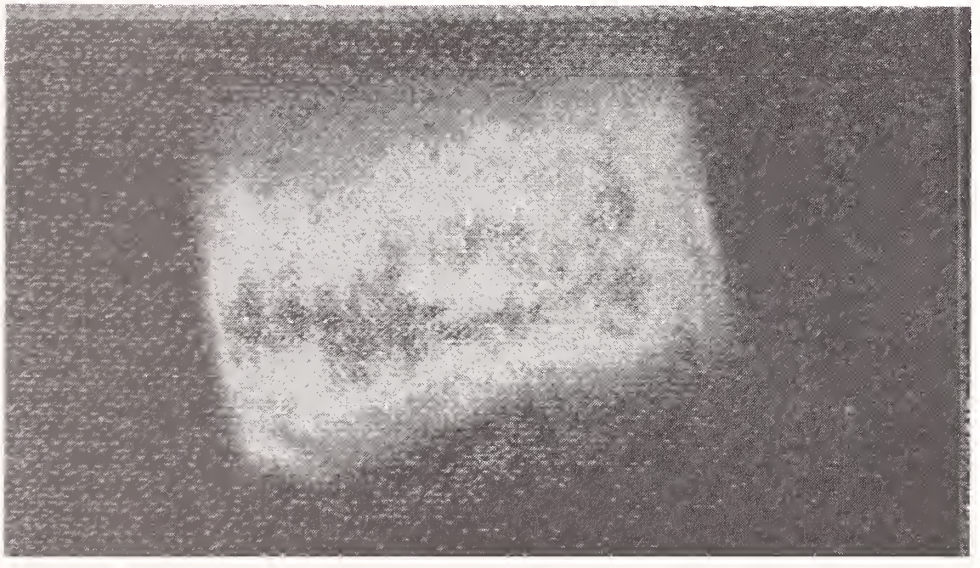

Figure 7 Test beam uniformity

Manuscript Received
2-19-88

On the Role of Water in the Laser Conditioning Effect

J.W. Arenberg and M.E. Frink
Hughes Aircraft Company
P.O. Box 902 Bldg. E1 M/S D127
El Segundo, CA 90245

Abstract

This paper reports on a series of experiments designed to collect phenomenological data regarding the role of water in the laser conditioning effect. To understand the data collected, a model of the mechanism of laser conditioning is introduced. The model posited is that water included in the coating absorbs some of the incident laser energy and this increased absorption causes lowered damage thresholds. Further, it is assumed that, during the sub-threshold irradiation of the surface under test, water is desorbed before damage occurs. The decreased water content in the coating leads to higher damage performance due to the decreased absorption of the incident laser energy.

Key Words; laser conditioning effect, water absorption, mechanisms of laser damage, laser cleaning effect, preconditioning, laser damage testing, conditioned damage testing.

Introduction

While performing laser induced damage threshold experiments many researchers have noted that sub-threshold laser irradiation of the test surface leads to higher damage threshold values. This effect has been attributed to some type of surface "cleaning" in which initiators (impurities, particles, solvent residue, etc) of damage are removed, thus enhancing the measured surface durability. This effect has been termed laser conditioning. Laser conditioning has been noted at many different wavelengths, 10.6 μm[1], 2.7 μm and 3.8 μm,[2] 1.06 μm[3,4], 0.694 μm, 0.532 μm[5] and at 0.248 μm[6].

Laser conditioning is interesting for several reasons. To optics and laser manufacturers, knowledge of the mechanism of conditioning allows for the development of novel processes for the hardening of optics and systems. To the researcher, comprehension of the laser conditioning mechanism(s) should give valuable insight as to the mechanism of laser damage in general.

One of the most striking features of the laser conditioning effect is that it is not generally permanent. The threshold enhancement due to conditioning has been shown to disappear over a period of days at 1.06 μm.[7] Investigations thus far have failed to conclusively identify the mechanisms controlling conditioning and its subsequent deactivation. There is a large and growing body of experimental evidence which infers that water is a primary contributing factor to laser damage in general as well as the conditioning effect in particular.[8,9,10] Furthermore, water has been directly measured as a species being desorbed from a surface subjected to laser irradiation, but these studies have not been made in conjunction with a study of the laser conditioning effect.[11,12,13]

In the first set of experiments, a set of coated optics were vacuum baked to remove volatile absorbing contaminants and therby simulate laser conditioning. In the second set of experiments, the effect of conditioning was measured at three different laser wavelengths, 1.06 μm, 0.694 μm and 0.532 μm.

Other possible actors are identified and compared with the observed phenomenology. The diffusion properties as inferred from the vacuum bake studies and the spectral properties taken together point strongly to water as a major actor in the laser conditioning mechanism.

The Water Only Model and Results

This paper presents qualitative data supporting the contention that the removal of water via sub-threshold laser irradiation is responsible for the threshold enhancement observed. Furthermore, the subsequent resorption of this environmental water is responsible for the deactivation of the threshold increases noted. The role of water is specified in the so called water-only-model (WOM) of laser conditioning. The WOM is stated as;

> The presence of included water in an optic under test decreases the measured laser damage threshold via the absorption of incident laser energy. Thus, the removal of this included water will lead to an increase in the laser damage threshold due to decreased absorption of laser energy by the optic under test.

The WOM will be tested in two ways in this study. The first is a simulation of the conditioning effect by vacuum baking. The second is a measure of the dispersion of the threshold enhancement due to conditioning. The results of these two tests considered together should provide solid evidence as to the role of water in the laser conditioning effect. The vacuum bake test allows for the preferential removal of less massive and small molecular species via diffusion over the heavier and larger molecules. The spectral measurement of the change in the threshold due to conditioning as a function of wavelength allows for further discrimination in the identification of the species playing a role in laser conditioning. This additional differentiation results from the fact that the conditioning should be large, at a wavelength where an included species is highly absorbant.

Vacuum Bake Test

A measure of the validity of the WOM is to condition, i.e. remove some of the smaller lighter molecular species, assumed to be water, without a laser to see if the laser damage threshold is enhanced. The method for removing the more volatile species study is a vacuum bake.

A previous bake study was performed in 1980 at LLNL.[14] It is worth noting that there were no significant conclusions drawn from the 1980 study on the correlation of baking and increases in laser damage threshold.

The vacuum bake performed in this study was carried out at, 10^{-3} torr and 125°C for 24 hours and on optics coated as anti-reflective and highly-reflective for 1.06 μm. These parts were then laser damage tested at 1.06 μm.

The effect of conditioning is quantified by comparing the conditioned and unconditioned laser damage thresholds.[15] The conditioned damage level of a particular site under test is the fluence at which the part fails catastrophically following irradiation at lower fluences on the same site. After a number of sites have been irradiated in this manner a sample of conditioned damage levels is generated. This sample may be described in many ways, the most common are the minimum conditioned damage level, also known as

the conditioned damage threshold, and the mean average of the conditioned failure levels, also known as the average conditioned threshold. The unconditioned threshold is determined by a binary search procedure where the fluence is different at each test site and new sites are taken until the smallest fluence causing damage has been unambiguously identified. Only one value results from an unconditioned damage test, the lowest damaging fluence and is called the unconditioned damage threshold.

The effect of the vacuum bake is specified by measuring both the conditioned and unconditioned damage thresholds at 1.06 μm, prior and subsequent to the vacuum bake. The entire sample is plotted using the so-called percentile box plots. An example of the plot is shown as Figure 1. The box plots show the location of five percentile levels, the 10th, the 25th, the 50th or median average, the 75th and the 90th.

In all, 12 parts were tested for unconditioned and conditioned thresholds both before and after vacuum baking. This data is presented in Figure 2.

The only case in which both the unconditioned and conditioned threshold did not increase is part number (P/N) 2. The decreases are small in both the mean average conditioned damage level and the unconditioned damage threshold. Since the uncertainties in those measured quantities is on the order of one unit, then the differences are smaller than the associated uncertainties. It is also possible that the observed decrease is due to contamination of the part during the vacuum bake and the subsequent damage tests.

In the case of P/N 4, the unconditioned threshold increases slightly, but the mean average conditioned level decreases slightly. These differences are smaller than the uncertainties and therefore not seen as significant.

In the other ten cases, the vacumm bake can be seen to "condition" the parts. That is, there is a threshold enhancement of both the unconditioned and the conditioned damage results. Further, it can be seen that the conditioned threshold is greater than the unconditioned threshold both pre and post vacuum bake. This indicates that the vacuum bake did not purge the coating entirely of volatile absorbants. The very large threshold enhancements possible by using a vacuum bake process and subsequent laser conditioning are evidenced on Figure 2. Thus, a user with a critical damage requirement might want to investigate the aforementioned process to realize higher damage thresholds.

Spectral Tests

In the spectral tests, conditioning was measured as a function of wavelength of the incident laser. The quantity of concern is the percent increase due to conditioning relative to the unconditioned threshold. Conditioning enhancement was measured at three wavelengths, 1.06 μm, 0.694 μm and 0.532 μm.

The WOM predicts that at the wavelengths where water is more absorbant there should be a more pronounced conditioning effect. The absorption spectra of water is given below as Figure 3. For the wavelengths used in this study, the absorbance of water is greatest at 1.06 μm, 0.15 cm^{-1}, next largest at 0.694 μm, 0.004 cm^{-1} and 0.0015 cm^{-1} at 0.532 μm. Thus, the WOM predicts that the conditioning effect should be most prominent at 1.06 μm, less at 0.694 μm and least at 0.532 μm.

The results of the spectral tests are given Figure 4. The plot shows the minimum, maximum and arithmetic mean average increase in the conditioned threshold relative to the unconditioned threshold as a function of the test wavelength. The sample sizes are 79, 5 and 50 for the 1.06 μm, the 0.694 μm and the 0.532 μm wavelengths respectively.

The error bar on the minimum conditioning line is intended to show the uncertainty in the location of the minimum and maximum values of conditioning

at each wavelength. The data represented in the minimum and maximum lines is uncertainty of the single most extreme part, and are typical of the uncertainty of a single point measurement. The mean average values are the result of many tests and thus have smaller error bars.

The curve showing the minimum threshold enhancement demonstrates no increase due to conditioning for the YAG and ruby laser wavelengths. The doubled YAG wavelength shows a slight decrease due to conditioning. This apparent "negative benefit" is an artifact of the damage definition employed. From studies conducted at 1.06 μm , it has been reported that it is relatively easy to define and accurately monitor catastrophic damage (flash, visible cratering, noise) on a sample.[16] At 1.06 μm there is a well defined onset of catastrophic damage. However, at 0.532 μm, the identification of the catastrophic failure level is more difficult. At 0.532 μm there is generally an accumulation of small damage sites which slowly grow into larger damage areas. Thus, there is no well defined catastrophic damage level. This may be due to a difference in the laser matter interaction at 0.532 μm versus 1.06 μm, or it may just be highlighting the change from a water dominated damage mechanism at 1.06 μm to another previously suppressed mechanism taking over at 0.532 μm. The difficulty in deciding upon an unambiguous definition of laser induced damage has been previously intorduced in the literature.[17]

It remains necessary to identify the most reasonable way to describe the data collected in the spectral testing. Since a part may be found in any reasonably large sample that does not condition, the minimum threshold is not a good way to describe the conditioning effect.

A similar argument may be made for the case that the maximum threshold is also not a good descriptor of the conditioning effect because it is determined by a single point.

The mean average increase in threshold is a good descriptor. It includes the information about the frequency and magnitude of the conditioning increases, although other statistical moments will do precisely the same, with different weighting. Thus, the choice of the mean is acknowleged to be somewhat arbitrary but not wholly without reason.

The mean increase in threshold due to conditioning is 0.34±0.01, 0.03±0.04 and 0.11±0.01 at 1.06 μm, 0.694 μm and 0.532 μm respectively. Viewed in this fashion, the effect due to conditioning is greatest at 1.06 μm, where water is the most absorbant. The differences between conditioni at 0.694 μm and 0.532 μm is small, 0.08±0.05 and the deviation from zero may be due to the very small number of parts tested at the ruby laser wavelength.

Discussion and Conclusions

Thus far, this paper has made the argument that there is removable contaminant in the coatings whose desorption increases the damage threshold. Qualitative evidence has been presented to support this contention. However, as the title of this paper indicates, it is believed that included water is the main species involved in the laser conditioning effect. This final section makes the case for water as the main actor in the laser conditioning effect.

The demonstrated qualities of the agent being desorbed by the sub-threshold irradiation in the laser conditioning effect are; the ability to diffuse out of the coating, and having greater absorbance at 1.06 μm than at 0.694 μm or 0.532 μm. These qualities, when considered together, make a strong, although circumstantial argument for water as the main actor in the conditioning effect.

The ability of a species to diffuse through a porous material like a thin film coating is characterized by its diffusion coefficient. This coefficient is defined by the size and mass of the diffusant and the material properties of the diffusion membrane, mainly pore size and shear modulus.

It is possible to compare estimates of the diffusion coefficients by using a model of the diffusion process. The model of the diffusion coefficient used as a paradigm for this study dealt with the diffusion of gasses through a silicon oxide film.[18] In this study, an estimate of the diffusion coefficient D, is given as,

$$D=D_0T^n\exp\left(-\frac{E}{KT}\right) \qquad [1]$$

where T is the temperature in K, D_0 is a function mainly of mass of the diffusant, n has a value of 0, 1/2 or 1 and E is the activation energy of the diffusion process that is a function of the diffusant size. By fitting an experimental curve it was found that each of the three values of n gave equally good fits. For the purposes of this paper n is taken to be zero. The functional form of D_0 contains geometric information about the membrane and varies inversely as the square root of the mass of the diffusant.[19] The activation energy of diffusion is modeled as the energy necessary to dilate an orifice of radius r to radius r_D, and is proportional to the square of the radius of the diffusant and linearly proportional to the shear modulus of the membrane.[20]

Using equation [1], the diffusion coefficient will be estimated for other possible actors in the conditioning effect. This estimation neglects any interaction, of chemical or other nature, between the diffusant and the coating. Using the diffusion coefficient of helium as the scale, the diffusion coefficient for a molecule of radius a and mass m is given as,

$$D(a,m)=\left(D_{0He}\sqrt{\frac{4}{m}}\right)\exp\left(-\frac{E_{He}\left(\frac{a}{r_{He}}\right)^2}{KT}\right). \qquad [2]$$

Equation [2] defines the value of D in the (a,m) plane. From [2] the contours of equal values of D, the isograms of D, may be identified. By identifying those combinations of a and m that give diffusion coefficients equal to or greater than that of water the other species that have equal or greater diffusion coefficients under both laser conditioning and vacuum baking are isolated.

Consider the plot given below. Figure 5 is a plot of three isograms of D as formulated in [2]. The three lines are the isogram of the diffusion coefficient of water, the isogram of 10 times, the diffusion coefficient of water and the third is the isogram relating to 0.1 of the diffusion coefficient of water. The a-axis is the molecular radius and is graduated in units of Å. The mass scale is in atomic mass units. As is evidenced by the plot there is a.precipitous drop at the molecular radius of water. This means that any alternate species playing a role in the conditioning effect must be equal to or smaller than the water molecule and may be up to 3.61, (65/18), times heavier. Thus, the other possible species playing a role in the conditioning effect must have a mass of less than 65 and a molecular size of 1.6 Å radius.

This leaves quite a number of species as possible actors. Previously, it was implicitly assumed that the source of the specie(s) deactivating the conditioning effect came from the atmosphere.[21] If this assumption is followed then other candidates should be present in the atmosphere and have greater a absorption at 1.06 μm than at 0.694 μm and 0.532 μm. Upon examination of the absorption spectra of dry air no such absorption is

evidenced. Thus, it is concluded that there is a strong case for water being the main actor in the laser conditioning effect.

The argument presented above is not conclusive, but is rather illustrative that there is strong circumstantial evidence that atmospheric water plays a major role in the mechanism governing conditioning effect. The nature of the water, physisorbed or chemisorbed[22], has yet to be determined and will hopefully be the result of the anticipated modeling effort to be reported in future conferences.

Acknowlegedements

The authors would like to acknowlegde the assistance of M.L.T. Crockett and C.L. Lopez in performing the the laser damage testing and D.E. Maguire for his assistance in the vacuum bake tests.

References

[1]Newnam, B.E., A.V. Nowak and D.H. Gill, "Short Pulse CO_2-Laser Damage Studies of NaCl and KCl Windows", in *Laser Damage in Optical Materials:1979*, H.E. Bennett, A.J. Glass, A.H. Guenther and B.E. Newnam editors, pp. 209-223, Nat. Bur. Stand.(U.S.) Spec. Pub. 620, U.S. Government Printing Office, Washington D.C., 1980.

[2]Porteus, J.O., T.M. Donovan, J.L. Jernigan and W.N. Faith,"Multithreshold Evaluation of 100-nsec Pulsed Laser Damage to Coated Materials at 2.7- and 3.8 μm Wavelengths" in *Laser Damage in Optical Materials:1978*, A.J. Glass and A.H. Guenther editors, pp. 202-211, Nat. Bur. Stand.(U.S.) Spec. Pub. 541, U.S. Government Printing Office, Washington D.C., 1978.

[3]Swain, J.E., S.E. Stowkowski, D. Milam and F. Rainer, "Improving the Bulk Damage Resistance of KDP by Baking and Pulsed Laser Irradiation", in *Laser Damage in Optical Materials:1981*, H.E. Bennett, D. Milam, A.H. Guenther and B.E. Newnam editors, pp. 119-128, Nat. Bur. Stand.(U.S.) Spec. Pub. 669, U.S. Government Printing Office, Washington D.C., 1982.

[4]Frink, M.E., J.W. Arenberg, D.W. Mordaunt, S.C. Seitel, M.T. Babb and E.A. Teppo,"Temporary Laser Threshold Enhancement by Laser Conditioning of Anti-reflection Coated Glass", *Applied Physics Letters*, volume 51, number 5,10 August 1987, pp 415-417.

[5]Present study.

[6]Rainer,F., D. Milam and W.H. Lowdermilk,"Laser Damage Thresholds of Thin Film Optical Coatings at 248 nm", in *Laser Damage in Optical Materials:1981*, H.E. Bennett, D. Milam, A.H. Guenther and B.E. Newnam editors, pp. 339-343, Nat. Bur. Stand.(U.S.) Spec. Pub. 669, U.S. Government Printing Office, Washington D.C., 1982.

[7]Frink et al, 1987, op. cit.

[8]Wood, R., *Laser Damage in Optical Materials*, Adam-Hilger, 1986.

[9]Porteus, J.O., W.N. Faith and S.D. Allen, "Laser Desorption Analysis of H_2O and Other Contaminants from Optical Surfaces", in *Laser Damage in Optical Materials:1981*, H.E. Bennett, D. Milam, A.H. Guenther and B.E. Newnam editors, pp. 273-279, Nat. Bur. Stand.(U.S.) Spec. Pub. 669, U.S. Government Printing Office, Washington D.C., 1982.

[10]Frink et al, 1987, op. cit.

[11]Wood, 1986, op. cit.

[12]Porteus et al, 1982, op. cit.

[13]Nogar, N.S. and R.C. Estler,"A Chemical Precursor to Optical Damage? Studies by Laser Ionization Mass Spectrometery"in *Laser Damage in Optical Materials:1987*, H.E. Bennett, D. Milam, A.H. Guenther and B.E. Newnam editors, to be published.

[14]Milam, D., F. Rainer and J.E. Swain, Laser Program Annual Report, 1980, Lawrence Livermore National Laboratory, 1980.

[15]Frink et al, 1987, op. cit.

[16]Arenberg, J.W., M.E. Frink, D.W. Mordaunt, G. Lee, S.C. Seitel and E.A. Teppo,"Correlation of Laser Damage at 1.06μm Varying Modal Content and Irradiance History",*Laser Damage in Optical Materials:1986,* H.E. Bennett, D. Milam, A.H. Guenther and B.E. Newnam editors, to be published.

[17]Foltyn, S.R. and L.J. Jolin, "Catastrophic versus Microscopic Damage: Applicability of Laboratory Measurements to Real Systems", in *Laser Damage in Optical Materials:1980*, H.E. Bennett, D. Milam, A.H. Guenther and B.E. Newnam editors, pp. 493-501, Nat. Bur. Stand.(U.S.) Spec. Pub. 620, U.S. Government Printing Office, Washington D.C., 1981.

[18] Perkins, W.G. and D.R. Beagal,"Diffusion and Permeation of He, Ne, Ar, Kr and D_2 Through Silicon Oxide Films", *Journal of Chemical Physics*, volume 54, number 6, pp 1683-1694, 15 February 1971.

[19] ibid.

[20] ibid.

[21] Frink et al, 1987, op. cit.

[22] Palik, E.D., J.W. Gibson, R.T. Holm, M. Hass, M. Braunstein and B. Garcia,"Infrared Characterization of Surfaces and Coatings by Internal-Reflection Spectroscopy", *Applied Optics*, volume 17, number 11, 1 June 1978, pp 1176.

FIGURE 1 - PERCENTILE BOX PLOT

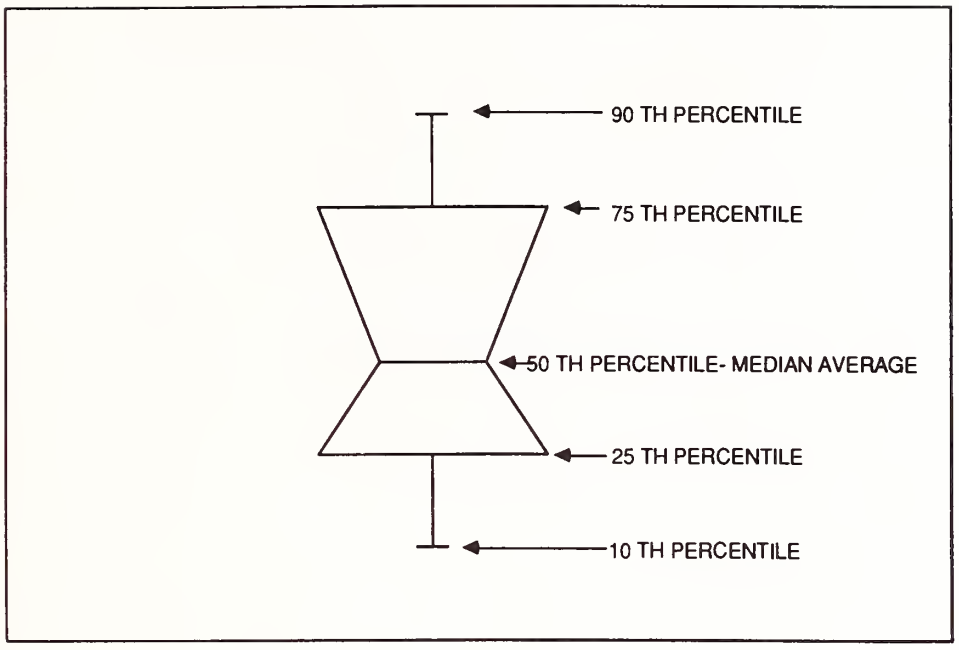

FIGURE 2 - RESULTS OF VACUUM BAKE

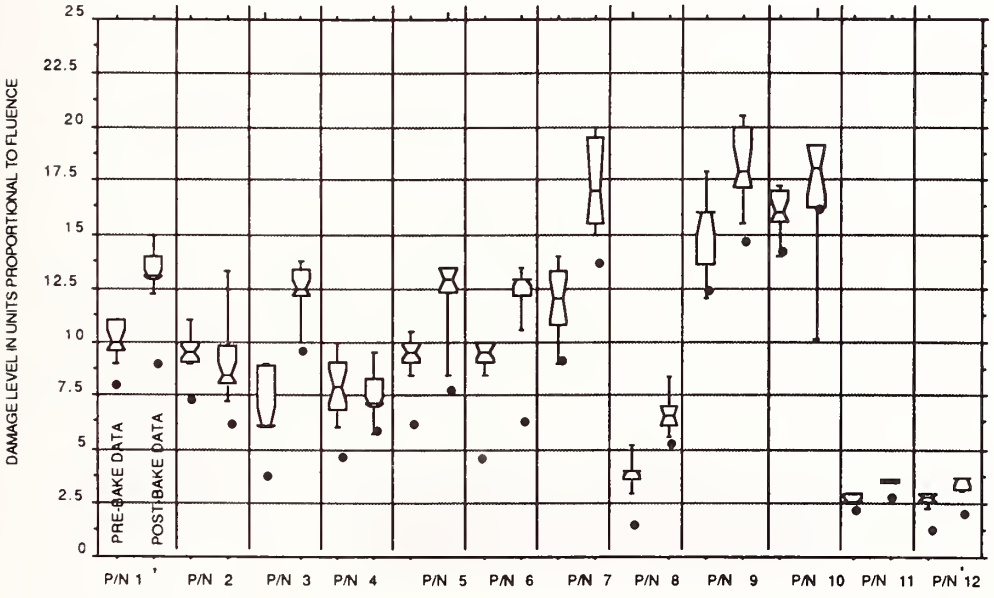

FOR ANY GIVEN PART, THE DATA SHOWN ON THE LEFT WAS TAKEN PRIOR TO THE VACUUM BAKE, AND THE DATA SHOWN ON THE RIGHT, WAS TAKEN FOLLOWING THE VACUUM BAKE

LEGEND

DENOTES CONDITIONED DAMAGE TEST DATA

DENOTES UNCONDITIONED DAMAGE THRESHOLD

FIGURE 3 - ABSORPTION SPECTRA OF WATER

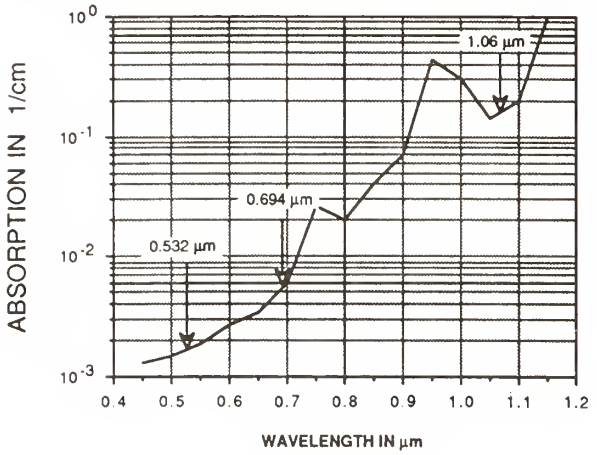

FIGURE 4 - RESULTS OF SPECTRAL TESTS

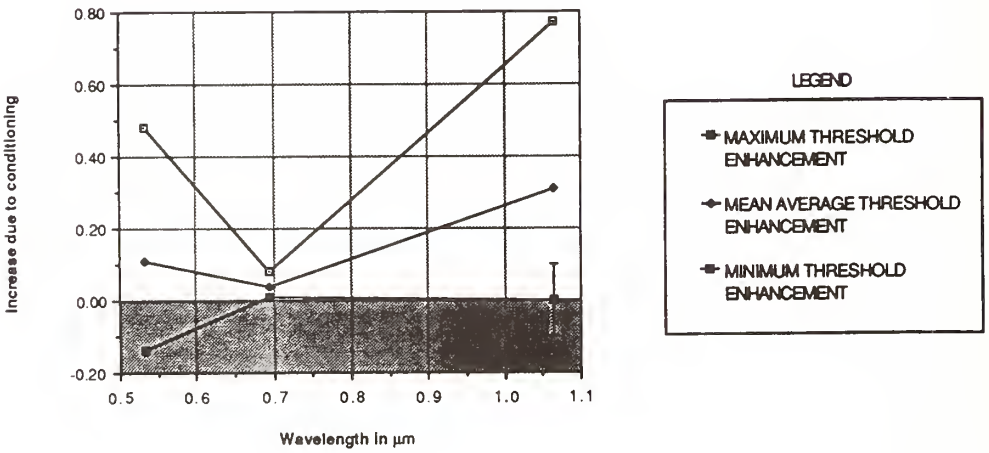

FIGURE 5 - ISOGRAMS OF D

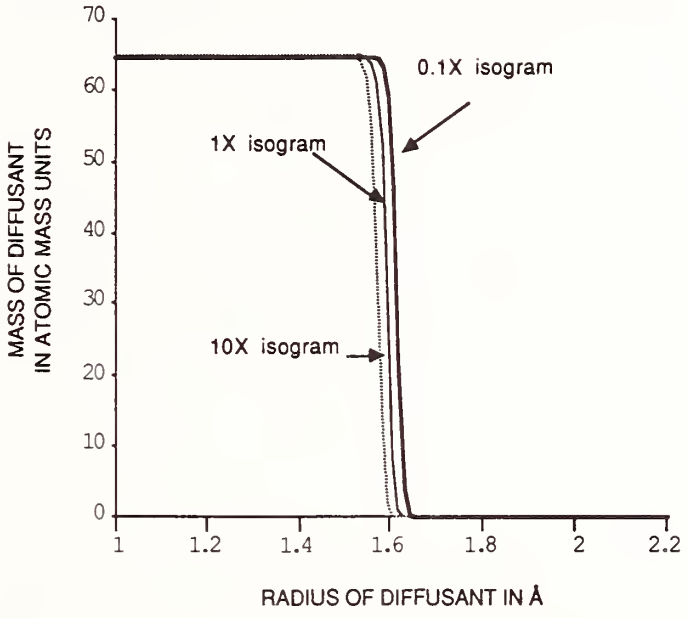

OPTICAL COATINGS FOR HIGH-POWER Nd-LASERS

F.S. Faizullov, A.I. Erokhin, V.I. Kovalev, and S.I. Sagitov
P.N. Lebedev Physical Institute, Ac.Sci., Moscow, USSR

B. Brauns, V. Goepner, G. Herrendorfer, and D. Schafer
Zentralinstitut fur Optik und Spektroskopie
DAW, DDR-1199, Berlin

W. Wolf and H. Zscherpe
Ingenieurhochschule Mittweida
DDR-9250, Mittweida

The influence of deposition technology and design of the dielectric optical thin film coating manufactured of refractory oxides and silicon dioxide on the damage thresholds of single and multilayer systems is investigated. It is shown that the damage threshold of reflection and antireflection coatings may be raised up to the damage threshold of pure glass surface for Nd-laser pulses in the range of 2 to 85 ns.

Key words: laser cleaning, laser damage, thin films, variations in film deposition parameters.

1. Introduction

The development and application of high power 1.06 μm Nd-lasers are placing heavy demands on optical elements, including thin layer interference coatings, such as cavity mirrors, light splitters, antireflection coatings and polarizers [1,2]. Beside the high laser damage resistance, thin layer systems must have a good spectral stability of the transmission and reflection under the changing temperature, humidity, and chemical and mechanical conditions. In order to attain such characteristics in the spectral region of one micron one usually employs thin layer systems prepared of refractory oxides. The quarter wave multilayer interference coatings prepared of alternating layers with high and low refractive index are usually used as cavity mirrors. The number of layers needed for improvement of high reflection is inversely proportional to the ratio of refractive index of the layer materials so that the highly refracting materials must have a possibly higher refractive index, while the low-refractive materials, the lesser one. In this connection we investigated Ta_2O_5, ZrO_2 and HfO_2 coatings as highly refracting, and SiO_2, as low refracting materials. We aimed at perfection of the coating technology of these materials with high resistance to 1.06 μm laser radiation.

2. Experimental Procedure

The coatings were deposited by the methods of thermal and electron beam evaporation in conventional vacuum chambers. The majority of oxides dissociate during evaporation, thus the correct stoichiometric composition of a film can be obtained only by depositing the films in a reactive atmosphere of oxygen. Ionized oxygen is used along with molecular oxygen to increase reactance. The ionization was performed by Heitmann-type source [3].

The laser evaporation technique was used in order to avoid the contamination of the coatings that usually result from thermal and e-beam evaporation [4,5]. A laser was placed outside the vacuum chamber. Its radiation was focused onto the coating material through an NaCl window by a system of plane and spherical mirrors. A schematic of the experimental arrangement for the laser evaporation is shown in Fig. 1. We used a cw CO_2 laser with output power of 200 W manufactured at VEB FEHA, in Halle, DDR.

The laser damage resistance of the coatings was studied using lasers operating at TEMoo transverse mode. Measurements were made at the Lebedev Physical Institute and the Central Institute of Optics and Spectroscopy, DDR, using a passively Q-switched Nd-glass laser.

At Lebedev, the experiments were performed with pulses of 3 and 30 ns duration. The spot size on the samples was varied from 60 micron to about 2 mm. Some measurements were made with the spot sizes of about 2 cm and pulse widths of 2 ns duration.

The experiments performed at Central Institute of Optics and Spectroscopy used a laser with pulse duration of about 25 ns, and focal spot size of about 85 micron.

The laser radiation was focused onto a sample surface by means of a lens with focal length from 30 cm to 2 m. Energy of the incident radiation varied from site to site. The damage on a coating was registered visually when a light flash appeared on the surface, or when there had been observed a sharp increase in the radiation scattering from a He-Ne laser beam placed coaxially with Nd-laser beam. The damage threshold, D, was found from mean damage energy.

Measurements made at the Higher Engineering School of Mittweida using an acousto-optical Q-switched Nd-YAG laser with pulse width of 85 ns. The measurements were made using a spot size of about 15 microns. This system was capable of delivering maximum energy density of 500 J/cm^2 at the sample surface. In the damage threshold measurements [6] the samples were scanned line by line using a pulse repetition frequency up to 760 Hz without overlapping irradiated spots. The power was reduced from line to line until no coating damage occurred. About 150 sites were irradiated in one line with constant energy density. The number of damage sites was then determined by inspection with an optical microscope. In this way the damage probability as a function of energy density was measured. The damage threshold D_o and D1, corresponding to the damage probabilities 0 and 1 were found in the same way [7].

It is known that absolute values of the laser damage threshold in optical materials depend on the spot size at the sample [8]. Therefore, comparative measurements of damage threshold were performed for the same samples on the three laser facilities, each having a characteristic spot size. The measurement results for four different samples having HfO_2 single layer coatings of $\lambda/4$ thickness at λ=1.06 μm are shown in Fig. 2. One can clearly see the dependence of damage threshold, D, on the spot size (the D dependence of oxide coatings on the pulse duration, in the range of 25-85 ns durations, is weak [9,10]). This shows that the coating is damaged due to the influence of local absorbing microdefects [11].

3. Investigating Results

3.1. Single-layer Coatings

Previous investigations in the development of quarter wave optical layers on the basis of low refracting material SiO2 showed that using the electron beam evaporation deposition technique one can produce layers whose damage threshold is close to that of a glass substrate surface [12]. In this work we studied such highly refracting materials, as HfO_2, Ta_2O_5, ZrO_2. We carefully examined the relation between the damage threshold of the quarter wave layers of these materials with substrate temperature and partial pressure of oxygen at e-beam deposition in the reactive atmosphere. Fig. 3 illustrates the dependence of D for HfO_2 and Ta_2O_5 coatings on the given parameters. Points and dashed lines denote the data obtained in IHS of Mittweida. The lower value corresponds to the energy density, D_o, in which no damage had been observed at any point of the coating. In those cases when the damage was observed in some but not all sites of the coating for the maximum fluence available of 400-500 J/cm^2, the damage probability is shown above the dotted line, that is, part of sites (in %) which had been damaged at these values of fluence.

Triangles and squares stand for the results obtained at Lebedev Institute with the spot size 550 and 60 microns, respectively. It is seen that the dependencies of Ta_2O_5 damage threshold obtained on two different laser facilities, are correlated with accuracy up to the measurement error. The data obtained for the spot diameter of 550 μm are close to D_o, and for 60 μm diameter, to D_1.

The results of more detailed measurements made with the help of YAG-laser showed (points and dots of Fig. 3.) that increasing oxygen pressure improves the damage

resistance of coatings, and that the resistance decreases with increased substrate temperature, T_s. For HfO_2 coatings the damage threshold is maximal, while the damage threshold changes considerably from site to site. The Ta_2O_5 coatings have lower damage threshold, D_1, but they are more homogeneous.

The experiments performed in the scanning regime showed that one can achieve high values of the damage threshold for each type of coating, under optimal conditions, not only in random sites of a sample, but also (and this is very important) in some regions as large as hundreds micrometers. This result indicates that the laser damage resistance of coatings can be significantly increased, if we understand the nature of enhanced resistance in these regions. In this respect, HfO_2 coatings are most promising because they have higher damage threshold, D_1.

3.2. Multilayer Systems

Under optimal deposition conditions by e-beam evaporation method we have manufactured 25 layer ZrO_2-SiO_2, HfO_2-SiO_2, and Ta_2O-SiO_2 optical quarter wave films with the reflection coefficient up to 99.9% at 1.06 μm wavelength. The measurement results of the laser damage resistance for multilayer systems are given in Fig. 4. The spread of damage threshold from site to site for multilayer Ta_2O_5 films is much less than for ZrO_2 and HfO_2 coatings. The Ta_2O_5-SiO_2 systems have the lowest damage threshold, which practically coincides with that of Ta_2O_5 single layer systems (see Fig.3.). The ZrO_2 and HfO_2 appear to be more promising films, because, as seen from Figs. 3 and 4, absolute values of minimal damage threshold, D_o, for multilayer films are higher than damage thresholds for single layers. Besides, the probability of damage of these coatings, at 500 J/cm^2 fluence is not higher than 8%, which is considerably less than for single layers.

The laser damage resistance of multilayer films can also be increased by means of the addition of halfwave silica overcoats [13]. Fig. 4 shows that D_o of multilayer films with halfwave silica overcoat has been doubled again, and the damage probability at 500 J/cm^2 is decreased. This effect is observed even when the deposition conditions are far from optimal (see Fig. 4., HfO_2-SiO_2 films at different values of oxygen pressure). The coatings without an "overcoat" layer and with it, in those experiments, were deposited by e-beam evaporation method in one cycle in order to provide identical deposition conditions.

The increase in the laser damage resistance of multilayer structures with deposition of halfwave overcoat is usually explained by the compensation of mechanical stress in the structure, or the decreasing influence of the atmosphere on properties of the coating. We should like to note another possible explanation to the observed effect.

The highly refractive oxides have, as a rule, higher absorption coefficients than SiO_2, so the first layer absorbs the greater part of energy incident on the coating. In this case the halfwave silica overcoat can serve as a kind of heatsink for the energy released in the outer coating layer.

We have calculated temperature profiles at laser pulseduration of 100 ns, by using the modal and the numerical integration method of thermoconductivity equation for the example of $\lambda/4$ thick ZrO_2 layer with overcoat [14]. The calculation results are shown in Figs. 5. a and b. It is seen that the halfwave silica overcoat reduces the temperature of the ZrO_2 by about 40%, and as a result, the damage threshold of this layer increases. As a result of our deposition experiments we have produced highly reflecting multilayer ZrO_2-SiO_2 and HfO_2-SiO_2 systems with damage threshold close to the damage threshold of pure optical glass K-8 (400 J/cm^2). The measurements of the damage threshold for such coatings with 2 cm diameter spots and 2 ns pulse duration gave values for the damage threshold from 5 to 7.5 J/cm^2.

3.3. Preliminary Treatment of Substrate by Laser Radiation

It is known that damage threshold of highly reflecting coatings weakly depends on quality of the substrate surface treatment, because the laser radiation practically does not penetrate the substrate surface [13]. The situation is

quite different for antireflection coatings and coatings with rather low reflection coefficient. The laser damage resistance, in this case, proves to be quite sensitive to the state of a substrate coating interface. The use found that conventional methods of surface cleaning before the deposition did not give the desired results. We, therefore, tried to use the laser cleaning method [15].

The experiments were done with coatings on fused silica substrates. The substrate treated by conventional methods was placed in a vacuum chamber which had been pumped out to the working vacuum. Then one of the substrates was irradiated within a few minutes by a cw 10 mm diameter CO_2 laser beam of 100 W power. After cooling, the coatings were deposited on substrates by e-beam evaporation technique. The experimental arrangement is schematically shown in Fig. 1. (dotted line).

Investigations in the laser damage resistance of ZrO_2 coating showed that the preliminary laser irradiation made it possible to raise the damage threshold of single layer coatings by nearly ten times. The results are illustrated in Fig. 6. Value D_o*/D_o determines the rise of the damage threshold after CO_2 laser treatment of the substrate. The result marked by A in Fig. 6. is for the case, when after the substrate irradiation, the vacuum chamber is being filled, for a short time, with atmospheric air, and then, after a subsequent pumping out, the deposition is performed. It is seen that the damage threshold, in this case, is not increased. This result shows that the vapor and gas adsorption has an essential influence on the damage threshold. One should further investigate what substance, after being adsorbed on the substrate surface, is most critical to the laser damage resistance. The similar results have been obtained with other oxides.

Fig. 7 illustrates, as an example, the dependencies ofabsorption and damage threshold of a single layer $\lambda/4$ TiO_2 coating on the distance from the CO_2 laser irradiation center. The absorption and the number of defects are seen to be decreased, and the damage threshold increases towards the center of the irradiated region (crater of the melt).

Beside single layer coatings we have performed the experiments on the ZrO_2-SiO_2 multilayer systems studying the influence of substrate cleaning by laser radiation on the damage threshold. These results are also shown in Fig. 6. It is seen that as the number of layers increases (or the reflection coefficient increases, which is the same), the effect of laser cleaning on the substrate decreases, and for a 25 layer system it is not effective at all.

4. Conclusions

This work showed that one can increase the laser damage resistance of multilayer dielectric oxide coatings up to the damage threshold of a cleaned glass substrate surface by a suitable choice of materials and the appropriate design of layers, as well as the optimization of deposition processes.

The best parameters have been obtained with highly refracting ZrO_2 and HfO_2 materials, and low refracting SiO_2. The highest laser damage thresholds are obtained with laser evaporation of these materials and vapor deposition in a reactive oxygen atmosphere on a cold substrate (20°).

The reliable characteristics and laser damage resistance of multilayer mirrors were considerably increased (almost doubled) due to the deposition of halfwave silica overcoat.

It was shown that cw CO_2 laser cleaning of the substrate surface in vacuum before the deposition makes it possible to increase laser resistance of single layer and multilayer coatings by about
3-10 times.

It was demonstrated that the adsorption of vapor and gas from the ambient atmosphere on the substrate decreased damage threshold of the deposited optical coatings.

In conclusion, the authors with to express their deep gratitude to G. V. Sklizkov for the opportunity to measure damage threshold on the laser facility "Delfin".

5. References

[1] Lowdermilk, W.H.; Milam, D. IEEE J. of Quantum Electron, QE-17, 1881 p., 1981.
[2] Lowdermilk, W.H. Proc.Soc.Photo-Opt.Instr.Eng., 325,(1982), 2.
[3] Heitmann, W. Appl.Opt., 10, 414 p., 1971.
[4] Brauns, B.; Schafer, D.; Wolf, R.; Zscherpe, G. Optica Acta, 33, 545 p., 1986.
[5] Morichev, L.; Savinov, V. Optiko-Mekhanich.Promyshl., N 2, 55 p., 1980 (in Russ.).
[6] Wolf, R.; Zscherpe, G.; Welsch, E.; Goepner, V.; Schafer, D. Optica Acta, 33, 919 p., 1986.
[7] Wolf, R.; Schafer, D. Potsdamer Forschungen Reihe B, 31, 173 p., 1982.
[8] Nesternov, L.; Poplavsky, A.; Fersman, I.; Khazov, L. Zhurn.Tekh. Fiz., 15, 651 p., 1970 (in Russ.).
[9] Lowdermilk, W.; Milam, D.; Rainer, F. Laser Induced Damage in Optical Materials: 1979 Spec.Publ. 568, US GPO, Washington, D.C. p. 391.
[10] Walker, T.W.; Guenther, A.H.; Fry, C.G.; Nielson, P. ibid., p 405
[11] De Shazer, L.G.; Newnam, B.E.; Leung, K.M. Appl.Phys.Lett., 27, 607 p. 1973.
[12] Wolf, R.; Schafer, D. 6 Arbeitstagung der HFR Greuzflaschen/Dunne Schichten, TH Karl Marx Stadt, Tagungsberichte, 1983.
[13] Carniglia, C.K.; Apfel, J.H.; Allen, T.H. et al., ibid. 9, p 377.
[14] Bierlein, Th.; Wolf, R.; Zscherpe, G.; Brauns, B.; Schafer, D. Vortrag ILA, Dresden 1986.
[15] Brauns, B.; Schafer, D.; Wolf, R.; Zscherpe, G. Thin Solid Films, 138, 157 (1986).

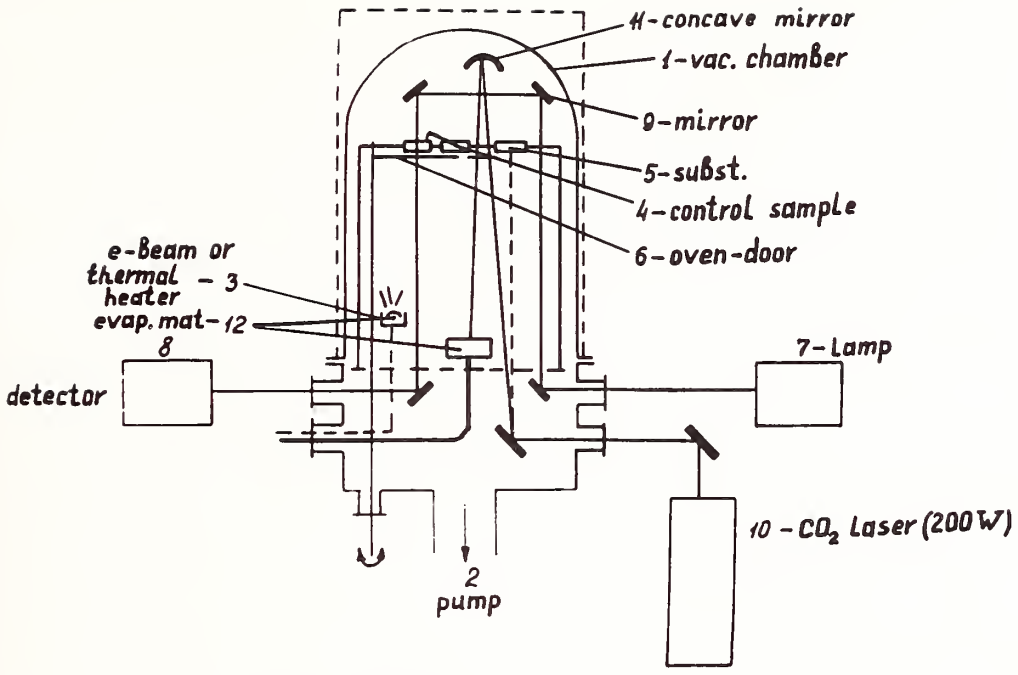

Fig. 1. Scheme of experimental set-up:
1-vacuum chamber, 2-vacuum pump, 3-electron-beam and thermal evaporator, 4-test sample, 5-sample, 6-oven door, 7,8-light source and detector of coating thickness test system, 9-mirror, 10-CO_2 laser, 11-concave mirror, 12-evaporating material.

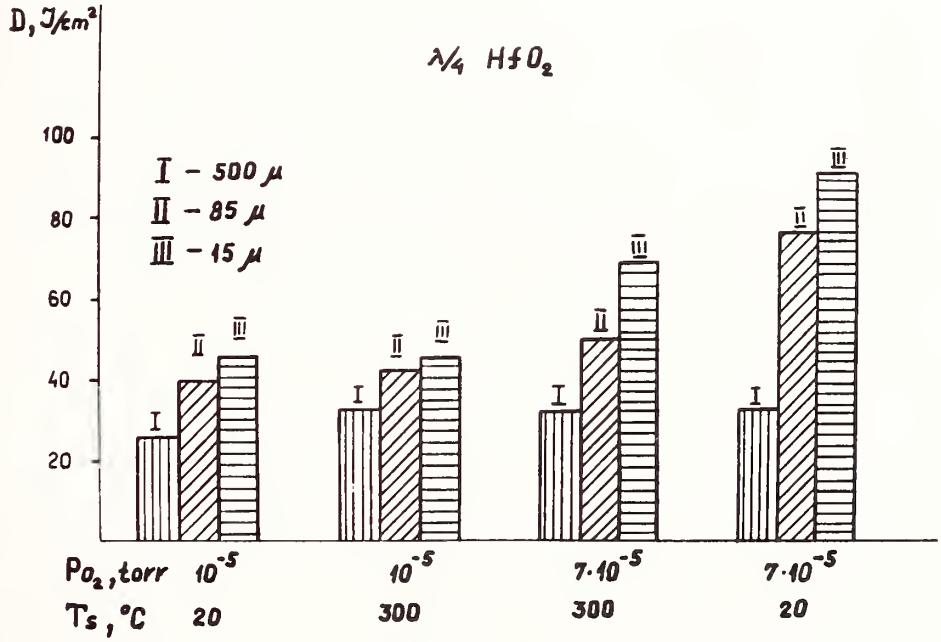

Fig. 2. Dependence of damage threshold, D, of $\lambda/4$-thick HfO_2 single-layer coating on the size of radiation spot, ϕ, at different pressures of oxygen, P_{O_2}, in vacuum chamber, and different substrate temperatures, T_s. ϕ = 500 (1), 85 (II), 15 μm (III); $P_{O_2} = 1.10^{-5}$ (1,2), 7.10^{-5} Torr (3,4); T_s = 20 (1,4), 300°C (2,3).

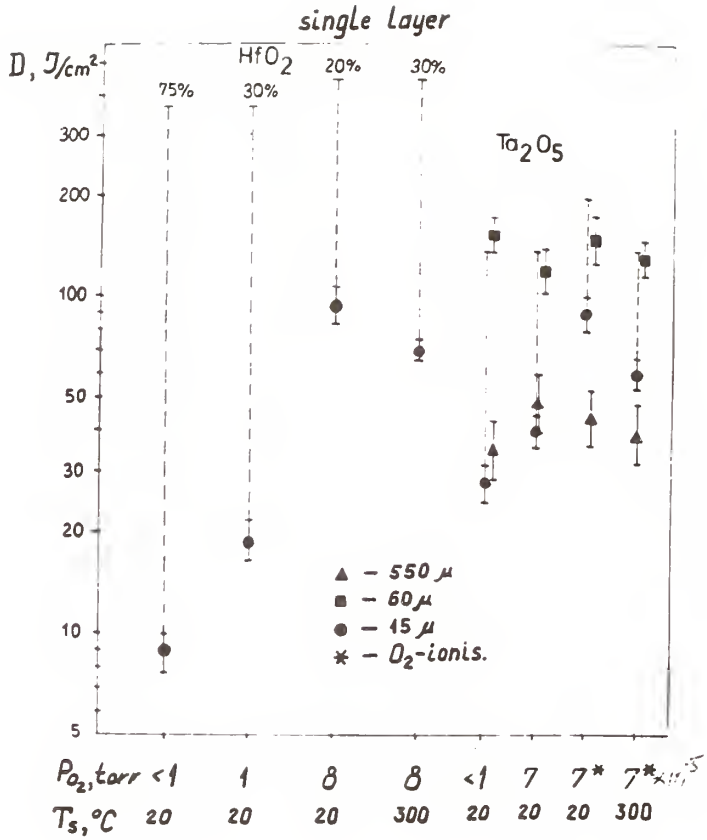

Fig. 3. Dependence of damage threshold, D, of $\lambda/4$-thick HfO_2 and Ta_2O_5 single-layer coatings on the oxygen pressure, P_{O2}, at different temperatures at 0 = 15 μm. T_s = 20 (1-3, 5-7), 300°C (4,8); * - ionized oxygen.

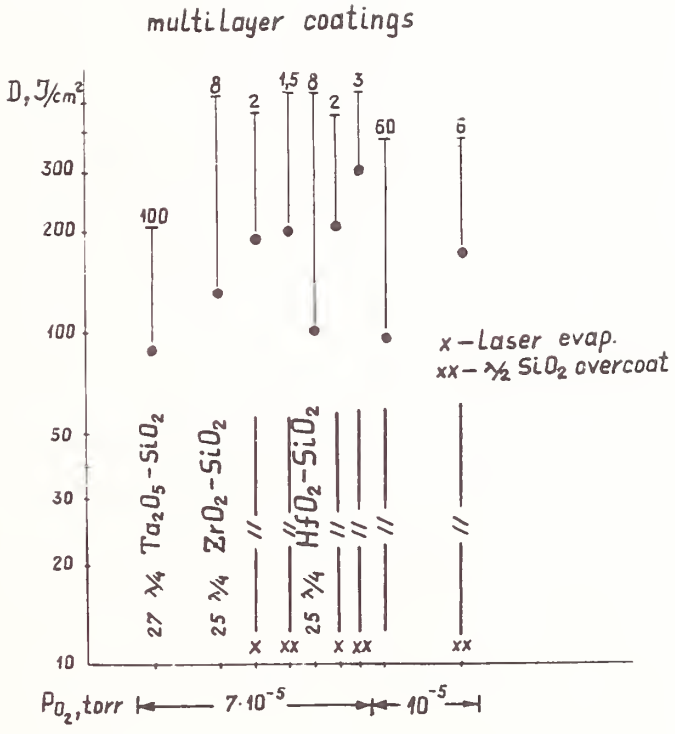

Fig. 4. Damage thresholds of multilayer coatings produced by e-beam and laser (X) evaporation methods: 1-27 $\lambda/4$ Ta_2O_5-SiO_2, 2-25 $\lambda/4$ ZrO_2-SiO_2, 3-25 $\lambda/4$ HfO_2-SiO_2 ($P_{O_2} = 7.10^{-5}$ Torr), 4-25 $\lambda/4$ f_2-SiO_2 ($P_{O_2} = 10^{-5}$ Torr); **) - coatings with halfwave silica overcaot.

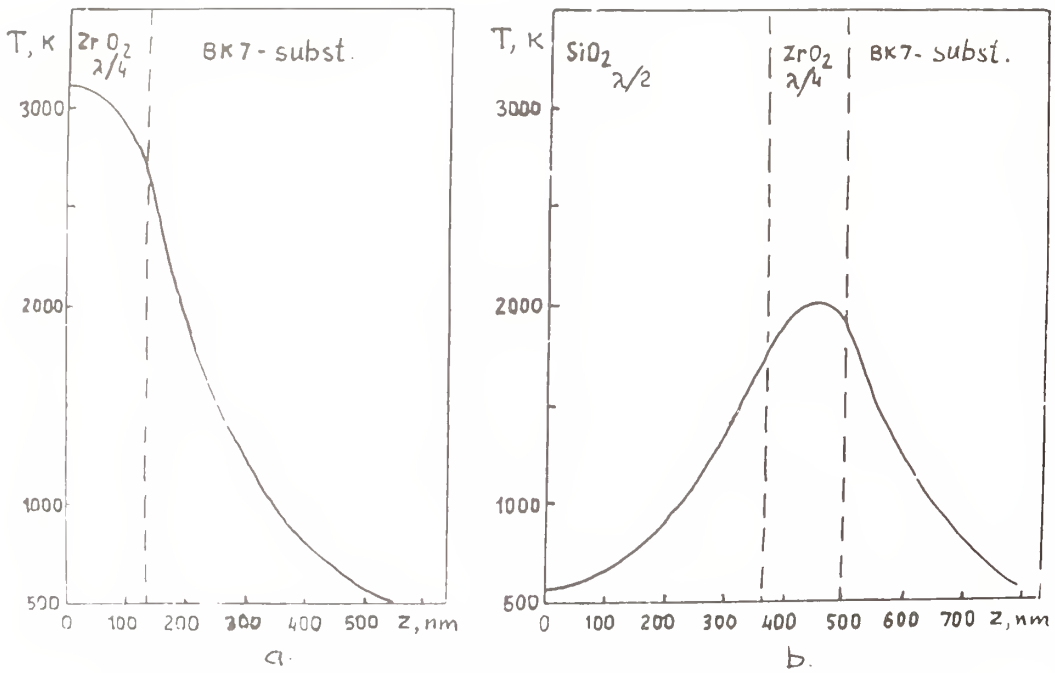

Fig. 5. Calculated temperature profiles in 132/4 ZrO_2 coating (a) and in the same coating with halfwave silica overcoat (b).

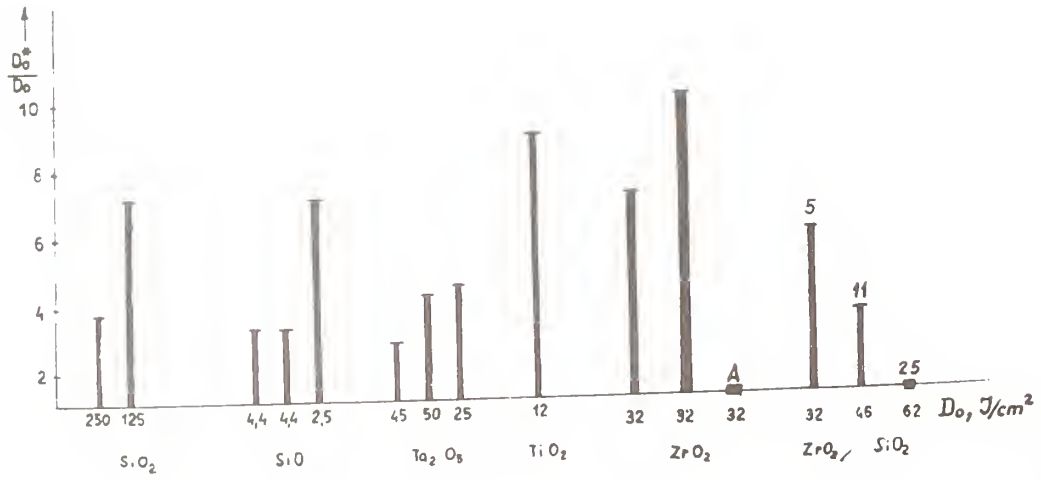

Fig. 6. Increase in the damage thresholds of coatings D*/D due to preliminary treatment of substrate with CW CO_2-laser radiation (P = 100 W, O = 10 mm).

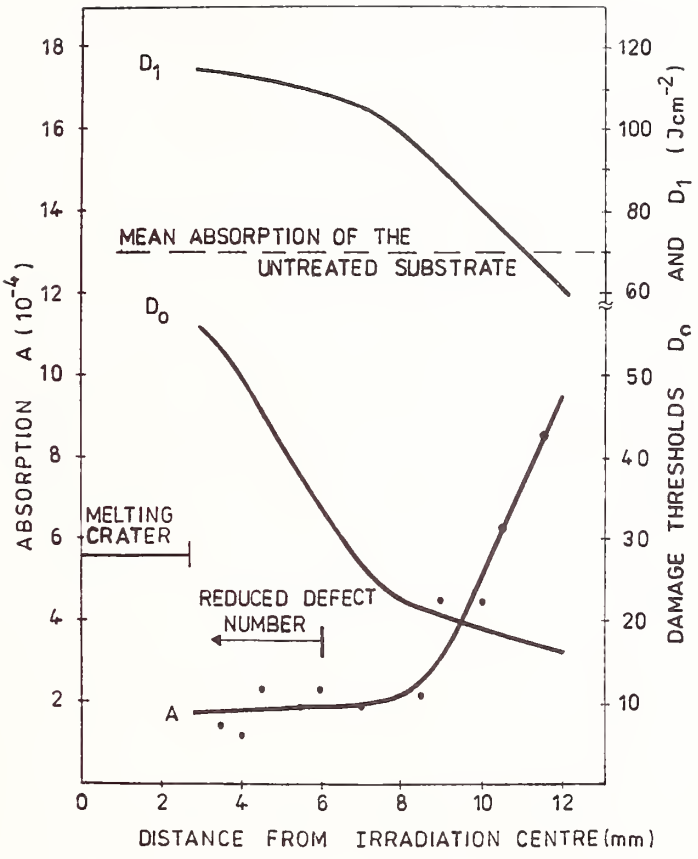

Fig. 7. Distribution of absorption and damage threshold of quarter wave single-layer TiO_2 coating in CO_2-laser irradiated region.

- MANUSCRIPT NOT RECEIVED -

PULSE LENGTH SCALING RESULTS AT 248 nm

J. Boyer
Los Alamos National Laboratory
Los Alamos, NM 87545

ABSTRACT

Damage thresholds were measured on a variety of optics at 248 nm for both 11 and 36 ns pulse lengths. Test at both pulse lengths were run on each optic. If a power law scaling is assumed, the mean exponent is 0.3 in agreement with results for other wavelengths. The exponents for individual optics range from 0.20 to 0.47. The experimental precision is such that variation in exponents is significant.

Manuscript Received 12/10/87/sar

Measurements of Ultra-wide Pulse Damage Thresholds of Anti-reflection Coated IR Materials at 10.6 μm

R. S. Eng, J. G. Grimm, J. Greene, J. A. Daley, N. W. Harris
Massachusetts Institute of Technology
Lincoln Laboratory
P.O. Box 73; Lexington, MA 02173-0073

A method has been developed to generate ultra-wide (10-100 μs regime) CO_2 laser pulses using a laser master oscillator-power amplifier configuration. These laser pulses have been used to conduct laser induced damage threshold measurements of anti-reflection coated cadmium telluride samples. The question of damage threshold dependence on the laser pulse width is discussed and compared with the results of other workers. The paper also addresses the effects of different types and physical properties of the AR-coating materials, and the effects of laser beam polarization on the damage thresholds of the materials.

KEY WORDS: Anti-reflection coatings; cadmium telluride; CO_2 laser MOPA; laser induced damage threshold; ultra-wide laser pulse lengths.

1. INTRODUCTION

While the damage thresholds of a number of commonly used, non-hygroscopic IR-transparent materials such as ZnSe, Ge, CdTe, and CdS have been measured at 10.6 μm using very narrow laser pulses,[1] very little is known about the laser induced damage threshold (LIDT) for much wider laser pulses. One of the main reasons is that it is rather difficult to generate flat-top pulses without severe pulse droop. We would like to report for the first time our method of generating ultra-wide, nearly flat-top CO_2 laser pulses of medium pulse energy and the results of measurements of damage thresholds on a number of AR-coated CdTe samples using these wide laser pulses. We have observed a LIDT exceeding 20 J/cm^2. Some of the samples have been tested successfully for several thousand laser shots without any observable surface damage.

2. EXPERIMENTAL SETUP

Figure 1 shows the experimental setup used to perform the CO_2 laser damage threshold measurements.

The laser beam pulses of several hundred millijoules are generated by a mechanically chopped cw CO_2 laser and an electrically pulsed amplifier chain. The beam is focussed by an ≈ f/30 lens onto the test sample which is located inside a cylindrical enclosed fixture constantly purged by filtered dry nitrogen and is shielded from room light so that free-carrier absorption in substrates such as CdTe need not be of concern.

Crucial to the measurement of the ultra-wide pulse damage thresholds is the generation of the wide CO_2 laser pulses, which are well behaved both temporally and spatially. We will discuss the details of the master oscillator-power amplifier (MOPA) chain.

Figure 2 shows a block diagram of the CO_2 laser MOPA chain. A cw CO_2 laser master oscillator (MO) with a 25 W nominal output is phase-locked by a stabilization loop to a 2 W CO_2 laser local oscillator. The latter is tuned to near the $^{12}C^{16}O_2$ I-P(20) line center but is not locked. A lens is used to form a small beam waist at the transmitting aperture of the high-speed chopper wheel. Another lens is used to transform the beam size, slightly convergent, through the low-pressure dc excited laser amplifier. A beam waist is formed slightly beyond the exit end of the first of the two InSb optical isolators. A pair of lenses is used as a beam expander to enlarge the beam being amplified by the first pulse excited laser amplifier. This beam is slightly convergent so that at the input to the second InSb optical isolator it is matched to the

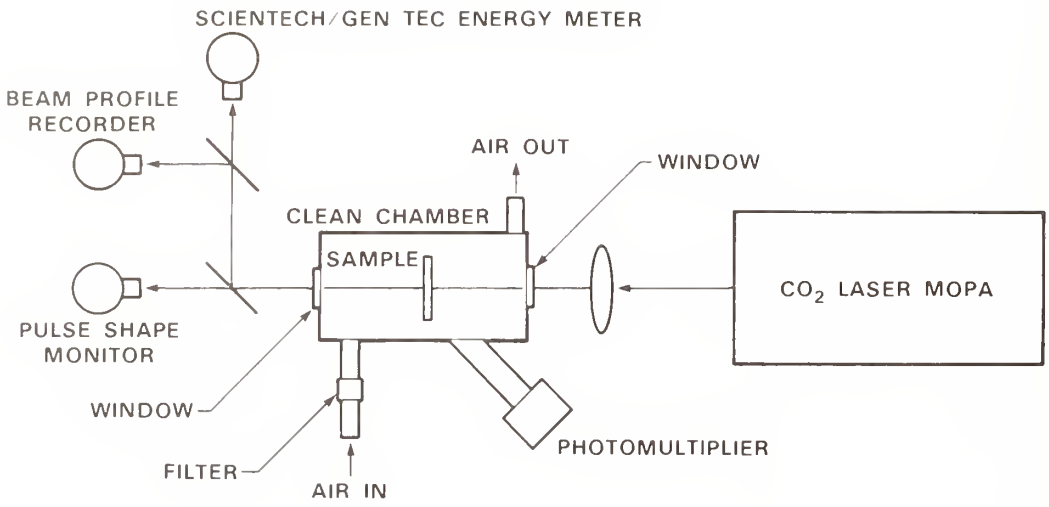

Figure 1. CO_2 laser damage threshold measurement setup.

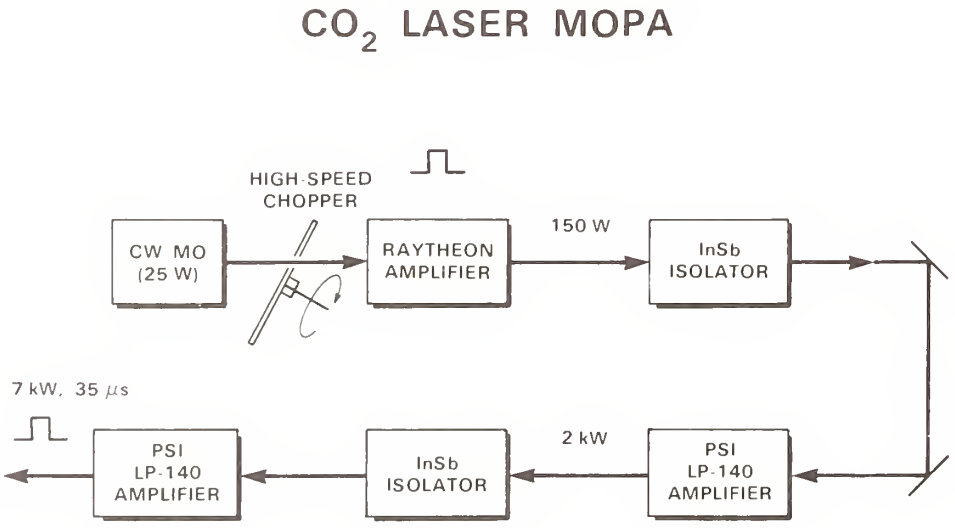

Figure 2. CO_2 laser MOPA schematic diagram.

clear aperture of the isolator. Brewster angle multi-plate polarizers are used next to the two InSb optical isolators to enhance the optical signal isolation.

Additional optics are used to control the beam diameter so that when it goes through the second pulse excited laser amplifier, the beam is sufficiently large to minimize gain saturation and at the same time not so large as to have any appreciable beam truncation. The two pulse excited laser amplifiers are low-pressure TE lasers manufactured by Pulse Systems, Inc. They are each operated at a total pressure of about 30 Torr.

With the above amplifier chain, pulse energy in excess of 300 mJ is easily obtained for pulse widths in the range of several tens of microseconds. However, when the optical delay is adjusted for maximum energy output, the optical pulse has a large droop. Due to their somewhat narrow and peaked leading edges, these pulses are not very useful for the determination of the effect of pulse width on the damage threshold. This is because it is difficult to assign an effective pulse width to these pulses unless one already has a good notion of the threshold-to-pulse-width dependence beforehand. For this reason, we shortened the optical pulse delay so that it fell on the rising portion of the temporal gain profile of the pulse amplifiers. This resulted in reasonably flat pulses, as shown in Figure 3, with only a moderate reduction in energy level, which we considered a good tradeoff.

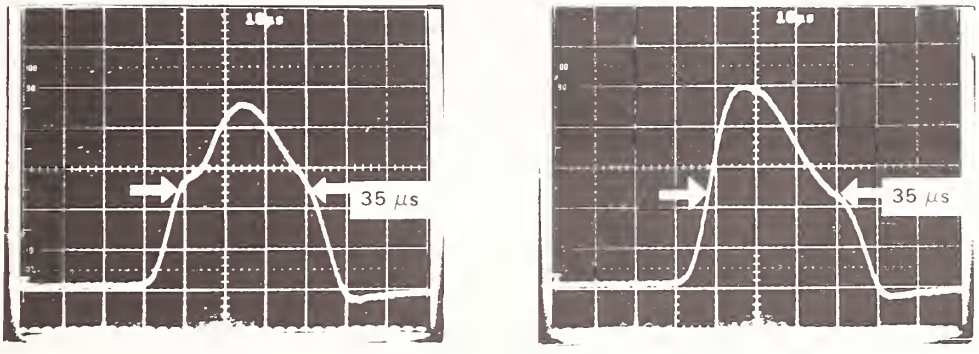

Figure 3. High-energy, coherent, wide pulses from a CO_2 laser MOPA for two delays of optical input.

Figure 4 shows the laser damage test fixture used to enclose and hold the test sample. AR/AR coated germanium windows are used at each end to shield off room light to prevent any free-carrier absorption by the CdTe test samples. The samples are placed at the center of the cylinder in the appropriate holder. A photomultiplier tube (PMT) is used to detect visible emissions prior to and during the onset of damage in some of the test runs. The fixture was cleaned initially and is purged with filtered N_2 during usage. It is completely portable so that it can be transported to a clean room for loading and microscopic inspection of the samples.

Some of the laser beam diagnostics, including pulse energy and temporal profile, are monitored simultaneously with the damage testing. A third diagnostic, the spatial profile, is measured on a periodic basis.

The pulse energy is meausured with a GenTec energy meter which was calibrated against a Scientech energy meter. The energy meter collects the pulse energy transmitted through the sample test fixture. The temporal pulse shape is measured using a Boston Electronics room temperature photoelectromagnetic (PEM) HgCdTe high-speed detector. The power that is reflected off of an AR/AR coated ZnSe window tilted at an angle of about 60° is focussed by an f/3 lens onto the active area of the detector. The losses in the test fixture were measured using a cw beam and a Coherent power meter. The losses, including the beamsplitter but not the actual test sample, were found to be 4%.

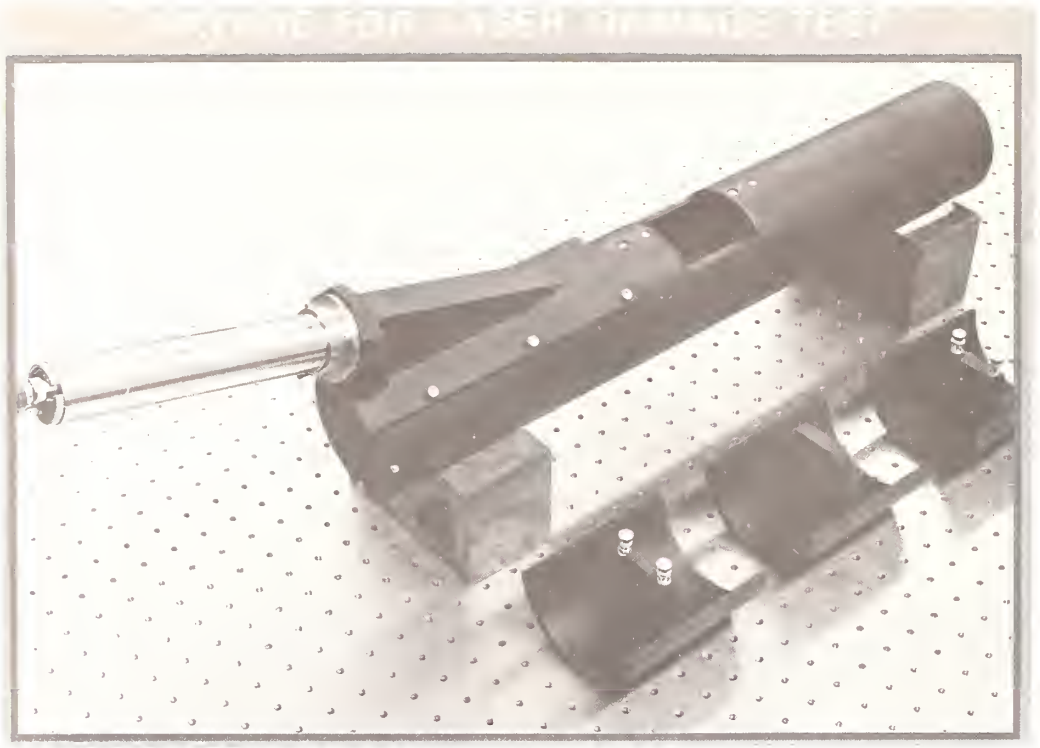

Figure 4. Photo of laser damage test fixture.

The spatial beam profile was recorded with a 16 x 15 pyroelectric detector array, made by Spiricon, Inc. This was done to ascertain that we had a Gaussian shape beam. Figure 5 shows both a contour and an isometric plot of the laser beam profile. It can be seen that the observed beam has a Gaussian profile. Based on the above plots of the beam profile, the following formula, which is appropriate for a Gaussian beam, is then used to determine the beam energy density, J, at the center of the beam:

$$J(r=0) = \frac{2E_t}{\pi w^2} \qquad (1)$$

where E_t is the total pulse energy and w is the beam spot radius.

By measuring the beam size and pulse energy, the peak or on-axis energy density was determined. The pulse repetition frequency was set at 1 Hz. For most of the samples we tested, a conditioning or hardening schedule was employed in that the sample was illuminated by the laser beam at an energy density about one half of the expected damage level. This conditioning was employed since a number of research workers previously reported that higher damage thresholds were achieved as a result.[1]

After each damage test run, black and white photographs of the irradiated spots were taken with a phase contrast Nomarski microscope in both dark-field and bright-field settings for detailed examination of any surface damage.

3. RESULTS AND DISCUSSION

Figure 6 shows typical damage sites. In the photo at the left there are two damage spots. Both of these occurred at the same damage threshold of 28 J/cm^2. They are slightly smaller than the measured beam spot size of 1.06 mm in diameter. The damage feature in the photo at the right is quite different. It is a hair-line crack that stretches diagonally across the AR-coating the width of the beam spot size. This damage occurred at an energy density of 38 J/cm^2; the coating is a three-layer coating of ZnSe, ThF_4, and ZnSe.

PULSED CO_2 LASER BEAM PROFILES

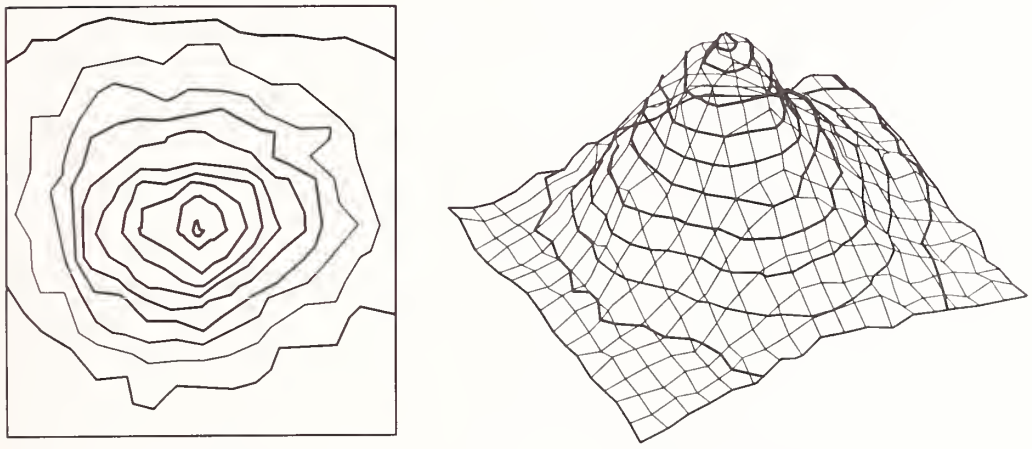

Figure 5. Pulsed CO_2 laser beam profiles.

TYPICAL CO_2 LASER DAMAGE SITES ON CdTe SAMPLES

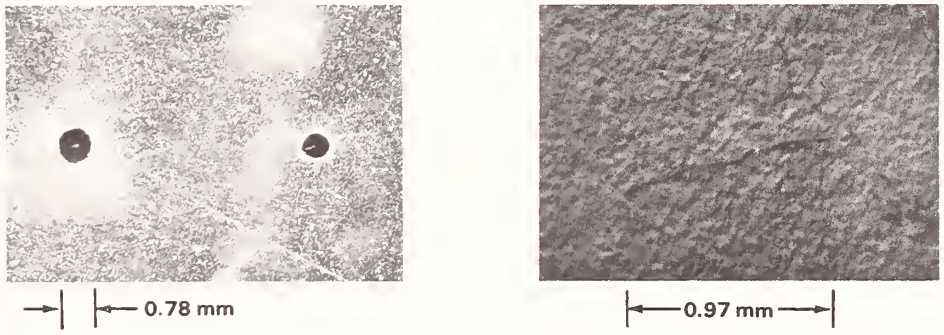

Figure 6. Typical CO_2 laser damage sites on CdTe samples.

The specifications for the AR-coated CdTe samples used in the damage tests are summarized in Table I. The samples were purchased from two sources and anti-reflection coated by a number of vendors. We see that only two materials were used for AR coatings, ThF_4 and ZnSe. Since ThF_4 has a higher absorption coefficient than ZnSe, this material has the higher impact on the damage threshold. Note optical polishing and cleaning techniques can also affect the LIDT.

TABLE 1. CdTe TEST SAMPLE SPECIFICATIONS

SAMPLE NUMBER	CT-1	CT-2	CT-3	CT-4	CT-5
CRYSTAL SURFACE	POLYCRYSTAL	POLYCRYSTAL	(111) OR $(1\bar{1}0)$	(111) OR $(1\bar{1}0)$	(111) OR $(1\bar{1}0)$
CRYSTAL GROWTH	II-VI INC.[a]	UNKNOWN	II-VI INC.[a]	II-VI INC.[a]	II-VI INC.[a]
AR-COAT TYPE	ThF_4/ZnSe	ThF_4	ZnSe/ThF_4/ZnSe	ThF_4/ZnSe	ThF_4/ZnSe
FINAL MECHAN. POLISH	0.3 μm	ULTRAFINE (M.M.)	0.3 μm	0.3 μm	0.3 μm
CHEM/RF CLEANING	YES/NO	NO/YES	YES/YES	YES/NO	YES/NO
EVAPORATION	THERMAL	E-BEAM	THERMAL	E-BEAM	THERMAL
SUBSTRATE TEMP. (°C)	150	100	200-250	150	200

a. MODIFIED BRIDGEMAN METHOD WITH In DOPING

Tables II-V show all the damage test results for damage test numbers ranging from 1-48. The parameters not listed on the tables are written here. The pulse repetition frequency was 1 Hz. The pulse width (FWHM) was 35 μs. The e^{-2} beam spot diameter was 2.73 mm for numbers 1-4 and was changed to 1.06 mm for damage test numbers 5-48.

Table II shows the results of damage tests on several CdTe samples. In damage test numbers 1-4 (samples CT-1 and CT-2), the beam spot size diameter was 2.73 mm. Using this diameter beam, it was not possible to damage the CT-1 sample, while sample CT-2 was damaged at rather low value of energy density due to a high density of surface defects. Damage test numbers 5-8 (sample number CT-1) represent a run series starting with low energy density to provide surface conditioning, then gradually increasing the energy density in subsequent test numbers until damage was observed. In this case, the damage occurred at test number 8 after two shots with the LIDT at about 30 J/cm^2. Similarly, using the same process, we obtained the LIDT of sample CT-6, which had the same sample specifications as those for CT-1. The damage thresholds for sample CT-1 and CT-6 were both in the 30-36 J/cm^2 levels. Tests numbers 5, 6, 7, and 9, 10, and 11 were conducted both as conditioning runs with the energy density gradually increasing to avoid passing the threshold level by a large margin. These tests show that the threshold width is reasonably narrow.

Table III shows similar test runs 13-16, 17-20, and 21-24 to obtain three damage sites on sample CT-3. Note that the sample is a single crystal of CdTe. For the (111) face, the threshold appeared to be 10-15% lower in comparison with the $(1\bar{1}0)$ face. The LIDT of these sites all fall in the range of 34-40 J/cm^2.

TABLE 2. DAMAGE TEST RESULTS ON CdTe SAMPLES

DAMAGE TEST NUMBER	SAMPLE NUMBER	PEAK ENERGY DENSITY (J/cm^2)	NUMBER OF SHOTS	POLARIZATION	RESULTS[a]
1	CT-1	7.4-9.6	900	LINEAR	ND
2	CT-1	5.1-6.7	3600	LINEAR	ND
3	CT-2	3.9-5.3	900	LINEAR	ND
4	CT-2	5.3	300	LINEAR	D
5	CT-1	6-8	600	LINEAR	ND
6	CT-1	12-16	600	LINEAR	ND
7	CT-1	20-25	600	LINEAR	ND
8	CT-1	30	2	LINEAR	D
9	CT-6[b]	8-10	1200	LINEAR	ND
10	CT-6	18-22	600	LINEAR	ND
11	CT-6	24-30	600	LINEAR	ND
12	CT-6	30-36	60	LINEAR	D

a. ND AND D DENOTE NO DAMAGE AND DAMAGE RESPECTIVELY;

b. THE FABRICATION PROCESS FOR SAMPLE CT-6 IS THE SAME AS THAT FOR CT-1.

TABLE 3. DAMAGE TEST RESULTS ON CdTe SAMPLES (Continued)

DAMAGE TEST NUMBER	SAMPLE NUMBER[a]	PEAK ENERGY DENSITY (J/cm^2)	NUMBER OF SHOTS	POLARIZATION	RESULTS[b]
13	CT-3(111)	16-22	600	LINEAR	ND
14	CT-3(111)	22-26	600	LINEAR	ND
15	CT-3(111)	26-30	600	LINEAR	ND
16	CT-3(111)	32-34	5	LINEAR	D
17	CT-3($1\bar{1}0$)	8-10	600	LINEAR	ND
18	CT-3($1\bar{1}0$)	16-20	600	LINEAR	ND
19	CT-3($1\bar{1}0$)	26-32	600	LINEAR	ND
20	CT-3($1\bar{1}0$)	38-40	5	LINEAR	D
21	CT-3($1\bar{1}0$)	10-16	600	LINEAR	ND
22	CT-3($1\bar{1}0$)	16-22	3600	LINEAR	ND
23	CT-3($1\bar{1}0$)	26-32	600	LINEAR	ND
24	CT-3($1\bar{1}0$)	38	5	LINEAR	D

a. NUMBERS WITHIN PARENTHESES DENOTE CRYSTAL SURFACE;

b. ND AND D DENOTE NO DAMAGE AND DAMAGE RESPECTIVELY.

Additional damage test results are summarized in Tables IV and V. It is to be noted that in damage test numbers 29-32 and 33-36, the incident laser polarization was changed during the measurements in order to determine whether the change in the electric field intensity has any effect on the damage threshold. Test number 32 shows that the damage threshold is about 10% higher than that achieved for an identically fabricated sample shown in test number 8 indicating that the 30% change in the laser electric field due to a change in the laser polarization has little effect on the LIDT. Therefore, we conclude that the cause of damage is mainly thermal in origin. This finding is further confirmed by test number 36 when the damage result is compared with those for test numbers 16, 20, 24, and 28, (all done on sample CT-3). In test number 43, the damage threshold reached 50 J/cm^2, which is nearly two orders of magnitude higher than those reported for nanosecond laser pulses. For the same sample in a subsequent test, however, the LIDT level came down to 32 J/cm^2. The cause of the reduction in threshold is believed to be surface contamination by debris from the adjacent damage site during the latter's damage run.

TABLE 4. DAMAGE TEST RESULTS ON CdTe SAMPLES (Continued)

DAMAGE TEST NUMBER	SAMPLE NUMBER[a]	PEAK ENERGY DENSITY (J/cm^2)	NUMBER DF SHDTS	PDLARIZATIDN	RESULTS[b]
25	CT-3(1$\bar{1}$0)	10-16	600	LINEAR	ND
26	CT-3(1$\bar{1}$0)	16-22	3600	LINEAR	ND
27	CT-3(1$\bar{1}$0)	26-32	600	LINEAR	ND
28	CT-3(1$\bar{1}$0)	38	5	LINEAR	D
29	CT-1	6-8	600	LINEAR	ND
30	CT-1	12-16	600	LINEAR	ND
31	CT-1	28-32	600	CIRCULAR	ND
32	CT-1	34	20	CIRCULAR	D
33	CT-3(1$\bar{1}$0)	7-10	1200	LINEAR	ND
34	CT-3(1$\bar{1}$0)	18-22	600	LINEAR	ND
35	CT-3(1$\bar{1}$0)	26-32	600	CIRCULAR	ND
36	CT-3(1$\bar{1}$0)	34-36	300	CIRCULAR	D

TABLE 5. DAMAGE TEST RESULTS ON CdTe SAMPLES (Continued)

DAMAGE TEST NUMBER	SAMPLE NUMBER[a]	PEAK ENERGY DENSITY (J/cm^2)	NUMBER DF SHOTS	PDLARIZATIDN	RESULTS[b]
37	CT-4(1$\bar{1}$0)	6-8	600	LINEAR	ND
38	CT-4(1$\bar{1}$0)	8-12	600	LINEAR	ND
39	CT-4(1$\bar{1}$0)	12-16	600	LINEAR	ND
40	CT-4(1$\bar{1}$0)	16-21	600	LINEAR	ND
41	CT-4(1$\bar{1}$0)	24-30	600	LINEAR	ND
42	CT-4(1$\bar{1}$0)	30-40	600	LINEAR	ND
43	CT-4(1$\bar{1}$0)	45-50	5	LINEAR	D
44	CT-4(1$\bar{1}$0)	6-8	600	LINEAR	ND
45	CT-4(1$\bar{1}$0)	16-20	600	LINEAR	ND
46	CT-4(1$\bar{1}$0)	20-24	600	LINEAR	ND
47	CT-4(1$\bar{1}$0)	24-28	600	LINEAR	ND
48	CT-4(1$\bar{1}$0)	30-32	15	LINEAR	D

a. NUMBERS WITHIN PARENTHESES DENOTE CRYSTAL SURFACE;

b. ND AND D DENOTE NO DAMAGE AND DAMAGE RESPECTIVELY.

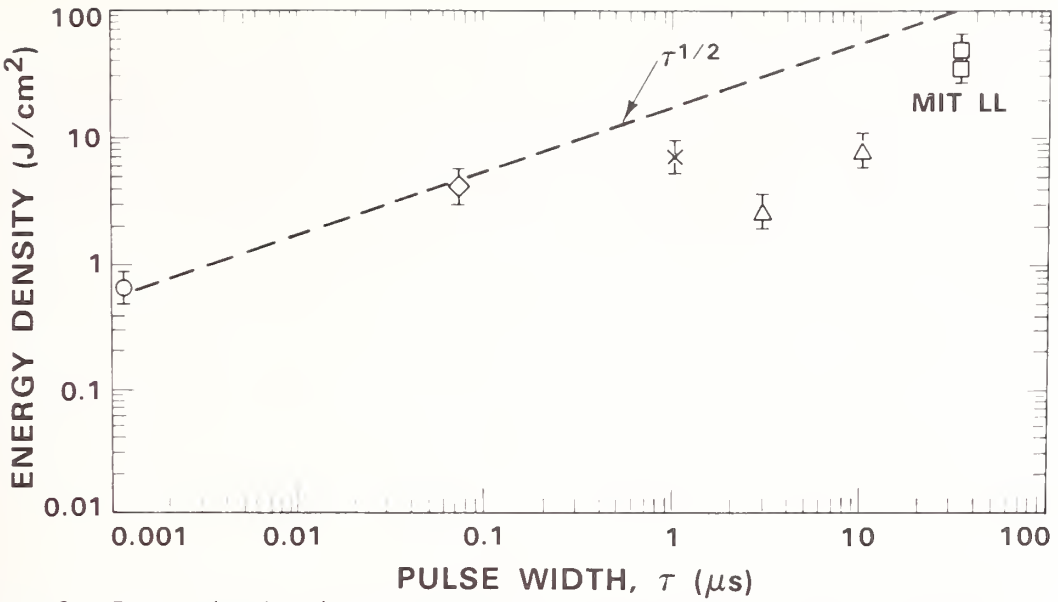

Figure 8. Energy density damage threshold vs. pulse width. The thresholds at 1.2 ns and 70 ns are from Refs. 1 and 2, that at 1 μs is from Ref. 3, and those at 3 μ and 10 vs are from Ref. 4.

4. CONCLUSION

Based on the present measurement results, we would like to conclude with the following remarks:

* The laser induced damage thresholds of a number of AR-coated CdTe samples have been measured using wide CO_2 laser pulses.

* The observed thresholds are more than one order of magnitude higher than those reported for very short pulses.

* The damage thresholds for long pulses fall below the square root of pulse width line extrapolated from short pulse data.

* The damage results for circularly polarized beam imply that the cause of damage is mainly thermal in origin.

* The effects of the types of AR coatings and damage site density were considered.

The authors would like to thank C. Freed, L. J. Sullivan, W. E Keicher, and B. E. Edwards for many helpful discussions, and R. A. Westberg, M. Mattei, and E. J. Christiansen for their able assistance with the experiment.

5. REFERENCES

[1] B. E. Newnam and D. H. Gill, "Damage Resistance of CO_2 Fusion Laser Optics," Optical Engineering, 18, 579 (1979).

[2] B. E. Newnam and D. H. Gill, "Damage Resistance of AR-coated Germanium Surfaces for Nanosecond CO_2 Laser Pulses," Laser Induced Damage in Optical Materials: 1977, NBS Spec. Pub. 509 pp.298-31. 1977.

[3] S. J. Thomas, Los Alamos National Laboratory, Reported damage threshold exceeding 7 J/cm² (4 J on 1.2 cm beam spot diameter) on AR-coated CdTe for 1 μs CO_2 laser pulses, private communications.

[4] Avco Everett Research Laboratory, Inc., "Radiation Damage Tests of Anti-reflection-coated Cadmium Telluride Modulator Crystals," Final Report, Contract No. F19628-85-C-0002, November 1985, prepared for MIT/Lincoln Laboratory, Lexington, MA.

Figure 7 is a plot of the CO_2 laser induced damage threshold level observed at those test numbers indicated on the abscissa. With the exception of test numbers 43 and 4 (the latter we can discard because of very poor optical surface quality) the damage levels show a rather small deviation of 5.7 J/cm² from the average of 36.6 J/cm². The present results imply that factors as crystal growth, mechanical polishing, and the supply source of ThF_4 (which are the same for almost all the samples tested) could have a much stronger effect on the threshold than the optical coating technique which varies somewhat from vendor to vendor.

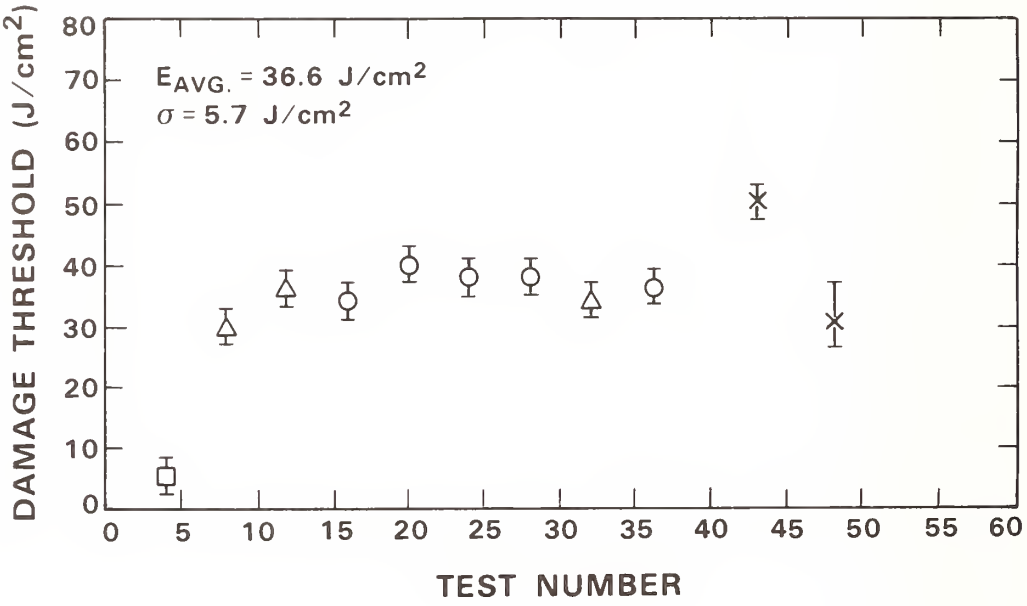

Figure 7. Damage threshold of CdTe vs. damage test number. Note that their area were a total of 48 damage tests conducted, but only 11 of them resulted in actual sample damage with thresholds plotted in the figure. Similar symbols denote different sites on the same sample.

For comparison purposes, we have plotted on Fig. 8 the laser damage thresholds of AR-coated CdTe samples as a function of the pulse width. The various experimental points on the plot were taken from a number of references.[1,2,3,4] It can be seen that the damage threshold goes up as the pulse width increases. Based on our present measured results using a long laser pulse width, the LIDT appears to fall slightly below the square root line. This is to be compared with the 3 μs and 10 μs data points from Ref. 4 which fall considerably below the square root line. The reasons for the much lower thresholds for these two data points are not known. However, the presence of a very sharp leading spike in the TEA laser oscillator output can not be excluded as a cause. As more data becomes available, the damage-vs-pulse-width relation will undoubtedly be improved further.

Was there much difference between the damage thresholds for various AR coating designs on different CdTe substrates? In tests done at Los Alamos in 1979, on many samples of Ge and some of CdTe they found that the design of the AR coating made no difference in the damage threshold. The substrate was damaging, not the coating. The speaker agreed, pointing out that the standard deviation of his damage thresholds was less than 15%, so the substrate was also damaging for the long pulses.

The reason that the measurements were carried out in the dark was that the band gap of CdTe is about 1.5 eV and the room temperature light would generate carrier pairs, lowering the resistivity.

Manuscript Received 12/23/87/sar

Sample Ranking vs. Damage Threshold Criteria in Small Spot Size Laser Damage Testing

S. D. Carson, P. Gorbett and S. L. Seiffert

The BDM Corporation
Albuquerque, NM 87106

F. P. Ernest and P. M. Schumacher

The Sierracin Research Corporation
Sylmar, CA 91342-3792

Small spot size (3.5 mm) laser damage testing at 10.6 μm has been used on samples which consisted of metallic and metallic oxide coatings on polymeric substrates. Three degrees of damage were used to define damage thresholds. While absolute threshold values were different for each of the three levels of damage, sample ranking did not change. As long as consistency is maintained, the degree of damage used to define the damage threshold does not appear to be significant for small spot size testing for these samples, where the goal is to screen the effectiveness of a series of hardening concepts.

Key words: damage threshold; defect density; laser damage; spot size.

1. Introduction

In any damage testing program, the question of what criteria will be used to define the damage threshold arises. We have defined three damage thresholds for our testing program: 1) the minimum energy level at which surface distortion due to heating effects is observed, 2) the minimum energy level at which coating damage (discoloration, cracking, crazing) occurs and 3) the minimum energy level at which substrate damage (melting, crazing) is observed. Equally important is the issue of spot size effects. Since damage thresholds are known to be a function of defect density within a sample, [1, 2] as the test spot size increases, the damage threshold decreases [3, 4]. Therefore, considerable skepticism surrounds small spot size testing, since resulting threshold values are felt to be artifically high. However, our results show that if the goal is relative, rather than "absolute" damage thresholds, then small spot size testing provides a rapid, efficient and economical approach to screening materials hardening concepts.

2. Experimental

Small spot size (3.5 mm) laser damage testing at 10.6 μm has been used for a series of twenty-two samples of metallic and metallic oxide coatings on polymeric substrates. The three damage thresholds defined above were determined for each sample. The experimental test setup is shown in figure 1. The laser source is a Spectra-Physics Spectra 810 CO_2 laser, maximum

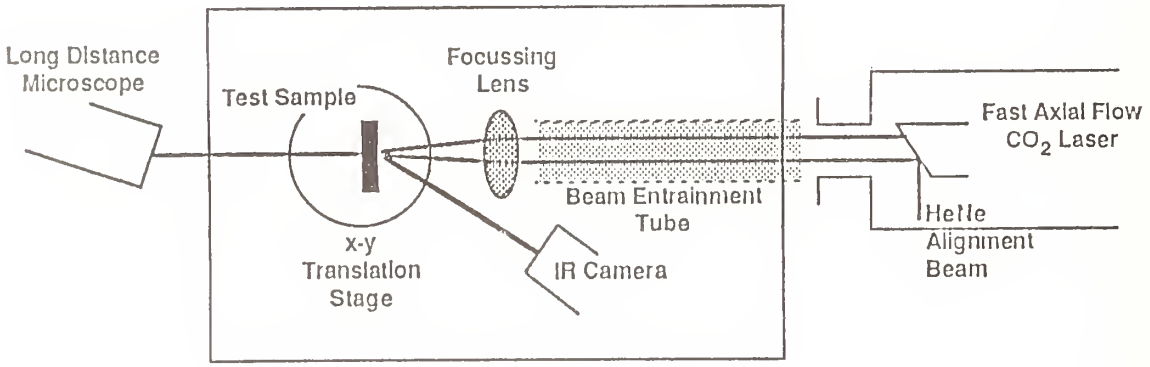

Figure 1. Experimental setup for damage testing.

power, 630 W (cw, TEM_{00}). Incident power density was the same for all tests, and the energy on target was varied by varying the irradiation time. A beam profile obtained using the scanning knife edge technique [5-7] is presented in figure 2. The transmitted power was measured with

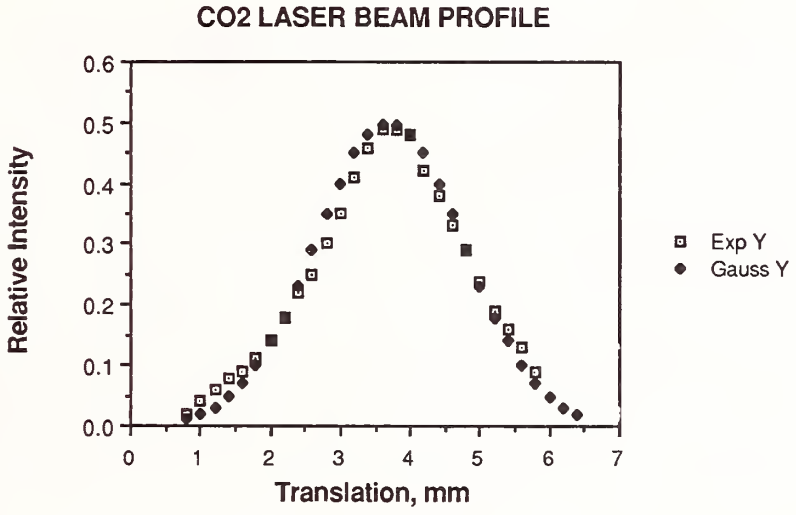

Figure 2. CO_2 laser beam profile obtained using the scanning knife edge technique.

a Laser Precision RT-3000 thermopile at 0.2 mm intervals as the knife edge traversed the beam cross section perpendicular to the transmission axis. The beam profile is essentially Gaussian with a diameter ($1/e^2$) at the target plane of 3.5 ± 0.2 mm. A Katoptaron LDM-1 long distance microscope with camera attachment was used to photograph damage and confirm that a particular degree of damage had occurred. Damage was further characterized by an AGA Model 782 Thermovision System.

Samples consisted of 3" square test coupons. Using the "up and down" statistical method of Detrio et. al. [8], up to 36 shots/sample were used to determine damage thresholds. If damage was produced at a particular energy level, irradiation time was decreased for the next shot. If no damage occurred at this fluence level, irradiation time was increased for the next test, and so on. In this manner, one can "zero in" on the damage threshold (corresponding roughly to the energy where 50% of the test sites damage).

3. Results and Discussions

Thresholds for each level of damage are shown in table 1.

Table 1. Test results

Sample	Damage Threshold, J/cm^2		
Uncoated Plexiglas (PL) and Polycarbonate (PC)	1	2	3
PL - 1, 2	16	N/A	72
PC - 3, 4	22	N/A	150
Metallic Oxide on PC			
5	*	12	290
6	"	13	315
7	"	28	342
8	"	55	615
9	"	119	1390
10	"	130	1400

Table 1. Test results (Continued)

Metallic Coating on PL and PC			
**PC - 11, 12, 13	284	293	359
PL - 14, 15, 16	300	320	381
PL - 17, 18, 19	***	1174	1777
PC - 20, 21, 22	706	1395	2114

*Coating exhibits no thermal distortion; the initial surface change is coating cracking or crazing.
**Values are the average for three samples of the same composition.
***Insufficient data to determine.

Sample ranking is seen to be independent of damage threshold criteria. This type of behavior is consistent with a simple thermal damage mechanism.

Using the CO_2 electric discharge coaxial laser (EDCL) at the Air Force Wright Aeronautical Laboratory (AFWAL), sample ranking was maintained under large spot size (one inch) testing conditions. Thus, small spot size testing has proved to be a fast, reliable screening method for hardening concepts.

This work was supported by the Air Force Wright Aeronautical Laboratory, AFWAL/MLPJ, Laser Hardened Materials Branch, under contract no. F33615-85-C-5144.

4. References

[1] DeShazer, L. G.; Newman, B. E.; Leung, K. M. The role of coating defects in laser induced damage to thin films. Nat. Bur. Stand. (U.S.) Spec. Publ. 387; 1973 December. 285 p.

[2] Aleshin, I. V.; Bonch-Bruevich, A. M.; Zinchenko, V. I.; Imas, Y. A.; Komolov, V. L. Effect of absorbing inhomogeneities on optical breakdown of transparent dielectrics. Sov. Phys. Tech. Phys. 18 (12): 1648-1650; 1974 June.

[3] Foltyn, S. R. Spot size effects in laser damage testing. Nat. Bur. Stand. (U.S.) Spec. Publ. 669; 1984 January. 499 p.

[4] Soileau, M. J.; Frank, J. B.; Veatch, T. C. On Self-focusing and spot size dependence of laser-induced breakdown. Nat. Bur. Stand. (U.S.) Spec. Publ. 620; 1981 October. 483 p.

[5] Khosrofian, J. M.; Garetz, B. A. Measurement of a Gaussian laser beam diameter through the direct inversion of knife-edge data. Appl. Opt. 22 (21): 3406-3410; 1983 November.

[6] Cohen, D. K.; Little, B.; Luecke, F. S. Techniques for measuring 1 μm diameter Gaussian beams. Appl. Opt. 23(4): 637-640; 1984 February.

[7] Hull, D.; Stewart, A. F. Laserbeam profiles - equipment and techniques. Lasers and Appl. 4(11): 71-76; 1985 November.

[8] Detrio, J. A; Berens, A. P. Statistical considerations of laser damage measurements. Nat. Bur. Stand. (U.S.) Spec. Publ. 509; 1977 December. 561 p.

Manuscript Received 12/21/87/sar

Intrinsic Optical Damage in Potassium Bromide at 532 nm

X. A. Shen, Peter Braunlich, and Scott C. Jones
Department of Physics, Washington State University
Pullman, WA 99164-2814

Paul Kelly
National Research Council, Ottawa, K1A 0R6, Canada

The nonlinear interaction of intense 100 ps laser pulses at 532 nm with KBr single crystals is monitored up to damage by measuring the resulting σ component of the self-trapped exciton recombination luminescence as a function of incident photon flux. Information on the temperature rise in the interaction volume is obtained from the σ-luminescence vs flux relation with the aid of the known temperature dependence of the luminous efficiency. We show that the mechanism of energy deposition is four-photon free carrier generation and ensuing free carrier heating with small contributions by self-trapped holes. Single-pulse damage occurs without electron avalanche formation at a temperature very close to the melting point.

Key Words: alkali halides; avalanche ionization; exciton recombination luminescence; 532 nm laser; four-photon absorption; free electron heating; polaron heating; KBr; self-trapped excitons.

1. Introduction

Historically, electron-avalanche impact ionization was believed to be the appropriate description for laser-induced damage of optical materials. The earlier damage measurements appeared to agree with predictions from the avalanche theory until 1977 when Manenkov [1] found discrepancies in the temperature dependence of the damage threshold in some alkali halides at 532 nm wavelength. He speculated that multiphoton absorption may be responsible for the observed damage events.

In the 18th Boulder Laser Damage Conference, Jones et al. [2] presented the first direct experimental evidence supporting the multiphoton theory. These authors measured, with a photoacoustic method, the prebreakdown energy deposition in NaCl exposed to intense laser pulses at 532 nm and showed that considerable energy can be deposited into the crystal via the four-photon absorption mechanism with no indication of electron avalanche. The temperature rise during the interaction can be as high as several hundred degrees. This motivated us to further study prebreakdown laser-matter interaction in other optical materials.

We report here the prebreakdown temperature measurements in KBr exposed to 532 nm laser pulses. Our results confirm that the primary charge carrier generation process in this case is also high-order multiphoton absorption by valence electrons. In addition, we show that the temperature rise resulting from the interaction with the laser pulses is primarily governed by the free carrier heating mechanism proposed by Epifanov [3], and intrinsic single-pulse damage occurs at a temperature very close to the melting point of the material.

The work reported here is an extension of the earlier investigation by Shen et al. [4] of the four-photon absorption cross section in KBr at 532 nm. The technique used is the self-trapped exciton recombination luminescence (STERL) method, which exploits the known temperature dependence of luminescence efficiency as a thermometer to measure the lattice temperature rise during the interaction with intense

532 nm laser pulses. This method is new, and data interpretation requires knowledge of the mechanism of charge carrier generation.

2. The STERL Method

Self-trapped exciton recombination luminescence is intrinsic to alkali halides. It results from electron-hole (e-h) pair generation (via various excitation processes) and their subsequent radiative recombination. The luminescence yield of self-trapped excitons (STE's) is determined by the formation efficiency of STE's, i.e., the probability to form an STE per e-h pair, and the probability for their radiative decay. The latter depends strongly on lattice temperature.

In most alkali halides, the radiative-decay efficiency of STE's, or the STE luminescence efficiency, obeys the relation

$$\eta = \frac{1}{1 + A \exp(-E/kT)}, \tag{1}$$

where E is the activation energy and T the lattice temperature. At low temperatures (below a critical temperature determined by the activation energy E) this efficiency is nearly unity and decreases rapidly with increasing T. The STERL method described below utilizes this property of STE's to measure the lattice temperature rise resulting from the interaction of a KBr crystal with intense laser pulses at 532 nm.

The technique requires that the initial temperature of a KBr crystal be below the onset of thermal quenching of STE luminescence. By exposing the crystal to intense 532 nm laser pulses, one can generate STE luminescence in the material via four-photon absorption [4]. If the temperature rise resulting from the interaction is not sufficient to affect the luminous efficiency, the dependence of the luminescence yield on photon flux will be of order four. This has been demonstrated by Shen et al. [4] in their measurement of the four-photon absorption cross section in the same material.

However, when the resulting temperature exceeds the onset of thermal quenching, this dependence will decrease according to $\eta(T)$. In principle, one can obtain directly the temperature rise from the luminescence versus photon flux measurement if one knows $\eta(T)$. However, due to the fact that the incident flux has Gaussian spatial and temporal distributions and thermal quenching does not occur uniformly in the crystal, the procedure of extracting the temperature in the interaction volume becomes much more complicated. Care must be taken in interpreting the data.

In the absence of thermal quenching, the spatial distribution of laser-induced STE luminescence is proportional to the fourth power of the flux distribution, $F^4(r)$, because the primary excitation process here is four-photon absorption. Any rise in temperature is due to the interaction of laser-generated charge carriers with the photon field; its spatial distribution is proportional to $F^4(r)$ as well. When thermal quenching takes place, it first occurs at the center of the interaction volume because there the temperature is highest. Increasing the laser flux enlarges the volume that undergoes thermal quenching as well as the peripheral area that emits luminescence photons. As a result, the detected spatially- and temporally-integrated luminescence still increases as photon flux increases even though the emission from the central region is quenched; but its dependence will be less than fourth order.

Knowing how the luminescence distribution changes with photon flux, one can determine the temperature rise from the log-log plot of the luminescence versus photon flux. The point on the curve at which the slope deviates from four indicates that the peak temperature in the interaction volume reaches the onset of thermal quenching. Thus, temperature calibration can be achieved (because its dependence on photon flux remains unchanged). The above analysis provides a direct temperature reading at each flux.

However, it can not identify which heating mechanism is responsible for the temperature rise because it does not require knowledge of laser-generated charge carrier density as a function of photon flux.

Computer simulation allows us to determine both the temperature and lattice heating mechanism at the same time. This is possible because in KBr at 532 nm the four-photon absorption cross section is known [4]. Thus, we can simulate the detected luminescence yield at different laser fluxes for a given heating mechanism and compare it with the experiment. By repeating this with different heating mechanisms, we can identify which theory is capable of describing the experimental results. Once it is determined, the temperature in the interaction volume for any photon flux can be calculated. The details of the analysis are described in section 5.

3. Experimental Details

3.1 Experimental Arrangement

The laser system used in our measurements is a Quantronix model 116 Q-switched and mode-locked Nd:YAG laser with a double pass amplifier. A single mode-locked pulse is selected by a pulse selector and converted to 532 nm by a second harmonic generator. The 532 nm laser pulse is focused into a KBr crystal mounted on a cold finger in a closed-cycle refrigerated optical cryostat operated at 50 K (fig. 1). A uv-grade optical fiber of 1 mm diameter is used to collect the induced STE luminescence in the interaction volume and guides it to an optical multichannel analyzer for detection. In the experiments, we monitor only the σ component of the STE luminescence for the same reason discussed in [4].

The samples are reactive-atmosphere-processed (to reduce the concentration of OH^-) ultrapure KBr single crystals obtained from the University of Utah. The size is approximately 4 x 4 x 25 mm^3. The front and the back surfaces of the samples are cleaved and the reflection loss per surface is measured to be approximately 5% at 532 nm. The sample can be moved in the direction perpendicular to the beam axis and that of the fiber so that different interaction sites can be chosen without affecting the collection efficiency of the fiber. Data are taken by exposing a virgin site to a single laser pulse. This is achieved by moving the sample between pulses.

3.2 Experimental Procedures

Experiments are carried out by carefully monitoring the σ component of the STE luminescence emitted from the interaction volume as a function of the incident photon flux. Measurements start from relatively low fluxes, where temperature increase is negligible, to the highest flux just prior to any indication of catastrophic damage.

In order to obtain the temperature in the interaction volume from the σ luminescence yield versus photon flux relation, careful measurement of the luminous efficiency as a function of lattice temperature is required. This is done as follows:

We use 266 nm (the fourth harmonic of Nd:YAG wavelength) laser pulses to produce the σ luminescence in KBr at different sample temperatures and measure its yields for a fixed photon flux. The measurement begins at 50 K, and the higher temperatures are obtained by switching off the refrigerator and letting the sample slowly warm up. Using 266 nm laser pulses precludes any temperature rise introduced by the laser-matter interaction, because this process is very efficient for the production of STE's (by two-photon absorption) but less efficient for energy deposition. Therefore, the measurement will reflect more closely the intrinsic efficiency of the σ luminescence.

The measured σ luminescence efficiency as a function of lattice temperature is given in figure 2. Here the dots are the experimental data obtained with single-pulse excitation and the solid line is the fit to eq (1) with $A = 3.8 \times 10^9$ and $E = 0.124$ eV. The results show that thermal quenching occurs above 60 K.

Damage is determined on the basis of two criteria: a) onset of a broad band emission in addition to the σ luminescence and b) the first detectable spatial distortion of the transmitted laser beam. The latter is monitored by looking at the far field pattern of the laser beam emerging from the sample. Any data taken with either effect present are considered to be due to damage.

The second criterion also provides information about imperfections of the sample surfaces. Since our measurements are carried out at different sample sites, variations of surface quality would introduce, e.g., via beam scattering on non-smooth surface areas, a large variation in the experimental results because of the highly nonlinear processes. Thus, any exposure to a laser pulse yielding a detectable beam distortion is considered to be due to roughness of either the front or back surface of the sample, or bulk damage. We judge whether damage is intrinsic or extrinsic based on the photon flux at which it occurs.

The origin of the broad background emission is unknown, but it is associated with some form of irreversible modification of the material. We will demonstrate below that the experimental data obtained, using this criterion, along with that of beam deformation, show that single-pulse damage occurs at a temperature very close to the melting point of the material.

We also inspected our samples under a microscope after the measurements using crossed polarizers and did not observe any visual damage of the material, such as crack and bubble formation. Therefore, all the results presented here are considered to be prebreakdown data.

The spatial profile of the laser pulses in the sample is obtained by measuring the beam cross section at the focusing-lens position with the slit-scanning technique and applying diffraction-limited optics. A typical spot radius (at 1/e intensity) at the focal plane is around 5×10^{-4} cm. The pulse length is 100 ps half width at 1/e intensity, measured with the second harmonic generation autocorrelation method. In order to simulate the experimental results for data analysis, we have to know precisely the collection efficiency of the fiber. The method to determine it has been described in [4].

3.3 Experimental Results

The measured total σ luminescence yield versus peak photon flux is plotted on a log-log scale in figure 3. At peak fluxes below 2.2×10^{29} photons/cm^{2}sec, the slope of the curves is approximately four, as was demonstrated in [4]. Thus, it confirms that the primary electron-hole pair generation process here is indeed four-photon absorption by valence electrons. Furthermore, it shows that the temperature rise resulting from the interaction with the laser pulses is not sufficient to affect the luminous efficiency because, otherwise, the dependence would be smaller. In this flux region, the four-photon absorption cross section is measured to be 2×10^{-112} cm^{8}sec^3 [4].

When the peak flux is above 2.2×10^{29} photons/cm^{2}sec, strong interaction with the photon field causes the lattice temperature to be higher than the onset of thermal quenching. As a result, the dependence of the σ luminescence yield on photon flux decreases; it becomes weaker as the flux becomes higher (see figure 3). Here the last data point corresponds to the highest non-damaging flux obtained in the experiments. As will be shown later, the peak temperature at this flux turns out to be very close to the melting point of the material, i.e., 1007 K.

4. Lattice Heating Theories

The data presented in the previous section show a clear temperature rise resulting from the interaction with the 532 nm laser pulses. The question of what heating mechanism is responsible for it needs to be answered. As we stated earlier, comparison with the available heating theories is our approach to the problem.

We consider two heating theories that have been proposed in the literature to describe the interaction of optical materials with laser pulses. They are the polaron heating mechanism [5]

$$c\rho \frac{dT}{dt} = (4\hbar\omega - E_g)N\sigma^{(4)}F^4 + \hbar\omega\sigma_p n_c F + W, \tag{2}$$

and the free carrier heating mechanism [2,3]

$$c\rho \frac{dT}{dt} = 1.09 \left(\frac{m^*kT}{2\pi}\right)^{\frac{1}{2}} \frac{n_c}{l_{ac} v_s} \left(\frac{eE}{m^*\omega}\right)^3 + W. \tag{3}$$

Here c is the specific heat, ρ the mass density, ω the laser frequency, n_c the conduction electron density, σ_p the polaron absorption cross section, F the photon flux, E_g the band gap, N the density of active atoms (i.e., Br^- ions in our case), $\sigma^{(4)}$ the four-photon absorption cross section, l_{ac} the mean free path of conduction electrons, v_s the longitudinal sound velocity, m^* the band mass of electrons, T the lattice temperature, E the instantaneous amplitude of the electric field, e the electron charge, k the Boltzmann constant and W consists of other possible contributions to the lattice heating, such as those from laser-generated primary defect formation, ionization and relaxation as well as direct recombination of charge carriers described in detail in [6].

These heating mechanisms were proposed in the 1970's, but it had not been proven which of them is appropriate to describe the interaction of any optical material with visible laser pulses. One of the important results of the present work is that it allows us to discriminate between them. We will discuss it in the following section.

5. Model Calculations

A detailed model describing the interaction of KBr with intense 532 nm laser pulses at 50 K has been provided by Shen et al. [4]. The calculation performed below is based on this model with some modifications. First, the temperature dependence of all the parameters has to be considered since the calculation is extended to higher temperature (up to 1007 K). Second, certain processes, such as diffusion of charge carriers and defects, which were not important at low temperature, have to be re-examined.

The calculation relies on the σ luminescence efficiency. This parameter has been carefully measured at different temperatures (see section 3). The efficiency of the π luminescence has a complicated dependence on temperature. However, it is not critical since we compute only the σ luminescence yield. We use an approximation in which we assume that the π luminescence efficiency also follows eq (1) with $A = 1.5 \times 10^{10}$ and $E = 0.126$ eV [6].

We choose the Huybrechts-Devreese expression [7] for the polaron absorption cross section:

$$\sigma_p \approx \left(\frac{4\pi e^2}{n c_l m^* \omega_o}\right) \left(\frac{2\alpha}{3}\right) \left(\frac{\omega_o}{\omega}\right)^{5/2} \left(1 + \frac{2}{\exp(\hbar\omega_o/kT) - 1}\right) . \qquad (4)$$

Here ω_o is the optical phonon frequency, m^* the band mass, α the polaron coupling constant, ω the laser frequency, n the refractive index, c_l the speed of light, and T the lattice temperature. This expression is valid for all temperatures and values of the coupling constant under the condition of $\omega/\omega_o >> 1$.

The lifetimes of STE's are chosen to be constant and their values at 50 K are used in the calculation. The error introduced with this approximation is estimated to be very small because the σ luminescence occurs only in a narrow temperature range from 50 to 60 K, in which the lifetimes do not change significantly. The temperature dependent specific heat is taken from the Debye theory with Debye temperature of 173 K.

Epifanov [3] calculated the electron diffusion in NaCl (with optical and thermal properties similar to KBr) exposed to 532 nm laser pulses and found its coefficient to be approximately 30 cm^2/sec. We estimated, using this value, the electron diffusion in KBr and found it to be negligible under our experimental conditions (the spot radius, $\omega_o \approx 5 \times 10^{-4}$ cm, and the pulse length, $\tau = 10^{-10}$ sec) [6]. Similar conclusions can be derived for the diffusion of V_k centers and STE's using the results reported by Tanimura and Itoh [8].

Jones et al. [9] have estimated the thermal diffusion in NaCl exposed to 80 ps laser pulses at 532 nm with a spatial profile of $\omega_o \approx 5 \times 10^{-4}$ cm and concluded that it is also a very weak effect.

We do not consider the formation of stable defects, such as F centers. Energy loss due to this is negligible compared to the total energy gained by the lattice [6].

For computational convenience, we express the laser pulse as $F(r,t) = F(r)\exp(-(t - \sqrt{5}\tau)^2/\tau^2)$ with the focal point being at $r = 0$. The calculation starts at $t = 0$ and is stopped when the σ luminescence emission and temperature rise are completed.

The calculated results of the total σ luminescence versus peak incident photon flux, $F_p = F(0, \sqrt{5}\tau)$, are plotted in figure 4 along with the experimental data. Here the dashed line is obtained with the polaron heating theory, while the solid line is free carrier heating. The vertical axis is the total number of photons collected by the optical fiber. The experimental results are normalized by fitting those below $F_p = 2.2 \times 10^{29}$ photons cm^2sec to the calculated curves, because in this region the temperature effect does not influence the dependence on photon flux in either theory, and the experimental results should follow the predictions of both theories.

The comparison in figure 4 clearly shows that the free carrier heating theory readily accounts for the experimental results, while the polaron theory does not. To ensure that the polaron heating theory indeed fails to explain the temperature rise observed here, we repeated the computation with a σ_p value up to two orders of magnitude larger. The polaron heating is still too inefficient to account for the thermal quenching occurring at 2.2×10^{29} photons/cm^2sec. The calculation of the σ luminescence yield versus photon flux is stopped when the peak temperature reaches the melting point. In the entire flux region, the agreement between the experimental results and the prediction of the free carrier heating theory is very satisfactory.

The above calculations are based on the assumption that the primary charge carrier generation process up to damage is four-photon absorption. This is clear at lower photon fluxes (below 2.2 x 10^{29} photons/cm^{2}sec), but whether it is still so at higher fluxes requires some analysis.

According to the calculation, the last data point corresponds to a peak temperature of 918 K, which provides a lower limit because any other conceivable process, e.g., avalanche ionization, would result in a higher temperature. On the other hand, we did not observe any catastrophic damage of the material up to this flux, which ensures that the temperature in the interaction volume has to be below the melting point. Thus, if any other contribution to the lattice heating, such as avalanche formation, were present, it would have to be less than 89 K. We can conclude, therefore, that the energy deposition process in the case of KBr exposed to 532 nm laser pulses up to melting is dominated by four-photon generated free carrier heating.

The above finding is very important. It is the first experimental evidence that the melting point can be indeed reached via four-photon absorption without electron avalanche. We take this and the fact that the measured prebreakdown phenomena can be explained by the theory described above as direct evidence that the interaction of intense 532 nm laser pulses with KBr is intrinsic in nature and not influenced by crystal imperfections or impurities.

With the experimental evidence that free carrier heating is the appropriate mechanism for energy deposition in the interaction of 532 nm laser pulses with KBr, the peak temperature rise versus laser flux relation can now be calculated with confidence and is shown in figure 5. The dependence of the peak temperature on photon flux is approximately fourth order as expected.

The uncertainty of the calculated temperature can be estimated from figure 4, where the luminescence serves as a thermometer and the fit to the experimental results is the calibration. The calculation of the temperature is based on this fit. Thus, estimating the uncertainty in temperature reduces to estimating the uncertainty in data fitting. The latter can be done by varying the adjustable parameters (e.g., l_{ac}, v_s or m*) in eq (3) or, equivalently, moving the solid curve in figure 4 along the dashed line in either direction, and examining the maximum allowable deviation from the calculation, $\Delta(\log F_p)$, which still provides a reasonable fit. By determining $\Delta(\log F_p)$, we can calculate the uncertainty in temperature from figure 5. Our results show that at the last data point, which corresponds to a temperature of 918 K, the uncertainty is less than 30%.

Our calculation shows that heating of four-photon generated free carriers [the first term in eq (3)] dominates the energy deposition in the case of KBr, contributing 93.3% of the heat to the lattice at F_p = 6.3 x 10^{29} photons/cm^{2}sec. Only 6.7% of the heat stems from direct charge carrier recombination and laser-generated defect absorption and relaxation, less than one tenth of which results from relaxation and ionization of STE's. The main contribution of W to lattice heating is due to V_k center ionization and subsequent reformation.

The time-integrated σ luminescence and temperature distributions, immediately after a laser pulse has passed through the interaction volume for a typical spatial pulse profile, are given in figures 6 and 7. At flux below 2.2 x 10^{29} photons/cm^{2}sec (fig. 6), the temperature rise is too small to influence the STE luminescence efficiency, and the temperature and luminescence distributions have approximately the same shape, namely the fourth power of the laser flux distribution. When the laser photon flux exceeds this value, however, the temperature at the center of the interaction volume rises above the onset of thermal quenching (60 K). Thus, in this region the σ luminescence yield is reduced, resulting in a distribution whose shape differs from that of the temperature distribution. An example is shown in figure 7 for a laser peak flux F_p = 6.3 x 10^{29} photons/cm^{2}sec. Here the total σ luminescence yield is determined by the regions of the spatial distribution where the flux level is below 2.2 x 10^{29} photons/cm^{2}sec. The regions with higher fluxes undergo thermal quenching, resulting in the distribution shown in figure 7(b). The fraction of the volume in which the luminescence is quenched increases as the peak flux of the pulse increases, until the peak temperature reaches the melting point. Then catastrophic damage of the material occurs.

6. Conclusions

We have demonstrated, using the STERL method, that the primary interaction process in KBr exposed to intense 532 nm laser pulses is governed by four-photon free-carrier generation and subsequent photon absorption by the free carriers with small contributions from laser-generated primary defect formation, ionization and recombination as well as direct charge carrier recombination. The lattice heating process is shown to occur according to the heating mechanism proposed by Epifanov [3]. The highest temperature reached in the interaction volume via four-photon generated free-carrier absorption just prior to any indication of catastrophic damage of the material is about 90 K below the melting point, which demonstrates that melting is indeed indicated as a failure mode of the optical material.

Our experiments show that the STERL method is a promising tool for the investigation of high-order nonlinear interaction processes in alkali halides. It allows one to study both the primary free carrier generation and the energy deposition processes in these materials as a consequence of nonlinear interaction with intense photon fields. Therefore, it should be useful in future work on optical damage. However, some peculiarities among the alkali halides, such as the absorption bands of the STE's, may interfere with its application, since it may be possible to bleach the STE luminescence with laser photons. A careful matching of laser wavelength with the particular material of interest is called for.

We would like to thank Mr. Tom Casper for his valuable assistance. This work was supported by the U.S. Air Force Office of Scientific Research under Grant No. AFOSR-87-0081.

7. References

[1] A. A. Manenkov, *Laser-Induced Damage in Optical Materials*, Natl. Bur. Stand. (U.S.) Spec. Publ. No. 509, edited by A. J. Glass and A. H. Guenther (U.S. GPO, Washington, D.C., 1978), p. 455.

[2] Scott C. Jones, X. A. Shen, P. Braunlich, P. Kelly, and A. S. Epifanov, Proc. 18th Boulder Damage Symposium (1986), to be published.

[3] A. S. Epifanov, Zh. Eksp. Teor. Fiz. **67**, 1805 (1974) [Sov. Phys. JETP **40**, 897 (1975)].

[4] X. A. Shen, Scott C. Jones, P. Braunlich, and P. Kelly, Phys. Rev. B**36**, 2831 (1987).

[5] A. Schmid, P. Kelly, and P. Braunlich, Phys. Rev. B**16**, 4569 (1977).

[6] X. A. Shen, Ph.D. dissertation, Washington State University, Pullman, WA, 1987.

[7] W. Huybrechts and J. Devreese, in *Elementary Excitations in Solids, Molecules and Atoms*, Vol. **B**, edited by J. Devreese, A. B. Kunz, and T. C. Collins (Plenum, New York, 1974).

[8] K. Tanimura and N. Itoh, J. Phys. Chem. Solids **42**, 901 (1981).

[9] Scott C. Jones, A. H. Fischer, Peter Braunlich, and Paul Kelly, Phys. Rev. B (Jan. 15, 1988).

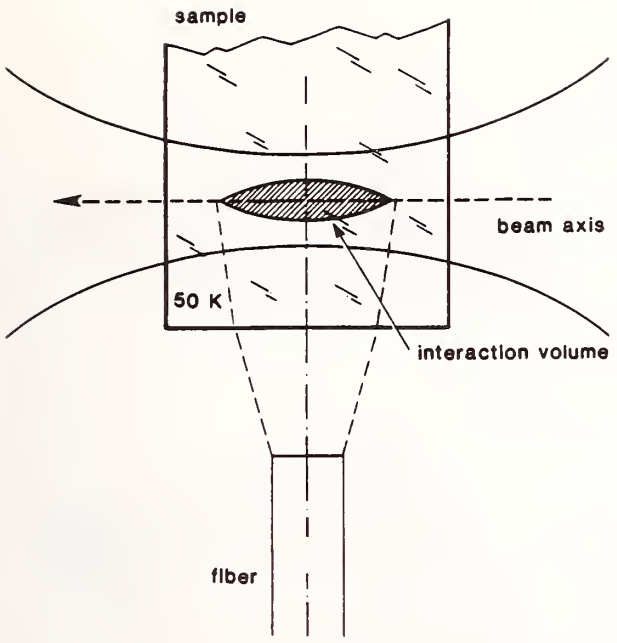

Figure 1. Experimental arrangement of the fiber with respect to the sample and the laser beam axis. The focal point of the incident laser pulses is located on the axis of the fiber. The sample can be moved in the direction perpendicular to the figure.

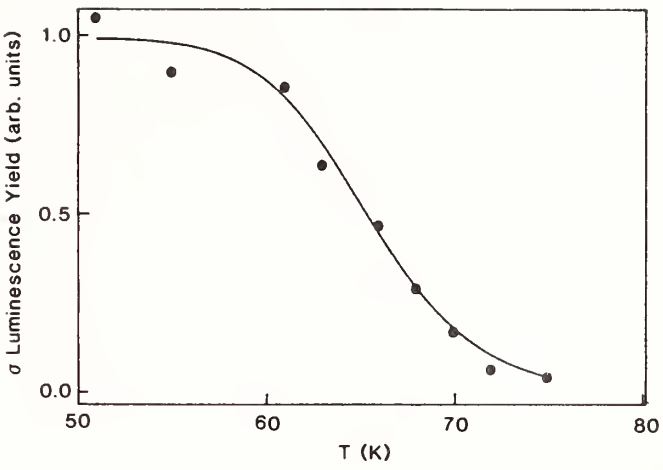

Figure 2. The σ luminescence efficiency versus temperature in KBr obtained with single 266 nm laser pulse excitation. The solid line is the fit to eq (1).

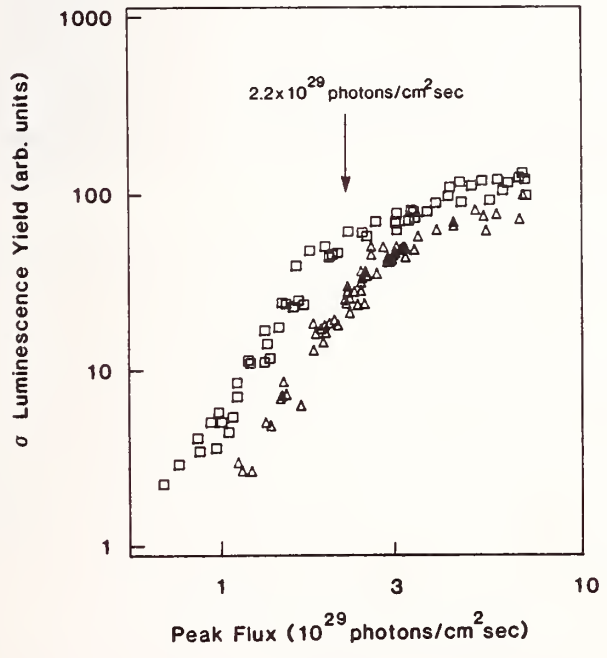

Figure 3. Total σ luminescence yield as a function of incident photon flux. The two sets of data (squares and triangles) are obtained from two separate measurements. Both exhibit a sudden decrease of slope at a flux of approximately 2.2×10^{29} photons/cm^{2}sec.

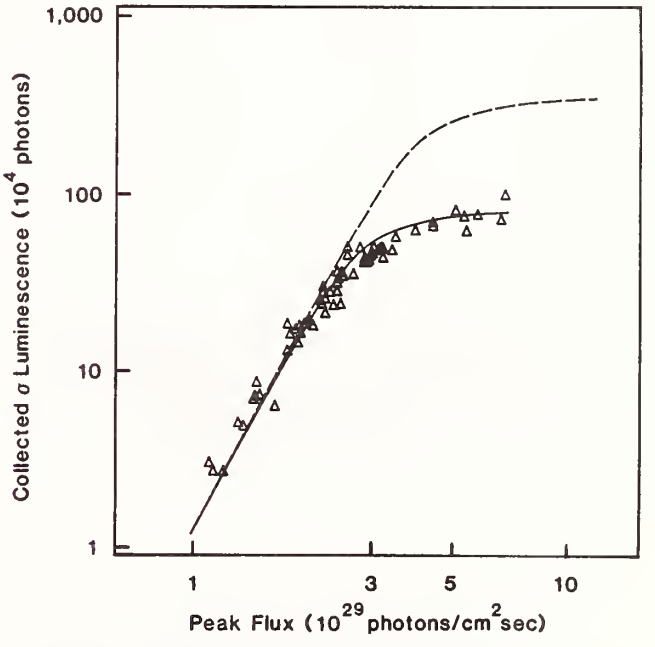

Figure 4. Calculated (solid and dashed lines) and measured (Δ) spatially- and temporally- integrated σ luminescence emission from KBr as a function of the peak photon flux in 532 nm laser pulses of 100 ps duration (1/e intensity halfwidth). The solid line is obtained using the free carrier heating model, while the dashed line is based on the polaron heating model.

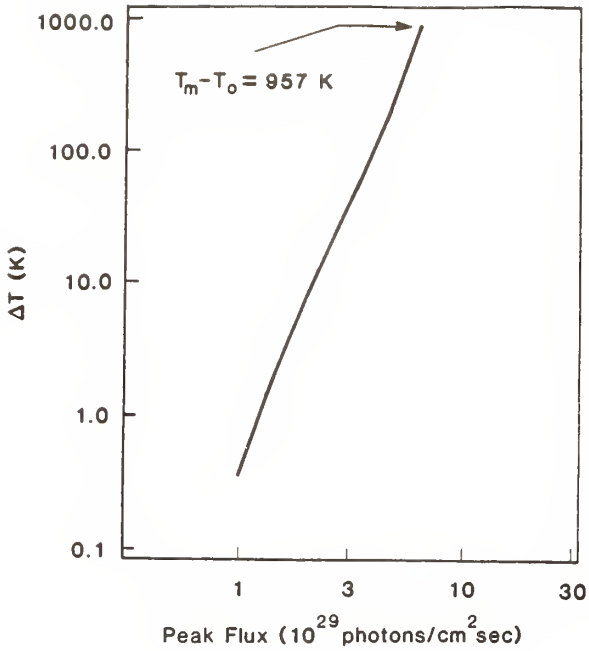

Figure 5. Calculated peak temperature rise as a function of photon flux in the interaction volume of KBr exposed to single 532 nm pulses of 100 ps 1/e halfwidth. Here T_m and T_o are the melting and initial temperatures, respectively. The slope of the curve is approximately four.

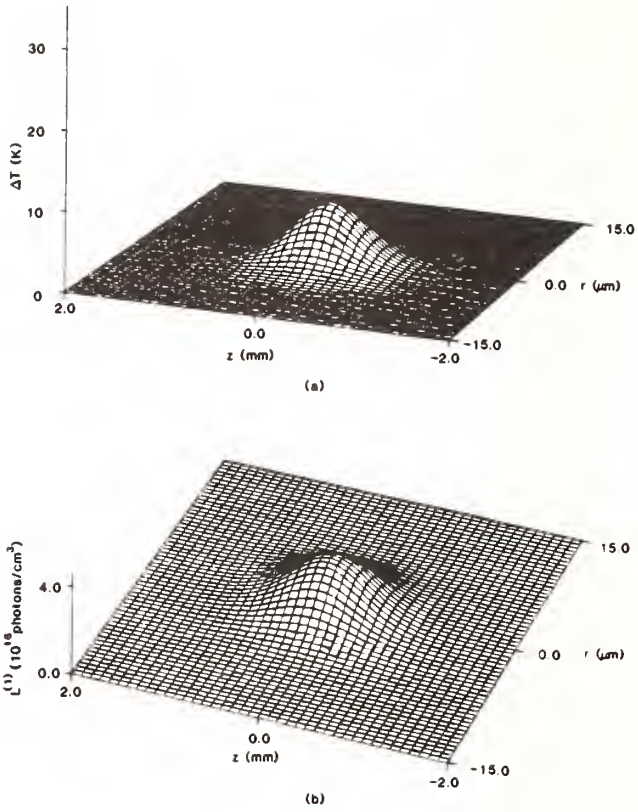

Figure 6. Temperature (a) and spatially resolved time integrated σ luminescence (b) distributions in KBr immediately after exposure to a single 532 nm pulse of peak flux 2.0 x 10^{29} photons/cm^{2}sec. The beam axis is the z axis and r is the radius in cylindrical coordinates from the optical axis. The geometrical focal point is (r,z) = (0,0). Note different scales of axes.

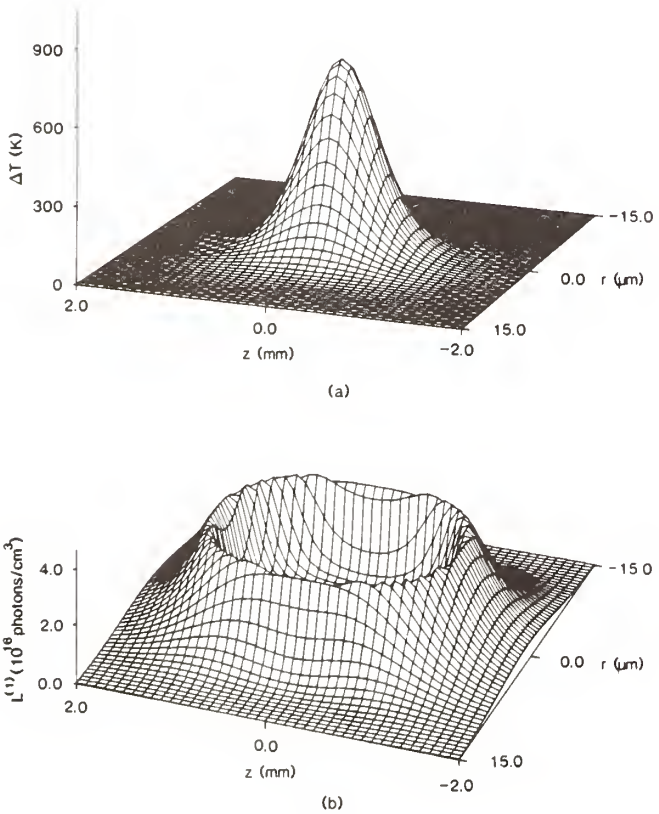

Figure 7. Same as figure 6 but with a peak flux of 6.3 x 10^{29} photons/cm^{2}sec.

The author reported a defect whose luminescence quenches at 60 K to 70 K and yet he inferred temperatures of some 900 K. Can he see luminescence down by a factor of e-10 or so from the peak luminescence? How can he be sure that he is not instead seeing the variation in temperature within the sample and only see the luminescence from the cool regions? The author replied that he measured luminescence versus flux. Luminescence versus temperature is known. In principle then one can deduce the dependence of temperature on flux. It is true that the luminescence starts to quench above 60 K. By very carefully mapping out the interaction volume and knowing that the primary process is a 4 photon process he can map out the 4 photon interaction volume, which is a Gaussian. We are looking here at time and spatially integrated luminescence yields. They stem from a luminescence emission volume which had that curious Mt. St. Helen dip in the middle. Knowing precisely the flux distribution he can calculate the peak temperature. However, he measures in effect only luminescence contributions from the fringes of the pulse in regions where the temperature has not yet increased to way above 60 K. He infers the peak temperature by knowing precisely the previously carefully measured shape of the interaction volume. That is all he has to do.

Another questioner asked: Since the author has high intensities and can create defect centers in materials like alkali halides at such high intensities by multiphoton-processes, has he considered the possibility that at higher intensities he is creating such centers and he has alternate paths for electron recombinations other than back down to the valence band? How would that effect the author's interpretation of the temperature rise? Also, he showed a temperature rise of 918 K, which is three significant figures. What are the error bars for that measurement? The author replied that the high temperature reported is based on the theory, not on a direct measurement. They prove that the experimentally observed photon flux dependence can be explained by the theory. If we have confidence in the theory, we can calculate the temperature. The questioner pointed out that although it is a theoretical calculation it is based on their measurements. Did they have any idea how good their extrapolated value was; could it be 500 K instead of 916 K? The author replied that the value could be higher than 916 K, but they saw no melting so it had to be less than the melting point. The calculated temperature was not based on a particular damage or interaction model. It was simply based on knowing that the basic mechanism is 4 photon absorption which is determined from the log-log slope of the effect versus photon flux diagram and on precise diagnostics of the laser beam profile. There is nothing in the temperature determination which biases in favor or against any of the many controversial intrinsic damage mechanisms. The accuracy of the temperature determination is a good question and is a bit hard to answer. You can only infer that from the accuracy of the luminescence yield measurements. It should be good within at least 20%, if not better. It is not off by 50%.

Another questioner pointed out that the optical properties of the alkali halides and especially KBr are notorious for their temperature cycling and impurity content. Where did the material tested come from, what are the impurities and how has he been able to rule out any impurity effects in the experiment? The author replied that the material came from the University of Utah and is a reactive atmosphere processed ultra-pure crystal. He did not know exactly what the impurity content was. He was asked how he could rule out that the effects he was observing were impurity effects and not intrinsic effects. He replied that they have come to the conclusion that impurities play a role only if their concentration reaches the concentration of free carriers at damage, which is about 10^{18}/cc.

Impurity concentrations of less than 1 ppm would not affect energy deposition whatsoever. The author claimed that several years back they had introduced the worries about primary defects which are a direct consequence of electron-hole pair formation. The sequence goes within 10-13 sec. Vk centers or self trapped excitons-self trapped hole formation traps free electrons. One effect of that recombination is the self trapped exciton luminescence, which is an intrinsic phenomena which was used here. One other effect of recombination is F center formation, and we have worried about that as well, and have studied F center formation directly. Unless you have repeated pulses and accumulate F centers in the 10+18 range jor you color your crystal with megarads and turn it completely opaque, they do not influence the single shot damage threshold. Unless they reach these high concentrations they can only contribute as many electrons to the available free carriers, which heat according to the Fanos mechanism, one electron per F center. Therefore you have a large number of defect centers. The model calculations take all of these primary defects and their various interaction mechanisms and recombination mechanisms during and after the laser pulse into account.

Manuscript Received 12/21/87/sar

The Discovery of Laser-Induced Intrinsic Optical Damage in Wide-Gap Materials at Visible Wavelength

Peter Braunlich, Scott C. Jones, X. A. Shen, and R. Thomas Casper
Department of Physics, Washington State University
Pullman, WA 99164-2814

Paul Kelly
Division of Physics, National Research Council
Ottawa, Ontario, Canada K1A OR6

After two decades of research, the question "What is the nature of intrinsic breakdown of wide-gap optical materials exposed to short laser pulses at visible wavelength?" has recently been answered unambiguously for two cases: 532 nm, picosecond pulses tightly focused in NaCl and KBr. This remarkable achievement warrants some reflection on its impact on the field of high laser power optical materials.

Clearly, the problem of extrinsic damage to coatings and surfaces remains unsolved and formidable, and the quest for higher damage thresholds will continue without any realistic hope to achieve intrinsic behavior in the foreseeable future. However, such pessimistic realism is no longer justified for bulk breakdown, because the possibility of fabricating intrinsic high-power optical materials—not just alkali halides, but also technologically important alkaline earth halides and metal oxides—must now be taken seriously.

In light of this new development we will re-examine the results of some classic damage experiments and the conclusions on the laser damage mechanisms that were based on erroneous assumptions of intrinsic material behavior. Extrinsic damage, presumed to be intrinsic for the purpose of data interpretation, will always appear to be avalanche formation via electron impact ionization if only damage thresholds are measured.

With this in mind, we will look again at self-focusing and defocusing effects, the traditional exclusive reliance on subjectively defined damage criteria and, thus, uncertain thresholds, and the role of primary laser-generated photo-chemical defects in the historical "workhorse" materials, the alkali halides.

Key Words: avalanche ionization; beam self-deformation; free electron heating; intrinsic laser damage; multiphoton absorption; prebreakdown absorption

1. Introduction

This paper does not present any new data on laser-induced damage of optical materials. Instead, it focuses on intrinsic bulk damage and the evolution of our present understanding of this complex nonlinear phenomenon. The purpose is to confront the reader with discrepancies between the recent unambiguous demonstration of intrinsic high-order multiphoton bulk damage in a wide-gap optical material [1-5] and the deeply ingrained and widely held current consensus that "such failure is due to avalanche breakdown initiated by multiphoton absorption associated with defects within the band gap." [6]

In the case of NaCl and KBr, exposed to 100 ps pulses at 532 nm, new experimental evidence [1-5] clashes head-on with this traditional view: It provides proof that a high-order multiphoton absorption process generates free carriers, and avalanche formation is negligible up to photon fluxes which cause the temperature in the interaction volume to soar close to the melting point.

Over the years there has been much fruitless and prejudiced debate on the relative merits of two theories of laser-induced damage, the avalanche and the multiphoton mechanisms. Both have their regime of applicability, which is often characterized by the order m of the multiphoton process required for the generation of conduction electrons. The argument is, however, not simply over the order m at which

avalanche formation becomes dominant. The cardinal problem is to establish, for a given experimental situation, what the detailed microscopic processes are that take place during the interaction of an intense laser pulse with an optical solid.

But why worry about or study intrinsic laser-induced bulk damage when it is obvious that the Achilles' heel of any high power laser system are optical surfaces and dielectric coatings? The answer is simple, albeit perhaps not obvious or acceptable to those struggling with the problem of producing damage resistant coatings:

> The fundamental interaction processes between the high-power laser photon field and the transparent solid are revealed by such studies, and the intrinsic damage thresholds are determined which then can serve as benchmarks for any configuration of optical materials, including free and coated surfaces, both of which are beset by structural imperfections and contaminants. Only after the complex microscopic processes leading to laser-induced intrinsic bulk damage are clearly understood can one hope to unravel the role of complicating factors associated with, e.g., laser-induced embrittlement in multi-shot damage [7-9], laser-caused photochemical surface reactions [10-14] and, eventually, adhesion, thermal mismatch and crystallinity of dielectric coatings.

To underscore this sweeping and general answer to the above question, we begin with a retrospective examination of our present view of the fundamental mechanisms of intrinsic laser damage and, thereafter, discuss two specific examples for damage phenomena whose physical nature could only be exposed because, in these cases, the basic photon-solid interaction processes were understood in detail.

2. Review

With the publication in 1978 of the review "Laser-Induced Breakdown in Optical Materials" by W. Lee Smith the classic and most active research period on the fundamental damage mechanism came to an end with the conclusion that the "experimental findings (are) mutually consistent with the notion of the avalanche model" for wide-gap solids and wavelengths $\lambda \geq 355$ nm [15].

All experiments reviewed by Smith concerned the measurement of subjective and, as became obvious only later, predominantly extrinsic damage thresholds, as a function of laser beam and material parameters. These were compared with a simple avalanche model advocated by Yablonovitch and Bloembergen [16] which is based on semi-empirical avalanche ionization coefficients (taken from dc breakdown data) and the Drude theory of ac conductivity. A much more rigorous theory of avalanche ionization published in 1975 by Epifanov [17,18] was not mentioned.

Smith also summarized the knowledge accumulated at that time of multiphoton absorption in transparent ionic solids as a mechanism for laser-induced damage. He concluded that only processes with multiphoton order $m < 3$ dominate the otherwise prevailing avalanche mechanism, and he dismisses the validity of the so-called multiphoton-polaron theory by Schmid et al. [19]. These authors included photon absorption by multiphoton-generated polarons (free carriers of low kinetic energy in ionic solids) as a process for energy deposition into the crystal lattice in addition to multiphoton absorption. Smith stated that the "model proposed by Schmid et al., which depends crucially on high-order MPI (multiphoton ionization), will be precluded from experimental observation by avalanche breakdown." [15]

The confidence expressed in Smith's review that the fundamental intrinsic optical damage mechanism had been discovered and only details need be filled in was, however, neither justified nor did this happy state of affairs last very long. Since 1980, mainly on the basis of careful work by Van Stryland, Soileau, and coworkers [20-22], cautious criticism can be found in the literature that the avalanche mechanism of laser-induced damage as reviewed by Smith [15] may after all not be valid for each wide-gap optical solid exposed to short laser pulses at visible wavelengths (cases: $m > 2$). Van Stryland et al. studied, among other phenomena, the dependence of the damage threshold on the size of the interaction volume in NaCl. Finding agreement of their results with neither the multiphoton nor the avalanche intrinsic damage models, they concluded: "It has been clearly established that, with the exception of a small number of specimens tested by Manenkov, the laser-induced breakdown fields are not intrinsic." [20] In other words, none of the data

published up to 1980 appears to pertain to intrinsic damage events with the likely exception of the results obtained by Manenkov and coworkers in a number of alkali halides at 532 nm [23], which Smith did not include in his review.

The inescapable consequence of these startling findings is that, since comparison of *extrinsic* damage thresholds with any theory of *intrinsic* laser-induced breakdown is impossible, Smith's 1978 assessment of the damage mechanism, in spite of its popularity to this date, must be viewed with extreme caution. His premature dismissal of high-order multiphoton processes serves as an example that erroneous conclusions may easily be drawn from experiments that depend solely on the measurement of damage thresholds in the absence of sufficient proof that the material under study is indeed intrinsic. The inability to measure third or higher order multiphoton absorption in extrinsic materials is not surprising to anyone who has ever attempted such a difficult experiment. Neither is the natural tendency a surprise to interpret the sudden explosive breakdown event in an *extrinsic* optical material above a threshold photon flux as avalanche formation, because such behavior, occurring without any advance warning, is precisely what one would expect from the theory of *intrinsic* avalanche damage [15,24].

The suspicion, that the pre-1980 work on laser-induced damage is apparently based on the erroneous assumption that the studied crystals were intrinsic in nature, had another consequence. The customary correction for presumed self-focusing effects in determining damage thresholds now turns out to be invalid on this basis. According to Zverev and Pashkov [25], the laser power at breakdown and the critical power of self-focusing can be determined by measuring the breakdown power density as a function of the laser spot size. Not only is the validity of this method predicated on intrinsic damage behavior, but, as Van Stryland and Soileau have shown [21,22] and Jones has confirmed recently [1,5], it simply does not work with data obtained from a number of "workhorse" materials such as quartz and intrinsic sodium chloride. In addition, recently measured values for the critical power of self-focusing in NaCl are much higher and, as a consequence, the nonlinear refractive index n_2 for these materials (and most likely that of other ionic optical solids) is considerably smaller than the values given in Ref. 15.

Similarly, studies of self-defocusing of Gaussian beams tightly focused in NaCl must also be revised. In their calculations, Kelly et al. [26] assumed polaron absorption as the process by which energy from the laser beam is deposited into the interaction volume. However, Shen et al. demonstrated recently [3,4,27] that in alkali halides polaron absorption is much weaker than free carrier absorption by the Epifanov mechanism [17] and, therefore, the reduction in refractive index due to free carriers and the resulting self-defocusing effects are much smaller than those calculated in Ref. [26].

For alkali halides and wavelengths in the visible it appears safe to neglect beam self-deformation because the free carrier density at breakdown is smaller than previously expected ($<10^{19}$ cm^{-3}) and as long as the focal spot radius (HW at 1/e square) of a laser beam tightly focused inside the crystal is less than 15 μm. We hasten to point out, however, that these are not general findings but pertain only to alkali halides and similar ionic wide-gap solids. Laser pulses tightly focused into other materials must be carefully tested for beam deformation. In fact, significant pre-breakdown self-defocusing can be observed in a number of III-V and II-VI compounds at 1.06 μm [28].

We summarize this short excursion into the history of research on intrinsic laser-induced damage with the following statement:

> There existed no direct experimental evidence in support of any intrinsic damage mechanism in wide-gap optical crystals at visible wavelengths prior to the work by Jones et al. [1,2] and Shen et al. [3,4], who performed the first unambiguous prebreakdown measurements of energy deposition from a laser beam into an intrinsic transparent optical solid. Only the studies by Manenkov and coworkers of the temperature dependence of the damage thresholds for 8 nsec pulses at 532 nm were retrospectively judged to have been performed with intrinsic crystals: NaCl, KCl, and KBr. Incidentally, these experiments provided an early indirect indication "...that at 532 nm laser damage of alkali halides is not explained by avalanche formation and is probably attributed to multiphoton ionization," [23] thus contradicting the U.S. literature available at that time [15].

3. Intrinsic Single Shot Bulk Damage

In perusing the classic literature on intrinsic laser-induced damage it becomes obvious that reliable information on the detailed damage mechanism cannot be had by measuring damage thresholds alone. The quality of the crystal can only be inferred indirectly in this way [20,23], and the question whether it exhibits intrinsic or extrinsic damage characteristics cannot be decided with any degree of confidence. Thus, comparison with theory is at best difficult.

The need for measurement of additional characteristic damage parameters had been recognized some time ago [15]. Specifically, Brawer suggested in 1979 that it might be possible to directly determine the energy deposited by the laser pulse into the optical solid prior to laser-induced damage "... by a calibrated photoacoustic experiment, [and] such an experiment may well be a good way to measure the existence of an electron avalanche." [28] Since then, nonlinear absorption has been detected photoacoustically in several optical solids, but, owing to experimental difficulties, direct demonstration of avalanche formation still remains an elusive goal.

Three-photon absorption was demonstrated by Van Stryland et al. [29]. Horn et al. [30] reported the first calibrated photoacoustic measurement of energy deposition by three-photon absorption in a solid. With the availability of reactive-atmosphere processed ultrapure alkali halide crystals and improved experimental techniques, Jones et al. [1,2] succeeded in photoacoustically monitoring focal point temperature increases of over 300 K in NaCl for non-damaging 80 ps pulses at 532 nm. They showed that the primary absorption process in this case is four-photon free carrier generation (with a cross section $\sigma^{(4)} \approx 5 \times 10^{-113}$ cm^{8}s^3), that avalanche formation was not evident even for these large temperature increases and that a high quality of the samples was of paramount importance for this first direct detection and study of intrinsic damage behavior.

Another major breakthrough in direct measurements of intrinsic laser-induced damage came with the so-called self-trapped exciton recombination luminescence method (STERL) pioneered by Brost et al. [31] and perfected by Shen et al. [2,3,32] who measured the σ component of the intrinsic exciton recombination luminescence as a function of pre-damage photon flux in KBr for 100 ps laser pulses at 532 nm. These pre-breakdown STERL experiments yielded the multiphoton absorption cross section ($\sigma^{(4)} = 2 \times 10^{-112}$ cm^{8}s^3) for free carrier generation, identified Epifanov's free carrier heating mechanism [17] rather than polaron absorption [19] as the main contribution to lattice heating in alkali halides and demonstrated that pre-breakdown temperature increases in the interaction volume can reach values very close to the melting point. Again, the intrinsic nature of the interaction between the laser pulse and the material was proven up to the single-shot damage threshold, and no evidence for avalanche formation could be detected.

The pre-breakdown experiments by Jones, Shen, and coworkers confirmed the theoretical prediction by Gorshkov et al. [33] and indications seen by Manenkov [23] that, for multiphoton order $m < 5$, the processes involved in energy deposition from the laser beam to an alkali halide are dominated by multiphoton free carrier generation and subsequent lattice heating via electron-phonon-photon collisions. This implies that in alkali halides the regime of validity for the avalanche mechanism is probably given by $m > 5$.

We refrain here from presenting details of the theories of intrinsic laser-induced damage, synopses of which can be found in the recent literature. The so-called "small quanta" ($E_g/h\nu > 5$, where E_g is the band gap and $h\nu$ the photon energy) avalanche mechanism was developed by Epifanov and coworkers [17,18,24] and again by Sparks et al. [34]. The "large quanta" ($3 < E_g/h\nu < 5$) version of this theory [33] was used by Jones [1,2], Shen [3,4], and Casper [7] to calculate possible contributions of avalanche ionization to the pre-breakdown energy deposition and damage thresholds in NaCl and KBr exposed to short 532 nm pulses, and its essential features are summarized in these papers.

The multiphoton-free carrier theory originated from the assumption that multiphoton absorption alone might account for the energy deposited from the laser beam into the transparent solid (originally believed to be the dominant process for $m < 3$) [15]. It then developed from initial attempts to include such secondary processes as absorption by multiphoton-generated polarons [19] and point defects [35] to its present form as applied in Refs. 1-7 to alkali halides.

An issue of considerable interest has always been the importance of avalanche-starting electrons and the role of point defects in optical breakdown. Contrary to the multiphoton mechanism, avalanche formation requires that a concentration of free electrons (approximately 10^8 to 10^{11} cm^{-3}) either be initially present or be generated early in the laser pulse by low-order multiphoton ionization of existing defects [15]. In 1981, Braunlich et al. [35] pointed out that in alkali halides efficient and extremely rapid formation of so-called primary defects (V_k-centers, self-trapped excitons, F- and H-centers) as recombination products of multiphoton-generated electron-hole pairs (excitons) might seriously affect the deposition of energy from the laser pulse to the crystal lattice by removing free carriers via recombination and by providing additional channels for efficient photon absorption. The relative importance of stable and/or laser-generated primary point defects in the myriad of dynamic microscopic processes that take place during the interaction of a short high-power laser pulse with a transparent (wide-gap) solid depends largely on the nature of the free carrier generation mechanism (avalanche ionization, multiphoton absorption or both) and the efficiency of free carrier absorption [1-4], but it is in general not the dominant mechanism of energy deposition to the lattice except for extreme point defect concentrations [3-5,7]. Nevertheless, any attempt to model a particular laser damage experiment must consider all of the processes that have been identified as playing a part in the overall laser-solid interaction, including point defects. In that sense, the calculation performed by Jones et al. [1,2], Shen et al. [3-5], and Casper et al. [7] represent the first realistic comparisons of intrinsic experimental laser bulk damage data with existing theory.

4. Intrinsic Surface Damage

Let us now turn to laser-induced intrinsic surface damage. To date there exists precious little clear experimental evidence of single shot damage events on an "intrinsic" optical surface for any laser wavelength. In light of the difficulties encountered in the identification of the processes leading to intrinsic bulk damage in a transparent solid, this state of affairs is not surprising considering the complexity of a surface. Yet, contrary to the bulk, manifestations of nonlinear laser-solid interactions at pre-breakdown photon fluxes can be measured with great sensitivity with a large variety of analytical tools. Most sensitive of all is the detection of charged particles; but neutrals have also been monitored successfully [10-14]. While laser-induced nonlinear photoelectron emission might not necessarily be associated with irreversible modifications of the surface, ion and neutral emission invariably is, and, by mass-spectrometric analysis or laser-induced fluorescence, it is always possible to identify whether the involved interaction process is intrinsic or extrinsic in nature.

The interest of the laser damage community in particle emission from optical surfaces exposed to intense laser pulses was prompted by the emission of halogen atoms into well defined crystallographic directions observed by Schmid et al. from NaCl, KCl, and KBr at pre-breakdown photon fluxes from a Q-switched ruby laser [10,11]. We include here two previously unpublished examples of the emission pattern obtained by these authors (fig. 1). With the clear picture now available of the processes that occur in the bulk of these alkali halides exposed to intense laser pulses at visible wavelengths, the tentative explanation of directional halogen emission given at that time and its relation to irreversible surface modifications (damage) is now confirmed: a high-order multiphoton process generates electron hole pairs. The holes are trapped on a time scale of 10^{-13} s to form V_k centers (X_2^- molecular ions, where X is a halogen atom). These recombine with free electrons to form self-trapped excitons (which eventually decay back to the crystalline ground state) or F-H pairs. On the surface, the X_2^- molecule is unstable and dissociates by emission of an X atom in a direction along its molecular axis in the <110> directions, leaving the surface alkali rich and prepared for subsequent laser-induced thermal desorption of neutral alkalis. The natural distortion of the crystalline structure in the upper most surface layers facilitates halogen emission in a direction close to a <221> axis in addition to <110> emission.

The importance of this discovery as a mechanism for intrinsic surface damage was immediately recognized [11], because the emission of only one halogen atom (or in the bulk, the formation of one single stable F-center) as a result of multi-photon exciton generation in the surface layer already constitutes, in principle, an intrinsic process of irreversible material modification. The intensity of directional emission was found to be very high, to depend nonlinearly on the photon flux and to occur prior to catastrophic breakdown by hot plasma formation. Since then, a number of studies have been performed on multiphoton-induced sputtering and desorption at pre-breakdown photon fluxes [12-14], and the intrinsic nature of most of the measured emission of ions and neutrals has been firmly established [12-14,36,37]. In fact, reports on these experiments have now become a regular feature of the Boulder Laser Damage Symposium.

Looking back to the early days of laser surface damage studies and the enormous difficulties encountered in explaining any of the microscopic laser-surface interaction processes, the progress made recently by applying the techniques of particle detection is undeniable, and, just as for further advancement in understanding laser-induced intrinsic bulk phenomena, the stage seems now set for further fruitful research in the physics of intrinsic laser-surface interactions.

A number of questions remain to be answered. Is Epifanov's free carrier heating the dominant heating process in the surface of alkali halides just like it is in the bulk, and is it ultimately responsible for single shot surface damage? Does the emission of halogen atoms from the surface layer affect the energy deposition from the laser pulse to the surface region? What fraction of halogen atoms has to be removed from the surface layer or how many surface layers have to be ablated and locally disturbed in successive shots to eventually facilitate catastrophic breakdown at fluxes lower than the single shot surface damage threshold? What is the relationship between intrinsic surface and bulk thresholds? How do the results obtained with intrinsic surfaces carry over to complicated structures such as dielectric coatings?

5. Multiple Shot Effects

With the availability of intrinsic optical materials (NaCl, KBr) and confidence in the laser-pulse solid interaction mechanisms established for them at 532 nm, it is intriguing to look again at multiple shot laser-induced bulk damage in these materials. Two distinct types of multiple pulse interactions are believed to exist [8]. One stipulates that a pulse of power density below the single shot damage threshold leaves the interaction volume unaltered, but repeated exposure to such pulses may eventually cause damage because the damage probability of any one of these pulses is presumably nonzero. The other type is due to the accumulation of microscopic damage which, after a number of shots, will lead to permanent macroscopic material modifications [9]. Since in all previous investigations of multiple shot failure *extrinsic* rather than *intrinsic* effects were most likely measured, the recent experiments with intrinsic crystals by Casper et al. [7] are of particular significance. Even though still preliminary, they have already provided new insight in the mechanism of accumulative damage at photon fluxes below the intrinsic single pulse damage threshold: 1. Changes of the optical properties of the materials due to the accumulation of laser-generated primary point defects (color centers) have been eliminated as a cause of multiple shot failure. 2. Laser pulses, which cause a peak temperature increase in the interaction volume of only 10 K, have been shown to damage the solid after fewer than ten successive shots at a low repetition rate. Taken together, these observations strongly suggest that, rather than changing those optical characteristics of the material that are relevant for intrinsic single shot damage behavior, the accumulation of certain microscopic defects must occur which alter the mechanical properties. One might term this phenomenon "laser-induced embrittlement," because the present preliminary experimental evidence supports a hypothesis by Manenkov et al. [9]: the observed accumulating effect is governed by an activation energy, which seems to decrease with the shot-to-shot buildup of localized stress. We reiterate that, just as in the case of intrinsic surface damage, these conclusions could be reached only because the detailed intrinsic processes involved in energy deposition from the laser beam to the solid are known in this case. Thus, irreversible and accumulating modifications due to phase transitions (melting) can most likely be excluded as can the probabilistic multi-shot damage theory discussed by Merkle and coworkers [8].

This work was supported by the Air Force Office of Scientific Research under grant number AFOSR-87-0081.

6. References

[1] S. C. Jones, X. A. Shen, P. F. Braunlich, P. Kelly, and A. S. Epifanov, Phys. Rev. B35, 894 (1987).

[2] S. C. Jones, X. A. Shen, P. F. Braunlich, P. Kelly, and A. S. Epifanov, Proceedings of the 18th Boulder Laser Damage Symposium 1986 (to be published).

[3] X. A. Shen, Peter Braunlich, S. C. Jones, and P. Kelly, Phys. Rev. Lett. 59, 1605 (1987).

[4] X. A. Shen, Peter Braunlich, S. C. Jones, and P. Kelly, Proceedings of the 19th Boulder Laser Damage Symposium October 26-28, 1987, Boulder, CO.

[5] S. C. Jones, Alfred H. Fischer, and Peter Braunlich, Phys. Rev. B38, January 15, 1988 (accepted for publication).

[6] M. J. Soileau, "Laser-Induced Damage" in Photonics Spectra, November 1987, pp. 109-114.

[7] R. Th. Casper, S. C. Jones, X. A. Shen, P. Braunlich, and P. Kelly, Proceedings of the 19th Boulder Laser Damage Symposium October 26-28, 1987, Boulder, CO (in preparation).

[8] L. D. Merkle, M. Bass, and R. T. Swimm, Natl, Bur. Stand. (US) Special Publication 669, 1982, 50-59.

[9] A. A. Manenkov, G. A. Matyushin, V. S. Nechitailo, A. M. Prokhorov, and A. S. Tsaprilov, Natl. Bur. Stand. (US) Special Publication 669, 1982, 436-447.

[10] A. Schmid, Peter Braunlich, and P. K. Rol, Phys. Rev. Lett. 35, 1382 (1975).

[11] A. Schmid, Peter Braunlich, and P. K. Rol, Natl. Bur. Stand. (US) Special Publication 435, 1975, 366-368.

[12] N. G. Stoffel, R. Riedel, E. Colavita, G. Margaritondo, R. F. Haglund, E. Taglauer, and N. H. Tolk, Phys. Rev. B32, 6805 (1985).

[13] J. Reif, H. Fallgren, W. E. Cooke, and E. Matthias, Appl. Phys. Lett. 49, 770 (1986).

[14] E. Matthias, J. Reif, H. B. Nielsen, E. Westin, and A. Rosen, Proceedings of the 19th Boulder Laser Damage Symposium, October 26-28, 1987, Boulder, CO (in preparation).

[15] W. Lee Smith, Optical Engineering 17, 489 (1978).

[16] E. Yablonovitch and N. Bloembergen, Phys. Rev. Lett. 29, 907 (1972).

[17] A. S. Epifanov, Sov. Phys.-JETP 40, 897 (1975).

[18] A. S. Epifanov, A. A. Manenkov, and A. M. Prokhorov, Sov. Phys.-JETP 43, 377 (1976).

[19] A. Schmid, P. Kelly, and Peter Braunlich, Phys. Rev. B16, 815 (1977).

[20] E. W. Van Stryland, M. J. Soileau, A. L. Smirl, and W. M. Williams, Nat. Bur. Stand. (US) Spec. Publ. 620, 1980, 375-384.

[21] M. J. Soileau, J. B. Franck, and T. C. Veatch, Nat. Bur. Stand. (US) Spec. Publ. 620, 1980, 385-393.

[22] M. J. Soileau, W. M. Williams, and E. W. Van Stryland, Nat. Bur. Stand. (US) Spec. Publ. 727, 1984, 394-403.

[23] A. A. Manenkov, Nat. Bur. Stand. (US) Spec. Publ. 509, 1976, 455-464.

[24] B. G. Gorshkov, A. S. Epifanov, and A. A. Manenkov, Sov. Phys.-JETP 49, 309 (1979).

[25] G. M. Zverev and V. A. Pashkov, Sov. Phys.-JETP 30, 616 (1970).

[26] P. Kelly, D. Ritchie, P. Braunlich, A. Schmid, and G. W. Bryant, Nat. Bur. Stand. (US) Spec. Publ. 620, 1980, 394-402.

[27] A. X. Shen, P. Braunlich, S. C. Jones, and P. Kelly (in preparation).

[28] S. Brawer, Phys. Rev. B20, 3422 (1979).

[29] E. W. Van Stryland, M. A. Woodall, W. E. Williams, and M. J. Soileau, Nat. Bur. Stand (US) Spec. Publ. 638, 1983, 589-600.

[30] P. Horn, A. Schmid, and P. Braunlich, IEEE J. Quantum Electron. QE-19, 1169 (1983).

[31] G. Brost, P. Braunlich, and P. Kelly, Phys. Rev. B30, 4675 (1984).

[32] X. A. Shen, S. C. Jones, P. Braunlich, and P. Kelly, Phys. Rev. B36, 2831 (1987).

[33] B. G. Gorshkov, Yu. K. Danileiko, A. S. Epifanov, V. A. Lobachev, A. A. Manenkov, and A. V. Sidorin, Sov. Phys.-JETP 45, 612 (1977).

[34] M. Sparks, D. L. Mills, R. Warren, T. Holstein, A. A. Maradudin, L. J. Sham, E. Loh, and D. F. King, Phys. Rev. B24, 3519 (1981).

[35] P. Braunlich, G. Brost, A. Schmid, and P. Kelly; IEEE J. Quantum Electron QE-17, 22-34 (1981).

[36] L. L. Chase and L. K. Smith, Proceedings of the 19th Boulder Laser Damage Symposium, October 26-28, 1987, Boulder, CO (in preparation).

[37] H. F. Arlinghaus, W. F. Calaway, C. E. Young, and D. M. Gruen, Proceedings of the 19th Boulder Laser Damage Symposium, October 26-28, 1987, Boulder, CO (in preparation).

A questioner pointed out that there are at least two errors in the equation used, one the assumptions which the speaker mentioned and the other that the critical power in that equation is incorrect. The speaker agreed, but pointed out that one needs to be careful about generalizing based on how large the spots are when self focussing is present. It depends on the power. The speaker agreed and pointed out that they had been very careful to scan the data for any effects which self focussing or defocussing would have, as well as monitoring the transmitted laser beam for deformations.

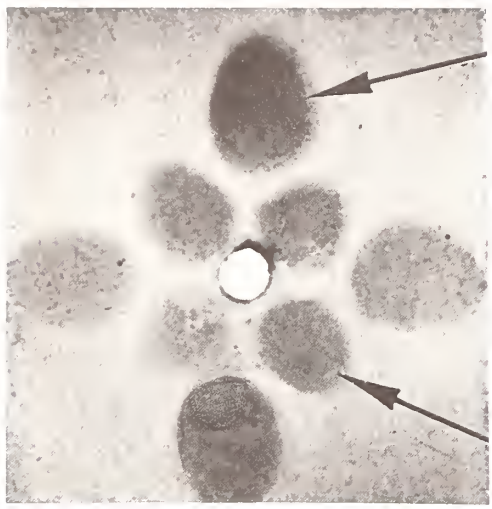

Br-atom emission pattern from KBr

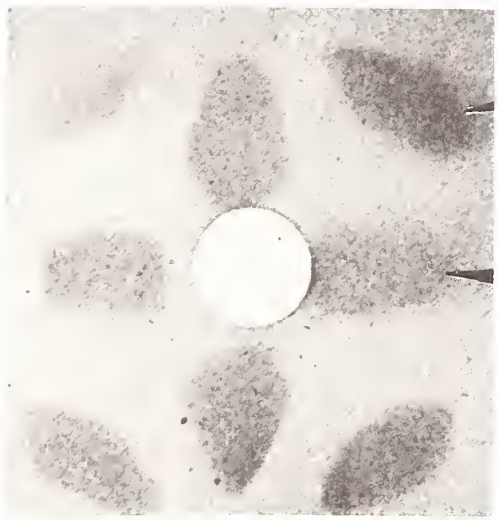

Cl-atom emission pattern from KCl

Figure 1. Halogen atom emission pattern obtained from the <100> planes of KBr and KCl single crystals exposed to focused pulses from a Q-switched ruby laser. A glass plate, coated with silver nitrate and having a small hole for passage of the laser beam, served as the detector. It was mounted 8 mm in front of and parallel to the <100> plane of the crystal (from unpublished work by A. Schmid and P. Braunlich).

Manuscript Received 12/21/87/sar

The Laser Damage Mechanism for NaCl and KBr at 532 nm - Theoretical Predictions and Experimental Tests

R. Thomas Casper, Scott C. Jones, X. A. Shen, and Peter Braunlich
Department of Physics, Washington State University
Pullman, WA 99164-2814

Paul Kelly
Division of Physics, National Research Council
Ottawa, Ontario, Canada K1A 0R6

Recent work by Jones et al. and Shen et al. established the detailed intrinsic damage mechanisms in NaCl and KBr exposed to short laser pulses at 532 nm. Predictions of the dependence on experimental and material parameters of energy deposition from the laser pulse to the wide-gap optical solid can now be made with confidence. We examine the effects of initial temperature and of pulse length on the damage threshold. We also discuss the role of defect accumulation in multiple shot damage in KBr.

Key Words: alkali halide; avalanche ionization; damage mechanism; defect accumulation; free electron heating; KBr; multiphoton absorption; multiple shot damage; NaCl; pulse length dependence; temperature dependence.

1. Introduction

As research in this field of laser damage progressed, two theories emerged as possible explanations for the phenomenon. The first of these, the avalanche theory, was a generalization of the d.c. dielectric breakdown phenomenon. This theory, however, was not successful at explaining all of the observed behaviors, and the multiphoton absorption mechanism was proposed to to account for these discrepancies. Over the years there has been much debate on the relative merits of these two possibilities. But the question has now shifted to which of the theories is valid in different regimes.

We examine here the cases of NaCl and KBr exposed to high power laser pulses at 532 nm. In the first part of this paper we are concerned with damage due to a single laser pulse, and later we consider multiple shot effects. For NaCl Jones et al. [1] used a photoacoustic technique to obtain a direct measure of the energy deposited in the crystal by a single laser pulse. In these experiments a temperature rise of several hundred degrees was observed with no indications of damage. They also determined that the primary mechanism involved was that of four photon absorption. Shen et al. [2, 3] used a technique with KBr which monitored the self-trapped exciton (STE) luminescence as a measure of the number of electron-hole pairs produced during the laser pulse to measure the four photon absorption cross section. Taking advantage of the thermal quenching of the STE luminescence they were also able to infer the temperature in the interaction volume without regard to any specific model of the laser-crystal interaction. Temperature increases up to 90 K below the melting point (T_m=1007 K) were observed for pulses, indicating that the intrinsic failure mode for single pulses is melting. Their conclusions were that the lattice heating is due to free electron absorption rather than polaron absorption and that avalanche ionization gives no significant contribution to the overall damage mechanism.

The work by Jones and Shen mentioned above comprised the first prebreakdown studies of intrinsic materials from which they were able to develop a theory which accounts for their observations. Of course it is not sufficient to judge the success of a theory solely on the observations used in its development. It is necessary to make additional predictions and then check their validity against experiments. In this work we present some of these tests.

2. Theory

As mentioned, the theory developed for these cases was one of a multiphoton absorption process. But the problem is more complicated than just the production of electron-hole pairs; a host of subsequent processes must also be considered. Figure 1 shows those which have been taken into account. In the end

the contributions of most of these additional processes to the lattice heating are relatively small so, for the purpose of clarity, a simplified set of model equations is presented here. The equations are shown in detail in papers by Shen et al. [2] and Jones et al. [4, 5].

The rate of change in the density of conduction electrons is

$$\frac{dn_c}{dt} = N\sigma^{(4)}F^4 + \gamma n_c - R + Q \ , \tag{1}$$

and the temperature rise at the center of the focal volume is given by

$$c\rho \frac{dT}{dt} = 1.09 \left(\frac{m^*kT}{2\pi}\right)^{1/2} \frac{n_c}{l_{ac}v_s} \left(\frac{eE}{m^*\omega}\right)^3 + W \ , \tag{2}$$

where the avalanche ionization coefficient is

$$\gamma = (aF)^5 T^4. \tag{3}$$

The first term on the right-hand-side of eq (1) represents the four photon absorption process, and the second term was included to allow for possible contributions from an avalanche mechanism. R accounts for various recombination routes of the conduction band electrons, whereas Q consists of additional sources of conduction electrons, such as defect ionization. In eq (2) the first term on the right-hand-side is that of free electron heating as developed by Epifanov [6]. W includes other sources of heating, such as non-radiative recombination events. The parameter a in eq (3) is an adjustable parameter which depends on material properties such as the effective mass of the electron and the collision frequency,and it is adjustable in the sense that these properties are not well determined. Definitions of the symbols are given in table 1.

Table 1. Symbols used in model equations

n_c	Conduction electron density
N	Density of active atoms (i.e., Cl^- or Br^- ions)
$\sigma^{(4)}$	Four photon absorption cross section
F	Photon flux
c	Specific heat
ρ	Density
m^*	Electron effective mass
T	Temperature
l_{ac}	Mean free path of conduction electrons
v_s	Sound velocity
E	Electric field strength
ω	Laser frequency

We are now in the position to make some predictions based on this theory. We will examine the damage threshold flux, F_D, as a function of initial temperature, T_0, and pulse width, τ. The method is to vary the peak flux until the melting temperature (1007 K for KBr and 1074 K for NaCl) is reached at the end of the pulse at the center of the focal volume. The end of the pulse was chosen to be the point at which the flux had dropped to 10 percent of its peak value. We cannot at this time, however, make predictions for the dependence of the damage threshold on the laser wavelength as this requires parameters which are unknown at wavelengths other than 532 nm, such as four-photon absorption cross section, $\sigma^{(4)}$.

3. Experimental Procedure

Figure 2 illustrates the experimental arrangement used to verify the predictions. The laser pulse is produced by a Q-switched and mode-locked Quantronix model 116 Nd:YAG laser system. A single mode-locked pulse is switched into a double pass Nd:YAG amplifier, and the second harmonic used in the experiments is produced in a KDP crystal. The spatial profile is checked at the entrance plane of the focusing lens using a scanning slit technique. The focal spot size is then calculated using diffraction limited gaussian optics. The temporal profile is measured by a zero background second harmonic generation autocorrelation procedure. The spot size was typically 6-8 μm, and the pulse width was 84 psec, where these values refer to the half-width at 1/ e of the peak flux.

The experimental procedure was to first expose the sample to a single high power laser pulse. A low power pulse was then used as a damage probe by checking for an increased scattering perpendicular to the beam axis. The scattered light is picked up by an optical fiber and guided to a photomultiplier tube which served as the detector. The site was considered damaged if the normalized scatter was two to three times as great as the scatter from a virgin site. The highest non-damaging flux was then chosen as the damage threshold. An example of the data obtained from one of these experiments is shown in figure 3. It should be noted that there is a low baseline for the scatter up to a flux of 6.5×10^{29} cm^{-2} sec^{-1}. At higher fluxes we no longer observe any points without a substantial increase in scatter. This flux is, therefore, chosen as the damage threshold. The points with large scattering for fluxes below the threshold are attributed to sites where extrinsic damage has occurred.

4. Results

We first examine the predicted temperature dependence of the damage threshold in KBr for the cases of multiphoton assisted avalanche and multiphoton mechanisms as illustrated in figure 4. In the avalanche calculation the value for a in eq (3) was chosen so that the contribution to heating from the conduction band electrons generated solely by the multiphoton process would yield a temperature increase of about 10 K. The important aspect here is the difference in the temperature dependence for the two cases. The dependence is strong for avalanche carrier generation (as indicated by a three-fold decrease in the threshold from 50 K to 300 K), and relatively weak for multiphoton carrier generation. In 1977 Manenkov [7] identified alkali halides as candidates for multiphoton absorption at 530 nm due to the lack of temperature dependence of their damage thresholds. Figure 5 then shows the thresholds measured in NaCl and KBr compared with the theoretical predictions for these materials. We again note no large temperature dependence, and the absolute numbers measured are in reasonable agreement with the predictions.

The pulse length dependence of the damage threshold is shown in figure 6, where the avalanche case has again been included for comparison. The points at 84 psec were measured in our laboratory, and those at 8 nsec were measured by Manenkov in 1977 [7], and are believed to be intrinsic values [8].

5. Multiple Shot Damage

Preliminary experiments were also performed to investigate the multiple shot damage mechanism. The experimental arrangement was the same as for the single shot studies with the exception that the scattered light was monitored during each shot rather than being probed afterwards. Damage was assumed to have occurred when a sudden increase in light scattering was observed. The laser repetition rate was approximately 1 Hz. Figure 7 shows the number of shots required to observe damage as a function of the peak flux for the temperatures of 300 K and 50 K. Although more data is required to determine whether there is a difference in the multishot thresholds for these two cases, the initial indications are that the threshold is somewhat higher for lower temperatures.

One must ask if the increased scattering observed is simply due to the accumulation of point defects which would then act as scattering centers for the laser light. If this were the case one would expect a much more gradual increase in the scattering than was observed. Also, as an experimental test of this possibility, several sites were heavily colored with low power UV (266nm) pulses. These sites showed no discernable increase in scattering over that of uncolored sites, indicating that the defects are not simply acting as scattering centers.

The next question is whether the accumulated defects, in particular F-centers, provide a sufficient number of starting electrons through single photon absorption to significantly reduce the damage threshold. A plot of the damage threshold as a function of the initial concentration of conduction band electrons is shown in figure 8. It is found that a ten percent reduction in the threshold requires a starting electron density equal to nearly half of the density obtained when the melting point is reached. The density of conduction band electrons at the melting point was calculated to be about 1.9×10^{18} cm^{-3}. This implies that it would require on the order of 10^{18} cm^{-3} defects present to significantly alter the damage threshold for the multiphoton process. This concentration, however, would not have been obtained in the number of shots required to observe damage at the fluxes in question. The case of defect assisted avalanche was not examined.

Finally, we must consider the possibility that the damage is due to an accumulated temperature increase. At a flux of 2.0×10^{29} cm^{-2} sec^{-1} the temperature rise from a single pulse is only 10 K , but at this flux it takes fewer than ten shots to damage the crystal. Therefore, even neglecting thermal diffusion, the total temperature increase would not be sufficient to reach the melting temperature.

These facts indicate that, rather than changing the optical properties of the material, the accumulation of point defects may alter the mechanical properties of the crystal. A method for studying such processes has been presented by Manenkov et al. [9]. This could then possibly make the sample more susceptible to crack formation due to the thermal stresses produced by the laser pulse.

6. Conclusion

The theory presented holds up well to the intrinsic data available for the materials which were studied, and similar models could now be developed for additional alkali halides and other wide-gapped materials. These would then enable predictions to be made of the material's response under a variety of experimental conditions.

In its present form this theory considers only single shot phenomena in that the model does not directly track the accumulation of defects nor thermal diffusion between shots. But by examining the dependence of single shot damage on the initial conditions some useful information concerning multiple shot damage can still be obtained. And it remains to be shown whether the accumulation of defects sufficiently alters the mechanical properties of the material to account for the observed multiple shot behavior.

This work was supported by the Air Force Office of Scientific Research under grant number AFOSR-87-0081.

7. References

[1] Scott C. Jones, X. A. Shen, P. F. Braunlich, Paul Kelly, and A. S. Epifanov, Phys. Rev. B, **35**, 894 (1987).

[2] X. A. Shen, Scott C. Jones, Peter Braunlich, and Paul Kelly, Phys. Rev. B, **36**, 2831 (1987).

[3] X. A. Shen, Peter Braunlich, Scott C. Jones, and Paul Kelly , Phys. Rev. Lett., **59**, 1605 (1987).

[4] Scott C. Jones, Alfred H. Fischer, Peter Braunlich, and Paul Kelly, accepted for publication in Phys. Rev. B, **37**, Jan. 15, 1988.

[5] S. C. Jones, X. A. Shen, P. F. Braunlich, Paul Kelly, and A. S. Epifanov, Proceedings of the 1986 Boulder Damage Symposium (to be published).

[6] A. S. Epifanov, Sov. Phys. JETP, **40**, 897 (1975).

[7] A. A. Manenkov, Nat. Bur. Stand. (U. S.) Spec. Publ. 509; 1977. 455-464.

[8] E. W. Van Stryland, M. J. Soileau, Arthur L. Smirl, and William E. Williams, Nat. Bur. Stand. (U. S.) Spec. Publ. 620; 1981. 375-384.

[9] A. A. Manenkov, G. A. Matyushin, V. S. Nechitailo, A. M. Prokhorov, and A. S. Tsaprilov, Nat. Bur. Stand. (U. S.) Spec. Publ. 669; 1984. 436-447.

A questioner asked if the picture presented is that all of the damage is due to four photon absorption and absorption from color centers, no avalanche. The speaker confirmed that this is his picture. Also, damage was assumed to occur at the end of the pulse. The questioner pointed out that in the experiments he was aware of damage occurred near the peak of the pulse, not at the end of the pulse. The speaker pointed out that they were not equipped to determine where temporally the damage occurred. The temperature tended to increase after the peak of the pulse so they used as their criterion that the melting point occurred at the end of the pulse.

Another questioner pointed out that although the picture presented was of an intrinsic, four photon process with no defect involvement, there was a substantial variation in the breakdown threshold for each shot. Why the variation? The speaker ascribed the variation to inhomogeneities in the material itself. It could also have something to do with fluctuations in laser parameters. They assume their pulse shape is consistent from one shot to the next. The questioner pointed out that in NdYAG lasers there can be differences in pulse width of up to a factor of 2 in pulses even in the same train, which could account for much of the scatter in the data presented.

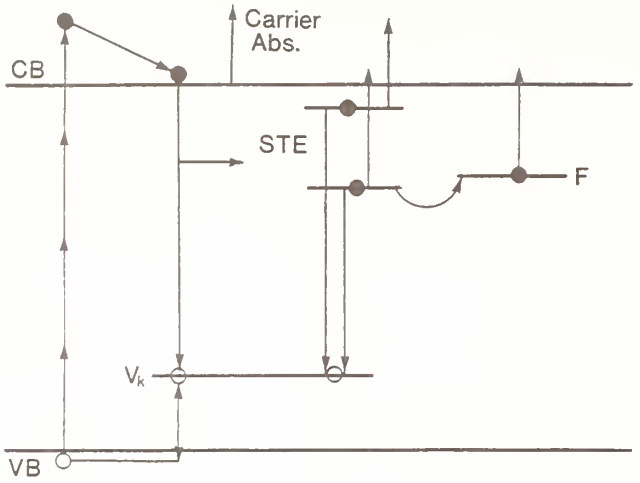

Figure 1. Processes considered in the model are production of electron-hole pairs by four photon absorption, trapping of holes to form V_k centers, trapping of electrons by V_k centers to form self-trapped excitons (STE), and F center production. Free carrier absorption, STE excitation, defect ionization, and electron-hole recombination are also considered.

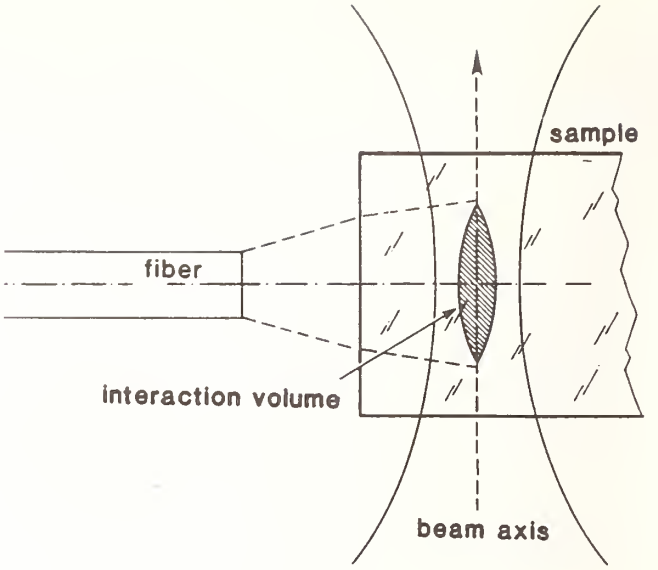

Figure 2. Experimental arrangement. The laser pulse is focused in the center of the sample, and the scattered light is detected by a fiber positioned perpendicular to the beam axis. The sample can be moved in a direction perpendicular to the page to obtain a new spot without changing the relative positions of the interaction volume and the collection fiber.

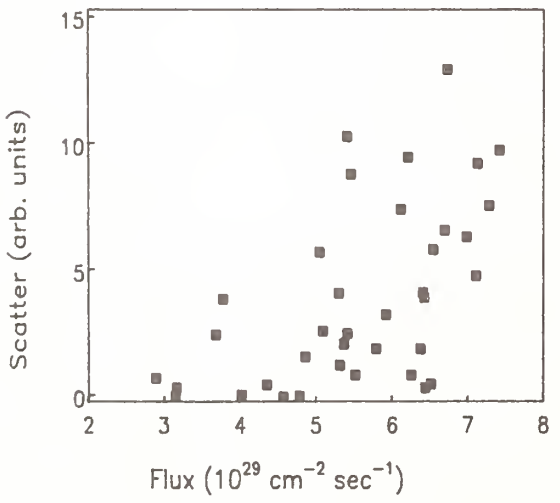

Figure 3. Damage threshold data for KBr at 50 K. Undamaged sites are indicated by points with low scatter. Above 6.5×10^{29} cm^{-2} sec^{-1} no non-damaging pulses are observed, therefore this point is chosen as the damage threshold. Points at lower fluxes with high scatter values are attributed to extrinsic damage.

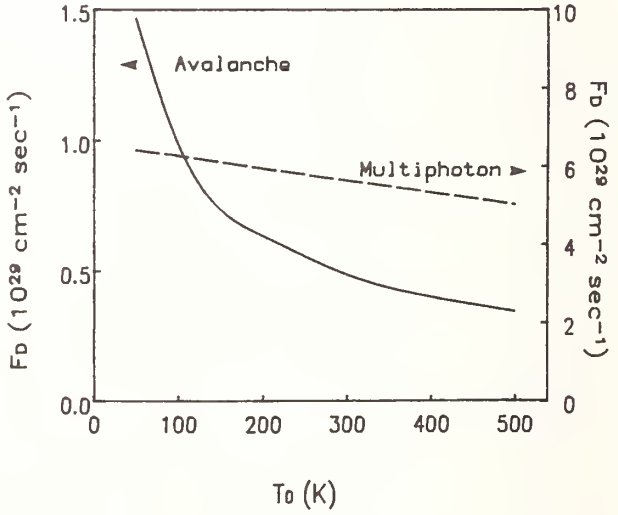

Figure 4. Temperature dependence of the damage threshold for multiphoton and multiphoton assisted avalanche mechanisms. The avalanche mechanism shows a strong temperature dependence, but the multiphoton case shows a much weaker dependence.

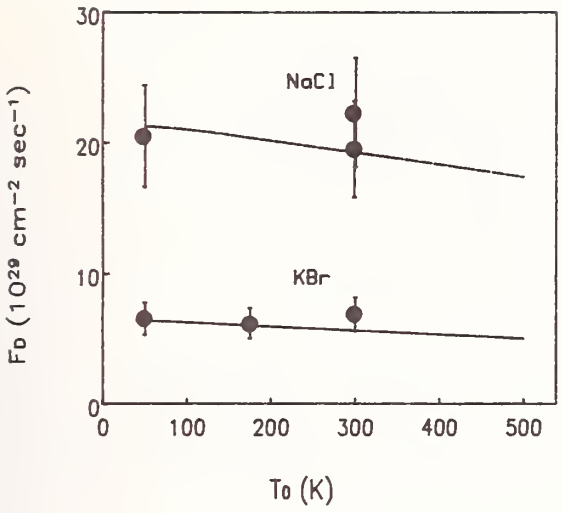

Figure 5. Measured damage thresholds (solid circles) compared to the values predicted by the multiphoton theory for NaCl and KBr as a function of temperatrure.

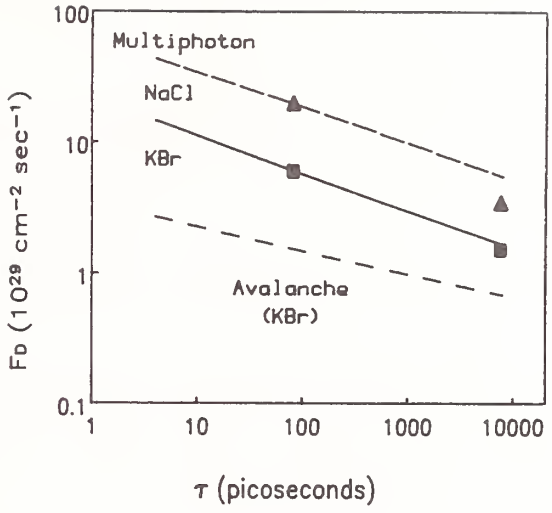

Figure 6. A double logarithmic plot of the pulse length dependence of the damage threshold for NaCl (top line and triangles) and KBr (center line and squares). The bottom line shows, for comparison, the dependence predicted for multiphoton assisted avalanche, whereas the top two lines were predicted using the multiphoton theory.

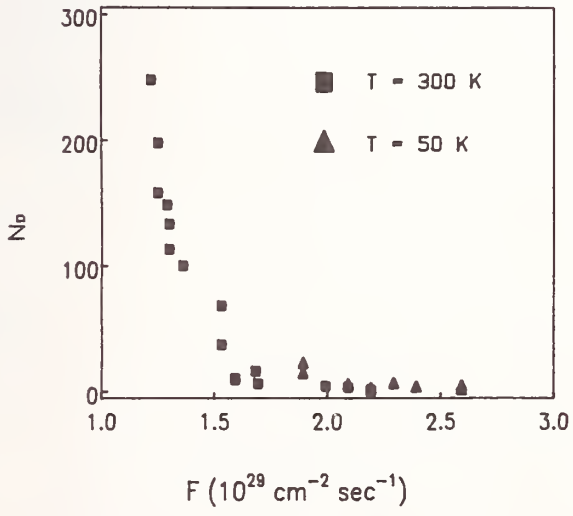

Figure 7. A plot of the number of shots required to observe damage as a function of the peak photon flux for KBr. Initial results indicate a temperature dependence of the multiple shot damage threshold.

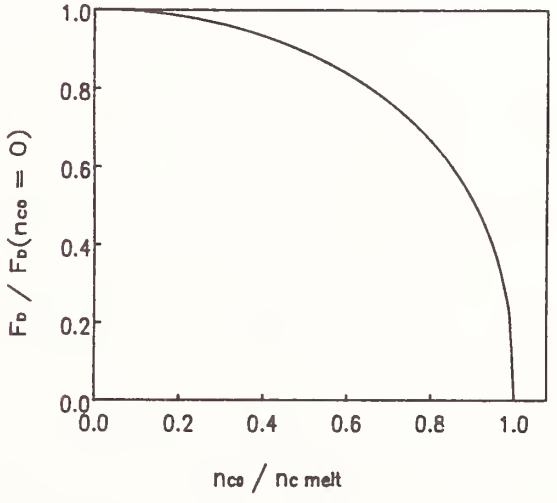

Figure 8. Calculated damage threshold as a function of the initial conduction electron concentration. For KBr $n_{c\ melt}=1.9\times10^{18}$ cm^{-3}.

New Data Regarding the Thermal Laser-Damage Model and the Accumulation Phenomena in Silicon

Stephen P. Fry, Rodger M. Walser and Michael F. Becker
The University of Texas at Austin
Center for Materials Science and Engineering and
Department of Electrical and Computer Engineering
Austin, TX 78712

In this paper we propose a new statistical framework from which to view laser-induced damage in silicon, particularly N-on-1 damage effects such as accumulation. To select between possible models for damage, we obtained a refined data set for the statistics of nanosecond pulsed Nd:YAG laser damage to Si surfaces. The implications of this data for modeling laser damage experiments will be discussed.

Key words: laser damage, silicon, accumulation, melting model, non-deterministic model.

1. Introduction and Background

There is a large and growing body of experimental evidence supporting a thermal model for the laser induced melting and damage of Si surfaces. In addition, there are related data describing the N-on-1 or accumulation damage behavior of Si. The possible implications of this data for a deterministic model of laser damage will be reviewed . In section 3 of this paper, we will introduce an alternative, non-deterministic model and investigate what experimental evidence could be used to discriminate between the two models. The theoretical framework developed here should be suitable for the study of laser damage of any material and for drawing inferences on the degree to which it is affected by accumulation or hardening.

For 1-on-1 nanosecond pulse damage of Si, microscopic examination of the damage morphology indicated that first a melt region was initiated at the center of the Gaussian beam and grew in diameter with increasing fluence [1,2,3,4]. At higher fluences, boiling initiated near the beam center and spread outward for further increasing fluence. This sequence of events conforms to thermal heating models proposed for laser induced damage, for example a model for damage to metals by Jee, *et al.* [5]. The model applies to any solid surface subject to one-dimensional surface heating. In other experiments, the onset of melting corresponding to an abrupt increase in reflectivity at 633 nm was detected by transient laser reflectivity. Data obtained in these experiments [6] indicated that the onset of laser induced damage of Si coincides with the onset of surface melting in agreement with the results of laser annealing experiments [7]. Finally, at substrate temperatures up to 500^{o}C [8] the damage threshold decreased as expected in melting. As a whole, this body of evidence indicates that 1-on-1 laser damage of Si due to nanosecond pulses occurred by a heating-melting-(and in some cases boiling) progression.

For N-on-1 laser damage, the situation is more complicated, and accumulation is always observed. That is, the onset and 50% probability fluences decreased as N increased. Figure 1 shows a typical result for Si in normalized form. Although a decrease in damage fluence to 80-85% of the single shot value was always observed at N=10-30, little further decrease occurred for further increases in N. The morphology observed for damage in this regime was not as consistent as for the N=1 case. For many samples, the usual melting-boiling progression was observed; but in others, particularly for large N or sub-nanosecond pulse lengths, local pitting damage was observed. Each pit of micron dimension had been both melted and explosively boiled with the ejection of material, while surrounding regions remained unmelted. As damage progressed, the pitted area increased, often in a coherent pattern. Unless the fluence was very high, this behavior was not accompanied by melting over the Gaussian beam area.

Previous attempts to ascertain the kinetics of an accumulated specie in N-on-1 YAG laser damage experiments on silicon gave negative results [8]. Accumulation was found to be independent of pulse repetition frequency (PRF) and independent of substrate temperature up to 500^{o}C, and pre-annealing had no effect on damage. In summary, no kinetic behavior for the accumulated specie was observed, even at elevated temperatures.

Finally, we have obtained new data on laser damage to Si as a function of substrate doping. The data are shown in figure 2 for n-type substrates with resistivities ranging from 0.01 to 10 Ω-cm. This corresponds to a range of doping densities from 4.6×10^{17} cm^{-3} to 4.6×10^{14} cm^{-3}. The experimental conditions were as

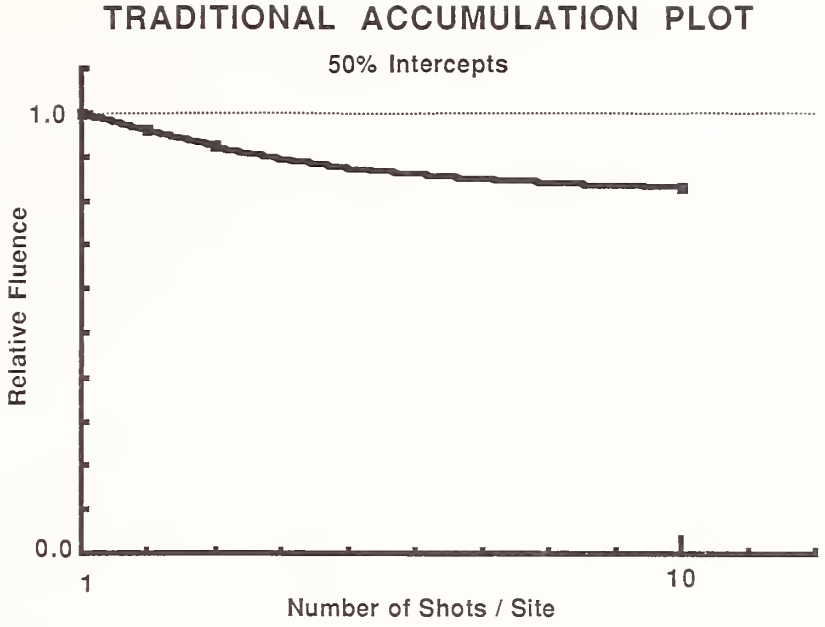

1. A traditional accumulation plot showing normalized damage threshold fluence versus number of pulses.

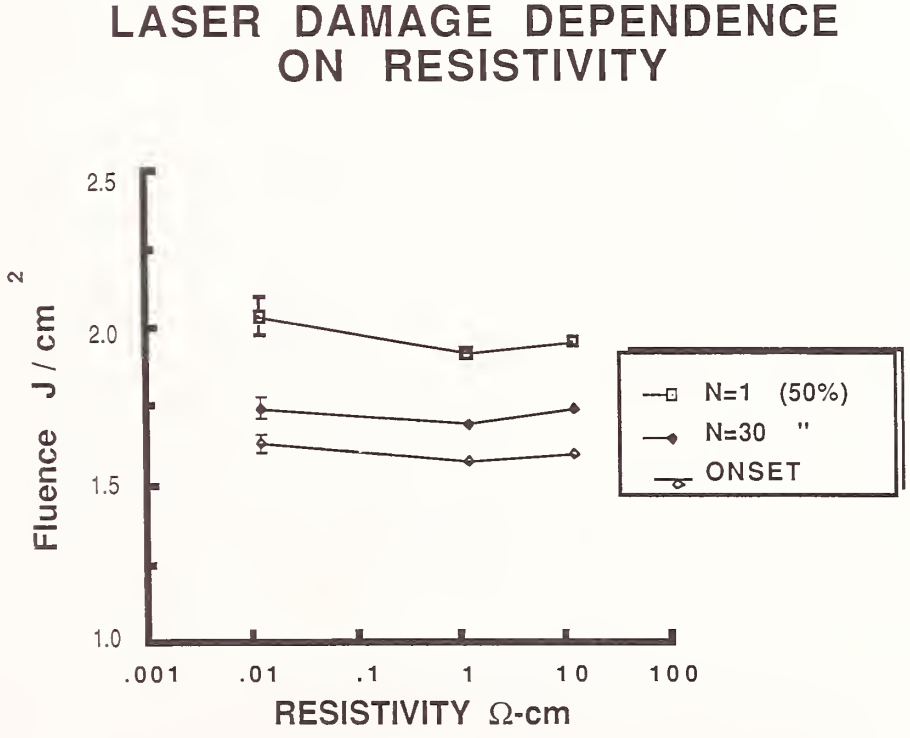

2. A plot of laser damage threshold versus Si wafer resistivity. The 50% damage probability is plotted for N=1 and 3, and the 0% probability intercept or onset is plotted for N=30.

described in the following section. As can be seen from the graph, no significant change in damage behavior was observed either in the onset fluence, 50% probability fluence or accumulation behavior. As the doping density was not sufficiently large to change the optical absorption, dopant impurity effects can be ruled out as a contributor to accumulation.

For these experiments, the observation of melting in conjunction with accumulation behavior suggests that a deterministic mechanism is involved in the nucleation of laser melting. In this view, there may be site-to-site fluctuations in a sample but each site has a unique and deterministic melt threshold. Damage ensues when the sample is irradiated by a laser pulse at or above this threshold. For accumulation in N-on-1 experiments, the deterministic melting threshold has been reduced by the previous pulses. This implies that some induced change or specie is accumulating. The negative results for experiments to determine the kinetics of accumulation have led us to theoretically and experimentally investigate an alternative viewpoint and a non-deterministic model for damage.

2. Experimental Methods and New Data

The laser used in these experiments was a Q-switched Nd:YAG laser operated at the fundamental wavelength of 1064 nm at a repetition rate of 10 Hz and with a 10 ns pulse length (FWHM). The optical layout was conventional and has been described previously [8]. The beam was attenuated with a fixed dielectric reflector and with a variable attenuator consisting of a rotating half-wave plate followed by a fixed thin-film polarizer. Irradiations were controlled by a computer driven shutter, and the computer also collected data from a reference energy meter on every laser pulse in order to compile irradiation statistics. In all cases, the pulse-to-pulse standard deviation in energy was less than 2% and less than 1% for most runs. The reference energy meter was calibrated at the start and end of each data taking session against another energy meter near the sample location. Each calibration also consisted of measuring the beam spot size at an equivalent focal plane using the knife edge method. A 78 cm focusing lens was used to obtain Gaussian spot sizes of about 300 μm ($1/e^2$ radius) incident normally on the sample surface. In studies of accumulation, the laser energy at the sample plane is of more interest than the fluence. Spot size measurements were, however, made to insure that the beam parameters did not change during an experimental run.

The Si wafers used in this study were (111) n-type wafers, 50 mm diameter, and polished on one side. Their resistivities ranged from 0.01 to 10 Ω-cm. The samples were cleaned in solvents to remove organic residue or contaminants before being placed in a dry pumped ($<10^{-4}$ Pa) vacuum chamber for laser damage testing. The vacuum was required for the collection charge emission data.

Test sites were arranged in a 1.5 mm grid pattern with markers at every fifth site. As testing proceeded, both the laser energy level and the number of pulses per site were varied in order to eliminate effects of slow variations across the wafer and changes in experimental parameters with time. This permitted the damage probability point for each fluence and pulse number N to be based on sites distributed across the wafer and in time. After irradiation, the sites were evaluated by Nomarski microscopy to 500x. Visible changes at any magnification were designated as damage.

Laser damage data was obtained for three resistivities of Si wafer. Most of the data reported in this paper was taken for the high resistivity (10 Ω-cm) wafers. The damage probability data were always plotted as damage probability versus fluence as first described by Foltyn [9]. Onset and 50% probability fluences were derived by least squares linear fits to the data. The generic accumulation curve shown in figure 1 was obtained in this way, as was the data showing damage fluence versus wafer resistivity in figure 2. In order to discuss models of accumulation, a data set for a single high resistivity wafer was chosen. It was typical of other wafers except that care was taken to obtain a sufficient number of data points at the high and low fluence ends of the curves and more different values of pulse number N were run. This data for N=1,2,3, and 10 is shown in figure 3 along with the number of sites upon which each curve is based. The analysis, modelling, and interpretation of this data is the subject of the remainder of this paper.

3. The Non-Deterministic Hypothesis

In this section we will introduce the non-deterministic model as an alternate way of viewing laser damage data and explore how this model can be distinguished experimentally from a deterministic one. The non-deterministic hypothesis asserts that the damage event is random with respect to laser fluence in an interval near threshold. That is, in the absence of site-to-site fluctuations, the damage frequency versus fluence curve would still have a finite slope and a finite overlap between the highest non-damaging fluence and the lowest damaging fluence. This behavior may be contrasted to the expected deterministic behavior, in the absence of site-to-site fluctuations, of a step function for the damage frequency versus fluence curve. A second independent assumption we shall make is that of non-accumulation. It states that if a given site is undamaged by previous pulses, it has the same probability of damage for subsequent pulses as it had for prior pulses. Under these conditions, N-on-1 non-damage probabilities are found by multiplying successive non-damage

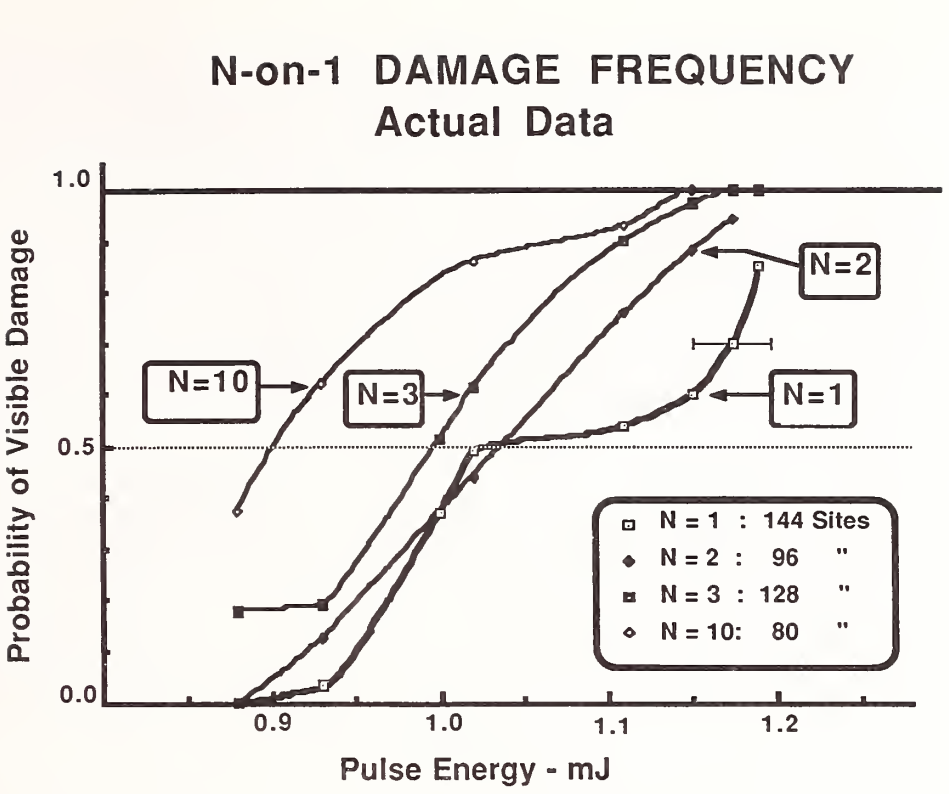

3. The silicon damage data set used for discussion in this paper. The data set is composed of a total of 448 individual sites distributed as shown in the inset.

probabilities for each pulse. This multiplication of probabilities to determine a cumulative damage probability leads to a reduced N-on-1 damage threshold and an "apparent" accumulation effect. In the following analysis we quantify this model and apply it to the experimental data to determine if a real accumulation effect is present .

The non-deterministic model implies that if the 1-on-1 damage probability, P1, for a given fluence is known, the N-on-1 damage probability, PN, for that fluence can be calculated or projected from this knowledge. In fact, if any PN is known, all the other PNs can be derived for that fluence. We denote a projected probability as P1*(m) where the N=1 damage probability is calculated from the m-shot data. A formula for the computation may be derived as follows. The probability of non-damage after one shot is (1-P1), and the probability of non-damage after n pulses is then $(1-P1)^n$. Hence the probability of damage after n shots is

$$Pn^*(1) = 1 - (1 - P1)^n \quad . \qquad (1)$$

The damage probability increases with increasing n as the non-damage probability simultaneously decreases. Equation (1) can be generalized to project the n shot probability from the m shot data as

$$Pn^*(m) = 1 - (1 - Pm)^{n/m} \quad . \qquad (2)$$

This relationship is illustrated on a damage probability versus fluence curve as shown in figure 4. The basis data is for N=3, and both the N=10 and N=1 damage probability curves are projected from the N=3 data. Since the projection process is applied at a constant fluence, the projection shifts the probability curve along vertical lines as illustrated by the arrows. As N increases, the probability curve shifts upward (not to the left) and vice versa for decreasing N.

The validity of the projection method was checked using the data set shown in figure 3 for N=1,2,3,and 10 pulse damage to Si. First, the P1 damage frequency was projected from N= 3 and 10 as shown in figure 5. Given the error range of the data, the agreement was quite good. The kink in the P1 curve at about the 50% damage probability was repeatable and seems to be a real feature of the damage statistics for this sample. A

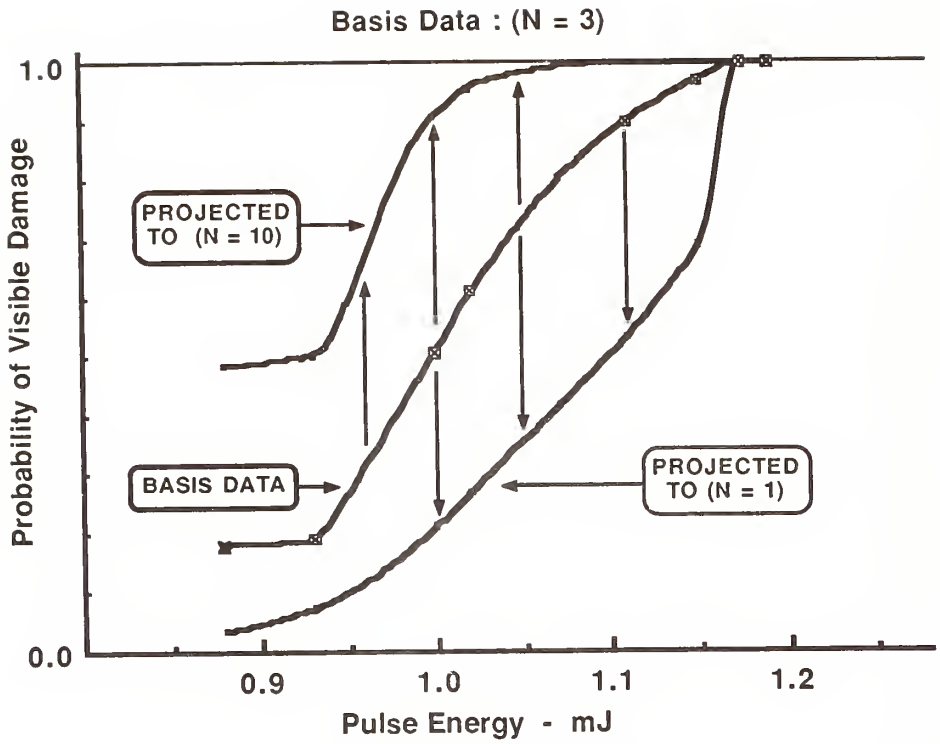

4. A graphical illustration of the result of projecting one damage probability curve from another as described in the text.

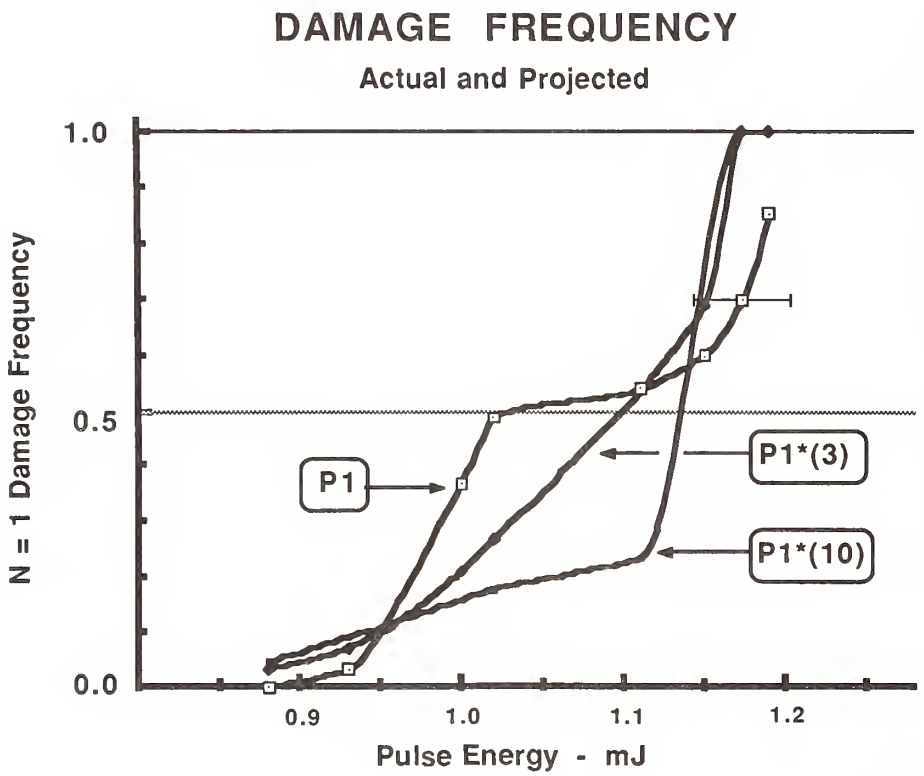

5. Projections of P1 from N=3 and 10 data compared to the actual P1 data.

projection from N=10 to N=1 might be an extreme test of the data accuracy because of the power law dependence involved; however, the agreement is still good. Projections from N=30 to N=1 were not as successful, however, the N=30 data was incomplete. Additional projections are shown in figure 6 for projecting P2 from N=3 data (top graph) and for projecting P10 from N=3 data (bottom graph). In both cases, the agreement between projected data and raw data for that value of N was remarkable.

A refined test of the non-deterministic hypothesis is to calculate the damage probability for a previously undamaged site and show that this probability is independent of the number of previous pulses incident on that site. This incremental probability can be calculated as follows. For illustration, the case of a third shot after two non-damaging shots is chosen. Recall that P3 is the probability of damage after three pulses, regardless of which shot initiated the damage. Define p3 as the probability that a previously undamaged site would damage on the third shot. We can write P3 as the sum of probabilities that damage occurred after two pulses, P2, and that damage occurred on the third pulse. The latter term is written as the product of the probability of non-damage after two pulses, (1-P2), and the probability of damage on the third pulse, p3:

$$P3 = P2 + [(1 - P2) \times p3] \quad . \qquad (3)$$

Equation (3) may be easily solved for p3, and used to calculate incremental probabilities such as p3 from experimental data. The only requirement is that damage probability versus fluence data be taken for adjacent values of N. In our data set, we have calculated p3 (since we had P2 and P3 data) and compared it to the P1 raw data as shown in figure 7. The agreement between these two curves supports the non-deterministic model. The non-deterministic model without any accumulation is adequate to describe the data, however, the deterministic model has not been eliminated. The existence of two possible models for laser damage of Si and the implications for how experiments should be conducted will be treated in the next section.

4. Discussion and Recommendations

In the discussion of the implications of our experiments, we will refer to a set of fictitious damage probability data shown in figure 8. The solid lines show the actual data which is perhaps unrealistically resolved in the regions of probability less than 0.1 and greater than 0.9. The data for each value of N has been least squares fitted to a linear curve shown as straight dashed lines in the figure. It is from these lines that the onset (0% probability intercept) and 50% threshold fluences are derived. According to these ways of defining damage threshold, this data shows accumulation. However, when the data in the upper and lower shaded boxes is considered, the non-deterministic model holds. There is really only a single onset energy, and all of the curves can be derived from a single curve for a given N using the projection method. Although the 50% thresholds decrease with increasing N, there is no real accumulation since there is a common onset threshold fluence and all the data may be projected from a single curve.

The implication for data collection is obvious but not very palatable; large amounts of data must be taken in order to resolve the damage probability curves in the shaded boxes, especially for probabilities less than 0.1. Even then, accumulation may not be unambiguously distinguished. A practical difficulty is that the data may be corrupted by site-to-site variations which, in an extreme case, could be a second cause for the data to have extended low probability tails as shown in figure 8. This case becomes nearly impossible to sort out. In a more optimum situation with minimal site-to-site fluctuations, onset is perhaps a better specifier for N-on-1 laser damage than is the 50% threshold. Complete specification of the damage probability curves is no doubt best. Other methods may be considered to resolve the situation. For example, probability curves for large values of N tend to be very steep and could be used to identify a possible common onset fluence value. It is still uncertain whether this onset is the same as that for lower values of N unless large amounts of data are taken.

Oddly enough, for some data taken for N>10 (not shown in this paper), there is an insignificant trend towards hardening or increasing damage threshold with increasing N. This effect was noticed when projections as from N=10 to 30 gave a higher damage probability than the N=30 data. This indicated that the N=30 data was based on a lower damage probability and, if significant, would have indicated the presence of hardening. The point of this example is that even though the onset and 50% damage fluences decreased from N=10 to N=30; if the decrease was not as large as projected by the non-deterministic model, then hardening would be indicated. Conversely, if the N=10 data projected to N=30 gave a lower damage probability than the N=30 data, accumulation would be indicated. This example illustrates how the non-deterministic model can be used to determine if accumulation or hardening is present.

The physical origins of the non-deterministic model may not be due to non-deterministic behavior of the sample but may arise due to small fluctuations in the laser pulses interacting with a strongly nonlinear response of the sample. The effect of small fluctuations will be greatly magnified in the damage probability curves and lead to non-deterministic behavior. On the other hand, the nucleation of melting is not a deterministic event but is strongly influenced by fluctuations near the critical point. These fluctuations could manifest themselves in the damage statistics.

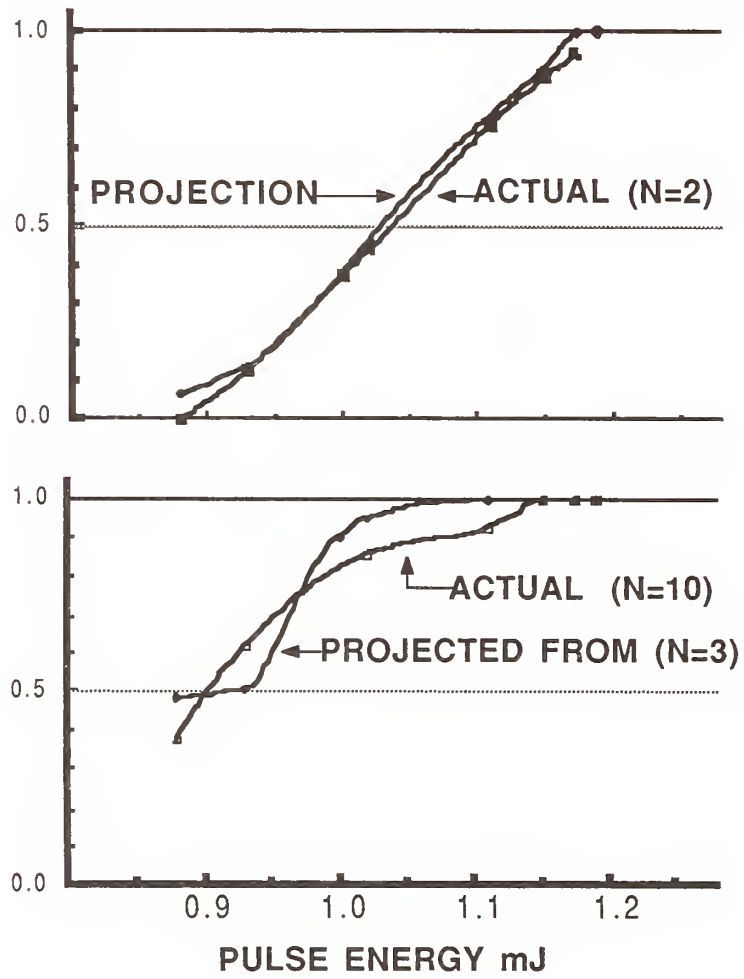

6. Projections of N=2 (top graph) and N=10 (bottom graph) from the N=3 data. Each projection is compared to the corresponding data for that value of N.

For the case of Si irradiated by a Q-switched Nd:YAG laser, neither the deterministic model nor the non-deterministic model has been unambiguously verified. Nor has the presence of a real accumulation been confirmed. Under these conditions, the threshold for multiple pulses is only reduced by at most 20%. This is not a strongly significant effect. It is possible that where the reduction in threshold with increasing N is large, accumulation may be unambiguously confirmed by experiments. Examples showing large apparent accumulation are Si irradiated with picosecond pulses [2] and GaAs irradiated with nanosecond pulses [10].

In conclusion, the hypothesized non-deterministic damage model is strongly supported by the reported damage data for Si. Unfortunately, neither the deterministic nor the non-deterministic model is unambiguously confirmed. The existence of real accumulation in this case is also still in doubt. Detailed data for damage probability less than 10% for a wide range of pulse numbers is required to make these fine distinctions, and such data is time consuming to acquire. Less data may be required to distinguish those cases where the apparent accumulation effect is larger than the 80-85% threshold reduction observed for Si damaged by nanosecond pulses.

This research was supported by the Texas Advanced Technology Research Program.

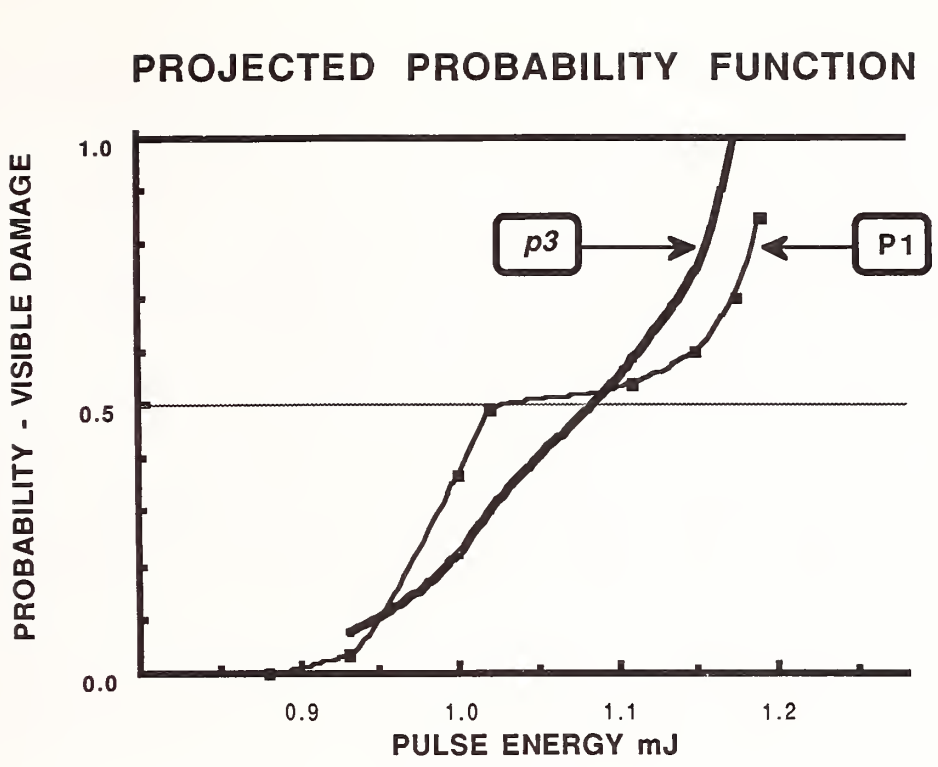

7. A comparison of the incremental damage probability on the third shot, p3, with the damage probability on the first shot, P1.

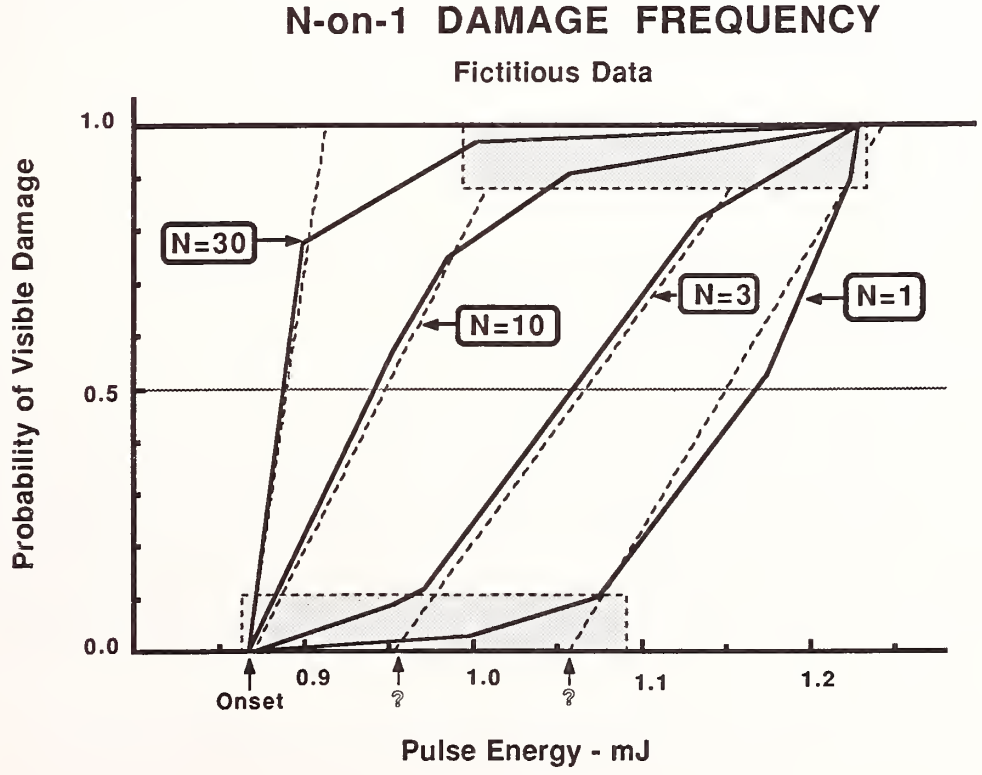

8. A set of fictitious damage probability curves which show apparent accumulation but actually obey the non-deterministic model. They are described more fully in the text.

5. References

[1] P.M. Fauchet and A.E. Siegman, "Surface ripples on silicon and gallium arsenide under picosecond laser illumination," Appl. Phys. Lett. **40**, 824 (1982).

[2] Y.K. Jee, M.F. Becker, and R.M. Walser, "Charge emission and precursor accumulation in the multiple-pulse damage regime of silicon," J. Opt Soc. Am. B **2**, 1626 (1985).

[3] Y. Kanemitsu, Y. Ishida, I. Nakada, and H. Kuroda, "Anomalous surface transformations in crystalline silicon induced by subpicosecond laser pulses," Appl. Phys. Lett. **48**, 209 (1986).

[4] A.L. Smirl, I.W. Boyd, T.F. Boggess, S.C. Moss, and H.M. van Driel, "Structural changes produced in silicon by intense 1-μm ps pulses,"J. Appl. Phys. **60**, 1169 (1986).

[5] Y. Jee, M.F. Becker, and R.M. Walser, "Laser-induced damage on single-crystal metal surfaces," J. Opt. Soc. Am. B **5**, 648 (1988).

[6] J.-D. Shin, M.F. Becker, and R.M. Walser, "Relating transient reflectivity to laser-induced damage of Si surfaces," to appear in the IEEE J. Quant. Elect. (1989).

[7] D.H. Auston, C.M. Surko, T.N.C. Venkatesan, R.E. Shlusher, and J.A. Golovchenko, "Time-resolved reflectivity of ion-implanted silicon during laser annealing," Appl. Phys. Lett. **33**, 437 (1978).

[8] J.R. Platenak, R.M. Walser, and M.F. Becker, "Temperature effects on laser induced damage and accumulation in silicon," Laser Induced Damage in Optical Materials: 1986, Nat. Bur. Stand. U.S. Spec. Publ. (1988).

[9] S.R. Foltyn, "Spotsize effects in laser damage testing," Laser Induced Damage in Optical Materials: 1982, Nat. Bur. Stand. U.S. Spec. Publ. #669, 368 (1983).

[10] D. K. Sardar, M.F. Becker and R.M. Walser , "Multipulse laser damage of GaAs surfaces," J. Appl. Phys. **62**, 3688 (1987).

The speaker was asked if he thought there was an accumulation effect in materials other than silicon. He answered that in metals they see amorphological evidence of slipping in n on 1 experiments. Using this data the onset is seen to shift downward slightly. There is then accumulation at 1 m wavelength on aluminum and copper curfaces, the ones studies. In gallium arsenide there may be some accumulation but a closer look is needed. In silicon for the pulse length used he did not see accumulation. Different damage morphology is found for silicon damaged by picosecond pulses or ion-beam implanted at low doses. The threshold is not affected but the morphology is and perhaps there is accumulation also but they do not have the data.

In response to another question the speaker stated that his results did not correspond to the theory proposed by Henry Musal in 1980. The calculated slip threshold was 1/5th to 1/10th of the threshold energy they observed damage at. It may have been that it would take several pulses to accumulate enough slip to see under Nomarski microscopy. However, they performed 30 to 100 shots per site.

- MANUSCRIPT NOT RECEIVED -

OBSERVATION OF TWO PHOTON ABSORPTION PRIOR TO LASER-INDUCED DAMAGE IN ZrO_2

Nastaran Mansour, Kamjou Mansour, M.J. Soileau
and Eric W. Van Stryland
Center for Research in Electro-Optics and Lasers
(CREOL)
University of Central Florida
Orlando, Florida 32817

ABSTRACT

We observed substantial dispersion in the breakdown electric field for yttria stabilized cubic zirconia (ZrO_2). The measured breakdown field at 1064 nm is a factor of 5 larger than that at 532 nm for 18 nsec (FWHM) pulses. For 532 nm pulses, we measured a significant decrease in transmission prior to the observation of catastrophic damage (i.e., damage accompanied by a spark and fracture of the sample). The observed nonlinear transmission is attributed to absorption by color centers generated by two-photon absorption (2PA). Presence of the color centers were directly monitored by transmission measurements. A permanent change in transmission was measured by irradiating the samples at high intensities (300 MW/cm^2). These induced defects are long lived (on the order of hours) but can be bleached by repeated irradiation with relatively low intensities (20 MW/cm^2). In a separate experiment, using picosecond pulses at 532 nm, the 2PA coefficient was determined to be 0.015 cm/GW.

Manuscript Received
3-8-88

Intense-Field Optical Interband Excitations in Semiconductors and Insulators

W. Becker and J.K. McIver

Center for Advanced Studies
and
Dept of Physics and Astronomy
University of New Mexico
Albuquerque, New Mexico 87131

and

A.H. Guenther

Air Force Weapons Laboratory
Kirtland Air Force Base, NM 87117

ABSTRACT

We enumerate a number of difficulties which one encounters in a nonperturbative treatment of optical interband excitations in semiconductors and insulators.

Key Words: semiconductors, insulators, and multi-photon excitations.

I. Introduction

In this paper we consider an external laser field so intense that it cannot adequately be dealt with in terms of perturbation theory. Whether or not perturbation theory is sufficient also depends to some extent on the physical quantity of interest. As a general rule, the more specific the question is that one asks the physical system, the less accessible is it to perturbation theory. For example, total ionization or excitation rates have been proven to allow for a calculation in terms of perturbation theory up to much higher intensities than differential ones. However, based on recent experience with multi-photon ionization of rare gases at high intensities (so called above-threshold ionization [1]) one may expect perturbation theory to become unreliable when the parameter $\eta=(eE_0)^2/(m\omega^3)$ approaches unity. Here E_0 and ω denote the field strength and frequency, respectively, of the laser field. For a CO_2-laser, $\eta=1$ corresponds to an intensity of about 10^{10} W/cm^2. Excitation from the valence into the conduction band, due to such a field, was first considered by Keldysh in a pioneering paper [2] and later elaborated on [3,4]. The approach was based on electron wave functions in the presence of both the periodic lattice and the laser field when neither one nor the other effect on the wave function could be considered as small. (It is interesting to notice the close relation to the problem of a periodic lattice in a constant electric field, viz. the controversial Wannier-Stark ladder [5]). In any event, the wave functions were essentially approximated by products of Bloch wave functions (describing the electron in the lattice without an external field) and Volkov wave functions (for a free electron in the laser field).

Up to quite recently, the problem might have been considered as a largely academic interest only. For a field that is intense in the above sense will so quickly destroy the lattice that the situation of an intact solid in an intense field never really arises. This has changed with the advent of high-intensity subpicosecond lasers so that for the first time one may be able to investigate "dressed bands" in a solid experimentally.

There is a close analogy between the present problem and electron-positron pair creation out of the vacuum in the presence of an intense external field. The analogy becomes particularly pronounced if one thinks of the vacuum of relativistic quantum electrodynamics in

terms of the filled Dirac Sea as the analog of the filled valence band. There are essentially two differences between the two cases. One is merely quantitative; while an electron only needs to absorb a small number of photons to be excited from the valence into the conduction band (leaving a hole in the former), a virtual electron-hole pair has to absorb on the order of $2mc^2/\hbar\omega$ photons to become a real pair. This fact is responsible for the different intensity scale of the two processes. However, a more important difference is the fact that the vacuum in the solid (i.e., the filled valence band plus the empty conduction band) has a structure given by the lattice, while the vacuum of relativistic QED does not. This difference is particularly important since electron-positron creation out of the vacuum in the presence of a purely plane wave laser field does not occur, no matter how intense the field is [6]. This result, surprising at first glance, becomes understandable if one tries to envision what the rate of pair creation per unit time and volume could be like [7]. Clearly, the rate can only depend on Lorentz and gauge scalars. Such can be constructed from the field tensor $F_{\mu\nu}(x)$ of the laser field and its dual $F^*_{\mu\nu}(x)$ as well as derivatives $\partial\mu=\partial/\partial x^\mu$. One easily sees [7] that all scalars which can be constructed out of these are zero. There are no other possible building blocks; for example, the vector potential $A_\mu(x)$ is not gauge invarient, and the total pair creation rate must not depend on any electron or positron velocities $p_\mu \mp \epsilon A_\mu$. This argument does not carry over to the solid due to the existence of additional vectors characterizing the vacuum, in this case, viz. the direct or reciprocal lattice vectors. (We here ignore the difficulties inherent in applying a genuinely relativistic argument to a nonrelativistic situation). It suggests, however, that umklapp processes might play an important role.

In this paper, we will pursue the analogy with the relativistic case and try to derive the excitation rate using the methods which have been developed [6] for electron-positron creation which, by necessity, are nonperturbative.

2. Electron Green's Functions

The field operator of the electron in the solid is

$$\psi(x) = \psi(\vec{x},t) = \sum_{\vec{k},i} \phi^{(i)}_{\vec{k}}(\vec{x},t) c^{(i)}_{\vec{k}} \qquad (2.1)$$

where the $c^{(i)}_{\vec{k}}$ are the electron annihilation operators, $\{c^{(i)}_{\vec{k}}, c^{(j)\dagger}_{\vec{l}}\} = \delta_{i,j}\delta_{\vec{k},\vec{l}}$, the sum over i is over the various bands and the sum over $\vec{k}$ over the first Brillouin zone. In the absence of the field, the wave functions are the Bloch functions

$$\phi^{(i)}_{\vec{k}}(\vec{x},t) = e^{i\vec{k}\vec{x}} u_{\vec{k}}(\vec{x}) e^{-iE_{\vec{k}}t}, \quad u_{\vec{k}}(\vec{x}+\vec{R}) = u_{\vec{k}}(\vec{x}) \qquad (2.2)$$

which satisfy the Schrodinger equation

$$\left(\frac{1}{2m}(\vec{p}+\hbar\vec{k})^2 + V(\vec{r})\right) u^{(i)}_{\vec{k}}(\vec{x}) = E^{(i)}_{\vec{k}} u^{(i)}_{\vec{k}}(\vec{x}) \qquad (2.3)$$

with V(r)=V(r+R) the periodic potential of the lattice. We will later restrict ourselves to just two bands, viz. the conduction and the valence band (i=c,v), and adopt the parabolic approximation so that

$$E_{\vec{k}}^{(c)} = \frac{\hbar^2 \vec{k}^2}{2m_c}, \quad E_{\vec{k}}^{(v)} = -E_v - \frac{\hbar^2 \vec{k}^2}{2m_v} \tag{2.4}$$

with effective masses m_c and m_v and gap enerty E_g.

In the presence of the laser field, which in the dipole approximation is described by the vector potential $\vec{A}(t)$, the wave functions satisfy

$$i\partial_t \phi_{\vec{k}}^{\vec{A}(i)}(x) = \left(\frac{1}{2m}\vec{p}^2 + V(\vec{r}) + H_I(t) \right) \phi_{\vec{k}}^{\vec{A}(i)} \tag{2.5}$$

where $H_I(t) = -e\vec{r}\vec{E}(t)$, or $H_I(t) = (2m)^{-1}(-2e\vec{p}\vec{A}(t) + e^2\vec{A}^2(t))$ depending on the gauge to be adopted. In the $\vec{p}\cdot\vec{A}$-gauge the periodicity of the lattice is preserved so that the crystal momentum $\vec{k}$ is conserved. We assume that when the field $\vec{A}(t)$ is turned off the band wave functions smoothly go over into those in the absence of the field

$$\phi_{\vec{k}}^{\vec{A}(i)}(x)\big|_{\vec{A}=0} = \phi_{\vec{k}}^{(i)}(x) \tag{2.6}$$

This assumption is far from evident [5] and may have to be abandoned. We also assume that the wave functions with or without the field are orthogonal and complete at any given time:

$$\int d^3x \phi_{\vec{k}}^{(i)}(\vec{x},t)^* \phi_{\vec{\ell}}^{(j)}(\vec{x},t) = \delta_{\vec{k},\vec{\ell}}\delta_{ij} \tag{2.7}$$

$$\sum_{\vec{k}\in 1^{st}BZ} \phi_{\vec{k}}^{(i)}(\vec{x},t)\phi_{\vec{k}}^{(i)}(\vec{x}',t)^* = \rho^{(i)}(\vec{x},\vec{x}',t) \tag{2.8}$$

$$\sum \rho^{(i)}(\vec{x},\vec{x}',t) = \delta(\vec{x}-\vec{x}') \tag{2.9}$$

(We drop the superscript $\vec{A}$ whenever possible.)

The ground state $|0\rangle$ (at temperature T=0) is defined by the condition that all bands above the Fermi energy are empty and all those below are filled, i.e.

$$c_{\vec{k}}^{(c)}|0\rangle = c_{\vec{k}}^{(v)\dagger}|0\rangle = 0 \tag{2.10}$$

for all $\vec{k}$. The Green's function, with respect to this vacuum state, is then defined by

$$\begin{aligned} iG(x,x') &= iG(\vec{x},t;\vec{x}',t') = \langle 0|T\psi(x)\psi^\dagger(x',|0\rangle \\ &= \theta(t-t')\langle 0|\psi(x)\psi^\dagger(x')|0\rangle - \theta(t'-t)\langle 0|\psi^\dagger(x')\psi(x)|0\rangle \\ &= \theta(t-t')\sum_{\vec{k}} \phi_{\vec{k}}^{(c)}(x)\phi_{\vec{k}}^{(c)}(x')^* - \theta(t'-t)\sum_{\vec{k}} \phi_{\vec{k}}^{(v)}(x)\phi_{\vec{k}}^{(v)}(x')^* \end{aligned} \tag{2.11}$$

with the wave functions (2.2) or (2.5), respectively, in the absence or in the presence of the field.

As a consequence of the orthogonality relation (2.7) the powers of the operator G which are defined by

$$G^n(x,x') = \int d^3y_1\, d\tau_1 \ldots d^3y_{n-1}\, d\tau_{n-1}\, G(\vec{x}t;\vec{y}_1\tau_1)\times \\ \times G(\vec{y}_1\tau_1;\vec{y}_2\tau_2)\times\ldots\times G(\vec{y}_{n-1}\tau_{n-1};\vec{x}'t') \tag{2.12}$$

satisfy

$$G^n(x,x') = \frac{(-i(t-t'))^{n-1}}{(n-1)!}G(x,x'). \tag{2.13}$$

The logarithm of G is defined by its power series and can be expressed as

$$\log G = \sum_{n=1}^{\infty}\frac{1}{n} + \frac{iG}{t-t'+i\epsilon} \tag{2.14}$$

The infinite constant cancels when the difference of the logarithms of two different Green's functions is considered.

3. Excitation Rate

All information about total excitation rates is contained in the vacuum persistence amplitude [6]

$$S_0 = \langle 0in|S|0in\rangle \tag{3.1}$$

where |0in> denotes the vacuum at the intitial time and S the time evolution operator from this initial to a later time. The probability that the vacuum remains the vacuum is given by $|S_0|^2$. It can be shown that [6] (see also [8])

$$S_0 = e^{-\mathrm{Tr}\log GG_0^{-1}} = e^{-\mathrm{Tr}(\log G - \log G_0)} \tag{3.2}$$

where G is the exact time-ordered Green's function of the electron in the presence of both the lattice and the field, and G_0 the Green's function in the absence of the field but with the lattice. Their matrix elements are defined in Eq. (2.11). The symbol Tr denotes the trace of the subsequent operator, i.e., integration over space and time:

$$\mathrm{Tr}A = \int d^3x dt\, A(\vec{x}t,\vec{x}t).$$

In view of Eq. (2.14) the vacuum persistence amplitude can be written in the form

$$S_0 = \exp -i \int dt \lim_{t' \to t} \int d^3x \frac{G(\vec{x}t;\vec{x}t') - G_0(\vec{x}t;\vec{x}t')}{t - t' + i\epsilon} \qquad (3.3)$$

The apparent singularity when t→t'is only superficial. For from Eqs. (2.11), (2.8), and the assumption (2.6) that the band wave functions change adiabatically when the field is turned on, we have that

$$G(\vec{x}t;\vec{x}t) - G_0(\vec{x}t;\vec{x}t) = 0$$

In order to make futher progress an explicit form for the Green's function $G(\vec{x}t,\vec{x}t')$ is required. A simple approximation is obtained if one adopts the product wave functions suggested by Keldyxh [2] and rewritten in the $\vec{p}\cdot\vec{A}$ gauge [3,4]. With the parabolic band approximation (2.4) they read

$$\phi_{\vec{k}}^{\vec{A}(c)}(\vec{x},t) = u_{\vec{k}}^{(c)}(\vec{x}) e^{i\vec{k}\vec{x}} e^{-\frac{1}{2mc}\int^t dr(\vec{k} - e\vec{A}(r))^2} \qquad (3.4a)$$

$$\phi_{\vec{k}}^{\vec{A}(v)}(\vec{x},t) = u_{\vec{k}}^{(v)}(\vec{x}) e^{i\vec{k}\vec{x}} e^{i\int^t dr(E_g + \frac{1}{2m_v}(\vec{k} - e\vec{A}(r))^2)} \qquad (3.4b)$$

With these wave functions, the Green's function (2.11) can be immediately constructed. We obtain

$$\begin{aligned}\lim_{t' \to t} \frac{G(\vec{x}t;\vec{x}t') - G_0(\vec{x}t;\vec{x}t')}{t - t'} = \lim_{t' \to t} \sum_{\vec{k}} (e\vec{k}\vec{A}(t) - \frac{e^2}{2}\vec{A}^2(t)) \\ \times (\frac{1}{m_c}\theta(t - t') u_{\vec{k}}^{(c)}(\vec{x}) u_{\vec{k}}^{(c)}(\vec{x})^* \\ + \frac{1}{m_v}(1 - \theta(t - t')) u_{\vec{k}}^{(v)}(\vec{x}) u_{\vec{k}}^{(v)}(\vec{x})^*). \qquad (3.5)\end{aligned}$$

In principle, at this point, the question comes up which value to assign to $\theta(0)$. However, we do not have to face this problem here since, in any event, the quantity (3.5) comes out to be real. Consequently, the vacuum persistence amplitude (3.3) is a pure phase, $|S_0|^2 = 1$, and no excitations take place. The immediate responsibility for this no-result has to be assumed by the wave functions (3.4). It is possible, however, that it has to be traced back ultimately to be adiabaticity assumption (2.6).

Alternatively, we may evaluate S_0 directly from Eq. (3.2). From the integral equation

$$G = G_0 + G_0 H_I G = G_0 + G H_I G_0$$

we have

$$G = (1 - G_0 H_I)^{-1} G_0 \qquad (3.6)$$

and

$$\log S_0 = \mathrm{Tr} \log(1 - G_0 H_I) \qquad (3.7)$$

Expasion of the logarithm then leads to straightforward perturbation theory with respect to H_1. The first order is purely imaginary, to second order we obtain

$$\mathrm{Re} \log S_0 = -\sum_{\vec{k},\vec{\ell}} \left| \int d^3x dt \phi_{\vec{\ell}}^{(e)}(x)^* H_I(x) \phi_{\vec{k}}^{(v)}(x) \right|^2 . \qquad (3.8)$$

This is the result of lowest order perturbation theory, which could have been written down right away. (It is, of course, only different from zero if $\hbar\omega > E_g$.)

It is tempting to try to improve on this expansion by using the alternative form

$$\log S_0 = -\mathrm{Tr} \log(1 + G H_I) \qquad (3.9)$$

in place of (3.7) and again expanding the logarithm. At first glance, one might expect this procedure to lead to an improved approximation scheme where the wave-functions $\phi_{\vec{k}}^{(i)}(x)$ in the absence of the field are replaced by the wave functions $\phi_{\vec{k}}^{A\,(i)}(x)$ in the presence of the field. However, while Eq. (3.9) is, of course, exact, an expansion of the logarithm does not afford a viable approximation scheme as different orders of the expansion will contain identical terms. An even more severe problem emerges if one considers

$$\mathrm{Tr} G H_I = \mathrm{Tr} G_0 H_I + \mathrm{Tr}(G_0 H_I)^2 + \mathrm{Tr}(G_0 H_I)^3 + \cdots \qquad (3.10)$$

where the right hand side is an expansion in terms of the interaction with the external field. (Incidentally, TrGH_1 is the leading term of an expansion of Eq. (3.9)). If the form (2.11) is used for both Green's functions (with wave functions $\phi_{\vec{k}}^{iA}(x)$ and $\phi_{\vec{k}}^{(i)}(x)$, respectively) the left hand side and the first, third,...term on the right hand side come out to be imaginary while the second, fourth,...terms are real. The latter terms cannot cancel each other as they are of different order in the interaction with the external field. This casts doubts on the legitimacy of the representation (2.11) of the Green's function in the field, and thereby, on the adiabaticity assumption (2.6).

REFERENCES

1. See, e.g. the Topical issue on "Multielectron excitations in atoms", J. Opt. Soc. Am. 4, (1987), No. 5.

2. L.V. Keldysh, Zh. Eksp. Teor. Fiz. 47 (1964) 1945; [Sov. Phys. JETP 20 (1965) 1307.

3. H.D. Jones and H.R. Reiss, Phys. Rev. B16 (1977) 2466.

4. L.C.M. Miranda, J. Phys. C9(1976) 2971; O.A.C. Nunes, J. Appl. Phys. 58 (1985) 2101.

5. G.H. Wannier and J.P. van Dyke, J. Math. Phys. 9 (1968) 899; J.N. Churchill and F.E. Holmstrom, Phys. Scripta 34 (1986) 269; J.B. Krieger and G.J. Iafrate, Phys. Rev. 33 (1968) 5494.

6. J. Schwinger, Phys. Rev. 82 (1951) 664.

7. S. Deser, J. Phys. A 8, 1638 (1975).

8. C. Itzykson and J.B. Zuber, Quantum Field Theory (McGraw Hill, 1980).

A question was raised as to the completeness of the Bloch functions. Do they cover extrinsic properties of the samples such as deep level impurities which are not periodic in the lattice? The author replied in the negative. The wave functions would have to be modified to do that.

Another question was raised as to the completeness of the combined wavefunctions. The speaker replied that that was hard to answer. They looked at a perturbation approach to explore that question. First indications are that they are not complete, although it is hard to prove. Orthogonality, at least within the second order perturbation approach taken, still holds but the completeness looks questionable.

Manuscript Received
12/21/87/sar

Behavior Studies on Dirt Spikes in Laser Discharge and Their Effects on Thyratron Operations

Chin E. Lin
Institute of Aeronautics and Astronautics

C. Y. Yang, C. L. Huang
Department of Electrical Engineering

Cheng Kung University
Tainan
Taiwan, China

In high repetition rate and high di/dt laser discharges, small concentrations of impurities in the laser tube may cause significant degradation to the laser output. More seriously, the presence of impurities in the discharge may cause dirt spikes on the thyratron, and will result damages to its anode. In this paper, the influences of impurities in laser discharge are investigated from the electrical viewpoints. The generation of dirt spikes is explained by the concept of Townsend discharge and electron attachment. Water vapor is found to be the dominant impurity to cause the dirt spike generation. The dirt spike effects on thyratron operation are studied. A new rating factor, termed as the D_b factor, is deduced from the π_b factor. This factor is proved with accuracy by comparisons with the experimental results. Measurement methods to reduce the damages of thyratron are discussed. Under well-characterized operation, the lifetime of thyratron can certainly be extended by the results of this study.

Keywords: Dirt Spikes, D_b Factor, Electron Attachment, Townsend Discharge.

1. INTRODUCTION

The presence of contaminants in high repetition rate and high di/dt laser discharges brings troubles in operations. It results very unstable discharges and causes dirt spikes on the thyratron anode. The dirt spikes increase additional loads to thyratron duties. Reliable operation and high power output can not be achieved unless the laser is free from contaminants. Significant damage and possible failure of thyratron operation may occur if the laser is not properly decontaminated.

By analyzing the electrical characteristics of the pulse circuit, the breakdown time of the laser tube is found to be a function of the amplitude of dirt spikes. From the relation between the effective primary electron number density and the critical avalanche electron number density of Townsend discharge, negative ion formation by the attachment of slow electrons is suggested to occure in the discharge when impurities appear in the laser tube. Quite frequently, these impurities are known as water vapor. The suggested mode is proved and supported by the analysis of mass spectrometer and by the observation of the characteristics of laser diacharges.

In the high repetition rate and high di/dt thyratron pulse generator, the thyratron is used as the main discharge switch. Most thyratron lifetime data, for either laser system applications or radar system applications, are obtained under such conditions that the thyratrons are operated close to their absolute maximum capabilities. In general, thyratron manufacturers specify an acceptable tube lifetime of 1000 hours. However, much longer lifetime for several thousand hours can be achieved if the thyratrons are operated under their absolute maximum capabilities.

Thyratron specifications include a plate breakdown factor, P_b, to limit the anode power dissipation to a tolerable level. Under high di/dt conditions, the P_b factor is inadequate to describe the power dissipation. Because the time scale is too short for thermal conduction to dissipate the heat, the anode surface is flashed to the vaporization point at the beginning of each pulse. Consequently, another factor is developed to include current risetime in this effect. This factor is termed as the π_b factor [1].

The analysis concerning in this paper discusses the dirt spike effects on thyratron operations. It has major contribution to the pulsed laser discharges from an electrical viewpoint. The theoretical analysis and experiments express the efforts of this study. In this paper, the

effects of dirt spike on thyratron operation is determined. A simple method which can be applied to monitor the appearance of dirt spikes in laser discharge is proposed. Two methods for minimizing the dirt spike effects on thyratron operation are presented. Their results are shown with significant improvements in laser operations.

2. ELECTRICAL BREAKDOWN OF CONTAMINATED LASERS

Figure 1 shows a typical pulse circuit for application in the high repetition rate and high di/dt laser discharges. The charging capacitor C_s is resonantly charged from the power supply, and then discharged to the laser tube through the thyratron. Under clean conditions, the discharge voltage on the thyratron is free from dirt spikes. However, if the laser tube is contaminated, the discharge voltage of thyratron will introduce dirt spikes. Figure 2 shows the appearance of the voltage waveforms from thyratron anode, both when the laser is clean and when the laser is contaminated. The generation of dirt spikes in the laser discharges can be explained by the result of characteristic study on the discharge circuit.

In the pulse circuit as shown in Figure 1, the charges stored on the charging capacitor C_s is transferred to the peaking capacitor C_p through thyratron when the thyratron is triggered. When the voltage applied between the electrodes of the laser tube becomes higher than the breakdown voltage, the laser current starts. If the breakdown time of the laser tube is sufficiently short, the charges stored on the peaking capacitor C_p will dump into the laser tube without any reflection on the arc level of thyratron. However, if the breakdown time of the laser tube is too long, the voltage across the peaking capacitor C_p will reflect to the charging capacitor C_s and will cause a reverse voltage on the arc level of thyratron. This reverse voltage is known as a dirt spike. Therefore, breakdown time of the laser tube is the dominant factor to result in dirt spike generation by the effect of impurities in the laser tube.

From the theory of Townsend discharge, the breakdown time T_b is equal to the discharge formation time from the generation of an effective primary electron number density N_0 to the beginning of discharge when the number density of electrons in an avalanche exceeds the critical number density N_c [2]. The relation between N_0 and N_c is given by:

$$\log_N(N_c) - \log_N(N_0) = \int_0^{T_b} \alpha v_d dt, \tag{1}$$

where α is the first Townsend coefficient for ionization by electron impact, v_d is the drift velocity, and both are a function of E/P, i.e., the electric field divided by the buffer gas pressure. At a given discharge condition, the integral of Equation (1) should always be constant, and the breakdown time T_b of each discharge should also be equal.

When contaminants present in the laser tube, the breakdown time of laser tube increases. It is shown that the electrical characteristics of the contaminated laser is smimilar to that of a laser with unsatisfactory preionization [3]. The presence of contaminants is assumed to reduce the number density of free electron which is caused by electron attachment. From the analyssis of mass spectrometer and reference [4] result, the dominant contaminant which causes dirt spikes is suggested to be water vapor. When low energy electrons pass through water vapor, electron attachment to the neutral molecules occurs. Electron attachment to H_2O may give rise to O^-, H^-, and OH^-. Each of these ions will be formed in the dissociation process with different kinetic energy.

$$e^- + H_2O \longrightarrow {}^*H_2O^- \longrightarrow \begin{matrix} H^- \\ O^- \\ OH^- \end{matrix} + \text{products}, \tag{2}$$

where the principle negative ion formed by electron impact in water is H^-, the negative atomic oxygen ion O^- is about ten times less abundant than H^-, the cross section for the production of OH^- is the lowest among them [5, 6, 7]. From the analysis of mass spectrometer, the relative intensities of H^+, O^+ and OH^+ are found to be increasing when dirt spike appears. Moreover, the cited effects, i.e., instabilities, striations, and bright glows near electrode surfaces, of adding an electronegative gas to a discharge are observed. It is sure that formation of negative ions by

attachment of slow electrons should occure when the impurity such as water vapor is presented in the laser tube.

When electron attachment occurres in the discharges, Equation (1) can be modified to include the effect of attachment, it becomes:

$$\log_N(N_c) - \log_N(N_0) = \int_0^{\bar{T}_b} \bar{\alpha} v_d dt, \tag{3}$$

and

$$\bar{\alpha} = \alpha - \beta, \tag{4}$$

where β is the attachment coefficient with the same factor as the first Townsned coefficient α, $\bar{\alpha}$ is the effective ionization coefficient. Compare Equation (1) with Equation (3), the breakdown time of a contaminated laser is found to be longer than that of a clean laser.

3. DIRT SPIKE EFFECTS

The critical component in the high repetition rate and high di/dt pulse generator is the thyratron. Table 1 shows the rating specifications of some different types of thyratrons [9]. To select a thyratron are usually determined by a combination of the following parameters:

a. e_{py} -- peak forward anode voltage,
b. I_b -- peak anode current,
c. f -- repetition rate,
d. di_b/dt -- rate of current rise in thyratron,
e. I_a -- average current.

Table 1. Tyratron Specifications.

Type	Mfg	Maximum Ratings			
		e_{py}(Kv)	I_b(KA)	I_a(A)	P_b
HY-32	EG&G	35	1.5	2.2	50
HY-53	EG&G	40	5.0	4.0	100
HY-7	EG&G	40	40.0	50.0	400
CX-1535	EEV	25	1.0	1.25	500
CX-1536	EEV	70	10.0	10.0	300
CX-1625	EEV	35	15.0	5.0	100
KU-275	ITT	50	5.0	8.0	400 ($\times 10^9$)

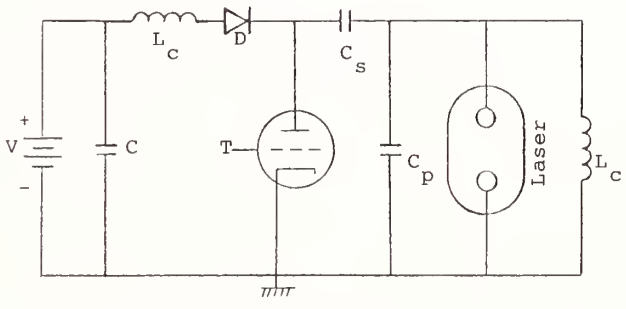

Figure 1. Typical high repetition rate, high di/dt thyratron pulse generator.

Two rating factors are to be checked to extend thyratron lifetime. The first rating factor is the plate breakdown factor P_b, where,

$$P_b = e_{py} \cdot I_b \cdot f, \quad \text{VA/sec} \tag{5}$$

The plate breakdown factor varies with different thyratrons. In general, it can be obtained from thyratron manufactures' data sheets. Another rating factor is developed to include the current risetime. This factor is denoted as π_b factor, where,

$$\pi_b = e_{py} \cdot (di_b/dt) \cdot f, \quad \text{VA/sec}^2 \tag{6}$$

The π_b factor, limited to be less than 10^{18} VA/sec^2, gives better assurance that the thyratron may have reasonable operating lifetime [10].

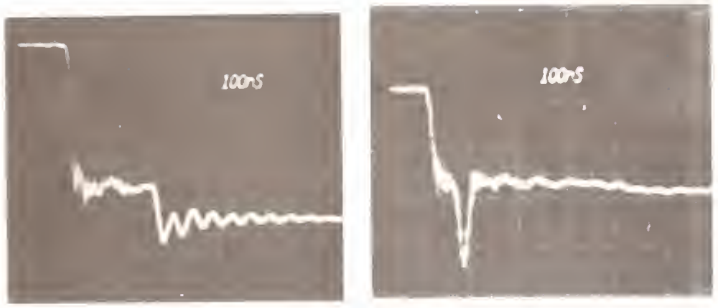

Figure 2. Voltage waveform on thyratron anode, (a) clean laser, (b) contaminated laser.

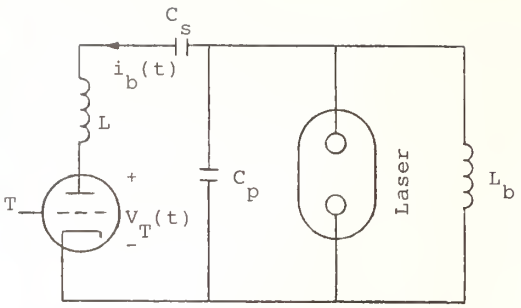

Figure 3. Circuit model of discharge circuit analysis.

If there are contaminants in the laser, the discharge voltage of thyratron will cause a dirt spike. Because of the influence of dirt spikes, a new π_b factor including the dirt spike effect can be formulated as:

$$\pi'_b = e_{py} \cdot (di_b/dt) \cdot f + e_r \cdot (di_r/dt) \cdot f, \tag{7}$$

where e_r is the peak reverse voltage of the dirt spike, di_r/dt is the rate of current change caused by the dirt spike.

In order to investigate the dirt spike effect, a circuit model for presenting the discharge current is shown in Figure 3. The circuit elements are:

L is the total switch and loop inductance, $i_b(t)$ is the tube current,

$V_T(t)$ is the voltage drop across the tube,

and other elements are as presented as in Figure 1. Figure 4 shows the parameter definitions of the anode voltage and the anode current. If the initial plasma conditions of laser are not properly established and $L \ll L_b$, then, the differential equation of discharge circuit before laser breakdown is:

$$V_T(t) + L di_b(t)/dt + 1/C_s \cdot \int_{-\infty}^{t} i_b(t)dt + 1/C_p \cdot \int_{-\infty}^{t} i_b(t)dt = 0. \tag{8}$$

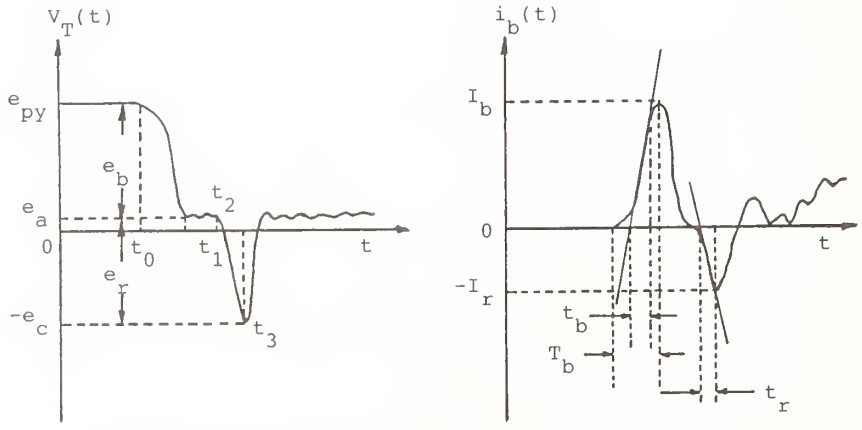

(a) Anode voltage (b) Anode current

Figure 4. Parameter definitions for thyratron waveform.

From Figure 3, and 4,

$$V_T(t_0) + Ldi_b(t_0)/dt + 1/C_s \cdot \int_{-\infty}^{t_0} i_b(t)dt + 1/C_p \cdot \int_{-\infty}^{t_0} i_b(t)dt =$$

$$e_{py} + Ldi_b(t_0)/dt + 1/C_s \cdot \int_{-\infty}^{t_0} i_b(t)dt + 1/C_p \cdot \int_{-\infty}^{t_0} i_b(t)dt = 0. \quad (9)$$

$$V_T(t_1) + Ldi_b(t_1)/dt + 1/C_s \cdot \int_{-\infty}^{t_1} i_b(t)dt + 1/C_p \cdot \int_{-\infty}^{t_1} i_b(t)dt =$$

$$e_a + Ldi_b(t_1)/dt + 1/C_s \cdot \int_{-\infty}^{t_1} i_b(t)dt + 1/C_p \cdot \int_{-\infty}^{t_1} i_b(t)dt = 0. \quad (10)$$

Combining Equation (9) and Equation (10), it becomes:

$$Ldi_b(t_1)/dt - Ldi_b(t_0)/dt = e_{py} - e_a - (C_s+C_p)/C_sC_p \cdot \int_{t_0}^{t_1} i_b(t)dt. \quad (11)$$

At the beginning of the conducting period, $di_b(t_0)/dt = 0$, and at high di/dt condition, the last term at right hand side of Equation (11) can be ignored. Then Equation (11) can be simplified to be:

$$\begin{aligned} di_b/dt_{max} &\doteqdot di_b(t_0)/dt \\ &= (e_{py} - e_a)/L \\ &\doteqdot e_b/L. \end{aligned} \quad (12)$$

Notice that all specified terms are defined and shown in Figure 4. The result of Equation (12) may not be the actual maximum rate of current rise. However, it is important that Equation (12) can determine at least an approximate maximum.

If the dirt spike appears, from Figure 3, and Figure 4, the discharge circuit becomes:

$$V_T(t_2) + Ldi_b(t_2)/dt + 1/C_s \cdot \int_{-\infty}^{t_2} i_b(t)dt + 1/C_p \cdot \int_{-\infty}^{t_2} i_b(t)dt =$$

$$e_a + Ldi_b(t_2)/dt + 1/C_s \cdot \int_{-\infty}^{t_2} i_b(t)/dt + 1/C_p \cdot \int_{-\infty}^{t_2} i_b(t)dt = 0. \quad (13)$$

$$V_T(t_3) + Ldi_b(t_3)/dt + 1/C_s \cdot \int_{-\infty}^{t_3} i_b(t)dt + 1/C_p \cdot \int_{-\infty}^{t_3} i_b(t)dt =$$

$$- e_c + Ldi_b(t_3)/dt + 1/C_s \cdot \int_{-\infty}^{t_3} i_b(t)dt + 1/C_p \cdot \int_{-\infty}^{t_3} i_b(t)dt = 0. \quad (14)$$

Combining Equation (13) and Equation (14), it becomes:

$$Ldi_b(t_3)/dt - Ldi_b(t_2)/dt = e_a + e_c - (C_s+C_p)/C_sC_p \cdot \int_{t_2}^{t_3} i_b(t)dt. \quad (15)$$

Because $i_b(t_3)$ is the maximum value of the reverse current, then $di_b(t_3)/dt = 0$; and at high di/dt condition, the last term at right hand side of Equation (15) can be ignored. Equation (15) can then be simplified as:

$$di_r/dt_{max} \doteq -\, di_b(t_2)/dt$$
$$= (e_a + e_c)/L$$
$$\doteq e_r/L. \tag{16}$$

Substituting Equations (12), and (16) into Equation (7), it becomes:

$$\pi'_b \doteq e_{py}\cdot(e_b/L)\cdot f + e_r\cdot(e_r/L)\cdot f$$
$$= e_{py}\cdot(e_b/L)\cdot f\cdot[\,1 + e_r^2/(e_{py}\cdot e_b)].$$
$$= \pi_b\,[\,1 + e_r^2/(e_{py}\cdot e_b)]. \tag{17}$$

In general $e_{py} >> e_a$, then,

$$\pi'_b \doteq \pi_b\cdot(\,1 + e_r^2/e_{py}^2\,)$$
$$= \pi_b\cdot D_b, \tag{18}$$

where D_b is a new factor in terms of the dirt spike factor for:

$$D_b = [\,1 + e_r^2/e_{py}^2\,]. \tag{19}$$

In order to verify the previous derivation, a pulse circuit as shown in Figure 1 by the circuit component C_s = 4 nf and C_p = 1 nf, and a plasma tube, with inner diameter 4.2 cm and length 150 cm, are used to measure the actual data. The instruments are composed of: (1) Tektronix 7834 oscilloscope, (2) Tektronix P-6015 high-voltage probe with 1000:1, (3) Rogowski coils with 2.5 V/KA. Tables 2 and 3 are the measurement data and their calculations.

Table 2. Experimental data and their calculation results.

e_{py} (Kv)	e_b (Kv)	I_b (A)	t_b (ns)	T_b (ns)	I_b/t_b ($\times 10^9$)	e_b/L ($\times 10^9$)	K_1	K_1' ($\times 10^{-2}$)
16	14.0	305	20	40	15.0	17.3	0.87	2.2
15	13.0	280	20	40	14.0	16.0	0.88	2.2
14	12.0	260	20	40	13.0	14.8	0.88	2.2
13	11.2	235	20	40	11.8	13.8	0.86	2.1
12	10.2	215	20	40	10.8	12.6	0.86	2.1
10	8.2	170	20	40	8.5	10.1	0.84	2.1
8	6.4	140	20	40	7.0	7.9	0.89	2.2

(L = 810 nH, $I_b/t_b = K_1 e_b/L$, $I_b = K_1' e_b$.)

Table 3. Experimental data and their calculation results.

e_r (Kv)	I_r (A)	t_r (nS)	I_r/t_r ($\times 10^9$)	e_r/L ($\times 10^9$)	K_2	K_2' ($\times 10^{-2}$)
10	100	10	10.0	12.0	0.83	1.0
8	80	10	8.0	9.8	0.82	1.0
6	70	10	7.0	7.4	0.94	1.2
5	60	10	6.0	6.2	0.97	1.2
4	50	10	5.0	4.9	1.02	1.2
3	40	10	4.0	3.7	1.08	1.3
2	32	10	3.2	2.5	1.28	1.6

(L = 810 nH, $I_r/t_r = K_2 e_r/L$, $I_r = K_2' e_r$.)

From Table 2 and Table 3,

$$di_b/dt = I_b/t_b$$
$$= K_1 e_b/L,$$

for K_1 = 0.84 to 0.89,

$$di_r/dt = I_r/t_r$$
$$= K_2 e_r/L,$$

for K_2 = 0.82 to 1.28. And, the π_b factor including the dirt spike effect is:

$$\pi'_b = e_{py} \cdot (di_b/dt) \cdot f + e_r \cdot (di_r/dt) \cdot f$$
$$= e_{py} \cdot K_1 (e_b/L) \cdot f + e_r \cdot K_2 (e_r/L) \cdot f$$
$$= e_{py} \cdot K_1 e_b/L \cdot f \cdot [\ 1 + (K_2/K_1)(e_r^2/e_{py} e_b)\ ]$$
$$\doteq \pi_b \cdot [\ 1 + (K_2/K_1)(e_r^2/e_{py}^2)\ ]$$
$$= \pi_b \cdot [\ 1 + K \cdot e_r^2/e_{py}^2\ ],$$

for $K = K_2/K_1$. From Table 2 and Table 3, K = 1 is a reasonable value. The previous calculation is concluded that Equations (12) and (16) have some error compared to the actual measurements. However, Equation (18) is correct to meet the measurements.

In the high repetition rate and high di/dt laser circuits, the D_b factor is very important. Under such conditions, that the thyratron is operated close to the margin of the upper limit of the π_b factor, i.e., 10^{18} VA/sec^2, even a small increase of the D_b factor can reduce the thyratron lifetime in a great deal. The dirt spike may cause a reverse current. This current will cause influence to the plate breakdown factor in Table 2 and Table 3,

$$P_b' = e_{py} \cdot I_b \cdot f + e_r \cdot I_r \cdot f$$
$$= e_{py} \cdot K_1' e_b \cdot f + e_r \cdot K_2' e_r \cdot f$$
$$= e_{py} \cdot K_1' e_b \cdot f\ [\ 1 + (K_2'/K_1') \cdot e_r^2/(e_{py} e_b)\ ]$$
$$\doteq P_b\ [\ 1 + K'(e_r^2/e_{py}^2)\ ]$$
$$\doteq P_b\ [\ 1 + 0.5(e_r^2/e_{py}^2)\ ],$$

where $K' = K_2'/K_1'$ is very close to 0.5 under the specified conditions. However, under high di/dt and high repetition rate conditions, the P_b factor is not the dominant limitation. If the reverse maximum current is limited to be less than 10 percent of the forward maximum current [11], the dirt spike effect on the P_b factor can be neglected.

4. DIRT SPIKE MEASUREMENT AND PROTECTION

4.1 Dirt Spike Measurements

Conventional method to monitor the appearance of dirt spike uses a high voltage probe to measure the anode voltage of thyratron together with a fast response oscilloscope. For continuous monitoring the discharge condition, this method is not economical. A null detector +/- 0.5A DC current meter is proposed [3] in series with the by-pass inductor L_b of Figure 1 as a dirt spike monitor. From the deflctions, the appearance of dirt spikes can be determined. Figure 5 shows the speified limits of the deflection of DC current meter for well discharge conditions. This method costs much less than the conventional method for the same purpose.

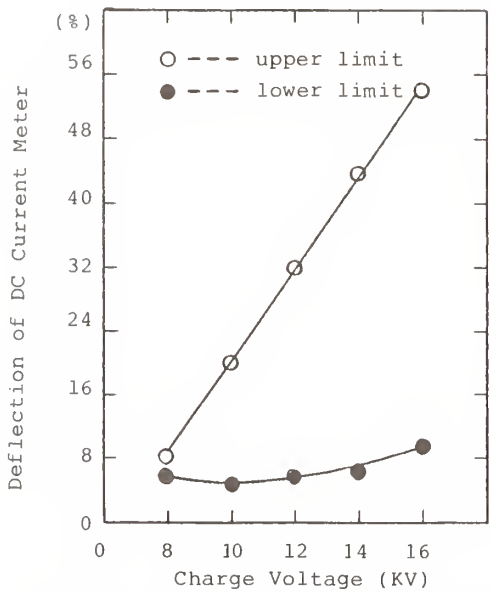

Figure 5. Specified limits of the deflection of the DC current meter under well discharge conditions.

4.2 Minimizing Dirt Spike Effects

Two methods which can effectively minimize the dirt spike effect are discussed. The first method is the series inductor method which introduces a small inductor in series with the thyratron anode. This application limits the rate of current rise and reduces the amplitude of the peak anode current which can also diminish the reverse current. Figure 6 shows the effect of the first method.

The second method is the peaking capacitor withdrawal method which withdraws the peaking capacitor from the pulse circuit to prevent the reflection of reverse voltage when the laser tube is contaminated. The experimental result indicates that the dirt spike can efficiently be removed. Figure 7 shows the effect of this method.

5. CONCLUSIONS

Dirt spike effect causes serious damage to thyratron operations in laser discharges, especially in high repetition rate and high di/dt lasers. The formations of dirt spike are studied, methods for measurement are investigated, and improvements on dirt spike effects are discussed. The aspects of behavior studies on dirt spikes and their effects on thyratron operations are consistent with the performance of high repetition rate, high di/dt laser discharges. The elimination or reduction of dirt spikes leads to longer operation lifetime of thyratrons.

6. ACKNOWLEDGEMENT

The technical assistants, Mr. Y. Y. Huang, Mr. C. H. Chen, and Mr. F. B. Luou, are greatly appreciated for their helps in experiments. Also, the authors would like to give their sincere thanks to Dr. T. C. Wang for his valuable guidance and advices.

7. REFERENCES

[1] Turnquist D., Caristi R., Friedman S., Merz S., Plante R., and Reinhardt N., New hydrogen thyratrons for advanced high power switching, IEEE Trans. on Plasma Science, PS-8, 185-190, 1980 Sept.

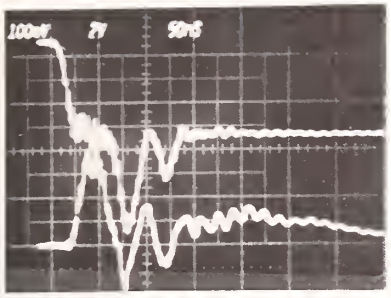

voltage

current

(a) without series inductor

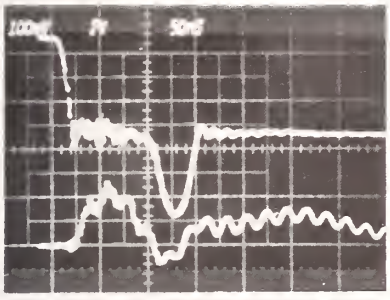

voltage

current

(b) with 2 uH series inductor

Figure 6. The effect of series inductor for dirt spike elimination.

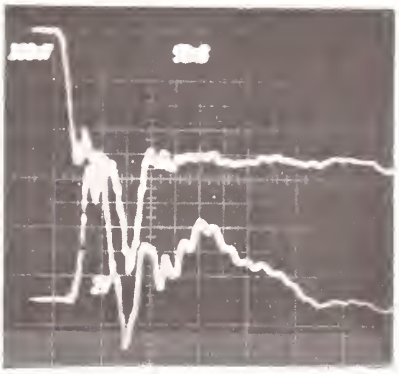

voltage

current

(a) with peaking capacitor

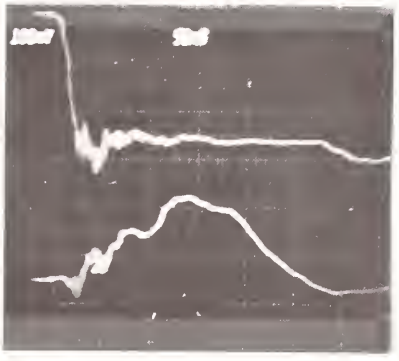

voltage

current

(b) without peaking capacitor

Figure 7. The effect of peaking capacitor withdrawal.

[2] Sakurai T., Watanabe T., Characteristics of the discharge current in the nanosecond-pulse breakdown, J. Appl. Phys., 59(12), 4007-4010, 1986 June.

[3] Lin C. E., Yang C. Y., Wang T. C., and Huang C. L., The dirt spike generation and measurement from a clean metal vapor laser, IEEE IMTC/88, San Diego, California, USA, April 19-22, 1988.

[4] Karras T. W., Contaminants in metal vapor laser, Proc. Int. Conf. on Laser'80, New Orleans, Louisiana, USA, 168-176, 1980 Dec.

[5] Compton R. N., and Christophoros L. G., Negative-ion formation in H_2O and D_2O, Phys. Rev. Vol. 154, 110-116, 1967 Feb.

[6] Stockdale J. A. D., Compton R. N., and Reinhardt P. W., Studies of negative-ion-molecule reactions in the energy region from 0 to 3 ev, Phys. Rev. Vol. 184, 81-93, 1969 Aug.

[7] Melton C. E., Cross sections and interpretation of dissociative attachment reaction producing OH^-, O^- and H^- in H_2O*, J. Chem. Phys. Vol. 57, 4218-4225, 1972 Nov.

[8] Gottscho R. A., and Gaebe C. E., Negative ion kinetics in RF glow discharges, IEEE Trans. on Plasma Science, PS-14, 92-102, 1986 Apr.

[9] Data Sheet of EEV/M-OV Electron tube abridgen data 1984-85; EG&G data sheets: H5000C-4, H5010A-3, H5008B-3; ITT data sheet: 4/67.

[10] Peter R. A., Zumdieck J. P., Demboski J., Smilanski I., Ewing J. J., and Center R. E., Magnetic pulse compression for copper vapour lasers, Pulse Power Conference, Albuquerque, New Mexico, U. S. A., June 1983.

[11] Basting D., Hohla K., Albers E., and Bergmann H. V., Thyratrons with magnetic switches: the key to reliable excimer lasers, Laser & Optoelektronik, 2/84, 128-131, 1984 Feb.

ADDENDUM

Presented by Title only

THERMAL SHOCK: A CONTRIBUTING FACTOR TO LASER DAMAGE IN OPTICAL THIN FILMS USED FOR HIGH POWER CONTINUOUS WAVE LASER OPTICS

J. R. Palmer

REVERSE THERMAL WAVE APPROCIMATION FOR TEMPERATURE TRANSIENTS IN OPTICAL THIN FILMS AND SUBSTRATES - REFLECTIVE OPTICS FOR HIGH POWER REPETITIVE PULSED LASERS

J. R. Palmer

REVERSE THERMAL WAVE APPROXIMATION FOR TEMPERATURE TRANSIENTS IN OPTICAL THIN FILMS AND SUBSTRATES REFLECTIVE OPTICS FOR HIGH POWER CONTINUOUS WAVE LASERS

J. R. Palmer

HIGH POWER CONTINUOUS WAVE AND REPETITIVE PULSED THERMAL SHOCK LASER DAMAGE TO METALLIC REFLECTIVE OPTICS

J. R. Palmer

Manuscript Received 12/14/87/sar

Thermal Shock: A Contributing Factor To Laser Damage In Optical Thin Films Used For High Power Continuous Wave Laser Optics

by

J. R. Palmer

The University of Alabama, Huntsville
Center For Applied Optics
Huntsville, Alabama 35899

Abstract

The direction of this paper is to provide a theoretical model and supporting empirical data for evaluation of laser damage to optical thin films subjected to high power Continuous Wave laser irradiation. Basically, there has been a seeming anomaly in the maximum temperature that optical thin films can withstand before they fail to perform their function. On the one hand, a paper was presented to the Laser Boulder Damage Symposium that clearly provided empirical data that a number of oxide coating materials could reach 590°C to 680°C before failure set in. On the other hand, many investigators have found that coatings have failed at temperatures of 200°C to 300°C.

In this paper we set out to demonstrate that both conditions could be correct, rather than just one or the other. The equations for the absorption and subsequent temperature rise in the multilayer stacks are provided. The temperature rise of the substrate is evaluated and the equations for the actual thermal shock resulting from the conditions in the optical thin films, the substrate, and sensitivity of both to the materials that comprise the optical thin films and the substrates combination. Several coating chemistry combinations and three diverse substrate materials are evaluated and plotted based on measurements made and reported some years ago.

Key Words: Optical Thin Films, High Energy Laser Optics, Mirror Damage

Introduction

The maximum usable temperature that optical thin films could be driven to has been a source of a lot of experiments. Kuster and Ebert[1] made a pyroelectric measurement of the average damage temperature of seven oxide single layer coatings on Suprasil I. The damage temperature ranged from ≈ 590°C for TiO_2 to ≈ 680°C for CeO_2. The coatings were quarter wave set at 1.06 μm for use with an acousto-optically Q-switched Nd-glass laser. Bennett[2] in citing the Kuster and Ebert paper goes on to say, "A more conservative value for coatings on ULE mirrors are temperatures in excess of 200°C. The fact that good multilayer coatings on ULE Mirrors will withstand surface temperatures as high as this without damage was demonstrated using a continuous wave 3.8 micrometer laser source and a very reliable temperature-measuring technique."[2] It should be pointed out that the Kuster and Ebert experiment used a pulsed source as opposed to the CW source used by Bennett. This becomes important for this evaluation.

Analysis Of Present Data

We can back calculate the absorption at the interface of the single layer coating and Suprasil I from the following expression.[3,4,5,6,7,8]

(1)

$$\Delta T_0 = 2\eta F_0(\alpha)^{0.5}\left\{\text{ierfc}(x)\right\}\ \left\{\tau^{0.5} - (\tau - \phi)^{0.5}\right\}/K$$

Where,

F_0 = Io/ ϕ = Absorbed incident flux density, W/cm^2
K = Thermal conductivity, W/cm-°C
x = $t / 2(\alpha\phi)^{0.5}$ at t = 0 ; ierfc(x) = $1/(\pi)^{0.5}$
Io = Absorbed fluence, Joules/cm^2
α = Thermal diffusivity, cm^2 /sec
ϕ = Pulse width FWHB, sec
t = Faceplate thickness, cm
η = Number of pulses

From Kuster and Ebert's data they have a pulse width of 800 nanoseconds, with 8 Joules outcoupled from the laser. They have a 50 μ sec delay before the next pulse. They used a total of fifteen pulses for each sample. The laser beam diameter at $1/e^2$ was 0.05cm. Based on the properties of Fused Silica[6,7,8,9] the samples were absorbing ≈93300W/cm ^{2} per pulse which is an absorption of ≈ 1.833(10 $^{-5}$) of the peak pulse output fluence. The temperature rise per peak pulse is found from,[3,4,5,6,7,8]

(2)

$$\Delta T_1 = 2F_0(\alpha\phi)^{0.5}\left\{\text{ierfc}(x)\right\}/K$$

We find then that the temperature rise at peak pulse is on the order of 630°C$_{\Delta T}$ from *Eq. (2)* and that the temperature at the end of the 50μ sec cool down period after each pulse would be 40°C$_{\Delta T}$. So that at end of the first pulse the surface would have cooled down from 630°C to 40°C so that for the second pulse the peak temperature on the surface would be 670°C$_{\Delta T}$.

Commensurately, by the fourteenth pulse the temperature after thermal relaxation of *Eq. (1)* would be 560°C$_{\Delta T}$ and the fifteenth pulse would provide a peak temperature of 1190°C$_{\Delta T}$. Even so, of course, the melting temperature of these materials is considerably higher than 1190°C. However, we would ask the reader to keep this value in mind for information that will be provided further on. Suffice to say that Bennett was able to do a similar calculation and determine that there was insufficient thermal relaxation between pulses to say that the one pulse represented the CW condition.

There is, however, a correlation to be made between the two experiments. In both the cases we find a representation of *Thermal Shock* which goes to the properties of the coating materials and the substrate. There have been a number of approaches given for mechanical thermal stress on metallic reflector optics and transmissive optics. Musal[10] describes the threshold for plastic deformation on good quality Copper mirror surfaces. And, he describes the temperature rise necessary for this to occur, so that,

(3)

$$\Delta T = Y\,(1-\nu)/(E\,\alpha)$$

Where,

Y = Yield Stress, N/cm^2
E = Young's Modulus, N/cm^2
α = Linear Coefficient of Expansion, °C^{-1}

ν = Poisson's Ratio (for metals on the order of 0.30)

Kreidl and Wood[11] have a thermal shock expression for glass and glassy like materials, such that,

$$\Delta T = 2000\ (1-\ 0.2)/\ (E\ \alpha) \qquad (4)$$

From Musikant[9] we find a term commonly used for dielectric materials known as the Modulus of Rupture. This value represents the maximum amount of allowable strain times Young's Modulus, or what may be called the fracture stress in bending.[12] We see from Musikant that the maximum strain rate ranges from $1.39(10^{-3})$ for ZnS to $4.54(10^{-4})$ for single crystal CaF. It appears that one could argue reasonable that the average strain rate is something on the order of $1(10^{-3})$ for most of the materials used for optical thin films. From Faupel and Fischer[12] we can look at the expression for thermal shock in the restrained environment of coatings mechanically bonded to a substrate. One will find that the substrates of metals and many oxides are very ductile compared to that of the dielectric materials that are used in optical thin films. The expression for thermal shock for the restrained environment will be,[12,13]

$$\Delta T_{shock} = \varepsilon E_c\ (1-\ 0.2)/\ \left\{ Ec\ (\alpha_s - \alpha_c) \right\} \qquad (5)$$

Where,

εE_c = Modulus of Rupture, N/cm^2

E_c = Young's Modulus, N/cm^2

α_c = Linear Coefficient of Expansion for the coating material, $°C^{-1}$

α_s = Linear Coefficient of Expansion for the substrate material, $°C^{-1}$

ν = Poisson's Ratio (for dielectrics on the order of 0.20)

We can, then, take some examples to find the thermal shock temperature (ΔT) for coatings on various types of substrates. We can use some of the values provided by Scott,[13] Barnes,[14] and Musikant.[9] For Al_2O_3 we have a Young's Modulus of $36.5(10^6)$ N/cm^2 and a coefficient of expansion of $6(10^{-6})°C^{-1}$. Using the strain rate of $1(10^{-3})$ our Modulus of Rupture would be $36.5\ (10^3)$ N/cm^2. If we were to put the Al_2O_3 on a Copper and Fused Silica substrate we can find from *Eq. (5)* what the respective thermal shock temperature may be. The coefficient of expansion for Copper is $16.6(10^{-6})°C^{-1}$ and for Fused Silica the coefficient of expansion is $0.56(10^{-6})°C^{-1}$.

$$\Delta T = \varepsilon E_c\ (1-\ 0.2)\ /\ \left\{ Ec\ (\alpha_s - \alpha_c) \right\}$$

For Copper,

$$\Delta T = 36.5\ (10^3)\ (1-\ 0.2)\ /\left\{ 36.5\ (10^6)\ \left(16.6\ (10^{-6}) - 6\ (10^{-6})\ \right) \right\}$$

ΔT = 75.48 temperature difference between the Al_2O_3 and the Copper

and, for Fused Silica,

$$\Delta T = 36.5\ (10^3)\ (1-\ 0.2)\ /\left\{ 36.5\ (10^6)\ \left(6\ (10^{-6}) - 0.56\ (10^{-6})\ \right) \right\}$$

ΔT = 147.05 temperature difference between the Al_2O_3 and the Fused Silica

However, Musikant[9] suggests that the maximum strain rate for Al_2O_3 is more on the order of $1.89(10^{-3})$ for crytalline material. With this strain rate, the thermal shock temperature would be $143°C_{\Delta T}$ for the Copper substrate and $434.3°C_{\Delta T}$ for the Fused Silica substrate. However, we have the ability to compare directly with an oxide used by Kuster and Ebert. We will use ZrO_2 for

our next example. Scott[14] shows that ZrO_2 has a Young's Modulus of 22.75(10^6) N/cm^2, and a coefficient of expansion of 4.2 (10^{-6})°C^{-1}. Using *Eq. (5)* then,

For Copper,

$$\Delta T = 22.75\ (10^3)(1-\ 0.2)\ /\{\ 22.75\ (10^6)\ (16.6\ (10^{-6})\ -\ 4.2\ (10^{-6})\ )\}$$

ΔT = 64.54 temperature difference between the ZrO_2 and the Copper

and,

For Fused Silica,

$$\Delta T = 22.75\ (10^3)(1-\ 0.2)\ /\{\ 22.75\ (10^6)\ (4.2\ (10^{-6})\ -\ 0.56\ (10^{-6})\ )\}$$

ΔT = 219.8 temperature difference between the ZrO_2 and the Fused Silica

There is, however, an interesting piece of work reported by our colleague Dr. Scott. He provides in his paper, measurements made on evaporated films and compares the values to the bulk materials. Interestingly, for ZrO_2 he reports that the Young's Modulus for the evaporated film is reduced from 22.75(10^6) to 11.72(10^6) N/cm^2 and the coefficient of expansion is reduced from 4.2(10^{-6})°C^{-1} to 1.1(10^{-6})°C^{-1}. For the materials that are shown by Scott, the Young's Modulus of the films are less than the bulk. However, for some of the cases the coefficient of expansion is increased markedly. Now then, if we use the new values shown by Dr. Scott, we find,

For Copper,

$$\Delta T = 11.72\ (10^3)(1-\ 0.2)\ /\{\ 11.72\ (10^6)\ (16.6\ (10^{-6})\ -\ 1.1\ (10^{-6})\ )\}$$

ΔT = 51.61 temperature difference between the ZrO_2 and the Copper

and, for Fused Silica,

$$\Delta T = 11.72\ (10^3)(1-\ 0.2)\ /\{\ 11.72\ (10^6)\ (1.1\ (10^{-6})\ -\ 0.56\ (10^{-6})\ )\}$$

ΔT = 148.15 temperature difference between the ZrO_2 and the Fused Silica

Now, then, if one looks at the thermal shock temperature of the Fused Silica that the coatings were placed on, that is, just the temperature rise of the first surface where the Young's Modulus of the Fused Silica is 7.31 (10^6) N/cm^2 we can find the thermal shock temperature for that material. So that,

$$\Delta T = 7.31\ (10^8)\ (1\ -\ 0.2)\ /\{\ 7.31\ (10^6)\ (\ 0.56\ (10^{-6})\ )\}$$

ΔT = 1428.6 temperature difference between the Fused Silica and the Air around the substrate.

If we look back at the Kuster and Ebert experiment we see that the temperature at the peak pulse after fifteen pulses should be on the order of 1200°C which is very close to the thermal shock temperature of the Fused Silica. Actually the value is within 85% of the value. Given that the absorption is more or less than calculated, and that the transport properties are not linear with temperature, it is more than possible, and should be expected, that the temperature that was achieved was very close to the thermal shock temperature. More importantly, the failure range from ≈ 590°C to ≈ 680°C would suggest that the substrate was beginning to fail from thermal shock and subsequently impacting the coating into failure. Kuster and Ebert did not discuss thermal shock, nor is there any calculation around that particular phenomena. The question may be rightly raised, well what about the thermal shock of the coating ZrO_2 in the temperature above the surrounding ambient. If we use the data from Dr. Scott, we can evaluate the thermal shock of the coating material as deposited. Then,

$$\Delta T = 11.75\ (103)(1-\ 0.2)\ /\left\{\ 11.75(10^{6})\left(1.1\ (10^{-6})\ \right)\right\}$$

$\Delta T = 727.3$ temperature difference between the ZrO_2 and the ambient temperature around the optic.

According to Kuster and Ebert,[1] the ZrO_2 had a failure temperature in the order of ≈ 640°C. We can look at yet another material, TiO_2. According to Scott, the Young's Modulus of the TiO_2 as deposited is $8.96(10^6)$ N/cm^2 and the coefficient of expansion is $2.1(10^{-6})°C^{-1}$. Using these values, we can look at the thermal shock of the TiO_2 deposited on the Fused Silica. So that,

$$\Delta T = 8.96\ (10^{3})\ (1-\ 0.2)\ /\left\{\ 8.96\ (10^{6})\left(2.1\ (10^{-6})\ -\ 0.56\ (10^{-6})\right)\right\}$$

$\Delta T = 519.5$ temperature difference between the TiO_2 and the Fused Silica.

$$\Delta T = 8.96\ (10^{3})\ (1-\ 0.2)\ /\left\{\ 8.96\ (10^{6})\left(2.1\ (10^{-6})\right)\right\}$$

$\Delta T = 380.9$ temperature difference between the TiO_2 and the Ambient surrounding air.

Kuster and Ebert report that the TiO_2 had a maximum damage temperature of ≈ 590°C. Again, given the exact amount of absorption and the non-linearity of the thermal transport properties with temperature, the experiment could have been very close to the thermal shock temperature. First of all, Temple, *et al*[16,17] and Bennett and Burge[18], have shown that the maximum absorption occurs at the interface of the coating and substrate. Since there is only one quarter wave thick coating on the Fused Silica substrate, the temperature of the coating and substrate should be virtually the same. Therefore, there is no thermal shock because of a gradient between the coating and the substrate. There is, however, the thermal shock between the coating and the ambient air and the substrate and the ambient air. It would seem that it is simply a foot race between the coating and the substrate as to when the failure will occur. As we have seen in the pulsed condition, you have the peak temperature rise due to the pulse and the slow temperature rise because of the lack of thermal relaxation between the pulses. Based upon the data we have presented here, it would seem that the thresholds of temperature are most likely caused by the Thermal Shock that is working on both the coating material and the substrate. The calculations would indicate that indeed, the coating/substrate failed at the appropriate point of temperature range. Neither of which have anything to do with the melting point of either material. Thermal Shock has nothing to do with the melting point and is only concerned with the strain rate that is allowed before reaching the Modulus of Rupture in the case of non-ductile materials and the plastic regime in the case of ductile materials. Bennett is correct to separate the pulsed from the Continuous Wave condition in his application. However, the problems that face the Continuous Wave applications are no less stringent, as we will see. It would have been interesting to see how the oxide coatings set out by Kuster and Ebert would have faired if they had been deposited on a more ductile material such as Copper. That, of course, is part of our experiment. If, for example, we put the ZrO_2 on Copper the required temperature differential between the coating and the substrate would have to be,

For Copper,

$$\Delta T = 11.75\ (10^{3})\ (1-\ 0.2)\ /\left\{\ 11.75\ (10^{6})\left(16.6\ (10^{-6})\ -\ 1.1\ (10^{-6})\ \right)\right\}$$

$\Delta T = 51.49$ temperature difference between the ZrO_2 and the Copper

and as we have already seen, the temperature difference with the air,

$$\Delta T = 11.75\ (10^{3})\ (1-\ 0.2)\ /\left\{\ 11.75\ (10^{6})\left(1.1\ (10^{-6})\ \right)\right\}$$

$\Delta T = 727.3$ temperature difference between the ZrO_2 and the surrounding ambient air.

Clearly, then, there is a very important part to be played by the substrate and the coating that is deposited on the surface. There are yet some additional factors that play in the thermal shock problem. The depositing of dielectric films very often leaves the material in a pre stressed condition. These stresses may be compressive or tensile.[19,20,21,22,23,24,25,26] The major point to be made in this connection is thermal creep and cycle life fatigue. In this connection, one would expect to see hysterisis in the coatings peak reflectance wavelength and a reduction in the reflectivity of the coating with use against the laser. Another major problem, of course, will be defects. If the coating have nodules such as are shown by Guenther[27,28] we now have notch points that will reduce the thermal shock temperature as a function of crack propagation at the nodule. Of course defects have a major impact on the coating temperature in any event.[29,30,31,32,33]

Temperature Distribution In Optical Thin Films Continuous Wave

Optical thin film coatings, manifestly, have very little thermal mass. The forces that bond the films may be Van Der Waal's forces, Electrostatic forces, or Chemical Bonding forces.[19,20] The experimental data would tend to indicate that the coating absorption takes place at the boundaries between the coating and the substrate; or coating-coating interface for multilayer systems.[2,16,17,18] Bennett and Burge[18] state that, " . . . And it has been found that the absorption in the vicinity of a thin-film interface may be as large or larger than that in the entire film volume." In discussing the results of absorption of an AsSe thin film on a CaF substrate, Temple states, "It was found that the predominant absorption was at the film-substrate interface."[17] For the analytical system of this paper, there is a concomitant statement that follows from the interfacial absorption. Temple, *et al*,[16] states, "Finally, we would like to make the point that while much attention has been given to the electric field plots for multilayer coatings in damage resistance discussions, it is the relative power density which must be considered in discussing thermal absorption since the local absorptance is the product of the relative power density and the absorption coefficient at that point." Fundamentally, then, the basis of the following treatment is underpinned with the basic premise that most, if not all, of the absorption takes place at the boundaries of the coatings. Further, that the temperature profile will follow the electric field.[34]

Heretofore, the conventional wisdom, when evaluating the temperature rise of an optical surface, has been to assume that the entire absorbed flux density goes into the substrate. Additionally, the belief continues, that the thin-film coatings equilibrate with the substrate in some instantaneous fashion. This technique would tend to indicate that these assumptions may not be accurate. At the outset, we will use an idealized case. The model assumes that the thermal transport properties do not change with temperature, recognizing that this is a fiction for the real world, for both the one dimensional and three dimensional case, and no heat is lost from the optic, i.e., no forced or free convection or radiation. The electric field strength and coating relationships will be as shown in Figure 1.

According to the electrical field plot of Figure 1, interfacial absorption will occur only at,

$$2E_o(\eta_o/\eta_H),\ 2E_o(\eta_o\eta_L/\eta_H^2),\ 2E_o(\eta_o\eta_L^2/\eta_H^3)\ldots$$

Even though the films are extremely thin, they are still amenable to joule heating. Consequently, the semi-infinite plate model is applicable. The model assumes that the layers of films are analogous to a series of composite layers. Each layer is bound by one, or a combination, of forces described earlier. This adhesive force is very important in determining the required transient and steady-state gradient through the film layers. If we assume, then, that the absorption and power densities are proportionate to the (E) field strength through the layers of the coatings, then,[34,35,36,37]

(6)

$$\alpha^{\bullet} = \left\{1 - R - \left[4(\psi)(\eta_L/\eta_H)^{2N}/(\varphi)\right] - \left[4\pi\sigma\cos(\theta)\left\{1.15 - 2.565(10^{-6}) \times \left[5(10^4) - \lambda\right]\right\}^{2N}/\lambda\right]^2\right\} \times \left\{\left[1 - (\eta_L/\eta_H)^{2N+1}\right]\left[\eta_H^2 - \eta_L^2\right]^{-1}(4)\right\}^{-1}$$

If the reflecting optic has a dielectric substrate:

low index next to the substrate, $\Psi = 1$, $\varphi = \eta_S$

high index next to the substrate, $\Psi = \eta_S$, $\varphi = \eta_H^2$

Where,

η_S = Substrate index, η_H = Index of the high index film.

For the case where the substrate is not a dielectric, i.e., is a metal, a quasi dielectric of the metal-film combination is generated, so that, for the low index next to the substrate,

(7)

$$\Psi = \eta_S \left\{ \left((1 \text{ (-/+) } \cos\delta) / 2 \right) \left\{ (\eta_S/\eta)^2 + (K_S/\eta)^2 \right\} + (1 \text{ (+/-) } \cos\delta) / 2 + (K_S/\eta) \sin\delta \right\}^{-1}$$

Where,

η = (η_L) low index film, at λ if next to substrate,
(η_H) if high index next to metal.

η_S = Index for metal substrate, at λ;

K_S = Extinction coefficient for metal substrate at λ.

$\tan\delta = 2\eta K_S / \left\{ \eta^2 - \eta_S^2 - K_s^2 \right\}$

$\varphi = \eta_H^2$

If the high index film is next to the substrate, $\Psi = 1.0$.

When, $\eta^2 > (\eta_S^2 + K_S^2)$, δ is in the first quadrant. Otherwise δ is in the second quadrant using the standard conventions.

σ = rms surface roughness, Å λ = Wavelength of interest, Å
R = Reflectivity N = Number of high-low coating pairs

For *Eq. (7)*, if the low index film is next to the metal substrate, use the upper sign in the denominator. If the high index is next to the substrate, use the lower sign in the denominator.

The value of $\left(4\pi\sigma \cos(\theta) / \lambda \right)^2$ represents the total integrated scatter from a surface. The expression $\left\{ 1.15\text{-}2.565\,(10^{-6}) \left[5(10^4) - \lambda \right] \right\}^{2N}$ represents the increase in scatter as a function of wavelength and number of coating pairs.

At each interface there will be a distribution of power density absorbed between the low and high index materials, as a function of their respective thermal transport properties, then,

(8)

$$2E_o \sum_{m=0}^{m} \left(\eta_o \eta_L^m / \eta_H^{m+1} \right) \left(F_1 \alpha^*_1{}^{0.5} / K_1 \right) = 2E_o \sum_{n=0}^{n} \left(\eta_o \eta_L^n / \eta_H^{n+1} \right)$$

$$\times \left(F_2 \alpha^*_2{}^{0.5} / K_2 \right) F_2 = F_1 \left(\alpha^*_1{}^{0.5} \right) K_2 / \left(K_1 (\alpha^*_1{}^{0.5}) \right)$$

$$\times \left\{ 2E_o \sum_{n=0}^{n} \left(\eta_o \eta_L^n / \eta_H^{n+1} \right) / 2E_o \sum_{m=0}^{m} \left(\eta_o \eta_L^m / \eta_H^{m+1} \right) \right\}$$

Where,

F_1 = Absorbed portion in low index material
F_2 = Absorbed portion in high index material
$\alpha^\bullet_1$ = Thermal diffusivity of low index material, cm^2/sec;
$\alpha^\bullet_2$ = Thermal diffusivity of high index material, cm^2/sec
K_1 = Thermal conductivity of low index material, W/cm-°C
K_2 = Thermal conductivity of high index material, W/cm-°C

So that,

$$F_1 + F_2 = 1.0 \qquad C = \left[\{ (\alpha^\bullet_{c1}{}^{0.5}) K_{c2} / (K_{c1} (\alpha^\bullet_{c2}{}^{0.5})) \} \right] \tag{9}$$

$$F_2 = 1.0 / (1.0 + C) \qquad F_1 = 1.0 - F_2 \tag{10}$$

From *Eqs. (8)* through *(11)*, the temperature rise for each element in the multilayer stack, and the substrate, may be evaluated. Using a modified form of the Palmer-Bennett model, to include source and multiple sink to the substrate,[7,8,32,33,34]

(11)

$$\Delta T_{F1-2} = 2 \mathcal{F}_{O1-2} (\alpha^\bullet_{1-2} \tau)^{0.5} \left[\{ \text{ierfc}(x) \} \right] / K_{1-2} - \mathcal{F}_{O1-2} / \Pi_{\zeta 1,2,3\ldots}$$

$$+ \mathcal{F}_{O1-2} / \Pi_{\zeta 1,2,3\ldots} \{ \exp (H_1{}^2 \alpha^\bullet_c \tau) \, \text{erfc}(\zeta) \}$$

$$+ 2 E_o \sum_{(m,n)=0}^{(m,n)} \left[\eta_o \eta_L{}^{(m,n)} / \eta_H{}^{(m,n)+1} \right] \Delta T_m + \Delta T_S$$

Where,

$X = t / 2(\alpha^\bullet \tau)^{0.5}$ at $t=0$
$\text{ierfc}(x) = 1/(\pi)^{0.5}$
$\text{erf}(x) = 0$
$Y = (\zeta) = H_1 (\alpha^\bullet \tau)^{0.5}$
$\alpha^\bullet_c = [\alpha^\bullet_1 + \alpha^\bullet_2] 2^{-1}$ $K_c = [K_1 + K_2] 2^{-1}$
$\alpha^\bullet_S$ = Thermal diffusivity of the substrate, cm^2/sec
K_S = Thermal conductivity of the substrate, W/cm-°C
$H_1 = \Pi_{\zeta 1,2,3\ldots} / K_S$
$H_2 = \Pi_{\zeta 1,2,3\ldots} / K_c$

The absorbed flux density $\mathcal{F}_{OL}$, $\mathcal{F}_{OH}$ are found from,[7,8,34]

$$\mathcal{F}_{OL} = I_O \alpha^\bullet_O F_1 \psi_N \left\{ 2 E_o \sum_{m=0}^{m} \left[\eta_O \eta_L{}^m / \eta_H{}^{m+1} \right] \right\}^{-1.0} \tag{12}$$

$$\mathcal{F}_{OH} = I_O \alpha^{\bullet}_O F_2 \Psi_N \left\{ 2 E_o \sum_{n=0}^{n} \left[\eta_O \eta_L^n / \eta_H^{n+1} \right] \right\}^{-1.0} \qquad (13)$$

Where,

$\mathcal{F}_{OL}, \mathcal{F}_{OH}$ = Absorbed flux density for the low and high index materials, W/cm^2.

I_O = Incident flux density, W/cm^2; N = High low pair number from Figure 1.

$\Psi_N = 2E_o(\eta_O/\eta_H)$, $2E_o(\eta_O\eta_L/\eta_H^2)$, $2E_o(\eta_O\eta_L^2/\eta_H^3)$, . . .

$\alpha^{\bullet}_O$ = Absorption value

The temperature rise at the low high index interface, where the electric field is cancelled, i.e., no absorption, is found from,[7,8,34]

(14)

$$\Delta T_{F1\text{-}2} = \left\{ 2\mathcal{F}_{OH} (\alpha^{\bullet}_1 \tau)^{0.5} \left[\{ \text{ierfc}(x) \} \right] / K_1 - \mathcal{F}_{OH} / \Pi_{\zeta 1,2,3\ldots} + \mathcal{F}_{OH} / \Pi_{\zeta 1,2,3\ldots} \right.$$
$$\times \exp\left(H_1^2 \alpha^{\bullet}_C \tau\right) \text{erfc}(\zeta) \Big\} + \Big\{ 2\mathcal{F}_{OL} (\alpha^{\bullet}_1 \tau)^{0.5} \left[\{ \text{ierfc}\ (x_o) \} \right] / K_2$$
$$\left. - \mathcal{F}_{OL} / \Pi_{\zeta 1,2,3\ldots} + \mathcal{F}_{OL} / \Pi_{\zeta 1,2,3\ldots} \times \exp\left(H_1^2\, \alpha^{\bullet}_C \tau\right) \text{erfc}(\zeta) \right\} \Big\}^{2\text{-}1}$$
$$+ 2 E_o \sum_{(m,n)=0}^{(m,n)} \left[\eta_O \eta_L^{(m,n)} / \eta_H^{(m,n)+1} \right] \Delta T_{(m,n)} + \Delta T_S$$

Where,

$X = t/2(\alpha^{\bullet}_1 \tau)^{0.5}$ at $t = 0$; ierfc $(x) = 1/(\pi)^{0.5}$; erf $(x) = 0$

$X_0 = t / 2(\alpha^{\bullet}_2 \tau)^{0.5}$ at $t = 0$; ierfc $(x_0) = 1/(\pi)^{0.5}$

$Y = H_{1,2,3\ldots}(\alpha^{\bullet}_1 \tau)^{0.5}$; $Y_1 = H_{1,2,3\ldots}(\alpha^{\bullet}_2 \tau)^{0.5}$

The temperature rise of the substrate will be found from,[7,8,34]

(15)

$$\Delta T_S = 2 E_o \left\{ \sum_{m=0}^{m} \left[\eta_O \eta_L^m / \eta_H^{m+1} \right] \mathcal{F}_{OL} \left\{ \text{erfc}\ (x) - \exp\left(H_2^2 \alpha^{\bullet}_S \tau\right) \text{erfc}\ (z) \right\} \right.$$
$$\left. + 2 E_o \sum_{n=0}^{n} \left[\eta_O \eta_L^n / \eta_H^{n+1} \right] \mathcal{F}_{OH} \left\{ \text{erfc}(x) - \exp\left(H_2^2 \alpha^{\bullet}_S \tau\right) \text{erfc}(z) \right\} \right\}$$
$$\times \left\{ 2 (\alpha^{\bullet}_S \tau)^{0.5} \left[\{ \text{ierfc}\ (Q) \} \right] / K_S \right\}$$

Where,

$Q = t/2(\alpha^{\bullet}_S \tau)^{0.5}$ at $t = 0$

ierfc(Q) $= 1/(\pi)^{0.5}$

erfc (x) $= 1$

$$Z = H_2 (\alpha^*_S \tau)^{0.5}$$

The problem is made simpler, of course, if we simply set,

$$\mathcal{F}_0 = 2E_0 \left\{ \sum_{m=0}^{m} \left[\eta_0 \eta_L^m / \eta_H^{m+1} \mathcal{F}_{0L} \right] \left\{ \text{erfc } (x) - \exp\left(H_2^2 \alpha^*_S \tau\right) \text{erfc } (z) \right\} \right.$$

$$\left. + 2E_0 \sum_{n=0}^{n} \left[\eta_0 \eta_L^n / \eta_H^{n+1} \mathcal{F}_{0H} \right] \left\{ \text{erfc } (x) - \exp\left(H_2^2 \alpha^*_S \tau\right) \text{erfc } (z) \right\} \right\} \qquad (16)$$

and, then, *Eq. (15)* becomes; $\Delta T_S = 2\mathcal{F}_0 (\alpha^*_S \tau)^{0.5} \left[\{ \text{ierfc } (Q) \} \right] / K_S$

Again, the above equations assume that the diameter of the laser beam will be $\geq 12[\alpha^* \tau]^{0.5}$ in order to be one dimensional. The steady-state gradient may be determined in a straight forward fashion. What makes the problem less than straight forward is knowing the binding forces between the coatings, i.e., adhesion. Pulker[19] suggests that the adhesive forces may be as low as 10^4 dynes/cm^2 for physisorption to greater than 10^{11} dynes/cm^2 for chemical bonding. Given this wide range, which, most probably, will be very susceptible to the coating technique and the environment, we will use a bonding force between the coatings of 10^{10} dynes/cm^2, for most analysis.

Based on a clamping force between the coatings of 10^{10} dynes/cm^2, or 9689 atmospheres, we can calculate a film coefficient between each layer. Schneider[38,39] states, ". . . heat transfer through an interface takes place by combined mechanisms of conduction across true contact points, conduction across entrapped interstitial fluid, and radiation across interstitial gaps. Resulting overall conductance of the joint is therefore a function of the material in contact (conductivity, surface finish, flatness, and hardness), the contact pressure, the mean temperature and the heat flux across the joint . . ."

The film coefficient is expected to increase with increased contact pressure. From this relationship, the film coefficient should follow from,[38,39,40,41]

$$\Pi_\zeta = (P^{2/3}) \ (1761)^{-1} \qquad (17)$$

Where

Π_ζ = W/cm^2-°C P = #/in^2

Based on the clamping force of 9689 atmospheres, 1.42(10^5)#/in^2, and very smooth surfaces,

$$\Pi_\zeta = \left[1.4(10^5)\right]^{2/3} \times (1761)^{-1} \qquad \Pi_\zeta = 1.55 \text{W/cm}^2\text{-°C}$$

Because the films are so thin, they will not present a thermal resistance of any magnitude. The basic expression for determining the overall film coefficient through a system of composite materials, is,[42,43]

$$U = 1 / \left\{ 1/\Pi_{\zeta 1} + L_1/K_1 + 1/\Pi_{\zeta 2} + L_2/K_2 + 1/\Pi_{\zeta 3} + \ldots \right\} \qquad (18)$$

So then, treating each absorbing electric field interface as a radiation boundary to the substrate, the first field interface (N=1), from Figure 1, the film coefficient will be,

$\Pi_{\zeta 1} = 1 / [2N_0 \times (1.55)^{-1}]$; $\Pi_{\zeta 2} = 1 / [2 (N_0 - 2) \times (1.55)^{-1}]$; *(19)*

$\Pi_{\zeta 3} = 1 / [2 (N_0 - 4) \times (1.55)^{-1}]$; $\Pi_{\zeta 4} = 1 / [2 (N_0 - 6) \times (1.55)^{-1}] \ldots$

From our model, then,

$H_1 = \Pi_{\zeta 1,2,3\ldots} / K_S$ $\quad N_0$ = Total number of coating pairs

$H_2 = \Pi_{\zeta 1,2,3\ldots} / K_C$

At this point it should be noted that amorphous dielectric as deposited materials have thermal transport properties on the order of ten to fifty times less than crystalline.[34,44,45,46,47]

However, if the substrate does not fit the semi-infinite plate boundary, that is, it is thinner than required by the boundary condition and thicker than 10% of what is required by the boundary condition,[5,7,8] where $\mathcal{F}_0$ follows from the simplification set forth above, then, the temperature rise of the first surface of the substrate may be determined from the Reverse Thermal Wave Approximation and will provide a temperature rise that will follow from,

(20)

$$\Delta T_S = 2\mathcal{F}_0 (\alpha^*_S \tau)^{0.5} \{\text{ierfc}(x)\} / K_S - 2\mathcal{F}_0 (\alpha^*_S \tau)^{0.5} \{\text{ierfc}(z)\} / K_S \{\text{erfc}(z) - \exp(t H_0 + H_0^2 \alpha^*_S \tau) + \text{erfc}(a)\} + 2\mathcal{F}_0 (\alpha^*_S \tau)^{0.5} \{\text{ierfc}(z)\} / K_S + 2\mathcal{F}_0 (\alpha^*_S \tau)^{0.5} \{\text{ierfc}(x)\} / K_S \{\text{erfc}(z) - \exp(t H_0 + H_0^2 \alpha^*_S \tau) \text{erfc}(a)\}$$

The temperature rise of the thin films, then, will follow from,

(21)

$$\Delta T_{F1-2} = \{ 2\mathcal{F}_{01-2} (\alpha^*_{1-2} \tau)^{0.5} \{\text{ierfc}(x)\} / K_{1-2} - \mathcal{F}_{01-2} / \Pi_{\zeta 1,2,3\ldots} + \mathcal{F}_{01-2} / \Pi_{\zeta 1,2,3\ldots} \{\exp(H_2^2 \alpha^*_S \tau) \text{erfc}(y)\}\} + 2 E_o \sum_{(m,n)=0}^{(m,n)} [\eta_0 \eta_L^{(m,n)} / \eta_H^{(m,n)+1}] \Delta T_m + \Delta T_S$$

and the temperature rise of the the second surface will follow from,

$$\Delta T_2 = 2\mathcal{F}_0 (\alpha^*_S \tau)^{0.5} \{\text{ierfc}(z)\} / K_S + 2\mathcal{F}_0 (\alpha^*_S \tau)^{0.5} \{\text{ierfc}(x)\} / K_S \{\text{erfc}(z) - \exp(t H_0 + H_0^2 \alpha^*_S \tau) \text{erfc}(a)\} \quad (22)$$

After the same fashion, we can treat with the repetitive pulsed case. We must look at the absorption in the coatings for the peak pulse and the residual temperature as a function of the cooling cycle.

Temperature Distribution In Optical Thin Films Repetitive Pulsed

The repetitive pulsed counterpart provides a different set of conditions for dielectric coatings on optics. Each cycle of a pulse has two components, a heating and cooling time line. Incorporated into *Eq (21)* will be the heating and cooling component so that the temperature rise in the coating layers will follow from,

(23)

$$\Delta T_{1-2} = \{2 \eta \mathcal{F}_{01-2} (\alpha^*_{1-2})^{0.5} / K_{1-2} \{\text{ierfc}(x)\} \{\Omega^{-0.5} - [\Omega^{-1} - \phi]^{0.5}\}$$

$$- 2\pi\Omega\phi\mathcal{F}_{01\text{-}2}/\Pi\zeta_{1,2,3\ldots} + 2\pi\Omega\phi\mathcal{F}_{01\text{-}2}/\Pi\zeta_{1,2,3\ldots}$$

$$\times\left\{\exp\left(H_1^2\alpha^{\bullet}{}_c\Omega^{-1}\eta\right)\operatorname{erfc}(y)\right\} + 2E_o\sum_{(m,n)=0}^{(m,n)}\left[\eta_0\eta_L^{(m,n)}/\eta_H^{(m,n)+1}\right]\Delta T_m+\Delta T_s$$

Where,

η = Number of cycles $\quad \mathcal{F}_{0\,1\text{-}2}$ = Absorbed fluence, W/cm^2

Ω = Cycles/sec $\quad x = t/2(\alpha^{\bullet}{}_c\Omega^{-1})^{0.5}$; at t = 0

ierfc(x) $= 1/\pi^{0.5}$ $\quad$ ierfc(Q) $= 1/\pi^{0.5}$

$y = H_1(\alpha^{\bullet}{}_c\Omega^{-1}\eta)^{0.5} \quad Q_1 = t/2(\alpha^{\bullet}{}_s\Omega^{-1}\eta)^{0.5}$, at t = 0

$z = H_2(\alpha^{\bullet}{}_s\Omega^{-1}\eta)^{0.5}$

$a = t/2(\alpha^{\bullet}{}_s\Omega^{-1}\eta)^{0.5} + H_0(\alpha^{\bullet}{}_s\Omega^{-1}\eta)^{0.5}$

The temperature rise in the substrate, however, is governed by the average power that may be conducted from the film interfaces to the substrate. The temperature rise in the substrate is described by,

(24)

$$\Delta T_{s1} = \left\{2E_o\sum_{m=0}^{m}\left[\eta_0\eta_L{}^m/\eta_H{}^{m+1}2\pi\Omega\phi\,\mathcal{F}_{0L}\right]\right.\left\{\operatorname{erfc}(x)\right.$$

$$\left.- \exp\left(H_2{}^2\alpha^{\bullet}{}_s\Omega^{-1}\eta\right)\operatorname{erfc}(z)\right\} + 2E_o\sum_{n=0}^{n}\left[\eta_0\eta_L{}^n/\eta_H{}^{n+1}2\pi\Omega\phi\mathcal{F}_{0H}\right]$$

$$\times\left\{\operatorname{erfc}(x) - \exp\left(H_2{}^2\alpha^{\bullet}{}_s\Omega^{-1}\eta\right)\operatorname{erfc}(z)\right\}\Big\}$$

$$\times\left\{2\left(\alpha^{\bullet}{}_s\Omega^{-1}\eta\right)^{0.5}\left\{\operatorname{ierfc}(Q)\right\}/K_s\right\}$$

We can simplify the complexity of the equations by setting $\mathcal{F}_0$ equal to,

(25)

$$\mathcal{F}_0 = \left\{2E_o\sum_{m=0}^{m}\left[\eta_0\eta_L{}^m/\eta_H{}^{m+1}2\pi\Omega\phi\,\mathcal{F}_{0L}\right]\right.\left\{\operatorname{erfc}(x)\right.$$

$$\left.- \exp\left(H_2{}^2\alpha^{\bullet}{}_s\Omega^{-1}\eta\right)\operatorname{erfc}(z)\right\} + 2E_o\sum_{n=0}^{n}\left[\eta_0\eta_L{}^n/\eta_H{}^{n+1}2\pi\Omega\phi\,\mathcal{F}_{0H}\right]$$

$$\times\left\{\operatorname{erfc}(x) - \exp\left(H_2{}^2\alpha^{\bullet}{}_s\Omega^{-1}\eta\right)\operatorname{erfc}(z)\right\}\Big\}$$

Again, for the one dimensional model that does not satisfy the semi-infinite plate model we can provide a similar expression from the *Reverse Thermal Wave Approximation*[5,6], so that,

(26)

$$\Delta T_s = 2\mathcal{F}_0(\alpha^{\bullet}{}_s\Omega^{-1}\eta)^{0.5}\left\{\operatorname{ierfc}(Q)\right\}/K_s - 2\mathcal{F}_0(\alpha^{\bullet}{}_s\Omega^{-1}\eta)^{0.5}/K_s\left\{\operatorname{ierfc}(Q_1)\right\}$$

$$\times \{\mathrm{erfc}(\varrho_1) - \exp(t H_o + H_o^2 \alpha^*_s \Omega^{-1}\eta) + \mathrm{erfc}(a)\}$$

$$+ 2\mathcal{F}_o (\alpha^*_s \Omega^{-1}\eta)^{0.5} \{\mathrm{ierfc}(\varrho_1)\} / K_s + 2\mathcal{F}_o (\alpha^*_s \Omega^{1}\eta)^{0.5} \{\mathrm{ierfc}(\varrho)\} / K_s$$

$$\times \{\mathrm{erfc}(\varrho_1) - \exp(t H_o + H_o^2 \alpha^*_s \Omega^{-1}\eta)\,\mathrm{erfc}(a)\}$$

And the temperature rise of the second surface will follow from,

(27)

$$\Delta T_2 = 2\mathcal{F}_o (\alpha^*_s \Omega^{-1}\eta)^{0.5} \{\mathrm{ierfc}(\varrho_1)\} / K_s + 2\mathcal{F}_o (\alpha^*_s \Omega^{-1}\eta)^{0.5} \{\mathrm{ierfc}(\varrho)\} / K_s$$

$$\times \{\mathrm{erfc}(\varrho_1) - \exp(t H_o + H_o^2 \alpha^*_s \Omega^{-1}\eta)\,\mathrm{erfc}(a)\}$$

Correlation With Previously Published Data

We can now look at the expressions set out above and relate some of this information to some actual coatings that have been very well characterized in the HF laser coating program undertaken by Holmes.[21] In this study a number of coating materials and combinations were studied to provide the best reflectors for the 2.8 μm wavelength. Four mirrors are shown to have been measured for reflection and absorption by Calorimetry and the Reflectometer at China Lake Naval Weapons Center. The basic substrate for all four coating combinations was Molybdenum. A Silver interface was placed on the Moly surface before the coating pairs were laid down. The author of the report states, "The reflectivity was calculated from calorimetry data using (Reflectivity = 1 - Absorptance), so that the differences in the two sets of measurements may be attributed to the effects of scattered light."[21] Indeed, as we will show, the difference was due to the total integrated scattered light. The first mirror in the table is composed of a Moly substrate with Silver overlay and $(ThF_4/ZnSe)^4$ coating. We have assumed for the purpose of our calculation that the Moly surface has a 20 Å surface roughness. The Reflectometer gave a reflectivity of 0.9991 and the Calorimeter gave a reflectivity of 0.9994. For 2.8 μm the index of refraction for ZnSe is shown to be 2.43.[21] The index of refraction for the ThF_4 is shown to be 1.50.[21] The optical constants for Silver at 2.8 μm are shown to be n=1.168 and k=17.1.[48] From *Eq. (6)* we find that the absorption will be $2.16(10^{-4})$, the scatter will be $3.37(10^{-4})$, and the transmission to the substrate will be $3.3\ (10^{-4})$ for a total of $8.83(10^{-3})$ vs. $9(10^{-4})$ which suggests that the surface scatter, i.e., roughness, was greater than 20Å RMS. One of the elements that should be impressed on our minds is that these three components must really be segregated in order to accurately calculate the maximum threshold flux density that will take the coating to thermal shock. In order to demonstrate the criticality of this segregation, we can look at the difference in flux density if we make the assumption that the coating is absorbing all of the flux density, i.e., 1-R, or only absorbing that portion which *Eq. (6)* indicates is the case. First, we will look at *Eq. (5)* to see what the thermal shock temperature difference may be between the Moly and the two materials. ThF_4 has a coefficient of expansion of $14.4(10^{-6})$ according to the report and a Young's Modulus of $4.7(10^6)$ N/cm^2. However, Scott's[14] data suggests the as-deposited value should be $2.9(10^{-6})$. We will use the data from the report for this analysis. The coefficient of expansion for ZnSe is $7.57(10^{-6})$ and the Young's Modulus is $6.24(10^6)$ N/cm^2.[9] For Moly the coefficient of expansion is $5.0\ (10^{-6})$.[15]

For ThF_4

$$\Delta T_{shock} = \varepsilon E_c\ (1 - 0.2) / \{Ec\ (\alpha_s - \alpha_c)\}$$

$$\Delta T = 4.7(10^3)(1 - 0.2) / \{4.7(10^6)\ (14.4(10^{-6}) - 5(10^{-6}))\}$$

$\Delta T = 85.11$ temperature difference between the ThF_4 and the Moly

and,

For the ZnSe,

$$\Delta T = 6.24\ (10^3)\ (1-\ 0.2)\ /\left\{\ 6.24(10^{\ 6})\ \left(7.57(10^{\ -6})\ -\ 5(10^{-6})\ \right)\right\}$$

ΔT = 311.3 temperature difference between the ZnSe and the Moly

If we were to use Scott's data for the ThF_4 the thermal shock temperature would be closer to,

$$\Delta T = 2.0\ (10^3)\ (1-\ 0.2)\ /\left\{\ 2.0\ (10^6)\ \left(5.0\ (10^{-6})\ -\ 2.9\ (10^{-6})\ \right)\right\}$$

ΔT = 381 temperature difference between the ThF_4 and the Moly

However, the maximum temperature difference of the as-deposited ThF_4 and the ambient air will be 275.8°C. Using *Eq. (11)* and *Eq. (15)* we can evaluate the temperature rise of the coating pairs and the substrate for a 10 second run time. And, for the first case, we will assume all of the 1 - R is absorbed in the four pairs. Figure 2 reflects the temperature rise in coating pairs N=1 to 4 and Moly substrate for a complete run time of 10 seconds. The amount of incident flux density to take coating pair N=1 to 275°$C_{\Delta T}$ in the 10 seconds will be 8.78(10^4)W/cm^2 or 8.78 (10^5) Joules/cm^2. If we use the partitioned energy where part of the energy is absorbed by the coating pairs and part is absorbed directly by the substrate, with the remainder going to scatter, we find from Figure 3 that for a 10 second run the maximum incident flux density to take coating pair N=1 to 275°$C_{\Delta T}$ in 10 seconds will be 1.98(10^5)W/cm^2 or 1.98(10^6) Joules/cm^2. This constitutes a factor of 2.25 greater by looking at the energy that really goes into the coating and into the substrate. This would appear to be a rather substantial amount, all things being equal. The reader should also notice that the upper limit for thermal shock in air for the ThF_4 is close to that value suggested by Bennett. Because we do not have the as-deposited values for ZnSe it would be hard to say what the in air thermal shock value will be for certain. However, we do not have the as-deposited values for the remaining coating chemistries either.

The second coating pair combination has the same substrate and Silver coating with a $(SiO/Si)^3$ combination. The index of refraction at 2.8 µm for SiO is 1.80, and for Si the index is 3.43. Young's Modulus for the Si is 6.76 (10^6) N/cm^2 and 3.45(10^6) for SiO. Commensurately, the coefficient of expansion for the Si is 2.44(10^{-6}) and for SiO the coefficient is 1.5(10^{-6}). We find from *Eq. (6)* for this pair, and the remaining two chemistries, that the equation overpredicts the absorption. It appears the equation is swamped by the scatter. Consequently, we will use the 1-R for absorption as shown by the calormetric measurement. As an aside, *Eq. (6)* predicts virtually no transmission to the substrate through the coating stack. From *Eq (5)* then,

For Si,

$$\Delta T_{shock} = \varepsilon E_c\ (1-\ 0.2)\ /\left\{\ Ec\ (\alpha_s - \alpha_c)\right\}$$

$$\Delta T = 6.76\ (10^3)\ (1-\ 0.2)\ /\left\{\ 6.76\ (10^6)\ \left(5\ (10^{-6})\ -\ 2.44\ (10^{-6})\ \right)\right\}$$

ΔT = 312.5 temperature difference between the Si and the Moly

and, For the SiO,

$$\Delta T = 3.45\ (10^3)\ (1-\ 0.2)\ /\left\{\ 3.45\ (10^6)\ \left(7.57\ (10^{-6})\ -\ 5\ (10^{-6})\ \right)\right\}$$

ΔT = 228.6 temperature difference between the SiO and the Moly

The absorption was measured calorimetrically and found to be 1.39 (10^{-3}) for this system. From Figure 4 we see that the temperature of coating pair N=1 will be 456°$C_{\Delta T}$ and the first surface of the Moly substrate will be 227°$C_{\Delta T}$ to achieve the thermal shock threshold after a 10 second laser run. The third coating pair consisted of $(SiO/Ge)^3$ on a Silvered Moly substrate. The index of refraction at 2.8µm for SiO is 1.80, and for Ge the index is 4.2. Young's Modulus for the Ge is

$10.27(10^{6})$ N/cm^2 and $3.45(10^6)$ for SiO. Commensurately, the coefficient of expansion for the Ge is $6.1(10^{-6})$ and for SiO the coefficient is $1.5(10^{-6})$. From *Eq (5)* then,

For Ge,

$$\Delta T_{shock} = \varepsilon E_c (1- 0.2) / \{ Ec (\alpha_s - \alpha_c) \}$$

$$\Delta T = 10.27\ (10^3)(1- 0.2) / \{ 10.27\ (10^6)(6.1\ (10^{-6}) - 5.0\ (10^{-6})) \}$$

ΔT = 727 temperature difference between the Ge and the Moly

and,

For the SiO,

$$\Delta T = 3.45\ (10^3)\ (1- 0.2) / \{ 3.45\ (10^6)(7.57\ (10^{-6}) - 5\ (10^{-6})) \}$$

ΔT = 228.6 temperature difference between the SiO and the Moly

The absorption was measured calorimetrically and found to be $1.40\ (10^{-3})$ for this system. From Figure 5 we see that the temperature of coating pair N=1 will be 461°C$_{\Delta T}$ and the first surface of the Moly substrate will be 232°C$_{\Delta T}$ to achieve the thermal shock threshold after a 10 second laser run. The fourth coating pair consisted of $(ZnS/Ge)^4$ on a Silvered Moly substrate. The index of refraction at 2.8μm for ZnS is 2.26, and for Ge the index is 4.2. Young's Modulus for the Ge is $10.27(10^6)$ N/cm^2 and $7.45(10^6)$ for ZnS. Commensurately, the coefficient of expansion for the Ge is $6.1(10^{-6})$ and for ZnS the coefficient is $7.85(10^{-6})$. From *Eq (5)* then,

For Ge,

$$\Delta T_{shock} = \varepsilon E_c (1- 0.2) / \{ Ec (\alpha_s - \alpha_c) \}$$

$$\Delta T = 10.27\ (10^3)(1- 0.2) / \{ 10.27\ (10^6)(6.1\ (10^{-6}) - 5.0\ (10^{-6})) \}$$

ΔT = 727 temperature difference between the Ge and the Moly

and,

For the ZnS,

$$\Delta T = 7.45\ (10^3)\ (1- 0.2) / \{ 7.45\ (10^6)(7.85\ (10^{-6}) - 5\ (10^{-6})) \}$$

ΔT = 280.7 temperature difference between the ZnS and the Moly

The absorption was measured calorimetrically and found to be $9.55\ (10^{-4})$ for this system. From Figure 6 we see that the temperature of coating pair N=1 will be 564°C$_{\Delta T}$ and the first surface of the Moly substrate will be 284°C$_{\Delta T}$ to achieve the thermal shock threshold after a 10 second laser run.

We see, then, that the temperature in the coatings can run quite high compared to the 200°C suggested by Bennett when the appropriate coatings are placed on the Moly substrate. We see, in fact, that the temperatures could run as high as the oxide coating in the Kuster and Ebert experiment. However, before we become too enthusiastic about the high thermal shock values, we should look at the remaining figures where we have clculated the thermal shock values for the same coatings on a Copper and Fused Silica substrate. For example, the $(ZnS/Ge)^4$ coating on Fused Silica will only be able to go to a temperature of 255°C$_{\Delta T}$ in the coating pair N=1 and 145°C$_{\Delta T}$ on the first surface of the substrate. In the case of a Copper substrate, the maximum temperature in coating pair N=1 can only go to a temperature of 154°C$_{\Delta T}$ and 77°C$_{\Delta T}$ on the first surface of the Copper. For the

$(SiO/Si)^3$ and the $(SiO/Ge)^6$ the calculated thermal shock sets in when the coating Pair N=1 achieves 112°$C_{\Delta T}$ and the substrates reaches 56°$C_{\Delta T}$ on the first surface of the Copper substrate. Clearly, then, the 200°$C_{\Delta T}$ is not a conservative value in some cases. However, it is not suitable to believe that all coatings will be able to withstand the ≈ 590 to ≈ 680°C temperature suggested by the Kuster and Ebert experiment. It would seem that the thermal shock criteria will have to be another component in the selection of the coatings and substrate when looking towards the maximum laser damage threshold of an optical component. There are some additional considerations that have fallen out of this analysis. It would seem that if one can transmit part of the energy to the substrate then there will be much less temperature difference between N=1 and the substrate. This would seem to provide a much higher possible temperature, and subsequently, a higher damage threshold for the optical component. As systems are pushed for higher flux densities, these seemingly small techniques may play a rather significant role in the design of optical thin films. Which leads to the last comment. If Rugate coatings are proven to be practical and repeatabale, the fact that they have only one resistance interface between N=1 and the substrate should make them substantially less victimized by thermal shock. They may prove to be the most viable technique for the next step toward higher flux densities.[49,50,51]

References

1. H. Kuster, and J. Ebert, "Pyroelectric Mesurement Of Absorption In Oxide Layers And Correlation To Damage Threshold," *Laser Induced Damage In Optical Materials: 1979*, NBS Spec. Pub. 568, 1980.

2. H. E. Bennett, *Large Optics Coating and Evaluation Facility Study*, NWC TP 6177, Naval Weapons Center, China Lake, CA, pp. 31 ff., 1980.

3. H. S. Carslaw, and J .C. Jaeger, *Conduction of Heat In Solids*, 2nd ed.,Oxford University Press, Oxford, England, 1978.

4. J.C Jaeger, "Pulsed Surface Heating of A Semi-Infinite Solid," *Quart. Appl. Math*, Vol 11, No. 1, 1953.

5. J. R. Palmer, "Reverse Thermal Wave Approximation For Temperature Transients In Coated Reflective Optics For High Power Repetitive Pulsed Lasers," *Optical Engineering* (to be published).

6. J. R. Palmer, "Reverse Thermal Wave Approximation For Temperature Transients In Coated Reflective Optics For High Power Continuous Wave Lasers," *Optical Engineering* (to be published).

7. J. R Palmer, *High Power Laser Optics*, Marcel Dekker, Inc., New York, NY, (to be published).

8. J. R. Palmer, *Laser Damage In Optical Thin Films*, MacMillan Publishing Co.,New York, N.Y., (to be published).

9. S. Musikant, *Optical Materials*, B. J. Thompson, ed., Marcel Dekker, Inc. New York, NY, 1985.

10. H. M. Musal, "Thermomechanical Stress Degradation Of Metal Mirror Surfaces Under Pulsed Irradiation," *Laser Induced Damage In Optical Materials: 1979*, NBS Spec. Pub. 568, 1980.

11. N. J. Kreidl, and J. L Rood, "Optical Materials," Chpt. 5, *Applied Optics And Optical Engineering* Vol. 1, R. Kingslake, ed., Academic Press, New York, NY., 1965.

12. J. H. Faupel, and F. E. Fisher,ed., *Engineering Design*, 2nd ed., John Wiley and Sons, Inc., New York, NY, 1981.

13. B. A. Boley, and J. H. Weiner, *Theory Of Thermal Stresses*, John Wiley and Sons, Inc., New York, NY, 1960.

14. M. L. Scott, "A Review Of UV Coating Material Properties," *Laser Induced Damage In Optical Materials: 1983*, NBS Spec. Pub. 688, 1985.

15. W. P Barnes, "Optical Materials - Reflective," *Applied Optics And Optical Engineering*, Vol. VII, R. R. Shannon, and J. C. Wyant, ed., Academic Press, New York, NY, 1979.

16. P. A.Temple, D. L. Decker, T. M. Donovan, and J. W. Bethke," Measured Thin Film Absorption At The Interface, The Thin Film Bulk, And The Film-Substrate Interface," *Laser Induced Damage in Optical Materials: 1978*, NBS Spec. Publ. 541, pp. 37-42. 1979.

17. P. A. Temple,"Measurement Of Thin-Film Optical Absorption At The Air-Film Interface Within The Film And At The Film-Substrate Interface," *Appl. Phys. Lett.* 34 (10), pp. 677-679, May 1979.

18. H. E. Bennett, and D. K. Burge, "Simple Expressions For Predicting The Effect Of Volume And Interface Absorption And Of Scattering In High-Reflectance Or Anti-Reflectance Multilayer Coatings," *J. Opt. Soc. AM*, Vol. (70), No. (3) pp. 268-276. March 1980.

19 H. K. Pulker, "Stress, Adherence, Hardness, And Density Of Optical Thin Films," *Optical Thin Films*, SPIE, Vol. 325, 1982.

20. R. W. Hoffman, "The Mechanical Properties Of Thin Condensed Films," *Physics of Thin Films*, Vol. 3, G. Hass and R. Thun ed., Academic Press, New York, pp. 211, ff. 1966.

21. S. J. Holmes, *Reflective Coating Development For HF Lasers*, AFWL-TR-82-12, Northrop Research And Technology Center, Palos Verdes Peninsula, CA.,1982.

22. O. S. Heavens, *Thin Film Physics*, Methuen and Co., Ltd., London, England, 1970.

23. H. K. Pulker, "Stress Mesaurements And Calculations For Vacuum Deposited MgF_2 Films," *Thin Solid Films*, Elsevier Sequoia S. A., Lausanne, Netherlands, 1978.

24. K. Kinosita, "Recent Developments In The Study Of Mechanical Properties Of Thin Films," *Thin Solid Films*, Elsevier Sequoia S. A., Lausanne, Netherlands, 1972.

25. H. K. Pulker, and J. Maser, "The Origin Of Mechanical Stress In Vacuum-Deposited MgF_2 And ZnS Films," *Thin Solid Films*, Elsevier Sequoia S. A., Lausanne, Netherlands, 1979.

26. A. E. Ennos, "Stresses Developed In Optical Thin Film Coatings," *Applied Optics*, Vol. 5, No. 1, 1966.

27. K. H. Guenther, Microstructure Of Vapor-Deposited Optical Coatings," *Applied Optics*, Vol. 23, No. 21, 1984

28. K. H. Guenther, "Physical And Chemical Aspects In The Application Of Thin Films On Optical Elements," *Applied Optics*, Vol. 23, No. 20, 1984.

29. M. Lange, J. McIver, and A. H. Guenther, "Thermal Considerations In The Selection Of Optical MaterialsFor Thin Film Laser Coatings," *Proc. IX IVC- V ICSS*, Madrid, Spain, 1983.

30. M. Lange, J. McIver, and A. H. Guenther, and T. W. Walker, "Pulsed Laser Induced Damage Of An Optical Material With A Spherical Inclusion: Influence Of The Thermal Properties Of The Materials," *Laser Induced Damage In Optical Materials: 1982*, NBS Spec. Pub. 669, 1984.

31. H. E. Bennett, "Insensitivity Of The Catastrophic Damage Threshold Of Laser Optics To Dust And Other Surface Defects," *Laser Induced Damage In Optical Materials: 1980*, NBS Spec. Pub. 620, 1981.

32. J. R. Palmer, and H. E. Bennett, "Relationship Between Coating Defects And The Limiting Flux Density A Cooled Laser Mirror Can Withstand," *Laser Induced Damage In Optical Materials: 1981*, NBS Spec. Pub. 638, 1983.

33 J. R. Palmer, "Continuous Wave Laser Damage On Optical Materials," *Optical Engineering* Vol. 22, No. 4, July/August 1983.

34. J. R. Palmer "Loss Of Infrared Optical System MTF Resulting From Damage Caused By High Power Continuous Wave An Low Average Power Repetitive Pulsed Visible - UV Lasers," *4th Int'l Symp. On Optical And Optoelectronic Applied Science And Engineering,* SPIE No. 806, The Hauge, The Netherlands, April 1987.

35. J. R Palmer, "Analytical Model For Determining Temperature Transients In Multilayer Thin Films With Uncooled And Cooled Soft X-Ray Optics," *International Conference On Soft X-Ray Optics And Technology,* SPIE No. 733, Berlin, West Germany, Dec. 1986.

36. J. R. Palmer, "Theoretical Model For Determining Temperature Transients In Multilayer Optical Thin Films Subjected To High Power Continuous Wave And Repetitive Pulsed Lasers: Part I-Continuous Wave," *Proc. 3rd. Int'l. Symp. On Optical And Optoelectronic Applied Science And Engineering,* SPIE Vol. No. 655,656,Innsbruck, Austria, April, 1986.

37. J. R. Palmer, "Theoretical Model For Determining Temperature Transients In Multilayer Optical Thin Films Subjected To High Power Continuous Wave And Repetitive Pulsed Lasers: Part II-Repetitive Pulsed," *Proc. 3rd. Int'l. Symp. On Optical And Optoelectronic Applied Science And Engineering,* SPIE Vol. No. 655, 656, Innsbruck, Austria, April, 1986.

38. P. J. Schneider, *Conduction Heat Transfer,* Addison-Wesley Publishing Co., Reading, MA., 1974.

39. P. J. Schneider, "Conduction," *Handbook of Heat Transfer Fundamentals* Section 4-1, 2nd. ed., W. M. Rohsneow, J. P. Hartnet, and E. N. Ganic', ed. McGraw-Hill Book Co. New York, NY, 1985.

40. D. M. Lewis, and H. J. Sailer, *Trans. J. Heat Transfer,* ASME, Vol. 87, 1965.

41. H. Fenech, and W. H. Rohsenow, *Trans. J. Heat Transfer,* ASME, Vol. 85, 1963.

42. M. Jakob, *Heat Transfer,* Vol. 1, John Wiley and Sons, New York, NY, 1949.

43. F. Kreith, *Principles of Heat Transfer,* 2nd. ed., International Textbook Co., Scranton, PA, 1966.

44. L. G. Koshigoe, and D. L. Decker, *Thermophysical Properties Of Thin Films,* NWC TM-5322, Naval Weapons Center, China Lake, CA, 1984

45. D. L. Decker, L. G. Koshigoe, and J. Ashely, "Thermal Properties Of Thin Films," *Laser Induced Damage In Optical Materials: 1984,* NBS Spec. Pub. 727, 1986.

46. M. McGuirk, and R. D. Poirier, "Thermal Conductivity Of Enhanced Reflectors," *Laser Induced Damage In Optical Materials: 1985,* NBS Spec. Publ. (to be published).

47. D. L. Decker, "Thermal Properties Of Optical Materials," *Laser Induced Damage In Optical Materials: 1986,* NBS Spec. Publ. (to be published).

48. D. W Lynch, and W. R. Hunter, "Comments On The Optical Constants Of Metals And A Introduction To The Data For Several Metals," Hanbook Of Optical Constants Of Solids, E. D. Palik, ed., Academic Press, Inc., New York, NY, 1985.

49 J. R. Palmer, "Theoretical Model For Evaluating Transient Temperature Distribution In Rugate Optical Thin Films Subjected To High Power Continuous Wave And Repetitive Pulsed Lasers: Part I-Continuous Wave," *Proc. 3rd. Int'l. Symp. On Optical And Optoelectronic Applied Science And Engineering,* SPIE Vol. No. 652,Innsbruck, Austria, April, 1986.

50 J. R. Palmer, "Theoretical Model For Evaluating Transient Temperature Distribution In Rugate Optical Thin Films Subjected To High Power Continuous Wave And Repetitive Pulsed Lasers: Part II-Repetitive Pulsed," *Proc. 3rd. Int'l. Symp. On Optical And Optoelectronic Applied Science And Engineering,* SPIE Vol. No. 652,Innsbruck, Austria, April, 1986.

51. J. R. Palmer "Optical Distortion Of Rugate Coated Optical Components Used In High Power Laser Systems," *4th Int'l Symp. On Optical And Optoelectronic Applied Science And Engineering* SPIE No. 805, The Hauge, The Netherlands, April 1987.

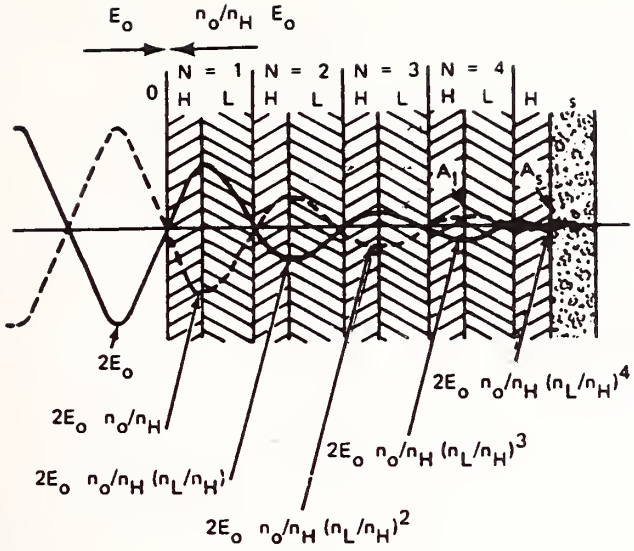
E_o
n_o/n_H E_o
N = 1
N = 2
N = 3
N = 4
0
H
L
H
L
H
L
H
L
H
S
A_1
A_2
$2E_o$
$2E_o$ n_o/n_H
$2E_o$ n_o/n_H (n_L/n_H)
$2E_o$ n_o/n_H $(n_L/n_H)^2$
$2E_o$ n_o/n_H $(n_L/n_H)^3$
$2E_o$ n_o/n_H $(n_L/n_H)^4$

Figure 1

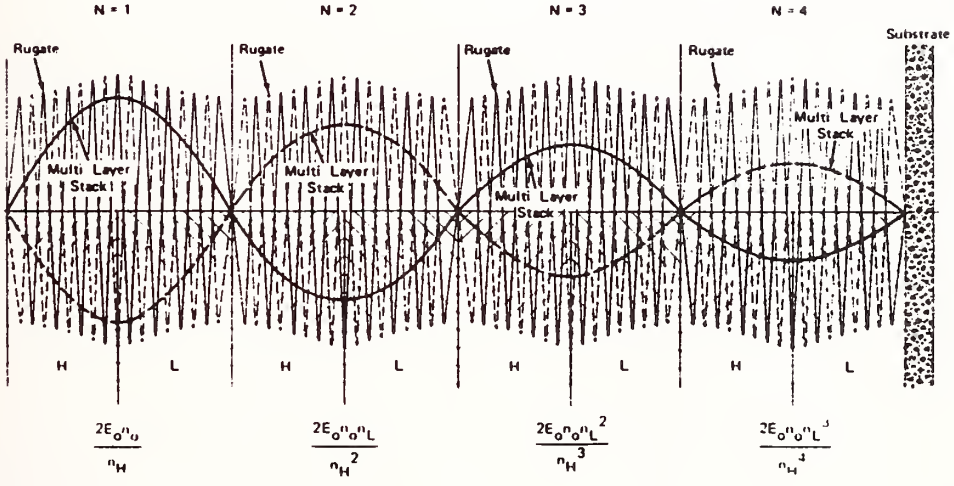
N = 1
N = 2
N = 3
N = 4
Substrate
Rugate
Rugate
Rugate
Rugate
Multi Layer Stack
Multi Layer Stack
Multi Layer Stack
Multi Layer Stack
H
L
H
L
H
L
H
L
$\frac{2E_o n_o}{n_H}$
$\frac{2E_o n_o n_L}{n_H^2}$
$\frac{2E_o n_o n_L^2}{n_H^3}$
$\frac{2E_o n_o n_L^3}{n_H^4}$

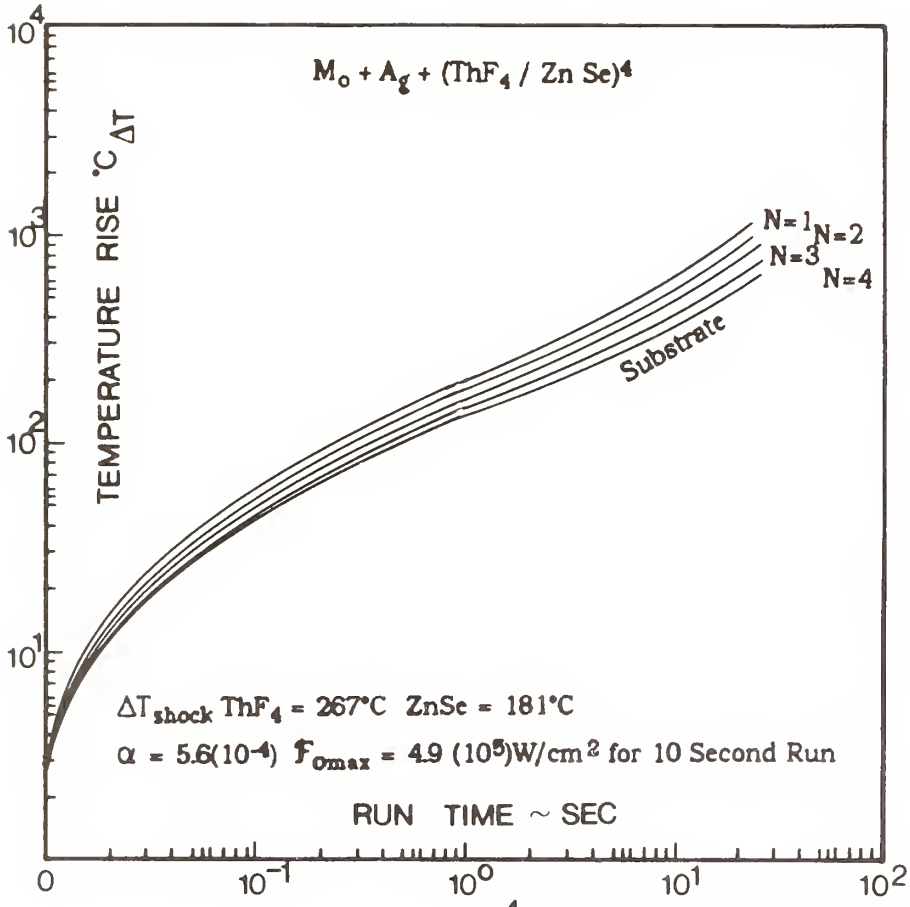

Figure 2

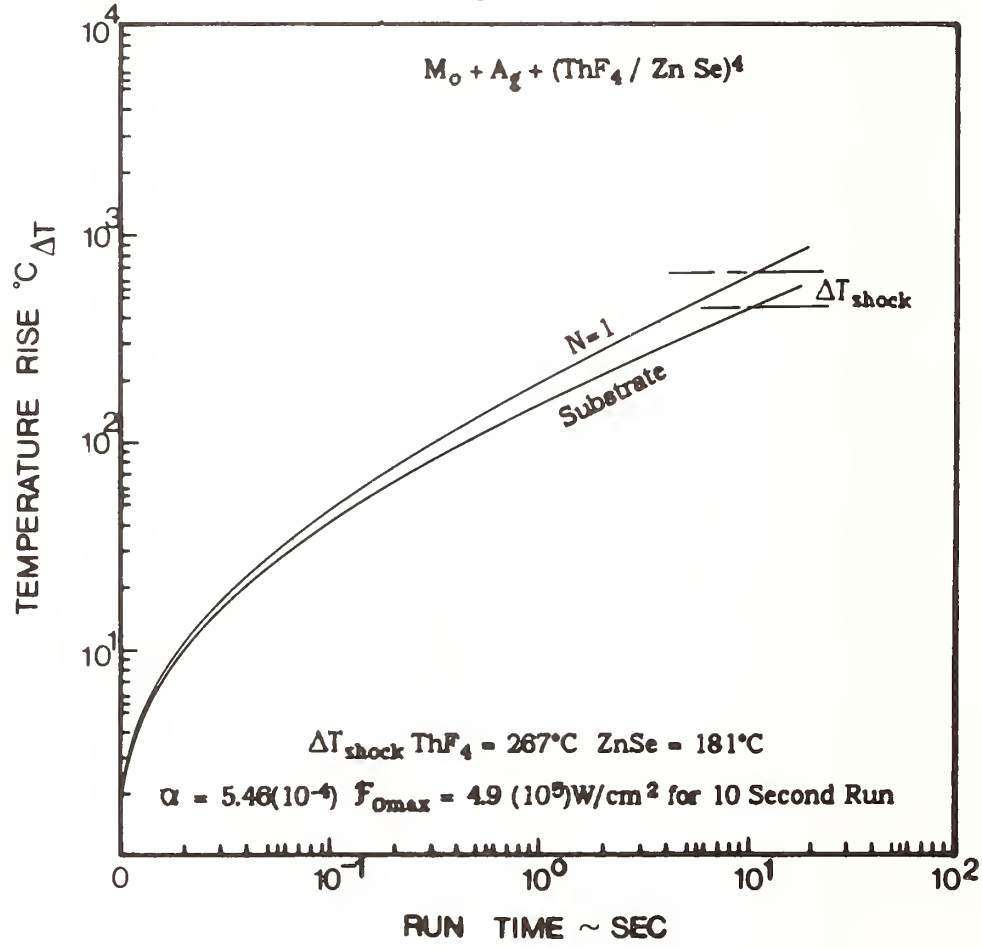

Figure 3

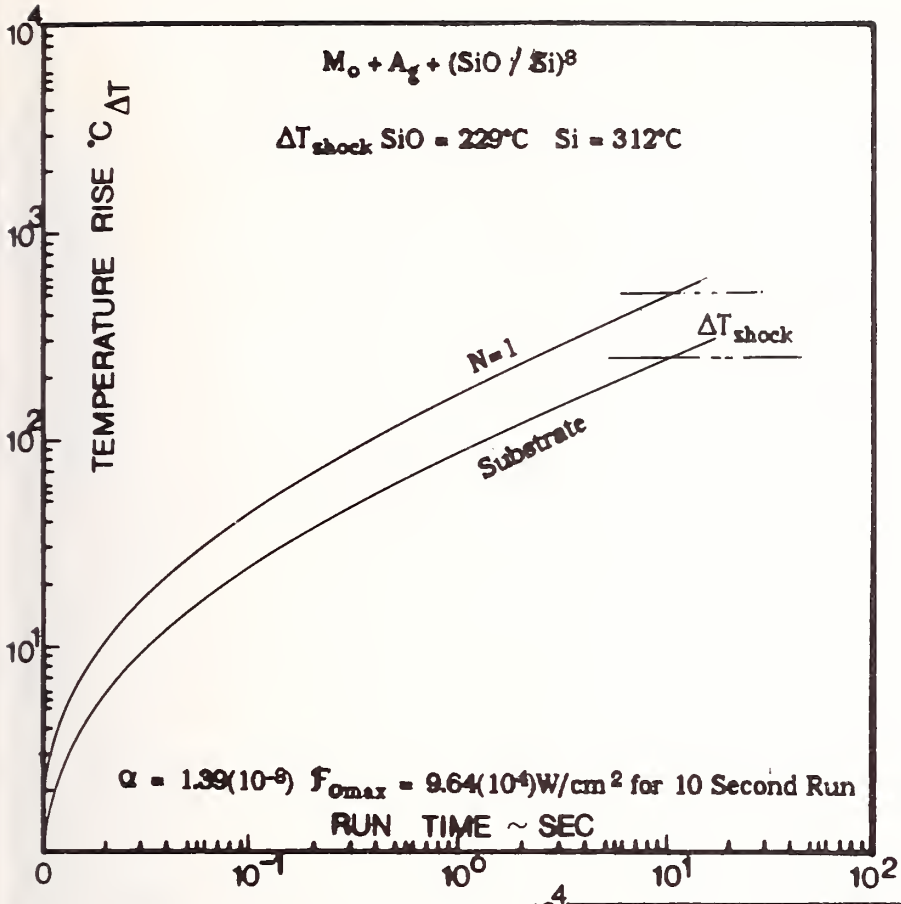

Figure 4

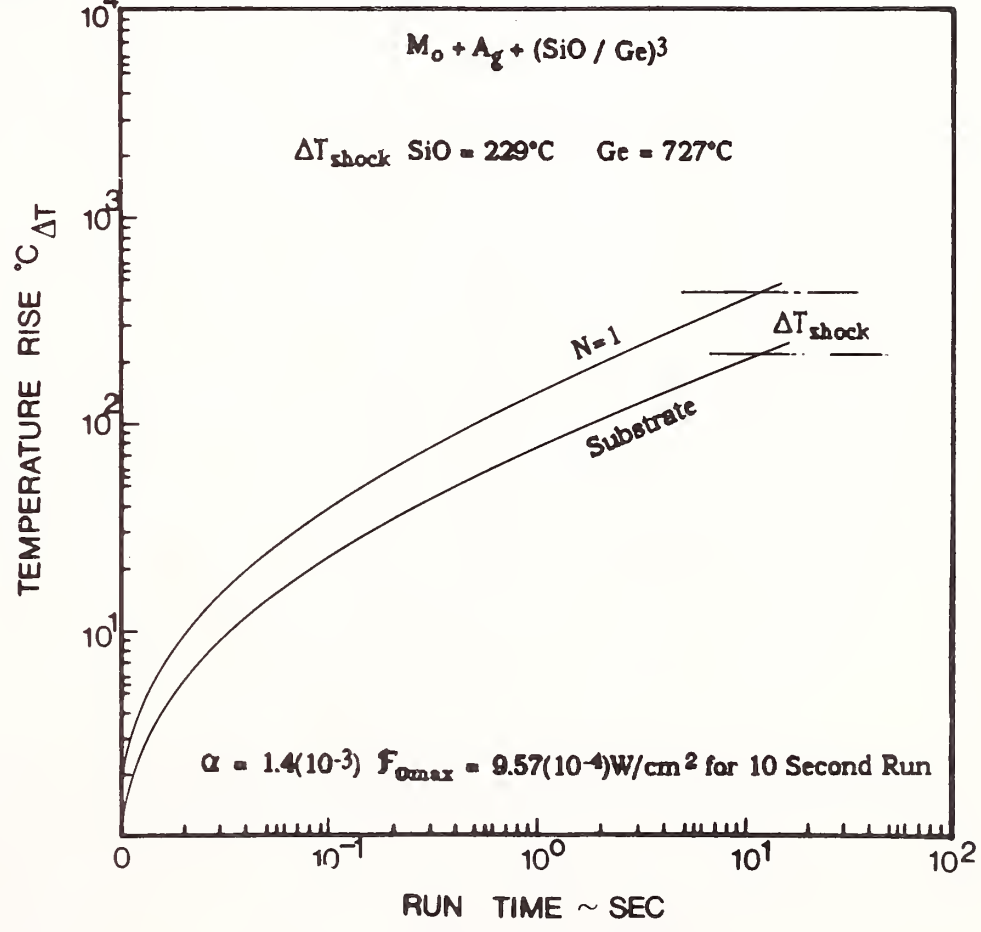

Figure 5

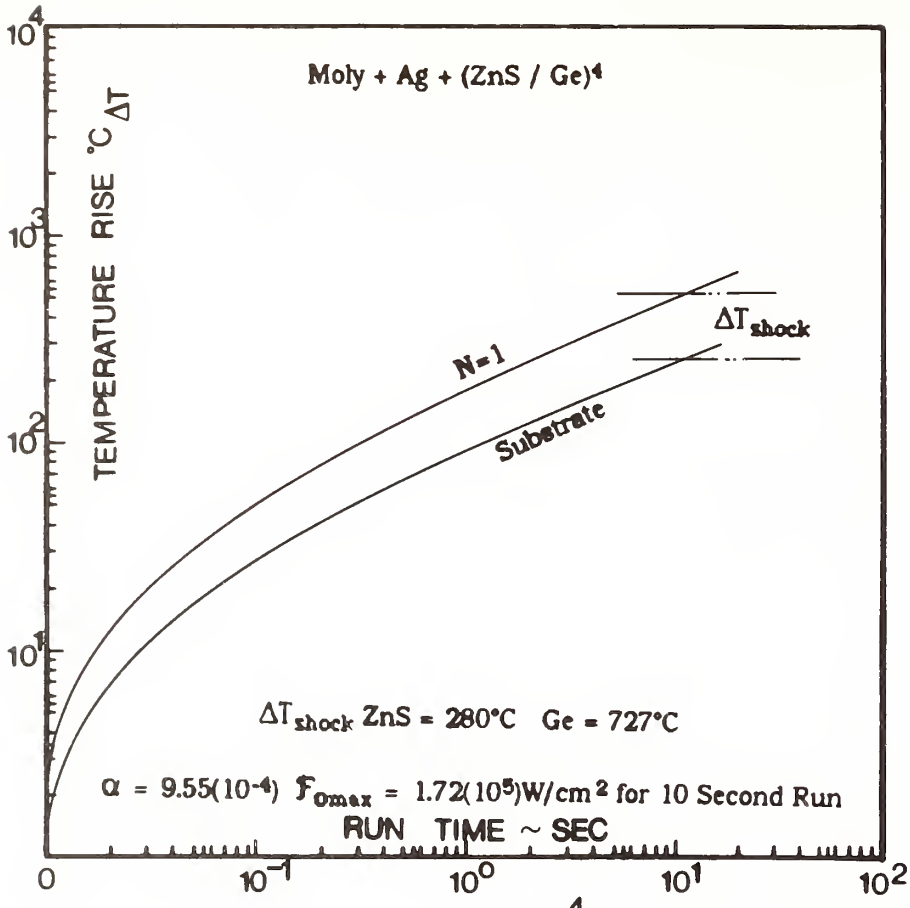

Figure 6

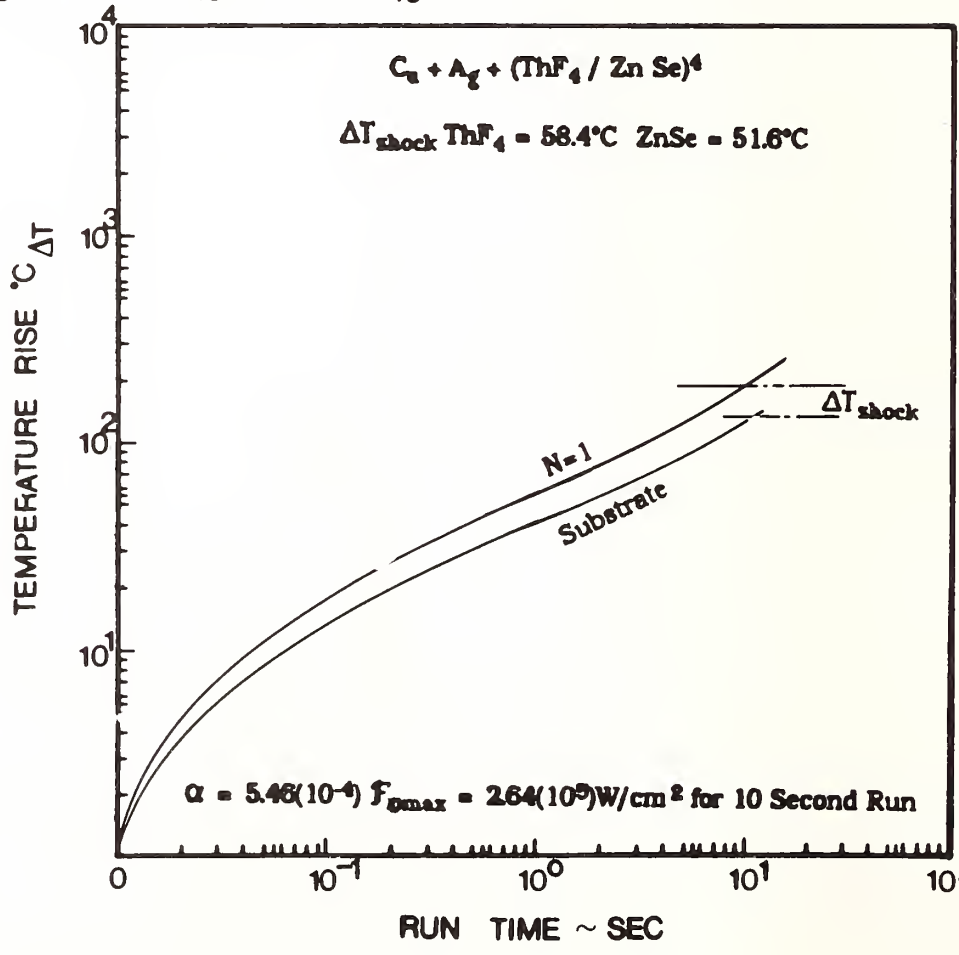

Figure 7

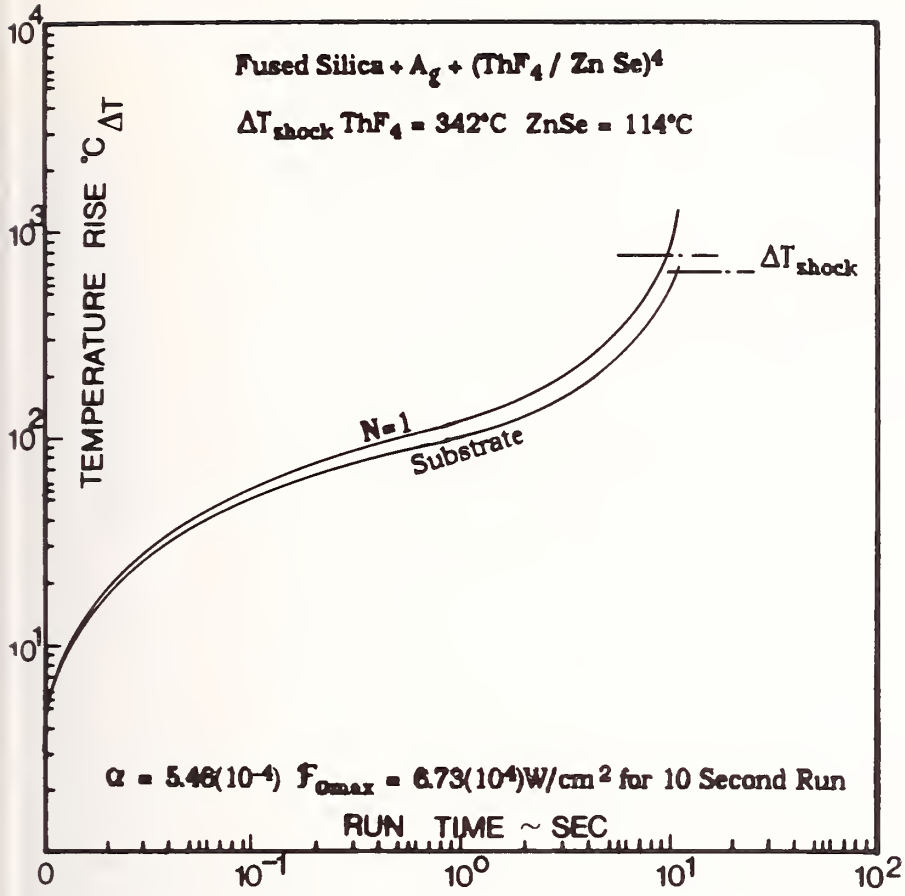

Figure 8

Figure 9

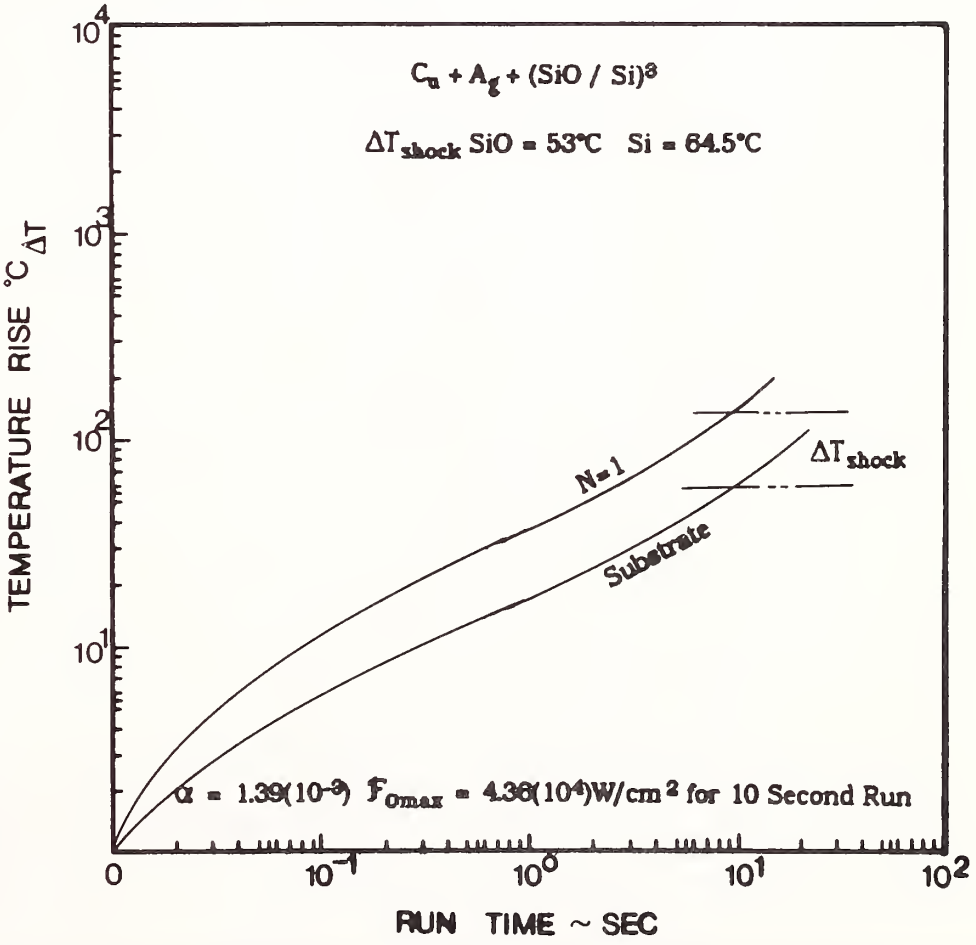

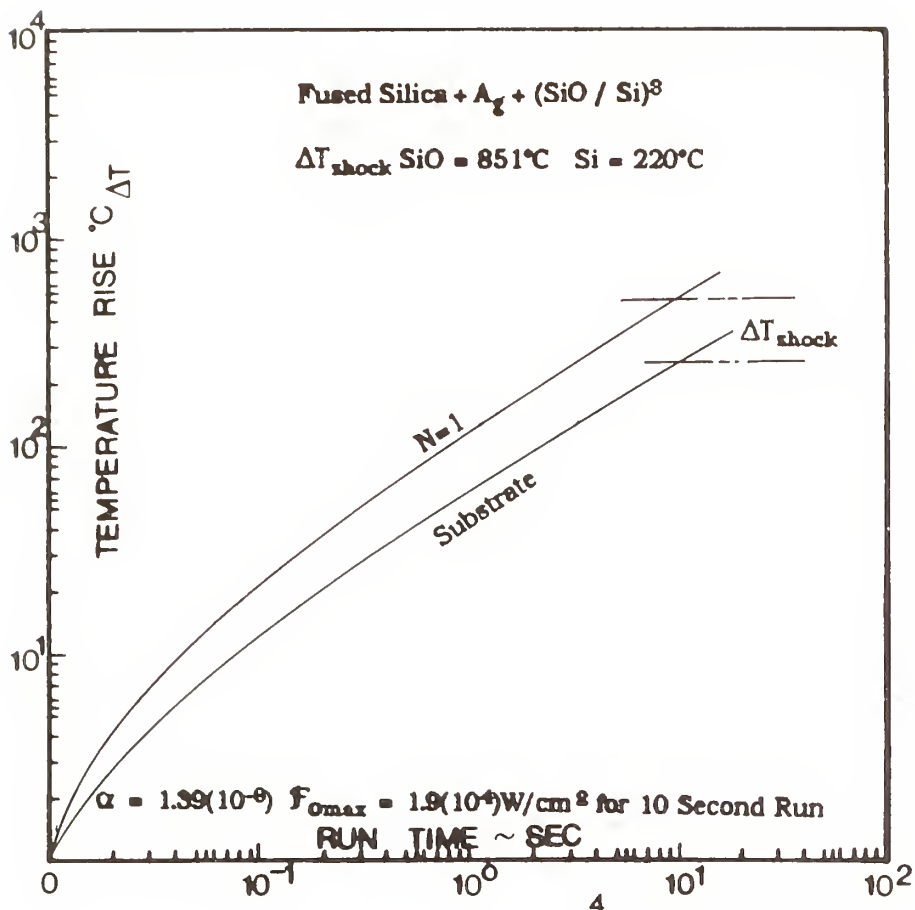

Figure 10

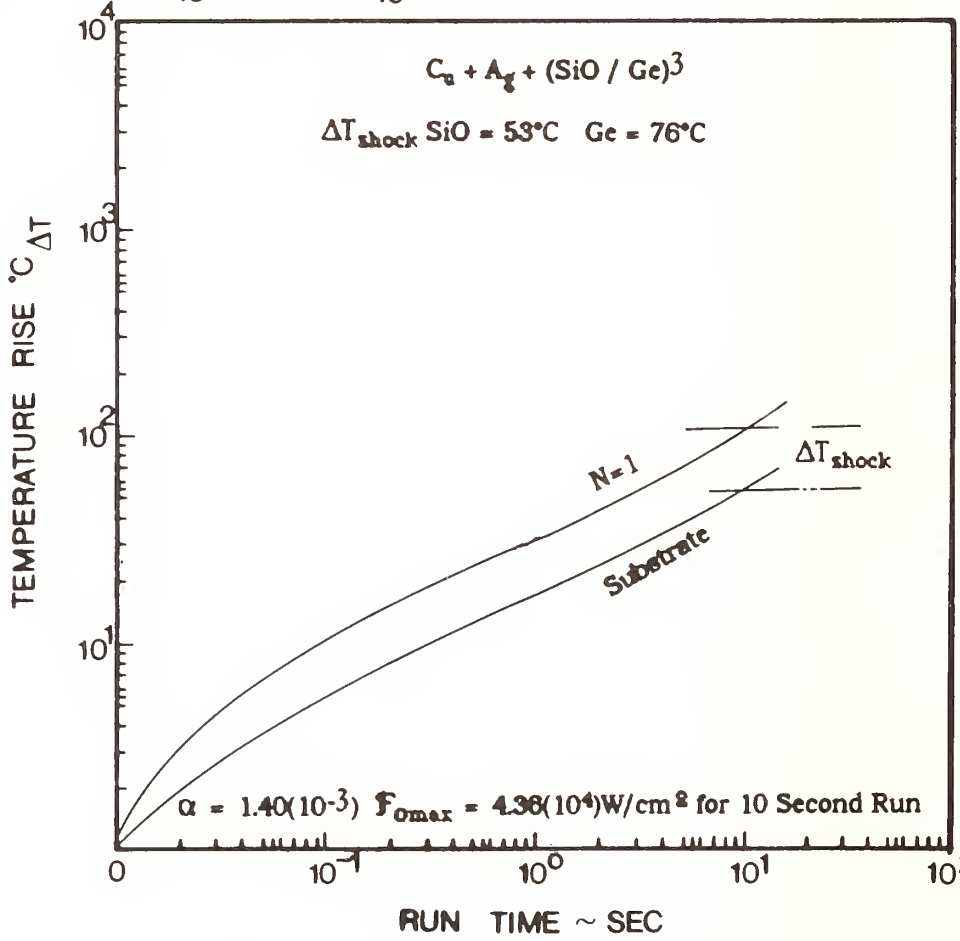

Figure 11

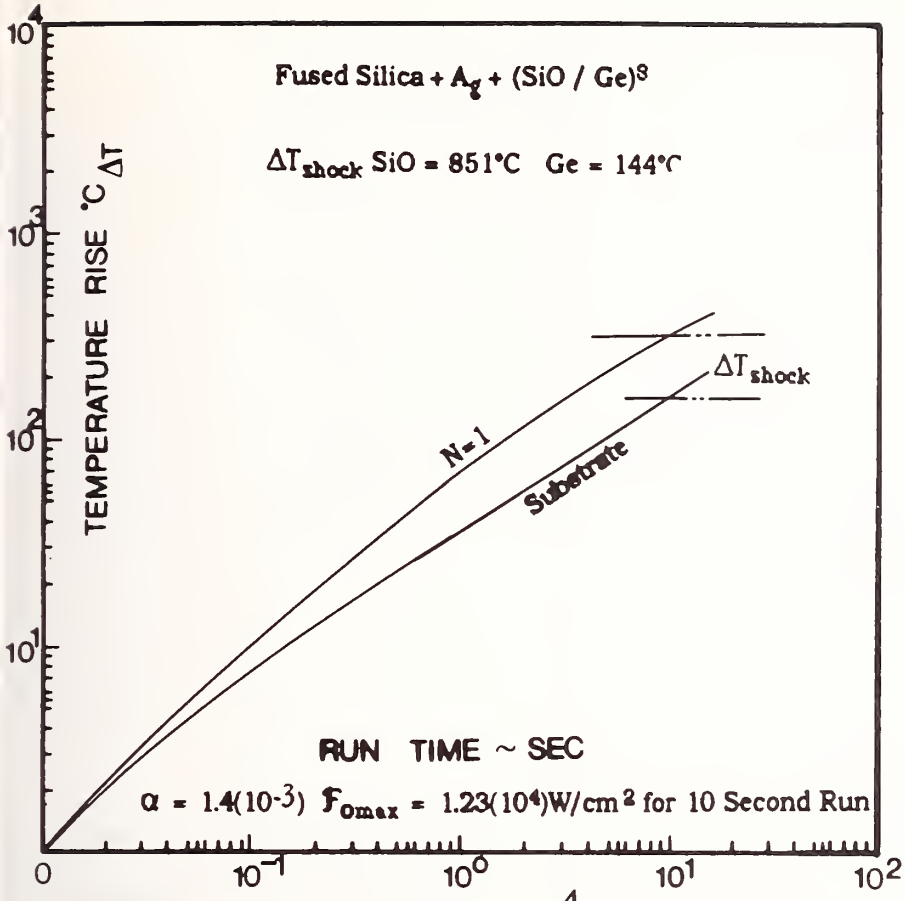

Figure 12

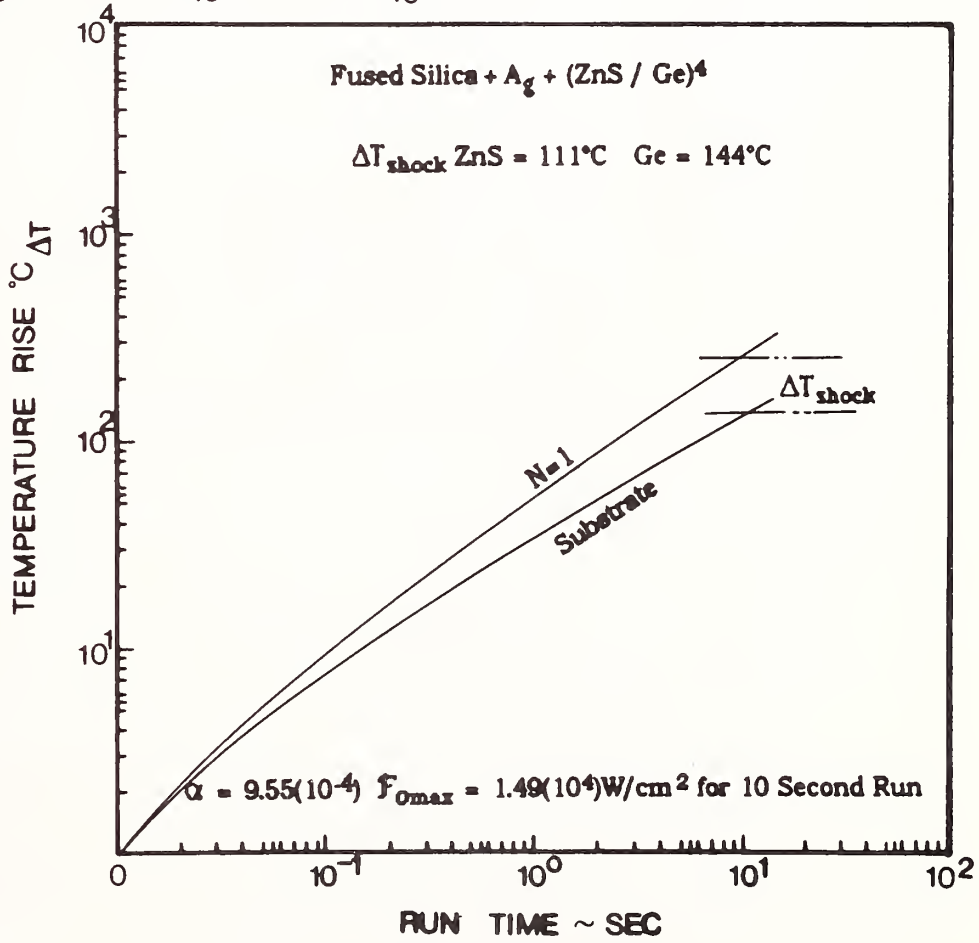

Figure 13

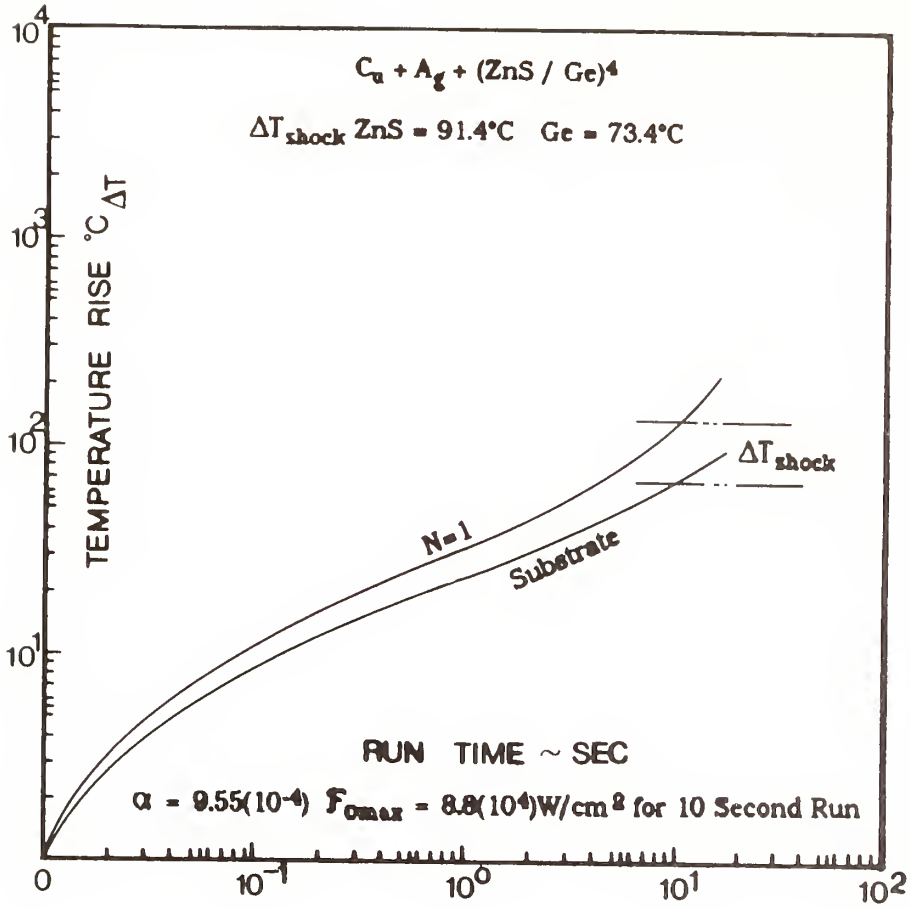

Figure 14

From the experiment: ZrO_2 failed at 640°C
TiO_2 failed at 590°C

$800(10^{-9})$ = ϕFWHB

50μ sec interval 15 Pulses

ΔT_{shock} ZrO_2 = 727°C TiO_2 = 520°C

Figure 15

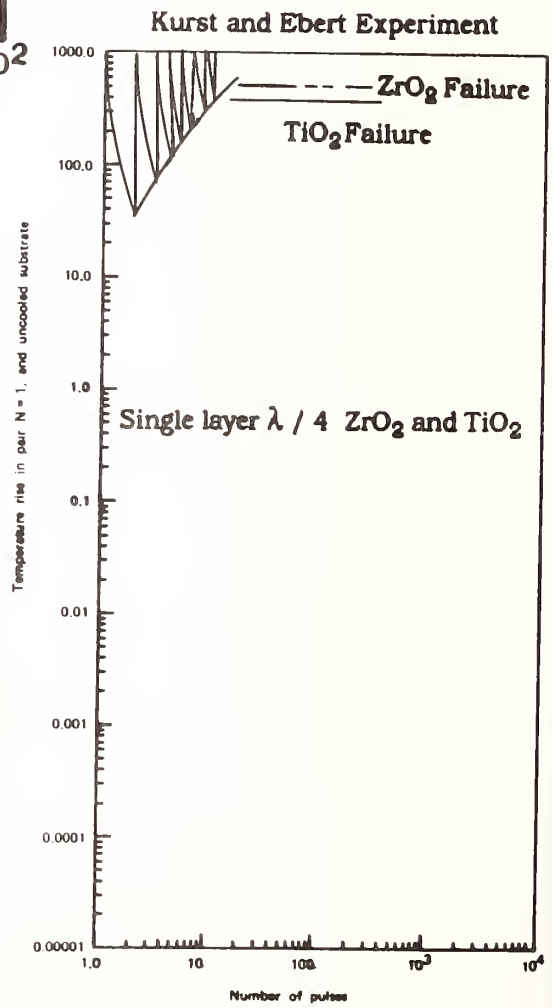

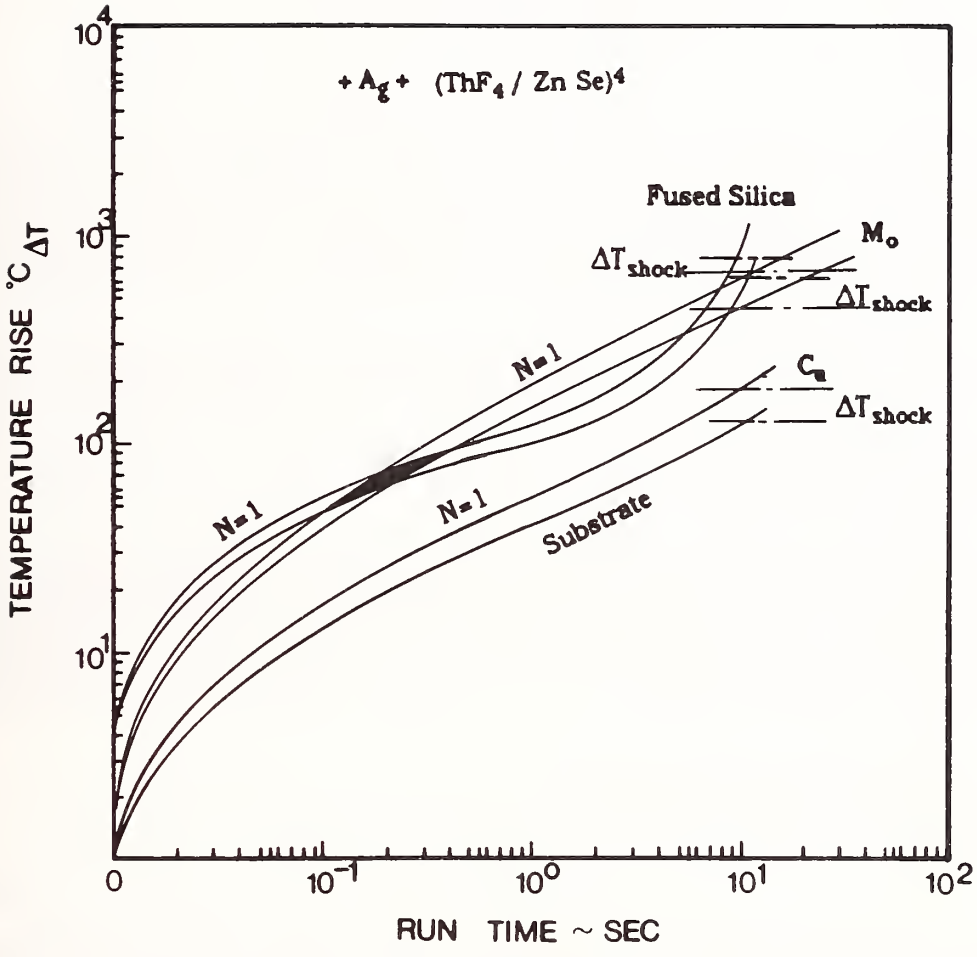
+ Ag + (ThF4 / Zn Se)4
Fused Silica
Mo
ΔTshock
ΔTshock
Cu
ΔTshock
N=1
N=1
N=1
Substrate
TEMPERATURE RISE °C ΔT
RUN TIME ~ SEC
0
10^-1
10^0
10^1
10^2
10^1
10^2
10^3
10^4

Figure 16

Reverse Thermal Wave Approximation For Temperature Transients In Optical Thin Films And Substrates - Reflective Optics For High Power Repetitive Pulsed Lasers

Manuscript Received
12/14/87/sar

J. R. Palmer

University Of Alabama, Huntsville
Center For Applied Optics

Abstract

This is the companion paper to the *Reverse Thermal Wave Approximations* for High Power Continuous Wave Lasers. The purpose of this paper is to provide equations that will allow the optical designer to evaluate the temperature gradient in optical thin films and substrates under transient conditions. The semi-infinite plate models have been described rather extensively in other publications. However, the problem that is treated in this paper is that set of boundary conditions that do not satisfy the semi-infinite plate condition.

It is not uncommon to have coated reflective optics that have very thin substrates. For those conditions it is necessary to evaluate the temperature transient much differently than one would if the substrates were of sufficient thickness to satisfy the semi-infinite plate boundary. One finds that the temperature rise and gradients are substantially different for very thin substrate conditions. The *Reverse Thermal Wave Model* will provide the ability to evaluate the temperature gradients during the transient with closed form approximations.

The repetitive pulsed case has a substantially different characteristic temperature profile from that of the continuous wave and in this paper the equations and figures are provided to reflect the unique character of the temperature gradients in the optical thin films and substrates as a function of the hertz rate and pulse width. It becomes clear that the duel cycle of heating and cooling coupled with the thermal shock play important roles in the damage thresholds of many optical components in high power laser systems.

Key Words: Optics, Transient Heat Transfer, Faceplates, Optical Distortion, and Repetitive Pulsed Lasers

Introduction

As we indicated before,[1,2] most authors dealing with transient thermodynamics rely almost exclusively on the semi-infinite plate model and the infinite plate model.[3,4,5,6] Carslaw and Jaeger,[3] of course, is the most seminal text in this area. However, the work of J. Crank,[4] E. L. Cussler,[5] and Tryyel and Harris[6] provide enormous insight into many of these problems. Even so, the problem of the boundary condition wherein the semi-infinite plate boundary is not met is given very little attention. And, for those people working in the optical field this provides little solace.

The thrust of this paper is to provide a set of approximations that will permit the analyst to evaluate the temperature transient through the optical thin films and a reflective optical faceplate that fails to meet the semi-infinite plate model boundary conditions. Obviously, if an analyst has access to a computer that has an appropriate finite difference heat transfer model, and the money to have the model put to use for the problem at hand, then these approximations may not be of any great concern. For those who do not always have these resources available to them, the approximations can be applied as a useful tool for evaluating their optical components and optical trains. Having said all that, the reader may find it very difficult to have a finite difference program work on the thin films. Most who have tried, including the author, have found that the films have such little thermal mass that the program goes unstable and blows up. The author has, however, provided mathematical closed form solutions which may be used in concert with a finite difference program.[7,8,9,10,11]

Repetitive Pulsed - One Dimensional

Basically, we begin with the semi-infinite plate boundary conditions. That is, energy, or temperature, is applied at one surface of the plate, no energy is lost from the plate to the surrounding environment, and the plate is of such a thickness that at the end of the time of the transient, the temperature rise on the back surface will be zero.[1,2,8,9] However, we must first treat with the energy absorbed in the optical thin films and transferred to the optical substrate.

Optical thin film coatings, manifestly, have very little thermal mass. The forces that bond the films may be Van Der Waal's forces, Electrostatic forces, or Chemical Bonding forces.[12,13] The experimental data would tend to indicate that the coating absorption takes place at the boundaries between the coating and the substrate; or coating-coating interface for multilayer systems.[14,15,16,17] Bennett and Burge[15] state that, " . . . And it has been found that the absorption in the vicinity of a thin-film interface may be as large or larger than that in the entire film volume." In discussing the results of absorption of an AsSe thin film on a CaF substrate, Temple states, "It was found that the predominant absorption was at the film-substrate interface."[17] For the analytical system of this paper, there is a concomitant statement that follows from the interfacial absorption. Temple, et.al.,[16] states, "Finally, we would like to make the point that while much attention has been given to the electric field plots for multilayer coatings in damage resistance discussions, it is the relative power density which must be considered in discussing thermal absorption since the local absorptance is the product of the relative power density and the absorption coefficient at that point." Fundamentally, then, the basis of the following treatment is underpinned with the basic premise that most, if not all, of the absorption takes place at the boundaries of the coatings. Further, that the temperature thermal profile will follow the electric field.

Heretofore, the conventional wisdom, when evaluating the temperature rise of an optical surface, has been to assume that the entire absorbed flux density goes into the substrate. Additionally, the belief continues, that the thin-film coatings equilibrate with the substrate in some instantaneous fashion. This technique would tend to indicate that these assumptions may not be accurate. At the outset, we will use an idealized case. The model assumes that the thermal transport properties do not change with temperature, for both the one dimensional and three dimensional case, and no heat is lost from the optic, i.e., no forced or free convection or radiation. The electric field strength and coating relationships will be as shown in *Figure 1*

Absorption Theory for Multilayer Optical Thin Films

According to the electrical field plot of *Figure 1*, interfacial absorption will occur only at,

$$2E_o(\eta_o/\eta_H),\ 2E_o(\eta_o\eta_L/\eta_H^2),\ 2E_o(\eta_o\eta_L^2/\eta_H^3)\ldots$$

Even though the films are extremely thin, they are still amenable to joule heating. Consequently, the semi-infinite plate model is applicable. The model assumes that the layers of films are analogous to a series of composite layers. Each layer is bound by one, or a combination, of forces described earlier. This adhesive force is very important in determining the required transient and steady-state gradient through the film layers. If we assume, then, that the absorption and power densities are proportionate to the (E) field strength through the layers of the coatings, then,

(1)

$$\alpha^* = \left\{1 - R - [4(\Psi)(\eta_L/\eta_H)^{2N}/(\varphi)] - [4\pi\sigma\cos(\theta)\{1.15 - 2.565(10^{-6}) \times [5(10^4) - \lambda]^{2N}/\lambda]^2\right\} \left\{[1 - (\eta_L/\eta_H)^{2N+1}][\eta_H^2 - \eta_L^2]^{-1}(4)\right\}^{-1}$$

If the reflecting optic has a dielectric substrate:

low index next to the substrate, then, $\Psi = 1$, $\varphi = \eta_S$:

high index next to the substrate, then, $\Psi = \eta_S$, $\varphi = \eta_H^2$:

where, η_S = Substrate index, η_H = Index of the high index film.

For the case where the substrate is not a dielectric, i.e., is a metal, a quasi dielectric of the metal-film combination is generated, so that, for the low index next to the substrate,

(2)

$$\Psi = \eta_S \left\{ \left((1 \; (-/+) \cos \delta) / 2 \right) \left\{ (\eta_S/\eta)^2 + (K_S/\eta)^2 \right\} + (1 \; (+/-) \cos \delta) / 2 + (K_S/\eta) \sin \delta \right\}^{-1}$$

where, η = (η_L) low index film, at λ if next to substrate.

(η_H) if high index next to metal.

η_S = Index for metal substrate, at λ.

K_S = Extinction coefficient for metal substrate at λ.

$\tan \delta = 2\eta K_S / \{\eta^2 - \eta_S^2 - K_s^2\}$

$\varphi = \eta_H^2$

If the high index film is next to the substrate, $\Psi = 1.0$.

When, $\eta^2 > (\eta_S^2 + K_S^2)$, δ is in the first quadrant. Otherwise, δ is in the second quadrant using the standard conventions.

σ = rms surface roughness, Å

λ = Wavelength of interest, Å

R = Reflectivity

N = Number of high-low coating pairs

For *Eq. (2)*, if the low index film is next to the metal substrate, use the upper sign in the denominator. If the high index is next to the substrate, use the lower sign in the denominator.

The value of $(4\pi\sigma \cos(\theta)/\lambda)^2$ represents the total integrated scatter from a surface. The expression $1.15\text{-}2.565(10^{-6})[5(10^4)\text{-}\lambda]^{2N}$ represents the increase in scatter as a function of wavelength and number of coating pairs.

Repetitive Pulsed Uncooled Coated Optics

At each interface there will be a distribution of power density absorbed between the low and high index materials, as a function of their respective thermal transport properties, then,

(3)

$$2E_o \sum_{m=0}^{m} \left(\eta_o \eta_L^m / \eta_H^{m+1} \right) \left(F_1 \alpha^*_1{}^{0.5} / K_1 \right) = 2E_o \sum_{n=0}^{n} \left(\eta_o \eta_L^n / \eta_H^{n+1} \right) \left(F_2 \alpha^*_2{}^{0.5} / K_2 \right)$$

$$F_2 = F_1 \left(\alpha^*_1{}^{0.5} \right) K_2 / \left(K_1 (\alpha^*_1{}^{0.5}) \right) \left\{ 2E_o \sum_{n=0}^{n} \left(\eta_o \eta_L^n / \eta_H^{n+1} \right) / 2E_o \sum_{m=0}^{m} \left(\eta_o \eta_L^m / \eta_H^{m+1} \right) \right\}$$

where, F_1 = Absorbed portion in low index material

F_2 = Absorbed portion in high index material

$\alpha^\bullet_1$ = Thermal diffusivity of low index material, cm^2/sec

$\alpha^\bullet_2$ = Thermal diffusivity of high index material, cm^2/sec

K_1 = Thermal conductivity of low index material, W/cm-°C

K_2 = Thermal conductivity of high index material, W/cm-°C

So that,

(4)

$$F_1 + F_2 = 1.0 \qquad C = ((a\bullet_1{}^{0.5})\, K_2 \;/\; (K1\ (a\bullet_2{}^{0.5}))$$

(5)

$$F_2 = 1.0 / (1.0 + C) \qquad F_1 = 1.0 - F_2$$

From *Eq. (1)* through *(5)*, the temperature rise for each element in the multilayer stack, and the substrate, may be evaluated. Using a modified form of the Palmer-Bennett model, to include source and multiple sink to the substrate,[7,8,9,18,19,20,21]

(6)

$$\Delta T_{F1\text{-}2} = \eta\left\{ 2\mathcal{F}_{O1\text{-}2}(\alpha^\bullet_{1\text{-}2})^{0.5}\left[\Omega^{-0.5} - \{\Omega^{-1} - \Phi\}^{-0.5}\right]\left[\{\text{ierfc}(x)\}\right]/K_{1\text{-}2} - \{2\pi\Omega\Phi\mathcal{F}_{O1\text{-}2}/h_c\}\right.$$
$$\left. + \{2\pi\,\Omega\,\Phi\,\mathcal{F}_{O1\text{-}2}/h_c\}\{\exp(H_1{}^2\alpha^\bullet_c\,\Omega^{-1}\eta)\,\text{erfc}(y)\}\right\}$$
$$+ 2E_o \sum_{(m,n)=0}^{(m,n)} \left[\eta_o\eta_L{}^{(m,n)}/\eta_H{}^{(m,n)+1}\right]\Delta T_m + \Delta T_S$$

where, $X = t/2(\alpha^\bullet\Omega^{-1}\eta)^{0.5}$ at $t=0$ $\quad \Omega$ = Hertz Rate, Cycles/sec

$\text{ierfc}(x) = 1/(\pi)^{0.5}$ $\quad \Phi$ = Pulse Width, FWHB, sec

$\text{erf}(x) = 0$ $\quad \eta$ = Number of Pulses

$h_c = 1./\{\Pi_\zeta{}^{-1}\ (2N)\}$ = W/cm^2 -°C

$Y = H_1(\alpha^\bullet\Omega^{-1}\eta)^{0.5}$

$\alpha^\bullet_c = [\alpha^\bullet_1 + \alpha^\bullet_2]\,2^{-1}$ $\quad K_c = [K_1 + K_2]\,2^{-1}$

$\alpha^\bullet_s$ = Thermal diffusivity of the substrate, cm^2/sec

K_S = Thermal conductivity of the substrate, W/cm -°C

$H_1 = \Pi_\zeta / K_C$

$H_2 = \Pi_\zeta / K_S$

The absorbed fluence $\mathcal{F}_{OL}$, $\mathcal{F}_{OH}$ are found from,[7,8,9,21]

(7)

$$\mathcal{F}_{OL} = I_o\alpha^\bullet{}_o F_1 \Psi_H \left\{ 2E_o \sum_{m=0}^{m} \left[\eta_O\eta_L{}^m/\eta_H{}^{m+1}\right]\right\}^{-1.0}\{\Phi\}^{-1.0}$$

$$\mathcal{F}_{OH} = I_o \alpha^{\bullet}_o F_2 \Psi_N \left\{ 2 E_o \sum_{n=0}^{n} \left[\eta_0 \eta_L^n / \eta_H^{n+1} \right] \right\}^{-1.0} \{\Phi\}^{-1.0} \qquad (8)$$

where,

$\mathcal{F}_{OL}$, $\mathcal{F}_{OH}$ = Absorbed flux density, W/cm^2

I_O = Incident fluence, Joules/cm^2

N = High low pair number from *Figure 1*

Ψ_N = $2E_o(\eta_O/\eta_H)$, $2E_o(\eta_O\eta_L/\eta_H^2)$, $2E_o(\eta_O\eta_L^2/\eta_H^3)$, . . .

$\alpha^{\bullet}_o$ = Absorption value

The temperature rise at the low - high index interface, where the electric field is cancelled, i.e., no absorption, is found from,[7,8,9,21]

$$\begin{aligned}
\Delta T_{F1\text{-}2} = & \left\{ 2 \mathcal{F}_{OH} (\alpha^{\bullet}_{1\text{-}2})^{0.5} \left[\Omega^{-0.5} - \{ \Omega^{-1} - \Phi \}^{-0.5} \right] \left[\{ \text{ierfc}(x) \} \right] / K_{1\text{-}2} - \{ 2 \pi \Omega \Phi \mathcal{F}_{OH} / h_c \} \right. \\
& + \{ 2 \pi \Omega \Phi \mathcal{F}_{OH} / h_c \} \{ \exp (H_1^2 \alpha^{\bullet}_c \Omega^{-1} \eta) \, \text{erfc}(y) \} - 2 \mathcal{F}_{OL} (\alpha^{\bullet}_{1\text{-}2})^{0.5} \\
& \times \left[\Omega^{-0.5} - \{ \Omega^{-1} - \Phi \}^{-0.5} \right] \left[\{ \text{ierfc}(x) \} \right] / K_{1\text{-}2} - \{ 2 \pi \Omega \Phi \mathcal{F}_{OL} / h_c \} \\
& \left. + \{ 2 \pi \Omega \Phi \mathcal{F}_{OH} / h_c \} \{ \exp (H_1^2 \alpha^{\bullet}_c \Omega^{-1} \eta) \, \text{erfc}(y) \} \right\} 2^{-1} \eta \\
& + 2 E_o \sum_{(m,n)=0}^{(m,n)} \left[\eta_0 \eta_L^{(m,n)} / \eta_H^{(m,n)+1} \right] \Delta T_{(m,n)} + \Delta T_S
\end{aligned} \qquad (9)$$

where, $X = t / 2(\alpha^{\bullet}_1 \Omega^{-1} \eta)^{0.5}$ at $t = 0$

$\text{ierfc}(x) = 1/(\pi)^{0.5}$;

$\text{erf}(x) = 0$

$Y = H_1(\alpha^{\bullet}_1 \Omega^{-1} \eta)^{0.5}$

$X_0 = t / 2(\alpha^{\bullet}_2 \Omega^{-1} \eta)^{0.5}$ at $t = 0$

$\text{ierfc}(x_0) = 1/(\pi)^{0.5}$

$Y_1 = H_1(\alpha^{\bullet}_2 \Omega^{-1} \eta)^{0.5}$

The temperature rise of the substrate will be found from,[7,8,9,21]

(10)

$$\Delta T_S = 2E_o\left\{\sum_{m=0}^{m}\left[\eta_o\eta_L{}^m/\eta_H{}^{m+1}\right]2\pi\,\Omega\,\Phi\,F_{oL}\left\{\mathrm{erfc}(x) - \exp\left(H_2{}^2\alpha^*{}_S\Omega^{-1}\eta\right)\mathrm{erfc}(z)\right\}\right.$$

$$\left. + 2E_o\sum_{n=0}^{n}\left[\eta_o\eta_L{}^n/\eta_H{}^{n+1}\right]2\pi\Omega\Phi\,F_{oH}\left\{\mathrm{erfc}(x) - \exp\left(H_2{}^2\alpha^*{}_S\Omega^{-1}\eta\right)\mathrm{erfc}\,(z)\right\}\right\}$$

$$\times\left\{2\left(\alpha^*{}_S\,\Omega^{-1}\eta\right)^{0.5}\left[\left\{\mathrm{ierfc}\,(Q)\right\}\right]/\,K_S\right\}$$

where, $Q = t\,/\,2(\alpha^*{}_S\,\Omega^{-1}\eta)^{0.5}$ at $t = 0$

$\mathrm{ierfc}(Q) = 1/(\pi)^{0.5}$

$\mathrm{erfc}\,(x) = 1$

$Z = H_2\,(\alpha^*{}_S\,\Omega^{-1}\eta)^{0.5}$

The problem is made simpler, of course, if we simply set,

$$F_o = 2E_o\left\{\sum_{m=0}^{m}\left[\eta_o\eta_L{}^m/\eta_H{}^{m+1}\,2\pi\,\Omega\,\Phi\,F_{oL}\right]\left\{\mathrm{erfc}(x) - \exp\left(H_2{}^2\alpha^*{}_S\Omega^{-1}\eta\right)\mathrm{erfc}(z)\right\}\right.$$

$$\left. + 2E_o\sum_{n=0}^{n}\left[\eta_o\eta_L{}^n/\eta_H{}^{n+1}\,2\pi\Omega\Phi F_{oH}\right]\left\{\mathrm{erfc}(x) - \exp\left(H_2{}^2\alpha^*{}_S\Omega^{-1}\eta\right)\mathrm{erfc}(z)\right\}\right\}$$

and, then, *Eq. (10)* becomes,

$$\Delta T_S = 2F_o\left(\alpha^*{}_S\,\Omega^{-1}\eta\right)^{0.5}\left[\left\{\mathrm{ierfc}(Q)\right\}\right]/\,K_S$$

There is yet a distinguishing feature of the repetitive pulse case that must be evaluated. The peak pulse temperature rise. In the repetitive pulsed case there are two elements of the cycle. We have the heating cycle and the cooling cycle. *Equation (6)* provides the residual temperature as a function the heating and cool down components of each cycle. However, there will be a peak temperature temperature rise before the cool down cycle begins, i. e., at the end of the pulse. The peak temperature rise will follow from,[8]

(11)

$$\Delta T_{Peak} = 2F_{o1\text{-}2}(\alpha\Phi)^{0.5}\left\{\mathrm{ierfc}(x)\right\}/K_{1\text{-}2} + 2E_o\sum_{(m,n)=0}^{(m,n)}\left[\eta_o\eta_L{}^{(m,n)}/\eta_H{}^{(m,n)+1}\right]\Delta T_m + \Delta T_S$$

For most all cases the ierfc(x) will equal $1/\pi^{0.5}$. Very often one will see a substantial temperature rise that will force the optical thin films into thermal shock and cause damage to the

optic. This phenomena is discussed a little later on in this paper. The residual temperature rise suggested by *Equation (6)* results from insufficient time for the material to dissipate the absorbed fluence from one pulse before the next pulse strikes. Consequently, we have the peak temperature rise and the slow temperature rise from the residual thermal load. The results can be just as damaging if the peak pulse does not thermally shock the coating, the residual temperature rise can shock the coating after sufficient number of pulses.

The above equations assume that the diameter of the laser beam will be greater than $12[\alpha^* \Omega^{-1} \eta]^{0.5}$ in order to be one dimensional.[1,2,7,8,9] The steady-state gradient may be determined in a straight forward fashion. What makes the problem less than straight forward is knowing the binding forces between the coatings, i.e., adhesion.

Pulker[12] suggests that the adhesive forces may be as low as 10^4 dynes/cm^2 for physisorption to greater than 10^{11} dynes/cm^2 for chemical bonding. Given this wide range, which, most probably, will be very susceptible to the coating technique and the environment, we will use a bonding force between the coatings of 10^{10} dynes/cm^2, for most analysis.

Based on a clamping force between the coatings of 10^{10} dynes/cm^2, or 9689 atmospheres, we can calculate a film coefficient between each layer. Schneider[22,23] states, ". . . heat transfer through an interface takes place by combined mechanisms of conduction across true contact points, conduction across entrapped interstitial fluid, and radiation across interstitial gaps. Resulting overall conductance of the joint is therefore a function of the material in contact (conductivity, surface finish, flatness, and hardness), the contact pressure, the mean temperature and the heat flux across the joint . . ."

The film coefficient is expected to increase with increased contact pressure. From this relationship, the film coefficient should follow from,[22,23,24,25]

(12)

$$\Pi_\zeta = (P^{2/3})\ (1761)^{-1}$$

where: Π_ζ = W/cm^2 -°C P = #/in^2

Based on the clamping force of 9689 atmospheres, $1.42(10^5)$#/in^2, and very smooth surfaces,

$$\Pi_\zeta = \left[1.4(10^5)\right]^{2/3} \times (1761)^{-1} \qquad \Pi_\zeta = 1.55 \text{W/cm}^2\text{-°C}$$

Because the films are so thin, they will not present a thermal resistance of any magnitude. The basic expression for determining the overall film coefficient through a system of composite materials, is,[26,27]

(13)

$$U = 1 / \left\{1/\Pi_{\zeta 1} + L_1/K_1 + 1/\Pi_{\zeta 2} + L_2/K_2 + 1/\Pi_{\zeta 3} + \ldots\right\}$$

So then, treating each absorbing electric field interface as a radiation boundary to the substrate, the first field interface (N=1), from *Fig. 1* the film coefficient will be:

(14)

$$\Pi_\zeta = 1 / \left[2N \times (1.55)^{-1}\right]$$

From our problem, then,

$$H_1 = \Pi_\zeta / K_S \qquad H_2 = \Pi_\zeta / K_C$$

We must remember that the value of (Π_ζ) changes with each pair of coatings as we work our way from N=1 to N = ∞. There are some additional issues that are not clearly defined. For example what are the correct thermal transport properties to use for the as deposited thin films, i.e.,

K_c, $\alpha^{\bullet}_c$. There is experimental work that has been performed that suggests that the thermal transport properties of the as deposited thin films may be lower than the crystalline values by a factor of 10 to 500.[28,29,30,31,32,33] For our analysis we will use the factor of ten reduction in the thermal transport properties of the various materials that are used for dielectric vapor deposited chemistries.

In evaluating the use of the *Reverse Thermal Wave Model*,[1] we began with a substrate of sufficient thickness to satisfy the semi-infinite plate boundary. However, our problem is more complicated with the absorption of the incident laser flux density in the optical thin films. Which leads us to another uncertainty, that of the maximum temperature for the optical thin films. Experiments have been made that suggest that the damaging temperature threshold for a single layer oxide coating on Suprasil I is 600°C irrespective of the melt temperature of the material.[14,34] However, there is also evidence to suggest that the real threshold of a multilayer optical thin film is in the range of 200°C.[14] This more conservative temperature is based upon thermal shock which occurs when the temperature difference between the substrate and the film interface is sufficient to push the coating material past the elastic limit. Even though coatings are very often evaporated on to substrates that are at 200°C, the substrates are completely thermalized and require many minutes for ramp down to ambient temperature. In this discussion, the temperatures are taken to 200°C in less than a second which provides for substantial thermal shock.

We can, for example, use the work of Kreidl and Wood,[35] which is not unlike the equation proposed by Musal,[36] for thermal shock of glass and glass like materials. They suggest the following expression as a first order analysis for thermal shock threshold, then,

(15)

$$\Delta T_{shock} = M(1-\nu)/ E \alpha$$

where,

ν = Poisson's Ratio

E = Young's Modulus, Newton's/cm^2

α = Coefficient of thermal expansion, °C^{-1}

M = Modulus of rupture, Newton's/cm^2

This equation is saying, fundamentally, that the temperature difference necessary to provide a stress that will impose cracking, or fracture of a glass, or a glass like material. What we see in this equation is that the coefficient of thermal expansion pretty much dominates. In another piece of work, Palmer, *et al*, evaluated the temperature rise in coating pair N=1 and the temperature rise of the first surface of the substrate for evaluating the thermal shock temperature differential.[38] For their application, the differential expansion between the coating pair N=1 and the substrate becomes the limiting criteria. In this paper, the seeming anomaly of the wide band of temperatures that coatings could withstand without damaging is resolved. In fact, both cases could very well be true. For this condition, they provide an equation, such that,

(16)

$$\Delta T_{shock} = M(1-\nu)/\{ E (\alpha_s - \alpha_c)\}$$

We can look at some standard materials used in optical thin films and see the respective thermal shock charateristics. For example, we can look at ZnS and Al_2O_3 and see what the relative temperature differential is needed to provide thermal shock. For ZnS the value for Poisson's ratio is on the order of 0.2, Young's Modulus is 1.06 (10^7)Newton's/cm^2, Modulus of rupture 2.05(10^4)Newton's/cm^2, and the expansion coefficient is 7.85 (10^{-6}).[35,37] Newton's/cm^2. For Copper the coefficient of expansion is 16.6 (10^{-6})[39] Newton's/cm^2. We find from *Eq. (15)* that the differential temperature for thermal shock is on the order of 177°C ΔT. For Al_2O_3 the value of Poisson ration is about 0.2, Young's Modulus is about 7.69 (10^7), Modulus of rupture is 1.451 (10^5), and the expansion coefficient is 7.7(10^{-6}).[35,37] The temperature differential for thermal shock will be 170°C ΔT. Based upon the thermal shock equation we are more inclined to use the more

conservative value of 200°C for the maximum threshold of as deposited optical thin films when using a Copper substrate.

Using a one dimensional condition, wherein the laser beam diameter meets the requirements of,

$$D \geq 12 \left(\alpha \Omega^{-1} \eta \right)^{0.5} \qquad (17)$$

where,

α = Thermal diffusivity, cm^2 / sec

$\Omega^{-1}\eta$= Transient time, sec

And the thickness of the substrate meets the requirements of,

$$t \geq 6 \left(\alpha \Omega^{-1} \eta \right)^{0.5} \qquad (18)$$

For the condition wherein constant flux density is applied to the first surface, the one dimensional semi-infinite plate model provides the temperature rise for the first surface,[1,2,3,9]

$$\Delta T_1 = 2 \mathcal{F}_0 (\alpha \Omega^{-1} \eta)^{0.5} \left\{ \text{ierfc}(x) \right\} / K \qquad (19)$$

where,

$\mathcal{F}_0$ = Absorbed incident flux density, W/cm^2

K = Thermal conductivity, W/cm-°C

x = $t / 2(\alpha \Omega^{-1}\eta)^{0.5}$ at t=0 ; ierfc(x) = $1/(\pi)^{0.5}$

And, at some depth into the faceplate, the temperature rise will be found from the following expression,[1,2,3,9]

(20)

$$\Delta T_{t>0} = 2 \mathcal{F}_0 (\alpha t)^{0.5} \left\{ \text{ierfc}(y) \right\} / K$$

where,

y = $t / 2(\alpha \Omega^{-1} \eta)^{0.5}$ at $t > 0$

We can now look at the end point and see if these equations correctly depict the temperature rise through the mass of material. To do this, we need to use the steady state solution.[26] Then,

(21)

$$\Delta T_{avg} = \Omega^{-1} \eta \, \mathcal{F}_0 / (\rho \, c_p \, t)$$

where,

ρ = Density , gm/cm^3

c_p= Specific heat, Joules/gm-°C

t = Thickness of the faceplate, cm

$\Omega^{-1}\eta$ = Time, sec

To demonstrate the relationships between *Eqs. (19), (20),* and *(21),* we can use an example. For our example, we will absorb 0.2 Joules/cm^2 with a pulse width of 2μsec, which provides

a peak flux density of (10^5) W/cm^2 on the first surface of a copper reflective mirror which has optical thin films vapor deposited on the first surface. We will use four pair of quarter wave coatings. The run time will be for 10^3 pulses. The diameter necessary to satisfy *Eq. (18)* for Copper will be 40.517cm.[1,2,3,4,9] The thickness to satisfy the semi infinite plate boundary is, according to *Eq. (19)* 20.258 cm. We will begin by using a high-low four pair stack of Al_2O_3 and ZnS for a wavelength of 2.7μm. The index for the ZnS will be 2.24 and for the Al_2O_3 will be 1.71.[39] From *Eq. (19)* we would find that the temperature rise of the first surface would be 92.15°C$_{\Delta T}$. And, of course, from *Eq. (20)* we would find that the temperature rise on the back surface would be zero for an average absorbed flux density of 125.66 W/cm^2, i. e., $2\pi\Omega\Phi\mathcal{F}_0$. If the problem were linear, the average temperature of the faceplate would be 61.07°C$_{\Delta T}$. However, from *Eq. (21)* we find that the linear condition would require an average temperature of 18.454°C$_{\Delta T}$. In order to get to this part of the problem, however, we must first obtain the energy distribution in the optical thin films. The film coefficient for the mechanical bonding is 1.55W/cm^2 -°C for each interface. Consequently, for the pair N=1, the overall film coefficient will be 0.19375 W/cm^2 -°C. For the second pair, N=2, the film coefficient will be 0.25833 W/cm^2 -°C. For the third pair, N=3, the film coefficient will be 0.3875 W/cm^2 -°C. And, for the fourth pair, N=4, the film coefficient will be 0.775 W/cm^2 -°C. The distribution of energy in the coating pairs will follow from *Figure 1*, so that, N=1 will absorb 35.83% of the total absorbed energy. N=2 will absorb 27.35% of the total absorbed energy. N=3 will absorb 20.88% of the total absorbed energy. And, N=4 will absorb 15.94% of the total amount absorbed. For the optical thin films the value of (α^*_c) will be 0.00698 cm^2/sec and the value of (K_c) will be 0.01698W/cm-°C.[39] For Copper, the value of (α^*_s) will be 1.14 cm^2/sec. The value of (K_c) will be 3.92W/cm-°C.[39] We can evaluate the maiximum temperature rise in the coating pairs as function of the amount of energy that is absorbed at each interface. For example, in coating pair N=1, the residual temperature will not rise above 232.39 °C because of the absorbed energy at the first pair interface. In other words, the steady state rise necessary to provide the absorbed energy sufficient gradient to drive the absorbed flux density to the substrate will be precisely that temperature differential. This does not include that total temperature rise that will occur in order to provide the temperature gradient necessaary to overcome the temperature build up of the other coating pairs and the substrate.

$$\Delta_T = \{2\pi\,\Omega\,\Phi\mathcal{F}_0/h_c\}\,\psi_N \,/\, 2E_o \sum_{(m,n)=0}^{(m,n)} \left[\eta_0\eta_L^{(m,n)} / \eta_H^{(m,n)+1}\right]$$

$$\Delta_T = 125.66\ (0.3583)\ /\ 0.19375$$

$$\Delta_T = 232.39\ ^\circ C$$

In like fashion, the other coating pairs have a temperature rise associated with the amount of flux density that can be stored and unloaded to the substrate under the steady-state conditions. It is now possible to look at the temperature distribution in the substrate. We know what happens to the flux density in the coatings and how that absorbed flux density is accommodated. Our problem now is to evaluate the temperature rise in the substrate for the conditions where the semi-infinite plate boundary is met and where it is not. We can look at the temperature gradient through a 17 cm thick optic, which pretty much fits the semi-infinfite plate condition, and determine if the average temperature accommodates the required flux density of 100 W/cm^2. We can use the *Lazor™Code*[40] to ease the calculations.

t_{cm}	Peak ΔT	ΔT
N=1	787.50	581.18
N=2	505.50	348.80
N=3	290.10	215.75
N=4	164.58	147.98
0		122.13
0.5		106.83
1.0		92.79
1.5		80.10
2.0		68.67
2.5		58.41
3.0		49.35
3.5		41.41
4.0		34.48
4.5		28.53
5.0		23.34
5.5		18.92
6.0		15.26
6.5		12.37
7.0		9.77
7.5		7.77
8.0		6.05
9.0		4.63
9.5		2.64
10.0		2.07
10.5		1.79
11.0		1.16
11.5		0.862
12.0		0.630
12.5		0.461
13.0		0.353
13.5		0.308
14.0		0.200
14.5		0.152
15.0		0.114
15.5		0.086
16.0		0.067
16.5		0.062
17.0		0.060
	$\Sigma =$	795.253

then, 795.253/35 = 22.72°C and rearranging *Eq (21)* we can evaluate the steady-state condition, so that,

$$F_0 = (\rho\, c_p\, t)\,(\Omega^{-1}\eta)^{-1}$$

where,

For Cu^{39} $\rho = 8.96$ g/cm^3; $c_p = 0.38$ Joules/gm-°C

$\Omega^{-1}\,\eta = 10$ sec; $t = 17.0$ cm

then, $F_0 = 8.96$ g/cm^3(0.38 W-sec/g-°C) 17.0cm (22.72°C) / 10sec

$F_0 = 131.51$ W/cm^2 vs 125.66 W/cm^2

It becomes clear, then, that we are dealing with a Gaussian Curve wherein we have made short straight lines between points. The problem, however, becomes somewhat more complex when the boundary condition of thickness is not satisfied, i.e., when the thickness does not satisfy *Eq (18)*.

As the faceplate becomes thinner, we have the front and back surfaces reinforcing one another in an ever increasing temperature rise with an ever decreasing gradient between the two faces. Again, one must keep in mind that the optic cannot lose any energy from the thermal mass. Based on this continuous reinforcement we have denominated this phenomena as a *Reverse Thermal Wave Approximation*. That is, as the temperature wave from the front surface travels to the back surface, it reverses and reinforces the temperature at the front. In like fashion, the back surface functions in much the same way. Consequently, the Gaussian Error Integrals become recursive in much the same way as the Fourier Series would be, with a similar result, it should be added. After the first few terms, the values become very small. The expression for the temperature rise on the first surface, using the *Reverse Thermal Wave Approximation* will follow from,[2]

(22)

$$\Delta T_1 = 2\mathcal{F}_0 (\alpha\Omega^{-1}\eta)^{0.5} \left\{ \text{ierfc}(x) \right\} / K - 2\mathcal{F}_0 (\alpha\Omega^{-1}\eta)^{0.5} \left\{ \text{ierfc}(y) \right\}$$
$$/ K \left\{ \text{erfc}(y) - \exp\left(t_o H_o + H_o^2 \alpha\Omega^{-1}\eta\right) \text{erfc}(z) \right\}$$
$$+ 2\mathcal{F}_0 (\alpha\Omega^{-1}\eta)^{0.5} \left\{ \text{ierfc}(y) \right\} / K + 2\mathcal{F}_0 (\alpha\Omega^{-1}\eta)^{0.5} \left\{ \text{ierfc}(x) \right\}$$
$$/ K \left\{ \text{erfc}(y) - \exp\left(t_o H_o + H_o^2 \alpha\Omega^{-1}\eta\right) \text{erfc}(z) \right\}$$

where,

$H_o = t_o^{-1}$, cm^{-1}; t_o = Thickness of faceplate, cm

$$z = \left\{ t_o / 2(\alpha\Omega^{-1}\eta)^{0.5} + H_o (\alpha\Omega^{-1}\eta)^{0.5} \right\};$$

$$y = t_o / 2(\alpha\Omega^{-1}\eta)^{0.5}$$

The temperature rise at any point below the first surface will follow from,

(23)

$$\Delta T_{t>0} = 2\mathcal{F}_0 (\alpha\Omega^{-1}\eta)^{0.5} \left\{ \text{ierfc}(y) \right\} / K + 2\mathcal{F}_0 (\alpha\Omega^{-1}\eta)^{0.5}$$
$$\times \left\{ \text{ierfc}(x) \right\} / K \left\{ \text{erfc}(y) - \exp\left(t_o H_o + H_o^2 \alpha\Omega^{-1}\eta\right) \text{erfc}(z) \right\}$$

We can, then, use *Eqs. (22)* and *(23)* in another example. In this case, we will use a Copper reflective optic faceplate that is only 5.0 cm thick. All the other conditions will remain the same.

t_{cm}	Peak ΔT/ Pulse	ΔT
N=1	787.50	614.66
N=2	505.50	382.30
N=3	290.10	249.25
N=4	164.59	181.48
0		155.67
0.50		119.43
1.00		105.40
1.50		92.67
2.00		81.27
2.50		71.02
3.00		61.95
3.50		54.01
4.00		47.10
4.50		41.13
5.00		35.95
	Σ =	865.60

then, 865.60/11 = 78.69°C and rearranging *Eq. (21)* we can evaluate the steady-state condition, so that,

$$\mathcal{F}_o = (\rho\, c_p\, t)\,(\Omega^{-1}\eta)^{-1}$$

then, $\mathcal{F}_o = 8.96\ g/cm^3 (0.38\ W\text{-}sec/g\text{-}°C)\ 5.0\ cm\ (78.59\ °C)\ /10\ sec$

$$\mathcal{F}_o = 134\ W/cm^2 \quad vs\ 125.66\ W/cm^2$$

If we were to look at the steady-state solution with *Eq. (21)* just by itself, we would find that the required average temperature would be 73.82 °C. And, if we were to evaluate the average temperature of the optical faceplate by taking the 95.81.26 °C. For this regime, the average of the front and back, without calculating the segments in between, will always be greater than the value calculated from *Eq. (21)*.

Equations (22) and *(23)* will do service for both the semi-infinite plate model and when the thickness does not satisfy the boundary condition. The reason for the satisfying of both conditions is to be found in the transport element of the equations, i.e.,

$$\left\{ \text{erfc}(y) - \exp\left(t_o H_o + H_o^2\, \alpha\, \Omega^{-1}\eta\right) \text{erfc}(z) \right\}$$

$Ho = t^{-1},\ cm^{-1}$

When, for example, $t_o \geq 6\,(\alpha\,\Omega^{-1}\eta)^{0.5}$ the value of erfc(y) and erfc(z) will be zero. We may say, then, that when the average temperature rise of the faceplate, based on the temperatures evaluated from *Eqs. (22)* and *(23)* are greater that the average temperature rise required by *Eq. (21* that *Eqs. (22)* and *(23)* are valid for this regime. If we describe the average temperature from *Eq. (21)* as $\Delta T_{\lambda 1}$ and the average from *Eqs. (22*) and *(23)* as $\Delta T_{\lambda 2}$, then, the regime of use for these equations will follow,

$$\Psi = 1 \text{ when } \Delta T_{\lambda 2} \geq \Delta T_{\lambda 1}$$

The reason for setting this regime will become clear as we do yet a third example. As the faceplate becomes substantially thinner than the thickness required by *Eq. (21)* the temperature of the two surfaces of the faceplate become very close to the same value. If we take our Copper example, again, except we now make the faceplate 2.0 cm thick, we will have the same absorbed value and the same number of pulses. From *Eq. (21)* the required temperature rise is 184.54°C, i.e.,

$$\Delta T_{avg} = 125.66\ W/cm^2\,(10\ sec)/\left\{ 8.96\ g/cm^8 (0.38\ W\text{-}sec/g\text{-}°C)\ 2.0\ cm \right\}$$

We find from *Eqs. (22)* and *(23)* the average temperature will only be 133.86°C. This is a lower prediction than what is required by *Eq. (21)*. That is, the equations predict a first surface temperature rise of 170.48°C and a second surface temperature rise of 97.24°C. In this regime, the average temperature of the faceplate $\Delta T_{\lambda 2}$ is lower than $\Delta T_{\lambda 1}$. For this regime, then, we would want to say that $\Psi = \Delta T_{\lambda 1}/\Delta T_{\lambda 2}$. And, we must modify *Eqs. (22)* and *(23)*, so that,

$$\Psi = \Delta T_{\lambda 1}/\Delta T_{\lambda 2} = 184.54°C\ /\ 134.08°C; \quad \Psi = 1.3847$$

(24)

$$\Delta T_1 = 2\mathcal{F}_o\,(\alpha\Omega^{-1}\eta)^{0.5}\,\Psi \left\{ \text{ierfc}(x) \right\}/K - 2\mathcal{F}_o\,(\alpha\Omega^{-1}\eta)^{0.5}\,\Psi\ \left\{ \text{ierfc}(y) \right\}/K \left\{ \text{erfc}(y) \right.$$
$$\left. - \exp\left(t_o H_o + H_o^2\,\alpha\,\Omega^{-1}\,\eta\right) \text{erfc}(z) \right\} + 2\mathcal{F}_o\,(\alpha\Omega^{-1}\,\eta)^{0.5}\,\Psi\ \left\{ \text{ierfc}(y) \right\}/K$$
$$+ 2\mathcal{F}_o\,(\alpha\Omega^{-1}\,\eta)^{0.5}\,\Psi\ \left\{ \text{ierfc}(x) \right\}/K \left\{ \text{erfc}(y) - \exp\left(t_o H_o + H_o^2\,\alpha\,\Omega^{-1}\eta\right)\ \text{erfc}(z) \right\}$$

And for the second surface, the temperature rise will be,

(25)

$$\Delta T_{t>0} = 2\,\mathbf{F_0}\,(\alpha\,\Omega^{-1}\,\eta)^{0.5}\,\Psi\left\{\,\text{ierfc}(y)\,\right\}/K + 2\,\mathbf{F_0}\,(\alpha\,\Omega^{-1}\,\eta)^{0.5}$$
$$\times\,\Psi\left\{\,\text{ierfc}(x)\,\right\}/K\left\{\,\text{erfc}(y) - \exp\left(t_o H_o + H_o^2\,\alpha\,\Omega^{-1}\eta\right)\,\text{erfc}(z)\,\right\}$$

When we use *Eqs. (24)* and *(25)* for the example of a 2.0 cm thick Copper faceplate, we find that the correct temperature for the first surface will be 236.05 °C vs 170.78 °C and the second surface temperature rise will be 134.66 °C vs 97.37 °C. The corrected temperatures will provide an average value in concert with *Eq. (20)*, i.e., 184.4 °C. The temperature rise of coating pair N=1 will be 695.10 °C. The temperature rise of coating pair N=2 will be 462.72 °C. The temperature rise of coating pair N=3 will be 329.67 °C. The temperature rise of coating pair N=4 will be 261.90 °C. In the same vein, if we were to use a 1.0cm thick faceplate, the required average temperature rise would be 369.08 °C and the initial calculation from *Eqs. (22)* and *(23)* would be 239.39 °C and 194.61 °C respectively, which would provide an average temperature of 217 °C. The value of (Ψ) would be 1.708. Using *Eqs. (24)* and *(25)*, the corrected temperatures would be 408.98°C and 332.48 °C respectively. The temperature rise of coating pair N=1 will be 867.97 °C. The temperature rise of coating pair N=2 will be 635.59 °C. The temperature rise of coating pair N=3 will be 502.54 °C. The temperature rise of coating pair N=4 will be 434.77 °C. The immediate question that comes to mind, of course, is, where is the break between the two regimes? The answer appears to be approximately when,

$$t_o \le 0.6\,(\alpha\,\Omega^{-1}\eta)^{0.5} \qquad (26)$$

That is, the break point appears to be when the thickness is approximately 10% of the required thickness to fulfill the semi-infinite plate boundary condition. We can say, then, that the regimes are bounded as follows,

Regime III

$$0 < t_o \le 0.6\,(\alpha\,\Omega^{-1}\eta)^{0.5} \qquad \Psi > 1 \text{ } \textit{Eq. (24)} \text{ and } \textit{(25)} \qquad (27)$$

Regime II

$$0.6\,(\alpha\Omega^{-1}\eta)^{0.5} < t_o < 6\,(\alpha\tau)^{0.5} \qquad \Psi \le 1 \text{ } \textit{Eq. (22)} \text{ and } \textit{(23)} \qquad (28)$$

Regime I

$$t_o \ge 0.6\,(\alpha\Omega^{-1}\eta)^{0.5} \qquad \Psi \le 1 \text{ } \textit{Eq. (19)} \text{ and } \textit{(20)} \qquad (29)$$

Reverse Thermal Wave - Three Dimensional Repetitive Pulsed

The problem becomes somewhat more complex when we treat with the problem in three dimension. There is a limitation in both the axial direction and in the radial component. In the one dimensional boundary condition, there was no radial component one had to accommodate. With the introduction of the radial component, the criteria for the laser beam diameter necessary to constitute a one dimensional condition is defined as,

$$\mathbf{D} \ge 12\,(\alpha\,\Omega^{-1}\,\eta)^{0.5} \qquad (30)$$

For this condition, the problem is one dimensional. When the laser beam diameter (D) on the optical surface is equal to, or greater than the value shown in *Eq. (30)* the problem is one dimensional and amenable to the equations described above. However, when,[1,2]

$$D < 12\,(\alpha\Omega^{-1}\eta)^{0.5} \qquad (31)$$

the problem is now three dimensional. We will begin with the first regime wherein the boundary conditions for the semi-infinite plate model are maintained. For the case of the optical thin films, the thermal diffusivity is so poor that one dimensional case is reached very early on. The temperature rise on the first surface of the faceplate follows from,[1,2,3,4,5,6,7,8,9]

$$\Delta T_1 = 2F_0\,(\alpha\Omega^{-1}\eta)^{0.5}\left\{\left(\text{ierfc}(x)\right) - \left(\text{ierfc}(x_1)\right)\right\}/K \qquad (32)$$

where,

$x_1 = R / 2(\alpha\Omega^{-1}\eta)^{0.5}$; R = Radius of the laser beam, cm

In similar fashion, the temperature rise at some depth into the faceplate will follow from,[1,2,3,4,5,6,7,8,9]

$$\Delta T_{t>0} = 2F_0\,(\alpha\Omega^{-1}\eta)^{0.5}\left\{\left(\text{ierfc}(y)\right) - \left(\text{ierfc}(y_1)\right)\right\}/K \qquad (33)$$

where,

$$y_1 = (t^2 + R^2)^{0.5} / 2(\alpha\Omega^{-1}\eta)^{0.5}$$

We can carry on the examples that we have provided before. However, the problem becomes a little more convoluted with the introduction of the radial component of diffusion. In any case, we will maintain the same boundary conditions as before except that we will provide a laser beam radius of 6.0 cm on the reflective optic. From *Eq. (30)*, we know that for a thousand pulses the laser beam needs to be equal to, or greater than, 40.5 cm. So, we know that a 12.0 cm diameter beam is completely within the three dimensional condition.

t_{cm}	Peak ΔT	ΔT
N=1	787.500	566.060
N=2	505.600	333.680
N=3	290.100	200.630
N=4	126.100	132.860
0		107.080
0.5		91.760
1.0		78.120
1.5		66.030
2.0		55.430
2.5		46.110
3.0		38.020
3.5		31.470
4.0		25.650
4.5		20.820
5.0		16.730
5.5		13.350
6.0		10.650
6.5		8.610
7.0		6.740
7.5		5.330
8.0		4.040
8.5		2.860
9.0		2.260
9.5		1.680

10.0	1.350
10.5	1.260
11.0	0.760
11.5	0.560
12.0	0.370
12.5	0.300
13.0	0.240
13.5	0.230
14.0	0.156
	Σ = 637.966

then, 637.966/29 = 22°C and rearranging *Eq. (21)* we can evaluate the steady-state condition, so that,

$$F_0 = (\rho\, c_p\, t)(\Omega^{-1}\eta)^{-1}$$

then, $F_0 = 8.96\ g/cm^3 (0.38\ W\text{-}sec/g\text{-}°C) 14\ cm\ (22°C) / 10\ sec$

$$F_0 = 104.86\ W/cm^2 \text{ vs } 125.66\ W/cm^2$$

Clearly, we can see from the calculation that we are missing some flux density. We can evaluate the amount of flux density that is being taken out in the radial component by either of two methods which we will describe. In the first method we would use the technique suggested by Carslaw and Jaeger.[3] A condition for the use of the following equations, however, is the requirement that the ΔT be of a constant value. In our case the temperature is constantly changing until the laser is turned off, or steady-state heat transfer is achieved. In order to use this technique, we have found that following the Gaussian nature of the temperature rise we can use the 50% point of the Gaussian form to evaluate the temperature change from $\Omega^{-1}\eta = 0$ to $\Omega^{-1}\eta > 0$. That is, we use $\Delta T \propto \ln(2)$ for our constant temperature source. For this case, they suggest that the amount of flux density may be evaluated from,

(34)

$$F_0 = \left\{ \ln(2)\ \Delta T\ K / R \right\} \left\{ (\pi\zeta)^{-0.5} + 0.50 - 0.25\ (\zeta/\pi)^{0.5} + 0.125\ \zeta \right\}$$

where,

$$\zeta = (\alpha\, \Omega^{-1}\, \eta) / R^2$$

Doing the arithmetic from *Eq. (34)* we find that the value for the W/cm^2 escaping into the radial component will be 14.57 W/cm^2. Adding this to the amount we found from the temperature gradient, we see that 104.86 + 14.57 = 119.43 W/cm^2. This is within 95% agreement with the W/cm^2 that are required.

We can look for the missing flux density, as before, using the work of Kern and Kraus.[41] The values for the temperatures for a radial fin are found from,

(35)

$$\Delta T_{20} = \Delta T_{10} \left\{ I_0(mR_e)\, K_1(mR) + K_0(mR_e)\, I_1(mR) \right.$$

$$\left. / \, I_0(mR_0)\, K_1(mR_e) + I_1(mR_e)\, K_0(mR_0) \right\}$$

where,

R_0 = The laser beam radius, cm; R_e = Radius of fin, cm

$m = (2h_c/Kt)^{0.5} = 0.378\ cm^{-1}$ $h_c = K / (R_e - R_0)$; $W/cm^2\text{-}°C$

I_1, K_1, I_0, K_0 = Bessel Functions; R = Radius-cm, $R_0 < R <= R_e$

t = faceplate thickness, 14 cm

For our problem we will use a fin height of 1.0 cm. R_o will be 6.0 cm and R_e will be 7.0cm. When one does the rough calculation,

$$\Delta T_{20} = .9298\ (\Delta T_{10}).$$

So, then, the average temperature along the 1.0 cm fin will be $\{.9298(\Delta T_{10}) + 22\}/2$ which will provide a value of 21.23°C$_{\Delta T}$. Then, using the same technique as before, we can evaluate the steady-state absorption in the fin, so that,

$$\mathcal{F}_o = (\rho\ c_p\ t)\ (\Omega^{-1}\eta)^{-1}$$

then, $\mathcal{F}_o$ = 8.96 g/cm^3 (0.38 W-sec/g-°C) 1.0 cm (21.23°C$_{\Delta T}$) / 10 sec

$$\mathcal{F}_o = 7.23\ \text{W/cm}^2$$

and adding the two values together we find 104.86 + 7.23 = 112.1 W/cm^2 which, does not provide a very good agreement with the escaping flux density. Again this is the steady-state value if the temperature of the cylinder were uniform and constant

If, however, we were to use another technique suggested by Kern and Kraus for the steady state flux density removed by the fin we would use the following,

(36)

$$\mathcal{F}_o = K\ m\ \Delta T\ \eta \{ I_o(mR_e)\ K_1(mR_o) - K_1(mR_e)\ I_1(mR_o) \\ / I_o(mR_o)\ K_1(mR_e) + I_1(mR_e)\ K_o(mR_o) \}$$

where,

$$\eta = \{ 2\pi\ R_o\ t\ K\ m\ \Delta T \} / \{ 2\pi\ (R_e^2 - R_o^2)\ h_c\ \Delta T \}$$

for our problem, then, η = 2.442 from the Lazor™Code.[40] After doing the calculation we find that $\mathcal{F}_o$= 32.21 W/cm^2. Again using the Gaussian 50% point, $\mathcal{F}_o$ = 22.33 W/cm^2. If we add the two values together, 104.8 + 22.33 = 127.18 W/cm^2. This is much better agreement.

At this point, we also need to look at the radial temperature distribution as a function of the laser run time. Carslaw and Jaeger[3] have provided a technique for evaluating the radial temperature distribution. Again, however, the technique has the boundary condition that temperature is constant. The radial temperature distribution then is found from,

(37)

$$\Delta T_R = \{ \Delta T (R_o / R_e)^{0.5}\ \text{erfc}(z) + \{ \Delta T\ (z)\ (\alpha\Omega^{-1}\eta)^{0.5} / (4\ R_o^{0.5}\ R_e^{1.5}) \}\ \text{ierfc}(z) \\ + \Delta T \{ (9\ R_o^2 - 2\ (R_o\ R_e) - 7\ R_e^2)\ (\alpha\ \Omega^{-1}\ \eta) / (32\ R_o^{1.5}\ R_e^{2.5}) \}\ i^2\text{erfc}(z) \}\ \ln(2)$$

where,

$$z = (R_e - R_o) / 2(\alpha\ \Omega^{-1}\ \eta)^{0.5}$$

Based on *Eq. (37)* we would find the average temperature at the tip of the fin, i.e., R_e will be 7.0 cm, will equal 12.16°C$_{\Delta T}$ at the end of a 10^3 pulses.

This would appear to be in reasonable agreement with the input flux density. We now shift our attention to the condition of Regime II. Again, this is the case where the thickness is less than the semi-infinite plate model requires and greater than 10% of that value. For this Regime, in the three dimensional case, we can evaluate the temperature rise of the first surface from,

(38)

$$\Delta T_1 = 2\mathcal{F}_o(\alpha\Omega^{-1}\eta)^{0.5}\left\{(\text{ierfc}(x)) - (\text{ierfc}(x_1))\right\}/K - 2\mathcal{F}_o(\alpha\Omega^{-1}\eta)^{0.5}\left\{(\text{ierfc}(y)) - (\text{ierfc}(y_1))\right\}/K\left\{\text{erfc}(y) - \exp(t_o H_o + H_o^2\alpha\Omega^{-1}\eta)\,\text{erfc}(z)\right\} + 2\mathcal{F}_o(\alpha\Omega^{-1}\eta)^{0.5}\left\{(\text{ierfc}(y)) - (\text{ierfc}(y_1))\right\}/K + 2\mathcal{F}_o(\alpha\Omega^{-1}\eta)^{0.5} \times \left\{(\text{ierfc}(x)) - (\text{ierfc}(x_1))\right\}/K\left\{\text{erfc}(y) - \exp(t_o H_o + H_o^2\alpha\Omega^{-1}\eta)\,\text{erfc}(z)\right\}$$

The temperature rise at some depth into the faceplate follows from,

(39)

$$\Delta T_{t>0} = 2\mathcal{F}_o(\alpha\Omega^{-1}\eta)^{0.5}\left\{(\text{ierfc}(y)) - (\text{ierfc}(y_1))\right\}/K + 2\mathcal{F}_o(\alpha\Omega^{-1}\eta)^{0.5}\left\{(\text{ierfc}(x)) - (\text{ierfc}(x_1))\right\}/K\left\{\text{erfc}(y) - \exp(t_o H_o + H_o^2\alpha\Omega^{-1}\eta)\,\text{erfc}(z)\right\}$$

The next example will use a 5.0 cm thick Copper substrate. We will use a 3.0 cm radius to alter the problem in order to compare the impact of a 6.0 cm and 3.0 cm laser beam radius. Of course, we are still absorbing $1(10^5)$W/cm^2 per pulse with a 2μsec pulse width with a hertz rate of 100 cycles/sec and 10^3 cycles on the first surface of the Copper faceplate that is coated with the optical thin films. Again, the energy is partitioned between the steady state flux density that is stored in the films and that which is stored in the substrate. Using *Eqs. (38)* and *(39)* we find the temperature of the front and back surface to be 86.59°$C_{\Delta T}$ and 14.47°$C_{\Delta T}$ respectively. We can, then, calculate the temperature gradient through the coating and through the 5.0 cm thick Copper faceplate and determine the average temperature, so that,

t_{cm}	Peak ΔT / Pulse	ΔT
N=1	787.5	545.600
N=2	505.5	313.220
N=3	290.4	180.170
N=4	126.1	112.400
0		86.590
0.5		65.720
1.0		53.680
1.5		44.000
2.0		36.330
2.5		30.260
3.0		25.390
3.5		21.630
4.0		18.680
4.5		16.400
5.0		14.470
	$\sum$ =	413.150

then, 413.150/11 = 37.56°C and rearranging *Eq. (21)* we can evaluate the steady-state condition, so that,

$$\mathcal{F}_o = (\rho\, c_p\, t)(\Omega^{-1}\eta)^{-1}$$

then, $\mathcal{F}_o$ = 8.96 g/cm^3(0.38 W-sec/g-°C) 5.0 cm (37.56 °C) / 10sec

$\mathcal{F}_o$ = 63.94 W/cm^2 vs 126.66 W/cm^2

Going back to the Kern and Kraus technique, we can use the fin analysis to evaluate the steady-state condition, where,

R_o = The laser beam radius, cm R_e = Radius of fin, cm

$m = (2h_c/Kt)^{0.5} = 0.6324\ cm^{-1}$ $h_c = K/(R_e - R_o)$; W/cm^2-°C

I_1, K_1, I_o, K_o = Bessel Functions R = Radius-cm, $R_o < R < = R_e$

t = faceplate thickness, 5.0 cm

Again we will use a fin height of 1.0 cm. R_o will be 3.0 cm and R_e will be 4.0 cm. When one does the rough calculation,

$$\mathcal{F}_o = K\, m\, \Delta T\, \eta \{ I_o(mR_e) K_1(mR_o) - K_1(mR_e) I_1(mR_o) / I_o(mR_o) K_1(mR_e) + I_1(mR_e) K_o(mR_o) \}$$

After doing the calculation from *Eq. (36)* we find that $\mathcal{F}_o = 80.773\ W/cm^2$. Again using the Gaussian 50% point, $\mathcal{F}_o = 55.99\ W/cm^2$. If we add the two values together, 63.94 + 55.99 = 120.0 W/cm^2. We will now do the same example except with a 6.0 cm laser beam radius to see that the technique tracks, then,

t_{cm}	Peak ΔT / Pulse	ΔT
N=1	787.5	591.930
N=2	505.5	359.550
N=3	290.4	226.500
N=4	126.1	158.730
0		132.940
0.5		102.770
1.0		89.130
1.5		77.040
2.0		66.450
2.5		57.120
3.0		49.040
3.5		42.490
4.0		36.670
4.5		31.840
5.0		27.750
	$\Sigma =$	683.240

then, 683.240/11 = 62.113°C and rearranging *Eq. (21)* we can evaluate the steady-state condition, so that,

$$\mathcal{F}_o = (\rho\, c_p\, t)(\Omega^{-1}\eta)^{-1}$$

then, $\mathcal{F}_o = 8.96\ g/cm^3 (0.38\ W\text{-}sec/g\text{-}°C)\ 5.0\ cm\ (62.113\ °C) / 10 sec$

$$\mathcal{F}_o = 105.74\ W/cm^2 \text{ vs } 125.66\ W/cm^2$$

Going back to the Kern and Kraus technique, we can use the fin analysis to evaluate the steady-state condition, where,

R_o = The laser beam radius, 6.0 cm R_e = Radius of fin, 7.0 cm

$m = (2h_c / Kt)^{0.5} = 0.6324\ cm^{-1}$ $h_c = K / (R_e - R_o)$; W/cm^2-°C

I_1, K_1, I_o, K_o = Bessel Functions R = Radius-cm, $R_o < R < = R_e$

t = faceplate thickness, 5.0 cm

$$\mathcal{F}_D = K\, m\, \Delta T\, \eta \left\{ I_o(mR_e)\, K_1(mR_o) - K_1(mR_e)\, I_1(mR_o) \right.$$

$$\left. / I_o(mR_o)\, K_1(mR_e) + I_1(mR_e)\, K_o(mR_o) \right\}$$

where,

$$\eta = \left\{ 2\pi R_o t\, K\, m\, \Delta T \right\} / \left\{ 2\pi (R_e^2 - R_o^2)\, h_c\, \Delta T \right\}$$

for our problem, then, η = 1.459 from the Lazor™Code.[40] After doing the calculation we find that $\mathcal{F}_D$ = 135.85 W/cm^2. Again using the Gaussian 50% point, $\mathcal{F}_D$ = 94.16 W/cm^2. If we add the two values together, 105.74+94.16 = 199.90 W/cm^2. This is hardly good agreement. However, if we use *Eq. (35)*,

$$\Delta T_{20} = \Delta T_{10} \left\{ I_o(mR_e)\, K_1(mR) + K_o(mR_e)\, I_1(mR) \right.$$

$$\left. / I_o(mR_o)\, K_1(mR_e) + I_1(mR_e)\, K_o(mR_o) \right\}$$

For our problem we have a fin height of 1.0 cm. R_o will be 6.0 cm and R_e will be 7.0 cm. When one does the rough calculation,

$$\Delta T_{20} = .8211\, (\Delta T_{10})\, \ln(2)$$

$$\Delta T_{20} = 35.35°C$$

then, $\mathcal{F}_D$ = 8.96 g/cm^3(0.38 W-sec/g-°C)1.0 cm (35.35°C) / 10 sec

$$\mathcal{F}_D = 12.06 \text{ W/cm}^2$$

If we add the two values together, 105.74 + 12.06 = 117.80 W/cm^2. This is a much better agreement. However, we can check the output with *Eq. (34)* for the transient condition,

$$\mathcal{F}_D = \left\{ \ln(2)\, \Delta T\, K / R \right\} \left\{ (\pi\, \zeta)^{-0.5} + 0.50 - 0.25\, (\zeta / \pi)^{0.5} + 0.125\, \zeta \right\}$$

Again, we see that the equation slightly over predicts the flux density, that is 105.74 + 41.15 = 146.89. If we use *Eq. (37)* for the temperature at the tip of the fin at the end of a ten second run, we find,

$$\Delta T_R = \left\{ \Delta T\, (R_o / R_e)^{0.5}\, \text{erfc}(z) + \left\{ \Delta T\, (z)\, (\alpha\tau)^{0.5} / (4\, R_o^{0.5}\, R_e^{1.5}) \right\} \text{ierfc}(z) \right.$$

$$\left. + \Delta T \left\{ (9\, R_o^2 - 2\, (R_o\, R_e) - 7\, R_e^2)\, (\alpha\tau) / (32\, R_o^{1.5}\, R_e^{2.5}) \right\} i^2\text{erfc}(z) \right\} \ln(2)$$

$$\Delta T_R = 51.00 \text{ °C}$$

The average temperature between the root and the tip will be (62.113 + 51)/2 = 56.56. Using our steady-state solution again from *Eq. (21)* we find,

$$\mathcal{F}_D = 8.96 \text{ g/cm}^3 (0.38 \text{ W-sec/g-°C})\, 1.0 \text{ cm}\, (56.56°C) / 10 \text{ sec}$$

$$\mathcal{F}_D = 19.26 \text{ W/cm}^2$$

If we add the two values together, 105.74 + 19.26 = 124.99 W/cm^2. This is a better agreement. What we find between the two techniques is that the further away from the steady-state condition we find ourselves, one technique works better than the other. Obviously, with the larger

the diameter approaching the one dimensional case the averaging of the fin-base technique is better. This is demonstrated because of the higher base temperature that permits a closer evaluation to the ultimate steady-state fin tip temperature. In the case of the smaller diameter, the flux density technique is more valuable because it is further from the steady state fin tip temperature. Because of this seeming anomaly, we wanted to provide the reader with the alternative approaches for finding the enthaply balance of Watts in and Watts out. There is yet a third way of evaluating the W/cm^2 that are going into the radial component. Using ***Lazor™Code***[40], we can evaluate the average temperature of the faceplate beyond the laser beam after a given run time. The temperature rise will be zero at a distance described by,

$$R_2 = 6\,(\alpha\,\tau)^{0.5} + R_1 \qquad (40)$$

Using a half centimeter increment in depth and a half centimeter increment in the radial component we calculated the temperature gradient out to a radius of 21 cm, see *Figure 2*. The ***Lazor™Code***[40] uses *Eq. (37)* to calculate the radial temperature distribution. Using *Eq. (37)*,

$$\Delta T_R = \left\{ \Delta T\,(R_o / R_e)^{0.5}\,\mathrm{erfc}(z) + \left\{ \Delta T\,(z)\,(\alpha\tau)^{0.5} / \left(4\,R_o^{0.5}\,R_e^{1.5}\right)\right\}\,\mathrm{ierfc}(z)\right.$$
$$\left. + \Delta T\left\{ \left(9\,R_o^2 - 2\,(R_o\,R_e) - 7\,R_e^2\right)(\alpha\tau) / \left(32\,R_o^{1.5}\,R_e^{2.5}\right)\right\}\,1^2\,\mathrm{erfc}(z)\right\}\ln(2)$$

This matrix provided a value of 3657.455 / 341 = 10.726°C average ΔT for the radial component. From *Eq. (21)* then, we can calculate the W/cm^2 that are going into the radial component, so that,

$$F_o = (\rho\,c_p\,t)\,(\Omega^{-1}\eta)^{-1}$$

then, $F_o = 8.96$ g/cm^3(0.38 W-sec/g-°C) 5.0 cm (10.726 °C) / 10sec

$$F_o = 18.26 \text{ W/cm}^2$$

We add the two together, (105.74 + 18.26) = 124.00 W/cm^2 vs 125.66 W/cm^2 which is the average power required. This provides a reasonable agreement with the required 112.66 W/cm^2.

The third regime for the three dimensional problem is much like the one dimensional model. In this regime, we must first calculate the values of (Ψ). This calculation is completed using *Eqs. (21)*, *(22)*, and *(23)* which is the one dimensional case provided above. Using our former example, 1(10^5)W/cm^2 per pulse will be absorbed on the first surface of a 2.0 cm thick copper faceplate coated with a a four pair stack of quarter wave optical thin films. From *Eq. (21)* we can find the required steady-state average temperature, so that,

$$\Delta T_{avg} = (\Omega^{-1}\eta)\,F_o / (\rho\,c_p\,t)$$

$$\Delta T_{avg} = 125.66 \text{ W/cm}^2(10 \text{ sec}) / \left\{ 8.96 \text{ g/cm}^3(0.38 \text{ W-sec/g-°C})\ 2.0 \right\}$$

$$\Delta T_{avg} = 184.54°C$$

And from *Eq. (22)*, we find the temperature rise of the first surface for the one dimensional case,

$$\Delta T_1 = 2\,F_o\,(\alpha\,\Omega^{-1}\eta)^{0.5}\left\{\mathrm{ierfc}(x)\right\}/K - 2\,F_o\,(\alpha\,\Omega^{-1}\eta)^{0.5}\left\{\mathrm{ierfc}(y)\right\}$$
$$/\,K\left\{\mathrm{erfc}(y) - \exp\left(t_o H_o + H_o^2\,\alpha\,\Omega^{-1}\eta\right)\mathrm{erfc}(z)\right\}$$
$$+ 2\,F_o\,(\alpha\,\Omega^{-1}\eta)^{0.5}\left\{\mathrm{ierfc}(y)\right\}/K + 2\,F_o\,(\alpha\,\Omega^{-1}\eta)^{0.5}\left\{\mathrm{ierfc}(x)\right\}$$

The temperature rise of the second surface for the one dimensional case comes from *Eq. (22)*, so that,

$$\Delta T_{t>0} = 2\mathcal{F}_o(\alpha\Omega^{-1}\eta)^{0.5}\{\,\text{ierfc}(y)\,\}/K + 2\mathcal{F}_o(\alpha\Omega^{-1}\eta)^{0.5}\{\,\text{ierfc}(x)\,\}/K$$
$$\times\{\,\text{erfc}(y) - \exp(t_oH_o + H_o^2\alpha\Omega^{-1}\eta)\,\text{erfc}(z)\,\}$$

$$\Delta T_2 = 122.20°C$$

$$\Delta T_{\lambda 2} = 168.217°C; \qquad \Delta T_{\lambda 1} = 184.54°C; \qquad \Psi = 1.097$$

At this point, we now calculate the temperature rise of the faceplate with a 6.0 cm laser beam diameter, in the three dimensional model, so that, from *Eq. (38)* the temperature rise will follow from,

(41)

$$\Delta T_1 = 2\mathcal{F}_o(\alpha\Omega^{-1}\eta)^{0.5}\Psi\{(\text{ierfc}(x)) - (\text{ierfc}(x_1))\}/K - 2\mathcal{F}_o(\alpha\Omega^{-1}\eta)^{0.5}\Psi\{(\text{ierfc}(y)) - (\text{ierfc}(y_1))\}/K\{\,\text{erfc}(y) - \exp(t_oH_o + H_o^2\alpha\Omega^{-1}\eta)\,\text{erfc}(z)\,\}$$
$$+ 2\mathcal{F}_o(\alpha\Omega^{-1}\eta)^{0.5}\Psi\{(\text{ierfc}(y)) - (\text{ierfc}(y_1))\}/K + 2\mathcal{F}_o(\alpha\Omega^{-1}\eta)^{0.5}\Psi\{(\text{ierfc}(x)) - (\text{ierfc}(x_1))\}/K\{\,\text{erfc}(y) - \exp(t_oH_o + H_o^2\alpha\Omega^{-1}\eta)\,\text{erfc}(z)\,\}$$

$$\Delta T_1 = 203.76°C$$

The second surface temperature rise for the 6.0 cm laser beam diameter in the three dimensional model will follow from,

(42)

$$\Delta T_{t>0} = 2\mathcal{F}_o(\alpha\Omega^{-1}\eta)^{0.5}\Psi\{(\text{ierfc}(y)) - (\text{ierfc}(y_1))\}/K + 2\mathcal{F}_o(\alpha\Omega^{-1}\eta)^{0.5}\Psi\{(\text{ierfc}(x)) - (\text{ierfc}(x_1))\}/K\{\,\text{erfc}(y) - \exp(t_oH_o + H_o^2\alpha\Omega^{-1}\eta)\,\text{erfc}(z)\,\}$$

$$\Delta T_2 = 112.71°C$$

The average temperature will be $\Delta T_{10} = 158.24°C$. And from *Eq.(21)*

$$\mathcal{F}_o = (\rho\, c_p\, t)(\Omega^{-1}\eta)^{-1}$$

then, $\mathcal{F}_o = 8.96\ \text{g/cm}^3\ (0.38\text{W-sec/g-}°C)\ 2.0\ \text{cm}\ (158.24°C)/10\ \text{sec}$

$$\mathcal{F}_o = 107.75\ \text{W/cm}^2$$

The temperature rise in coating pair N=1 will be 662.75 °C. The temperature rise in coating pair N=2 will be 430.37 °C. The temperature rise in coating pair N=3 will be 297.32 °C. The temperature rise in coating pair N=4 will be 229.55 °C. We can look for the missing flux density as before. Using *Eq.(34)* again,

$$\mathcal{F}_o = \{\ln(2)\,\Delta T\ K/R\}\{(\pi\zeta)^{-0.5} + 0.50 - 0.25(\zeta/\pi)^{0.5} + 0.125\,\zeta\}$$

and $\mathcal{F}_o = 104.82\ \text{W/cm}^2$. Adding the two together (107.75+104.82) = 212.57 W/cm^2. This is not reasonable agreement for the approximation. Again, we find that this expression over predicts the flux density that exits to the radial component. Fundamentally, what we see, then, is that the steady-state temperature expressions do not provide as close an approximation as one would like. However, using the *Lazor™Code*[40] we can do a course nodal temperature distribution through the radial

component out to the point where the temperature increase is equal to zero. The Lazor™Code[40] uses *Eq. (37)* for evaluating the temperature distribution.

$$\Delta T_R = \left\{ \Delta T (R_o / R_e)^{0.5} \operatorname{erfc}(z) + \left\{ \Delta T (z) (\alpha\tau)^{0.5} / (4 R_o^{0.5} R_e^{1.5}) \right\} \operatorname{ierfc}(z) \right.$$
$$\left. + \Delta T \left\{ (9 R_o^2 - 2 (R_o R_e) - 7 R_e^2) (\alpha\tau) / (32 R_o^{1.5} R_e^{2.5}) \right\} i^2 \operatorname{erfc}(z) \right\} \ln(2)$$

The temperature increase is zero when,

$$R_2 = 6 (\alpha \tau)^{0.5} + R_1$$

Using a half centimeter increment in depth and a half centimeter increment in the radial component we calculated the temperature gradient out to a radius of 21 cm, (see *Figure 3*). This matrix provided a value of 3750 / 155 = 24.194 °C average ΔT for the radial component. Using *Eq. (21)*, we find,

$$F_o = (\rho\, c_p\, t) (\Omega^{-1}\eta)^{-1}$$

then, $F_o = 8.96$ g/cm^3 (0.38 W-sec/g-°C) 2.0 cm (24.194°C) / 10 sec

$$F_o = 16.475 \text{ W/cm}^2$$

Adding (105.74 + 16.475) = 122.21 W/cm^2 which is very close to the 125.66 W/cm^2 that we are looking for. What we find, then, is that we can describe the temperature rise of an optical faceplate that is not in concert with the semi-infinite plate model. The above models square with the steady-state requirements and these approximations will provide a first order analysis to evaluate the temperature rise through thin optical faceplates. They may also be used to check numerical codes for accuracy of modeling. We can define the three regimes for the three dimensional case, then, so that,

Regime III

$$0 < t_o \leq 0.6 (\alpha\tau)^{0.5} \qquad \Psi > 1 \quad \textit{Eqs. (41)} \text{ and } \textit{(42)} \qquad \textit{(43)}$$

Regime II

$$0.6 (\alpha\tau)^{0.5} < t_o < 6 (\alpha\tau)^{0.5} \qquad \Psi \leq 1 \quad \textit{Eqs. (38)} \text{ and } \textit{(39)} \qquad \textit{(44)}$$

Regime I

$$t_o \geq 6 (\alpha\tau)^{0.5} \qquad \Psi \leq 1 \quad \textit{Eqs. (32)} \text{ and } \textit{(33)} \qquad \textit{(45)}$$

References

1. J. R. Palmer, "Reverse Thermal Wave Approximation For Temperature Transients In Uncoated Reflective Optics For High Power Continuous Wave Lasers," *Optical Engineering* (to be published).

2. J. R. Palmer, "Transient Temperature Distribution In Multi-Component Optical Faceplate Using Reverse Thermal Wave Approximations: High Power Repetitive Pulsed Lasers," *Optical Engineering* (to be published in 1987-88).

3. H.S. Carslaw, and J.C. Jaeger, *Conduction of Heat In Solids*, 2nd ed.,Oxford University Press, Oxford, England, 1978.

4. J. Crank, *The Mathematics Of Diffusion* 2nd ed., Oxford University Press, Oxford, England, 1983.

5. E. L. Cussler, *Diffusion: Mass Transfer In Fluid Systems* Cambridge University Press, London, England, 1984.

6. H. J. V. Tyrrell, and K.R. Harris, *Diffusion In Liquids: A Theoretical And Experimental Study*, Butterworths, London, England, 1984.

7. J. R. Palmer, "Theoretical Model For Determining Temperature Transients In Multilayer Optical Thin Films Subjected To High Power Continuous Wave And Repetitive Pulsed Lasers: Part I- Continuous Wave," *Proc. 3rd. Int. Symp. On Optical And Optoelectronic Applied Science And Engineering* SPIE Vol. No. 655,656, Innsbruck, Austria, April, 1986.

8. J. R. Palmer, "Theoretical Model For Determining Temperature Transients In Multilayer Optical Thin Films Subjected To High Power Continuous Wave And Repetitive Pulsed Lasers: Part II- Repetitive Pulsed," *Proc. 3rd. Int. Symp. On Optical And Optoelectronic Applied Science And Engineering* SPIE Vol. No. 655, 656, Innsbruck, Austria, April, 1986.

9. J. R. Palmer "Loss Of Infrared Optical System MTF Resulting From Damage Caused By High Power Continuous Wave And Low Average Power Repetitive Pulsed Visible - UV Lasers," *4th Int'l Symp. On Optical And Optoelectronic Applied Science And Engineering* SPIE No. 806, The Hauge, The Netherlands, April, 1987.

10. J. R. Palmer "Optical Distortion Of Multilayer Coated Optical Components Used In HIgh Power Laser Systems," *4th Int'l Symp. On Optical And Optoelectronic Applied Science And Engineering* SPIE No. 805, The Hauge, The Netherlands, April, 1987.

11. J. R. Palmer "Optical Distortion Of Rugate Coated Optical Components Used In High Power Laser Systems," *4th Int'l Symp. On Optical And Optoelectronic Applied Science And Engineering* SPIE No. 805, The Hauge, The Netherlands, April, 1987.

12 H. K. Pulker, "Stress, Adherence, Hardness, And Density Of Optical Thin Films," *Optical Thin Films*, SPIE, Vol. 325, 1982.

13. R. W. Hoffman, "The Mechanical Properties Of Thin Condensed Films," *Physics of Thin Films*, Vol. 3, G. Hass and R. Thun ed., Academic Press, New York, pp. 211, ff. 1966.

14. H. E. Bennett, *Large Optics Coating and Evaluation Facility Study*, NWC TP 6177, Naval Weapons Center, China Lake, CA, pp. 31 ff. 1980.

15. H. E. Bennett, and D. K. Burge, "Simple Expressions For Predicting The Effect Of Volume And Interface Absorption And Of Scattering In High-Reflectance Or Anti-Reflectance Multilayer Coatings," *J. Opt. Soc. AM*, Vol. (70), No. (3) pp. 268-276, March, 1980.

16. P. A.Temple, D. L. Decker, T. M. Donovan, and J. W. Bethke," Measured Thin Film Absorption At The Interface, The Thin Film Bulk, And The Film-Substrate Interface," *Laser Induced Damage in Optical Materials: 1978*, NBS Spec. Publ. 541, pp. 37-42, 1979.

17. P. A. Temple,"Measurement Of Thin-Film Optical Absorption At The Air-Film Interface Within The Film And At The Film-Substrate Interface," *Appl. Phys. Lett.* 34 (10), pp. 677-679, May, 1979.

18. J. R. Palmer, and H. E. Bennett, "Relationship Between Coating Defects And The Limiting Flux Density A Cooled Laser Mirror Can Withstand," *Laser Induced Damage In Optical Materials: 1981*, NBS Spec. Pub. 638, 1983.

19 J. R. Palmer, "Continuous Wave Laser Damage On Optical Materials," *Optical Engineering* Vol. 22, No. 4, July/August, 1983.

20. H. E. Bennett, "Insensitivity Of The Catastrophic Damage Threshold Of Laser Optics To Dust And Other Surface Defects," *Laser Induced Damage In Optical Materials: 1980,* NBS Spec. Pub. 620, 1981.

21 J. R. Palmer, *Laser Damage In Optical Thin Films,* MacMillan Publishing Co., New York, NY (to be published).

22. P. J. Schneider, "Conduction," *Handbook of Heat Transfer Fundamentals* Section 4-1, 2nd. ed., W. M. Rohsneow, J. P. Hartnet, and E. N. Ganic', ed., McGraw-Hill Book Co., New York, NY, 1985.

23. P. J. Schneider, *Handbook of Heat Transfer,* W. M. Rohsenow, and J. R. Hartnett, ed., McGraw-Hill Book Co., New York, NY, pp. 3-14 ff. 1973.

24. D. M.Lewis, and H. J. Sailer, *J. Heat Transfer,* Trans., ASME, Vol. 87, pp. 310-311, 1965.

25. H. Fenech, and W. H. Rohsenow, *J. Heat Transfer,* Trans., ASME, Vol. 85, pp. 15-24, 1963.

26. F. Kreith, *Principles of Heat Transfer,* 2nd. ed., International Textbook Co., Scranton, PA, 1966.

27. M. Jakob, *Heat Transfer,* Vol. 1, John Wiley and Sons, New York, NY, 1949.

28. M. McGuirk, and R. D. Poirier, "Thermal Conductivity Of Enhanced Reflectors," *Laser Induced Damage In Optical Materials: 1985,* NBS Spec. Publ. (to be published).

29. D. L. Decker, "Thermal Properties Of Optical Materials," *Laser Induced Damage In Optical Materials: 1986,* NBS Spec. Publ. (to be published).

30. S. M. J. Akhtar, D. Ristau, and J. Ebert, "Thermal Conductivity Of Dielectric Film And Correlation To Damage Threshold At 1064 nm," *Laser Induced Damage In Optical Materials: 1986,* NBS Spec. Publ. (to be published).

31. R. T. Swimm, "Photothermal Measurement Of Optical Coating Thermal Transport Properties," *Laser Induced Damage In Optical Materials: 1986,* NBS Spec. Publ. (to be published).

32. L. G. Koshigoe, and D. L. Decker, *Thermophysical Properties Of Thin Films,* NWC TM-5322, Naval Weapons Center, China Lake, CA, 1984.

33. D. L. Decker, L. G. Koshigoe, and J. Ashely, "Thermal Properties Of Thin Films," *Laser Induced Damage In Optical Materials: 1984,* NBS Spec. Pub. 727, 1986.

34. H. Kuster, and J. Ebert, "Pyroelectric Measurement Of Absorption In Oxide Layers And Correlation To Damage Threshold," *Laser Induced Damage In Optical Materials: 1979,* NBS Spec. Pub. 568, 1980.

35. N. J. Kreidl, and J. L. Rood, "Optical Materials," Chpt. 5, *Applied Optics And Optical Engineering* Vol. 1, R. Kingslake, ed., Academic Press, New York, NY, 1965.

36. H. M. Musal, "Thermomechanical Stress Degradation Of Metal Mirror Surfaces Under Pulsed Irradiation," *Laser Induced Damage In Optical Materials: 1979,* NBS Spec. Pub. 568, 1980.

37. S. J. Holmes, *Reflective Coating Development For HF Lasers,* AFWL-TR-82-12, Northrop Research And Technology Center, Palos Verdes Peninsula, CA, 1982.

38. J. R. Palmer, "Thermal Shock: A Contributing Factor To Laser Damage In Optical Thin Films Used For High Power Continuous Wave Laser Optics," *Laser Induced Damage In Optical Materials: 1987,* (to be published).

39. S. Musikant, *Optical Materials: An Introduction To Selection And Application,* Marcel Dekker, Inc., New York, NY, 1985.

40. This is a new code developed by Lazor Inc. for evaluating the temperature transients in optics for coated and uncoated, CW and Repetitive Pulsed laser optical components. This system runs on a Macintosh Plus™. Lazor Inc, P.O. Box 613311, So. Lake Tahoe. CA. 95761.

41. D. Q. Kern, and A. D. Kraus, *Extended Surface Heat Transfer*, McGraw-Hill Book Co., Inc., New York, NY, pg. 103 ff, (1972).

42. J. R. Palmer, *High Power Laser Optics*, Marcel Dekker, New York, NY, (to be published in 1989).

Appendix

2 ierfc, 4i^2 erfc, and erfc functions[2,3,42]

(X) Interval	**2 ierfc (X)**
0 to 0.299	$1.1284 - 1.998(X) + 1.11(X)^2$
0.30 to 0.5499	$1.115074 - 1.90863(X) + 0.9543(X)^2$
0.55 to 0.999	$1.012 - 1.5525(X) + 0.64346(X)^2$
1.0 to 1.599	$0.6271 - 0.76914(X) + 0.241964(X)^2$
1.6 to 2.0	$0.21573 - 0.21165(X) + 0.0525(X)^2$
2.001 to 2.4	$0.05124 - 0.041425(X) + 0.008393(X)^2$

(X) Interval	**erfc (X)**
0 to 0.299	$1.0 - 1.1408(X) + 0.1377(X)^2$
0.30 to 0.5499	$1.0167 - 1.2658(X) + 0.38269(X)^2$
0.55 to 0.99	$1.0394 - 1.35775(X) + 0.47606(X)^2$
1.0 to 1.599	$0.84562 - 0.98479(X) + 0.29598(X)^2$
1.6 to 2.09	$0.359744 - 0.34066(X) + 0.081586(X)^2$
2.1 to 2.5	$0.045779 - 0.032871(X) + 0.005892(X)^2$

(X) Interval	$4\,i^2\mathrm{erfc}\,(X)$
0 to 0.299	$1.0171964 - 2.497286(X) + 2.4798872(X)^2$
0.30 to 0.5499	$0.74768 - 1.21279697(X) + 0.522727(X)^2$
0.55 to 0.999	$0.9441262 - 1.854143(X) + 1.049524(X)^2$
1.0 to 1.599	$0.3642714 - 0.4490714(X) + 0.1417143(X)^2$
1.6 to 2.0	$0.09558 - 0.093086(X) + 0.022857(X)^2$
2.001 to 2.4	$0.021334 - 0.0174143(X) + 0.0035714(X)^2$

Thermal Properties of Some Optical Materials [39,42]

material	α cm²/sec	K W/cm-°C	ρ g/cm³	cp Joules/g-°C
Aluminum	0.98	2.37	2.70	0.870
Copper	1.14	3.92	8.96	0.380
Beryllium	0.467	1.61	1.83	1.884
Gold	1.20	3.18	19.30	0.140
Molybdenum	0.52	1.34	10.20	0.250
Nickel	0.18	0.85	8.90	0.450
Rhodium	0.292	0.90	12.40	0.248
Silver	1.68	4.20	10.50	0.230
Berylco-10	0.61	2.09	4.03	0.850
Chromium	0.25	0.95	7.20	0.500
ULE	0.0078	0.0131	2.20	0.766
Silicon	0.48	0.847	2.33	0.758
Silicon Carb.	0.37	1.270	3.14	1.320
Cervit	0.0081	0.017	2.50	0.840
Pyrex	0.0065	0.0113	2.35	0.740
Zerodur	0.008	0.0165	2.21	0.934
Al_2O_3	0.0625	0.1771	3.98	0.712
Fused Silica	0.0084	0.0137	2.20	0.741

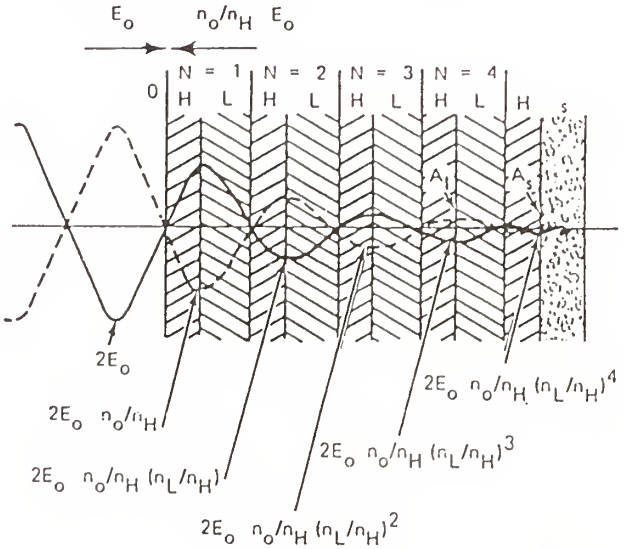

Figure 1.0

Lazor™ Code

Temperarature Rise ΔT – °C

Radius – cm

6	6.5	7	7.5	8	8.5	9	9.5	Thickness – cm
132.94	81.38	71.58	62.61	54.36	47.10	40.42	34.44	0
107.77	62.91	55.34	48.40	42.02	36.40	31.25	26.63	.5
89.13	54.56	48.00	41.98	36.45	31.56	27.10	23.10	1
77.04	47.16	41.48	36.29	31.50	27.28	23.42	19.96	1.5
66.45	40.67	35.78	31.30	27.17	23.53	20.20	17.22	2
57.12	34.97	30.76	26.90	23.36	20.23	17.37	14.80	2.5
49.04	30.02	26.40	23.10	20.05	17.36	14.91	12.70	3
42.49	26.01	22.88	20.01	17.36	15.05	12.92	11.01	3.5
36.67	22.44	19.74	17.27	15.00	12.98	11.15	9.50	4
31.84	19.49	17.14	15.00	13.02	11.27	9.68	8.25	4.5
27.75	16.98	14.94	13.07	11.34	9.83	8.44	7.19	5

Absorbed Average Fluence: 125.66 W/cm²
Laser Beam Diameter: 12 cm

Substrate: Copper
Run Time : 10^5 Pulses

Figure 2.0

Lazor™ Code

Temperarature Rise ΔT – °C

Radius – cm

Thickness – cm

10	10.5	11	11.5	12	12.5	13	13.5	
29.16	24.50	20.42	16.87	13.81	11.22	9.11	7.32	0
22.54	18.94	15.78	13.04	10.68	8.68	7.04	5.66	.5
19.55	16.43	13.69	11.31	9.26	7.53	6.11	4.91	1
16.90	14.20	11.83	9.77	8.01	6.50	5.28	4.24	1.5
14.57	12.25	10.20	8.43	6.90	5.61	4.55	3.66	2
12.53	10.53	8.77	7.25	5.94	4.82	3.91	3.14	2.5
10.76	9.04	7.53	6.22	5.10	4.14	3.36	2.70	3
9.32	7.83	6.52	5.39	4.41	3.59	2.91	2.34	3.5
8.04	6.76	5.63	4.65	3.81	3.10	2.51	2.02	4
6.98	5.87	4.89	4.04	3.31	2.69	2.18	1.75	4.5
6.09	5.11	4.26	3.52	2.88	2.34	1.90	1.53	5

Lazor™ Code

Temperarature Rise ΔT – °C

Radius – cm

Thickness – cm

14	14.5	15	15.5	16	16.5	17	17.5	
5.80	4.53	3.49	2.68	2.10	1.70	1.19	0.891	0
4.48	3.50	2.70	2.07	1.61	1.31	0.919	0.689	.5
3.89	3.03	2.34	1.80	1.40	1.14	0.797	0.600	1
3.36	2.62	2.02	1.56	1.21	0.984	0.689	0.516	1.5
2.90	2.26	1.75	1.34	1.04	0.848	0.594	0.445	2
2.49	1.94	1.50	1.15	0.897	0.729	0.511	0.383	2.5
2.14	1.67	1.29	1.00	0.770	0.626	0.438	0.329	3
1.85	1.45	1.12	0.858	0.667	0.542	0.380	0.285	3.5
1.60	1.25	0.963	0.740	0.576	0.468	0.328	0.246	4
1.39	1.08	0.836	0.643	0.50	0.407	0.285	0.213	4.5
1.21	0.945	0.729	0.560	0.436	0.354	0.248	0.186	5

Lazor™ Code

Temperarature Rise ΔT – °C

Radius – cm

18	18.5	19	19.5	20	20.5	21	Thickness – cm
0.651	0.465	0.332	0.250	0.213	0.120	0.092	0
0.503	0.360	0.257	0.193	0.165	0.093	0.071	.5
0.436	0.312	0.223	0.167	0.143	0.080	0.061	1
0.377	0.270	0.193	0.145	0.123	0.070	0.053	1.5
0.325	0.233	0.166	0.125	0.106	0.060	0.050	2
0.280	0.200	0.143	0.107	0.091	0.052	0.039	2.5
0.240	0.172	0.123	0.092	0.079	0.044	0.034	3
0.208	0.149	0.106	0.080	0.068	0.038	0.029	3.5
0.180	0.128	0.092	0.070	0.059	0.033	0.025	4
0.156	0.111	0.080	0.060	0.051	0.029	0.022	4.5
0.136	0.097	0.069	0.052	0.044	0.025	0.019	5

PEAK PULSE TEMPERATURE RISE IN MULTILAYER STACK

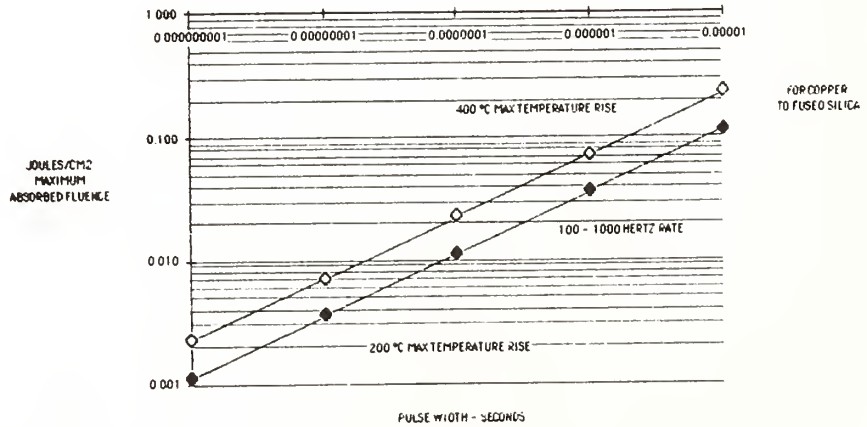

FIGURE 4.0

Lazor™ Code

Temperarature Rise ΔT – °C

Radius – cm

6	6.5	7	7.5	8	8.5	9	9.5	
203.76	124.72	109.71	95.97	83.31	72.16	61.95	52.79	0
152.74	93.45	82.21	71.94	62.45	54.10	46.44	39.57	.5
137.71	84.25	74.15	64.86	56.31	48.77	41.87	35.68	1
124.38	76.14	66.97	58.58	50.86	44.05	37.82	32.23	1.5
112.71	69.00	60.69	53.08	46.08	39.91	34.27	29.20	2

Thickness – cm

Absorbed Average Fluence: 125.66 W/cm²
Laser Beam Diameter: 12 cm

Substrate: Copper
Run Time : 10^5 Pulses

Figure 3.0

Lazor™ Code

Temperarature Rise ΔT – °C

Radius – cm

10	10.5	11	11.5	12	12.5	13	13.5	
44.69	37.55	31.29	25.85	21.17	17.20	13.96	11.22	0
33.50	28.15	23.46	19.39	15.87	12.89	10.46	8.41	.5
30.20	25.38	21.15	17.47	14.31	11.63	9.43	7.58	1
27.28	22.92	19.10	15.78	12.92	10.50	8.52	6.85	1.5
24.72	20.77	17.31	14.30	11.71	9.52	7.72	6.21	2

Thickness – cm

Lazor™ Code

Temperarature Rise ΔT – °C

Radius – cm

14	14.5	15	15.5	16	16.5	17	17.5	
8.89	6.94	5.35	4.11	3.20	2.60	1.82	1.37	0
6.66	5.20	4.01	3.08	2.40	1.95	1.37	1.02	.5
6.01	4.69	3.62	2.78	2.16	1.76	1.23	0.923	1
5.42	4.24	3.27	2.51	1.95	1.59	1.11	0.833	1.5
4.92	3.84	2.96	2.28	1.77	1.44	1.01	0.755	2

Thickness – cm

Lazor™ Code

Temperarature Rise ΔT – °C

Radius – cm

18	18.5	19	19.5	20	20.5	21		
0.997	0.713	0.510	0.383	0.326	0.184	0.141		0
0.748	0.534	0.382	0.287	0.245	0.138	0.105		.5
0.674	0.482	0.344	0.259	0.221	0.124	0.095		1
0.609	0.435	0.311	0.234	0.20	0.112	0.086		1.5
0.552	0.394	0.282	0.212	0.182	0.102	0.078		2

Thickness – cm

Manuscript Received 12/14/87/sar

Reverse Thermal Wave Approximation For Temperature Transients In Optical Thin Films And Substrates Reflective Optics For High Power Continuous Wave Lasers

J. R. Palmer

University Of Alabama, Huntsville
Center For Applied Optics
Huntsville, Alabama 35899

Abstract

It is the intent for the purpose of this paper to continue with the application of the *Reverse Thermal Wave Model* to problems associated with the damage thresholds and temperature gradients for optical components which are provided with optical thin films. This problem is particularly acute for those optical components which are part of a high power Continuous Wave laser system.

In this paper are descriptions of how the approximations provide techniques for evaluating the maximum threshold for optical thin films deposited on components with very thick and very thin optical faceplates. The *Reverse Thermal Wave Model*provides some rather dramatic results for those optical systems that are used for imaging in the infrared portion of the spectrum, in as much as these optical elements are generally very thin faceplates and may be subject to damage from very high power lasers.

Both mathematical descriptions and figures are provided to show the damage thresholds predicted by the model and correlated to one dimensional semi-infinite plate experimental data. For the most part, authors have treated with infinite and semi-infinite walls. The attention for this article is to treat with those conditions that do not meet the boundary requirements for the semi-infinite plate. Given this boundary, the use of what we describe as the *Reverse Thermal Wave Approximations* will be implemented to allow the calculation of the transient temperature rise in thin optical faceplates. Equations are described and the regimes of their application are outlined. Additionally, curves are generated to provide the reader examples of how to implement the equations.

Key Words: Optics, Transient Heat Transfer, Faceplates, Optical Distortion, and Continuous Wave Lasers

Introduction

As we indicated before,[1,2] most authors dealing with transient thermodynamics rely almost exclusively on the semi-infinite plate model and the infinite plate model.[3,4,5,6] Carslaw and Jaeger,[3] of course, is the most seminal text in this area. However, the work of J. Crank,[4] E. L. Cussler,[5] and Tyrrell and Harris[6] provide enormous insight into many of these problems. Even so, the problem of the boundary condition wherein the semi-infinite plate boundary is not met is given very little attention. And, for those people working in the optical field this provides little solace.

The thrust of this paper is to provide a set of approximations that will permit the analyst to evaluate the temperature transient through the optical thin films and a reflective optical faceplate that fails to meet the semi-infinite plate model boundary conditions. Obviously, if an analyst has access to a computer that has an appropriate finite difference heat transfer model, and the money to

have the model put to use for the problem at hand, then these approximations may not be of any great concern. For those who do not always have these resources available to them, the approximations can be applied as a useful tool for evaluating their optical components and optical trains. Having said all that, the reader may find it very difficult to have a finite difference program work on the thin films. Most who have tried, including the author, have found that the films have such little thermal mass that the program goes unstable and blows up. The author has, however, provided mathematical closed form solutions which may be used in concert with a finite difference program.[7,8,9,10,11]

Continuous Wave - One Dimensional

Basically, we begin with the semi-infinite plate boundary conditions. That is, energy, or temperature, is applied at one surface of the plate, no energy is lost from the plate to the surrounding environment, and the plate is of such a thickness that at the end of the time of the transient, the temperature rise on the back surface will be zero.[1,2,8,9] However, we must first treat with the energy absorbed in the optical thin films and transferred to the optical substrate.

Optical thin film coatings, manifestly, have very little thermal mass. The forces that bond the films may be Van Der Waal's forces, Electrostatic forces, or Chemical Bonding forces.[12,13] The experimental data would tend to indicate that the coating absorption takes place at the boundaries between the coating and the substrate; or coating-coating interface for multilayer systems.[14,15,16,17] Bennett and Burge[15] state that, " . . . And it has been found that the absorption in the vicinity of a thin-film interface may be as large or larger than that in the entire film volume." In discussing the results of absorption of an AsSe thin film on a CaF substrate, Temple states, "It was found that the predominant absorption was at the film-substrate interface."[17] For the analytical system of this paper, there is a concomitant statement that follows from the interfacial absorption. Temple, et.al.,[16] states, "Finally, we would like to make the point that while much attention has been given to the electric field plots for multilayer coatings in damage resistance discussions, it is the relative power density which must be considered in discussing thermal absorption since the local absorptance is the product of the relative power density and the absorption coefficient at that point." Fundamentally, then, the basis of the following treatment is underpinned with the basic premise that most, if not all, of the absorption takes place at the boundaries of the coatings. Further, that the temperature thermal profile will follow the electric field.

Heretofore, the conventional wisdom, when evaluating the temperature rise of an optical surface, has been to assume that the entire absorbed flux density goes into the substrate. Additionally, the belief continues, that the thin-film coatings equilibrate with the substrate in some instantaneous fashion. This technique would tend to indicate that these assumptions may not be accurate. At the outset, we will use an idealized case. The model assumes that the thermal transport properties do not change with temperature, for both the one dimensional and three dimensional case, and no heat is lost from the optic, i.e., no forced or free convection or radiation. The electric field strength and coating relationships will be as shown in *Figure 1*.

Absorption Theory for Multilayer Optical Thin Films

According to the electrical field plot of *Figure 1*, interfacial absorption will occur only at,

$$2E_o\{\eta_o/\eta_H\},\ 2E_o\{\eta_o\eta_L/\eta_H^2\},\ 2E_o\{\eta_o\eta_L^2/\eta_H^3\}\ldots$$

Even though the films are extremely thin, they are still amenable to joule heating. Consequently, the semi-infinite plate model is applicable. The model assumes that the layers of films are analogous to a series of composite layers. Each layer is bound by one, or a combination, of forces described earlier. This adhesive force is very important in determining the required transient and steady-state gradient through the film layers. If we assume, then, that the absorption and power densities are proportionate to the (E) field strength through the layers of the coatings, then,

(1)

$$\alpha^{\bullet} = \left\{1 - R - \left[4(\psi)(\eta_L/\eta_H)^{2N}/(\varphi)\right] - \left[4\pi\sigma\cos(\theta)\left\{1.15 - 2.565(10^{-6}) \times \left[5(10^4) - \lambda\right]\right\}^{2N}/\lambda\right]^2\right\} \left\{\left[1 - (\eta_L/\eta_H)^{2N+1}\right]\left[\eta_H^2 - \eta_L^2\right]^{-1}(4)\right\}^{-1}$$

If the reflecting optic has a dielectric substrate:

low index next to the substrate, then, $\Psi = 1$, $\varphi = \eta_S$:

high index next to the substrate, then, $\Psi = \eta_S$, $\varphi = \eta_H^2$:

where, η_S = Substrate index, η_H = Index of the high index film.

For the case where the substrate is not a dielectric, i.e., is a metal, a quasi dielectric of the metal-film combination is generated, so that, for the low index next to the substrate,

(2)

$$\psi = \eta_S\left\{\left((1 (-/+) \cos\delta)/2\right)\left\{(\eta_S/\eta)^2 + (K_S/\eta)^2\right\} + (1 (+/-) \cos\delta)/2 + (K_S/\eta)\sin\delta\right\}^{-1}$$

where, $\eta = (\eta_L)$ low index film, at λ if next to substrate.

(η_H) if high index next to metal.

η_S = Index for metal substrate, at λ

K_S = Extinction coefficient for metal substrate at λ.

$\tan\delta = 2\eta K_S / \left\{\eta^2 - \eta_S^2 - K_s^2\right\}$

$\varphi = \eta_H^2$

If the high index film is next to the substrate, $\psi = 1.0$

When, $\eta^2 > (\eta_S^2 + K_S^2)$, δ is in the first quadrant. Otherwise, δ is in the second quadrant using the standard conventions.

σ = rms surface roughness, Å

λ = Wavelength of interest, Å

R = Reflectivity

N = Number of high-low coating pairs

For *Eq. (2)*, if the low index film is next to the metal substrate, use the upper sign in the denominator. If the high index is next to the substrate, use the lower sign in the denominator.

The value of $\left(4\pi\sigma\cos(\theta)/\lambda\right)^2$ represents the total integrated scatter from a surface. The expression $1.15\text{-}2.565(10^{-6})\left[5(10^4)\text{-}\lambda\right]^{2N}$ represents the increase in scatter as a function of wavelength and number of coating pairs.

Continuous Wave Uncooled Coated Optics

At each interface there will be a distribution of power density absorbed between the low and high index materials, as a function of their respective thermal transport properties, then,

(3)

$$2E_o \sum_{m=0}^{m} \left(\eta_o \eta_L^m / \eta_H^{m+1} \right) \left(F_1 \alpha^*_1{}^{0.5} / K_1 \right) = 2E_o \sum_{n=0}^{n} \left(\eta_o \eta_L^n / \eta_H^{n+1} \right) \left(F_2 \alpha^*_2{}^{0.5} / K_2 \right)$$

$$F_2 = F_1 \left(\alpha^*_1{}^{0.5} \right) K_2 / \left(K_1 (\alpha^*_1{}^{0.5}) \right) \left\{ 2E_o \sum_{n=0}^{n} \left(\eta_o \eta_L^n / \eta_H^{n+1} \right) / 2E_o \sum_{m=0}^{m} \left(\eta_o \eta_L^m / \eta_H^{m+1} \right) \right\}$$

where, F_1 = Absorbed portion in low index material

F_2 = Absorbed portion in high index material

α^*_1 = Thermal diffusivity of low index material, cm^2/sec

α^*_2 = Thermal diffusivity of high index material, cm^2/sec

K_1 = Thermal conductivity of low index material, W/cm-°C

K_2 = Thermal conductivity of high index material, W/cm-°C

So that,

(4)

$$F_1 + F_2 = 1.0 \qquad C = ((\alpha^*_1{}^{0.5}) K_2 / (K_1 (\alpha^*_2{}^{0.5})))$$

(5)

$$F_2 = 1.0 / (1.0 + C) \qquad F_1 = 1.0 - F_2$$

From *Eq. (1)* through *(5)*, the temperature rise for each element in the multilayer stack, and the substrate, may be evaluated. Using a modified form of the Palmer-Bennett model, to include source and multiple sink to the substrate,[7,8,9,18,19,20,21]

(6)

$$\Delta T_{F1-2} = 2 \mathcal{F}_{o1-2} (\alpha^*_{1-2} \tau)^{0.5} \left[\{ \text{ierfc}(x) \} \right] / K_{1-2} - \{ \mathcal{F}_{o1-2} / h_c \} + \{ \mathcal{F}_{o1-2} / h_c \}$$

$$X \{ \exp (H_1{}^2 \alpha^*_c \tau) \, \text{erfc}(y) \} + 2E_o \sum_{(m,n)=0}^{(m,n)} \left[\eta_o \eta_L{}^{(m,n)} / \eta_H{}^{(m,n)+1} \right] \Delta T_m + \Delta T_s$$

where, $X = t / 2(\alpha^* \tau)^{0.5}$ at $t=0$

$\text{ierfc}(x) = 1/(\pi)^{0.5}$

$\text{erf}(x) = 0$

$h_c = 1/\{\Pi_\zeta{}^{-1} (2N)\} = W/cm^2 \text{-°C}$

$Y = H_1 (\alpha^* \tau)^{0.5}$

$\alpha^*_c = [\alpha^*_1 + \alpha^*_2] 2^{-1} \quad K_c = [K_1 + K_2] 2^{-1}$

α^*_s = Thermal diffusivity of the substrate, cm^2/sec

K_s = Thermal conductivity of the substrate, W/cm -°C

$$H_1 = \Pi_\zeta / K_C$$

$$H_2 = \Pi_\zeta / K_S$$

The absorbed flux density $\mathcal{F}_{OL}$, $\mathcal{F}_{OH}$ are found from,[7,8,9,21]

$$\mathcal{F}_{OL} = I_o \alpha^\bullet_o F_1 \psi_N \left\{ 2 E_o \sum_{m=0}^{m} \left[\eta_O \eta_L^m / \eta_H^{m+1} \right] \right\} -1.0 \qquad (7)$$

$$\mathcal{F}_{OH} = I_o \alpha^\bullet_o F_2 \psi_N \left\{ 2 E_o \sum_{n=0}^{n} \left[\eta_O \eta_L^n / \eta_H^{n+1} \right] \right\} -1.0 \qquad (8)$$

where,

$\mathcal{F}_{OL}$, $\mathcal{F}_{OH}$ = Absorbed flux density, W/cm^2

I_O = Incident flux density, W/cm^2

N = High low pair number from *Figure 1*

ψ_N = $2E_o(\eta_O/\eta_H)$, $2E_o(\eta_O\eta_L/\eta_H^2)$, $2E_o(\eta_O\eta_L^2/\eta_H^3)$, . . .

$\alpha^\bullet_o$ = Absorption value

The temperature rise at the low - high index interface, where the electric field is cancelled, i.e., no absorption, is found from,[7,8,9,21]

$$\Delta T_{F1\text{-}2} = \left\{ 2 \mathcal{F}_{OH} (\alpha^\bullet_1 \tau)^{0.5} \left[\{ \text{ierfc } (x) \} \right] / K_1 - \{ \mathcal{F}_{OH} / h_c \} + \{ \mathcal{F}_{OH} / h_c \} \right.$$
$$\times \{ \exp (H_1^2 \alpha^\bullet_c \tau) \text{ erfc}(y) \} + 2 \mathcal{F}_{OL} (\alpha^\bullet_1 \tau)^{0.5} \left[\{ \text{ierfc } (x_o) \} \right] / K_2$$
$$\left. - \{ \mathcal{F}_{OL} / h_c \} + \{ \mathcal{F}_{OL} / h_c \} \{ \exp (H_1^2 \alpha^\bullet_c \tau) \text{ erfc}(y) \} \right\} 2^{-1} \qquad (9)$$

$$+ 2 E_o \sum_{(m,n)=0}^{(m,n)} \left[\eta_O \eta_L^{(m,n)} / \eta_H^{(m,n)+1} \right] \Delta T_{(m,n)} + \Delta T_S$$

where, X = $t / 2(\alpha^\bullet_1 \tau)^{0.5}$ at $t = 0$

ierfc (x) = $1/(\pi)^{0.5}$;

erf (x) = 0

Y = $H_1(\alpha^\bullet_1 \tau)^{0.5}$

X_0 = $t / 2(\alpha^\bullet_2 \tau)^{0.5}$ at $t = 0$

ierfc (x_0) = $1/(\pi)^{0.5}$

Y_1 = $H_1(\alpha^\bullet_2 \tau)^{0.5}$

The temperature rise of the substrate will be found from,[7,8,9,21]

(10)

$$\Delta T_S = 2E_o\left\{\sum_{m=0}^{m}\left[\eta_o\eta_L{}^m/\eta_H{}^{m+1}\right]\mathcal{F}_{oL}\left\{\text{erfc }(x)-\exp\left(H_2{}^2\alpha^*{}_S\,\tau\right)\text{erfc }(z)\right\}\right.$$

$$\left.+\,2E_o\sum_{n=0}^{n}\left[\eta_o\eta_L{}^n/\eta_H{}^{n+1}\right]\mathcal{F}_{oH}\left\{\text{erfc }(x)-\exp\left(H_2{}^2\alpha^*{}_S\tau\right)\text{erfc }(z)\right\}\right\}$$

$$\times\left\{2\left(\alpha^*{}_S\,\tau\right)^{0.5}\left[\left\{\text{ierfc }(Q)\right\}\right]/K_S\right\}$$

where, $Q = t/2(\alpha^*{}_S\,\tau)^{0.5}$ at $t=0$

$\text{ierfc}(Q) = 1/(\pi)^{0.5}$

$\text{erfc }(x) = 1$

$Z = H_2\,(\alpha^*{}_S\,\tau)^{0.5}$

The problem is made simpler, of course, if we simply set,

$$\mathcal{F}_o = 2E_o\left\{\sum_{m=0}^{m}\left[\eta_o\eta_L{}^m/\eta_H{}^{m+1}\mathcal{F}_{oL}\right]\left\{\text{erfc }(x)-\exp\left(H_2{}^2\alpha^*{}_S\,\tau\right)\text{erfc }(z)\right\}\right.$$

$$\left.+\,2E_o\sum_{n=0}^{n}\left[\eta_o\eta_L{}^n/\eta_H{}^{n+1}\mathcal{F}_{oH}\right]\left\{\text{erfc }(x)-\exp\left(H_2{}^2\alpha^*{}_S\,\tau\right)\text{erfc }(z)\right\}\right\}$$

and, then, *Eq. (10)* becomes,

$$\Delta T_S = 2\mathcal{F}_o\left(\alpha^*{}_S\,\tau\right)^{0.5}\left[\left\{\text{ierfc}(Q)\right\}\right]/K_S$$

The above equations assume that the diameter of the laser beam will be greater than $12[\alpha^*\,\tau]^{0.5}$ in order to be one dimensional.[1,2,7,8,9] The steady-state gradient may be determined in a straight forward fashion. What makes the problem less than straight forward is knowing the binding forces between the coatings, i.e., adhesion.

Pulker[12] suggests that the adhesive forces may be as low as 10^4 dynes/cm^2 for physisorption to greater than 10^{11} dynes/cm^2 for chemical bonding. Given this wide range, which, most probably, will be very susceptible to the coating technique and the environment, we will use a bonding force between the coatings of 10^{10} dynes/cm^2, for most analysis.

Based on a clamping force between the coatings of 10^{10} dynes/cm^2, or 9689 atmospheres, we can calculate a film coefficient between each layer. Schneider[22,23] states, ". . . heat transfer through an interface takes place by combined mechanisms of conduction across true contact points, conduction across entrapped interstitial fluid, and radiation across interstitial gaps. Resulting

overall conductance of the joint is therefore a function of the material in contact (conductivity, surface finish, flatness, and hardness), the contact pressure, the mean temperature and the heat flux across the joint . . ."

The film coefficient is expected to increase with increased contact pressure. From this relationship, the film coefficient should follow from,[22,23,24,25]

(11)

$$\Pi_\zeta = (P^{2/3})\ (1761)^{-1}$$

where, $\Pi_\zeta = W/cm^2\text{-}°C$ $\quad P = \#/in^2$

Based on the clamping force of 9689 atmospheres, $1.42(10^5)\#/in^2$, and very smooth surfaces,

$$\Pi_\zeta = \left[1.4(10^5)\right]^{2/3} \times (1761)^{-1} \qquad \Pi_\zeta = 1.55\ W/cm^2\text{-}°C$$

Because the films are so thin, they will not present a thermal resistance of any magnitude. The basic expression for determining the overall film coefficient through a system of composite materials, is,[26,27]

(12)

$$U = 1 / \left\{1 / \Pi_{\zeta 1} + L_1 / K_1 + 1 / \Pi_{\zeta 2} + L_2 / K_2 + 1 / \Pi_{\zeta 3} + \ldots\right\}$$

So then, treating each absorbing electric field interface as a radiation boundary to the substrate, the first field interface (N=1), from *Fig. 1* the film coefficient will be,

(13)

$$\Pi_\zeta = 1 / \left[2N \times (1.55)^{-1}\right]$$

From our problem, then,

$$H_1 = \Pi_\zeta / K_S \qquad H_2 = \Pi_\zeta / K_C$$

We must remember that the value of (Π_ζ) changes with each pair of coatings as we work our way from N=1 to N = ∞. There are some additional issues that are not clearly defined. For example what are the correct thermal transport properties to use for the as deposited thin films, i.e., K_C, α^*_C. There is experimental work that has been performed that suggests that the thermal transport properties of the as deposited thin films may be lower than the crystalline values by a factor of 10 to 500.[28,29,30,31,32,33] For our analysis we will use the factor of ten reduction in the thermal transport properties of the various materials that are used for dielectric vapor deposited chemistries.

In evaluating the use of the *Reverse Thermal Wave Model*[1] we began with a substrate of sufficient thickness to satisfy the semi-infinite plate boundary. However, our problem is more complicated with the absorption of the incident laser flux density in the optical thin films. Which leads us to another uncertainty, that of the maximum temperature for the optical thin films. Experiments have been made that suggest that the damaging temperature threshold for a single layer oxide coating on Suprasil I is 600°C irrespective of the melt temperature of the material.[14,34] However, there is also evidence to suggest that the real threshold of a multilayer optical thin film is in the range of 200°C.[14] This more conservative temperature is based upon thermal shock which occurs when the temperature difference between the substrate and the film interface is sufficient to push the coating material past the elastic limit. Even though coatings are very often evaporated on to substrates that are at 200°C, the substrates are completely thermalized and require many minutes for ramp down to ambient temperature. In this discussion, the temperatures are taken to 200°C in less than a second which provides for substantial thermal shock.

We can, for example, use the work of Kreidl and Wood,[35] which is not unlike the equation proposed by Musal,[36] for thermal shock of glass and glass like materials. They suggest the following expression as a first order analysis for thermal shock threshold. Then,

(14)

$$\Delta T_{shock} = M(1-\nu) / E\,\alpha$$

where,

ν = Poisson's Ratio

E = Young's Modulus, Newton's/cm^2

α = Coefficient of thermal expansion, °C^{-1}

M = Modulus of rupture, Newton's/cm^2

This equation is saying, fundamentally, that the temperature difference necessary to provide a stress that will impose cracking, or fracture of a glass, or a glass like material. What we see in this equation is that the coefficient of thermal expansion pretty much dominates. In another piece of work, Palmer, *et al*, evaluated the temperature rise in coating pair N=1 and the temperature rise of the first surface of the substrate for evaluating the thermal shock temperature differential.[38] For their application, the differential expansion between the coating pair N=1 and the substrate becomes the limiting criteria. In this paper, the seeming anomaly of the wide band of temperatures that coatings could withstand without damaging is resolved. In fact, both cases could very well be true. For this condition, they provide an equation, such that,

(15)

$$\Delta T_{shock} = M(1-\nu)/\left\{ E\,(\alpha_S - \alpha_C)\right\}$$

We can look at some standard materials used in optical thin films and see the respective thermal shock charateristics. For example, we can look at ZnS and Al_2O_3 and see what the relative temperature differential is needed to provide thermal shock. For ZnS the value for Poisson's ratio is on the order of 0.2, Young's Modulus is 1.06(10^7) Newton's/cm^2, Modulus of rupture 2.05(10^4) Newton's/cm^2, and the expansion coefficient is 7.85(10^{-6}). [35,37] Newton's/cm^2. For Copper the coefficient of expansion is 16.6 (10^{-6})[39] Newton's/cm^2. We find from *Eq. (15)* that the differential temperature for thermal shock is on the order of 177 °C ΔT. For Al_2O_3 the value of Poisson ration is about 0.2, Young's Modulus is about 7.69 (10^7), Modulus of rupture is 1.451 (10^5), and the expansion coefficient is 7.7(10^{-6}).[35,37] The temperature differential for thermal shock will be 170 °C ΔT. Based upon the thermal shock equation we are more inclined to use the more conservative value of 200°C for the maximum threshold of as deposited optical thin films when using a Copper substrate.

Using a one dimensional condition, wherein the laser beam diameter meets the requirements of,

(16)

$$D \geq 12\,(\alpha\tau)^{0.5}$$

where,

α = Thermal diffusivity, cm^2 / sec

τ = Transient time, sec

And the thickness of the substrate meets the requirements of,

$$t \geq 6\,(\alpha\tau)^{0.5} \qquad (17)$$

For the condition wherein constant flux density is applied to the first surface, the one dimensional semi-infinite plate model provides the temperature rise for the first surface,[1,2,3,9]

$$\Delta T_1 = 2F_0\,(\alpha\tau)^{0.5}\left\{ \text{ierfc}(x) \right\}/K \qquad (18)$$

where,

$\mathcal{F}_o$ = Absorbed incident flux density, W/cm^2

K = Thermal conductivity, W/cm-°C

x = $t / 2(\alpha\tau)^{0.5}$ at t=0 ; ierfc(x) = $1/(\pi)^{0.5}$

And, at some depth into the faceplate, the temperature rise will be found from the following expression,[1,2,3,9]

(19)

$$\Delta T_{t>0} = 2\mathcal{F}_o (\alpha\tau)^{0.5} \{ \text{ierfc}(y) \} / K$$

where,

$y = t / 2(\alpha\tau)^{0.5}$ at $t > 0$

We can now look at the end point and see if these equations correctly depict the temperature rise through the mass of material. To do this, we need to use the steady state solution.[26] Then,

(20)

$$\Delta T_{avg} = \tau \mathcal{F}_o / (\rho c_p t)$$

where,

ρ = Density , gm/cm^3

c_p= Specific heat, Joules/gm-°C

t = Thickness of the faceplate, cm

τ = Time, sec

To demonstrate the relationships between *Eq. (18)*, *(19)*, and *(20)*, we can use an example. For our example, we will absorb 100 W/cm^2 on the first surface of a copper reflective mirror which has optical thin flims vapor deposited on the first surface. We will use four pair of quarter wave coatings. The run time will be for ten seconds. The diameter necessary to satisfy *Eq. (16)* for Copper will be 40.517cm.[1,2,3,4,9] The thickness to satisfy the semi-infinite plate boundary is, according to *Eq. (17)*, 20.258 cm. We will begin by using a high-low four pair stack of Al_2O_3 and ZnS for a wavelength of 2.7μm. The index for the ZnS will be 2.24 and for the Al_2O_3 will be 1.71.[39] From *Eq. (18)* we would find that the temperature rise of the first surface would be 92.15°C$_{\Delta T}$. And, of course, from *Eq. (19)* we would find that the temperature rise on the back surface would be zero. If the problem were linear, the average temperature of the faceplate would be 46.08°C$_{\Delta T}$. However, from *Eq. (20)* we find that the linear condition would require an average temperature of 16.37°C$_{\Delta T}$. In order to get to this part of the problem, however, we must first obtain the energy distribution in the optical thin films. The film coefficient for the mechanical bonding is 1.55 W/cm^2-°C for each interface. Consequently, for the pair N=1, the overall film coefficient will be 0.19375 W/cm^2 -°C. For the second pair, N=2, the film coefficient will be 0.25833 W/cm^2 -°C. For the third pair, N=3, the film coefficient will be 0.3875 W/cm^2 -°C. And, for the fourth pair, N=4, the film coefficient will be 0.775 W/cm^2 -°C. The distribution of energy in the coating pairs will follow from *Figure 1* So that, N=1 will absorb 35.83% of the total absorbed energy. N=2 will absorb 27.35% of the total absorbed energy. N=3 will absorb 20.88% of the total absorbed energy. And, N=4 will absorb 15.94% of the total amount absorbed. For the optical thin films the value of ($\alpha^\bullet_c$) will be 0.00698 cm^2/sec and the value of (K_c) will be 0.01698 W/cm-°C.[39] For Copper, the value of ($\alpha^\bullet_s$) will be 1.14 cm^2/sec. The

value of (K_c) will be 3.92 W/cm-°C.[39] We can evaluate the maximum temperature rise in the coating pairs as a function of the amount of energy that is absorbed at each interface. For example, in coating pair N=1, the temperature will not rise above 184.92°C because of the absorbed energy at the first pair interface. In other words, the steady state rise necessary to provide the absorbed energy sufficient gradient to drive the absorbed flux density to the substrate will be precisely that temperature differential. This does not include that total temperature rise that will occur in order to provide the temperature gradient necessaary to overcome the temperature build up of the other coating pairs and the substrate.

$$\Delta_T = \{F_0/h_c\}\,\psi_N \,/\, 2E_o \sum_{(m,n)=0}^{(m,n)} \left[\eta_0 \eta_L^{(m,n)} / \eta_H^{(m,n)+1}\right]$$

$$\Delta_T = 100\ (0.3583)\ /\ 0.19375$$

$$\Delta_T = 184.92\ °C$$

In like fashion, the other coating pairs have a temperature rise associated with the amount of flux density that can be stored and unloaded to the substrate under the steady state conditions. It is now possible to look at the temperature distribution in the substrate. We know what happens to the flux density in the coatings and how that absorbed flux density is accommodated. Our problem now is to evaluate the temperature rise in the substrate for the conditions where the semi infinite plate boundary is met and where it is not. We can look at the temperature gradient through a 17 cm thick optic, which pretty much fits the semi-infinfite plate condition, and determine if the average temperature accommodates the required flux density of 100 W/cm^2. We can use the Lazor™Code[40] to ease the calculations.

t_{cm}	ΔT
N=1	462.49
N=2	277.57
N=3	171.69
N=4	117.81
0	97.74
1.0	73.84
2.0	54.74
2.5	46.48
3.0	39.27
3.5	32.95
4.0	27.44
4.5	22.70
5.0	18.58
5.5	15.06
6.0	12.14
6.5	9.58
7.0	7.77
7.5	6.18
8.0	4.82
9.0	2.78
10.0	2.10
10.5	1.65
12.0	0.50
12.5	0.37
13.0	0.28
13.5	0.25
14.0	0.16
14.5	0.12
15.0	0.09

16.0	0.05
17.0	0.05
$\Sigma =$	477.69

then, 477.69/27 = 17.67°C and rearranging *Eq. (4)* we can evaluate the steady-state condition, so that,

$$\mathcal{F}_0 = (\rho\, c_p\, t)\, \tau^{-1}$$

where,

For Cu^{39} ρ = 8.96 g/cm^3; c_p = 0.38 Joules/gm-°C

τ = 10 sec; t = 17.0 cm

then, $\mathcal{F}_0 = 8.96\ \text{g/cm}^3 (0.38\ \text{W-sec/g-°C}) 17.0\text{cm} (17.67\text{°C}) / 10\text{sec}$

$\mathcal{F}_0 = 102.3\ \text{W/cm}^2$ vs $100\ \text{W/cm}^2$

It becomes clear, then, that we are dealing with a Gaussian Curve wherein we have made short straight lines between points. The problem, however, becomes somewhat more complex when the boundary condition of thickness is not satisfied, i.e., when the thickness does not satisfy *Eq. (17)*. As the faceplate becomes thinner, we have the front and back surfaces reinforcing one another in an ever increasing temperature rise with an ever decreasing gradient between the two faces. Again, one must keep in mind that the optic cannot lose any energy from the thermal mass. Based on this continuous reinforcement we have denominated this phenomena as a *Reverse Thermal Wave Approximation*. That is, as the temperature wave from the front surface travels to the back surface, it reverses and reinforces the temperature at the front. In like fashion, the back surface functions in much the same way. Consequently, the Gaussian Error Integrals become recursive in much the same way as the Fourier Series would be, with a similar result, it should be added. After the first few terms, the values become very small. The expression for the temperature rise on the first surface, using the *Reverse Thermal Wave Approximation* will follow from,[2]

(21)

$$\Delta T_1 = 2\mathcal{F}_0 (\alpha\tau)^{0.5} \{ \text{ierfc}(x) \} / K - 2\mathcal{F}_0 (\alpha\tau)^{0.5} \{ \text{ierfc}(y) \}$$
$$/ K \{ \text{erfc}(y) - \mathbf{exp}(t_o H_o + H_o^2 \alpha\tau)\, \text{erfc}(z) \}$$
$$+ 2\mathcal{F}_0 (\alpha\tau)^{0.5} \{ \text{ierfc}(y) \} / K + 2\mathcal{F}_0 (\alpha\tau)^{0.5} \{ \text{ierfc}(x) \}$$
$$/ K \{ \text{erfc}(y) - \mathbf{exp}(t_o H_o + H_o^2 \alpha\tau)\, \text{erfc}(z) \}$$

where,

$H_o = t_o^{-1}$, cm^{-1}; t_o = Thickness of faceplate, cm

$z = \{ t_o / 2(\alpha\tau)^{0.5} + H_o (\alpha\tau)^{0.5} \}$;

$y = t_o / 2(\alpha\tau)^{0.5}$

The temperature rise at any point below the first surface will follow from,

(22)

$$\Delta T_{\tau>0} = 2\mathcal{F}_0 (\alpha\tau)^{0.5} \{ \text{ierfc}(y) \} / K + 2\mathcal{F}_0 (\alpha\tau)^{0.5} \{ \text{ierfc}(x) \} / K$$
$$\times \{ \text{erfc}(y) - \mathbf{exp}(t_o H_o + H_o^2 \alpha\tau)\, \text{erfc}(z) \}$$

We can, then, use *Eq. (21)* and *(22)* in another example. In this case, we will use a Copper reflective optic faceplate that is only 5 cm thick. All the other conditions will remain the same.

t_{cm}	ΔT
N=1	489.13
N=2	304.21
N=3	198.33
N=4	144.45
0	123.88
0.25	101.02
0.75	89.32
1.00	83.87
1.25	78.68
1.75	69.08
2.00	64.67
2.25	60.46
2.75	52.79
3.00	49.30
3.25	46.03
3.75	40.06
4.00	37.47
4.25	35.02
4.75	30.59
5.00	28.60
	$\sum$ = 990.84

then, 990.84/16 = 61.93°C and rearranging *Eq. (20)* we can evaluate the steady-state condition, so that,

$$\mathcal{F}_0 = (\rho\, c_p\, t)\, \tau^{-1}$$

then, $\mathcal{F}_0 = 8.96\ g/cm^3 (0.38\ W\text{-}sec/g\text{-}°C)\ 5.0cm\ (61.93°C)\ /10\ sec$

$$\mathcal{F}_0 = 105.43\ W/cm^2 \quad vs\ 100\ W/cm^2$$

If we were to look at the steady-state solution with *Eq. (20)* just by itself, we would find that the required average temperature would be 58.74°C. And, if we were to evaluate the average temperature of the optical faceplate by taking the average of the front and back only, we would find that this average would be 76.24°C. For this regime, the average of the front and back, without calculating the segments in between, will always be greater than the value calculated from *Eq. (20)*.

Equations (21) and *(22)* will do service for both the semi-infinite plate model and when the thickness does not satisfy the boundary condition. The reason for the satisfying of both conditions is to be found in the transport element of the equations, i.e.,

$$\left\{ \text{erfc}(y) - \exp\left(t_o H_o + H_o^2\, \alpha\tau\right) \text{erfc}(z) \right\}$$

$Ho = t^{-1},\ cm^{-1}$

When, for example, $t_o \geq 6\,(\alpha\tau)^{0.5}$ the value of erfc(y) and erfc(z) will be zero. We may say, then, that when the average temperature rise of the faceplate, based on the temperatures evaluated from *Eqs. (21)* and *(22)* are greater that the average temperature rise required by *Eq. (20)* that *Eqs. (21)* and *(22)* are valid for this regime. If we describe the average temperature from *Eq. (20)* as $\Delta T_{\lambda 1}$ and the average from *Eqs. (21)* and *(22)* as $\Delta T_{\lambda 2}$, then, the regime of use for these equations will follow,

$$\Psi = 1 \text{ when } \Delta T_{\lambda 2} \geq \Delta T_{\lambda 1}$$

The reason for setting this regime will become clear as we do yet a third example. As the faceplate becomes substantially thinner than the thickness required by *Eq. (20)* the temperature of the two surfaces of the faceplate become very close to the same value. If we take our Copper example, again, except we now make the faceplate 2.0 cm thick, we will have the same absorbed value and the same run time. From *Eq. (20)* the required temperature rise is 146.854°C, i.e.,

$$\Delta T_{avg} = 100\ W/cm^2\ (10\ sec) / \{ 8.96\ g/cm^3 (0.38\ W\text{-}sec/g\text{-}°C)\ 2.0\ cm \}$$

We find from *Eqs. (21)* and *(22)* the average temperature will only be 134.08°C. This is a lower prediction than what is required by *Eq. (20)*. That is, the equations predict a first surface temperature rise of 170.48°C and a second surface temperature rise of 97.24°C. In this regime, the average temperature of the faceplate $\Delta T_{\lambda 2}$ is lower than $\Delta T_{\lambda 1}$. For this regime, then, we would want to say that $\Psi = \Delta T_{\lambda 1}/\Delta T_{\lambda 2}$. And, we must modify *Eqs. (21)* and *(22)*, so that,

$$\Psi = \Delta T_{\lambda 1}/\Delta T_{\lambda 2} = 146.854°C\ /\ 134.08°C; \quad \Psi = 1.10 \qquad (23)$$

$$\Delta T_1 = 2 F_0 (\alpha\tau)^{0.5} \Psi \{ ierfc(x) \}/K - 2 F_0 (\alpha\tau)^{0.5} \Psi \{ ierfc(y) \}/K$$
$$\propto \{ erfc(y) - \exp(t_o H_o + H_o^2 \alpha\tau)\ erfc(z) \} + 2 F_0 (\alpha\tau)^{0.5} \Psi$$
$$\propto \{ ierfc(y) \}/K + 2 F_0 (\alpha\tau)^{0.5} \Psi \{ ierfc(x) \}/K \{ erfc(y)$$
$$- \exp(t_o H_o + H_o^2 \alpha\tau)\ erfc(z) \}$$

And for the second surface, the temperature rise will be,

$$\Delta T_{t>0} = 2 F_0 (\alpha\tau)^{0.5} \Psi \{ ierfc(y) \}/K + 2 F_0 (\alpha\tau)^{0.5}\ \Psi \{ ierfc(x) \} \qquad (24)$$
$$/ K \{ erfc(y) - \exp(t_o H_o + H_o^2 \alpha\tau)\ erfc(z) \}$$

When we use *Eqs. (23)* and *(24)* for the example of a 2.0 cm thick Copper faceplate, we find that the correct temperature for the first surface will be 187.86°C vs 170.78°C and the second surface temperature rise will be 101.55°C vs 97.37°C. The corrected temperatures will provide an average value in concert with *Eq. (20)*, i.e., 146.85°C. The temperature rise of coating pair N=1 will be 553.11°C. The temperature rise of coating pair N=2 will be 368.19°C. The temperature rise of coating pair N=3 will be 262. 31°C. The temperature rise of coating pair N=4 will be 208.43°C. In the same vein, if we were to use a 1.0 cm thick faceplate, the required average temperature rise would be 293.05°C and the initial calculation from *Eqs. (21)* and *(22)* would be 190.55°C and 154.907°C respectively, which would provide an average temperature of 172.73. The value of (Ψ) would be 1.70. Using *Eqs. (23)* and *(24)*, the corrected temperatures would be 325.46°C and 264.58°C respectively. The temperature rise of coating pair N=1 will be 690.71°C. The temperature rise of coating pair N=2 will be 505.79°C. The temperature rise of coating pair N=3 will be 399.90°C. The temperature rise of coating pair N=4 will be 346.03°C. The immediate question that comes to mind, of course, is, where is the break between the two regimes? The answer appears to be approximately when,

$$t_o \leq 0.6 (\alpha\tau)^{0.5} \qquad (25)$$

That is, the break point appears to be when the thickness is approximately 10% of the required thickness to fulfill the semi-infinite plate boundary condition. We can say, then, that the regimes are bounded as follows,

Regime III

$$0 < t_o \leq 0.6\,(\alpha\tau)^{0.5} \qquad \Psi > 1 \quad \textit{Eqs. (23)} \text{ and } \textit{(24)} \qquad \textit{(26)}$$

Regime II

$$0.6\,(\alpha\tau)^{0.5} < t_o < 0.6\,(\alpha\tau)^{0.5} \qquad \Psi \leq 1 \quad \textit{Eqs. (21)} \text{ and } \textit{(22)} \qquad \textit{(27)}$$

Regime I

$$t_o \geq 0.6\,(\alpha\tau)^{0.5} \qquad \Psi \leq 1 \quad \textit{Eqs. (18)} \text{ and } \textit{(19)} \qquad \textit{(28)}$$

Reverse Thermal Wave - Three Dimensional Continuous Wave

The problem becomes somewhat more complex when we treat with the problem in three dimension. There is a limitation in both the axial direction and in the radial component. In the one dimensional boundary condition, there was no radial component one had to accommodate. With the introduction of the radial component, the criteria for the laser beam diameter necessary to constitute a one dimensional condition is defined as,

$$\mathbf{D} \geq 12\,(\alpha\tau)^{0.5} \qquad \textit{(29)}$$

For this condition, the problem is one dimensional. When the laser beam diameter (**D**) on the optical surface is equal to, or greater than the value shown in *Eq. (29)* the problem is one dimensional and amenable to the equations described above. However, when,[1,2]

$$\mathbf{D} < 12\,(\alpha\tau)^{0.5} \qquad \textit{(30)}$$

the problem is now three dimensional. We will begin with the first regime wherein the boundary conditions for the semi-infinite plate model are maintained. For the case of the optical thin films, the thermal diffusivity is so poor that one dimensional case is reached very early on. The temperature rise on the first surface of the faceplate follows from,[1,2,3,4,5,6,7,8,9]

$$\Delta T_1 = 2\mathbf{F_o}\,(\alpha\tau)^{0.5} \left\{ \left(\text{ierfc}(x)\right) - \left(\text{ierfc}(x_1)\right) \right\} / K \qquad \textit{(31)}$$

where,

$x_1 = R / 2(\alpha\tau)^{0.5}$; R = Radius of the laser beam, cm

In similar fashion, the temperature rise at some depth into the faceplate will follow from,[1,2,3,4,5,6,7,8,9]

$$\Delta T_{t>0} = 2\mathbf{F_o}\,(\alpha\tau)^{0.5} \left\{ \left(\text{ierfc}(y)\right) - \left(\text{ierfc}(y_1)\right) \right\} / K \qquad \textit{(32)}$$

where,

$$y_1 = \left(t^2 + R^2\right)^{0.5} / 2(\alpha\tau)^{0.5}$$

We can carry on the examples that we have provided before. However, the problem becomes a little more convoluted with the introduction of the radial component of diffusion. In any case, we will maintain the same boundary conditions as before except that we will provide a laser beam radius of 6.0 cm on the reflective optic. From *Eq. (29)* we know that for a ten second run time

the laser beam needs to be equal to, or greater than, 40.5 cm. So, we know that a 12.0 cm diameter beam is completely within the three dimensional condition.

t_{cm}	ΔT
N=1	456.460
N=2	265.540
N=3	159.660
N=4	105.780
0	85.210
0.5	73.020
1.0	62.160
1.5	52.540
2.0	44.110
2.5	36.690
3.0	30.260
3.5	25.040
4.0	20.410
4.5	16.570
5.0	13.310
5.5	10.620
6.0	8.480
6.5	6.850
7.0	5.370
7.5	4.240
8.0	3.210
8.5	2.270
9.0	1.800
9.5	1.340
10.0	1.070
10.5	1.000
11.0	0.605
11.5	0.450
12.0	0.298
12.5	0.240
13.0	0.191
13.5	0.186
14.0	0.124
	Σ = 507.664

then, 507.664/29 = 17.506°C and rearranging *Eq. (20)* we can evaluate the steady-state condition, so that,

$$F_0 = (\rho\, c_p\, t)\, \tau^{-1}$$

then, F_0 = 8.96 g/cm^3(0.38 W-sec/g-°C) 14 cm (17.506°C) /10 sec

$$F_0 = 83.444 \text{ W/cm}^2 \text{ vs } 100 \text{ W/cm}^2$$

Clearly, we can see from the calculation that we are missing some flux density. We can evaluate the amount of flux density that is being taken out in the radial component by either of two methods which we will describe. In the first method we would use the technique suggested by Carslaw and Jaeger.[3] A condition for the use of the following equations, however, is the requirement that the ΔT be of a constant value. In our case the temperature is constantly changing until the laser is turned off, or steady-state heat transfer is achieved. In order to use this technique, we have found that following the Gaussian nature of the temperature rise we can use the 50% point of the Gaussian form to evaluate the temperature change from τ=0 to τ>0. That is, we use $\Delta T \times \ln(2)$ for our

constant temperature source. For this case, they suggest that the amount of flux density may be evaluated from,

(33)

$$\mathcal{F}_o = \left\{ \ln(2)\ \Delta T\ K/R \right\} \left\{ (\pi\zeta)^{-0.5} + 0.50 - 0.25(\zeta/\pi)^{0.5} + 0.125\ \zeta \right\}$$

where,

$$\zeta = (\alpha t) / R^2$$

Doing the arithmetic from *Eq. (33)* we find that the value for the W/cm^2 escaping into the radial component will be 11.6 W/cm^2. Adding this to the amount we found from the temperature gradient, we see that 83.444 + 11.6 = 95.04 W/cm^2. This is somewhat close agreement with the W/cm^2 that are required.

We can look for the missing flux density, as before, using the work of Kern and Kraus.[41] The values for the temperatures for a radial fin are found from,

(34)

$$\Delta T_{20} = \Delta T_{10} \left\{ I_o(mR_e)\ K_1(mR) + K_o(mR_e)\ I_1(mR) \right.$$

$$\left. / \ I_o(mR_o)\ K_1(mR_e) + I_1(mR_e)\ K_o(mR_o) \right\}$$

where,

R_o = The laser beam radius, cm; R_e = Radius of fin, cm

$m = (2h_c/Kt)^{0.5} = 0.378\ cm^{-1}$ $h_c = K/(R_e - R_o)$; W/cm^2-°C

I_1, K_1, I_o, K_o = Bessel Functions; R = Radius-cm, $R_o < R <= R_e$

t = faceplate thickness, 14 cm

For our problem we will use a fin height of 1.0 cm. R_o will be 6.0cm and R_e will be 7.0cm. When one does the rough calculation,

$$\Delta T_{20} = .9298(\Delta T_{10}).$$

So, then, the average temperature along the 1.0 cm fin will be $\left\{ .9298\ (\Delta T_{10}) + 17.506 \right\} / 2$ which will provide a value of 16.892°C$_{\Delta T}$. Then, using the same technique as before, we can evaluate the steady-state absorption in the fin, so that,

$$\mathcal{F}_o = (\rho\ c_p\ t)\ \tau^{-1}$$

then, $\mathcal{F}_o = 8.96\ g/cm^3 (0.38\ W\text{-}sec/g\text{-}°C)\ 1.0\ cm\ (16.892°C_{\Delta T}) / 10\ sec$

$$\mathcal{F}_o = 5.75\ W/cm^2$$

and adding the two values together we find 83.444 + 5.75 = 89.20 W/cm^2 which does not provide a very good agreement with the escaping flux density. Again, this is the steady-state value if the temperature of the cylinder were uniform and constant

If, however, we were to use another technique suggested by Kern and Kraus for the steady-state flux density removed by the fin we would use the following,

(35)

$$\mathcal{F}_o = K\ m\ \Delta T\ \eta \left\{ I_o(mR_e)\ K_1(mR_o) - K_1(mR_e)\ I_1(mR_o) \right.$$

$$\left. / \ I_o(mR_o)\ K_1(mR_e) + I_1(mR_e)\ K_o(mR_o) \right\}$$

where,

$$\eta = \left\{ 2\pi R_o t K m \Delta T \right\} / \left\{ 2\pi (R_e^2 - R_o^2) h_c \Delta T \right\}$$

For our problem, then, η = 2.442 from the Lazor™Code.[40] After doing the calculation we find that F_O = 24.87 W/cm^2. Again using the Gaussian 50% point, F_O = 16.34 W/cm^2. If we add the two values together, 83.444 + 16.34 = 99.78 W/cm^2. This is much better agreement.

At this point, we also need to look at the radial temperature distribution as a function of the laser run time. Carslaw and Jaeger[3] have provided a technique for evaluating the radial temperature distribution. Again, however, the technique has the boundary condition that temperature is constant. The radial temperature distribution then is found from,

(36)

$$\Delta T_R = \left\{ \Delta T (R_o / R_e)^{0.5} \operatorname{erfc}(z) + \left\{ \Delta T (z) (\alpha\tau)^{0.5} / (4 R_o^{0.5} R_e^{1.5}) \right\} \operatorname{ierfc}(z) \right.$$
$$\left. + \Delta T \left\{ (9 R_o^2 - 2 (R_o R_e) - 7 R_e^2)(\alpha\tau) / (32 R_o^{1.5} R_e^{2.5}) \right\} i^2 \operatorname{erfc}(z) \right\} \ln(2)$$

where,

$$z = (R_e - R_o) / 2 (\alpha\tau)^{0.5}$$

Based on *Eq. (36)* we would find the temperature at the tip of the fin, i.e., R_e will be 7.0 cm, will equal 9.426°C$_{\Delta T}$ at the end of a ten second run.

This would appear to be in reasonable agreement with the input flux density. We now shift our attention to the condition of Regime II. Again, this is the case where the thickness is less than the semi-infinite plate model requires and greater than 10% of that value. For this Regime, in the three dimensional case, we can evaluate the temperature rise of the first surface from,

(37)

$$\Delta T_1 = 2 F_O (\alpha\tau)^{0.5} \left\{ (\operatorname{ierfc}(x)) - (\operatorname{ierfc}(x_1)) \right\} / K - 2 F_O (\alpha\tau)^{0.5} \left\{ (\operatorname{ierfc}(y)) - (\operatorname{ierfc}(y_1)) \right\}$$
$$/ K \left\{ \operatorname{erfc}(y) - \exp(t_O H_O + H_O^2 \alpha\tau) \operatorname{erfc}(z) \right\} + 2 F_O (\alpha\tau)^{0.5} \left\{ (\operatorname{ierfc}(y)) - (\operatorname{ierfc}(y_1)) \right\}$$
$$/ K + 2 F_O (\alpha\tau)^{0.5} \left\{ (\operatorname{ierfc}(x)) - (\operatorname{ierfc}(x_1)) \right\} / K$$
$$\times \left\{ \operatorname{erfc}(y) - \exp(t_O H_O + H_O^2 \alpha\tau) \operatorname{erfc}(z) \right\}$$

The temperature rise at some depth into the faceplate follows from,

(38)

$$\Delta T_{\tau>0} = 2 F_O (\alpha\tau)^{0.5} \left\{ (\operatorname{ierfc}(y)) - (\operatorname{ierfc}(y_1)) \right\} / K$$
$$+ 2 F_O (\alpha\tau)^{0.5} \left\{ (\operatorname{ierfc}(x)) - (\operatorname{ierfc}(x_1)) \right\} / K$$
$$\times \left\{ \operatorname{erfc}(y) - \exp(t_O H_O + H_O^2 \alpha\tau) \operatorname{erfc}(z) \right\}$$

The next example will use a 5.0 cm thick Copper substrate. We will use a 3.0 cm radius to alter the problem in order to compare the impact of a 6.0 cm and 3.0 cm laser beam radius. Of course, we are still absorbing 100 W/cm^2 on the first surface of the Copper faceplate that is coated with the optical thin films. Using *Eqs. (37)* and *(38)* we find the temperature of the front and back

surface to be 68.90°$C_{\Delta T}$ and 11.52°$C_{\Delta T}$ respectively. We can, then, calculate the temperature gradient through the 5.0 cm thick Copper faceplate and determine the average temperature, so that,

t_{cm}	ΔT
N=1	434.160
N=2	249.240
N=3	143.360
N=4	89.480
0	68.900
0.5	52.300
1.0	42.720
1.5	35.020
2.0	28.910
2.5	24.080
3.0	20.210
3.5	17.210
4.0	14.870
4.5	13.050
5.0	11.520
	$\sum$ = 328.790

then, 328.790/11 = 29.89°C and rearranging *Eq. (20)* we can evaluate the steady-state condition, so that,

$$F_0 = (\rho\, c_p\, t)\, \tau^{-1}$$

then, F_0 = 8.96 g/cm^3 (0.38 W-sec/g-°C) 5.0 cm (29.89 °C) / 10sec

F_0 = 50.884 W/cm^2 vs 100 W/cm^2

Going back to the Kern and Kraus technique, we can use the fin analysis to evaluate the steady-state condition,

where,

R_0 = The laser beam radius, cm; R_e = Radius of fin, cm

$m = (2h_C/Kt)^{0.5}$ = 0.6324 cm^{-1} $h_C = K/(R_e - R_0)$; W/cm^2-°C

I_1, K_1, I_0, K_0 = Bessel Functions; R = Radius-cm, $R_0 < R < = R_e$

t = faceplate thickness, 5.0 cm

Again we will use a fin height of 1.0 cm. R_0 will be 3.0 cm and R_e will be 4.0 cm. When one does the rough calculation,

$$\Delta T_{20} = .8406(\Delta T_{10}).$$

After doing the calculation from *Eq. (35)* we find that F_0 = 64.28 W/cm^2. Again using the Gaussian 50% point, F_0 = 42.23 W/cm^2. If we add the two values together, 50.884 + 42.23 = 93.114 W/cm^2. We will now do the same example except with a 6.0 cm laser beam radius to see that the technique tracks, then,

t_{cm}	ΔT
N=1	471.040
N=2	286.120
N=3	180.240
N=4	126.360
0	105.790
0.5	81.790
1.0	70.930
1.5	61.310
2.0	52.880
2.5	45.460
3.0	39.020
3.5	33.810
4.0	29.180
4.5	25.330
5.0	22.080
	$\sum$ = 567.580

then, 567.580/11 = 51.598°C and rearranging *Eq. (20)* we can evaluate the steady-state condition, so that,

$$\mathcal{F}_o = (\rho\, c_p\, t)\, \tau^{-1}$$

then, $\mathcal{F}_o$ = 8.96 g/cm^3 (0.38 W-sec/g-°C) 5.0 cm (51.598 °C) / 10sec

$$\mathcal{F}_o = 87.84 \text{ W/cm}^2 \text{ vs } 100 \text{ W/cm}^2$$

Going back to the Kern and Kraus technique, we can use the fin analysis to evaluate the steady-state condition, where,

R_o = The laser beam radius, 6.0 cm; R_e = Radius of fin, 7.0 cm

$m = (2h_c/Kt)^{0.5} = 0.6324 \text{ cm}^{-1}$ $h_c = K/(R_e - R_o)$; W/cm^2 -°C

I_1, K_1, I_o, K_o = Bessel Functions; R = Radius-cm, $R_o < R < = R_e$

t = faceplate thickness, 5.0 cm

$$\mathcal{F}_o = K\, m\, \Delta T\, \eta \left\{ I_o(mR_e)\, K_1(mR_o) - K_1(mR_e)\, I_1(mR_o) \right.$$

$$\left. / I_o(mR_o)\, K_1(mR_e) + I_1(mR_e)\, K_o(mR_o) \right\}$$

where,

$$\eta = \left\{ 2\pi\, R_o\, t\, K\, m\, \Delta T \right\} / \left\{ 2\pi\, (R_e^2 - R_o^2)\, h_c\, \Delta T \right\}$$

for our problem, then, η = 1.459 from the **Lazor™Code.**[40] After doing the calculation we find that $\mathcal{F}_o$ = 112.9 W/cm^2. Again using the Gaussian 50% point, $\mathcal{F}_o$ = 78.3 W/cm^2. If we add the two values together, 87.84 + 78.3 = 166.1 W/cm^2. This is hardly good agreement. However, if we use *Eq. (34)*

$$\Delta T_{20} = \Delta T_{10} \left\{ I_o(mR_e)\, K_1(mR) + K_o(mR_e)\, I_1(mR) \right.$$

$$\left. / I_o(mR_o)\, K_1(mR_e) + I_1(mR_e)\, K_o(mR_o) \right\}$$

For our problem we have a fin height of 1.0 cm. R_o will be 6.0 cm and R_e will be 7.0 cm. When one does the rough calculation,

$$\Delta T_{20} = .8211\ (\Delta T_{10})\ \ln(2)$$

$$\Delta T_{20} = 29.38°C$$

then,

$$\mathcal{F}_0 = 8.96\ g/cm^3 (0.38\ W\text{-}sec/g\text{-}°C)\ 1.0\ cm\ (29.38°C)\ /10\ sec$$

$$\mathcal{F}_0 = 10.01\ W/cm^2$$

If we add the two values together, 87.84 + 10.01 = 97.85 W/cm^2. This is a much better agreement. However, we can check the output with *Eq. (33)* for the transient condition,

$$\mathcal{F}_0 = \left\{ \ln(2)\ \Delta T\ K/R \right\} \left\{ (\pi\ \zeta)^{-0.5} + 0.50 - 0.25(\zeta/\pi)^{0.5} + 0.125\ \zeta \right\}$$

Again, we see that the equation slightly over predicts the flux density, that is 87.84 + 18.15 = 105.99. If we use *Eq. (36)* for the temperature at the tip of the fin at the end of a ten second run, we find,

$$\Delta T_R = \left\{ \Delta T\ (R_0 / R_e)^{0.5}\ \text{erfc}(z) + \left\{ \Delta T\ (z)\ (\alpha\tau)^{0.5} / (4\ R_0^{0.5}\ R_e^{1.5}) \right\} \right.$$

$$\times\ \text{ierfc}(z) + \Delta T \left\{ (9\ R_0^2 - 2\ (R_0\ R_e) - 7\ R_e^2)\ (\alpha\tau) \right.$$

$$\left. \left. / (32\ R_0^{1.5}\ R_e^{2.5}) \right\}\ i^2\text{erfc}(z) \right\} \ln(2)$$

$$\Delta T_R = 27.814\ °C$$

The average temperature between the root and the tip will be (51.616 + 27.814)/2 = 39.715. Using our steady state solution again from *Eq. (20)* we find,

$$\mathcal{F}_0 = 8.96\ g/cm^3 (0.38\ W\text{-}sec/g\text{-}°C)\ 1.0\ cm\ (39.715°C)\ /10\ sec$$

$$\mathcal{F}_0 = 13.522\ W/cm^2$$

If we add the two values together, 87.84 + 13.522 = 101.36 W/cm^2. This is a better agreement. What we find between the two techniques is that the further away from the steady-state condition we find ourselves, one technique works better than the other. Obviously, with the larger the diameter approaching the one dimensional case the averaging of the fin-base technique is better. This is demonstrated because of the higher base temperature that permits a closer evaluation to the ultimate steady-state fin tip temperature. In the case of the smaller diameter, the flux density technique is more valuable because it is further from the steady-state fin tip temperature. Because of this seeming anomaly we wanted to provide the reader with the alternative approaches for finding the enthaply balance of Watts in and Watts out. There is yet a third way of evaluating the W/cm^2 that are going into the radial component. Using Lazor™Code[40], we can evaluate the average temperature of the faceplate beyond the laser beam after a given run time. The temperature rise will be zero at a distance described by,

$$R_2 = 6\ (\alpha\ \tau)^{0.5} + R_1 \qquad (39)$$

Using a half centimeter increment in depth and a half centimeter increment in the radial component we calculated the temperature gradient out to a radius of 21 cm (see *Figure 2*) . The Lazor™Code[40] uses *Eq. (36)* to calculate the radial temperature distribution. Using *Eq. (36),*

$$\Delta T_R = \left\{ \Delta T \left(R_o / R_e\right)^{0.5} \text{erfc}(z) + \left\{ \Delta T\,(z)\,(\alpha\tau)^{0.5} / \left(4\, R_o^{0.5}\, R_e^{1.5}\right) \right\} \text{ ierfc}(z) \right.$$

$$\left. + \Delta T \left\{ \left(9\, R_o^2 - 2\,(R_o\, R_e) - 7\, R_e^2\right)(\alpha\tau) / \left(32\, R_o^{1.5}\, R_e^{2.5}\right) \right\} \text{ i}^2\text{erfc}(z) \right\} \ln(2)$$

This matrix provided a value of 2910.503 / 341 = 8.535°C average Δt for the radial component. From *Eq. (20)* then, we can calculate the W/cm^2 that are going into the radial component, so that,

$$\mathcal{F}_o = (\rho\, c_p\, t)\, \tau^{-1}$$

then, $\mathcal{F}_o = 8.96$ g/cm^3 (0.38 W-sec/g-°C) 5.0 cm (8.535 °C) / 10sec

$$\mathcal{F}_o = 14.53 \text{ W/cm}^2$$

We add the two together, (87.84 + 14.53) = 102.40 W/cm^2. This provides a reasonable agreement with the required 100 W/cm^2.

The third regime for the three dimensional problem is much like the one dimensional model. In this regime, we must first calculate the values of (Ψ). This calculation is completed using *Eqs. (20), (21),* and *(22)* which is the one dimensional case provided above. Using our former example, 100 W/cm^2 will be absorbed on the first surface of a 2.0 cm thick copper faceplate coated with a a four pair stack of quarter wave optical thin films. From *Eq. (20)* we can find the required steady-state average temperature, so that,

$$\Delta T_{avg} = \tau\, \mathcal{F}_o / (\rho\, c_p\, t)$$

$$\Delta T_{avg} = 100 \text{ W/cm}^2 (10 \text{ sec}) / \left\{ 8.96 \text{ g/cm}^3 (0.38 \text{ W-sec/g-°C})\, 2.0 \right\}$$

$$\Delta T_{avg} = 146.85°\text{C}$$

And from *Eq. (21),* we find the temperature rise of the first surface for the one dimensional case,

$$\Delta T_1 = 2\,\mathcal{F}_o\,(\alpha\tau)^{0.5} \left\{ \text{ierfc}(x) \right\} / K - 2\,\mathcal{F}_o\,(\alpha\tau)^{0.5} \left\{ \text{ierfc}(y) \right\} / K$$

$$\times \left\{ \text{erfc}(y) - \exp\left(t_o\, H_o + H_o^2\, \alpha\tau\right) \text{erfc}(z) \right\} + 2\,\mathcal{F}_o\,(\alpha\tau)^{0.5}$$

$$\times \left\{ \text{ierfc}(y) \right\} / K + 2\,\mathcal{F}_o\,(\alpha\tau)^{0.5} \left\{ \text{ierfc}(x) \right\} / K \left\{ \text{erfc}(y) \right.$$

$$\left. - \exp\left(t_o\, H_o + H_o^2\, \alpha\tau\right) \text{erfc}(z) \right\}$$

$$\Delta T_1 = 170.48°\text{C}$$

The temperature rise of the second surface for the one dimensional case comes from *Eq. (22),* so that,

$$\Delta T_2 = 2\,\mathcal{F}_o\,(\alpha\tau)^{0.5} \left\{ \text{ierfc}(y) \right\} / K + 2\,\mathcal{F}_o\,(\alpha\tau)^{0.5} \left\{ \text{ierfc}(x) \right\}$$

$$/ K \left\{ \text{erfc}(y) - \exp\left(t_o\, H_o + H_o^2\, \alpha\tau\right) \text{erfc}(z) \right\}$$

$\Delta T_2 = 97.25°C$

$\Delta T_{\lambda 2} = 133.865°C$; $\Delta T_{\lambda 1} = 146.85°C$; $\Psi = 1.097$

At this point, we now calculate the temperature rise of the faceplate with a 6.0 cm laser beam diameter, in the three dimensional model, so that, from *Eq. (37)* the temperature rise will follow from,

(40)

$$\Delta T_1 = 2\mathcal{F}_o (\alpha\tau)^{0.5} \Psi \left\{ (\text{ierfc}(x)) - (\text{ierfc}(x_1)) \right\}/K - 2\mathcal{F}_o (\alpha\tau)^{0.5} \Psi$$
$$\times \left\{ (\text{ierfc}(y)) - (\text{ierfc}(y_1)) \right\}/K \left\{ \text{erfc}(y) - \exp(t_o H_o + H_o^2 \alpha\tau) \text{ erfc}(z) \right\}$$
$$+ 2\mathcal{F}_o (\alpha\tau)^{0.5} \Psi \left\{ (\text{ierfc}(y)) - (\text{ierfc}(y_1)) \right\}/K + 2\mathcal{F}_o (\alpha\tau)^{0.5} \Psi \left\{ (\text{ierfc}(x)) \right.$$
$$\left. - (\text{ierfc}(x_1)) \right\}/K \left\{ \text{erfc}(y) - \exp(t_o H_o + H_o^2 \alpha\tau) \text{ erfc}(z) \right\}$$

$\Delta T_1 = 162.15°C$

The second surface temperature rise for the 6.0 cm laser beam diameter in the three dimensional model will follow from,

(41)

$$\Delta T_2 = 2\mathcal{F}_o (\alpha\tau)^{0.5} \Psi \left\{ (\text{ierfc}(y)) - (\text{ierfc}(y_1)) \right\}/K$$
$$+ 2\mathcal{F}_o (\alpha\tau)^{0.5} \Psi \left\{ (\text{ierfc}(x)) - (\text{ierfc}(x_1)) \right\}/K$$
$$\times \left\{ \text{erfc}(y) - \exp(t_o H_o + H_o^2 \alpha\tau) \text{ erfc}(z) \right\}$$

$\Delta T_2 = 89.69°C$

The average temperature will be $\Delta T_{10} = 125.92°C$. And from *Eq.(20)*

$$\mathcal{F}_o = (\rho\, c_p\, t)\, \tau^{-1}$$

then, $\mathcal{F}_o = 8.96\ g/cm^3\ (0.38\ W\text{-}sec/g\text{-}°C)\ 2.0\ cm\ (125.92°C)\ /10\ sec$

$\mathcal{F}_o = 85.75\ W/cm^2$

The temperature rise in coating pair N=1 will be 527.40 °C. The temperature rise in coating pair N= 2 will be 342.48 °C. The temperature rise in coating pair N=3 will be 236.60 °C. The temperature rise in coating pair N=4 will be 182.72 °C. We can look for the missing flux density as before. Using *Eq.(33)* again,

$$\mathcal{F}_o = \left\{ \ln(2)\ \Delta T\ K/R \right\} \left\{ (\pi\zeta)^{-0.5} + 0.50 - 0.25(\zeta/\pi)^{0.5} + 0.125\ \zeta \right\}$$

and $\mathcal{F}_o = 83.41\ W/cm^2$.

Adding the two together (85.75 + 83.41) = 160.10 W/cm^2. This is not reasonable agreement for the approximation. Again, we find that this expression over predicts the flux density that exits to the radial component. Fundamentally, what we see, then, is that the steady temperature expressions do not provide as close an approximation as one would like. However, using the ***Lazor™Code***[40] we can do a course nodal temperature distribution through the radial component out to the point where the temperature increase is equal to zero. The ***Lazor™Code***[40] uses *Eq. (36)* for evaluating the temperature distribution.

$$\Delta T_R = \left\{ \Delta T (R_o / R_e)^{0.5} \, \mathrm{erfc}(z) + \left\{ \Delta T (z) (\alpha\tau)^{0.5} \right.\right.$$

$$\left. / \left(4 R_o^{0.5} R_e^{1.5}\right) \right\} \, \mathrm{ierfc}(z) + \Delta T \left\{ \left(9 R_o^2 - 2 (R_o R_e) - 7 R_e^2\right) \right.$$

$$\left. \left. \times (\alpha\tau) / \left(32 R_o^{1.5} R_e^{2.5}\right) \right\} i^2 \, \mathrm{erfc}(z) \right\} \ln(2)$$

The temperature increase is zero when,

$$R_2 = 6 (\alpha \tau)^{0.5} + R_1$$

Using a half centimeter increment in depth and a half centimeter increment in the radial component, we calculated the temperature gradient out to a radius of 21 cm (see *Figure 3*). This matrix provided a value of 2984.638 / 155 = 19.256 °C average ΔT for the radial component. Using *Equation (20)* we find,

$$F_o = (\rho \, c_p \, t) \, \tau^{-1}$$

then, $F_o = 8.96$ g/cm^3 (0.38 W-sec/g-°C) 2.0 cm (19.256°C) / 10 sec

$$F_o = 13.1123 \text{ W/cm}^2$$

Adding (85.75 + 13.1123) = 98.86 W/cm^2 which is very close to the 100 W/cm^2 that we are looking for. What we find, then, is that we can describe the temperature rise of an optical faceplate that is not in concert with the semi-infinite plate model. The above models square with the steady-state requirements and these approximations will provide a first order analysis to evaluate the temperature rise through thin optical faceplates. They may also be used to check numerical codes for accuracy of modeling. We can define the three regimes for the three dimensional case, then, so that,

Regime III

$$0 < t_o \leq 0.6 (\alpha\tau)^{0.5} \qquad \Psi > 1 \text{ } \textit{Eqs. (40)} \text{ and } \textit{(41)} \qquad \textit{(42)}$$

Regime II

$$0.6 (\alpha\tau)^{0.5} < t_o < 6 (\alpha\tau)^{0.5} \qquad \Psi \leq 1 \text{ } \textit{Eqs. (37)} \text{ and } \textit{(38)} \qquad \textit{(43)}$$

Regime I

$$t_o \geq 6 (\alpha\tau)^{0.5} \qquad \Psi \leq 1 \text{ } \textit{Eqs. (31)} \text{ and } \textit{(32)} \qquad \textit{(44)}$$

References

1. J. R. Palmer, "Reverse Thermal Wave Approximation For Temperature Transients In Uncoated Reflective Optics For High Power Continuous Wave Lasers," *Optical Engineering* (to be published).

2. J.R. Palmer, "Transient Temperature Distribution In Multi-Component Optical Faceplate Using Reverse Thermal Wave Approximations: High Power Repetitive Pulsed Lasers," *Optical Engineering* (to be published in 1987-88).

3. H.S. Carslaw, and J.C. Jaeger, *Conduction of Heat In Solids*, 2nd ed.,Oxford University Press, Oxford, England, 1978.

4. J. Crank, *The Mathematics Of Diffusion*, 2nd ed., Oxford University Press, Oxford, England, 1983.

5 E. L. Cussler, *Diffusion: Mass Transfer In Fluid Systems*, Cambridge University Press, London, England, 1984.

6. H.J.V. Tyrrell, and K.R. Harris, *Diffusion In Liquids: A Theoretical And Experimental Study*, Butterworths, London, England, 1984.

7. J.R. Palmer, "Theoretical Model For Determining Temperature Transients In Multilayer Optical Thin Films Subjected To High Power Continuous Wave And Repetitive Pulsed Lasers: Part I- Continuous Wave," *Proc. 3rd. Int. Symp. On Optical And Optoelectronic Applied Science And Engineering*, SPIE Vol. No. 655,656, Innsbruck, Austria, April, 1986.

8. J.R. Palmer, "Theoretical Model For Determining Temperature Transients In Multilayer Optical Thin Films Subjected To High Power Continuous Wave And Repetitive Pulsed Lasers: Part II- Repetitive Pulsed," *Proc. 3rd Int. Symp. On Optical And Optoelectronic Applied Science And Engineering*, SPIE Vol. No. 655,656, Innsbruck, Austria, April, 1986.

9. J.R. Palmer "Loss Of Infrared Optical System MTF Resulting From Damage Caused By High Power Continuous Wave And Low Average Power Repetitive Pulsed Visible - UV Lasers," *4th Int'l Symp. On Optical And Optoelectronic Applied Science And Engineering* SPIE No. 806, The Hauge, The Netherlands, April, 1987.

10. J.R. Palmer "Optical Distortion Of Multilayer Coated Optical Components Used In HIgh Power Laser Systems," *4th Int'l Symp. On Optical And Optoelectronic Applied Science And Engineering* SPIE No. 805, The Hauge, The Netherlands, April, 1987.

11. J.R. Palmer "Optical Distortion Of Rugate Coated Optical Components Used In HIgh Power Laser Systems," *4th Int'l Symp. On Optical And Optoelectronic Applied Science And Engineering* SPIE No. 805, The Hauge, The Netherlands, April, 1987.

12. H.K. Pulker, "Stress, Adherence, Hardness, And Density Of Optical Thin Films," *Optical Thin Films*, SPIE, Vol. 325, 1982.

13. R.W. Hoffman, "The Mechanical Properties Of Thin Condensed Films," *Physics of Thin Films*, Vol. 3, G. Hass and R. Thun ed., Academic Press, New York, NY, pp. 211, ff. 1966.

14. H.E. Bennett, *Large Optics Coating and Evaluation Facility Study*, NWC TP 6177, Naval Weapons Center, China Lake, CA, pp. 31 ff. 1980.

15. H.E. Bennett, and D.K. Burge, "Simple Expressions For Predicting The Effect Of Volume And Interface Absorption And Of Scattering In High-Reflectance Or Anti-Reflectance Multilayer Coatings," *J. Opt. Soc. AM*, Vol. (70), No. (3) pp. 268-276, March, 1980.

16. P.A.Temple, D.L. Decker, T.M. Donovan, and J.W. Bethke," Measured Thin Film Absorption At The Interface, The Thin Film Bulk, And The Film-Substrate Interface," *Laser Induced Damage in Optical Materials: 1978*, NBS Spec. Publ. 541, pp. 37-42, 1979.

17. P.A. Temple,"Measurement Of Thin-Film Optical Absorption At The Air-Film Interface Within The Film And At The Film-Substrate Interface," *Appl. Phys. Lett.* 34 (10), pp. 677-679, May, 1979.

18. J.R. Palmer, and H.E. Bennett, "Relationship Between Coating Defects And The Limiting Flux Density A Cooled Laser Mirror Can Withstand," *Laser Induced Damage In Optical Materials: 1981*, NBS Spec. Pub. 638, 1983.

19. J.R. Palmer, "Continuous Wave Laser Damage On Optical Materials," *Optical Engineering* Vol. 22, No. 4, July/August, 1983.

20. H.E. Bennett, "Insensitivity Of The Catastrophic Damage Threshold Of Laser Optics To Dust And Other Surface Defects," *Laser Induced Damage In Optical Materials: 1980*, NBS Spec. Pub. 620, 1981.

21. J.R. Palmer, *Laser Damage In Optical Thin Films,* MacMillan Publishing Co., New York, NY, (to be published).

22. P.J. Schneider, "Conduction," *Handbook of Heat Transfer Fundamentals* Section 4-1, 2nd. ed., W. M. Rohsneow, J. P. Hartnet, and E. N. Ganic', ed., McGraw-Hill Book Co., New York, NY, 1985.

23. P.J. Schneider, *Handbook of Heat Transfer,* W.M. Rohsenow, and J.R. Hartnett, ed., McGraw-Hill Book Co., New York, NY, pp. 3-14 ff. 1973.

24. D.M.Lewis, and H.J. Sailer, *J. Heat Transfer,* Trans., ASME, Vol. 87, pp. 310-311, 1965.

25. H. Fenech, and W.H. Rohsenow, *J. Heat Transfer,* Trans., ASME, Vol. 85, pp. 15-24,1963.

26. F.Kreith, *Principles of Heat Transfer,* 2nd. ed., International Textbook Co., Scranton, PA, 1966.

27. M. Jakob, *Heat Transfer,* Vol. 1, John Wiley and Sons, New York, NY, 1949.

28. M. McGuirk, and R.D. Poirier, "Thermal Conductivity Of Enhanced Reflectors," *Laser Induced Damage In Optical Materials: 1985,* NBS Spec. Publ. (to be published).

29. D.L. Decker, "Thermal Properties Of Optical Materials," *Laser Induced Damage In Optical Materials: 1986,* NBS Spec. Publ. (to be published).

30. S.M.J. Akhtar, D. Ristau, and J. Ebert, "Thermal Conductivity Of Dielectric Film And Correlation To Damage Threshold At 1064 nm," *Laser Induced Damage In Optical Materials: 1986,* NBS Spec. Publ. (to be published).

31. R.T. Swimm, "Photothermal Measurement Of Optical Coating Thermal Transport Properties," *Laser Induced Damage In Optical Materials: 1986,* NBS Spec. Publ. (to be published).

32. L.G. Koshigoe, and D.L. Decker, *Thermophysical Properties Of Thin Films,* NWC TM-5322, Naval Weapons Center, China Lake, CA, 1984.

33. D.L. Decker, L.G. Koshigoe, and J. Ashely, "Thermal Properties Of Thin Films," *Laser Induced Damage In Optical Materials: 1984,* NBS Spec. Pub. 727, 1986.

34. H. Kuster, and J. Ebert, "Pyroelectric Measurement Of Absorption In Oxide Layers And Correlation To Damage Threshold," *Laser Induced Damage In Optical Materials: 1979,* NBS Spec. Pub. 568, 1980.

35. N.J. Kreidl, and J.L Rood, "Optical Materials," Chpt. 5, *Applied Optics And Optical Engineering,* Vol. 1, R. Kingslake, ed., Academic Press, New York, NY, 1965.

36. H.M. Musal, "Thermomechanical Stress Degradation Of Metal Mirror Surfaces Under Pulsed Irradiation," *Laser Induced Damage In Optical Materials: 1979,* NBS Spec. Pub. 568, 1980.

37. S.J. Holmes, *Reflective Coating Development For HF Lasers,* AFWL-TR-82-12, Northrop Research And Technology Center, Palos Verdes Peninsula, CA.,1982.

38. J.R. Palmer, "Thermal Shock: A Contributing Factor To Laser Damage In Optical Thin Films Used For High Power Continuous Wave Laser Optics," *Laser Induced Damage In Optical Materials: 1987,* (to be presented to the Laser Damage Symposium, October, 1987 and submitted for review in Applied Optics, 1988).

39. S. Musikant, *Optical Materials: An Introduction To Selection And Application,* Marcel Dekker, Inc., New York, NY, 1985.

40. This is a new code developed by Lazor Inc. for evaluating the temperature transients in optics for coated and uncoated, CW and Repetitive Pulsed laser optical components. This system runs on a Macintosh™ Plus. Lazor Inc, P.O. Box 613311, So. Lake Tahoe, CA 95761

41. D.Q. Kern, and A.D. Kraus, *Extended Surface Heat Transfer*, McGraw-Hill Book Co., Inc., New York, NY, pg. 103 ff, (1972).

42. J.R. Palmer, *High Power Laser Optics*, Marcel Dekker, New York, NY (to be published in 1989).

Appendix

2 ierfc, $4i^2$ erfc, and erfc functions [2,3,42]

(X) Interval	2 ierfc (X)
0 to 0.299	$1.1284 - 1.998(X) + 1.11(X)^2$
0.30 to 0.5499	$1.115074 - 1.90863(X) + 0.9543(X)^2$
0.55 to 0.999	$1.012 - 1.5525(X) + 0.64346(X)^2$
1.0 to 1.599	$0.6271 - 0.76914(X) + 0.241964(X)^2$
1.6 to 2.0	$0.21573 - 0.21165(X) + 0.0525(X)^2$
2.001 to 2.4	$0.05124 - 0.041425(X) + 0.008393(X)^2$

(X) Interval	erfc (X)
0 to 0.299	$1.0 - 1.1408(X) + 0.1377(X)^2$
0.30 to 0.5499	$1.0167 - 1.2658(X) + 0.38269(X)^2$
0.55 to 0.99	$1.0394 - 1.35775(X) + 0.47606(X)^2$
1.0 to 1.599	$0.84562 - 0.98479(X) + 0.29598(X)^2$
1.6 to 2.09	$0.359744 - 0.34066(X) + 0.081586(X)^2$
2.1 to 2.5	$0.045779 - 0.032871(X) + 0.005892(X)^2$

(X) Interval	$4\,i^2\mathrm{erfc}\,(X)$
0 to 0.299	$1.0171964 - 2.497286(X) + 2.4798872(X)^2$
0.30 to 0.5499	$0.74768 - 1.21279697(X) + 0.522727(X)^2$
0.55 to 0.999	$0.9441262 - 1.854143(X) + 1.049524(X)^2$
1.0 to 1.599	$0.3642714 - 0.4490714(X) + 0.1417143(X)^2$
1.6 to 2.0	$0.09558 - 0.093086(X) + 0.022857(X)^2$
2.001 to 2.4	$0.021334 - 0.0174143(X) + 0.0035714(X)^2$

Thermal Properties of Some Optical Materials[39,42]

material	α cm²/sec	K W/cm-°C	ρ g/cm³	cp Joules/g-°C
Aluminum	0.98	2.37	2.70	0.870
Copper	1.14	3.92	8.96	0.380
Beryllium	0.467	1.61	1.83	1.884
Gold	1.20	3.18	19.30	0.140
Molybdenum	0.52	1.34	10.20	0.250
Nickel	0.18	0.85	8.90	0.450
Rhodium	0.292	0.90	12.40	0.248
Silver	1.68	4.20	10.50	0.230
Berylco-10	0.61	2.09	4.03	0.850
Chromium	0.25	0.95	7.20	0.500
ULE	0.0078	0.0131	2.20	0.766
Silicon	0.48	0.847	2.33	0.758
Silicon Carb.	0.37	1.270	3.14	1.320
Cervit	0.0081	0.017	2.50	0.840
Pyrex	0.0065	0.0113	2.35	0.740
Zerodur	0.008	0.0165	2.21	0.934
Al_2O_3	0.0625	0.1771	3.98	0.712
Fused Silica	0.0084	0.0137	2.20	0.741

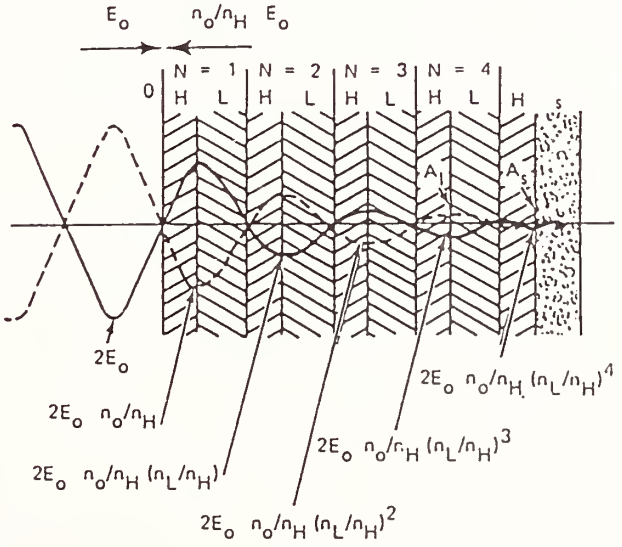

Figure 1.0

Lazor™ Code

Temperarature Rise ΔT - °C

Radius - cm

6	6.5	7	7.5	8	8.5	9	9.5	
105.79	64.76	56.96	49.83	43.26	37.46	32.16	27.41	0
81.785	50.06	44.04	38.52	33.44	28.96	24.87	21.19	.5
70.93	43.42	38.20	33.41	29.00	25.12	21.57	18.38	1
61.31	37.53	33.00	28.87	25.07	21.71	18.64	15.88	1.5
52.88	32.37	28.47	24.90	21.62	18.73	16.08	13.70	2
45.46	27.82	24.48	21.41	18.59	16.10	13.82	11.78	2.5
39.02	23.89	21.01	18.38	15.96	13.82	11.86	10.11	3
33.81	20.70	18.20	15.92	13.82	11.97	10.28	8.76	3.5
29.18	17.86	15.71	13.74	11.93	10.33	8.87	7.56	4
25.33	15.51	13.64	11.93	10.36	8.97	7.70	6.56	4.5
22.08	13.52	11.89	10.40	9.03	7.82	6.71	5.72	5

Thickness - cm

Absorbed Flux density: 100 W/cm^2

Laser Beam Diameter: 12 cm

Substrate: Copper

Run Time: 10 sec

Figure 2.0

Lazor™ Code

Temperarature Rise ΔT – °C

Radius – cm

Thickness – cm

10	10.5	11	11.5	12	12.5	13	13.5	
23.20	19.50	16.25	13.42	11.00	8.93	7.25	5.82	0
17.94	15.07	12.56	10.38	8.50	6.90	5.60	4.50	.5
15.56	13.07	10.90	9.00	7.37	6.00	4.90	3.91	1
13.45	11.30	9.42	7.78	6.37	5.18	4.20	3.38	1.5
11.60	9.74	8.12	6.71	5.49	4.46	3.62	2.91	2
9.97	8.38	6.98	5.77	4.72	3.84	3.11	2.50	2.5
8.56	7.19	5.99	4.95	4.05	3.29	2.67	2.15	3
7.42	6.23	5.19	4.29	3.51	2.85	2.32	1.86	3.5
6.40	5.38	4.48	3.70	3.03	2.46	2.00	1.61	4
5.56	4.67	3.89	3.21	2.63	2.14	1.74	1.39	4.5
4.84	4.07	3.39	2.80	2.29	1.86	1.51	1.22	5

Lazor™ Code

Temperarature Rise ΔT – °C

Radius – cm

Thickness – cm

14	14.5	15	15.5	16	16.5	17	17.5	
4.61	3.60	2.78	2.14	1.66	1.35	0.95	0.71	0
3.57	2.78	2.15	1.65	1.28	1.04	0.73	0.55	.5
3.17	2.42	1.86	1.43	1.11	0.91	0.63	0.48	1
2.67	2.09	1.61	1.24	0.96	0.78	0.55	0.41	1.5
2.31	1.80	1.39	1.07	0.83	0.68	0.47	0.35	2
1.98	1.55	1.19	0.92	0.71	0.58	0.41	0.30	2.5
1.70	1.33	1.03	0.79	0.61	0.50	0.35	0.26	3
1.47	1.15	0.89	0.68	0.53	0.43	0.30	0.23	3.5
1.27	0.99	0.77	0.59	0.46	0.37	0.26	0.20	4
1.10	0.86	0.67	0.51	0.40	0.32	0.23	0.17	4.5
0.96	0.75	0.58	0.45	0.35	0.28	0.20	0.15	5

Lazor™ Code

Temperarature Rise ΔT - °C

Radius - cm

Thickness - cm

18	18.5	19	19.5	20	20.5	21	
0.52	0.37	0.26	0.20	0.17	0.10	0.070	0
0.40	0.29	0.20	0.15	0.13	0.070	0.060	.5
0.35	0.25	0.18	0.13	0.11	0.060	0.050	1
0.30	0.21	0.15	0.12	0.10	0.055	0.040	1.5
0.26	0.19	0.13	0.10	0.080	0.050	0.036	2
0.22	0.16	0.11	0.090	0.070	0.040	0.03	2.5
0.19	0.14	0.10	0.070	0.060	0.035	0.027	3
0.17	0.12	0.080	0.060	0.050	0.030	0.020	3.5
0.14	0.10	0.070	0.055	0.047	0.026	0.019	4
0.12	0.090	0.060	0.050	0.040	0.022	0.017	4.5
0.11	0.080	0.055	0.040	0.035	0.020	0.015	5

Lazor™ Code

Temperarature Rise ΔT – °C

Radius – cm

6	6.5	7	7.5	8	8.5	9	9.5	Thickness – cm
162.15	99.25	87.31	76.37	66.30	57.42	49.30	42.01	0
121.54	74.40	65.44	57.24	49.70	43.04	36.95	31.49	.5
109.58	67.08	59.00	51.61	44.81	38.81	33.32	28.39	1
98.98	60.59	53.29	46.62	40.47	35.05	30.10	25.64	1.5
89.69	54.90	48.29	42.24	36.67	31.76	27.27	23.24	2

Absorbed Flux density: 100 W/cm²

Laser Beam Diameter: 12 cm

Run Time : 10 sec

Substrate: Copper

Figure 3.0

Lazor™ Code

Temperarature Rise ΔT – °C

Radius – cm

10	10.5	11	11.5	12	12.5	13	13.5	Thickness – cm
35.60	29.88	24.90	20.57	16.85	13.69	11.11	8.93	0
26.66	22.40	18.67	15.42	12.63	10.26	8.33	6.69	.5
24.04	20.19	16.82	13.9	11.39	9.25	7.51	6.03	1
21.71	18.24	15.20	12.56	10.29	8.36	6.78	5.45	1.5
19.67	16.53	13.77	11.38	9.32	7.57	6.14	4.94	2

Lazor™ Code

Temperarature Rise ΔT – °C

Radius – cm

14	14.5	15	15.5	16	16.5	17	17.5	Thickness – cm
7.07	5.52	4.26	3.27	2.55	2.07	1.45	1.09	0
5.30	4.14	3.19	2.45	1.91	1.55	1.09	0.814	.5
4.78	3.73	2.88	2.21	1.72	1.40	0.98	0.734	1
4.32	3.37	2.60	2.00	1.56	1.26	0.885	0.663	1.5
3.91	3.05	2.36	1.81	1.41	1.15	0.801	0.601	2

Lazor™ Code

Temperarature Rise ΔT – °C

Radius – cm

18	18.5	19	19.5	20	20.5	21		Thickness – cm
0.794	0.567	0.405	0.305	0.260	0.146	0.112		0
0.595	0.425	0.304	0.228	0.195	0.110	0.084		.5
0.536	0.383	0.274	0.206	0.175	0.099	0.076		1
0.484	0.346	0.247	0.186	0.159	0.089	0.068		1.5
0.439	0.314	0.224	0.168	0.144	0.081	0.062		2

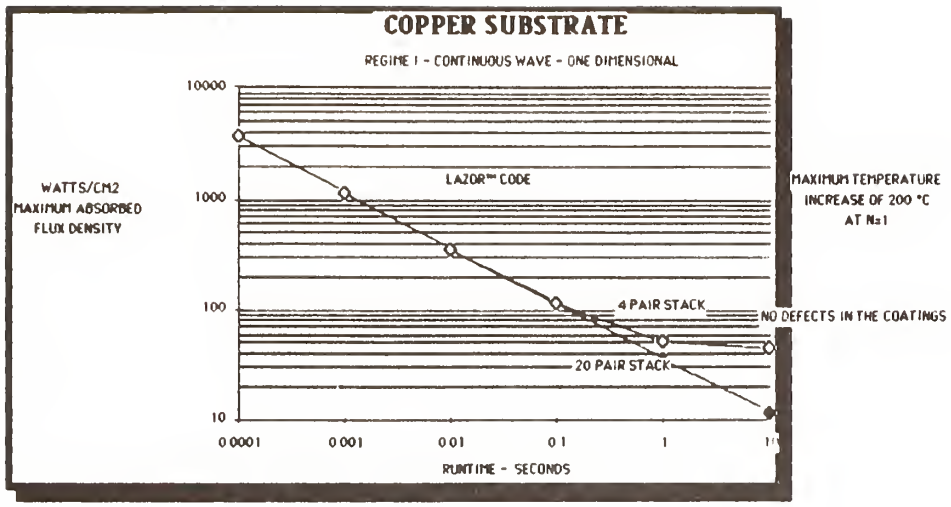

FIGURE 4.0

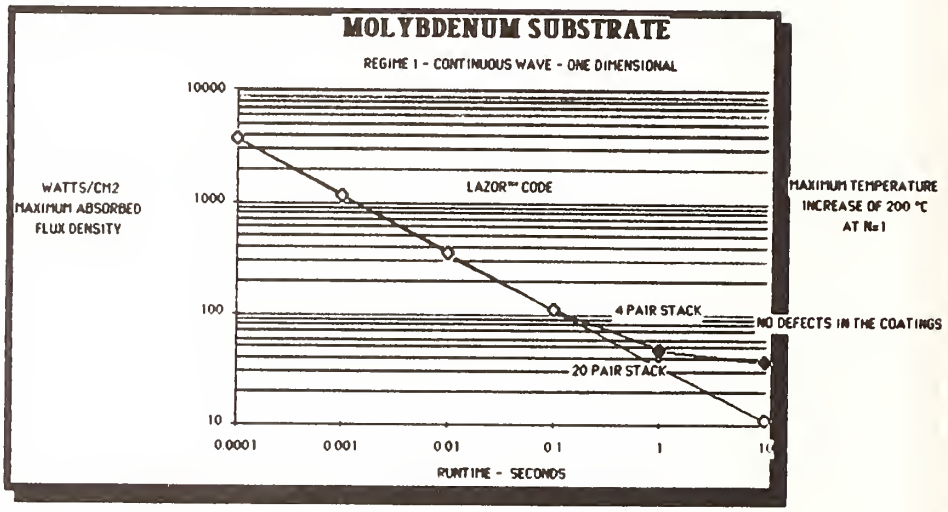

FIGURE 5.0

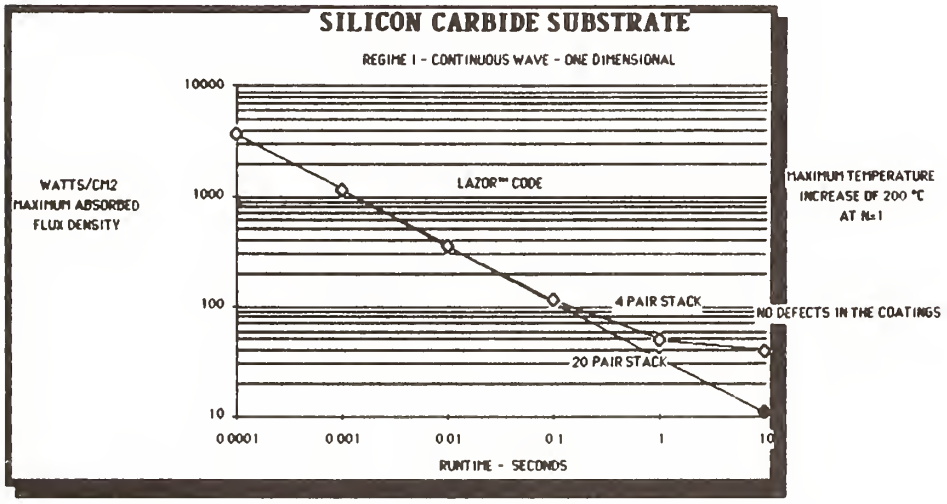

FIGURE 6.0

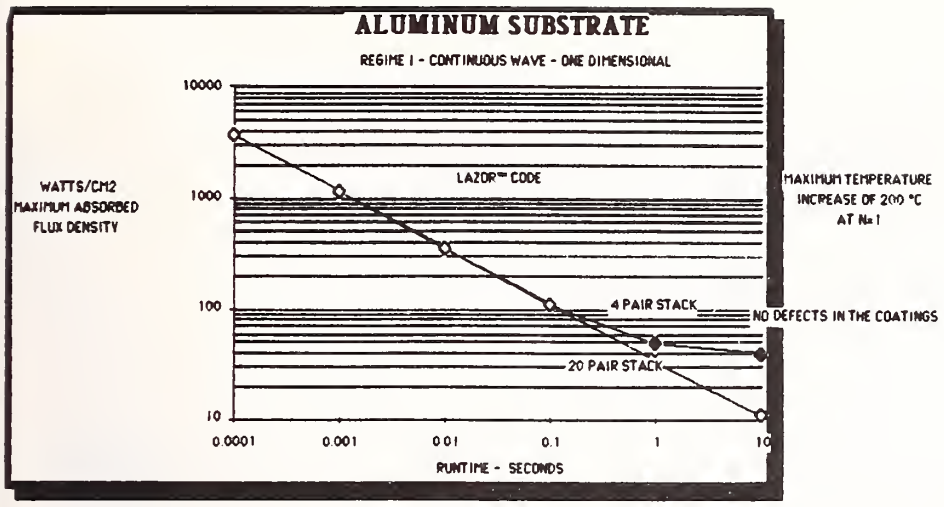

FIGURE 7.0

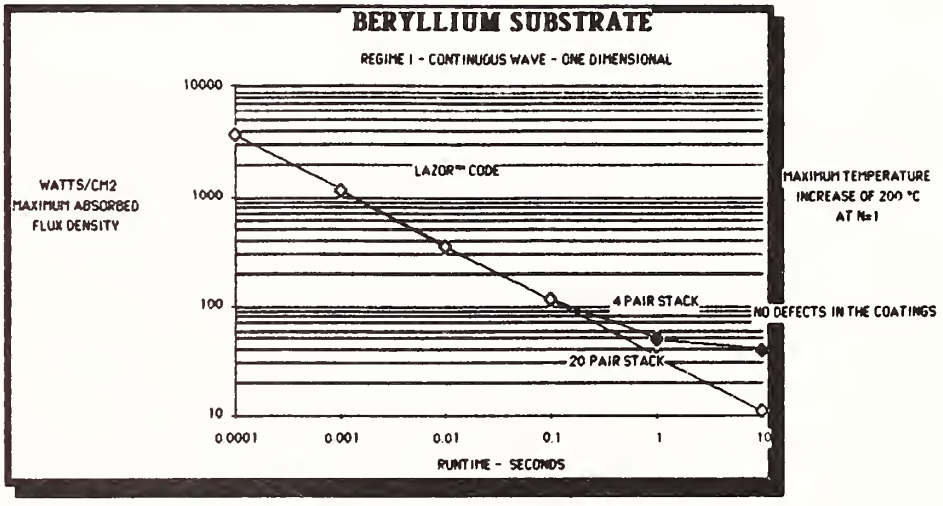

FIGURE 8.0

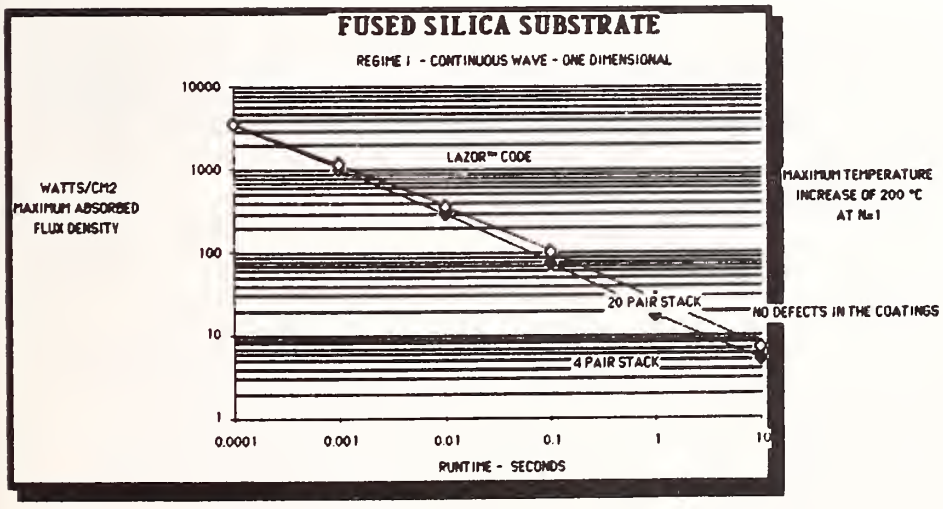

FIGURE 9.0

Manuscript Received 12/14/87/sar

High Power Continuous Wave And Repetitive Pulsed Thermal Shock Laser Damage To Metallic Reflective Optics

J. R. Palmer

University of Alabama, Huntsville
Center For Applied Optics
Huntsville, Alabama 35899

Abstract

Thermal shock damage may be a precursor to the melting and disordering of metallic reflector surfaces. A number of investigators have reported in these proceedings the phenomena of slip fracture on the surfaces of both polished and diamond turned optics. In this paper, a model is presented using elastic-plastic technique coupled with the transient thermal response of an optical surface.

Equations are presented to reflect the thermal shock threshold for major metals that are commonly used for high power laser reflective optics. The models for the continuous wave and repetitive pulsed conditions have some similarities in evaluating the strain and rupture. However, because of the two cycle nature of the Repetitive Pulse condition, the thresholds are demonstrably lower than those that are shown for the Continuous Wave situation.

Key Words: Optics, Transient Heat Transfer, Faceplates, Distortion, Repetitive Pulsed Lasers, Continuous Wave Lasers, and Thermal Shock

Introduction

There have been a number of discussions over the years, in this forum, about slip and disordering of optical surfaces that are subjected to high power Continuous Wave and Repetitive Pulsed laser. In this paper we will present some approximations that will allow a designer to perform a first order analysis of the thresholds of flux density or fluence that one may expect for their respective system or component.

Thermal Shock

One can look at the phenomena of thermal shock and the elastic-plastic response of metals to both Continuous Wave and Repetitive Pulsed imposition of flux density or fluence. Dr. Musal presented a paper at this conference some years ago that described the response of metals and demonstrated how thermal shock could affect the optical surface.[1] In that paper he described an expression that would permit the evaluation of the maximum allowable flux density or fluence on the optical surface, so that,

$$\Delta T = Y (1 - \nu) / (E \alpha) \qquad (1)$$

where,

Y = Yield Stress, N/cm^2

E = Young's Modulus, N/cm^2

α = Linear Coefficient of Expansion, $°C^{-1}$

ν = Poisson's Ratio (for metals on the order of 0.30)

Faupel and Fischer,[2] however, suggest that one use the following expression,

$$\Delta T_{shock} = \varepsilon E\ (1-\ 0.3) / \{ E\ \alpha \} \qquad (2)$$

where,

εE = Maximum Bending Stress, N/cm^2

E = Young's Modulus, N/cm^2

α = Linear Coefficient of Expansion for the substrate material, °C^{-1}

ν = Poisson's Ratio (for metals on the order of 0.30)

ε = Strain Rate

The same authors, however, suggest that *Eq. (2)* is not adequate because of the plastic hinge phenomena and the subsequent elongation before the material actually begins to separate. The suggestion, then, is that one should use the pseudoelastic modulus to accommodate the propensity for metals to elongate after they have gone through plastic hinge. The modified expression to accommodate the elastic-plastic condition would follow from,

$$\Delta T_{shock} = \varepsilon^{0.7} E\ (1-\ 0.3) / \{ E\ \alpha \} \qquad (3)$$

where,

$\varepsilon^{0.7}E$ = Modulus of Rupture, N/cm^2

E = Young's Modulus, N/cm^2

α = Linear Coefficient of Expansion for the substrate material, °C^{-1}

ν = Poisson's Ratio (for metals on the order of 0.30)

$\varepsilon^{0.7}$ = Strain Rate, which includes the pseudoelastic modulus

We can look at the thermal shock temperature for Copper. For Copper the coefficient of expansion is 16.6 (10^{-6}) °C^{-1}. The Young's Modulus is 11.7(10^6) Newtons/cm^2. The strain rate is of the order of 0.004.[3,4] Using *Eq. (3)*, then, the temperature rise to cause thermal shock will follow from,

$$\Delta T = 0.004^{0.7}\ (11.7)10^6\ (.7)\ /\ \{ (11.7)10^{\ 6}\ \ (16.6)10^{-6} \}$$

$$\Delta T = 883.96\ °C$$

There is yet another set of nuances that must be applied. *Equation (3)* does not have a time dependence, nor a thickness dependence associated with the steep gradient necessary to cause thermal shock. Manson[5,6] has developed an empirical expression based on test data that incorporates a time and thickness variable into the equation,

$$\Delta T_{shock} = \{ \varepsilon^{0.7} E\ (1-\ 0.3) / \{ E\ \alpha \} \} \{ K(6.25) / t_o(h_c) \} \qquad (4)$$

where,

t_o = Thickness of the substrate, cm

For Continuous Wave, the heat transfer coefficient will be,

$h_c = (K/2)\ \{ \pi/(\alpha\ \tau) \}^{0.5}$, Heat transfer Coefficient[7], W/cm^2-°C

For Repetitive Pulse, the heat transfer coefficient will be,

$h_c = (K/2)\ \{ \pi/(\alpha\ \Omega^{-1}\ \eta) \}^{0.5}$, Heat transfer Coefficient[7], W/cm^2-°C

K = Thermal Conductivity of Faceplate,W/cm-°C

Ω = Hertz rate, cycles/sec

η = Number of Cycles

Equation (4) is to be used when $t_o(h_c) < K(6.25)$ or the Biot Modulus[7,8,9] is greater than K(6.25). The Biot Modulus is defined as,[7,8,9]

$$B_i = t_o(h_c) / 2(K) \qquad (5)$$

For the continuous wave problem using a semi-infinite plate model, we can calculate the amount of flux density and the thermal shock temperature limit for a semi-infinite plate boundary. The thickness that will satisfy the semi-infinite plate boundary will be $t_o = 6\ (\alpha\tau)^{0.5}$. The thickness of our Copper faceplate will have to be 6.4062 cm for a one second run time. The temperature rise of the first surface is found from,[4,10,11,12]

$$\Delta T_1 = 2F_o\ (\alpha\tau)^{0.5} \left\{ \text{ierfc}(x) \right\} / K \qquad (6)$$

where,

F_o = Absorbed incident flux density, W/cm^2

K = Thermal conductivity, W/cm-°C

x = $t / 2(\alpha\tau)^{0.5}$ at t=0 ; ierfc(x) = $1/(\pi)^{0.5}$

And, at some depth into the faceplate, the temperature rise will be found from the following expression,[4,10,11,12]

$$\Delta T_{t>0} = 2F_o\ (\alpha\tau)^{0.5} \left\{ \text{ierfc}(y) \right\} / K \qquad (7)$$

where,

$y = t / 2(\alpha\tau)^{0.5}$ at $t > 0$

The thermal diffusivity of Copper is 1.14 cm^2/sec and the conductivity will be[3] 3.92 W/cm-°C. The heat transfer film coefficient will be 3.2537 and the product of $t_o(h_c)$ = 20.844. This value is less than K(6.25) = 24.50. Based on the criteria suggested by Manson, we would use *Eq. (4)* rather than *Eq. (3)* We would find from *Eq. (4)*

$$\Delta T_{shock} = \left\{ \varepsilon^{0.7} E\ (1 - 0.3) / (E\ \alpha) \right\} \left\{ K(6.25) / t_o(h_c) \right\}$$

ΔT_{shock} = 1039 °C vs 883.96 found from *Eq(3)*

For a one second run time, the maximum absorbed flux density would be 2876 W/cm^2 for a thermal shock temperature of 883.96 °C and 3381 W/cm^2 for a thermal shock temperature of 1039°C for our our minimal thickness faceplate. However, if our faceplate were 7.53 cm thick, we would fall into *Eq. (3)* with the lower thermal shock temperature value. For a ten second run time the values shown above would still be applicable. That is, the film coefficient would drop to 1.209 but the thickness increases with the time constant in the exact same way. This would provide the same constants for falling into the regime of *Eq. (4)* Fundamentally, we have the same thermal shock temperature as before. The maximum absorbed flux density would be 910 W/cm^2 for the 883.96°C thermal shock temperature of *Eq. (3)* For the thermal shock temperature of 1039°C the maximum absorbed flux density would be 1069 W/cm^2. For the repetitive pulsed case, however, we have to treat with both elements of the thermal cycle. So that, treating with the peak pulse temperature rise we would use,[4,10,11,12,13]

$$\Delta T_1 = 2F_0 (\alpha \phi)^{0.5} \{ \text{ierfc}(x) \} / K \qquad (8)$$

where,

F_0 = Absorbed incident fluence, W/cm^2

K = Thermal conductivity, W/cm-°C

x = $t / 2(\alpha \phi)^{0.5}$ at t=0 ; $\text{ierfc}(x) = 1/(\pi)^{0.5}$

For this problem we would have an enormous heat transfer film coefficient. Consequently, this problem falls within the range of *Eq. (3)* For a pulse width of $1(10^{-8})$ the required absorbed fluence would be $2.88(10^7)$ W/cm^2, i.e., 0.288 Joules/cm^2. For a pulse width of $1(10^{-5})$ the required absorbed fluence would be $9.1(10^5)$ W/cm^2 i.e., 9.1 Joules/cm^2. However, this only reflects the heat up cycle and does not reflect the cooling portion of the cycle. The complete temperature rise of the first surface of the optical component at the end of one complete cycle is found from,[4,10,11,12,13,14,15]

$$\Delta T_0 = 2\eta F_0 (\alpha)^{0.5} \{ \text{ierfc}(x) \} \{ \Omega^{-0.5} - (\Omega^{-1} - \phi)^{0.5} \} / K \qquad (9)$$

where,

Ω = Hertz rate, cycles / sec

η = Number of pulses

So, then, if we had a laser that had a pulse width of $1(10^{-8})$sec, and was pulsing at 100 cycles/sec, the fluence per pulse necessary to raise the surface temperature to 883.96°C at the end of 1000 cycles would be,

$$F_0 = 883.96°C \ (3.92 \text{ W/cm-°C}) / \{ (1.1284)(1.14)^{0.5} (5)10^{-8} \text{sec/cyc} \ (1000) \}$$

$F_0 = 5.752(10^7)$ W/cm^2 - pulse = 0.5752 Joules/cm^2 - pulse

We see, however, that the fluence per pulse necessary to bring the surface temperature up to thermal shock has already raised the temperature above thermal shock at each pulse. We can look at the same problem, however, we will use a pulse width of $1(10^{-5})$.

$$F_0 = 883.96°C \ (3.92 \text{ W/cm-°C}) / \{ (1.1284)(1.14)^{0.5} (5)10^{-5} \text{sec/cyc} (1000) \}$$

$F_0 = 5.75(10^4)$ W/cm^2 - pulse = 0.575 Joules/cm^2 - pulse

It would seem that the shorter the pulse width, a single pulse can bring the surface temperature to the thermal shock level with a smaller amount of fluence than with a longer pulse. This observation has been made by a multitude of investigators. In terms of the repetitive pulsed condition, the short pulse width also allows the longer cool down cycle. This in turn requires an even greater fluence density for the long term temperature rise over a number of pulses. As the pulse width grows longer, the cool down portion of the cycle grows shorter and less fluence density is required to bring the first surface to thermal shock temperature. For the short pulse width of $1(10^{-8})$sec we see that at the end of one cycle, the residual temperature will be 0.884 °C ΔT, using the $5.752(10^7)$ W/cm^2 - pulse. At the same time, we would see the same residual temperature rise at the end of 10^3 cycles using the longer pulse width of $1(10^{-5})$sec using only $5.752(10^4)$ W/cm^2 - pulse. some implications of what we see would be that one would require a higher hertz rate as the pulse width grows shorter. For example, if we use 500 cycles/sec with the $1(10^{-8})$sec pulse width, we would find that the required fluence to achieve thermal shock would be,

$\mathcal{F}_D$ = 883.96°C (3.92 W/cm-°C) / $\{(1.1284)(1.14)^{0.5}(1.12)10^{-7}$sec/cyc(1000)$\}$

$\mathcal{F}_D$ = 2.568(10 ^{6}) W/cm^2 - pulse = 0.02568 Joules/cm^2 - pulse

At this point, we should also add, that with each heat up and cool down the peak pulse temperature rise is additive. So that at the end of 999 pulses in our last example the next peak pulse will raise the peak temperature to 1673 °C ΔT at the 10^3 pulse.

Non Semi-Infinite Plate Boundary

The problem of the non semi-infinite boundary is not an issue that has been well addressed by many of the authors dealing with transient thermodynamics. However, it is a problem that must be addressed when discussing the problem of high power laser optics. In this symposia, the author has dealt with the issue of otical faceplates that do not satisfy the condition of the semi-infinite plate boundary.[16,17] The problem is equally acute for the continuous wave and repetitive pulsed type of laser. There are, of course, many of the same issues between the two phenomena as discussed above. The optical faceplate fails to meet the semi-infinite boundary condition when the thickness of the optical faceplate is within the boundary of the following equation for the continuous wave problem,

$$t < 6\,(\alpha\tau)^{0.5} \qquad (10)$$

where,

α = Thermal diffusivity, cm^2 / sec

τ = Transient time, sec

and for the repetitive pulsed problem,

$$t < 6\,(\alpha\,\Omega^{-1}\,\eta)^{0.5} \qquad (11)$$

where,

α = Thermal diffusivity, cm^2 / sec

$\Omega^{-1}\,\eta$ = Transient time, sec

For this boundary condition, the author has constructed a set of approximations that will permit the reader to perform a first order analysis to determine the temperature rise of the first and second surface of the uncooled optical component. Using the *Reverse Thermal Wave Approximations* we can determine the temperature rise of the first surface from,

(12)

$$\Delta T_1 = 2\mathcal{F}_D\,(\alpha\tau)^{0.5}\left\{\text{ierfc}(x)\right\}/K - 2\mathcal{F}_D(\alpha\tau)^{0.5}\left\{\text{ierfc}(y)\right\}/K\left\{\text{erfc}(y) - \exp\left(t_O H_O + H_O^2\alpha\,\tau\right)\,\text{erfc}(z)\right\} + 2\mathcal{F}_D\,(\alpha\tau)^{0.5}\left\{\text{ierfc}(y)\right\}/K + 2\mathcal{F}_D(\alpha\tau)^{0.5}\left\{\text{ierfc}(x)\right\}/K \times \left\{\text{erfc}(y) - \exp\left(t_O\,H_O + H_O^2\,\alpha\,\tau\right)\,\text{erfc}(z)\right\}$$

where,

$H_o = t_o^{-1}$, cm^{-1}; t_o= Thickness of faceplate, cm

$z = \left\{t_o / 2(\alpha\,\tau)^{0.5} + H_O\,(\alpha\,\tau)^{0.5}\right\}$;

$y = t_o / 2(\alpha\,\tau)^{0.5}$

The temperature rise at any point below the first surface will follow from,

(13)

$$\Delta T_{t>0} = 2\,\mathbf{F}_0\,(\alpha\tau)^{0.5}\{\,\mathrm{ierfc}(y)\,\}/K + 2\,\mathbf{F}_0\,(\alpha\tau)^{0.5}\{\,\mathrm{ierfc}(x)\,\}/K$$
$$\times\,\{\,\mathrm{erfc}(y) - \exp(t_0H_0 + H_0^2\,\alpha\,\tau)\,\mathrm{erfc}(z)\,\}$$

These expressions work for Regime II. This regime is the condition where $0.6\,(\alpha\tau)^{0.5} < t_o < 6\,(\alpha\tau)^{0.5}$. Using *Eq. (12)* and *(13)* we can take our sample problem and look for thermal shock on a Copper substrate that is 4.0 cm thick for our one sec run time . The problem is made simpler using the **Lazor™Code.**[18] The value of $t_0\,(h_c) = 13.01$. What we find is that the thermal shock temperature is achieved much more quickly, as one might expect. For our example, the thermal shock temperature is 1730.56°C for this much thinner faceplate which falls within the regime of *Eq. (4)*. This temperature is above the melt point of the Copper. Consequently, we see that the thinner the material of the faceplate the more rapidly the front and back surfaces increase in temperature and begin to close on one another, i.e., the temperature gradient is diminishing rapidly.

For the repetitive pulsed condition, we would begin to see that the faceplate will begin to recede from *Eq. (3)* and, begin as, expected to enter the arena of *Eq. (4)* We will take a sample problem using the $1(10^{-5})$ pulse width, 100 Hertz, and total 10^2 pulses. From *Eq. (11)* the required thickness would be 6.406 cm. We will use the 4.0 cm thickness of the continuous wave problem. The value of $t_0\,(h_c) = 13.01$. Again we would find that the thermal shock temperature would be greater than the melt temperature of the Copper. For completeness, however, the temperature rise of the first surface with residual temperature, excluding peak pulse will follow from,[16,17]

(14)

$$\Delta T_1 = 2\,\eta\,\mathbf{F}_0(\alpha)^{0.5}\,\{\,(\mathrm{ierfc}(x_o))\,\}\,\{\,\Omega^{-0.5} - (\Omega^{-1} - \phi)^{0.5}\,\}/K - 4\,\pi\,\Omega\,\phi\,\mathbf{F}_0\,(\alpha\,\Omega^{-1}\,\eta)^{0.5}$$
$$\times\{\,(\mathrm{ierfc}(y))\,\}/K\{\,\mathrm{erfc}(y) - \exp(t_0H_0 + H_0^2\,\alpha\,\Omega^{-1}\,\eta)\,\mathrm{erfc}(z)\,\}$$
$$+ 4\,\pi\,\Omega\,\phi\,\mathbf{F}_0\,(\alpha\,\Omega^{-1}\eta)^{0.5}\{\,(\mathrm{ierfc}(y))\,\}/K + 4\,\pi\,\Omega\,\phi\,\mathbf{F}_0\,(\alpha\,\Omega^{-1}\,\eta)^{0.5}$$
$$\times\{\,(\mathrm{ierfc}(x))\,\}/K\times\,\{\,\mathrm{erfc}(y) - \exp(t_0H_0 + H_0^2\,\alpha\,\Omega^{-1}\,\eta)\,\mathrm{erfc}(z)\,\}$$

The temperature rise at some some depth into the faceplate follows in like fashion from,

(15)

$$\Delta T_2 = 4\,\pi\,\Omega\,\phi\,\mathbf{F}_0\,(\alpha\,\Omega^{-1}\,\eta)^{0.5}\,\{\,(\mathrm{ierfc}(y))\,\}/K + 4\,\pi\,\Omega\,\phi\,\mathbf{F}_0\,(\alpha\,\Omega^{-1}\,\eta)^{0.5}\,\{\,(\mathrm{ierfc}(x))\,\}/K$$
$$\times\,\{\,\mathrm{erfc}(y) - \exp(t_0H_0 + H_0^2\,\alpha\,\Omega^{-1}\,\eta)\,\mathrm{erfc}(z)\,\}$$

where,

$x_o = t / 2\{\,\alpha\,(\Omega^{-1} - \phi)\,\}^{0.5}$ at t=0; $\quad \mathrm{ierfc}\,(x_o) = 1/(\pi)^{0.5}$

$y = t / 2\,(\alpha\,\Omega^{-1}\eta)^{0.5}$; $\quad z = t / 2\,(\alpha\,\Omega^{-1}\eta)^{0.5} + H_o\,(\alpha\,\Omega^{-1}\eta)^{0.5}$

$H_0 = t_0^{-1}$, cm^{-1}; $\quad t_0$ = Thickness of faceplate, cm

Conclusion

It would seem, then, that one can use the elastic-plastic analytical technique for evaluating the thermal shock threshold for various metallic optical components. By using the heat transfer coefficient which is time dependent, coupled with the thickness of the optical component, we see that the thermal shock threshold can change dramatically. Further, it appears that the thinner the optical faceplate, the higher the thermal shock threshold. This results from the rapid temperature convergence with time. Conversely, for those optical components that are thicker than

that required by the semi-infinite boundary condition, there is a lower thermal shock threshold, as shown by *Eq. (3)* This should be as expected in that the temperature gradient will be very steep for the thicker faceplate. We find, however, that the single pulse condition falls within *Eq. (3)* because the heat transfer coefficient is so large and the thickness, will most generally, always be tremendously large compared to the pulse width. Even for a number of repetitive pulse cases, the film coefficient and the thickness will be substantially larger than that required for the semi-infinite boundary problem.

References

1. H. M. Musal, "Thermomechanical Stress Degradation Of Metal Mirror Surfaces Under Pulsed Irradiation," *Laser Induced Damage In Optical Materials: 1979,* NBS Spec. Pub. 568, 1980.

2. J. H. Faupel, and F. E. Fisher,ed., *Engineering Design,* 2nd ed., John Wiley and Sons, Inc., New York, NY, 1981.

3. S. Musikant, *Optical Materials,* B.J. Thompson, ed., Marcel Dekker, Inc., New York, NY, 1985.

4. J. R. Palmer, *High Power Laser Optics,* Marcel Dekker, Inc., New York, NY, (to be published).

5. S. S. Manson, "Behavior Of Materials Under Conditions Of Thermal Stress - Part I," *Machine Design,* Vol. 30, No. 6, 1958.

6. S. S. Manson, "Behavior Of Materials Under Conditions Of Thermal Stress - Part II," *Machine Design,* Vol. 30, No. 9, 1958.

7. M. Jakob, *Heat Transfer,* Vol. 1, John Wiley and Sons, New York, NY, 1949.

8. J. Crank, *The Mathematics Of Diffusion,* 2nd ed., Oxford University Press, Oxford, England, 1983

9. E. L. Cussler, *Diffusion: Mass Transfer In Fluid Systems,* Cambridge University Press, London, England, 1984.

10. J.R. Palmer "Loss Of Infrared Optical System MTF Resulting From Damage Caused By High Power Continuous Wave And Low Average Power Repetitive Pulsed Visible - UV Lasers," *4th Int'l. Symp. On Optical And Optoelectronic Applied Science And Engineering,* SPIE No. 806, The Hauge, The Netherlands, April, 1987.

11. J.R. Palmer, "Reverse Thermal Wave Approximation For Temperature Transients In Uncoated Reflective Optics For High Power Continuous Wave Lasers," *Optical Engineering* (to be published).

12. J.R. Palmer, "Reverse Thermal Wave Approximation For Temperature Transients In Uncoated Reflective Optics For High Power Repetitive Pulsed Lasers," *Optical Engineering* (to be published).

13. J.C Jaeger, "Pulsed Surface Heating of A Semi-Infinite Solid," *Quart. Appl. Math,* Vol 11, No. 1, 1953.

14. J.R. Palmer, *Laser Damage In Optical Thin Films,* MacMillan Publishing Co., New York, NY, (to be published).

15. H S. Carslaw, and J.C. Jaeger, *Conduction of Heat In Solids,* 2nd ed., Oxford University Press, Oxford, England, 1978.

16. J.R. Palmer, "Reverse Thermal Wave Approximations For Temperature Transients In Optical Thin Films And Substrates-Reflective Optics For High Power Continuous Wave Lasers," *Laser Induced Damage In Optical Materials: 1987,* (proceedings of this symposia to be published).

17. J.R. Palmer, "Reverse Thermal Wave Approximations For Temperature Transients In Optical Thin Films And Substrates-Reflective Optics For High Power Repetitive Pulsed Lasers," *Laser Induced Damage In Optical Materials: 1987,* (proceedings of this symposia to be published).

18. **Lazor™Code** is a transient heat transfer program that treats with optical components that are provided with optical thin films and metal reflective optical substrates. **Lazor Inc.** P.O. Box 613311, So. Lake Tahoe, CA, 95761.

Appendix

2 ierfc, 4i^2 erfc, and erfc functions [3,4,16,17]

(X) Interval	**2 ierfc (X)**
0 to 0.299	$1.1284 - 1.998(X) + 1.11(X)^2$
0.30 to 0.5499	$1.115074 - 1.90863(X) + 0.9543(X)^2$
0.55 to 0.999	$1.012 - 1.5525(X) + 0.64346(X)^2$
1.0 to 1.599	$0.6271 - 0.76914(X) + 0.241964(X)^2$
1.6 to 2.0	$0.21573 - 0.21165(X) + 0.0525(X)^2$
2.001 to 2.4	$0.05124 - 0.041425(X) + 0.008393(X)^2$

(X) Interval	**erfc (X)**
0 to 0.299	$1.0 - 1.1408(X) + 0.1377(X)^2$
0.30 to 0.5499	$1.0167 - 1.2658(X) + 0.38269(X)^2$
0.55 to 0.99	$1.0394 - 1.35775(X) + 0.47606(X)^2$
1.0 to 1.599	$0.84562 - 0.98479(X) + 0.29598(X)^2$
1.6 to 2.09	$0.359744 - 0.34066(X) + 0.081586(X)^2$
2.1 to 2.5	$0.045779 - 0.032871(X) + 0.005892(X)^2$

(X) Interval	$4\,i^2\mathrm{erfc}\,(X)$
0 to 0.299	$1.0171964 - 2.497286(X) + 2.4798872(X)^2$
0.30 to 0.5499	$0.74768 - 1.21279697(X) + 0.522727(X)^2$
0.55 to 0.999	$0.9441262 - 1.854143(X) + 1.049524(X)^2$
1.0 to 1.599	$0.3642714 - 0.4490714(X) + 0.1417143(X)^2$
1.6 to 2.0	$0.09558 - 0.093086(X) + 0.022857(X)^2$
2.001 to 2.4	$0.021334 - 0.0174143(X) + 0.0035714(X)^2$

Thermal Properties of Some Optical Materials [3,4,16,17]

material	α cm^2/sec	K w/cm-°C	ρ g/cm^3	cp Joules/g-°C
Aluminum	0.98	2.37	2.70	0.870
Copper	1.14	3.92	8.96	0.380
Beryllium	0.467	1.61	1.83	1.884
Gold	1.20	3.18	19.30	0.140
Molybdenum	0.52	1.34	10.20	0.250
Nickel	0.18	0.85	8.90	0.450
Rhodium	0.292	0.90	12.40	0.248
Silver	1.68	4.20	10.50	0.230
Beryico-10	0.61	2.09	4.03	0.850
Chromium	0.25	0.95	7.20	0.500
ULE	0.0078	0.0131	2.20	0.766
Silicon	0.48	0.847	2.33	0.758
Silicon Carb.	0.37	1.270	3.14	1.320
Cervit	0.0081	0.017	2.50	0.840
Pyrex	0.0065	0.0113	2.35	0.740
Zerodur	0.008	0.0165	2.21	0.934
Al_2O_3	0.0625	0.1771	3.98	0.712
Fused Silica	0.0084	0.0137	2.20	0.741

BOULDER DAMAGE SYMPOSIUM
October 26 - 28, 1987

LIST OF ATTENDEES

Joseph Abate
Hampshire Instruments, Inc.
P.O. Box 10159
10 Carlson Road
Rochester, NY 14610
(716) 482-4070

M. A. Acharekar
Litton Laser Systems
Apopka, FL 32854-7300
(305) 295-4010

Paul M. Adams
The Aerospace Corporation
P.O. Box 92957 MS M2-250
Los Angeles, CA 90009
(213) 336-6927

Chris Adams
McDonnell Douglas
P.O. Box 516
E467/287/3/309H
St. Louis, MO 63166
(314) 234-6426

David M. Aikens
Lawrence Livermore Nat'l Lab
P.O. Box 808, L-443
Livermore, CA 94550
(415) 423-8392

Claude Amra
Laboratoire d'Optique
E.N.SP.M.
Domaine Universitaire de St. Jerome
13397 Marseilles Cedex 13
FRANCE
(33) 91 67 96 87

Jonathan W. Arenberg
Hughes Aircraft Co.
P. O. Box 902
Bldg. E1 M/S D126
El Segundo, CA 90245
(213) 616-3090

Heinrich F. Arlinghaus
Argonne National Laboratory
Bldg. 200
9700 S. Cass Ave.
Argonne, IL 60439
(312)972-7520/3513

Mark T. Babb
Montana Laser Optics, Inc.
P.O. Box 4151
Bozeman, MT 59772
(406) 586-5100

Mira Bakshi
Deacon Research
900 Welch Rd. Suite 203
Palo Alto, CA 94304
(415) 326-1520

P. J. Baron
Laboratoires de Marcoussis
91460 Marcoussis
FRANCE

Michael F. Becker
University of Texas at Austin
Dept. of Elec. & Comp. Engr. ENS 143
133 Engineering Science Building
Austin, TX 78712-1084
(512) 471-3628

Harold E. Bennett
Michelson Labs
Naval Weapons Center
Code 38101
China Lake, CA 93555
(619) 939-1440

James D. Boyer
Los Alamos Nat'l Laboratory
CLS-5 MS J566
P.O. Box 1663
Los Alamos, NM 87545
(505) 667-0041/9222

Peter Braunlich
Physics Dept.
Washington State Univ.
Pullman, WA 99164-2814
(509) 335-4946

Ernie Braunschweig
R & D Associates
P.O. Box 9377
Albuquerque, MN 87119
(505) 842-8911

Ronald Braustein
Corion Corporation
73 Jeffrey Avenue
Holliston, MA 01746
(617) 429-5065

Raymond Brusasco
Lawrence Livermore Nat'l Lab
P.O. Box 5508, L-483
Livermore, CA 94550

Dr. Wallis F. Calaway
Argonne Nat'l Laboratory
Building 200
9700 S. Cass Ave.
Argonne, IL 60439
(313) 972-3514/5313

John H. Campbell
Lawrence Livermore Nat'l Lab
P.O. Box 5508, L-490
Livermore, CA 94550
(415) 422-6497

Charles K. Carniglia
Martin Marietta Aerospace
P.O. Box 9316
International Airport
Albuquerque, NM 87119
(505) 844-1064

Susan D. Carson
The BDM Corporation
1801 Randolph Road, S.E.
Albuquerque, NM 87106
(505) 848-5696

R. Thomas Casper
Physics Department
Washington State Univ.
Pullman, WA 99164-2814
(509) 335-8613

Jack P. Chambers
II-VI, Inc.
Saxonburg Blvd.
Saxonburg, PA 16001
(412) 352-4455

Randall Chapman
University of Illinois
Dept. of Nuclear Eng.
Urbana, IL 61801
(217) 244-4943

Lloyd L. Chase
Lawrence Livermore Nat'l Lab
P.O. Box 5508, L-490
Livermore, CA 94550
(415) 422-6151

James W. Cheely
NASA - Langley Res. Center
Mail Stop 434
Hampton, VA 23665
(804) 865-4571

Stephen Chelli
McDonnell Douglas
MDAS-STL Astronautics
Dept. E467-101D-2-200
P.O. Box 516
St. Louis, MO 63166
(314) 233-4603

Raymond Clarke
M.C.M. Laboratories
1945 Charleston Road
Suite 103
Mountain View, CA 94043
(415) 961-2347

Charles S. Cockrum
Rocky Mountain Instruments
1501 So. Sunset
Longmont, CO 80501
(303) 651-2211

Simon A. Cross
Technical Optics Ltd.
Second Avenue
Onchan
Isle of Man
0624-74443

Alain Culoma
ETCA
16 bis Avenue Prieur de la Coted'Or
94114 Arcueil Cedex
FRANCE
16 1 42.31.92.71.

John G. Daly
Litton Laser Systems
P.O. Box 7300
Orlando, FL 32954
(305) 297-4457

Colin Danson
Rutherford Appleton Laboratory
Building RI
Chilton, DIDCOT
Oxon
GREAT BRITAIN
0235-21900 XT 6340

Barbara A. Darnell
OPTOVAC
E. Brookfield Road
N. Brookfield, MA 01535
(617) 867-6444

William J. Davis
Litton-Itek Optical Systems Div.
20 Maguire Road
Lexington, MA 02173
(617) 276-2233

Arthur C. Day
Photon Sciences
11816 North Creek Parkway N.
Bothell, WA 98011
(206) 486-8883

David A. G. Deacon
Deacon Research
900 Welch Road
Suite 203
Palo Alto, CA 94304
(415) 326-1520

Fred Domann
UW-Platteville, WI
Dept. of Physics
UW-Platteville
Platteville, WI 53818
(608) 342-1657

David Doryland
USAF
AFWL/ARBD
Kirtland AFB, MN 87117-6008
(505) 844-1776

Fred W.Doss
Spectra Physics
Optics Division
1250 W. Middlefield Road
P.O. Box 7013
Mountain View, CA 94039-7013
(415) 961-2550

David F. Edwards
Lawrence Livermore Nat'l Lab
P.O. Box 808, L-332
Livermore, CA 94550
(415) 422-0747

Edward A. Enemark
Optical Coating Laboratory, Inc.
P.O. Box 1599
Santa Rosa, CA 95402
(707) 525-7108

Richard S. Eng
Mass. Inst. of Technology
Lincoln Laboratory
Lexington, MA 02173-0073
(617) 863-5500 X3695

W. W. Ernst
Space-Forschungsgruppe
Schlosshofstr. 9
7801 Buchenbach
FRG

Gregory J. Exarhos
Battelle Northwest
Battelle Boulevard
PSL/1108
Richland, WA 99352
(509) 375-2440

Albert Feldman
National Bureau of Standards
Bldg. 223, Room 20899
Gaithersburg, MD 200899
(301) 975-5740

Kim F. Ferris
Pacific Northwest Laboratory
P.O. Box 999
Richland, WA 99352
(509) 375-3754

Dale Figart
USAF
AFWL/ARBD
Kirtland AFB, NM 87117
(505) 844-3616

Herve Floch
Commissariat a l'Energie Atomique
Centre d'Etudes de Limeil
B.P. 27
94190 Villeneuve-St-Georges
FRANCE
(1)45.95.64.73

E. Joseph Friebele
Naval Research Laboratory
Code 6570
Washington, DC 20375
(202) 767-2270

Stephen P. Fry
Univ. of Texas at Austin
Dept. of Electrical and
Computer Engineering
Austin, TX 78712
(512) 343-2777

Wendy S. Frydrych
Battelle Northwest
P.O. Box 999
Richland, WA 99352
(509) 946-2394

David J. Gallant
Rockwell International
Rocketdyne Division
P.O. Box 5670
Kirtland AFB, NM 87185
(505) 844-2065

Gerald A. Gallegos
Los Alamos Nat'l Laboratory
CLS-6, MS J566
P.O. Box 1663
Los Alamos, NM 87545
(505) 667-9926/6448

Dr. Adolf Giesen
Inst. fur Strahlwerkzeuge
Universitat Stuttgart
Pfaffenwaldring 38
7000 Stuttgart 80
WEST-GERMANY
0711-6862-705

Dennis H. Gill
Los Alamos National Labs.
Chemistry Division, J563
P.O. Box 1663
Los Alamos, NM 87545
(505) 667-6250

Philip Goede
W.J. Schafer Associates
20501 Ventura Blvd.
Woodland Hills, CA 91364
(818) 704-1455

Robert Goedert
U.S. Army Tank-Auto. Command
AMSTA-RSC
Warren, MI 48397-5000
(313) 574-5325

Ray Gonzales
Lawrence Livermore Nat'l Lab
P.O. Box 5508, L-490
Livermore, CA 94550
(415) 422-6059

Erik D. Grann
Union Carbide Corp.
750 S. 32nd Street
Washoulga, WA 98617
(206) 835-8566

John S. Greene, Jr.
Ford Aerospace & Comm. Corp.
MIT/Lincoln Laboratory
P.O. Box 73
Lexington, MA 02173
(617) 863-5235

Joel G. Grimm
MIT/Lincoln Laboratory
244 Wood Street
Room L-384
Lexington, MA 02173
(617) 863-5500 X3835

Arthur H. Guenther
AFWL/CCN
Kirtland AFB, NM 87117
(505) 844-9856

Sandra R. Gyetvay
The Aerospace Corporation
P.O. Box 92957
Mail Station M2/241
Los Angeles, CA 90009
(213) 336-8239

Robert Harrach
Lawrence Livermore Nat'l Lab
P.O. Box 808, L-297
Livermore, CA 94550
(415) 422-4069

Francis B. Harrison
Los Alamos Nat'l Laboratory
P.O. Box 1663 MS J564
Los Alamos, NM 877545
(505) 665-0041

Paige L. Higby
NRL/SFA
Code 6575
Naval Research Lab
Washington, DC 20375
(202) 767-6493

Edward A. Hildum
Lawrence Livermore Nat'l Lab
P.O. Box 5508, L-490
Livermore, CA 94550
(415) 422-8726

Carl E. Hittle
Naval Ordn. Miss. Test Sta.
Code 301B
White Sands Missile Range
NM 88002
(505) 679-5345

Lowell M. Hobrock
Hughes Aircraft Company
2000 E. El Segundo Blvd.
P.O. Box 902
El Segundo, CA 90245
(213) 616-9620

Samuel J. Holmes
Northrop Research & Tech. Center
One Research Park
Palos Verdes Peninsula, CA 90274
(213) 544-5314

Alan K. Hopkins
AF Weapons Laboratory
AFWL/AR2
Kirtland AFB, NM 87117
(505) 844-6176

Richard F. Horton
MIT/Lincoln Laboratory
P.O. Box 427
White Sands Missile Range, NM 88002
(505) 679-5284

Tetsurou Izumitani
Hoya Corporation
3-3-1 Musashino
Akishima-shi
Tokyo 196
JAPAN
(0425) 46-2705

Yong Jee
MCC
12100A Technology Blvd.
Austin, TX 78727
(512) 250-2704

Linda F. Johnson
Naval Weapons Center
Physics Division, Code 3818
China Lake, CA 93555
(619) 939-1422

Jerry Johnston
Optical Coating Lab., Inc.
2789 Northpoint Parkway
Mail Station 474-F
Santa Rosa, CA 95401-7397
(707) 525-7148

L. John Jolin
Los Alamos Nat'l Laboratory
P.O. Box 1663
CLS-6 MS-J566
Los Alamos, NM 87544
(505) 667-7314/2151

Scott C. Jones
Physics Department
Washington State Univ.
Pullman, WA 99164-2814
(509) 335-4672

Doug Jungwirth
Northrop Electronics Division
2301 West 120th Street
Hawthorne, CA 90250
(213) 606-6744

Bill Kastanis
OCLI
2789 Northpoint Parkway
Mail Station 449-F
Santa Rosa, CA 95407-7397
(707) 525-7664

Geza L. Keller
Continental Optical Corp.
15 Power Drive
Hauppauge, NY 11788
(516) 582-3388

Paul Kelly
Physics Division
National Research Council
Ottawa, Ontario
CANADA
993-0347 (1-613)

Stephen E. Kendrick
Itek Optical Systems Div.
10 Maguire Road
Lexington, MA 02173
(617) 276-3752

A. Alexander Kennel
Ball Aerospace Systems Div.
Mail Stop TO-3
P.O. Box 1062
Boulder, CO 80306
(303) 939-5831

Hackjin Kim
School of Chemical Sciences
University of Illinois at
Urbana-Champaign
505 S. Mathews Ave.
Urbana, IL 61801
(217) 333-8382

Floyd Kinden
COMARCO
1201 N. China Lake Blvd.
Ridgecrest, CA
(619) 446-7671

C. William King
Harshaw/Filtrol
6801 Cochran Road
Solon, OH 44139
(216) 349-6556

Theodore Kohane
Raytheon Research Division
131 Spring Street
Lexington, MA 02173
(617) 860-3073

William A. Koldewyne
Scientech, Inc.
5649 Arapahoe
Boulder, CO 80303
(303) 444-1361

G. Edward Kuhl
W. Schafer Associates, Inc.
5100 Springfield Pike
Suite 311
Dayton, OH 45431-1231
(513) 253-9572

Nisso Lagnado
Hughes Santa Barbara Res. Center
75 Coromar Drive
Goleta, CA 93117
(805) 562-2615

Ramin Lalezari
PMS Electro Optics
1855 S. 57th Ct.
Boulder, CO 800301
(303) 443-7100

William A. Leamon
Los Alamos Nat'l Laboratory
P.O. Box 1663
MS J564
Los Alamos, NM 87545
(505) 667-3422

Olive Lee
Deacon Research
900 Welch Road
Suite 203
Palo Alto, CA 94304
(415) 326-1520

Thomas A. Leonard
Ball Systems
Engineering/ADI Division
5100 Springfield Pike
Suite 211
Dayton, OH 45431
(513) 258-1192

C. E. Lin
Inst. for Aeronautics and
Astronautics
Inst. of Elec. Engineering
Cheng Kung University
Tainan
TAIWAN

Michael Lunt
Technical Optics Ltd.
Second Avenue,
Onchan, Isle of Man
UNITED KINGDOM 0624 4443
44 624 74443

Swarnalatha Mallavarapu
AFWL
Kirtland AFB, NM 87117

John E. Marion
Lawrence Livermore Nat'l Lab
P.O. Box 808, L-490
Livermore, CA 94550
(415) 423-6788

Diane J. Martin
USAF
AFWL/ARBD
Kirtland AFB, NM 87117-6008
(505) 844-1776

Prof. Eckart Matthias
Freie Universitat Berlin
Department of Physics
Arnimallee 14
D-1000 Berlin 33
WEST GERMANY
30-838 3340

Billie R. Mauro
Los Alamos National Lab.
CLS-6, MS/J-564
P.O. Box 1663
Los Alamos, NM 87545
(505) 667-5663

Theresa McCarthy Brow
AFWL/ARBD
Kirtland AFB, NM 87117-6008
(505) 844-3616

David E. McCready
Martin Marietta Aerospace
P.O. Box 9316
International Airport
Albuquerque, NM 87119
(505) 844-1064

John K. McIver
Univ. of New Mexico
Dept. Physics & Astronomy
Albuquerque, NM 87131
(505) 277-8484

Theodore S. McMinn
McDonnell Douglas Corporation
P.O. Box 516
Bldg. 106, Level 2
MS/8
St. Louis, MO 63166
(314) 234-4321

James F. McNally
United States Air Force
Department of Physics
U.S. Air Force Academy
Colorado Springs, CO 80840
(303) 472-2240

David Milam
Lawrence Livermore
National Laboratory
PO Box 5508, L-490
Livermore, CA 94550
(415) 422-5499

Stephen A. Miller
Naval Ocean Systems Center
Code 562
San Diego, CA 92152
(619) 225-6591

S. Mohan
Indian Institute of Science
Bangalore-560012
INDIA
364411 Ext. 270

Kent Moncur
KMS Fusion, Inc.
3621 S. State
Ann Arbor, MI 48104
(313) 769-8500

Mark B. Moran
Naval Weapons Center
Code 3817
China Lake, CA 93555
(619) 939-3827

David Mordaunt
Hughes Aircraft Company
P. O. Box 902, E1/B129
El Segundo, CA 90245
(213) 616-5422

Dennis Morelli
Optical Coating Laboratory, Inc.
2789 Northpoint Parkway
Dept. 428-1
Santa Rosa, CA 95407-7397
(707) 525-7024

Ross E. Muenchausen
Los Alamos Nat'l Laboratory
CLS-2, MS G738
P.O. Box 1663
Los Alamos, NM 87545
(505) 667-3018

Ian T. Muirhead
OCLI Optical Coatings LTD
Hillend Industrial Estate
Dunfermline, Fife
SCOTLAND
(0383)823631

Tatsuji Nagai
Canon Sales Corp.
3-11-28 Mita Minato
Tokyo
JAPAN
03-455-9565

Prof. Yoshiharu Namba
Chubu University
1200 Matsumotocho, Kasugai
Aichi 487
JAPAN
0568-51-111 Ext. 2306

Dan Neal
Sandia Nat'l Laboratory
Div. 1128
P.O. Box 5800
Albuquerque, NM 87185

Ontario H. Nestor
Harshaw/Filtrol Partnership
Cleveland, OH
(216) 349-6586

Brian E. Newnam
Los Alamos Nat'l Laboratory
MS-J564
Los Alamos, NM 87545
(505) 667-7979

Davis B. Nichols
Boeing Aerospace Co.
Mail Stop 8H-29
PO Box 3999
Seattle, WA 98124
(206) 773-8938

Daniel E. Nieuwsma
Hughes Aircraft Co.
P.O. Box 902
M/S E1/D126
El Segundo, CA 90245
(213) 616-4962

Nicholas S. Nogar
Los Alamos National Labs.
CLS-2 G738
Los Alamos, NM 87545
(505) 667-9305

Robert M. O'Connell
Univ. of Missouri - Columbia
Elect. Engineering Dept.
College of Engineering
Columbia, MO 65201
(314) 882-8373

Robert O'Shaughnessy
US Army
ARDEC
Picatinny. NJ 07806-5000
(201) 724-6223

Robert W. Odom
Charles Evans & Associates
301 Chesapeake Drive
Redwood City, CA 94063
(415) 369-4567

Dr. Inki Oh
Kollsman
MS/2-B12-2
220 Daniel Webster Highway
Merrimack, NH 03054
(603) 595-6034

Yoshiaki Okamoto
Okamoto Optics Work, Inc.
8-34 Haramachi, Isogoku
Yokohama 235
JAPAN
(045) 752-2233

Garl P. Owen
British Defence Staff
British Embassy
3100 Massachusetts Ave. NW
Washington, DC 20008
(202) 898-4398

Roger A. Paquin
Perkin-Elmer Corporation
Optical Group Research
100 Wooster Heights Road
MS/848
Danbury, CT 06810
(203) 797-6130

Peter S. Parkinson
General Electric, SCO
P.O. Box 8555
Philadelphia, PA 19087
(215) 354-5672

Emile Pelletier
University of Marseilles
ENSP
Domaine Universitaire St. Jerome
13397 Marseilles Cedex 13
FRANCE
(33) 91 68 25 0 6

Dennis D. Phillips
McDonnel Douglas Corp.
MS E804/101A/3/340
P.O. Box 516
St. Louis, MO 63166
(314) 232-8835

Robert D. Poirier
Perkin Elmer Corp.
761 Main Avenue
Norwalk, CT 06859-0420
(203) 834-6272

Bradley Pond
Martin Marietta
P.O. Box 9316
Albuquerque, NM 87119
(505) 844-1064

Lawrence R. Pratt
Los Alamos Nat'l Laboratory
MS G738
Chemistry Division
Los Alamos, NM 87545
(505) 667-8624

William P. Proffitt
Rockwell International
6633 Canoga Ave.
M/S FA03
Canoga Park, CA 91304
(818) 700-4716

Rod K. Quinn
Los Alamos Nat'l Laboratory
P.O. Box 1663/CLS-DO
MS - J563
Los Alamos, NM 87545
(505) 667-6250

Frank Rainer
Lawerence Livermore
National Laboratory
P. O. Box 5508, L-490
Livermore, CA 94550
(415) 423-4376

Tilak Raj
Martin Marietta Denver Aerospace
P.O. Box 9316
International Airport
Albuquerque, NM 87119
(505) 844-1064

David Reicher
Univ. of New Mexico
4120 Mesa Verde N.E. #B
Albuquerque, NM 87110
(505) 265-6364

Steven J. Salazar
Los Alamos Nat'l Laboratory
P.O. Box 1663
CLS-6, MS J564
Los Alamos, NM 87545
(505) 667-7148

Aaron Sanders
724.02
National Bureau of Standards
325 Broadway
Boulder, CO 80303
(303) 497-5341

Virgil E. Sanders
Los Alamos Nat'l Laboratory
MS J564
P.O. Box 1663
Los Alamos, NM 87545
(505) 667-0041

Paul Schall, Jr.
JAYCOR
2811 Wilshire Blvd.
Suite 690
Santa Monica, CA 90403
(213) 829-0584

Ansgar Schmid
Laboratory of Laser Energetics
University of Rochester
250 East River Rd.
Rochester, NY 14623
(716)275-5764

Dr. Arnulf Schultz
URANIT
D-5170 Juelich
Germany
(02461)-65350

Marion L. Scott
Los Alamos Nat'l Laboratory
P.O. Box 1663, MS E549
Albuquerque, NM 87545
(505) 667-7557

Steven C. Seitel
Montana Laser Optics, Inc.
P.O. Box 4151
Bozeman, MT 559772-4151
(406) 586-5100

Xiao-An Shen
Washington State Univ.
Physics Department
Pullman, WA 99164-2814
(509) 335-8613

Mary F. Singleton
Lawrence Livermore National Lab
P.O. Box 5508, L-490
Livermore, CA 94550
(415) 422-6649

James G. Sliney, Jr.
Rockwell International
Rocketdyne Division
MS-FA 03
6633 Canoga Ave.
Canoga Park, CA 91304
((818) 700-4900

Andrew M. Smith
AWE (Aldermaston)
Aldermaston, Reading, Berks.
England

Freddie W. Smith
Ktech Corporation
901 Pennsylvania, N.E.
Albuquerque, NM 87110
(505) 268-3379

M. J. Soileau
University of Central Florida
P.O. Box 25000
Orlando, FL 32816-0115

Alan F. Stewart
Air Force Weapons Lab.
AFWL/ARBD
Kirtland AFB, NM 87117-6008
(505) 844-7368

W. Kent Stowell
USAF
AFWL/ARBD
Kirtland AFB, NM
(505) 844-1776

Randall T. Swimm
U.S.C., Center for Laser Studies
University Park, DRB 17
Los Angeles, CA 90089-1112
(213) 743-4370

Eric B. Szarmes
Stanford Photon Res. Lab
Stanford University
Stanford, CA 94022
(415) 725-6708

Michael Tarasevich
Singer Co.
1225 McBride Ave.
MS/ 3B55
Little Falls, NJ 07470
(201) 785-2623

John R. Taylor
Lawrence Livermore Nat'l Lab
P.O. Box 808, L-462
Livermore, CA 94550
(415) 423-4438

Ian Thomas
Lawrence Livermore Nat'l Lab
P.O. Box 5808, L-483
Livermaore, CA 94550
(415) 423-3896

James H. Tillotson
Northrop Corporation
2301 W. 120th Street
Hawthorne, CA 90251-5032
(213) 600-3874

Marion N. Todd
Talandic Res. Corp.
2793 East Foothill Blvd.
Pasadena, CA 91107
(818) 793-4161

Michael J. Treadaway
JAYCOR
P.O. Box 85154
San Diego, CA 92138
(619) 453-6580

Tom Turner
Los Alamos Nat'l Lab
Mail Stop J564
P.O. Box 1663
Los Alamos, NM 87545
(505) 667-7102

Trudy Tuttle Hart
Optical Coating Laboratory, Inc.
2789 Northpoint Parkway
Santa Rosa, CA 95407-7397
(707) 525-7192

Marc Von Gunten
Spectra-Physics, Inc.
Optics Division
1250 West Middlefield Rd.
Mountain View, CA 94043-3196
(415) 961-2550 Ext 3008

E. W. Waddell
Pilkington Defence Systems
Barr & Stroud
Caxton Street, Anniesland
Glasgow
SCOTLAND G13 1HZ

Carlton Walker
Arthur D. Little Inc.
Acorn Park
Cambridge, MA 01742
(617) 864-5770

Dr. Alan J. Watts
Ktech Corporation
901 Pennsylvania N.E.
Albuquerque, NM 87110
(505) 268-3379

Carolyn Weinzapfel
Lawrence Livermore Nat'l Lab.
P.O. Box 5508, L-491
Livermore, CA 94550
(415) 423-3987

Major John J. Wharton
DARPA
1400 Wilson Blvd.
Arlington, VA 22039
(202) 694-3783

Patty White
W.J. Schafer, Assoc.
2000 Randolph Dr. #205
Albuquerque, NM 87107
(505) 242-9992

Keith Wier
Scientech Inc.
5649 Arapahoe
Boulder, CO 80303
(303) 444-1361

John G. Wilder
Lawrence Livermore National Lab
P.O. Box 5508, L-483
Livermore, CA 94550
(415) 423-3896

Gregg Wilensky
R & D Associates
P.O. Box 9695
Marina del Rey, CA 90295
(213) 822-1715 Ext.369

Forrest L. Williams
Univ. of New Mexico
Center for High Technology
Materials
Albuquerque, NM 87131

G. Richard Wirtenson
Lawrence Livermore Nat'l Lab
P.O. Box 5508, L-491
Livermore, CA 94550
(415) 422-1332

Jurgen Wisotzki
Talandic Res. Corp.
2703 East Foothill Blvd.
Pasadena, CA 91107
(818) 793-4161

Charles V. Woerner
NASA
Langley Research Center
Mail Stop 356
Hampton, VA 23665
(804) 865-2303

Mikio Yamashita
Mitsubishi Electric Corp.
8-1-1 Tsukaguchi Honmachi
Amagasaki City, Hyogo Pref.
JAPAN
(06) 491-8021

A. Yokotoni
Osaka University
Institute of Laser Engineering
2-6 Yamada-oka
Suita Osaka 565
JAPAN

Kunio Yoshida
Institute of Laser Engineering
Osaka University
2-6 Yamada-oka
Suita Osaka, 565
JAPAN
(06) 877-5111 Ext. 6561

Richard Zoborowski
OCLI
2789 Northpoint Parkway
Dept. 428-1
Santa Rosa, CA 95407-7397
(707) 525-7709

NBS-114A (REV. 2-8C)

U.S. DEPT. OF COMM. BIBLIOGRAPHIC DATA SHEET (See instructions)	1. PUBLICATION OR REPORT NO. NIST/SP-756	2. Performing Organ. Report No.	3. Publication Date October 1988

4. TITLE AND SUBTITLE

Laser Induced Damage in Optical Materials: 1987

5. AUTHOR(S) Harold E. Bennett (NWC), Arthur H. Guenther (AFWL) David Milam (LLNL), Brian E. Newnam (LLNL), and M. J. Soileau (UCF)

6. PERFORMING ORGANIZATION (If joint or other than NBS, see instructions)
National Institute of Standards and Technology
~~NATIONAL BUREAU OF STANDARDS~~
DEPARTMENT OF COMMERCE
WASHINGTON, D.C. 20234

7. Contract/Grant No.

8. Type of Report & Period Covered
Final

9. SPONSORING ORGANIZATION NAME AND COMPLETE ADDRESS (Street, City, State, ZIP)
Nat'l Institute of Standards and Technology (NIST)
American Society for Testing and Materials (ASTM)
Office of Naval Research (ONR)
Department of Energy (DOE)
Defense Advanced Research Project Agency (DARPA)
Air Force Office of Scientific Research (AFOSR)

10. SUPPLEMENTARY NOTES

Library of Congress Catalog Card Number: 88-600576

☐ Document describes a computer program; SF-185, FIPS Software Summary, is attached.

11. ABSTRACT (A 200-word or less factual summary of most significant information. If document includes a significant bibliography or literature survey, mention it here)

The Nineteenth Annual Symposium on Optical Materials for High-Power Lasers (Boulder Damage Symposium) was held at the National Institute of Standards and Technology in Boulder, Colorado, October 26-28, 1987. The Symposium was held under the auspices of ASTM Committee F-1, Subcommittee on Laser Standards, with the joint sponsorship of NIST, the Defense Adavanced Research Project Agency, the Department of Energy, the Office of Naval Research, and the Air Force Office of Scientific Research. Over 190 scientists attended the Symposium, including representatives of the United Kingdom, France, Japan, India, Canada, and the Federal Republic of Germany. The Symposium was divided into sessions concerning Materials and Measurements, Mirrors and Surfaces, Thin Films, and, finally, Fundamental Mechanisms. As in previous years, the emphasis of the papers presented at the Symposium was directed toward new frontiers and new developments. Particular emphasis was given to materials for high power systems. The wavelength range of prime interest was from 10.6 μm to the uv region. Highlights included surface characterization, thin film substrate boundaries, and advances in fundamental laser-matter threshold interactions and mechanisms. The scaling of damage thresholds with pulse duration, focal area, and wavelength was discussed in detail. Harold E. Bennett of the Naval Weapons Center, Arthur H. Guenther of the Air Force Weapons Laboratory, David Milam of the Lawrence Livermore National Laboratory, Brian E. Newnam of the Los Alamos National Laboratory and M. J. Soileau of the University of Central Florida were co-chairmen of the Symposium. The Tewntieth Annual Symposium is scheduled for October 26-28, 1988, at the National Institute of Standards and Technology, Boulder, Colorado.

12. KEY WORDS (Six to twelve entries; alphabetical order; capitalize only proper names; and separate key words by semicolons)

laser damage; laser interaction; optical components; optical fabrication; optical materials and properties; thin film coatings.

13. AVAILABILITY

☐ Unlimited
☐ For Official Distribution. Do Not Release to NTIS
☒ Order From Superintendent of Documents, U.S. Government Printing Office, Washington, D.C. 20402.
☐ Order From National Technical Information Service (NTIS), Springfield, VA. 22161

14. NO. OF PRINTED PAGES
650

15. Price

USCOMM-DC 6043-P80

☆U.S. GOVERNMENT PRINTING OFFICE: 1989-675-330/5071

NIST Technical Publications

Periodical

Journal of Research of the National Institute of Standards and Technology—Reports NIST research and development in those disciplines of the physical and engineering sciences in which the Institute is active. These include physics, chemistry, engineering, mathematics, and computer sciences. Papers cover a broad range of subjects, with major emphasis on measurement methodology and the basic technology underlying standardization. Also included from time to time are survey articles on topics closely related to the Institute's technical and scientific programs. Issued six times a year.

Nonperiodicals

Monographs—Major contributions to the technical literature on various subjects related to the Institute's scientific and technical activities.

Handbooks—Recommended codes of engineering and industrial practice (including safety codes) developed in cooperation with interested industries, professional organizations, and regulatory bodies.

Special Publications—Include proceedings of conferences sponsored by NIST, NIST annual reports, and other special publications appropriate to this grouping such as wall charts, pocket cards, and bibliographies.

Applied Mathematics Series—Mathematical tables, manuals, and studies of special interest to physicists, engineers, chemists, biologists, mathematicians, computer programmers, and others engaged in scientific and technical work.

National Standard Reference Data Series—Provides quantitative data on the physical and chemical properties of materials, compiled from the world's literature and critically evaluated. Developed under a worldwide program coordinated by NIST under the authority of the National Standard Data Act (Public Law 90-396). NOTE: The Journal of Physical and Chemical Reference Data (JPCRD) is published quarterly for NIST by the American Chemical Society (ACS) and the American Institute of Physics (AIP). Subscriptions, reprints, and supplements are available from ACS, 1155 Sixteenth St., NW., Washington, DC 20056.

Building Science Series—Disseminates technical information developed at the Institute on building materials, components, systems, and whole structures. The series presents research results, test methods, and performance criteria related to the structural and environmental functions and the durability and safety characteristics of building elements and systems.

Technical Notes—Studies or reports which are complete in themselves but restrictive in their treatment of a subject. Analogous to monographs but not so comprehensive in scope or definitive in treatment of the subject area. Often serve as a vehicle for final reports of work performed at NIST under the sponsorship of other government agencies.

Voluntary Product Standards—Developed under procedures published by the Department of Commerce in Part 10, Title 15, of the Code of Federal Regulations. The standards establish nationally recognized requirements for products, and provide all concerned interests with a basis for common understanding of the characteristics of the products. NIST administers this program as a supplement to the activities of the private sector standardizing organizations.

Consumer Information Series—Practical information, based on NIST research and experience, covering areas of interest to the consumer. Easily understandable language and illustrations provide useful background knowledge for shopping in today's technological marketplace.

Order the **above** *NIST publications from: Superintendent of Documents, Government Printing Office, Washington, DC 20402.*

Order the **following** *NIST publications—FIPS and NISTIRs—from the National Technical Information Service, Springfield, VA 22161.*

Federal Information Processing Standards Publications (FIPS PUB)—Publications in this series collectively constitute the Federal Information Processing Standards Register. The Register serves as the official source of information in the Federal Government regarding standards issued by NIST pursuant to the Federal Property and Administrative Services Act of 1949 as amended, Public Law 89-306 (79 Stat. 1127), and as implemented by Executive Order 11717 (38 FR 12315, dated May 11, 1973) and Part 6 of Title 15 CFR (Code of Federal Regulations).

NIST Interagency Reports (NISTIR)—A special series of interim or final reports on work performed by NIST for outside sponsors (both government and non-government). In general, initial distribution is handled by the sponsor; public distribution is by the National Technical Information Service, Springfield, VA 22161, in paper copy or microfiche form.

U.S. Department of Commerce
National Institute of Standards and Technology
(formerly National Bureau of Standards)
Gaithersburg, MD 20899